20th AOCMP
18th SEACOMP
120th JSMP
12th TMPS

AOCMP SEACOMP JSMP TMPS

3-5 December 2020
Phuket, Thailand

20th Asia-Oceania Congress on Medical Physics (AOCMP)
18th South-East Asia Congress of Medical Physics (SEACOMP)
120th Scientific Meeting of Japan Society of Medical Physics (JSMP)
12th Annual Meeting of Thai Medical Physicist Society (TMPS)

PROCEEDINGS

20th AOCMP
18th SEACOMP
120th JSMP
12th TMPS

AOCMP SEACOMP JSMP TMPS

3-5 December 2020
Phuket, Thailand

20th Asia-Oceania Congress on Medical Physics (AOCMP)
18th South-East Asia Congress of Medical Physics (SEACOMP)
120th Scientific Meeting of Japan Society of Medical Physics (JSMP)
12th Annual Meeting of Thai Medical Physicist Society (TMPS)

PROCEEDINGS

Organizing Committee

President	Anchali Krisanachinda
Vice President, Treasurer	Tanawat Sontrapornpol
Scientific	Puangpen Tangboonduangjit Chirapha Tannanonta Chumpot Kakanaporn Sawwanee Asavaphatiboon Napapong Pongnapang Nauljun Stansook Suphaluck Khajonkom
Registration	Paranee Sahachjesdakul Lakkana Apipanyasopon
Commercial Exhibitor	Sivalee Suriyapee Panya Pasawang Petcharleeya Suwanpradit
Social and Audiovisual	Kitiwat Khamwan
Social and Transportation	Amporn Funsian
International Cooperation	Thitithip Tippayamontri
Webmaster	Tawatchai Chaiwatanarat
Secretary General and Audiovisual	Taweap Sanghangthum

Organizing and Endorsing Professional Bodies

Thai Medical Physicists Society (TMPS)

President	Anchali Krisanachinda
Vice President	Tanawat Sontrapornpol
Secretary General	Taweap Sanghangthum
Treasurer	Tanawat Sontrapornpol

Japan Society of Medical Physics (120th Congress JSMP)

President	Shigekazu Fukuda
Executive Committee	Naoki Hayashi
Program Committee	Shuichi Ozawa

Asia Oceania Federation of Organizations for Medical Physics (AFOMP)

President	Arun Chougule
Vice President	Eva Bezak
Secretary General	Anupama Azhari
Treasurer	Kwan Hoong Ng
Chairman Scientific Committee	Tomas Kron

South East Asian Federation of Organizations for Medical Physics (SEAFOMP)

President	Freddy Haryanto
Vice President	Chai Hong Yeong
Secretary General	Supriyanto Pawiro
Treasurer	Taweap Sanghangthum

International Organization of Medical Physics (IOMP)

President	Madan Rehani
Vice President	John Damilakis
Secretary General	Eva Bezak
Treasurer	Ibrahim Duhaini

Greetings from President AFOMP

I am delighted to note that the 20th Asia-Oceania Congress on Medical Physics (AOCMP), the 18th South-East Asia Congress of Medical Physics (SEACOMP), 120th Scientific Meeting of Japan Society of Medical Physics (JSMP) and the 12th Annual Meeting of Thai Medical Physicist Society (TMPS) are jointly organized at Phuket, Thailand during 3rd to 5th December 2020. The theme of the conference is 'Medical Physics- Achievements, Challenges and Horizons'. Many congratulations to the organizing team especially Prof Anchali Krisanachinda for making it happen despite the unprecedented pandemic situation worldwide.

This congress is unique as it's the 20th anniversary of AFOMP and four very active medical physics associations of Asia-Oceania are joined together in organizing this mega scientific event. It is heartening to note that the 1st AOCMP was held in Thailand and afterwards 9th, 12th and 16th AOCMP's were also hosted by Thailand. It's the 5th time AOCMP is being held in Thailand marking the 20th Anniversary of AFOMP celebrating it in a big way associating with SEACOMP, JSMP and TMPS which shows the acumen of Prof Anchali and team and the great hospitality of Thailand.

AFOMP has started many activities to encourage professional and academic excellence. Prof Kiyonari Inamura Memorial AFOMP Oration awarded for 2020 is awarded to Prof K Y Cheung of Hong Kong, AFOMP lifetime achievement award 2020 to Prof Anchali Krisanachinda, Thailand and Prof Donald McLean, Australia and to celebrate the 20th anniversary, AFOMP is honouring 21 medical physicists with AFOMP outstanding medical physicist award. In addition to encourage publication of scientific papers in AFOMP journals, best paper published award is also started by AFOMP.

Education and training is the key to accelerated professional achievements. As healthcare professionals, education cannot wait or stop for the pandemic. Despite all the hurdles, the organizers have done tremendous efforts to materialize this conference a reality though the dates were postponed and this shows the resolute determination of the organizers. I would like to thank JSMP also for being a partner. The organizers have arranged virtual as well as face to face opportunity this time so that everyone may get benefitted.

Let me also urge the participants of this conference not only be confined with the challenges at their own field of specialization but take it as a moral responsibility to be proactive and enthusiastic in learning about the contemporary cutting edge tools in all aspects of physics in medicine. This pandemic was an eye opener for all of us to realize the necessity of being proactive to be successful in the changing world.

Wishing you all, a pleasant and fruitful conference and continued success in all your professional endeavours. I am sure this will be an academic feast satisfying the diverse interests of all participants giving novel ideas and new insights. Wish you all a very fruitful attending of the conference and pleasant stay in Phuket.

Arun Chougule

Prof Arun Chougule
President- AFOMP
Chair- ETC and accreditation board, IOMP
Senior Professor and Head, Dept of Radiological Physics
SMS Medical College and Hospitals
Jaipur, INDIA

Welcome Message from President of SEAFOMP

Dear colleagues and friends,

On Behalf of the President of South East Asian Federation of Organizations for Medical Physics (SEAFOMP), allow me to warmly thank the organizers of this Joint Conference among the AFOMP, SEAFOMP, JSMP, and TMPS for giving me the privilege of welcoming and addressing you all. For me, it is an honor and a pleasure.

I would also like to thank Prof. Anchali and her team for bringing us together on the first hybrid Conference for our society. Due to Covid-19 Pandemic, we could not meet all to gather in wonderful and beautiful Phuket Island, Thailand, to discuss the achievements, challenges, and horizons in our medical physics word.

The Conference, composed of 3 parallel sessions, tackles important topics on medical physics. There are also mini-symposium and workshops. I am sure that each of you will identify subjects of his/her interest and benefit from many fruitful and enriching discussions.

I am incredibly happy to be virtually present in this unique event today and to exchange views and share experiences with colleagues and friends. For the participants who come to Phuket Island, please to have time also for exploring the island.

I congratulate you on your commitment and active participation and wish you all the success.

Thank you,

Freddy Haryanto

President SEAFOMP

Welcome Message From President of JSMP

It is a great pleasure for me to hold the 120th Scientific Meeting of Japan Society of Medical Physics jointly with 20th Asia-Oceania Congress on Medical Physics, 18th South-East Asia Congress of Medical Physics, and 12th Annual Meeting of Thai Medical Physicist Society.

First of all, I would like to thank Dr. Anchali Krisanachinda, the mother of medical physics of Thailand, and also Dr. Arun Chougule, President of AFOMP. Despite the uncertain and difficult situation of the impact of COVID-19, they have committed very hard to the holding of this conference, which resulted in the successful opening today.

The recent environmental conditions surrounding radiotherapy, radiodiagnosis, and nuclear medicine have changed significantly due to the popularization of advanced radiotherapy such as IGRT and particle therapy, the introduction of AI, the fusion of diagnosis and therapy and so on. The education and training for these advanced technique in medical physics are becoming increasingly important. However, the environment for education and training for them is still insufficient in Asian region. So JSMP wants to contribute to improving this environmental situation in the Asian region with our resources and experiences through the international collaboration.

Although the COVID-19 pandemic is a disaster, if we think positively, due to this situation, we are able to hold the JSMP scientific meeting jointly with the AOCMP, SEACOMP, and TMPS scientific meeting. This JSMP scientific meeting is held overseas for the first time except Japan-Korea Joint Meeting of Medical Physics, which is held once every three years. So, I'd like to regard this opportunity as an important steppingstone to make an international contribution to the development of medical physics in the Asian region.

I hope this conference will be a successful and fruitful to all participants. Thank you.

Shigekazu Fukuda

Shigekazu Fukuda, Ph. D
President of the 120th Scientific Meeting of Japan Society of Medical Physics,
President of JSMP

TMPS President Message

In the name of Thai Medical Physicist Society, I am pleased to welcome you to the 20th Asia Oceania Congress on Medical Physics, the 18th South-East Asian Congress of Medical Physics, the 120th Scientific Meeting of Japan Society of Medical Physics and the 12th Annual Meeting of Thai Medical Physicist Society. This Congress had been endorsed by the International Organization on Medical Physics.

This is the fifth time Thailand has hosted the Congress for AFOMP:

First: 2001 Royal Jubilee 50th year Coronation Medical Society Building Petchaburi Road, Bangkok
Second: 2009 Pang Suan Kaew Convention Hall, Chiang Mai
Third: 2012 Kum Poo Come Chiang Mai
Fourth: 2016 ICMP at Shangari La Hotel Bangkok
Fifth: 2020 Duangjitt Resort and Spa Phuket

This is the first time to host the Congress for Japan Society of Medical Physics especially on the 120th. It is genuinely our great honor to host on hybrid at virtual and in person. Hopefully, we can co-host the annual Scientific Meeting for JSMP again in the future.

We plan to celebrate the 20th Anniversary for AFOMP at the Gala Dinner on December 3rd, 2020, Thai and seafood are arranging on Phuket style.

Scientific program had been arranged as following: John Cameron Memorial Lecture, Professor Kiyonari Inamura Oration Lecture, JSMP Honor Lecture, Proton Therapy Mini Symposium, JSRT Mini Symposium, 49 Invited Lectures, 6 Mini Symposia, 121 Oral and 54 e-poster presentations. The Convention Hall consists of 2 Grand Lecture Rooms for Radiotherapy and one Commercial Exhibition room. Outside the Convention Hall there are 3 rooms for Medical Imaging - Diagnostic Radiology and Nuclear Medicine for Oral and e Poster presentations. Beverages and lunch are arranged during the Congress.

Certification for Clinically Qualified Medical Physicists is arranged at the Gala Dinner, including TMPS Outstanding Medical Physicists, AFOMP and TMPS Awards.

Please enjoy your time at the Congress in Phuket for In Person and Virtual participations.

Anchali Krisanachinda, Ph.D.
Chair, 20th AOCMP, 18th SEACOMP, 120th JSMP, 12th TMPS

Contents

Organizing Committee ... 1
Organizing and Endorsing Professional Bodies ... 2
Greetings from President AFOMP ... 3
Welcome Message from President of SEAFOMP ... 4
Welcome Message From President of JSMP ... 5
TMPS President Message ... 6
Contents ... 7
Floor Plan ... 16
Program at a glance
3 December 2020 ... 17
4 December 2020 ... 18
5 December2020 ... 19
Program in detail
3 December 2020 ... 20
Room: Duangchanok Convention 1-2 ... 20
Room: Duangchanok, Radiotherapy ... 21
Room: Duangkaew, Diagnostic ... 21
Room: Duangmanee, Nuclear Medicine ... 21
4 December 2020 ... 22
Room: Duangchanok, Radiotherapy ... 22
Room: Duangkaew, Diagnostic ... 22
Room: Duangmanee, Nuclear Medicine ... 22
Room: Duangchanok Convention 1-2 ... 22
Room: Duangchanok ... 22
Room: Duangkaew ... 22
Proffered Papers in Radiotherapy (Face-to-face) ... 23
Room: Duangchanok ... 23
Proffered Papers in Radiotherapy (Virtual) ... 25
Room: Duangthip ... 25
Proffered Papers in Nuclear Medicine, Diagnostic, Radiotherapy (Face-to-face) ... 27
Room: Duangkeaw ... 27
Nuclear Medicine ... 27
Diagnostic ... 27
Radiotherapy ... 28
Proffered Papers in Diagnostic, Nuclear Medicine, Radiotherapy (Virtual) ... 29
Room: Duangmanee ... 29
Diagnostic ... 29
Nuclear Medicine ... 30
Radiotherapy ... 30
5 December 2020 ... 31
Room: Duangchanok ... 31
Room: Duangkaew ... 31
Room: Duangmanee ... 32
Room: Duangmanee ... 32
Room: Duangchanok Convention 1-2 ... 32
E-Posters ... 33
Radiotherapy ... 33
Diagnostic ... 34
Nuclear Medicine ... 36

Abstract

Invited Presentations
JOHN CAMERON MEMORIAL LECTURE: New Additions to the Scientific Dictionary and Encyclopaedia on Medical Physics ... 39
Professor Kiyonari Inamura Memorial AFOMP Oration 2020 ... 40

JSMP INVITED LECTURE: Evaluation of ionising radiation induced DNA damage on a cell and prediction of biological response by integrated track structure Monte Carlo simulations using Geant4-DNA 41
Impact of radiosensitivity and gender on paediatric cranial tumours following proton and photon intensity modulated radiation therapy – A radiobiological response modelling study 43
Comparisons of DNA damage in HPV negative and positive head and neck cancer cell lines following fractionated irradiation 44
MS 1: Proton Therapy in Hong Kong 45
MS 2: JSRT Clinical application of the latest radiation technology – CT 46
MS 2: JSRT Clinical application of the latest radiation technology in Magnetic Resonance Imaging 47
MS 2: JSRT Clinical application of the latest radiation technology in Nuclear Medicine 48
IAEA Activities in Support of Recognition of the Medical Physics Profession 49
South Asia Centre for Medical Physics and Cancer Research (SCMPCR): A Centre of Excellence to Fight against Cancer in South Asia Region 50
Radiation incidents and accidents in radiotherapy 51
National Diagnostic Reference Level (NDRLs) of Procedures in Cardiac Catheterization Laboratory in Thailand: A Multi Center Survey 52
Outline of updated national diagnostic reference levels in Japan (Japan DRLs 2020) 53
National DRLs in Thailand 54
Dose monitoring and audit, tools for patient dose optimization 55
Clinical Aspects for Theranostics in the Era of Precision Medicine 56
Interesting Radiation Protection Issues in Theranostic Radiopharmaceutical; Workers, Caregivers, Members of the Public and Waste Management 57
How to make a research plan for young investigators 58
e-Learning in Medical Physics: Building Educational Modules with Moodle VLE 59
Role of Radiation and Caution in the Management of Covid-19 60
AFOMP Medical Physics Education and Clinical Training 61
Postgraduate medical physics programmes in Asia Pacific countries - A survey study 62
Imaging-based Biomarkers 63
Teaching Linear Accelerator Physics using a Web Based Simulator 64
Automating Plan Checking Tasks by Scripting 65
Principle and Application of MR-Linac 66
Extreme hypofractionated radiotherapy – Radiobiology and radiobiological models 67
High patient radiation doses from recurrent CT exams 68
Patients who receive high radiation doses in a single day 69
Challenges in CT with photon counting detectors 70
Physicists and Clinical Trials: Support and Evidence for New Technology and Techniques 71
Novel technologies for advanced radiomics for clinical practices 72
Consideration of stochastic risks in interventional procedures 73
MS 5: Eye Lens Dose Measurements of Medical Staffs in Thailand 74
Rapid estimation of muscle transverse relaxation time (T_2) based on ultrafast magnetic resonance imaging at 3.0 Tesla 75
Optimization of Cone Beam Breast CT – Radiation Dose and Image Quality 76
The Establishment of UNSCEAR Report in Thailand 77
MS 6: Facility design of a PETCT 78
MS 6: Facility design of a cyclotron 79
MS 6: Radiation Emergency Preparedness in Nuclear Medicine 80
Theranostics in Nuclear Medicine 81
Preparation and Application of Ga-68 in Nuclear Medicine 82
Radiomics in Radiation Oncology 83
Patient specific quality assurance by log file-based software: a multi-institutional study in Thailand 84

Oral Presentations

Radiotherapy: Dosimetry 85
Parametric impact study of interplay effects in 6 MV flattening filter free (FFF) of photon beams 86
Development and dosimetric verification of 3D customized bolus in radiotherapy 87
Tuning effective spot size parameter in Acuros XB algorithm for Edge™ radiosurgery machine 88
Investigation of field output correction factors in small elongated fields for 6 MV photon beam 89

Comparison of field output factors of different detectors in small field for 6 MV flattening filter and flattening filter free photon beams 90
Evaluation of detectors on relative dosimetric measurement for CyberKnife M6 System 91
Surface and Build Up Doses Comparison between Analytical Anisotropic Algorithm and Acuros XB for Various Treatment Parameters 92
Determination of small field output factors and specific correction factors for various diodes and microDiamond detector for CyberKnife M6 system equipped with fixed collimator 93
Efficiency of EPID dosimetry based software compared with ion chamber 94
An update on local blood irradiation technique using medical LINAC: Blood Irradiation Kit 95
Radiotherapy: Monte Carlo Simulation 96
Determination of fetal dose and health effect to the fetus from breast cancer radiotherapy during pregnancy 97
Calculation of field output correction factors for radiophotoluminescence glass dosimeter in 6 MV WFF and FFF small photon beams using Monte Carlo simulation 98
Investigation of dose perturbations around brachytherapy seeds in high-energy photon beams 99
Monte Carlo Simulation of semiflex chamber in Megavoltage Photon Beam 100
Estimation of Linear and Mass Attenuation Coefficients of Soy-lignin Bonded Rhizophora spp. Particleboard as a Potential Phantom Material for Low- and High-energy Studies using Monte Carlo Simulation 101
Comparison simulation treatment between Gamma Knife and Linac Stereoradiosugery on small target volume by using GEANT 4 Monte Carlo Simulation 102
Monte Carlo calculation of beam quality correction factors in proton beams using PTSIM/GEANT4 103
VDOSE: A tools to analyze dose distribution from Monte Carlo dose Calculation 104
Radiotherapy: Radiobiology 105
Low-dose radiation enhance cytotoxicity of chemotherapeutic agent (pirarubicin) in K562 and K562/adr leukemic cancer cells 106
Radioprotective effect of interruptin derived from Cyclosorus terminans could protect cell damage of irradiated normal cells from radiotherapy 107
Temperature variation of stimulated diabetic blood and its effects on Evaluated specific absorption rate (SAR) when used a 532 nm wavelength laser for therapeutics 108
The Effect of Different Sizes of Bismuth Oxide Nanorods on Radiosensitization Enhancement Ratio 109
The Effect of Different Sizes of Bismuth Oxide Nanorods on Cancer Cells 110
Influence of PEG-coated Bismuth Oxide Nanoparticles on ROS Generation for Electron Beam Radiotherapy 111
Radiotherapy: Treatment planning 112
Dosimetric Validation of Monaco Treatment Planning System 113
Evaluation of dose calculation algorithm accuracy in Eclipse treatment planning system for jaw-defined and MLC-defined small fields 114
The quality improvement of dose escalation plan of prostate cancer using an integration of biological parameters for optimization and evaluation 115
Treatment planning evaluation of 3D-printed Anthropomorphic Head Phantom 116
Comparison of different treatment planning techniques for left-sided breast cancer: A dosimetric study 117
Investigation of the optimal cost function for pelvic CT-MR deformable image registration 118
Dosimetric comparison between 3D and IMRT treatment techniques for whole breast radiotherapy 119
Radiotherapy: Big data, Deep learning, AI and Modeling 120
Development of automated prostate VMAT treatment planning system using deep learning-based predictive dose distribution 121
Automated fast data collection and organization for medical artificial intelligence 122
A feasibility study of kVCBCT-based radiomics for radiological complication prediction 123
Evaluation of machine learning-based prediction model for radiation pneumonitis in NSCLC patients 124
Impact of image type and deep learning architecture in deep learning radiomics on the accuracy of lung cancer prediction 125
Prognostic analysis of CT-based radiomics focusing on a subgroup of NSCLC patients 126
Radiotherapy: Patient-specific QA 127
Preliminary evaluation of the performance of an EPID-based in vivo dosimetry for advanced radiotherapy treatment verification 128
Patient-specific quality assurance for IMRT delivery: A multi-centre study 129

Pilot study of remote clinical dosimetry auditing for IMRT using virtual EPID standard phantom audit (VESPA) in Thailand 130
Evaluation of Mobius and Portal dosimetry Quality Assurance tools for volumetric modulated arc therapy plans 131
Effect of plan complexity to gantry angle uncertainty for VMAT delivery 132
Development of novel x-ray-opaque-marker system for improvement and quantification of phantom positioning accuracy in patient-specific quality assurance 133
Radiotherapy: Particle beam therapy 134
Dosimetric validation of the commercial dose calculation algorithm for carbon ion therapy in a heterogeneous phantom 135
Simulation of the efficiency of rescanning with respiratory gating technique in pencil beam scanning proton therapy for lung cancer 136
Dosimetric comparison of normal liver sparing in hepatocellular carcinoma between intensity modulated proton therapy and volumetric modulated arc therapy 137
Development of Ultra-fast Irradiation for Proton Therapy 138
Radiotherapy: IGRT 139
Tolerance level determination for automated EPID-based deep inspiration breath-hold (DIBH) instability evaluation in breast cancer patients 140
A simulation study of fractional image guidance protocol contributing to the dosimetric accuracy of patients treated on Halcyon system 141
Localization accuracy of off-isocenter multi-target brain stereotactic radiosurgery using SyncTraX FX4. 142
Evaluation of tumor delineation accuracy in denoised contrast enhancement four-dimension CT using deformable image registration method 143
Radiotherapy: Radiation Safety / DRL 144
Acceptance Test and Commissioning of Tomotherapy Radixact X5 series in LBCH 145
The preliminary survey report of the compact proton therapy unit 146
Mitigation of Error Propagation in Tele-cobalt Treatment: An Institutional Assessment 147
Evaluation of radionuclides and activation detected by a 15 MeV medical linear accelerator 148
Radiotherapy: Others 149
Dosimetric comparison of manual and library applicator reconstruction in MRI image-based for gynecological brachytherapy 150
Verification of Treatment Time in Interstitial Brachytherapy using Paris System 151
Dosimetric evaluation of the uncorrectable rotational setup error in total body irradiation using helical tomotherapy system 152
Investigating the effect of material absorber the source of Gamma Knife PerfexionTM based on Monte Carlo simulations 153
Development of an In-house MATLAB code for dynamic multileaf collimator quality assurance based on EPID 154
Dosimetric evaluation of photon beam-matching for two similar linear accelerators 155
Assessment of Radiation Protection and Radiation Safety Awareness among Radiation Professionals in a Tertiary Care Teaching Hospital 156
Design of universal 3D-printed oral stent for head and neck radiotherapy 157
Fabrication and validation of cubic phantom embed with an accelerometer sensor for verifying six-degrees-of-freedom couch 158
Daily machine-specific performance monitoring through clinical treatment delivery using Statistical Process Control and MobiusFX 159
Establishment of MOH Medical Physics Research Task Force 160
CT Density Profile and Physicochemical Study of Soy-Lignin Bonded Rhizophora spp. Particleboard as Phantom Material in Medical Physics Application 161
Dignostic: Imaging 162
Correlation of Ultrasound Attenuation Imaging versus MRI Proton Density Fat Fraction in Non-alcoholic Fatty Liver 163
Sonographic predictors for developing cholangiocarcinoma: A cohort study from an endemic area. 164
Value of Superb Microvascular Imaging (SMI) in characterize of nodular type focal fat sparing lesion and true hepatic nodules in the background of fatty liver 165
Predicting Treatment Response in Nasopharyngeal Cancer Using Radiomics: A Preliminary Study 166
Performance of quantitative lesion measurement in hepatic dual-energy computed tomography (DECT): Phantom study 167

Automatic QC Analysis Program in Digital Radiography System 168
Correlation between renal histological fibrosis and renal cortical thickness using shear wave elastography in patients with kidney disease 169
Automatic stratification of prostate cancer patients into low- and high-grade groups based on multiparametric MR image feature analysis 170
Image analysis of pancreatic cancer tissues using Haralick Features 171
Digital Breast Tomosynthesis (DBT): Dose and image quality assessment of man-made breast phantom 172
Grey Matter Segmentation of T1-Weighted MR Image in Ischemic Stroke Patients using k-Means Clustering 173
Diagnostic: Big data, Deep learning, AI and Modeling 174
The effective methods for liver cyst labelling in ultrasound images by using R-CNN 175
Quantitative Assessment of Breast Density Using Pixel Intensity Threshold 176
Overall Survival Prediction of Nasopharyngeal Carcinoma using Radiomics 177
Machine Learning model for Alzheimer's disease prediction and classification using T1-weighted MR Brain imaging based on SVM algorithm 178
The Breast Microcalcification Detection in Mammogram Image by Using the Deep Convolutional Neural Network 179
Prediction of Tumor Growth Trajectories During Molecularly Targeted Therapy Based on Mathematical Models 180
Quantitative evaluation of deep convolutional neural network based denoising for ultra-low-dose CT 181
A Preliminary Study of Various Augmentation Techniques on Deep-learning Based Classification of Lung Squamous Cell Carcinoma using Chest X-Ray 182
A Computational Study on Deep-learning Based Classification of Lung Adenocarcinoma using Chest X-Ray 183
Dignostic: Dosimetry 184
Patient-specific organ dose calculated using dose tracking software based on Monte Carlo simulation in pediatric abdominal CT 185
Size-Specific Dose Estimates (SSDE) for Head CT in Pediatric Patients 186
Preliminary investigation on performance of photodiode sensor as a dosimeter 187
Evaluation of scattering spectra from an examinee during in CT scans 188
Diagnostic: Radiation Safety / DRL 189
The Study of Local Diagnostic Reference Levels at Unit of Vascular and Interventional Radiology, King Chulalongkorn Memorial Hospital 190
Local Diagnostic Reference Levels (DRLs) of Interventional Radiology Procedures in Thailand: A Single Center 191
Estimation the effective and skin doses for pediatric and adult patients undergoing cardiac interventional examination using five PMMA phantoms and TLD/ionization chamber technique 192
Facility reference level for common x-ray procedures: a preliminary study 193
Evaluation of gonad shielding in digital radiography: Based on clinically adjustable controls. 194
Diagnostic: Others 195
Evaluation of student skill competency on accuracy of mid-trimester fetal sonography scan following the newly-established Master degree in medical sonography 196
The teaching and learning of postgraduate medical physics using Internet-based e-learning during the COVID-19 pandemic 197
Analysis of NTCP Based Radiobiological Models: A Systematic Review of Literatures 198
Evaluation of Visually Induced Motion Sickness During Virtual Reality based Head-mounted Display Viewing using Electroencephalography 199
Nuclear Medicine: Imaging 200
The comparison between planar gated blood pool imaging and gated blood pool SPECT to evaluate ventricular function in breast cancer patients receiving cardiotoxic cancer treatments 201
Diagnostic performance of dual-tracer subtraction, single-tracer dual-phase 99mTc-MIBI parathyroid scintigraphy, and 99mTc-MIBI SPECT/CT for preoperative localization in patients with hyperparathyroidism. 202
Clearance Patterns of Tc-99m ECD Using Serial SPECT Imaging to Define Seizure Onset Zone 203
Monte Carlo simulation for high resolution imaging of Rb-82 with bremsstrahlung X-ray camera for small animals 204
Nuclear Medicine: Radiation Safety / DRL 205

Size specific dose estimate (SSDE) for estimating CT doses in SPECT/CT and PET/CT examinations.... 206
Flexible, Lightweight and Lead-free Radiation Shielding for Nuclear Medicine from Natural Rubber with Barium Sulfate Composite 207
Investigation of position and angle effects of nanoDot OSL dosimeter for the eye lens dose measurement 208
Determination for current status of environmental radioactivity in Fukushima, using NaI (Tl) scintillation survey meter 209
Nuclear Medicine: Others 210
The labeling of 99mTc-PSMA-HBED-CC for prostate cancer imaging 211
Gamma Scintigraphy for Hepatic Radioembolization: Comparison between Different Radionuclides using GATE Monte Carlo Simulation 212
Positron Range Correction in Positron Emission Tomography 213
Evaluation of patient doses from 177Lu-PSMA in metastases prostate cancer treatment at King Chulalongkorn Memorial Hospital 214
Development of Flexible Radiotherapeutic Bandage Containing Samarium-153 for the Treatment of Skin Cancer 215

E-Poster Presentations

Radiotherapy 216
Real-time in vivo dose verification using Metal-Oxide Semiconductor Field Effect Transistor (MOSFET) in HDR brachytherapy 217
Development of external dosimetry audit system for image-guided brachytherapy in Asian Countries..... 218
Comparison of ICRU Point Doses and Volumetric Doses to the Rectum High Dose Rate Cobalt-60 Brachytherapy of Cervical Cancer 219
Correlation analysis of CT-based rectal planning dosimetric parameters with in vivo dosimetry of MOSkin and PTW 9112 detectors in Co-60 source HDR intracavitary cervix brachytherapy 220
A development of a primary standard of absorbed dose to water for a small field in high-energy photon beam 221
Construction of regional network and remote support system for linac output dose difference facilities. .. 222
Investigation for measurement of photon depth dose using UVC camera 223
Impact of the Frequency of Verification with In-room CT on Setup Errors in Carbon Ion Radiotherapy for Prostate Cancer 224
Determination of the beam quality correction factors for carbon-ion beams by Monte Carlo simulations and measurements 225
Effects of parallax error and light refraction on estimation for dose distribution of proton beams using luminescence in water 226
Time dependence of intra-fractional motion for spine stereotactic body radiotherapy 227
Calculation of an automatic irradiation path for dynamic-wave-arc irradiation 228
Dosimetric effect of the baseline shift in the phase and amplitude gated lung SBRT 229
The Proposal of the Simple Alternative Planning Method for Lung/Esophageal IMRT plan in case of failure in Varian Halcyon 230
Evaluate the dose distribution of mono-isocenter and dual-isoncenter volumetric modulated arc therapy for synchronous bilateral breast cancer 231
Remote Monte Carlo verification system of radiotherapy with multiple processor 232
Detection of multi-leaf collimator errors in a small-field volumetric modulated arc therapy plan using portal dosimetry 233
Focus control of electron beam for arbitrary field formation 234
Feasibility test of independent dose verification with Monte Carlo simulation tool at Osaka Heavy Ion Therapy Center 235
Development of method to cancel the calculation direction dependence for image processing applying diffusion equation 236
Impact of automatic image registration with contrast enhancement filter in head and neck cancer 237
Development of facial recognition system for patient safety: Analysis of benchmark data 238
Development of Real – time Radioluminescence Dosimetry System for External Beam Radiotherapy: A Preliminary Study 239
Diagnostic 240
LORETA as a Method of Brain Activation Analysis for Autism Spectrum Disorder: an Evaluation using Traditional Benchmarks 241

Material decomposition of photon-counting CT spectra with Machine Learning 242
The Study of Correlation Between Water-equivalent Diameter (Dw) and Age on CT Examination in Pediatric Head Patient with Tube Current Modulation (TCM) Technique 243
Spectral distortion correction caused by pulse-pileup effects with a machine learning technique for a photon counting x-ray detector 244
The method to estimate source position for mobile tomosynthesis 245
Evaluation method of isotropic performance of CT system using “Spiral Micro Holes Phantom” 246
Effect of Various Hybrid Iterative Reconstruction Method on High Resolution Scan Mode in Abdominal CT 247
Investigation on dose assessment and image quality evaluation of selected dental fillings in dental radiography. 248
Image Quality Evaluation of a Hybrid Iterative Reconstruction Algorithm in the Multi-Slice Computed Tomography Scanner for the Pediatric Head Diagnostic Procedure 249
Denoising of OCT images with a bandelet transform for feature extractions 250
Comparison of compensation effect for non-uniform magnetic field with major grains 251
Metal Artifact Reduction using Tilt Scan Technique in CT 252
Bone mineral density screening in a rural population, Ayutthaya, Thailand 253
The study of Power Spectral Density Value Ratio between Wet and Dry Electrodes with Electroencephalography (EEG) Using Audio Stimulus 254
Investigating the current status of Medical Physics in Sri Lanka 255
The role of a medical physicist in an advanced emergency pediatric hospital 256
Deploying Long Short-Term Memory (LSTM) Network to Classify EEG Signal for Epileptic Seizure Detection 257
Using Radial Basis Function-Kernel Support Vector Machine with Tree-Based Feature Selection for Cancer Type Prediction Based from Gene Expressions 258
CT-based convolutional-neural-network segmentation of poorly differentiated HCCs with lung-cancer-based transfer learning 259
Fabrication of Bismuth-Polymer Composite for Additive Manufacturing of Radiation Shielding 260
Change of CTDIvol in medical exposure management of computed tomography 261
Effects of Quercetin on adipogenesis by studying the metabolic profiles by NMR 262
Single-scan method for the inner ear in cone-beam computed tomography 263
Nuclear Medicine 264
Diagnostic performance of I-131 MIBG scintigraphy in 101 patients suspected for pheochromocytoma/paraganglioma: A comparison between visual and semi-quantitative planar analyses and a hybrid SPECT/CT imaging 265
99mTc-Labeled Bismuth Nanoparticles for Contrast Enhancement in SPECT-CT Imaging: A Phantom Study 266
Image reconstruction method based on a deep learning in a multi-pinhole SPECT system 267
Improvement of the spatial resolution with a deconvolution method in a pinhole SPECT system 268
Estimated Radiation Dose Received By Resuscitation Providers Following the CPR Operation of a Patient Undergoing a Nuclear Medicine Studies 269
Optimal administered activity for Tc99m MDP SPECT-Bone scan patients in relation to body mass index 270
Shielding Calculation for a Diagnostic Nuclear Medicine Facility 271
Inter-laboratory comparisons of ring dosimeters in term of Hp(0.07) 272

Full Papers

Correlation of Ultrasound Attenuation Imaging versus MRI Proton Density Fat Fraction in Non-alcoholic Fatty Liver 274
Shielding Calculation for a Diagnostic Nuclear Medicine Facility 279
The Study of Local Diagnostic Reference Levels at Unit of Vascular and Interventional Radiology, King Chulalongkorn Memorial Hospital 285
Sonographic predictors for developing cholangiocarcinoma: A cohort study from an endemic area 289
Using Radial Basis Function-Kernel Support Vector Machine with Tree-Based Feature Selection for Cancer Type Prediction Based on Gene Expressions 293
The role of a medical physicist in an advanced emergency pediatric hospital 297
Time dependence of intra-fractional motion for spine stereotactic body radiotherapy 299
Effect of Various Hybrid Iterative Reconstruction Method on High Resolution Scan Mode in Abdominal CT 303

Facility reference level for common x-ray procedures: A preliminary study 307
The method to estimate source position for mobile tomosynthesis 311
Quantitative evaluation of deep convolutional neural network- based denoising for ultra-low-dose CT ... 315
Evaluation of student competency on mid-trimester fetal sonography scan following the newly-established Master degree in medical sonography 320
The Study of Correlation Between Water-equivalent Diameter (Dw) and Age on CT Examination in Pediatric's Head Patient with Tube Current Modulation (TCM) Technique 324
Size specific dose estimate (SSDE) for estimating CT doses in SPECT/CT and PET/CT examinations ... 328
Single-scan method for the inner ear in cone-beam computed tomography 332
Comparison simulation treatment between Gamma Knife and Linac Stereoradiosugery on small target volume by using GEANT 4 Monte Carlo simulation 336
Value of Superb Microvascular Imaging in characterize of nodular type focal fat sparing lesion and actual hepatic nodules in the background of fatty liver 340
Mitigation of error propagation in tele cobalt treatment 344
Assessment of Radiation Protection and Radiation Safety Awareness among Radiation Professionals in a Tertiary Care Teaching Hospital 346
Localization accuracy of off-isocenter multi-target brain stereotactic radiosurgery using SyncTraX FX4. 349
The current status of Medical Physics in Sri Lanka 353
Dosimetric evaluation of uncorrectable rotational setup error in total body irradiation using helical tomotherapy 356
Investigation of dose perturbations around brachytherapy seeds in high-energy photon beams 360
Efficiency of EPID dosimetry based software compared with ion chamber 363
Improvement of the spatial resolution with a deconvolution method in a pinhole SPECT system 366
The effective methods for liver cyst labelling in ultrasound images by using R-CNN 369
Image reconstruction method based on a deep learning in a multi-pinhole SPECT system 373
Preliminary investigation on performance of photodiode sensor as a dosimeter 375
Flexible, Lightweight and Lead-free Radiation Shielding for Nuclear Medicine from Natural Rubber with Barium Sulfate Composite 380
Predicting Treatment Response in Nasopharyngeal Cancer Using Radiomics: a Preliminary Study 384
The Labeling of 99mTc-PSMA-HBED-CC for Prostate Cancer Imaging 388
Development of method to cancel the calculation direction dependence for image processing applying diffusion equation 392
Impact of automatic image registration with contrast enhancement filter in head and neck cancer 396
Monte Carlo calculation of beam quality correction factors in proton beams using PTSIM/GEANT4 399
The comparison between planar gated blood pool imaging and gated blood pool SPECT to evaluate ventricular function in breast cancer patients receiving cardiotoxic cancer treatments 402
Patient-specific organ dose calculated using dose tracking software based on Monte Carlo simulation in pediatric abdominal CT 406
Material decomposition of photon-counting CT spectra with machine learning 410
How to create a conversion IMRT plan for lung / esophageal cancer using the fluence reversible computing function on HalcyonTM 412
Evaluation of patient doses from 177Lu-PSMA in metastases prostate cancer treatment at King Chulalongkorn Memorial Hospital 416
Development of facial recognition system for patient safety : Analysis of benchmark data 420
Dosimetric effect of the baseline shift in the phase and amplitude gating lung SBRT 424
Development and dosimetric verification of 3D customized bolus in radiotherapy 428
Remote clinical dosimetry auditing for IMRT using virtual EPID standard phantom audit (VESPA) in Thailand: Preliminary results 432
Evaluation of Scattering Spectra from Examinee during CT Scans 436
Diagnostic performance of I-131 MIBG scintigraphy in 101 patients suspected for pheochromocytoma/paraganglioma: a comparison between visual and semi-quantitative planar analyses and a hybrid SPECT/CT imaging 440
Detection of multi-leaf collimator errors in a small-field volumetric modulated arc therapy plan using portal dosimetry 444
Tuning effective spot size parameter in Acuros XB algorithm for Edge™ radiosurgery machine 446
Denoising of OCT images with a bandelet transform for feature extractions 450
Evaluation of dose calculation algorithm accuracy in Eclipse treatment planning system for jaw-defined and MLC-defined small fields 453

Spectral distortion correction caused by pulse-pileup effects with a machine learning technique for a photon counting x-ray detector 457
Determination for current status of environmental radioactivity in Fukushima, using NaI(Tl) scintillation survey meter 460
Effect of plan complexity to gantry angle uncertainty for VMAT delivery 463
Calculation of an automatic irradiation path for dynamic-wave-arc irradiation 467
Comparison of field output factors of different detectors in small field for 6 MV flattening filter and flattening filter free photon beams 471
Grey Matter Segmentation of T1-Weighted MR Image in Ischemic Stroke Patients using k-Means Clustering 475
Evaluation of the effectiveness of gonad shielding in digital radiography 479
Focus control of electron beam for arbitrary field formation 483
Quantitative Assessment of Breast Density Using Pixel Intensity Threshold 486
Diagnostic performance of dual-tracer subtraction, single-tracer dual-phase 99mTc-MIBI parathyroid scintigraphy, and 99mTc-MIBI SPECT/CT for preoperative localization in patients with hyperparathyroidism. 490
Linear accelerator performance monitoring through clinical treatment delivery using Statistical Process Control and MobiusFX 494
Surface and Buildup Doses Comparison between Analytical Anisotropic Algorithm and Acuros XB for Various Treatment Parameters 498
Determination of small field output factors and specific correction factors for various diodes and microDiamond detector for CyberKnife M6 system equipped with fixed collimator 502
Tolerance level determination for automated EPID-based deep inspiration breath-hold (DIBH) instability evaluation in breast cancer patients 506
Fabrication and validation of cubic phantom embed with an accelerometer sensor for verifying six-degrees-of-freedom couch 510
Automatic QC Analysis Program in Digital Radiography System 514
Investigation of position and angle effects of nanoDot OSL dosimeter for the eye lens dose measurement 518
Development of an In-house MATLAB code for dynamic multileaf collimator quality assurance based on EPID 521
Predicting 3D dose distribution from patient CT images alone for prostate VMAT using deep learning 525
Size-Specific Dose Estimates (SSDE) for Head CT in Pediatric Patients 528
Design of universal 3D-printed oral stent for head and neck radiotherapy 532
The Breast Microcalcification Detection in Mammogram Image by Using the Deep Convolutional Neural Network 536

Participants 539
Author Index 545
Commercial Exhibition Floor Plan 547
Sponsors 548

Floor Plan

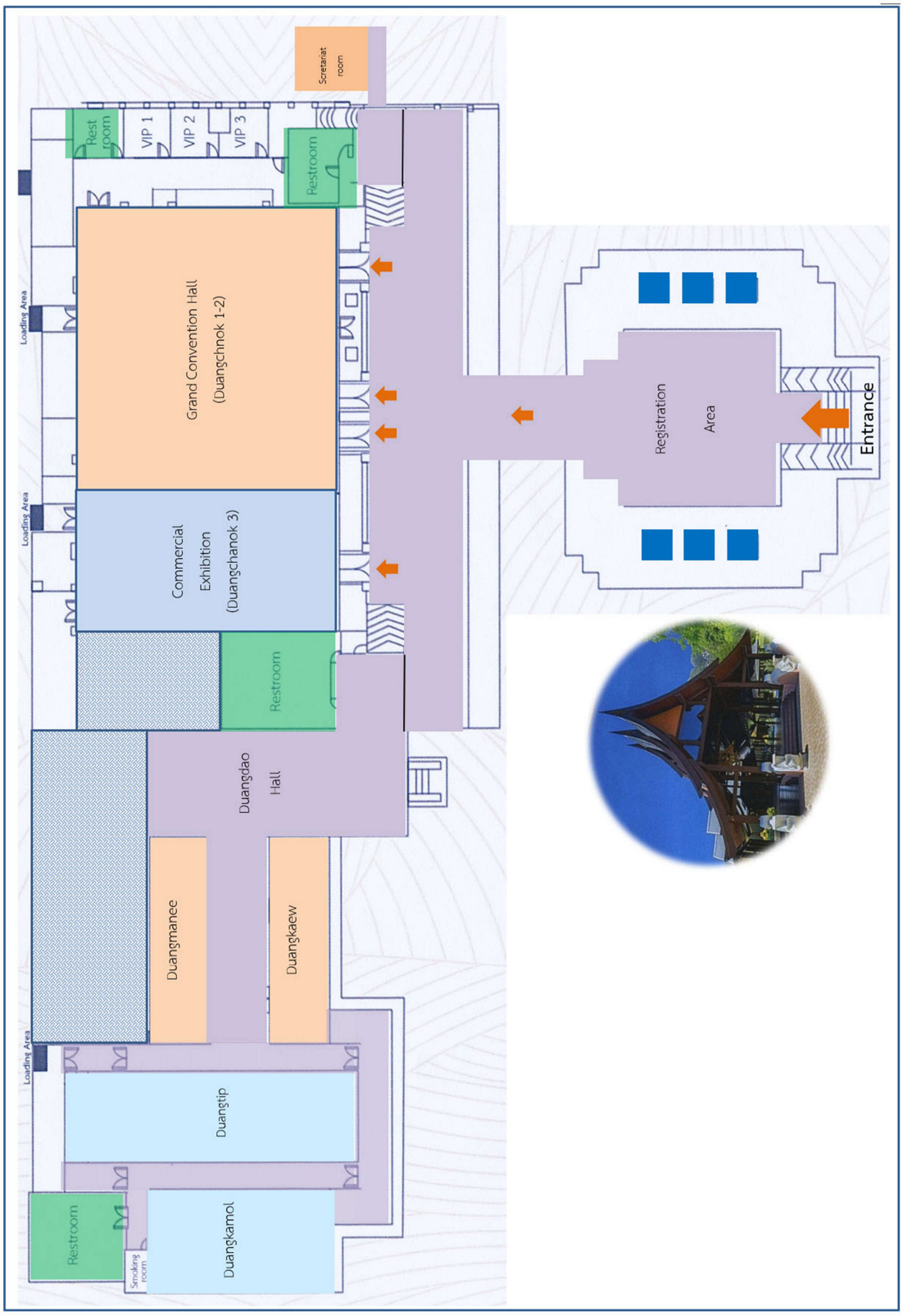
Secretariat room
Rest room
VIP 1
VIP 2
VIP 3
Restroom
Grand Convention Hall (Duangchnok 1-2)
Loading Area
Commercial Exhibition (Duangchanok 3)
Loading Area
Restroom
Duangdao Hall
Duangmanee
Duangkaew
Loading Area
Duangtip
Restroom
Smoking room
Duangkamol
Registration Area
Entrance

Program at a glance

Time	3 December 2020		
08:00-08:30	**Registration**		
Room	Duangchanok Convention 1-2		
08:30-09:00	**Opening Ceremony** *Arun Chougule, Freddy Haryanto, Shigekasu Fukuda, Anchali Krisanachinda, Madan Rehani* *(MC: Kitiwat & Thititip)*		
09:00-09:30	John Cameron Memorial Lecture: "New Additions to the Scientific Dictionary and Encyclopaedia on Medical Physics" *Slavik Tabakov*		
09:30-10:00	Prof. Kiyonari Inamura Memorial AFOMP Oration *Kin Yin Cheung*		
10:00-10:30	Coffee Break		
Chair	Shigekasu Fukuda		
10:30-11:00	JSMP Invited Lecture: Evaluation of ionising radiation induced DNA damage on a cell and prediction of biological response by integrated track structure Monte Carlo simulations using Geant4-DNA *Dousatsu Sakata*		
11:00-12:00	**MS 1**: Proton Therapy *Facilitator: Napapat Amornwichet* *Speakers: Chonlakiet Khorprasert (Thailand), Kin Yin Cheung (Hong Kong)* *James Lee Cheow Lei (Singapore)*		
12:00-13:00	Lunch / AFOMP EXCOM Meeting (Room: Duangmanee)		
Chair	Nisa, Puangpen		
13:00-13:20	Impact of radiosensitivity and gender on paediatric cranial tumours following proton and photon intensity modulated radiation therapy – A radiobiological response modelling study *Eva Bezak*		
13:20-13:30	Comparison of DNA damage in HPV negative and positive head and neck cancer cell lines following fractionated irradiation *Eva Bezak*		
13:30-14:20	**MS 2 JSRT**: Clinical application of the latest radiation technology: Research and Activities *Facilitator: Kohei Hanaoka* *Speakers*: *Kosuke Matsubara, Yasuo Takatsu, Kohei Hanaoka*		
14:20-14:50	IAEA Global Activities related to Professional Issues in Medical Physics and their Harmonization *Giorgia Loreti*		
14:50-15:00	Coffee Break		
	Radiotherapy	**Diagnostic**	**Nuclear Medicine**
Room	Duangchanok	Duangkaew	Duangmanee
Chair	Sivalee / Wannapa	Anchali / Napapong	Tanawat / Panya
15:00-15:20	3D-Based Brachytherapy *Christian Kirisits*	NDRLs in Cardiac Cath in Thailand *Suphot Srimahachota*	Clinical Aspects for Theranostics in the Era of Precision Medicine *Maythinee Chantadisai*
15:20-15:30		Updated NDRLs in Japan *Kosuke Matsubara*	
15:30-15:40	SCMPCR: A Centre of Excellence to fight against Cancer in South Asia Region *Hasin Anupama Azhari, Golam Abu Zakaria, Volker Steil, Frank Hensley*		Theranostic dosimetry *Kitiwat Khamwan*
15:40-16:00		NDRLs in Thailand *Panruethai Trinavarat*	
16:00-16:10		Dose Monitoring and Audit, Tools for Patient Dose Optimization *Napapong Pongnapang*	Interesting Radiation Protection Issues in Theranostic Radiopharmaceutical *Krisanat Chuamsaamarkkee*
16:10-16:30	Radiation Incident and Accident in RT *Golam Abu Zakaria*		
16:30-17:30	TMPS Business Meeting		
18:00-21:00	Gala Dinner		

<table>
<tr><th>Time</th><th colspan="4">4 December 2020</th></tr>
<tr><th></th><th>Radiotherapy</th><th colspan="2">Diagnostic</th><th>Nuclear Medicine</th></tr>
<tr><td>Room</td><td>Duangchanok</td><td colspan="2">Duangkaew</td><td>Duangmanee</td></tr>
<tr><td>Chair</td><td>Puangpen / Nualjun</td><td colspan="2">Anchali</td><td>Kitiwat</td></tr>
<tr><td>08:00-08:30</td><td rowspan="2">MS 3: Medical Physics Practice and Science in Times of COVID
Facilitator: Tomas Kron
Speakers: Chai Hong Yeong, Xiance Jin, Jeanie Hsiu Ding Wong, Arun Chougule, Hasin Anupama Azhari</td><td colspan="2">ACOMP:
SSDE dosimetrie in CT-Scan
Freddy Haryanto</td><td></td></tr>
<tr><td>08:30-09:00</td><td colspan="2">Large Scale Data curation for AI in Mammography
Rasika Rajapakshe</td><td>How to Make a Research Plan for Young Investigator
Hidetaka Arimura</td></tr>
<tr><td>Room</td><td colspan="4">Duangchanok Convention 1-2</td></tr>
<tr><td>Chair</td><td colspan="4">Napapong</td></tr>
<tr><td>09:00-09:20</td><td colspan="4">ACOMP: How the Life of Medical Physicists Changed During the COVID-19 Pandemic?
Ng Kwan Hoong</td></tr>
<tr><td>09:20-09:40</td><td colspan="4">ACOMP: Role of Medical Physicists in the Clinic during COVID-19 Pandemic
Mahadevappa Mahesh</td></tr>
<tr><td>09:40-10:00</td><td colspan="4">ACOMP: E-learning in Medical Physics: Building Education Modules with Moodle VLE
Vassilka Tabakova</td></tr>
<tr><td>10:00-10:30</td><td colspan="4">Coffee Break</td></tr>
<tr><td>Room</td><td>Duangchanok</td><td colspan="3">Duangkaew</td></tr>
<tr><td>Chair</td><td>Chumpot / Taweap</td><td colspan="3">Amporn / Panya</td></tr>
<tr><td>10:30-10:50</td><td rowspan="2">Role of Radiation and Caution in the Management of Covid-19
Indra J Das</td><td colspan="3">AFOMP Medical Physics Education and Clinical Training
Arun Chougule</td></tr>
<tr><td>10:50-11:00</td><td colspan="3" rowspan="2">Postgraduate Medical Physics Programmes in Asia Pacific Countries - A Survey Study
Sivananthan Sarasanandarajah</td></tr>
<tr><td>11:00-11:10</td><td rowspan="2">Patient-specific QA by Log File Based Software
Sornjarod Oonsiri, Pichet Uber</td></tr>
<tr><td>11:10-11:30</td><td colspan="3" rowspan="2">MS4: Women in Medical Physics
Facilitators: Eva Bezak, Hasin Anupama Azhari
Speakers: Eva Bezak, Hasin Anupama Azhari, Anchali Krisanachinda, Azleen Mohd Zain</td></tr>
<tr><td>11:30-12:00</td><td>Radiomics in Radiation Oncology
Yothin Rakvongthai, Anussara Prayongrat</td></tr>
<tr><td>12:00-13:00</td><td colspan="4">Lunch / AFOMP Council Meeting (Room: Duangmanee)</td></tr>
<tr><td>Room</td><td>Duangchanok</td><td>Duangthip</td><td>Duangkeaw</td><td>Duangmanee</td></tr>
<tr><td>Chair</td><td>Sivalee / Taweap)
Chumpot / Wannapa</td><td>Puangpen / Nualjun
Chirapha / Supalak</td><td>Tanawat / Panya
Lakkana / Thititip</td><td>Anchali / Krisanat)
Kittiwat / Yothin</td></tr>
<tr><td>13:00-..</td><td>13:00-17:50
Proffered Papers in RT
(Face-to-face)</td><td>12:00-17:00
Proffered Papers in RT
(Virtual)</td><td>13:00-18:00
Proffered Papers in NM+Dx+RT
(Face-to-face)</td><td>12:00-17:00
Proffered Papers in NM+Dx+RT
(Virtual)</td></tr>
</table>

Time	5 December2020		
	Radiotherapy	**Diagnostic**	**Nuclear Medicine**
Room	Duangchanok	Duangkaew	Duangmanee
Chair	Chirapha / Nualjun	Anchali / Thititip	Kitiwat / Shuichi
08:00-08:30	Clinical Application of Small Field Dosimetry *Jan Seuntjens*	High Patient Rad Doses from Recurrent CT Exams *Madan Rehani*	The Establishment of UNSCEAR Report in Thailand *Anchali Krisanachinda*
08:30-08:40		Patients who received more than 100 mSv in a single day *Madan Rehani*	Challenges in CT with Photon Counting Detectors *Picha Shunhavanich*
08:40-09:00	Physicists and Clinical Trails: Support and Evidence for New Technology and Techniques *Tomas Kron*		
09:00-09:30	SIMAC (Linac Simulation Education Tool) *Marco Carlone*	Spectral CT *Mahadevappa Mahesh*	MS 6: Facility Design of a Cyclotron Facility Design of a PET/CT *Somanesan S.*
09:30-10:00	Automatic Plan Checking Tasks by Scripting *Michael Lamey*	Novel Technologies for Advanced Radiomics for Clinical Practices *Hidetaka Arimura*	MS 6: Radiation Emergency Preparedness in Nuclear Medicine *Chai Hong Yeong*
10:00-10:30	Coffee Break		
Room	Duangchanok	Duangkaew	Duangmanee
Chair	Sivalee/ Supalak	Anchali/ Lakkana	Tanawat/ Kitiwat
10:30-10:50	Proton Flash Therapy Adam Harrington (*Varian)*	Consideration of Stochastic Risk in Intervetional Procedures *Madan Rehani*	Theranostics in Nuclear Medicine *Shuichi Shiratori*
10:50-11:00		Imaging-based Biomarkers *Yothin Rakvongthai*	
11:00-11:10	Introduction to MR-Linac *Kin Yin Cheung*		Preparation and Application of Ga-68 in Nuclear Medicine *Shuichi Shiratori*
11:10-11:20		MS5: Eye Lens Dose of Medical Staffs in Thailand *Waraporn Sudchai, Suphot Srimahachota, Anchali Krisanachinda*	
11:20-11:30	Extreme Hypofractionated RT - Radiobiology & Radiobiological Models *Arun Chougule*		
11:30-11:40			Rapid Estimation of Muscle Tranverse Relaxation Time (T2) based on Ultrafast Magnetic Resonance Imaging at 3.0 Tesla *Noriyuki Tawara*
11:40-12:00	Patient-Specific QA Management using Cloud Based *Todsaporn Fuangrod*	Optimization of CBBCT patient dose and image quality *Kanlayanee Theerakul, Apawadee Chakrapong, Anchali Krisanachinda*	
Room	Duangchanok Convention 1-2		Duangmanee
12:00-12:10			Lunch Box / SEAFOMP Council Meeting
12:10-12:30	First Demonstration of the FLASH Effect Using the MEVION S250i and Future Development of Ultra-High Dose Rate Delivery Technology *James Cooley (Mevion/ Nuclear System)*		
12:30-12:50	GE Healthcare CT Sim Solutions for Radiation Oncology *Manmohan Singh (GE)*		
12:50-13:10	QA in the Time of COVID *Yamini Sivashunmugam (Sun Nuclear)*		
13:10-13:30	Filmless End-to-End Stereotactic QA *Greg Robinson (Sun Nuclear)*		
13:30-13:50	RadCalc - Independent 3D QA Software *Elaine Theresa Mathews (Lap Laser)*		
13:50-14:10	New Products – RUBY & OCTAVIUS 1600 SRS) *Edmund Lo (PTW)*		
14:10-14:30	IBA ProteusCLASS, ARC, FLASH & Motion Management *(Gavin Choo)* IBA Sphinx COMPACT and Phonix, New Development of Detector for Particle Therapy *(Kuan Chuan Yeh)*		
14:30-14:50	Ethos™ Therapy: A Deep Dive into the Future of Intelligent Cancer Care *Takahiro Hara (Varian/ BA)*		
14:50-15:10	MR-RT BBRT and Pinnacle Evolution for Brain Stereotactic Radiosurgery *(Philips)*		
15:10-15:30	Presentation Awards and Closing		

Program in detail

3 December 2020

08:00-08:30 Registration

Room: Duangchanok Convention 1-2

08:30-09:00 Opening Ceremony
Arun Chougule, Freddy Haryanto, Shigekasu Fukuda, Anchali Krisanachinda, Madan Rehani
(MC: Kitiwat & Thititip)

09:00-09:30 John Cameron Memorial Lecture:
"New Additions to the Scientific Dictionary and Encyclopaedia on Medical Physics"
Slavik Tabakov

09:30-10:00 Prof. Kiyonari Inamura Memorial AFOMP Oration
Kin Yin Cheung

10:00-10:30 Coffee Break

Chair: Shigekasu Fukuda

10:30-11:00 JSMP Invited Lecture: Evaluation of ionising radiation induced DNA damage on a cell and prediction of biological response by integrated track structure Monte Carlo simulations using Geant4-DNA
Dousatsu Sakata

11:00-12:00 MS 1: Proton Therapy
Facilitator: Napapat Amornwichet
Speakers: Chonlakiet Khorprasert (Thailand), Kin Yin Cheung (Hong Kong) James Lee Cheow Lei (Singapore)

12:00-13:00 Lunch / AFOMP EXCOM Meeting (Room: Duangmanee)

Chair: Nisa, Puangpen

13:00-13:20 Impact of radiosensitivity and gender on paediatric cranial tumours following proton and photon intensity modulated radiation therapy – A radiobiological response modelling study
Eva Bezak

13:20-13:30 Comparison of DNA damage in HPV negative and positive head and neck cancer cell lines following fractionated irradiation
Eva Bezak

13:30-14:20 MS 2 JSRT: Clinical application of the latest radiation technology: Research and Activities
Facilitator: Kohei Hanaoka
Speakers: Kosuke Matsubara, Yasuo Takatsu, Kohei Hanaoka

14:20-14:50 IAEA Global Activities related to Professional Issues in Medical Physics and their Harmonization
Giorgia Loreti

14:50-15:00 Coffee Break

Room: Duangchanok, Radiotherapy
Chair: Sivalee / Wannapa

15:00-15:30 3D-Based Brachytherapy
Christian Kirisits

15:30-16:10 SCMPCR: A Centre of Excellence to fight against Cancer in South Asia Region
Hasin Anupama Azhari, Golam Abu Zakaria, Volker Steil, Frank Hensley

16:10-16:30 Radiation Incident and Accident in RT
Golam Abu Zakaria

16:30-17:30 TMPS Business Meeting

18:00-21:00 Gala Dinner

Room: Duangkaew, Diagnostic
Chair: Anchali / Napapong

15:00-15:20 NDRLs in Cardiac Cath in Thailand
Suphot Srimahachota

15:20-15:40 Updated NDRLs in Japan
Kosuke Matsubara

15:40-16:00 NDRLs in Thailand
Panruethai Trinavarat

16:00-16:30 Dose Monitoring and Audit, Tools for Patient Dose Optimization
Napapong Pongnapang

Room: Duangmanee, Nuclear Medicine
Chair: Tanawat / Panya

15:00-15:30 Clinical Aspects for Theranostics in the Era of Precision Medicine
Maythinee Chantadisai

15:30-16:00 Theranostic dosimetry
Kitiwat Khamwan

16:00-16:30 Interesting Radiation Protection Issues in Theranostic Radiopharmaceutical
Krisanat Chuamsaamarkkee

4 December 2020

Room: Duangchanok, Radiotherapy
Chair: Puangpen / Nualjun

08:00-09:00 MS 3: Medical Physics Practice and Science in Times of COVID
Facilitator: Tomas Kron
Speakers: Chai Hong Yeong, Xiance Jin, Jeanie Hsiu Ding Wong, Arun Chougule, Hasin Anupama Azhari

Room: Duangkaew, Diagnostic
Chair: Anchali

08:00-08:30 ACOMP: SSDE dosimetrie in CT-Scan
Freddy Haryanto

08:30-09:00 Large Scale Data curation for AI in Mammography
Rasika Rajapakshe

Room: Duangmanee, Nuclear Medicine
Chair: Kitiwat

08:30-09:00 How to Make a Research Plan for Young Investigator
Hidetaka Arimura

Room: Duangchanok Convention 1-2
Chair: Napapong

09:00-09:20 ACOMP: How the Life of Medical Physicists Changed During the COVID-19 Pandemic?
Ng Kwan Hoong

09:20-09:40 Role of Medical Physicists in the Clinic during COVID-19 Pandemic
Mahadevappa Mahesh

09:40-10:00 E-learning in Medical Physics: Building Education Modules with Moodle VLE
Vassilka Tabakova

10:00-10:30 Coffee Break

Room: Duangchanok
Chair: Chumpot / Taweap

10:30-11:00 Role of Radiation and Caution in the Management of Covid-19
Indra J Das

11:00-11:30 Patient-specific QA by Log File Based Software
Sornjarod Oonsiri, Pichet Uber

11:30-12:00 Radiomics in Radiation Oncology
Yothin Rakvongthai, Anussara Prayongrat

Room: Duangkaew
Chair: Amporn / Panya

10:30-10:50 AFOMP Medical Physics Education and Clinical Training
Arun Chougule

10:50-11:10 Postgraduate Medical Physics Programmes in Asia Pacific Countries - A Survey Study
Sivananthan Sarasanandarajah

11:10-12:00 MS4: Women in Medical Physics
Facilitators: Eva Bezak, Hasin Anupama Azhari
Speakers: Eva Bezak, Hasin Anupama Azhari, Anchali Krisanachinda, Azleen Mohd Zain

12:00-13:00 Lunch / AFOMP Council Meeting (Room: Duangmanee)

Proffered Papers in Radiotherapy (Face-to-face)

Room: Duangchanok
Chair: Sivalee / Taweap)

Time	Paper no.	
13:00	198	Development of automated prostate VMAT treatment planning system using deep learning-based predictive dose distribution *Patiparn Kummanee (Thailand)*
13:10	20	Low-dose radiation enhance cytotoxicity of chemotherapeutic agent (pirarubicin) in K562 and K562/adr leukemic cancer cells *Khin The Nu Aye (Thailand)*
13:20	113	Radioprotective effect of interruptin derived from Cyclosorus terminans could protect cell damage of irradiated normal cells from radiotherapy *Miss Nipha Chumsuwan (Thailand)*
13:30	128	Dosimetric comparison of manual and library applicator reconstruction in MRI image-based for gynecological brachytherapy *Sakda kingkaew (Thailand)*
13:40	89	Parametric impact study of interplay effects in 6 MV flattening filter free (FFF) of photon beams *Vanida Poolnapol (Thailand)*
13:50	117	Development and dosimetric verification of 3D customized bolus in radiotherapy *Miss Nichakan Chatchumnan (Thailand)*
14:00	125	Tuning effective spot size parameter in Acuros XB algorithm for Edge(TM) radiosurgery machine *Warinthorn Rattanaareeyakorn (Thailand)*
14:10	130	Investigation of field output correction factors in small elongated fields for 6 MV photon beam *Mananchaya Vimolnoch (Thailand)*
14:20	140	Comparison of field output factors of different detectors in small field for 6 MV flattening filter and flattening filter free photon beams *Mr. Surendra Dhungana (Thailand)*
14:30	141	Evaluation of detectors on relative dosimetric measurement for CyberKnife M6 System *Mr. Wisawa Phongprapun (Thailand)*
14:40	165	Surface and Build Up Doses Comparison between Analytical Anisotropic Algorithm and Acuros XB for Various Treatment Parameters *Miss Sonam Choki (Thailand)*
14:50	166	Determination of small field output factors and specific correction factors for various diodes and microDiamond detector for CyberKnife M6 system equipped with fixed collimator *Penpisuth Suksawang (Thailand)*
15:00		Break

Chair: Chumpot / Wannapa

Time	Paper no.	
15:10	61	Efficiency of EPID dosimetry based software compared with ion chamber *Mrs. Wanwanat Sumanaphan (Thailand)*
15:20	167	Tolerance level determination for automated EPID-based deep inspiration breath-hold (DIBH) instability evaluation in breast cancer patients *Miss Aphisara Deeharing (Thailand)*
15:30	101	Determination of fetal dose and health effect to the fetus from breast cancer radiotherapy during pregnancy *Pattarakan Suwanbut (Thailand)*
15:40	146	Calculation of field output correction factors for radiophotoluminescence glass dosimeter in 6 MV WFF and FFF small photon beams using Monte Carlo simulation *Sumalee Yabsantia (Thailand)*
15:50	205	Design of universal 3D-printed oral stent for head and neck radiotherapy *Thunphisit Mundee (Thailand)*
16:00	53	Dosimetric validation of the commercial dose calculation algorithm for carbon ion therapy in a heterogeneous phantom *Sirinya Ruangchan (Thailand)*
16:10	102	Simulation of the efficiency of rescanning with respiratory gating technique in pencil beam scanning proton therapy for lung cancer *Nattakarn Kittiva (Thailand)*
16:20	129	Dosimetric comparison of normal liver sparing in hepatocellular carcinoma between intensity modulated proton therapy and volumetric modulated arc therapy *Mintra Keawsamur (Thailand)*
16:30	114	Dosimetric Validation of Monaco Treatment Planning System *Viphaphone INPHAVONG (Thailand)*
16:40	134	Evaluation of dose calculation algorithm accuracy in Eclipse treatment planning system for jaw-defined and MLC-defined small fields *Panun Sritubtim (Thailand)*
16:50	174	The quality improvement of dose escalation plan of prostate cancer using an integration of biological parameters for optimization and evaluation *Mr. Tanwiwat Jaikuna (Thailand)*
17:00	118	Pilot study of remote clinical dosimetry auditing for IMRT using virtual EPID standard phantom audit (VESPA) in Thailand *Pavarit Pojanapreecha (Thailand)*
17:10	121	Evaluation of Mobius and Portal dosimetry Quality Assurance tools for volumetric modulated arc therapy plans *Chulee Vannavijit (Thailand)*
17:20	137	Effect of plan complexity to gantry angle uncertainty for VMAT delivery *Thananya Chanpanya (Thailand)*
17:30	139	Dosimetric evaluation of photon beam-matching for two similar linear accelerators *Ms. Kanogpan Prasartvit (Thailand)*

Proffered Papers in Radiotherapy (Virtual)

Room: Duangthip

Chair: Puangpen / Nualjun

Time	Paper no.	
13:00	3	Automated fast data collection and organization for medical artificial intelligence *Hongjia Liu or Yibao Zhang (China (Peoples Rep.))*
13:10	4	A feasibility study of kVCBCT-based radiomics for radiological complication prediction *Yuliang Huang or Yibao Zhang (China (Peoples Rep.))*
13:20	93	Evaluation of machine learning-based prediction model for radiation pneumonitis in NSCLC patients *Shiina Mouri (Japan)*
13:30	94	Impact of image type and deep learning architecture in deep learning radiomics on the accuracy of lung cancer prediction *Shumpei Tanabe (Japan)*
13:40	95	Prognostic analysis of CT-based radiomics focusing on a subgroup of NSCLC patients *Yuto Sugai (Japan)*
13:50	10	Temperature variation of stimulated diabetic blood and its effects on Evaluated specific absorption rate (SAR) when used a 532 nm wavelength laser for therapeutics. *Sylvester Jande Gemanam (Malaysia)*
14:00	64	The Effect of Different Sizes of Bismuth Oxide Nanorods on Radiosensitization Enhancement Ratio *Amirah binti Jamil (Malaysia)*
14:10	65	The Effect of Different Sizes of Bismuth Oxide Nanorods on Cancer Cells *Amirah binti Jamil (Malaysia)*
14:20	91	Influence of PEG-coated Bismuth Oxide Nanoparticles on ROS Generation for Electron Beam Radiotherapy *Noor Nabilah Binti Talik Sisin (Malaysia)*
14:30	5	Verification of Treatment Time in Interstitial Brachytherapy using Paris System *Sujan Mahamud (Bangladesh)*
14:40	58	Investigation of dose perturbations around brachytherapy seeds in high-energy photon beams *Shuta Ogawa (Japan)*
14:50	153	An update on local blood irradiation technique using medical LINAC: Blood Irradiation Kit *Janatul Madinah Wahabi (Malaysia)*
15:00	51	Assessment of Radiation Protection and Radiation Safety Awareness among Radiation Professionals in a Tertiary Care Teaching Hospital *Mary Joan (India)*
15:10	163	Establishment of MOH Medical Physics Research Task Force *Ng Aik Hao (Malaysia)*
15:20	2	A simulation study of fractional image guidance protocol contributing to the dosimetric accuracy of patients treated on Halcyon system *Chenguang Li or Yibao Zhang (China (Peoples Rep.))*
15:30	52	Localization accuracy of off-isocenter multi-target brain stereotactic radiosurgery using SyncTraX FX4 *Jun Tomihara (Japan)*

15:40	87	Evaluation of tumor delineation accuracy in denoised contrast enhancement four-dimension CT using deformable image registration method *Kentarou Suzuki (Japan)*
15:50	40	CT Density Profile and Physicochemical Study of Soy-Lignin Bonded Rhizophora spp. Particleboard as Phantom Material in Medical Physics Application *Siti Hajar binti Zuber (Malaysia)*
16:00		Break
16:10	14	Monte Carlo Simulation of semiflex chamber in Megavoltage Photon Beam *Suresh Poudel (India)*
16:20	39	Estimation of Linear and Mass Attenuation Coefficients of Soy-lignin Bonded Rhizophora spp. Particleboard as a Potential Phantom Material for Low- and High-energy Studies using Monte Carlo Simulation *Siti Hajar binti Zuber (Malaysia)*
16:30	48	Comparison simulation treatment between Gamma Knife and Linac Stereoradiosugery on small target volume by using GEANT 4 Monte Carlo Simulation *Shazmi MR (Malaysia)*
16:40	98	Monte Carlo calculation of beam quality correction factors in proton beams using PTSIM/GEANT4 *Masaya Ichihara (Japan)*
16:50	155	VDOSE: A tools to analyze dose distribution from Monte Carlo dose Calculation *Sitti Yani (Indonesia)*
17:00	80	Development of Ultra-fast Irradiation for Proton Therapy *Nagaaki Kamiguchi (Japan)*
17:10	57	Treatment planning evaluation of 3D-printed Anthropomorphic Head Phantom *Nur Emirah Zain (Malaysia)*
17:20	86	Comparison of different treatment planning techniques for left-sided breast cancer: A dosimetric study *Dr Md Akhtaruzzaman (Bangladesh)*
17:30	96	Investigation of the optimal cost function for pelvic CT-MR deformable image registration *Tomoya Ishida (Japan)*
17:40	180	Dosimetric comparison between 3D and IMRT treatment techniques for whole breast radiotherapy *Miss Yin Yin Pyone (Myanmar)*
17:50	43	Development of novel x-ray-opaque-marker system for improvement and quantification of phantom positioning accuracy in patient-specific quality assurance *Kentaro Suzuki (Japan)*

Proffered Papers in Nuclear Medicine, Diagnostic, Radiotherapy (Face-to-face)

Room: Duangkeaw

Chair: Tanawat / Panya

Nuclear Medicine

Time	Paper no.	
13:00	112	Evaluation of patient doses from 177Lu-PSMA in metastases prostate cancer treatment at King Chulalongkorn Memorial Hospital *Kotchakorn Chatachot (Thailand)*
13:10	106	The comparison between planar gated blood pool imaging and gated blood pool SPECT to evaluate ventricular function in breast cancer patients receiving cardiotoxic cancer treatments *Kanokpich Khwaipha (Thailand)*
13:20	156	Diagnostic performance of dual-tracer subtraction, single-tracer dual-phase 99mTc-MIBI parathyroid scintigraphy, and 99mTc-MIBI SPECT/CT for preoperative localization in patients with hyperparathyroidism. *Warissara Wittayapasitti (Thailand)*
13:30	209	Clearance Patterns of Tc-99m ECD Using Serial SPECT Imaging to Define Seizure Onset Zone *Chanan Sukprakun (Thailand)*
13:40	44	Size specific dose estimate (SSDE) for estimating CT doses in SPECT/CT and PET/CT examinations *Prajaree Mayomthong (Thailand)*
13:50	73	Flexible, Lightweight and Lead-free Radiation Shielding for Nuclear Medicine from Natural Rubber with Barium Sulfate Composite *Nattha Plangpleng (Thailand)*
14:00	195	Investigation of position and angle effects of nanoDot OSL dosimeter for the eye lens dose measurement *Pattaravarin Rattanamongkonkul (Thailand)*
14:10	84	The labeling of 99mTc-PSMA-HBED-CC for prostate cancer imaging *Miss Benchamat Phromphao (Thailand)*
14:20		Break

Chair: Lakkana / Thititip

Diagnostic

Time	Paper no.	
14:30	66	The effective methods for liver cyst labelling in ultrasound images by using R-CNN *Mrs.Sutthirak Tangruangkiat (Thailand)*
14:40	149	Quantitative Assessment of Breast Density Using Pixel Intensity Threshold *Mr. Jaroonroj Wongnil (Thailand)*
14:50	187	Overall Survival Prediction of Nasopharyngeal Carcinoma using Radiomics *Sararas Intarak (Thailand)*
15:00	212	Machine Learning model for Alzheimer's disease prediction and classification using T1-weighted MR Brain imaging based on SVM algorithm *Mr. Chayanon Pamarapa (Thailand)*
15:10	107	Patient-specific organ dose calculated using dose tracking software based on Monte Carlo simulation in pediatric abdominal CT *Miss Yuparak Innan (Thailand)*
15:20	204	Size-Specific Dose Estimates (SSDE) for Head CT in Pediatric Patients *Saowapark Poosiri (Thailand)*

15:30 41 Evaluation of student skill competency on accuracy of mid-trimester fetal sonography scan following the newly-established Master degree in medical sonography
Surapa Hairunpijit (Thailand)

15:40 11 Correlation of Ultrasound Attenuation Imaging versus MRI Proton Density Fat Fraction in Non-alcoholic Fatty Liver
Miss.Pantajaree Hiranrat (Thailand)

15:50 19 Sonographic predictors for developing cholangiocarcinoma: A cohort study from an endemic area
Natcha Thanakijsombat (Thailand)

16:00 28 Correlation of Intraabdominal and Intrahepatic lipid content assessed by MRI/MRS with biofluid lipid and glucose metabolic profiles
Miss Khin Thandar Htun (Thailand)

16:10 49 Value of Superb Microvascular Imaging (SMI) in characterize of nodular type focal fat sparing lesion and true hepatic nodules in the background of fatty liver
Songpon Srisittimongkon (Thailand)

16:20 77 Predicting Treatment Response in Nasopharyngeal Cancer Using Radiomics: A Preliminary Study
Miss Sasawan Wongpisarn (Thailand)

16:30 181 Performance of quantitative lesion measurement in hepatic dual-energy computed tomography (DECT): Phantom study
Miss Hataipat Jantawong (Thailand)

16:40 184 Automatic QC Analysis Program in Digital Radiography System
Jongwat Cheewakul (Thailand)

16:50 18 The Study of Local Diagnostic Reference Levels at Unit of Vascular and Interventional Radiology, King Chulalongkorn Memorial Hospital
Miss Kornkamol Prajamchuea (Thailand)

17:00 83 Local Diagnostic Reference Levels (DRLs) of Interventional Radiology Procedures in Thailand: A Single Center
Miss Rasalin Thana (Thailand)

17:10 214 The Breast Microcalcification Detection in Mammogram Image by Using the Deep Convolutional Neural Network
Miss Chatsuda Songsaeng (Thailand)

17:20 Break

Radiotherapy

Time Paper no.

17:30 168 Fabrication and validation of cubic phantom embed with an accelerometer sensor for verifying six-degrees-of-freedom couch
Tippawan Popreeda (Thailand)

17:40 197 Development of an In-house MATLAB code for dynamic multileaf collimator quality assurance based on EPID
Aiyara Pishyapan (Thailand)

17:50 160 Daily machine-specific performance monitoring through clinical treatment delivery using Statistical Process Control and MobiusFX
Piyakan Wongsaroj (Thailand)

18:00 108 Acceptance Test and Commissioning of Tomotherapy Radixact X5 series in LBCH
Chonlathorn Pihusut (Thailand)

18:10 157 The preliminary survey report of the compact proton therapy unit
Mr. Tanawat Tawonwong (Thailand)

Proffered Papers in Diagnostic, Nuclear Medicine, Radiotherapy (Virtual)

Room: Duangmanee
Chair: Anchali / Krisanat

Diagnostic

Time	Paper no.	
13:00	12	Correlation between renal histological fibrosis and renal cortical thickness using shear wave elastography in patients with kidney disease *Sook Sam Leong (Malaysia)*
13:10	30	Automatic stratification of prostate cancer patients into low- and high-grade groups based on multiparametric MR image feature analysis *Akimasa Urakami (Japan)*
13:20	36	Image analysis of pancreatic cancer tissues using Haralick Features *Ashleigh Hull (Australia)*
13:30	71	Digital Breast Tomosynthesis (DBT): Dose and image quality assessment of man-made breast phantom *Nur Farrah Ezlyn Mohammad Rusdi / Nur Afizatul Izni Mohd Jasri (Malaysia)*
13:40	142	Grey Matter Segmentation of T1-Weighted MR Image in Ischemic Stroke Patients using k-Means Clustering *Dian Yuliani Alam (Indonesia)*
13:50	68	Preliminary investigation on performance of photodiode sensor as a dosimeter. *Nur Farah Huda Zulkafli (Malaysia)*
14:00	119	Evaluation of scattering spectra from an examinee during in CT scans *Kota Tsurusawa (Japan)*
14:10	6	Prediction of Tumor Growth Trajectories During Molecularly Targeted Therapy Based on Mathematical Models *Truong Gia Huy (Japan)*
14:20	38	Quantitative evaluation of deep convolutional neural network based denoising for ultra-low-dose CT *Keisuke Usui (Japan)*
14:30	161	A Preliminary Study of Various Augmentation Techniques on Deep-learning Based Classification of Lung Squamous Cell Carcinoma using Chest X-Ray *Mohammad Haekal (Indonesia)*
14:40	162	A Computational Study on Deep-learning Based Classification of Lung Adenocarcinoma using Chest X-Ray *Reza Rendian Septiawan (Indonesia)*
14:50	103	Analysis of NTCP Based Radiobiological Models: A Systematic Review of Literatures *Mahfuzur Rahman (Bangladesh)*
15:00	16	Estimation the effective and skin doses for pediatric and adult patients undergoing cardiac interventional examination using five PMMA phantoms and TLD/ionization chamber technique *Wu Keng-Yi (China (Taiwan))*
15:10	35	Facility reference level for common x-ray procedures: a preliminary study *D.M Satharasinghe (Sri Lanka)*
15:20	144	Evaluation of gonad shielding in digital radiography: Based on clinically adjustable controls. *Elly Kombo (Malaysia)*
15:30	158	Evaluation of Visually Induced Motion Sickness During Virtual Reality based Head-mounted Display Viewing using Electroencephalography

Galih Restu Fardian Suwandi (Indonesia)

15:40 13 The teaching and learning of postgraduate medical physics using Internet-based e-learning during the COVID-19 pandemic
Jeannie Wong Hsiu Ding (Malaysia)

15:50 Break

Chair: Kittiwat / Yothin

Nuclear Medicine

Time Paper no.

16:00 24 Monte Carlo simulation for high resolution imaging of Rb-82 with bremsstrahlung X-ray camera for small animals
Kouhei Nakanishi (Japan)

16:10 34 Positron Range Correction in Positron Emission Tomography
Rukiah A. Latiff (Australia)

16:20 178 Development of Flexible Radiotherapeutic Bandage Containing Samarium-153 for the Treatment of Skin Cancer
Wong Yin How (Malaysia)

16:30 136 Determination for current status of environmental radioactivity in Fukushima, using NaI (Tl) scintillation survey meter
Natsuki Miura (Japan)

16:40 46 Gamma Scintigraphy for Hepatic Radioembolization: Comparison between Different Radionuclides using GATE Monte Carlo Simulation
Fahmi MR (Malaysia)

16:50 Break

Radiotherapy

17:00 69 Preliminary evaluation of the performance of an EPID-based in vivo dosimetry for advanced radiotherapy treatment verification
Nur Nabilah Roskhahar (Malaysia)

17:10 152 Patient-specific quality assurance for IMRT delivery: A multi-centre study
Nur Diyana Afrina Hizam (Malaysia)

17:20 50 Mitigation of Error Propagation in Tele-cobalt Treatment: An Institutional Assessment
Mary Joan (India)

17:30 173 Evaluation of radionuclides and activation detected by a 15 MeV medical linear accelerator
Ryosei Ogata (Japan)

17:40 56 Dosimetric evaluation of the uncorrectable rotational setup error in total body irradiation using helical tomotherapy system
Akira Isobe (Japan)

17:50 70 Investigating the effect of material absorber the source of Gamma Knife Perfexion[TM] based on Monte Carlo simulations
Junios (Indonesia)

5 December 2020

Room: Duangchanok

Chair: Chirapha / Nualjun

08:00-08:40 Clinical Application of Small Field Dosimetry
Jan Seuntjens

08:40-09:00 Physicists and Clinical Trails: Support and Evidence for New Technology and Techniques
Tomas Kron

09:00-09:30 SIMAC (Linac Simulation Education Tool)
Marco Carlone

09:30-10:00 Automatic Plan Checking Tasks by Scripting
Michael Lamey

10:00-10:30 Coffee Break

Chair: Sivalee / Supalak

10:30-11:00 Proton Flash Therapy
Adam Harrington (Varian)

11:00-11:20 Introduction to MR-Linac
Kin Yin Cheung

11:20-11:40 Extreme Hypofractionated RT - Radiobiology & Radiobiological Models
Arun Chougule

11:40-12:00 Patient-Specific QA Management using Cloud Based
Todsaporn Fuangrod

Room: Duangkaew

Chair: Anchali / Thititip

08:00-08:30 High Patient Rad Doses from Recurrent CT Exams
Madan Rehani

08:30-09:00 Patients who received more than 100 mSv in a single day
Madan Rehani

09:00-09:30 Spectral CT
Mahadevappa Mahesh

09:30-10:00 Novel Technologies for Advanced Radiomics for Clinical Practices
Hidetaka Arimura

10:00-10:30 Coffee Break

Chair: Anchili/ Lakkana

10:30-10:50 Consideration of Stochastic Risk in Intervetional Procedures
Madan Rehani

10:50-11:10 Imaging-based Biomarkers
Yothin Rakvongthai

11:10-11:40 MS5: Eye Lens Dose of Medical Staffs in Thailand
Waraporn Sudchai, Suphot Srimahachota, Anchali Krisanachinda

11:40-12:00 Optimization of CBBCT patient dose and image quality
Kanlayanee Theerakul, Apawadee Chakrapong, Anchali Krisanachinda

Room: Duangmanee

Chair: Kitiwat / Shuichi

08:00-08:30 The Establishment of UNSCEAR Report in Thailand
Anchali Krisanachinda

08:30-09:00 Challenges in CT with Photon Counting Detectors
Picha Shunhavanich

09:00-09:30 MS 6: Facility Design of a Cyclotron, Facility Design of a PET/CT
Somanesan S.

09:30-10:00 MS 6: Radiation Emergency Preparedness in Nuclear Medicine
Chai Hong Yeong

10:00-10:30 Coffee Break

Chair: Tanawat/ Kitiwat

10:30-11:00 Theranostics in Nuclear Medicine
Shuichi Shiratori

11:00-11:30 Preparation and Application of Ga-68 in Nuclear Medicine
Shuichi Shiratori

11:30-12:00 Rapid Estimation of Muscle Tranverse Relaxation Time (T2) based on Ultrafast Magnetic Resonance Imaging at 3.0 Tesla
Noriyuki Tawara

Room: Duangmanee

12:00-13:00 Lunch Box / SEAFOMP Council Meeting

Room: Duangchanok Convention 1-2

12:10-12:30 First Demonstration of the FLASH Effect Using the MEVION S250i and Future Development of Ultra-High Dose Rate Delivery Technology
James Cooley (Mevion/ Nuclear System)

12:30-12:50 GE Healthcare CT Sim Solutions for Radiation Oncology
Manmohan Singh (GE)

12:50-13:10 QA in the Time of COVID
Yamini Sivashunmugam (Sun Nuclear)

13:10-13:30 Filmless End-to-End Stereotactic QA
Greg Robinson (Sun Nuclear)

13:30-13:50 RadCalc - Independent 3D QA Software
Elaine Theresa Mathews (Lap Laser)

13:50-14:10 New Products – RUBY & OCTAVIUS 1600 SRS)
Edmund Lo (PTW)

14:10-14:30 IBA ProteusCLASS, ARC, FLASH & Motion Management
Gavin Choo

IBA Sphinx COMPACT and Phonix, New Development of Detector for Particle Therapy
Kuan Chuan Yeh

14:30-14:50 Ethos™ Therapy: A Deep Dive into the Future of Intelligent Cancer Care
Takahiro Hara (Varian / BA)

14:50-15:10 MR-RT BBRT and Pinnacle Evolution for Brain Stereotactic Radiosurgery
(Philips)

15:10-15:30 Presentation Awards and Closing

E-Posters

Radiotherapy

Seq.	Paper no.	
1	55	Real-time in vivo dose verification using Metal-Oxide Semiconductor Field Effect Transistor (MOSFET) in HDR brachytherapy *Siti Hajar Binti Abdul Rahman (Malaysia)*
2	82	Development of external dosimetry audit system for image-guided brachytherapy in Asian Countries *Hideyuki Mizuno (Japan)*
3	124	Comparison of ICRU Point Doses and Volumetric Doses to the Rectum High Dose Rate Cobalt-60 Brachytherapy of Cervical Cancer *Yun Seang Yi (Malaysia)*
4	182	Correlation analysis of CT-based rectal planning dosimetric parameters with in vivo dosimetry of MOSkin and PTW 9112 detectors in Co-60 source HDR intracavitary cervix brachytherapy *Zulaikha Jamalludin (Malaysia)*
5	60	A development of a primary standard of absorbed dose to water for a small field in high-energy photon beam *Masakatsu Takeda (Japan)*
6	131	Construction of regional network and remote support system for linac output dose difference facilities. *Shinji Kawamura (Japan)*
7	175	Investigation for measurement of photon depth dose using UVC camera *Kengo Miyazaki (Japan)*
8	159	Impact of the Frequency of Verification with In-room CT on Setup Errors in Carbon Ion Radiotherapy for Prostate Cancer *Yushi Wakisaka (Japan)*
9	132	Determination of the beam quality correction factors for carbon-ion beams by Monte Carlo simulations and measurements *Yuka Urago (Japan)*
10	26	Effects of parallax error and light refraction on estimation for dose distribution of proton beams using luminescence in water *Koki Furuo (Japan)*
11	27	Time dependence of intra-fractional motion for spine stereotactic body radiotherapy *Ryuta Hirai (Japan)*
12	138	Calculation of an automatic irradiation path for dynamic-wave-arc irradiation *Kouichi Murashima (Japan)*
13	116	Dosimetric effect of the baseline shift in the phase and amplitude gated lung SBRT *Kenji Yasue (Japan)*
14	111	The Proposal of the Simple Alternative Planning Method for Lung/Esophageal IMRT plan in case of failure in Varian Halcyon *Yuki Tanaka (Japan)*

15 15 Evaluate the dose distribution of mono-isocenter and dual-isoncenter volumetric modulated arc therapy for synchronous bilateral breast cancer
Chung-Hsien Ho (China (Taiwan))

16 59 Remote Monte Carlo verification system of radiotherapy with multiple processor
Hiraku Fuse (Japan)

17 122 Detection of multi-leaf collimator errors in a small-field volumetric modulated arc therapy plan using portal dosimetry
Yuichi Saito (Japan)

18 147 Focus control of electron beam for arbitrary field formation
Atsushi Myojoyama (Japan)

19 143 Feasibility test of independent dose verification with Monte Carlo simulation tool at Osaka Heavy Ion Therapy Center
Taku Nakaji (Japan)

20 90 Development of method to cancel the calculation direction dependence for image processing applying diffusion equation
Kentaro Doi (Japan)

21 97 Impact of automatic image registration with contrast enhancement filter in head and neck cancer
Kouta Hirotaki (Japan)

22 115 Development of facial recognition system for patient safety : Analysis of benchmark data
Takatomo Ezura (Japan)

23 154 Development of Real - time Radioluminescence Dosimetry System for External Beam Radiotherapy: A Preliminary Study
Janatul Madinah Wahabi (Malaysia)

Diagnostic

Seq. Paper no.

24 177 LORETA as a Method of Brain Activation Analysis for Autism Spectrum Disorder: an Evaluation using Traditional Benchmarks
Sra H. Pratama (Indonesia)

25 109 Material decomposition of photon-counting CT spectra with Machine Learning
Kazumi Murata (Japan)

26 42 The Study of Correlation Between Water-equivalent Diameter (Dw) and Age on CT Examination in Pediatric Head Patient with Tube Current Modulation (TCM) Technique
Khoerun Nisa Syaja'ah (Indonesia)

27 135 Spectral distortion correction caused by pulse-pileup effects with a machine learning technique for a photon counting x-ray detector
Kohei Koyama (Japan)

28 37 The method to estimate source position for mobile tomosynthesis
Kensuke Hori (Japan)

29 33 Evaluation method of isotropic performance of CT system using "Spiral Micro Holes Phantom"
Katsumi Tsujioka (Japan)

30 31 Effect of Various Hybrid Iterative Reconstruction Method on High Resolution Scan Mode in Abdominal CT
Masato Yoshida (Japan)

31	72	Investigation on dose assessment and image quality evaluation of selected dental fillings in dental radiography. *Nur Aina Najwa Mohamad Feriza / Amira Nabila Yahaya (Malaysia)*
32	9	Image Quality Evaluation of a Hybrid Iterative Reconstruction Algorithm in the Multi-Slice Computed Tomography Scanner for the Pediatric Head Diagnostic Procedure *Mark Anthony C Burgonio (Philippines)*
33	133	Denoising of OCT images with a bandelet transform for feature extractions *Keito Sato (Japan)*
34	123	Comparison of compensation effect for non-uniform magnetic field with major grains *Kouhei Nakanishi (Japan)*
35	32	Metal Artifact Reduction using Tilt Scan Technique in CT *Katsumi Tsujioka (Japan)*
36	216	Bone mineral density screening in a rural population, Ayutthaya, Thailand *Chatnapa Nuntue (Thailand)*
37	62	The study of Power Spectral Density Value Ratio between Wet and Dry Electrodes with Electroencephalography (EEG) Using Audio Stimulus *Nur Faadhilah Afif (Indonesia)*
38	54	Investigating the current status of Medical Physics in Sri Lanka. *Dr. Vijitha Ramanathan (Sri Lanka)*
39	23	The role of a medical physicist in an advanced emergency pediatric hospital *Manabu Yoshimoto (Japan)*
40	164	Deploying Long Short-Term Memory (LSTM) Network to Classify EEG Signal for Epileptic Seizure Detection *Sra H. Pratama (Indonesia)*
41	151	The Optimal Number of Features in Epileptic Seizure Detection Using K-Nearest Neighbor Classification *Fauzia Puspa Lestari (Indonesia)*
42	21	Using Radial Basis Function-Kernel Support Vector Machine with Tree-Based Feature Selection for Cancer Type Prediction Based from Gene Expressions *Adrian S. Remigio (Australia)*
43	104	CT-based convolutional-neural-network segmentation of poorly differentiated HCCs with lung-cancer-based transfer learning *Noriyuki Nagami (Japan)*
44	179	Fabrication of Bismuth-Polymer Composite for Additive Manufacturing of Radiation Shielding *Wong Yin How (Malaysia)*
45	25	Change of CTDIvol in medical exposure management of computed tomography. *Hiroki Ohtani (Japan)*
46	29	Effects of Quercetin on adipogenesis by studying the metabolic profiles by NMR *Aye Thidar Moe Moe (Thailand)*
47	47	Single-scan method for the inner ear in cone-beam computed tomography *Yuki HAYAKAWA (Japan)*

Nuclear Medicine

Seq.	Paper no.	
48	120	Diagnostic performance of I-131 MIBG scintigraphy in 101 patients suspected for pheochromocytoma/paraganglioma: a comparison between visual and semi-quantitative planar analyses and a hybrid SPECT/CT imaging *Pikom Sirisopausa (Thailand)*
49	110	99mTc-Labeled Bismuth Nanoparticles for Contrast Enhancement in SPECT-CT Imaging: A Phantom Study *Fazizulafizi Bin Madin (Malaysia)*
50	67	Image reconstruction method based on a deep learning in a multi-pinhole SPECT system *Hiroaki Konno (Japan)*
51	63	Improvement of the spatial resolution with a deconvolution method in a pinhole SPECT system *Michi Okoshi (Japan)*
52	105	Estimated Radiation Dose Received By Resuscitation Providers Following the CPR Operation of a Patient Undergoing a Nuclear Medicine Studies *Paya Dardaranonda, Prapapan Saenbandit (Thailand)*
53	186	Optimal administered activity for Tc99m MDP SPECT-Bone scan patients in relation to body mass index *Ms. Wasinee Thiangsook (Thailand)*
54	17	Shielding Calculation for a Diagnostic Nuclear Medicine Facility *Marlon Raul Z (Philippines)*
55	193	Inter-laboratory comparisons of ring dosimeters in term of Hp(0.07) *Nittima Rungpin (Thailand)*

Abstract

Invited Presentations

JOHN CAMERON MEMORIAL LECTURE:
New Additions to the Scientific Dictionary and Encyclopaedia on Medical Physics

Slavik Tabakov[1,2,3]

1 King's College London, UK
2 IUPESM Vice-President
3 Chair Editorial Board of Scientific Dictionary and Encyclopaedia on Medical Physics

Introduction: The Scientific Dictionary and Encyclopaedia on Medical Physics exist 10 years as a free reference resource for the profession. The project for their development attracted over 320 specialists from 36 countries. Their dedicated web site (www.emitel2.eu) has over 5,000 visits per month worldwide. The development of this huge project passed through 6 phases. The current 6th phase was completed during 2017-2020 – new additions including new articles and languages.

Purpose: The purpose of the Scientific Dictionary and Encyclopaedia on Medical Physics is to support the education of medical physicists worldwide. Over the past 10 years the profession developed further - new methods and equipment were introduced in clinical practice. Due to this reason new encyclopaedic articles were added to the existing ones.

Methods: The new materials for the Encyclopaedia were distributed as per the existing Workgroups. Additionally new Groups were introduced – on Non-ionising radiation and Clinical engineering. The update phase used the original methodology of the Encyclopaedia – Workgroups of specialists with internal and external reviewing of the articles. The translation of the new terms was made on national basis, in parallel with the encyclopaedic articles update.

Results: The updated edition of the Encyclopaedia of Medical Physics contains over 3300 cross-referenced articles related to medical physics and associated technologies. The materials are supported by over 1300 figures and diagrams. Additionally the Encyclopaedia includes over 600 synonyms, abbreviations and other linked entries. The existing materials were organised as per the main fields of the profession: X-ray Diagnostic Radiology, Nuclear Medicine, Radiotherapy, Ultrasound Imaging, Magnetic Resonance Imaging, Radiation Protection, General Terms. The Scientific Dictionary was updated by translating all new terms into 31 languages.

Conclusion: These free reference materials support medical physics students worldwide. They are especially useful for the colleagues from Low and Middle Income (LMI) Countries.

Keywords: Education, Encyclopaedia of Medical Physics, Scientific Dictionary of Medical Physics, Online Reference resources

Professor Kiyonari Inamura Memorial AFOMP Oration 2020

Kin Yin Cheung

Hong Kong Sanatorium & Hospital, Hong Kong SAR

The medical physics profession in the AFOMP region in general has gone through admirable development since year 2000 when the Federation was founded. The enormous achievements could be the outcome of increasing demands for quality medical services that was driven by economic prosperity in the region during this period of time. In the case of radiation medicine, provision of advanced disease diagnosis and treatment services demanded the implementation in large scale of sophisticated equipment technologies in the clinics and the corresponding demand for manpower to operate the service. This in turn paved the way for establishing the infrastructure and resources for training of healthcare professionals, including medical physicists. The speed and scale of the developments in AFOMP could not have been possible without the vision, efforts and contributions of the leaders and grandfather medical physicists in the respective countries or regions. The contributions of AFOMP together with IOMP in setting international standards on such issues as education and training requirements for medical physicists, and provision of guidance, resources and supports in establishing a platform for networking, collaboration and mutual support amongst the medical physics organizations on such matters as education and training, scientific exchange and experience sharing also played an important part in the development of the profession. The inclusion by IAEA in their new International Safety Standard (a document endorsed by the relevant UN Agencies including WHO and ILO) the definition and the role and responsibility of medical physicist has also helped promoting the recognition of medical physicists as health professionals by national health and regulatory authorities in IAEA member countries. The initiatives of the individual national organizations in establishing national professional certification boards have helped promoting the standard of practice of the medical physicists. IMPCB also contributed to the AFOMP success from the aspect of quality audit on medical physicist certification boards.

JSMP INVITED LECTURE:

Evaluation of ionising radiation induced DNA damage on a cell and prediction of biological response by integrated track structure Monte Carlo simulations using Geant4-DNA

Dousatsu Sakata[1], Nathanael Lampe[2], Mathieu Karamitros[2], Ioanna Kyriakou[3], Oleg Belov[4], Marie-Claude Bordage[5,6], Vladimir Ivanchenko[7,8], Ivan Petrovic[9], Aleksandra Ristic-Fira[9], Wook-Geun Shin[2,10], Dimitris Emfietzoglou[3], Susanna Guatelli[11] and Sebastien Incerti[2,10]

1 Department of Accelerator and Medical Physics, National Institute of Radiological Sciences, QST, Chiba, Japan,
2 CNRS, IN2P3, CENBG, UMR 5797, Gradignan, France,
3 Medical Physics Laboratory, University of Ioannina, Medical School, GR-45110 Ioannina, Greece,
4 Joint Institute for Nuclear Research, Dubna, Russia,
5 INSERM, Université Paul Sabatier, UMR 1037, CRCT, Toulouse, France,
6 Université Toulouse III-Paul Sabatier, UMR 1037, CRCT, Toulouse, France,
7 Geant4 Associates International Ltd, Hebden Bridge, UK,
8 Tomsk State University, Tomsk, Russia,
9 Vinca Institute of Nuclear Science, University of Belgrade, Belgrade, Serbia,
10 Université de Bordeaux, CENBG, UMR 5737, Gradignan, France,
11 Centre for Medical Radiation Physics, University of Wollongong, Wollongong, NSW, Australias
Corresponding author: Dousatsu Sakata [4-9-1 Anagawa, Inage-ku, Chiba- shi, Chiba 263-8555, Japan]・ sakata.dousatsu@qst.go.jp

1. Introduction

Simulation of radiation induced DNA damage and following biological repair is still a challenging issue due to their complexity. Monte Carlo (MC) mechanistic simulations are a promising tool for the modelling of DNA damage induction by ionising radiation. They indeed provide functionalities which allow us to simulate physical interactions and radiolysis chemical processes in combination with simplified geometries of biological targets for the prediction of such damage. In the last decades, several MC codes were developed to predict DNA damage, like KURBUC, PARTRAC and Geant4- DNA. Recently, Geant4-DNA has demonstrated the possibility to evaluate early DNA damage in an E. coli bacterium and in a fibroblast cell nucleus irradiated by protons. In particular, we have presented for the first time the combination of the features across physics, chemistry and biological geometry, in a single Geant4-DNA application for the modelling of early DNA damage induction in a cell nucleus [1]. However, it is still a challenge to model biological response against such early DNA damage. In this talk, we present our progress on the extension of Geant4-DNA for the early biological DNA damage and repair.

2. Materials and Methods

As used in our previous work, we have built a fractal-based cell nucleus geometry composed by double-helix DNA fibre and histone [1]. We simulated physical particle interactions followed by the production of radiolysis molecular species, diffusion of free radicals and ions as well as chemical reactions under gamma and proton irradiation. Through "track-structure simulations, early DNA damage (typically, created within 1 μ s after irradiation) can be calculated by the microscopic energy deposition pattern in the region surrounding DNA molecules, as well as by the interaction of molecular species created during water radiolysis (typically hydroxyl radicals). Then, resulting damage clusters are classified according to the damage type definition proposed by Nikjoo, for the purpose of calculating damage complexity used in biological prediction models. The simulations provide two biological predictions for the γ H2AX foci yield and the survival fraction. The biological prediction model for foci yield has been developed by one of our collaborators, Dr Oleg Belov [2], and the survival fractions obtained by the Two-Lesion Kinetic model [3] using the optimized model parameters for proton irradiation.

3. Results and Discussion

Using the Geant4-DNA, it's possible to simulate early

DNA damage when a cell is irradiated by protons and gamma from ^{60}Co. The simulated numbers of DSB for protons and gamma are in agreement with the corresponding experimental data within 13.3% and 2.5% respectively. With the numbers of DSB and complexity of DSB as inputs, survival fraction and foci yields can be calculated by the use of the corresponding prediction model. For instance, Figure 1 shows the survival fraction of V79 cell after 1.5 MeV proton irradiation and the scaled yield of γ H2AX till 24 hours after from gamma irradiation from a ^{60}Co radiation source. Both the simulated survival fraction and foci yield show a good agreement with experimental data.

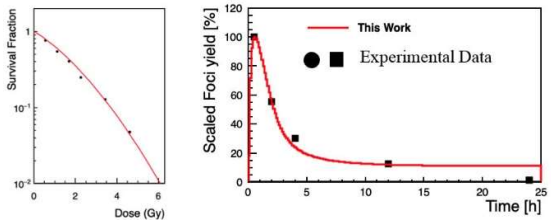

Figure1: Left; Survival fraction of V79 after proton irradiation as a function of dose. Right; γ H2Ax yield after gamma irradiation as a function of time up to 24 hours.

4. Conclusion

We have developed for the first time a Monte Carlo simulation model based on Geant4-DNA that calculates, in addition to early DNA damage, biological quantities such as survival fraction and foci accumulation for γ H2AX. This integrated simulation chain will allow us to further explore the mechanisms of ionising radiation induced DNA damage.

References

1) D. Sakata et al, "Evaluation of early radiation DNA damage in a fractal cell nucleus model using Geant4-DNA", Phys. Med. 62 (2019) 152-157
2) O. Belov et al, "A quantitative model of the major pathways for radiation-induced DNA double-strand break repair", Journal of Theoretical Biology 366 (2015) 115–130
3) R. D. Stewart, "Two-Lesion Kinetic Model of Double-Strand Break Rejoining and Cell Killing", Rad. Res. 156 (2001), 365–378

Impact of radiosensitivity and gender on paediatric cranial tumours following proton and photon intensity modulated radiation therapy – A radiobiological response modelling study

Mikaela Dell'Oro[1,2], Michala Short[1], Puthenparampil Wilson[2,3], Eva Bezak[1,4]

1 Cancer Research Institute, University of South Australia, Adelaide, SA 5001, Australia,
2 Department of Radiation Oncology, Royal Adelaide Hospital, Adelaide, SA 5000, Australia,
3 UniSA STEM, University of South Australia, Adelaide, SA 5001, Australia,
4 Department of Physics, University of Adelaide, Adelaide, SA 5005, Australia

Introduction: Medulloblastoma is the most diagnosed paediatric malignancy of the central nervous system. Despite the high number of paediatric patients treated with intensity-modulated photon (IMRT) and proton (IMPT) radiotherapy, risk factors for increased normal tissue complication probability (NTCP) are still not fully understood. Disparities in intrinsic radiosensitivity (α/β ratio) for paediatric patients exist, influencing NTCP outcomes. Additionally, literature suggests that TD50 can be ~20% lower in female patients.

Purpose: Following this data, our aim was to model the impact of gender and intrinsic radiosensitivity on paediatric brain tumour IMRT and IMPT outcomes.

Methods: 216 comparative IMRT and IMPT plans were created for six paediatric patients, using Varian Eclipse software. Relative-seriality and Lyman-Kutcher-Burman models were used to calculate NTCP values for cranial irradiation of several anatomical structures. Evaluated complication endpoints included brainstem necrosis, blindness, and deafness. Sensitivity analyses were performed to gauge the impact of α/β values and TD50 on radiation response.

Results: IMPT plans demonstrated smaller side-effect risks compared to IMRT across all NTCP models. For medulloblastoma, tinnitus and brainstem necrosis NTCP depended on modality and TD50 of irradiated normal tissue, therefore NTCP could be potentially underestimated in female paediatric patients (Graph 1). Similarly, IMPT demonstrated advantages for NTCP across all tested α/β values compared to IMRT, with lower α/β values estimating a reduced risk of adverse side effects (Graph 2). If the true α/β of these paediatric tissues are higher than predicted (α/β ~3), planning could severely increase risk of cochlea tinnitus for IMRT. In general, NTCP for IMPT was not as influenced when changing parameters in the model compared to IMRT.

Conclusion: This study aimed to estimate the impact of gender on NTCP for paediatric cranial critical structures. Modified NTCP calculations can be used for ranking of treatment plans to better stratify patients who would benefit most from IMPT.

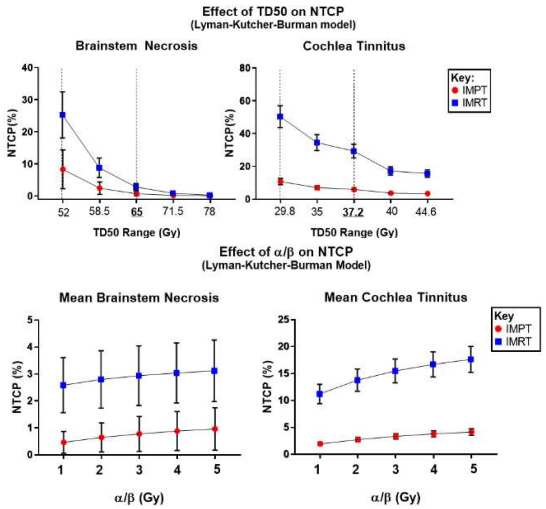

Graph 1. Effect of TD50 on NTCP of brainstem necrosis and cochlea tinnitus for medulloblastoma patients. TD50 for females is approximately 20% lower than males, this is represented by the first dashed line compare to the second line (underlined TD50) which illustrates the mean value. Therefore, females will potentially have a higher NTCP for the given dose distribution.

Graph 2. Effect of α/β on NTCP of brainstem necrosis and cochlea tinnitus for medulloblastoma patients.

Comparisons of DNA damage in HPV negative and positive head and neck cancer cell lines following fractionated irradiation.

Paul Reid[1,2*], Alexander H. Staudacher[6,8], Loredana G. Marcu[1,3], Ian Olver[2,7], Leyla Moghaddasi[4,5], Eva Bezak[1, 2, 4]

1 School of Health Sciences, University of South Australia, Adelaide, SA 5001, Australia.
2 Cancer Research Institute, University of South Australia, Adelaide, SA 5001, Australia.
3 Faculty of Science, University of Oradea, Oradea 410087, Romania.
4 Department of Physics, University of Adelaide, Adelaide, SA 5005, Australia.
5 Genesis Care, Adelaide Radiotherapy Centre, Adelaide, SA 5000, Australia
6 Translational Oncology Laboratory, Centre for Cancer Biology, SA Pathology and University of South Australia, Adelaide, SA 5000, Australia.
7 School of Psychology, University of Adelaide, Adelaide, SA 5000, Australia.
8 School of Medicine, University of Adelaide, Adelaide, SA 5000, Australia.

Introduction: Significantly better responses to treatment for head and neck squamous cell carcinoma (HNSCC) resulting from human papillomavirus (HPV), compared to other causes, is an important focus of research for dose de-escalation.

Purpose: To examine the intrinsic response of HNSCC cell lines to fractionated X-radiation, comparing between HPV positive and negative groups. Potential to repair DNA, using measures of γH2AX resolution, and the accumulation of chromosomal damage following 4 Gy fractions were investigated.

Methods: Three cell lines of each HPV status were irradiated with 4 Gy fractions. Cells surviving 4 Gy were re-cultured to become the next generation of that cell line before reirradiation and plating for microscopy. Expression of γH2AX was measured by flow cytometry at ½ and 24 hours post 4 Gy irradiation.

Results: γH2AX resolution was greatest in the first generation of all cell lines but the extent of recovery varied, ranging from 60.6% for the cell line UM-SCC-17a to 11.8% for cell line UM-SCC-1(figure 1). All cell lines displayed deceasing γH2AX response at 30 min post 4 Gy and increasing residual expression at 24 hours with accumulating absorbed dose. Cross-sectional area of nuclei increased 158% and 303% in HPV negative and HPV positive cell lines respectively after three 4 Gy fractions. The extent of γH2AX recovery and the accumulation of residual expression was mixed between cell lines and HPV status. All lines however, showed a decreasing ability to resolve γH2AX in subsequent generations. This was supported by increasing signs of nuclear disfunction and chromosomal anomaly in the later generations of cells by micrograph.

Conclusion: HPV positive and HPV negative cell lines demonstrate accumulation of DNA damage while HPV positive cell lines, as a group, demonstrate significantly greater change in nuclear size with progressive fractional dose.

Keywords: Head and neck cancers; HPV; γH2AX: Radiation; DNA.

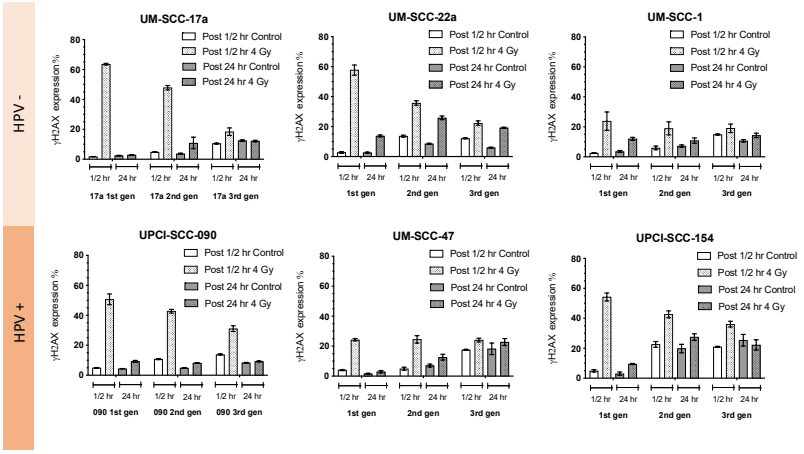

Figure 1. Change in γH2AX expression post 4 Gy fractions.

MS 1:
Proton Therapy in Hong Kong

Kin Yin Cheung

Hong Kong Sanatorium & Hospital, Hong Kong SAR

An overview on the design philosophy and site specific requirements and features of the first proton therapy facility in Hong Kong will be presented together with the key milestone developments of the project such as site planning and design, equipment installation, testing and commissioning for clinical service. Some of the challenges encountered from physics perspective during the various stages of the project will also be discussed.

MS 2: JSRT

Clinical application of the latest radiation technology – CT

Kosuke Matsubara

Department of Quantum Medical Technology, Faculty of Health Sciences, Institute of Medical, Pharmaceutical and Health Sciences, Kanazawa University, Kanazawa, Japan

Introduction: Significant technological improvements of CT are still going on, and they shifted from increasing the gantry rotation speed and adding more detector rows toward developing technologies such as dual-energy imaging and applications, new image reconstruction algorithms, and applications of dose reduction. It is necessary for physicists/technologists to evaluate the usefulness of those new technologies in CT and determine whether they can be applied to clinical practice based on the evaluation results.

Purpose: This presentation shows some examples of the latest technologies in CT and the possibility of their clinical application.

Dual-energy imaging and application: Dual-energy CT is provided by all major CT manufacturers, and there are different implementations of dual-energy CT in clinical routine. Various clinical applications of dual-energy CT have been developed and evaluated such as virtual nonenhanced imaging, automated bone removal, urinary stone classification, and metal artifact reduction.

Image reconstruction algorithm: Filtered back projection (FBP) is being replaced by iterative reconstruction (IR) algorithms. Because IR exhibits more nonlinear behaviour than FBP, task-transfer function is useful for characterizing the properties that are introduced by IR algorithms. Recently, image reconstruction algorithms based on deep learning has been introduced, and their effectiveness in clinical practice needs to be proven.

Application of dose reduction: In CT, automatic exposure control (AEC) is essential to ensure proper dose management for patients. A systematic approach for characterizing AEC is needed when optimizing acquisition protocols, and the Mercury 4.0 phantom can assist physicists/technologists in completing these tasks.

Keywords: CT, dual-energy, iterative reconstruction, automatic exposure control

MS 2: JSRT

Clinical application of the latest radiation technology in Magnetic Resonance Imaging

Yasuo TAKATSU, Ph.D.[1,2]

1 Department of System Control Engineering, Graduate School of Engineering, Tokushima Bunri University
2 Department of Radiological Technology, Faculty of Health and Welfare, Tokushima Bunri University

Topics of Magnetic Resonance Imaging

Amide proton transfer (APT) imaging
Chemical exchange saturation transfer (CEST) imaging is a method of molecular imaging in MRI, and its representative one is APT imaging. APT imaging gives contrast based on the concentration of peptide (amide group) in mobile protein and exchange rate, and is applied to the assessment of malignancy of brain tumours and differentiation between radiation necrosis and brain tumour recurrence.

3D nerve view
3D SHINKEI (nerve view) is based on 3D fast spin echo T2-weighted images Selective fat suppression pulses for suppressing signals from bone and adipose tissue existing around peripheral nerves, iMSDE pulse suppresses blood vessel signal and short T2 value; such as muscle tissue. As a result, it becomes possible to suppress background signals and selectively visualize nerves.

Gd-EOB-DTPA
Basically, MR examination takes long scanning time; therefore, long examination. Especially Liver MRI using Gd-EOB-DTPA.
The management about throughput or avoiding fatigue for the patient due to long examination, based on the cutoff value of quantitative liver-spleen contrast ratio, was performed.

MS 2: JSRT

Clinical application of the latest radiation technology in Nuclear Medicine

Kohei HANAOKA, Ph.D.

Institute of Advanced Clinical Medicine, Division of Positron Tomography, KINDAI University

Nuclear medicine and molecular imaging has been developed tremendously. Radionuclides have been used for the diagnosis and therapy of cancers. In Japan, about 1.8 million studies are performed annually, especially on bone, the heart, the brain and cancer. 18F-FDG, which images glucose metabolism, has been widely used as the management of lung, colorectal and other cancers. Currently, there are more than 500 scanners have been installed in most of the prefectures. Furthermore, radionuclides are also employed in the therapy of cancer.

Hybrid imaging systems integrating nuclear medicine imaging and CT or MRI into PET/CT, SPECT/CT and PET/MRI provide important functional and anatomical information. And the development of modern technology can make new applications safer.

The Nuclear Medicine Division is the Japanese Society of Radiological Technology's sub group which consists of members who share an interest in the improvement of academic levels in the field of nuclear medicine scanning and nuclear medicine imaging.

The contents of this presentation are as follows.
1. Current Development and Strengths of Nuclear Medicine Technology
2. JSRT's activities in Nuclear Medicine
- introduction of related papers from JSRT members
- group research for technical evaluation
- joint research with other institutions

IAEA Activities in Support of Recognition of the Medical Physics Profession

Giorgia Loreti[1], Debbie van der Merwe[1]

1 IAEA, Vienna

Introduction: Despite the inclusion of medical physics as a health profession by ILO in 2008, the recognition of medical physics in Member States has been limited. The IAEA aims to promote and support medical uses of radiation in order to ensure that all patients have access to safe and effective services, provided in accordance with international best practices.

Purpose: For more than a decade, the IAEA has made concerted efforts to highlight medical physics professional recognition, through the support of appropriate education and training, amongst other activities. This presentation describes this approach, as well as some efforts that have been made to track outcomes.

Methods: To support the medical physics profession, the IAEA works simultaneously on:
- coordination of an international postgraduate programme in Medical Physics and its monitoring
- development and dissemination of harmonized guidelines
- provision of support to Member States through national or regional technical cooperation projects, facilitated through the use of online tools
- support to clinically qualified medical physicists.

Results: The IAEA-supported ICTP/UT Master of Advanced Studies in Medical Physics (MMP) has been instrumental in disseminating best practices and in producing professionals who could lead in the establishment and development of the medical physics profession in their national settings. Surveys of graduates have revealed limited brain drain; however, recognition is still a challenge.

Instruments such as AMPLE, MRP Net and other regionally driven tools help enhance networking and community. Specific guidelines focussing on supporting quality education and continuous professional development are made available to underpin the work of medical physicists.

Professional guidelines continue to be developed and updated.

Conclusion: To support the medical physics profession, the IAEA has aimed at a coordinated multi-facetted outreach converging on promoting the recognition of the profession with activities that favour Member States' ownership and have fostered regional collaborations.

Keywords: Medical Physics, Recognition, Healthcare

South Asia Centre for Medical Physics and Cancer Research (SCMPCR): A Centre of Excellence to Fight against Cancer in South Asia Region

H.A. Azhari[1,3], G.A. Zakaria[1,2,3], V. Steil[4], F. Hensley[5]

1 South Asia Centre for Medical Physics and Cancer Research, Dhaka, Bangladesh
2 Ex-Gummersbach Hospital of Klinikum Oberberg, Medical Radiation Physics, Teaching Hospital of the University Cologne, Gummersbach, Germany
3 Gono Bishwabidyalay (University), Department of Medical Physics and Biomedical Engineering (MPBME), Savar, Bangladesh
4 Radiooncology, University Medical Center Mannheim, Mannheim, Germany
5 Ex-Department of Radiation Oncology, Heidelberg University, Heidelberg, Germany

Introduction: Cancer is one of the major causes of morbidity and mortality among non-communicable diseases in the world. South Asian countries face a big challenge in all four key components of cancer control such as prevention, early detection, diagnosis and treatment. This well-known fact indicates that this region of the world requires improvement strategies in cancer management. In order to address the aforementioned issues, Medical Physics education starts through some seminars at Bangladesh in 1996 in cooperation with the Task group K16 "Medical Physics in the Developing Countries" of the German Society of Medical Physics (DGMP). With the help of German collaboration and DAAD, the Medical Physics education and research is still developing sector in Bangladesh. To extend the Medical Physics education and research and fight against cancer, SCMPCR started its journey in 2018 with a mission to advance cancer care practice in Bangladesh and in other countries in South Asia by disseminating scientific information, fostering the educational and professional development and promoting the highest quality medical services for patients.

Material and Methods: SCMPCR does awareness campaign about cancer, its warning signs with a focus on the importance of early diagnosis in treatment of cancer, by visiting into the rural area over Bangladesh. Alongside, a screening program will be executed in parallel with the awareness program. In addition, SCMPCR made a self-group of the cancer patient for increasing cancer awareness, patient support and patient to patient communication. On the other hand, capacity building of cancer professionals is made by the hands-on training program by the highly experienced international trainer.

Results: Until now, SCMPCR was arranged five hands-on training programs for the cancer professionals of South Asia region (4 for medical physicists, 1 for radiation oncologists). The trainers of those training programs came from Germany, Japan, India, Canada and Taiwan and Bangladesh. The training program of SCMPCR maintains the international standard and accredited by the international organization. In the COVID 19 pandemic situation from 2020 first online program on medical physics in Bangladesh is organized by SCMPCR three times in a year.

Conclusion: SCMPCR works as a model cancer centre with the cancer professionals, local government community health workers and increasing awareness and provision of support for the cancer patient in the South Asia region. Our centre is a good example of south-south cooperation in South Asia region and it will also expand its activities in other developing countries especially in Africa continent.

Keywords: SCMPCR, hands on traing, Awareness, Self Help Group, Welfare home

Radiation incidents and accidents in radiotherapy

Golam Abu Zakaria, Ph.D

South Asia Centre for Medical Physics and Cancer Research (SCMPCR), Dhaka, Bangladesh and
Former Chairman, Department of Medical Radiation Physics, Gummersbach Hospital of Klinikum Oberberg, Academic Teaching Hospital of the University of Cologne, Gummersbach, Germany

The aim in radiotherapy is to deliver a precisely predetermined dose to the malignant target region without causing injury to surrounding healthy tissue. An accident or a miss-administration in radiotherapy is significant if it results in either an underdose or overdose, whereas in conventional radiation protection only overdoses are generally of concern. Therefore all procedures should be performed in such a way as to optimize the dose to tumor volume and to minimize the dose to healthy tissue.

According to ICRU Publication 112, a quality assurance program should be established to implement a new technology considering the following points for an overall preventive measure:

- Lessons from conventional techniques
- Safety awareness of all responsible persons for radiotherapy
- Manufacturers responsibility
- Program of purchasing, acceptance and commissioning
- Need for new protocols for treatment prescription and dosimeter
- Decision of dose escalation
- Safety-critical communication and notifications
- Computers and data integrity
- Updating of quality control tests
- Using lessons from experience
- Overcoming the lack of experience when introducing new technologies

National Diagnostic Reference Level (NDRLs) of Procedures in Cardiac Catheterization Laboratory in Thailand: A Multi Center Survey

Suphot Srimahachota[1], Panruethai Trinavarat[2], Anchali Krisanachinda[2], Kornkamol Prajumchuae[3], Waraporn Sudchai[4]

1 Cardiac center and Department of Medicine, Faculty of Medicine, Chulalongkorn University, Bangkok 10330, Thailand
2 Department of Radiology, Faculty of Medicine, Chulalongkorn University, Bangkok 10330, Thailand,
3 Department of Radiology, King Chulalongkorn Memorial Hospital, Bangkok 10330, Thailand
4 Thailand Institute of Nuclear Technology (Public Office)

Introduction: The International Commission on Radiological Protection (ICRP) recommended the establishment of reference levels as the method for optimization of the radiation exposure. Diagnostic Reference Level (DRLs) was introduced by ICRP Publication 73 in 1996. Cardiac angiography and interventional procedures constitute one of the examination major methods applied to the diagnosis and therapeutic procedures. During CAG and PCI, the same area is exposed to radiation for a long period, and therefore, there is a high possibility of occurrence of radiation injury to the skin. In this survey on national diagnostic reference level (NDRLs) for coronary angiography (CAG), percutaneous transluminal coronary intervention (PCI) procedures and PPM (Permanent Pacemaker implantation) at ten centers of tertiary healthcare hospitals had been studied in 2019 in Thailand.

Purpose: To determine the National Diagnostic Reference Levels (NDRLs) of procedures in cardiac catheterization laboratory.

Methods: The survey covered 1102 common procedures, 366 CAG procedures, 397 PCI procedures, 339 permanent pacemaker implantation (PPM), and 29 R/F equipment had been used in this survey. **Results:** In CAG, 75th Percentile (DRLs) of total kerma-area–product (KAP) and air kerma were 28 $Gy.cm^2$ and 379 mGy respectively. In PCI, DRLs for KAP and AK were 82.2 $Gy.cm^2$ and 1332 mGy respectively. For PPM, the DRLs for total KAP and AK were 5.8 $Gy.cm^2$ and 58.5 mGy respectively.

Conclusion: This is the first study to introduce the DRLs for common interventional cardiovascular procedures in Thailand. The results will help the optimization of patient dose in the interventional cardiology procedures at some center in Thailand. When we compare our DRLs with Jung Su Kim et al[3] studies, our DRLs are lower than Korean DRLs of CAG of 47.0 $Gy.cm^2$ and PCI DRLs 171.38$Gy.cm^2$

Keywords: DRL, coronary angiography, percutaneous transluminal intervention (PCI), ICRP, 75th percentile.

Outline of updated national diagnostic reference levels in Japan (Japan DRLs 2020)

Kosuke Matsubara

Department of Quantum Medical Technology, Faculty of Health Sciences, Institute of Medical, Pharmaceutical and Health Sciences, Kanazawa University, Kanazawa, Japan

Introduction: National diagnostic reference levels (NDRLs) were updated in Japan after five years since the first NDRLs had been published in 2015. According to the International Commission on Radiological Protection (ICRP) Publication 135, NDRLs should be reviewed at regular intervals (3–5 years) in order to promote the optimization of protection by implementing them and to respond to changes in technical progress and clinical demands.

Purpose: This lecture offers an outline of the updated NDRLs in Japan (Japan DRLs 2020) especially those for CT and diagnostic fluoroscopy.

Details: During the updating process of the NDRLs in Japan, ICRP Publication 135 was used as a reference. Japan DRLs 2020 includes DRLs for CT (adult CT and pediatric CT), general radiography, mammography, dental radiography (intraoral radiography, panoramic radiography, and dental cone beam CT), interventional radiology, diagnostic fluoroscopy, and nuclear medicine (SPECT radiopharmaceuticals, PET radiopharmaceuticals, SPECT/CT hybrid CT, and PET/CT hybrid CT). In the DRLs for adult CT, the DRL values were updated, those for "acute pulmonary thromboembolism and deep vein thrombosis" and "whole-body CT for trauma" were newly added, and the weight range of the standard-sized patient changed from 50–60 kg to 50–70 kg. In the DRLs for pediatric CT, weight bands in addition to age bands were introduced for setting DRL values. The DRLs for diagnostic fluoroscopy, which included 12 examination types, were newly set although they had not been set in the first NDRLs in Japan (Japan DRLs 2015). Incident air kerma at the patient entrance reference point, air kerma-area product, fluoroscopic time, and number of images per examination were selected as DRL quantities.

Expected outcome: By enforcing the partial revision of the Enforcement Regulations of the Medical Care Law that includes the safety management of radiation for medical use in April 2020 in Japan, the optimization at each institution is expected to be promoted using these updated NDRLs.

Keywords: diagnostic reference level, optimization, safety management, CT, diagnostic fluoroscopy

National DRLs in Thailand

Panruethai Trinavarat[1], Anong Singkavongsay[2], Tawatchai Chaiwatanarat[1], Suphot Srimahachota[1], Pisit Wattanaruangkowit[3], Jiraporn Laothamatas[4], Anchalee Churojana[5], Nucharin Supakul[4], Napapong Pongnapang[6]

1 Faculty of Medicine, Chulalongkorn University,
2 Department of Medical Sciences, Ministry of Public Health,
3 Faculty of Medicine, Thammasat University,
4 Faculty of Health Science Technology, HRH Princess Chulabhorn College of Medical Sciences, Chulabhorn Royal Academy,
5 Faculty of Medicine, Siriraj Hospital, Mahidol University,
6 Faculty of Medical Technology, Mahidol University

National DRLs in Thailand for "Projection Radiography" have been established in 2017, "Computed Tomography" in 2018, "Mammography" in 2019, and "Interventional Radiography" in 2020, from the surveys performed by the Department of Medical Sciences, Ministry of Public Health (DMSc, MoPH) on the most common examinations performed in each imaging modality. The project of DRLs in Interventional Radiology was under the cooperation of DMSc, MoPH and the Thai Society of Vascular & Interventional Radiology and also the Royal College of Radiologists of Thailand.

Additional DRLs have also been established or are during the process of survey by the groups leaded by radiologists and cardiologists in University Hospitals since 2018, some projects coordinating with the Office of Atom for Peace (OAP) passing the ad hoc subcommittee for national DRLs of the OAP.

The values of the DRLs in Thailand comparing to those of other countries will be presented in the meeting. Official report of national DRLs in Thailand will be announced in 2021.

Beside the survey with manual record, a pilot project of Thailand CT dose registry is getting started in 2021 by installation of dose tracking software in 9 public hospitals and sending CT dose data to the central server at the OAP. This project was initially started by radiologists in University Hospitals and has been assisted by the IAEA, then transferring to the OAP with the cooperation of the hospitals in the MoPH.

Dose monitoring and audit, tools for patient dose optimization

Napapong Pongnapang

Department of Radiological Technology, Faculty of Medical Technology, Mahidol University

Throughout the past decades, diagnostic and interventional radiology have been known as major sources of radiation dose exposed to the world population. The International Basic Safety Standard (BSS) issued by the International Atomic Energy Agency (IAEA) clearly outlines key activities in radiation protection from medical exposure. Those activities include justification, optimization and limitation of dose. The BSS requires optimization of protection and safety for each and every medical exposure. Key components of optimization include patient dosimetry and Dose Reference Levels (DRLs). Patient dose monitoring and audit have been used as tools for optimization and required by either regulation or accreditation such as the Joint Commission (JCI).

The speaker aims to provide information regarding the use of dose monitoring software in radiological practice. How to start up the monitoring, important role of clinical medical physicists in diagnostic radiology, JCI compliance issues, DRLs and audit systems. Benefits of the dose monitoring software in a purpose of national dose index registry will also be discussed.

Clinical Aspects for Theranostics in the Era of Precision Medicine

Maythinee Chantadisai, MD.

Division of Nuclear Medicine, Department of Radiology, Faculty of Medicine, Chulalongkorn University,
King Chulalongkorn Memorial Hospital, The Thai Red Cross Society, Bangkok, Thailand.

The term “theranostics” is a combination of diagnostics and therapy by using the same/ or very similar molecule labelled with diagnostic and therapeutic radionuclides for treating patients within a concept of targeted therapy and precision medicine. The first theranostic radiopharmaceutical was radioiodine, which was used for therapy and imaging in thyroid diseases. In recent years, the theranostics concept then progressed through the treatment of other advanced cancers mainly in neuroendocrine neoplasia (NEN) and prostate cancer. Numerous clinical trials and practice guidelines were established for radiolabeled somatostatin analogs called peptide receptor radionuclide therapy (PRRT) in treating NEN, mostly in patients with advanced metastatic gastroenteropancreatic tumors. The well-known randomized controlled phase III study (NETTER-1 trial) showed a significant clinical benefit of PRRT plus octreotide over octreotide alone, with some common adverse events such as mild nausea and vomiting. Grade 3 or 4 hematologic toxicity rate were low (9%) and transient. No evidence of renal toxicity was seen.

Lutetium-177-labelled prostate specific membrane antigen (PSMA)-ligand is also another established treatment within the theranostics concept by directing to PSMA expression on prostate cancer cells. Several studies reported on safety and efficacy of ^{177}Lu-PSMA treatment in men with metastatic castration resistant prostate cancer (mCRPC) who previously failed conventional therapies showing the clinical benefit of ^{177}Lu-PSMA with low rate of grade 3 or 4 hematologic toxicity (2%).

In summary, ^{177}Lu-Dotatate PRRT, and ^{177}Lu-PSMA radioligand therapy appear to have clinical benefits in patients with advanced NEN and mCRPC, respectively with tolerable/ acceptable adverse effects. The next challenges are to evaluate the efficacy of these targeted treatments in an earlier phase of diseases, the use of alpha-emitting radionuclides, and selective approaches (e.g. intraarterial injection) in patients with some specific conditions.

Keywords: Theranostics, neuroendocrine neoplasia, prostate cancer, PRRT, Lu-177 PSMA

Interesting Radiation Protection Issues in Theranostic Radiopharmaceutical; Workers, Caregivers, Members of the Public and Waste Management

Krisanat Chuamsaamarkkee[1,2]

1 Master of Science Program in Medical Physics, Department of Diagnostic and therapeutic Radiology, Faculty of Medicine Ramathibodi Hospital, Mahidol University, Thailand
2 Division of Nuclear Medicine, Department of Diagnostic and therapeutic Radiology, Faculty of Medicine Ramathibodi Hospital, Mahidol University, Thailand

Radiation protection is required in all processes of theranostic nuclear medicine because it utilizes unsealed radionuclides and delivers high radiation doses to patient. For radiation protection framework, medical, occupational, and public exposures are important in nuclear medicine practices. Medical exposure is involved mainly patients and it also includes their caregivers since the treated patient is acted as the radioactive source. According to the International Commission on Radiological Protection (ICRP), the dose limit for caregiver is established as the whole-body effective dose of 5 mSv per treatment episode. Occupational dose for radiation worker is also essential topic in theranostic. The multidisciplinary healthcare professionals are involved in theranostic for example nuclear medicine physician, radiopharmacist, radiopharmaceutical scientist, medical physicist, nurse, nuclear medicine technologist. The annual occupational dose limit is not only the whole-body effective dose, more importantly, doses to the eyes and the extremities are of particular concern. Therefore, investigation of occupation dose for those radiation workers are necessitated. For members of the public, the effective dose should not exceed 1 mSv in a year. This limit could be achieved by limiting the dose when release the treated patient, controlling the exposure in unrestricted area and radioactive waste management and the sanitary sewerage.

Keywords: radiation protection, theranostic, radioactive waste

How to make a research plan for young investigators

Hidetaka Arimura

Division of Medical Quantum Science, Department of Health Sciences, Faculty of Medical Sciences, Kyushu University

It would be substantially difficult for young students or researchers even the author to make a research plan. After you find a new research theme, you have to confirm four items in the following checklist to make a research plan. (1) Why do you do the research? (2) What are known and what are unknown? (3) What is the purpose of your research? (4) What is the working (tentative) hypothesis?

A tip of doing your research is to logically but “slowly” or “thoroughly” (Stay foolish?) think the research and actually perform it based on practices. You should not conclude that you do not have to do it based on your “smart” understanding. In this case, you have never done anything, and thus you may miss substantially important things. Please seek for the reasons why you do the research, what is the hypothesis, why you use the method, and why you got the results. Eventually, you can find something new and meaningful from academic and clinical point of view.

In this lecture, the author will describe how to make a research plan.

e-Learning in Medical Physics: Building Educational Modules with Moodle VLE

Vassilka Tabakova

King's College London

Introduction: Professional bodies predict the necessity of almost tripling the number of medical physicists by 2035, most significant growth being expected in Lower- and Middle- Income countries. Efficient and fast increasing of these specialists will have to rely on broad implementation of e-Learning and a free and open source Virtual Learning Platform (VLE) such as Moodle will be very useful for providing this on a limited budget.

Purpose: The presentation aims to provide a concise guide to educators in Medical Physics to build their own e-Learning course or a whole educational programme while enhancing the overall quality of education. It is based on the free and open source Moodle VLE, but the general principles are applicable to many other popular VLE platforms for Higher Education.

Methods: The major roles on the VLE are outlined with special focus on the Teacher's preliminary preparation of material for the VLE and his/her role in editing, creating content (such as course works and quizzes), performing assessment and initiating communication with Students on the VLE (through forums, chats etc.). Illustration is given as well of Student functions (submitting assignments and forum participation) and Manager functions such as organising and managing the structure of an educational programme.

Results: A concise guide for building an e-Learning educational programme with a limited budget is given, with detailed results, in the new book e-Learning in Medical Physics and Engineering: Building Educational Modules with Moodle, CRC Press, 2020, ISBN-13: 978-1138347328

Conclusion: e-Learning provides a quick, effective and efficient way to transfer knowledge. However the quality of education is best achieved by providing blended learning through combining e-Learning with classical teaching.

Keywords: e-Learning in Medical Physics; blended learning in Medical Physics; Moodle VLE; Medical Physics education in Lower and Middle Income countries

Role of Radiation and Caution in the Management of Covid-19

Indra J Das, PhD, FACR, FASTRO

Northwestern Memorial Hospital, Northwestern University Feinberg of Medicine, Chicago, IL, USA

Abstract: Covid-19, a highly contagious and deadly disease that started in Dec 2019 in Wuhan China has spread rapidly to entire globe and has no medicine and relatively no cure. This has created a pandemic of epic proportion worldwide and have touched every part of the society. This is compared to the 1918 Spanish flue pandemic that killed nearly 50 million people. Covid-19 has infected over 35.3 million people and > 1.04 million death worldwide as the end of September 2020.

Since there is no cure, a few in radiation oncology community is proposing to use low-dose radiation treatment (LDRT) for the management of Covid-19. This is anecdotal to century old data where radiation was used for every possible illness. Such practices faded away with improvement in medical care and development of anti-viral and antibody therapies. Low-dose (<50 cGy) has shown to produce immunomodulatory that produces cytokines interlukin-8 (IL-8), granulocyte microphage colony stimulating factor (G-CSF) and platelet derived growth factor (PDGF). These cytokines are time and dose dependent and are shown in cell culture. These findings suggest that low-dose can help coordinate related patients with management of pneumonia but this is an extrapolated view as no data in animal nor in human has proven this hypothesis. On the other hand, there is a vast amount of data on LDRT associated with long terms serious complications. For example, LDRT in childhood for tinea-captitis, and thymic abnormalities are associated with long term development of cancer. In adult patients with mastitis where radiation was practiced in the past is associated with severe complications with secondary cancer. Additionally the atomic bomb survivor data are also indicative of long term LDRT complications.

This aspect has been discussed and cautioned for use in Covid-19. It is recommended that without a clinical trial with positive results, LDRT is unethical and should not be attempted.

AFOMP Medical Physics Education and Clinical Training

Arun Chougule

President AFOMP
Senior Professor & Head Department of Radiological Physics
SMS Medical College & hospital, Jaipur, India
Arunchougule11@gmail.com

Clinical Medical physicists are health professionals and therefore medical physicists working in clinical environment should have required competency and therefore undergo structured clinical training program and residency under experienced medical physicist in recognized institution. Further medical physics is a fast growing area needing high degree of knowledge and professional competency due to the rise in complexity of treatment procedures, increasing access to medical technology and the requirement of coordination between medicine, physics and biomedical engineering areas. The unprecedented surge in medical physics competency in the last 2- 3 decades is due to implementation of specialized physics intensive procedures such as particle therapy, image guided & intra operative radiotherapy ,advanced imaging and nuclear medicine techniques. In this scenario to handle this new technology era the quantity of qualified medical physicist needs to be in consonance with the competency needed. There is a special requirement for education and training of medical physicists which lead to opening of numerous educational programs around the world and so in AFOMP region. However if we look at socio-economic & educational status of AFOMP countries we find huge diversity, further there are no unified guidelines as Euroatom for European region/EU and therefore task of AFOMP to homogenise the medical Physics education and profession is quite challenging.

To cater to the needs of the medical physicists and their education, AFOMP has created three main committees to work on number of important tasks.
1. Professional development committee (PDC)
2. Education and training Committee (ETC)
3. Scientific Committee (SC)

These committees have drafted policy statements to deal with minimum level of education and training of medical physics, continuous professional development and career progression for clinical medical physicist in AFOMP countries. We have conducted a survey to access the medical physics and education status in AFOMP region and found that out 21 countries, 14 countries has the structured medical physics education program and only 07 countries has the mandatory residency program and accreditation. Further there is huge gap in availability of CQMP in AFOMP region, 18 MP/ million population [Australia] to 0.5 MP/ million population [Myanmar] whereas compared to US-Canada [25 MP/ million] and Europe [13 MP/ million] the number of medical physicists for one million population is in AFOMP region is only 2.0, that shows huge potential to ramp up the structured education and training of medical physicists in AFOMP region to cope up the need.

Keywords: Education, Residency, Medical Physicists, accreditation

Postgraduate medical physics programmes in Asia Pacific countries - A survey study

Sivananthan Sarasanandarajah[1], Jeannie Hsiu Ding Wong[2], Kwan Hoong Ng[2]

1 Peter MacCallum Cancer Centre and RMIT University, Melbourne, Australia
2 University of Malaya, Malaysia

The increased use of medical imaging and radiation therapies has resulted in a high demand for medical physicists. Although medical physics programmes are well established in advanced countries, the same cannot be said for many low- and medium-income countries. In some countries, there may be huge variations in the graduates' skill and quality, which pose a problem in ensuring patient safety, providing quality assurance in treatments, optimisation of protocols and standardisation of quality. It also makes any yet-to-be-established regional peer recognition efforts problematic. In order to understand the depth of this problem, a survey was carried out as part of the home-based assignment under the RAS 6088 IAEA programme. A large diversity in terms of course content, duration, clinical training and student profile could be observed across the Asia-Oceania universities surveyed. Out of 25 programmes, only six received recognition from professional bodies, and they were mostly in Australia and New Zealand. Hence, to ensure quality education, a regional curriculum model needs to be developed to harmonise standards. And there is still a long way to go towards standardizing medical physics education and clinical training in the region.

Imaging-based Biomarkers

Yothin Rakvongthai

Chulalongkorn University Biomedical Imaging Group and Division of Nuclear Medicine, Department of Radiology, Faculty of Medicine, Chulalongkorn University, Bangkok, Thailand

Advances in medical imaging enable us to gain useful anatomical and functional information inside the human body. To leverage this technology, imaging-based biomarkers, especially quantitative biomarkers, have been developed as numerical metrics derived from an image to indicate biological processes, pathogenic processes, or treatment response. In this session, we will discuss a framework for imaging-based biomarker research, summarize challenges and obstacles in imaging-based biomarker development, and outline current and potential uses of these biomarkers in clinical practice.

Teaching Linear Accelerator Physics using a Web Based Simulator

Marco Carlone[1,2]

1 BC Cancer Kelowna, British Columbia, Canada,
2 Linax Technologies Ltd., Ke;owna, British Columbia, Canada,

Introduction: Linear accelerators are the most important equipment used in radiotherapy as they create the beams used for irradiating patients. Medical Physicists are responsible for the safe operation of the device and must ensure that the radiation beams are calibrated and reflect the beam models in planning systems. Other than two textbooks (Karzmark and Green), there are few resources for teaching medical physicists their operating principles. Learning their functionality is also challenging since linear accelerators must be operated within a narrow set of parameter ranges, making it difficult for a student to experiment with the device to learn its operating principles. This presentation will describe a linear accelerator simulator that is designed to assist medical physicists in learning their operating principles.

Methods and Materials: SIMAC is a linear accelerator simulator. It simulates the electron acceleration in an accelerating waveguide as well as microwave production, electron injection, the bending chamber, and the photon production and transport. The web environment was designed to include sections for didactic material as well as a virtual laboratory, which complement the accelerator and reinforce the learning objectives.

Results: SIMAC is hosted in a web environment at https://linax.ca. It includes the ability to create unique flattening filters, and to swap them in customized beam configurations, and examining their effect on beam flatness. Steering coils are also simulated so that symmetry errors can be recreated. There are thirteen linac lessons covering all aspects of linear accelerator functionality with evaluations for each lesson. As well, certain features of the simulator have been automated so that a learner can study the effect of adjusting one parameter, there are 8 linear accelerator exercises in total. The website has over 300 registered users; at present it is accessed about 20 times per day.

Conclusion: A linear accelerator simulator has been constructed and is available on a public website for anyone interested in using it to learn about linear accelerator functionality.

Automating Plan Checking Tasks by Scripting

Michael Lamey[1,2]

1 BC Cancer Kelowna, British Columbia, Canada,
2 University of British Columbia Okanagan, British Columbia, Canada,

The purpose of this work is to illustrate how scripting can be used in the clinical environment to automate many of the tasks associated with Radiation Therapy Plan checks and the associated workflow. In this work the C# programming language was applied to the Varian Eclipse Scripting API to program many of the plan check tasks. Windows presentation foundation is used for the graphical user interface.

Vendors as well as many Cancer Centres involved in research continue work on applying machine learning and big data strategies to Radiation Therapy Planning (RTP). This work is the future of RTP but, as there are process differences from center-to-center, there are still opportunities for scripting of the practical nature at the individual center level. In this work I will discuss and illustrate how we have integrated scrips into our clinical workflow, the scripts are of the practical nature which could be of interest to and integrated by most centers. Many plan checking tasks can be time consuming and mundane by nature, automating these tasks gives the plan checker more time to evaluate plan quality. Some of these checks include: ICRU point location warnings, VMAT collimator angle warnings, appropriate tolerance table, dose calc. warnings, appropriate plan approver, appropriate beam model, appropriate dose rate, overridden structures, Bolus HU values, optimizer settings, checks for MLC end-of-travel and beam on time for deep inspiration breath hold patients. Scripts have also been used to standardize instructions for secondary calculation phantom setup checks and increase plan export speed. Automating these plan check tasks and improving workflow efficiency at our center has improved staff morale and increased plan check efficiency. As patient numbers increase improvements in workflow are necessary to keep up with the increasing demands of the cancer center.

Principle and Application of MR-Linac

Kin Yin Cheung

Hong Kong Sanatorium & Hospital, Hong Kong SAR

A brief overview on physics and unique characteristics of an Elekta Unity MR-Linac and the principle and rationale behind the clinical applications of on-line MR-guided adaptive radiotherapy will be presented. The adaptation treatment planning and delivery workflow, and QA measures will also be discussed.

Extreme hypofractionated radiotherapy – Radiobiology and radiobiological models

Arun Chougule

Senior Professor Radiological Physics
SMS Medical College & Hospitals
Jaipur, India
arunchougule11@gmail.com

Radiotherapy started within few months of discovery of X- rays and today it is the main modality of cancer treatment. In last 124 years radiotherapy has seen tremendous technological developments in dose delivery systems, imaging modalities, accuracy of dosimetry, planning, execution and at the same time improved understanding of underlying radiobiology. The aim of radiotherapy is to deliver lethal dose to tumour at the same time spare the organ at risk [OAR] and keep the normal tissue complication probability [NTPC] clinically manageable. To achieve the goals various radiotherapy fractionation schedules were tried such as conventional fractionation, hypofractionation, accelerated fractionation, hypo and extreme hypofractionation. The imaging techniques such as CT, MRI, CT-PET, MR-PET combined with computerised treatment planning systems [TPS] and stable radiotherapy machines have given rise to techniques like conformal radiotherapy [CRT], Intensity modulated radiotherapy [IMRT], image guided radiotherapy [IGRT], stereotactic radiosurgery [SRS], and stereotactic body radiotherapy [SBRT] where in the normal tissue and/or OAR irradiated volume is minimised thereby by escalating the tumour dose leading to better tumour control probability [TCP].

With increased understanding of radiobiology, to compare the efficacy in terms TCP & NTCP of various fractionation schedules, various empirical and biological models were introduced and used. One of the radiobiological models widely used is linear quadratic [LQ] model. To achieve the goal of radiotherapy, more than the physical dose, the radiobiological effectivity of the dose on various tissues and tumour is of importance and therefore the newer versions of TPS are providing radiobiological optimisation with iso- ERD plots, paradigm shift from dose volume optimisation [DVO] to biological model optimisation [BMO] leading to the concept is biologically guided radiotherapy [BGRT] so as to ultimately maximise the tumour lethality with moderate normal tissue complications.

Questions are raised regarding predictability accuracy, validity of LQ model to extremely hypofractionated radiotherapy especially SRS and SBRT. In this presentation, attempts are made to analyse validity, predictability and limitations of LQ model.

Keyword: Radiobiology, hypofractionation, SRS, LQ

High patient radiation doses from recurrent CT exams

Madan M. Rehani

Massachusetts General Hospital, USA
(madan.rehani@gmail.com; mrehani@mgh.harvard,edu)

Computed tomography (CT) has remained the most important imaging modality in medical practice. One cannot imagine modern medicine without CT and thus it has indispensable role. There have been reports from time to time raising radiation risk concerns associated with CT. They have helped to make CT safer as the dose for a defined level of diagnostic information has gone down substantially. A large number of publications have assessed how a different technology or technique has helped to reduce the dose in a single CT exam to maintain the same level of noise in the image or how and how much dose reduction could be achieved for the same CT exam. Despite that, we have not reached a point where one can say that CT is a low dose imaging modality. The concept of low or high is always relative and is related to use and risks. The risk depends on how recurrent the use is. Three papers published recently from our group covering data of 3.2 million patients undergoing CT exams in 344 hospitals in 20 countries have shown that 0.64% to 3.4% of the patients undergoing CT exams reach the cumulative effective dose (CED) of ≥ 100 mSv in 1 to 5 years period. The papers estimated that about 0.9 million patients probably reach a CED ≥ 100 mSv every year globally through recurrent CT exams alone. About every fifth patient who was exposed to more than 100 mSv in this study was ≤ 50 years old. Further, these papers identified patients in this cohort who are < 40 years of age and with no malignant disease. Another paper reported that total number of patients with CED ≥100 mSv for all 35 OECD countries combined in a 5-year period is around 2.5 million (2,493,685) in a population of 1.2 billion (1,176,641,900), i.e., 0.21% of the population. Expressed per 1,000 population, the range is from 0.51 for Finland to 2.94 for the US, a nearly six-fold difference. Countries with more than 2 patients with CED ≥100 mSv in a 5-yr period per 1,000 population are: Belgium, France, Iceland, Japan, Korea, Luxembourg, Portugal, Turkey, and US.

Despite significant advances in CT technology, unfortunately, we are not at a stage to tell millions of these patients that CT is a low dose imaging modality. It will be so if we consider our responsibility to lie up to the level of a single CT exam rather than the patient as a whole. We have responsibility towards patient radiation safety and that is what creates requirements in national regulations for their appointment at first place. We need to create awareness about these facts and continue actions at all levels to make CT safe for patients.

Patients who receive high radiation doses in a single day

Madan M. Rehani

Massachusetts General Hospital, Boston, USA
(madan.rehani@gmail.com; mrehani@mgh.harvard,edu)

Our recent studies had indicated that there are patients who might be receiving relatively high doses such as 100 mSv in a single day through computed tomography (CT). We had just flagged this issues in our earlier paper (Rehani et al. Eur Radiol. 2020 Apr;30(4):1828-1836). Since this was a new observation not reported before, we wanted to study further if this was an incidental and rare finding or there could be sizable number of patients with such doses. We have just completed analysis of a big study covering nearly 4 million CT exams. We are finding that the percentage of cases with effective dose of ≥ 50 mSv in a single day with respect to total patient-days are below 1% and cases with dose ≥ 100 mSv are below 0.1%. These are not ignorable figures. Further >90% of the cases had only one CT procedure in a day and thus such doses are in fact in a single procedure. Our analysis shows that CT imaging of body region (chest or abdomen and pelvis) are responsible for such high doses including multiphasic angiographic studies. Once again these are new findings under publication for the first time. They highlight the need strengthen actions on radiation protection of patients. The most prominent action is to use alternative imaging techniques that do not utilize ionizing radiation.

Challenges in CT with photon counting detectors

Picha Shunhavanich, PhD

Department of Radiology, Faculty of Medicine, Chulalongkorn University

With many attractive attributes including improved tissue characterization, reduced noise, and lower dose, photon counting detectors (PCDs) with multiple energy bins are being considered for clinical CT systems. A major problem with PCDs is the slow count rate, resulting in count rate loss and pulse pileup. Another challenge to PCDs with multiple energy bins is the large amount of projection data acquired that must be transferred in real time through slip rings to data storage subsystems, causing a bandwidth bottleneck problem. Our goal is to address these two challenges with a dynamic bowtie filter and a compression algorithm for PCD projection data, respectively. A dynamic bowtie modulates flux distribution as a function of fan and view angles to reduce dose, scatter, and detector dynamic range. One approach, the piecewise-linear attenuator (Hsieh and Pelc, *Med Phys* 2013), consists of multiple wedges, each of which covers a different fan angle range and is moved in the axial direction to change the thickness seen in an axial slice. The filter was implemented and tested. Another dynamic bowtie design, called a fluid-filled dynamic bowtie filter (Shunhavanich et al., *Med Phys* 2019) was also proposed, aiming for potentially more reproducibility due to digital control of the filter thickness. For the bandwidth problem, the use of data compression was explored. The compression process could be performed prior to transmission through the slip ring.

Keywords: dynamic bowtie filter, fluence field modulation, photon counting detector, data compression

Physicists and Clinical Trials: Support and Evidence for New Technology and Techniques

Tomas Kron

Peter MacCallum Cancer Centre, Melbourne, Australia

Introduction Clinical trials are the backbone of evidence based medicine. Whilst most clearly visible in the context of drugs and more recently vaccines, also technology and its judicious application must be tested rigorously not only in terms of technical performance but also in relation to its clinical objectives. This presentation aims to explore the role of medical physicists in clinical trials.

Methods Motion management is one of the key areas of concern in modern radiotherapy and deep inhalation breath hold (DIBH) is one of the methods to optimise patient preparation for example in breast cancer radiotherapy where DIBH can reduce dose to the heart in left sided breast cancer patients. We are exploring the role of a physicist in a multicentre trial testing feasibility, cost and patient anxiety in DIBH for breast cancer patients.

Results The trial needed to define, which was captured through ability of patients to hold their breath, the quality of the DIBH plans and the reproducibility of breast position in breath hold. The latter was assessed using mid-lung-distance (MLD) as shown on electronic portal images acquired during treatment. The trial enrolled 30 left sided (DIBH) patients and 30 right sided patients treated in free breathing who serve as a control in terms of reproducibility and treatment time as a measure of additional resource requirements for DIBH.

Discussion The trial was physics led and just completed accrual. It helps to demonstrate the contributions physicists can make to trials that test new techniques in particular if more than one technology can be utilised to achieve a similar goal.

Conclusions Medical physicists are at the interface between technology and patients. They must actively engage not just in quality assurance of technology in trials but also help to define endpoints with the aim to better introduce new technology and techniques into clinical practice.

Acknowledgement: The support of our work by the Gross Foundation is greatly appreciated

Novel technologies for advanced radiomics for clinical practices

Hidetaka Arimura

Division of Medical Quantum Science, Department of Health Sciences, Faculty of Medical Sciences, Kyushu University

Radiomics is one of omics research fields where medical image features are considered “radiome” like genome, transcriptome, proteome, metabolome, and so on. The aim of the radiomics is to find the relationships between image features in pretreatment images and patients’ prognoses, and make advantages of them in decision making of treatment policies. We assume that the image features could mathematically characterize the heterogeneity of tumors in medical images, which could be associated with the patients’ prognoses. Since the radiomics concept has been introduced, image features have been based on classical medical image processing, i.e., histogram and texture analysis. The problem of the conventional image features is vulnerable to variations of image quality for imaging scanners and protocols.

A number of researchers in various fields could not resist the large wave of deep learning (DL) technologies. Therefore, many medical researchers are moving on the DL-based radiomics, where you do not have to subjectively use hand-crafted features in a happy-go-lucky manner, but image features will be automatically and objectively derived. All that you can do are to find a problem, collect the large number of data, train DL networks, and test them. After you found the problem, the procedure with changing many parameters may be tedious, but recently we have DL systems whose parameters will be automatically determined. However, there are mainly two issues in DL, i.e., black box and overfitting problems (requirement of the large number of data).

To overcome these issues, the author of a classical medical image processing researcher thought that one of the approaches would be to employ mathematical models which will be white or comprehensive, and will not require the large number of data.

The purpose of this lecture is to introduce mathematical models for advanced radiomics in clinical practices which could characterize tumor heterogeneity, such as homology of topology [1-3]. The homology can quantify the cavitation derived from pixel value heterogeneity in cancerous regions using Betti numbers, which are mathematically invariant. The persistent homology is defined as a data analytical approach for computing topological features of data with increasing spatial resolutions.

Keywords: radiomics, mathematical models, homology, classical image processing, deep learning

Consideration of stochastic risks in interventional procedures

Madan M. Rehani

Massachusetts General Hospital, USA
(madan.rehani@gmail.com; mrehani@mgh.harvard,edu)

Interventional procedures using fluoroscopy are well known to impart high radiation doses to patients. The usual emphasis of radiation protection actions in interventional procedures has been to lay emphasis on avoidance of skin injuries (tissue reactions) in adults and limiting stochastic risks in children. However, recent studies from group at our hospital have drawn attention to the risk of stochastic effects in adults also as high effective doses have been observed. We have recently reported that patients undergoing fluoroscopy guided interventional procedures at our hospital during the 9-year period (excluding cardiac cases) were found to have radiation dose of ≥ 100 mSv in the 9-year period studt [Li et al. AJR Am J Roentgenol. 2020 Aug;215(2):433-440]. It may be noted that majority (about 90%) of their procedures were within 12 months, and 10.7% patients were under 40 years age. It is commonly believed that most patients undergoing long and complicated interventional procedures are old people and with conditions that imply shorter life expectancy. But our studies indicate that this may not be a correct notion. This was the first such report that studied medical condition of these patients receiving substantial cumulative doses.

Radiation dose information should always be recorded in the patient's medical record after completion of the procedure. For patients who have received a radiation dose greater than the defined level during the procedure, additional actions are necessary. The interventionalist should write an appropriate note in the patient's medical record indicating that the substantial dose level has been exceeded.

MS 5:
Eye Lens Dose Measurements of Medical Staffs in Thailand

Waraporn Sudchai[1], Suphot Srimahachota[2], Anchali Krisanachinda[3]

1 Thaland Institute of Technology, Bangkok, Thailand
2 Cardiac Center, Department of Medicine, Faculty of Medicine, Chulalongkorn University, Bangkok, Thailand,
3 Department of Radiology, Faculty of Medicine, Chulalongkorn University, Bangkok, Thailand

Introduction: Due to the epidemiology evidence of cataract and eye lens opacity, ICRP Publication 118 in 2012, decreased the dose limit for the eye lens from 150 to 20 mSv per year, averaged over 5 year period, no single year exceeding 50 mSv. On 5 October 2018, the Royal Thai Government announced in the Royal Gazette on the reduction of eye lens dose limit from 150 to 20 mSv per year averaged over 5 year period. Thailand Institute of Nuclear Technology, TINT, (Public Organization) proposed a national research project on eye lens dose measurement in medical staff in 2016-2020.

Purpose: To measure the eye lens dose in medical staff performed various procedures in interventional cardiology, interventional radiology and nuclear medicine and to investigate the deterministic effects of radiation on eye lens upon the new dose limit

Methods: The eye lens doses were measured in 182 medical staffs in Thailand. 8 Cardiac Centers of 111 medical staffs, 3 Interventional Radiology Units of 15 medical staffs, and 6 Nuclear Medicine Sections of 56 medical staff were included. OSLD, Model nanoDot used for eye lens dose monitoring, were supplied and calibrated by TINT. The annual eye investigations were performed to check the effects of radiation on the eye lens.

Results: The average left and right eye lens doses, mSv/year, in interventional cardiology staffs, interventional radiologists and nuclear medicine staff were 2.06 and 1.90, 6.32 and 2.83 and 1.89 and 1.90 respectively.

Conclusion: The average doses were less than the new dose limit recommended by ICRP publication 118. Both interventional cardiologists and radiologists received the higher left eye lens doses than the right eye, while nuclear medicine staff received similar dose on both eyes. The interventional cardiology (IC) staffs, and the age- and sex-matched controls were investigated on the prevalence of radiation-associated posterior lens opacities at 3-year follow-up period. Relative risk was determined using 95% confidence interval from 0.535 to 3.075.

Keywords: eye lens dose, interventional cardiology, interventional radiology, nuclear medicine, OSLD

Rapid estimation of muscle transverse relaxation time (T_2) based on ultrafast magnetic resonance imaging at 3.0 Tesla

Noriyuki Tawara[1,2], Atsushi Nishiyama[1]

1 Department of Radiological Sciences, Faculty of Health Sciences, Japan Health Care College, Sapporo, JAPAN
2 Department of Radiology, Faculty of Medicine, Chulalongkorn University, Bangkok, Thailand

Introduction: Exercise-induced muscle activity is essential in sports medicine and rehabilitation medicine. Magnetic resonance imaging (MRI) can evaluate muscle activity; transverse relaxation time (T_2) of exercised muscle is increased compared to that of rested muscle. The pulse sequence for calculating T_2 is spin echo (SE), but it has been pointed out the problems about temporal resolution and spatial resolution. Therefore, it is necessary to consider the pulse sequence for solving these problems, we focused on spin-echo echo-planar-imaging (SE-EPI) and double-echo-steady-state (DESS) as the pulse sequences for shortening the acquisition time and increasing the spatial resolution.

Purpose: The aim of this study was to assess the utility of SE-EPI and DESS pulse sequences for T_2 measurement at 3.0T by comparing them with multiple spin echo (MSE) sequences in order to determine which protocol would best reduce the image acquisition time for the calculation of muscle T_2.

Methods: The data for comparison of T_2 were obtained using the same 3.0 Tesla whole body scanner with an eight-channel knee coil. The comparison of T_2 was performed using T_2 relaxation curve and calculated T_2. Regions of interest (ROI) for comparison of T_2 were placed in m. semitendinosus (semi).

Results: This result indicates that it is possible to calculate T_2 from SE-EPI if the TE is short, but that errors may arise with longer TE values. Regarding calculated T_2 from DESS, there was no significant difference in T_2 with and without fat suppression.

Conclusion: In this study we demonstrated the feasibility of calculating T_2 values using ultrafast imaging. The muscle T_2 calculating using 3 Tesla MRI units were uninfluenced by intramuscular lipids. The ultrafast imaging T_2 method can be creatively used with each sequence type depending on the reason for performing the scan.

Keywords: transverse relaxation time (T_2), muscle, spin-echo echo-planar-imaging (SE-EPI), double-echo-steady-state (DESS).

Optimization of Cone Beam Breast CT – Radiation Dose and Image Quality

Kanlayanee Theerakul[1], Porjai Techanitisawat[1], Wasinee Panomsert[1], Apawadee Chackrapong[2], Anchali Krisanachinda[3]

1 Queen Sirikit Centre for Breast Cancer, King Chulalongkorn Memorial Hospital, The Thai Red Cross Society, Bangkok, Thailand
2 Medical Physics Program, Department of Radiology, Faculty of Medicine, Chulalongkorn University, Bangkok, Thailand,
3 Department of Radiology, Faculty of Medicine, Chulalongkorn University, Bangkok 10330, Thailand

Introduction: Cone Beam Breast CT (CBBCT) uses projections acquired in a 360-degree scan to reconstruct the 3D image of the breast. The ultrasound image is scanned to confirm the findings. ACR BI-RADS had also been reported. However, the optimization of the breast dose can also greatly reduce the image quality and the diagnostic performance.

Purpose: The purpose of the study is to optimize the patient breast dose from CBBCT imaging using manufacturer default technique and reduced tube current technique with the analyses on the related image quality of both groups.

Study Design: In this retrospective study, 213 patients received CBBCT scans, had ACR BI-RADS report, ultrasound scan, were selected from the facility's patient database as the control group: cases with original CBBCT images. The second group of 201 patients with reduced tube current received CBBCT scan to optimize the breast dose. The breast dose was compared between two groups as well as the image quality. The breast dose reduction of 40 percent has been observed. Radiologists specialized in CBBCT evaluated the image quality by scoring to confirm the second technique for optimization is applicable for the diagnostic performance of CBBCT. The readers were blinded to the group allocation of each case.

Keywords: cone beam breast CT, dose optimization, image quality

The Establishment of UNSCEAR Report in Thailand

Anchali Krisanachinda

Department of Radiology, Faculty of Medicine, Chulalongkorn University, Bangkok 10330, Thailand

Introduction: The radiation medicine has been established in Thailand in 1921. The rules and regulations on the use of ionizing radiation had been enacted by the Atomic Energy for Peace of Thailand in 1961. After that the application of radiation in various fields had been grown up rapidly. There was no official report on the increasing use of radiation in any fields until the year 2019. The Office of Atoms for Peace had set up the Sub Committee on the use of ionizing radiation in medical field with the main objective is to collect data according to the UNSCEAR requirements on medical exposure and occupational exposure.

Methods: In September 2019, the UNSCEAR data had been gathered and analyzed from major centers represent all parts of the country. The information on the number of populations, physicians, radiologists, dentists, radiation oncologists, nuclear medicine physicians, medical physicists, technologists, nurses, etc. and the number of equipment in diagnostic radiology, radiotherapy and nuclear medicine in 2018 in Thailand had been collected. Furthermore, the number on procedures in radiotherapy and nuclear medicine as well as the patient radiation dose had been estimated to obtain the effective dose as detail in UNSCEAR manual. Unfortunately, the data on diagnostic radiology on estimated number of procedures and patient dose could not be collected in time. UNSCEAR data on medical exposures in radiation oncology and nuclear medicine and occupational radiation exposure had already been submitted to the UNSCEAR Headquarter via OAP official channel. That information, hopefully, should be published in UNSCEAR 2020 Report

Conclusion: The data on the exposure of patients and radiation workers on national level are valuable. The data collection should provide further relevant data about healthcare level, effects and risk of radiation exposure from various sources. The data should be published annually on website.

Keywords: medical exposure, occupational exposure, healthcare level, frequency, effective dose

MS 6:
Facility design of a PETCT

Mr Somanesan S

Department of Nuclear Medicine and Molecular Imaging, Singapore General Hospital

Introduction: The design elements and critical aspects of a facility design for a PETCT imaging facility shall be presented.

Purpose: To ensure a PETCT facility is set up for a safe, efficient that is compliant with local and international practises such as the IAEA Basic Safety Standards for PETCT molecular imaging.

Methods: The conflicting requirements of a PETCT facility design will be reviewed with an emphasis on facilitating a safe and efficient eventual operation of the PETCT to ensure a safe and efficient PETCT imaging operation that is compliant with local and international regulations.

Conclusion: Design of a safe, efficient, effective PETCT imaging facility that is future proofed.

Keywords: PETCT, Facility, radiation safety

MS 6:
Facility design of a cyclotron

Mr Somanesan S

Department of Nuclear Medicine and Molecular Imaging, Singapore General Hospital

Introduction: The design elements and critical aspects of a facility design for a cyclotron shall be presented.

Purpose: To ensure a cyclotron facility is set up for a safe, efficient and compliant with the current Good Manufacturing Production (cGMP) practises in PET radiopharmaceutical production.

Methods: The conflicting requirements of a cyclotron facility design will be reviewed with an emphasis on facilitating a safe and efficient eventual operation of the cyclotron to ensure a safe, steady and consistent PET radiopharmaceutical production that is compliant with local and international regulations.

Results: NA

Conclusion: Design of a safe, efficient, effective cyclotron facility that is future proofed.

Keywords: Cyclotron, radiation safety, shielding, radiopharmaceutical

MS 6:
Radiation Emergency Preparedness in Nuclear Medicine

Chai Hong Yeong

School of Medicine, Faculty of Health and Medical Sciences, Taylor's University, 47500 Subang Jaya, Malaysia

Radiological accidents can have a lasting impact on public health and environment. In nuclear medicine, large amounts of sealed and unsealed radionuclides are used for diagnosis and therapy of various diseases. During the planning of a nuclear medicine facility, it is important to include a detailed emergency and contingency plan towards any possibilities of radiation emergency or accidents. Some of the examples of emergency and radiation incidents in nuclear medicine department include spillage of radionuclides, mis-administration of radiopharmaceutical to patients, loss of radioactive source in the department or in transit, death of patient with administered radiopharmaceutical in the body, vomiting of radiopharmaceutical by the patient, accidental radiation exposure to pregnant women, etc. An accident in a nuclear medicine laboratory may cause personnel exposure, internal/external contamination, or both. Hence it is essential that sufficient level of emergency preparedness be ensured and practised in the department. Medical physicist, who is a professional in radiation applications and protection, should take an active role in the planning and implementation of the emergency preparedness programme in the nuclear medicine department.

Keywords: nuclear medicine, emergency preparedness, contingency plan, medical physicist

Theranostics in Nuclear Medicine

Shuichi Shiratori

Division of Nuclear Medicine, Department of Radiology, Faculty of Medicine Siriraj Hospital, Mahidol University, Bangkok, Thailand

Theranostic concept has coined as a part of personalized medicine since last two decades. Up-to-date, theranostic approach is clinically tailored utilizing specific ligand **labelled with** gamma or positron emitter **for diagnosis** and consequent alpha or beta emitter for therapeutic purpose. The first proof-of-concept theranostic in Thailand has been successfully applied to prostate cancer and neuroendocrine tumor (NET) in King Chulalongkorn Memorial Hospital since February 2018.

A highly promising therapeutic ^{177}Lu-PSMA has a palliative effect, particularly, in patients with metastatic castration-resistant prostate cancer (mCRPC) as well as improvement of disease progression and overall survival. An imaging of ^{68}Ga-PSMA is very useful not only planning before treatment but also monitoring and evaluation of therapeutic outcome. Recently, ^{18}F-PSMA is addressed as alternative option for prostate cancer diagnosis due to a better benefit in daily multiple-case management. In the other hands, a group of somatostatin receptor agonists, known as DOTATATE, DOTANOC, DOTATOC, can be labelled with gallium-68 and lutetium-177 in the same manner to PSMA. Therefore, for example, ^{68}Ga-DOTATATE provides high resolution medical image before administration of ^{177}Lu-DOTATATE to treat NET.

Moreover, Ac-225 is an alpha emitter which has remarkable advantage on anticancer activity over Lu-177. There are some evidences of both ^{225}Ac-PSMA and 225Ac-DOTATATE which are effectively utilized in clinic in many countries. However, xerostrommia was found more severe than its ^{177}Lu-labelled analogues. The fixed dose of 100kBq/kg became dose-limiting regimen for alpha therapy.

Besides mCRPC and NET, more advance theranostics is expanded to others common cancers such as non-small cell lung cancer, breast cancer, ovarian cancer, colorectal carcinoma, pancreatic carcinoma which express fibloblast activation protein (FAP) over 90% of epithelial cancers. Well-developed small molecule FAP inhibitor, called FAPI04, can be utilized as a novel potential ligand under the same theranostic concept in near future.

Preparation and Application of Ga-68 in Nuclear Medicine

Shuichi Shiratori

Division of Nuclear Medicine, Department of Radiology, Faculty of Medicine Siriraj Hospital, Mahidol University, Bangkok, Thailand

Over past two decades, positron emission tomography (PET) has increasingly utilized in diagnosis and treatment evaluation. Especially, ^{18}F-FDG became clinically routine PET radiotracer used in worldwide. However, its availability depends on on-site or nearby cyclotron facility which requires significant high investment and maintenance. One potentially interesting PET radionuclide that relevant to fluorine-18 is generator-based gallium-68 (Ga-68).

To-date, Ga-68 becomes one of the most frequently used radionuclide in nuclear medicine due to its nearly ideal physicochemical properties together with feasible ^{68}Ge/^{68}Ga generators and commercially available cold kits. Among positron emitters, Ga-68 is very convenient to produce and label compare to carbon-11 or fluorine-18. Moreover, Ga-68 chemistry principle based on well-defined chelation to various chelators or macrocyclic molecules.

Ga-68 is obtained by eluting of hydrochloric acid to a ^{68}Ge/^{68}Ga generator that prompts to label with bifunctional chelating agents to form complexation of $^{68}Ga^{3+}$ ion. Subsequently, loading crude Ga-68 labelled product to C-18 cartridge then washing with mixture solution of ethanol:water (1:1) via 0.22μ filter to receive >99% radiochemical purity. After quality control process according to requirements, certain ^{68}Ga-labelled radiopharmaceuticals can be administered to patient.

Due to its robust and simple preparation, Ga-68 is extensively utilized to label with many specific ligands to have high resolution imaging in oncology for example ^{68}Ga-PSMA for prostate cancer, ^{68}Ga-DOTATATE for neuroendocrine tumor, ^{68}Ga-FAPI for various cancers. Moreover, Ga-68 is one of the most necessary radionuclide in research field. Many novel PET tracers are previously composed of Ga-68, then adapted to its fluorine-18 analogue in clinical service.

Radiomics in Radiation Oncology

Yothin Rakvongthai[1] and Anussara Prayongrat[2]

1 Chulalongkorn University Biomedical Imaging Group and Division of Nuclear Medicine, Department of Radiology, Faculty of Medicine, Chulalongkorn University, Bangkok, Thailand
2 Division of Radiation Oncology, Department of Radiology, King Chulalongkorn Memorial Hospital, Bangkok, Thailand

Radiomics is an evolving field which utilizes the extraction of large amounts of quantitative features, termed radiomic features, from medical images. These radiomic features can capture tumor characteristics such as intratumoral heterogeneity, which can be used for decision making in radiation oncology. The goal of this session is to provide an overview of fundamentals and workflow of radiomics as well as technical limitations. Clinical applications in radiation oncology such as prognosis and treatment response prediction will also be covered.

Patient specific quality assurance by log file-based software: a multi-institutional study in Thailand

Sornjarod Oonsiri[1], Chulee Vannavijit[1], Puntiwa Oonsiri[1], Weerachai Injai[2], Rosarin Sintiprom[2], Pichet Uber[3], Paya Dardaranonda[3], Chalermchart Bunsong[3], Issara Lekkong[3], Pubade Kaewpruk[3], Phattarawat Junpue[4], Sowitchaya Huakham[4], Rusdchai Chaisuttee[5], Nataporn Buakaew[5], Jongchai Tinlapat[5], Chanidapa Kanchanawaleekun[6], Taweap Sanghangthum[7], Sivalee Suriyapee[7]

1 Division of Radiation Oncology, Department of Radiology, King Chulalongkorn Memorial Hospital, Bangkok, Thailand
2 Division of Radiation Oncology, Department of Radiology, Bhumibol Adulyadej Hospital, Directorate of Medical Service, Royal Thai Airforce, Bangkok, Thailand
3 Department of Radiation Oncology, Chonburi Cancer Hospital, Chonburi, Thailand.
4 Radiation Therapy and Oncology Division, Chiwamitra Hospital, Ubon Ratchathani, Thailand.
5 Division of Radiation Oncology, Department of Radiology, Phrapokklao Hospital, Chanthaburi, Thailand.
6 Department of Radiology, Cancer Alliance Hospital, Chonburi, Thailand
7 Department of Radiology, Faculty of Medicine, Chulalongkorn University, Bangkok, Thailand

There is an evident increase in the trend of volumetric modulated arc therapy practice over the years, which will necessitate measures to address quality assurance concerns in Thailand. Over recent years, as the complexity of treatment techniques evolved alongside technology, log file-based software is the new trend of patient specific quality assurance for advanced technique. This project aims to determine the patient specific quality assurance result of measurement-based and log file-based software and to set the confidence limits for log file-based software. Six institutions participated in the multi-institutional study in Thailand. A total of 167 plans for volumetric modulated arc therapy patients with head and neck, lung and prostate cancer were examined. The gamma evaluation of 3% and 3 mm criteria for both methods were used in this project. The results of gamma evaluation for measurement-based and log file-based methods were 99.0 ± 1.6% and 96.6 ± 3.4%, respectively. The statistical analysis showed that there was no noticeable correlation between measurement-based and log file-based methods. Our multi-institutional study suggested that the confidence limit for clinical practice is 90% for log file-based patient specific quality assurance.

Keywords: Patient specific quality assurance, Log file-based software

Radiotherapy: Dosimetry

Parametric impact study of interplay effects in 6 MV flattening filter free (FFF) of photon beams

Vanida Poolnapol[1], Mintra Keawsamur[2], Taweap Sanghangthum[3]

1 Medical Physics Program, Faculty of Medicine, Chulalongkorn University, Bangkok, Thailand.
2 Division of Radiation Oncology, Department of Radiology, King Chulalongkorn Memorial Hospital , Bangkok, Thailand.
3 Division of Radiation Oncology, Department of Radiology, Faculty of Medicine, Chulalongkorn University, Bangkok, Thailand.

Introduction: Tumour moving induced interplay effects in stereotactic body radiotherapy (SBRT) of lung cancer patients, which lead to non-uniform doses within the target volume and unwanted dose to the surrounding tissues.

Purpose: To investigate the interplay effects from parameters of breathing amplitudes and phases, dose levels, dose rates, field sizes, and fractionations.

Methods: The standard AP-field plans of 6 MV FFF photon beams were created on Eclipse treatment planning system version 15. The moving patterns were simulated on a robotic platform (MotionSimXY/4D, Sun Nuclear, Melbourne, FL) for different breathing amplitudes and phases, dose levels, dose rates, field sizes, and number of fractions. The 2D diode array (MapCHECK2; Sun Nuclear, Melbourne, FL) with 3 cm of solid water phantom buildup was placed above robotic platform. The measurements were performed on a TrueBeam linear accelerator (Varian Medical Systems, Palo Alto, CA). The measured and calculated doses were compared by using gamma analysis with 1%/1 mm criteria.

Results: The gamma passing rates decreased for higher amplitudes (especially for 2D phantom motion compered to 1D phantom motion) and dose rates, these results were agreement with Edvardsson A and Mukhlisin M studied. However, gamma passing rates increased with larger field sizes (32.7%, 46.4%, and 54.1% for 4x4 cm^2, 6x6 cm^2, and 10x10 cm^2, respectively), dose level (32.7% for 5 Gy and 38.8% for 8 and 12 Gy), and number of fractions (32.7%, 34.7%, and 36.7% for 1, 2, and 5 fractions, respectively). For phase parameter, no interplay effect was detected.

Conclusion: The tumor motion induced interplay effects were verified with the robotic platform motion measurements. The interplay effects are pronounced for higher breathing amplitudes, higher dose rates, smaller field sizes, lower dose level and lesser fractionation numbers.

Keywords: FFF, interplay effects, photon beams, and robotic platform

Development and dosimetric verification of 3D customized bolus in radiotherapy

Nichakan Chatchumnan[1], Sakda Kingkeaw [2], Taweap Sanghangthum[3]

1 Master of Medical Physics Program, Faculty of Medicine, Chulalongkorn University, Bangkok, Thailand
2 Division of Radiation Oncology, Department of Radiology, King Chulalongkorn Memorial Hospital, Bangkok, Thailand
3 Division of Radiation Oncology, Department of Radiology, Faculty of Medicine, Chulalongkorn University, Bangkok, Thailand

Introduction: Bolus is a tissue equivalent material that commonly used to reduce skin-sparing effect in radiotherapy. The commercial flat bolus cannot form perfect contact with irregular surface of the patient's skin, resulting in air gap, especially in irregular surface shape.

Purpose: The purpose of this study was to evaluate the feasibility of two kinds of silicone rubber bolus, RA-00AB and RA-05AB that were made as the fabricated flat and 3D customized bolus using 3D printing technology.

Methods: The 1 cm boluses were made from two kinds of silicone rubber solutions. The planar dose differences were evaluated at 1.5 cm depth by comparing with virtual bolus using gamma index from SNC-patient software. For 3D customized bolus, the bolus shell was designed at nose region by Fusion 360 program. Then print out the shell by 3D printer and fill the shell with silicone rubber solution. The dosimetric effect of 3D customized bolus was compared to without bolus situation.

Results: The planar dose differences presented the excellent agreement with 100% passing rate at 2%/2 mm gamma criteria in both types of flat bolus. However, RA-00AB showed lower passing rate to 80% when the criteria was reduced to 1%/1 mm, while RA-05AB still presented 100%. When 3D customized bolus was placed on the RANDO phantom, surface and build up doses increased and the target volume was obviously presented more uniform doses compared to the without bolus situation.

Conclusion: A silicone rubber bolus produced the feasible dosimetric properties to a commercial bolus and could save cost when compared to commercial bolus. The 3D printed customized bolus is a good buildup material and could potentially replace and improve commercially flat bolus [2].

Keywords: silicone rubber, flat bolus, 3D Customize bolus

Tuning effective spot size parameter in Acuros XB algorithm for Edge™ radiosurgery machine

Warinthorn Rattanaareeyakorn[1], Suphalak Khachonkham[1], Pimolpun Changkaew[1], Panun Sritubtim[1], Surendra Dhungana[1], Nauljun Stansook[1], Pornpan Yongvithisatid[2], Puangpen Tangboonduangjit[1]

1 Master of Science Program in Medical Physics, Department of Diagnostic and Therapeutic Radiology, Faculty of Medicine Ramathibodi Hospital, Mahidol University, Thailand
2 Radiosurgery center, Faculty of Medicine Ramathibodi Hospital, Mahidol University, Thailand

Introduction: The effective spot size parameter (ESS) is an important parameter that can affect to a beam profile shaping and output factor in a small beam such as in radiosurgical beam. Inappropriate ESS can lead improper isodose distribution in treatment planning system. Vendor suggested to use a film to fine-tune ESS by beam profile matching. However, because of film processing complication, the microDiamond detector was used for derived beam profile.

Purpose: To tune an effective spot size parameter in Acuros XB for radiosurgical beam defined by MLCs for Edge™ machine.

Methods: MLC field size of 0.5, 1, 2 cm square field with 3×3 cm^2 Jaw fixing was scanned in crossline and inline. The ESS was varied separately in X and Y directions from 0 to 1.5 mm with 0.25 mm increment. The calculated profile was compared with the measured profile using beam profile matching and penumbra difference in both directions for selecting ESS. The field output factors between default and selecting parameter were compared with measured field output factors followed TRS-483 CoP [5].

Results: The selecting parameter was 0.75 and 0 in X and Y directions, respectively. This parameter showed a good beam profile agreement in shoulder of high dose region for 0.5, 1, 2 cm MLC square fields. The field output factors of selecting parameter showed an excellent agreement (0.02%) in 0.5 cm MLC delimited field while default demonstrate poor agreement (6.66%). However, the field output factors were independent with an ESS for larger fields.

Conclusion: The ESS can improve an accuracy of field output factor calculation in Acuros XB algorithm for a radiosurgical beam size but this parameter is not affected in large field. However, other parameters should be considered such as DLG. More evaluation should be performed to make more confidence of selecting ESS.

Keywords: effective spot size parameter, Acuros XB, field output factor, the microDiamond

Investigation of field output correction factors in small elongated fields for 6 MV photon beam

Mananchaya Vimlnoch[1], Sornjarod Oonsiri[1], Taweap Sanghangthum[2], Sivalee Suriyapee[2], Jan Seuntjens[3]

1 Radiation Oncology Division. King Chulalongkorn Memorial Hospital, Thai Red Cross Society, Bangkok, Thailand
2 Radiation Oncology Division, Radiology Department, Faculty of Medicine, Chulalongkorn University, Bangkok, Thailand
3 Medical Physics Unit, McGill University, Montreal, Québec H3G 1A4, Canada

Introduction: The recent publication of IAEA TRS-483 has clarified the dosimetry of small static fields. The protocol provides the field output correction factors ($k_{Q_{clin},Q_{msr}}^{f_{clin},f_{msr}}$) for symmetry field or when the field is not too elongated (0.7<Y/X<1.4). However, a clinical implementation of these new recommendations may require absorbed dose to be specified in elongated fields which TRS-483 had not yet been issued.

Purpose: To investigate the field output correction factors of the small elongated fields in 6 MV photon beam.

Methods: Three different detectors, including an ion chamber (IBA CC01), a natural diamond (PTW), and a diode detector (Sun Nuclear Edge) were used to determine $k_{\mathbf{Q_{clin},Q_{msr}}}^{\mathbf{f_{clin},f_{msr}}}$ for 20 field sizes of small symmetry and elongated fields. The jaw sizes of symmetric field were 0.6, 1, 1.5, 2, 3, 4, 6, and 10 cm^2. The elongated field sizes with X and Y jaw were 0.6×1, 0.6×1.5, 0.6×3, 1×0.6, 1×1.5, 1×3, 1.5×0.6, 1.5×1, 1.5×3, 3×0.6, 3×1, and 3×1.5 cm^2. The ratio of meter reading of any field sizes and 10×10 cm^2 field size were determined. Then, the averaged ratio of meter reading for three detectors was used as the reference value to determine $k_{Q_{clin},Q_{msr}}^{f_{clin},f_{msr}}$. Then these factors were compared with $k_{Q_{clin},Q_{msr}}^{f_{clin},f_{msr}}$ from TRS-483[1] and Francescon studied.

Results: The calculated $k_{Q_{cli},Q_{msr}}^{f_{clin},f_{msr}}$ of each three detectors for symmetry fields were in good agreement with literatures within 1.2% for field size larger than 0.6x0.6 cm^2. The large differences were observed for all detectors when comparing the $k_{Q_{clin},Q_{msr}}^{f_{clin},f_{msr}}$ of elongated fields with TRS-483. These belonged to fields with either jaw set at 0.6 cm.

Conclusion: The calculated $k_{Q_{clin},Q_{msr}}^{f_{clin},f_{msr}}$ can be used if the jaw Y/X is in the range of 0.7-1.4 if one of the jaw set larger than 0.6 cm.

Keywords: small field, small elongated field, field output correction factors

Comparison of field output factors of different detectors in small field for 6 MV flattening filter and flattening filter free photon beams

Surendra Dhungana [1], Suphalak Khachonkham [1], Pimolpun Changkaew [1], Warinthorn Rattanaareeyakorn [1], Panun Sritubtim [1], Nauljun Stansook [1], Supakiet Piasanthia [1] Pornpan Yongvithisatid [2], Puangpen Tangboonduangjit [1]

1 Masters of Science Program in Medical Physics, Department of Diagnostic and Therapeutic Radiology, Faculty of Medicine Ramathibodi Hospital, Mahidol University, Thailand
2 Radiosurgery Centre, Faculty of Medicine Ramathibodi Hospital, Mahidol University, Thailand

Introduction: The conventional output factors (OF) differ significantly from small field output factors (FOF). At small fields; application of detector specific output correction factors is essential. The difference in detectors response in clinical and reference field size are considered by these correction factors. The higher dose rate in flattening filter free (FFF) compared to with flattening filter (WFF) beams can alter detector responses in small fields.

Purpose: This work aims to compare the FOF of detectors in WFF and FFF modes.

Methods: Small field output factors were measured with 5 detectors (Electron Field Diode-3G, Microdiamond, Ionization chamber - CC01, Dosimetric diode SRS and Edge) for 6 MV WFF and FFF modes in Varian's Edge accelerator. Field sizes (FS) range of 0.6×0.6 - 3×3 cm^2 with a reference field of 10×10 cm^2 were scanned in Blue Phantom^2 system controlled by OMNIPRO-ACCEPT software. Individual detector equivalent square field sizes (S_{clin}) were used for calculation of field output factors except for CC01 for which Microdiamond's S_{clin} was considered.

Results: The mean (reference) FOF of all detectors for nominal square fields of 0.6, 1, 1.5 ,2, 2.5 and 3 cm^2 are 0.498, 0.671 ,0.751 ,0.790, 0.813, 0.831 in WFF mode and 0.529 ,0.688,0.762, 0.797, 0.821, 0.839 in FFF mode respectively. The Standard error of the mean (SEM) are 0.0032, 0.0016, 0.0013, 0.0014, 0.0011, 0.0013 for WFF and 0.0014, 0.0033, 0.0032, 0.0030, 0.0029 ,0.0025 for FFF modes for the respective field sizes mentioned above.

Conclusion: The SEM is higher for FFF than WFF mode in all FS except 0.6×0.6 cm^2. There is the decreasing trend of SEM with an increase in F.S in both modes for FS >0.6×0.6 cm^2.

Keywords: Small field output factors, Detectors, Flattening filter, Flattening filter free

Evaluation of detectors on relative dosimetric measurement for CyberKnife M6 System

Wisawa Phongprapun[1], Siwadol Pleanarom[1], Penpisuth Suksawang[2], Putthipong Chanwichu[1], Chumpot Kakanaporn[1]

1 Division of Radiation Oncology, Faculty of Medicine Siriraj Hospital, Mahidol University, Bangkok, Thailand,
2 Master of Science Program in Medical Physics, Faculty of Medicine Ramathibodi Hospital, Mahidol University, Bangkok, Thailand

Introduction: CyberKnife-M6 machine is normally used for stereotactic radiotherapy especially in small lesion cases with small field for treatment. Thus, small field dosimetry has been challenged for accuracy measurement. From a study of Francescon and Vanessa et al proposed that unshielded diode and synthetic diamond were suitable for small field dosimetry. However, most of diodes still confront with a problem of dose rate dependence and over-response to low energy.

Purpose: The aim of study was to compare the unshielded-diode and synthetic diamond detector effect on relative dosimetry measurement of small field including output factors(OFs), percentage depth doses(PDDs), and beam profiles (BPs) by using PTW-60019, PTW-60017, PTW-60018, and Razor diode.

Methods: The OFs, PDDs, and BPs of CyberKnife-M6 were measured by four detector types with MP3-XS water phantom system for eight fixed circular cone sizes including 5, 7.5, 10, 15, 20, 30, 40, and 60 mm in diameter. Measurement conditions of OFs were at 785 mm source to surface distance(SSD), and 15 mm depth in water. For PDDs, setup condition was at 800 mm SSD by ranging 0 to 280 cm depth in water. In term of BPs, measurement condition was at 800 mm SSD with measurement of four depth in water including 15, 50, 100, and 200 mm.

Results: The OFs before used field output correction factor from TRS-483 and study of Francescon et al. for Razor diode showed more difference of range OFs than the OFs factors with field output correction factor (Mean of max-min OF value; 0.0126, and 0.0082, maximum difference of range, 0.0375, and 0.0260, respectively). The PDDs of PTW-60017, PTW-60018, and Razor diode yielded similar result, but PTW-60019 showed over-response in depth more than 15cm. Field size of BFs had little difference value in each detector. PTW-60019 possessed more penumbra width than another detector.

Conclusion: Type of unshielded diode had effect of relative dosimetric measurement.

Keywords: Relative doismetry, CyberKnife-M6, small-field dosimetry

Surface and Build Up Doses Comparison between Analytical Anisotropic Algorithm and Acuros XB for Various Treatment Parameters

Sonam Choki[1], Sivalee Suriyapee[2], Chulee Vannavijit[3], Taweap Sanghangthum[2]

1 Medical Physics Program, Department of Radiology, Faculty of Medicine, Chulalongkorn University, Bangkok, Thailand
2 Division of Radiation Oncology, Department of Radiology, Faculty of Medicine, Chulalongkorn University, Bangkok, Thailand
3 Division of Radiation Oncology, Department of Radiology, King Chulalongkorn Memorial Hospital, Thai Red Cross Society, Bangkok, Thailand

Introduction: Surface and build up region doses are important for superficial cancer, however, dose calculation and measurement in these regions are challenging because charged particle equilibrium does not exist. The Eclipse treatment planning system has dose calculation algorithms like standard of Analytical Anisotropic Algorithm (AAA) and new algorithm of Acuros XB (AXB).

Purpose: To compare the surface and build-up region doses under various treatment parameters between AAA and AXB algorithms.

Methods: Surface and build up region doses were calculated in a solid water phantom using AAA and AXB algorithms. Doses at the surface and build up region were calculated based on four treatment parameters of energy (6, 10 and 15 MV), field size (1x1 to 40x40 cm^2), dynamic wedge angle (10 to 60 degree), and bolus thickness (0, 1.0 and 1.5 cm). Moreover, the out-of-field doses from 0 to 20 cm from field edge were evaluated.

Results: Surface dose increases linearly with field size and photon energy, with AAA showing higher dose than AXB. The dose differences between two algorithms were ranged approximately from 0.1% to 36% at depth 0.07 cm and 0 cm. With dynamic wedges, surface dose decreases for both algorithms, with difference of about 21% and AAA also showing higher doses. The differences in out-of- field surface dose decreased with distance from the beam edge for both algorithms. The calculated surface dose increases linearly with respect to bolus thickness for both algorithms and for all depths.

Conclusion: Differences in surface dose calculations are observed between AAA and AXB algorithms for all conditions. **At deeper depths, the differences in dose between AAA and AXB become lesser.**

Keywords: Surface dose, Build up region, AAA, AXB.

Determination of small field output factors and specific correction factors for various diodes and microDiamond detector for CyberKnife M6 system equipped with fixed collimator

Penpisuth Suksawang[1], Sawwanee Asavaphatiboon[1], Lakkana Apipunyasopon[2], Wisawa Phongprapun[3], Chumpot Kakanaporn[3]

1 Master of Science Program in Medical Physics, Faculty of Medicine Ramathibodi Hospital, Mahidol University, Bangkok 10400, Thailand
2 Department of Radiological Technology and Medical Physics, Faculty of Allied Health Sciences, Chulalongkorn University, Bangkok 10330, Thailand
3 Division of Radiation Oncology, Faculty of Medicine Siriraj Hospital, Mahidol University, Bangkok 10700, Thailand

Introduction: The CyberKnife M6 (Accuray Incorporated, Sunnyvale, CA, USA), which is a robotic manipulator LINAC delivered small field in radiosurgery techniques. The small field has a challenge on the dosimetric measurements due to characteristics of the beam such as steep dose gradient and unflattened profile. According to TRS483 and Russo S. et al., one of the suggested detectors as a reference is microDiamond PTW60019 because of the material of detector has much better water equivalence than other diodes and provide agreement of Monte Carlo simulation within 0.6%.

Purpose: This study was designed to determine small field output factors and specific output correction factors of CyberKnife M6 equipped with fixed collimators using various detector measurements, including microDiamond PTW60019, diode SRS PTW60018, diode E PTW60017, and IBA RAZOR.

Methods: Measured the relative output factors of PTW60019, PTW60018, PTW60017, and IBA RAZOR. Then calculated the output factors for each detector and used microdiamond as the reference detector to calculate the specific output correction factors for various detectors.

Results: The result showed good agreement of output factors between PTW60019, PTW60018 and PTW60017 at smallest circular field sizes of 7.5mm and 5mm, which the percentage difference compare to PTW60019 are 1.3% and 1.8%**,** respectively. Specific output correction factors does not exceed than 1% ,when compared to TRS483 percentage difference within. 1%.

Conclusion: The result shown the comparable output factor of Cyberknife M6 with fixed collimator between various diodes with percentage difference criteria 1%. The specific output correction factors does not exceed than 1%. In future work should be investigate the measurements of reference detector with Extradin W1, radiochromic film or Monte Carlo simulation.

Keywords: CyberKnife M6, Small field, Output factors, Specific output correction factors

Efficiency of EPID dosimetry based software compared with ion chamber

Wanwanat Sumanaphan[1], Jumneanphan Rueansri[2], Wannita Malila[2], Patsuree Cheebsumon[3]

1 Master of Science Program in Medical Physics, Faculty of Allied Health Science, Naresuan University, Thailand
2 Division of Medical Physics, Department of Radiation Therapy, Lampang Cancer Hospital, Thailand
3 Department of Radiologic Technology, Faculty of Allied Health Science, Naresuan University, Thailand

Introduction: Electronic portal imaging device (EPID) is an essential part of LINAC for patient dosimetry and verification. PerFRACTION™ is EPID dosimetry program. Accessibility of program reduces time to setup. Before using EPID dosimetric program, point dose measurement is a necessary process to confirm software efficiency.

Purpose: To validate point dose measurement in EPID dosimetric program.

Methods: Square fields sizes between 3×3 and 20×20 cm^2 at 5, 10, and 15 cm depth in virtual water phantom on Raysearch (version 9A) TPS for 6 and 10 MV were investigated with collapse cone convolution (CCC) algorithm. Beam output was measured in water phantom as condition of TRS-398, and also square fields sizes were tested. PerFRACTION™ obtained data from TPS and ELEKTA Versa HD™ that delivered directly to EPID in air without phantom to calculate point dose with CCC algorithm. Dose difference from IC and PerFRACTION™ was evaluated, compared with that from TPS.

Results: Average of percentage difference between ion chamber and TPS in 6 MV was 1.16±0.59, 0.66±0.24 and 2.21±0.50 for depth 5, 10 and 15 cm, respectively, between PerFRACTION™ and TPS was 0.29±0.31, 0.63±0.46 and 0.58±0.45.. In 10 MV, average of percentage difference of all field sizes from IC was less than 1.40, except 2.54 at 15 cm depth. In contrast, result from PerFRACTION™ remained relatively stable < 0.74. Field size lower than 5x5 cm^2 dose not received full scatter factor. More different result found in the smallest field. The maximum different found at depth 15 because higher MU effect to scatter.

Conclusion: Point dose good agreements (<3%) between measurements and TPS data were found in 6 and 10 MV. However, maximum different (3.34%) was found in 3×3 cm^2 at depth 15 cm for 10 MV. Measured point doses obtained from PerFRACTION™ were accepted as recommendation of TG-119 report.

Keywords: EPID, Dosimetry, PerFRACTION™, Delta4+™, Validation

An update on local blood irradiation technique using medical LINAC: Blood Irradiation Kit

Janatul Madinah Wahabi[1, 2, 3], Noor Zati Hani Abu Hanifah[1], Manshahruddin Sawal[1], Md Faziali Sulaiman[1], Musa Mohd Salehuddin[1]

1 Pusat Rawatan Onkologi, Hospital Sultan Ismail, Malaysia
2 Department of Radiotherapy and Oncology, National Cancer Institute, Malaysia
3 Department of Biomedical Imaging, University of Malaya, Malaysia

Introduction: Blood irradiation is a procedure of irradiating blood and its component using ionising radiation prior to blood transfusion. The purpose of blood irradiation is to prevent the risk of Transfusion Associated Graft versus Host Disease (TA-GvHD) to the receiver.

Purpose: The objective of this study is to improve blood irradiation technique that has been employed previously and increase the amount of irradiated packed cells to cater for increasing local demand.

Methods: In this study, plastic acrylic was assembled into a box and a homogeneous material was then used to increase dose homogeneity around the packed cells. A treatment plan was then created and the dose distribution around the box was evaluated. The dose delivered to the box was measured using Optically Stimulated Luminescent Dosimeter (OSLDs) to compare between calculated dose and measured dose.

Results: The dose distribution calculated was within 95% to 106% of prescribed dose inside the blood irradiation kit. The box can fill up to 7 units of packed cells and irradiation time was 20 minutes per box. Furthermore, the measured dose using OSLDs were within 5% of the prescribed dose.

Conclusion: The box provides better dose homogeneity and better dose accuracy compared to previous technique adopted. It also simplifies the workflow and is easy to understand by the operators.

Keywords: Blood irradiation, Radiotherapy, OSLD, TA-GvHD

Radiotherapy: Monte Carlo Simulation

Determination of fetal dose and health effect to the fetus from breast cancer radiotherapy during pregnancy

Pattarakan Suwanbut[1], Wilai Masa-nga[2], Chirapha Tannanonta[2], Danupon Nantajit[1], Thiansin Liamsuwan[1]

1 Medical Physics Program, Faculty of Medicine and Public Health, HRH Princess Chulabhorn College of Medical Science, Chulabhorn Royal Academy, Bangkok, Thailand
2 Radiation Oncology Department, Chulabhorn Hospital, Chulabhorn Royal Academy, Bangkok, Thailand

Introduction: Radiotherapy treatment planning during pregnancy must be considered both in-field radiation dose for the patient and out-of-field radiation dose to avoid deterministic effects and minimize stochastic effects for the fetus. According to AAPM TG-36, the fetus must receive dose of less than 10 cGy, which is the threshold dose for deterministic effects. However, the fetal dose also increases the likelihood of cancer development in the fetus. There are many methods used to assess fetal dose, each of which has some limitations. Monte Carlo simulations with realistic patient and radiation field characteristics can help to achieve an accurate assessment of the fetal dose.

Purpose: The objective of this study is to evaluate fetal dose and associated deterministic effects and risks from breast cancer radiotherapy during pregnancy using a Monte Carlo simulation and computational pregnancy phantoms.

Methods: The fetal dose will be simulated with the J-45 computational pregnant female phantom at 8 weeks post-conception receiving dose from a Varian TrueBeam linear accelerator using the Monte Carlo simulation code PHITS version 3.20. The treatment plan used to assess the fetal dose has been used for a breast cancer pregnant patient, for which the planning target volume received a total dose of 50 Gy of 10 MV photons with three-dimensional conformal radiotherapy for the breast tumor. Once the fetal dose is evaluated from the simulation, the occurrence of deterministic effects and the risks for developing stochastic effects will be assessed using the recommendations of NCRP Report No. 174, AAPM Report No. 50 and ICRP Publication 84.

Results: Validation of the Monte Carlo simulation will be presented to assure the accuracy of the calculation. Moreover, the fetal dose and associated deterministic effects and risks will be evaluated and discussed for the case studied.

Conclusion: The Monte Carlo simulation with computational phantoms are mathematical tools that can be used for evaluation of the fetal dose and associated deterministic effects and risks from radiotherapy treatment of pregnant breast cancer patients.

Keywords: Fetal dose, Monte Carlo simulation, Computational phantom, Deterministic effect, Stochastic effect

Calculation of field output correction factors for radiophotoluminescence glass dosimeter in 6 MV WFF and FFF small photon beams using Monte Carlo simulation

Sumalee Yabsantia[1], Sivalee Suriyapee[1], Nakorn Phaisangittisakul[2], Sornjarod Oonsiri[3], Taweap Sanghangthum[1], Jan Seuntjens[4]

1 Department of Radiology, Faculty of Medicine, Chulalongkorn University, Bangkok, Thailand
2 Department of Physics, Faculty of Science, Chulalongkorn University, Bangkok, Thailand
3 Department of Radiation Oncology, King Chulalongkorn Memorial Hospital, Thai Red Cross Society, Bangkok, Thailand
4 Medical Physics Unit, McGill University, Montreal, Québec H3G 1A4, Canada

Introduction: The high atomic number, density, and volume of radiophotoluminescence glass dosimeter (RPLGD) affect the perturbation factor in small field dosimetry. Therefore, the field output correction factor should be employed when using RPLGD for determining field output factors.

Purpose: To determine the field output correction factors of RPLGD for 6 MV flattened (WFF) and unflattened (FFF) beams using Monte Carlo simulation

Methods: The ratio of absorbed dose to a small water volume and sensitive volume of RPLGD were determined at 90-cm SSD, 10-cm depth for 6 MV WFF, and FFF beams using egs_chamber user-code. The field output correction factors of RPLGD for jaw field size range from 0.5×0.5 to 10×10 cm^2 were determined. The orientations of RPLGD were perpendicular and parallel.

Results: The RPLGD in perpendicular orientation for both energies exhibited underestimation for all field sizes. For the parallel orientation, the detector showed underestimation for field size down to 1×1 cm^2, while overestimations were observed for lower field sizes. In the smallest field size, the corrections of RPLGD in parallel & perpendicular orientations for 6 MV WFF and FFF were respectively within 5% & 19% and 3% & 21%.

Conclusion: The field output correction factors of RPLGD in parallel orientation are suitable for determining field output factors down to 0.5×0.5 cm^2 field size for 6 MV WFF and FFF beams. However, the RPLGD in the perpendicular direction can determine field output factors to 1×1 cm^2 field size.

Keywords: egs_chamber, Field output correction factors, Small field, Radiophotoluminescence glass dosimeter

Investigation of dose perturbations around brachytherapy seeds in high-energy photon beams

Shuta Ogawa[1], Keisuke Yasui[2], Yasunori Saito[3], Kazuki Ouchi[1], Junya Nagata[1], and Naoki Hayashi[2]

1 Graduate School of Health Sciences, Fujita Health University
2 School of Medical Sciences, Fujita Health University
3 Division of Radiology, Fujita Health University Hospital

Introduction: A combination of external-beam radiation therapy and brachytherapy (combo-RT) is useful for the treatment of high-risk prostate cancer. However, the dose perturbations around seeds due to backscatter and attenuation during combo-RT is difficult to calculate on treatment planning systems.

Purpose: The purpose of this study was to investigate the dose perturbations around seeds in high-energy photon beams (6 MV, 10 MV; with flattening filter (WFF), flattening filter-free (FFF)).

Methods: TheraAgX100 (TAX) and Bard BRACHYSOURCE STM125I (BBS) were used for seed models. We calculated the dose distribution around seeds by Monte Carlo (MC) code (PHITS ver.3.11) under the following geometric conditions: (a) One seed at the depth of 5.0 cm on the beam axis in water (b) Three seeds at the depths of 4.8, 5.0 and 5.2 cm on the beam axis in water (c) One seed at the center of the elliptical columnar water phantom. It was irradiated from one direction under the condition (a) and (b); five directions under the condition (c). The measurement using GafchromicEBT3 films under the condition (a) with TAX carried out to verify the accuracy of the MC calculation. The dose perturbation is defined as the difference between the dose with and without the seed.

Results: The result of MC simulations was coincident with film measurements within 4%. The dose perturbations were ranging from -14.9% (condition (b), on the downstream of TAX, 10 MV-WFF) to 13.0% (condition (b), on the upstream of BBS, 6 MV-WFF) on the beam axis under the condition (a) and (b). Only dose enhancements of up to 9.0% were observed under the condition (c).

Conclusion: The dose perturbations around seeds in high-energy photon beams were investigated by the MC simulation and film measurements. The seeds located close to organs at risk may cause excessive irradiation.

Keywords: Monte Carlo simulation, prostate cancer, brachytherapy, external-beam radiation therapy

Monte Carlo Simulation of semiflex chamber in Megavoltage Photon Beam

Suresh Poudel[1], Gunter Hartmann[2], Golam Abu Zakaria[3], ***Asita Kulshreshtha[1]***

1 Amity School of Applied Sciences, Amity University, Lucknow Campus, Lucknow, India,
2 German Cancer Research Center, Heidelberg, Germany
3 Klinikum Oberberg, Teaching Hospital of University of Colonge, Germany

Introduction: Monte Carlo (MC) method provides a numerical solution to a problem that can be described as a temporal evolution of objects interacting with other objects based upon object−object interaction relationships. It is a numerical method to solve equation or to calculate integrals based on random number sampling and statistical analysis to compute results. MC is used when it is difficult to solve a problem analytically, for example, there are too many particles in the system and have complex interactions among the particles or with the external field.

Purpose: The main purpose of this study is to perform MC simulation with PTW semiflex chamber in 6 MV photon beams. The specific purposes are to determine the appropriate profile estimator at and to utilize the same estimator to predict the profiles at other depths, hence, to explain the differences between measured profile and MC generated profiles.

Methods: Assuming point source (isource=3) incident on the water phantom from front, for PTW semiflex chamber, MC simulation program is written in Visual Studio Fortran Compiler to generate a random profile, field size= 4*4 cm^2 at SSD= 100 cm and 0.5 cm depth in water from an ideal estimator, which is a rectangular profile. Thus generated MC profile is compared with measured profile in same depth. The differences between the MC profile and measured profile are accounted to adjust the estimator to proper shape. Hence, the adjusted estimator is used to generate the profiles at 5 cm and 10 cm depths in water.

Results: A parameter a=2 mm is added to the field border where the profile changes from 0 to 1, and the contribution outside the field is accounted to define appropriate shape of the estimator, which is trapezoid shaped. This estimator appropriately generated the profiles at 5 cm and 10 cm depths in water at SSD=100.

Conclusion: The estimator could appropriately generate the MC profiles at any depths in water for semiflex chamber. The success of this study will reduce the time in measuring the profiles at different depths during commissioning of external beam radiotherapy.

Keywords: Monte Carlo Simulation, Random Number Sampling, Profiles

Estimation of Linear and Mass Attenuation Coefficients of Soy-lignin Bonded *Rhizophora* spp. Particleboard as a Potential Phantom Material for Low- and High-energy Studies using Monte Carlo Simulation

Siti Hajar Zuber[1], Muhammad Rizal Fahmi[1], Nurul Ab. Aziz Hashikin[1], Mohd Fahmi Mohd Yusof[2], Rokiah Hashim[3]

1 School of Physics, Universiti Sains Malaysia, 11800, Penang, MALAYSIA.
2 School of Health Sciences, Universiti Sains Malaysia, 16150, Kelantan, MALAYSIA.
3 School of Industrial Technology, Universiti Sains Malaysia, 11800, Penang, MALAYSIA.

Introduction: Estimation of linear and mass attenuation coefficients of materials for medical physics application is important, as they affect the interactions of radiations with the material, among other factors.

Purpose: We aim to estimate the linear and mass attenuation coefficients of a fabricated particleboard intended for use as a phantom material, using GATE Monte Carlo (MC) package at low- and high-energy photons. The results were compared with experimental measurements.

Methods: Particleboard made of *Rhizophora* spp. wood trunk bonded with soy-flour and lignin were fabricated at target density of 1.0 $g.cm^{-3}$. The elemental composition of the sample was obtained from Energy Dispersive X-ray (EDX) spectroscopy. Americium-241 (^{241}Am) was used for low energy, while Cobalt-60 (^{60}Co) and Cesium-137 (^{137}Cs) were used for high energy. For low energy, samples were placed at 6.0 cm from the source, and 7.0 cm from the LEGe detector. For high energy, samples were placed at 20.0 cm from the source, and 10.0 cm from the NaI detector. Similar setups were simulated via GATE (version 1.2.3) MC package, with histories of 1×10^6 to 1×10^8. Finally, the linear and mass attenuation coefficients obtained from the experimental measurements and simulations were compared and discussed.

Results: The percentage differences between the experimentally measured and calculated (via GATE) linear and mass attenuation coefficients of the samples at high energies were smaller (6.4% for ^{137}Cs and 5.4% for ^{60}Co) compared to that of the low energy (56%). This could be due to the boundary conditions and device limitation of the simulated model in correspond to the experimental setup. Regardless, all the recorded attenuation coefficients obtained were in good agreement to the attenuation coefficient of water based on XCOM data.

Conclusion: The particleboard has the potential to be used as a phantom material as the attenuation coefficients obtained were in good agreement to that of water. Verification of experimental measurement via GATE simulation has been shown crucial in providing reliable data for high energy studies.

Keywords: Monte Carlo Simulation; X-Ray Fluorescence; Energy Dispersive X-ray Spectroscopy; particleboard; soy-lignin adhesive

Comparison simulation treatment between Gamma Knife and Linac Stereoradiosugery on small target volume by using GEANT 4 Monte Carlo Simulation.

Mohammad Shazmi bin Sapeei[1], Muhammad Rizal Fahmi[1], Nik Noor Ashikin Nik Ab Razak[1], Nurul Ab. Aziz Hashikin[1]

1 School of Physics, Universiti Sains Malaysia, Pulau Pinang, 11800, MALAYSIA

Introduction: Stereotactic radiosurgery (SRS) is a radiation therapy technique that delivers an accurate and efficient high radiation dose to smaller diameter of target tumor that able deliver in single fraction. These studies were simulating Stereotactic radiosurgery (SRS) techniques used by Linac-based SRS and Gamma Knife based on real treatment setup.

Purpose: We aimed to compare absorbed dose received by organ at risk (OAR) by simulating IMRT, SRS VMAT coplanar, SRS VMAT with non-coplanar and Gamma Knife technique to treat 1.8 mm diameter of parasellar meningiomas using GEANT 4 Application.

Methods These simulations were using GEANT 4 Montecarlo Simulation using MIRD5 human_phantom (readily available in GEANT 4 Monte Carlo package) with additional active volume for OARs such as brain, brain stem, optic chiasm, optic nerve, eyeball, lens, parotid gland and upper spine. Other than that, these simulations are involve the placement of beam arrangement for Linac-based SRS and Gamma Knife to treat 18 mm diameter tumor using 24 Gy prescribed dose. Additionally, in this study the effect of 6 MV and 18 MV photon of Linac-based SRS for IMRT-8 fields, SRS VMAT with coplanar, SRS VMAT with non-coplanar were measured.

Results: From the result obtained, dose falloff of SRS VMAT non-coplanar techniques using 18 MV photon was sharper than Gamma Knife, SRS VMAT coplanar and IMRT technique. Other than that, IMRT technique shows higher absorbed dose to cochlear and optic chiasm as compared to other therapy simulation techniques.

Conclusions: In conclusion, the comparison between all the techniques shows SRS VMAT with non-coplanar technique using 18 MV photon is the most efficient technique for treatment small brain tumor near the OARs.

Keywords: GEANT 4, Stereotactic radiosurgery (SRS), Monte Carlo simulation

Monte Carlo calculation of beam quality correction factors in proton beams using PTSIM/GEANT4

Masaya Ichihara[1], Keisuke Yasui[2], Chihiro Omachi[3], Toshiyuki Toshito[3], Junya Nagata[1], Riki Oshika[1], Shun Kurata[1] and Naoki Hayashi[2]

1 Graduate school of Health Sciences, Fujita Health University,
2 School of Medical Sciences, Fujita Health University,
3 Nagoya Proton Therapy Center

Introduction/Purpose: In radiotherapy, determination and management of delivery dose by measuring the absolute dose are important. The reference dose for clinical proton beams is based on ionization chamber dosimetry. However, there are few data on the beam quality correction factors (k_Q) required for calculating the absolute dose for the proton beam. Furthermore, the perturbation correction factor (P_Q) of ionization chambers is assumed to be unity for proton beams in the IAEA TRS-398 CoP. Hence, the aim of this study is to calculate k_Q factors for ionization chambers in proton beams using the Monte Carlo simulation (MC), and also calculated P_Q to clarify whether the assumption from the IAEA TRS-398 CoP is sufficiently accurate or not.

Methods: We used PTSIM version 10.05.p01, a toolkit based on the Monte Carlo code GEANT4. As reference beam quality Q_0, we used a ^{60}Co source. We reproduced a spot scanning nozzle at the Nagoya Proton Therapy Center and calculated the k_Q for the cylindrical ionization chamber (30013: PTW). We investigated four different monoenergetic beams (150,160,200 and 250 MeV). To estimate the P_Q, the water to air stopping power ratios ($S_{w,air)}$ calculated in the previous report were used for each beam.

Results: The f_{Q0} was agreed with previous study within a standard deviation. The k_Q was the agreement with previous studies at 150 MeV, however, there was a difference of up to 2.2% at 250 MeV. The total perturbation correction factor for PTW 30013 was 0.990 at 200 MeV.

Conclusion: We calculated the k_Q factors under the clinical condition in proton beams using PTSIM/GEANT4. We need to further investigate the k_Q for high proton energies. Additionally, P_Q are different than unity in contrast to the assumption from the IAEA TRS-398 CoP.

Keywords: proton dosimetry, beam quality correction factors, perturbation correction factors, Monte Carlo

VDOSE: A tools to analyze dose distribution from Monte Carlo dose Calculation

Sitti Yani[1], Kamirul[2], Mohamad Fahdillah Rhani[3], Choirul Anam[4], Freddy Haryanto[5]

1 Department of Physics, Faculty of Mathematics and Natural Sciences, IPB University (Bogor Agricultural University), West Java, 16680, Indonesia,
2 Indonesian National Institute of Aeronautics and Space, Jl. Goa Jepang, Sumberker, Samofa, Kabupaten Biak Numfor, Papua 98118, Indonesia,
3 Radiolology Department, National University Cancer Institute, Singapore, 119074, Singapore,
4 Department of Physics, Faculty of Sciences and Mathematics, Diponegoro University, Central Java, 50275, Indonesia,
5 Department of Physics, Faculty of Mathematics and Natural Sciences, Institut Teknologi Bandung, West Java, 40132, Indonesia

Introduction: DOSZYZnrc Monte Carlo code can be used to simulate IMRT planning with several different beam angles. At the end of simulation, the several dose distribution data will be produced. Each beam angle produces one distribution data. To obtain the real dose distribution, the data must be combined into one file and cannot be done with DOSXYZnrc.

Purpose: Therefore, the graphical user interface based on MATLAB namely VDOSE GUI was developed to combine the dose distribution data from some beam angles and produce the dose volume histogram (DVH) curve.

Methods: The VDOSE GUI inputs required only the 3ddose and egsphant files. These files obtained from each simulation with different beam angle using DOSXYZnrc can be read by dosxyz_show. However, this dosxyz_show program still have some drawbacks in displaying more than one 3ddose data at the same time, especially for IMRT. In this study, IMRT simulation with seven beam angles was used to produce seven different 3ddose and one egsphant files. These files were combined using VDOSE GUI in the end of simulation. The isodose curve obtained from one angle using dosxyz_show and VDOSE GUI was compared.

Results: The VDOSE GUI can assist to combine more than one dose distribution in one. 3ddose file and calculate the DVH. The similar contour was obtained from dosxyz_show and VDOSE GUI. The relative dose error in the dose distribution for body from VDOSE GUI and anisotropic analytical algorithm (AAA) was 51.23%.

Conclusion: The isodose contour and DVH curve formed from the IMRT simulation using EGSnrc have a pattern that is similar to the isodose and DVH from AAA TPS. Although some slices show different isodose curve.

Keywords: VDOSE GUI, EGSnrc, MATLAB, IMRT

Radiotherapy: Radiobiology

Low-dose radiation enhance cytotoxicity of chemotherapeutic agent (pirarubicin) in K562 and K562/adr leukemic cancer cells

Khin The Nu Aye[1], Benjamaporn Supawat[1], Suchart Kothan[1], Chatchanok Udomtanakunchai[1], Singkome Tima[2], Montree Tungjai[1]

1 Department of Radiologic Technology, Faculty of Associated Medical Sciences, Chiang Mai University, Chiang Mai, Thailand, 50200
2 Division of Clinical Microscopy, Department of Medical Technology, Faculty of Associated Medical Sciences, Chiang Mai University, Chiang Mai, Thailand, 50200

Introduction: Cancer disease is a major cause of death in the world. There are several strategies to overcome cancer disease is used for cancer treatment. Radio-and Chemo-therapy, one of these strategies play important rule in cancer treatment especially for systemic cancer. Recently, the evidences suggest no deleterious effect of low-dose radiation (<100 mGy) in normal cell. In contrast, low-dose radiation can induce the hyper-radiosensitivity in a number of cancer cells. In this study, low-dose radiation and chemotherapeutic agent (pirarubicin) was used for treating in cancer cells. Pirarubicin (4'-O-tetrahydropyranyl doxorubicin), one of the anthracycline groups is clinical anticancer drug.

Purpose: To determine effect of low-dose radiation on cytotoxicity of pirarubicin in K562 and K562/adr leukemic cancer cells.

Methods: The K562 and K562/adr cancer cells were exposed to X-radiation at 0.02, 0.05 and 0.1 Gy of X-radiation doses. At 24 hours after irradiation, cells were treated with 10 nM pirarubicin. Cells were not exposed to X-radiation and not treated with pirarubicin serve as a control. The cell viability was determined by using resazurin assay at 24 hours after treatment with pirarubicin. In addition, cell morphology was observed under light microscope.

Results: The cell viability was decreased in both K562 and K562/adr cancer cells after exposure to X-radiation followed by treatment with 10 nM pirarubicin, as compared to control. Also the change of cell morphology in exposed cells was found.

Conclusion: This finding suggested that low-dose radiation could enhance cytotoxicity of pirarubicin in K562 and K562/adr leukemic cancer cells. The mechanism should be further investigation.

Keywords: ionizing radiation, chemotherapeutic agent, cancer cells

Radioprotective effect of interruptin derived from *Cyclosorus terminans* could protect cell damage of irradiated normal cells from radiotherapy

Nipha Chumsuwan[1,2], Pasarat Khongkow[1], Sireewan Kaewsuwan[3], ***Kanyanatt Kanokwiroon***[1*]

1 Department of Biomedical Sciences and Biomedical Engineering, Faculty of Medicine, Prince of Songkla University,
2 Department of Radiology, Faculty of Medicine, Prince of Songkla University,
3 Department of Pharmacognosy and Pharmaceutical Botany, Faculty of Pharmaceutical Sciences, Prince of Songkla University

Introduction: Radiotherapy is one of the most common method to treat cancers. The irradiation of tissues during radiotherapy leading to various complications. The main radiation damage occurs from free radicals generated by interaction of radiation with water. Radioprotectors are the agents administered to reduce toxicity of normal tissues from radiotherapy. The natural compounds with free radicals scavenging activity were shown to be the effective radioprotectors. Thus, interruptin derived from *C. terminans* may be use as the radioprotector to reduce the effect from radiotherapy in normal cells.

Purpose: To investigate radioprotective activity of interruptin in x-ray irradiated normal cells.

Methods: The radioprotective effect of interruptin was demonstrated in HaCat skin keratinocyte and MCF-10A normal breast cell lines. MDA-MB-231 and Hs578T human breast cancer cell lines were used as cancer cell models. Irradiation was performed using 6 MV x-ray linac. After irradiation, the clonogenic cell survival assay was carried out to evaluate cell survival. SOD activity assay was used to investigate the antioxidant enzyme activity. The investigation of DNA repair dynamic was performed by γ-H2AX assay. Micronuclei formation assay was detected DNA damage and cell cycle progression.

Results: Our results showed that pre-treatment of interruptin in irradiated normal cells showed more cell survival than irradiated-normal cells alone. However, interruptin did not promote cell proliferation in cancer cells. Antioxidant activity also increased in interruptin pre-treatment normal cells while significantly decreased DNA damage by reducing γ-H2AX foci and micronucleus formation (p value < 0.05).

Conclusion: The radioprotective effects of interruptin could recover the cell viability of x-ray irradiated normal cells in both HaCat skin keratinocyte and MCF-10A cells. Moreover, interruptin did not enhance cell viability of cancer cells. Finally, interruptin may be a potential compound for developing as the radioprotective agent to reduce the complication in radiotherapy patients.

Keywords: radioprotective effect, interruptin, cell damage, radiotherapy, breast cancer

Temperature variation of stimulated diabetic blood and its effects on Evaluated specific absorption rate (SAR) when used a 532 nm wavelength laser for therapeutics.

Sylvester J. Gemanam[1,2], Nursakinah Suardi[1], Barnabas A. Ikyo[2], Samson Damilola Oluwafemi[1], Soheila Mokmeli[2]

1 School of Physics, Universiti Sains Malaysia (USM), Pulau Pinang, Penang, 11800, Malaysia.
2 Department of Physics, Faculty of Science, Benue State University, Makurdi, 102119, Nigeria.
3 Canadian Optic and Laser Center, COL Center, Victoria, Canada.

Introduction: Human blood exposed to irradiation absorbed electromagnetic energy which consequently effect temperature variation. The evaluation of Specific Absorption Rate (SAR) of human blood helps to determine the values for optimum laser power, time and temperature variation for fair therapy to avoid blood-irradiation pollution but improving its rheological properties in using lasers. The prior knowledge of blood SAR evaluating its dielectric properties is important; however, this is under investigated.

Purpose: We investigate the appropriate SAR threshold value as affected temperature variation using fundamental blood dielectric parameters for the optimal effect of low level laser therapy based on the physiological and morphological changes of the stimulated diabetic blood.

Methods: Studies were carried out with Agilent 4294A impedance analyser at frequencies (40Hz – 30MHz) and designed cells (cuvettes) comprises of electrodes were used in the measurements before and after irradiations. Blood samples were exposed at various irradiation therapy durations using portable laser diode-pumped solid state with wavelength 532 nm at different laser power output.

Results: Result showed laser at low energy is capable of moderating morphologically the proportion of abnormal diabetic red blood cells. Hence, there is a significance effect using laser at low energy, as non-medicinal therapy in controlling diabetic health conditions.
The positive biostimulation effects on the irradiated diabetic blood occurred within absorbance threshold SAR values range $0.140 \leq 0.695$ W/kg and average temperatures range $24.2 \leq 26.0\ ^{0}$C before blood saturation absorbance peak.

Conclusion: There is morphological stimulation at laser power of 50 mW for exposure time of 10-15 minutes and 60 mW for 5 -10 minutes of laser therapy that demonstrates better blood rejuvenated conditions. This occurred within the threshold SAR of $0.140 \leq 0.695$ W/kg and average temperatures range $24.2 \leq 26.0\ ^{0}$C. The diabetic blood irradiated using laser output powers of 70 and 80 mW within exposure durations of 5-20 minutes rather bio-inhibits positive blood stimulation therefore resulted to crenation due to excessive irradiation.

Keywords: Dielectric properties, specific absorption rates, diabetic blood, low level laser therapy.

The Effect of Different Sizes of Bismuth Oxide Nanorods on Radiosensitization Enhancement Ratio

Amirah Jamil, Safri Zainal Abidin, Wan Nordiana Wan Abd Rahman

School of Medical Sciences, Health Campus, Universiti Sains Malaysia, 16150 Kubang Kerian, Kota Bharu, Kelantan, Malaysia

Introduction: Years after the discovery of metal nanoparticles, it is recognised that synthesized nanoparticles have unique physical and chemical properties (Conde et al., 2012) especially in increasing the radiosensitization effects to cancer tissue, including hypoxic cancers. High atomic number (Z) properties which is the main determinant factor that increase the probability of radiation interaction through secondary electron effects are well-known concept in radiation physics.

Purpose: In this study, hydrothermal technique was implemented for the synthesis of 60, 70, 80, and 90 nm bismuth oxide nanorod (Bi_2O_3-NR) to investigate the radiosensitization enhancement of Bi_2O_3-NR of different sizes in radiotherapy.

Methods: A total of 1 x 10^4 cells was inserted into 10 sterile microvial tubes for every nanoparticles size (60, 70, 80, and 90 nm) including control groups, and the samples were exposed to different radiation doses using photon beam and electron beam irradiation. For photon beam irradiation, the samples were placed onto a 10 cm solid water phantom, and then the bolus of 1.5 cm was placed on top of the samples for 6 MV photon beam irradiation. Meanwhile, 2.5 cm bolus was used for 10 MV photon beam energy to deliver maximum dose. The samples were placed on solid water phantom (10 cm) and covered with 2.5 cm bolus to deliver maximum dose for 6 MeV and bolus of 3.5 cm for 12 MeV for electron beam protocol. All samples were irradiated with different radiation doses (0.0, 0.5, 1.0, 1.5, 2.0, 4.0, 6.0, 8.0, 9.0 and 10.0 Gy). Cell colony formed after irradiation could be visible on the plate and the colour was purple after staining with crystal violet. The data was fitted based on linear quadratic model and the sensitization enhancement ratio (SER) was determined to indicate radiosensitizing effects of Bi_2O_3-NR.

Results: Analysis of different sizes of Bi_2O_3-NR conducted in this study showed that the enhancement of radiosensitization is influenced by smaller size of Bi_2O_3-NR. From Figure 1, the result reveals that SER value was higher for Bi_2O_3-NR of 60 nm upon radiation of 6 MV photon beam. Furthermore, upon irradiation with 10 MV photon beam, 60 nm Bi_2O_3-NR yielded the highest SER value. Radiosensitization effect experiment using electron beam as shown in Figure 2 showed that the size of Bi_2O_3-NR plays important factor in enhancing radiotherapy outcome in cancer cell killing. It was found that 60 nm Bi_2O_3-NR yielded the highest SER value for both 6 and 12 MeV electron beam. Meanwhile for 70 nm Bi_2O_3-NR, the SER value was the second highest followed by 80 and 90 nm in size. The results generated from this study showed that 60 nm Bi_2O_3-NR resulted in the most optimum enhancement of radiosensitization, followed by 70 nm. Meanwhile, 80 and 90 nm Bi_2O_3-NR were not effective in increasing radiosensitization effect on cancer cells.

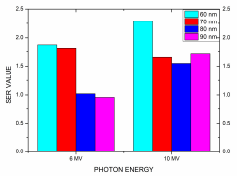

Figure 1 Effect of different size of Bi_2O_3-NR on MCF-7 cell using 6 and 10 MV photon beam.

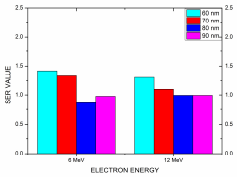

Figure 2 Effect of different size of Bi_2O_3-NR on MCF-7 cell using 6 and 12 MeV electron beam.

Conclusion: In this study, it was discovered that Bi_2O_3-NR of 60 nm generated the highest SER, and it has the potential to destroy cancer cells. This is presumably due to the nanoparticles being absorbed into the cells and interact with radiation. However, the use of high concentration and very small nanoparticles can cause cytotoxicity to the normal cells. Therefore, determination of the most optimum concentration and size of nanoparticles is very important for future research.

Keywords: Bismuth nanorods, nanoparticles, radiotherapy, cancer cells, SER

The Effect of Different Sizes of Bismuth Oxide Nanorods on Cancer Cells

Amirah Jamil, Safri Zainal Abidin, Wan Nordiana Wan Abd Rahman

School of Medical Sciences, Health Campus, Universiti Sains Malaysia, 16150 Kubang Kerian, Kota Bharu, Kelantan, Malaysia

Introduction: With the advancement of technology, various approaches have been developed to increase radiation intensity to cancer tissue, which in turn increasing the effectiveness of killing radioresistant cancer cells. Therefore, abundance of research has studied the potentials of various metallic nanoparticles increasing the effectiveness of radiotherapy.

Purpose: This study is conducted to investigate the effect of different size of bismuth oxide nanorods (Bi_2O_3-NR) on MCF-7 and HeLa cancer cells.

Methods: A total of 1 x 10^4 MCF-7 and HeLa cells were inserted into sterile microvial tubes. Then, Bi2O3-NR of different concentrations (0.05, 0.25, and 0.5 µMol/L) were added and was gently mixed with the cells using pipette. Meanwhile for control samples, both cells were prepared without Bi_2O_3-NR. A total of 10 microvials were prepared for every nanoparticles size (60, 70, 80, and 90 nm) including control, and were exposed to different radiation dose (0-10 Gy). For 6 MV photon beam irradiation, the samples were placed onto a solid water phantom (10 cm), and then the bolus of 1.5 cm (depth of maximum dose) was placed on top of the samples. Meanwhile, 2.5 cm bolus was used for 10 MV photon beam energy to deliver maximum dose. The samples for electron beam irradiation were set up according to the photon beam procedure, in which the samples were placed on solid water phantom (10 cm) and covered with 2.5 cm bolus to deliver maximum dose for 6 MeV and bolus of 3.5 cm for 12 MeV.

Results:

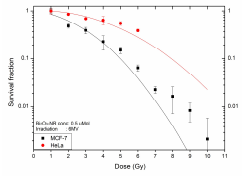

Figure 1 *Comparison between MCF-7 and HeLa cell line treated with Bi_2O_3-NR and irradiated using 6 MV photon beam.*

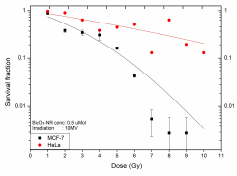

Figure 2 *Comparison between MCF-7 and HeLa cell line treated with Bi_2O_3-NR and irradiated using 10 MV photon beam*

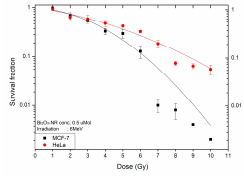

Figure 3 *Comparison between MCF-7 and HeLa cell line treated with Bi_2O_3-NR and irradiated using 6 MeV electron beam.*

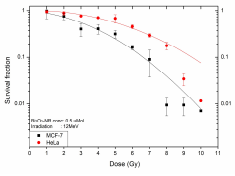

Figure 4 *Comparison between MCF-7 and HeLa cell line treated with Bi_2O_3-NR and irradiated using 12 MeV electron beam.*

Cell survival curves from Figure 1 to 4 showed that MCF-7 cell experienced more death compared to HeLa cells when irradiated with photon and electron beam. These results indicated that the Bi_2O_3-NR inflicted more radiosensitization in MCF-7 cells. Khoshgard (2017) reported that dextran-coated iron oxide nanoparticles increase the effect of radiosensitivity when irradiated with 6 MV photon beam. It was discovered from the study that MCF-7 cell produced higher SER value (1.21 ± 0.06) compared to HeLa cell (1.19 ± 0.04). The difference is presumably due to the different characteristics of the cells such as type of receptors, number of mitochondria, chromatin structure, all of which affect the cell radiation sensitivity.

Conclusion: This study discovered that MCF-7 has higher radiosensitivity and increased cell death compared to HeLa when Bi_2O_3-NR was used. Therefore, different cell types exhibit different level of radiosensitivity.

Keywords: Bismuth oxide nanorods, nanoparticles, radiotherapy, MCF-7, HeLa

Influence of PEG-coated Bismuth Oxide Nanoparticles on ROS Generation for Electron Beam Radiotherapy

Noor Nabilah Talik Sisin[1], Nur Fatin Amirah Radzuan[1], Muhammad Afiq Khairil Anuar[1], Norhayati Dollah[2], Khairunisak Abdul Razak[3], Wan Nordiana Rahman[1]

1 School of Health Sciences, Universiti Sains Malaysia, Malaysia.
2 Department of Nuclear Medicine, Radiotherapy and Oncology, Hospital Universiti Sains Malaysia, Malaysia
3 School of Materials and Mineral Resources Engineering, Universiti Sains Malaysia, Malaysia.

Introduction: Nanoparticles (NPs) have been proven to enhance radiotherapy efficacy. The introduction of coating materials such as PEG to NPs is found to impact the NPs' biocompatibility and effectiveness as a radiosensitizer. Optimization of surface coating is a crucial element to ensure the successful application of NPs as a radiosensitizer in radiotherapy.

Purpose: This study aims to investigate the influence of bismuth oxide NPs (BiONPs) coated with different PEG concentrations on reactive oxygen species (ROS) generation after electron beams irradiation on HeLa cervical cancer cell line.

Methods: The HeLa cells were treated with BiONPs coated with different PEG concentrations (0.05, 0.10, 0.15 and 0.20 mM). The samples were irradiated under 3 Gy dose of electron beam energies (6 and 12 MeV). ROS generation was measured immediately after irradiation and after 3 hours of incubation.

Results: The percentages of ROS generated in the presence of PEG-BiONPs were higher than the uncoated-BiONPs. It also found that a high energy electron beam plays a role in increasing the ROS generation. The ROS generated for 6 MeV electron beam, and BiONPs with 0.05 mM of PEG was found to induce the highest ROS with 234%, with a slightly different result of 232% for 12 MeV. Data showed that higher concentration of PEG (0.2 mM) decreased the ROS generation to 225% for 6 MeV and 229% for 12 MeV. There were also linear increments of ROS after 3 hours of incubation, up to 339% for 6 MeV and 357% for 12 MeV**.**

Conclusion: Slight increase of the ROS by the PEG-BiONPs relative to the uncoated-BiONPs indicated the non-toxicity of the surface coating. Higher PEG concentrations also perhaps more biocompatible. Finally, the PEG coating might not contribute substantial effects towards the ROS generated, emphasizing the BiONPs application as the radiosensitizer for HeLa cells.

Keywords: PEG, Bismuth oxide, Reactive oxygen species, Radiotherapy

Radiotherapy: Treatment planning

Dosimetric Validation of Monaco Treatment Planning System

Viphophone Inphavong[1], Thibaud Saibaing[2], David Little[3], Taweap Sanghangthum[4]

1 Radiotherapy Center, Mittaphab Hospital, Vientiane Capital, Lao PDR.
2 Medical Physics and Radiation Safety Department, Hospices Civils de Lyon, France
3 Medical Physics and Bioengineering, Canterbury District Health Board, New Zealand
4 Division of Radiation Oncology, Department of Radiology, Faculty of Medicine, Chulalongkorn University, Bangkok, Thailand.

Introduction: The error in dose calculation can lead to tumor control probability change. The accuracy of dose distribution is necessary to validate.

Purpose: To study the dosimetric influences of photon beams for Collapse Cone Algorithm in Monaco TPS calculation.

Methods: Photon beam characteristics of Collapse Cone Algorithm in Monaco TPS were verified in various square fields by comparing with measured PDDs and profiles in water phantom using 0.125CC cylindrical chamber. Moreover, the squares, rectangular, complex MLC shapes and wedge fields have been calculated following IAEA TRS-430 guideline in homogeneous and heterogeneous slab phantoms. All plans were exported to Mosaiq sequencer and Elekta Synergy Platform for beam delivery. Point dose at central axis and off-axis were measured using 0.6CC Farmer and 0.125CC cylindrical chamber. In clinical assessment, relative electron density (RED) curves on TPS were created based on universal curve and Elekta robust curve data. The 22 cases of brain, head&neck, lung, breast and cervix regions of 3D-CRT were planned on both types of RED curves. The absolute dose differences at isocentre were compared, and D_{90} of PTV was also evaluated.

Results: The measured PDDs and profiles of square fields showed good agreement to TPS with maximum dose difference of 1%. For point-dose at various situations, average dose differences were -1.20±0.013% and 0.2±0.011% in homogeneous phantom, -1.0±0.002% and -0.4±0.004% in heterogeneous phantom for 0.6CC and 0.125CC chambers, respectively. Therefore, these differences were within the limits as the recommendation from IAEA TRS-430 and AAPM TG-53. For clinical assessment, average dose difference between 2 types of RED curves was 0.1±0.6% and D_{90} difference of PTV was 0.1±0.1%.

Conclusion: **The accuracy of dose calculation in** Monaco TPS based on the Collapse Cone Algorithm meets international recommendations and can be implemented in clinic for patient treatments.

Keywords: PDD, Collapsed Cone Algorithm, Monaco TPS, 3D-CRT

Evaluation of dose calculation algorithm accuracy in Eclipse treatment planning system for jaw-defined and MLC-defined small fields

Panun Sritubtim[1], Suphalak Khachonkham[1], Pimolpun Changkaew[1], Warinthorn Rattanaareeyakorn[1], Surendra Dhungana[1], Nauljun Stansook[1], Pornpan Yongvithisatid[2], Puangpen Tangboonduangjit[1]

1 Master of Science Program in Medical Physics, Division of Radiotherapy and Oncology, Department of Diagnostic and Therapeutic Radiology, Faculty of Medicine Ramathibodi Hospital, Mahidol University, Thailand
2 Radiosurgery center, Faculty of Medicine Ramathibodi Hospital, Mahidol University, Thailand

Introduction: Basic concepts for the AAA and Acuros XB dose calculation algorithms employed in the Eclipse™ TPS have not been designed for small field planning. This might lead to dosimetric errors in the SBRT planning if the commissioning process is not aware of.

Purpose: To evaluate dosimetric accuracy of the AAA and Acuros XB algorithms implemented in the Eclipse TPS version 13.6.23 in a homogeneous phantom for small static fields defined by the MLCs and jaws.

Methods: Comparison between calculation of both algorithms and reference measurements was conducted for the 6 MV photon beams and delivered using the Varian Edge linac. Field output factors were measured in the water phantom for small static fields collimated by jaws (0.6×0.6, 1×1, 2×2, 3×3, 5×5 cm^2) and MLCs (0.5×0.5, 1×1, 2×2; fixed jaw at 3×3 cm^2). The PTW SRS diode and microdiamond detectors were used by following the protocol of TRS-483 CoP. Calculated field output were acquired from the central axis point dose of any field sizes normalized with those of the 10×10 cm^2 field with 0.1 cm calculation grid size.

Results: Percentage differences between measurements and calculation by both algorithms were <3% in MLC-and jaw-defined field down to 1×1 cm^2 and 3×3 cm^2, respectively. In the smallest MLC field size (0.5×0.5 cm^2), the agreement was up to 9% and 8% for AAA and Acuros XB, respectively. For jaw-defined fields smaller than 3×3 cm^2, the result showed unacceptable agreement up to 15% and 19% for AAA and Acuros XB, respectively.

Conclusion: The accuracy of small field dose calculation for both algorithms was within 3% for field sizes defined by MLC and jaw down to 1×1 cm^2 and 3×3 cm^2, respectively.

Keywords: small static fields, Eclipse dose algorithms, AAA, Acuros XB, collimation devices, dose calculation accuracy

The quality improvement of dose escalation plan of prostate cancer using an integration of biological parameters for optimization and evaluation

Tanwiwat Jaikuna[1], Wiwatchai Sittiwong[1], Pittaya Dankulchai[1]

1 Division of Radiation Oncology, Department of Radiology, Faculty of Medicine Siriraj Hospital, Mahidol University, Thailand

Introduction: The inverse optimization for Volumetric Modulated Arc Radiotherapy (VMAT) normally based on physically dose volume-based parameters (DV-based), but it not tendency related to clinical outcome. The biological optimization as the parameter of tumour control probability (TCP), normal tissue complication probability (NTCP), and equivalent uniform doses (EUD) provided superior clinical relevance.

Purpose: This study aimed to investigate the plan quality improvement for dose escalation plan of prostate cancer using physical and biological indices in three optimization techniques, DV-based, biological-based, and integrated-based.

Methods: Ten prostate cancer patient cases have delineated the organ-at-risk; bladder and rectum, and the multi-dose targets of the planning target volume, dominant intraprostatic lesion, prostate gland (PG), and seminal vesicle (SV) using multi-parametric magnetic resonance image-guided by the experienced radiation oncologist and the VMAT plans were generated using Raystation version 9B with the different optimization techniques. Physical dosimetric indices and biological indices included $D_{98\%}$, $D_{2\%}$, $V_{95\%}$, D_{mean}, TCP, Heterogeneity index (HI), and Conformity index (CI) for Target as well as $V_{40Gy,}$ V_{60Gy}, $D_{2\%}$, $D_{1\%}$, D_{mean}, and NTCP for OARs were evaluated.

Results: All plan-optimized techniques provided a similar result for target coverage when considering the physical indices; $D_{98\%}$ of PTV DIL=87.22±0.76, 86.07±0.47, 86.54±0.17, $D_{98\%}$ of PTV PG=77.86±0.63, 77.69±0.47, 77.19±0.22, and D98% of PTV SV=62.20±0.81, 73.03±0.71, 73.47±1.60 for physical, biological, and integrated-based optimization, respectively. Although TCP of PTV DIL and PG showed similar value in all optimization technique (TCP=1), the higher TCP value in PTV SV was obtained when biological parameters are applied (TPC=0.98±0.01) when compared to physical optimization only (TCP=0.74±0.07). However, the overdose region is showed significantly different as the biological optimization provided higher dose compared to other plan-optimization technique except in PTV SV which showed the integrated-based yield a similar result with biological-based optimization (about 5% increased). The OARs tend to receive a lower dose in biological and integrated-based optimization in all parameters with lower NTCP (decreased to less than 5%) when considering the same biological endpoint.

Conclusion: The quality of the prostate plan can improve by using the integration of DV and biological-based optimization.

Keywords: Biological Optimization, Prostate Cancer, Volumetric Modulated Radiation Therapy

Treatment planning evaluation of 3D-printed Anthropomorphic Head Phantom

Nur Emirah Zain[1], Reduan Abdullah[2], Wan Fatihah Wan Sohaimi[2], Wan Nordiana Rahman[1]

1 School of Health Sciences, Health Campus, Universiti Sains Malaysia, Malaysia,
2 Departments of Oncology, Radiotherapy and Nuclear Medicine, Hospital Universiti Sains Malaysia, Malaysia,

Introduction: Radiotherapy phantom is used as a patient replacement to run the quality assurance and advanced treatment verification. Standard commercial phantom is very costly which leads to the development of low cost custom made 3 Dimensional (3D) printed phantoms. 3D printing technique is currently a popular method to fabricate a low cost radiotherapy phantom. The quality of the phantom requires evaluation to fulfil dosimetric standard in radiotherapy.

Purpose: To evaluate the 3D printed anthropomorphic phantom in comparison to standard commercial RANDO® Head Phantom treatment planning based on treatment planning system (TPS) and radiochromic EBT3 films dosimetry.

Methods: The RANDO® Head Phantom and 3D printed anthropomorphic head phantom were scanned using CT-simulation for 3D data acquisition. The topographic data from CT-sim were transferred to the Oncentra TPS in the DICOM format. Image registration manoeuvred by contouring all organs at risk and whole brain as the target area. The treatment planning was based on neck and head consisting of two opposite-field beams. Later, the planning proceeds to the beam insertion in the plan manager segment with prescribed dose recommended followed by the dose calculation process. The plan was then exported to the LINAC through ARIA's electronic medical record system. The treatment delivery was conducted on both the RANDO® Head Phantom and 3D printed head phantom with GafChromic EBT3 films for dose verification.

Results: The dosimetric accuracy measured on 3D printed head phantom is found to be less compared to the RANDO® head phantom. The measured dose from the EBT3 film on the RANDO® head phantom is in average 80% passed according to the gamma analysis. While dose received in 3D printed head phantom displayed high error due to the presence of air gap between the slices. This 3D printed head phantom requires further optimization to reduce the air gaps between the slices.

Conclusion: The 3D-printed head phantom has been developed and its show potential to be used in radiotherapy treatment planning and dose verification. However further optimization is required to comply with the dosimetric standard in radiotherapy.

Keywords: 3D-printing, radiotherapy phantom, radiochromic films, treatment planning

Comparison of different treatment planning techniques for left-sided breast cancer: A dosimetric study

Md Akhtaruzzaman[1], Md Abdus Sabur[2], Md Shoriful Islam[3]

1 Ahsania Mission Cancer and General Hospital, Dhaka, Bangladesh
2 Square Hospital Limited, Dhaka, Bangladesh
3 National Institute of Cancer Research and Hospital, Dhaka, Bangladesh

Introduction: Cancer is a significant healthcare problem. Breast cancer is the most common type of cancer among women. Radiotherapy is one of the most effective treatment techniques after breast conserving surgery.

Purpose: To investigate the suitable radiotherapy treatment plan and delivery method for left-sided breast cancer after breast conserving surgery by comparing different treatment planning techniques.

Materials and methods: Ten patients with left breast cancer who underwent breast conserving surgery were selected. For each patient, three different whole breast irradiation techniques including Field in Field (FiF), Intensity Modulated Radiation Therapy (IMRT) and Volumetric Modulated Arc Therapy (VMAT) with free breathing were compared. Treatment plans were prepared with Eclipse treatment planning system (Varian Medical System Inc) using Anisotropic Analytical Algorithm (AAA). The prescribed dose was 50 Gy in 25 fractions (2 Gy/fraction). Plans were compared for target coverage (V95% and V107%) and doses of the lungs, heart, and spinal cord. Conformity index (CI) and homogeneity index (HI) were also assessed in this study.

Results: Mean maximum point dose (D_{max}) and minimum point dose at target (PTV50) for planning techniques were 106%-107% (±0.83) and 83%-84% respectively. The mean V95 for FiF and IMRT was almost same (97.5%), which is higher than VMAT (95.2%). Only FiF had a lower mean dose (ipsilateral lung-1089cGy, heart-1087cGy) in compare to IMRT (ipsilateral lung-1260 cGy, heart-1308 cGy) and VMAT (ipsilateral lung-1386 cGy, heart-1301 cGy). In contrast, V20 was lower for IMRT (16.8%) than FiF (18.0%) and VMAT (24.0%) techniques for ipsilateral lung. All planning techniques demonstrated excellent CI and HI.

Conclusion: The all three techniques provide adequate dose coverage. The IMRT had significantly smaller dose than VMAT in ipsilateral lung. VMAT demonstrated excellent dose homogeneity and conformity but an increased low-dose volume outside the target should be of concern.

Keywords: Breast cancer- radiotherapy planning technique- VMAT, IMRT, FiF

Investigation of the optimal cost function for pelvic CT-MR deformable image registration

Tomoya Ishida[1], Noriyuki Kadoya[1], Shunpei Tanabe[1], Haruna Ohashi[2], Ken Takeda[2], Suguru Dobashi[2], Keiichi Jingu[1]

1 Department of Radiation Oncology Tohoku University Graduate School of Medicine,
2 Department of Therapeutic Radiology Tohoku University Graduate School of Medicine,

Introduction: In recent years, the development of magnetic resonance imaging (MRI)-guided radiotherapy systems has resulted in an increased use of MRI in radiotherapy planning. To transfer contour and electron density information between computed tomography (CT) and MR images, image intensity-based deformable image registration (DIR) is used. In general, the DIR accuracy between different modalities is lower than that between the same modalities, and to date, reports on the evaluation of CT-MR DIR accuracy have been scarce.

Purpose: We evaluated the CT-MR DIR accuracy by validating the optimal cost function in pelvic images.

Methods: CT, T1-weighted MR (T1w), and T2-weighted MR (T2w) images from five male pelvic images (data by Tufve et al.) were included in the study. B spline-based DIR (elastix) was used for DIR, mutual information was used for the similarity term, and Bending energy penalty for the regularization term as cost functions. Six patterns of regularization weights were considered for determining the optimal cost function: 0.01, 0.1, 1, 10, 100, and 200.

Results: The mean dice similarity coefficients of the bladder in T1w images were 0.74 ± 0.11 (rigid), 0.85 ± 0.04 (DIR, $\lambda = 0.1$), 0.74 ± 0.10 (DIR, $\lambda = 200$). Those of the rectum in T1w images were 0.77 ± 0.13, (rigid), 0.80 ± 0.04 (DIR, $\lambda = 0.1$), 0.78 ± 0.12 (DIR, $\lambda = 200$). A similar trend was observed for T2w images. The most accurate value of λ varied from case to case, with $\lambda = 0.1$ for T1w and $\lambda = 1$ for T2w being the most common. These results indicate that the optimal cost function vary by case and MRI sequences.

Conclusion: This study suggested that optimization of the cost function might improve the accuracy of CT-MR DIR.

Keywords: MRI-guided radiotherapy, deformable image registration, cost function, pelvis, dice similarity coefficient

Dosimetric comparison between 3D and IMRT treatment techniques for whole breast radiotherapy

Yin Yin Pyone[1], Taweap Sanghangthum[2]

1 Department of Radiation Oncology, Pinlon Cancer Center, Pinlon Hospital, Yangon, Myanmar
2 Division of Radiation Oncology, Department of Radiology, Faculty of Medicine, Chulalongkorn University, Bangkok, Thailand

Introduction: In worldwide, breast cancer is the most common cancer in women that contributing 25.4% of the total number of new cases diagnosed in 2018 and also, it is the second most common women cancer in Myanmar and late toxicity could lead to secondary cancer for the contralateral breast.

Purpose: To determine the dosimetric effects of 3D and IMRT treatment techniques for whole breast radiotherapy.

Methods: The 10 left-sided and 5 right-sided women breast patients in Pinlon Cancer Center were randomly selected. The clinical target volume (CTV), planning target volume (PTV) and OARs: right lung, left lung, heart and contralateral breast were contoured according to the RTOG breast contouring guideline. All plans were performed by Varian Eclipse Treatment Planning System (Version 13.1) for; (1) standard wedge tangent (SWT), (2) Field in Field (FiF), (3) electronic compensator (E-Comp), (4) tangential-IMRT (T-IMRT), and (5) multiple field-IMRT (MF-IMRT). The PTV was evaluated by D95%, conformity index (CI), and Homogeneity Index (HI). Also for the OARs, the mean dose of heart, ipsilateral lung and contralateral breast were compared for all plans.

Results: The D95% of PTV was higher than prescribed dose for all techniques. The IMRT plans (T-IMRT and MF-IMRT) showed superior to PTV CI and HI compared with 3D plans (SWT, FiF and E-Comp). Among 3D-CRT techniques, E-Comp technique results better CI and HI. MF-IMRT presented the highest HI but also showed the highest dose at contralateral breast, while SWT showed the highest ipsilateral lung and heart doses, especially left breast side.

Conclusion: Different planning techniques present differ dosimetric on PTV and OARs. E-Comp is a good choice of radiotherapy. The advanced technique of IMRT can increase CI and HI parameters.

Keywords: Breast cancer, 3D-CRT, IMRT

Radiotherapy: Big data, Deep learning, AI and Modeling

Development of automated prostate VMAT treatment planning system using deep learning-based predictive dose distribution

Patiparn Kummanee[1], Sangutid Thongsawad[1,2], Wares Chancharoen[1], Todsaporn Fuangrod[1]

*1 Faculty of Medici*ne and Public Health, HRH Princess Chulabhorn College of Medical Science, Chulabhorn Royal Academy, Bangkok, Thailand
2 Department of Radiation Oncology, Chulabhorn Hospital, Chulabhorn Royal Academy, Bangkok, Thailand

Introduction: Treatment planning process for volumetric modulated arc therapy (VMAT) is considered as the time-consuming process due to manual trail-and-errors (iteration of planning from unapproved plan). An automated treatment planning can accelerate this process and reduce the number of iterations during the plan optimization. The predictive dose distribution can be generated directly from patient CT data using artificial intelligence method. The automatic treatment plan can be developed if the predicted dose is provided.

Purpose: The automated prostate VMAT treatment planning system was designed and developed. The predictive dose distribution model was developed using deep learning algorithm.

Methods: A generative adversarial network (GAN) approach was used to generate the predictive model, which consists of a pair of deep learning model including U-net generator and discriminator. To train the model, the inputs were the CT images and its dose distribution. Fifteen patients of VMAT prostate cancer were collected in this study. Ten patients were randomly chosen as training set and the remaining were the test set. The trained model was tested by input CT images from test set and evaluated the dose distribution output with the corresponding dose using 3D gamma analysis and dose-volume histogram (DVH).

Results: The trained model could predict the accurate dose distribution from input CT image. The passing rates of 3D gamma analysis were 49.44% with 2%/2 mm criteria. The usage time of deep learning-based treatment planning were 30 minutes which approximately 80% faster than conventional planning.

Conclusion: Our proposed automated treatment planning system using deep learning predictive model of prostate cancer could generate acceptable dose distribution from input CT images which could help medical physicists to get the acceptable quality of treatment plan with less time in the process.

Keywords: VMAT, deep learning, prostate cancer, dose distribution prediction.

Automated fast data collection and organization for medical artificial intelligence

Hongjia Liu[1], Yibao Zhang[1] (Corresponding Author)

1 Key Laboratory of Carcinogenesis and Translational Research (Ministry of Education/Beijing), Peking University Cancer Hospital & Institute, Beijing 100142 China

Introduction: The medical applications of artificial intelligence have been strongly dependent on the data aggregation and organization. Conventional manual collection is labour-intensive and time-consuming.

Purpose: This work aims to develop and validate a Web-Crawler-based medical records information aggregation tool for effective data mining from existing electronic information systems.

Methods: Based on Selenium framework and Python programming language, a Web-Crawler-based medical records information aggregation tool was designed, which was validated under two illustrative scenarios: 1. To identify radiation pneumonitis (RP) cases from Hospital Information System (HIS), as an application example of quick data search; 2. To summarize an organized table combining desired data from various examination reports, to test the application of facilitating clinical workflow. Automated and manual methods were compared in terms of efficiency and accuracy.

Results: The automated tool showed superior efficiency and accuracy than manual method. For the first scenario, automated method identified 110 RP cases out of 3541 patients in about 54 seconds per patient based on a Raspberry Pi 4B, without any human interference. Manual methods identified the same group of RP cases but took about 90 seconds per patient. It took longer to confirm a non-RP case because more data need to be excluded to avoid false-negative, suggesting even greater advantage of automated method in searching small-probability events, especially from huge patient volume. For the other scenario, automated and manual methods needed about 10 or 75 seconds respectively for each patient. Automated method also avoided typos that were frequently observed in manual report filling.

Conclusion: A Web-Crawler-based medical records information aggregation tool has been successfully developed. The superior efficiency and accuracy of auto-aggregation has been validated based on specific clinical scenarios. With the advantage of cross-platform and easy-to-extend, this application could improve radiologists' and physicists' productivity in their clinical and research practice.

Keywords: Web-Crawler; data aggregation; automation

A feasibility study of kVCBCT-based radiomics for radiological complication prediction

Yuliang Huang[1], Yibao Zhang[1] (Corresponding Author)

1 Key Laboratory of Carcinogenesis and Translational Research (Ministry of Education/Beijing), Peking University Cancer Hospital & Institute, Beijing 100142 China

Introduction: Considering the well-reported feasibility of planning CT (pCT)-based radiomics, the consistent features of kilovoltage cone-beam CT (kVCBCT) are complementary if not intersubstitutable with pCT for radiomics.

Purpose: To validate the feasibility of radiomic feature extraction from kVCBCT images and to investigate potential application of kVCBCT-based radiomics in predicting radiation-induced pneumonitis (RP).

Methods: 193 thoracic cancer patients treated with radiotherapy during January, 2017 and December, 2019 in our centre were retrospectively selected, including 70 patients who reported RP after the treatment. Contoured pCT and kVCBCT acquired at the initial treatment fraction were collected from clinical database for each patient. The dataset was split to training and test groups with the ratio of 4:1. Concordance correlation coefficients (CCC) of 1275 radiomic features extracted from pCT and kVCBCT were calculated. Stable radiomic features (CCC>0.99) were selected to train a logistic regression model that predicted radiation-induced pneumonitis for the 193 patients. Performance of the model was compared with that of another logistic model based on dose statistics (V5Gy, V10Gy, V20Gy, mean dose of lung).

Results: In addition to shape and volume, 50 more texture features were found to be consistent between pCT and kVCBCT (CCC>0.99). Tracking the changing kVCBCT radiomic features during the IGRT course might provide prompt and quantified evaluation of tumour response and OAR risks. AUC values of the two logistic models based on radiomics and dosimetrics were 0.84 and 0.73 respectively. Although RP was directly related to dose, varieties in individual's radiological sensitivity could undermine the accuracy of dosimetric model, while radiomics model provides additional patient-specific and dynamic indicators.

Conclusion: KVCBCT images are interchangeable with pCT providing a subset of reliable radiomics features. The prognostic value of kVCBCT-based radiomics in predicting RP has been evaluated, which encourages future study on temporal radiomics tracking based on kVCBCT sequence in IGRT.

Keywords: Radiomics; kVCBCT; Radiological complication

Evaluation of machine learning-based prediction model for radiation pneumonitis in NSCLC patients

Shiina Mouri[1], Noriyuki Kadoya[1], Yoshiyuki Katuta[1], Takayuki Kanai[3], Yujiro Nakajima[1,4], Shunpei Tanabe[1], Yuto Sugai[1], Mariko Umeda[1], Suguru Dobashi[2], Ken Takeda[2], Keiichi Jingu[1]

1 Department of Radiation Oncology, Tohoku University Graduate School of Medicine, Sendai, Japan
2 Department of Radiological Technology, School of Health Sciences, Faculty of Medicine, Tohoku University, Sendai, Japan
3 Department of Radiation Oncology, Yamagata University Faculty of Medicine, Yamagata, Japan
4 Tokyo Metropolitan Cancer and Infectious Diseases Center Komagome Hospital, Tokyo, Japan

Introduction: Radiation pneumonitis (RP) is a vital toxicity in non-small cell lung cancer (NSCLC) patients who are treated using radiotherapy. DVH parameters have been employed to predict the risk of RP. Machine learning has great potential in enhancing the prediction accuracy. However, there are only a few studies on this matter.

Purpose: We assessed the accuracy of machine learning-based prediction model for RP in NSCLC patients.

Methods: 186 lung cancer patients (stage I: 51, stage II: 17, stage III: 54, stage IV: 13, and unknown: 51), were treated at our hospital. The number of patients who were treated using conventional and stereotactic radiotherapy were 107 and 79, respectively. We predicted the risk of Grade 2+ pneumonitis (rate = 28%). DVH parameters of V5, V10, V20, V30, and MLD provided as equivalent dose in 2Gy fractions (EQD2) were utilized as predictive indicators. For the multivariate analysis, random forest (R package) was used to build the machine-learning model. All data were split into two sets: 80% for training, and 20% for testing. Two models were developed: model A employed all the DVH parameters and model B employed three parameters that were selected based on their importance in random forest[2)].

Results: The AUC values for V5, V20, and MLD in the univariate analysis were 0.74, 0.73, and 0.65, respectively, for the training data and 0.68, 0.61, and 0.58 for the test data, respectively. In the multivariate analysis, the AUC values were 0.74 (training) and 0.71 (testing) in model A, and 0.77 and 0.72, in model B, indicating that these values were higher than those in the univariate analysis. Three indicators of high importance were V5, V10, and MLD.

Conclusion: Multivariate analysis using machine learning may improve the accuracy of predicting RP in NSCLC patients.

Keywords: Radiation therapy, Machine learning, Lung cancer, Radiation pneumonitis

Impact of image type and deep learning architecture in deep learning radiomics on the accuracy of lung cancer prediction

Shumpei Tanabe[1], Noriyuki Kadoya[1], Shohei Tanaka[1], Ken Takeda[2], Suguru Dobashi[2], Keiichi Jingu[1]

1 Department of Radiation Oncology Tohoku University Graduate School of Medicine
2 Department of Therapeutic Radiology Tohoku University Graduate School of Medicine

Introduction: Conventional radiomics typically extracts predesigned features from a segmented region of interest (ROI). Recently, radiomics with deep learning (DL) has been actively researched. It automatically extracts features using a convolutional neural network from an image patch without segmenting the ROI. However, there has been no study on the impact of the type of input images and DL architecture on prediction accuracy.

Purpose: In this study, we evaluated the impact of input image type and DL architectures on the accuracy of prognostication of patients with lung cancer.

Methods: From the Cancer Imaging Achieve database, 418 patients with nonsmall cell lung cancer, including their CT images and GTV contour, were included. We created four types of input images that focused on the center of gravity of the GTV, as follows: 1) 50 × 50 mm with CT value outside the GTV set at 0 (masked 50 × 50 mm); 2) 50 × 50 mm; 3) 100 × 100 mm; and 4) 150 × 150 mm. We employed three types of DL architectures, including a simple model that comprised three convolution layers; a medium model that comprised four convolution layers; and a complex model that comprised 152 convolution layers. For all combinations of input image and DL architecture, we evaluated the accuracy of prognostication by area under the curve (AUC).

Results: The best performance AUCs were 0.64 with 150 × 150 mm for the simple model, 0.65 with 50 × 50 mm for the medium model, and 0.66 with masked 50 × 50 mm for the complex model. This result showed that a more complex model could achieve high prediction accuracy with input image and less information.

Conclusion: The prediction accuracy of radiomics with DL depended on the DL architecture and the input image.

Keyword: radiomics, deep learning, prognostic, radiotherapy

Prognostic analysis of CT-based radiomics focusing on a subgroup of NSCLC patients

Yuto Sugai[1], Noriyuki Kadoya[1], Shohei Tanaka[1], Shunpei Tanabe[1], Mariko Umeda[1], Takaya Yamamoto[1], Kazuya Takeda[1], Suguru Dobashi[2], Haruna Ohashi[3], Ken Takeda[2], Keiichi Jingu[1]

1 Department of Radiation Oncology, Tohoku University Graduate School of Medicine, Sendai, Japan
2 Department of Radiological Technology, School of Health Sciences, Faculty of Medicine, Tohoku University, Sendai, Japan
3 Department of Radiation Technology, Tohoku University Graduate School of Health Sciences, Sendai, Japan

Introduction: Radiomics is an emerging field wherein quantitative features extracted from medical images are used to noninvasively predict survival prognosis. Recent studies have described the feasibility of predicting the prognosis in patients with non-small-cell lung cancer (NSCLC) using this ingenious approach; however, its prognostic accuracy can certainly be improved. Hence, we focused on the prognostic analysis in subgroups with identical characteristics.

Purpose: We investigated the survival prediction of specific NSCLC subtypes and T stages using radiomics.

Methods: Images from 304 NSCLC patients (Stages I-IV) who had been treated with radiotherapy in our hospital were used in this study. 107 radiomic features (14 shape features, 18 first-order statistical features, and 75 textural features) were extracted from the GTV in CT images (free-breathing) acquired during treatment planning. Three different feature selection methods were used: test-retest and multiple-segmentation (FS1), Pearson's correlation analysis (FS2), and features suggested as useful in previous studies (FS3), and a least absolute shrinkage and selection operator-cox regression model was constructed using selected features. Prognostic analyses were performed for each NSCLC subtype and each T stage, and their accuracy was evaluated using the C-index with five-fold cross-validation and the Kaplan-Meier method.

Results: The C-index for all data were 0.629 ± 0.023 (FS1), 0.626 ± 0.023 (FS2), and 0.636 ± 0.023 (FS3), respectively. In subgroup analysis, the prediction models for specific NSCLC subtypes and T stages showed higher C-index than that for all data, especially in the T4 subgroup (0.687 ± 0.05). Moreover, the prediction models for each T stage in adenocarcinoma (ADC) had a higher C-index than that of ADC.

Conclusion: Our results showed that feature selection methods had a moderate impact on prognostic accuracy, and that prediction models that use specific NSCLC subtypes and T stages could improve prediction accuracy.

Keywords: Radiomics, prognosis prediction, subgroup analysis, lung cancer

Radiotherapy: Patient-specific QA

Preliminary evaluation of the performance of an EPID-based in vivo dosimetry for advanced radiotherapy treatment verification

Yasmin Md Radzi[1], Nur Nabilah Roskhahar[1], Nur Fatin Fariha Abd Latif[1], Noor Naslinda Noor Rizan[2]

1 School of Physics, Universiti Sains Malaysia, Penang, Malaysia,
2 Radiotherapy and Oncology Department, Gleneagles Hospital, Penang, Malaysia.

Introduction: Patient specific QA dose verification has been widely discussed and has proposed a way to achieve treatment delivery accuracy and patient safety. While in vivo dosimetry verification is currently is a necessity in radiotherapy centres in Europe countries, its demand currently rising in developed countries especially in Malaysia.

Purpose: In this work, the sensitivity and performance of EPID-based in vivo dosimetry, EPIgray® (DOSIsoft, Cachan, France) were evaluated for its use in clinical treatment verification for our centre.

Methods: Sensitivity tests such as dose linearity, field size, off-axis, position as well as angle dependency were performed to observe the response of EPIgray measured dose against TPS calculated dose for 6 MV and 10 MV photon beam. The relative deviation of the total dose was evaluated at isocentre point for different depth in water. EPIgray was also validated by using IMRT and VMAT prostate plan to be compared with the dose in TPS. All calculation points were at the beam isocentre and at additional points suggested by TG-119 and following the accepted tolerance of 10% dose threshold.

Results: EPIgray reported good agreement for linearity, field size, off-axis and position dependency with TPS dose being within 5% tolerance for both energy ranges. For angle dependency test, average agreement between TPS and EPIgray dose is less than 2% in 6 MV while 7% in 10 MV photon beam. The clinical evaluation performed for IMRT prostate plan gave average agreement 5-6% at the plan isocentre for both energies. While for VMAT, 94% and 100% of all points created lies within 5% for 6 MV and 10 MV photon beam energy respectively.

Conclusion: Based on the work presented in this paper, in vivo dosimetry is deemed as an essential need as one of the verification tools for advanced treatment techniques in Malaysia alongside pre-treatment verification.

Keywords: Epigray, in vivo dose measurement, IMRT, VMAT, Patient-specific QA

Patient-specific quality assurance for IMRT delivery: A multi-centre study

Nur Diyana Afrina Hizam[1], Wei Loong Jong[1,2], Hafiz Mohd Zin[3], Kwan Hoong Ng[4], Ngie Min Ung[1]

1 Clinical Oncology Unit, Faculty of Medicine, University of Malaya, Kuala Lumpur, Malaysia,
2 Department of Radiation Oncology, Auckland City Hospital, Auckland 1023, New Zealand,
3 Advanced Medical and Dental Institute, Universiti Sains Malaysia, Penang, Malaysia
4 Department of Biomedical Imaging, University of Malaya, Kuala Lumpur, Malaysia

Introduction: IMRT technique requires multi-centre quality assurance programs for verification due to its increased complexity. This study is the first trial of multi-centre audit in Malaysia

Purpose: To verify accuracy of IMRT delivery by using independent tools and to investigate the feasibility of using MO*Skin* detectors for multi-centre study

Methods: Physicists from participating centre required to produce a head & neck plan by using a case study given as per their clinical practice. The MO*Skin* detector and PTW Octavius 1500 detector were used to verify the point dose and dose distribution plane respectively.

Results: A total of 12 measurements were performed across 11 radiotherapy centres between May to September 2019. Overall mean difference of MO*Skin* detectors are 3.3% ± 3.2%. 82% of the results were within the tolerance level of ±5% recommended by IAEA for on-site IMRT/VMAT audits. Gamma passing rates of 3%/3 mm for most of the centres were within 95% passing rates using Octavius 1500.

Conclusion: A first dosimetric audit has been successfully conducted from 11 centres in Malaysia. Results showed that the standard of IMRT delivery in participating centres were, in general, met the standard recommended by international guidelines.

Keywords: Audit dosimetry; IMRT/VMAT; MO*Skin*

Pilot study of remote clinical dosimetry auditing for IMRT using virtual EPID standard phantom audit (VESPA) in Thailand

Pavarit Pojanapreecha[1], Puangpen Tangboonduangjit[4], Sangutid Thongsawad[1], Peter Greer[2, 3], Todsaporn Fuangrod[1]

1 Faculty of Medicine and Public Health, HRH Princess Chulabhorn College of Medical Science, Chulabhorn Royal Academy, Bangkok,10210, Thailand
2 Department of Radiation Oncology, Calvary Mater Hospital Newcastle, NSW, 2298, Australia
3 School of Mathematical and Physical Sciences, University of Newcastle, Newcastle, NSW, 2308, Australia
4 Department of Radiology, Faculty of Medicine, Ramathibodi Hospital, Mahidol University, Bangkok 10400, Thailand

Introduction: Since many centers applies the modern radiotherapy technique, it require the complex treatment plan resulting the need of highly efficient quality assurance (QA) to ensure the beam is delivered precisely. Although the standard of QA (such as TG-142) is recommended for implementation in all centers, the variation across center-to-center remains exist. To face with this situation, the machine audit with simulated beam delivery in end-to-end test perspective becomes essential. However, the audit process requires resource intensive and time consuming.

Purpose: The remote auditing for IMRT using virtual EPID standard phantom audit was implemented and promoted as an alternative auditing tool to solve the traditional auditing limitations. This project was implemented as a pilot study.

Methods: The workflow of remote auditing using the virtual EPID standard phantom for IMRT has developed and implemented in four centers in Thailand. All process guidelines and data were communicated and transferred online. Each center was required to set trial plan data to the auditors, which including plan files, dose files and EPID images. After the participant transferred data, the auditor analyzed the data using in-house software programmed in MATLAB/Simulink. As clinical dosimetry auditing, The accuracy of beam delivery was evaluated using Gamma passing rate. Geometric error was investigated using the calculated data from the software.

Results: All of the participated centres passed the tolerance. (3%/2mm) .The mean percentage gamma pass rates for the 4 centres were 99.7 % (for the 3%/2 mm criterion) and 98.05 % (for the 2%/2 mm criterion). The geometric error was detected for some centre.

Conclusion: The remote clinical dosimetry auditing process and tool can be used to evaluate the participant center's current dosimetric quality level of IMRT process. The benefit of remote auditing shows resource intensive, time efficient, and high flexibility.

Keywords: IMRT; Quality Assurance; Dosimetry Auditing;

Evaluation of Mobius and Portal dosimetry Quality Assurance tools for volumetric modulated arc therapy plans

Chulee Vannavijit[1], Sornjarod Oonsiri[1], Taweap Sanghangthum[2], Sivalee Suriyapee[2]

1 Division of Radiation Oncology, Department of Radiology, King Chulalongkorn Memorial Hospital, Thai Red Cross Society, Bangkok, Thailand.
2 Division of Radiation Oncology, Department of Radiology, Faculty of Medicine, Chulalongkorn University, Bangkok, Thailand.

Introduction: Mobius is a software-based verification tool for patient specific quality assurance (QA) and treatment delivery. The distinctive point of Mobius system is no uncertainty from setup error of the measurement tools.

Purpose: To evaluate the dosimetric performance of Mobius system (Mobius3D and MobiusFx) by comparison with electronic portal imaging device (EPID), which is routinely used for patient specific QA.

Methods: Total of 30 volumetric modulated arc therapy (VMAT) plans consisted of 10 head-neck, 10 chest and 10 prostate plans using Eclipse with AAA algorithm. Mobius 3D independently verified the pre-treatment plans by re-calculation with collapsed-cone algorithm. The MobiusFx used the Mobius3D and the machine log files to calculate 3D dose during treatment. The verification with EPID was undertaken at the same time. All plans were delivered with 6 and 10 MV photon beams of 2 to 4 arcs per plan by Varian TrueBeam linac. The percent gamma passing rate were compared using criteria of 3%/3mm for the composited dose between Portal dosimetry, Mobius3D and MobiusFx with TPS.

Results: The average gamma passing rate for EPID, Mobius3D and MobiusFx for head-neck plans were 98.5±1.4%, 97.2±2.0% and 97.2±2.0%, for chest plans were 97.4±1.8%, 98.3±1.5% and 97.8±2.2%, for prostate plans were 97.6±2.3%, 99.3±0.7%, and 99.3±0.7%, respectively. The relative percentage dose differences between EPID and Mobius3D were 0.40±2.8%, while EPID and MobiusFx dose differences were 0.30±2.8%.

Conclusion: Mobius3D and MobiusFX are capable to produce the comparable results to EPID for patient specific pre-treatment QA. Therefore, Mobius system can be applied interchangeably with EPID, which are commonly used as a patient specific QA tool, especially under the criteria of 3%/3 mm and 95% pass rate.

Keywords: Mobius3D, MobiusFx, Patient specific QA, VMAT.

Effect of plan complexity to gantry angle uncertainty for VMAT delivery

Thananya Chanpanya[1], Sangutid Thongsawad[1], Todsaporn Fuangrod[1]

1 Medical Physics Program, Faculty of Medicine and Public Health, HRH Princess Chulabhorn College of Medical Science, Chulabhorn Royal Academy, Bangkok, Thailand

Introduction: Volumetric modulated arc therapy (VMAT) is the radiation therapy technique with beam modulation during gantry rotation. Beam is modulated using leaf speed, gantry speed instead of dose rate. Gantry speed is the crucial parameter that can influence to beam delivery especially in VMAT plan. Increasing of beam modulation represented by plan complexity score may influenced to treatment error delivery. Hence, the effect of plan complexity to gantry uncertainty need to be investigated for setting the optimal plan complexity.

Purpose: The aim of this study was to investigate the correlation between gantry angle uncertainty and plan complexity in VMAT plan by using in-house Quality Assurance (QA) tool.

Methods: Ten VMAT plans included head and neck (5 plans) and prostate (5 plans) were selected for measurement gantry angle uncertainty and assessment beam complexity. Gantry speed and acceleration were used to determined plan complexity by retrieving from DICOM plan. The gantry angle measurement was performed using in-house QA tool namely double dot QA. Briefly explain here, double dot QA is gantry angle measurement tool using VDO processing method. To evaluate gantry angle uncertainty, the gantry difference between measurement and plan were determined. Finally, the correlation between gantry angle uncertainty and plan complexity was evaluated with Spearman correlation method.

Results: The result of 10 VMAT plans showed a strong correlation between plan complexity and gantry angle uncertainty.

Conclusion: This study indicated that the beam complexity in term of gantry speed and acceleration has a strong correlation with gantry uncertainty, and the optimal gantry speed and acceleration was suggested to reduce gantry uncertainty for VMAT plan.

Keywords: Volumetric modulated arc therapy (VMAT), gantry speed and acceleration, gantry angle QA

Development of novel x-ray-opaque-marker system for improvement and quantification of phantom positioning accuracy in patient-specific quality assurance

Kentaro Suzuki[1], Takeshi Kamomae[2], Hiroshi Oguchi[1], Fumitaka Kawabata[3], Kazuma Sugita[3], Kuniyasu Okudaira[3], Kazuhiro Ohtakara[2], and Yoshiyuki Itoh[2]

1 Department of Radiological and Medical Laboratory Sciences, Nagoya University Graduate School of Medicine, 1-1-20 Daiko-Minami, Higashi-ku, Nagoya, Aichi 461-8673, Japan,
2 Department of Radiology, Nagoya University Graduate School of Medicine, 65 Tsurumai-cho, Showa-ku, Nagoya, Aichi 466-8550, Japan,
3 Department of Radiological Technology, Nagoya University Hospital, 65 Tsurumai-cho, Showa-ku, Nagoya, Aichi 466-8560, Japan

Introduction: It is essential to perform patient-specific quality assurance (QA) in radiotherapy. However, the conventional phantom positioning with the room lasers includes a subjective process. For improvement and quantification of phantom positioning accuracy, we newly developed the x-ray-opaque-marker system which had seven fiducial markers inserted in the RW3 plate. This system is easily removable from the existing patient-specific QA phantoms. Furthermore, the positions of the markers were logically arranged to be recognized by the image guidance systems equipped in the treatment systems.

Purpose: The aim of this study is to assess the clinical utility of our system by (1) evaluating the accuracy of the phantom positioning and (2) estimating the dose perturbation around a marker.

Methods: The phantom positioning accuracy was quantified by using the I'mRT phantom (IBA) with CyberKnife (Accuray) and Clinac iX (Varian). The known displacements of the phantom positioning were compared with the measured displacements by Target Locating System (TLS) and on-board imager (OBI) image guidance systems. While, the dose perturbation was evaluated for 6 MV photon beam through experimental measurements and Monte Carlo simulations.

Results: The root mean square (RMS) of the discrepancies in translations between the measured and the known displacements was found to be ≤0.07 mm with TLS and ≤0.30 mm with OBI. The RMS of the discrepancies in rotations was found to be ≤0.13° with TLS and ≤0.15° with OBI. While, the dose perturbation along the beam axis was observed within about 1.5 mm from the marker.

Conclusion: The results demonstrated the sufficient accuracy of phantom positioning by using our system. While, the distance between the markers and the measurement equipment should be kept at least 1.5 mm to avoid the dose perturbation from the markers. We conclude that it's feasible to set up the phantom accurately and quantitatively by using our system.

Keywords: fiducial marker, CyberKnife, patient-specific QA, image-guided radiotherapy (IGRT), dose perturbation

Radiotherapy: Particle beam therapy

Dosimetric validation of the commercial dose calculation algorithm for carbon ion therapy in a heterogeneous phantom

Sirinya Ruangchan[1, 4], Dietmar Georg[1, 2], Barbara Knäusl[1, 2], Hugo Palmans[2, 3], and Monika Clausen[1]

1 Division of Medical Radiation Physics, Department of Radiation Oncology, Medical University of Vienna, Austria
2 Division of Medical Physics, MedAustron Ion Therapy Center, Wiener Neustadt, Austria
3 National Physical Laboratory, Teddington, United Kingdom
4 Division of Therapeutic Radiation and Oncology, Department of Radiology, King Chulalongkorn Memorial Hospital, Bangkok, Thailand

Introduction: Carbon ion therapy is an advanced treatment technique in radiation oncology that enable well-targeted dose escalation to a tumor with a dose minimization to surrounding healthy tissues. The treatment planning system (TPS) RayStation (RaySearch Laboratories, Sweden) offers a Pencil Beam (PB) algorithm for carbon ion therapy and provides rapid and efficient dose calculations.

Purpose: The purpose of this work was to dosimetrically validate the dose calculation algorithm in RayStation for carbon ion therapy, both inside and outside the target, in the presence of heterogeneous phantom geometries. Predictions of the PB algorithm and the results from the experimental dosimetric validation will be presented.

Methods: Measurements were performed in a large water phantom with embedded bone-lung and bone-soft tissue inserts using 24 pinpoint ionization chambers (T31015, PTW, Germany). The target of 4 x 4 x 4 cm^3 was located behind the heterogeneous tissues at two different depths. Treatment plans were optimized and calculated by the TPS with a prescribed physical dose of 1 Gy. Configurations with and without the range shifter and different air gaps were investigated.

Results: The dose calculations performed with the PB algorithm showed a good dosimetric agreement with experimental measurements. The mean dose difference was 2% (5% range shifter), and maximal dose difference of up to 3% (7% range shifter) was observed inside the target. However, significant local discrepancies were found in the regions behind the target, with a maximum dose difference of 15%. Dose uncertainties of 17% were even more pronounced behind the target for configurations with the range shifter.

Conclusion: The RayStation PB algorithm applied for heterogeneous geometries provided an acceptable calculated dose inside the target. However, significant dose discrepancies were observed behind the target. The potentially larger dosimetric errors outside the target volumes might lead to an increased risk of side effects for the treatment of heterogeneous structures.

Keywords: Dose calculation algorithm, Carbon ions, Heterogeneous phantom

Simulation of the efficiency of rescanning with respiratory gating technique in pencil beam scanning proton therapy for lung cancer

Nattakarn Kittiva[1], Sumana Paduka[2], Sangutid Thongsawad[1], Thiansin Liamsuwan[1]

1 Medical Physics Program, Faculty of Medicine and Public Health, HRH Princess Chulabhorn College of Medical Science, Chulabhorn Royal Academy, Bangkok, Thailand
2 Chulabhorn Hospital, Bangkok, Thailand

Introduction: Currently, pencil beam scanning proton therapy is increasingly used in particle therapy centers but the problem is that it is sensitive to the motion causing the interplay effect and reducing the efficiency of the treatment. The gating technique and the rescanning technique have been used to reduce the interplay effect.

Purpose: This study aims to evaluate the interplay effect and the efficiency of pencil beam scanning proton therapy with (i) breath-sample layered rescanning alone and (ii) breath-sampled layered rescanning combined with the gating technique for the treatment of lung cancer with the motion of larger than 1 cm in term of dose metrics and the treatment time.

Methods: The treatment plans were created with the open source software for radiation treatment planning matRad using the 4-dimensional computed tomography (4DCT) data of a four-dimensional phantom. The internal motion in each breathing phase was defined by deformable image registration of the CTV on each phase to the end of exhalation, while the external motion was defined by using the breathing cycle collected from the RPM^{TM} signal. The mitigation efficiency of the interplay effect was evaluated in term of homogeneity and conformity of CTV and OARs, dose volume histograms, and the treatment time compared to the static case.

Results: The mitigation efficiency of the interplay effect using breath-sampled layered rescanning combined with the gating technique and breath-sample layered rescanning alone will be presented and discussed in term of dose metrics and treatment time.

Conclusion: The efficiency evaluation of breath-sampled layered rescanning combined with the gating technique will assist proton pencil beam scanning for cancer patients with large motions.

Keywords: Proton therapy, pencil beam scanning, breath-sample layered rescanning, gating technique, deformable registration

Dosimetric comparison of normal liver sparing in hepatocellular carcinoma between intensity modulated proton therapy and volumetric modulated arc therapy

Mintra Keawsamur[1], Taweap Sanghangthum[2], Napapat Amornwichet[2], Sivalee Suriyapee[2], Chonlakiet Khorprasert[2]

1 Division of Radiation Oncology, Department of Radiology, King Chulalongkorn Memorial Hospital, Thai Red Cross Society, Bangkok, Thailand.
2 Division of Radiation Oncology, Department of Radiology, Faculty of Medicine, Chulalongkorn University, Bangkok, Thailand.

Introduction: Hepatocellular carcinoma (HCC) is one of the cancers expected to receive the greatest benefit from the radiotherapy. Radiation-induced liver disease is commonly occurred when the dose exceed limitation.

Purpose: The aim was to estimate quantitatively the dose-escalation of IMPT and VMAT in terms of sparing of the normal liver.

Methods: Ten selected liver cancer patients who underwent volumetric modulated arc therapy (VMAT) plan that used 6MV and 10 MV with 3 arcs were re-planned with 1 or 2 fields of intensity modulated proton therapy (IMPT) using Eclipse software (Version 15.6). A relative biological effectiveness (RBE) weighted dose of the PTV was escalated with three treatment protocols (a) 66 GyE in 10 fractions, (b) 72.6 GyE in 22 fractions, and (c) 77 GyE in 35 fractions and the endpoints defined by the dose to normal liver $D_{mean} \leq 13$ GyE were used in both IMPT and VMAT plans.

Results: Ten patients had an average tumor volume of 140.0 cm^3 ± 97 SD (range from 23.5 – 286.6 cm^3). In all cases at least 95% of the PTV received the prescription dose. For all cases, the spared liver volume with $D_{mean} \leq 13$ GyE for IMPT plans were larger compared to VMAT plans. For dose protocols (a), IMPT met the dose criteria for 7 from 10 cases and for protocol (b) and (c) 6 of the 10 cases pass the criteria. For VMAT plans, only 2 cases met normal liver dose criteria for all dose protocols. The results showed that IMPT was significantly superior to VMAT when evaluating the integral dose to the normal liver.

Conclusion: In our study, the evidence of escalating the radiation dose is only significant factor. The present treatment planning study comparing IMPT and VMAT of HCC showed that the most advantageous treatment plans could be obtained by IMPT when considering the liver to be the most important critical organ. The study strongly indicates that IMPT may allow dose-escalation and result in improved outcome in HCC.

Keywords: Proton therapy, IMPT, HCC, Liver dose, Dose-escalation

Development of Ultra-fast Irradiation for Proton Therapy

Nagaaki Kamiguchi, Kenzo Sasai, Takuya Miyashita, Nobuaki Takahashi, Yukio Mikami

Sumitomo Heavy Industries, Ltd.,

Introduction: The breath holding method is one of the methods for moving target with respiration in the radiation treatment field. The other hands, the proton therapy system which consists of a cyclotron can deliver rather high beam current (few 10 nA) potentially. High beam current can make dose rate higher and it makes short time dose delivery into targets possible within single breath holding.

Purpose: Evaluation and development of fast scanning method for breath holding method.

Methods: Sumitomo Heavy Industries have employed the Line scanning method as PBS method, which scans the beam continuously with scan speed modulated as intensity modulation method. The beam current is determined from the minimum weight of irradiation unit in each single layer. The beam currents may get higher if the maximum scanning speed becomes higher. The effect of the shortening irradiation time by scan speed was evaluated for each clinical case with treatment planning study. The proton therapy system simulated in this study corresponds to Sumitomo new model machine which can emit 1000 nA beam at exit of the cyclotron and equips fast layer switching system which can change an energy layer within 0.2 s and scanners which can scan 100 mm/ms at most.

Results: It was made clear that 1.8 s irradiation is potentially possible for lung cancer case about 100 ml with 1 Gy. For liver cancer case, it took 4.3 s to 700 ml with 1 Gy. In case of combination of three times rescanning, the irradiation time for lung case did not differ from the case without rescan but the liver case required 6.2 s to complete irradiation.

Conclusion: Since the tolerance of breath holding time is known as 6-7s, this new system can deliver the less stress treatment for patients.

Keywords: proton, fast scan, high current, fast switching, breath hold

Radiotherapy: IGRT

Tolerance level determination for automated EPID-based deep inspiration breath-hold (DIBH) instability evaluation in breast cancer patients

Aphisara Deeharing[1], Puangpen Tangboonduangjit[1, 2], Todsaporn Fuangdrod[3]

1 Master of Science Program in Medical Physics, Department of Diagnostic and Therapeutic Radiology, Faculty of Medicine Ramathibodi Hospital, Mahidol University, Bangkok, Thailand
2 Division of Radiation Oncology, Department of Diagnostic and Therapeutic Radiology, Faculty of Medicine Ramathibodi Hospital, Mahidol University, Bangkok, Thailand
3 Faculty of Medicine and Public Health, HRH Princess Chulabhorn College of Medical Science, Chulabhorn Royal Academy, Bangkok, Thailand

Introduction: Deep Inspiration Breath Hold (DIBH) is used during radiotherapy for left-sided breast cancer to reduce the cardiac and LAD dose. This technique requires monitoring for the stability of DIBH during treatment. In addition, there is no current system to monitor daily intra-fractional patient DIBH motion. The cinematographic image (cine) is selected for DIBH monitoring because it does not add the dose to the patient. Then, it can measure geometrical setup errors in Beam's-Eye-View (BEV) according to the actual field

Purpose: To develop a daily patient DIBH instability assessment as an intra-fractional motion verification tool using a cine-electronic portal imaging device (cine-EPID).

Methods: The cine images were acquired and analysed to find the stability of the breath-hold during treatment by using in house MATLAB program with Canny's edge algorithm. Then the lung depth distance was calculated automatically to evaluate the stable of DIBH. Moreover, the performance of assessment tools was studied from the phantom by testing the accuracy and capability. Then applying in clinical from three patients.

Results: The maximum difference of the accuracy test of the in house assessment tool from the phantom is -0.996 ±0.246 mm. For capability test with adding blur in the image, this program can be analysed quite accurately with a maximum difference of 1.400 ±0.460 mm but reduce noise very poorly with maximum difference 73.2±13.89 mm. However, in clinical found that the results correspond amplitude setting from the treatment room.

Conclusion: The in-house automated program with EPID based is suitable for clinical treatment with a millimetre error**.**

Keywords: Deep Inspiration Breath Hold (DIBH), cine EPID, Whole Breast Radiation Therapy (WBRT)

A simulation study of fractional image guidance protocol contributing to the dosimetric accuracy of patients treated on Halcyon system

Chenguang Li[1], Yibao Zhang[1] (Corresponding Author)

1 Key Laboratory of Carcinogenesis and Translational Research (Ministry of Education/Beijing), Peking University Cancer Hospital & Institute, Beijing 100142 China

Introduction: Frequency of conventional kV-image guidance is sometimes sacrificed to reduce concomitant risk, leaving deviations of unguided fractions unknown. MV-imaging and treatment dose can be collectively optimized on Halcyon, where fractional MVCBCT provides complete anatomic records for course-wide dose reconstruction.

Purpose: By resampling, this work simulated the impact of imaging frequency on patient treatment dose.

Methods: Using Velocity software, deformable image registration was performed on 416 MVCBCTs from 16 patients of various tumour sites to cast the HU of planning CT onto MVCBCT images representing actual anatomies on the treatment day. Fractional reconstructed dose (1f_fractional) was accumulated representing the actual dose distribution (1f_sum). To simulate weekly guidance, only the first couch shift of every 5 fractions was applied to the reconstructed dose (5f_fractional) and accumulated without remaining 4 setup corrections every week (5f_sum). Limited by partially imaged volumes and different organs-at-risk of various sites, only target dose-volume parameters were compared.

Results: GTV_D98%, CTV_D98%, PTV_D90%, PTV_D95%, PGTV_D90% and PGTV_D95% were evaluated (Dx%: the minimal dose received by x% volume). Pairwise comparisons were made between 5f_fractional and 1f_fractional, 5f_sum and 1f_sum, 1f_sum and planned dose, respectively. All the difference are (former - latter)/prescription×100%. All parameter mean difference between 5f_sum and 1f_sum were negative, suggesting that weekly-guidance can result in an average under-dose of 1.54% to the target. The maximum difference of PTV_D95% and PGTV_D95% between 1f_sum and 5f_sum reached -10.37% and -32.90% respectively, suggesting larger dose unreliability in the margins of the planned target volumes associated with reduced imaging frequency and increased setup errors. Slight target under-dose was observed on daily reconstructed results compared with planned dose, but is clinically acceptable.

Conclusion: Weekly guidance protocol may introduce dose error up to 32.9% over one course. Fractional image guidance on Halcyon provides more reliable treatment results than IGRT using sacrificed imaging frequency.

Keywords: IGRT; Halcyon; deformable registration

Localization accuracy of off-isocenter multi-target brain stereotactic radiosurgery using SyncTraX FX4

Jun Tomihara[1, 2], Jun Takatsu[3], Naoya Hara[2], Naoto Shikama[3], Keisuke Sasai[3]

1 Department of Radiation Oncology, Graduate School of Medicine, Juntendo University,
2 Department of Radiology, Juntendo University Hospital,
3 Department of Radiation Oncology, Faculty of Medicine, Juntendo University.

Introduction: Localization accuracy of linac-based brain stereotactic radiosurgery (SRS) has been previously evaluated. Verifying the localization accuracy of off-isocenter target is necessary when using a single isocenter. The SyncTraX FX4 (Shimadzu, Kyoto, Japan) device offers fast and accurate patient setup. It consists of four X-ray tubes and four flat panel detectors. Although the positioning accuracy of SyncTraX for isocenter targets has been previously investigated, off-isocenter positioning accuracy of SyncTraX is still unclear.

Purpose: To evaluate the localization accuracy of SyncTraX for off-isocenter targets, and the correlation between intracranial isocenter position and setup accuracy.

Methods: First, localization accuracy of an off-isocenter target was evaluated utilizing MAX-EI (IMT, NY), which was designed for SRS QA. The MAX-EI phantom consists of anthropomorphic bone structures and two targets, one each at a center and an offset position. Following phantom setup using SyncTraX, 15 fields of various gantry and couch angles were delivered to EPID. The delivered field size was approximately 2×2 cm^2. Second, RAND phantom (The Phantom Laboratory, NY) was used for evaluating the setup accuracy against the cranial isocenter position. The isocenter was shifted from the phantom center in three different directions from 0 to 9 cm. After bone matching using SyncTraX, cone beam CT (CBCT) images were taken. Differences between SyncTraX and CBCT were analyzed.

Results: The maximum localization error of an off-isocenter target was 0.57 mm. The results of setup accuracy relative to isocenter shift were 0.0 ± 0.2 mm, 0.2 ± 0.2 mm, and 0.3 ± 0.1 mm for AP, SI, and LR directions, respectively. Additionally, rotational differences between SyncTraX and CBCT were -0.1 ± 0.1 degree, 0.0 ± 0.1 degree, and -0.1 ± 0.1 degree for yaw, pitch, and roll, respectively.

Conclusion: We clarified that SyncTraX provides satisfactory setup accuracy for brain SRS.

Keywords: SyncTraX, SRS, off-isocenter

Evaluation of tumor delineation accuracy in denoised contrast enhancement four-dimension CT using deformable image registration method

Kentarou Suzuki [1, 2], Keisuke Usui [3, 4], Akira Isobe [1], Keisuke Sasai [1, 4]

1 Department of Radiation Oncology, Graduated School of Medicine, Juntendo University, Tokyo, Japan
2 Department of Radiology, Toranomon Hospital
3 Department of Radiological Technology, Faculty of Health Science, Juntendo University, Tokyo, Japan
4 Department of Radiation Oncology, Faculty of Medicine, Juntendo University, Tokyo, Japan

Introduction: Tumor motion by the respiration needs to be reflected in the treatment planning in stereotactic radiotherapy for hepatocellular carcinoma. A contrast enhanced four-dimensional computed tomography (4DCT) using a 320-area detector CT (ADCT) can accurately delineate variations of tumor position associated with respiration; however, excessive imaging doses are required. Nevertheless, low exposure dose causes image noise leading to inaccurate tumor delineation. Therefore, we developed a noise reduction method for the contrast enhanced 4DCT using the deformable image registration (DIR) method.

Purpose: This study aimed to evaluate the tumor delineation accuracy depending on the deformation accuracy in our proposed method using a digital pseudo CT.

Methods: Positional variation associated with respiratory motion was corrected using a DIR process in all respiratory phase images to the intermediate phase image, and image noise was reduced by image average addition processing. To quantitatively evaluate the accuracy of tumor delineation, we generated 4DCT images with liver pseudo tumors using a digital phantom (extended cardiac torso (XCAT), Duke University, Durham, USA)[3]. Subsequently, we added the CT specific noise and made pseudo tumors with various sizes and intensities of the Hounsfield Unit (HU). Moreover, the contour of the tumor was delineated by the thresholding method, and the similarity to the ground truth was evaluated using the Dice similarity coefficient (DSC).

Results: The DSC at the tumor size of 15, 25, and 35 mm were 0.96, 0.85, and 0.89, and the contrast of HU in tumor to normal tissue of 5, 15, and 30 HU; results of DSC were 0.99, 0.96, and 0.97, respectively.

Conclusion: This proposed method can improve the image noise and the accuracy of tumor delineation for low intensity and small size tumors without the need for additional imaging doses.

Keywords: Four-dimension computed tomography, Deformable image registration, Denoise

Radiotherapy: Radiation Safety / DRL

Acceptance Test and Commissioning of Tomotherapy Radixact X5 series in LBCH

Chonlathorn Pihusut[1], Jitlada Jitmon[1], Komkrit Krongkietlearts[1], Kananan Utitsarn[1],
Thepphithak Watthanasarn[1], Jeerawat Pimthong[1], Wirasinee Chaloemchawalit[1], Taweap Sanghangthum[2]

1 Department of Radiotherapy, Lopburi Cancer Hospital, Lopburi, Thailand 15000
2 Division of Radiation Oncology, Department of Radiology, Faculty of Medicine, Chulalongkorn University, Bangkok, Thailand 10330

Introduction: The first Radixact X5 machine was installed at Lopburi Cancer Hospital (LBCH) in August 2019. Machine acceptance testing and commissioning is an essential procedure to clarify that the machine meet the defined specification before start operating the treatment machine.

Purpose: To perform the acceptance testing and commissioning of the Radixact X5 and to create the machine QA baseline for LBCH.

Methods: The acceptance test and commissioning was performed follow the manufacture checklist and TG148 protocol. Mechanical alignments were performed using cheese phantom, virtual water phantom, EBT3 film and RIT film software. Radiation beam profile measurements (longitudinal profile, transverse profile and PDD) were measured with A1SL in water scanning system. For E2E testing, beam data from iDMS of 3 selected cases was imported to the RayStation TPS. Point dose measurement using A1SL and planar dose measurement using ArcCHECK phantom was performed to verify the machine beam modelling.

Results: The acceptance test and commissioning showed compatible results with the manufacturer's specifications. The mechanical alignment and synchronicity test showed good agreement with criteria. The beam parameters test corresponded to the gold standard data (less than 1%) in every field width. TomoHelical delivery test in cheese phantom presented a good match between measured and calculated dose (3%/3 mm) in all plans. The static output (1.5 cm) was 836.53cGy/min. The PDD ratios were within the acceptable criteria. For E2E test, measured point dose of 3 plans corresponded to calculated dose (<3%). The passing rate of >95% measured by ArcCHECK was presented (3%/2mm) in all plans.

Conclusion: The Radixact X5 acceptance and commissioning testing is compatible with the manufacturers' specification. The collected beam data shows excellent agreement with bunker data. This Radixact system is proven and ready to be used for accuracy and safety clinical performance.

Keywords: Radixact X5; Tomotherapy; Acceptance test and commissioning

The preliminary survey report of the compact proton therapy unit

Tanawat Tawonwong[1,2], Sivalee Suriyapee[3], Sornjarod Oonsiri[2], Taweap Sanghangthum[3]

1 Medical Physics Program, Department of Radiology, Chulalongkorn University, Bangkok, Thailand
2 Division of Radiation Oncology, Department of Radiology, King Chulalongkorn Memorial Hospital, Bangkok, Thailand,
3 Division of Radiation Oncology, Department of Radiology, Faculty of Medicine, Chulalongkorn University, Bangkok, Thailand

Introduction: The number of compact proton therapy center is rapidly increasing. Her Royal Highness Princess Chakri Sirindhorn Proton Therapy center located at King Chulalongkorn Memorial Hospital is the one which will be operating by early 2021. The radiation safety of shielding and operation must be considered.

Purpose: To verify the efficiency of the shielding and create the guideline for the treatment room entering after beam off at Her Royal Highness Princess Chakri Sirindhorn Proton Therapy center by measuring the ambient dose equivalent.

Methods: The proton beam energy of 230 MeV was delivered to the water phantom at the isocenter with the current about 2 nA. The Wendi II was used to measure the ambient dose equivalent both outside and inside the treatment room. Outside the treatment room, the measurements were performed in front of the shielding door, the control room, and the service engineer room. Inside the treatment room, the ambient dose equivalent was measured beside the treatment couch, 140 cm away from the isocenter. The measurement was prolonged for 6 minutes to observe the possible value.

Results: The ambient dose equivalent outside the treatment room was about the background, 0.5 μSv/hr, for all measurement locations. In the treatment room, the ambient dose equivalent at 1, 2, 3, 4, 5 and 6 minutes after the beam off were 40.86, 1.17, 0.93, 0.78, 0.66, and 0.58μSv/hr, respectively.

Conclusion: For outside the treatment room, the shielding efficiency was under the shielding constrain of 1 mSv/year at the measured condition. The recommendation of the guideline for room entering after beam off was at least 2 minutes where the ambient dose equivalent was lower than 1.17 μSv/hr to achieve the personal dose limit lower than 5 mSv/year.

Keywords: Compact proton therapy, Ambient dose equivalent, Personal dose limit

Mitigation of Error Propagation in Tele-cobalt Treatment: An Institutional Assessment

Mary Joan[1], Priya Saini [1], Mukesh Jain[1], Ramesh Sharma[1], Ajay Prajapathi[1], Arun Chougule[1]

1 Department of Radiological Physics, S.M.S Medical College and Hospitals, Jaipur

Introduction: Radiotherapy is a multilevel process, which requires a working group that consists of Radiation Oncologists (RO), Medical Physicists (MP) and Radiotherapy Technologists (RT) and the treatment delivery requires a lot of information transfer amongst them. Any discrepancy in this information can lead to erroneous patient record and, in worst cases, wrong treatment. The objective of this work is to analyse the possible scenarios of errors and incidents in conventional tele-cobalt treatment procedure, and to introduce methods that could minimize their occurrences in our system.

Materials and Methods: Patients treated over a period of one year in tele-cobalt machines were evaluated. All relevant data were recorded. Different steps of the treatment were analysed systematically to look for possible errors. The treatment prescriptions were thoroughly checked to find any discrepancy. Weekly audits were done to check for any overlooked facts or errors. The RO, MP and RTT were requested to report any kind of discrepancy. The discrepancies and errors were recorded and their in depth analysis was done.

Results: The errors found were related to the dose prescription, SAD/SSD, writing down the field size dimensions and depth of treatment, change of field size during the course of treatment or treatment course defaulted by the patient. Other issues like change in dose fractionation, inclusion of blocks etc. were also found. All these were recognized before the initiation of treatment. The main reason recognized was the lack of communication regarding the change in the treatment parameters. Improper transfer of facts and knowledge or the lack of it also led to such issues. Interestingly, none of these errors resulted in incorrect treatment due to the conscious involvement of the professionals and timely communication with the others. The discrepancies were resolved and proper documentation was maintained.

Conclusion: Manual record systems are prone to human error. The errors can be minimized by strictly following departmental procedure protocols, maintaining proper records, good communication among all the professionals involved and with the patient. A strong communication system between the ROs, MPs & RTTs is essential for easy creation of robust documentation. Regular evaluation of departmental protocols, common sessions of RO, MP, RTT to discuss issues, proper counselling of patients to make them aware of the importance of the protocols are some other solutions. Double stage verification needs to be performed at every major step of the treatment.

Keywords: Tele-cobalt, Mitigation of error propagation, Conventional radiotherapy

Evaluation of radionuclides and activation detected by a 15 MeV medical linear accelerator

Ryosei Ogata[1], Shinji Kawamura[1], Hiroyuki Okamoto[2], Shouichi Katsuta Katsuta[3], Tomonori Goka[3]

1 Division of Radiological Sciences, Graduate School of Health Sciences, Teikyo University
2 Department of medical physics, National Cancer Center Hospital
3 Department of Radiological Technology, National Cancer Center Hospital

Introduction: It is known that gantry parts are activated by photonuclear reaction in a medical linac device with energy of 10 MeV or more. At present, the increase of radioactive waste and the cost for disposal are becoming a problem in Japan.

Purpose: The NaI spectrometer has the advantages of being cheaper, lighter, and easier to operate than the Ge detector. According to the Japanese medical care law, medical facilities are obliged to measure the activation of parts by NaI(Tl) scintillation survey meter when the linac is discarded. In this study, we evaluated the radioactivity of 12 components of the medical linear accelerator (target, flattening filter, upperJAW, lower JAW, shielded lead, etc.) using the NaI spectrometer.

Methods: We measured the parts of the 15 MeV energy linac device CLINAC iX, which was discarded at the National Cancer Center Hospital. The components were placed in close contact with the detector and each part was measured for 30 minutes. Radioactivity was evaluated by calculating the detection efficiency of NaI spectrometer using Monte Carlo simulation PHITS.

Results: Co-60 and Co-58 were detected in tungsten and copper materials such as upper JAW, lower JAW, flattening filter and MLC. Au-196 and Au-198 were detected from the target. In addition, Sb-124 was detected in the lead shielding material. The reason why Au-196 and Au-198 were detected from the target is because NICRO is used as an adhesive for copper and tungsten, and it is considered that this component has been activated.

Conclusion: The activation of the components of a medical linear accelerator with 15 MeV energy was evaluated using a NaI spectrometer. We consider that the evaluation of radioactive materials using a portable spectrometer is useful.

Keywords: Activation, Medical linear accelerator, NaI spectrometer, Monte Carlo simulation, Radioactive waste

Radiotherapy: Others

Dosimetric comparison of manual and library applicator reconstruction in MRI image-based for gynecological brachytherapy

Sakda Kingkaew[1], Puntiwa Oonsiri[1], Sornjarod Oonsiri[1], Taweap Sanghangthum[2], Sivalee Suriyapee[2]

1 Radiation Oncology Division, King Chulalongkorn Memorial Hospital, The Thai Red Cross Society, Bangkok, Thailand.,
2 Radiation Oncology Division, Radiology Department, Faculty of Medicine, Chulalongkorn University, Bangkok, Thailand.

Introduction: MRI-image is increased usage in brachytherapy. Applicator reconstruction may be the factors that introduce the dose errors of the treatment planning process.

Purpose: To investigate the dose difference between manual and library applicator reconstruction in MRI-based brachytherapy for gynecological malignancies.

Methods: Sixty-four plans of library applicator reconstruction were re-planed by manual applicator reconstruction. There were different applicator sets of; 20 plans for vagina cylinder applicator, 30 plans for Fletcher applicator, and 14 plans for Venezia applicator. The dosimetric parameters were compared in term of dose delivered to 98% and 90% of the HR-CTV volume (D_{98}, D_{90}), The high dose regions was volume receiving 200% and 100% of the prescription dose (V_{200}, V_{100}) for HR-CTV also investigated. The bladder, rectum, and sigmoid were evaluated in the dose received by a volume of 2 cm^3 (D_{2cc}).

Results: For the fixed applicator set like a vagina cylinder and the Venezia applicator, the result showed no significant dose difference in most of the parameters, except the sigmoid of the Venezia applicator. The dose difference at sigmoid from the manual reconstruction applicator was lower than the library applicator reconstruction. The Fletcher applicator plans showed significant doses difference for all parameters of HR-CTV (D_{98}, D_{90}, V_{200}, and V_{100} ($P < 0.05$)) and bladder. The rectum and sigmoid were not significantly different, $P = 0.23$ and 0.06, respectively.

Conclusion: The dose difference between manual and library reconstruction applicator is significant in Fletcher applicator plans. The vagina cylinder and Venezia applicator showed no significant difference. So, the Fletcher applicator reconstruction by manual in MRI-based brachytherapy should be careful investigation.

Keywords: Applicator reconstruction; MRI 3D image brachytherapy; gynecological brachytherapy.

Verification of Treatment Time in Interstitial Brachytherapy using Paris System

Mahamud S[1], H.A.Azhari[1], G.A. Zakaria[1,2], Ahmed S[3]

Gono Bishwabidyalay (University), Dhaka, Bangladesh

Introduction: Brachytherapy (BT) is a one kind of radiation therapy where sources are placed into or near the tumor for giving a high radiation dose. Now a day, most of the hospitals are doing intra cavitory treatment in Bangladesh and interstitial brachytherapy is rarely practiced.

Purpose: To verify the treatment time in interstitial brachytherapy using Paris System.

Methods: MATLAB (2016 a) and a test case of Paris system has been used in this method. This study has been done according to the principle of Paris System, all catheters have been inserted according to the ICRU 58 and dose rate calculation was done according to TG 43 protocol.

Results: The total treatment time for calculated and test case were 225.4 sec. and 225.7 sec. The deviation between these is only 0 .3 second, which is acceptable.

Conclusion: It is standard practice in BT to have a second, independent check of the treatment plan. It is one and utmost duty of a medical physicist to perform the TPS dose verification other than electrical check, mechanical check, dosimetry and radiation safety check Therefore this study will be helpful for the practicing of Paris system for the interstitial brachytherapy besides intracavitary brachytherapy that might open the new era of cancer treatment in Bangladesh.

Keywords: Interstitial Brachytherapy, Paris system, Treatment time verification.

Dosimetric evaluation of the uncorrectable rotational setup error in total body irradiation using helical tomotherapy system

Akira Isobe[1,3], Keisuke Usui[2,4], Haruka Katou[3], Junpei Ohbuchi[3], Naoya Hara[3], Keisuke Sasai[4]

1 Department of Radiation Oncology, Graduated School of Medicine, Juntendo University, Tokyo, Japan
2 Department of Radiological Technology, Faculty of Health Science, Juntendo University, Tokyo, Japan
3 Department of Radiology, Juntendo University Hospital, Tokyo, Japan
4 Department of Radiation Oncology, Faculty of Medicine, Juntendo University, Tokyo, Japan

Introduction: Total body irradiation (TBI) using helical tomotherapy (HT) has proven to safe. However, since TBI targets the entire body, the rotational setup error (SE) in the sagittal (pitch) direction may cause a large SE in the field edge. Additionally, when irradiating a large target such as TBI, the patient couch sag, which is characteristic the HT apparatus, increases so that a systematic pitch error is generated in the vertical direction.

Purpose: This study aimed to clarify the effects of rotational SE on dose distribution for TBI using HT.

Methods: The planning computed tomography (CT) images of 10 patients were rotated to 1 degree–5 degrees in the pitch direction in order to simulate the effects of rotational SE on dose distribution. The clinical target volume (CTV) was the whole-body contour excluding the lung, which is an organ at risk. The prescription dose was optimized by a radiation treatment planning system using a constraint to cover 95% of the target with 12 Gy on original image. The effects of rotational SE on dose distribution was quantitatively determined by recalculating the treatment plan with the rotated images.

Results: As a result of the simulation, the dose uniformity within the target deteriorated as the rotational SE increased. Even when the rotational SE of 1.0 degree occurred, the high-dose regions in CTV showed a significant difference from that of the planned dose distribution. The average of high-dose regions in the CTV was 5.1% with 2 degree of SE and 7.6% with 3 degree of SE.

Conclusion: If the rotational SE was less than 2.0 degree, the CTV dose heterogeneity could be kept within ± 10% of the prescribed dose in at least 95% of the cases. Therefore, we conclude that dose errors induced by rotational SE of less than 2.0 degree are acceptable.

Keywords: TBI, Helical tomotherapy, rotational setup error

Investigating the effect of material absorber the source of Gamma Knife Perfexion^{TM} based on Monte Carlo simulations

J. Junios[1*], I. Irhas[1], Novitrian[1], E. Soediatmoko[2], F. Haryanto[1], Z. Su'ud[1] and A. L. Fielding[3]

1 Faculty of Mathematics and Natural Sciences, Institut Teknologi Bandung, Jalan Ganesha 10 Bandung 40132, Indonesia
2 Gamma Knife Centre Indonesia, Siloam Hospital Lippo Karawaci, Tangerang, Banten 15811, Indonesia
3 Science and Engineering Faculty, Queensland University of Technology, Brisbane Qld, 4001, Australia
*e-mail: junios@s.itb.ac.id

Introduction: Gamma Knife Perfexion^{TM} (GKP) is a stereotactic surgical device that uses Cobalt-60 sources. For radiation protection purposes, it's encapsulated from certain materials. When the source beam is emitted, the interaction between the photons and absorber atoms produces two possibilities: (1) photons are absorbed with some of its energy transferred to charged particles and (2) scattered photons.

Purpose: These studies were very encouraging, as the effect associated with the use of absorber capsule, and PB materials on the Cobalt-60 GKP source with the Monte Carlo simulation technique will be studied.

Methods: The geometry of the accelerator to be simulated is built up from a series of predefined component modules (CMs) on the BEAMnrc program. The CMs used is FLATFILT, owing to its ability to produce cylindrical sources, capsules, and areas around the source. A cylindrical Cobalt-60 source with a diameter of 1 mm and length of 17 mm is packaged in stainless steel capsules, with a density (ρ) of 8.9 x10^3 Kg/m^3. The absorber used in this simulation is a PB material taken from the ICRU and a capsule material from the ELEKTA AB blueprint.

Results: The results show the effect of Capsule, and PB material absorbers on the source beam output on the total photons with a sequential increase influence at the Compton region was 62.49%, 58.54%. in the secondary photons found an increasing influence in the Compton region was 61.84%, 59.87%.

Conclusion: This increase occurs due to scattered photons when concerning capsules and PB material.

Keywords: The Cobalt-60 source, material absorber, Gamma Knife PerfexionTM, Monte Carlo simulation

Development of an In-house MATLAB code for dynamic multileaf collimator quality assurance based on EPID

Aiyara Pishyapan[1], Nauljun Stansook[1], Pimolpun Changkaew[1], Suphalak Khachonkham[1], Puangpen Tangboonduangjit[1]

1 Master of Science Program in Medical Physics, Department of Diagnostic and Therapeutic Radiology, Faculty of Medicine Ramathibodi Hospital, Mahidol University, Thailand

Introduction: In advanced radiotherapy treatments, verification of the performance of the multileaf collimator (MLC) is an essential part of the linac QA program. However, time-consuming is one of the issues of the MLC QA analysis procedure. There is some commercial software that can be used in combination with EPID information in saving time for MLC QA analysis. Unfortunately, there is an expensive product cost.

Purpose: To develop an In-house MATLAB code for evaluating the MLC leaf position accuracy based on EPID images following the TG-142 guideline.

Methods: This study tested with the Varian Clinac® iX which has 60 leaf pairs. The picket fence IMRT were generated for two plans. The standard has 11 strips separated by a 1 mm gap and the other has an individual intentional error of 1 and 2 mm to the specific knowing leaf number. All plans were delivered using 6 MV x-rays and acquired by EPID aS1000. The EPID images were imported to MATLAB. The standard of picket fence without error data was used as a baseline. The MATLAB code was generated based on image subtraction to find the error point. After that, the size of leaf error was detected.

Results: The MATLAB code was able to detect the error with 0.26 mm per pixel resolution. The position of error corresponding to leaf position and agrees to within ±0.15 mm of the intentional preset value by showing of 1.05 mm and 1.85 mm for 1 mm and 2 mm intent errors, respectively.

Conclusion: This developing MATLAB code provides a sufficient MLC leaf position accuracy. It is useful and convenient for routine MLC QA.

Keywords: Multileaf collimator, EPID, quality assurance, MATLAB

Dosimetric evaluation of photon beam-matching for two similar linear accelerators

Kanogpan Prasartvit, Porntip Iampongpaiboon, Chumpot Kakanaporn

Division of Radiation Oncology, Department of Radiology, Faculty of Medicine Siriraj Hospital, Mahidol University, Bangkok, Thailand

Introduction: In radiation therapy center, linear accelerators (linac) from the same model and vendor are usually tuned as beam-matched since it can increase the resilience for a treatment process. As long as two linacs are in beam-matching criteria, when one of the machines has been down, patients can continue their treatment at another machine with no dose recalculation required. Hence, to verify that machines are not unaltered from original specifications in commissioning process, the most practical way is to ensure that accelerators are acceptable to interchanged use.

Purpose: The study was aimed to evaluate the similarity of dose characteristic between two new Elekta Versa HD installed at Siriraj Hospital.

Methods: The output factor (OF), percentage depth dose (PDD), cross- and in-plane beam profiles and $TPR_{20,10}$ for the flattening and non-flattening filters of 6 and 10 MV photon beams were measured. Then, to include the treatment planning calculation, ten VMAT plans in various site of patient were generated using the same beam model. The doses were measured using Octavius 1500 and compared with 2%, 2mm gamma criteria.

Results: The measured output factor in each field sizes varied by less than 1%. The maximum and minimum different values in each depth of PDD varied within 1%. The difference of measured point dose in cross-and in-plane profiles were within 2%. $TPR_{20,10}$ were a few difference by less than 1% in all photon energies. All VMAT plans passed more than 95%.

Conclusion: By comparing all measurement criteria, the results show that there is good agreement in term of the similarity of the dosimetric characteristics between the two linacs. These findings also prove that our beam matching requirements have been satisfied.

Keywords: beam-matching, similar linear accelerator, dose characteristic

Assessment of Radiation Protection and Radiation Safety Awareness among Radiation Professionals in a Tertiary Care Teaching Hospital

Mary Joan[1], Priya Saini [1], Mukesh Jain[1], Ramesh Sharma[1], Ajay Prajapathi[1], Arun Chougule[1]

1 Department of Radiological Physics, S.M.S Medical College and Hospitals, Jaipur

Introduction: As the use of radiation in healthcare has increased, the probability of occurrence of radiation injuries and hazards has also increased. Hence, proper training and education of the radiation professional, which encompasses the radiation protection and safety aspects, instils confidence in the radiation professionals and reduces the anxiety and fear that surrounds radiation use. This training program can be conducted by the medical physicists in their respective hospitals on a regular basis.

Purpose: It is noticed that the medical professionals who perform interventional procedures are the most exposed to radiation and yet not thorough with the safety aspects. Hence, an assessment of the various radiation professionals was done to evaluate their knowledge about radiation hazards and radiation safety. This was followed by a training program which highlights the importance of such training sessions in radiation safety.

Materials & Methods: A questionnaire related to radiation protection, safety, regulatory norms and safe practices was formulated and the radiation and non-radiation medical professionals were asked to fill it. They then underwent a training program on radiation safety and were asked to submit the same questionnaire. A comparison was done to analyze the improvement through the training program.

Results: On comparing the results of pre and post training questionnaires, an increase in the score was seen for almost every participant. The average score of the 275 medical professionals of different background (Anaesthesiology, Cardiology, Gastroenterology and Orthopaedics) increased from 67% to 78% and 200 radiation professionals (Radiology and Radiotherapy) increased from 75% to 84%.

Discussions & Conclusions: The non-radiation medical professionals were found to be less confident in applying radiation safety knowledge in routine practice. The training program threw light on the importance of regular training sessions and the role of medical physicist in radiation protection and safety. The medical/radiation physicists are the key persons in establishing a safe and fearless atmosphere in a hospital when it comes to radiation usage. It is hence a responsibility of the medical physicist to hold regular training sessions for all the radiation and non-radiation professionals using ionizing radiation.

Keywords: Radiation protection and safety, Radiation awareness, Medical Physicists

Design of universal 3D-printed oral stent for head and neck radiotherapy

Thunphisit Mundee[1], Teerawit Eakpatcha[2], Chavin Jongwannasiri[1], Todsaporn Fuangrod[1]

1 Faculty of Medicine and Public Health, HRH Princess Chulabhorn College of Medical Science, Chulabhorn Royal Academy, Bangkok, Thailand
2 Department of Radiation Oncology, Chulabhorn Hospital, Chulabhorn Royal Academy

Introduction: The primary treatment of head and neck cancer is external beam radiation therapy. The complications from radiation include speech, taste, saliva production, and swallowing. An oral stent immobilization equipment is applied to minimize dose in the tongue (or hard palate) and can improve the patient setup accuracy between fractions. The oral stent remains not widely used due to the unaffordable price.

Purpose: We aim to design the universal oral stent, which is an affordable cost but high efficiency. The universal oral stent was physically evaluated using the Finite Element Analysis (FEA) to demonstrate the structural components and physical property. The first prototype was fabricated using 3D printing.

Methods: The universal oral stent was designed in 3D using CAD modeling software. The design consists of two components: mouthpiece and tongue displacer. The tongue displacer has three lengths 40, 45, and 50 mm according to the Asian patient's tongue length. The 3D model of the oral stent was evaluated using the FEA by simulating the realistic environment parameters, including maximum patient bites force (350 N) and average human breath airflow (1.3 m/s). The 3D printed oral stent was tested by experienced radiation therapists.

Results: The results of FEA presented the total deformation from the maximum bite force on the mouthpiece was 0.1282 mm. The deformation test showed that the mouthpiece is unbreakable with human bite force. The airflow line had the range between 0.6 - 1.3 m/s through the airway, and the mainline was 1.3 m/s. The patient can breathing from using. The function and usability of oral stent were satisfied by the experienced radiation therapists.

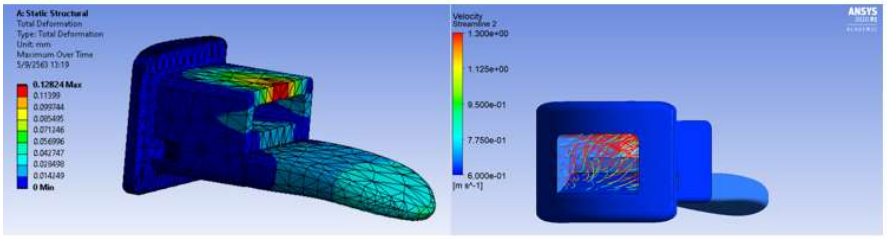

Conclusion: This universal oral stent contains the physical tolerance for the patient normal bite force due to the less deformation, and the level of airflow is suitable for the patient's normal breathing.

Keywords: oral stent, 3D printed fabrication, immobilization

Fabrication and validation of cubic phantom embed with an accelerometer sensor for verifying six-degrees-of-freedom couch

T. Popreeda[1], S. Thongsawad[2], N. Udee[1]

1 Department of Radiological Technology, Faculty of Allied Health Sciences, Naresuan University, Mueang, Phitsanulok 65000, Thailand.,
2 Radiation Oncology Unit, Chulabhorn Hospital, HRH Princess Chulabhorn College of Medical Science, Chulabhorn Royal Academy, Laksi, Bangkok 10210, Thailand.

Introduction: In modern medical linacs, the six-degrees-of-freedom (6DOF) couch have been implemented to machine for improving the accuracy of beam delivery. Especially in Stereotactic Radiosurgery (SRS) and Stereotactic Radiotherapy (SRT), couch can be shifted in pitch, roll, and yaw direction. However, the accuracy of couch shifted needs to be investigated with comprehensive Quality Assurance (QA).

Purpose: The purpose of this study was to develop cubic phantom embed with an accelerometer sensor for verifying 6DOF couch.

Methods: Cubic phantom was fabricated by using 3D printing, and an accelerometer sensor was imbedded inside the phantom to measure couch angle. The study was classified in two main tests: printing accuracy test, and angle measurement accuracy test. For printing accuracy test, printing parameter included printing speed and fill density were varied to find optimal parameter. For angle measurement accuracy test, accelerometer sensor was calibrated with referent spirit level in different angles, and the accuracy was validated in term of precision and reproducibility. The precision was determined by using difference between cubic phantom measurement and digital spirit level, whereas the reproducibility was determined by using standard deviation (sd.) of 10-time repeated measurements.

Results: The optimal parameter was found at printing speed of 50 mm/s, and fill density of 40%. The maximum difference between cubic phantom measurement and spirit level was -0.05±0.07 degree, and 0.05±0.22 degree for pitch, and roll direction, respectively. The maximum sd. of 10-time repeated measurements was found at 5 degree with ± 0.09 for pitch direction, and at -4 degree with ±0.19 for roll direction.

Conclusion: In this study, we have developed the new QA tool for verifying 6DOF couch with self-measurement method, and the accuracy of cubic phantom embed accelerometer sensor was enough for verifying six-degrees-of-freedom couch.

Keywords: six-degrees-of-freedom (6DOF) couch QA, 3D printing, accelerometer sensor

Daily machine-specific performance monitoring through clinical treatment delivery using Statistical Process Control and MobiusFX

Piyakan Wongsaroj[1], Taweap Sanghangthum[2], Todsaporn Fuangrod[1]

1 Medical ***Physics*** Program, Faculty of Medicine and Pubic Health, HRH Princess Chulabhorn College of Medical Science, Chulabhorn Royal Academy, Bangkok, Thailand,
2 Division of Radiation Oncology, Department of Radiology, Faculty of Medicine, Chulalongkorn University, Bangkok, Thailand

Introduction: Linear accelerator (linac) quality assurance (QA) aims to check the machine does not significantly deviate from the controlled values in various both mechanics and dosimetric parts. A machine-specific performance monitoring through process can enhance the treatment quality, reducing the systematic errors, and benefit to proactive linac maintenance management.

Purpose: To develop the daily machine-specific performance monitoring using MobiusFX (log-file) with statistical process control (SPC).

Methods: The daily machine-specific performance monitoring was performed to capture patient delivery data (machine log-file) in daily bias from Varian Clinac iX linac for 60 days. Total data of 385 log-files were analysed using MobiusFX (V.2.1.2). SPC in form of X/MR charts was constructed from the first 30 days then used to monitor linac machine performance including 3D gamma analysis values, root-mean-square (RMS) error analysis values for gantry, collimator, jaw and MLC motor.

Results: X/MR charts of SPC showed the lower control limits (LCL) of 3D gamma at 95% (as baseline). The upper control limits (UCL) of RMS error for gantry, collimator, jaws in X1, X2, Y1, Y2 and MLC motor were 1.05 mm, 0.106 mm, 0.33 mm, 0.708 mm, 0.71 mm, 0.607 mm and 1.19 mm, respectively. The LCL of RMS error values for MLC motor was 0.61 mm. During the linac machine monitoring (since day 31 to 60), the system flagged the issue twice on Y1-jaw, and once on Y2-jaw. This required setting-up the preventive maintenance for Y-jaw.

Conclusion: The linac machine performance monitoring through the clinical treatment delivery evaluation using MobiusFX with SPC demonstrate the potential system to flag the possible malfunction of machine parts (focusing on finding the systematic errors). This can help medical physicist to manage their preventive maintenance efficiently and minimizing the unexpected machine downtime in the future.

Keywords: Daily machine-specific performance monitoring, Statistical process control, MobiusFX

Establishment of MOH Medical Physics Research Task Force

Aik Hao Ng[1], Hwee Shin Soh[2]

1 Department of Radiotherapy and Oncology, National Cancer Institute, Putrajaya, Malaysia.
2 Medical Radiation Surveillance Division, Ministry of Health Malaysia.

Introduction: Medical physicist is a relatively small profession in the Malaysian Ministry of Health (MOH) settings. The core businesses of the profession within the organisation are to provide clinical support and regulatory services. Some of the medical physicists have limited access to adequate research support and felt isolated in their work environment.

Purpose: This presentation sets out to report the establishment the research task force. This initiative aims to cultivate research culture amongst the medical physicists in the MOH and to provide research support.

Methods: The task force was formed in 2019, consisted of 21 volunteered medical physicists nationwide from both clinical and regulatory sectors. A SWOT analysis was carried out to examine the current status of research activities within the organisation.

Results: Four sub-groups have been established to execute the aims of the task force, namely research (1) promotion, (2) support, (3) requirements as well as (4) activities and database. The group outreaches the profession through scientific meetings, email and mobile instant messaging application (WhatsApp) to continuously promote research awareness and to share timely information. Workshop and consultation were organised to provide guidance and support to the young professionals. The group also explored potential research collaboration with academic and industrial partners.

Conclusion: The initiative offers a new platform to cultivate research culture and encourage more research activities to be carried out, which could provide added values to the healthcare services. We hope to continue to explore different ways to succeed this work and encourage more volunteers to join us.

Keywords: research, medical physicists, task force

CT Density Profile and Physicochemical Study of Soy-Lignin Bonded *Rhizophora* spp. Particleboard as Phantom Material in Medical Physics Application

Siti Hajar Zuber[1], Nurul Ab. Aziz Hashikin[1], Mohd Fahmi Mohd Yusof[2], Rokiah Hashim[3]

1 School of Physics, Universiti Sains Malaysia, 11800, Penang, MALAYSIA.
2 School of Health Sciences, Universiti Sains Malaysia, 16150, Kelantan, MALAYSIA.
3 School of Industrial Technology, Universiti Sains Malaysia, 11800, Penang, MALAYSIA.

Introduction: The utilization of natural adhesive in the fabrication of particleboard for medical physics application has been investigated and many proved capable of replacing the well-integrated formaldehyde adhesive. Soy flour and lignin had been extensively used as adhesive and more studies had proved the suitability of both adhesives in the production of sturdier particleboards. CT study can accurately estimate the attenuation coefficients for soft tissue, thus providing an accurate determination of density, electron density and density profile of the fabricated particleboard.

Purpose: We aim to evaluate the physical and mechanical properties of the particleboards, the determination of CT number, electron density and density profile of the material using fabricated density plug phantom.

Methods: Density determination, internal bonding, modulus of rupture, water absorption, and thickness swelling were performed. Microstructure study using scanning electron microscopy (SEM) and elemental analysis by carbon hydrogen nitrogen (CHN) analyser were also investigated. We also study the Computed Tomography (CT) number, relative electron density and the density profile analysis of the phantoms.

Results: Particleboards with adhesives improved internal bond strength. Smaller particle sizes also have shown to be able to improve the thickness swelling outcomes, with lower hygroscopic properties. The SEM images showed that smaller particle size allowed better bonding with adhesives and provided superior strength. The CHN ratio revealed no major difference when compared with the samples which were crucial in the fabrication of tissue-mimicking phantom. The bonded particleboard showed close similarities with water, based on the average CT numbers, CT calibration curve, electron density calibration curve and the analysis of CT density profile, compared to the binderless particleboard.

Conclusion: The CT and physiochemical study of soy-lignin bonded *Rhizophora* spp. particleboard exhibited its suitability as an alternative phantom material for applications in medical physics.

Keywords: Physical properties; Mechanical properties; CT Electron Density phantom; particleboard fabrication; soy-lignin adhesive

Dignostic: Imaging

Correlation of Ultrasound Attenuation Imaging versus MRI Proton Density Fat Fraction in Non-alcoholic Fatty Liver

Pantajaree Hiranrat[1], B.Sc., Surachate Siripongsakun[1], M.D., Kamonwan Soonklang[2], M.Sc., Chanisa Chotipanich[1], M.D.

1 Sonographer School, Faculty of Health Science Technology, Chulabhorn Royal Academy, Bangkok 10210, Thailand,
2 Data ***Management*** Unit, HRH Princess Chulabhorn College of Medical Science, Chulabhorn Royal Academy, Bangkok 10210, Thailand,

Introduction: Attenuation Imaging (ATI) is a novel ultrasound method for assessment degree of hepatic steatosis, based on ultrasound attenuation by calculating attenuation coefficient which will increase in fatty liver condition. The previous published data comparing ATI and Magnetic Resonance Proton Density Fat Fraction (MR-PDFF) has moderate to high correlation coefficient (r = 0.66-0.81). However, fatty liver is commonly associated with obesity which may be an influencing factor of the ATI measurement.

Purpose: The purpose of this study was to evaluate correlations and interobserver liability of ATI comparing with MRI-PDFF in obese patients.

Methods: In this study, the non-alcoholic fatty liver disease (NAFLD) patients with available ATI and MRI-PDFF examination, excluding cirrhosis, history of significant alcohol drinking, and chronic liver condition were evaluated. Correlation of ATI and MRI-PDFF values and interobserver's concordance of ATI measurements were evaluated, using Spearman rank correlation and Cohen's kappa coefficient. Statistical significance is considered at 2 side p value < 0.05.

Results: There were 62 patients included with average BMI of 27.4 kg/m2. The correlation coefficient (r) of ATI vs MRI-PDFF were in moderate correlation ($r = 0.63$-0.69, $p<0.001$). With the highest correlation coefficient at right posterior segment measurement ($r=0.69$). The inter-observer reliability of two observers were 100% with Cohen kappa coefficient of 1.00 ($p < 0.001$).

Conclusion: ATI is a novel ultrasound method to quantify degree of fat deposition with good correlation to MRI-PDFF with high interobservers' reliability. Obesity commonly associated with fatty liver may be an interfering factor of ATI measurement.

Keywords: Attenuation Imaging, Fatty liver, Steatosis, MRI-PDFF, MRE, NAFLD

Sonographic predictors for developing cholangiocarcinoma: A cohort study from an endemic area.

Natcha Thanakijsombat[1,2], Jiraporn Laothamatas[1], Kamonwan Soonklang[3], Surachate Siripongsakun[1]

1 Sonographer School, Faculty of Heath Science Technology HRH Princess Chulabhorn College of Medical Science, Bangkok, Thailand
2 Department of Emergency Medicine, Police General Hospital, Bangkok, Thailand
3 Data Management Unit, HRH Princess Chulabhorn College of Medical Science, Chulabhorn Royal Academy, Bangkok, Thailand

Introduction: Cholangiocarcinoma (CCA) is an aggressive malignancy with rapid progression and poor prognosis. Bile duct and peribiliary changes related to cholangiocarcinogenesis may present on sonographic findings for example; periportal fibrosis, and non-specific diffuse bile duct dilatation without obstruction.

Purpose: This study aim is to evaluate ultrasound findings which could be used as predictors for developing CCA through our surveillance program in an endemic area, Nan province, Thailand.

Methods: The surveillance population-based cohort was 4,337 villagers in Northern Thailand, aged 30-60 years, who consented to a 5-year abdominal ultrasound surveillance program which included interval ultrasound examinations every 6 months. Patient's demographics including age and gender, family history of CCA, ultrasound findings including the presence of calcifications, diffuse biliary dilatation, and periportal fibrosis were included. A logistic regression model was used to determine significant predictors using forward stepwise generalized linear model for multivariate analysis.

Results: In this cohort, there were 4,337 patients, between 30-60 years, with average age of 45.37±7.7 years, consisted of 2,360 females and 1,977 males, respectively. On univariate analysis; the significant predictors with increased risk of developing CCA included age (relative risk (RR) = 1.11, $p < 0.001$), family history of CCA (RR = 2.58, $p < 0.001$), hepatic calcifications/granuloma (RR = 0.74, P=0.38), diffuse biliary system dilatation (RR = 5.02-17.62, both $p < 0.001$, respectively), periportal fibrosis (RR 3.11, $p < 0.001$). On multivariate analysis the significant independent predictors associated with developing CCA include age (RR = 1.09, $p < 0.001$), diffuse biliary system dilatation (RR = 7.03-22.59, $p < 0.001$)

Conclusion: Sonographic predictors of CCA development including age and diffuse bile duct dilatation may be helpful in identifying the population at risk in order to target for surveillance in CCAs endemic areas.

Keywords: Cholangiocarcinoma, Predictor, Sonography, Surveillance

Value of Superb Microvascular Imaging (SMI) in characterize of nodular type focal fat sparing lesion and true hepatic nodules in the background of fatty liver

Songpon Srisittimongkon[1], Surada Vichitpunt[1], Siwat Bhumiwat[1], Pantajaree Hiranrat[1], Surachate Siripongsakun[1]

1 Sonographer School, Faculty of Health Science Technology, Chulabhorn Royal Academy, Bangkok 10210, Thailand,

Introduction: Fatty liver is a common condition which increases liver parenchyma echogenicity. This condition often associated with an area of **f**ocal fat sparring (FFS) due to inhomogenous fatty deposition**.** Increase parenchymal background from the fatty liver also alters the echogenic appearance of liver lesions which will be relatively hypo-echogenic**.** Superb microvascular imaging (SMI) is a novel microvascular imaging technique that allows visualization of vascular architectures of the lesions which potentially distinguish true nodules from FFS pseudo-lesions.

Purpose: The study was to evaluate the value of SMI in characterizing hypoechoic lesion in fatty liver background.

Methods: This prospective study recruited patients who had fatty liver with hypoechoic nodular lesions, between 0.8-4.0 cm in size, which had definite characterization on CT or MRI. Size, margin, and SMI patterns, of hypoechoic lesions of true and FFS psudeo-lesions were evaluated using t-test and Fischer's exact test. SMI vascular patterns are classified according to Lee et al.

Results: There were 44 patients with fifty-seven hypoechoic lesions, consisting of 22 FFS lesions and 35 true hepatic nodules including twenty-two hemangiomas, seven metastases, three focal nodular hyperplasias (FNHs), two regenerating nodules and two parasitic related abscesses. True nodules and FFS pseudo-lesions showed well-defined margin in 34/35(97%) and 8/22 (36%, $p < 0.001$), respectively. Almost all FFS showed non-specific or no signal pattern (19/22, 85%), which overlapped with true nodules in (17/35, 57%). Rarely FFS has other patterns including nodular rim and staining (3/22, 15%). Nodular rim with dot-like and spoke-wheel SMI patterns were found only in hemangiomas and FNHs, respectively.

Conclusion: In fatty liver, FFS and true nodules are overlapped in US appearance. A few patterns of SMI including nodular-rim with dot-like and spoke-wheel patterns may suggest a specific type of lesions including hemangiomas and FNHs.

Keywords: Fatty liver, Hypoechoic, Superb Microvascular Imaging, Ultrasound

Predicting Treatment Response in Nasopharyngeal Cancer Using Radiomics: A Preliminary Study

Sasawan Wongpisarn[1,5], Chawalit Lertbutsayanukul[2], Nutchawan Jittapiromsak[3], Yothin Rakvongthai[4,5]

1 Medical Physics Program, Department of Radiology, Faculty of Medicine, Chulalongkorn University, Bangkok, Thailand
2 Division of Radiation Oncology, Department of Radiology, Faculty of Medicine, Chulalongkorn University, Bangkok, Thailand
3 Division of Diagnostic Radiology, Department of Radiology, Faculty of Medicine, Chulalongkorn University, Bangkok, Thailand
4 Division of Nuclear Medicine, Department of Radiology, Faculty of Medicine, Chulalongkorn University, Bangkok, Thailand
5 Chulalongkorn University Biomedical Imaging Group, Department of Radiology, Faculty of Medicine, Chulalongkorn University, Bangkok, Thailand

Introduction: It is necessary to monitor a treatment for nasopharyngeal cancer (NPC) to assess its response. Radiomics is a technique that extracts large amount of data from medical images in terms of features which reflect tumor characteristics.

Purpose: Our hypothesis was that radiomics features from diffusion-weighted imaging (DWI) could be used as imaging biomarkers for concurrent chemoradiation therapy (CCRT) treatment response. Here we investigated the use of such radiomics features for treatment response prediction in NPC patients.

Methods: We collected seventeen patient datasets including thirteen complete response (CR) patients and four partial response (PR) patients where one patient dataset consisted of DWI and apparent diffusion coefficient (ADC) data acquired before (i.e. pre-treatment) and at five weeks after (i.e. mid-treatment) initiation of CCRT. For each dataset, we calculated the radiomic feature values using PyRadiomics software from pre-treatment and mid-treatment, and computed the percentage change of each feature, called Delta Radiomic (ΔRadiomic) feature. To validate the performance in differentiating CR and PR patients, we calculated the mean, standard deviation (SD) across CR and PR patients, and area under the receiver operating characteristic (ROC) curve (AUC) of each feature and its ΔRadiomic, where tumor response was from 6-month follow-up data using RECIST1.1 guideline.

Results: There were 1 radiomic feature value at pre-treatment and 32 ΔRadiomic feature values that yielded a significant difference ($p<0.05$) between CR and PR groups. The AUC values from these 32 ΔRadiomic feature values ranged from 0.85 to 0.94, which were all higher than those from percentage change values of conventional imaging biomarkers such as volume, mean, uniformity and entropy (0.48, 0.81, 0.44, and 0.46, respectively). ΔRadiomic feature values that yielded the highest AUC value were from sphericity and wavelet-LLH_glcm_DifferenceVariance.

Conclusion: Radiomics-based biomarkers could potentially be used for early treatment response prediction in NPC patients.

Keywords: Radiomics, Nasopharyngeal cancer, DWI

Performance of quantitative lesion measurement in hepatic dual-energy computed tomography (DECT): Phantom study

Hataipat Jantawong[1], Anchali Krisanachinda[2]

1 Doctor of Philosophy Program in Medical Physics, Faculty of Medicine, Chulalongkorn University, Bangkok, Thailand
2 Department of Radiology, Faculty of Medicine, Chulalongkorn University, Bangkok, Thailand

Introduction: The quantitative measurements of iodine uptake, size and volume of liver lesion are essential for diagnostic and treatment response assessment of HCC. Recently, the dual energy computed tomography (DECT) acquisition has been adopted and widely used in abdominal imaging.

Purpose: To evaluate the performance of quantitative lesion measurements (both the iodine enhancement and size) in hepatic DECT as a function of imaging parameters using 3D-printing liver lesion phantom.

Methods: The three-dimensional printing technique was used to construct liver phantom with various in size of synthetic hyperenhancement spherical liver lesions; 6,8,10,15,19,20,25 mm in diameter and different iodine concentrations of 18,20,22,24,26 mg-iodine per mL (mgI/mL). Total of 35 lesions were scanned using DE acquisition with the third generation of dual source DECT (DS-DECT). The kV-combination was selected as 80/150Sn,90/150Sn and 100/150Sn. The radiation dose levels were varied to achieve targeted $CTDI_{vol}$ of 15,20, and 25 mGy. The images of low-and high-kV were sent to vendor-specific DE software to measure the iodine quantification for each lesion size and iodine concentration. Absolute error of iodine quantification was measured. The virtual monoenergetic images (VMIs) were created at different photon energy from 40- 80-keV(10 keV interval) images and were sent to commercial software to perform semi-automated measurements of diameter and volume of various liver lesions and then estimated for the measurement error.

Results: Among different DE parameters, the iodine quantification error was lower when increasing the lesion size and iodine concentration. However, at higher dose level, size and volume, the errors were improved. In addition, at the standard and high dose level, lower photon energy of VMIs provided the better performance.

Conclusion: The scanning and post-processing DE parameters have potential impact on iodine quantification error and volumetric measurement. In addition, the lesion characteristics (size and iodine concentration) affect the accuracy of iodine quantification and volumetry.

Keywords: dual-energy computed tomography, hepatocellular carcinoma, iodine quantification, virtual monoenergetic images, liver 3D-priting phantom

Automatic QC Analysis Program in Digital Radiography System

Jongwat Cheewakul[1], Natee Ina

1 Department of Radiology Faculty of Medicine Prince of Songkla University, Songkla, Thailand

Introduction: Quality Control of the diagnostic radiology system is the test of the quality and function of the X-ray machine and to observe the defects, deterioration or damage of the equipment by Medical Physicist. The developed program analyses the automatic image quality control in digital x-ray systems can help Medical Physicist to reduce the time spent in the analysis the test results with more convenience.

Purpose: The purpose of this study was to design automatic quality control analysis program and to compare the test results from this program with the results from three observers.

Methods: This developed analysis program using MATLAB could assess the image quality in terms of the spatial resolution, low contrast detail detectability and high contrast detail detectability. The Routine Test Object for conventional and non-subtractive digital radiography, TOR CDR test tool was exposed by three digital X-ray machines, one image for each X-ray machine was obtained. Then three images were assessed by developed software and three observers.

Results: The results show that the evaluation from the developed software and three observers are comparable. The spatial resolution evaluated by the developed software were 3.55, 3.15, 2.80 lp/mm and by three observers was 3.55, 2.80, 2.80 lp/mm respectively. The low-contrast detectability evaluated by the developed software was 16, 15, 17 and by three observers were 16, 16, 15 respectively. The high-contrast detectability evaluated by the developed software was 17, 17, 17, and by three observers were 16, 17, 17 respectively. The average assessment time evaluated by the developed software was 1.30 min and by manual procedure was 3.15 min.

Conclusion: This automatic QC analysis program can be used with the reduction in the assessment time and be able to record the results to compare with the previous results.

Keywords: Quality Control, Spatial Resolution, Low and High Contrast Detectability, Digital Radiography System

Correlation between renal histological fibrosis and renal cortical thickness using shear wave elastography in patients with kidney disease

Sook Sam Leong[1,2], Jeannie Hsiu Ding Wong[1,3], Mohammad Nazri Md Shah[1,3], Anushya Vijayananthan[1,3], Maisarah Jalalonmuhali[4], Tak Kuan Chow[5], Nur Hidayati Mohd Sharif[6], Kwan Hoong Ng[1,3]

1 Department of Biomedical Imaging, University of Malaya, 50603 Kuala Lumpur, Malaysia
2 Department of Biomedical Imaging, University of Malaya Medical Centre, 50603 Kuala Lumpur, Malaysia
3 University of Malaya Research Imaging Centre, University of Malaya, 50603 Kuala Lumpur, Malaysia
4 Department of Medicine, University of Malaya, 50603 Kuala Lumpur, Malaysia
5 Department of Pathology, University of Malaya, 50603 Kuala Lumpur, Malaysia
6 Renal Unit, Faculty of Medicine, University Teknologi MARA, 47000 Sungai Buloh, Malaysia

Introduction: Renal biopsy is the gold standard for the histological characterisation of chronic kidney disease (CKD), of which renal fibrosis is a dominant component, affecting its stiffness.

Purpose: This study aims to investigate the correlation between kidney stiffness obtained by SWE and renal histological fibrosis.

Methods: SWE assessments were performed in 75 CKD patients who underwent renal biopsy. The SWE-derived estimates of the tissue Young's modulus (YM), given as kilopascals (kPa), were measured. YM was compared to patients' renal histological scores, broadly categorised into glomerular, tubulointerstitial and vascular scores.

Results: YM correlates significantly with tubular interstitial score ($\rho = 0.442$, $p < 0.001$) and glomerular score ($\rho = 0.375$, $p = 0.001$). Patients with no glomerular sclerosis showed lower mean YM measurements compared those with glomerular sclerosis. The mean YM increased as the percentage of interstitial fibrosis and tubular atrophy increased. The area under the ROC curve for SWE in differentiating between mildly and moderately impaired kidneys was 0.702.

Conclusion: SWE accurately detects chronic renal damage resulting from glomerular sclerosis, interstitial fibrosis and tubular atrophy, using the optimal cut-off YM value of ≥5.81 kPa.

Keywords: Biopsy; Fibrosis; Kidney; Shear wave elastography; Young's modulus

Automatic stratification of prostate cancer patients into low- and high-grade groups based on multiparametric MR image feature analysis

Akimasa Urakami[1], Hidetaka Arimura[2], Fumio Kinoshita[3] Kenta Ninomiya[1], Sumiko Watanabe[2], Kenjiro Imada[4], Yoshinao Oda[3]

1 Department of Health Sciences, Graduate School of Medical Sciences, Kyushu University
2 Department of Health Sciences, Faculty of Medical Sciences, Kyushu University
3 Department of Anatomic Pathology, Graduate School of Medical Sciences, Kyushu University
4 Department of Urology, Prostate, Kidney, Adrenal Surgery, Kyushu University Hospital

Introduction: Multiparametric magnetic resonance (MR) imaging could be utilized for non-invasive grading of prostate cancer[1,2].

Purpose: This study aimed to investigate the potential of automatic stratification of prostate cancer patients into low- and high-grade groups based on multiparametric MR image feature analysis.

Methods: MR images of 66 cancer regions corresponding to histopathological images were identified and divided into a training (n = 40) and test datasets (n = 26). Each dataset was divided into two groups, low-grade tumors (≤GG2) and high-grade tumors (GG3≤), based on their grade groups. A total of 4320 MR image features were calculated from 16 types of images in 5 sequences for each cancer region and some of them were selected by using a least absolute shrinkage and selection operator (LASSO) and regularized logistic regression using elastic net algorithm as a signature candidate. Next, a combination strategy was used to extract a signature from the signature candidate. Finally, support vector machines (SVM) models were built using the signature in the training dataset. Leave-one-out cross validation was applied to feature extraction and training of the models. Model performances were evaluated using areas under receiver operating characteristic curves (AUCs).

Results: The AUC based on the SVM models of the stratification of prostate cancer patients into two groups were 0.993 in the training dataset and 0.550 in the test dataset.

Conclusion: This study showed the potential of automatic stratification of prostate cancer patients into low- and high-grade groups based on multiparametric MR image feature analysis.

Keywords: prostate cancer, grade group, MR image features, regularized logistic regression using elastic net, support vector machine

Image analysis of pancreatic cancer tissues using Haralick Features

Ashleigh Hull[1], Yanrui Li[1], Dylan Bartholomeusz[2,3], William Hsieh[1,2] & Eva Bezak[1,4]

1 Cancer Research Institute & Allied Health and Human Performance Academic Unit, University of South Australia, Adelaide, Australia,
2 Department of PET, Nuclear Medicine & Bone Densitometry, Royal Adelaide Hospital, SA Medical Imaging, Adelaide, Australia,
3 Adelaide Medical School, The University of Adelaide, Adelaide, Australia,
4 Department of Physics, The University of Adelaide, Adelaide, Australia

Introduction: Cellular heterogeneity complicates the development of targeted therapies for pancreatic cancer. Despite studies assessing the molecular basis of this heterogeneity, few studies have established the implications of heterogeneity on the overall texture of pancreatic cancer. Haralick Features (HF) provide 14 textural descriptors, such as contrast and homogeneity, to characterise images based on the spatial distribution of pixel values.

Purpose: The aim of this study was to identify textural differences between images of normal, pancreatic cancer and chronic pancreatitis tissues using HF.

Methods: Two-hundred and eighty pancreatic tissue samples consisting of normal (n = 97), primary pancreatic cancer (n = 106) and chronic pancreatitis (n = 77) pathology were immunohistochemically stained using C595, an anti-mucin 1 antibody. Stained tissue samples were imaged using a NanoZoomer Digital Slide Scanner (Hamamatsu Photonics, Japan), with images converted to 8-bit grayscale by Image J (v.1.52, National Institutes of Health, USA). A gray level co-occurrence matrix was determined for each image, allowing for calculation of HF values using MATLAB (v. 2020a, MathWorks, USA). Statistical analysis of the HF across the disease groups was performed using GraphPad Prism (v.8.2.0, GraphPad Software, USA).

Results: Preliminary results demonstrated significant differences for all 14 HF between the pancreatic cancer and normal pancreatic tissue samples ($p < 0.0006$). There were significant differences between chronic pancreatitis and pancreatic cancer tissues for 12 HF ($p < 0.03$). Correlation ($p = 0.36$) and Information Measure of Correlation I ($p = 0.7915$) demonstrated no significant differences between the chronic pancreatitis and pancreatic cancer groups.

Conclusion: This study demonstrates quantifiable differences between the texture of pancreatic cancer tissue to both normal tissue and pancreatitis. Consideration of these textural differences may be valuable for the development of targeted therapies by improving treatment stratification with potential extension into artificial intelligence.

Keywords: Haralick Features, pancreatic cancer, textural analysis.

Digital Breast Tomosynthesis (DBT): Dose and image quality assessment of man-made breast phantom

Nur Farrah Ezlyn Mohammad Rusdi[1], Nur Afizatul Izni Mohd Jasri[1], Yasmin Md Radzi[1], Noor Diyana Osman[2]

1 School of Physics, USM, Malaysia,
2 Advanced Medical and Dental Institute, Universiti Sains Malaysia, Penang, Malaysia.

Introduction: Digital Breast Tomosynthesis (DBT) system offers a gain in sensitivity and specificity in breast cancer detection of overlying tissues compared to the existing 2D mammography. To truly evaluate the clinical systems of intended diagnostic tasks, a realistic three dimensional (3D) anthropomorphic breast phantom is essential but 3D prototyping is very expensive. Therefore, a simple phantom is vital to practice good and efficient breast screening while capable of providing optimum compromise between dose and image quality.

Purpose: In this study, we aim to optimize the parameters in 3D breast screening with excellent compromise between dose and image quality in addition to determine the ideal breast thickness to provide good image quality while minimizing dose exposure to the patient.

Methods: A simple customized gelatine-based[2] phantom with two different overlying masses mimicking tumour and microcalcification was used throughout the study in order to assess the dose and image quality during breast screening. Mean Glandular Dose and Signal-Noise-Ratio are assessed for the absorbed dose and image quality assessment at different thicknesses of breast phantom using 2D and 3D tomosynthesis of 45° arc movement (Siemens Healthineers, USA). Optimum parameters are evaluated, and comparison between both methods are discussed.

Results: An ideal breast thickness (approximately 36.78mm) was determined from the intercept point of Average Glandular Dose (AGD) and Optical Density as well as Signal-to-Noise Ratio (SNR). The benefits of 3D imaging compared to 2D imaging were also observed in determining the optimum parameter for a thorough patient's breast screening.

Conclusion: Understanding the image creation process as it relates to the interplay of contrast, noise, patient dose, and diagnostic performance is vital in the practice of modern radiology including mammography. When a lesion needs to be more visible, this could be achieved by increasing the contrast, reducing noise, or by a judicious combination of both aspects.

Keywords: Digital breast tomosynthesis (DBT), Average Glandular Dose (AGD), Mean Glandular Dose (MGD), Signal-to-Noise Ratio (SNR), Optical density,

Grey Matter Segmentation of T1-Weighted MR Image in Ischemic Stroke Patients using *k*-Means Clustering

Dian Yuliani Alam

Department of Physics, University of Brawijaya, Malang, Indonesia

Introduction: The grey matter in the brain plays an important role to process the information. In ischemic stroke patients, it could experience some change. This could be diagnosed through the T1-weighted MR (Magnetic Resonance) image, since it shows the grey matter brighter. The T1-weighted MR image is based on the longitudinal relaxation, which the energy of radio-frequency is released to the surrounding tissue.

Purpose: In this research, the grey matter segmentation was conducted to confirm the principle of T1-weighted image as well as the results of researches in ischemic stroke patients related to the grey matter.

Methods: The MRI data were collected in 10 ischemic stroke patients and 10 healthy controls. The Time Echo (TE) parameter in the T1-weighted image was analysed. The used image segmentation method was k-means clustering based on the pixel intensity using MATLAB software.

Results: The obtained result showed that the T1-weighted axial images of all patients had short TE values (less than 20 ms). The pixel intensity of grey matter was higher than cerebrospinal fluid and white matter. This had a correlation with short TE values. As for the mean pixel intensity of grey matter in ischemic stroke patients and healthy controls were 135.53 and 150.76, respectively.

Conclusion: Since the mean pixel intensity of grey matter in ischemic stroke patients was lower than healthy controls, it could be concluded that the ischemic stroke reduces the grey matter in the brain.

Keywords: Grey matter, T1-weighted image, ischemic stroke, *k*-means clustering

Diagnostic: Big data, Deep learning, AI and Modeling

The effective methods for liver cyst labelling in ultrasound images by using R-CNN

Sutthirak Tangruangkiat[1], Anchali Krisanachinda[2], Supatana Auetavekiat[3]

1 Ph.D. program in Medical Physics, Faculty of Medicine, Chulalongkorn University, Thailand.
2 Department of Radiology, Faculty of Medicine, Chulalongkorn University, Thailand.
3 Department of Electrical Engineering, Faculty of Engineering, Chulalongkorn University, Thailand.

Introduction: Ultrasound imaging is one of the most popular medical imaging modality because of its non-ionizing radiation and real time imaging. Deep learning has been successfully applied in medical imaging as computer aided diagnosis (CAD). However, the limitation on ultrasound imaging of the same target can be variable according to the users' technique and the equipment setup, leading to the inaccurate classification.

Purpose: To design the training data for a region-based convolution neural network (R-CNN) for cyst detection in liver ultrasound images.

Methods: R-CNN using ResNet50 as a classifier was used as an object detector. The ground truth of a cyst was provided in two sets. On the first set, only the area of the cyst was used as a ground truth. On the second set, in addition to the cyst, the acoustic enhancement artefact below the cyst, the distinct feature of the cyst, was included into the ground truth. The five-fold cross validation was performed on 615 liver cyst images to evaluate the classification accuracy.

Results: The classification accuracy was 84.39% and 90.73% for the R-CNN trained using only cysts and the combination of a cyst and its enhancement artefact, respectively. Two main causes of error are: (1) failure to detect the cyst in a low-resolution image and (2) the detection of a vessel as a cyst. Both errors were reduced when the artefact was included to the training image.

Conclusion: The distinct feature of a target should be included into the training data of R-CNN to improve classification accuracy.

Keywords: Deep learning, ultrasound image, liver, cyst, artefact, R-CNN

Quantitative Assessment of Breast Density Using Pixel Intensity Threshold

Jaroonroj Wongnil[1], Anchali Krisanachinda[1], Rajalida Lipikorn[2]

1 Ph.D.in Medical Physics, Department of Radiology Faculty of Medicine, Chulalongkorn University, Bangkok, Thailand
2 Department of Mathematics and Computer Science, Faculty of Science, Chulalongkorn University, Bangkok, Thailand

Introduction: Breast cancer is the most common cancer with the highest mortality in women worldwide. Breast density can be used to evaluate the risk of breast cancer and the routine visually assessment. It is difficult to distinguish variably assigned BI-RADS categories. The visual assessment is still important where automated assessment systems had not been available.

Purpose: To evaluate quantitative breast density using pixel intensity threshold correlate to visual assessment method.

Methods: The study consists of 2,000 full-field digital screening mammogram with 1,000 craniocaudal (CC) and 1,000 mediolateral oblique (MLO) views in Thai patients. Breast density of almost entirely fatty (AF), scatter areas of fibro-glandular density (SD), heterogeneous dense (HD) and extremely dense (ED) at 400, 600, 600 and 400 images had been collected on both views (CC and MLO). All mammograms were classified using BI-RADS, along with the radiologist classification and retrieved from PACS (Picture Archiving and Communication System). The pre-process covers the identification of the breast region, the background removal, and labelling pectoral muscle areas using MATLAB Image segmentation. The ratio of breast density was calculated by summation of specific breast areas divided by total breast area. The breast density ratio of each breast classification was obtained and validated by using the new set of mammographic images.

Results: The average (min-max) breast density ratio of AF, SD, HD and ED were 0.366 (0.319-0.427), 0.392(0.309-0.460), 0.445(0.408-0.491) and 0.446(0.400-0.541), respectively. The results were concordant with visual assessment by radiologist which are difficult in distinguish between HD and ED.

Conclusion: The quantitative assessment of breast density using pixel intensity threshold conformed to visual assessment methods. The classification of breast density between HD and ED are still challenging, using both quantitative and qualitative methods to assess which may improve the accuracy and consistency of breast density classification.

Keywords: Breast density, histogram, BI-RADS, pixel intensity threshold

Overall Survival Prediction of Nasopharyngeal Carcinoma using Radiomics

Sararas Intarak[1,2], Yothin Rakvongthai[2,3]

1 Medical Physics program, Department of Radiology, Faculty of Medicine, Chulalongkorn University
2 Chulalongkorn University Biomedical Imaging Group, Department of Radiology, Faculty of Medicine, Chulalongkorn University
3 Division of Nuclear Medicine, Department of Radiology, Faculty of Medicine, Chulalongkorn University

Introduction: Nasopharyngeal carcinoma (NPC) is endemic disease in Southeast Asia and Southern China. The current patient stratification is based on TNM staging and Epstein-Barr Virus (EBV) DNA concentration level test. Patients are categorized into high-risk and low-risk group to provide appropriate treatment according to tumor prognosis. However, EBV value undetectable in 41 percent of the patients (1), for which an appropriate treatment option is difficult to choose. Radiomics, an emerging field for data mining of medical images (2), was used in this study. The underlying hypothesis is that radiomics features describing size, shape, texture, and voxel intensity in the images may reflects the characteristics of the tumor. The quantitative analysis may provide better risk stratification for NPC.

Purpose: To investigate the prognostic value of radiomics in NPC from pre-treatment CT images.

Methods: A total of 197 patients were collected retrospectively. They had CT examinations prior to treatment and had at least 3 years of follow-up data. The radiomic features were extracted through Pyradiomics version 2.7. The tumor delineation was performed by board-certified radiation oncologists. 158 and 39 patients were randomly classified into train group and test group, respectively. The radiomic feature selection and model construction were performed by STATA version 15. The univariate and multi-variable analyses were performed by logistic regression and ROC analysis was constructed.

Results: The AUC of radiomics model was 0.7927 in train group and 0.7463 in test group.

Conclusion: Our preliminary results demonstrated the usefulness of radiomics in tumor prognosis for nasopharyngeal cancer. Radiomics could potentially be applied to improve decision making in clinical practice throughout cancer therapy process at low cost.

Keywords: Radiomics, Overall Survival, Nasopharyngeal Carcinoma

Machine Learning model for Alzheimer's disease prediction and classification using T1-weighted MR Brain imaging based on SVM algorithm

Chayanon Pamarapa[1], Yudthaphon Vichianin[1]

1 Department of Radiological Technology, Faculty of Medical Technology, Mahidol University, Thailand.

Introduction: Nowadays, Alzheimer's disease is worldwide health issue. The clinical information especially the imaging data from MRI is one of the key biomarkers for diagnosis and importantly, the early stage detection could prevent high progression of disease. Moreover, in era of 'Big data' and the machine learning, a number of data could be used to construct a classification model for Alzheimer's staging prediction.

Purpose: To create a machine learning model for prediction the patient who under an Alzheimer's Disease (AD), Mild cognitive implement (MCI) and cognitive normal (CN) patient for patient aged 65-80 by using T1-weighted MR Brain imaging based on Support Vector Machine (SVM) classification algorithm

Methods: In this work there are three main steps to construct a medical prediction model called 'Computer-aided diagnostic' (CAD) consists of i) Pre-processing, ii) Feature extraction, in the first two steps were using FreeSurfer software to normalize and extract the feature of interest which are Entorhinal cortex, Hippocampus, Amygdala, Thalamus, Lateral ventricle and Total gray matter volume iii) Classification, process of classification performance by statistical analysis based on Support vector machine (SVM) algorithm. The classification performance was evaluated by using the cross-validation and Principle component analysis (PCA) by MATLAB classification learner.

Results: The performance of prediction model were evaluated by Receiver Operating Characteristics (ROC) curve. The model achieved Area under the ROC curve of 0.87 [AD vs. CN with PCA], 0.73 [AD vs. MCI with non-PCA] and 0.60 [MCI vs. CN with PCA]

Conclusion: By using T1-weighted MR Brain imaging, a machine learning model based on SVM algorithm designed for prediction of AD, MCI achieved a great performance 0.87 [AD vs. CN] with accuracy, sensitivity, specification and precision equal to 80.0%, 75.0%, 87.5%, 90.0%, respectively.

Keywords: Alzheimer's Disease, T1-weighted MR Brain image, Machine Learning, Support Vector Machine

The Breast Microcalcification Detection in Mammogram Image by Using the Deep Convolutional Neural Network

Chatsuda Songsaeng [1], Sitthichok Chaichulee [2]

1 Department of Radiology, Faculty of Medicine, Prince of Songkla University, Hat Yai, Songkhla 90110, Thailand.
2 Institute of Biomedical Engineering, Department of Biomedical Sciences and Biomedical Engineering, Faculty of Medicine, Prince of Songkla University, Hat Yai, Songkhla 90110, Thailand.

Introduction: The deep convolutional neural network (DCNN) is one of the methods in artificial intelligence to automatically recognize and classify the images and help the radiologists to detect the microcalcifications in mammography assessment.

Purpose: To develop and evaluate the efficiency of the computer model in the detection of microcalcification in mammogram images and compare with the radiologist's assessment.

Methods: This retrospective study included 814 mammogram images of the patients who undertaken screening mammogram between 1 January 2017 to 30 September 2019 at Tanyawej Breast Cancer, Songklanagarind Hospital. The data was collected 214 mammogram images with breast calcification and 600 mammogram images without breast calcification. The following data were collected: age (year), breast side, type of microcalcification, position of calcification and BI-RADS assessment. In this study, the data were divided into 2 sets, the first dataset was used for training model and the second dataset was used for testing model. The training and testing model of deep learning is the methods to classify the microcalcification in mammogram images and performed on MATLAB R2019a.

Results: The sensitivity of model 1, 2, 3 was 74.3%, 82.1% and 76.5%, respectively. The specificity of model 1,2,3 was 100%, 87.5% and 100%, respectively. The precision of model 1,2,3 was 100%, 88.5% and 100%, respectively. The negative value prediction of model 1,2,3 was 65.4%, 80.8% and 69.2%, respectively. The accuracy of model 1,2,3 was 82.7%, 84.6% and 84.6%, respectively. The area under the receiver operating characteristic curve (AUC-ROC) of model 1,2,3 was 0.91568, 0.92012 and 0.97781, respectively.

Conclusion: The computer models were efficient to predict the groups of microcalcification in mammogram images which resembles to the radiologists' assessments.

Keywords: Microcalcification, Deep Convolutional Neural Network (DCNN), Mammogram images, MATLAB

Prediction of Tumor Growth Trajectories During Molecularly Targeted Therapy Based on Mathematical Models

Truong Gia Huy[1], Arimura Hidetaka[2], Tanaka Kentaro[3], Ninomiya Kenta[1]

1 Division of Medical Quantum Science, Department of Health Sciences, Graduate School of Medical Sciences, Kyushu University
2 Division of Medical Quantum Science, Department of Health Sciences, Faculty of Medical Sciences, Kyushu University
3 Respiratory Medicine, Kyushu University Hospital

Introduction: Tyrosine kinase inhibitors (TKIs) therapy has been widely applied to epidermal growth factor receptor (EGFR) mutated patients with non-small cell lung cancer (NSCLC) as a molecularly targeted therapy in order to reduce the tumor growth. However, the outcomes of TKIs therapy for the NSCLC patients depend on sensitive, resistant, and persister cell populations in the tumors. Therefore, prior to the treatment, it could be nece ssary to predict whether each patient could be curable with the TKI therapy.

Purpose: This study aims for investigating mathematical models to predict the tumor growth trajectories during the TKI therapy for the EGFR-mutated NSCLC patients, based on tumor volumes derived from CT images.

Methods: The Gompertz tumor growth model combined with a cell loss (tumor shrinkage) model were implemented under the assumption that each tumor could contain three components: sensitive, persister and resistant populations, which have different responses to TKI drugs. The parameters in the tumor growth model for each tumor was optimized with a Levenberg-Marquardt method to minimize the difference between the predicted and reference tumor growth trajectories. The model was applied to 10 patients with 10 tumors at stages III and IV, who were treated by 4 types of TKI drugs (Erlotinib, Gefitinib, Afatinib and Osimertinib).

Results: Seven parameters were employed in the model which had different ranges. The percentage error between predicted and reference data varied from 0.02 to 46.3%, and the average error was 12.18%.

Conclusion: The mathematical tumor growth model could provide oncologists the information to manage the TKIs therapy and/or combined therapies with other treatment approaches such as radiotherapy and conventional chemotherapy.

Keywords: epidermal growth factor receptor (EGFR) mutation, non-small cell lung cancer (NSCLC), tyrosine kinase inhibitors (TKI), Gompertz tumor growth model, tumor growth trajectory

Quantitative evaluation of deep convolutional neural network based denoising for ultra-low-dose CT

Keisuke Usui[1, 2], Kentarou Suzuki[3], Akira Isobe[3], Kazumi Murata[4], Koichi Ogawa[4]

1 Department of Radiological Technology, Faculty of Health Science, Juntendo University, Tokyo, Japan
2 Department of Radiation Oncology, Faculty of Medicine, Juntendo University, Tokyo, Japan
3 Department of Radiation Oncology, Graduated School of Medicine, Juntendo University, Tokyo, Japan
4 Faculty of Science and Engineering, Hosei University, Tokyo, Japan

Introduction: Dose reduction is important in diagnostic and therapeutic applications of computed tomography (CT). Reducing the number of X-ray photons using tube current modulation is achieved using low-dose CT. However, image noise does occur, resulting in degradation of image quality caused by the reduction in X-ray dose. Various image correction methods have been investigated to obtain a clear reconstructed image. Recently, deep-learning approaches based on including extensive data and powerful graphical processing units have been used in image denoising and have achieved great success.

Purpose: This study aimed to evaluate the general convolutional neural network (CNN) for denoising with ultra-low-dose CT and to compare it with another noise-reduction method against unique CT noise simulation images.

Methods: Dominant noise statistics in X-ray reduction images have a Poisson distribution. Therefore, to simulate an ultra-low-dose CT image, we added Poisson noise to the normal-dose images based on the CT unit–specific modulation transfer function. We created simulated low-dose images with a dose reduction of 10–90% from the original image. These images were denoised using a trained denoising CNN (DnCNN) and assessed over various dose reduction levels. To determine the image quality quantitatively, we compared the performance of DnCNN with other methods in Median, Gaussian, Winner, and Wavelet filters.

Results: The DnCNN image provided significant improvement in the signal-to-noise ratio (SNR), especially at the ultra-low-dose level. With DnCNN denoising on 50%-dose cases, SNR improved by 12 times, and the contrast-to-noise ratio improved by 14 times. Image noise was improved in other denoising filter methods, and high-frequency components were degraded simultaneously. In contrast, DnCNN images achieved the highest structural similarity index and closely matched the original-dose image.

Conclusion: The DnCNN denoising method significantly improves ultra-low-dose CT in quantitative evaluations.

Keywords: CNN, Low-dose-CT, Denoise, image quality

A Preliminary Study of Various Augmentation Techniques on Deep-learning Based Classification of Lung Squamous Cell Carcinoma using Chest X-Ray

Mohammad Haekal[1], Reza Rendian Septiawan[2], Freddy Haryanto[3], Idam Arif[3]

1 Laboratory of Medical Physics and Biophysics, Department of Physics, Faculty of Sciences and Data Analytics, Institut Teknologi Sepuluh Nopember, Kampus ITS Sukolilo - Surabaya, Jawa Timur 60111 Indonesia
2 Computer Engineering Study Program, School of Electrical Engineering, Telkom University, Jl. Telekomunikasi No.1, Bandung, Jawa Barat 40257 Indonesia
3 Faculty of Mathematics and Natural Sciences, Institut Teknologi Bandung, Jl. Ganeca 10, Bandung, Jawa Barat 40132 Indonesia

Introduction: There are still many challenges existed in the application of deep learning in classifying medical images. One of them including image quality difference which may occurred if the test datasets were acquired with different acquisition protocols from the training datasets. This condition could affect the classification process of deep learning algorithm. The increase of training datasets number from various image quality are usually performed to produce better accuracy of the algorithm. However, the number of datasets that could be used as training datasets are usually limited. Therefore, augmentation process was used to compensate for the lack of datasets.

Purpose: To analyze the performance of deep learning algorithm in classifying medical images with augmentation techniques.

Methods: Chest X-rays from patients diagnosed with squamous cell carcinoma in the lung were selected from The Cancer Imaging Archive (TCIA) database. The datasets were divided randomly between training, validation, and test datasets. The test datasets were then divided into original and artificially induced noise datasets. The training dataset were augmented by changing the shape (rotation, skew) and feature of the image. The trained algorithm were then tested using the test datasets and the results were compared with those trained without augmentation.

Results: The preliminary results showed that the augmentation increased the performance of the algorithm in detecting image with noise.

Conclusion: Proper augmentation process would be beneficial in increasing the deep learning algorithm process.

Keywords: Deep learning, medical image, augmentation

A Computational Study on Deep-learning Based Classification of Lung Adenocarcinoma using Chest X-Ray

Reza Rendian Septiawan[1], Mohammad Haekal[2], Freddy Haryanto[3], Idam Arif[3]

1 Computer Engineering Study Program, School of Electrical Engineering, Telkom University, Jl. Telekomunikasi No.1, Bandung, Jawa Barat 40257 Indonesia
2 Laboratory of Medical Physics and Biophysics, Department of Physics, Faculty of Sciences and Data Analytics, Institut Teknologi Sepuluh Nopember, Kampus ITS Sukolilo - Surabaya, Jawa Timur 60111 Indonesia
3 Faculty of Mathematics and Natural Sciences, Institut Teknologi Bandung, Jl. Ganeca 10, Bandung, Jawa Barat 40132 Indonesia

Introduction: The difference in imaging modalities and image acquisition protocol may affect the robustness of deep learning when classifying medical images. The use of X-ray as an early screening process of detecting lung cancer is preferable due to its low cost. However, the image quality is sometimes poor compared with other imaging modalities. The use of deep learning can help to better identify and classify the abnormalities in X-ray image that might be unseen by the naked eye. The difference in image protocol acquisition could sometimes worsen the performance of the deep learning, therefore, an augmentation process are usually done in the training process.

Purpose: To analyze the performance of deep learning algorithm in classifying X-ray images of patient diagnosed with adenocarcinoma.

Methods: Chest X-rays from patients diagnosed with adenocarcinoma in the lung were selected from The Cancer Imaging Archive (TCIA) database. The datasets were divided randomly between training, validation, and test datasets. The test datasets were then divided into original and artificially induced noise datasets. The training dataset were augmented by changing the shape (rotation, skew) and feature of the image. The trained algorithm were then tested using the test datasets and the results were compared with those trained without augmentation.

Results: The preliminary results showed that the performance of the algorithm is increased in detecting X-rays of patients with adenocarcinoma.

Conclusion: The deep learning method may be used to identify patients with adenocarcinoma using X-ray images.

Keywords: Deep learning, medical image, X-ray

Dignostic: Dosimetry

Patient-specific organ dose calculated using dose tracking software based on Monte Carlo simulation in pediatric abdominal CT

Yuparak Innan[1,3,4], Kitiwat Khamwan[2,3,4]

1 Medical Physics Program, Faculty of Medicine, Chulalongkorn University, Bangkok 10330, Thailand
2 Division of Diagnostic Imaging, Department of Radiology, Praram9 Hospital, Bangkok 10310, Thailand
3 Division of Nuclear Medicine, Department of Radiology, Faculty of Medicine, Chulalongkorn University and King Chulalongkorn Memorial Hospital, The Thai Red Cross Society, Bangkok 10300, Thailand
4 Chulalongkorn University Biomedical Imaging Group, Department of Radiology, Faculty of Medicine, Chulalongkorn University, Bangkok 10330, Thailand

Introduction: As the children are more sensitive from ionizing radiation compared to the adults, assessing the individual organ doses accurately in CT scan is still a challenging task.

Purpose: To determine the patient-specific organ doses using dose tracking software in pediatric abdominal CT.

Methods: The retrospective data were collected from 78 pediatric patients (168 studies, age range 0-15 years-old), who underwent single phase abdominal CT at Praram9 Hospital. The tube voltages ranged between 80 and 135 kVp were adjusted according to the size and age of patients, and rotation time 0.35-0.5 sec. All of patients were acquired using the automatic exposure control (AEC) protocol. The organ doses were calculated based on the Monte Carlo simulation using the Radimetrics dose tracking software in accordance with patient age derived from stylized computational phantom model. The size-specific dose estimates (SSDE) were calculated based on the effective diameter method. The organ doses obtained from pediatric abdominal CT were then compared among age group.

Conclusion: Average patient body weights of 38.6±18.5 kg (range 3.89 - 94.00 kg) were obtained in this study. Five highest organ doses for 15-yr patients were found in kidneys, urinary bladder, stomach, spleen, and liver with the values of 16.48, 15.56, 15.39, 14.79, 14.60 mGy, respectively. The average effective dose (ED) for pediatrics abdominal CT in newborn, 1, 5, 10 and 15 years-old were 2.24±0.07, 3.23, 3.82±1.63, 4.89±2.01 and 9.19±1.46 mSv, respectively. Average SSDE were 2.72±1.14, 4.52, 5.82±2.10, 8.02±2.77 and 13.05±1.83 mGy, respectively.

Keywords: Dose tracking software, Monte carlo simulation, Effective dose (ED), Size-specific dose estimates (SSDE), Organ doses

Size-Specific Dose Estimates (SSDE) for Head CT in Pediatric Patients

Saowapark Poosiri[1], Kanokkwan Chuboonlap[2], Nuttita Kaewlaied[3], Supika Kritsaneepaiboon[4]

1,2,3 Department of Radiology, Faculty of Medicine, Prince of Songkla University, Hat Yai, Thailand.

Introduction: The dose from CT examination is normally displayed as volume CT dose index ($CTDI_{VOL}$). Actually, $CTDI_{vol}$ is estimated by using two cylindrical phantoms of different diameters. In order to estimate patient radiation dose, $CTDI_{vol}$ is only an indicator as it does not address the patient size. AAPM Report no.293[1] on the size-specific dose estimates (SSDEs) for CT head examination provides the conversion factors for the estimation of the patient radiation dose at higher accuracy.

Purpose: The purpose of this study was to estimate the size-specific dose estimation (SSDE) for head examination in the Computed Tomography of pediatric patients.

Methods: This study is the retrospective analysis of 191 cases which the inclusion criteria covers the age range from 0 to 15 years old. The patients had been scanned by CT Toshiba Aquilion Prime with 80 detectors without contrast media enhancement, from September 2015 to October 2019. The conversion factors from AAPM No.293 report were selected to calculate $SSDE_{Dw}$ by using the equation, $SSDE_{Dw}$ = conversion factor x $CTDI_{VOL.}$ The $SSDE_{Dw}$ had been compared to $CTDI_{VOL}$. The average $SSDE_{Dw}$ of head partial is calculated by the division of $SSDE_{Dw}$ by the patient age level.

Results: The mean $SSDE_{Dw}$ with four age ranges of less than 1, 1 to less than 5, 5 to less than 10 and 10 to 15 years old were 19.38, 22.82, 28.74 and 38.20 mGy, respectively while the mean $CTDI_{VOL}$ were 18.82, 24.36, 31.87, and 43.71 mGy respectively.

Conclusion: The $SSDE_{Dw}$ in all age ranges were less than $CTDI_{VOL}$ except at the age of less than 1, the $SSDE_{Dw}$ were greater than $CTDI_{VOL}$ due to the conversion factor that included the patient body composition. The $SSDE_{Dw}$ is more appropriate indicator for CT patient dose because the patient size and composition had been considered to provide higher accuracy.

Keywords: Size-specific dose estimates (SSDE), Volume CT dose index (CTDIVOL), Radiation dose

Preliminary investigation on performance of photodiode sensor as a dosimeter

Nur Farah Huda Zulkafli[1], Yasmin Md Radzi[1], Ahmad Fairuz Omar[1]

1 School of Physics, Universiti Sains Malaysia, Penang, Malaysia,

Introduction: Dosimeter is an important device to measure the ionizing radiation exposure while serving as radiation surveillance in controlled areas to ensure there is no unnecessary radiation exposure to patient and personnel. There are various dosimeters available in the market nowadays, but their prices are remarkably expensive. Therefore, many types of diodes were tested as a dosimeter to produce a cost-effective dosimeter[1].

Purpose: This study investigates the capabilities of OPT101 (Texas Instruments, USA) monolithic photodiode[2] with an on-chip trans-impedance amplifier as a dosimeter for diagnostic radiology.

Methods: An OPT101 photodiode covered with black insulation tape was irradiated with diagnostic x-ray (range from 40 to 90 kVp) with constant tube current-time product, 50 mAs at 60 cm source-to-detector distance (SDD)[3, 4]. Subsequently, exposures of different tube current at the range of 10 to 250 mA with a constant tube voltage of 70 kVp at the same setup are made. The direct read-output of the photodiode sensor in the millivolt (mV) and semiconductor detector connected to an electrometer were recorded. The photodiode's energy dependency, reproducibility, and linearity were evaluated as the preliminary investigation of the photodiode to use as an immediate dosimeter[5,6].

Results: It has been demonstrated in this experiment that linearity of photodiode energy dependency has the value of R^2=0.9458. While, for the response to increasing tube current with constant tube voltage showed R^2=0.912. However, OPT101 photodiode has failed to show good response during the reproducibility test which a reliable dosimeter should behave mainly due to its large self-capacitance.

Conclusion: This monolithic photodiode with an on-chip transimpedance amplifier has demonstrated good results for energy dependency and dose linearity but poor results for reproducibility. However, more detailed work could be improvised in the future to ensure it is suitability as an immediate dosimeter by compromising many factors.

Keywords: radiation dosimetry, dosimeter, photodiode, sensor

Evaluation of scattering spectra from an examinee during in CT scans

Kota Tsurusawa[1], Daisuke Shimao[1,2]

1 Hokkaido University of Science Graduate School of Health Science,
2 Hokkaido University of Science

Introduction: Medical staffs occasionally stand by the gantry during X-ray CT scans for patient care or biopsy under X-ray CT scans. The staffs will be exposed the scattering X-rays from examinees in these cases. It is important to reveal the characteristics of scattering X-rays from examinees in order to evaluate the influence on each tissue of the staffs exposed.

Purpose: To measure and characterize scattering X-rays spectra from a subject during X-ray CT scans at various locations by an X-ray spectrometer.

Methods: Chest level of human phantom manufacturer, Kyoto Kagaku, was scanned by non-helical mode using CT scanner (4 row MDCT) [Alexion, Canon]. The scan conditions were: tube voltage of 120 kV, tube current of 10 mA, and scan speed of 0.75 sec/rot. The energy spectra of scattering X-rays from the phantom were measured using an X-ray spectrometer (CdTe) [EMF Japan] by changing the measurement locations during each scan fixing the distance of 270 cm from isocenter. After the measurements, the effective energies of the scattering X-rays were calculated from corresponding spectrum.

Results: The spectra and effective energies of scattering X-rays from the phantom did not change significantly at the location of 45 degrees lateral from long axis of the scanner's bed even when the height of the measuring point were varied. When the measurement positions were changed to the gantry or scanner's bed direction, differences of their spectra were within 1 keV of the effective energies, however the energy peak at around 17.5 keV was found changing the position to the gantry direction. It is assumed that fluorescent X-rays from a certain component which includes molybdenum were detected.

Conclusion: The spectra of scattering X-rays from a subject during X-ray CT scans at various locations were revealed by an X-ray spectrometer. Our result will be useful for evaluating the exposure to medical staffs serving in the X-ray CT room.

Keywords: X-ray CT, scatter, spectrum

Diagnostic: Radiation Safety / DRL

The Study of Local Diagnostic Reference Levels at Unit of Vascular and Interventional Radiology, King Chulalongkorn Memorial Hospital

Kornkamol Prajamchuea[1], Anchali Krisanachinda[2]

1 Master of Science in Medical Physics Program, Faculty of Medicine, Chulalongkorn University, Bangkok 10330, Thailand
2 Department of Radiology, Faculty of Medicine Chulalongkorn University Bangkok 10330, Thailand

Introduction: ICRP Publication 135 title Diagnostic Reference Levels in Medical Imaging recommended on the DRLs to be an effective tool that aids in optimization of protection of patients for diagnostic and interventional procedures. Currently, there are no DRLs in interventional radiology procedures in Thailand.

Purpose: To study the local DRLs of patient radiation dose in interventional radiology procedures in standard-sized of Thai patients.

Methods: Collect the exposure and related parameters of at least 240 cases based on standard size of Thai patients of 9 body intervention procedures and 3 neuro-intervention procedures to distribute LDRLs based on 75th percentile of the radiation exposure levels of median values. Compare LDRLs to NDRLs.

Results: 398 body intervention and 87 neuro-intervention procedures were reported as median of fluoroscopy time and DRLs of total KAP as: *CT-guided TACE* 58.30 min, 459 Gy.cm^2, *CBCT-guided TACE* 53.75 min, 357 Gy.cm^2, *PICC line* 0.80 min, 2 Gy.cm^2, *Perm cath* 1.65 min, 4 Gy.cm^2, *PCD* 1.50 min, 5 Gy.cm^2, *PTBD* 4.65 min, 14 Gy.cm^2, *Peripheral angiogram* 5.61 min, 25 Gy.cm^2, *Peripheral angioplasty* 15.40 min, 16 Gy.cm^2, and *CBCT-guided biopsy* 2.19 min, 17 Gy.cm^2 respectively. For neuro-interventional radiology, *Cerebral angiogram* 6.53 min, 61 Gy.cm^2, *Embolization of intracranial aneurysm* 39.48 min,144 Gy.cm^2, and *Embolization of brain AVM* 44.16 min, 224 Gy.cm^2 respectively.

Conclusion: The LDRLs for interventional radiology procedures had been reported and compared to Japan DRLs 2020. Our DRLs on body intervention procedures were higher than Japan DRLs as our procedures using CT and CBCT guided while Japan used only fluoroscopy guided. As the centre covers both clinical services and training fellows, the patients received higher doses. For neuro interventional procedures, senior interventional radiologists play an import role on complicated procedures, therefore, the LDRLs were comparable and lower than Japan DRLs.

Keywords: Local DRLs, interventional radiology, body intervention, neuro-intervention, 75th percentile

Local Diagnostic Reference Levels (DRLs) of Interventional Radiology Procedures in Thailand: A Single Center

Rasalin Thana[1], Anchali Krisanachinda[2]

1 Department of Imaging, Bumrungrad International Hospital, Bangkok 10110, Thailand
2 Department of Radiology, Faculty of Medicine, Chulalongkorn University, Bangkok 10330, Thailand

Introduction: The Diagnostic Reference Levels (DRLs) are an important tool for optimizing radiological diagnosis and interventional radiology (IR). The DRLs has been recommended by the International Commission on Radiological Protection (ICRP) Publication 135. IR is a medical subspecialty procedure and offered the opportunity of the patient survival rate. However, IR procedure delivers the high radiation dose as a complex study inducing skin injury. Therefore, DRLs is recommended for the methodology in patient dose optimization.

Purpose: To determine the local, LDRLs of interventional radiology procedures at a single center for the establishment of the National Diagnostic Reference Levels (NDRLs) in Thailand.

Methods: 491 cases (184 female, 307 male) of nonvascular and vascular IR procedures were surveyed from January 2019 to May 2020. The patient weight ranges from 45.2-74.8 kg for female and 50.9-80 kg for male. The data includes 59 transarterial chemoembolization (TACE), 27 percutaneous transhepatic biliary drainage (PTBD), 22 IVC filter placement and 21 percutaneous nephrostomy (PCN). Patient dose surrogates such as Kerma-area product (KAP), Air-kerma (AK) and Fluoroscopic time (FT) were recorded.

Results: Local DRLs at 75th percentile of total KAP, and cumulative AK in TACE were 374 Gy.cm^2, 1.1 Gy respectively. In PTBD, KAP were 50 Gy.cm^2, AK 0.12 Gy respectively. In IVC filter placement, KAP were 67 Gy.cm^2, AK 0.26 Gy, respectively and PCN KAP were 37 Gy.cm^2, AK 0.11Gy, respectively.

Conclusion: In comparison, DRLs of TACE, PTBD and PCN from our study are lower than US practice[2] of TACE 400 Gy.cm^2, PTBD 100 Gy.cm^2 and PCN 40 Gy.cm^2. Japan DRLs 2020[3] report DRLs for TACE KAP at 270 Gy.cm^2 which is lower than ours, AK at 1.4 Gy which is higher than ours.

Keywords: Local DRLs, Interventional Radiology, TACE, KAP, AK, ICRP Publication 135

Estimation the effective and skin doses for pediatric and adult patients undergoing cardiac interventional examination using five PMMA phantoms and TLD/ionization chamber technique

Keng-Yi Wu[1,2,3], Wei-Ting Chen[1,4], Hsun-Nan Kuo[1,5], Samrit Kittipayak[6], Lung-Fa Pan[1,2*], Lung-Kwang Pan[1*]

1 Graduate Institute of Radiological Science, Central Taiwan University of Science and Technology, Takun, Taichung, Taiwan
2 Department of Cardiology, Taichung Armed Forces General Hospital, Taichung, Taiwan
3 Division of Cardiology, Department of Internal Medicine, Tri-Service General Hospital, National Defense Medical Center, Taipei, Taiwan
4 Department of Psychiatry, Zuoying Branch of Kaohsiung Armed Forces General Hospital, Kaohsiung, Taiwan
5 Division of Cardiology, Yuan Rung Hospital, Yuanlin, Changhua, Taiwan
6 Department of Radiological Technology, Faculty of Medical Technology, Mahidol University, Bangkok, Thailand

Purpose: Dose**s** for pediatric and adult patients undergone cardiac interventional examination were simulated and evaluated using five PMMA phantoms with various weights and thermoluminescence dosimeter (TLD)/ionization chamber technique in this work with follow-up clinical verification from the real patients.

Methods: Five PMMA phantoms (different sizes to well simulate the 10, 30, 50, 70, and 90 kg patients) were customized to represent the trunk (thorax, abdomen, and pelvic cavity) of baby, child, adult female, adult male, and overweight adult (by Asian complexion standards), respectively, in accordance with the ICRU-48 report. Each phantom could be disassembled into 31 plates to insert TLD chips for measuring X-ray exposed dose or assisted with an auxiliary plate to insert high-sensitivity ionization chamber for surveying low-energy fluoroscopy dose. Specifically, the skin doses were measured only by TLD chips that were attached on the surface of phantom, whereas the effective dose from either exposed or fluoroscopy were derived mostly from ion chamber that was cooperated with an auxiliary plate. The empirical data were integrated altogether to construct 4 groups of datasets for estimating the semi-empirical formulas. In doing so, five PMMA phantoms were converted to different BMIs and cooperated with the assigned DAP to derive the binary quadratic form for skin or effective dose. Moreover, the estimated doses were categorized into by exposed or fluoroscopy one, respectively. The estimated doses were verified by 30 follow-up patients undergone real cardiac examination and had an acceptable accuracy with minor fluctuation.

Results: The data acquired from five phantoms were integrated into four semi-empirical formulas, in order to fit the binary quadratic form "Dose = $A \cdot BMI^2 + B \cdot DAP^2 + C \cdot BMI + D \cdot DAP + E$". The latter linked the X-ray and fluoroscopy effective/ skin doses, respectively, with a high coefficient of determination R^2 (from 0.888 to 0.986).

Conclusion: The model refinement with DAP share adjustment is envisaged in diagnostic coronary angiography exam.

Keywords: effective dose, TLD, cardiac interventional examination, phantom, semi-empirical formula

Facility reference level for common x-ray procedures: a preliminary study

DM Satharasinghe[1,2#], J Jeyasugiththan[1], AS Pallewatte[3] and WMNMB Wanninayake[2]

1 Department of Nuclear Science, Faculty of Science, University of Colombo, Sri Lanka.
2 Horizon Campus, Malabe, Sri Lanka.
3 Department of Radiology, National Hospital of Sri Lanka, Colombo, Sri Lanka.

Introduction: Ionizing radiation is an essential tool in medical diagnosis and it brings great benefit to the patient. However, the associated risks due to the radiation is unavoidable. Therefore, close monitoring of radiation exposure should be performed in order to control the potential harm. As an advisory measure to improve optimization of patient's radiation protection, Diagnostic Reference Levels (DRLs) was introduced by the International Commission on Radiation Protection (ICRP).

Purpose: The present study aims on the evaluation of the doses and its variation for selected x-ray procedures used by a single institution in Sri Lanka to determine a possible institutional DRL.

Methods: The study included dose data and exposure parameters from 218 chest-Postero Anterior (PA), 33 abdomen-Antero Posterior (AP), 85 lumbar spine AP and 88 lumbar spine-Lateral (LAT) projections of patients (age between 19-78 years). The 3rd quartile of the distribution for each projection was compared with international DRLs to identify the projections which requires a dose optimization.

Results: The 3rd quartile dose values obtained for chest PA, abdomen AP, lumbar spine AP and LAT were 16, 256, 155, 455 μGy.m^2 respectively. The dose values for chest PA and lumbar spine AP were below or comparable with the international DRLs.

Conclusion: In the present study the 3rd quartile values for chest PA and lumbar spine AP projections are suggested as the facility reference levels (16 and 155 μGy.m^2 respectively).The tube current used in lumbar spine lateral and abdomen AP projections were comparatively higher. Also they are with higher dose levels compared to international DRLs. Therefore, utilization of high tube current should be justified based on the image quality requirement. This preliminary study provides information on a selected radiology facility only, however can be used as a reference for quality improvement programs in future.

Keywords: Institutional diagnostic reference level, IDRL, Diagnostic reference level, DRL, Ionizing radiation, x-ray.

Evaluation of gonad shielding in digital radiography: Based on clinically adjustable controls.

E.W Kombo[1] J. H. D. Wong[1,2] MS Nizam[1,2] KH Ng[1,2]

1 Department of Biomedical Imaging, Faculty of Medicine, University of Malaya, Kuala Lumpur 50603, Malaysia
2 University of Malaya Research Imaging Centre, Faculty of Medicine, University of Malaya, Kuala Lumpur 50603, Malaysia

Introduction: The effectiveness of gonad shielding in general x-ray radiography in recent years has been questioned because of the risk of obscuring important information. Previous literature studies were based on Kerma Air Product (KAP) and do not show the absorbed dose-based reductions on the gonads and image quality considerations for clinical practicability[1]. With radiographers having the option of choosing to use AEC or not there is a need to justify the continued practice by some centres.

Purpose: To determine the percentage dose reduction achieved when gonad shields are in place and how it is affected by varying the parameters of interest, which include tube potential and current-time product (mAs), AEC.

Methods: An adult anthropomorphic phantom was exposed in anteroposterior pelvic projection study. Exposure was done for shielded and unshielded gonads in various adjustments. Using tube voltages (70-100kVp) and mAs (16-25mAs) adjustments when AEC turned off and measured organ absorbed dose at four internal sites and three on the surface points for male study using nanoDot™ optically stimulated luminescence dosimeter (OSLD).

Results: In males, absorbed dose to the testes was reduced by > 87% (87.9 - 90.8%) and range of values from 60 - 70% in females when automated exposure was used. With manual control of mAs and standard voltage (70kVp) similar dose reduction in males of >88.5% (88.5 - 88.7%) however, in female reduction was slightly lower with 45-70%. Various tube potential values with constant mAs dose reductions with values > 84% (85- 89%) and female 57-70% range were obtained.

Conclusion: The effectiveness of gonad shielding is affected by the location of gonads. The location of male gonads, being more easily identified are more easily shielded and benefited from larger dose reduction due to reduced scattering[2]. In contrast, the actual positions of the female ovaries are not visible and often estimated. This resulted in poorer gonad shielding.

Keywords: contact shields, dose reduction factor, mAs, Tube voltage, AEC.

Diagnostic: Others

Evaluation of student skill competency on accuracy of mid-trimester fetal sonography scan following the newly-established Master degree in medical sonography

Surapa Hirunpijit[1,3], Surachate Siripongsakun[1], Chanisa Chotipanich[1], Pantajaree Hiranrat[1], Amarin Narkwichean[2], Wipada Laosooksathit[2]

1 Sonographer School, Faculty of Health Science Technology, Chulabhorn Royal Academy, Bangkok 10210, Thailand,
2 Faculty of Medicine, Srinakharinwirot University, HRH Maha Chakri Sirindhorn Medical Centre Nakhon Nayok, 26120 Thailand,
3 Department of Radiology, Central Chest Institute of Thailand, Nonthaburi, 11000, Thailand.

Introduction: Mid-trimester scan is recommended in all pregnancies nonetheless the obstetrician's workload can be extensive. Thailand first postgraduate, a 2-year master's degree in medical sonography has only been established in 2019 aiming to produce sonographers providing support on sonographic examination. Students underwent 8-week obstetric module during their first-year study, attending lectures, workshops and real clinical practice. Assessment of student competency is required as parts of the program/module evaluation.

Purpose: To evaluate skills of medical sonography students particularly an accuracy of biometric measurement and gestational age estimation, in comparison to qualified obstetricians, upon completion of the obstetric module of the newly-established program

Method: A cross-sectional observational study was conducted on the first batch medical sonographer students. A total of 81 participating pregnancies in their mid-trimester (18-24 weeks) underwent ultrasound scans firstly performed by either of 2 students. Parameters; biparietal diameter (BPD) head circumference (HC), abdominal circumference (AC), femur length (FL), were measured to calculate the gestational age. The scan was confirmed by a qualified obstetrician on-duty. Comparisons between the first and subsequent scan were made. Recorded images were then subsequently reviewed by a maternal-fetal-medicine specialist to assess student performance of the scan and measurement

Results: Although there was a significant difference in HC and AC measurement, Gestational age (mean difference 0.01± 2.92 days, p=0.969) and some parameters (BPD and FL) measurement were not difference between the students and obstetricians. Intraobserver and Interobserver (n=2) variability were not observed. Review performance of students regarding scanning and measuring skills, utilising standard criteria recommended by the ISUOG, was considered good to excellence (77.5-80%).

Conclusion: The study demonstrates that medical sonography students are competent regarding second trimester scan in terms of biometric measurement and gestational age estimation. The outcomes help verifying the Master degree program.

Keyword: Competency, Fetal biometry, Obstetric sonography, Medical sonographer student.

The teaching and learning of postgraduate medical physics using Internet-based e-learning during the COVID-19 pandemic

Che Ahmad Azlan[1], Jeannie Hsiu Ding Wong[1*], Li Kuo Tan[1], Muhammad Shahrun Nizam A Daman Huri[1], Ngie Min Ung[2], Vinod Pallath[3], Christina Phoay Lay Tan [4], Chai Hong Yeong[5], Kwan Hoong Ng[1]

1 Department of Biomedical Imaging, Faculty of Medicine, University of Malaya, 50603 Kuala Lumpur, Malaysia.
2 Clinical Oncology Unit, Faculty of Medicine, University of Malaya, 50603 Kuala Lumpur, Malaysia.
3 Medical Education and Research Development Unit, Faculty of Medicine, University of Malaya, 50603 Kuala Lumpur, Malaysia.
4 Department of Primary Care Medicine, Faculty of Medicine, University of Malaya, 50603 Kuala Lumpur, Malaysia.
5 School of Medicine, Faculty of Health and Medical Sciences, Taylor's University, 47500 Subang Jaya, Malaysia

Introduction: Many countries around the world imposed lockdowns or other forms of movement restrictions to stop the pandemic of COVID-19 in their communities, Malaysia included. These unprecedented measures caused the closure of school and universities and disrupted the teaching and learning (T&L) activities. To continue the instructional delivery, most universities implemented Internet-based e-learning.

Purpose: We intend to share our approach in the implementation of Internet-based e-learning in the Master of Medical Physics programme at the University of Malaya, Malaysia.

Methods: In March 2020, we surveyed the e-learning readiness of the students at the beginning of the nationwide lockdown. We implemented T&L activities via various virtual learning environments and e-learning platforms. We present the pros and cons of selected online teaching platforms. An evaluation survey was carried out after 15 weeks to evaluate the students' experience during this period of e-learning.

Results: We found that while students still preferred physical face-to-face teaching, they were able to adapt to the new norm of instructional delivery. More than 60% of the students agreed that the various e-learning approaches were useful in the learning process. The e-learning and study from home environment allowed most students the flexibility of learning at any time they preferred. However, for some students, they found it difficult to focus on their studies because of various distractions and lack of morale. Technical problems such as intermittent disruption of internet connectivity and limited internet data availability were the challenges of the e-learning process.

Conclusion: We expect that this method of distance learning (emergency remote learning) will continue to prevail in the near future and could become a new norm. It is also predicted that blended learning strategies which include e-learning, would become more common for the T&L of postgraduate medical physics programmes even after the COVID-19 crisis.

Keywords: Medical physics education, online teaching, virtual learning, COVID-19

Analysis of NTCP Based Radiobiological Models: A Systematic Review of Literatures

Rahman M[1], Kausar A[1], Mondol M[1], Sujan M[1], Azhari HA[1] and Zakaria GA[1,2]

1 Dept of Medical Physics and Biomedical Engineering, Gono Bishwabidyalay, Savar, Dhaka, Bangladesh
1,2 Dept. of medical Radiation Physics, Gummersbach Hospital, Academic Teaching Hospital of the University of Cologne, Gummersbach, Germany

Introduction: To achieve the optimal treatment goal, radiobiological parameters has to evaluate and predict the outcome of this treatment plan in terms of both TCP and NTCP. Different types of radiobiological model were used to achieve prescribed treatment dose of radiation during the tumor control. Where TCP models play a important role in order to achieve desired dose to the tumor. A suitable NTCP model was theoretically found among different models that can be used in treatment plan evaluation.

Materials and Methods: Theoretically, six different radiobiological dose response models such as Lyman–Kutcher–Burman, Critical element, critical volume, Relative Seriality, Parallel architecture, Weibull distribution were analyzed in this project. All models were discussed elaborately with its various parameters and were used in the calculation of normal tissue complication probability during the treatment in radiotherapy. Further, all models were compared with each other.

Results: The models denote the dose for 50% complication probability (D50) parameters is the most commonly used radiobiological models for the normal tissues. The functional subunit response models (critical element & Relative seriality, Critical Volume, parallel architecture) are used in the derivation of the formulae for the normal tissue. Since all complicated NTCP model predict same as the simple NTCP model that is Lyman–Kutcher–Burman model as well as it is computationally efficient. Also Lyman–Kutcher–Burman model can be used in different treatment planning system incorporating with other model. For this reason our suggested model is Lyman–Kutcher–Burman NTCP model which can be used in treatment plan evaluation.

Conclusion: After analyzing six different model of NTCP, finding of the study is the treatment plan evaluation in where Lyman–Kutcher–Burman model may be considered as a better option for biological plan evaluation

Keywords: Radiobiological Model, TCP, NTCP

Evaluation of Visually Induced Motion Sickness During Virtual Reality based Head-mounted Display Viewing using Electroencephalography

Galih Restu Fardian Suwandi[1], Siti Nurul Khotimah[1], Freddy Haryanto[1], and Suprijadi[2]

1 Nuclear Physics and Biophysics Research Group, Department of Physics, Faculty of Mathematics and Natural Sciences, Institut Teknologi Bandung, Indonesia
2 Instrumentation and Computational Physics Research Group, Department of Physics, Faculty of Mathematics and Natural Sciences, Institut Teknologi Bandung, Indonesia

Introduction: Virtual reality (VR) technology has advanced significantly in recent years. However, visually induced motion sickness (VIMS) may occur when a person immerses into the VR environment. A person with VIMS suffers from headaches, stomach awareness, nausea, disorientation, sweating, fatigue, and even vomiting, which raises safety and health concerns for current VR platforms. Therefore, VIMS is considered a major hurdle for wide acceptance of VR applications.

Purpose: To investigate any VIMS reduction methods, it is necessary to have tools to evaluate VIMS efficiently and effectively. In this study, we will use electroencephalography (EEG) as a tool for evaluated VIMS.

Methods: The subjects are 10-20 high school and undergraduate students (male, age of 16-24 years). All subjects have no pre-existing neurological problems and not wearing glasses. In this study, brain waves for all subjects are read using wireless electroencephalography (EEG) with 14 channels for six conditions: (i) one minute in relax condition with open eyes, (ii) three minutes watching neutral video, (iii) five minutes watching action video 1, (iv) five minutes watching action video 2, (v) five minutes watching action video 3, and (vi) one minute in relax condition with open eyes. Data recording results from EEG will be extracted by centering in order to remove the DC offset of each electrode and then filtered from the noise and artifacts. The algorithm of power spectra and brain mapping has been described in the previously study.

Results: We compared two conditions of the participants which are eyes open and movie watching condition. The data of all the channels from each participant was transformed into frequency domain using FFT. The power of all the channels was computed by squaring the amplitude of the frequency domain signal. The power signal from 14 channels was averaged out to get a single power spectrum for each participant. It is evident that relative alpha power is higher in rest condition compared to virtual reality condition. The drop in alpha power is expected to occur due to changes in brain activity.

Conclusion: From the results we conclude that there is a change in the electrical activity of the brain. After watching the video, the alpha power is reduced. From this change in brain activity we deduce that participant is not comfortable from watching the video using head-mounted display. Therefore, this discomfort can be reported as visually induced motion sickness because it occurs due to visual changes in stimulus.

Keywords: brain, electroencephalography, virtual reality, visually induced motion sickness

Nuclear Medicine: Imaging

The comparison between planar gated blood pool imaging and gated blood pool SPECT to evaluate ventricular function in breast cancer patients receiving cardiotoxic cancer treatments

Kanokpich Khwaiphan[1], Benjapa Khiewvan[2], Pinyaporn On-Ekkasit[2], Thonnapong Thongpraparn[2], Sunanta Chiewvit[2]

1 Division of Radiological Science, Department of Radiology, Faculty of Medicine Siriraj Hospital, Mahidol University
2 Division of Nuclear Medicine, Department of Radiology, Faculty of Medicine Siriraj Hospital, Mahidol University

Introduction: Multiple Gated Acquisition (MUGA) is study to evaluate ventricular functions. Planar gated blood pool (GBP) imaging is commonly used to evaluate left ventricle performance in cancer patients who received treatment related cardiotoxicity.

Purpose: Compare left ventricular ejection fraction (LVEF), right ventrocular ejection fraction (RVEF), left end diastolic volume (LEDV), left end systolic volume (LESV) and wall motion between planar and Single Photon Emission Tomography (SPECT) GBP techniques in breast cancer patients.

Methods: Fifty-seven MUGA studies in 20 breast cancer patients were performed. Planar and SPECT MUGA were performed in patients who received treatment related cardiotoxicity (Anthracyclines or Transtuzumab) before and during chemotherapy every 3 months in Siriraj hospital between April 1, 2019 and July 21,2020. The correlation and agreement of LVEF, RVEF, ESV, and EDV were compared between two techniques. Wall motions of both ventricles were also observed.

Results: The mean LVEF, RVEF, left EDV and left ESV of planar GBP were 66.12±5.21%, 45.07±6.19%, 117.67±28.38 mL and 40.04±12.62 mL. The mean LVEF, RVEF, left EDV and left ESV of SPECT GBP were 67.21±8.11%, 45.35±6.44%, 87.75±13.22mL, 29.14±9.95mL. There was no significant different LVEF ($p=0.082$) and RVEF ($p=0.760$) between both techniques using by Paired samples t-test. However, there was significantly different in EDV and ESV ($p<0.001$) between both techniques. LVEF showed good agreement (ICC=0.865, 95% confidence interval (CI) 0.771-0.921) and strong correlation ($r=0.846$, p-value<0.001). RVEF showed moderate agreement (ICC=0.577, 95% CI 0.278-0.751) with low correlation ($r=0.402$, p-value=0.002). EDV showed very poor agreement (ICC=0.167, 95% CI-0.165-0.440) and very poor correlation ($r=0.225$, p-value=0.092). ESV showed moderate agreement (ICC=0.559, 95% CI -0.095-0.799) with moderate correlation ($r=0.579$, p-value<0.001). SPECT GBP showed abnormal wall motion in 11 patients (55%) which is normal on planar images.

Conclusion: Gated blood pool SPECT technique can be used to evaluate left ventricular function in cancer patients receiving treatment related cardiotoxicity. SPECT seems to detect abnormality of wall motion which cannot be determined by planar technique.

Keywords: Gated blood pool, left ventricular ejection fraction, Planar gated blood pool, gated blood pool SPECT

Diagnostic performance of dual-tracer subtraction, single-tracer dual-phase 99mTc-MIBI parathyroid scintigraphy, and 99mTc-MIBI SPECT/CT for preoperative localization in patients with hyperparathyroidism.

Warissara Wittayapasitti[1], Kijja Rhoongsittichai[1], Jiraporn Sriprapaporn[1]

1 Division of Nuclear Medicine, Department of Radiology, Faculty of medicine, Siriraj hospital, Mahidol University,

Introduction: Preoperative imaging is performed to localize the hyperfunctioning parathyroid glands to facilitate a minimally invasive surgical approach. The parathyroid glands can be imaged with different modalities. However, parathyroid scintigraphy has been the investigation of choice for decades. When analyzing the published data, it can be stated that parathyroid scintigraphy was mainly performed using double-phase, dual-tracer subtraction, SPECT/CT methods. Furthermore, it is still debated which protocols should be preferred for localizing abnormal parathyroid glands.

Purpose: To evaluate the diagnostic performance of dual-tracer subtraction (DT), dual-phase 99mTc-MIBI (DP) and, 99mTc-MIBI SPECT/CT parathyroid scintigraphy for preoperative localization in patients with hyperparathyroidism.

Methods: This retrospective study of consecutive 100 patients who underwent parathyroid scintigraphy at the division of nuclear medicine department of radiology Siriraj hospital from 30 July 2013 to 10 September 2019. All the parathyroid scintigraphy were reinterpreted using nuclear medicine physicians by reading 3 sets of image data of DT, DP, and SPECT/CT. Finally, all the data were statistically analyzed by using pathological results as a gold standard and to statistically compare the diagnostic performance among these 3 techniques.

Results: A total of 242 parathyroid lesions were excised. Parathyroid scintigraphy was compared with pathological results. In this series, most the lesions were parathyroid hyperplasia (204 lesions), 28 were parathyroid adenomas, and two were carcinoma. The rest eight foci represent normal parathyroid tissue. The overall sensitivities of DT, DP, and SPECT/CT techniques were 44.4%, 35.5%, and 40.2%, respectively and the overall specificities of these techniques were 87.5%, 87.5%, and 87.5%, respectively. Nevertheless, in the subgroup analysis, the sensitivities of adenoma glands were 78.6%, 82.1%, 82.1% and those for hyperplastic glands were 39.2%, 28.5%, 33.8% respectively.

Conclusion: The 3 imaging techniques have a low sensitivity similarly, but it shows insignificant result in preoperative localization of parathyroid in hyperparathyroidism. Although the sensitivities of 3 techniques were low, parathyroid scintigraphy were of benefit in identifying adenoma glands.

Keywrds: Hyperparathyroidism / 99mTc-MIBI / Parathyroid scan / MIBI / SPECT/CT

Clearance Patterns of Tc-99m ECD Using Serial SPECT Imaging to Define Seizure Onset Zone

Chanan Sukprakun[1], Chusak Limotai[2,3], Kitiwat Khamwan[4,5,6], Panya Pasawang[1], Supatporn Tepmongkol[3,4,5,6]

1 Division of Nuclear Medicine, Department of Radiology, King Chulalongkorn Memorial Hospital, Thai Red Cross Society, Bangkok, Thailand
2 Division of Neurology, Department of Medicine, Faculty of Medicine, Chulalongkorn University, Bangkok, Thailand
3 Chulalongkorn Comprehensive Epilepsy Center of Excellence (CCEC), King Chulalongkorn Memorial Hospital, Thai Red Cross Society, Bangkok, Thailand
4 Division of Nuclear Medicine, Department of Radiology, Faculty of Medicine, Chulalongkorn University, Bangkok, Thailand
5 Chulalongkorn University Biomedical Imaging Group (CUBIG), Faculty of Medicine, Chulalongkorn University, Bangkok, Thailand
6 Chula Neuroscience Center, King Chulalongkorn Memorial Hospital, Thai Red Cross Society, Bangkok, Thailand

Introduction: If there is a difference of ethyl cysteinate dimer (ECD) clearance pattern between the seizure onset zone (SOZ) and other brain regions, adding serial single photon emission computed tomography (SPECT) may give benefit for seizure focus localization.

Purpose: To define the SOZ by clearance patterns and rates of Tc-99m ECD using serial brain SPECT.

Methods: A total of 22 serial brain SPECT scans were prospectively collected from 12 subjects, including 9 patients with drug-resistant epilepsy (DRE) and 3 normal volunteers from Mar 2018 to Sep 2019 at King Chulalongkorn Memorial Hospital. Slope maps and clearance rates were calculated by regression model analysis. Visual grading of clearance patterns and statistical analysis of clearance rates in the SOZs were done.

Results: There were 12 SOZs in nine patients. The average Tc-99m ECD clearance rates of all SOZs were +0.46 % ± 2.71 %/hr (wash in), -4.97 % ± 2.83 %/hr (washout), and -5.16% ± 1.81 %/hr (washout) in ictal, aura and interictal phases, respectively. Matched pair t-tests between the SOZ and contralateral regions showed statistically significant difference ($p = 0.013$ and $p = 0.009$ in ictal and interictal phases, respectively). From 5 slope patterns found in 12 SOZs, which were wash in, mixed wash in and slow washout, slow washout, normal washout, and fast washout patterns, clearance patterns that can define the SOZs were 1) wash in and slow washout on ictal slope, 2) slow washout or fast washout on aura slope and 3) fast washout on interictal slope with percent localization of 100% (10/10), 100% (4/4) and 83.33% (10/12) in ictal, aura, and interictal slope maps, respectively.

Conclusion: Brain ECD clearance patterns using the slope map can define the SOZs with high percent localization (83.33%-100%). Thus, clearance pattern methods are potential diagnostic or confirmation tools for the SOZ localization.

Keywords: epilepsy, ECD, clearance, SPECT, localization

Monte Carlo simulation for high resolution imaging of Rb-82 with bremsstrahlung X-ray camera for small animals

Kouhei Nakanishi[1, 2], Seiichi Yamamoto[1]

1 Radiological and Medical Laboratory Sciences, Nagoya University Graduate School of Medicine, Nagoya, Japan,
2 Department of Radiology, Akita Hospital, Chiryu, Japan,

Introduction: Although Rb-82 is most common tracer for the myocardial perfusion imaging with PET, Rb-82 emits high energy positrons which have long range resulting in blurring of spatial resolution of PET image. Due to the limitation of spatial resolution, imaging of Rb-82 in mouse is not reported.

Purpose: Our purposes are proposing new method for high resolution imaging of Rb-82 in small animal by detecting bremsstrahlung X-rays emitted by the positron and validating the feasibility of the method using Monte Carlo simulation.

Methods: We simulated previously developed pinhole collimator camera based on 0.5-mm thick YAP scintillator and measured performance of the camera for the bremsstrahlung X-rays emitted by positron of Rb-82. Also, we simulated imaging of mouse heart phantom filled with Rb-82 of 67 MBq per milliliter in the heart phantom.

Results: The spatial resolution of simulated camera with 1.0-mm pinhole collimator was 2.6 mm FWHM at 17.5 mm from surface of collimator. We could observe shape of the phantom in the image measured in 4 minutes.

Conclusion: We conclude that high resolution imaging for high-energy positron emitter is possible by detecting bremsstrahlung X-rays emitted by the positron and the spatial resolution is superior to that of PET images.

Keywords: bremsstrahlung X-ray, Rb-82, high-resolution, scintillation camera, PET

Nuclear Medicine: Radiation Safety / DRL

Size specific dose estimate (SSDE) for estimating CT doses in SPECT/CT and PET/CT examinations

Mayomthong P, Khiewvan B, Tongpraparn T, Mali P, Chaudakshetrin P, Sritongkul N, Tuntawiroon M.

Section of Nuclear Medicine, Department of Radiology,
Faculty of medicine Siriraj Hospital, Mahidol University, Bangkok 10700, Thailand

Introduction: $CTDI_{vol}$ and DLP are frequently used parameters for estimation of patient's absorbed dose from CT examination. Until recently, the SSDE, which takes into account the patient size in terms of effective diameter and the output of the CT scanner in terms of $CTDI_{vol}$ has been proposed by the AAPM 204.

Purpose: To find out if there is a relationship between patient size and the parameters, SSDE and $CTDI_{vol}$.

Methods: CT data from 16 children and 109 adult patients performing PET/CT oncology; SPECT/CT myocardial perfusion, bone, parathyroid, and infection/inflammation were retrospectively collected for 3 months. Effective diameter of each patient was calculated as geometric mean of the anterior-posterior (AP) and lateral dimensions measured on axial CT images. Conversion factors corresponding to effective diameters were obtained from AAPM report 204 and the radiation dose were converted to SSDE. Linear regression model was used to evaluate the relationship between patient size and the parameters SSDE and $CTDI_{vol}$.

Results: The study shows that SSDE was larger than the $CTDI_{vol}$ in all patients. A positive correlation between SSDE and $CTDI_{vol}$ was observed ($r = 0.9730$). Patients with small body size have higher SSDE as demonstrated by the higher $SSDE/CTDI_{vol}$ ratio, more than 1.8-fold for children and lower than 1.8 for adult patients. Calculated ED based on DLP and SSDE values were found to present no correlation.

Conclusion: $CTDI_{vol}$ is an important indicator for calculating the SSDE. Both $CTDI_{vol}$ and SSDE vary with patient size. When there was no available organ dose to calculate an ED by SSDE/ICRP method, SSDE is a better estimate of average patient dose from CT than $CTDI_{vol}$ because the dose not only depends on output dose but also on the patient's characteristics. However, SSDE cannot be used to compute ED using *k-factors* for risk estimation as in DLP method.

Keywords: Size specific dose estimate (SSDE), Volume CT dose index ($CTDI_{vol}$), CT dose in nuclear medicine

Flexible, Lightweight and Lead-free Radiation Shielding for Nuclear Medicine from Natural Rubber with Barium Sulfate Composite

Nattha Plangpleng[1], Kartpan Sakulkaew[2], Nichapa Buasuwan[2], Putthiporn Charoenphan[3], Krisanat Chuamsaamarkkee[3]

1 Master of Science Program in Medical Physics, Department of Diagnostic and Therapeutic Radiology, Faculty of Medicine Ramathibodi Hospital, Mahidol University, Thailand,
2 Department of Science Services, Ministry of Higher Education, Science, Research and Innovation, Thailand,
3 Division of Nuclear Medicine, Department of Diagnostic and Therapeutic Radiology, Faculty of Medicine Ramathibodi Hospital, Mahidol University, Thailand

Introduction: Radiation shielding is an important tool for the protection of patient and medical staffs from radiation. Generally, lead provides the efficient high atomic number with greatest attenuated of radiation. However, the lead shielding is heavy and inflexible leading to inconvenient to use. Furthermore, lead is a highly toxic substance and a very strong poison which may present an insidious health hazard.

Purpose: The aim of this work was to develop the flexible, lightweight and lead-free shielding from natural rubber with barium sulfate ($BaSO_4$) composite for radiation shielding in nuclear medicine.

Methods: Natural rubber was filled with $BaSO_4$ of 0, 10, 20, 30 and 50 parts per hundred of natural rubber (phr) using the two roll mills. The physical and mechanical properties of these shielding have been tested. The shielding properties were measured using the 3-inch x 3-inch NaI(Tl) scintillation detector with ^{57}Co (122 keV) and ^{133}Ba (356 keV) for representative of commonly used radionuclides in nuclear medicine ^{99m}Tc (140 keV) and ^{131}I (364 keV) respectively.

Results: The results showed that increasing of $BaSO_4$ into natural rubber raised the hardness and density whereas the flexible properties were reduced. For radiation shielding properties, the mass attenuation coefficient (μ_m) were found to increase with the $BaSO_4$ concentrations for ^{57}Co and ^{133}Ba radionuclides. The highest mass attenuation coefficient was observed in natural rubber with $BaSO_4$ 50 phr, the μ_m were calculated to be 0.29 cm^2/g and 0.21 cm^2/g for ^{57}Co and ^{133}Ba respectively.

Conclusion: Natural rubber with $BaSO_4$ showed a promising result for developing potential shielding in nuclear medicine due to their flexibility, lightweight and lead-free composite. However, it is important to note that this study used the ^{57}Co and ^{133}Ba to represent the energy peak of ^{99m}Tc and ^{131}I respectively. Hence, it might not be the same in the term of radioactivity. Further study could be focused on enhancing the shielding properties by increasing the concentration of $BaSO_4$ or adding novel composites such as nanofiller in natural rubber and testing the shielding with the clinical used radioactive.

Keywords: Natural rubber, Barium Sulfate, Flexible shielding, Radiation protection

Investigation of position and angle effects of nanoDot OSL dosimeter for the eye lens dose measurement

Pattaravarin Rattanamongkonkul[1], Putthiporn Charoenphun[1], Krisanat Chuamsaamarkkee[2], Tanapol Dachviriyakij[3], Korawee Saejia[3]

1 Master of Science Program in Medical Physics, Department of Diagnostic and Therapeutic Radiology, Faculty of Medicine Ramathibodi Hospital, Mahidol University, Thailand,
2 Division of Nuclear Medicine, Department of Diagnostic and Therapeutic Radiology, Faculty of Medicine Ramathibodi Hospital, Mahidol University, Thailand,
3 Regulatory Technical Support Division, Office of Atoms for Peace, Thailand.

Introduction: Radiation dose to the eye lens are more consideration since ICRP decreased the equivalent dose limit of the eye lens in 2011. The nanoDot dosimeter has been used to measure the eye lens dose due to its characteristic which should appropriate for point dose measurement in term of Hp(3). However, several studies exhibited angular dependence of the nanoDot OSL. Moreover, the position of nanoDot could be varied depended on the individual face.

Purpose: The aim of the study was to investigate simultaneously the effects of position and angle of the nanoDot OSL for the eye lens dose measurement.

Methods: The responses of nanoDot OSL dosimeters were carried out on the PMMA water-filled cylindrical phantom behind the build-up region using ^{137}Cs as a calibration and reference source. The position and angular dependence were tested by setting up the source at 0º to the phantom. The nanoDots were placed at the centre (0º) and the various angles of 15º, 30º, 45º, 75º and 90º to the left and right side of the ^{137}Cs source. Then Hp(3) was evaluated correspondence to each dosimeter.

Results: The mean, standard deviation and the range of evaluated Hp(3) at the left and right side were 1137.13 ± 74.13 µSv ranging of 988.87 µSv to 1285.39 µSv and 1152.36 ± 51.64 µSv ranging of 1049.08 µSv to 1255.65 µSv, respectively. The Hp(3) results from various positions and angles indicated no difference at 95% confidence interval.

Conclusion: The nanoDot OSL dosimeter exhibited no effects of position and angle for the eye lens dose measurement in term of Hp(3). Therefore, nanoDot OSL dosimeter could be feasible for measurement of the eye lens dose whether the workers wear nanoDots in different positions and angles.

Keywords: nanoDot OSL dosimeter, Hp(3), effect of position and angle

Determination for current status of environmental radioactivity in Fukushima, using NaI (Tl) scintillation survey meter

Natsuki Miura[1], Daisuke Shimao[1], Tetsuya Sanada[1]

1 Department of Radiological Technology, Faculty of Health, Hokkaido University of Science

Introduction: Fukushima Daiichi nuclear power plant accident following the Great East Japan Earthquake and tsunami on March 11, 2011 caused radiation contamination in Fukushima prefecture. The evaluation of environmental radiation dose by the artificial radionuclides in Fukushima have been carried out by governments and many researchers. According to published investigation, in the environmental radiation dose has been reduced to background level in major cities in Fukushima due to decontamination and reaching half-life. Nevertheless, someone is concerned about the external radiation exposure visiting Fukushima.

Purpose: The purpose is to evaluate the environmental radiation dose at major sightseeing areas and roadside stations in Fukushima and to provide current status to public.

Methods: Ambient dose rates were measured in air 1 m above the ground at all sampling points using a NaI (Tl) scintillation survey meter (TCS-172B, Hitachi-Aloka Medical, Ltd., Tokyo, Japan), which can measure gamma rays with a time constant of 30 sec. Environmental radioactivity measurements were carried out at 12 areas which are over 800 thousand people visit annually in Aizu, Iwaki and Northern area. The environmental radiation dose was derived from 5 measurement points in each 12 areas.

Results: The environmental radiation doses obtained this study suggested that it has become background level and almost the same as other areas. These results could be useful and available data to obtain understanding safety of Fukushima.

Conclusion: We measured current environmental radiation doses at major sightseeing areas and roadside stations in Fukushima. The results indicated that there is no health hazard because the external radiation exposure is the same level as other cities and no concerned about additional exposure even when someone visiting Fukushima.

Keywords: Fukushima, environmental radioactivity measurement, NaI (Tl) scintillation survey meter

Nuclear Medicine: Others

The labeling of ^{99m}Tc-PSMA-HBED-CC for prostate cancer imaging

Benchamat Phromphao[1,3], Shuichi Shiratori[2,3]

1 Department of Radiology, Faculty of Medicine, Chulalongkorn University, Bangkok 10330, Thailand
2 Department of Radiology, Faculty of Medicine Siriraj Hospital, Mahidol University, Bangkok 10700, Thailand
3 Chulalongkorn University Biomedical Imaging Group, Department of Radiology, Faculty of Medicine, Chulalongkorn University, Bangkok 10330, Thailand

Introduction: Prostate cancer (PCa) is the second most common cancer and the fifth leading cause of death worldwide in 2018. Initially, PCa diagnosis based on Prostate-Specific Antigen (PSA) blood test, sonography guided needle biopsy which are invasive manner. Moreover, these two methods provided low sensitivity and low specificity. Therefore, molecular imaging recently enrolls as an important technique in PCa diagnosis using some small molecules which well developed to bind to overexpressed Prostate Specific Membrane Antigen (PSMA). The small molecules, for example PSMA-HBED-CC, PSMA I&T, chelate with Ga-68 for diagnostic purpose and Lu-177 for therapeutic purpose under theranostic concept. Herein, we report a new tracer using Tc-99m labeled with PSMA-HBED-CC aim to alternative option for PCa diagnosis.

Purpose: To develop in-house preparation of ^{99m}Tc-PSMA-HBED-CC for prostate cancer imaging.

Methods: ^{99m}Tc-pertechnetate 370 MBq was added to mixture solution of PSMA-HBED-CC 10 µg and 4% $SnCl_2 \bullet 2H_2O$, then heated to 100 ºC 15 minutes and incubated while cool down to room temperature. Labeling parameters were optimized to obtain the maximum radiochemical yield of ^{99m}Tc-PSMA-HBED-CC. The completeness chelation was determined by instant thin layer chromatography (iTLC) and pH of ^{99m}Tc-PSMA-HBED-CC was measured.

Results: ^{99m}Tc-PSMA HBED-CC was successfully chelated using ^{99m}Tc-pertechnetate solution in high radiochemical yield and purity which is sufficient to administer to patient for SPECT imaging of PCa diagnosis.

Conclusion: The preliminary labeling method of ^{99m}Tc-PSMA-HBED-CC can prepare a new promising SPECT tracer for PCa diagnosis. Animal experiment using PCa xenograft nude mouses is under investigation in our laboratory before apply to clinical use of ^{99m}Tc-PSMA-HBED-CC in human.

Keywords: Prostate cancer imaging, Technetium-99m, PSMA, ^{99m}Tc-PSMA

Gamma Scintigraphy for Hepatic Radioembolization: Comparison between Different Radionuclides using GATE Monte Carlo Simulation

Muhammad Rizal Fahmi[1], Nurul Ab. Aziz Hashikin[1], Ying Chee Keat[2]

1 School of Physics, Universiti Sains Malaysia, 11800, Penang, MALAYSIA.
2 Oncological & Radiological Science Cluster, Advanced Medical and Dental Institute, Universiti Sains Malaysia, 11900, Penang, MALAYSIA.

Introduction: Radioembolization using Yttrium-90 (^{90}Y) allows delivery of high-dose beta radiation to tumour. Post-treatment imaging is possible via Bremsstrahlung radiation, however with significantly lower quality. Alternative radionuclides have been investigated as potential substitutes for ^{90}Y, i.e. Lutetium-177 (^{177}Lu), Holmium-166 (^{166}Ho), and Samarium-153 (^{153}Sm), able to deliver equivalent tumour doses and emit gamma radiations ideal for post-treatment imaging.

Purpose: We aimed to evaluate the image quality from gamma (planar) scintigraphy following hepatic radioembolization with different radionuclides, using GATE Monte Carlo simulation.

Methods: A spherical tumour (diameter = 1.0 cm) was created inside a trapezoidal-shaped liver and placed inside a cylindrical torso phantom using GATE v8.2. For image acquisition, a gamma head (with NaI detector) was modelled using SPECTHead example from GateContrib(GitHub), with dimension of $21 \times 30 \times 7$ cm^3, and positioned 3.5 cm from the phantom. Technetium-99m (^{99m}Tc) source was uniformly distributed within the liver and tumour volumes (assuming tumour-to-normal ratio of 2:1) during image acquisition. Imaging was later repeated using ^{90}Y, ^{153}Sm, ^{166}Ho, and ^{177}Lu (using optimised protocols suggested by previous studies**).** All planar images were evaluated based on image quality, signal-to-background ratio (SBR) and coefficient of variation (CV). Image acquired using ^{99m}Tc was used as reference.

Results: Results show that the image acquired using ^{177}Lu gave the best SBR (13.23), followed by ^{99m}Tc(7.31), ^{90}Y(6.12), ^{153}Sm(5.68), and ^{166}Ho (4.36). For CV, ^{99m}Tc(0.46) resulted in the best value, followed by ^{177}Lu(0.50), ^{153}Sm(0.51), ^{166}Ho(0.66), and ^{90}Y(0.80). Higher SBR indicated superior spatial information, while lower CV indicated lower variation (better estimation).

Conclusion: Image acquired using ^{177}Lu shows the most superior quality compared to other radionuclides, at the same time able to deliver comparable tumour dose**.** Nevertheless, all alternative radionuclides offer better imaging capability via gamma emission compared to bremsstrahlung imaging via ^{90}Y.

Keywords: GATE, radioembolization, Monte Carlo simulation, Yttrium-90.

Positron Range Correction in Positron Emission Tomography

Rukiah A. Latiff[1, 2], Steve R Meikle[1], John E Gillam[1, 3], Peter L Kench[1]

1 The Brain and Mind Centre, Faculty of Medical and Health Sciences, The University of Sydney, Australia.
2 Faculty of Health Sciences, The National University of Malaysia, Malaysia.
3 Land Division, Defence Science and Technology Group, Fishermans Bend, *Australia.*

Introduction: Gallium-68 (^{68}Ga) gives more blur to Positron Emission Tomography (PET) image due to its higher positron range (PR), compared to ^{18}F. The blurring effect resulting in loss of spatial resolution and quantitative accuracy. The magnitude of PR blurring is proportional to the energy of the radionuclide used and inversely proportional to the density of the medium it travels through. The contribution of image blur was approximately 10% in bone and soft-tissue compared to 100% in lung medium. Besides, the blurring effect is independent of the acquisition system and parameters.

Purpose: This Monte-Carlo simulation study aims to develop an iterative post-reconstructed tissue-dependant spatially-variant positron range correction (PRC) deconvolution method and investigate its performance on PET National Electrical Manufacturer Association (NEMA) image quality phantom.

Methods: The PRC method proposed is implemented directly onto image space. Geant4 Application on Tomography and Emission (GATE) was used to model the NEMA phantom annihilation image from its PET-measured image. The simulated annihilation image takes into account the material in which the positron is originated and annihilated, obtained from a CT-segmented image. The correction factor of PET-measured image and GATE-annihilation image was calculated and employed in the forward projection to update the image estimate. We compare the image quality of the images before and after PRC.

Results: The preliminary results demonstrate an improvement in target-to-background ratio, contrast recovery and resolution after implementation of PRC with manageable noise as the iteration increases. This method also obtains artefact-free PR-corrected images especially in a lung region.

Conclusion: The performance of proposed PRC methods provides a resolution and quantitative improvement in PET phantom image. It can be implemented onto any PET image regardless of scanner geometry properties and type of radionuclides used. Future investigation is required by implementing this PRC method onto patients image.

Keywords: Positron range, PET, Monte Carlo simulation, NEMA phantom

Evaluation of patient doses from ^{177}Lu-PSMA in metastases prostate cancer treatment at King Chulalongkorn Memorial Hospital

Kotchakorn Chatachot[1,2], Kitiwat Khamwan[1,3,4]

1 Medical Physics Program, Faculty of Medicine, Chulalongkorn University, Bangkok, Thailand
2 Division of Nuclear Medicine, Department of Radiology, Buddhachinaraj Hospital, Phitsanulok, Thailand
3 Division of Nuclear Medicine, Department of Radiology, Faculty of Medicine, Chulalongkorn University and King Chulalongkorn Memorial Hospital, The Thai Red Cross Society, Bangkok, Thailand
4 Chulalongkorn University Biomedical Imaging Group, Department of Radiology, Faculty of Medicine, Chulalongkorn University, Bangkok, Thailand

Introduction: ^{177}Lu-PSMA has increasingly used for targeted radionuclide therapy of prostate cancer and its metastases. Dosimetric calculation, therefore, is critical to achieve the optimal therapeutic activity with limited side effects.

Purpose: To perform the image-based absorbed doses calculation to the normal organs for patients who treated by ^{177}Lu- PSMA for prostate cancer.

Methods: Whole-body planar images and SPECT/CT images were acquired in eight patients at immediately, 4 and 24 h after injection of ^{177}Lu-PSMA (range 4.37 to 8.58 GBq). To generate the time-integrated activity (TIA) in source organs, region of interests (ROIs) were manually contoured in whole-body, liver, spleen, urinary bladder, lacrimal gland, and bone marrow using the Osirix MD program. The geometric mean of anterior and posterior counts was determined through the ROI analysis. The TIA in each source organ was calculated by integrating area under time-activity curve using MATLAB. The s-values were extracted from OLINDA/EXM version 2.0. in order to calculate the absorbed dose coefficient in target organs according to the Medical Internal Radiation Dose (MIRD) scheme. The absorbed doses to bone marrow were estimated using the two-compartment method by dividing high-uptake and low-uptake compartment. The spherical model was used to calculate the lacrimal gland absorbed doses.

Results: The average absorbed dose coefficients per cycle were 0.56±0.16 mGy/MBq for the bone marrow [3], 0.62±0.13 mGy/MBq for the kidneys [1,2], 0.11±0.08 mGy/MBq for the liver [1], 0.18±0.14 mGy/MBq for the urinary bladder wall, 0.14±0.05 mGy/MBq for the spleen, and 2.86±0.78 mGy/MBq for the lacrimal glands [1,2]. The critical absorbed doses reported for the kidneys of 23 Gy, and for bone marrow of 2 Gy were not reached in any patients.

Conclusion: Our dosimetry results suggest that ^{177}Lu-PSMA treatment with higher activities and more cycles is possible without the risk of damaging the critical organ in metastasis prostate cancer patients.

Keywords: PSMA; ^{177}Lu-PSMA; theranostics; MIRD; radionuclide therapy

Development of Flexible Radiotherapeutic Bandage Containing Samarium-153 for the Treatment of Skin Cancer

Yin How Wong[1], Azahari Kasbollah[2], Basri Johan Jeet Abdullah[1] and Chai Hong Yeong[1]

1 School of Medicine, Faculty of Health and Medical Sciences, Taylor's University, 47500 Subang Jaya, Selangor
2 Malaysian Nuclear Agency, 43000 Kajang, Selangor, Malaysia

Introduction: Skin cancer is a common type of cancer that emerges from the skin due to the development of abnormal growth of cells. Radiation therapy is used as a primary treatment for inoperable tumors and in patients who are unfit for surgery. Radioactive samarium-153 (^{153}Sm) is a viable candidate for use against skin cancer.

Purpose: The aim of this study was to develop a flexible, neutron activatable radiotherapeutic bandage containing ^{153}Sm for treatment of skin cancer.

Methods: Electrospinning technique was used to prepare the flexible radiotherapeutic bandage from polyurethane (PU) and samarium-152 acetylacetonate (^{152}SmAcAc) crystal. The ^{152}SmAcAc-labeled PU bandage was then activated in a nuclear reactor, converting ^{152}Sm to ^{153}Sm (E_{max} = 807.6 keV, half-life = 46.3 hours) via ^{152}Sm(n,γ)^{153}Sm reaction. The ^{152}SmAcAc-labeled PU bandage before and after neutron activation were characterized using scanning electron microscope (SEM), energy dispersive X-ray (EDX) spectroscopy, gamma spectroscopy, Fourier transformed infrared spectroscopy, thermogravimetric analysis (TGA) and differential scanning calorimetry (DSC) . The in-vitro retention efficiency of ^{153}SmAcAc on the PU bandage was performed in saline solution over a duration of 120 h.

Results: The ^{153}SmAcAc-labeled PU bandage achieved nominal activity of 272 ± 9.6 μCi/mg or 1680 ± 52.6 μCi/cm^2 after 6 h neutron activation. SEM results shows the morphology of the bandage remained the same after neutron activation. The gamma and EDX spectroscopy indicated that no radionuclide and elemental impurities was observed after neutron activation. The TGA and DSC analysis suggested that the bandage was stable up to 200°C. By manipulating the neutron activation duration, different amounts of radioactivity were produced to meet the desired dosage for different stages or conditions of skin cancer. Furthermore, the radioactive bandage can be cut into specific shapes and sizes to cover only the treatment area and hence minimizing radiation exposure to the healthy tissues. The in-vitro retention efficiency of ^{153}SmAcAc was more than 95% in saline solution for 120 h.

Conclusion: The ^{153}SmAcAc-labeled flexible radiotherapeutic bandage are potentially useful for radiation therapy of skin cancer in view of its favorable physicochemical characteristics and excellent retention efficiency.

Keywords: Samarium-153, Radiotherapeutic Bandage, Skin Cancer, Radiation Therapy, Electrospinning

Radiotherapy

Real-time in vivo dose verification using Metal-Oxide Semiconductor Field Effect Transistor (MOSFET) in HDR brachytherapy

Siti Hajar Abdul Rahman[1], Yasmin Md Radzi[1], Mohd Zahri Abdul Aziz[2], Ahmad Naqiuddin Azahari[2]

1 School of Physics, Universiti Sains Malaysia, Penang, Malaysia,
2 Advanced Medical and Dental Institute (AMDI), Universiti Sains Malaysia, Penang, Malaysia.

Introduction: High dose rate (HDR) brachytherapy requires a highly conformal dose to the tumour volume. Hence, in vivo dosimetric for verification during treatment is deeming very important and crucial to provide an accurate, highly reliable and precise dose delivery.

Purpose: In this work, we introduce the use of real-time in vivo dosimetry using MOSFET as a reliable quality assurance tool for HDR brachytherapy instead of widely used thermoluminescence dosimeters (TLDs).

Methods: Calibration of MOSFETs detector was done following the vendor's specification under HDR Ir-192 brachytherapy source available at our centre. The distance of the source-to-detector (SDD) was measured at 3cm. The detectors and source were positioned in a "sandwich set-up". The positional accuracy of the source was verified using Gafchromic EBT3 film. A plan was optimised to deliver 100 cGy at 3cm depth using Oncentra Treatment Planning System (TPS). The detector's reproducibility, linearity, distance dependency and in-phantom verification were tested for its suitability as an in vivo detector.

Results: Five individual detectors gave maximum sensitivity deviation of 2.66%. Measured values for the reference dose data showed a good agreement with the calculated data, with maximum deviation of –2.86%. The calibration factors were ranged from 1.40 to 1.44 mV/cGy. The MOSFET detector has good reproducibility (<3%) and excellent dose linearity (R^2=1). While distance dependency response showed a linear fit with R^2 value of 0.9844 (2cm to 5.5cm). In-phantom dose measurements using MOSFET detectors showed that maximum deviation was -4.35%. The percentage deviations between the measured doses and the TPS doses were below 5% for all measurements.

Conclusion: MOSFET has demonstrated as a suitable and good detector of choice for real-time in-vivo dosimetry in HDR brachytherapy. Additionally, MOSFET can be used as one of the reliable QA tools for HDR brachytherapy due to its special characteristic of being small in size.

Keywords: MOSFET, HDR brachytherapy, In vivo dosimetry, real-time, quality assurance

Development of external dosimetry audit system for image-guided brachytherapy in Asian Countries

Hideyuki Mizuno[1], Taku Nakaji[1], Shigekazu Fukuda[1], Shingo Kato[2]

1 QST hospital, National Institutes for Quantum and Radiological Science and Technology,
2 Saitama medical university International medical Center

Introduction: Clinical study on standardized radiation therapy for uterine cervical cancer has been carried out within the frame work of The Forum for Nuclear Cooperation in Asia (FNCA). Eleven Asian countries (Bangladesh, China, Indonesia, Japan, Kazakhstan, Korea, Malaysia, Mongolia, Philippines, Thailand and Vietnam) participate in this study. To improve the quality of multi-center clinical study using image-guided brachytherapy (IGBT), QA activity should be performed.

Purpose: The purpose of this study is to develop the external dosimetry system of IGBT through end-to-end test among Asian countries.

Methods: Sophisticated water phantom was developed to support various shapes of applicators used in Asian countries. A tandem holder was inserted into the water phantom to hold the applicator in water. The root part of the applicator was fixed by an arm. A Pinpoint ionization chamber (PTW, TN31013) and a radiophotoluminescent glass dosimeter (RPLD; AGC, DoseAce GD-302M) were used as dosimeters. The left and right A points dose were measured by pinpoint chamber, and the rectal and bladder dose, represented as an ICRU reference points, were measured by RPLD. In order to precisely calculate the dose points with the IGBT, a dummy dosimeter which has a cavity with a diameter of 2 mm was placed at a position corresponding to the effective center of the dosimeter at the CT image acquisition. The cavity center dose is calculated by TPS and compared with the measured dose by dosimeters which is placed at the IGBT irradiation.

Results: The on-site audit was performed to 5 hospitals from 3 countries, Korea, China and Philippines. All audit was successfully completed and feasibility of this audit procedure was confirmed. Preliminary results of the audit will be presented at the conference.

Conclusion: External dosimetry system of IGBT through end-to-end test procedure was developed.

Acknowledgement: This work was supported by JSPS KAKENHI Grant Number JP 17K09075.

Keywords: Audit, Image-guided-brachytherapy, end-to-end test

Comparison of ICRU Point Doses and Volumetric Doses to the Rectum High Dose Rate Cobalt-60 Brachytherapy of Cervical Cancer

Yun Seang Yi[1], Zulaikha Binti Jamalludin[2], Rozita Malik[1], Ung Ngie Min[1]

1 Clinical Oncology Unit, Faculty of Medicine, University of Malaya, Kuala Lumpur, Malaysia
2 Medical Physics Unit, University of Malaya Medical Centre, Kuala Lumpur, Malaysia

Introduction: Brachytherapy is a common option to treat cervical cancer. High dose rate (HDR) intracavitary brachytherapy (ICBT) is one of the currently used techniques for cervical cancer treatment. The volume-based brachytherapy planning method recommended in the International Commission on Radiation Units and Measurements (ICRU) report No. 89 is widely believed to be more useful compared to the conventional point-based method recommended in ICRU report No. 38 in terms of OARs dosimetry. However, more resources in terms of manpower and time are required to implement volume-based brachytherapy planning.

Purpose: This study aims to evaluate the point-based and volume-based methods for rectal dose estimation in HDR Co-60 brachytherapy of cervical cancer.

Methods: A total of 150 patients receiving full insertion HDR ICBT treatment in University of Malaya Medical Centre from 2017 to 2019 were retrospectively selected. The patients' data including rectal volume and rectal dose parameter calculated using both point-based and volume-based techniques were extracted from the brachytherapy treatment planning system. Data were compared and investigated for possible correlations using the SPSS software version 23.0.

Results: The results showed significant differences between rectal point dose ($ICRU_r$) with doses to most exposed rectal volumes of 0.1 cm^3 ($D_{0.1cc}$), 1 cm^3 (D_{1cc}) and 5 cm^3 (D_{5cc}) ($p<0.05$). The $ICRU_r$ was shown to have no significant difference with the most exposed rectal volumes of 2 cm^3 (D_{2cc}) ($p=0.960$). The results of correlation analyses indicated weak correlations between $ICRU_r$ with $D_{0.1cc}$, D_{1cc}, D_{2cc}, and D_{5cc} with the correlation coefficients of 0.184, 0.351, 0.371, 0.384, and 0.397 respectively ($p<0.01$). The strongest correlations between rectal point and volumetric dose were observed to be between $ICRU_r$ and D_{1cc} and D_{2cc} with the correlation coefficients of 0.674 and 0.669 ($p<0.05$) respectively.

Conclusion: In conclusion, the D_{1cc} and D_{2cc} were the volumetric rectal doses that can be explained better by the $ICRU_r$.

Keywords: ICRU point dose, volumetric dose, rectal dose

Correlation analysis of CT-based rectal planning dosimetric parameters with *in vivo* dosimetry of MO*Skin* and PTW 9112 detectors in Co-60 source HDR intracavitary cervix brachytherapy

Zulaikha Jamalludin[1,2,3], Rozita Abdul Malik[2,3], Zamzarinah KamarulZaman[1,3], Munira Rejab[1,3], Nurul Hidayah Moksem[1,3] and Ngie Min Ung[2,3]

1 Medical Physics Unit, University of Malaya Medical Centre, Kuala Lumpur, 59100, Malaysia,
2 Department of Clinical Oncology, University of Malaya Medical Centre, Kuala Lumpur, 59100, Malaysia,
3 Clinical Oncology Unit, Faculty of Medicine, University of Malaya, 50603, Kuala Lumpur, Malaysia

Introduction: Intracavitary brachytherapy (ICBT) for the treatment of cervical cancer while delivering high doses to the target will also delivered portion of doses to rectal organ due to close proximity to the cervico-uterus organ. Rectal dose assessment was evaluated with the use planning and *in vivo* based dose parameters.

Purpose: This study conducted to analyze the correlation between rectal *in vivo* measured dose with selected volume and point-based dose parameters.

Methods: In 48 insertions of CT-based high dose rate ICBT, *in vivo* dose measurement performed with commercial PTW 9112 semiconductor diode probe. In 18/48 insertions, a single MO*Skin* detector was attached on the PTW 9112 probe surface, at 50 mm from the probe tip. Four types of dosimetric parameters were retrospectively collected from treatment planning system (TPS) in these insertions; a) TPS planned doses from the maximum reported dose of PTW 9112 diode (RP_{max}) and single MO*Skin* detector, b) minimum dose to 2 cc rectal organ (D_{2cc}), c) ICRU reference point ($ICRU_r$), d) maximum dose from additional rectal points (R_{max}). The measured *in vivo* doses from both detectors were analyzed for any correlation with the above-mentioned dosimetric parameters.

Results: There was significant high correlation strength between *in vivo* measured dose from RP_{max} and MO*Skin* with TPS planned dose with correlation coefficient (r) to be 0.916 and 0.959 respectively. The correlation between measured RP_{max} dose with both D_{2cc} and R_{max} revealed high correlation strength with $r > 0.7$ while resulted in moderate correlation strength with ICRUr of $r = 0.525$. Analysis of relationship found no significant correlation (p-value > 0.05) between MO*Skin* in vivo measured dose with D_{2cc}, $ICRU_r$ and R_{max}.

Conclusion: The non-significant correlation between parameters ascribable to the differences in both detectors position within the patient and dosimetric volume and point location determined on 3D images from TPS rather than detectors uncertainties.

A development of a primary standard of absorbed dose to water for a small field in high-energy photon beam

Masakatsu Takeda[1, 2], Morihito Shimizu[2], Yuichiro Morishita[2], Masao Hoshina[1] and Masanori Sato[1]

1 Graduate School of Health Sciences, Komazawa Univ
2 National Metrology Institute of Japan (NMIJ), AIST

Introduction: The use of a small field photon beam is indispensable in modern high-precision radiotherapy, and accurate measurement of absorbed dose to water for a small field is important. The NMIJ are developing a primary standard of absorbed dose to water for a small field in high-energy photon beam.

Purpose: In order to determine the absorbed dose to water for the small field, we developed dose measurement method using a compact graphite calorimeter.

Methods: The absorbed dose to water for the small field in a 6 MV photon beam from a clinical linac were determined using the compact graphite calorimeter with core diameter of 2 cm. The field size of the photon beams was 2 cm × 2 cm − 10 cm × 10 cm. The absorbed dose to graphite calorimeter was converted to dose to water by Monte Carlo simulation (EGS5). A short Farmer-type ionization chamber (IBA, FC-23C) was calibrated with the determined dose to water.

Results: The calibration coefficients of the ionization chamber were 137.06±0.51 mGy nC^{-1} for the field size from 4 cm × 4 cm to 10 cm × 10 cm. In the field size of 3 cm × 3 cm and 2 cm × 2 cm, the calibration coefficients were 2 % and 11 % larger than that on 10 cm × 10 cm, respectively. This difference between the field size might come from the conversion factor was calculated for that of 10 × 10 cm.

Conclusion: The absorbed dose to water calibration coefficient for field size of 4 cm × 4 cm to 10 cm × 10 cm was determined with a relative standard uncertainty of 0.38 % in the small field photon beams.

Keywords: small field, Absorbed dose to water, high-energy photon beam, graphite calorimeter

Construction of regional network and remote support system for linac output dose difference facilities.

Shinji Kawamura[1], Yoshinori Tanabe[2], Shuichi Ozawa[3], Toshiyuki Minemura[4], Katsuhisa Narita[5], Kazushige Hayakawa[6]

1 Graduate school of health sciences, Fukuoka, 836-8505, Japan
2 Yamaguchi University Hospital, Ube, Yamaguchi, 755-8505, Japan
3 Hiroshima high-precision radiation therapy cancer center, Hiroshima, 732-0057, Japan
4 Center for cancer control and information services, Tokyo, 104-0045, Japan
5 Association for Nuclear Technology in Medicine, Chiba, 263-0041, Japan
6 National Hospital Organization Disaster medical center, Tokyo, 190-0014, Japan

Introduction: In Japan, there are some facilities with dose difference exceeding 3% in the linac output dose audit. Support for these facilities is an issue.

Purpose: We have established a system to provide aid to these facilities by utilizing regional networks and remote support system. We examined the effectiveness and issues of this system.

Methods: The Japanese Organization of Radiotherapy Quality Management (JORQM) has been conducting a pilot study of output dosimetry support since 2018. This study is being conducted for each region divided into nine regional blocks and is scheduled to be completed in 2020. Through this study, a regional network for quality control of radiation therapy will be established. In addition, the remote support system STD-Audit will be constructed. We will introduce the efforts to standardize the output dose through the regional network and remote support in Japan.

Results: As a result of output dose audit in Japan, the dose difference facilities exceeding 3% were about 10% of the audit facilities. The output doses measured by the two quality managers who visited the facility were automatically transferred to the remote server, and the cause of the difference in output doses was discussed by the facility manager, two visiting quality managers, and the remote supporters. Reasonable and optimal support can be provided by adding a regional network and remote support system.

Conclusion: We constructed a local network and remote support system for facilities with different linac output dose, and evaluated its effectiveness and issues in a pilot study.

Keywords: Audit, Output dose difference, Regional network, Remote support, STD-audit

Investigation for measurement of photon depth dose using UVC camera

Kengo Miyazaki[1], Atsushi Myojoyama[1]

1 Graduate School of Human Health Science, Tokyo Metropolitan University

Introduction: When a photon output from a linear accelerator was incident on a UVC (USB Video Class) camera, noise was detected on the output images. We considered that the detail information of photons or electrons with a high dose rate can be obtained by analysing the noise because the generated noise increases as the dose rate.

Purpose: In this study, we investigated the radiation response characteristics of a UVC camera in order to develop an inexpensive semiconductor detector.

Methods: UVC camera was placed 15 cm below the ^{137}Cs radiation source and connected to the noise analysis program that we developed. The copper block was placed directly above the UVC camera, and the number of noise generated for 10 minutes was counted for each 1 mm thickness. In order to investigate the number of noise in detail, the measured results were compared with EGSnrc simulation. In the simulation, the thickness of the copper block was increased by 1 μm from 0 cm to 3 cm, and the number and energy of electrons generated from the bottom surface of the copper block at each thickness were investigated.

Results: It was observed in actual measurement that the noise amount decreases as the copper block becomes thicker. As a result of comparison between actual measurement and simulation, it was confirmed that the number of noise generated from the UVC camera conforms to the depth dose obtained from the simulation.

Conclusion: It was suggested that the UVC camera could be a semiconductor detector for depth dose measurement.

Keywords: UVC camera, noise, depth dose, metal block

Impact of the Frequency of Verification with In-room CT on Setup Errors in Carbon Ion Radiotherapy for Prostate Cancer

Yushi Wakisaka[1,2], Hiroyasu Maruo[1], Takayoshi Ishii[1]

1 Department of Radiation Technology, Osaka Heavy Ion Therapy Center, Osaka, Japan,
2 Department of Medical Physics and Engineering, Osaka University Graduate School of Medicine, Suita, Japan

Introduction: In our facility, the position of the prostate was verified by daily in-room CT when the patient was inapplicable to implement fiducial markers. The reduction of the number of taking in-room CT is desired for the viewpoint of exposure dose and occupation time of the treatment room within acceptable setup errors.

Purpose: To evaluate the impact of the frequency of verification with in-room CT on setup errors.

Methods: Because of lack of cases taking in-room CT, inter-fractional errors of 350 patients with fiducial markers were analyzed. Intra-fractional errors were assumed to be 1 mm based on clinical experiments, and expressed by the random numbers following a normal distribution. When assuming verification with in-room CT, the inter-fractional error of that day should be zero, while it must be estimated by averaging previous trends for the other day. Following our treatment protocols, total errors (i.e. the sum of inter-fractional errors and intra-fractional errors) with 12 fractions were simulated for the different number of verifications with in-room CT.

Results: When in-room CT was not taken at all (i.e. matched only by bone every fractions), the total error was 2.1±1.6 mm. Assuming taking in-room CT for equal intervals, total errors were 1.7±1.4 mm, 1.4±1.3 mm, 1.2±1.1 mm, 0.8±0.6 mm when taking in-room CT 2, 4, 6, 12 (all) times, respectively.

Conclusion: Even if the frequency of verification with in-room CT was decreased, setup errors could be less than the case that in-room CT was never taken. However, margins of treatment planning might be revised because the reduction of the number of taking in-room CT leads to the increase of setup error.

Keywords: In-room CT, Prostate cancer, Carbon ion radiotherapy, Setup error, Fiducial marker

Determination of the beam quality correction factors for carbon-ion beams by Monte Carlo simulations and measurements

Yuka Urago[1,2], Makoto Sakama[2], and Hidetoshi Saitoh[1]

1 Department of Radiological Science, Graduate school of Human Health Science, Tokyo Metropolitan University
2 Department of Accelerator and Medical Physics, NIRS, QST

Introduction: The beam quality correction factor k_{Q,Q_0} obtained by the water-to-air stopping power ratio $s_{water,air}$, the energy to form an electron-ion pair in air W_{air}, and chamber-specific perturbation correction factor P. The uncertainties of $s_{water,air}$, W_{air}, and P are large at 2 %, 1.5 %, and 1 %, respectively in the IAEA TRS-398. In addition, despite these factors change with irradiated particle and its energy, a constant value is adopted. Consequently, the uncertainty of k_{Q,Q_0} for carbon-ion beams is estimated to be 3 %, which is larger than 1 % for photon.

Purpose: The aim of this study is determination of k_{Q,Q_0} of ionization chambers for carbon-ion beams by Monte Carlo (MC) simulation with Geant4 and evaluation by comparison with that obtained by measurements and literature values.

Methods: k_{Q,Q_0} can be obtained as the ratio of a chamber-specific calibration factor N_{D,w,Q_0} and $N_{D,w,Q}$. Since there is no primary standard of absorbed dose to water for carbon-ion beams, however, it is impossible to determine k_{Q,Q_0} by the dosimetry for each ionization chamber. Therefore, the ratio of the beam quality correction factor of the ionization chamber k_Q to that of the reference chamber k_Q^{ref} was evaluated under the same irradiation conditions.

Results: Figure 1 shows the results for 290 MeV/u carbon-ion beams. The measured values and the literature values of the ionization chambers agreed within the standard uncertainty of TRS-398.

Conclusion: The k_{Q,Q_0} of carbon-ion beams were evaluated by measurements with various ionization chambers. The measured values and the literature values of the ionization chambers agreed within the standard uncertainty. We plan to evaluate k_{Q,Q_0} of various ionization chambers by MC simulation and analyze in detail.

Keywords: carbon ion therapy, carbon ion dosimetry, Monte Carlo simulation, beam quality correction factor, ionization chamber

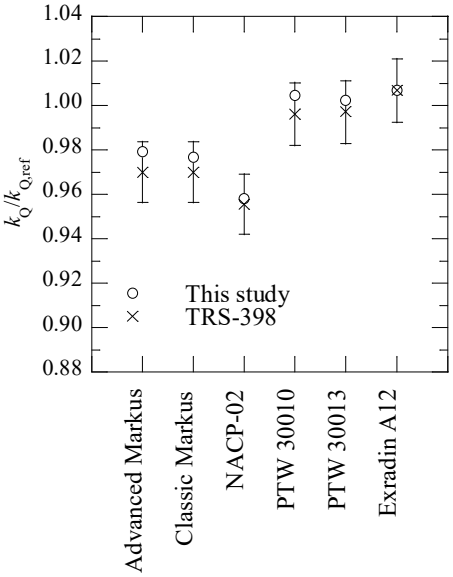

Fig.1 Comparison of k_{Q,Q_0} measurements and literature values for 290 MeV/u carbon-ion beams: Error bars show the standard uncertainty of TRS-398.

Effects of parallax error and light refraction on estimation for dose distribution of proton beams using luminescence in water

Koki Furuo[1], Masataka Komori[1], Hiroto Ushiba[1], Toshiyuki Toshito[2]

1 Nagoya University Graduate School of Medicine, 1-1-20 Daiko-Minami, Higashi-ku, Nagoya 461-8673, Japan,
2 Nagoya Proton Therapy Center, Nagoya City West Medical Center, 1-1-1, Hirate-cho, Kita-ku, Nagoya 462-8508, Japan

Introduction: A previous study confirmed that weak luminescence was observed by CCD (Charge Coupled Device) camera when water was irradiated with proton beams having energy lower than the threshold for Cherenkov-light emission. Furthermore, the luminescence distribution was found out to almost correspond with the dose distribution. Therefore, the luminescence imaging has great potential to estimate the dose distribution of proton beam. However, the parallax error of the CCD camera and the refraction of the luminescence at the surface of the water phantom affects the dose estimation.

Purpose: We evaluated the effects of the parallax error and the refraction of the luminescence for the dose estimation with uniform-field irradiation of proton beams.

Methods: The calculated dose distribution by treatment planning system (TPS) was corrected for the parallax and refraction errors and compared with the luminescence distribution measured from lateral side. Field size of 6×6 cm2, range of 12 cm and SOBP of 6 cm were used for the uniform-field irradiation of proton beams. The parallax error and refraction depend on the distance between the CCD camera and the luminescence emission point (from 42 to 48 cm). Therefore, the calculated dose distribution was corrected for the parallax error and refraction at every 1 mm steps of the distance and summed up to one dose distribution.

Results: By correcting the parallax error in the dose distribution, the slope at the end of the ranges became gentle, and the inclination was 32% improved to the luminescence distribution. Further, the correction of the refraction was found to 4.5% expand the dose distribution.

Conclusion: The correction of the parallax error and refraction was found to improve the dose estimation by luminescence imaging for uniform-field irradiation of proton beams.

Keywords: luminescence imaging, dose estimation, parallax error, refraction

Time dependence of intra-fractional motion for spine stereotactic body radiotherapy

Ryuta Hirai[1], Yu Ohkubo[2], Mitsunobu Igari[1], Yu Kumazaki[1], Tomomi Aoshika[1], Yasuhiro Ryuno[1], Satoshi Saito[1], Takanori Abe[1], Shin-ei Noda[1], Shingo Kato[1]

1 Department of Radiation Oncology, Saitama Medical University International Medical Center
2 Department of Radiation Oncology, Saku Central Hospital Advanced Care Center,

Introduction: Recently the usefulness of stereotactic body radiotherapy (SBRT) for spinal metastases has been reported, however, the treatment could require a long time. Therefore, the intra-fractional spinal motion must be taken into account.

Purpose: We investigated intra-fractional spinal motion during SBRT and its time dependency.

Methods: Thirty-one patients who received SBRT using CyberKnife at our hospital were enrolled in the study. Two-dimensional kV X-ray spine images in two directions were taken before and during treatment. Image acquisition intervals during treatment were set at 35-60 sec. Automatic image matchings were performed between the reference digital reconstructed radiography (DRR) images and live images, and the spinal position displacements were recorded on three translations and rotations (Right-Left, Superior-Inferior, Anterior-Posterior, Roll, Pitch, Yaw). The amount of couch adjustments was also recorded when the spine position was corrected by moving couch. From these values, the over-time accumulated translational and rotational displacements without any couch adjustments were calculated. Pearson's correlation coefficients were used to evaluate the correlations between the displacements and the elapsed treatment time.

Results: Spinal position displacements in all translational and rotational directions were correlated with the elapsed treatment time. Especially, Right-Left displacements of >1 mm and >2 mm were observed at 4-6 minutes and 8-10 minutes after initiation of treatments, respectively. Rotational displacements in Yaw direction >1° were observed 8-10 minutes after treatment initiation.

Conclusion: The translational and rotational displacements systematically increased with the elapsed treatment time. It is suggested that the spine position should be checked every 4-6 minutes or irradiation time should be limited within 4-6 minutes to assure the irradiation accuracy with a millimeter or submillimeter range.

Keywords: Stereotactic body radiotherapy, Spine metastasis, Intra-fractional motion

Calculation of an automatic irradiation path for dynamic-wave-arc irradiation

Kouichi Murashima[1], Akira Sawada[2], Masaki Sueoka[3], Yoshitomo Ishihara[4], Masaki Kokubo[3], Masamitsu Moriyama[1]

1 Kindai University, Osaka, Japan,
2 Kyoto College of Medical Science, Kyoto, Japan,
3 Kobe City Medical Center General Hospital, Hyogo, Japan
4 Japanese Red Cross Wakayama Medical Center, Wakayama, Japan

Introduction: Dynamic-wave-arc irradiation enables 3D rotational irradiation along a unicursal path with dynamic tumor tracking functionality of Vero4DRT system. It is a burden to determine an irradiation path.

Purpose: The purpose of this study was to calculate a dynamic-wave-arc irradiation path which has passed over normal tissues reduced as much as possible.

Methods: First, distance from each point inside irradiation area to normal tissue was measured using the structure data of DICOM. From a starting point to the end, points having the smallest value among 8-neighborhood points on the above distance map showing risk score were selected successively. The treatment plan along the calculated irradiation path for a phantom was created and dose distribution was calculated using a treatment planning system (Eclipse TPS Ver. 15.1 (Varian Medical Systems, Palo Alto, USA)).

Results: For the lung phantom, an irradiation path and the DVH were calculated. It has been observed that radiation dose to normal tissues was minimized while the prescribed dose was delivered to the target.

Conclusion: From this preliminary phantom study, it will be feasible to calculate a dynamic-wave-arc irradiation path which has passed over normal tissues reduced as much as possible, further investigation is required though.

Keywords: dynamic-wave-arc, dynamic tumor tracking, Vero4DRT

Dosimetric effect of the baseline shift in the phase and amplitude gated lung SBRT

Kenji Yasue[1,2], Hiraku Fuse[3], Kazuya Shinoda[2], Hideaki Ikoma[2], Tatsuya Fujisaki[3], Yoshio Tamaki[4]

1 Ibaraki Prefectural University of Health Sciences, Graduate School of Health Sciences
2 Ibaraki Prefectural Central Hospital, Department of Radiation Technology
3 Ibaraki Prefectural University of Health Sciences, Department of Radiation Technology
4 Ibaraki Prefectural Central Hospital, Department of Radiation Oncology

Introduction: The lung stereotactic body radiation therapy (SBRT) must be considered the intra-fractional motion for prescribing the target with high dose and small field. The previous study was showed about 30% reduction in the residual motion for three of irregular respiratory patients using amplitude gated, compared with phase gated. The dosimetric effect of the baseline shift has not been revealed in phase and amplitude gated lung SBRT, although the baseline shift was reported the target coverage was decrease in lung SBRT to the residual motion was increase with the magnitude of the baseline shift.

Purpose: To quantify the dosimetric effect of the baseline shift in respiratory gated lung SBRT, the dose distribution is measured using the motion phantom that reproduced the respiratory motion with the baseline shift.

Methods: The patient specific phantom was designed by QUASAR^{TM} Respiratory Motion Platform and IMRT thorax phantom. The phantom was moved by the sample waveforms reproduced the respiratory motion with the baseline shift. The shape of target in the IMRT thorax phantom was assumed to be a sphere. The dose distribution of the lung SBRT was calculated by the treatment planning system and delivered on a TrueBeam STx and Real-time Positioning Management (RPM) system for respiratory gating.

Results: The target coverage was decrease with the magnitude of the baseline shift in phase and amplitude gated method. The dose distribution of the amplitude gated method was less effected by the baseline shift since the residual motion was small, compared with the phase gated method.

Conclusion: The dosimetric effect of the baseline shift was measured using the motion phantom that reproduced the respiratory motion with the baseline shift in phase and amplitude gated lung SBRT. Amplitude gated method was more appropriate than phase gated method in lung SBRT with the baseline shift.

Keywords: Respiratory gated method Baseline shift Phase gated Amplitude gated Intra-fractional motion

The Proposal of the Simple Alternative Planning Method for Lung/Esophageal IMRT plan in case of failure in Varian Halcyon

Yuki Tanaka [1], Haruki Tougou [1], Toshiya Rachi[1]

1 Nationol Cancer Center Hospital East,

Introduction: If a conventional linear accelerator (LINAC) fails, a LINAC with similar or the same mechanical structure may allow treatment to be performed without changing the plan. In the re-creation of the intensity-modulated radiotherapy (IMRT) plan using the treatment planning system (TPS), it is considered that there is no substantial difference in the dose distribution by using the same optimization parameters for similar LINAC. However, Varian Halcyon has a mechanical structure of flattening filter free (FFF), so it differs from the existing LINAC. Therefore, to change the IMRT plan created on Halcyon into another LINAC, it is necessary to reconsider the TPS's optimization carefully.

Purpose: We propose a simple method to convert the lung/esophageal IMRT plan created on Halcyon into another LINAC.

Methods: Fallback Planning of RayStation v9.0 was used to convert the already created dose distribution for Halycon 6XFFF into another LINAC. The dose distribution created using Halcyon 6XFFF was converted to that using Varian TrueBeam 6X. 4 patients with esophageal cancer and 9 patients with lung cancer were planned using IMRT. Dose-volume histogram (DVH), conformity index (CI), and homogeneity index (HI) in the converted plans were evaluated. Additionally, the shapes of these isodose curves for each 10% were compared using the Dice coefficient (DC).

Results: All DVHs evaluated were within the specified values; HI and CI were equivalent or better than the original plans. The minimum DC in the isodose curve of all patients was 0.86, and the average was 0.90. From these results, it was considered that the converted plans have the same dose distribution as the original plans created on Halcyon.

Conclusion: A simple re-planning method was proposed that can convert the dose distribution planned in Varian Halcyon into the conventional LINAC.

Keywords: Varian Halcyon, IMRT, Lung Cancer, Esopheal Cancer, Plan conversion

Evaluate the dose distribution of mono-isocenter and dual-isoncenter volumetric modulated arc therapy for synchronous bilateral breast cancer

Chung-Hsien Ho[1], Tzu-Hsuan Kuo[1], Ming-Feng Lee[1], Bi-Ching Hsu[1], Chiao-Chi Yang[1], Shang-Chien Lin[1], Pai-Hseun Chen[1]

1 Department of Oncology and Radiology, Lo-Hsu Medical Foundation Lotung Poh-Ai Hospita, Taiwan

Introduction: Lots of reports pointed out that VMAT improved dosimetry and reduced treatment time, but there were few reports evaluated the difference of dose distribution between mono-isocenter VMAT plan and dual-isocenter VMAT plan.

Purpose: We modified the tangential based multiple partial arcs VMAT and the purpose of this study is to evaluate the dose distribution difference of mono-/dual- isocenter VMAT plan.

Methods: Four patients with synchronous bilateral breast cancers after BCS were included. The PTV included the whole breast and tumor bed, and PTV prescription dose for the whole breast is 50 Gy in 30 fractions and SIB for tumor bed is 60 Gy in 30 fractions. VMAT plans for mono-isocenter and dual-isocenter contain eight and ten partial arcs, respectively. DVH of PTV and OAR's were analyzed for mono-/dual- isocenter plan.

Results: The mono-/dual- isocenter plan had similar PTV CI and HI. The dose distribution of heart and LAD was no significantly difference. Dual-isocenter plan reduced the total lung dose compared to mono-isocenter plan. The V5Gy, V10Gy, V20Gy and mean lung dose of dual-isocenter plan were reduced from 45.92%±12.62% to 29.75%±9.75%, 24.80%±8.00% to 16.61%±7.34%, 11.43%±5.44% to 8.10%±4.69%, and 8.11 Gy±2.37 Gy to 6.00 Gy±1.93 Gy, respectively.

Conclusion: Dual-isocenter plan significantly reduced the total lung dose for synchronous bilateral breast cancer patients compared with mono-isocenter plan and did not affecte the PTV CI and HI. With the similar treatment time but significantly better dose distribution for total lung, we think the dual-isocenter VMAT technique more suitable for synchronous bilateral breast.

Keywords: mono-isocenter VMAT, dual-isocenter VMAT, synchronous bilateral breast

Remote Monte Carlo verification system of radiotherapy with multiple processor

Hiraku Fuse[1], Kenji Yasue[2], Tatsuya Fujisaki[1], Shinji Abe[1]

1 Department of Radiological Sciences, Ibaraki Prefectural University of Health Sciences,
2 Graduate School of Health Sciences, Ibaraki Prefectural University of Health Sciences.

Introduction: The indications for radiation therapy are widely used in many areas, and in the body where low density and high-density substances are mixed, calculation may be difficult with a commercial treatment planning device, and its verification may be similarly difficult. Several algorithms installed in the general-purpose treatment planning device, are reported to have 5% uncertainty compared to Monte carlo simulation (MC). Verification by MC is effective to guarantee the quality of the treatment plan in the heterogeneous area created by the commercial treatment planning device.

Purpose: To verify the dose distribution created in the treatment planning system, highly accurate remote MC simulation system developed based on multiple processors server. Also, the interface for sending and receiving data with DICOM-RT was created so that medical institutions can compare and verify the dose distribution.

Methods: This computing system has two configurations of Intel Xeon Phi Processor mounted cluster with storage server as compute node as login node accessed by user. The MC code used for dose calculation was EGSnrc. The linac head model can be selected according to the medical institution's linac by the Web access interface. Finally, generated dose distribution data (3 ddose file) were used to verify the dose distribution from treatment planning.

Results: VMAT produces a dose distribution with a 2σ uncertainty of around 3% in the PTV, while for Breast Tangential irradiation, history is increased due to fewer beams, below 2% in the PTV. It was confirmed that the dose distributions in heterogeneity differed by up to 6%.

Conclusion: Differences in dose distribution due to inhomogeneity in the head and neck and spread of dose distribution in the lung were clarified by MC simulation.

Keywords: Remote treatment planning verification, Monte Carlo, Radiotherapy

Detection of multi-leaf collimator errors in a small-field volumetric modulated arc therapy plan using portal dosimetry

Yuichi Saito[1], Suguru Kimura[1], Hiroaki Kobayashi[1], Kohei Shibayama[1], Takahisa Suzuki[1], Koudai Hoshino[1], Yuki Murayama[1], Kento Miyata[1], Katsumi Shima[1]

1 National Hospital Organization Hokkaido Cancer Center, Sapporo, Hokkaido, 003-0804, Japan

Introduction: In volumetric modulated arc therapy (VMAT), multi-leaf collimator (MLC) errors cause significant dose discrepancy, especially in small fields. Therefore, patient-specific quality assurance (QA) using any metrics should be performed to detect MLC errors in advance.

Purpose: This study was conducted to investigate the effect of MLC errors on dose distribution in small-field VMAT plans and to determine the suitable criteria for detecting MLC errors using the gamma index in portal dosimetry (PD) for patient-specific QA.

Methods: A small-field VMAT plan for a sphere considered as a PTV of 1-cm diameter in the phantom was created as an original plan. The original plan was modified according to the following three error types: (1) both MLC banks are open, (2) both MLC banks are closed, and (3) both MLC banks are shifted. The sizes of MLC errors for the original plan were 0.2 and 0.5 mm, respectively. The predicted fluence of the original plan was calculated in a treatment planning system, and the fluence of the original plan and error plans were measured by EPID. The consistency of the predicted and measured fluence distribution was evaluated using the gamma index of 2%/0.5 and 1%/1 mm.

Result: The minimum MLC errors that failed the >95% criteria with the gamma index of 2%/0.5 mm were (1) 0.2 mm, (2) 0.2 mm, and (3) 0.5 mm, corresponding to the error types. In contrast, no MLC errors were detected with the gamma index of 1%/1 mm because all error plans passed the >95% criteria.

Conclusion: Small-field VMAT plans for a sphere of 1-cm diameter are required to pass the >95% criteria in the gamma index of 2%/0.5 mm, which was also determined as the criteria for detecting MLC errors in patient-specific QA with PD.

Keywords: Quality assurance, Portal dosimetry, Gamma-index

Focus control of electron beam for arbitrary field formation

Atsushi Myojoyama[1], Minami Nakao[1] and Hidetoshi Saitoh[1]

1 Graduate School of Tokyo Metropolitan University

Introduction: Currently, scanning irradiation is used to form irradiation fields in proton beam and heavy particle beam therapy. In contrast, electron beam therapy uses a mold and a bolus to form an appropriate dose distribution. If an equivalent dose distribution can be produced without using them, high-accuracy and short-time electron beam therapy can be realized. Moreover, if the irradiation field dependence of the electron beam is used, there is a possibility that the maximum treatment depth can be changed and the treatment depth can be adjusted by changing the size of the electron beam. In scanning irradiation with an electron beam, it is necessary to realize convergence and deflection of the electron beam with high accuracy.

Purpose: The purpose of this study was to confirm the convergence of the electron beam using a solenoid and its effect on the dose distribution by simulation.

Methods: Monte Carlo simulation was performed using Geant4, and the solenoid conditions suitable for convergence control were obtained. The simulation geometry assumed that a solenoid coil was attached to the accelerator gantry. When the energy of the electron beam was changed, the magnetic flux density was changed, and the solenoid shape was devised.

Results: From the result of Monte Carlo simulation, it was confirmed that the electron beam could be converged by using a solenoid. It was suggested that the conditions suitable for convergence differ depending on the energy of the electron beam, and the conditions of the appropriate solenoid differ, and that the solenoids of the same size and shape can be used for all energies by adjusting the applied voltage.

Conclusion: It was confirmed that the electron beam was converged by Lorentz force based on the theoretical formula when irradiated in a magnetic field. Detailed experiments are ongoing.

Keywords: Monte Carlo, Geant4, electron beam therapy

Feasibility test of independent dose verification with Monte Carlo simulation tool at Osaka Heavy Ion Therapy Center

Taku Nakaji[1], Masaaki Takashina[2], Masashi Yagi[3], Noriaki Hamatani[2], Toshiro Tsubouchi[2], Tastuaki Kanai[2]

1 QST hospital, National Institutes for Quantum and Radiological Science and Technology,
2 Osaka Heavy Ion Therapy Center,
3 Graduate School of Medicine, Osaka University

Introduction: Osaka Heavy Ion Therapy Center (HIMAK) is the clinic facility dedicated to carbon ion radiotherapy (CIRT) and adopts the hybrid depth scanning system. One of our tasks is the development of effective and efficiency dose verification tool for patient-specific QA for CIRT. It is based on 3D dose distribution data calculated by the Monte Carlo code. Therapeutic C-ion beams were modelled in PTSim framework mounted over Monte Carlo toolkit Geant4 (version 10.02.p03) with beam line constructions, including peculiar ripple filter, wire monitors, etc. Moreover, the development of the system for dose verification of volume irradiation was attempted.

Purpose: The purpose of this study is the verification of dose distribution based on Monte Carlo simulation (MCS).

Methods: This feasibility study consists of two steps; one is for MCS of spot beams, other is for volume irradiation. In the first step, the adjustment of parameters for incident beams was carried out to realize the measured dose distributions in MCS. This modification was based on measured three profiles, which were the integrated dose distribution in water with the Stingray ion chamber (IBA dosimetry), lateral dose distribution at the several depths in air with 2D scintillator XRV-2000 (Logos Systems) and same one in water 3D pinpoint chamber (PTW) for the therapeutic carbon ion spot beams. In the second step, the comparison between the measurements and calculations of the point dose at center of pattern irradiations was performed. These pattern irradiations have rectangular arrangements of irradiation spots with inside length from 0 to 84 mm and outside length from 18 to 96 mm, and measured at several water depths.

Results: Calculation doses were reproduced by the arrangements of 3D dose distribution of one spot beam simulated by MCS.

Conclusion: The system for dose verification of volume irradiation in water was developed.

Keywords: Carbon ion radiotherapy, Monte Carlo simulation, Dose verification

Development of method to cancel the calculation direction dependence for image processing applying diffusion equation

Kentaro Doi[1], Yusuke Anetai[2], Hideki Takegawa[2], Yuhei Koike[2], Satoaki Nakamura[2], and Masahiko Koizumi[1]

1 Department of Medical Physics and Engineering, Osaka University Graduate School of Medicine, Osaka, Japan,
2 Department of Radiation Oncology, Kansai Medical University Hospital, Osaka, Japan

Introduction: Manually extracting bone metastases (BM) lesions from computed tomography (CT) images generally depends on individual criteria and leads to overlooking lesions. Therefore, a system for efficiently extracting BM lesions (BML) is needed, and we are developing a BML extraction system for screening. We reported calculation model applying diffusion equation (DEQ) for BML extraction in the previous study. To improve the accuracy of calculation model, we developed a method for cancelling calculation direction dependence (CDD), which is well-known in numerical fluid physics fields.

Methods: DICOM CT images of multiple BM patients were used for DEQ calculation. The cases of calculation dependency for starting point (CSP) and end point (CEP) were verified. CSP was selected one of four corners and CEP was defined as the diagonal point of CSP. A total calculated image for evaluation was obtained as follows: (a) four image sets received DEQ calculation every 20 iterations of each CSP to CEP were combined by Hadamard products with normalization 0 to 1, and (b) one image set succeeded previous CSP to CEP calculation with rescaled to original CT value received 20 iterated DEQ calculation at each CSP to CEP respectively. Noise reduction were compared with from upper-left CSP to CEP DEQ calculated image as a control.

Results and Discussion: By using our methods successfully achieved noise reduction by 26% and 17% against the control, we achieved to cancel CDD and improved accuracy for our developing DEQ calculation model. However, further study is needed to differentiate between BML and physiological high CT value regions clearly.

Conclusion: We developed valid calculation methods to cancel CDD for our DEQ calculation system.

Keywords: Image processing, Diffusion equation, Bone metastasis

Impact of automatic image registration with contrast enhancement filter in head and neck cancer

Kouta Hirotaki[1,2], Akita Tsunemichi[1], Kitou Satoe[1], Moriya Syunsuke[3]

1 National Cancer Center Hospital East Department of Radiology
2 University of Tsukuba Master's Program in Medical Sciences
3 Graduate School of Comprehensive Human Sciences, University of Tsukuba

Introduction: Automatic image registration benefits from objectivity in the registrations as the registration quality is observer independent. Current image-guided proton beam therapy (IGPBT) utilize orthogonal two-dimensional (2D) kV X-ray images. Automatic image registration performance is dependent on the quality of the image and there is some preprocessing filter in commercial IGPBT systems.

Purpose: To evaluate the effectiveness of using the contrast enhancement filter for improvement of the matching accuracy of automatic image registration.

Methods: A retrospective analysis of 20 head and neck cancer patients who received proton beam therapy was performed. The 2D-kV images were acquired per fraction. Bone registration was performed on each pretreatment daily 2D-kV image using the VeriSuite software (MedCom, Germany). The algorithms used in the software were based on a mutual information algorithm. The weights of contrast enhancement filter were set 0%, 60%, 75%, and 95%. The accuracy of automatic image registration using different contrast enhancement filters were compared with the manual registration. A typically acceptable clinical specifications was set at <1.0 mm and <0.5 degree.

Results: The automatic image registration without filter (i.e. 0%-contrast enhancement filter) and with filter (i.e. 60%-, 75%-, and 95%-contrast enhancement filter) provided acceptable matches in >35.0% and >92.5% of registrations, respectively. The computed mean translational difference was 0.65±0.98 (mean±1SD), 0.32±0.37, 0.34±0.37, and 0.27±0.34 mm and the computed mean rotational difference was 0.71±1.32, 0.18±0.25, 0.16±0.20, and 0.08±0.11 degree in the 0%-, 60%-, 75%-, and 95%-contrast enhancement filter, respectively. The automatic registration using 95%-contrast enhancement filter achieved most similar registration to the manual registration.

Conclusion: Automatic image registration with the contrast enhancement filter would achieve a higher accuracy. The increase of weight may contribute to the improvement of the rotation-error.

Keywords: IGRT, Automatic image registration, 2D-Xray image, Head and Neck cancer

Development of facial recognition system for patient safety: Analysis of benchmark data

Takatomo Ezura[1,2], Atsushi Myojoyama[1], Terufumi Kusunoki[2] and Daisaku Yoshida[3]

1 Graduate School of Human Health Sciences, Tokyo Metropolitan University, Tokyo, JP
2 Division of Radiation Medical Physics, Kanagawa Cancer Center, Kanagawa, JP,
3 Department of Radiation Oncology, Kanagawa Cancer Center, Kanagawa, JP

Introduction: For patient safety, various clinics have implemented individual authentication methods using several identifiers. Facial recognition method does not require physical contact with the device for authentication and there is no risk of infection. Therefore, we have developed the facial recognition system using Xbox One Kinect sensor and facial mapping API. Our system has made it possible to identify individuals with a greater than 95 % probability. However, it was unclear whether the daily identification would be performed correctly.

Purpose: The purpose of this study is to quantitatively analyze the variability of daily scans as part of developing the present system.

Methods: Qt (ver.5.7.0) on Visual C++ 2015 was used as the development environment for the system. Kinect for Windows SDK 2.0, OpenCV 3.1 were applied as development libraries and MySQL was used as a database management system. For facial identification, arbitrary 31 points were selectively used from 1347 points of feature points, and the matching algorithm is based on the comparison of coordinates between facial characteristic points in a reference data and collected real-time data. To verify the accuracy of the system, the same person was scanned once or twice a day for 2 months and 80 facial mapping data were collected.

Results: In the current system environment, only one case deviated from the threshold range set for personal identification. The characteristic points with a small variability were located around the inner canthus and from the upper lip to below the nose, while the points of high movement were located on the whole nose and outer corners of the mouth.

Conclusion: This study clarified that a facial recognition system using Kinect sensor is correct for day-to-day identification. The present system was shown to have satisfactory performance for use in clinical practice.

Keywords: Radiation therapy, Patient safety, Facial recognition, Kinect

Development of Real – time Radioluminescence Dosimetry System for External Beam Radiotherapy: A Preliminary Study

Janatul Madinah Wahabi[1], Jeannie Wong Hsiu Ding[1], Ung Ngie Min[2], Ghafour Amouzad Mahdiraji[3,4]

1 Department of Biomedical Imaging, University of Malaya, Malaysia
2 Clinical Oncology Unit, University of Malaya, Malaysia
3 Dura-Mine Sdn. Bhd., Branang, Selangor, Malaysia
4 Flexilicate Sdn. Bhd., University of Malaya, Malaysia

Introduction: Radioluminescence (RL) dosimetry has been one of the options to determine the accuracy of radiotherapy beam. When ionising radiation strikes a scintillating material, light photons will be produced and guided to the photodetector where it will be counted. Hence relationship between ionising radiation and light signal can be established.

Purpose: This study explored the development of real – time RL dosimetry system by assembling a basic single point RL dosimetry system and verify the functionality of the assembled system in megavoltage (MV) photon range.

Methods: The system consists of a photomultiplier (PMT), a counter and a power supply. The sensor was made out of blue emitting plastic scintillator and the light signal generated was carried to the PMT by using optical fibre. Multiple doses of MV photon were delivered by using Linear Accelerator (LINAC) and the measured doses were analysed using Matlab.

Results: Difference of signals between permanent and non – permanent coupling was 21.42 %. Dose reduction of 95.03 % was observed when changing the fibre's core from 110 μm to 9 μm. Meanwhile reducing sampling time and optical fibre length also contributed to dose reduction. The system showed great stability with 0.1 % variation between readings.

Conclusion: The real – time RL dosimetry system was assembled and able to perform reliable dose measurement in MV photon range. Further development and verification of the system will be carried out to study the characteristics of the system.

Keywords: Radioluminescence, Real – time, Scintillator, Radiotherapy

Diagnostic

LORETA as a Method of Brain Activation Analysis for Autism Spectrum Disorder: an Evaluation using Traditional Benchmarks

Sra H. Pratama, Nita Handayani, Ernawatil Gani, Freddy Haryanto, and Siti N. Khotimah

Faculty of Mathematics and Natural Sciences, Institut Teknologi Bandung, Indonesia

Introduction: The prevalence of Autism Spectrum Disorder (ASD) is known to increase over the years globally. Various analysis methods have been developed worldwide to observe ASD using electroencephalography (EEG) measurement. A system named LORETA (Low-Resolution Brain Electromagnetic Tomography) is known as a relatively new and progressively developed method to analyse EEG signal. Previously, we have conducted EEG measurements on children with ASD and performed the analysis using several traditional methods and algorithms, such as power spectral analysis, interhemisphere coherence, and spectral entropy analysis. In this research, LORETA was employed to analyse the ASD data and compared with our previous findings as the benchmarks.

Purpose: This research aims to evaluate LORETA method in comparison to our previously conducted analysis methods on the ASD analysis.

Methods: For this study, 6 children with ASD and 5 normal children were recruited as the subjects (10-15 years old). The EEG recordings were conducted using Emotiv EPOC (14 channels). The EEG signal acquisitions were conducted on resting condition and closed eyes in 5 minutes duration. The acquired data were then normalized and filtered from unwanted noise and artefacts. The clean data were then analysed using LORETA system to evaluate the activated brain areas. A voxel-wise *t*-tests was used on LORETA to examine the ASD data compared to normal in six frequency bands. The results were then evaluated through comparison analysis with our previous employed methods and results.

Results: Differences on brain activation of children with ASD compared to normal were detected by LORETA on certain brain areas. Compared to our previous findings, the results from LORETA were mostly similar. A few differences of activated areas were found on LORETA.

Conclusion: LORETA was evaluated to work very well and showed close results with popular and traditional algorithm on EEG analysis for ASD condition, such as power spectral analysis and coherence. With its ability on detecting activated brain areas, the usage of LORETA for ASD analysis was found to enrich the previously conducted methods by showing more detail activated areas compared to traditional methods.

Keywords: Electroencephalography, LORETA, Autism Spectrum Disorder, power spectral analysis, functional connectivity

Material decomposition of photon-counting CT spectra with Machine Learning

Kazumi Murata[1] and Koichi Ogawa[2]

1 National Astronomical Observatory of Japan,
2 Faculty of Science and Engineering, Hosei University

Introduction: Photon-counting CT is an emergence technology which measures X-ray intensity with multiple energy bins. These data enable us to perform material decomposition and multi-contrast-agent imaging. However, simple material decomposition such as a singular value decomposition method is highly affected by statistical and systematic noises. Hence, material decomposition with less dependence on these noises should be provided.

Purpose: The aim of this study is to provide a machine-learning based method which simultaneously performs both denoising and material decomposition.

Methods: We performed a material-decomposition simulation using a photon-counting CT system with attenuation spectra with solutions having various concentrations of water, iodine, and gold. Statistical Gaussian noises with a standard deviation of 1% were also added to the spectra. Material decomposition was conducted on these spectra with a network similar to a denoising auto encoder. The network compressed input spectra and estimated concentration of each material, from which predicted spectra were produced. The optimization was conducted to minimize square of difference between predicted and input spectra.

Results: Our network successfully reduced the spectral noise; from 1.0% to 0.5 %. Furthermore, the concentrations produced from the network were consistent with the original values; The RMSEs were 0.7-0.8 wt% for all material (i.e. water, iodine, and gold). These results were valid for any concentrations adopted in this work.

Conclusion: Our results suggest that the material decomposition based on a machine-learning method is effective even for a spectrum with strong noises.

Keywords: photon-counting CT, material decomposition, machine learning

The Study of Correlation Between Water-equivalent Diameter (Dw) and Age on CT Examination in Pediatric Head Patient with Tube Current Modulation (TCM) Technique

Khoerun Nisa Syaja'ah[1], Choirul Anam[1], Freddy Haryanto[1], Idam Arif[1]

1 Department of Physics, Faculty of Mathematic and Natural Science, Institut Teknologi, Bandung, Indonesia

Introduction: Computed Tomography (CT) examination in pediatric head patient is sensitive to ionizing radiation with long-term risk effect to cell or tissue injury. In addition, the actual patient dose delivered during CT examinations has not been well-define especially when using tube current modulation (TCM) technique. The tube current is dynamically changed after on the patient size (region) along the Z-axis (longitudinal TCM).

Purpose: To calculate and compare the correlation between two parameters, Dw and age in pediatric head patient for tube current modulation (TCM) technique.

Methods: The data were retrospectively collected from CT head in the DICOM, six pediatric patients 0-12-year-old age groups were examined in Hasan Sadikin hospital using Somatom Definition Flash with variation in the number of slices. We calculate using programming python with automated contouring algorithm, there are two main parts in this step. The first is thresholding process and contouring using morphological gradient method after images CT data were read and converted to Hounsfield Units (HU). The second is calculating of Dw based on American Association of Physicists in Medicine (AAPM) report 220. The value of average Dw was correlated with age of patients using regression analysis.

Results: The result showed the average Dw of the age groups (0-6th years) were 9.6-12 cm, and it increases compared to the age of 7^{th} to reach 12^{th} years with the average value 13-15.6 cm. The Dw size was linearly correlated with R^2 values of 0.66 with gradient 0.85 and R^2 0.83 with gradient 0.06 for age and tube current, respectively.

Conclusion: The correlation between Dw and age in pediatric head patient for TCM technique indicates that the average Dw has changed and increased in comparison to every age group and the Dw was linearly correlated with patient age and average tube current.

Keywords: Water-equivalent Diameter (Dw), Tube Current Modulation (TCM), Age, CT, Automated Contouring

Spectral distortion correction caused by pulse-pileup effects with a machine learning technique for a photon counting x-ray detector

Kohei Koyama[1], Kazumi Murata[2,3], Koichi Ogawa[2]

1 Graduate School of Science and Engineering, Hosei University,
2 Faculty of Science and Engineering, Hosei University,
3 National Astronomical Observatory Japan

Introduction: Owing to the spectral capabilities, a photon counting CT system has generated considerable recent research interest. It can distinguish materials of target objects and enables us to perform a K-edge imaging. However, the photon-counting CT has a serious issue; spectral distortion mainly due to a pulse-pileup effect, which is caused by multiple photons simultaneously incident on the detector. In this work, we focus on the capability of nonlinear regression of machine learning and propose a neural network-based method to correct the spectral distortion.

Purpose: The aim of this study is to develop a neural-network based correction method of spectral distortion due to pulse-pileup effects for a photon-counting detector.

Methods: We investigated the feasibility of our method with a simulation. We produced a training network which transformed a distorted spectrum to an original spectrum. The distorted spectra were produced with an analytical pulse-pileup model for a non-paralyzable detector. The original spectra were obtained by using the IPEM program. We trained the network using distorted/original spectral pairs with various levels of pulse-pileup effects. The correction accuracy was investigated via a mean absolute error of output spectra from the trained network.

Results: Our trained network significantly reduced the spectral distortion and the output spectra were in good agreement with the original spectra for any pileup levels adopted in our study.

Conclusion: The results demonstrate the feasibility of our neural network-based correction method for spectral distortion caused by pulse-pileup effects.

Keywords: Photon-counting CT, Pulse-pileup, Distortion correction, Machine learning

The method to estimate source position for mobile tomosynthesis

Kensuke Hori[1], Takahisa Koike[1], Kiichi Tadano[1], Takeyuki Hashimoto[1]

1 Kyorin University Graduate School of Health Sciences

Introduction: Mobile x-ray radiography is often used for follow-ups in clinical. The tomosynthesis can reconstruct the tomogram and improve the quality of diagnosis. For the tomosynthesis reconstruction, the geometrical relationship between the source and the detector is critically needed. In mobile imaging, the geometry is adjusted by radiological technologist, but it is actually too difficult to keep the detector and the x-ray source in the same position. In this study, we developed the technique that can estimate the x-ray source position simultaneously with the tomosynthesis scan.

Purpose: The purpose of this study is to estimate the source position from the projection images using the markers.

Methods: We developed the marker panel that was consisted with a Styrofoam ($400\times300\times10$ mm^3) and four tungsten sheets ($20\times20\times1$ mm^3). While tomosynthesis scanning, the marker panel was attached to the detector and the position of projected markers was calculated by template matching. The x-ray source position was estimated by the position of projected markers and original markers. In this study, numerical simulation was performed.

Results and Discussions: The detector was placed in the xz plane and the y-axis perpendicularly directed to the source from the detector. The estimation error of source position was 2.08±2.35%, 3.36±1.22% and 0.00±0.00% in the x, y and z direction when the x-ray source moved along the x axis. The normalized root mean squared error of reconstructed image was about 20% and there were visually errors only in the edge part.

Conclusion: The method to estimate the x-ray source position was proposed and the error was less than few percent. This method was considered to be practically useful because it can be performed simultaneously with the tomosynthesis scan.

Keywords: Tomosynthesis, mobile imaging, estimation of source location

Evaluation method of isotropic performance of CT system using "Spiral Micro Holes Phantom"

Katsumi Tsujioka[1], Yujiro Doi[2], Kyohei Yamada[3], Masato Yoshida[3], Masayoshi Niwa[3]

1 Faculty of Radiological Technology, School of Health Sciences, Fujita Health University,
2 Department of Radiology, Fujita Health University Hospital,
3 Department of Radiology, Yokkaichi Municipal Hospital

Introduction: In CT, not only the X-Y plane but the spatial resolution in the Z-axis direction is the target of image evaluation. However, conventionally, the spatial resolutions in the X-Y plane and the Z-axis direction have been evaluated separately. We propose isotropic performance as a method to simultaneously evaluate the spatial resolution in the X-Y plane and the Z-axis direction.

Purpose: We report on evaluation methods of isotropic performance using "Spiral Micro Holes Phantom" for CT systems.

Methods: This phantom is made of an acrylic Column with 40mm diameter. We used two types of phantoms. Phantom A has holes with diameter of 0.5mm and phantom B has holes with diameter of 0.3mm. CT scans were performed with the long axis of phantom placed parallel to the X-Y plane of the CT system. For the experiment, we used a conventional CT system and an UHR-CT system. MinIP, VE and curved MPR were performed on the obtained volume data, and the displaying of the holes in each direction was studied.

Results: In the MinIP, since the air layer of the acrylic Column is detected, the comparison between the X-Y plane to the Z axis was performed accurately. VE and curved MPR were able to be evaluated continuously from the X - Y plane to the Z axis.

Conclusion: In clinical image diagnosis, MPR, MIP, MinIP, VR and VE are performed for each case. Evaluation by Spiral Micro Holes Phantom is also useful for explaining the characteristics of each display method to the radiologist.

Keywords: computed tomography, Image quality, Spatial resolution, Isotropic performance, Phantom

Effect of Various Hybrid Iterative Reconstruction Method on High Resolution Scan Mode in Abdominal CT

Masato Yoshida[1], Masayoshi Niwa[1], Yasukata Takahashi[1], Yosuke Kuratani[1], Katsumi Tsujioka[2]

1 Department of Radiology, Yokkaichi Municipal Hospital,
2 Faculty of Radiological Technology, School of Health Sciences, Fujita Health University

Introduction: Discovery CT750HD (GE Healthcare) is equipped with High Resolution scan mode (HRmode). Recently, it became possible to use new generation adaptive statistical iterative reconstruction (ASiR-V) on the data scanned not only with conventional scan mode (NRmode) but also with HRmode. If HRmode can provide good low-contrast detectability by using ASiR-V, we use HRmode in more cases requiring high resolution. [1]

Purpose: The goal of our study was to evaluate image quality improvement by using ASiR-V on the data scanned with NRmode and HRmode in comparison to conventional Hybrid IR method (ASiR).

Methods: We scanned Catphan604 (Phantom Laboratory) and a columned acryl phantom made for observer test with NRmode and HRmode, and reconstructed each of the scanned data with ASiR and ASiR-V. We measured task transfer function (TTF) by applying a radial edge technique to acryl rod inserted in Catphan604. We measured standard deviation (SD) and noise power spectrum (NPS) in the uniform region. We evaluated low-contrast detectability by requesting fifteen observers to evaluate the certainty of existence of a low contrast signal in images of a columned acryl phantom by continuously-distributed method.

Results: In the data scanned with HRmode, the NPS of ASiR-V was lower than that of ASiR at low frequency regions. Although the TTF of ASiR-V was lower than ASiR at low frequency regions, they coincided at high frequency regions. Observer test showed that positive certainty degree of ASiR-V was slightly higher than that of ASiR. When using ASiR-V on both scan modes, HRmode showed higher TTF and NPS than NRmode at high frequency regions. Positive and negative certainty degree of HRmode and NRmode roughly coincided from the result of observer test.

Conclusion: Using ASiR-V on the data scanned HRmode brought higher noise reduction rate than ASiR and good low-contrast detectability similar to NRmode.

Keywords: computed tomography, iteractive reconstruction, high resolution, low contrast

Investigation on dose assessment and image quality evaluation of selected dental fillings in dental radiography.

Nur Aina Najwa Mohamad Feriza[1], Amira Nabila Yahaya[1], Yasmin Md Radzi[1], Ramzun Maizan Ramli[1]

1 School of Physics, Universiti Sains Malaysia, Penang, Malaysia.

Introduction: Dental radiography accounts for the most examination perform in diagnostic x-ray imaging by giving small dose of ionizing radiation to produce image of the internal structure of the mouth. Variation of tube voltage affects the radiation dose delivered which correspond to biological risks to adjacent soft tissues and image quality produced. Hence, optimum tube voltage is needed for producing good quality of dental radiograph with the lowest possible of absorbed dose by the oral sensitive tissues.

Purpose: This study was to investigate the optimisation parameter between the absorbed dose and image quality assessment on selected dental fillings (composite and amalgam) under the diagnostic x-ray range and estimate dose absorbed by the surrounding vital oral soft tissues.

Methods: Studies were conducted by using two types of dental fillings (amalgam and composite) embedded in a teeth model that was attached with borax slime to represent the surrounding tissues (tongue and lips). Absorbed dose measurement was performed by varying tube voltage potential using calibrated Thermoluminescence (TLD) detector chips were placed on the dental fillings and the soft tissues. by each of the material and analysing the image quality produced in terms of optical density and signal-to-noise-ratio. Evaluation of image quality in terms of signal-to-noise ratio (SNR) and optical density (OD) were observed respectively.

Results: The absorbed dose to the dental fillings was increased as kVp increased. A similar trend was observed in the estimation of dose absorbed by the adjacent soft tissues created within the teeth model. For image quality assessment, the optical density seemed to be increased as the kVp increased while the signal-to-noise ratio decreased as the kVp increased.

Conclusion: It is essential to determine the optimum tube voltage for good image quality while sparing healthy oral soft tissues like lips and tongue.

Keywords: Dental radiograph, amalgam restoration, composite restoration, absorbed dose, image quality

Image Quality Evaluation of a Hybrid Iterative Reconstruction Algorithm in the Multi-Slice Computed Tomography Scanner for the Pediatric Head Diagnostic Procedure

Mark Anthony C. Burgonio[1], Princess Jara M. Castillo[2], Janet Caraan[2], Nathaniel De Vera[2], Roland Cristopher Caballar[1,3] and Agnette P. Peralta[1]

1 The Graduate School, University of Santo Tomas, España Blvd. Sampaloc Manila, 1008 Philippines
2 Ancillary Services, St. Luke's Medical Center, Quezon City, 1112 Philippines
3 Department of Radiological Sciences, Quirino Memorial Medical Center, Quezon City, 1109 Philippines

Despite high radiation doses from computed tomography (CT), pediatric head CT procedures have increased. Dose reduction protocols – such as the iterative reconstruction (IR) algorithm – have been developed. Dose reduction is essential, especially for children. However, it is also necessary to ensure that the implementation of a dose reduction CT protocol does not degrade CT image quality. This study focused on the image quality characteristics and dose reduction capability of the hybrid IR algorithm in the 256-slice CT scanner of St. Luke's Medical Center-Quezon City for the pediatric head diagnostic procedure. The ACR CT phantom was used for image quality evaluation. The displayed $CTDI_{vol}$ values were used for dose reduction assessment. For the image quality evaluation, the calculated objective metric parameters were the contrast-to-noise ratio (CNR), signal-to-noise ratio (SNR), standard deviation (SD), noise power spectrum (NPS), modulation transfer function (MTF) and task transfer function (TTF). Three different pediatric age groups were considered. First, the parameters were determined from the images produced at the tube current-time product (mAs) and the filtered backprojection (FBP) algorithm currently used. The mAs values were then reduced and the different level settings of the hybrid IR algorithm were applied. The CNR and SNR increased, the SD and NPS_r peak curve amplitude decreased, and the spatial resolution improved for the images reconstructed using the hybrid IR algorithm. The noise texture appearance of images reconstructed at different level settings of the hybrid IR algorithm became smoother and less grainy when compared to the FBP images. The hybrid IR algorithm also showed a $CTDI_{vol}$ reduction of 8.42% to 26.19% without degrading image quality. Moreover, it has been shown that reduced mAs setting paired with specific hybrid IR level for each age group could be utilized in a dose-reduced pediatric brain plain CT protocol.

Keywords: Computed Tomography, Hybrid Iterative Reconstruction Algorithm, Dose Reduction, Image Quality

Denoising of OCT images with a bandelet transform for feature extractions

Keito Sato[1], Kazumi Murata[2,3], Koichi Ogawa[2]

1 Graduate School of Science and Engineering, Hosei University,
2 Faculty of Science and Engineering, Hosei University,
3 National Astronomical Observatory Japan

Introduction: Optical coherence tomography (OCT) is a diagnostic imaging system for ophthalmologic applications. Making use of interferometry, the OCT system provides high resolution images, from which retinal layers are extracted for ophthalmologic diagnostics. However, the images tend to be degraded by speckle noise produced by coherent light. Although many studies have addressed this issue, the state-of-the-art noise reduction method is still far from optimal. In this work, we focus on the layer shape as *a priori* knowledge and produce a denoising method based on a bandelet transform.

Purpose: The aim of this study is to provide a new bandelet-based denoising method optimized for feature extractions from OCT images.

Methods: We investigated the feasibility of our method with real OCT images. The proposed method identified the directions of retinal layers in the OCT images with the bandelet transform and smoothed the images along with the directions. This analysis produced a flat profile of each layer.

Results: Our method successfully reduced the noise in the OCT images along the direction of each layer without degradation of detail features. This enables us to easily extract each retinal layer.

Conclusion: The results suggest that out method is appropriate for noise reduction in OCT images for feature extractions.

Keywords: optical coherence tomography, denoising, bandelet transform, wavelet transform

Comparison of compensation effect for non-uniform magnetic field with major grains

Kouhei Nakanishi [1], Keita Someya[1]

1 Department of Radiology, Akita Hospital, Chiryu, Japan

Introduction: It was reported that rice and wheat flour are useful for compensation of non-uniform fat suppression in MRI because they compensate non-uniform magnetic field which is due to difference of magnetic susceptibilities of air and patient's body. However, availability of other grains for the compensation is not unclear.

Purpose: The purpose of this study was to clarify availability of soybean, potato and corn for compensation for non-uniform magnetic field.

Methods: We developed a phantom using agar and purified water. The phantom had cylindrical empty structure at center. With a 1.5-tesla MR imaging system (Vantage Elan, Canon Medical Systems), we acquired images of the phantom of which cavity filled with commercial rice, corn starch, potato starch, roasted soybean flour and barium sulfate, respectively. We compared distortion of images which were acquired with 2-dimensional EPI.

Results: The reduction of susceptibility artifacts in images of phantom filled with corm and potato starch were similar to that with rice.

Conclusion: Corn and potato can be inexpensive alternative to rice and flour for compensation for non-uniform magnetic field. The method is promising for not only diagnosis image but also image for treatment planning.

Keywords: MRI, non-uniformity, susceptibility artifact, compensation, magnetic field

Metal Artifact Reduction using Tilt Scan Technique in CT

Katsumi Tsujioka[1], Yujiro Doi[2], Kyohei Yamada[3], Masato Yoshida[3], Masayoshi Niwa[3]

1 Faculty of Radiological Technology, School of Health Sciences, Fujita Health University,
2 Department of Radiology, Fujita Health University Hospital,
3 Department of Radiology, Yokkaichi Municipal Hospital

Introduction: In clinical CT examination, metal artifacts caused by screw bolt fixed in the posterior lumbar interbody become a problem. In particular, loose bolts may not be accurately diagnosed due to the occurrence of metal artifacts. In this case, the major axis of the bolt and the scan plane are often in parallel.

Purpose: In this report, we discuss the reduction of metal artifact by tilting the gantry during CT scan.

Methods: The phantom has a brass rod with a diameter of 8mm and a different length, and an acrylic surface is placed on the tips of a brass rods. The gap between the brass rod and the acrylic surface can be changed to 0mm, 2mm. We performed a self-made phantom scan at tilt angles of 0 and 30degrees, visual evaluation of metal artifacts on coronal and sagittal surfaces in MPR display, and measurement of gap between brass rod and acrylic surface.

Results: The occurrence of metal artifacts due to metal bars is due to beam hardening. Metal artifacts could be reduced by tilting the CT. Especially, it is clinically effective to be able to accurately perform the gap of the tip of the brass rod.

Conclusion: Currently, many CT devices cannot perform gantry tilt. However, gantry tilt is effective in reducing metal artifacts. In addition, gantry tilt is also effective in reducing exposure dose to the patient's eye.

Keywords: computed tomography, Metal Artifact, Gantry tilt, Image quality

Bone mineral density screening in a rural population, Ayutthaya, Thailand

Chatnapa Nuntue[1], Khemipa Sanklaa[1]

1 Department of Radiological technology, Faculty of Allied Health Science, Thammasat University

Introduction: Osteoporosis is one of the non-transmissible diseases that turn into a crucial challenge and it is relevant to the morbidity and increased prevalence fractures in the population.

Purpose: To assess the bone mineral density of rural population in the age group of 25-88 years by using calcaneus quantitative ultrasound bone densitometer.

Methods: One hundred and twenty-four people whose ages ranged from 25 to 88 years in Ayutthaya, Thailand participated in the bone mineral density screening using calcaneal ultrasound bone. Age, weight, height, bone mass index, working status, education, medication condition were recorded.

Results: Out of 75 women, 25.3% and 17.3% had osteopenia and osteoporosis, respectively. Mean age was 53.33±17.63 years (25 to 82 years). Within 49 males, 30.6% and 16.3% had osteopenia and osteoporosis, respectively. Mean age was 53.10±18.54 years (26 to 88 years). Body Mass Index range between 12.8 to 40.23. Work is another factor that contributed to low bone mass. Based on 124 subjects collected, approximately 62.1% who does not work has osteoporosis compared to 38.9% who are working.

Conclusion: Approximately 50% of women and men had low bone mass. The working status and aging were the main detriments.

Keywords: Bone density, Ultrasound bone densitometer, osteoporosis, aging

The study of Power Spectral Density Value Ratio between Wet and Dry Electrodes with Electroencephalography (EEG) Using Audio Stimulus

Nur Faadhilah Afif*, Ernawatil Gani, Sra Harke Pratama, Freddy Haryanto and Siti Nurul Khotimah

Faculty of Mathematics and Natural Sciences, Institut Teknologi Bandung, Indonesia
*E-mail: faadhilahafif18@gmail.com

Introduction: Electroencephalography (EEG) electrodes are divided into two types: dry and wet. Wet and dry electrodes have different amounts of propagation media. Wet electrodes have three propagation mediums which are the electrodes, the saline liquid and the head skin, while the dry electrodes have two media of propagation which are the electrodes and the head skin. The difference in the amount of propagation media between the two types of the electrodes are represented through the characteristic of Power Spectral Density (PSD) calculated from brain signal which is acquired by the receiver.

Purpose: The focus of this study was to determine the ratio of PSD value between wet and dry electrodes.

Methods: This study was conducted using Emotiv EPOC (wet) and Insight (dry). An audio stimulus that contains a story was chosen followed by a small task related to the story. The brainwave signals were acquired from eight males (20-25 years old) as the participant in this experiment. The data acquisition was performed in 36 minutes to maintain the stability of the two types of electrodes. Three minutes of recordings in resting condition were conducted on both before and after given audio stimulus. Audio stimulation followed by a small task was performed for 30 minutes. Data analysis methods included the pre-processing using bandpass filter and processing steps using Periodogram Welch.

Results: The result showed that the PSD of wet and dry electrodes were $1,34 \pm 0,55$ and $2,12 \pm 0,54$ (μv^2). So, the ratio of PSD value between wet and dry electrode was 0,63.

Conclusion: It was gathered that the differences of PSD value on both electrodes was high.

Keywords: Wet and Dry electrodes, Power Spectral Density (PSD), Periodogram Welch, Window Hanning

Investigating the current status of Medical Physics in Sri Lanka

Vijitha Ramanathan

Department of Radiography & Radiotherapy, Faculty of Allied Health Sciences, General Sir John Kotelawala Defence University, Werahera, Sri Lanka

Introduction: Medical physics plays a major role in medicine. It uses concepts, theories, and applications of physics in medicine to prevent, diagnosis, and treat the diseases. And the most important areas of medical physics are radiation oncology, radiology, nuclear medicine, and radiation protection.

Purpose: To investigate the current practice, education, staffing, continuous professional development program in medical physics.

Methods: Radiotherapy treatment centres were identified all over the Sri Lanka. All information about medical physics such as staffing, education, medical physicist requirement, and continuous development programs were collected by on site visit, conservation over the phone, and from other available cancer resources in Sri Lanka.

Results: There are 7 government and 2 private radiotherapy centres are currently available in Sri Lanka for about 21 million population. Total number of medical physicists are 38. Only 3 medical physicists are working in radiology departments as a diagnostic medical physicist. None of the medical physicists are involved directly in nuclear medicine in Sri Lanka. The minimum education requirement for medical physicist is special degree in physics which is a four-year program. The medical physicists are recruited by Sri Lanka Scientific Service (SLSS) in government radiotherapy treatment centres. The medical physicists are rarely involving in research and continuous development program.

Conclusion: The current status of medical physics in Sri Lanka is far behind the International Atomic Energy Agency (IAEA) recommendation. It is necessary to expand the medical physics service to diagnostic radiology and nuclear medicine as these areas also require dosimetry and radiation protection. The research activities need to be improved. Nationwide professional accreditation system for certification of medical physicist should be implemented.

Keywords: Medical physics, Radiation oncology, Sri Lanka

The role of a medical physicist in an advanced emergency pediatric hospital

Manabu Yoshimoto[1], Hiroyasu Iwasaki[1], Yuji Yonezawa[1], Makoto Hayashi[1], Masaki Andou[1], Manabu Iwata[1], Kazuya Takahashi[1], Junpei Kurokawa[1], Yuma Shibutami[1], Akari Murai[1], Ayaka Kumazawa[1], Ai Naitou[1], and Kyoka Kobayashi[1]

1 Aichi Children's Health and Medical Center, Japan

Introduction, Purpose: Our hospital specializes in advanced pediatric emergency care as a children's hospital, and promotes advanced team medical care before birth. Taking into account the trends in the radiation department, we will consider the future involvement, medical cooperation, and hospital contribution in the charge of the medical physicist.

Methods: Extract the latest trends and current status of each examination in the radiation department over the past five years, verify the current job description, and examine future job description.

Results: The results for each quarter (three months) show an increasing trend on average for radiological examinations that are less affected by time frames other than CT, MRI, Radio Isotope, Cardio angiography. The number of images taken per 100 patients per year is about twice that of 5 years ago.

In the radiation department

- Enhancement of safety management of radiation equipment.
- Selection of radiation dose that understands the output characteristics of each device.
- Reduction of radiation exposure of radiologists in pediatric imaging.
- Participating in conferences before some examinations.

Currently focusing on the above items.

Conclusion: As necessary items for the number of examinations that are increasing year by year, there are problems of safety management of radiation equipment, proper use of radiation equipment including radiation dose, and radiation exposure of medical personnel. As a short-term goal, it is considered necessary for radiation technologists to select an appropriate radiation dose by taking into account factors such as age, body shape, and past images when taking images by reducing radiation exposure. From a long-term perspective, team medical care is very important, and strengthening collaboration with various occupations, including participation in meetings, is a major issue. We would like to continue our efforts as a facility that can efficiently provide high-quality and appropriate medical care for children.

Keywords: Medical physicist, Reduction of exposure, Pediatric medical

Deploying Long Short-Term Memory (LSTM) Network to Classify EEG Signal for Epileptic Seizure Detection

Achmad M. Gani, Freddy Haryanto, Sra H. Pratama, and Siti N. Khotimah

Faculty of Mathematics and Natural Sciences, Institut Teknologi Bandung, Indonesia

Introduction: Electroencephalography (EEG) is an electrophysiological monitoring method to tracks and record brain wave patterns. The emerge of epileptic seizure in brain wave is sometimes unidentified by visual inspection. In this research, multiple domain feature extraction is developed to tackle this problem since it offers a wide range of important information that is fed into the classification system.

Purpose: The aim of this research is to design a robust signal processing algorithm that extracts epilepsy information and classify the diagnosed patients according to the epilepsy detection algorithm.

Methods: The subject recordings were based on CHB-MIT datasets, grouped into 23 cases, collected from 22 subjects which consist of 5 males and 17 females in the 3-22 age range. The Discrete Wavelet Transform (DWT) and Statistical Moments were implemented for extracting the spectral and temporal information of epileptic seizures. The spectral analysis aimed to extract the brain rhythmic information, while the temporal analysis aimed to extract the distribution insights between seizure and non-seizures. The wavelet was used to divide a signal in the sum of scaled and shifted versions of the wavelet function and the wavelet coefficients were computed. The performance of the designed classification algorithm was then tested to the epilepsy dataset.

Results: The results show that the system achieved high accuracy in determining each class, providing reasonable seizure prediction sensitivity and specificity.

Conclusion: The developed method and algorithms are reliable as the automatic detection and classification of epileptic seizure from EEG dataset.

Keywords: Electroencephalography, Epileptic seizure, Long Short-Term Memory, Automatic detection

Using Radial Basis Function-Kernel Support Vector Machine with Tree-Based Feature Selection for Cancer Type Prediction Based from Gene Expressions

Adrian S. Remigio

School of Science, Royal Melbourne Institute of Technology, Australia

Introduction: Different treatment responses, survival characteristics and proliferation rate among different cancer types are attributed to their variation of genotypes. Gene expression analysis in conjunction with machine learning methods are helpful tools in cancer diagnosis and treatment prognosis.

Purpose: Our study aims to develop a cancer type classifier with reduced gene expressions required using tree-based feature selection.

Methods: Dataset was obtained from the Pan-cancer analysis project, which contains 801 patients with 5 different cancer types and 20,531 gene expression measurements. Gini impurity function from decision trees was used to rank the 20,531 in terms of feature importance for the cancer type classification. The top 5 genes with the smallest impurities were utilized as features for the support vector machine (SVM). Radial basis function (RBF) kernel was implemented for the hyperplane or decision boundary in the SVM classification method.

Results: Results show that the sets of genes obtained resulted in high accuracy for the SVM. Density distribution of selected gene expressions provide an illustration of differences in gene expressions for different cancer types, which supports further the outcome of feature selection.

Conclusion: Although the gene expression feature space was greatly reduced from 20,531 to 5, the accuracy scores of the developed classifier range from 0.955 to 0.980. Thus, 5 gene expression are sufficient for 5 cancer type classification, reducing the need for gene expression measurements from thousands of genes.

Keywords: Cancer type, Feature space, Hyperplane

CT-based convolutional-neural-network segmentation of poorly differentiated HCCs with lung-cancer-based transfer learning

Noriyuki Nagami[1,2], Hidetaka Arimura[3], Junichi Nojiri[4], Kenta Ninomiya[2], Reika Ohgushi[1], Satoshi Takita[1], Manabu Ogata[1], Shigetoshi Kitamura[1], Hiroyuki Irie[4]

1 Department of Radiology, Saga University Hospital
2 Graduate School of Medical Sciences, Kyushu University
3 Faculty of Medical Sciences, Kyushu University
4 Department of Radiology, Faculty of Medicine, Saga University

Introduction: According to the guideline for modified response evaluation criteria in solid tumors assessment for hepatocellular carcinoma (HCC), the one of important factors in decision making of HCC treatment strategies is the longest viable tumor diameter, which should be correctly and automatically measured on contrast-enhanced arterial phase computed tomography (CT) images to reduce inter- and intra-observer variabilities. Transfer learning of convolutional-neural-network (CNN) pretrained by a lung cancer segmentation task to segmentation of HCC regions may be promising due to the larger number of lung cancer patients than that of HCC patients.

Purpose: To investigate CT-based CNN segmentation of HCC regions with transfer learning based on lung cancer data.

Methods: Sixty cases with poorly differentiated HCC, who received treatments based on tumor size, underlying liver disease and functional status of the patient, were selected from HCC patients. A deep learning architecture was a tensor-flow-based open-source CNNs (NiftyNet) for researches in medical imaging. The CNN model pre-trained with lung cancer CT images was retrained as an HCC-CNN segmentation model to segment HCC regions using CT images in training datasets. An average Dice's similarity coefficient (DSC) and Hausdorff distance (HD) were employed for evaluation of the segmentation accuracy based on a 5-fold cross-validation test. The DSC denotes the degree of region similarity between HCC regions annotated by a radiologist and the regions estimated with the proposed model. The HD is defined as the distance that measures how far two subsets of a metric space are from each other.

Results: The proposed segmentation model achieved the average DSC of 0.783 ± 0.09 and HD of 2.15 ± 1.46 mm, whereas the model without pre-training produced the average DSC of 0.665 ± 0.16 and HD of 3.03 ± 2.26 mm.

Conclusion: The proposed approach with lung-cancer-based transfer learning showed the potential to automatically delineate poorly differentiated HCC regions on CT images.

Keywords: deep learning, segmentation, transfer learning, HCC.

Fabrication of Bismuth-Polymer Composite for Additive Manufacturing of Radiation Shielding

Adam Effendi bin Ashaari[1], Yin How Wong[2], Hui Leng Choo[1] and Chai Hong Yeong[2]

1 School of Computer Science and Engineering, Taylor's University, 47500 Subang Jaya, Selangor
2 School of Medicine, Faculty of Health and Medical Sciences, Taylor's University, 47500 Subang Jaya, Selangor

Introduction: Fused deposition modeling (FDM) 3D printing is an additive manufacturing process capable of rapidly building three-dimensional computer-modeled objects. The technology offers an inexpensive and efficient technique to manufacture customized objects with intricate geometries using a simple printing process. Bismuth-based compounds, which share similar radiation attenuation properties with lead, has the potential to be used as alternative to the conventional radiation shielding produced from lead-based materials.

Purpose: The aim of this study was to investigate the feasibility of using a bismuth (Bi) and polyactic acid (PLA) composite material to fabricate customizable radiation shields through material extrusion additive manufacturing.

Methods: The Bi-PLA composite material with different Bi content has been formulated in this study. The Bi-PLA composite material then extruded into the 3D printing filament using single screw extruder. The Bi-PLA composite filament was used to 3D print a CAD designed model with a dimension of 3 x 3 x 1 mm. The X-ray attenuation ability of the prepared Bi-PLA composite sample were determined at different X-ray tube voltages (50–140 kV) using a general radiography unit.

Results: The CAD designed sample was successfully printed using the fabricated Bi-PLA composite filament. The X-ray attenuation ability of the Bi-PLA composite material increased with the increase in the thickness of the Bi-PLA composite samples. About 80% attenuation was achieved using Bi-PLA composite sample of ~3 mm thickness at 140 kV.

Conclusion: A novel 3D printing filament made of Bi-PLA (60:40) composite material has been successfully fabricated in this study. The filament can be used to print customized radiation shielding designs as a substitute to conventional lead-based materials.

Keywords: Additive manufacture, 3D Printing, Radiation Shielding, Bi-PLA composite

Change of $CTDI_{vol}$ in medical exposure management of computed tomography

Hiroki Ohtani[1], Kazuki Kitayama[1], Kojiro Ohno[1], Junya Yamamoto[1], Ryuki Kikuchi[1]

1 Teikyo University

Introduction: Despite displaying $CTDI_{vol}$ on equipment, this is not exposure of patient each. $CTDI_{vol}$ shows the same value of the same radiography conditions even if they differ in the patient's figure.

Purpose: The purpose of this research is to clarify change of $CTDI_{vol}$ by a patient's figure.

Methods: The pillar type acrylics phantom twisted in agar equivalent to water scanned by computed tomography. $CTDI_{vol}$ was measured using the ionization chamber. Change of $CTDI_{vol}$ at the time of transmuting the thickness on the surface of a phantom by fluctuating the layer of agar was investigated. The tube voltage for radiography was changed and same measurement was performed.

Results: $CTDI_{vol}$ of the theoretical value in tube voltage 100 kV and 200 kV did not change. $CTDI_{vol}$ of the actual measurement decreased with the increasing thickness of agar. The values of $CTDI_{vol}$ displayed on the screen of computed tomography equipment and $CTDI_{vol}$ measured using the dosimeter was different. As for reduction of $CTDI_{vol}$ accompanying thickness increase of the agar in an approximate expression, the actual measurement of 120kV became larger than the actual measurement of 100 kV.

Conclusion: It was confirmed that the difference of $CTDI_{vol}$ displayed on computed tomography equipment and an actual measurement changes with the differences in a patient's figure. Change appeared in the difference of $CTDI_{vol}$ and an actual measurement also by the difference in tube voltage.

Keywords: The diagnostic reference level, Radiation Safety, $CTDI_{vol}$, Medical Exposure, Radiation Protection

Effects of Quercetin on adipogenesis by studying the metabolic profiles by NMR

Aye Thidar Moe Moe[1], Jie Pan[2], Montree Tungjai[1], Chatchanok Udomtanakunchai[1], Suchart Kothan[1]

1 Department of Radiologic Technology, Faculty of Associated Medical Sciences, Chiang Mai University, Chiang Mai, Thailand, 50200
2 Shandong Provincial Key Laboratory of Animal Resistant Biology, College of Life Sciences, Shandong Normal University, Jinan, China, 250014

Introduction: Obesity is a major health obstacle for the modernized world. It is induced by the hypertrophy of adipocytes and proliferation of new adipocytes; two processes that are dependent on the regulation of adipocyte differentiation. Potential therapeutic agents that inhibit adipogenesis or increase adipocyte death by apoptosis could be important tools in preventing obesity. Quercetin, is one of the most common dietary flavanols with a well characterized in vitro antioxidant activity. It is found in fruits, vegetables, tea, wine, nuts, and seeds, and represents an integral part of the human diet. It has been shown to inhibit glucose uptake in isolated rat adipocytes and to increase lipolysis. It also reduces cell proliferation and causes cell cycle arrest and apoptosis in vitro experiments with various cell lines, including 3T3-L1 preadipocytes.

Purpose: To study the effects of Quercetin on the differentiation of mature adipocyte by examining the metabolites found in NMR

Methods: 3T3-L1 fibroblasts were maintained in high glucose complete DMEM containing Sodium Pyruvate at 37°C and 5% CO2. Cells were subcultured at 90% confluence and plated in 12-well plates at a density that allowed them to reach confluence in 3 days. At this point (day 0), cells were switched to MDI-differentiation medium (complete DMEM with BS, dexamethasone (1 μM), IBMX (0.5 μM), and insulin (1.5 μM)) for 8 days. Meanwhile, 6 wells were treated with Quercetin (10 μM). On Day8, MDI was switched to the original medium. At D16, the experiment was finished. Collected supernatant at D2, D8, D16, and cell palates at D16 were analyzed by NMR.

Results: The metabolites (glucose, lactate, citrate, acetate) found in quercetin containing supernatant is significantly lower than that of without quercetin in all D0, D8, and D16. All of the metabolic cells is reduced to about half of the control.

Conclusion: This finding suggested that quercetin can enhance the metabolism of 3T3-L1 cells in the adipogenesis process. These results showed that quercetin affected by mitochondrial biogenesis, mitochondrial membrane potential, oxidative respiration, and ATP anabolism.

Keywords: Quercetin, 3T3L1 preadipocytes, adipogenesis, NMR

Single-scan method for the inner ear in cone-beam computed tomography

Yuki HAYAKAWA[1], Mitsuharu OOSAWA[1], Yuka TAWADA[1], Ryousuke SANO[1], Masaru NAKAMURA[1]

1 Department of Radiology, Aichi Medical University Hospital

Introduction: Imaging of the inner ear in cone-beam computed tomography (CBCT) generally involves the double-scan method, in which the left and right inner ears are separately imaged. However, the CBCT system introduced by our institute is equipped with a wide range scan mode (field of view [FOV] 170 mm), and it is possible to scan both inner ears at the same time.

Purpose: This study aimed to use the single-scan method clinically and compare this method with the double-scan method.

Methods: For physical evaluation, a wire phantom was scanned at the center and the edge in CBCT, and the 10% modulation transfer function was calculated. For visual evaluation, head phantom images from the single-scan method were evaluated by otolaryngologist using five-level evaluation (excellent, very good, good, poor, and very poor) compared with the images from the double-scan method. Further, the exposure of the lens was measured by attaching optically stimulated luminescence dosimeters to the orbit of the head phantom, and the examination time was calculated from clinical cases. The scan parameters were as follows: double-scan method, 90 kV, 7 mA and FOV 100 mm; single-scan method, 90 kV, 10 mA and FOV 170 mm. The reconstruction parameters were as follows: double-scan method, slice thickness 0.5 mm; single-scan method, slice thickness 0.4 mm and FOV 100 mm using zoom reconstruction.

Results: There was a 5% decrease at the center and a 19% decrease at the edge for physical evaluation with the single-scan method compared with the double-scan method, but there was no significant difference for visual evaluation. Further, the single-scan method decreased the exposure of the lens by 20% and examination time by 28%.

Conclusion: Our findings suggest that the single-scan method for the inner ear in CBCT can be used clinically.

Keywords: inner ear, CBCT, scan method

Nuclear Medicine

Diagnostic performance of I-131 MIBG scintigraphy in 101 patients suspected for pheochromocytoma/paraganglioma: A comparison between visual and semi-quantitative planar analyses and a hybrid SPECT/CT imaging

Pikom Sirisopausa, M.D.[1], Chulaluk Komontri, PhD.[2], Jiraporn Sriprapaporn, M.D.[3]

1 Diagnostic Radiology and Nuclear Medicine Unit, National Cancer Institute of Thailand,
2 Division of Research Development, Faculty of Medicine, Siriraj Hospital,
3 Division of Nuclear Medicine, Department of Radiology, Faculty of Medicine Siriraj Hospital

Introduction: Pheochromocytoma and paraganglioma (PPGL) are rare diseases. The diagnosis is based on documentation of catecholamine excess by clinical context, biochemical testing, and imaging localization. I-131 MIBG imaging is a high specific imaging modality for these diseases. Due to impaired image quality of I-131 radionuclide, different techniques of image interpretation were compared.

Purpose: To compare the diagnostic performance of planar I-131 MIBG imaging using visual and semi-quantitative techniques and visual interpretation of SPECT/CT images in the diagnosis of PPGL.

Methods: This is a cross-sectional retrospective review of 101 consecutive patients, being suspected for PPGL. I-131 MIBG imaging was performed 24 hours and 48 hours after intravenous administration of 37 MBq I-131 MIBG. All I-131 MIBG images were blindly interpreted by two physicians. The planar images were read by visual analysis and semi-quantitative scoring (score 0-3, relative to uptake in the liver). In addition, I-131 MIBG SPECT/CT images were read as positive or negative. Pathological report had been used as a gold standard, otherwise clinical follow-up combined with a contrast CT scan was incorporated.

Results: Prevalence of PPGL was 45.5%. Total 214 lesions were studied, which 69 were pathologically proved. The sensitivity, specificity, and accuracy of planar images using visual analysis were 92.59%, 97.5%, and 96.26%, respectively. Those interpreted using semi-quantitative method were 92.59%, 96.88%, and 95.79%, respectively. In addition, those for I-131 MIBG SPECT/CT imaging were 90.48%, 98.26%, and 96.18%, respectively. Each technique shows similar diagnostic performance.

Conclusion: This study showed excellent diagnostic performance of I-131 MIBG scan for the diagnosis of PPGL, both interpreted by visual analysis and semi-quantitative techniques. SPECT/CT imaging provided additional benefit in a few cases with visualized physiologic adrenal gland uptake.

Keywords: I-131 MIBG; pheochromocytoma; paraganglioma; Semiquantitative; SPECT/CT

^{99m}Tc-Labeled Bismuth Nanoparticles for Contrast Enhancement in SPECT-CT Imaging: A Phantom Study

Fazizulafizi Madin[1], Azahari Kasbollah[2], Siti Selina Abd Hamid[2], Khairunisak Ab Razak[3], Aimi Anisa Asdi[1], Wan Fatihah Wan Sohaimi[4], Wan Nordiana Rahman[1]

1 School of Health Sciences, Universiti Sains Malaysia, Malaysia.
2 Medical Technology Department, Agensi Nuklear Malaysia, Malaysia
3 School of Materials and Mineral Resources Engineering, Universiti Sains Malaysia, Malaysia.
4 School of Medical Sciences, Universiti Sains Malaysia, Malaysia
Corresponding Author: wandiana@usm.my

Introduction: Dual modality Single Photon Emission Computed Tomography (SPECT) and computed tomography (CT) imaging has been playing an important role in nuclear medicine. The development of SPECT-CT not only provides high contrast anatomical details but also physiological and functional information that improved the cancer diagnosis. This dual modality imaging technique could be integrated with molecular imaging agent to enhance the contrast of the image and hence improved disease detection.

Purpose: The purpose of this study is to investigate the potential of ^{99m}Tc-Labeled Bismuth Nanoparticles (^{99m}Tc-BiNPs) as contrast agent to enhance SPECT-CT imaging.

Methods: The Bismuth Nanoparticles (BiNPs) were synthesized using hydrothermal process which yields rod shape BiNPs with diameter of 60 nm and length approximately around 5 μm in powders form. The BiNPs were diluted in phosphate buffer saline before being tagged to ^{99m}Tc. The ^{99m}Tc-BiNPs samples in vial were prepared into a custom-made phantom filled with water. Other samples prepared are ^{99m}Tc, BiNPs, H_2O and Iodine contrast agents. The phantom was scanned using Discovery NM/CT 670 Pro (GE Healthcare) with Low Energy High-Resolution (LEHR) collimator and 512×512 matrix size. CT imaging was carried out with a tube voltage of 120 kV, smart mA current and a slice thickness of 5 mm. Image reconstruction were conducted with 1.25 mm thickness and abdomen window. Hounsfield unit (HU) for each sample were analyzed.

Results: Our results show that ^{99m}Tc-BiNPs samples indicate higher contrast in term of Hounsfield Unit (HU) in comparison to SPECT-CT image of ^{99m}Tc alone. The maximum contrast with HU of 1135 is found for concentrated BiNPs samples followed by ^{99m}Tc-BiNPs with HU of 812. The HU for ^{99m}Tc, water and iodine are used for references which present with value of 2, 0, and 80 respectively. Additions of BiNPs are found to increase the opacity of CT image contrast.

Conclusion: Contrast agent offers a potential to assist the image analysis and interpretation by providing high quality anatomic information and aiding in functional detection. The ^{99m}Tc-BiNPs could be applied as contrast agent for use in SPECT-CT hybrid imaging systems due to their ability to increase contrast information. Further optimization might facilitate ^{99m}Tc-BiNPs as an effective contrast or molecular imaging agent for SPECT-CT imaging.

Keywords: ^{99m}Tc-BiNPs, SPECT-CT, Contrast agent

Image reconstruction method based on a deep learning in a multi-pinhole SPECT system

Hiroaki Konno[1], Michi Okoshi[1] Kazumi Murata[2], Koichi Ogawa[2]

1 Graduate School of Science and Engineering, Hosei University,
2 Faculty of Science and Engineering, Hosei University

Introduction: A multi-detector SPECT system equipped with multi-pinhole collimators has great advantages compared with a conventional one owing to a data acquisition without rotating a gamma camera. It reduces the data acquisition time and obtains dynamic information of tracers. However, it has a problem in the image reconstruction; reconstructed images are highly degraded when the size of a pinhole is large. This is caused by the exact detection probability could not be calculated and a correction method such as a 7-rays method could not compensate the influence of the large pinhole size. Hence, a new image reconstruction method is required for the case with a large pinhole collimator.

Purpose: We propose a deep-learning based image-reconstruction method for a multi-pinhole static SPECT system.

Methods: To investigate the feasibility of our method, we performed an image-reconstruction simulation. We constructed a CNN-based learning network which transforms an input sinogram into a reconstructed image. The input sinograms were obtained with Monte-Carlo simulations with a multi-pinhole static SPECT system.

Results: Our network successfully reconstructed the images and the spatial resolution was significantly higher than those with a conventional method.

Conclusion: Our results indicate that the machine-learning based method is effective for the image reconstruction of a multi-pinhole static SPECT system.

Keywords: SPECT, image reconstruction, deep learning

Improvement of the spatial resolution with a deconvolution method in a pinhole SPECT system

Michi Okoshi[1], Kazumi Murata[2], Koichi Ogawa[2]

1 Graduate School of Science and Engineering, Hosei University,
2 Faculty of Science and Engineering, Hosei University,

Introduction: As a conventional SPECT system rotates detectors to acquire projection data, it takes long time and cannot perform a dynamic study of an organ. In contrast, a multi-detector SPECT system with multi-pinhole collimator requires no detector rotation in data acquisition. In this pinhole SPECT system, the quality of images strongly depends on a pinhole size, i.e. a large pinhole size leads to high sensitivity but low spatial resolution. To improve the spatial resolution of reconstructed images, a 7-rays method is sometimes effective, but it requires large computation load to correct attenuation and scatter effects in the process of image reconstruction.

Purpose: The purpose of our study is to improve the spatial resolution of reconstructed images acquired with a multi-pinhole SPECT system.

Methods: To improve the spatial resolution, we used a deconvolution method. The deconvolution kernel used was a point spread function (PSF) of a point source located at the center of the imaging area. For simplicity, we used a single PSF measured with a pinhole at the center of the detector. The deconvolution process was performed on the projection plane. Several phantoms were used to confirm the feasibility of our proposed method.

Results: Reconstructed images were evaluated with a peak signal to noise ratio. The results showed that our proposed method could improve the spatial resolution of reconstructed images compared with that corrected with the 7-rays method.

Conclusion: The proposed deconvolution method in projection domain was effective to obtain a high spatial resolution image in a pinhole SPECT system.

Keywords: static SPECT system, pinhole collimator, deconvolution, point spread function

Estimated Radiation Dose Received By Resuscitation Providers Following the CPR Operation of a Patient Undergoing a Nuclear Medicine Studies

Paya Dardaranonda[1], Prapapan Saenbandit[2], Benjarat Dardaranonda[3]

1 Department of Radiation Oncology, Chonburi Cancer Hospital, Chonburi,
2 Department of Diagnostic Radiology and Nuclear Medicine, Chonburi Cancer Hospital, Chonburi,
3 Faculty of Medicine, Burapha University, Chonburi, THAILAND

Introduction: Emergency calls in nuclear medicine studies were reported. The resuscitation were operated by both radiological staff and the emergency team. This emergency team members were well-trained advance CPR professional. However, they were considered volunteers and non-radiation workers. Thus, radiation protection and radiation risk information providing were necessary and should be done by the radiation profession ethically.

Purpose: To estimate the radiation dose received by resuscitation providers from patient undergoing nuclear medicine studies.

Methods: The study was performed with 75 randomized patients underwent nuclear medicine studies of Tc99m MDP bone scan or Tc99m Multiple Gated Acquisition (MUGA) scan at the Department of Diagnostic Radiology and Nuclear Medicine, Chonburi Cancer Hospital. The Instant radiation dose rate in air were measured at 1.0 cm away from patient's body at positions according to pit crew CPR method including vertex, chest, lateral of forearm, and pelvis. Each position was measured at the first minute after Radiopharmaceutical injection, pre-voiding and post-voiding.

Results: The maximum dose rate at the vertex, chest, forearm, and pelvis were 202.77 μSvh^{-1}, 979.83 μSvh^{-1}, 652.85 μSvh^{-1}, 777.87 μSvh^{-1} respectively. The pre-voiding measurements showed the dose rate decreased from the first minute of 22.02%, 47.27%, and 36.15% at the positions of vertex, chest, and forearm respectively while the dose rate at pelvis was increased to 377.60%. The possible radiation dose received by resuscitation providers in 40 minutes of typical operation time were 0.135 mSv for the airway position, 0.653 mSv for the chest compression position, and 0.519 mSv for the medication and monitor position.

Conclusion: The resuscitation providers will receive radiation dose up to 0.653 mSv especially the CPR provider at the chest compression crew position. The CPR providers who are not radiation workers should be informed of the received dose and the risk. Pocket dosimeter was recommended for dose monitoring. To avoid any undesirable result, a specific nuclear medicine CPR guideline was established and practical drill was recommended. A further studies are recommended.

Keywords: Radiation Safety, Radiation Dose, Pit Crew CPR, Resuscitation Provider

Optimal administered activity for Tc99m MDP SPECT-Bone scan patients in relation to body mass index

Wasinee Thiangsook[1], Thanyalak Samphantharat[1], Siwaporn Rattanamanee[1], ***Anchali Krisanachinda[2]***

1 Department of Radiology, Faculty of Medicine, Prince of Songkla University,
2 Department of Radiology, Faculty of Medicine, Chulalongkorn Hospital

Introduction: Bone scan using radiopharmaceuticals, Tc99m-MDP, administered to the patients remains clinically useful until now because it provides an earlier diagnosis with more sensitive of cancer detection than many radiographic procedures. In practice, the administered activities in bone scan patients at the Division of Nuclear Medicine, Songklanagarind Hospital, is fixed at 740 MBq (20 mCi) for all patients (except in children), at all weights and sizes. These result in patients received unnecessary higher radiation doses.

Purpose: To determine the optimal administered activity of Tc99m-MDP in relation to BMI of bone scan patients

Methods: A retrospective study of 180 bone scan patients' data was collected and divided into five groups based on body mass index criteria. Each group is divided into four subgroups according to the dose levels by comparing the administered activity to the calculated activity base on the guideline of the IAEA. (1) a group with administered activity is less than the calculated activity (2) a group with administered activity is more than the calculated activity in the range of 10% (3) a group with administered activity is higher than the calculated activity between 10% and 20% and (4) a group with administered activity is higher than the calculated activity 20%. The qualitative and quantitative image quality was assessed.

Results: The result shows that administered activity in each group of BMI did not affect the image quality evaluated by both methods using two-way ANOVA testing.

Conclusion: The administered activity should be considered to optimize the patient radiation dose. Consequently, the administered activity can be calculated in relation to BMI without losing image quality.

Keywords: Body Mass Index, Administered Activity, Bone Scan, Technetium-99m MDP

Shielding Calculation for a Diagnostic Nuclear Medicine Facility

M.R.Z. Tecson[1, 2], A.K.M. Garcia[1], J.M.G.F. Gonzales[1, 2], J.D.O. De Guzman[1, 2], A.B. Galay[1, 2], N.A.A. Madrigal[1, 2], & M.M. Ramirez[1]

1 Medical Physics & Health Physics Services, Inc., 2310 Taft Ave., Malate, Manila, Philippines 1004,
2 The Graduate School, University of Santo Tomas, España Blvd. Sampaloc, Manila, Philippines 1008

Introduction: Nuclear medicine refers to the introduction of unsealed radionuclides into the body mostly to diagnose organ structures and assess bodily functions. Upon patient administration, the radiopharmaceuticals in the body are unsealed sources that emit additional doses to nearby areas. Consequently, the dose emitted can produce unacceptable public and occupational exposure on its surroundings. Therefore, radiation protection through an appropriate shielding design is necessary to limit the doses to their respective safe limits as recommended by ICRP 103.

Purpose: This paper aims to demonstrate a method for the shielding calculations, based on AAPM Task Group 108: PET and PET/CT Shielding Requirements and NCRP Report No. 147 recommendations, of a diagnostic nuclear medicine facility.

Methods: A method for the shielding calculations of a diagnostic nuclear medicine facility, based on the AAPM Task Group 108: PET and PET/CT Shielding Requirements and NCRP Report No. 147 recommendations, was demonstrated. It was applied to a proposed floor plan of a facility in conjunction to its proposed nuclear medicine services: PET/CT imaging, SPECT/CT imaging, DEXA, thread mill myocardial stress tests, and thyroid uptake probe measurements. The following radiation sources were considered: F-18, Tc-99m, I-131, I-125 and x-ray sources from CT and DEXA. Typical scan parameters in accordance to international standards and guidelines for each diagnostic procedure, the physical characteristics of each radiation source, the expected workload of the facility, and regulatory requirements were considered.

Results: The method was able to provide shielding requirements in terms of pure lead or concrete walls. Also, the method showed that areas with calculated doses lower than the weekly dose goal do not need radiation shielding.

Conclusion: The method demonstrated in this paper can be used for shielding calculations in a new nuclear medicine department. The proposed scan protocols and technical specifications of the equipment should be considered in performing shielding calculations. Prior to the completion of the construction, an on-site evaluation of the facility may be conducted. The "inspection is to verify that barriers are properly placed, contiguous and free of voids or defects; and the evaluation of shielding adequacy is to verify that barriers adequately attenuate exposures in nearby occupied areas to the relevant shielding design goal".

Keywords: Radiation Shielding, Nuclear Medicine, Radiopharmaceuticals, X-Rays, Shielding Calculation

Inter-laboratory comparisons of ring dosimeters in term of $H_p(0.07)$

Nittima Rungpin[1], Natch Rattanarungruangchai[1], Tanapol Dachviriyakij[2], Krittayot Koonkana[2], Tewit Tungkasereeruk[3]

1 Thailand Institute of Nuclear Technology, Bangkok, Thailand,
2 Office of Atoms for Peace, Thailand
3 Department of Medical sciences, Ministry of Public Health, Thailand

Introduction: The Inter-laboratory comparison programme was organized for setting up quality assurance for individual monitoring services laboratories to assist in implementation of measurement accuracy and on their quality control procedures.

Purpose: The overall objective of this inter-laboratory comparison programme was to verify the performance of ring dosimeters to improve standard and accuracy of personal dose equivalent evaluation to measure extremity ($H_p(0.07)$) for gamma and beta radiations.

Methods: OSL, nanoDot dosimeters inserted in ring dosimeters were provided in this inter-laboratory comparison to compare the assessment data in term of $H_p(0.07)$. Ring dosimeters attached on rod phantom were irradiated at beam qualities of Cs-137 and Sr-90. Air kerma for Cs-137 can traceable to National Institute Metrology of Japan (NMIJ) and absorbed dose for Sr-90 can traceable to Physikalisch-Techische Bundesanstalt (PTB).

Results: The ratios of $H_{\text{measured doses}}/H_{\text{reference doses}}$ after subtracting their background from three participants were calculated. For Cs-137 gamma dose comparison, the results were overestimated from all participants with maximum value around 15%. For Sr-90 beta dose comparison, most of the participant results were overestimated with maximum value around 10%.

Conclusion: The summary of inter-laboratories comparisons results for each irradiated qualities, reference doses and uncertainty (k=2), ratios of $H_{\text{measured doses}}/H_{\text{reference doses}}$ and number of participants that fulfil the “trumpet curve” limits. The results show a good performance between individual monitoring services laboratories.

Keywords: Inter-laboratory comparison, Extremity

Full Papers

Correlation of Ultrasound Attenuation Imaging versus MRI Proton Density Fat Fraction in Non-alcoholic Fatty Liver

Pantajaree Hiranrat[1], B.Sc., Surachate Siripongsakun[1], M.D., Kamonwan Soonklang[2], M.Sc., Chanisa Chotipanich[1], M.D.

1 Sonographer School, Faculty of Health Science Technology, Chulabhorn Royal Academy, Bangkok, Thailand,
2 Data Management Unit, HRH Princess Chulabhorn College of Medical Science, Chulabhorn Royal Academy, Bangkok, Thailand

Abstract

The purpose of this study was to evaluate correlations and interobserver liability of Attenuation Imaging (ATI) comparing with MRI-Proton Density Fat Fraction (PDFF) in the non-alcoholic fatty liver disease (NAFLD) patients. The NAFLD patient with available ATI and MRI-PDFF examination, excluding cirrhosis, history of significant alcohol drinking, and chronic liver condition were evaluated. Correlation of ATI and MRI-PDFF values and interobserver's concordance of ATI measurements were evaluated, using Spearman rank correlation and Cohen's kappa coefficient. Statistical significance is considered at 2 side p-value < 0.05. There were 62 patients included with an average BMI of 27.4 kg/m2. The correlation coefficient (r) of ATI vs MRI-PDFF were in moderate correlation (r = 0.63-0.69, p<0.001). With the highest correlation coefficient at right posterior segment measurement (r=0.69). The inter-observer reliability of two observers was 100% with the Cohen kappa coefficient of 1.00 (p < 0.001). ATI is a novel ultrasound method to quantify the degree of fat deposition with a good correlation to MRI-PDFF with high interobserver reliability. Obesity commonly associated with fatty liver may be an interfering factor of ATI measurement.

Keywords: Attenuation Imaging, Fatty liver, Steatosis, MRI-PDFF, MRE, NAFLD

1. INTRODUCTION

Non-alcoholic fatty liver disease (NAFLD) is the excessive quantity of triglyceride in the hepatocyte, which could also relate to liver impairment. Advancement of the disease process could induce liver inflammation, resulting in non-alcoholic steatohepatitis (NASH) which is one of the leading causes of hepatic cirrhosis and hepatocellular carcinoma (HCC) (1). The overall prevalence of NAFLD is estimated at 25.24%, 20-30%, and 9.26% in global, Western countries, and Asia, respectively (1, 2). NAFLD is commonly found in the obese population, associated with metabolic risk factors including type 2 diabetes mellitus, and hyperlipidemia. The estimated prevalence of NAFLD in the obese population who has body mass index (BMI) >25 kg/m^2, hyperlipidemia, and diabetic patients have been reported 67% - 94%, 50%, and 70%, respectively(3, 4).

The gold standard in the diagnosis of NAFLD depends on histopathology by liver biopsy, which is invasive. However, liver biopsy still has many disadvantages and complications; including, sampling error, bleeding, and infection risks. With the invasive risk and inappropriate use for monitoring of liver biopsy, non-invasive imaging method for diagnosis and quantification liver fat have been using as surrogate methods.

Conventional ultrasound is widely used for the detection of fatty liver because the ultrasound examination is inexpensive and widely accessible. Under routine liver ultrasound examination, bright liver score, a semi-quantitative scale, is used to grade hepatic steatosis by comparing liver parenchymal echogenicity to kidney and wall of hepatic vessels (5). Many studies showed a good correlation between bright liver score and liver biopsy in the detection of fatty liver (28, 29). However, liver bright score has limited sensitivity in detecting mild fatty liver (6), decreased sensitivity/specificity in high BMI patients (7).

To overcome the ultrasound limitations, the novel technique implemented in the ultrasound system for assessment of hepatic steatosis based on ultrasound attenuation properties has been developed. ATI (Canon Medical Systems Corporation, Otawara, Tochigi, Japan) as a potential tool for quantifying fat in the liver calculating the attenuation coefficient of ultrasound in tissue, presuming that higher fat composition will increase ultrasound attenuation. This method eliminated the interfering factors including time gain compensation and beam focusing in order to receive simple signal intensity profile of the sound to calculate attenuation coefficient of the liver (8, 9).

A few recent studies showed a moderate to high correlation between ATI and MRI-PDFF (r =0.66-0.81, p<0.001) (8, 9). Tada et al, have assessed the performance of ATI comparing with liver biopsy, showing good accuracy between 76.4-85.1% with area under the receiver operating characteristic curve (AUROC) between 0.85-0.91. However, in Tada et al study, the subgroup of the obese patient groups showed decrease diagnostic accuracy from 76-85% to 58-68% in the significant fatty liver group (grade ≥ 2) (8). With the recent information, ATI could potentially be another non-invasive method to evaluate hepatic steatosis but need more validation especially in the obese population.

The purpose of this study was to evaluate the correlations and the interobserver liability of ATI comparing with MRI-PDFF in NAFLD patients.

2. MATERIAL AND METHODS

In this retrospective study, all consecutive NAFLD patients who underwent MR elastography, MRI-PDFF with available ATI information at Chulahborn hospital from August to October 2019 were included.

Inclusion criteria were patients at age of 18 or above, patients who clinically diagnosed as having the non-alcoholic fatty liver disease (NAFLD) defined by elevated ALT (≥ 40 U/L) with liver sonography findings suggestive of fatty liver

Exclusion criteria included known cirrhosis, Daily alcohol drinking > 30 g in men, 20 g in women, Chronic viral hepatitis B, C, and other known chronic liver diseases such as autoimmune hepatitis, primary biliary cholangitis, etc.

2.1 ATI evaluation technique

All patients who underwent conventional gray-scale US and ATI examinations were performed by two operators (S.S. and P.H.) with 12 and 3 years of experience in abdominal US imaging respectively. Both operators were blinded to the patient's clinical details as well as MRI-PDFF and laboratory results. Liver sonography and ATI examinations were performed using an ultrasound scanner (Aplio i800, Canon Medical Systems, Otawara, Japan) with a 1-8 MHz multi-frequency convex probe. All patients who underwent ATI had been fasted for at least 6 hours before examination. All images were obtained in the supine position via intercostal approach.

The included ROI was placed on the liver parenchyma, avoiding internal vessels, with the upper margin at least 2 cm below the liver capsule (Fig. 1).

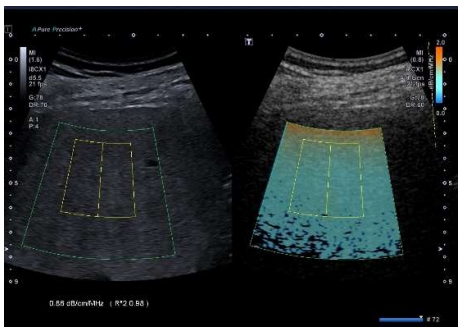

Figure 1. The green box in the right side image shows the attenuation color map of ROI (region of interest). The upper margin of the ROI should be about 2 cm below liver capsule. The measurement area, a yellow box of a fixed 4X2cm as shown in the right side image, should be placed at the center of ROI, avoiding major vasculatures.

The degree of attenuation was color-coded and displayed in the sampling box of ATI. The resulting attenuation coefficient was displayed in the units of dB/cm/MHz. Automated linear regression comparing the observed and the expected values by the machine represents as R^2 values, which are classified as poor ($R^2 < 0.80$), good ($R^2 = 0.80$-0.89), or excellent ($R^2 \geq 0.90$) (10).

For the evaluation of inter-observer reliability, the assessment was conducted in a series of 18 subjects. Two operators (S.S. and P.H) performed two sets of 5 ATI measurements on the same subject by an alternating set of measurements between two operators.

2.2 MRI-PDFF and MR elastography

MRI-PDFF and MRE are incorporated into the routine MRI protocol to assess hepatic steatosis and fibrosis in NAFLD patients. MRI was performed with 3.0T (Ingenia; Philips Healthcare, Best, Netherlands) Protocol of MR-PDFF and MRE are shown in table 1.

Table 1. MRI technique for MRI proton density fat fraction and MR elastography

Parameter	MRI-PDFF	MRE
Pulse sequence	FSPGR	GRE
Matrix	300x300	300x85
No. of signal acquired	1	1
Echo time (msec)	5.9	20
Repetition time (msec)	1.05	50
Delta echo time (msec)	0.7	-
Flip angle (deg)	5	30
Bandwidth (kHz)	-	287
No. of sections	64	4
Section thickness (mm)	5	10
Section gab (mm)	10	1
No. of phases	-	4
MEG frequency (Hz)	-	60
Axis of MEG	-	Z
Driver frequency (Hz)	-	60
Driver cycles per trigger	-	3
No. of breath holds	1	4
Breath hold mode	Expiration	Expiration
Acceleration factor	-	2
Imaging time	7 sec	1.10 min
mDIXON images	Water, fat, fat fraction, T2*	-

Percentage fat fraction measurement on the MRI-PDFF were performed using a 3x3 cm ROI at the parenchyma of left lateral hepatic lobe, right anterior and posterior of right hepatic lobe, respectively. (Fig. 2)

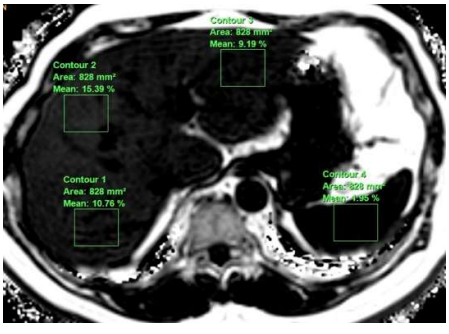

Figure 2. Fast-spoiled gradient echo MR image of fat mapping image, showing measurement area including posterior segment of right hepatic lobe (contour 1), anterior segment of right hepatic lobe (contour 2), left hepatic lobe (contour 3), and spleen (contour 4)

Quantification of liver fat was categorized by MRI-PDFF as follows; ≥5% (S>0: steatosis), ≥16.3% (S>1: significant steatosis), and ≥21.6% (S>3: severe steatosis)(36), and MRE was categorized into fibrosis

stage f1-f2, f2-f3, f3-f4 and f4 at the cut off value 2.9–3.5 kPa, 3.5–4.0 kPa, 4.0–5.0 kPa, >5.0 kPa respectively (11).

2.3 Statistical analysis

Demographic and anthropometric data of the patients, including age, gender, Body mass index (BMI), and liver function test were evaluated using an independent t-test for comparing demographic data.

The univariate r coefficient was tested to compare between ATI and MRI-PDFF using the Spearman rank correlation method and categorized as follows: 0.00-0.25 none or slight; 0.26 to 0.50 fair to moderate; 0.51-0.75 moderate to good; 0.76-1.00; almost perfect (12).

Concordance between inter-observer was assessed by Cohen's kappa coefficient, which result can be interpreted as follow; 0 as an agreement equivalent to chance: 0.01-0.20 as slight agreement; 0.21-0.4 as fair agreement; 0.41-0.60 as moderate agreement; 0.61-0.80 as substantial agreement; 0.81-0.90 as near perfect agreement; 1.00 as a perfect agreement (13).

Analyses were conducted using STATA version 12; Stata Corporation, College Station, Tx) at 2 side p-value < 0.05 as the level of significance.

3. RESULTS

There were 64 patients were included, two patients were excluded due to incomplete data of ATI. Of all 62 patients (31 women and 31 men), average BMI and percentage of patient BMI ≥ 25 kg/m2 were 27.4 kg/m2, and 72%, respectively. None of the patients has significant liver fibrosis with mean stiffness of 2.1±0.4 kPa.

The characteristics of all patients, including gender, weight, height, BMI, liver stiffness, serum aspartate aminotransferase (AST), alanine aminotransferase (ALT), fasting blood glucose (FBG), triglycerides (TG), cholesterol (CHOL), and platelet count (PLT) are summarized in table 2.

The correlation of ATI vs MRI-PDFF values at lateral segment of left lobe, anterior and posterior of right hepatic lobe, and average value correlation of ATI vs MRI-PDFF showed a moderate to good correlation with the highest correlation of right posterior segment. ($r = 0.63$, $p < 0.001$, $r = 0.66$, $p < 0.001$; $r = 0.69$, $p < 0.001$, $r = 0.67$, $p < 0.001$; respectively) (Figure 3a-d).

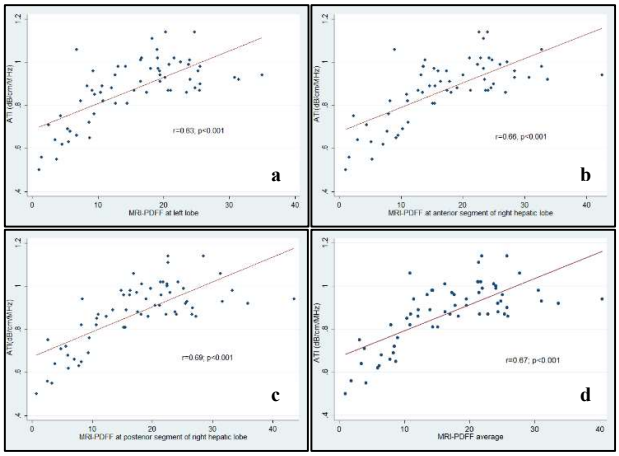

Figure 3. The Spearman's correlation analysis between ATI of liver and MRI-PDFF of different hepatic areas and the average MRI-PDFF value (a) left lobe liver (r = 0.63). (b) anterior segments of right hepatic lobe (r = 0.66). (c) posterior segments of right hepatic lobe (r = 0.69). (d) average value of different hepatic areas (r = 0.67).

The agreement of the inter-observer reliability of two observers were 100% with the Cohen kappa coefficient of 1.00 ($p < 0.001$).

4. DISCUSSION

ATI is a novel method that has the basic concept of sound attenuation measurement base on fatty tissue that should have higher sound attenuation compare to normal liver tissue (20). Measurement of attenuation coefficient allows quantitative measurement addition to conventional US imaging and potential for follow up indication.

In our study, the correlation coefficient between ATI and MRI-PDFF are concordant to previously published

Table 2. Demographic data of patients

	Female (n=31)	Male (n=31)	All patients (n=62)	p-value*
Age (mean ± SD)	54.8±10.6	46.9±11.1	50.9±11.5	0.0054*
Weight (kg)	70.4±8.5	78.2±10.6	74.3±10.4	0.0022*
Height (cm)	159.5±6.6	170.0±4.1	164.8±7.6	<0.001*
Waist circumference (cm)	92.8±6.1	97.8±7.0	95.8±7.0	0.0255*
BMI (kg/m2)	27.7±3.5	27.1±3.4	27.4±3.4	0.4418
< 25	8 (25.8%)	8 (25.8%)	16 (25.8%)	-
≥ 25	23 (74.2%)	23 (74.2%)	46 (74.2%)	-
Stiffness* (kPa)	2.0±0.4	2.2±0.3	2.1±0.4	0.107
Baseline Laboratory values (mean ± SD)				
AST (IU/L)	34.9±20.5	28.2±6.2	30.9±14.0	0.750
ALT (IU/L)	49.7±27.5	48.5±19.4	49.0±22.7	0.499
FBG (mg/dL)	114.4±42.2	98.2±21.9	104.7±32.1	0.0323*
TG (mg/dL)	123.3±45.4	146.0±83.4	136.9±70.9	0.525
CHOL (mg/dL)	190.0±43.0	194.5±31.2	192.7±35.9	0.294
Plt(x10^3/ul)	298.1±58.2	266.6±51.3	279.2±55.7	0.122

Stiffness* (kPa) by MR scanner 3.0 Tesla (Ingenia; Philips Healthcare, Best, Netherlands) with MRE protocol

studies with slightly in lower correlation coefficient r = 0.63-0.69 comparing to r = 0.66 – 0.81 (9, 21). There are potential interfering factors of the ATI measurement which may cause less reliability. Jeon et al have found that the patients with skin-to-liver distance greater than 20 mm significantly less correlation between ATI and MRI-PDFF (9).

The majority study comparing ATI and MRI-PDFF has limited data on obese patients (8, 21). Tada et al have reported that the subgroup of higher grading of fatty liver tends to have less diagnostic performance (8). Our study may substantiate these interfering factors since 75% of our population have BMI over 25 and all patients are diagnosed with fatty liver. The findings that ATI is less reliable in an obese patient are possible due to the deeper the sound passes through, the greater the attenuation and eventually create a higher attenuation coefficient (22). Due to in obese patients, presume that patient might have a thicker abdominal wall and preperitoneal fat which increase the distance between transducer and fixed measurement area. This factor may interfere with ATI measurement, causing decreased correlation.

Overall ATI value shows a better correlation to MRI-PDFF at right posterior hepatic lobe as compared with other locations. This could be explained by the technique of ATI measurement at the right intercostal approach, mainly representing the posterior right hepatic lobe, therefore correlation of ATI is more concordant with measurement of fat at right posterior hepatic lobe than other places.

Perfect interobserver reliability (k = 1.0) in grading liver steatosis is observed in our study, this is maybe because ATI is relatively non-complicated to use with fix both measurement ROI box and measurable area. Jeon et al have also reported with high reliability in both interobserver and intraobserver (k = 0.8-1.0) (9). With this high reproducibility, ATI may be a good candidate method for monitoring the treatment of NAFLD.

In this regard, ATI equipped in the US system allows additional quantitative measurement of liver steatosis in the same setting of liver US study. ATI may potentially be a surrogate method to evaluate and assess the degree of fatty liver in the routine clinical setting.

5. CONCLUSION

ATI is an emerging quantitative ultrasound-based approach, using sound attenuation property to evaluate fatty liver conditions with the potential to be a surrogate for MRI-PDFF measurement. However, interfering factors eg. high BMI may decrease the accuracy of ATI comparing to MRI-PDFF as a reference.

REFERENCES

1. Younossi ZM, Koenig AB, Abdelatif D, Fazel Y, Henry L, Wymer M. Global epidemiology of nonalcoholic fatty liver disease-Meta-analytic assessment of prevalence, incidence, and outcomes. Hepatology. 2016;64(1):73-84.
2. Sayiner M, Koenig A, Henry L, Younossi ZM. Epidemiology of Nonalcoholic Fatty Liver Disease and Nonalcoholic Steatohepatitis in the United States and the Rest of the World. Clin Liver Dis. 2016;20(2):205-14.
3. Argo CK, Caldwell SH. Epidemiology and natural history of non-alcoholic steatohepatitis. Clin Liver Dis. 2009;13(4):511-31.
4. Bellentani S, Bedogni G, Miglioli L, Tiribelli C. The epidemiology of fatty liver. Eur J Gastroenterol Hepatol. 2004;16(11):1087-93.
5. Ricci C, Longo R, Gioulis E, Bosco M, Pollesello P, Masutti F, et al. Noninvasive in vivo quantitative assessment of fat content in human liver. J Hepatol. 1997;27(1):108-13.
6. Shannon A, Alkhouri N, Carter-Kent C, Monti L, Devito R, Lopez R, et al. Ultrasonographic quantitative estimation of hepatic steatosis in children With NAFLD. J Pediatr Gastroenterol Nutr. 2011;53(2):190-5.
7. Fitzpatrick E, Dhawan A. Noninvasive biomarkers in non-alcoholic fatty liver disease: current status and a glimpse of the future. World J Gastroenterol. 2014;20(31):10851-63.
8. Tada T, Iijima H, Kobayashi N, Yoshida M, Nishimura T, Kumada T, et al. Usefulness of Attenuation Imaging with an Ultrasound Scanner for the Evaluation of Hepatic Steatosis. Ultrasound Med Biol. 2019;45(10):2679-87.
9. Jeon SK, Lee JM, Joo I, Yoon JH, Lee DH, Lee JY, et al. Prospective Evaluation of Hepatic Steatosis Using Ultrasound Attenuation Imaging in Patients with Chronic Liver Disease with Magnetic Resonance Imaging Proton Density Fat Fraction as the Reference Standard. Ultrasound Med Biol. 2019;45(6):1407-16.
10. Bae JS, Lee DH, Lee JY, Kim H, Yu SJ, Lee JH, et al. Assessment of hepatic steatosis by using attenuation imaging: a quantitative, easy-to-perform ultrasound technique. Eur Radiol. 2019;29(12):6499-507.
11. Hoodeshenas S, Yin M, Venkatesh SK. Magnetic Resonance Elastography of Liver: Current Update. Top Magn Reson Imaging. 2018;27(5):319-33.
12. Johnson AF. Statistics in Medicine. T. Colton. Little, Brown and Company, Boston, Mass. 02106, 1974, xii + 372 pp. Paperback. $22.50. Clinical Chemistry. 1975;21(6):789-90.
13. McHugh ML. Interrater reliability: the kappa statistic. Biochem Med (Zagreb). 2012;22(3):276-82.
14. Caussy C, Reeder SB, Sirlin CB, Loomba R. Noninvasive, Quantitative Assessment of Liver Fat by MRI-PDFF as an Endpoint in NASH Trials. Hepatology. 2018;68(2):763-72.
15. Permutt Z, Le TA, Peterson MR, Seki E, Brenner DA, Sirlin C, et al. Correlation between liver histology and novel magnetic resonance imaging in adult patients with non-alcoholic fatty liver disease - MRI accurately quantifies hepatic steatosis in NAFLD. Aliment Pharmacol Ther. 2012;36(1):22-9.
16. Middleton MS, Heba ER, Hooker CA, Bashir MR, Fowler KJ, Sandrasegaran K, et al. Agreement Between Magnetic Resonance Imaging Proton Density Fat Fraction Measurements and Pathologist-Assigned Steatosis Grades of Liver Biopsies From Adults With Nonalcoholic Steatohepatitis. Gastroenterology. 2017;153(3):753-61.
17. Saverymuttu SH, Joseph AE, Maxwell JD. Ultrasound scanning in the detection of hepatic fibrosis and steatosis. Br Med J (Clin Res Ed). 1986;292(6512):13-5.
18. Palmentieri B, de Sio I, La Mura V, Masarone M, Vecchione R, Bruno S, et al. The role of bright liver echo pattern on ultrasound B-mode examination in the diagnosis of liver steatosis. Dig Liver Dis. 2006;38(7):485-9.

19. Hepburn MJ, Vos JA, Fillman EP, Lawitz EJ. The accuracy of the report of hepatic steatosis on ultrasonography in patients infected with hepatitis C in a clinical setting: a retrospective observational study. BMC Gastroenterol. 2005;5:14.
20. Culjat MO, Goldenberg D, Tewari P, Singh RS. A review of tissue substitutes for ultrasound imaging. Ultrasound Med Biol. 2010;36(6):861-73.
21. Ferraioli G, Maiocchi L, Raciti MV, Tinelli C, De Silvestri A, Nichetti M, et al. Detection of Liver Steatosis With a Novel Ultrasound-Based Technique: A Pilot Study Using MRI-Derived Proton Density Fat Fraction as the Gold Standard. Clin Transl Gastroenterol. 2019;10(10):e00081.
22. Frederick WK. Sonography: Principles and Instruments. Ninth ed. Missouri: Loren Wilson; 2016.

Shielding Calculation for a Diagnostic Nuclear Medicine Facility

M.R.Z. Tecson[1,2], A.K.M. Garcia[1], J.M.G.F. Gonzales[1,2], J.D.O. De Guzman[1,2], A.B. Galay[1,2], N.A.A Madrigal[1,2], & M.M. Ramirez[1]

1 Medical Physics & Health Physics Services, Inc., 2310 Taft Ave., Malate, Manila, Philippines 1004
2 The Graduate School, University of Santo Tomas, España Blvd. Sampaloc, Manila, Philippines 1008
**mphps@yahoo.com.ph*

Abstract

Nuclear medicine refers to the introduction of unsealed radionuclides into the body mostly to diagnose organ structures and assess bodily functions. Upon patient administration, the radiopharmaceuticals in the body are unsealed sources that emit doses to nearby areas and can produce unacceptable public and occupational exposure on its surroundings. Therefore, radiation protection through an appropriate shielding design is necessary to limit the doses to their respective safe limits as recommended by ICRP 103. This paper presents a method adapted from the AAPM Task Group 108: PET and PET/CT Shielding Requirements and NCRP Report No. 147 recommendations for the shielding calculation of a nuclear medicine facility. The method was able to provide shielding requirements in terms of lead or concrete walls from the emitted doses contributed by the following sources on different areas: x-rays emitted by CT and DEXA scanners for anatomical imaging, F-18 used for PET imaging, Tc-99m used for SPECT imaging and myocardial perfusion stress tests, I-125 for radioimmunoassay, and I-131 for thyroid uptake measurements.

Keywords: Radiation Shielding, Nuclear Medicine, Radiopharmaceuticals, X-Rays, Shielding Calculation

1. INTRODUCTION

Guidelines such as NCRP Report No. 147 and AAPM Task Group 108 are being followed to conduct proper shielding of PET and PET/CT facilities. [2] [3] In this study, the objective is to demonstrate a method for the shielding calculation of a diagnostic nuclear medicine facility. The study presents a shielding calculation example whereas a nuclear medicine facility aims to provide the following services: PET/CT imaging, SPECT/CT imaging, thyroid uptake probe measurements, treadmill cardiac stress tests, DEXA, and radioimmunoassay.

2. MATERIAL AND METHODS

A nuclear medicine facility aims to cater the following services: PET/CT imaging, SPECT/CT imaging, thyroid uptake probe measurements using I-131, treadmill cardiac stress tests, bone densitometry (DEXA) using x-rays, and radioimmunoassay. Also, the facility plans to use 18-Fluorodeoxygluocose for PET/CT functional imaging, Technetium-99m sestamibi/tetrofosmin for SPECT/CT functional imaging and treadmill cardiac stress tests, Iodine-131 for thyroid uptake probe measurements, and I-125 for radioimmunoassay as their respective primary radionuclides. Meanwhile, x-rays from CT and DEXA scanners will be used for anatomical imaging. Physical characteristics of these radionuclides are taken from several references. [3] [4] [5] [6] [7]

2.1 Floor Plan and Proposed Scan Protocols

Figures 1a and 1b show the 1st and 2nd floor plan of the nuclear medicine facility, respectively. For each room in the facility where shielding requirements are determined, the surrounding zone/area around each room was assigned with weekly design goals and occupancy factors in accordance to NCRP 147 and AAPM Task Group 108 recommendations. [2] [3]

The facility reported that proposed scan protocols will follow the international standardized guidelines (e.g. EANM guidelines). Thus, the DLP emitted from CT imaging as well as the administered activity, uptake time, and imaging time used in PET/CT imaging, SPECT/CT imaging, thyroid uptake probe measurements, treadmill cardiac stress tests, bone densitometry and radioimmunoassay typically encountered in medical facilities are lifted from several international guidelines. The typical scattered dose rate from pencil and fan beam scanners used in bone densitometry are also included. These parameters will be used for the shielding calculation and are cited in the references. [2] [8] [9] [10] [11] [12] Furthermore, assumptions are established to simplify the shielding calculation:

1. The uptake process of I-131 for the thyroid uptake probe measurements will take place in the thyroid uptake room.
2. The Post-Admin room is an uptake room.
3. The height of the ground floor to the second floor is 3 meters.
4. The thickness of the 2nd floor slabs is four inches of concrete.
5. The density of the walls is in compliance to DOH A.O. 35 Section 6.2.: 2.35 g/cm^3 for concrete walls or 11.36 g/cm^3 for lead walls. [13]
6. The facility will use a fan-beam type bone densitometry scanner.
7. The facility will conduct CT procedures with or without contrast media.
8. The treadmill room has the same procedure with SPECT/CT.
9. The number of patients per week will be 8 for PET/CT, 10 for SPECT/CT, 10 for treadmill

cardiac stress tests, and 10 for thyroid uptake measurements.

10. For the second floor slabs calculation, the patient is assumed to be 1 m above the floor. Thus, the dose rate is calculated 0.5 m above the source and at 1.7 m above the floor for rooms below the source.
11. An individual will typically stay at least 0.3 m beyond a wall. Hence, the dose rate is calculated at 0.3 m beyond a wall for rooms near the source at the same floor.
12. The radionuclide inside the patient and the scattered radiation coming from x-ray sources are isotropic sources.
13. There is no patient attenuation.
14. The amount of patient voiding for F-18 is the same for Tc-99m.
15. The dose rate constants have a cutoff energy of 20 keV. This means that emitted particles and photons by the source with energies below 20 keV are assumed to be absorbed by the medium (air or patient). Hence, these particles and photons do not contribute to the dose. [4][6][14]
16. For the radioimmunoassay room and hotlab shielding calculations, the following assumptions were taken:
    a. The number of individual sources per radionuclide will depend on the number of patients per week for each modality that uses that radionuclide. For instance, the thread mill room is expected to have 10 procedures per week while the SPECT/CT is expected to have 10 scans per week. Assuming that the SPECT/CT and threadmill will use Tc-99m and the same activity per procedure/scan, the hotlab will have a total of 20 individual Tc-99m vials (i.e. one for each patient) with the same activity.
    b. The quantity of the vials will not be diminished. Only the physical decay of the radionuclide will occur.
    c. The vials contain unsealed sources (i.e. no lead containers or lead bricks sufficiently contain the emitted charged and uncharged particles). Also, the atoms in the vials do not interact with the emitted radiation.
    d. The following sources are stored in the hotlab - 18-FDG, Tc-99m, and I-131.

e. An individual is expected to be maximally exposed for 8 hours (equivalent to 1 working day) per day.
f. For RIA room calculation: there are 3 sources in the RIA room (1 per RIA test kit). Each source contains 3 MBq at the tabletop as advised. The sources are typically placed on the radioimmunoassay equipment. Scan time for the radioimmunoassay equipment is assumed to be 2 hours.

2.2 Transmission Factor Calculation

The dose calculations used are adapted from NCRP Report No. 147 and AAPM Task Group 108 recommendations. Meanwhile, the RIA room and Hotlab dose calculations are lifted from Andreo et.al (2017). [2] [3] [6] Afterwards, the transmission factor was calculated simply by getting the ratio of the weekly design goal and the product of the occupancy factor and the calculated weekly dose by an individual at a given point.

2.1 Shielding Calculation

The required thickness of a wall, x, arising from the transmission factor, B, was obtained using Archer's Formula. [2] [15] The α, β, and γ parameters used in this study are lifted from NCRP Report No. 147, AAPM Task Group 108, Kusano & Caldwell (2014), & Kharrati (2007) for lead and concrete. [2] [3] [4] [16]

3. RESULTS

Figure 1a and 1b shows the required shielding thicknesses based from the calculations done. The required shielding thickness of each wall and floor slab (in inches) is presented in terms of lead equivalence. The reported shielding thickness were consulted with the available lead sheet thickness in the market. [17] The facility reported that the proposed slabs would be 4 inches of concrete. Using the shielding calculation method, the slabs require additional shielding (3/16 inches lead equivalent).

4. DISCUSSION

The calculated shielding requirements depends on several factors. First, it depends on the expected radiation sources involved in a specific area. Each radiation source has different dose-rate constants which predicts the amount of dose emitted at 1 meter by the radiation source. Consequently, the shielding requirements depends on the dose-rate constant used in the calculation as remarked by Kusano & Caldwell (2014). "According to Kusano & Caldwell (2014), the choice of the dose-rate constant models in their study yielded different transmission factors with Smith & Stabin (2012) and NCRP Report No. 124. This variation was caused by the differences in the cutoff energy considered and the calculation of the nuclide f-factor which pertains to the stopping power ratios of air to tissue. The calculation of the nuclide f-factor depends on the tissue model at hand. For instance, the tissue model used in the research of Smith & Stabin (2012) was the one described in ICRU-44." [4] [5] Second, the shielding requirement depends on the technical specifications of the equipment. For instance, the technical specifications of a CT scanner declare normalized CTDI values and isodose curves which can be used for planning the shielding calculations as

recommended by NCRP Report no. 147. [2] Third, the shielding requirement depends on the scan protocols to be used (i.e. administered activity, imaging time, uptake time, use of contrast media, scan parameters for the CT component, etc.). This is essential for uptake and imaging room calculations. Lastly, the shielding requirement depends on the composition of the proposed shielding material, expected workload of the facility, the area of the rooms, and the choice of weekly design goal and occupancy factor for each area of the facility.[2][3][4][5]

For hybrid systems, the nuclear medicine facility can add diagnostic services. Thus, CT component of the PET/CT and SPECT/CT will have an additional workload. Consequently, the extended use of the CT component of the hybrid systems increases the dose to be considered for shielding design. Considerations to impose additional shielding might be needed in these situations. A separate shielding calculation to estimate the dose contributions from the CT component of the PET/CT and SPECT/CT systems should be done. This is because we cannot easily accept the following assumption: that the shielding calculations in accordance to the PET or SPECT dose contributions will sufficiently attenuate the CT dose contributions due to the higher energy considerations of PET and SPECT over CT. This is because of the higher workload imposed in the CT component. [3] The shielding requirements should also consider the viewing conditions of the leaded glass because it typically gives a pale, yellow color which darkens over time as it is being exposed to ionizing radiation. Viewing conditions might be affected should thicker leaded glasses be used. Care in purchasing leaded glasses in accordance to visual clarity should be done. [18] [19]

After conducting the shielding calculations, the results should be compared with the regulatory requirements. In the Philippines, it should be compared with the DOH A.O 35 requirements and PNRI-CPR requirements. [13] [20] The reported calculated shielding requirements should satisfy regulatory requirements. For instance, DOH A.O 35 requires at least 1.5 mm Pb equivalent (or approximately 0.06 inches) shielding for x-ray facilities. Thus, the walls of the PET/CT room, SPECT/CT room, and DEXA room will be required to have at least 1.5 mm Pb equivalent. The proposed shielding requirements upon installation requires to be verified as recommended by NCRP Report No. 147 and AAPM Task Group 108 guidelines. In particular, the actual composition and density of the shielding material as well as the actual thickness and the transmission response of each wall should be verified after the initial construction of the facility. The shielding verification procedure can be done in accordance to the AAPM Task Group 108 and NCRP Report No. 147 recommendations. Particularly, it requires an experimental simulation involving transmission measurements using the radiation sources to be used and radiation detectors such as ionization chambers. [2] [3] Findings must be discussed with the facility representative, engineers, and architects in order to discuss the corrective actions, if any, needed to partake.

5. CONCLUSION

The shielding calculation method demonstrated in this paper can be used for shielding calculations in a new nuclear medicine department. The proposed scan protocols and technical specifications of the equipment should be considered in performing shielding calculations. Prior to the completion of the construction, an on-site evaluation of the facility may be conducted. The "inspection is to verify that barriers are properly placed, contiguous and free of voids or defects; and the evaluation of shielding adequacy is to verify that barriers adequately attenuate exposures in nearby occupied areas to the relevant shielding design goal".

REFERENCES

[1] Cherry, S.R, Sorenson, J.A., Phelps, M.E. (2012) *Physics in Nuclear Medicine: 4th Edition* Elsevier Sanders. 2012

[2] NCRP (2005) *NCRP Report no. 147: Structural shielding design for medical X-ray imaging facilities.* National Council on Radiation Protection and Measurements, 2004

[3] Madsen, M.T., Anderson, J.A., Halama, J.R., Kleck, J., Simpkin, D.J, Votaw, J.R., Wendt, R.E. III, Williams, L.E, Yester, M.V. (2006) *AAPM Task Group 108: PET and PET/CT Shielding Requirements.* Medical Physics, 33(1), 14-15 doi: 10.1118/1.2135911

[4] Kusano, M. & Caldwell, C.B. (2014) *Dose Rate Equivalent Constants and Barrier Transmission Data for Nuclear Medicine Facility Dose Calculations and Shielding Design.* Health Physics, 107(1), 60-72 doi: 10.1097/HP.0000000000000051

[5] Smith, D.S. & Stabin, M.G. (2012) *Exposure Rate Constants and Lead Shielding Values for over 1,100 Radionuclides*. Health Physics, 102(3), 271-291 doi: 10.1097/HP.0b013e318235153a

[6] Andreo, P., Burns, D.T., Nahum, A.E., Seuntjens, J., & Attix, F.H. (2017) *Fundamentals of Ionizing Radiation Dosimetry* Wiley-VCH Verlag GmbH & Co. KGaA. 12, 69469 Weinheim, Germany

[7] Eckerman, K. & Endo, A. (2008) *Annals of the ICRP: Nuclear Decay Data for Dosimetric Calculations. ICRP Publication 107* Ann ICRP. 2008;38(3):7-96. doi: 10.1016/j.icrp.2008.10.004.

[8] IAEA (2010) *IAEA Human Health Series No. 15: Dual Energy X-Ray Absorptiometry for Bone Mineral Density and Body Composition Assessment* IAEA, 2010 retrieved from: https://www-pub.iaea.org/MTCD/Publications/PDF/PUB1797_web.pdf

[9] Varrone, A., Asenbaum, S., Vander Borght, T., Booij, J., Nobili, F., Någren, K., Darcourt, J., Kapucu, Ö. L., Tatsch, K., Bartenstein, P., & Van Laere, K. (2009). *EANM procedure guidelines for PET brain imaging using [18F] FDG, version 2.* European Journal of Nuclear Medicine and Molecular Imaging, 36(12), 2103–2110. doi: 10.1007/s00259-009-1264-0

[10] Verbene, H.J., Acampa, W., Anagnostopoulos, C., Ballinger, J., Bengel, F., De Bondt, P., Buechel, R.R., Cuocolo, A., van Eck-Smit, B.LF, Flotats, A., Hacker, M., Hindorf, C., Kaufmann, P.A., Lindner, O., Ljungberg, M., Londsale, M., Manrique, A., Minarik, D., Scholte, A.J.H.A, Slart, R.H.J.A., Trägårdh, E., de Wit, T.C., & Hesse, B. (2015) *EANM procedural guidelines for radionuclide myocardial perfusion imaging with SPECT and SPECT/CT:2015 revision.* European Journal of Nuclear Medicine and Molecular Imaging, 42(12), 1929-1940. doi: 10.1007/s00259-015-3139-x

[11] Balon, H.R., Silberstein, E.B., Meier, D.A, Charckes, N.D., Sarkar, S.D., Royal, H.D., & Donohoe, K.J. (2006) *Society of Nuclear Medicine Procedure Guideline for Thyroid Scintigraphy version 3.* Retrieved from: http://s3.amazonaws.com/rdcms-snmmi/files/production/public/docs/Thyroid_Scintigraphy_V3.pdf

[12] Siegel, J.A., (2001) *Guide for Diagnostic Nuclear Medicine.* Society of Nuclear Medicine, 2001. Retrieved from: https://www.nrc.gov/materials/miau/miau-reg-initiatives/guide_2002.pdf

[13] Department of Health (1994) *Administrative Order No. 35: Requirements for the control of radiation hazards from clinical diagnostic x-ray facilities*

[14] Loevinger, R., Budinger, T.F., & Watson, E.E., Atkins, H.L, Blau, M., Lathrop, K.A., Poston, J.W., Robertson, J.S., Thomas, S.R., & Weber, D.A. (1998) *MIRD Primer for Absorbed Dose Calculations.* The Society of Nuclear Medicine, Inc.

[15] Archer, B.J. (1983) *Diagnostic X-Ray Shielding Design based on an Empirical Model of Photon Attenuation*. Health Physics 44(5) pp. 507-517

[16] Kharrati, H., Agebi, A., & Karaoui, M.K. (2007) *Monte Carlo Simulation of x-ray buildup factors of lead and its applications in shielding of diagnostic x-ray facilities* Med. Phys. 34 1398 (2007); doi: 10.1118/1.2710333

[17] *Ray-Bar Stock Sheet Lead Standard Thickness, Weights and Conversions* (2020) Retrieved from: https://www.xrayprotection.com/lead-thickness-chart-2

[18] Rochus, P. (2020) *Shielding solutions you can look through: Leaded glass and leaded acrylic* Vertical Media Retrieved from: https://hospitalnews.com/shielding-solutions-you-can-look-through-leaded-glass-and-leaded-acrylic/

[19] Jones, D. E. A. (1956). Solid Lead-glass Viewing Windows for High Energy Radiotherapy Installations. The British Journal of Radiology, 29(340), 230–231. doi:10.1259/0007-1285-29-340-230

[20] Department of Science and Technology – Philippine Nuclear Research Institute (2014) *CPR Part 13: License for Use of Unsealed Radioactive Material* Official Gazette Vol. 110, No. 12. Retrieved from: https://pnri.dost.gov.ph/images/safetyregulatorydocs/CPR/cpr_part_13_final_copy.pdf

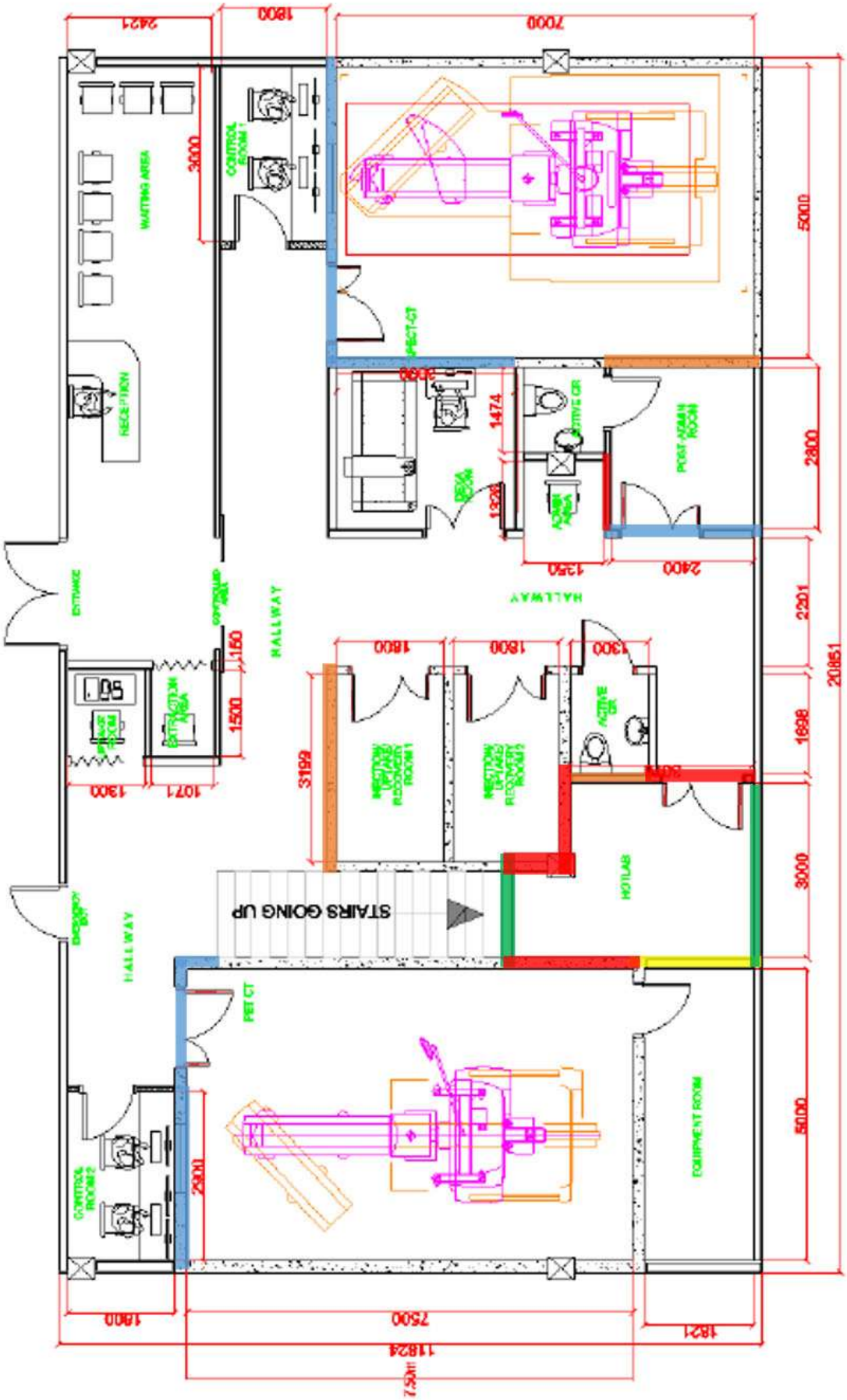

Figure 1a. *Proposed 1st floor plan of the nuclear medicine facility with the minimum required shielding highlighted in different colors. Blue = 1/64 in. Pb equivalent; Green = 1/32 in. Pb equivalent; Yellow = 3/64 in. Pb equivalent; Orange = ¼ in. Pb equivalent; Red = ½ in. Pb equivalent. The proposed 2nd floor slabs would be 4 inches of concrete. Using the shielding calculation method, the slabs need additional shielding (3/16 in. Pb equivalent).*

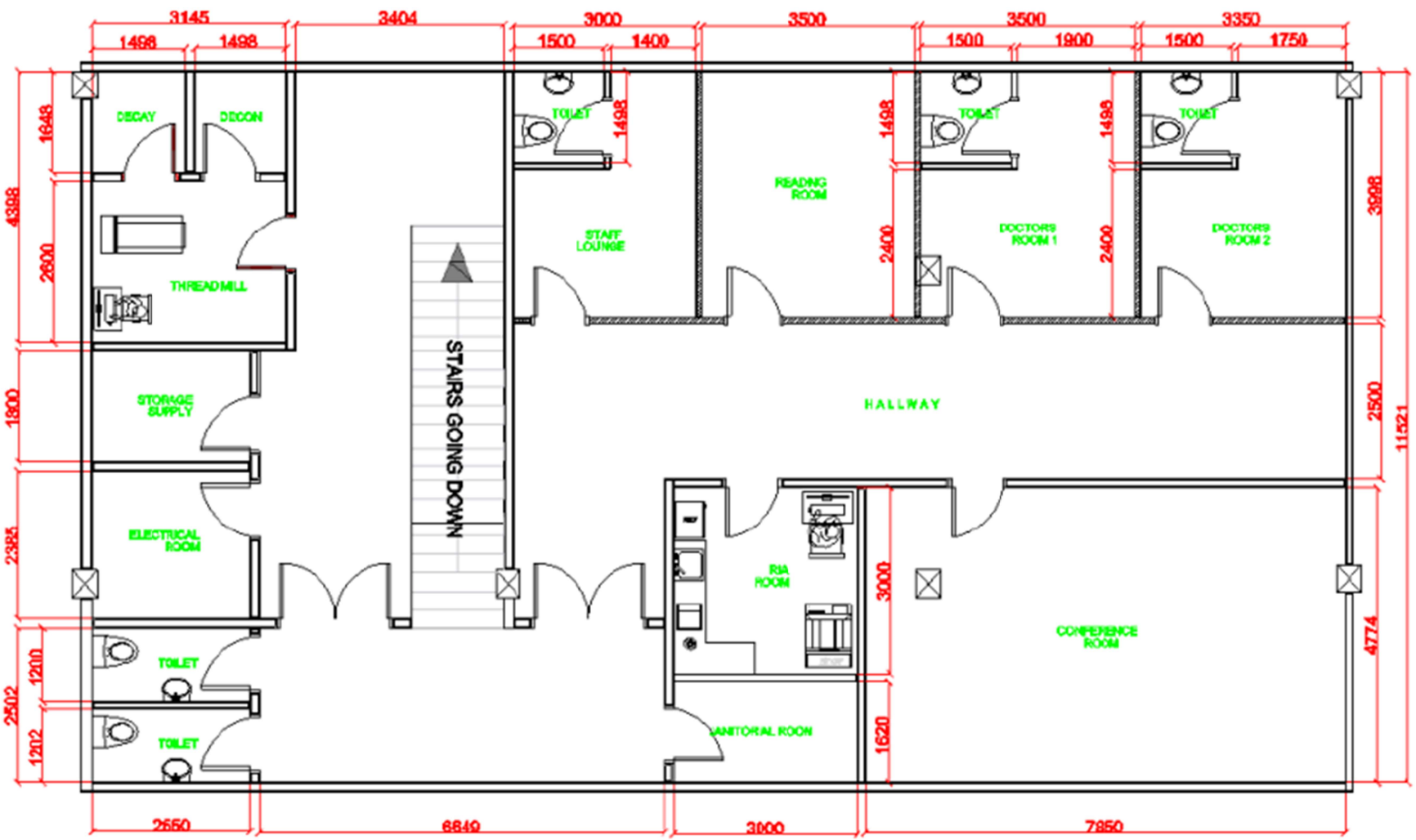

Figure 1b. *Proposed 2nd floor plan of the nuclear medicine facility with the required shielding highlighted in different colors. Blue = 1/64 in. Pb equivalent; Green = 1/32 in. Pb equivalent; Yellow = 3/64 in. Pb equivalent; Orange = ¼ in. Pb equivalent; Red = ½ in. Pb equivalent. The proposed 2nd floor slabs would be 4 inches of concrete. Using the shielding calculation method, the slabs need additional shielding (3/16 in. Pb equivalent).*

The Study of Local Diagnostic Reference Levels at Unit of Vascular and Interventional Radiology, King Chulalongkorn Memorial Hospital

Kornkamol Prajamchuea[1] Anchali Krisanachinda[2]

[1]*Master of Science in Medical Physics Program, Faculty of Medicine, Chulalongkorn University, Bangkok 10330, Thailand*
[2]*Department of Radiology, Faculty of Medicine, Chulalongkorn university, Bangkok 10330, Thailand*

Abstract

The purpose of this research is to study the local DRLs in interventional radiology procedures at King Chulalongkorn Memorial Hospital. DRLs is an effective tool for the optimization of patient protection for diagnostic and interventional radiology procedures. As DRLs in interventional radiology procedures are not available in Thailand, the medical exposure and related parameters from 9 body interventional procedures and 3 neuro-interventional procedures have been surveyed for local DRLs in standard-sized of Thai patients. 387 body intervention and 87 neuro-intervention procedures were reported as median of fluoroscopy time and DRLs of total KAP. The results had been compared to Japan DRLs 2020. The DRLs of body intervention procedures were higher than Japan DRLs as our procedures using CT and CBCT guided while Japan used fluoroscopy guided. As the purposes of our center cover both clinical services and training of many related professions, the patients received higher doses. For neuro-interventional procedures, senior interventional radiologists play an import role on complicated procedures, therefore, the Local DRLs were comparable to and lower than Japan DRLs. Local DRLs will help optimize the interventional radiology procedures for the Unit of Vascular and Interventional Radiology and contribute to the National Diagnostic Reference Level.

Keywords: Local DRLs, interventional radiology, body intervention, neuro-intervention, 75th percentile

1. INTRODUCTION

ICRP Publication 135 on Diagnostic Reference Levels in Medical Imaging (2017) [(1)] recommended the DRLs to be an effective tool that aids in optimization of protection of patients for diagnostic and interventional procedures. Diagnostic Reference Levels (DRLs) in medical imaging is defined as a practical tool to optimize the patient radiation dose to the lowest possible exposure, but the image quality is still maintained for the diagnostic and therapeutic procedures. DRLs is a general guideline based on 75th percentile of the median dose for a sample of standard sized of patients. This means the optimization of patient radiation dose should be more than 25th percentile of the median, while 75th percentile is Diagnostic Reference Levels (DRLs). In order to encourage the optimization of patient radiation dose, a concept of achievable dose has been introduced by National Radiological Protection Board (NRPB) [(2)] and is also recommended by the National Council on Radiation Protection and Measurements (NCRP) [(3)]. The achievable dose is set at the median (50th percentile) of the survey of dose distribution. The optimization of patient radiation dose should be, in the future, below the achievable dose level at 50th percentile level. The DRLs distribution is used for clinical operation and do not apply directly to individual patient and examination. There are three types of DRLs, Local Diagnostic Reference Levels (LDRLs), National Diagnostic Reference Levels (NDRLs) and Regional Diagnostic Reference Levels (RDRLs) [(4)] The Local DRLs should be reviewed annually and National DRLs should be reviewed every 5 years.

Interventional radiology (IR) procedure is defined as a medical sub-specialty of radiology utilizing minimally-invasive technique for diagnostic or therapeutic procedures using medical imaging guidance interventional procedure (IGIP) such as fluoroscopy, CT, MRI or ultrasound, to precisely guide medical devices into the internal structures of the body through very small incision. There are two parts of interventional radiology procedures follow the human body such as body intervention and neuro-intervention. The procedures are also separated into two groups that are a group of endovascular procedure and a group of non-vascular procedure. The interventional radiology staffs and patients usually receive high radiation dose during the procedures according to the increasing number of workloads and complexity of the procedures. Furthermore, the NDRLs report of interventional radiology procedures are not available in Thailand which will result in the increasing of both patients and staff doses.

The patient doses depend on a variety of factors in addition to patient size. The DRLs process should be applied to both interventional fluoroscopy and interventional CT. If the values of LDRLs for patients are higher than the NDRLs, the investigation should be started with the evaluation of the problem, then the procedure protocols, and finally the exposure techniques.

In this study, we investigated 9 body intervention and 3 neuro intervention procedures at the unit of vascular and interventional radiology, King Chulalongkorn Memorial hospital.

2. MATERIALS AND METHODS

A total of 474 examinations (387 body interventional procedures *and 87* neuro-interventional procedures*) were surveyed from* January 2019 to June 2020.

The basic adult patients (over 15 years old) information such as patient age, gender, weight (45-75kg. for female and 50-80kg. for male to macth the standard size of Thai patients), height and medical exposure information such as cumulative fluoroscopy time (min), cumulative air kerma (mGy)*, cumulative kerma area product (*Gy.cm^2*) and total number of images were collected from the dose summary report of each case in PACS and Radimetrics (the program of dose reporting and tracking, protocol management). The data were collected from 4 angiographic equipment such as CT-guided TACE with* Canon (Toshiba) hybrid angiography CT system*, CBCT-guided TACE, PICC line, Perm cath, PCD and PTBD with Siemens* single plane fluoroscopy*,* Peripheral angiogram and Peripheral angioplasty with Siemens biplane fluoroscopy, CBCT-guided Biopsy*,* Cerebral angiogram, Embolization of intracranial aneurysm and Embolization of brain AVM *with* Philips biplane fluoroscopy.

LDRLs based on the 75th percentile was determined in terms of the KAP value for all procedures included 25th, 50th (Achievable dose) and 95th percentiles to demonstrate the spread of data. Effective dose (mSv) was taken into radiation risk consideration. The LDRLs of interventional radiology procedures were grouped into two main categories of body interventional procedures and neuro- interventional procedures.

3. RESULTS

The LDRLs based on 75th percentile of 9 body interventional procedures and 3 neuro-interventional procedures were reported as median of fluoroscopy times and the 25th, 50th, 75th and 95th percentiles for the KAP values for each procedure. The number of sample size of PTBD, Peripheral angiogram and Embolization of brain AVM were less than other procedures, at 20 cases at least.

The total KAP values for body interventional procedures, vascular procedures, were: CT-guided TACE 58.30 min, 459 Gy.cm^2, CBCT-guided TACE 53.75 min, 357 Gy.cm^2, PICC line 0.70 min,1 Gy.cm^2, Perm Cath 1.65 min, 4 Gy.cm^2, Peripheral angiogram 5.25 min, 18 Gy.cm^2, and Peripheral angioplasty 15.40 min, 16 Gy.cm^2. Nonvascular procedures, PCD 1.40 min, 4 Gy.cm^2, PTBD 4.65 min, 14 Gy.cm^2, and CBCT-guided biopsy 2.19 min, 17 Gy.cm^2. The total KAP values for neuro-interventional procedures were: Cerebral angiogram 6.53 min, 61 Gy.cm^2, Embolization of intracranial aneurysm 39.48 min, 144 Gy.cm^2, and Embolization of brain AVM 44.16 min, 224 Gy.cm^2 respectively as Table 1.

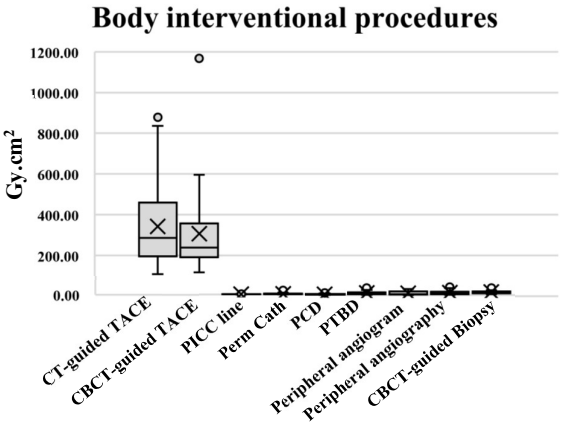

Figure 1 *Minimum, maximum, 75th percentile (DRLs) and 50th percentile (AD) values of the body interventional procedures.*

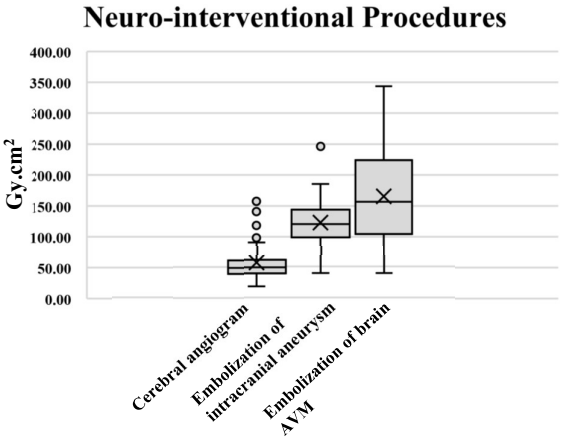

Figure 2 *Minimum, maximum, 75th percentile (DRLs) and 50th percentile (AD) values of the neuro-interventional procedures.*

4. DISCUSSION

The patients received the highest doses from CT guided TACE procedures. Followed by CBCT guided TACE and embolization of brain AVM. The patient dose optimization is seriously considered because the biological effects of radiation on skin will occur.

4.1 Body interventional procedures

The highest KAP values were abdominal part of body interventional procedures: CT-guided and CBCT-guided TACE procedures. Hybrid angiography CT system and Single plane fluoroscopy for guided had been operated for those procedures. The equipment selection depends on case complexity index and the decision of the interventional radiologists. Even though the DRLs (75th percentiles) and AD (50th percentiles) of CT-guided TACE are higher than CBCT-guided TACE, the accuracy of small vessel selection technique is necessary in complicated cases.

Table 1 *Median of Fluoroscopy time, 25th percentile, and 50th percentile (AD), percentile of KAP values, Number of cases of each procedures and Effective dos procedures.*

Interventional radiology procedures	Flu. Time (min)	KAP (Gy.cm^2)				No. of cases	Effective dose (mSv)
		25th percentile	50th percentile (Achievable Dose)	75th percentile (DRLs)	95th percentile		
Body intervention							
CT-guided TACE	58.30	195.73	286.68	459.27	748.13	112	119.41
CBCT-guided TACE	53.75	190.39	238.27	356.97	576.05	26	92.81
PICC line	0.70	0.48	0.70	1.19	2.57	58	
Perm cath	1.65	0.85	1.16	3.96	7.83	24	
PCD	1.40	1.29	2.29	3.99	6.76	34	
PTBD	4.65	3.96	5.56	13.77	25.00	20	
Peripheral angiogram	5.25	2.10	3.73	17.61	26.46	20	4.58
Peripheral angioplasty	15.40	4.09	7.00	16.20	31.76	48	4.21
CBCT-guided Biopsy	2.19	8.06	11.65	17.39	32.16	45	
Neurointervention							
Cerebral angiogram	6.53	39.13	48.82	60.73	116.82	44	5.28
Embolization of intracranial aneurysm	39.48	98.87	120.50	143.78	240.38	23	37.38
Embolization of brain AVM	44.16	104.20	156.84	224.29	298.51	20	58.32

The DRLs (75th percentiles) of the catheter placement procedures, PICC line and Perm Cath, and the nonvascular procedures, PCD, PTBD and CBCT-guided biopsy are quite low. These procedures were acquired by the single plane fluoroscopy equipment, the CBCT-guided biopsy operated by the biplane fluoroscopy equipment resulted in the maximum DRLs of nonvascular procedures. The KAP values of each procedure depends on the thickness of the body part and the complexity index.

The KAP values for DRL, AD and median of fluoroscopy time of the endovascular procedure, Peripheral angiogram and Peripheral angioplasty, were not available because of pulse rate, acquisition mode and the spreading of limited number of sample size as well as Peripheral Angiogram.

4.2 Neuro-interventional procedures

The diagnostic procedure, cerebral angiogram showed the lowest median of fluoroscopy time and KAP values. The specificity of the disease and acquisition mode influenced on the KAP value at DRL of therapeutic procedures. The KAP value of Embolization of intracranial aneurysm is less than Embolization of brain AVM. The median of fluoroscopy time of these procedures was relevant.

The data spreading in the Box plots showed that the 25th percentile was close to the median and the patient doses during this procedure were quite low.

The DRLs (75th percentiles) and AD (50th percentiles) are increasingly important especially for the interventional radiology procedures which the patient radiation doses should be under controlled.

The Local DRLs in this study had been compared to Japan DRLs 2020. The DRL of TACE procedure at our center, 459 Gy.cm^2*, was higher than Japan DRLs, 270* Gy.cm^2*. The CT and CBCT guided used at our center resulting in high doses while the fluoroscopy guided is used Japan. Furthermore, our center is a training center for interventional fellows with many cases of complexity, thus the patients received higher doses. For neuro interventional procedures, the DRL of* Embolization of brain AVM *at our center was 224* Gy.cm^2 *which was less than Japan DRLs at 410* Gy.cm^2*. The senior with high experienced interventional radiologists mostly conducted the complicated procedures; therefore, the Local DRLs was lower than Japan DRLs.*

5. CONCLUSION

The Local DRLs of interventional radiology procedures has been initially established in 2020. The outcome of this study will help optimize the patient radiation dose during procedures for the unit of vascular and interventional radiology, King Chulalongkorn Memorial Hospital. The Local DRLs report is useful to provide guidance on diagnostic reference level (DRLs), achievable dose levels (AD) and the National DRLs database are established.

ACKNOWLEDGEMENTS

The authors are pleased to acknowledge with thanks to the Radiological Society of Thailand for the awards offer to participate to this Congress. The acknowledgement is also forwarded to the interventional radiologists, nurses and radiological technologists at the unit of vascular and interventional radiology, King Chulalongkorn Memorial Hospital.

REFERENCES

1. International Commission on Radiological Protection. ICRP publication 135: Diagnostic reference levels in medical imaging. Annals of ICRP 2017; 46(1): 1–144.
2. National Radiological Protection Board (NRPB). Guidelines on patient dose to promote the optimization of protection for diagnostic medical exposure. Document of NRPB 1999; 10(1).
3. National Council on Radiation Protection and Measurements (NCRP). Reference levels and achievable doses in medical and dental imaging: Recommendations for The United States. NCRP report 2012; 172.
4. Australian Radiation Protection and Nuclear Safety Agency (ARPANSA). Code of practice for the radiation protection in the medical applications of ionizing radiation, Radiation Protection series 2008; 14.
5. International Atomic Energy Agency (IAEA). Patient dose optimization in fluoroscopically guided interventional procedures. IAEA-TECDOC 2010; 1641: 1–66.
6. Erskine BJ, Brady Z, Marshall EM. Local diagnostic reference levels for angiographic and fluoroscopic procedures: Australian practice. Australasian College of Physical Scientists and Engineers in Medicine 2014; 37: 75-82.
7. Kim JS, Lee BK, Ryu DR, Chu KJ, Choi HH, Roh YH, et al. A Multicenter survey of local diagnostic reference levels and achievable dose for coronary angiography and percutaneous transluminal coronary intervention procedures in Korea. Radiation Protection Dosimetry 2019; 178: 1-5.
8. Schegerer A, Loose R, Heuser LJ, et al. Diagnostic Reference Levels for diagnostic and interventional X-Ray procedures in Germany: update and handling. Fortschr Röntgenstr 2019; 191: 739-751.
9. Etard C, Bigand E, Salvat C, Vidal V, Beregi JP, Hornbeck A, et al. Patient dose in interventional radiology: a multicentre study of the most frequent procedures in France. European Radiology 2017; 27: 4281–4290.

Sonographic predictors for developing cholangiocarcinoma: A cohort study from an endemic area

Natcha Thanakijsombat[1,2], Jiraporn Laothamatas[1], Kamonwan Soonklang[3] , Surachate Siripongsakun[1]

1 Sonographer School, Faculty of Heath Science Technology, HRH Princess Chulabhorn College of Medical Science, Bangkok, Thailand,
2 Department of Emergency Medicine, Police General Hospital, Bangkok, Thailand,
3 Data Management Unit, HRH Princess Chulabhorn College of Medical Science, Chulabhorn Royal Academy, Bangkok, Thailand

Abstract

Cholangiocarcinoma (CCA) is an aggressive malignancy with rapid progression and poor prognosis. Bile duct and peribiliary changes related to cholangiocarcinogenesis may present on sonographic findings, for example, periductal fibrosis and diffuse bile duct dilatation without obstruction.

This study aims to evaluate ultrasound findings that could be used as predictors for developing CCA through our surveillance program in an endemic area, Nan province, Thailand. The surveillance population-based cohort was 4,337 villagers in Northern Thailand, aged 30-60 years, who consented to a 5-year abdominal ultrasound surveillance program, which included interval ultrasound examinations every six months. Patient demographics, including age and gender, family history of CCA, and ultrasound findings, including calcifications/ granuloma, diffuse biliary dilatation, and periductal fibrosis, were included. A logistic regression model was used to determine significant predictors using forward stepwise generalized linear model for multivariate analysis. A total of 4,225 people included in the study consisted of 1,919 males and 2,306 females with an average age of 45.49±7.66 years. Prevalence of calcifications/granuloma, periductal fibrosis, and diffuse bile duct dilatation detected on baseline sonographic surveillance was 497 (11.76%), 868 (20.54%), 478 (11.31%), respectively. The univariate analysis for significant predictors for development of CCA includes age (RR = 1.12, $p < 0.001$), family history of CCA (RR= 2.29, p= 0.002), periductal fibrosis (RR= 2.38, p= 0.001) and diffuse bile duct dilatation (RR = 7.59, $p < 0.001$).The multivariate analysis the independent predictors were age (RR= 1.12, $p <0.001$), family history of CCA (RR = 2.37, p = 0.001), and bile duct dilatation (RR= 5.94, $p <0.001$). Sonographic predictors of CCA development, including age and diffuse bile duct dilatation, may help identify the population at risk to target for surveillance in CCAs endemic areas.

Keywords: cholangiocarcinoma, predictor, sonography, surveillance

1. INTRODUCTION

Cholangiocarcinoma (CCA) is the most common primary malignancy of the biliary tract, originating in the biliary epithelial cells. The etiology of CCA is related to chronic inflammation and cholestasis of the biliary system. Several risk factors have been identified, such as liver fluke infestation, biliary stones (1). CCA's natural course is aggressive, with a median survival of fewer than 24 months following diagnosis and a 5-year survival rate of less than 5% (2). Thus CCA is highly aggressive with a dismal prognosis, especially in advanced stages. Early detection, diagnosis, and treatment of CCA patients is still a tough challenge for experts, at present.

CCA incidence rates vary markedly worldwide, presumably reflecting differences in local risk factors and genetics. The highest known prevalent rate are in southeast Asia, with an enormous burden of the disease reported in Thailand, particularly in the northeastern and northern regions (3). For Thailand, the disease's severity has caused awareness and prompt responses and the 1987 Campaign of "No raw fish consumption" in the endemic areas. Many research papers confirming that liver-fluke is a significant risk for developing CCA (3) and are found in uncooked fish. The campaign was successful, but still, the incidence rate has only minimally declined. Mortality rates are still high since patients present to hospital at a late stage of the disease, as the tumors are clinically silent in the early stages (4). Thus, Thailand's Ministry of Health decreed an endemic screening program (Cholangiocarcinoma Screening and Care Program: CASCAP). Results from 2019 confirm the effectiveness and viability as a tool for early detection of early-stage, operable CCA in high-risk areas (5).

At present, there has no consensus on the specific ultrasonographic findings that can serve as predictors of CCA (6,7). However, a current imaging study can identify early premalignant CCA lesions, including Biliary Intraepithelial Neoplasia (Bil-IN) and Intraductal Papillary Neoplasm of Biliary tract (IPNB), potentially in the curative resectable stage (8). In the premalignant CCA stage, especially IPNB, the dysplastic changes could produce mucin, which causes dilatation of the biliary system without detectable mass obstruction (9). The finding of biliary dilatation on ultrasound imaging may potentially be related to premalignant CCA change. This finding has been supported by a large cross-sectional CCA screening study, which found a significant association between bile duct dilatation and CCA (10).

There is limited research data about imaging predictors that could serve as independent biomarkers to predict CCA development, potentially useful for CCA surveillance. Therefore, this study aims to evaluate ultrasound findings, which could utilize as predictors for

developing CCA through our surveillance program in an endemic area, Nan province, Thailand.

2. MATERIAL AND METHODS

2.1 Study design and population

This historical cohort study included the residents of Ban Luang District, Nan Province, as the study population. Aged between 30 to 60 years, those recruited were not having any cancer or pregnancy. Village health care volunteers recruited subject registration with the Ban Luang district hospital's cooperation under the list of 6,327 target populations based on a district census registration. This study received approval by the Institutional board review and Ethics committee for Human Research (Certification No. 0052/2661), and the need for individual consent was waived. The recruitment flow of the patient is shown in Figure 1.

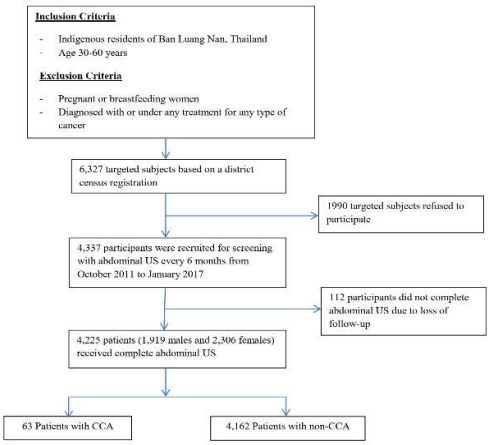

Figure 1 *Recruitment flow chart*

2.2 Subheading

Periductal fibrosis is defined as increasing periportal echo on sonography, caused by thickening of the bile duct wall, which runs parallel to the portal vein (11). Diffuse bile duct dilatation defines as the dilatation of the intrahepatic bile duct when the diameter exceeds 3 mm or more than 40% of the accompanying portal vein and without other associated abnormality (12). Calcifications/granuloma defined as hyperechoic nodules with posterior acoustic shadow within the liver parenchyma.

2.3 Statistical analysis

Demographic and anthropometric data of the patients, including age, gender, Body mass index Demographic data of the patients, including age, gender, and family history of CCA (first-degree relative), sonographic findings including hepatic calcifications/granuloma, diffuse bile duct dilatation, and periductal fibrosis were analyzed using chi-square and student t-test. A logistic regression analysis was used to determine significant predictors for developing CCA, including gender, age, family history of CCA, hepatic calcifications/granuloma, diffuse biliary system dilatation, and periductal fibrosis**.** The multivariate analysis was performed with forward stepwise selection to identify the independent predictive variables with $p<0.05$ level of significance. The analysis was conducted using Stata version12; Stata Corporation, College Station, and significance was defined as a two-sided p-value < 0.05.

3. RESULTS

A total of 4,225 people included in the study consisted of 1,919 males and 2,306 females with an average age of 45.49±7.66 years. Prevalence of calcifications, periductal fibrosis, and diffuse bile duct dilatation detected on baseline sonographic surveillance was 497 (11.76%), 868 (20.54%), 478 (11.31%), respectively. Demographic data are shown in Table 1.

Table 1 *Demographic data and presence of key US findings of the patients*

Table 1 Demographic data and presence of key US findings of the patients

	CCA (63 cases)	Non- CCA (4,162 case)	Total (4,225)	p value
Age (years)	51.41±5.85	45.40±7.65	45.49±7.66	<0.001
Gender				0.263
Male	33 (52.4%)	1,886 (45.31%)	1,919 (45.42%)	
Female	30 (47.6%)	2,276 (54.69%)	2,306 (54.58%)	
Family history of Cholangiocarcinoma*				0.002
No	44 (69.84%)	3,511 (84.36%)	3,555 (84.14%)	
Yes	19 (30.16%)	651 (15.64%)	670 (15.56%)	
Calcifications/granuloma				0.578
No	57 (90.48%)	3,671 (88.20%)	3,728 (88.24%)	
Yes	6 (9.52%)	491 (11.80%)	497 (11.76%)	
Diffuse bile duct dilatation				<0.001
No	32 (50.79%)	3,715 (89.26%)	3,747(88.69%)	
Yes	31 (49.21%)	447 (10.74%)	478 (11.31%)	
Periductal fibrosis				<0.001
No	39 (61.90%)	3,318 (79.72%)	3,357 (79.46%)	
Yes	24 (38.10%)	844 (20.28%)	868(20.54%)	

* Family history of first degree relative for Cholangiocarcinoma

The univariate analysis for the independent predictors of CCA's development includes age (RR = 1.12, $p < 0.001$), family history of CCA (RR= 2.29, p= 0.002), periductal fibrosis (RR= 2.38, p= 0.001) and diffuse bile duct dilatation (RR = 7.59, $p < 0.001$). The multivariate analysis of the independent predictors for CCA development were age (RR= 1.12, $p <0.001$), family history of CCA (RR = 1.92, p = 0.015), and bile duct dilatation (RR= 5.94, $p <0.001$). The univariate and multivariate analysis are shown in Table 2.

Table 2 *Univariate and Multivariate Analysis of CCA's Predictors*

Table 2. Univariate and Multivariate Analysis of CCA's Predictors

	Univariate Analysis			Multivariate Analysis		
	RR	95% CI	*p*-value	RR	95% CI	*p*-value
Age (years)	1.12	1.08-1.16	<0.001	1.12	1.08-1.16	<0.001
Gender (male vs female)	1.32	0.81-2.16	0.265			
Family history of CCA* (Yes vs No)	2.29	1.35-3.90	0.002	1.92	1.14-3.26	0.015
Calcifications/granuloma (Yes vs No)	0.79	0.34-1.32	0.580			
Diffuse bile duct dilatation (Yes vs No)	7.59	4.68-12.33	<0.001	5.94	3.65-9.66	<0.001
Periductal fibrosis (Yes vs No)	2.38	1.44-3.94	0.001			

* Family history of first degree relative for Cholangiocarcinoma

4. DISCUSSION

Of all demographic predictors, age and family history of CCA are significant independent predictors for developing CCA. Worldwide the incidence of CCA is increasing with age. This finding probably due to

CCA's evolution involves multiple carcinogenesis steps, starting from chronic bile duct inflammation to genetic alteration, premalignant bile duct change, and eventually to malignant transformation (13). Globally, age is one of the CCA risk factors, regardless of etiology (7). CCA's development has an average peak incident around 50 years and above but uncommon before 40 (6); this reflected that cholangiocarcinogenesis might take a significant time to develop invasive carcinoma. In Thailand, the incidence of CCA starts to rise at around age 40 and peak at age 60 (14). In our cohort study, most subjects detected by abdominal ultrasound surveillance to have CCA were in their late 40s and early 50s, and none was younger than 40 years of age (15).

Family factors influencing CCA development are believed to be solely from inheriting genetic factors and exposure to carcinogens (16). In the setting of liver fluke related CCA development, house-hold lifestyle may play a significant role in risk exposure (17). For example, people who live in the same area or close family tend similar lifestyles and similar eating habits. These factors would be poor sanitation practices, inadequate sewage infrastructure, and uncooked crypnoid fish consumption. This lifestyle leads to an increased risk of liver-fluke infection, class I carcinogen (18). Therefore, CCA's positive first-degree family history appears to be a good predictor for CCA development and should incorporate for surveillance scheme.

Interestingly, our data support that diffuse bile duct dilatation and periductal fibrosis are significant predictors for developing CCA. These two findings are related to the inflammation process, which eventually leads to the development of CCA. In a large cross-sectional CCA cohort study has reported an association between bile duct dilatation and CCA (8). However, our long-term follow-up study found that only diffuse bile duct dilatation was a strong independent predictor for CCA development. We postulate that because diffuse bile duct dilatation is bile duct changes related to inflammation (mucin production) (9) and potential premalignant change, e.g., IPNB, therefore, is a more specific risk factor in the development of CCA (8).

Thailand has the highest prevalence of CCA- with the highest incidence rate in the Northeastern region- which is considered a significant healthcare burden (19). Although there have been many studies on the characteristics of the specific liver and biliary tract imaging used to predict CCA development (8,10). Still, inconclusive to use as predictors for CCA to guide surveillance and follow-up. Our previous report on cholangiocarcinoma surveillance in the endemic area has proved to the survival benefit by detecting cholangiocarcinoma in the resectable stage and potentially received curative R0 resection (15). There are no specific serum biomarkers available for CCA screening due to insufficient sensitivity and specificity (20). Abdominal US is an effective method in detecting CCA and premalignant lesions; therefore, incorporating high-risk US features may help triage the high-risk population for close follow-up and potentially provide more extended surveillance for lower-risk patients (8).

5. CONCLUSION

Diffuse bile duct dilatation is an independent predictor for the development of CCA in the patients at risk in the endemic area of OV infestation. This imaging finding is potentially useful in identifying patients at risk for close CCA surveillance in the endemic area.

REFERENCES

1. Rizvi S, Gores GJ. Pathogenesis, diagnosis, and management of cholangiocarcinoma. Gastroenterology. 2013;145(6):1215-29.
2. Mosconi S, Beretta GD, Labianca R, Zampino MG, Gatta G, Heinemann V. Cholangiocarcinoma. Crit Rev Oncol Hematol. 2009;69(3):259-70.
3. Sripa B, Pairojkul C. Cholangiocarcinoma: lessons from Thailand. Current opinion in gastroenterology. 2008;24(3):349-56.
4. Thunyaharn N, Promthet S, Wiangnon S, Suwanrungruang K, Kamsa-ard S. Survival of cholangiocarcinoma patients in northeastern Thailand after supportive treatment. Asian Pac J Cancer Prev. 2013;14(11): 7029-32.
5. Khuntikeo N, Koonmee S, Sa-Ngiamwibool P, Chamadol N, Laopaiboon V, Titapun A, et al. A comparison of the proportion of early stage cholangiocarcinoma found in an ultrasound-screening program compared to walk-in patients. HPB (Oxford). 2020;22(6):874-83.
6. Blechacz B. Cholangiocarcinoma: Current Knowledge and New Developments. Gut Liver. 2017;11(1): 13-26.
7. Kamsa-Ard S, Luvira V, Suwanrungruang K, Kamsa-Ard S, Luvira V, Santong C, et al. Cholangiocarcinoma Trends, Incidence, and Relative Survival in Khon Kaen, Thailand From 1989 Through 2013: A Population-Based Cancer Registry Study. J Epidemiol. 2019;29(5):197-204.
8. Siripongsakun S, Sapthanakorn W, Mekraksakit P, Vichitpunt S, Chonyuen S, Seetasarn J, et al. Premalignant lesions of cholangiocarcinoma: characteristics on ultrasonography and MRI. Abdominal Radiology. 2019;44(6):2133-46.
9. Shimonishi T, Sasaki M, Nakanuma Y. Precancerous lesions of intrahepatic cholangiocarcinoma. Journal of hepato-biliary-pancreatic surgery. 2000;7(6): 542-50.
10. Chamadol N, Khuntikeo N, Thinkhamrop B, Thinkhamrop K, Suwannatrai AT, Kelly M, et al. Association between periductal fibrosis and bile duct dilatation among a population at high risk of cholangiocarcinoma: a cross-sectional study of cholangiocarcinoma screening in Northeast Thailand. BMJ open. 2019;9(3):e023217.

11. Sungkasubun P, Siripongsakun S, Akkarachinorate K, Vidhyarkorn S, Worakitsitisatorn A, Sricharunrat T, et al. Ultrasound screening for cholangiocarcinoma could detect premalignant lesions and early-stage diseases with survival benefits: a population-based prospective study of 4,225 subjects in an endemic area. BMC Cancer. 2016;16:346.
12. Benedetti NJ, Desser TS, Jeffrey RB. Imaging of Hepatic Infections. Ultrasound quarterly. 2008;24 4): 267-78.
13. Weill F, Eisencher A, Zeltner F. Ultrasonic study of the normal and dilated biliary tree. The "shotgun" sign. Radiology. 1978;127(1):221-4.
14. Nakanuma Y, Sasaki M, Sato Y, Ren X, Ikeda H, Harada K. Multistep carcinogenesis of perihilar cholangiocarcinoma arising in the intrahepatic large bile ducts. World J Hepatol. 2009;1(1):35-42.
15. Shaib Y, El-Serag HB. The epidemiology of cholangiocarcinoma. Seminars in liver disease. 2004;24(2):115-25.
16. Siripongsakun S, Vidhyarkorn S, Charuswattanakul S, Mekraksakit P, Sungkasubun P, Yodkhunnathum N, et al. Ultrasound surveillance for cholangiocarcinoma in an endemic area: A prove of survival benefits. Journal of gastroenterology and hepatology. 2018; 33(7):1383-8.
17. Songserm N, Promthet S, Pientong C, Ekalaksananan T, Chopjitt P, Wiangnon S. Gene-environment interaction involved in cholangiocarcinoma in the Thai population: polymorphisms of DNA repair genes, smoking and use of alcohol. BMJ open. 2014;4(10):e005447.
18. Pengput A, Schwartz DG. Risk Factors for Opisthorchis Viverrini Infection: A Systematic Review. J Infect Public Health. 2020.
19. Sripa B, Kaewkes S, Sithithaworn P, Mairiang E, Laha T, Smout M, et al. Liver fluke induces cholangiocarcinoma. PLoS medicine. 2007;4(7):e201
20. Sithithaworn P, Yongvanit P, Duenngai K, Kiatsopit N, Pairojkul C. Roles of liver fluke infection as risk factor for cholangiocarcinoma. Journal of Hepato-Biliary-Pancreatic Sciences. 2014;21(5):301-8.
21. Alvaro D. Serum and bile biomarkers for cholangiocarcinoma. Current opinion in gastroenterology. 2009;25(3):279-84.

Using Radial Basis Function-Kernel Support Vector Machine with Tree-Based Feature Selection for Cancer Type Prediction Based on Gene Expressions

Adrian Remigio[1]

1 School of Science, Royal Melbourne Institute of Technology, Australia

Abstract

Different treatment responses, survival characteristics and proliferation rate among different cancer types are attributed to their variation of genotypes. Gene expression analysis in conjunction with machine learning methods are helpful tools in cancer diagnosis and treatment prognosis. Our study aims to develop a cancer type classifier with reduced gene expressions needed. Dataset was obtained from the Pan-cancer analysis project, which contains 801 patients with 5 different cancer types and 20,531 gene expression measurements. Gini impurity function from decision trees was used to rank the 20,531 in terms of feature importance for the cancer type classification. The top 5 genes with the smallest impurities were utilized as features for the support vector machine (SVM). Radial basis function (RBF) kernel was implemented for the hyperplane or decision boundary in the SVM classification method. Results show that the sets of genes obtained resulted in high accuracy for the SVM. Density distribution of selected gene expressions provide an illustration of differences in gene expressions for different cancer types, which supports further the outcome of feature selection. Although the gene expression feature space was greatly reduced from 20,531 to 5, the accuracy scores of the developed classifier range from 0.955 to 0.980. Thus, 5 gene expression are sufficient for 5 cancer type classification, reducing the need for gene expression measurements from thousands of genes.

Keywords: Cancer type, Feature space, Hyperplane

1. INTRODUCTION

Different physiologic conditions, such as abundance of transcription factors, modulate the characteristic differentiation and differentiation rate of cells (1). Malignancy arises as a result of defective cell cycle and cell death regulations in cells that are in vegetative state. Cancer cells often exhibit abnormal cell cycle mechanisms that neglect control signals from inhibiting factors. Some tumors can manipulate its microenvironment to promote survival. Overall, these mechanisms help cancer cells to prolong their lifetime, and to continue colony formation (2).

The heterogeneity of tumor genotype, as a result of variable genetic alterations, leads to different sensitivities and response to cancer treatment modalities. As a complex network of signaling pathways, different gene expressions and protein levels modulate the interplay and dynamics of biochemical process involved in cell repair, proliferation, metabolism, and survival. For example, the mutations in von Hippen-Lindau (VHL) gene in renal cell tumors triggers an increased expression of HIF. HIF expression may increase or decrease the radiosensitivity of cells, depending on the signaling network and influence of HIF. HIF may increase susceptibility to radiation-induced cell death by amplification of p53-mediated apoptosis (2).

Gene expression defines the amount and rate of transcription and translation of a particular gene. Since cancer cell characteristics depend on a repertoire of gene networks, gene expression profiling of tumors is a helpful technique for classifying cancer type, estimating risks, and predicting prognosis (2,3). Fluorescence in situ hybridization (FISH) is used to determine the presence and amplification of mRNA expression of FGFR2 gene in the suspected bladder cancer. Using the obtained gene expression data and data-derived cancer characteristics, anti-cancer drugs, such as erdafitnib, are prescribed. Real-time quantitative reverse transcription PCR and microarray assays are also used for gene expression measurements (3).

Computer-aided methods for cancer therapies were developed through the application of mathematical and statistical techniques to help improve diagnostic accuracy and treatment selection. Data extracted from imaging studies and laboratory tests are used in supervised and unsupervised learning algorithms to establish a mathematical correlation between the extracted information and the predicted outcome. An example of diagnostic application of supervised learning is the use of convolutional neural network for breast cancer detection in mammograms (4).

In this study, we focused on classification of 5 cancer types using support vector machines (SVM). Various feature selection methods were implemented in the field of cancer classification such as double radial basis function-kernels in (5). The Pan-Cancer Analysis (PANCAN) Project is a compilation of gene expressions from 20,531 genes for different tumor types (6). We used feature importance based on decision trees to recommend sets of gene biomarkers significant for cancer type classification, which were subsequently used as features for the developed SVM with radial basis function (RBF) kernel classifier. This classifier can be used in clinical pathology characterization with the advantage of minimal gene expression data required as a result of top feature selection. In addition, the classifier

can also be used for identifying probable primary tumors using metastases in the examined region.

2. MATERIAL AND METHODS

2.1 Dataset Acquisition

Dataset used for the feature selection, and training and testing of classifiers was obtained from the PANCAN project. The dataset consists of RNA-sequence gene expressions from 20,531 genes for 5 tumor types and 801 patients. Each patient was diagnosed with one of the 5 tumor types, which are breast carcinoma (BRCA), kidney renal-cell carcinoma (KRCC), prostate adenocarcinoma (PRAD), lung adenocarcinoma (LUAD), and colon adenocarcinoma (COAD).

2.2 Data Preprocessing

The initial processing involves the normalization of gene expression values in the dataset through the following equation:

$$x_{ij} = norm(g_{ij}) = \frac{g_{ij} - E_{j,min}}{E_{j,max} - E_{j,min}},$$

where g_{ij} is the gene expression for patient i and gene j; $E_{j,min}$ is the minimum gene expression of gene j for all patient i; $E_{j,max}$ is the minimum gene expression of gene j for all patient i; and $norm(g_{ij})$ is the normalized value of g_{ij}.This procedure allows equal influence of varying gene expression ranges for different genes, as justified in (7). The dataset was also equally partitioned into feature selection dataset, and classifier training and testing dataset. This eliminates classification bias that would arise if the dataset used for feature selection is reused in training and testing of the classifiers.

2.3 Feature Selection Using Decision Trees

Decision trees is a supervised learning algorithm for classification based on a series of data splitting procedures, with the goal of producing homogeneous nodes with corresponding labels of classification (8). In the study, the gene expressions from 20,531 genes were the original features. Recall that class labels, which are the 5 tumor types, are dependent on some or all of the features.

At the start of the classifier training procedure, the root node contains the whole training dataset. The root node is split and branches into two subsets according to a certain feature decision function. The node is split further for other features until certain stopping criteria, such as minimum number of samples per node, are met. These nodes that do not split further, referred to as the terminal nodes, become the basis of class label assignment through identification of the mode of the samples in the terminal node. For example, if the terminal node contains 5 patients with BRCA, 2 patients with KRCC, and 2 patients with COAD, then the class label BRCA will be assigned to the terminal node.

The feature selection procedure utilized the first half of the original dataset. Let x_i be the datapoints in the 20,531-dimensional gene expression feature space with corresponding cancer type class labels y_i. For a given data Q in node m, there exists a split candidate $\theta = (j, t_m)$ for feature or gene j, where t_m is the threshold gene expression for splitting. The splitting candidate divides the dataset into:

$$Q_{left}(\theta) = (x, y), x_j \geq t_m$$

$$Q_{right}(\theta) = (x, y), x_j \leq t_m$$

which shows that all patients with gene expression j greater than or equal to t_m are included to $Q_{left}(\theta)$, while the other remaining patients are included in $Q_{right}(\theta)$. If gene expression j is an efficient biomarker that differentiates between cancer types, then almost or all patients included in $Q_{left}(\theta)$ will have similar cancer types different from the cancer types in $Q_{right}(\theta)$. A common measure of the quality of splitting is the impurity of nodes given by:

$$G(Q, \theta) = \frac{n_{left}}{N_m} H\left(Q_{left}(\theta)\right) + \frac{n_{right}}{N_m} H\left(Q_{right}(\theta)\right),$$

where n_{left} is the number of patients in $Q_{left}(\theta)$; n_{right} is the number of patients in Q_{righ} (θ); N_m is the number of patients in the parent node m; and H is the impurity function. In the study, we selected the Gini impurity function:

$$H(Q) = \sum_k p_k(Q)(1 - p_k(Q))$$

where k are the cancer types as labels; and p_k is the ratio of patients with cancer type k to the total number of patients in Q.

Iteration of the process of node splitting and impurity measurement were performed for all gene expression feature j or until the minimum number of samples per node is achieved. The branching patterns formed by different feature sequences and the threshold t_m in each node were optimized such that $G(Q, \theta)$ is minimized. Small impurity $G(Q, \theta)$ indicates that the splitting is able to effectively separate different cancer types according to the set of features (8).

Top 5 genes were recommended based on features in nodes with the smallest $G(Q, \theta)$. Due to the random selection of splitting candidates, top genes from feature ranking may vary for different simulations. We recommended 5 sets of top genes that were acquired from different simulation runs. Genes from each set were tested as input features for the SVM. Some of the top genes were investigated by plotting their gene expression density distribution for the whole dataset.

2.4 Training of SVM with RBF Kernel

In SVM, classification is performed by establishment of hyperplanes or decision boundaries that divide the feature space, where each region corresponds to a class label. The hyperplanes are enclosed by margins, such that there are no datapoints within the defined margins. Datapoints nearest to the margins are defined as the support vectors. SVM aims to maximize the margin distance from the hyperplane to lower the generalization error during classification (8). The maximization of margin is similar to minimizing the distance between the support vectors and margin boundaries.

Using the definition of x_i and y_i in Section 2.3, the weight vector $\boldsymbol{w}$ is defined as the vector that has a magnitude equal to the distance from the hyperplane to the outer boundary of the margin, with the maximum margin equal to $2/\|\boldsymbol{w}\|$. $\boldsymbol{w}$ is perpendicular to the tangent of hyperplane and margin boundary. The SVM training for the hyperplane and margin definition was considered as an optimization problem. The hyperplane used was a radial basis function of the form:

$$K(x, x') = \exp(-\gamma\|x - x'\|^2),$$

where $\|x - x'\|$ is the Euclidean distance from two points in the feature space (8).

Selection of 5 gene expressions from the employed tree-based feature selection reduces the dimensions of the feature space from 20,531 to 5, which implies that the SVM was trained only for the 5 selected gene expressions. Moreover, the SVM can classify cancer types using only the provided 5 gene types used for training.

2.5 Accuracy Evaluation of the SVM Classifier

Following the training of the SVM with RBF kernel classifier using the gene expression data, the classifier was subjected to prediction of testing patient dataset. It is important that the data utilized in training of the SVM classifier is not reused in the testing of the same classifier to prevent classification bias. Accuracy scores, which is the ratio of the number of correct predictions to the total number of predictions made, were obtained by benchmarking of the predicted cancer type to the true cancer type defined in the testing dataset. 5-fold cross-validation method was used to ensure that all patients in the training and testing dataset are sampled. Feature selection, SVM training, and testing were implemented using Scikit learn toolkit in Python (8).

3. RESULTS

3.1 Selected Top Genes from the PANCAN Dataset

Results from tree-based feature selection after 5 simulation runs are shown in Table 1. Each set corresponds to a single simulation run. As already noted in Section 2.3, the stochastic approach of minimizing the impurity function for different candidate splits may result to different rankings with different simulation runs. The process of feature selection entails that the gene expression of genes shown in Table 1 are relevant in the identification of cancer type of the patient.

Table 1 *Top genes obtained from decision tress feature importance selection.*

Set	5 Most Important Genes
1	TRPS1, PAX2, SCGB3A2, PLEK2, NSFL1C
2	TRPS1, ESRP1, SLC45A3, SFTPA1, ATOX1
3	TRPS1, FXYD2, SCGB3A2, ANXA4, SPRY2
4	TRPS1, PAX2, SCGB3A2, AURKB, AQPEP
5	TRPS1, SCGB3A2, ST6GALNAC1, LOC286002, HBM

3.2 SVM with RBF Kernel Accuracy

The accuracies of the trained SVM for different sets of gene expression features are shown in Table 2. The different gene sets have high accuracy scores, indicating the effectiveness of tree-based feature selection for identifying important gene expression biomarkers in cancer type classification. We recommend the use of SVM trained using features from Set 2, which has the highest accuracy score among the other sets.

Table 2 *Respective accuracies for different classifiers using the decision tree recommended genes.*

Set	SVM Accuracy Score
1	0.955±0.030
2	0.980±0.013
3	0.950±0.026
4	0.957±0.036
5	0.955±0.023

The importance of these genes can be visualized using density plots of gene expression for the 801 patients. In Figure 1, the density distribution of FXYD domain containing ion transport regulator 2 (FXYD2) gene expression in the PANCAN dataset for different cancer types is plotted. The density plot of FXYD2 gene expression demonstrates that almost all patients with KRCC have higher FXYD2 gene expressions compared to patients with other cancer types. Thus, measurement of FXYD2 gene expression is an important biomarker for differentiating KIRCC from other cancer types. For comparison purposes, we also plotted the density distribution for the transcriptional repressor GATA binding 1 (TRPS1) in Figure 2. TPRS1 density distribution of gene expression demonstrates that TPRS1 is highly expressed in BRCA. Using both

FXYD2 and TPRS1 gene expressions as bases, BRCA and KRCC can be identified from other cancer types. Combination with other genes listed in Table 1 allows accurate classification for all 5 cancer types.

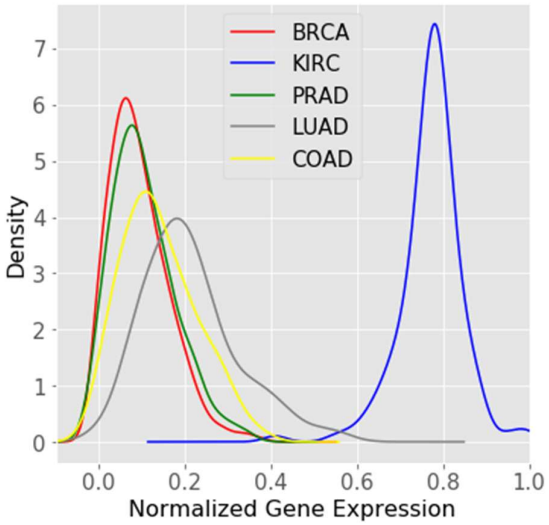

Figure 1 *Gene expression density Plot of FXYD2 gene in Set 3.*

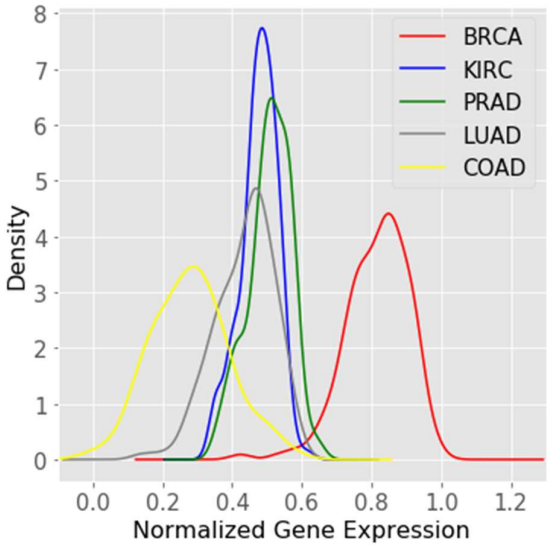

Figure 2 *Gene expression density plot of TPRS1 gene.*

4. DISCUSSION

The main advantage of the SVM classifier developed in this study is that it relies only on 5 gene expression measurements. This eliminates the need of performing gene expression measurements from thousands of genes for cancer type identification. The model can be expanded to include other cancer types. However, the number of recommended genes should be greater or equal to the number of cancer type labels, such that there is an assurance that at least a single gene will be found to be relevant for each cancer type. The SVM classifier can also be used in primary cancer localization during treatment assessment. During metastasis, cancer cells from the primary tumor may migrate to other distant organs through blood or lymph vessels. If the metastatic growth location was found and the primary tumor location remains undetected, gene expression measurements may be performed and used as input to the SVM classifier. The predicted cancer type may suggest the origin of the metastatic tumor, leading to primary tumor localization.

5. CONCLUSION

Feature selection using decision trees supervised learning significantly reduces the feature space while yielding good prediction accuracies for the 5 cancer types. Density plots of the PANCAN dataset show that the gene expressions from the selected feature genes varies for different cancer types. Since the genes selected are relevant in discriminating between cancer types, these genes can also be utilized as imaging biomarkers and therapeutic agents.

REFERENCES

1. Newman, S.A., 2020. Cell differentiation: What we have learned in 50 years. Journal of Theoretical Biology. 485.
2. Hall, E.J., Giaccia, A.J., 2012. Radiobiology for the Radiologists. WOLTERS KLUWER, Philadelphia.
3. Malone, E.R. et al., 2020. Molecular profiling for precision cancer therapies. Genome Med. 12(8). https://doi.org/10.1186/s13073-019-0703-1.
4. Katzen, J., Dodelzon, K., 2018. A review of computer aided detection in mammography. Clinical Imaging. 52, 305-309. DOI: 10.1016/j.clinimag.2018.08.014.
5. Liu, S. et al., 2018. Feature selection of gene expression data for cancer classification using double RBF-kernels. BMC Bioinformatics. 19(1). DOI:10.1186/s12859-018-2400-2.
6. Weinstein, J.N. et al., 2013. The cancer genome atlas pan-cancer analysis project. Nature Genetics. 45(10), 1113-1120.
7. Higuera, C., Gardiner, K.J., Cios, K.J., 2015. Self-organizing feature maps identify proteins critical to learning in a mouse model of down syndrome. PLoS ONE. 10(6): e0129126. DOI:10.1371/journal.pone.0129126.
8. Pedregosa, F. et al., 2011. Machine Learning in Python. Journal of Machine Learning Research. 12, 2825-2830.

The role of a medical physicist in an advanced emergency pediatric hospital

Manabu Yoshimoto[1], Hiroyasu Iwasaki[1], Yuji Yonezawa[1], Makoto Hayashi[1], Masaki Andou[1], Manabu Iwata[1], Kazuya Takahashi[1], Junpei Kurokawa[1], Yuma Shibutami[1], Akari Murai[1], Ayaka Kumazawa[1], Ai Naitou[1], and Kyoka Kobayashi[1]

1 Aichi Children's Health and Medical Center, Japan

Abstract

Most Japanese medical physicists are involved in radiation therapy in the medical field. We had the opportunity to have a medical physicist in the diagnostic field specializing in pediatric emergency medicine due to the reorganization of the hospital. With the birth rate of children declining in recent years, hospitals specializing in pediatric medicine play a very important role in the community. Medical physics needs to continue to develop in the diagnostic department as well. Looking at the past and future, in order to think about how we can contribute to the hospital as a medical physicist in the future, we examined the work from the past to the present and examined how it will contribute to pediatric medicine.

Keywords: Medical physicist, Reduction of exposure, Pediatric medical

1. INTRODUCTION

This center was newly constructed in November 2001, and is a characteristic facility with major pillars of health and medical care based on a new concept for the 21st century. As of March 2020, we have 31 medical care departments and 200 beds. With the birthrate generally stagnant, the significance of existence and demand for this hospital are increasing. In 2019, with the closure of the radiation department due to the merger of hospitals, we had the opportunity to assign a medical physicist to a hospital specializing in pediatric care. As a pediatric hospital, our hospital specializes in advanced pediatric emergency medical care and promotes advanced team medical care even before childbirth. One of the roles of medical physicists is to train team members who are practicing team medical care and have excellent knowledge and skills, and who are capable of accepting pediatric patients with high severity and urgency. It is necessary to contribute to quality improvement. Taking into account the trends in the radiation department, we will consider the future involvement, medical cooperation, and hospital contribution in the charge of the medical physicist.

2. MATERIAL AND METHODS

Extract the latest trends and current status of each examination in the radiation department over the past five years, verify the current job description, and examine future job description.

3. RESULTS

The situation regarding the number of past cases is summarized in Figures 1. It shows a temporary increase in the number of examinations every spring, summer, and winter. This indicates that the number of patients is increasing during the child-specific school holidays. The results for each quarter (three months) show an increasing trend on average for radiological examinations that are less affected by time frames other than CT, MRI, Radio Isotope, Cardio angiography. The number of radiological examinations per number of patients per year was about twice that of 5 years ago. (The previous value was 17.7 and the latter value was 35.8)

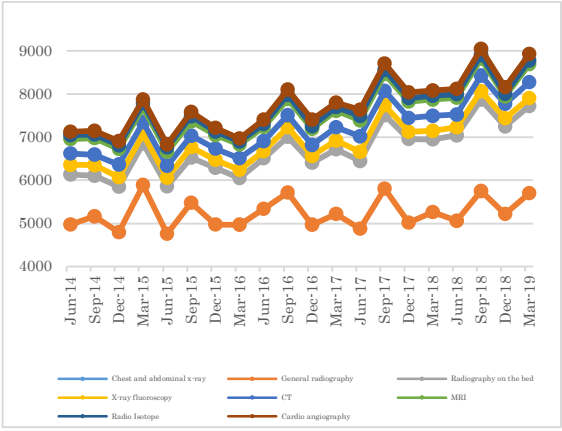

Figure 1 Number of each radiological examination every quarter (every 3 months) in the past 5 years.

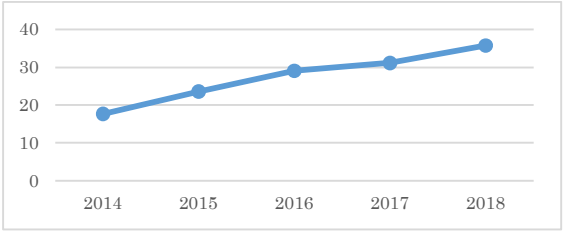

Figure 2 Number of radiological examinations per number of patients per year

4. DISCUSSION

In the radiation department

・Enhancement of safety management of radiation equipment. (Device QA・QC)

・Selection of radiation dose that understands the output characteristics of each device. (Understand radiation dose by patient age and site)
・Introduction and management of individual patient radiation exposure management software in cooperation with the radiology information system and each radiation device.
・Reduction of radiation exposure of radiologists in pediatric imaging. (Exposure of radiologists' hands and fingers within the radiation imaging range is a major issue, and the use of patient fixtures and promotion of the use of lead-containing gloves and lead-containing aprons)
・Participating in conferences before some examinations.

Currently focusing on the above items.

5. CONCLUSION

As necessary items for the number of examinations that are increasing year by year, there are problems of safety management of radiation equipment, proper use of radiation equipment including radiation dose, and radiation exposure of medical personnel.We have been actively introducing cutting-edge medical equipment since the operation of the facility started. Taking general radiography and ward radiography as examples, the introduction of the flat-panel x-ray imaging detector is not only patient exposure but also simple and immediate, it can be said that it had a great effect in aiming for easy medical care. However, there are large variations in radiation imaging conditions of radiologists. As a short-term goal, it is considered necessary for radiation technologists to select an appropriate radiation dose by taking into account factors such as age, body shape, and past images when taking images by reducing radiation exposure. From a long-term perspective, team medical care is very important, and strengthening collaboration with various occupations, including participation in meetings, is a major issue. We would like to continue our efforts as a facility that can efficiently provide high-quality and appropriate medical care for children.

ACKNOWLEDGEMENTS

We will continue to make further progress and will make further efforts so that it will be widely recognized as a mature facility and meet the expectations of everyone. Thank you for your special support and cooperation.

Time dependence of intra-fractional motion for spine stereotactic body radiotherapy

Ryuta Hirai[1], Yu Ohkubo[2], Mitsunobu Igari[1], Yu Kumazaki[1], Tomomi Aoshika[1], Yasuhiro Ryuno[1], Satoshi Saito[1], Takanori Abe[1], Shin-ei Noda[1], Shingo Kato[1]

1 Department of Radiation Oncology, Saitama Medical University International Medical Center,
2 Department of Radiation Oncology, Saku Central Hospital Advanced Care Center

Abstract

Recently the usefulness of stereotactic body radiotherapy (SBRT) for spinal metastases has been reported, however, the treatment could require a long time. Therefore, the intra-fractional spinal motion must be taken into account. We investigated intra-fractional spinal motion during SBRT and its time dependency.

Thirty-one patients who received SBRT using CyberKnife at our hospital were enrolled in the study. Two-dimensional kV X-ray spine images in two directions were taken before and during treatment. Image acquisition intervals during treatment were set at 35-60 sec. Automatic image matchings were performed between the reference digital reconstructed radiography (DRR) images and live images, and the spinal position displacements were recorded on three translations and rotations (Right-Left, Superior-Inferior, Anterior-Posterior, Roll, Pitch, Yaw). The amount of couch adjustments was also recorded when the spine position was corrected by moving couch. From these values, the over-time accumulated translational and rotational displacements without any couch adjustments were calculated. Pearson's correlation coefficients were used to evaluate the correlations between the displacements and the elapsed treatment time.

Spinal position displacements in all translational and rotational directions were correlated with the elapsed treatment time. Especially, Right-Left displacements of >1 mm and >2 mm were observed at 4-6 minutes and 8-10 minutes after initiation of treatments, respectively. Rotational displacements in Yaw direction >1° were observed 8-10 minutes after treatment initiation.

The translational and rotational displacements systematically increased with the elapsed treatment time. It is suggested that the spine position should be checked every 4-6 minutes or irradiation time should be limited within 4-6 minutes to assure the irradiation accuracy with a millimeter or submillimeter range.

Keywords: Stereotactic body radiotherapy, Spine metastasis, Intra-fractional motion

1. INTRODUCTION

The spine is one of the most common sites of metastasis, causing pain and negatively impacting QOL. Typically, palliative irradiation at 8-30 Gy is performed to treat spinal metastases. However, dose escalation using stereotactic body radiotherapy (SBRT) for spinal metastases may provide better long-term pain control and local control compared to conventional palliative radiotherapy [1, 2]. Recently, re-irradiation of spinal metastases using SBRT has also been reported [3, 4].

Spine SBRT is performed using various image guides and irradiation devices [5, 6]. Intra-fractional motion errors of the spine are minimized when patient displacements are corrected during treatment using image guidance systems [7, 8]. However, depending on the treatment device, it may be difficult to perform real-time position correction during irradiation. The time required for SBRT depends on the particular treatment device, the site of irradiation, and prescribed dose, but is generally longer than that of conventional three-dimensional conformal radiotherapy (3DCRT). SBRT planning studies for spinal metastases have reported an irradiation time of about 10 minutes with TrueBeam (Varian Medical systems, Palo Alto, CA) and 20-30 minutes with Tomotherapy (Accuray, Inc., Sunnyvale, CA) [9, 10]. As treatment time increases, positional displacement of the patient may occur. Therefore, intra-fractional motion should be accurately determined and taken into account during treatment planning.

In this study, we investigated intra-fractional spinal motion during SBRT and its time dependency by analyzing tracking log data of a CyberKnife (Accuray, Inc., CA) room-mounted X-ray imaging system.

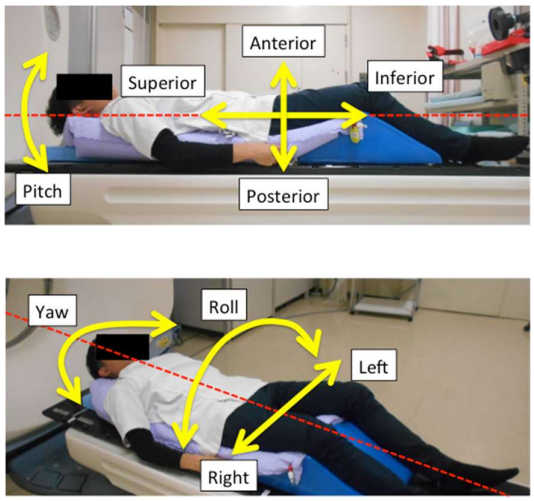

Figure 1 *Patient set-up.*

Table 1 *Patient characteristics.*

	Detail	No. of cases
Tumor location	Lung	22
	Rectum (pelvic recurrence)	1
	Prostate (pelvic recurrence)	1
	vertebral body	2
	lymph node metastasis	6
Tracking location	Cervical	3
	Thoracic	22
	Lumbar	7
Prescribed dose	12-60 Gy	—
Fractions	3-8 fractions	—
Image interval	1 min 9 sec ± 11 sec	—
Mean treatment time	34 min 12 sec ± 10 min 34 sec	—

2. MATERIAL AND METHODS

A total of 31 patients (32 plans) who received SBRT using CyberKnife at our hospital from April 2014 to March 2020 were enrolled in this study. Patient characteristics are summarized in Table 1. Patients were immobilized with a vacuum bag and a cushion placed below the knees (Fig. 1). All treatments were delivered with a real-time tracking system using the vertebral body near the tumor as a landmark. Log data from 32 plans conducted as initial treatment were analyzed.

Two-dimensional kV X-ray spine images in two directions were taken before and during SBRT with a room-mounted X-ray imaging system associated with the CyberKnife. Image acquisition intervals during treatment were set at 35-60 sec. Since the CyberKnife system did not allow imaging during treatment beams, images were acquired approximately once every minute (Table 1). The timestamps of each image were logged. Automatic image matching using the vertebral body was performed between reference digital reconstructed radiography (DRR) images and live images with the Xsight Spine Tracking System, and mismatches in three sets of translations and rotations (Right-Left (R-L), Superior-Inferior (S-I), Anterior-Posterior (A-P), Roll, Pitch, and Yaw) were recorded. The arrows in Fig. 1 show the direction of spine movement. If spine position was corrected by altering the position of the couch, the amount of couch adjustments was also recorded. Based on this information, the time-dependent accumulation of translational and rotational displacements without couch adjustments was analyzed. Positional displacements were calculated by averaging every 2 minutes for 0-10 minutes and every 5 minutes for 10-20 minutes. Pearson's correlation coefficients (r) were used to evaluate correlations between vertebral body displacements and elapsed treatment time. $P<0.05$ was considered statistically significant. This study was approved by the Institutional Review Board of our institute.

3. RESULTS

Figures 2(a)-(f) show the mean time-dependent accumulation of translational and rotational displacements of the vertebral body in all cases. Relatively large displacements in the R-L direction were observed, and the displacements tended to increase with time. Spinal position displacements in all translational and rotational directions were correlated with elapsed treatment time. In particular, there was a moderate correction ($r>0.4$) between the R-L and S-I directions. Mean ± 1 SD maximum translational displacements within 20 minutes for all patients were 1.3 ± 0.9 mm, 0.8 ± 0.4 mm, and 0.6 ± 0.4 mm in the R-L, S-I, and A-P directions, respectively, and mean ± 1 SD maximum rotational displacements in the Yaw, Pitch, and Roll directions were 0.6 ± 0.3°, 0.4 ± 0.2°, and 0. 5 ± 0.3°, respectively. Table 2 shows the proportion of patients with displacements of >1 mm, >2 mm, >1°, or >2° according to elapsed treatment time. Right-Left displacements of >1 mm and >2 mm were observed at 4-6 minutes and 8-10 minutes after treatment initiation, respectively. No displacement of ≥2 mm was observed within 20 minutes in the S-I and A-P directions. Rotational displacements in the Yaw direction of >1° were observed at 10-15 minutes after treatment initiation.

4. DISCUSSION

Some studies have evaluated intra-fractional spinal motion during SBRT using ExacTrac (BrainLab, Heimstetten, Germany) [13] and Cone-Beam CT [14-16]. However, these studies analyzed motion only pre- and post-irradiation, or for a limited duration during

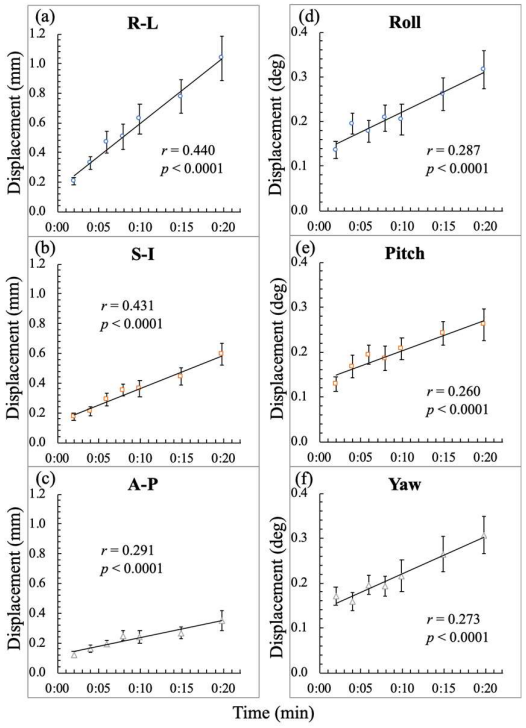

Figure 2 *Time dependence of translational and rotational displacements of the vertebral body.* Error bars represent standard errors.

treatment, and did not continuously evaluate motion during the entire treatment fraction. Murphy et al. [17] and Chuang et al. [18] measured intra-fractional motion with the CyberKnife X-ray imaging system, but only analyzed positional displacements between consecutive image acquisitions taken in 1-2 minute intervals, rather than the positional displacement over the entire treatment fraction. To the best of our knowledge, no study has reported on the temporal aspects of intra-fractional spinal motion in SBRT, although intra-fractional motion of the skull and metal markers has been reported [11].

Mean translational and rotational displacements were correlated with elapsed treatment time (Figure 2), indicating that the spine is systematically displaced during treatment and this displacement increases with time. However, as shown in Table 2, there were no cases in which the maximum rotational displacement exceeded 1° within 10 minutes. Moreover, in spine SBRT, the influence of rotational displacement is limited because the beam isocenter is set near the center of the target in most cases. In contrast, translational displacements, especially in the R-L direction, were relatively large, with displacements of >1 mm at 4-6 minutes and >2 mm at 8-10 minutes in some cases (Table 2). Hoogeman et al. recommended patient position matching at least every 5 minutes in order to achieve irradiation accuracy in the millimeter or sub-millimeter range for skull or metal marker tracking [11]. Our findings for spine tracking were similar, suggesting

Table 2 *Percentage of cases with mean translational and rotational displacements of >1 mm, >2 mm, >1°, or >2° according to elapsed treatment time.*

		0-2 min	2-4 min	4-6 min	6-8 min	8-10 min	10-15 min	15-20 min
R-L	> 1 mm	0.0	0.0	12.5	12.5	21.9	31.3	40.6
	> 2 mm	0.0	0.0	0.0	0.0	3.1	6.3	12.5
S-I	> 1 mm	0.0	0.0	0.0	3.1	3.1	3.1	12.5
	> 2 mm	0.0	0.0	0.0	0.0	0.0	0.0	0.0
A-P	> 1 mm	0.0	0.0	0.0	0.0	0.0	0.0	9.4
	> 2 mm	0.0	0.0	0.0	0.0	0.0	0.0	0.0
Roll	> 1°	0.0	0.0	0.0	0.0	0.0	0.0	0.0
	> 2°	0.0	0.0	0.0	0.0	0.0	0.0	0.0
Pitch	> 1°	0.0	0.0	0.0	0.0	0.0	0.0	0.0
	> 2°	0.0	0.0	0.0	0.0	0.0	0.0	0.0
Yaw	> 1°	0.0	0.0	0.0	0.0	0.0	3.1	3.1
	> 2°	0.0	0.0	0.0	0.0	0.0	0.0	0.0

R-L = Right-Left. S-I = Superior-Inferior. A-P = Anterior-Posterior.

the importance of frequent image guidance for spine SBRT due to the proximity of organs at risk (OARs), especially the spinal cord.

In SBRT, a steep dose distribution is applied to deliver large doses to the tumor while reducing the dose to adjacent OARs. Serious adverse events could occur if large doses are delivered to OARs due to intra-fractional motion. Therefore, when treating patients with an IGRT device that does not allow for real-time positional correction during irradiation, an appropriate setup margin must be used to account for intra-fractional motion. However, expanding the setup margin may cause overlap between the PTV and OARs, making it impossible to irradiate the tumor with a sufficient dose. In the present study, intra-fractional motion of the vertebral body was found to increase as treatment time elapsed. In such cases, irradiation time should be shortened or frequent image guidance should be performed. For instance, when treating patients with volumetric modulated arc therapy (VMAT), the number of arcs can be increased and positional correction repeated with each arc irradiation.

This study has several limitations worth noting. First, the sample size was small, and thus we could not assess the influence of differences in tracking sites (cervical, thoracic, and lumbar spine). Depending on the fixation method, the cervical or upper thoracic spine may exhibit more positional displacement due to the curvature. Second, given the small proportion of patients with spinal metastases, intra-fractional motion may in fact be greater than that observed in the present study, for example, in patients suffering from pain. Spine SBRT for patients with bone metastases would

require the active use of analgesics to maintain the patient's posture during treatment.

5. CONCLUSION

Translational and rotational displacements systematically increased as treatment time elapsed. Spine position should be checked every 4-6 minutes, or irradiation time should be limited to within 4-6 minutes, in order to ensure irradiation accuracy within the millimeter or submillimeter range.

ACKNOWLEDGEMENTS

The authors thank Jun Teranishi, Tomohito Nakada, Tohru Azami, and Haruka Yoshida (Division of Radiology, Saitama Medical University International Medical Center) for their assistance in data collection.

REFERENCES

1. Kumar R, Nater A, Hashmi A, et al. The era of stereotactic body radiotherapy for spinal metastases and the multidisciplinary management of complex cases. Neurooncol Pract. 2016;3(1):48–58. 2.
2. Zeng KL, Tseng CL, Soliman H et al. Stereotactic Body Radiotherapy (SBRT) for Oligometastatic Spine Metastases: An Overview. Front Oncol. 2019;9:337. Published 2019 May 1. 3.
3. Kawashiro S, Harada H, Katagiri H, et al. Reirradiation of spinal metastases with intensity-modulated radiation therapy: an analysis of 23 patients. J Radiat Res. 2016;57(2):150–6. 4.
4. Myrehaug S, Sahgal A, Hayashi M, et al. Reirradiation spine stereotactic body radiation therapy for spinal metastases: systematic review. J Neurosurg Spine. 2017;27(4):428–35. 5.
5. Benedict SH, Yenice KM, Followill D, et al. Stereotactic body radiation therapy: the report of AAPM Task Group 101. Med Phys. 2010 37(8):4078–101. 6.
6. Alaei P, Ding GX. Overview of Image Guidance in Radiation Therapy. In: Alaei P, Ding GX, editors. Image Guidance in Radiation Therapy: Techniques, Accuracy, and Limitations. 1st ed. Tennessee: American Association of Physicists in Medicine by Medical Physics Publishing; 2018. pp. 1–22. 7.
7. Chang EL, Shiu AS, Lii MF et al. Phase I clinical evaluation of near-simultaneous computed tomographic image-guided stereotactic body radiotherapy for spinal metastases. Int J Radiat Oncol Biol Phys. 2004;59(5):1288–94. 8.
8. Verellen D, Soete G, Linthout N et al. Quality assurance of a system for improved target localization and patient set-up that combines real-time infrared tracking and stereoscopic X-ray imaging. Radiother. Oncol. 2003;67, 129–141. 9.
9. Gallo JJ, Kaufman I, Powell R et al. Single-fraction spine SBRT end-to-end testing on TomoTherapy, Vero, TrueBeam, and CyberKnife treatment platforms using a novel anthropomorphic phantom. J Appl Clin Med Phys. 2015;16(1):5120. 10.
10. Yang J, Ma L, Wang XS et al. Dosimetric evaluation of 4 different treatment modalities for curative-intent stereotactic body radiation therapy for isolated thoracic spinal metastases. Med Dosim. 2016;41(2):105–12. 11.
11. Hoogeman MS, Nuyttens JJ, Levendag PC et al. Time dependence of intrafraction patient motion assessed by repeat stereoscopic imaging. Int J Radiat Oncol Biol Phys. 2008;70(2):609–18. 12.
12. Chuang C, Sahgal A, Lee L et al. Effects of residual target motion for image-tracked spine radiosurgery. Med Phys. 2007;34(11):4484–90. 13.
13. Jin JY, Ryu S, Rock J et al. Evaluation of residual patient position variation for spinal radiosurgery using the Novalis image guided system. Med Phys. 2008;35(3):1087–93. 14.
14. Li W, Sahgal A, Foote M et al. Impact of immobilization on intrafraction motion for spine stereotactic body radiotherapy using cone beam computed tomography. Int J Radiat Oncol Biol Phys. 2012;84(2):520–6. 15.
15. Hyde D, Lochray F, Korol R et al. Spine stereotactic body radiotherapy utilizing cone-beam CT image-guidance with a robotic couch: intrafraction motion analysis accounting for all six degrees of freedom. Int J Radiat Oncol Biol Phys. 2012;82(3):e555–62. 16.
16. Finnigan R, Lamprecht B, Barry T et al. Inter- and intra-fraction motion in stereotactic body radiotherapy for spinal and paraspinal tumours using cone-beam CT and positional correction in six degrees of freedom. J Med Imaging Radiat Oncol. 2016;60(1):112–8. 17.
17. Murphy MJ, Chang SD, Gibbs IC et al. Patterns of patient movement during frameless image-guided radiosurgery. Int J Radiat Oncol Biol Phys. 2003;55(5):1400–8. 18.
18. Nataf F, Schlienger M, Liu Z et al. Radiosurgery With or Without A 2-mm Margin for 93 Single Brain Metastases. Int J Radiat Oncol Biol Phys. 2008;70(3):766–72.

Effect of Various Hybrid Iterative Reconstruction Method on High Resolution Scan Mode in Abdominal CT

Masato Yoshida[1], Masayoshi Niwa[1], Yasukata Takahashi[1], Yosuke Kuratani[1], Katsumi Tsujioka[2]

1 Department of Radiology, Yokkaichi Municipal Hospital,
2 Faculty of Radiological Technology, Fujita Health University

Abstract

Discovery CT750HD (GE Healthcare) is equipped with High Resolution scan mode (HRmode). Recently, it became possible to use new generation adaptive statistical iterative reconstruction (ASiR-V) on the data scanned not only with conventional scan mode (NRmode) but also with HRmode. If HRmode can provide good low-contrast detectability by using ASiR-V, we use HRmode in more cases requiring high resolution. The goal of our study was to evaluate image quality improvement by using ASiR-V on the data scanned with NRmode and HRmode in comparison to conventional Hybrid IR method (ASiR). We scanned Catphan604 (Phantom Laboratory) and a columned acryl phantom made for observer test with NRmode and HRmode, and reconstructed each of the scanned data with ASiR and ASiR-V. We measured task transfer function (TTF) by applying a radial edge technique to acryl rod inserted in Catphan604. We measured standard deviation (SD) and noise power spectrum (NPS) in the uniform region. We evaluated low-contrast detectability by requesting fifteen observers to evaluate the certainty of existence of a low contrast signal in images of a columned acryl phantom by continuously-distributed method. In the data scanned with HRmode, the NPS of ASiR-V was lower than that of ASiR at low frequency regions. Although the TTF of ASiR-V was lower than ASiR at low frequency regions, they coincided at high frequency regions. Observer test showed that positive certainty degree of ASiR-V was slightly higher than that of ASiR. When using ASiR-V on both scan modes, HRmode showed higher TTF and NPS than NRmode at high frequency regions. Positive and negative certainty degree of HRmode and NRmode roughly coincided from the result of observer test. Using ASiR-V on the data scanned HRmode brought higher noise reduction rate than ASiR and good low-contrast detectability similar to NRmode.

Keywords: computed tomography, high resolution, low contrast, iterative reconstruction

1. INTRODUCTION

High Resolution (Hi-Res) CT scan mode (Hi-Res, GE Healthcare, Waukesha, WI) can improve spatial resolution by increasing the number of views per rotation and oversampling in *X-Y* direction with focal spot deflection system.[1] Hi-res scan mode was accompanied by a set of High Definition (HD) reconstruction kernels that are specifically designed for Hi-res scan mode. When using Hi-res scan mode clinically to improve vessel visibility in Abdominal CT, we combine HD standard kernel generally to effectively take advantage of the resolution provided by the scan mode. (combined use of Hi-res scan and HD standard kernel is reffered to as HRmode in this paper). We use conventional normal resolution scan mode (it is reffered to as NRmode in this paper) in abdominal CT in most cases, because HRmode may increase noise and affect detectability of low-contrast objects. The adaptive statistical iterative reconstruction (ASiR-V) is relatively new iterative reconstruction (IR) algorithm by GE. ASiR-V has characteristics between those of conventional ASiR and VEO, a full model-based IR algorithm. Recently, it became possible to use ASiR-V on the data scanned with HRmode by updating the system console, so further noise reduction can be expected in HRmode. If HRmode can provide good low-contrast detectability under clinical abdominal CT condition by using ASiR-V, we use HRmode in more cases requiring high resolution. The goal of our study was to evaluate image quality improvement by using ASiR-V on the data scanned with NRmode and HRmode in comparison to ASiR.

2. MATERIAL AND METHODS

2.1 CT system and Measurement setup

CT scan was performed on a Discovery CT750HD (GE Healthcare, Waukesha, WI) equipped with the Hi-res scan mode. We are available to two kinds of hybrid IR algorithms, ASiR and ASiR-V, on the CT scanner. The noise reduction levels of them are from 0% to 100%, with 100% corresponding to the most intense noise reduction.

For measuring task-based transfer function (TTF), which has been used to evaluate the spatial resolution of images processed with IR, we used a rod-shaped object with a diameter of 1 cm inside a commercially available CT phantom (Catphan604, The Phantom Laboratory, Greenwich, NY). The rod was made from acrylic with 60 HU contrasts to the surroundings at 120 kV. We accurately positioned to match the central axis of the phantom with the rotation axis of the CT system, and the center of the rod was 5cm away from the isocenter. We used the uniform region of the phantom to measure standard deviation (SD) and noise power spectrum (NPS).

To evaluate the low-contrast detectability by observer-based image evaluation, we created a phantom by putting 6mm diameter acrylic rod in a 250mm wide

container, fixing it with a magnet from the outside, and filling the container with a diluted contrast media. The approximate CT value difference between diluted contrast media and acrylic was 30HU. The position of the acrylic rod can be changed arbitrarily by moving the magnet from the outside of the container.

2.2 Data acquisition

The acquisition parameters to scan a Catphan604 for quantitative measurement were listed as follows: applied tube voltage of 120 kVp, tube current of 100mA (volume CT dose index $CTDI_{vol}$ of 4mGy), rotation time of 0.5 s, pitch factor of 0.984 using a detector of 64×0.625mm, scan modes of Hi-res mode and conventional mode without Hi-res. The acquired data were reconstructed with a display field of view of 320 mm, nominal slice thickness of 0.625mm, and 512×512 image matrix. Radiation exposure level was determined based on clinical practice by adjusting the tube current so that the image noise was comparable to clinical condition. When scanning with tube current of 100mA, the SD measured in uniform regions of phantom images reconstructed with a layer thickness of 5mm by FBP algorithm with Standard kernel was 10HU.

The imaging condition scanning the observer-test phantom for obtain the sample images were listed as follows: applied tube voltage of 120 kVp, tube current of 200mA ($CTDI_{vol}$ of 8mGy), rotation time of 0.5 s, pitch factor of 0.984 using a detector of 64×0.625mm, scan modes of Hi-res mode and conventional mode without Hi-res. The acquired data were reconstructed with a display field of view of 320 mm, nominal slice thickness of 2.5mm, and 512×512 image matrix. The radiation dose level was determined so that the observer test was of appropriate difficulty. When scanning with tube current of 200mA, the SD measured in uniform regions of phantom images reconstructed with a layer thickness of 2.5mm by ASiR-V algorithm with Standard kernel was 10HU.

We applied HD Standard reconstruction kernel to the data acquired with Hi-res scan mode (it is reffered to as HRmode) and Standard reconstruction kernel to the data acquired without Hi-res scan mode (it is reffered to as NRmode). The noise reduction level of ASiR and ASiR-V were set to 60 % (ASiR 60% and ASiR-V 60%, respectively).

2.3 Quantitative measurements

We quantified image noise by measuring SD and NPS from a central square-shaped ROI of 128×128 pixels on the image of the uniform water phantom. We averaged the results of SD measured from 10 images obtained from 10 acquisitions. We used the radial frequency method based on two-dimensional Fourier transform to obtain the radially averaged NPS. To improve the accuracy of the measurements, we averaged the results of NPS measured from 100 images obtained from 10 acquisitions.

We evaluated in-plane contrast-dependent spatial resolution by measuring TTF from the image of the acrylic rod with diameter of 1cm and contrast of 60HU. To improve the accuracy of the measurements in the condition of low contrast-to-noise ratio (CNR), we averaged 400 images of the rod obtained from 20 acquisitions. We used the circular edge method to obtain a one-dimensional edge spread function from an averaged image of the rod.

To evaluate the noise reduction performance for the specific low-contrast condition like abdominal CT, we calculated system performance (SP) function as follows:

$$SP^2(u) = \frac{TTF^2(u)}{NPS(u)}$$

where u denotes the spatial frequency. TTF(u) and NPS(u) were measured as described above. This index is similar to the signal-to-noise ratio based on ideal observer model only for the specific conditions where TTF was measured.[2]

2.4 Observer-based image evaluation

We used a ROC viewer (ForMethod1 Ver.1.0.1), which is a software distributed by image science division of Japanese society of radiological technology (JSRT), to show the human observer a series of three axial images in a task (*Fig.1*). Observers evaluated the certainty of the existence of a low contrast signal by continuously-distributed method. A total of 200 series, in which 100 series out of 200 series had a signal and another 100 series had no signal, were presented randomly to the observer. Fifteen observers with over 4 years of experience as a radiological technologist participated in the evaluation.

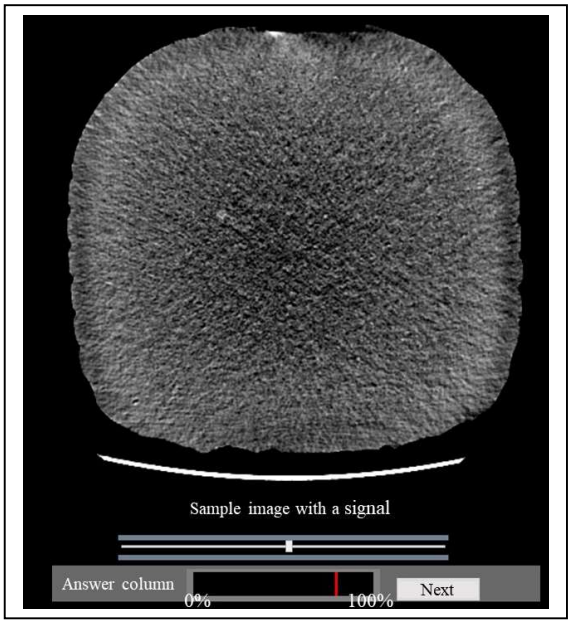

Figure 1 *Screenshot of the ROC viewer during observer test. This software required the observer to click on a point between 0% and 100% based on the certainty of existence of a signal.*

We created a frequency distribution map based on the continuously obtained values of certainty degree, how much confidence the observer had in the presence of the signal. We obtained receiver operating characteristics (ROC) curve from the frequency distribution map and calculated the value of area under curve (AUC). We also calculated sensitivity, specificity, and accuracy by checking whether the answers obtained in the test were correct or incorrect.

3. RESULTS

3.1 Quantitative measurements

Figure 2 shows the results of SD values at same radiation dose. ASiR-V showed a higher SD reduction rate than ASiR at the same 60% intensity. SD was higher in HRmode than NRmode, but the difference was relatively small when using ASiR-V.

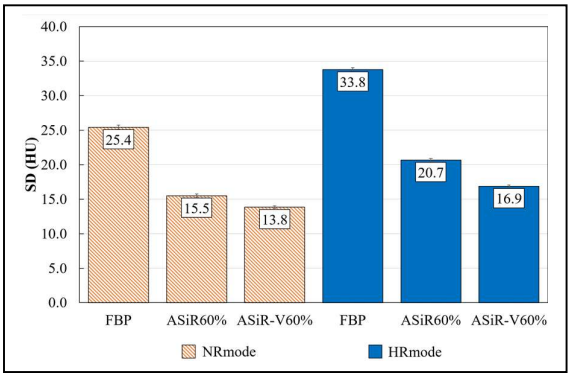

Figure 2 *SD values of NRmode and HRmode when reconstructed with FBP, ASiR60% and ASiR-V60%.*

Figure 3 shows the results of NPS. ASiR decreased noise mainly at high frequencies, but ASiR-V achieved noise reduction over the entire frequency range. The NPS of HRmode was higher at high frequencies and lower at low frequencies than NRmode.

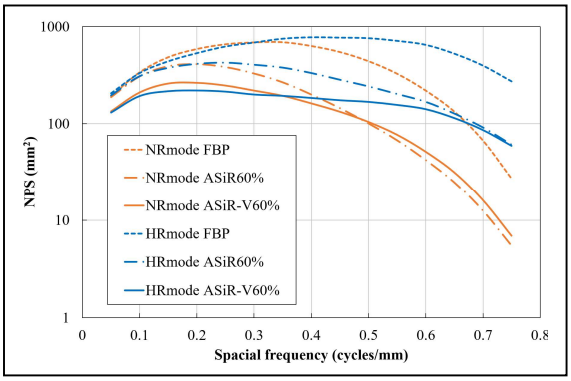

Figure 3 *NPS of NRmode and HRmode when reconstructed with FBP, ASiR60% and ASiR-V60%.*

Figure 4 shows the results of TTF. ASiR and ASiR-V showed lower TTF than FBP, because it is difficult to preserve the edge under low CNR condition. TTF of ASiR-V was lower than ASiR at low frequencies, but the same at high frequencies. The TTF of HRmode was higher at high frequencies than NRmode.

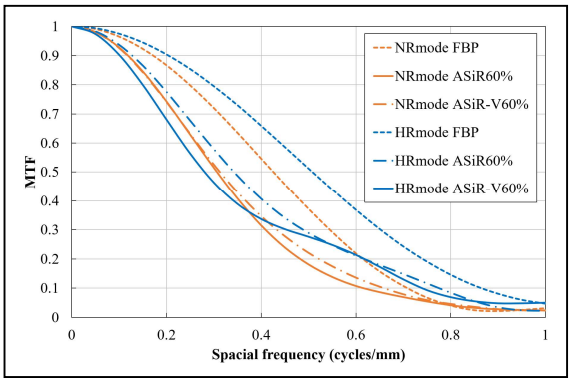

Figure 4 *TTF of NRmode and HRmode when reconstructed with FBP, ASiR60% and ASiR-V60%.*

Figure 5 shows SP function calculated from TTF and NPS. SP of ASiR-V increased compared to FBP by an average of 30%. SP of HRmode was not much different from that of NRmode when using ASiR-V.

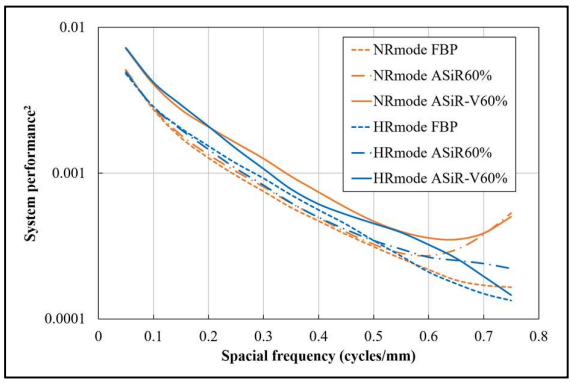

Figure 5 *SP function of NRmode and HRmode when reconstructed with FBP, ASiR60% and ASiR-V60%.*

3.2 Observer-based image evaluation

Figure 6 shows a frequency distribution map of certainty degree obtained from the result of observer test comparing ASiR and ASiR-V when scanned with HRmode. ASiR-V enabled the observers to detect a signal with a higher degree of certainty than ASiR. Table 1 shows the index values of the observer test comparing ASiR and ASiR-V. Sensitivity and AUC of ASiR-V were slightly higher than those of ASiR, but the difference was not significant. Figure 7 and Table 2 show the results of the observer test comparing NRmode and HRmode using the data reconstructed with ASiR-V. There was no significant difference between the results of NRmode and HRmode. It may be because the signal was too easy to detect and the difference could not be evaluated.

Table 1 *Index values of the observer test comparing ASiR60% and ASiR-V60% when scanned with HRmode.*

	ASiR60%	ASiR-V60%
Sensitivity	97.6%	100%
Specificity	94.7%	93.6%
Accuracy	96.1%	96.8%
AUC	0.987	0.996

Table 2 *Index values of the observer test comparing NRmode and HRmode when reconstructed with ASiR-V.*

	NRmode	HRmode
Sensitivity	97.6%	96.3%
Specificity	93.6%	93.9%
Accuracy	95.6%	95.1%
AUC	0.981	0.978

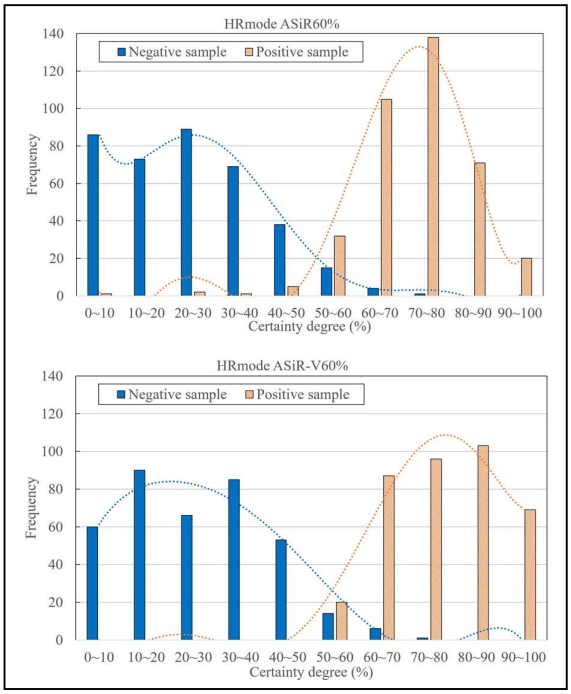

Figure 6 *Frequency distribution map comparing ASiR60% and ASiR-V60% when scanned with HRmode.*

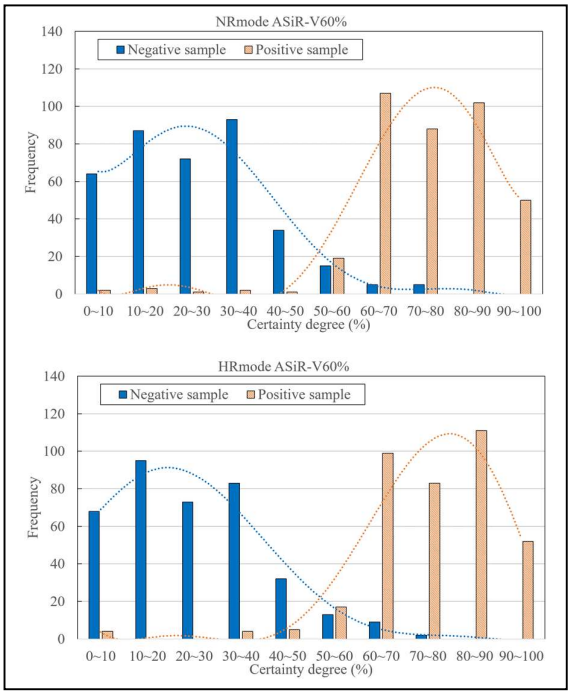

Figure 7 *Frequency distribution map comparing NRmode and HRmode when reconstructed with ASiR-V.*

4. DISCUSSION

NPS of ASiR-V was lower than that of ASiR at low frequencies. Although both ASiR and ASiR-V show NPS peak shifts towards lower frequencies in relation to changes in noise texture,[3] our results suggested that the shifts were relatively small for ASiR-V at the same radiation level. TTF of ASiR-V was lower than ASiR at low frequencies, but they were almost equal at high frequencies. The noise reduction at low frequencies of ASiR-V may be obtained by the compromise of resolution at low frequencies at low CNR condition. SP function of ASiR-V increased compared to ASiR by an average of 30%. In observer test, positive certainty degree of ASiR-V was slightly higher than that of ASiR. ASiR-V may improve low-contrast detectability when limited to in-plane property, but our evaluation neglected degradation of longitudinal resolution by using ASiR-V at low CNR conditions.[4] This is one of a few limitations of our study.

Although SD value was higher in HRmode than NRmode, NPS of HRmode was slightly lower at low frequencies. The results of SP function and observer test roughly coincided between NRmode and HRmode. The characteristics of noise increased by HRmode was mainly high frequency and may not affect the low-contrast detectability. Therefore, HRmode could provide as good low-contrast detectability as NRmode at same radiation dose level, and in addition HRmode also provides significant improvement of resolution at high contrast condition as previously reported.[1]

5. CONCLUSION

Using ASiR-V on the data scanned HRmode brought higher noise reduction rate than ASiR and good low-contrast detectability similar to NRmode.

ACKNOWLEDGEMENTS

We thank Mr. Katsumi Tsujioka for providing invaluable insights for our study.

REFERENCES

1. Juan PC, Daniel GC, et al. Hi-Res scan mode in clinical MDCT systems: Experimental assessment of spatial resolution performance. Med Phys 2016; 43(5): 2399–2409
2. Kawashima H, Ichikawa K, et al. Quality evaluation of image-based iterative reconstruction for CT: Comparion with hybrid iterative reconstruction. Med Phys 2019; 20(6): 199–205
3. Achille M, David AZ, et al. CT Detectability of Small Low-Contrast Hypoattenuating Focal Lesions: Iterative Reconstructions versus Filtered Back Projection. Radiology 2018; 289(2): 443-454
4. Goto M, Tominaga C, et al. A method to measure slice sensitivity profiles of CT images under low-contrast and high-noise conditions. Physica Medica 2019; 60: 100-110

Facility reference level for common x-ray procedures: A preliminary study

DM Satharasinghe[1,2#], J Jeyasugiththan[1], AS Pallewatte[3] and WMNMB Wanninayake[2]

1 Department of Nuclear Science, Faculty of Science, University of Colombo, Sri Lanka.
2 Horizon Campus, Malabe, Sri Lanka.
3 Department of Radiology, National Hospital of Sri Lanka, Colombo, Sri Lanka.

Abstract

Ionizing radiation is an essential tool in medical diagnosis and it brings great benefit to the patient. However, the associated risks due to the radiation is unavoidable. Therefore, close monitoring of radiation exposure should be performed in order to control the potential harm. As an advisory measure to improve optimization of patient's radiation protection, Diagnostic Reference Levels (DRLs) was introduced by the International Commission on Radiation Protection (ICRP). The present study aims on the evaluation of the doses and its variation for selected x-ray procedures used by a single institution in Sri Lanka to determine a possible institutional DRL. The study included dose data and exposure parameters from 218 chest-Postero Anterior (PA), 33 abdomen-Antero Posterior (AP), 85 lumbar spine AP and 88 lumbar spine-Lateral (LAT) projections of patients (age between 19-78 years). The 3rd quartile dose values for above projections were 16, 256, 155, 455 μGy.m^2 respectively. Further, the above dose values were compared with international DRLs and we found that the lumbar spine lateral projection and abdomen AP are with higher dose levels. This preliminary study provides information on the selected study setting only however, can be used as a reference for quality improvement programs by others.

Keywords: institutional diagnostic reference level, IDRL, Diagnostic reference level, DRL, ionizing radiation, x-ray

1. INTRODUCTION

The optimization of radiation protection in diagnostic radiology requires the use of appropriate examination-specific protocols tailored well with the patient age, size or body mass, region of imaging and clinical indication. This will ensure that the received doses are kept as low as reasonably achievable (ALARA) [1]. Accordingly, major national and international surveys had conducted on medical radiation exposures as early as in 1950 [2-3]. The aforementioned surveys that conducted in UK and USA mainly focussed only on diagnostic x-ray examinations. However, due to the varying definition used by different authors, comparison of values between publications were impossible. Therefore, the term "Diagnostic Reference Level" was introduced by the International commission on Radiation protection (ICRP) in 1996 [4]. This concept was subsequently developed further and guidance document for establishing DRLs were introduced in 2001 and 2017 [5-6]. According to the ICRP, DRL is considered as an advisory measure to improve optimization of patient protection by identifying high patient dose levels which might not be justified on the basis of image quality requirements [6]. This is applicable for all patients groups irrespective of age, gender or any other category. The main objective of DRL is to avoid radiation overdose to the patient that doesn't account for clinical requirement. However, the DRL is not intended to provide dose constrains to individual patients or studies to demarcate the good and bad practices [6].

During the present study, the variation of doses among most common x-ray procedures in a radiology facility were evaluated. The obtained results were compared with the international published DRLs to identify the procedures which required optimization. Finally the necessary recommendations were given. This is the first preliminary study conducted in Sri Lanka. Therefore, the results from present study would escalate the concern on use of appropriate exposures during x-ray procedures and to optimize the radiation dose received by the patient.

2. MATERIALS AND METHODS

This study was conducted in a radiology department of a well-established private hospital equipped with a digital flat panel system made of caesium iodide and amorphous silicon. The dimension of the fixed detector is 42.5 X 42.6 cm with pixel matrix of 2880 X 2880 X 148 μm. The dimension of the wireless detector is 35.3 X 42.4 cm with pixel matrix of 3072 X 2560 X 139 μm.

The permission was granted by the Head of the relevant department to conduct the study and ethical approval was waived since the patient identification data is not required. This respective department provides services to nearly 3000 patients per month covering range of plain radiographic studies.

The exposure parameters were recorded retrospectively. This includes 218 chest Posteroanterior (PA), 33 abdomens Anteroposterior (AP), 85 lumbar spine AP and 88 lumbar spine Lateral (LAT) projections of patients aged 19-78 years. The Doses were extracted from the Digital Image Communication in Medicine (DICOM) header in the form of Dose Area Product (DAP) measured in μGy.m^2. This value is automatically appearing on the viewing monitor immediately following the exposure. For majority of exposures, Automatic Exposure Control (AEC) were utilized. During the AEC mode the mAs is automatically decided by the machine depending on the selected combination of the dose and the kVp which were set by the user. However, manual exposures were employed when imaging over or underbuilt patients to ensure an adequate quality image. Except for chest radiography other projections were done on table buckey with using a portable Wi-Fi flat panel x-ray detector. The chest PA projections were performed in the fixed detector wall

***Table 1**: Descriptive statistics of the technical parameters (tube current (mAs) and tube voltage (kVp)) and dose data (DAP µGy.m2) in the study sample. Mean value and standard deviation (range in parenthesis) are given.*

Region	Projection	Sample size (n)	Age (years)	kVp	mAs	DAP µGy.m^2	3rd quartile of the DAP-µGy.m^2
Chest	PA	218	38.2 ± 13.7 (19-78)	124.9 ± 0.2 (124.3- 125.6)	2.8 ± 0.9 (1.6-6.6)	13.7 ±5.6 (3.6-37.8)	16
Abdomen	AP	33	41.8 ± 14.3 (20-68)	75.8 ± 5.4 (65.9-81.3)	38.9 ± 40.3 (6.8-211.1)	192.4±165 (34.3-860.6)	256
Lumbar Spine	AP	85	41.5 ± 13.5 (19-66)	72.5±3.6 (61.5-80.8)	40.9±26.1 (6.5-157.9)	124 ±82.5 (17.6-490.5)	155
	LAT	88	42 ±13.3 (19-66)	75.7 ±6.4 (62.9-90.3)	81.2 ±61.6 (3.6-312.7)	336.3 ±241.8 (11.2-1265)	455

buckey. The system was commissioned a year ago and calibrations were done regularly by the vendor.

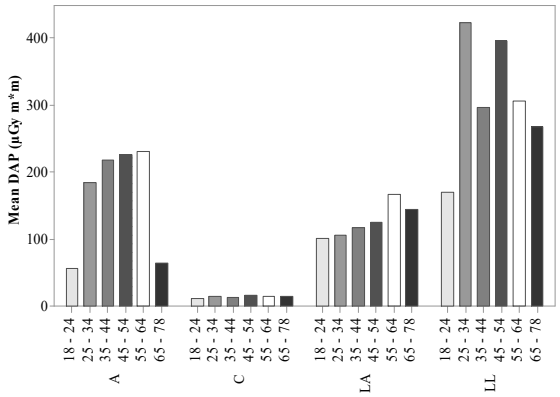

***Figure 1.** Histogram showing the mean DAP (µGy.m^2) values as a function of age categories for four different x-ray projections. **A**-Abdomen AP, **C** – Chest PA, **LA**-Lumbar Spine AP, **LL**-Lumbar Spine Lateral.*

Therefore, the displayed doses were considered accurate and reliable. The mean and third quartile value of the dose data and exposure parameters were calculated for each projection. Statistical analysis was done using Minitab® 17.1.0 statistical software.

3. RESULTS

The dose data with exposure parameter of 424 patients aged between 19 and 78 years (60.8% male) belongs to four different anatomical projections (chest, abdomen and lumbar spine AP and LAT) were evaluated. The mean, third quartile value and the range of the dose distribution were calculated. The obtained DAP values (µGy.m^2), kVp and mAs for each of the above projections are summarized in table 1.

***Table 2.** Comparison of 3rd quartile values of the present study with the international DRLs.*

Anatomy	Projection	DRL (µGy.m^2)			
		Present study	UK [7]	Austria [8]	Germany [9]
Chest	PA	16	15	15	15
Abdomen	AP	256	250	210	230
Lumbar Spine	AP	155	150	200	200
	LAT	455	250	320	350

3.1 International comparison of DRLs

The obtained 3rd quartile dose values were compared with the established DRLs of England, Austria and Germany (see table 2). These countries had followed the similar concept and established their own DRL through nationwide patient's dose surveys. The DRLs are defined for an average adult and it differs from country to country [7-9]. The average adult is considered as a person with 70 kg [6]. But, the dose values in the present study are obtained for range of adult patients (19-78 years) without considering weight. This is a one limitation of the present study.

4. DISCUSSION

The 3rd quartile dose values for chest PA and lumbar spine AP are closely agreed with the international DRLs. The abdomen AP projection shows nearly a similar trend when compared to UK, but greater than the Austria (21%) and Germany (2.4%). Moreover, the 3rd quartile dose value for lumbar spine LAT projection is not comparable with those three countries. There is a large difference against UK study (82%).

Abnormally higher doses for the abdomen AP and lumber spin LAT projections may be due to several factors such as utilizing of inappropriately high radiographic technical parameters, patient positioning errors, calibration discrepancies of the equipment and many more. The DR system is more likely to result in overexposures due to its high exposure latitude compared to the conventional x-ray [10]. Consequently, it requires several times higher exposures until the signal saturation occurs and result in noticeable image quality degradation [10]. Regrettably, the patient in this situation received unnecessary radiation exposure, often without the knowledge of the technologist who involved in the image acquisition. Therefore, it is essential to evaluate the technical and the practice parameters of the above projection in order to identify the causes for the high exposure.

The figure 1 illustrates the mean DAP values for different x-ray projections and for different age groups. These dose values are demonstrated without biasing to the gender and it is observed that the mean dose for chest

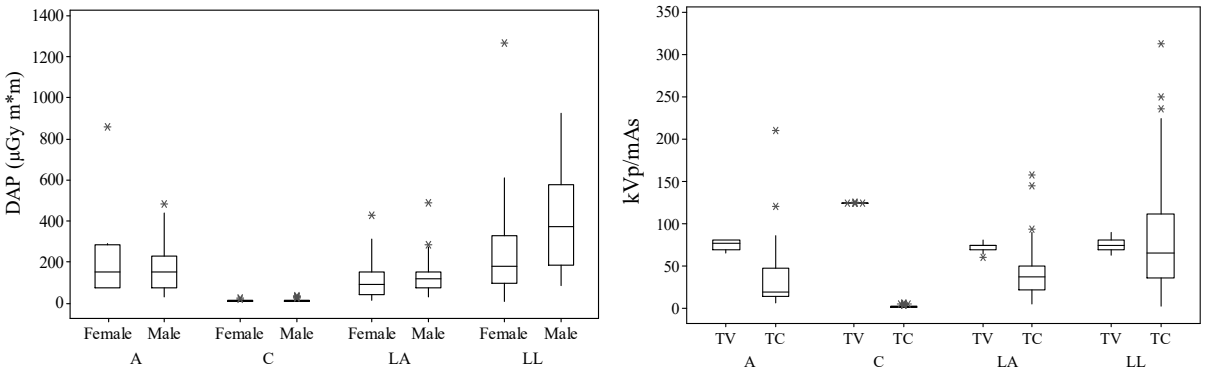

(a) (b)

Figure 2 *Box-whisker plot of (a) gender wise variation of DAP per projection (b) kVp and mAs per projection. Abdomen AP (n=33), Chest PA (n=218), Lumbar spine AP (n=85) and Lumbar spine LAT (n=88). The 25th and 75th percentile marks the box and whiskers extend to the range outliers. The median is marked in the box. The asterisks (*) represent extreme values.* ***TV****- Tube Voltage,* ***TC****- Tube current,* ***A****-Abdomen AP,* ***C*** *– Chest PA,* ***LA****-Lumbar Spine AP,* ***LL****-Lumbar Spine Lateral.*

region is uniformly distributed among all age ranges. Patients aged, 18-24 years had exposed to the lowest dose of radiation during all procedures. However, there is no significant between age ranges and dose for all projections ($p < 0.05$).

Additionally, the influence of gender on delivered dose were also evaluated. Figure 2(a) demonstrates the resultant relationship between DAP and gender. The median dose delivered during abdomen AP, lumbar spine AP and chest PA were almost constant for both males and females. But male patients were receiving higher doses during lumbar spine lateral projections.

The median tube voltage is almost constant for all projections except for chest PA (figure 2(b)). For the chest PA projection, it is clearly seen that the highest tube voltage and lowest tube currents were used. This is due to the fact that chest region contain both high and low attenuation structures such as denser mediastinum and less dense lung tissue [10]. This will make a greater variation in subject contrast. Therefore, the utilization of high tube voltage with low tube current is recommended to visualize the lower lying lung field [11].

However, tube current utilized for the lumbar spine lateral projection is high and widely distributed. The higher tube current increases the production of electrons (or the quantity of radiation) [12]. This enables more photons to reach the x-ray detector and creates a greater signal intensity, i.e. a high quality image. Moreover, the median of the tube current used for the abdomen AP is more towards the 1st quartile. So, higher tube currents are used for abdomen AP and it may be a reason for the abnormally higher dose. A recent study carried out by Hawal and Hariwan (2017) confirmed that users always tend to set the tube lower voltages in the DR system. Therefore it will result in high tube current (i.e. High patient doses) [13]. Furthermore a phantom study showed that the entrance dose (ED) of 0.002 mSv is adequate to visualize the anatomical structures of the lumbar spine LAT projection [14]. In addition, they emphasize that exposure of 95 kVp and 4.5 mAs can reduce the ED by 63%. Therefore, utilization of high tube current should be justified based on the image quality requirement since tube current directly influence the dose delivered during an imaging procedure [15].

Finally, the radiologic technologists of the relevant institution were informed about these findings to emphasize the immediate requirement of a dose optimization protocol to avoid unnecessary radiation dose given to the patient. Also, it is very essential to evaluate the image quality of the projections which have higher dose levels so that an accurate diagnosis could be obtained with considerable dose saving.

This study will be extended in future and the post optimized protocols will be evaluated to quantify the achievement of the dose reduction. Therefore, we are recommending not only the dose reference levels for the aforementioned institution but also emphasize the requirement of regular dose and image quality monitoring. Furthermore, the 3rd quartile values of the dose distribution for chest PA, abdomen AP, LAT and lumbar spine AP can be used as the facility reference levels. The suggested reference values can be used to identify the unnecessary over exposures until the establishment of the DRL values matches for Sri Lankan context.

5. CONCLUSION

This is considered as a preliminary study to initiate a dose evaluation programmes in Sri Lanka. In the present study, the projections such as chest PA and lumbar spine AP were below or comparable with the international DRLs. Therefore, the 3rd quartile value of the dose distribution for the above projections are suggested as the facility reference levels which are 16 and 155 µGy.m^2 respectively. The lumbar spine LAT and abdomen AP shows abnormally higher doses (3rd quartile values 455 and 256 µGy.m^2 respectively) than that of the international reference levels. Therefore, optimization actions should be implemented for the above projection and should be followed by a re-evaluation survey. This preliminary study provides

information on a selected radiology facility only, however this result can be used as a reference for quality improvement programs. In the future, in-depth study is essential to cover all the procedures which involves ionizing radiation for the medical diagnosis purposes.

ACKNOWLEDGEMENTS

This work was supported by the by the project "Accelerating Higher Education Expansion and Development (AHEAD)" which is a World Bank funded Sri Lankan government operation to support the higher education sector (AHEAD 6026-LK/8743-LK).

REFERENCES

[1] C. E. Willis and T. L. Slovis, "The ALARA concept in pediatric CR and DR: Dose reduction in pediatric radiographic exams - A white paper conference Executive Summary," *Pediatr. Radiol.*, vol. 34, no. SUPPL. 3, pp. 162–164, 2004, doi: 10.1007/s00247-004-1264-y.

[2] B. F. Wall and P. C. Shrimpton, "The Historical Development of Reference Doses in Diagnostic Radiology," *Radiat. Prot. Dosimetry*, vol. 80, no. 1, pp. 15–19, 1998, doi: 10.1093/oxfordjournals.rpd.a032492.

[3] UNSCEAR, "United Nations Scientific Committee on the Effects of Atomic Radiation 1958." 1958, [Online]. Available: http://www.iaea.org/inis/collection/NCLCollectionStore/_Public/41/084/41084475.pdf.

[4] ICRP, "Radiological Protection and Safety in Medicine (ICRP publication 73)," 1996.

[5] ICRP, "Doses to the Embryo and Fetus from Intakes of Radionuclides by the Mother," 2001. doi: 10.1016/0146-6453(81)90127-5.

[6] ICRP, "Diagnostic Reference Levels in Medical Imaging, The International Commission on Radiological Protection," 2017.

[7] D. Hart, M. Hillier, and P. Shrimpton, *Doses to patients from radiographic and fluoroscopic X-ray imaging procedures in the UK—2010 Review*, no. May. 2010.

[8] D. Wachabauer, F. Röthlin, H. M. Moshammer, and P. Homolka, "Diagnostic Reference Levels for conventional radiography and fluoroscopy in Austria: Results and updated National Diagnostic Reference Levels derived from a nationwide survey," *Eur. J. Radiol.*, vol. 113, no. February, pp. 135–139, 2019, doi: 10.1016/j.ejrad.2019.02.015.

[9] A. Schegerer, R. Loose, L. J. Heuser, and G. Brix, "Diagnostic Reference Levels for Diagnostic and Interventional X-Ray Procedures in Germany: Update and Handling," *RoFo Fortschritte auf dem Gebiet der Rontgenstrahlen und der Bildgeb. Verfahren*, vol. 191, no. 8, pp. 739–751, 2019, doi: 10.1055/a-0824-7603.

[10] J. A. Seibert, "Digital radiography: Image quality and radiation dose," *Health Phys.*, vol. 95, no. 5, pp. 586–598, 2008, doi: 10.1097/01.HP.0000326338.14198.a2.

[11] K. C. CLARK, "Positioning in Radiography," *Am. J. Med. Sci.*, vol. 233, no. 1, p. 491, 1957, doi: 10.1097/00000441-195710000-00024.

[12] K. Holmes, *CLARK ' S eSSentiAL PHYSiCS in imAging FoR RADiogRAPHeRS. .*

[13] H. Y. Yacoob and H. A. Mohammed, "Assessment of patients X-ray doses at three government hospitals in Duhok city lacking requirements of effective quality control," *J. Radiat. Res. Appl. Sci.*, vol. 10, no. 3, pp. 183–187, 2017, doi: 10.1016/j.jrras.2017.04.005.

[14] Z. H. Lai, C. Sá dos Reis, and Z. Sun, "Effective dose and image optimisation of lateral lumbar spine radiography: a phantom study," *Eur. Radiol. Exp.*, vol. 4, no. 1, 2020, doi: 10.1186/s41747-019-0132-3.

[15] E. G. Walter Huda, J. Anthony Seibert, Kent Ogden, "Upstate Medical University-Physics Teaching File for Radiology Residents." https://www.upstate.edu/radiology/education/rsna/radiography/mas.php (accessed Jul. 18, 2020).

The method to estimate source position for mobile tomosynthesis

Kensuke Hori[1], Takahisa Koike[1], Kiichi Tadano[1], Takeyuki Hashimoto[1]

1 Kyorin University Graduate School of Health Sciences

Abstract

Mobile X-ray radiography is often used for follow-ups in a clinical context. Tomosynthesis can reconstruct a tomogram and improve the quality of diagnosis. For tomosynthesis reconstruction, it is critically important to determine the geometrical relationship between the source and the detector. In mobile imaging, the geometry is adjusted by a radiology technologist, but it is actually extremely difficult to keep the detector and the X-ray source in the same position. In this study, we developed a technique that can estimate the X-ray source position simultaneously during a tomosynthesis scan. The purpose of this study was to estimate the source position from projection images using markers. We developed a marker panel consisting of a base panel and four markers. During tomosynthesis scanning, the marker panel was attached to the detector and the position of the projected markers was calculated by template matching. The X-ray source position was estimated using the positions of the projected markers and original markers. In this study, numerical simulation was performed to evaluate the accuracy of our proposing method quantitatively. The detector was placed in the *xz*-plane with the *y*-axis perpendicularly directed to the source from the detector. The estimated errors of the source position were 7.8%, 1.7%, and 4.7% in the *x*, *y*, and *z* directions, respectively. The normalized root mean squared error of a mobile tomosynthesis image was about 30% and there were visualizable errors only in the image's edge. This paper proposes a method of estimating the X-ray source position, having error of a few percent. This method is considered to be practically useful because it can be performed simultaneously during a tomosynthesis scan.

Keywords: Tomosynthesis, mobile imaging, estimation of source location

1. INTRODUCTION

Mobile X-ray radiography is widely used for follow-ups and confirmation after treatment at the bedside in a clinical context (1). Tomosynthesis can reconstruct a tomogram using projections acquired from a limited range of angles and improve the quality of diagnosis compared with X-ray radiography (2). For image reconstruction, it is critically important to determine the geometrical relationship between the source and the detector. In mobile imaging, the X-ray source position is adjusted by a radiology technologist, but it is actually extremely difficult to keep the detector and the X-ray source in the same position. Therefore, for mobile tomosynthesis, there is a need for a system that can specify geometrical information on the X-ray source and the detector without additional scanning. Sato et al. proposed a method of using a calibration object attached to an X-ray source to conduct 2D-3D registration (3). However, too many calibration images were needed for the calculation of 2D-3D registration. In this study, we developed a novel mobile X-ray imaging system that can estimate geometrical information on the X-ray source and detector positions using template matching. Moreover, we reconstructed and evaluated a mobile tomosynthesis image.

2. MATERIAL AND METHODS

In our method, a marker panel consisting of a base panel (462mm×372mm×10mm) and four markers (1.95mm×1.95mm×1.0mm) was used. The X-ray absorption of the base panel was sufficiently small to be ignored. On the other hand, all of the markers had sufficiently high X-ray absorption and it was assumed that the X-ray was not transmitted through them.

2.1 Estimation method

Our proposed method mainly involved calculation by a geometrical algorithm and consisted of two steps. The first step involved estimating the *x* and *z* coordinates of the X-ray source position (Figure 1). A line could be specified by the original and projected marker coordinates and was found at each marker. The coordinates of the projected marker position were calculated by a template matching technique, as explained in section 2.2. Two lines that were drawn from neighboring markers should intersect and the *x* and *z* coordinates of the X-ray source position should match those of this intersection.

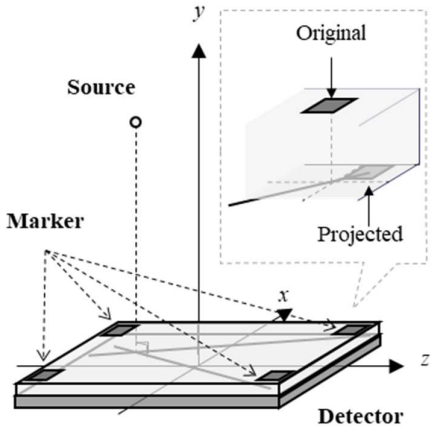

Figure 1 The first step of the estimation method.

The second step involved estimating the *y* coordinate based on similarity, as shown in Figure 2. The points of the large triangle in this figure include the source position (*x, y, z*), a position defined by (*x*, 0, *z*), and the projected marker position (*px*, 0, *pz*). The points of the small triangle include the original marker position (*mx*, *my*, *mz*), a position defined by (*mx*, 0, *mz*), and the projected marker position (*px*, 0, *pz*). Thus, the large and small triangles are similar. Because the coordinates other than *z* are known, the *z* coordinate can easily be calculated.

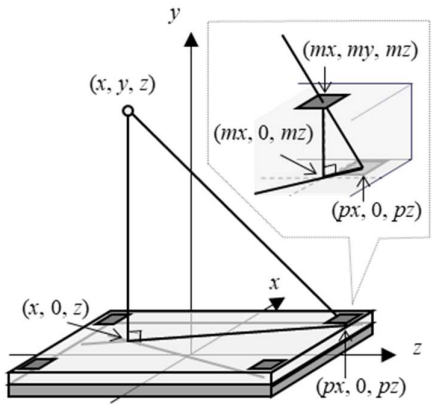

Figure 2 The second step of the estimation method. The large and small triangles are similar to each other.

2.2 Template matching technique

The template matching involves calculation of the similarity between the template image prepared in advance and a sub-window of the input image. The template image assumed as a marker was prepared, and its matrix size was 13×13 pixels. The similarity was calculated using the sum of squared difference (SSD) between the template image and a sub-window of the input image. The SSD can be represented by the following equation:

$$SSD(x,y)=\sum_{i=1}^{I}\sum_{j=1}^{J}\left[T(j,i)-I(x+j,y+i)\right]^2$$

where $T(j, i)$ is the template image, $I(x, y)$ is the input image, and the matrix size of the template and sub-window is $I \times J$ pixels.

2.3 Image reconstruction

Image reconstruction is the inverse problem of Radon transform. An algorithm that can reconstruct a tomogram analytically was used in this study, represented by the following equation:

$$f(x,y)=\int_0^{\pi}\left\{\int_{-\infty}^{\infty}G(\rho,\theta)|\rho|e^{i2\pi\rho(x\cos\theta+y\sin\theta)}d\rho\right\}dv$$

where $f(x, y)$ is the reconstructed image, $G(\rho, \theta)$ is calculated by Fourier transform of the projection data from scan angle θ, represented by $g(x', \theta)$, (x, y) is the fixed coordinate system for the object, and (x', θ) is the detector coordinate system rotated around the object.

2.4 Numerical simulation

The projection images are acquired by an X-ray source moving along a linear trajectory in a tomosynthesis scan (4). In this study, the distance that the X-ray source moved was 317 mm and the trajectory was any straight line. The matrix size and voxel size of the digital phantom were 256×256×256 voxels and 0.15mm×0.15mm×0.15mm, respectively. The geometry of the numerical simulation is shown in Figure 3.

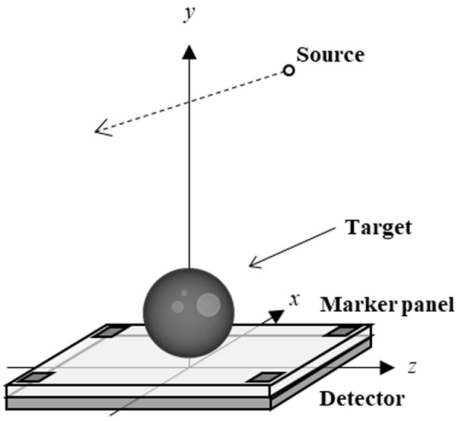

Figure 3 The geometry of numerical simulation. The source moved along any straight line and its position was estimated by our proposed method.

The reconstructed image was evaluated by normalized root mean squared error (NRMSE), represented by the following equation:

$$NRMSE=100\times\sqrt{\frac{\sum_{i=1}^{I}(g_m-f_m)^2}{\sum_{i=1}^{I}(f_m)^2}}$$

where f_m and g_m are tomosynthesis images reconstructed using true and estimated X-ray source positions, respectively.

3. RESULTS

3.1 Estimation of X-ray source position

The accuracy of estimating the X-ray source position was evaluated by changing the *x* and *z* coordinates of the X-ray source from 0 mm to +300 mm in 100 mm increments. In *xz*-plane, the reference position that was the true position of the X-ray source and the estimated position are shown in Figure 4. The X-ray source

estimation error of *y*-axis was shown in Figure 5. For the *x*, *y*, and *z* coordinates, the average estimation errors were 7.8%, 1.7%, and 4.7%, respectively.

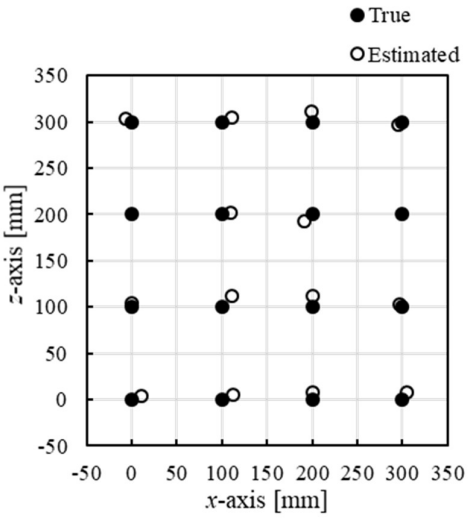

Figure 4 The true and estimated X-ray source positions in *xz*-plane. The true and estimated positions of the X-ray source was shown by filled and open circle, respectively.

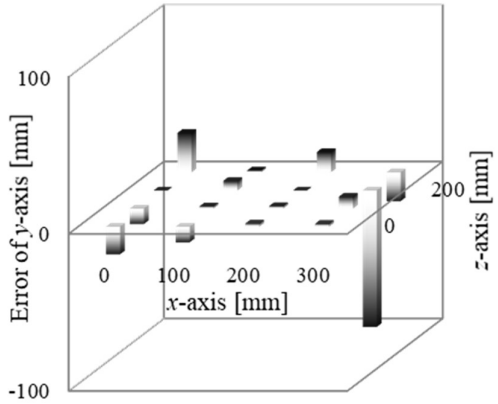

Figure 5 The estimation error of X-ray source position in *y*-axis.

3.2 Mobile tomosynthesis images

Mobile tomosynthesis images were reconstructed using true and estimated X-ray source positions (Figure 6). The error image was calculated using the difference between images that were reconstructed using true and estimated X-ray source positions. There was reconstruction error in the image's edge, but no major artifact was observed and the NRMSE was about 30%.

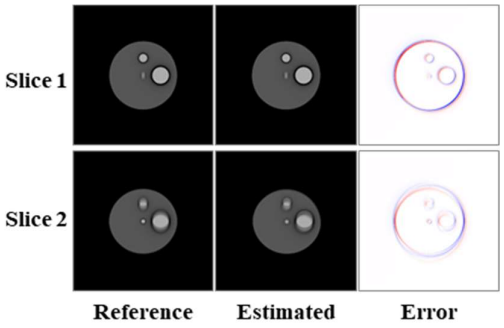

Figure 6 *Mobile tomosynthesis image* that was reconstructed using the true X-ray source position (Reference image) and the estimated one (Estimated image). The error images were calculated using the difference between reference and estimated images.

4. DISCUSSION

This study showed that mobile tomosynthesis images can be reconstructed by a novel method for estimating the position of the X-ray source. The estimation error was considered to be due to the error of calculating the projected marker position. In this study, the calculation of template matching was performed in the unit of pixels. Therefore, it may be possible to improve the calculation accuracy by processing with a sub-pixel unit.

The marker panel consisted of a base panel and markers. It is considered to be better for the material of the base panel to have negligibly small X-ray absorption, like the case for Styrofoam. Moreover, it is considered to be better for the material of the markers to have high X-ray absorption enough to prevent it from passing through, like the case for tungsten.

Our proposed method can be easily performed by attaching a marker panel to the detector, without the need for additional scanning or exposure of the patient to radiation. Using our proposed method, a tomogram can be acquired at the bedside; therefore, it could be especially useful for patients with monitors like an ECG in intensive care units.

5. CONCLUSION

A method for estimating the X-ray source position was developed for mobile tomosynthesis. The estimation error was a few percent and no major artifact was observed in reconstructed images. It was suggested that our method is useful for mobile tomosynthesis at the bedside.

REFERENCES

1. Henschke CI, Passternack GS, Schroeder S, Hart K, Herman PG. Bedside chest radiography: diagnostic efficacy. Radiology. 1983; 149: 23-6
2. Dobbins JT III, McAdams HP, Song JW, Li CM, Godfrey DJ, Delong DM, et al. Digital tomosynthesis of the chest for lung nodule detection:

Interim sensitivity results from an ongoing NIH-sponsored trial. Med Phys. 2008; 35: 2554-7
3. Sato K, Ohnishi T, Sekine M and Haneishi H. Geometry calibration between X-ray source and detector for tomosynthesis with a portable X-ray system. Int J CARS. 2017; 12: 707-17
4. Dobbins JT III, Godfrey DJ. Digital x-ray tomosynthesis: current of the art and clinical potential. Phys Med Biol. 2003; 48: R65-106

Quantitative evaluation of deep convolutional neural network- based denoising for ultra-low-dose CT

Keisuke Usui [1, 2], Kentarou Suzuki [3], Akira Isobe [3], Kazumi Murata [4], Koichi Ogawa [4]

1 Department of Radiological Technology, Faculty of Health Science, Juntendo University, Tokyo, Japan,
2 Department of Radiation Oncology, Faculty of Medicine, Juntendo University, Tokyo, Japan,
3 Department of Radiation Oncology, Graduated School of Medicine, Juntendo University, Tokyo, Japan,
4 Faculty of Science and Engineering, Hosei University, Tokyo, Japan

Abstract

Introduction: Dose reduction is important for diagnostic and therapeutic applications of computed tomography (CT). However, image noise still occurs, resulting in degradation of image quality caused by the reduction in X-ray dose. Recently, deep learning approaches based on including extensive data and powerful graphical processing units have been used within image denoising and have achieved great success.

Purpose: This study aimed to evaluate the general convolutional neural network (CNN) for denoising of ultra-low-dose CT and to compare this technique with an alternate noise reduction method against unique CT simulation images containing noise.

Methods: To simulate an ultra-low-dose CT image, we added Salt & pepper noise to normal-dose images based on the CT unit-specific modulation transfer function. We generated simulated low-dose images with a dose reduction of 10%–99% from the original images, which were then denoised using a trained denoising CNN (DnCNN). Moreover, we evaluated the influence of transfer learning from DnCNN via fine-tuning. We compared the performance of DnCNN with other methods using Median, Gaussian, Winner filters.

Results: DnCNN images were significantly improved in terms of the signal-to-noise ratio (SNR), especially at the ultra-low-dose level. With DnCNN denoising for 50% dose cases, SNR improved 12-fold, and the contrast-to-noise ratio improved 14-fold, simultaneously, high-frequency components were degraded. In contrast, trained DnCNN images achieved the highest structural similarity index and closely matched the original dose image.

Conclusion: The DnCNN denoising method significantly improves ultra-low-dose CT within quantitative evaluations.

Keywords: Deep learning, CNN, low-dose CT, denoise, image quality

1. INTRODUCTION

Computed tomography (CT) is widely used by clinicians for screening scans to diagnose. However, high exposure scans that can make patients suffer with several biological effects of cancer risks (1, 2). To decrease radiation risk, reduction of the number of X-ray photons employed during tube current modulation is considered as a solution. This incurs a drawback as low-dose CT results in image quality degradation. Thus, lower dose of X-ray photons leads to degrades the signal-to-noise ratio (SNR) in CT images and may reduce the value of diagnostic performance (3).

To address the issues, many techniques have proposed to improve the image quality of low-dose CT, such as sinogram domain filtration, iterative reconstruction, and reconstructed image processing (i.e. image space denoising). However, these methods depend on the CT manufacturer's specifications. And, computational costs are needed, then the process of reconstruction is quite slow. Moreover, they have the risk of either generating new image artifacts or losing original structural information through post-processing, all of which limits their clinical applications (4–6).

Deep learning approaches have been widely used for image denoising due to their high computational efficiency leading to efficient algorithms (7–9). In addition, particularly convolutional deep neural networks (CNN) based on the including extensive data and powerful graphical processing units (GPU) have achieved great success. Several CNN-based methods have been proposed for natural image denoising and low-dose CT. However, these CNNs may introduce image blurring, and suffers from loss of gradients. The denoising network, known as DnCNN incorporating with residual learning and batch normalization, can yield better improvements for Gaussian denoising tasks with unknown noises. However, it has been shown to be inferior for correction of more realistic and complicated noise (10, 11).

In the current study, we implemented the general CNN for denoising with ultra-low-dose CT and compared it with another noise-reduction method against unique CT noise simulation images, in order to better understand the dose-dependent properties of CNN-based denoising methods. Moreover, to adapt the CNN model for denoising of ultra-low-dose CT, we evaluated the influence of transfer learning from the DnCNN via fine-tuning.

2. MATERIAL AND METHODS

2.1 Network architecture

We used a network structure of DnCNN as the general CNN model (10). This model was pretrained on 400 gray images with a Gaussian noise level of 25 for natural image denoising. The size of input image for training was 50 × 50 pixels, the convolution layers were

set to 20, and 64 convolutional filters were used at a size of 3 × 3 pixels for generating the feature maps. To enhance denoising performance and learning speedup, residual learning and batch normalization was used in this model. Moreover, to be defined as the positive part of its value, rectified linear units (ReLU) were used for faster training of deep neural networks. DnCNN learns residual map data and generates a noise reduction image, which can yield more efficient training and accurate results within very deep networks. Batch normalization is utilized between the convolution filters, and ReLU in all middle layers for enabling higher learning rates with normalization of each sub-sample set. The architecture of the DnCNN network is shown in Figure 1.

2.2 Transfer learning

The concept of our transfer learning is to update the pretrained model of DnCNN for adapting CT-specific dose reduction images. In this study, abdominal CT images acquired with an original dose using 159 images were used for transfer learning. These CT images were taken from a publicly available dataset (The Cancer Imaging Archive), which is an open access information resource created by Washington University (12). We generated simulated dose reduction image within these abdominal images, with a 10-step dose reduction rate from the original dose to 1/100. Therefore, the number of training images in our transfer learning totaled 1590. We then selected these images in three cases, 5% of the data were separated for validation during the training, and 2.5% of the data for evaluation of denoising performance. Training images were randomly divided in small patches of 50 × 50 pixels, with 25 patches per image. Moreover, the input image was randomly rotated from 0 to 90 degrees horizontally. These learning methods can prevent overfitting with the training datasets. The Adam optimizer was used for training at a learning rate of 10^{-3} and networks were trained in 20 epochs.

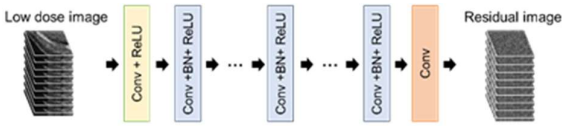

Figure 1 *Overall architecture of the DnCNN network with transfer learning using simulated noise images. This network learns residual mapping for noise image. The main modules include covolutional filtering (Conv), ReLU, and batch normalization (BN).*

2.3 CT noise simulation image

Dominant CT noise statistics in X-ray reduction is known to be in a Poisson distribution. Therefore, to simulate a low-dose CT image, we added a salt and pepper distribution while convoluting the CT unit-specific modulation transfer function (MTF) (13). Figure 2 shows the MTF curve applied during this noise simulation process. Here, we added the simulated noise with 10-step standard deviation in 10, 20, … and 100 times to the original image for creating 1/10, 1/20, … and 1/100 dose equivalent images. In this way, the unique dose reduction image was created to reflect the CT-unit noise characteristics, and these images were used within the transfer learning for adapting the CT-specific noise reduction process.

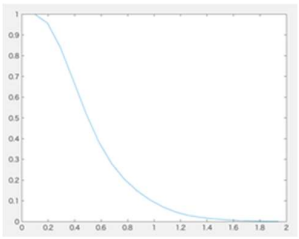

Figure 2 *CT unit-specific modulation transfer function.*

2.4 Evaluation of image quality

To evaluate the image quality of denoised images using the DnCNN and to compare efficacy with another noise reduction method, the contrast-to-noise ratio (CNR), peak signal-to-noise ratio (PSNR) and Structural Similarity Index (SSIM) were calculated in denoised images (14). The CNR was calculated using equation (1) as follows:

$$CNR = \frac{Signal_{liver} - Signal_{vein}}{SD_{vein}} \quad (1)$$

We evaluated the CNR between regions of liver tissue and veins, each region of interest (ROI) to measure signal and standard deviation (SD) values are shown in Figure 3. The PSNR was calculated using equation (2) as follows:

$$MSE = \frac{1}{M \times N} \sum_{i=1}^{M} \sum_{j=1}^{N} (x(i,j) - y(i,j))^2,$$

$$PSNR = 10 \log_{10} \frac{max|x(i,j)|^2}{MSE} \quad (2)$$

Figure 3 *ROI placement onto the CT image in the axial direction. We measured pixel values at regions of liver tissue and veins. ROIs = 10 mm φ (red and blue circles).*

The PSNR was denoted by maximum value in input image data ($x(i,j)$) divided by the mean square error between the image x (denoise low-dose image) and image y (original full-dose image). M and N indicate the width and height of the images, respectively. Furthermore, the SSIM was calculated using equation (3) as follows:

$$SSIM(x, y) = \frac{(2\mu_x\mu_y + C_1)(2\sigma_{xy} + C_2)}{(\mu^2{}_x + \mu^2{}_y + C_1)(\sigma^2{}_x + \sigma^2{}_y + C_2)} \quad (3)$$

where μ represents the signal mean value; σ represents variance value; C indicates regularization constants; and x, y represent each evaluation image, respectively.

In this study, we compared the performance of DnCNN with another noise reduction method using Media, Gaussian, and Winner filters. Within the Median filter method, output value is the median value of 3 × 3 neighboring pixels. In the Gaussian filter method, isotropic Gaussian smoothing kernel with an SD of 1.0 is applied to a two-dimensional image. For the Winner filter method, smoothing kernel in mean and variance of 5 × 5 neighboring pixels are used in the denoising process. Moreover, post-transfer learned DnCNN was compared with these noise reduction methods, included with original DnCNN. To compare image quality using the CNR index, PSNR and SSIM, an abdominal CT image composed of 350 × 250 pixels with 1 mm slice thickness was used as a denoised image. The simulated noise images were created in 75%, 50%, 10% and 5% equivalent dose level as compared to the original dose.

3. RESULTS

Figure 4 shows the results of a denoised image using several filtering and CNN-based methods. DnCNN_Tra represents application of transfer learning for the original DnCNN-based model. Figure 4 (b) depicts a comparison of the zoomed images of a specific region (indicated by the red ROI in Figure 4 (a)). Noise artifacts caused by the lack of incident photons severely degrades image quality, particularly in the in the ultra-low dose levels equivalent to 10% and 5% doses. It can also be observed that the CNN-based methods reduced the noise effectively at these ultra-low dose levels. However, within the results of original DnCNN method, although the noise has been removed, image blurring has been introduced in the ultra-low dose levels. On the other hand, DnCNN using the transfer learning method can be used to preserve the edge sharpness of the images (Figure 4b). Nevertheless, excessive smoothing occurred at the dose reduction levels of 75% and 50%.

In Figures 5, 6, and 7, we also compared the denoising results in terms of CNR, PSNR and SSIM, respectively, among noise suppression filters, original DnCNN and DnCNN_Tra over different dose reduction levels. For CNN, the DnCNN-based methods can be improved by 4~7 times to the ultra-low dose image. We observed that both DnCNN methods improved PSNR and SSIM even within high degradation images, while the original DnCNN yielded less improvement at ultra-low dose levels. For DnCNN_Tra, we accomplished improvement of SSIM by approximately 9% as compared to that of the original method in 5% and 10% dose equivalent images.

4. DISCUSSION

In this study, we assessed function of CNN image denoising caused by lack of incident photons in CT images. For diagnostic purposes, denoised images should have sufficient quality to facilitate a clinically sound decision. Therefore, we evaluated image quality based on image contrast, smoothing and similarity, while comparing this technique with other noise reduction methods.

The DnCNN demonstrated significant performance of denoising in terms of image PSNR and SSIM compared to another image space denoising methods. Significant improvement in the CNR and SNR were demonstrated, especially at the ultra-low-dose level with 5% and 10% dose equivalent images. However, it has been observed that over-smoothing behavior is associated with original DnCNN in denoising very low-dose CT data. This is the same tendency as described in a previous study (8). The tailored DnCNN (DnCNN_Tra) was able to remove noise and maintain image sharpness within ultra-low dose levels. Therefore, we can update the current denoising model, which was pre-trained on natural/synthetic images using Gaussian noise, by the simulated dose reduction images. However, at the noise reduction levels of 75% and 50%, the results of DnCNN_Tra images also exhibited excessive smoothing. It is possible that the distribution of high noise components was significant for the training data. Therefore, adjustment of noise distribution of training data and improvement of CNN architecture are required for applying noise reduction for any levels.

5. CONCLUSION

The DnCNN-based denoising method is appropriate for denoising of CT-specific noise resulting from low X-ray exposure. Moreover, its denoising properties were more suitable than those of other noise reduction methods, particularly for ultra-low dose levels. Transfer learning with tailored DnCNN could help to prevent noise removal and over-smoothing at ultra-low doses, and is able to improve image similarity by about 9%. Developing a generally applicable denoising network via optimal network design and training data modification is necessary for appropriate noise reduction at all noise levels.

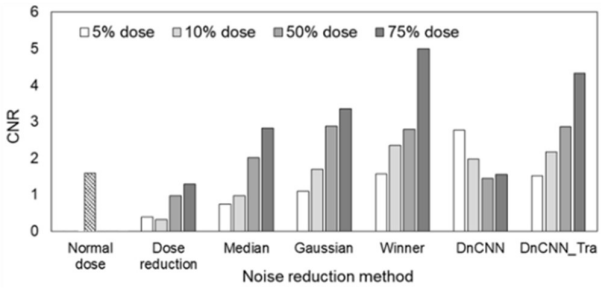

Figure 5 *Result of CNN within differing noise reduction methods for each dose reduction simulated image.*

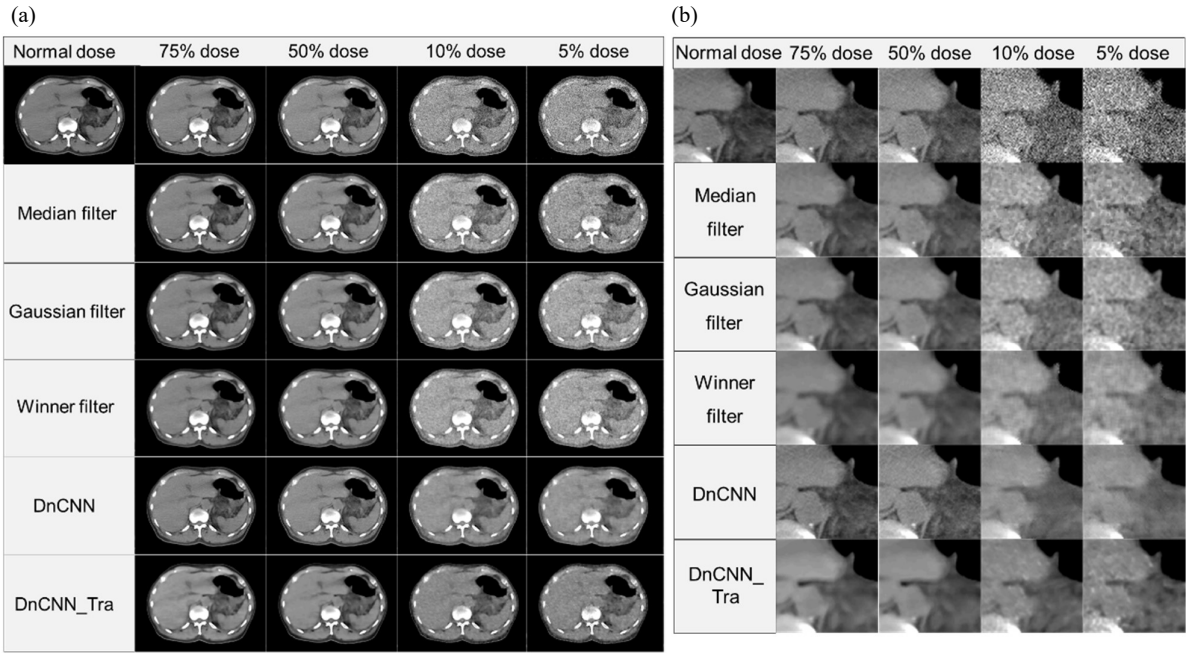

Figure 4 *The denoised image with contaminating noise artifacts, which was simulated for reduction of dose exposure in the image at four different dose levels. (a) Results of noise reduction in the whole abdominal image. (b) Zoomed images indicated within the red ROI; all images are shown with the same window width and level. Median, Gaussian, Winner, original DnCNN and optimized DnCNN (DnCNN_Tra) were applied for noise reduction at each dose reduction level.*

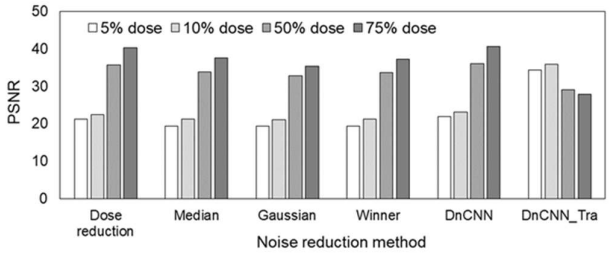

Figure 6 *PSNR results within differing noise reduction methods for each dose reduction simulated image.*

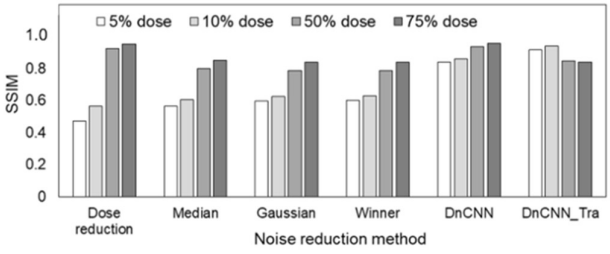

Figure 7 *Result of SSIM within differing noise reduction methods for each dose reduction simulated image.*

REFERENCES

1. Brenner DJ, Hall EJ. Computed tomography—an increasing source of radiation exposure. New Engl J of Med. 2007;357:2277–2284.
2. National Lung Screening Trial Research Team. Reduced lung-cancer mortality with low-dose computed tomographic screening. N Engl J Med. 2011;365:395–409.
3. Brenner DJ, Hall EJ. Computed tomography-an increasing source of radiation exposure. N Engl J Med. 2007;357:2277–2284.
4. Wang J, Li T, Lu H, et al. Penalized weighted least-squares approach to sinogram noise reduction and image reconstruction for low-dose X-ray computed tomography. IEEE Trans Med Imaging. 2006;25(10):1272–1283.
5. Pickhardt Pj, Lubner Mg, Kim Dh, et al. Abdominal CT with model-based iterative reconstruction (MBIR): initial results of a prospective trial comparing ultralow-dose with standard-dose imaging. AJR Am J Roentgenol. 2012;199(6):1266–1274.
6. Chen H, Zhang Y, Kalra MK, et al. Low-Dose CT With a Residual Encoder-Decoder Convolutional Neural Network, IEEE Trans Med Imaging. 2017;36(12):2524–2535.
7. Zhao T, McNitt-Gray M, Ruan D. A convolutional neural network for ultra-low-dose CT denoising and emphysema screening, Med Phys. 2019;46(9):3941–3950.
8. Kim B, Han M, Shim H, et al. A performance comparison of convolutional neural network-based image denoising methods: The effect of loss functions on low-dose CT images. Med Phys. 2019;46(9):3906–3923.
9. Wolterink JM, Leiner T, Viergever MA, et al. Generative Adversarial Networks for Noise Reduction in Low-Dose CT. IEEE Trans Med Imaging. 2017;36(12):2536–2545.
10. Zhang K, Zuo W, Chen Y, Meng D, Zhang L. Beyond a gaussian denoiser: residual learning of deep CNN for image denoising. IEEE Trans Image Process. 2017;26:3142–3155.
11. Plotz T, Roth S. Benchmarking denoising algorithms with real photographs. 2017 IEEE Conference on Computer Vision and Pattern Recognition (CVPR) 2017:1:6.
12. Clark K, Vendt B, Smith K, et.al., The Cancer Imaging Archive (TCIA): maintaining and operating a public information repository. J Digit Imaging. 2013;26(6):1045–1057.
13. Kim CW, Kim JH, Realistic simulation of reduced-dose CT with noise modeling and sinogram synthesis using DICOM CT images. Med Phys. 2014;41(1):011901.

14. Wang Z, Bovik AC, Sheikh HR, Simoncelli EP. Image quality assessment: from error visibility to structural similarity. IEEE Trans Image Process. 2004;13:600–612.

Evaluation of student competency on mid-trimester fetal sonography scan following the newly-established Master degree in medical sonography

Surapa Hirunpijit[1,3], B.Sc., Surachate Siripongsakun[1], M.D., Chanisa Chotipanich[1], M.D.,
Pantajaree Hiranrat[1], B.Sc., Amarin Narkwichean[2], M.D. PhD., Wipada Laosooksathit[2], M.D.

1 Sonographer School, Faculty of Health Science Technology, Chulabhorn Royal Academy, Bangkok, Thailand,
2 Department of Obstetrics and Gynecology, Faculty of Medicine, Srinakharinwirot University, Nakornnayok, Thailand2
3. Radiological Department of Central Chest Institute of Thailand, Bangkok, Thailand3

Abstract

Introduction: The medical sonographer plays a role in assisting specialized physicians in the ultrasound (US) examination, especially in obstetric sonography services. The significant assistance, including antenatal ultrasound evaluation of gestational age, improves the detection of fetal anomalies. Currently, Thailand has a first formal master's degree sonographer training program. However, competency level after completing the obstetric sonography training is not formally assessed.

Purpose: The study aims to evaluate medical sonography students' competency who have completed obstetric sonography training to estimate gestational ages (GA) and fetal biometric measurement, compared to obstetricians.

Method: A cross-sectional observational study at the end of the medical sonographer student's practice session had been conducted. Eighty pregnant undergoing mid-trimesters (18-24 weeks) were recruited and ultrasound using the International Society of Sonography in Obstetrics and Gynecology (ISUOG) guideline. Estimated GA calculated from biometric measurements were compared between medical sonographer students and qualified obstetricians. Subsequently, images were randomly evaluated by maternal-fetal medicine specialists to assess the performance of the measurement.

Results: There was no significant difference in terms of estimated gestational age (GA) between medical sonographer students and obstetrician. The mean difference of ultrasound estimated gestational ages between medical sonographer students and obstetricians were 0.01 day ± 2.92, p-value = 0.89. A significant difference in the measurement of head circumference (HC) and abdominal circumference (AC) ($p<0.001$). The overall image quality of fetal head, abdomen, and femur are good to excellence (77.5-80%). Perfect and nearly perfect agreement on the presence of placenta previa, adequacy of amniotic fluid, and position of the placenta ($k = 0.9$-1.0).

Conclusion: Medical sonographer students have proved competency in GA estimation by fetal biometry measurement as compared to obstetricians. However, the quality of the acquired images, according to ISUOG recommendation, needs to be improved and should be emphasized in the curriculum. Thus, medical sonographer students can potentially assist to decrease obstetrician workload in screening in mid-trimesters US.

Keywords: Competency, Fetal biometry, Obstetric sonography, Medical sonographer, Sonographer

1. INTRODUCTION

Antenatal care should advocate for all pregnant women to ensure the well-being of mother and child during antepartum and postpartum periods. The necessary antenatal evaluation should include GA estimation, evaluation of fetal development/well-being, estimated delivery date, and proper mode of delivery[(1)].

The ISUOG recommends a sonography assessment practice guideline for fetal biometry and growth and a practice guidelines for performance of the routine mid-trimester fetal ultrasound scan[(2, 3)], which included; measurement of important fetal structures and development parameters. Accurate measurement for estimation of gestational age, fetal weight, interval fetal growth and development, and fetal anomaly[(4)].

In Europe, USA, and Australia, the medical sonographers perform US scanning to assist specialized physicians. Medical sonographers' primary work is performing US scanning and giving preliminary findings to radiologists and obstetricians, who will be responsible for interpreting the reports and covered only problematic cases. The sonographer's assistance allows reducing waiting time and promoting more efficiency in the diagnostic examination.

In Thailand, most obstetrics US studies require specialized physicians, especially obstetricians and radiologists, to perform the exams, resulting in limitations in availability and accessibility. In 2018, a new established Master program for training sonographer at Chulabhorn College of Medical Science[(5)] had been started, to recruit competent medical sonographers to perform proper US scanning. Master degree in medical sonography covers the competency in abdominal, obstetrics, reproductive, small parts, and vascular scanning.

An established training program, the competency of the first batch of Master degree students on competency assessment study is vital to improve the program's curriculum.

Since US examination is operator dependent, operators' competency is essential, which impacts the result of the studies. A few studies have proved that well-trained medical sonographers can perform US scanning and detect hepatic and biliary lesions comparable to radiologists [6, 7].

In Thailand, obstetric US scanning is solely performed by physician and never have formally trained sonographers to assist. In the Master degree curriculum, the student will have core training in obstetrics sonography which consists of two subjects including; 1. Core training two credits with fifteen hours of didactic lectures and thirty hours of laboratory practices with allotment of forty-five hours of self-learning and 2. Clinical clerkship which accounts one hundred seventy-five hours of obstetrics sonography scanning.

This study aims to compare the competency of Medical sonography students who have completed obstetric sonography training in the Master degree curriculum compared to obstetricians.

2. MATERIAL AND METHODS

This observational study evaluated medical sonographer students' competencies after completing their obstetrics modules to perform a mid-trimester US scan, comparing to obstetricians at Srinakharinwirot University Hospital, Thailand. The study was approved by the Ethics Committee for Human Research, the Chulabhorn Research Institute (CRI 073/2562). The research was conducted following all relevant international ethical guidelines. The inclusion criteria were women aged > 20 years old carrying singleton pregnancy visiting the antenatal clinic during their second trimester (18-24 weeks). Their gestational age had to be confirmed by at least once a first-trimester ultrasound scan. The exclusion criteria were the presence of fetal anomaly detected during the scan.

All participants, following written informed consent given, were enrolled in the study. Demographic data, including age, GA, height, weight, previous pregnancy history, and menstrual period information was collected. The participants then underwent two ultrasound scans, firstly by a medical sonographer student, then a qualified obstetrician. Two medical sonographer students in the first batch involve in this study. The US scans were confirmed by an on-duty obstetrician of the day. Each medical sonographer student and the obstetrician measured biometric parameters, according to ISUOG guideline, which includes biparietal diameter (BPD), HC, AC and femur length (FL)[3]. The sonographer students performed the measurement three times for reproducibility assessment. Information regarding correct image planes/measurement techniques and criteria of the best-quality biometric images were demonstrated in figure 1 and table 1, respectively. The estimation of GA is calculated by the Hadlock formula[8], and the placenta site and adequacy of amniotic fluid were recorded. Also, three sonographic images demonstrating i) fetal head on the transthalamic plane, ii) Transverse section of the fetal abdomen (as circular as possible), iii) Femur diaphysis length, were recorded in all participants during the medical sonographer student scan. Subsequently, 60 images from 20 studies were randomly selected to be evaluated (and marked) for the image quality by a maternal-fetal medicine specialist (WL) using ISUOG guideline assessment of fetal biometry and growth (Table 1)[2, 4, 9]. US machine included LOGIQ S7 GE Healthcare Austria for sonographers and Voluson E6 GE Healthcare Austria for obstetricians.

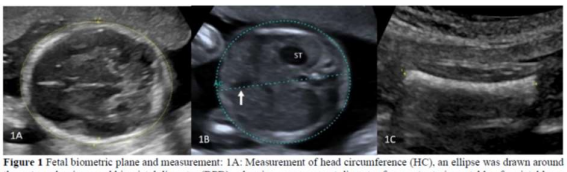

Figure 1 Fetal biometric plane and measurement: 1A: Measurement of head circumference (HC), an ellipse was drawn around the outer calvarium; and biparietal diameter (BPD) , showing measurement diameter from outer to inner table of parietal bone (cross mark measurement), 1B: Measurement of abdominal Circumference (AC) in transverse abdominal view approach, showing symmetry of abdomen with presence of fluid-filled stomach (ST) and portal sinus (arrow), 1C: Measurement of femur length (FL) in longitudinal view, showing presence of distal and proximal ends of diaphysis and measurement points should be placed at mid of each diaphyseal end (cross mark measurement).

Table 1 Criteria for score-base objective evaluation quality of biometric image

Biometric Parts	Criteria of biometric image	Diagrams	Ultrasound images
BPD & HC	* Symmetrical plane * Plane showing thalami * Plane showing cavum septi pellucidi * Cerebellum not visible * Head plane occupying more than half of total image size * Calipers and dotted ellipse placed correctly	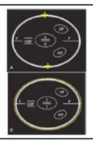	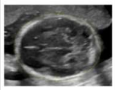
AC	* Symmetrical plane * Plane showing portal sinus * Plane showing stomach bubble * Kidneys not visible of total image * Abdomen plane occupying more than half of total image size * Calipers and dotted ellipse placed correctly		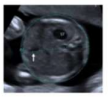
FL	* Both ends of bone clearly visible * Femur occupying more than half total image * <45° angle to horizontal * Calipers placed correctly		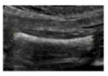

2.1 Statistical analysis

Mean gestational age and fetal biometry measurement between medical sonographer students and obstetricians were compared using the Wilcoxon signed-rank test. Interobserver-variability, mean difference of GA of each sonographer student and obstetrician was analyzed using the Mann Whitney U test. Intra-observer reliability of fetal biometry measurement was calculated used the intra-subject coefficient of variation (CV%)[10]. Correlation agreement between medical sonographer students and obstetricians for assessing the placenta site, presence of placenta previa, and adequacy of amniotic fluid were assessed by Fleiss and Cohen's Kappa statistics, respectively. Kappa coefficient was determined as following; 0 as agreement equivalent to chance; 0.01-0.20 as slight agreement; 0.21-0.40 as fair agreement; 0.41-0.60 as moderate agreement; 0.61-0.80 as substantial agreement; 0.81-0.90 as near perfect agreement; 1.00 as perfect agreement.

Statistical analysis was performed utilizing the IBM Statistical Package for the Social Sciences (SPSS) version 20 (IBM, Inc., New York, NY), and significance

was defined as a two-sided p-value <0.05. Demographic data were presented using descriptive statistics.

3. RESULTS

Eighty-one pregnant participants were enrolled in the study, with one being excluded due to the presence of fetal cleft lip/palate anomaly. Participants' average age and BMI were 29.6±4.6 years and 23.97 ± 3.86 kg/m^2, respectively. Their average gestational age on the study date was at 20.8±7.5 weeks. Participant demographic data is demonstrated in Table 2.

Table 2 Participants demographic data

	N=80
Age (years)*	29.58 ± 4.58
Weight (kg)*	61.10 ± 11.56
Height (cm)*	1.59 ± 0.06
Gestational age on study date*	20.8 ±7.5
Body mass index (BMI) *	23.97 ±3.86
Normal (BMI < 23)	41 (51.3%)
Overweight (BMI at 23.5-27)	20 (25%)
Obesity (BMI > 27 to 30)	13 (16.3%)
Morbid obesity (> 30)	6 (7.5%)

* mean ± standard deviation

There was no significant difference in terms of estimated gestational age (biometric calculation) measured between medical sonographer students and obstetricians (mean difference of GA measured 0.01 ± 2.92 days, p = 0.89). Regarding each biometry parameters, BPD and FL measurements were also not significance difference (mean difference BPD 0.39 ± 1.94 mm, p = 0.07; FL 0.12 ± 1.73 mm, p = 0.94). Nonetheless, circumferential measurement (HC and AC) were measured slightly larger by medical sonographer students when compared to obstetricians (mean difference; 4.08 ± 5.88 mm, p<0.001, and 2.86 ± 7.23, p<0.001, respectively). Mean differences of fetal biometry and estimated GA, comparisons between a medical sonographer student and an obstetrician are shown in table 3. Overall, interobserver variability between medical sonographer students when compared mean difference gestational age from obstetrician was 0.39. Interobserver variability between sonographers were not significance difference in BPD, HC and AC measurements (p = 0.78, 0.20 and 0.14), only FL measurement was a significant difference (p<0.001).

Intra-observer variation of the two medical sonographer students' measurement shows no significant difference in BPD, HC, AC, and FL during three repeated measurements. The intra-subject coefficient of variation (%CV) of BPD, HC, AC, and FL in medical sonographer student 1 was 1.68%, 1.28%, 1.54% and 1.61% and medical sonographer student 2 was 1.53%, 1.43%, 1.96%, and 2.43%.

Table 3 Comparison biometry measurement between sonographers with obstetrician

	Obstetrician (n=80)	Mean difference of obstetrician and sonographer	P-value	Mean difference		P-value
				Sonographer 1	Sonographer 2	
BPD (mm± SD)	47.92 ± (3.89)	0.39 ± (1.94)	0.07	0.37 ± (1.95)	0.44 ± (1.95)	0.78
HC (mm± SD)	180.54 ± (13.66)	4.08 ± (5.88)	<0.001	3.48 ± (5.64)	6.32 ± (6.37)	0.20
AC (mm± SD)	157.35 ± (14.66)	2.86 ± (7.23)	<0.001	2.24 ± (6.77)	5.13 ± (8.58)	0.14
FL (mm± SD)	33.77 ± (3.53)	0.12 ± (1.73)	0.94	0.25 ± (1.39)	1.50 ± (2.14)	<0.001
Estimated GA by ultrasound (days ± SD)	20w4d ± (8.05)	0.01d ± (2.92)	0.89	0.20 ± (2.81)	0.64 ± (3.31)	0.39

A perfect agreement on detecting placenta previa and evaluating amniotic fluid between medical sonographer students and obstetricians (kappa = 1) is observed. A near-perfect agreement on determination of placental location was demonstrated (k=0.9).

Overall average scores between 77.5 - 80% were achieved across all biometric parameters regarding sonographer students' skills on quality of image caption and measurement. Nonetheless, breakdown analysis demonstrated student defects on obtaining i) symmetrical abdominal plane (45%), ii) adequate fetal head plane showing thalami (55%), and iii) captured fetal part more than half of the total image (AC 60%, FL 55%) (Table 4).

Table 4 Quality of biometric ultrasound images.

Biometric Parts	Criteria of biometric image	n =20 (%)	Overall average of achievement
Head	* Symmetrical plane	16 (80%)	4.8/6 (80%)
	* Plane showing thalami	11 (55%)	
	* Plane showing cavum septi pellucidi	16 (80%)	
	* Cerebellum not visible	20 (100%)	
	* Head plane occupying more than half of total image size	17 (85%)	
	* Calipers and dotted ellipse placed correctly	16 (80%)	
Abdomen	* Symmetrical plane	9 (45%)	4.65/6 (77.5%)
	* Plane showing portal sinus	14 (70%)	
	* Plane showing stomach bubble	19 (95%)	
	* Kidneys not visible of total image	19 (95%)	
	* Abdomen plane occupying more than half of total image size	12 (60%)	
	* Calipers and dotted ellipse placed correctly	20 (100%)	
Femur	* Both ends of bone clearly visible	16 (80%)	3.15/4 (78.75%)
	* Femur occupying more than half total image	11 (55%)	
	* <45° angle to horizontal	20 (100%)	
	* Calipers placed correctly	16 (80%)	

4. DISCUSSION

In Thailand, ultrasonography still requires specialized physicians, especially radiologists, and obstetricians, resulting in some limitations with increasing services and long waiting times of patients in government hospitals before examinations, which could delay diagnosis and treatments. An official sonographer school in Thailand has been new established. The competent sonographer in obstetrics sonography may potentially help the shortage of sonography providers.

Of all fetal biometry measurements and the GA estimation, there are two parameters, including HC and AC, that have significantly different measurement values between sonographers and obstetricians. This variation may be explained that HC and AC are the measurements in two dimensions[3]; therefore, HC and AC more prone to error than one dimension of measurement e.g. BPD and FL. Interobserver variability of *sonographers*' measurement on BPD has accuracy

and reliability, compared to obstetricians. While HC and AC *measurement may not be quite accurate. This finding may be caused by US scan technique, improper measurement, or borderline image quality. FL has the least reliability between the students; because the fetal leg's position has the most mobility during scanning, resulting in less repeatability of measurement.*

Although there are differences in AC and HC measurement, the GA estimation has no effect on this variability and clinical impact of GA measurement between sonographers and obstetrician. In a report of a well-established sonographer program had shown that the certified sonographers have excellent concordance measurement of fetal biometry (AC, FL and EFW)[11]. This study probably supports the potential of sonographer training, which can be trained at the level of expectations depending on the quality of the training program.

Both intra-operator fetal biometry measurement variation and inter-operator agreement, on placenta location and amniotic fluid adequacy, reveal no significant difference and nearly perfect agreement, respectively. This finding support students' competency in detecting life-threatening maternal conditions such as placenta previa, oligohydramnios, and polyhydramnios[12, 13].

The evaluation of image quality shows average optimal image achievement of head, abdomen, and femur planes about 77.5-80.0%. The fetal head thalamic plane, a symmetrical plane of abdomen, and femur occupying more than half of image are the least achievable for imaging quality, which are only about 55%, 45%, and 55%, respectively. To achieve a good quality of images, sonographer student needs to develop combined multiple sonography skills, including hand-eye coordination, image optimization, and anatomical recognition, which needs to build up to be competent in sonography [14, 15]

5. CONCLUSION

Medical sonographer students who have complete clinical training of obstetrics sonography have proved a certain competency level in ultrasound mid-trimester, including confirming GA estimation by fetal biometry measurement. However, the quality of the acquired images, according to ISUOG recommendation, need to be improved and should be emphasized in the curriculum. Thus, medical sonographer students can potentially assist to decrease obstetrician workload in screening in mid-trimesters US.

REFERENCES

1. Tunçalp Ö, Pena-Rosas J, Lawrie T, Bucagu M, Oladapo O, Portela A, et al. WHO recommendations on antenatal care for a positive pregnancy experience—going beyond survival. BJOG: An International Journal of Obstetrics & Gynaecology. 2017;124(6):860-2.
2. Salomon LJ, Alfirevic Z, Da Silva Costa F, Deter RL, Figueras F, Ghi T, et al. ISUOG Practice Guidelines: ultrasound assessment of fetal biometry and growth. Ultrasound Obstet Gynecol. 2019;53(6):715-23.
3. Salomon LJ, Alfirevic Z, Berghella V, Bilardo C, Hernandez-Andrade E, Johnsen SL, et al. Practice guidelines for performance of the routine mid-trimester fetal ultrasound scan. Ultrasound Obstet Gynecol. 2011;37(1):116-26.
4. Benson CB, Doubilet PM. Fetal Biometry and Growth. In: Mary E. Norton LMS, Vickie A. Feldstein., editor. Callen's ultrasonography in obstetrics and gynecology. 6 ed. Philadelphia: Elsevier; 2017. p. 118-31.
5. http://www.asean-journal-radiology.org/index.php/ajr/article/view/63 SSMcJ-Af. The first step of the sonographer system in Thailand. . The Asean Journal of Radiology. 2020;21:68-72.
6. Tangruangkiat S, Phonlakrai M, Ritlumlert N, Siripongsakun S, Vidhyarkorn S, Thitisitthikorn W. Ultrasonography detection of liver lesions: A Pilot comparison study between radiologists and sonographers. J Med Assoc Thai. 2018;101:37-41.
7. Dawkins A, George N, Ganesh H, Ayoob A, Lee J, Nair R, et al. Radiologist and Sonographer Interpretation Discrepancies for Biliary Sonographic Findings: Our Experience. Ultrasound Q. 2017;33(4):261-4.
8. Hadlock FP, Deter RL, Carpenter RJ, Park SK. Estimating fetal age: effect of head shape on BPD. AJR Am J Roentgenol. 1981;137(1):83-5.
9. Salomon LJ, Bernard JP, Duyme M, Doris B, Mas N, Ville Y. Feasibility and reproducibility of an image-scoring method for quality control of fetal biometry in the second trimester. Ultrasound Obstet Gynecol. 2006;27(1):34-40.
10. Reed GF, Lynn F, Meade BD. Use of coefficient of variation in assessing variability of quantitative assays. Clin Diagn Lab Immunol. 2002;9(6):1235-9.
11. Gregory Ward D, Bolaños R, Blaskiewicz RJ, Xiao T, Gavard JA. Concordance Rates Between Resident-Performed Ultrasound Measurements and Certified Sonographer Measurements. J Ultrasound Med. 2019;38(9):2389-94.
12. Dashe JS, Hoffman BL. Ultrasound Evaluation of the Placenta, Membranes, and Umbilical Cord. In: Mary E. Norton LMS, Vickie A. Feldstein., editor. Callen's ultrasonography in obstetrics and gynecology. 6 ed. Philadelphia: Elsevier; 2017. p. 674-703 (679).
13. Magann EF, Sandlin AT. Amniotic Fluid Volume in Fetal Health and Disease. In: Mary E. Norton LMS, Vickie A. Feldstein., editor. Callen's ultrasonography in obstetrics and gynecology. 6 ed. Philadelphia: Elsevie; 2017. p. 704-19.
14. Tolsgaard MG. A multiple-perspective approach for the assessment and learning of ultrasound skills. Perspect Med Educ. 2018;7(3):211-3.
15. Tolsgaard MG, Todsen T, Sorensen JL, Ringsted C, Lorentzen T, Ottesen B, et al. International multispecialty consensus on how to evaluate ultrasound competence: a Delphi consensus survey. PLoS One. 2013;8(2):e57687.

The Study of Correlation Between Water-equivalent Diameter (Dw) and Age on CT Examination in Pediatric's Head Patient with Tube Current Modulation (TCM) Technique

Khoerun Nisa Syaja'ah[1], Choirul Anam[2], Freddy Haryanto[1], Idam Arif[1]

1 Department of Physics, Faculty of Mathematic and Natural Science, Institut Teknologi, Bandung, Indonesia,
2 Department of Physics, Faculty of Mathematics and Natural Sciences, Diponegoro University, Semarang, Indonesia

Abstract

Computed Tomography (CT) examination in pediatric's head patient is known to have a hypersensitive reaction of ionizing radiation. Therefore, it gives a long-term risk effect on cell or tissue injury. Besides, the actual patient dose delivered during CT examinations has not been well-defined, especially when using the tube current modulation (TCM) technique. The tube current is changed dynamically after the patient's size (region) along the Z-axis (longitudinal TCM). This study aims to calculate and compare the correlation between two parameters D_w and age, in pediatric's head patient for tube current modulation (TCM) technique. Six pediatric patients 0-12-year-old age groups underwent a CT head examination in Hasan Sadikin hospital using Somatom Definition Flash with variation in the number of slices. We calculate using programming python with an automated contouring algorithm. There are three main parts to this step. The first is thresholding process and contouring using a morphological gradient method after images CT data were reading and converted to Hounsfield units (HU). The second is Calculating D_w based on the American Association of Physicists in Medicine (AAPM) report 220. the third is Extracting the data tube current. **The value of average D_w was a correlation with the age of patients using regression analysis. The result showed that the average Dw of the age groups (0-6th years) was 9.6-12 cm, and it was increases compared to the age of seventh to reach 12th years with the average value 13-15.6 cm. The D_w size was linearly correlated with R^2 0.96 with gradient 0.52 and R^2 0.83 with gradient 22.85 for age and tube current. The correlation between D_w and age in Pediatric's head patient for TCM technique indicates that average D_w's value has changed and increase compared to every age group. The D_w correlates with the age of the patient and the average tube current.**

Keywords: Water-equivalent Diameter (D_w), Tube Current Modulation (TCM), Age, CT, Automated Contouring,

1. INTRODUCTION

Computed Tomography (CT) is one of the tool diagnostic imaging devices that use radiation from X-ray to produce a cross-sectional (trans-axial) of the patient's anatomy without surgery. Recently, CT's technology has facilitated the expansion to provide fast, complex, and accurate diagnostic results (1-3). In many aspects, CT has to turn into a reliable option for clinical imaging purposes. However, the radiation dose in these methods also increases the risk of cumulative exposure for patients and significantly increasing the risk of cancer in the sensitive organ (4) The method for analyzing to reduce the risk of excessive radiation exposure, optimization, and evaluation dose from CT is very concerning, especially in pediatric patients as small as possible to estimate patient dose efficiently (4)(5). One method to quantify radiation dose from CT examination using data Volumetric Computed Tomography Dose Index ($CTDI_{vol}$). $CTDI_{vol}$ is calculated based on measurement using cylindrical phantom PPMA 16 cm for head and 32 cm for body region (6). Besides, the dose for an individual patient depends on the size (7).

The American Association of Physicists in Medicine (AAPM) introduces a method to estimate individual dose using Specific Size Dose Estimation (SSDE) (8). SSDE method calculate by data normalizing $CTDI_{vol}$ with correction factor number from diameter size patient such as effective diameter (D_{eff}) or water equivalent diameter (D_w) (8)(9).

D_{eff} and D_w measure diameter size from an image Dicom file. The difference from the method is the D_{eff} measure without calculating the composition of attenuation effect to material or patients. At the same time, D_w quantifies the composition of attenuation from x-ray when interacting with the matter or tissue in the human body (11)(12). Therefore, D_w gives a more accurate evaluation size for the patient's dose than Deff (13). D_w is one of the parameters to estimate the dose using SSDE. The relationship between D_w and age or other parameters for pediatric's patients has not been established. Besides, the actual patient dose delivered during CT examinations has not been well-defined, especially when using the tube current modulation (TCM) technique.

Therefore, this study aimed to calculate and compare the correlation between two parameters D_w and age, in pediatric's head patient for tube current modulation (TCM) technique.

2. MATERIAL AND METHODS

2.1 The Images of Patients

The data collected from CT head in the DICOM, six pediatric patients 0-12-year-old age groups were examined in Hasan Sadikin hospital using Somatom Definition Flash with variation in the number of slices

2.2 The algorithm for automated D_w and extracted data tube current

We calculated using programming python with an automated contouring algorithm based on Figure 1. There are three main parts to this step. The first is the thresholding process, and contouring using morphological gradient dilation and erosion method

after images CT data converted to Hounsfield units (HU) using equation 1. The second calculates D_w based on the American Association of Physicists in Medicine (AAPM) report 220 using equation 2. The third is extracting of tube current data for every slice on image patient from Dicom image. The info patients and parameter machines in the examination can obtain from this file format, such as tube current, tube voltage, $CTDI_{vol}$. Finally, the average value D_w was analyzed with the average tube current using regression analysis.

$$HU = CTdata \times S_l + l_n \quad \text{.....(1)}$$

$$D_w = 2 \times \sqrt{\left(\frac{\overline{HU(x,y)}}{1000} + 1\right) \times \frac{A_{ROI}}{\pi}} \quad \text{.....(2)}$$

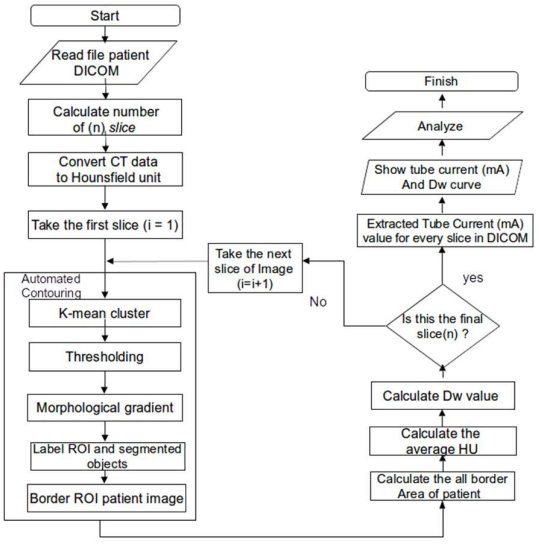

Figure 1 Flow chart for automated conturing and extrated data from DICOM file

3. RESULTS

3.1 Automated D_w Calculation Based on Conturing Process

Figure 2(a) shows an original input image pediatric head patient with precise slices. Figure 2(b) shows the gradient morphology erosion and dilatation process. Before this process, we use the thresholding process. This process aims to determine the image boundary. The value of thresholding was 200 to 700 HU. Figure 2(c) shows the result of the process labeling it is to make sure the region that will be analyzed, and Figure 2(d) is the result of contouring with borders or outlines of the image. The blue one line bordered by the original image is the limit area of the calculation, or we can call it the Region of Interest (ROI) image of the head.

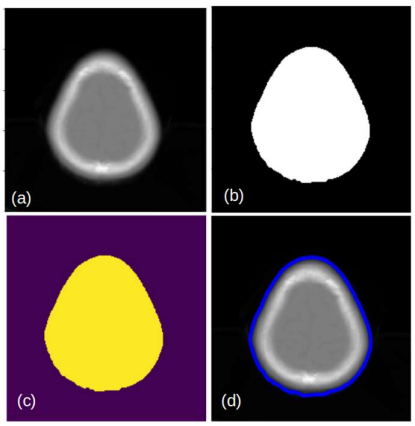

Figure 2 *Steps for the automatic contouring process:(a) original input file image patient from the axial slice, (b) the result of morphological gradient algorithm and thresholding process,(c) the labeling object ROI, (d) result of border auto contouring to calculate the D_w.*

3.2 Tube Current Modulation (mA)

Figure 3 shows a tube current value for every slice in the TCM technique's longitudinal axis from image one of the pediatric's head patient. It can be seen that the tube current value fluctuated for every slice and has a different value for a specific region

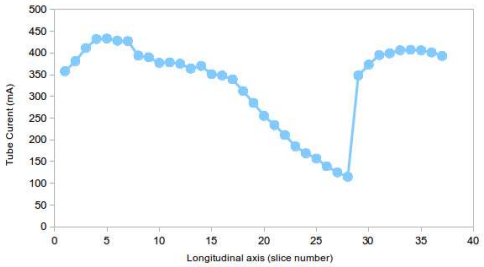

Figure 3 *Extracted data for tube current value using the TCM technique in the image of the patient.*

3.3 Correlation between D_w and Age Patients

Figure 4 shows a correlation between the two parameters; the x-axis is age patients and on the y-axis is D_w. We analyzed using linear regression. It can be seen that the D_w and age patient has a strong correlation with the R^2 is 0.96, and the gradient is 0.52.

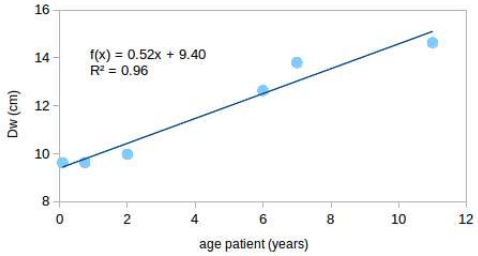

Figure 4 *Relationship between D_w (cm) and age patients (years)*

3.4 Correlation between D_w and Tube Current Modulation

Figure 5 shows a correlation between D_w and the tube current with the TCM technique. It can be seen that Figure 5 below the D_w and tube current TCM technique has linearly correlated with the R^2 is 0.83 and the gradient is 22.85.

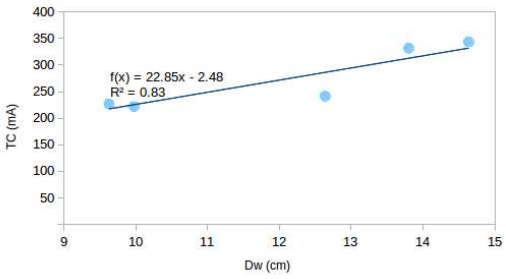

Figure 5 *Relationship between tube current (mA) and D_w (cm) value*

4. DISCUSSION

The tube current modulation technique's result will be fluctuated dynamically or change in every slice as a longitudinal axis, as shown in Figure 3. It is because of the effect of the attenuating area in the water-equivalent diameter (D_w) method. This current study showed a relationship between D_w linearly correlated with average tube current in TCM technique with R^2 values 0.83, and the gradient or slope is 22.85, as shown in Figure 5. So, we can estimate the average tube current value using the TCM technique from the D_w value.

The D_w also has a relationship with patients' age when the scanning process is using the TCM technique. This study showed that the value of average D_w was correlated with patients' age using regression analysis. The result showed that the average D_w of the age groups (0-6th years) was 9.6-12 cm, and it was increases compared to the age of seventh -12th years with the average value 13-15.6 cm. The D_w size was linearly correlated with R^2 0.96 with gradient 0.52. D_w's value will determine the SSDE value, so the accurate calculation of this parameter correlates with each other to the final value as dose radiation. It is an exciting point and message that the pediatric CT protocol should be comprehensive and accurately evaluated. A limitation from this study has the small pediatric patients only a few age-group that can be examined. So this study needs to develop further research in large-scale populations.

5. CONCLUSION

From this study, it can be assumed that the D_w size was linearly correlated with R^2 values of 0.96 with gradient 0.52 and R^2 0.83 with gradient 22.85 for age and tube current, respectively. The correlation between D_w and age in Pediatric's head patient for TCM technique indicates that the value of average D_w has changed and increased compared to every age group and the D_w was found linearly correlated with age patient and average tube current.

ACKNOWLEDGEMENTS

This study was funded by the Penelitian Dasar Unggulan Perguruan Tinggi (PDUPT). Ministry of Research Technology and Higher Education of Republic of Indonesia. The authors would like to thank Dwi Siwi Retnoningsih from Hasan Sadikin Hospital, Bandung, Indonesia.

REFERENCES

1. A.B. Kharbanda, E. Krause, Y. Lu, and K.Blumberg, Analysis of Radiation Dose to Pediatric Patients During Computed
2. Kalender WA. X-ray computed tomography. Phys Med Biol. 2006;51(13):R29-R43.
3. Tootell A, Szczepura A, Hogg P. Analysis of effective and organ dose estimation in CT when using mA modulation: a single scanner
4. pilot study. Radiography. 2017;23(2):159-166.
5. Khoerun Nisa Syaja'ah, Choirul Anam, Fauzia P Lestari, Mochamad Haekal, Freddy Haryanto, Calculation of Size-Specific Dose Estimation (SSDE) of The Pediatric's Head for Tube Current Modulation (TCM) CT Examinations. Journal of Physics: Conference Series. Doi:10.1088/1742-6596/1505/1/012036. 2020
6. Arif Fahmi, Choirul Anam, Suryono, Mohd Hanafi Ali, Arif Jauhari. Correlation between age and head diameters in the paediatric patients during CT examination of the head. The Journal of Polish Society of Medical Physics.Vol 25, Issue 4. 2019
7. Anam, F. Haryanto, R. Widita, I. Arif and G. Dougherty, Automated Calculation of Water-equivalentDiameter (D W) Based on AAPM Task Group 220, Journal of Applied Clinical Medical Physics, Volume 17, No 4, 2016.
8. C. Anam, F. Haryanto, R. Widita, I. Arif, G. Dougherty, D. McLean Volume computed tomography dose index (CTDI vol) and size-specific dose estimate (SSDE) for tube current modulation (TCM) in CT scanning, International Journal of Radiation Research, Volume 16, No 3, 2018.
9. AAPM 2011 Size Specific Dose Estimates (SSDE) in Pediatric and Adult Body CT Examinations (College Park: AAPM)McCollough, D.M. Bakalyar, M.Bostani, S.Brady, K.Boedeker, J.M. Boone,H. H.Chen-Mayer, O.I. Christianson, S.Leng B. Li, Michael F. McNitt-Gray, R.A. Nilsen, Mark P. Supanich, and J. Wang The Measurement, Reporting, and Management of Radiation Dose in CT, Report of AAPM Task Group 220: CT Dosimetry Diagnostic Imaging Council CT Committee 2014.
10. Anam C, Fujibuchi T, Haryanto F, et al. An evaluation of computed tomography dose index

measurements using a pencil ionisation chamber and small detectors. J Radiol Prot. 2019;39(1):112-124.
11. Dawson P Patient dose in multislice CT: Why is it increasing and does it matter ? British Journal of Radiology, 77, S10-S13, 2004
12. Wang J, Duan X, Christner JA, et al. Attenuation-based estimation of patient size for the purpose of size specific dose estimation in CT. Part I. Development and validation of methods using the CT image. Med Phys. 2012;39(11):6764-6771.
13. Wang J, Christner JA, Duan Y, et al. Attenuation-based estimation of patient size for the purpose of size specific dose estimation in CT. Part II. Implementation on abdomen and thorax phantoms using cross sectional CT images and scanned projection radiograph images. Med Phys. 2012;39(11):6772-6778.
14. The Report of AAPM Task Group 220. Use of water equivalent diameter for calculating patient size and size-specific dose estimates
15. (SSDE) in CT. 2014. https://www.aapm.org/pubs/reports/RPT_220.pdf.

Size specific dose estimate (SSDE) for estimating CT doses in SPECT/CT and PET/CT examinations

Mayomthong P, Khiewvan B, Thongpraparn T, Mali P, Chaudakshetrin P, Sritongkul N, Tuntawiroon M.

Section of Nuclear Medicine, Department of Radiology, Faculty of medicine Siriraj Hospital, Mahidol University, Bangkok 10700, Thailand

Abstract

Introduction: $CTDI_{vol}$ and DLP are frequently used parameters for estimation of patient's absorbed dose from CT examination. Until recently, the SSDE, which takes into account the patient size in terms of effective diameter and the output of the CT scanner in terms of $CTDI_{vol}$ has been proposed by the AAPM 204. The objective of the study was to find out if there is a relationship between patient size and the parameters, SSDE and $CTDI_{vol}$.

Material and methods: CT data from 16 children and 109 adult patients performing PET/CT oncology; SPECT/CT myocardial perfusion, bone, parathyroid, and infection/inflammation were retrospectively collected for 3 months. Effective diameter of each patient was calculated as geometric mean of the anterior-posterior (AP) and lateral dimensions measured on axial CT images. Conversion factors corresponding to effective diameters were obtained from AAPM report 204 and the radiation dose were converted to SSDE. Linear regression model was used to evaluate the relationship between patient size and the parameters SSDE and $CTDI_{vol}$.

Results: The study shows that SSDE was larger than the $CTDI_{vol}$ in all patients. A positive correlation between SSDE and $CTDI_{vol}$ was observed (r = 0.9730). Patients with small body size have higher SSDE as demonstrated by the higher SSDE/$CTDI_{vol}$ ratio, more than 1.8-fold for children and lower than 1.8 for adult patients. Calculated ED based on DLP and SSDE values were found to present no correlation.

Conclusion: $CTDI_{vol}$ is an important indicator for calculating the SSDE. SSDE vary with patient size. When there was no available organ dose to calculate an ED by SSDE/ICRP method, SSDE is a better estimate of average patient dose from CT than $CTDI_{vol}$ because the dose not only depends on output dose but also on the patient's characteristics. However, SSDE cannot be used to compute ED using *k-factors* for risk estimation as in DLP method.

Keywords: Size specific dose estimate (SSDE), Volume CT dose index ($CTDI_{vol}$), CT dose in nuclear medicine

1. INTRODUCTION

Hybrid SPECT/CT and PET/CT examinations improve diagnostic accuracy by allowing better localization, detection, and monitoring of many disease mechanisms compared to SPECT, PET, or CT alone (1, 2).

Various parameters were used for estimating patient dose from CT, the commonly used parameters being volumetric CT dose index ($CTDI_{vol}$) and dose length product (DLP). $CTDI_{vol}$ is used to compare the dose delivered by various scanners or various protocols, which represents the average dose within the scan volume for a standard phantom (3). The dose obtains from $CTDI_{vol}$ and DLP, only depends on scanner radiation output, therefore, dose estimation in patients of different body sizes may make the values not represent the actual patient radiation dose. Until recently, size-specific dose estimates (SSDE) has been proposed by the American Association of Physicists in Medicine (AAPM) in an effort to adapt $CTDI_{vol}$ to patients' cross-sectional size in the body region being imaged (4-6). This study aims to determine if there is any relationship among the parameters, SSDE, $CTDI_{vol}$ and patient size.

2. MATERIAL AND METHODS

CT data were collected on patients diagnosed with SPECT/CT and PET/CT during 3 months from August 2019 to October 2019 at the Department of Nuclear Medicine Siriraj Hospital. They were 16 children and 109 adults. Most common SPECT/CT and PET/CT examinations were analyzed (Table 1). The collected data were gender, age, weight, $CTDI_{vol}$, DLP, and effective diameter. The effective diameter of each patient was calculated as geometric mean of the anterior-posterior (AP) and lateral (LAT) dimensions measured on axial CT images.

2.1 Size specific dose estimate (SSDE)

The calculation of SSDE was based on the effective diameter obtained from the AP and LAT dimension of the cross-section in the central slides of the examined

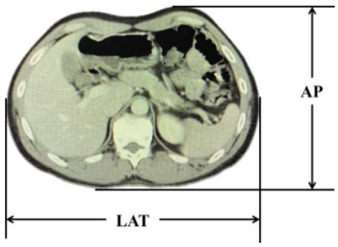

Figure 1: *The anterior-posterior (AP) and lateral (LAT) dimensions on axial CT images.*

Table 1 *Most common SPECT/CT and PET/CT examinations underwent between August 2019 to October 2019*

	Most common SPECT/CT and PET/CT examinations	Radiopharmaceutical	No. of Patients
Children	Infection/inflammation scan	^{67}Ga-Citrate	9
	Oncology scan	^{131}I-MIBG	7
Adult	Myocardial perfusion scan	^{99m}Tc-MIBI (rest & stress)	23
	Bone scan	^{99m}Tc-MDP	20
	Parathyroid scan	^{99m}Tc-Pertechnetate & ^{99m}Tc-MIBI	16
	Infection/inflammation scan	^{67}Ga-Citrate	11
	Oncology scan	^{131}I-MIBG	3
	Gate Blood pool	^{99m}Tc-RBC	2
	Oncology scan	^{18}F-FDG	41

part (Figure 1). AAPM conversion factors based on effective diameter for $CTDI_{vol}32$ (7). The following formula was used to calculate effective diameter:

$$\text{Effective diameter} = \sqrt{\text{AP} \times \text{LAT}}$$

SSDE was calculated for each patient as the product of conversion factor and $CTDI_{vol}32$.

2.2 Effective dose (ED)

ED was estimated from DLP method based on the National Radiological Protection Board (NRPB). Effective dose was calculated using the following formula:

$$\text{ED} = k - factors \times \text{DLP}$$

2.3 Data analysis

Spearman correlation was used for determining the correlation between SSDE, $CTDI_{vol}$ and effective diameter. A P-value less than 0.05 were considered significant.

3. RESULTS

Children patients' weight range was 9 - 52 kg and an average effective diameter was 18.35 ± 4.05 cm. Adult patients' weight range was 55-85 kg and an average effective diameter was 24.34 ± 3.08 cm. The relationship between average body weight and effective diameter for each type of nuclear medicine examination presents a strong positive correlation between the two (r = 0.9688), so can be describing the patient size in terms of weight (Figure 2).

SSDE values are calculated using $CTDI_{vol}$ and patient size. SSDE decreases as the patient size increases. The relationship between SSDE and weight presents a moderate negative correlation (r = - 0.4028). The resulting shows in Figure 3.

This study shows that SSDE is larger than the $CTDI_{vol}$ in all patients, which is confirmed by using a linear regression test between the SSDE and the $CTDI_{vol}$. A strong positive correlation is observed (r = 0.9730). The resulting shows in Figure 4.

Small size patients have higher SSDE as demonstrated by higher $SSDE/CTDI_{vol}$ ratio, more than 1.8-fold for children and lower than 1.8 for adult patients. This can see from a linear regression test between the $SSDE/CTDI_{vol}$ ratio and the weight presents a strong negative correlation (r = - 0.9588) (Figure 5).

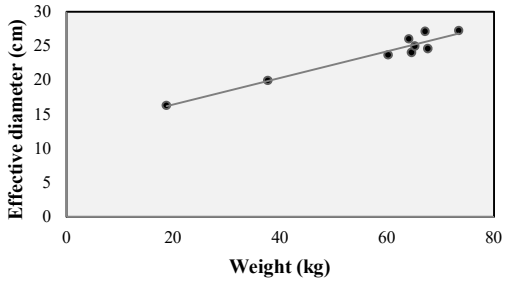

Figure 2: *Linear regression between the average effective diameter and the average weight. A strong positive correlation is observed (Pearson correlation, r = 0.9688; P < 0.0005).*

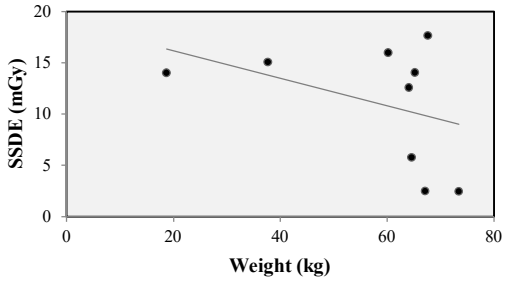

Figure 3: *Linear regression between the average SSDE and the average weight. A moderate negative correlation is observed (Pearson correlation, r = - 0.4028; P = 0.1).*

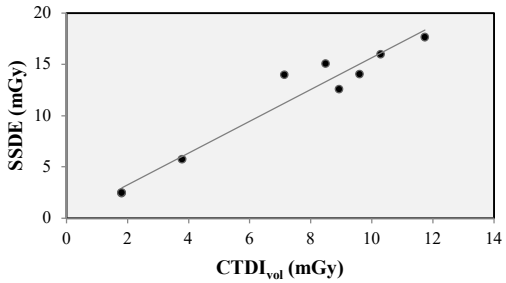

Figure 4: *Linear regression between the average SSDE and the average $CTDI_{vol}$. A strong positive correlation is observed (Pearson correlation, r = 0.9730; P < 0.0005).*

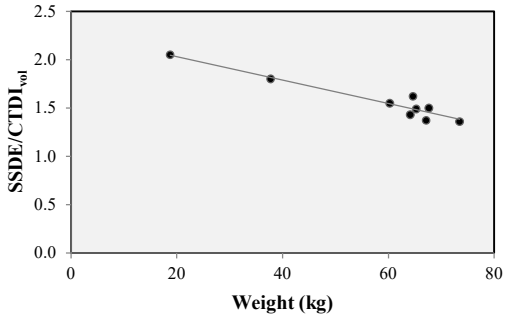

Figure 5: *Linear regression between the average SSDE/CTDI$_{vol}$ ratio and the average weight. A strong negative correlation is observed (Pearson correlation, r = - 0.9588; P < 0.0005).*

The ED from CT is calculated using a DLP method. DLP values are not based on patient size, but that are calculated based on CT scan length. As a result, no linear correlation is seen between the DLP and patient body weight (r = - 0.0960) and no linear correlation is seen between the ED and patient body weight (r = - 0.2328).

4. DISCUSSION

CTDI$_{vol}$ is commonly used to estimate the patient dose obtained by processing the scanner and displaying on the CT console. CTDI$_{vol}$ reported is based on a standard phantom. The dose is not representative of all patients, because the actual size of each patient is different. Therefore, SSDE is a better estimate of average patient dose than CTDI$_{vol}$ because SSDE is a correction of the CTDI$_{vol}$ to relate the patient size using an axial CT image (Figure 4).

A reference body size is a person weighing approximately 70 kg (8). In this study, adult patients have an average weight of 65.40 kg, which are not much different from the reference body size. For children patients have an average weight of 27.50 kg, which are significantly different from the reference body size, resulting in a difference in SSDE and CTDI$_{vol}$ values. The ratio of SSDE/CTDI$_{vol}$ is more than 1.8 fold for children and lower than 1.8 for adult (Figure 5). It is suggested that SSDE value is better estimate of the patient dose of patient with size differs from the reference body size.

Although SSDE is a value that takes the patient size into account, a linear regression test between SSDE and weight presents only a moderate negative correlation. This could result from less variation in patient's weight.

DLP is a value independent of body size but depends on CT scan length, so DLP has no correlation to patient size. The ED is calculated using by DLP values, therefore, there is no correlation between ED and patient size as well.

ED is a measure of radiological safety, which can be calculated in several ways. The calculation from SSDE can be performed by SSDE/ICRP method if the organ dose is measured using MOSFET dosimeters in anthropomorphic phantoms (9). But in this study, the organ dose was not studied. Therefore, the ED can be calculated from the DLP method by using the *k-factors*; the coefficient of the body regions for CT scans. The average ED of children and adult patients were 7.59 ± 3.10 and 6.96 ± 7.01 mSv respectively.

5. CONCLUSION

To calculate the dose in the patient whose size was significantly different from reference body size, SSDE value should be used. The SSDE vary with patient size, which is a better estimate of average patient dose from CT than CTDI$_{vol}$ because the dose not only depends on output dose but also on the patient's characteristics. However, CTDI$_{vol}$ is an important indicator for calculating SSDE.

ED does not take into account patient body size. SSDE cannot be used to compute ED using *k-factors* for risk estimation as in DLP method.

ACKNOWLEDGEMENTS

The authors would like to thank doctors, radiologists, physicists, and staff members at the Department of Nuclear Medicine Siriraj Hospital, Mahidol University for their sincere cooperation.

REFERENCES

1. Mattsson, S., Andersson, M., Sderberg, M. Technological advances in hybrid imaging and impaction dose. *Radiation Protection Dosimetry.* 165(1-4), (2015): 410–415.
2. Montes, C., Tamayo, P., Hernandez, J., Gomez-Caminero, F., Garcia, S., Martin, C., Rosero, A. Estimation of the total effective dose from low-dose CT scans and radiopharmaceutical administrations delivered to patients undergoing SPECT/CT explorations. *Ann Nucl Med.* 27, (2013): 610–617.
3. AAPM Report 96. The Measurement, Reporting, and Management of Radiation Dose in CT, American Association of Physicists in Medicine, (2008).
4. Abdollahi, H., Shiri, I., Salimi, Y., Sarebani, M., Mehdini, R., Deevband, M. R., Mahdavi, S. R., Sohrabi, A., Bitarafan-Rajabi, A. Radiation dose in cardiac SPECT/CT: An estimation of SSDE and effective dose. *European Journal of Radiology.* 85, (2016): 2257–2261.
5. Anam, C., Haryanto, F., Widita, R., Arif, I., Dougherty, G. A fully automated calculation of size-specific dose estimates (SSDE) in thoracic and head CT examinations. *Journal of Physics: Conference Series.* 694, (2016). doi:10.1088/1742-6596/694/1/012030.
6. Choudhary, N., Rana, B. S., Shukla, A., Oinam, A. S., Singh, N. P., Kumar, S. Patients dose estimation in CT examinations using size specific dose estimates. *Radiation Protection Dosimetry.* 184(2), (2019): 256–262.

7. AAPM Report 204. Size-Specific Dose Estimates (SSDE) in Pediatric and Adult Body CT Examinations, American Association of Physicists in Medicine, (2011).
8. Rizzo,S., Kalra, M., Schmidt, B., Dalal, T., Suess, C., Flohr, T., Blake, M., Saini, S. Comparison of Angular and Combined Automatic Tube Current Modulation Techniques with Constant Tube Current CT of the Abdomen and Pelvis. *AJR.* 186, (2006): 673–679.
9. Moore, B. M., Brady, S. L., Mirro, A. E., Kaufman, R. A. Size-specific dose estimate (SSDE) provides a simple method to calculate organ dose for pediatric CT examinations. *Med. Phys.* 41(7), (2014): 071917 1-9.

Single-scan method for the inner ear in cone-beam computed tomography

Yuki HAYAKAWA, Mitsuharu OOSAWA, Ryousuke SANO, Masaru NAKAMURA

Department of Radiology, Aichi Medical University Hospital

Abstract

Purpose: We examined the utility of the single-scan method using the zoom reconstruction function compared to the double-scan method for the inner ear in cone-beam computed tomography (CBCT).

Methods: The wire phantom was scanned at the evaluation points on the XY axes, from the isocenter of the CBCT toward the edge of the FOV, and spatial resolution for the physical evaluation was measured as a 10% modulation transfer function (MTF). Visual evaluation of head phantom images for the single-scan method compared to that for the double-scan method was conducted by nine otolaryngologists. Radiation exposure dose to the lens in the eye was measured by the optically stimulated luminescence (OSL) dosimeters attached to the orbits of the head phantom.

Results: In the single-scan method, the 10% MTF decreased by 5% at the evaluation point equivalent to the cochlea, and by19% at that to external ear canal, as compared to the double-scan method. But the results of the visual evaluation were equivalent. Further, the single-scan method decreased the exposure dose of the lens by 20%.

Conclusion: These results suggest the single-scan method using the zoom reconstruction function for the inner ear imaging in CBCT can be a very useful technique.

Keywords: inner ear, CBCT, scan method

1. INTRODUCTION

The number of examinations using radiation is rising due to an increase radiodiagnosis equipment. Therefore, all medical workers who handle radiation must optimize the patient's radiation exposure dose [1]. Since the temporal bone has a fine and complicated anatomical structure, such as the cochlea and ossicles, radiodiagnosis plays an important role in the diagnosings of middle ear and inner ear diseases [2]. Cone-beam computed tomography (CBCT) is one of the radiodiagnosis methods used for the temporal bone. The CBCT uses cone-shaped X-rays and Flat panels to limit the scan area to the temporal bone, enabling acquisition of high-resolution images and device miniaturization.

3D Accuitomo-F17 (Morita, Kyoto, Japan) is a CBCT device developed for the diagnosis of dental and otolaryngology. This device is equipped with a wide field of view (FOV) scan mode and zoom reconstruction function. This function is a technology that can acquire detailed information on the local area by determining the voxel size and region of interest (ROI) after the scan. Conventionally, the inner ear imaging in CBCT involves the double-scan method, where the left and right inner ears are separately imaged due to limitations in FOV [3]. However, 3D Accuitomo-F17 has made a single-scan method possible. The single-scan method scans both inner ears simultaneously, followed by zoom reconstruction of the left and right inner ears separately (Fig.1). This method involves fewer scans, which is expected to decrease exposure dose of the lens. However, there have been no reports evaluating the image quality of the inner ear by the single-scan method.

Therefore, we examined the utility of the single-scan method using the zoom reconstruction function compared to the double-scan method for the inner ear in CBCT.

2. MATERIAL AND METHODS

The evaluation items were physical evaluation, visual evaluation, and radiation exposure dose to the lens in the eye.

2.1 Physical evaluation

2. 1. 1 Evaluation of spatial resolution

Spatial resolution was evaluated using a self-made wire phantom consisting of a 0.2 mm copper wire in the center of a water-filled syringe 50 mm in diameter. In the double-scan method, the scan parameters were 90 kV, 7 mA, 100 mm in FOV, and 17.5 sec in scan time; in the single-scan method, 90 kV, 10 mA, FOV 170 mm, and 17.5sec in scan time. In the double-scan method, the reconstruction parameters were 0.50 mm in slice thickness and 0.25mm in voxel size; in the single-scan method using zoom reconstruction centered on the wire, 0.40 mm in slice thickness, 0.20 mm in voxel size, and 100 mm in FOV. The wire phantom was scanned at the evaluation points on the XY axes, from the isocenter of the CBCT toward the edge of the FOV (Fig.2). The evaluation points on the X and Y directions from the isocenter for the double-scan method were ± 5, 15, 25, 35, and 45 mm, and for the single-scan method were ± 5, 15, 25, 35, 45, 55, 65, and 75 mm. Spatial resolution for the physical evaluation was measured as a 10% modulation transfer function (MTF) at each evaluation point, according to the methodology of Ichikawa et al. [4].

2. 1. 2 Evaluation of practical aspects

In the double-scan method, the centers of scan are set at the right and left middle ears, whereas in the single-scan method the center is set at the midline of the skull. Accordingly, in the single-scan method, the center of the zoom reconstruction was off-centered to compare the single-scan method and the double-scan method. The

single-scan method images acquired in 2.1.1 was off-centered by + 33 mm in the X direction using zoom reconstruction, and the reconstruction parameters were 0.40 mm in slice thickness, 0.20 mm in voxel size, and 100 mm in FOV (Fig. 3). For comparison, we used the double-scan method acquired in 2.1.1. Considering the anatomical position of the temporal bone, the cochlea and the external ear canal were defined as the evaluation points of 10% MTF. Evaluation point of the cochlea was -11 mm and that of the external ear canal was + 34 mm in the X direction from the middle ear. The 10% MTF at these coordinates was extrapolated from the measurements acquired in 2.1.1.

2.2 Visual evaluation

Fig. 4 shows images of the head phantom PH-47 41301-200 (Kyoto Kagaku, Co., Ltd., Kyoto, Japan) that were visually evaluated by nine otolaryngologists. The evaluation target was bone structure visibility, and a five-level scoring system, ranging from *excellent*, *very good*, *good, poor*, to *very poor*, was used to compare single-scan and double-scan images. In the double-scan method, the scan parameters were 90 kV, 7 mA, 100 mm in FOV, and 17.5 sec in scan time; in the single-scan method, 90 kV, 10 mA, FOV 170 mm, and 17.5sec in scan time. In the double-scan method, the reconstruction parameters were 0.50 mm in slice thickness and 0.25mm in voxel size; in the single-scan method off-centered in the middle ear (+ 33 mm in the X direction) using zoom reconstruction, 0.40 mm in slice thickness, 0.20 mm in voxel size, and 100 mm in FOV..

2.3 Radiation exposure dose to the lens in the eye

The exposure dose of the lens was measured by the optically stimulated luminescence (OSL) dosimeters nanoDot (Nagase Landauer Ltd., Tsukuba, Japan). The head phantom attached nanoDot to the left and right orbits and was scanned by the single-scan method and double-scan method. The exposure dose was the average of the values taken 5 times. In the double-scan method, the left and right inner ears were scanned once separately, and the scan parameters were 90 kV, 7 mA, 100 mm in FOV, and 17.5 sec in scan time; in the single-scan method, both inner ears were scanned a simultaneously, and the scan parameters were 90 kV, 10 mA, FOV 170 mm, and 17.5sec in scan time.

3. RESULTS

3.1 Evaluation of spatial resolution

Fig.5 shows the 10% MTF of each evaluation point in the both scan methods. In both cases, the 10% MTF was highest at the isocenter and decreased towards the edge of the FOV. The 10% MTF at the outmost edge of the FOV was 18% lower for the double-scan method and 32% lower for the single-scan method than the isocenter. Further, the difference between the 10% MTF at each evaluation point (± 5, 15, 25, 35, 45 mm) for the single-scan and the double-scan methods was 4.5% or less.

3.2 Evaluation of practical aspects

The 10% MTF of the evaluation point equivalent to the cochlea was 1.86 for the double-scan method and 1.76 for the single-scan method. That of the evaluation point equivalent to the external ear canal was 1.73 for the double-scan method and 1.38 for the single-scan method. Therefore, in the single-scan method, the 10% MTF decreased by 5% at the evaluation point equivalent to the cochlea, and by19% at that to external ear canal, as compared to the double-scan method.

3.3 Visual evaluation

Table 1 shows the results of the visual evaluation. The scores were *good* for the median and mode.

3.4 Exposure dose of the lens

The average exposure dose of the left and right lens was 10.5 mGy for the double-scan method and 8.4 mGy for the single-scan method. Therefore, The exposure dose to the lens decreased by about 20% in the single-scan method, compared to the double-scan method.

4. DISCUSSION

CBCT for otolaryngology is used for radiodiagnosis of the inner ear and middle ear. High-resolution images are required to observe fine bone structures, such as the cochlea and ossicles. However, since CBCT is also used for preoperative planning and postoperative follow-up, there is concern that radiation exposure will increase based on scan frequency. As the ICRP 2011 Recommendations have reduced the acceptable exposure dose of the lens, further optimization of the radiation exposure dose will be required in the future.

We examined the utility of the single-scan method using the zoom reconstruction function for the inner ear in CBCT, which is expected to reduce the number of scans and decrease the exposure dose.

For spatial resolution, we observed that the 10% MTF tended to decrease from the isocenter toward the edge of the FOV in both methods. This was similar to a report by Ozaki et al., who evaluated CBCT's spatial resolution [5]. We speculate that the blurring effect increased with increasing distance from the isocenter due to the geometrical configuration, because the CBCT device's X-ray beam was fan-shaped [6]. Since the FOV of the single-scan method is larger than that of the double-scan method, the 10% MTF of the evaluation point farthest from the isocenter for the single-scan method (75mm) has a larger rate of decrease than that of the double-scan method (45mm). However, CBCT using a detector with a flat panel results in images with a pixel size of 0.1- 0.4 mm, so CBCT images have a higher resolution compared to general diagnostic CT images [7, 8]. Therefore, it is considered that the decrease in 10% MTF at the edge of the FOV in the

CBCT images does not have a large effect on radiodiagnosis of the inner ear.

In the single-scan method, the 10% MTF decreased by 5% at the evaluation point equivalent to the cochlea, and by19% at that to external ear canal, as compared to the double-scan method. When either the left or right middle ear was set to the isocenter for the double-scan method, the distances from the isocenter to the cochlea and the external ear canal were 11mm and 34 mm, respectively. When the midline of the skull was set to the isocenter for the single-scan method, the distances from the isocenter to the cochlea and the external ear canal was 22 mm and 67 mm, respectively. In other words, in the CBCT device, which has decreased resolution depending on the distance from the isocenter, the single-scan method (in which the isocenter cannot be proximal to the cochlea and the external ear canal) had inferior spatial resolution compared double-scan method.

However, the visual evaluation of nine observers using images of the head phantom was equivalent in both the median and mode. This suggests that when evaluating visibility of bone structures, as according to Webber's law, those with high pixel values, such as bone, were less likely to be visually affected even if there was a difference in the physical evaluation. Therefore, we speculate that both scan methods were clinically sufficient CBCT images of the inner ear.

In the single-scan method made it possible to decrease the exposure dose of the lens by 20%. Due to the recently increasing use of radiodiagnosis, we believe that this contributes significantly to the optimization of the radiation dose.

The limitation is, if the subject size exceeds the maximum FOV size in single-scan method, both the left and right temporal bones cannot be included in the scan range at once. That is, as it is not always possible to scan for the inner ear by the single-scan method in clinical practice, the single-scan method and the double-scan method should be selected according to subject size.

5. CONCLUSION

We examined the utility of the single-scan method using the zoom reconstruction function compared to the double-scan method for the inner ear imaging in CBCT. In the single scan method, the physical evaluation was not as good as the conventional double scan method, but the results of the visual evaluation were equivalent, and exposure dose can be reduced by 20%. These results suggest the single-scan method using the zoom reconstruction function can be a very useful technique.

ACKNOWLEDGEMENTS

We are grateful to Dr. Uchida (the Department of Otorhinolaryngology, Aichi Medical University Hospital) for helpful discussions and Ms. Yukiko Kuru (Aichi Medical University) for language support. Additionally, we thank you to the Department of Radiology (Aichi Medical University Hospital).

REFERENCES

1. Tsapaki V: Radiation dose optimization in diagnostic and interventional radiology: Current issues and future perspectives. Physica Medica, 79:16-21, 2020
2. Hiroshi Ogawa, et al: Clinical Evaluation of Multislice CT Scan for the Temporal Bone. Otol Jpn, 11(2): 121-126, 2001
3. Shingo Murakami, et al: Imaging of Middle Ear Disease -State of the Art-. Otol Jpn, 12(2): 86-90, 2002
4. Katsuhiro Ichikawa, et al: Method of Measuring Modulation Transfer Function Using Metal Wire in Computed Tomography. Japanese Journal of Radiological Technology, 64(6): 672-680, 2016.
5. Ozaki Yoshihiro, et al: Location dependency of the spatial resolution of cone beam computed tomography for dental use. Oral Surgery, Oral Medicine, Oral Pathology and Oral Radiology, 116(5): 648-655, 2013
6. Hara Takanori, et al: Image quality dependence on in-plane positions and directions for MDCT images. European journal of radiology, 75(1): 114-121, 2010
7. Güldner C., et al: Potential of dosage reduction in cone-beam-computed tomography (CBCT) for radiological diagnostics of the paranasal sinuses. European Archives of Oto-Rhino-Laryngology, 270(4): 307-1315, 2013
8. Watanabe Hiroshi, et al: A comparative study for spatial resolution and subjective image characteristics of a multi-slice CT and a cone-beam CT for dental use. European journal of radiology, 77(3): 397-402, 2011

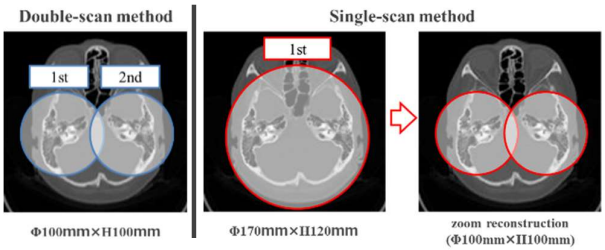

a|b

Figure 1. a) Double-scan method, b) Single-scan method

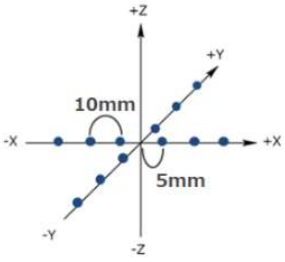

Figure 2. Evaluation points in the XY axes

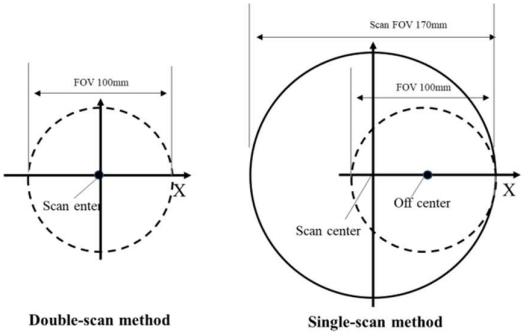

Figure 3. Schema of zoom reconstruction in single-scan method

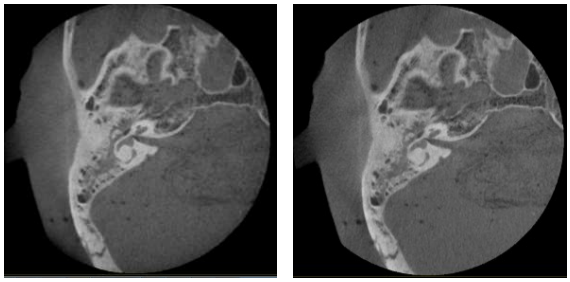

a|b

Figure 4. Visual evaluation images a) Double-scan method (reference image), b) Single-scan method

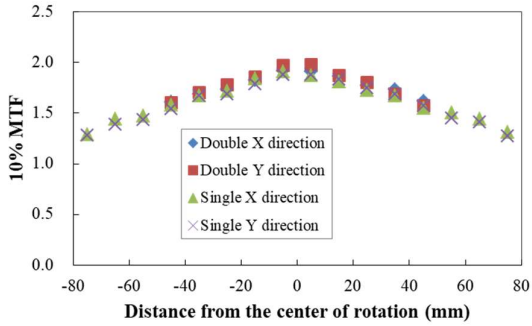

Figure 5. 10% MTF in the XY axes

Table 1 Visual evaluation results

Evaluator Score									Mode	Median
A	B	C	D	E	F	G	H	I		
3	4	2	5	3	4	2	3	4	3	3

5:excellent, 4:very good, 3:good, 2:poor, 1:very poor

Comparison simulation treatment between Gamma Knife and Linac Stereoradiosugery on small target volume by using GEANT 4 Monte Carlo simulation

Mohammad Shazmi bin Sapeei[1], Nik Noor Ashikin Nik Ab Razak[1], Nurul Ab. Aziz Hashikin[1], Muhammad Rizal Fahmi[1]

1 School of Physics, Universiti Sains Malaysia, Pulau Pinang, 11800, MALAYSIA

Abstract

Introduction: Stereotactic radiosurgery (SRS) is a radiation therapy technique that delivers an accurate and efficient high radiation dose to smaller diameter of target tumor in single fraction [1]. These studies were simulating stereotactic radiosurgery (SRS) techniques real treatment setup by using Linac-based SRS and Gamma Knife.

Purpose: To compare the absorbed dose of tumor and organ at risk (OAR) by simulating IMRT, SRS VMAT coplanar [2], SRS VMAT with non-coplanar [2,3] and Gamma Knife [4] technique to treat 18 mm diameter of parasellar meningiomas using GEANT 4 Application.

Methods These simulations were using GEANT 4 Montecarlo simulation with MIRD5 human phantom (readily available in GEANT 4 Monte Carlo package) with additional active volume for OARs (brain, brain stem, optic chiasm, optic nerve, eyeball, lens, parotid gland and upper spine). The beam placement arrangement for Linac-based SRS and Gamma Knife were stimulate to treat 18 mm diameter tumor with a total of 24 Gy prescribed dose [1]. Additionally, the effect of 6 MV and 18 MV photon of Linac-based SRS for IMRT-8 fields, SRS VMAT with coplanar, SRS VMAT with non-coplanar were measured.

Results: The dose falloff of SRS VMAT non-coplanar techniques [5] using 18 MV photon was sharper than Gamma Knife, SRS VMAT coplanar and IMRT technique. Other than that, IMRT technique shows higher absorbed dose to cochlear and optic chiasm as compared to other therapy simulation techniques.

Conclusions: The comparison between all the techniques shows SRS VMAT with non-coplanar technique using 18 MV photon is the most efficient technique to treat small brain tumor near the OARs.

Keywords: GEANT 4, Gamma Knife, Stereotactic radiosurgery (SRS), Monte Carlo simulation

1. INTRODUCTION

Stereotactic radiosurgery (SRS) uses multiple, convergent beams of high energy X-rays, gamma rays, or protons beam, delivered to a discrete, radiographically-defined treatment volume [6]. The delivery of radiation is highly conformal. By using multiple, intersecting beams of radiation, the treatment volume receives a high, therapeutic prescription dose, while surrounding normal brain tissue receives a relatively low dose.

Radiation therapy aims to destroy abnormal tissue, notably tumor cells, with minimal damage to surrounding normal tissue. Stereotactic radiosurgery has played a central role in the treatment of parasellar meningioma. The complex anatomy of base of skull, tumor adherence to bony structures and the close proximity to sensitive organs at risk (OAR) has been the major problem in treating the c [7]. Thus, SRS is the best method to deliver the radiation beam due to rapid dose falls off allows for sparing of normal tissues and critical structures with minimal radiation-associated adverse effects [5]. However, there have many techniques in Linac-based SRS treatment with different advantages and disadvantages in term of sparring healthy tissue near organ at risk. Therefore, in these studies we want to compare the parasellar meningioma treatment technique between IMRT, VMAT with non-coplanar and VMAT with coplanar techniques.

Gamma Knife (GK) radiosurgery uses multiple Cobalt-60 sources arranged hemispherically around a single isocentre to treat tumors from at least 192 angles simultaneously and deliver highly conformal dose distributions. Stereotaxis is achieved with a fixed alignment of the patient to a physical coordinate system via a specialized stereotactic head frame. In contrast, linear accelerator (LINAC)-based radiosurgery was developed as an alternative to GK SRS in the 1980s, using a standard LINAC modified for stereotactic purposes [8]. This technique uses a collimated X-ray beam focused on an intracranial target, around which the LINAC gantry and couch can rotate to produce multiple noncoplanar intersecting arcs of radiation [9]. Following improvements in these modifications and treatment planning systems, LINAC-based SRS was marketed as having acceptably similar precision, accuracy, and mechanical stability [10]. From this study we can determine the effectiveness between both modalities in treating the small diameter of brain tumor and effective in sparring the healthy tissue by using GEANT 4 Monte Carlo simulation.

2. MATERIAL AND METHODS

2.1 MIRD-5 adult human phantom

The study was performed using Geant4 version 10.0.0.p03 by utilising the 'human phantom' advanced example. The example consists of a mathematical adult

male phantom based on the Medical Internal Radiation Dose (MIRD) Pamphlet 5, as shown in Figure 1.

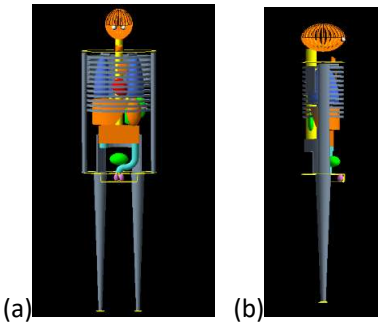

Figure 1: The MIRD-5 adult human phantom (a) frontal and (b) lateral view

2.2 Organ at risks (OARs)

The simulation of additional organ at risk such as eye ball, eye lens, optic chiasm, brain stem, cochlear, parotid gland and upper spine as shown in Figure 2 was created based on reference measurement for an adult organ. The simulation of parasellar meningioma was created using sphere shape at diameter 18mm and located at central base of skull [9].

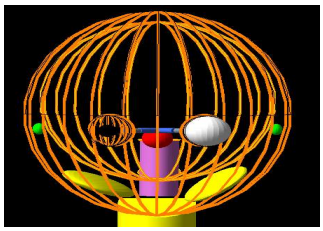

Figure 2: The MIRD-5 adult human head phantom with additional organ at risk (OAR)

2.3 Gamma Knife helmet

Based on the simulation, the helmet was made of semi spherical shape (3 cm thickness of lead) with 192 circular holes that can allow the gamma beam radiation can be centralize to the brain tumor. This helmet consists of 6 level of holes (total of 192 holes) that arranged hemispherically around a single isocentre as shown in Figure 3.

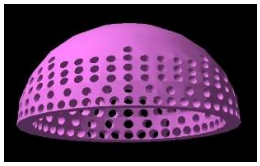

Figure 1: Gamma Knife helmet with 192 holes.

2.4 Beam geometry of SRS Intensity Modulated Radiotherapy (IMRT)

Figure 4 (a) and (b) shows the simulated IMRT planning with 8 different beam angles (0°, 45°, 90°, 135°, 180°, 225°, 270° and 315° angles). The field size diameter used was 18 mm which is the same as the tumor diameter size. The photon beam weighting for each of the beam was chosen as 1.

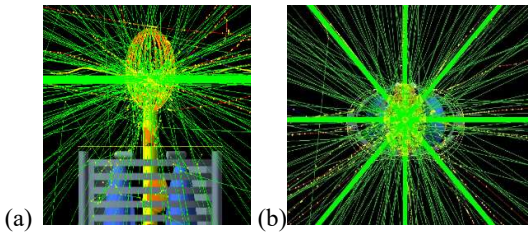

Figure 4: The IMRT beam planning (a) Anterior view (b) Superior view

2.5 Beam geometry of SRS (VMAT) with coplanar technique

Volumetric modulated arc therapy (VMAT) with coplanar technique is radiation therapy technique that delivers the radiation dose continuously as the treatment machine rotates in one plane. The beam simulation was delivered in 5° gap for each of angle, from 0° until 360° degree in one plane (Figure 5).

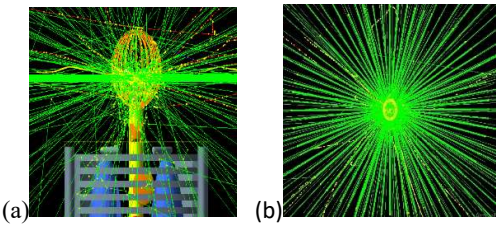

Figure 5: The VMAT with coplanar beam planning (a) Anterior view (b) Superior view

2.6 Beam geometry of SRS Volumetric Modulated Arc Therapy (VMAT) with Non-Coplanar technique.

Volumetric Modulated Arc Therapy (VMAT) is a radiation therapy technique that delivers the radiation dose continuously as the treatment machine rotates in 3 full plane rotation. This VMAT simulation was using the non-coplanar technique with 3 different planes (at 0° no movement of couch, 45° the couch move to the right and -45° the couch move to the left) as shown at Figure 6 (a).

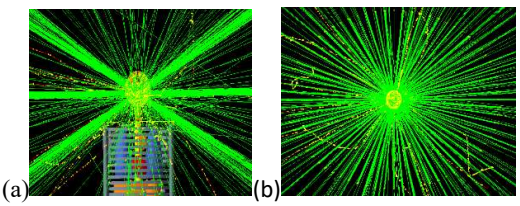

Figure 6: The VMAT with non coplanar beam planning (a) Anterior view (b) Superior view

2.7 Beam geometry of Gamma Knife

Stereotactic Gamma Knife was simulated from 192 Cobalt-60 sources that are focused to the centre of collimator helmet to deliver high dose of radiation with minimal irradiation of proximal structures. For each Cobalt-60 source, energy spectrum has been simulated from GEANT 4. The Gamma Knife utilizes a fixed arrangement of 192 isocentrically arranged non-opposed beams. In these simulations, it requires 6 level of circular beam where a total amount of 192 holes was created on lead helmet and Cobalt-60 source was planned to be focused on the target tumor at SAD 40 cm[11].

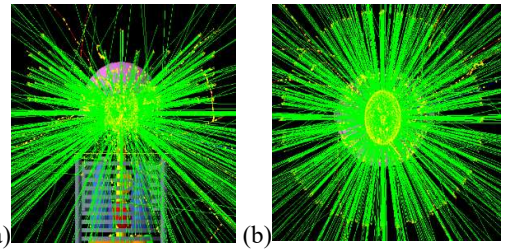

(a) (b)

Figure 7: The Gamma Knife simulation with 192 Cobalt-60 showing the beam targeted to the tumor volume.

3. *RESULTS*

The obtained results were tabulated in Table 1 and Table 2.

Table 1: Absorbed dose for tumor and organ at risk (OAR) for Linac based SRS using 6 MV photon

Table 2: Absorbed dose for tumor and (OAR) for Linac based SRS using 18 MV photon and Gamma knife

4. *DICUSSION*

The simulation was programmed to irradiate prescribed dose of 24 Gy to the tumor volume. The measured absorbed dose was then compared to QUANTEC guideline to make sure that the dose been received by the organ at risk are within the tolerance value. Table 1 shows that the SRS VMAT with Non-Coplanar techniques using 6 MV photon provide a good technique for sparing effect to OARs. This is due to the beam arrangement of this technique (Figure 6 (b)) allowed the multiple beam to be pointed at the target tumor and the beam intensity was equally distributed at three different plane of arc rotation.

Organ	Dose (Gy)		
	6 MV photon beam		
	SRS VMAT C	SRS VMAT NC	IMRT
Tumor	23.97	24.00	24.00
Brain	0.53	0.54	0.52
Brain Stem	0.39	0.40	0.52
Optic Chiasm	0.96	1.04	2.16
Lt Parotid	0.01	0.20	0.01
Lt Cochlear	0.90	0.34	3.39
Lt Eye	0.46	0.31	0.02
Lt Lens	0.55	0.37	0.02
Lt Optic Nerve	0.82	0.92	0.28
Rt Parotid	0.01	0.17	0.01
Rt Cochlear	0.90	0.34	3.38
Rt Eye	0.46	0.31	0.02
Rt Lens	0.54	0.37	0.02
Rt Optic Nerve	0.81	0.91	0.28
Upper spine	0.00	0.00	0.00

Organ	Dose (Gy)			
	18 MV photon beam			Gamma Knife
	SRS VMAT C	SRS VMAT NC	IMRT	
Tumor	24.03	23.99	24.04	23.99
Brain	0.64	0.73	0.63	0.51
Brain Stem	0.59	0.01	0.72	0.49
Optic Chiasm	1.09	0.10	2.27	0.60
Lt Parotid	0.02	0.00	0.02	0.10
Lt Cochlear	0.84	0.10	2.71	0.90
Lt Eye	0.49	0.18	0.05	0.30
Lt Lens	0.56	0.22	0.05	0.25
Lt Optic Nerve	0.76	0.09	0.36	0.45
Rt Parotid	0.02	0.00	0.02	0.11
Rt Cochlear	0.84	0.10	2.70	0.90
Rt Eye	0.49	0.18	0.05	0.30
Rt Lens	0.57	0.22	0.05	0.20
Rt Optic Nerve	0.76	0.09	0.37	0.51
Upper spine	0.00	0.00	0.00	0.02

Table 2 shows that SRS VMAT with Non-Coplanar technique using 18 MV measures the best performance in preserving the healthy tissue as the dose to OARs showed the lowest. As stated by (Chen, 2005)[12] the radiation energy is focused so that the treatment volume receives a high, therapeutic prescription dose while surrounding normal tissue is given a relatively low dose.

For IMRT technique, both of the energy (6 MV and 18 MV) show highest absorbed dose to left cochlear, right cochlear and optic chiasm due to high intensity of radiation received by the OAR. However, when the enry of photon beam is increased to 10 MV, the dose of right cochlear was reduced to 20.24 % and the dose to left cochlear was reduced to 19.80 %. The reduction of dose to certain OARs can be achieved by increasing the energy treatment.

From the comparison between Gamma Knife technique and Linac-based SRS, there is no significant different of absorbed dose to OARs between both tehniques. Other than that, Gamma Knife is better than IMRT technique because of ability Gamma Knife to irradiate a lower dose than IMRT to critical organs such as right cochlear, left cochlear and optic chiasm. As a conclusion, Gamma Knife, SRS VMAT Coplanar, SRS VMAT Non coplanar is good techniques in order to treat small tumor volume that close to OARs.

5. CONCLUSION

From the overall comparison between all of the techniques, the SRS VMAT with non-Coplanar technique using 18 MV photon is the most efficient technique for treating brain tumor near the OARs. Additionally, the dose falloff of SRS VMAT non-coplanar techniques using 18 MV photon was sharper than SRS VMAT Coplanar, IMRT and Gamma Knife technique. It is proven that the SRS VMAT Non Coplanar technique measure a better sparing effect to all OARs. For the IMRT technique, higher absorbed dose were measured at right cochlear, left cochlear and optic chiasm when compared to other techniques.

REFERENCES

1. Shaw, E., Scott, C., Souhami, L., Dinapoli, R., Kline, R., Loeffler, J., & Farnan, N. (2000). Single dose radiosurgical treatment of recurrent previously irradiated primary brain tumors and brain metastases: Final report of RTOG protocol 90- 05. *International Journal of Radiation Oncology Biology Physics*, *47*(2), 291–298.
2. Zhang, S., Yang, R., Shi, C., Li, J., Zhuang, H., Tian, S., & Wang, J. (2019). Noncoplanar VMAT for Brain Metastases: A Plan Quality and Delivery Efficiency Comparison With Coplanar VMAT, IMRT, and CyberKnife. *Technology in Cancer Research & Treatment*.
3. Smyth, G., Evans, P. M., Bamber, J. C., & Bedford, J. L. (2019). Recent developments in non-coplanar radiotherapy. In *British Journal of Radiology*.
4. Stieber, V. W., Bourland, J. D., Tomé, W. A., & Mehta, M. P. (2003). Gentlemen (and ladies), choose your weapons: Gamma Knife vs. linear accelerator radiosurgery. *Technology in Cancer Research and Treatment*, *2*(2), 79–85.
5. Sharma, S. D., Kumar, S., Dagaonkar, S. S., Bisht, G., Dayanand, S., Devi, R., Deshpande, S. S., Chaudhary, S., Bhatt, B. C., & Kannan, S. (2007). Dosimetric comparison of linear accelerator-based stereotactic radiosurgery systems. *Journal of Medical Physics*.
6. Baschnagel, A., Wolters, P. L., & Camphausen, K. (2008). Neuropsychological testing and biomarkers in the management of brain metastases. In *Radiation Oncology*
7. Combs, S. E., Ganswindt, U., Foote, R. L., Kondziolka, D., & Tonn, J. C. (2012). State-of-the-art treatment alternatives for base of skull meningiomas: Complementing and controversial indications for neurosurgery, stereotactic and robotic based radiosurgery or modern fractionated radiation techniques. In *Radiation Oncology*.
8. Deinsberger, R., & Tidstrand, J. (2005). LINAC Radiosurgery as Single Treatment in Cerebral Metastases. *Journal of Neuro-Oncology, 76*(1), 77-83.
9. Niranjan, A., Maitz, A., Lunsford, A., Gerszten, P., Flickinger, J., Kondziolka, D., & Lunsford, L. (2007). 5. Radiosurgery techniques and current devices. *Progress in Neurological Surgery*.
10. Andrews, D. W., Bednarz, G., Evans, J. J., & Downes, B. (2006). A review of 3 current radiosurgery systems. *Surgical Neurology*.
11. Goetsch, S. J. (2008). Linear Accelerator and Gamma Knife-Based Stereotactic Cranial Radiosurgery: Challenges and Successes of Existing Quality Assurance Guidelines and Paradigms. *International Journal of Radiation Oncology Biology Physics*, *71*(1 SUPPL.), 118–121.
12. Chen, J. (2005). Stereotactic Radiosurgery: Instrumentation and Theoretical Aspects--Part 1. *The Permanente Journal*.

Value of Superb Microvascular Imaging in characterize of nodular type focal fat sparing lesion and actual hepatic nodules in the background of fatty liver

Songpon Srisittimongkon, B.Sc., Surada Vichitpunt, M.D., Siwat Bhumiwat, M.D.,
Pantajaree Hiranrat, B.Sc., Surachate Siripongsakun, M.D.

Sonographer School, Faculty of Health Science Technology, Chulabhorn Royal Academy, Bangkok, Thailand,

Abstract

Fatty liver is a common condition which increases liver parenchyma echogenicity(1), which is often associated with an area of focal fat sparring (FFS) due to inhomogenous fatty deposition. Increase parenchymal background from the fatty liver also alters the echogenic appearance of liver lesions, in which the majority will be relatively hypo-echogenic. (2) Superb microvascular imaging (SMI) is a novel microvascular imaging technique that allows visualization of the lesions' vascular architectures, potentially distinguishing actual nodules from FFS. (3) The study's purpose was to evaluate the value of SMI in characterizing hypoechoic lesion in fatty liver background. This prospective study recruited patients who had fatty liver with hypoechoic nodular lesions, between 0.8-4.0 cm in size, which had definite characterization on CT or MRI. Size, margin, and SMI patterns, of hypoechoic lesions of actual and FFS psuedo-lesions, were evaluated using the t-test and Fischer's exact test. SMI vascular patterns are classified, according to Lee et al.(4) There were 44 patients with fifty-seven hypoechoic lesions, consisting of 22 FFS lesions and 35 actual hepatic nodules, including twenty-two hemangiomas, seven metastases, three focal nodular hyperplasias (FNHs), two regenerating nodules, and two parasitic related abscesses. Actual nodules and FFS pseudo-lesions showed well-defined margin in 34/35(97%) and 8/22 (36%, $p < 0.001$), respectively. Almost all FFS showed non-specific or no signal patterns (19/22, 85%), overlapping with actual nodules (17/35, 57%). Rarely FFS has other patterns, including nodular rim and staining (3/22, 15%). Nodular rim with dot-like and spoke-wheel SMI patterns were found only in hemangiomas and FNHs, respectively. In fatty liver, FFS and actual nodules are overlapped in sonographic appearance. A few patterns of SMI, including nodular-rim with dot-like and spoke-wheel patterns, may suggest a specific type of lesions, including hemangiomas and FNHs.

Keywords: Fatty liver, Hypoechoic, Superb Microvascular Imaging, Ultrasound

1. INTRODUCTION

Ultrasonography (US) is frequently used as the first-line imaging modality for focal liver lesion screening, follow-up, and further evaluation because it is safe, non-invasive, no ionizing radiation, and widely available. (5) In particular, the liver US every six months is recommended as the primary surveillance of hepatocellular carcinoma (HCC) in high-risk populations, such as those with chronic hepatitis B viral infection and liver cirrhosis due to reducing the mortality rate related to HCCs.(6) Therefore, focal liver lesions are frequently found incidentally. However, the characterization for differentiation between each focal liver lesions using US imaging is often difficult.(7) Moreover, in the presence of fatty liver background, focal liver lesions often show different imaging features than those in normal parenchyma, which usually appear as hypoechoic lesions.(2) For example, hemangioma usually presents as hyperechoic in the normal liver parenchyma but appears hypoechoic in the fatty liver, complicating the diagnosis.(8) Fatty pseudo-lesion or focal fatty sparing is a common finding in fatty liver.(8) It usually appears as a geographic configuration, poorly delineated margins, absence of a mass effect on other liver structures, and location in a specific area (e.g., adjacent to the falciform ligament, ligamentum venosum, porta hepatis, and gallbladder fossa).(1) Some atypical focal fatty sparing, such as a well-defined round or oval shape, can make the wrong differential diagnosis, and further investigation is required. On the other hand, some tumors may be misdiagnosis as focal fatty sparing(8) Consequently, the differentiation between FFS and the actual liver lesion in the fatty liver background is essential.

Some previous studies have reported the limitation of using conventional Color Doppler and Power Doppler ultrasound in the differentiation pattern distribution of focal liver lesions because they cannot detect slow microvascular flow.(9) Contrast-enhanced ultrasound (CEUS) has been reported as the imaging modality that can establish the diagnosis, especially for benign liver lesions, due to its capacity to detect microvascular structure in the focal liver lesion.(10) Nevertheless, it required the usage of a contrast agent, which has a higher cost.

Superb microvascular imaging (SMI) is a technology that expands the range of visible blood flow and provides visualization of low microvascular flow without a use of a contrast agent by analyzing clutter motion and uses a new adaptive algorithm to identify and remove tissue motion.(11) Several studies have reported that SMI can improve the diagnostic performance of ultrasound in the differentiation between benign and malignant breast and thyroid masses.(12, 13) Moreover, few studies have

demonstrated the usefulness of SMI in the microvascular evaluation of focal liver lesion (3, 4); however, no study has used SMI for the differentiation of focal fatty sparing from an actual lesion in the fatty liver background to our knowledge. Therefore, the purpose of our study was to evaluate the diagnostic performance of SMI for differentiation between focal fatty sparing and the actual liver lesion in fatty liver background.

2. MATERIAL AND METHODS

2.1 Patient

This prospective study was performed from January 2016 to December 2018 at Chulabhorn Hospital, Bangkok, and Banluang hospital, Nan province, Thailand. The ethical committee approved the study of the Chulabhorn hospital. No 036/2559, and each patient provided informed consent before the examination.

Eighty-five patients with 95 focal liver lesions were included in our study. Among of focal liver lesions patients, 44 patients with 57 focal liver lesions were included in this study based on the following inclusion criteria; 1) the presence of a hypoechoic lesion on the fatty liver background from ultrasound, 2) size of the lesion between 0.8-4.0 cm in maximum diameter, 3) definite diagnosis by contrast-enhanced CT and/or MRI at least 2-year follow-up period with a stable lesion.

Among the 44 patients (23 females and 21 males, mean age 52.9±10.4 years, range 26-60 years), 57 hypoechoic lesions on the fatty liver background were divided into 35 actual lesions (28 benign and seven malignant lesions) and 22 focal fatty sparing. Twenty-eight benign lesions included 21 hemangiomas, three focal nodular hyperplasias (FNH), two benign regenerative nodules, and two inflammatory lesions (e.g., parasite infection) that were diagnoses by typical contrast-enhanced CT or MRI imaging findings. In comparison, the malignant lesions are metastasis lesions diagnosed by typical MRI imaging findings and confirmed by pathology. The MRI confirmed the 22 pseudo-lesions (focal fatty sparing) in 20 patients in 15 lesions, contrast-enhanced CT in 1 lesion, and four lesions with insignificant change at least 2-years follow-up.

2.2 Ultrasound examination

All ultrasound examinations were performed using Aplio500, Toshiba Medical Systems Corporation, Japan, with a curved transducer. The radiologist initially scanned the liver thoroughly with the B-mode US to characterize liver parenchyma and identify the focal liver lesion. When the focal liver lesions were identified, the focal liver lesion's location, size, and margin were recorded. Subsequently, the SMI mode was performed to characterize the SMI pattern of the focal liver lesion. For the SMI patterns, they were classified into eight patterns (figure1) including; (A) nodular rim pattern, (B) nodular rim with a dot-like pattern, (C) spotty dot-like pattern, (D) spoked-wheel pattern, (E) radiating pattern, (F) non-specific vascular pattern, (G) staining pattern, and (H) no signal.(4) The radiologist recorded the SMI pattern for each focal liver lesions.

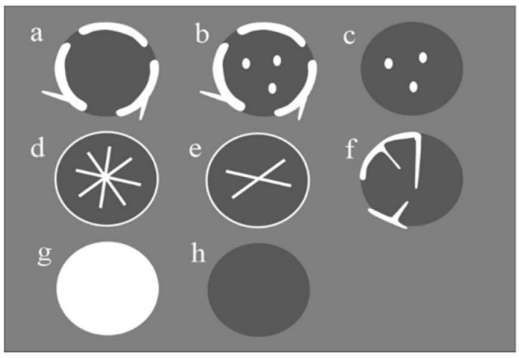

Figure 1: SMI pattern according to Lee et al.(4) : (a) nodular rim pattern, (b) nodular rim with a dot-like pattern, (c) spotty dot-like pattern, (d) spoked-wheel pattern, (e) radiating pattern, (f) non-specific vascular pattern, (g)staining pattern, and (h)no signal.

Criteria for the interpretation of fatty liver included the liver's echogenicity exceeding that of the renal cortex and spleen.(1) Furthermore, according to the bright liver echogenicity score, grading of fatty liver have been done, including; grade 1 fatty liver with increased liver echogenicity, grade 2 fatty liver with the echogenic liver obscuring the echogenic walls of the portal venous branches, and grade 3 fatty liver in which the diaphragmatic outline is obscured.(1)

2.3 Statistical analysis

All qualitative data are reported as the means ± standard deviation. Fisher exact and Chi-squared tests were used to evaluate the differences between the qualitative data. P values < 0.05 indicated a statistically significant difference. The statistical analyses were performed using the statistical software Stata.

3. RESULTS

There were 57 focal liver lesions in 44 patients were included. Demographic data and underlying liver condition of the patients were shown in Table 1.

The average size of the 57 focal liver lesions was 1.5 cm, with a range of 0.8 cm to 3.5 cm. The mean size of focal fatty sparing was 1.3 cm with a range of 1.0-1.6 cm, and a non-specific SMI pattern is the most common presentation (45%, 10/22). Nine of twenty-two (40%, 9/22) FFS were not detected vascularity by SMI mode. Two focal fatty sparing exhibited a nodular rim (10%, 2/22), and the remaining focal fatty sparing exhibited a staining pattern (5%, 1/22).

Table 1 demographic data and underlying liver condition of the patients

	Total (N=44)
Age (years)	52.9±10.4
Gender	
Female	23 (52%)
Male	21 (48%)
Underlying disease	
Hepatitis B	32 (73%)
Unknown	5 (11%)
underlying malignancy	7 (16%)
Underlying fatty liver (bright score)	
grade 0 (normal)	0
grade 1 (mild)	30 (68%)
grade 2 (moderate)	14 (32%)
grade 3 (severe)	0

Among 35 actual lesions (mean size 1.5 cm, ranging from 0.8-3.5 cm), the non-specific lesion was the most common SMI pattern (31%, 11/35) followed by a nodular rim pattern (20%, 7/35). Six actual lesions were not detected signal by SMI mode (17%, 6/35). The remaining lesions show nodular rim with a dot-like pattern (20%, 7/35) and staining pattern (6%, 2/35). The SMI pattern distribution between the pseudo-lesion and the actual liver lesion was not significantly different ($p = 0.306$, $p > 0.05$).

For the actual lesions, we categorized into benign and malignant lesions. There were 35 benign liver lesions, as in table 2.

Table 2. Superb microvascular imaging (SMI) features of the lesions

SMI pattern*	Total	A	B	C	D	E	F	G	H
FFS	22	2 (10%)	0 (0%)	0 (0%)	0 (0%)	0 (0%)	10 (45%)	1 (5%)	9 (40%)
Actual nodules	35	7(20%)	7 (20%)	0 (0%)	2 (6%)	0 (0%)	11 (31%)	2 (6%)	6 (17%)
Benign RN	2	0 (0%)	0 (0%)	0 (0%)	0 (0%)	0 (0%)	0 (0%)	1 (50%)	1 (50%)
FNH	3	1(33%)	0 (0%)	0 (0%)	2 (67%)	0 (0%)	0 (0%)	0 (0%)	0 (0%)
Hemangioma	21	5(24%)	7 (33%)	0 (0%)	0 (0%)	0 (0%)	5 (24%)	1 (5%)	3 (14%)
Inflammation	2	1(50%)	0 (0%)	0 (0%)	0 (0%)	0 (0%)	0 (0%)	0 (0%)	1 (50%)
Metastasis	7	0 (0%)	0 (0%)	0 (0%)	0 (0%)	0 (0%)	6 (86%)	0 (0%)	1 (14%)
Total	57	9 (16%)	7 (8%)	0 (0%)	2 (4%)	0 (0%)	21 (37%)	3 (5%)	15 (26%)

*SMI pattern: (A) nodular rim pattern, (B) nodular rim with a dot-like pattern, (C) spotty dot-like pattern, (D) spoked-wheel pattern, (E) radiating pattern (F) non-specific vascular pattern, (G) staining pattern; (H) no signal pattern, FFS=focal fatty sparing RN = regenerating nodule, FNH = focal nodular hyperplasia,

The mean size of 21 hemangiomas was 1.7 cm, with a range of 0.7-3.5 cm. The most common SMI patterns of hemangioma is a nodular rim with dot-like (33%,7/21,), which were not found in the other lesions (specificity 100%, sensitivity 22%). However, three of the hemangioma were not detected by SMI (14%, 3/21). The SMI pattern of the two inflammation benign lesions was as follows: one was defined as a nodular rim pattern (50%, 1/2), and another was defined as no signal pattern (50%, 1/2). Two benign regenerative nodules (mean size 1.2 cm) were described as no signal pattern and staining pattern. One focal nodular hyperplasia (FNH) (size 1.0 cm) was defined as a spoked-wheel pattern (67%, 2/3), and another was defined as a nodular rim pattern (33%,1/3)

There were seven metastatic lesions with mean size 1.1 cm, and ranging from 0.8-1.4 cm, six lesions were demonstrated as a non-specific pattern (86%, 6/7), and only one lesion could not detect flow (14%, 1/7). The distribution of SMI types between the benign and the malignant lesions was not significantly different ($p = 0.051$).

Regarding the FFS, ill-defined was detected in 14 of 22 lesions (64%), and a well-defined border was detected in 8 of 22 lesions (36%). For the actual lesion, a well-defined lesion was the majority feature (34/35, 97%). Only one lesion (1/35, 3%) exhibited the ill-defined lesion. In conclusion, borders between actual and pseudo-lesion were significantly different ($p < 0.001$).

4. DISCUSSION

According to the difference of vascularity and vascular pattern of the hepatic tumors, the differential diagnosis of hepatic tumors on imaging study has been dependent on the tumor structure and its related vasculature. For ultrasound imaging, the application of color and power Doppler ultrasound has been used to detect vascular signals for many years. Nevertheless, the detection ability of those technologies is insufficient, as only significant vessels could be shown.(9)

SMI examination is an innovative ultrasound Doppler technique that allows visualization of minute vessels with slow velocity without using a contrast agent. Moreover, some studies have reported that the SMI features to aid in diagnosing focal liver tumor. (3, 4) In our study found that the distribution of SMI types between the pseudo-lesion and actual lesion as well as benign and the malignant lesions were not significantly different.

The non-specific pattern was the most common focal fatty sparing (10/22, 45%). It can explain by the aberrant blood supply, including the aberrant artery and vein.(14) Also, hemangioma and malignant lesions found that non-specific pattern was the most common pattern. Consequently, SMI mode could not significantly distinguish focal fatty sparing from a malignant lesion. However, a combination of the other characters, such as the border, helps distinguish. ill-defined was found in focal fatty sparing 64% (14/22), while actual lesions were found only 3% (1/35).

Meanwhile, we found that nodular rim with dot-like SMI patterns was detected in 7 (33%) hemangioma, which is not demonstrated in the other lesions (specificity 100%, sensitivity 22%). Moreover, sensitivity and sensitivity of the nodular rim pattern for hemangioma were 87% and 50%, respectively. These findings correspond to the previous study, which has been reported by Lee et al. 2016.(4) Consequently, these patterns were sufficiently distinctive as to discriminate hemangioma from other lesions. According to Lee et al. 2016 (4), our study also showed that the peripheral nodular enhancement pattern on contrast-enhanced CT or MRI and nodular rim pattern in SMI are not related. In our study, among 11

hemangiomas showing peripheral nodular enhancement on contrast-enhanced CT or MRI, five hemangiomas did not exhibit nodular rim pattern on SMI (5/21, 24%).

Regarding metastasis lesions, the non-specific pattern was the most common in the SMI examination (86%, 6/7), and one lesion could not detect flow (14%, 1/7). In contrast, in contrast-enhanced CT, all metastasis lesions exhibited arterial rim enhancement and hypo-enhancing nodules in venous phases. Consequently, there is a limitation of SMI examination in detecting vascularity and diagnosing of a metastatic lesion. Patients with primary cancer should be considered as further investigation.

There are some limitations to our study. Firstly, the study included a relatively small number of hepatic tumors and FFS. Secondly, most of the hepatic lesions in our study were not pathologically diagnosed, especially FFS, which clinically do not need any pathological confirmation. However, all of the examined exhibited typical imaging features on contrast-enhanced CT or MRI which are imaging gold standard.

To accurately assess the role of SMI examination in evaluating hepatic tumors, further studies with a larger number of lesions may be needed.

5. CONCLUSION

SMI examination can assess the vascularity of focal liver lesions, but the pattern distribution of SMI does not provide reliable to the differentiation between pseudo-lesion and actual lesion and benign and malignant lesions. Also, hemangioma was significantly correlated with nodular rim and nodular rim with dot-like SMI patterns with high sensitivity and specificity

REFERENCES

1. Hamer OW, Aguirre DA, Casola G, Lavine JE, Woenckhaus M, Sirlin CB. Fatty Liver : Imaging Pattern and Pitfalls. Radiographics. 2006;26(6):1637-53.

2. Shan QY, Chen LD, Zhou LY, Wang Z, Liu GJ, Huang Y, et al. Focal Lesions in Fatty Liver: If Quantitative Analysis Facilitates the Differentiation of Atypical Benign from Malignant Lesions. Sci Rep. 2016;6:18640.

3. He MN, Lv K, Jiang YX, Jiang TA. Application of superb microvascular imaging in focal liver lesions. World J Gastroenterol. 2017;23(43):7765-75.

4. Lee DH, Lee JY, Han JK. Superb microvascular imaging technology for ultrasound examinations: Initial experiences for hepatic tumors. Eur J Radiol. 2016;85(11):2090-5.

5. Marrero JA, Ahn J, Reddy RK, Gastroenterology PPCotACo. ACG clinical guideline: the diagnosis and management of focal liver lesions. American Journal of Gastroenterology. 2014;109(9):1328-47.

6. Association E. European Association For The Study Of The L, European Organisation For R, Treatment Of C. EASLEORTC clinical practice guidelines: management of hepatocellular carcinoma. J Hepatol. 2012;56(4):908-43.

7. D'Onofrio M, Crosara S, De Robertis R, Canestrini S, Mucelli RP. Contrast-Enhanced Ultrasound of Focal Liver Lesions. AJR Am J Roentgenol. 2015;205(1):W56-66.

8. Wu S, Tu R, Liu G, Li H, Zhao Y. Characteristics suggestive of focal Fatty sparing from liver malignancy on ultrasound in liver screening. Ultrasound Quarterly. 2014;30(4):276.

9. Gaiani S, Casali A, Serra C, Piscaglia F, Gramantieri L, Volpe L, et al. Assessment of vascular patterns of small liver mass lesions: value and limitation of the different Doppler ultrasound modalities. The American journal of gastroenterology. 2000;95(12):3537-46.

10. Burrowes DP, Medellin A, Harris AC, Milot L, Wilson SR. Contrast-enhanced US Approach to the Diagnosis of Focal Liver Masses. Radiographics. 2017;37(5):1388-400.

11. Naganuma H, Ishida H, Ogawa M, Suzuki K. Visualization of draining vein in focal nodular hyperplasia by superb microvascular imaging: report of two cases. J Med Ultrason (2001). 2017;44(4):323-8.

12. Ahn HS, Lee JB, Seo M, Park SH, Choi BI. Distinguishing benign from malignant thyroid nodules using thyroid ultrasonography: utility of adding superb microvascular imaging and elastography. Radiol Med. 2018;123(4):260-70.

13. Ma Y, Li G, Li J, Ren WD. The Diagnostic Value of Superb Microvascular Imaging (SMI) in Detecting Blood Flow Signals of Breast Lesions: A Preliminary Study Comparing SMI to Color Doppler Flow Imaging. Medicine (Baltimore). 2015;94(36):e1502.

14. Liu L-P, Dong B-W, Yu X-L, Zhang D-K, Li X, LI H. Analysis of Focal Spared Areas In Fatty Liver Using Color Doppler Imaging And Contrast-Enhanced Microvessel Display Sonography. J Ultrasound Med. 2008;27:387-94.

Mitigation of error propagation in tele cobalt treatment

Mary Joan[1], Priya Saini[2], Mukesh Jain[3], Ramesh Sharma[4], Ajay Prajapathi[5], Arun Chougule[6]

1, 2, 3, 4, 5, 6 Department of Radiological Physics, SMS Medical College and Hospitals, Jaipur

Abstract

Radiotherapy is a multilevel process, which requires a working group that consists of Radiation Oncologists, Medical Physicists and Radiotherapy Technologists. Each treatment procedure consists of several steps such as assessment of patient, prescription of treatment dose, imaging and target delineation, treatment planning and treatment delivery. There are many chances for errors whose consequences may be extremely critical. The objective of this work is to analyze the possible scenarios of errors and incidents in radiotherapy tele cobalt treatment procedure, and to introduce methods that could minimize their occurrences.

Keywords: patient safety, quality control, error mitigation, tele cobalt, radiotherapy

1. INTRODUCTION

Radiotherapy plays an important role in the treatment of cancer. The gamma radiation from the Cobalt 60 radioisotope is used for cancer treatment in the form of external beam radiotherapy or teletherapy as early as 1950's. The tele cobalt machines are the primary work horse of radiotherapy cancer treatments in India starting in 1950's till date.

Radiotherapy is a multilevel process, which requires a working group that consists of Radiation Oncologists (RO), Medical Physicists (MP) and Radiotherapy Technologists (RT). Each treatment procedure consists of several steps such as assessment of patient, prescription of treatment dose, imaging and target delineation, treatment planning and treatment delivery. There are many chances for errors whose consequences may be extremely critical (1). The objective of this work is to analyze the possible scenarios of errors and incidents in tele cobalt radiotherapy treatment procedure, and to introduce methods that could minimize their occurrences.

2. MATERIAL AND METHODS

Patients treated over a period of one year in tele cobalt machines were evaluated. Two tele cobalt machines ATC C9 and Bhabhatron II TAW are there at the institute where about 4016 patients enumerated together are treated in a year. All relevant data were recorded. Different steps of the treatment were analyzed systematically to look for possible errors. The treatment prescriptions were thoroughly checked to find any discrepancy. Weekly audits were done to check for any overlooked facts or errors. The RO, MP and RTT were requested to report any kind of discrepancy. 60% of the medical physicists, 11% of the radiation oncologists and 17% of the radiotherapy technologists of the institute are part of the task group to analyze the possible scenarios of error in tele cobalt radiotherapy treatment and their mitigation. The discrepancies and errors were recorded and their in depth analysis was done. All the relevant data was recorded and studied in form of case studies. Similar kind of issues were grouped together and studied as a single case study.

2.1 Identification of errors

A departmental protocol of cross verification is implemented at radiation oncologists, medical physicists and radiotherapy technologist level. Potential errors were identified for various steps of radiotherapy treatment planning and dose delivery. The type of discrepancies identified are incorrect field size on prescription, incorrect depth mentioned on prescription, incorrect dose fractionation, field size changed in middle of treatment, blocks and wedges missed during calculation.

2.2 Analysis of errors

Weekly assessment by the multidisciplinary task group of medical physicist, radiation oncologist and radiotherapy technologist were conducted. Medical physicists focuses on performing and supervising quality assurance tasks, such as tele cobalt output checks, weekly chart checks, etc. Members of the radiation oncology team review the prescription and treatment technique for patients that began treatment during the previous week. Verification of the departmental standard operating procedures in the tele cobalt radiotherapy treatment implementation was carried out by the radiotherapy technologist (2).

3. RESULTS

Errors were found in writing down the field size dimensions and depth of treatment. Errors related to dose prescription, treatment technique (SAD/SSD) and change of field size during the course of treatment were also common. Other issues like change in dose fractionation, inclusion of blocks were also found. However, all these were recognized before the initiation of treatment. The main reason recognized was the lack of communication regarding the change in the treatment parameters. Improper transfer of facts and knowledge or the lack of it also led to such issues. Interestingly, none of these errors resulted in incorrect treatment due to the agility of the professionals involved and timely communication with the others involved. The departmental protocol of cross verification at clinical planning, physics planning and treatment implementation enabled identification of errors before

radiation dose delivery. The discrepancies were resolved and proper documentation was maintained.

Table 1 *Classification of errors, identification, action taken and remedial implemented for tele cobalt.*

Case Study	Type of Discrepancy	Identified By	Action Taken	Remedial Action
1	Incorrect Field Size on Paper	RTT	Referred to the concerned RO and resolved	Double check at RO level.
2	Incorrect Depth mentioned on paper	MP	Referred to the concerned RO and resolved	Double check at RO level.
3	Incorrect Dose Fractionation	RO. In some cases, MP.	Confirmed with RO and Consultants.	Double check at RO level.
4	Field Size changed in middle of treatment.	RTT	Recalculation done and treatment started.	Proper communication to the MP. Replan.
5	Blocks and wedges missed during calculation.	RTT	Resent to MP and recalculation done.	Double check at MP level.

3.1 Discerning of errors

It is observed that most of the discrepancies/ errors observed could be stopped from further escalation by vigilance and strict adherence to the standard operating procedure of the department.

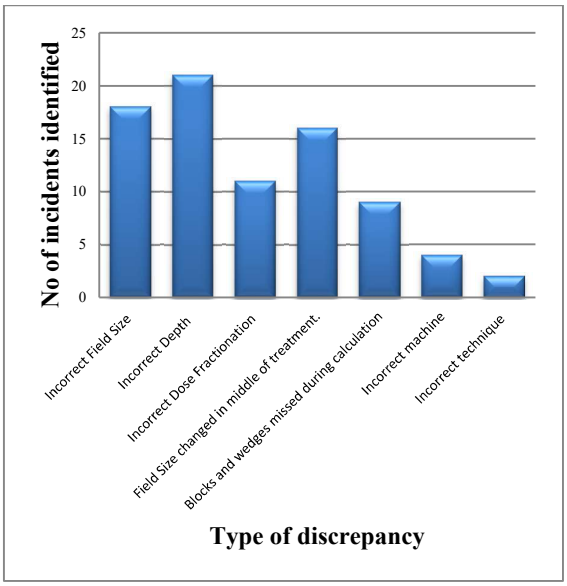

Figure 1 *Discrepancies detected.*

4. DISCUSSION

This study was about finding, examine and analyze the possible errors in tele cobalt radiotherapy. Data of one year at two tele cobalt radiotherapy machines were evaluated, considering limitations and problems.

In this study 100% of the discrepancies were identified before treatment execution. The independent multi layered manual verification and confirmation at every step aided in achieving this. Although, strict adherence to the well-defined and clear standard operating protocol helped in avoiding wrong radiation delivery, one should be alert for possible inaccuracies otherwise accidental error propagation may still occur.

This investigation emphasis on the need to have more serious attention to establish a peer review system and routine cross verification in all steps of the radiotherapy treatment planning and execution on tele cobalt machines (3). The established departmental protocol to take a critical look at each step of the system for multilayered prevention of accidental exposures enabled in prevention of errors in radiotherapy treatment (4).

4.1 Genesis of errors

Large workload, rush and stress in combination with inadequate experience and knowledge lead to oversight of the professional and resulted in the maximum number of errors identified. The communication gap between clinical groups of oncologist, physicist and technologist was another major reason. Insufficient patient counselling also propagated into errors.

5. CONCLUSION

The errors can be minimized by strictly following departmental procedure protocols, maintaining proper records, good communication among all the professionals involved and with the patient. Proper counselling can improve the awareness of the patient regarding the importance of adhering to the treatment protocol. Double stage verification needs to be performed at every major step of the treatment.

ACKNOWLEDGEMENTS

The authors acknowledge the co-operation and participation of radiation oncologists, medical physicists and radiotherapy technologists of the institute.

REFERENCES

1. Asnaashari K, Gholami S, Khosravi H R. Lessons learnt from errors in radiotherapy centers. Int. J. Radiat. Res., 2014; 12(4): 361-67.
2. Cox B W, Teckie S, Kapur a, Chou H, Potters L. Prospective peer review in radiation therapy treatment planning: Long-term results from a longitudinal study. Pract Rad Onc 2020; 10(4): e199-e206.
3. Ford E et al, Strategies for effective physics plan and chart review in radiation therapy: Report of AAPM Task Group 275. Med Phys 2020; 47(6): e236-272.
4. Fraass B A. Errors in radiotherapy: motivation for development of new radiotherapy quality assurance paradigms. Int. J. Radiation Oncology Biol. Phys., 2008; 71(1): S162–S165.

Assessment of Radiation Protection and Radiation Safety Awareness among Radiation Professionals in a Tertiary Care Teaching Hospital

Mary Joan[1], Priya Saini[2], Mukesh Jain[3], Ramesh Sharma[4], Arun Chougule[5]

1, 2, 3, 4, 5 *Department of Radiological Physics, SMS Medical College and Hospitals, Jaipur*

Abstract

As the use of radiation in healthcare has increased, the probability of occurrence of radiation injuries and hazards has also increased. Hence, proper training and education of the radiation professional, which encompasses the radiation protection and safety aspects, instills confidence in the radiation professionals and reduces the anxiety and fear that surrounds radiation use. It is noticed that the medical professionals who perform interventional procedures are the most exposed to radiation and yet not thorough with the safety aspects. Hence, an assessment of the various radiation professionals was done to evaluate their knowledge about radiation safety. This was followed by a training program which highlights the importance of such training sessions in radiation safety.

Keywords: awareness, radiation safety, radiation protection, radiation hazards, radiation professionals

1. INTRODUCTION

Modern evidence based clinical practice is dependent on routine as well as interventional radiological procedures. With the increase in the use of radiological procedures fears regarding radiation exposure to patients and personnel continue to emerge (1).

As the use of radiation in healthcare has increased, the probability of occurrence of radiation injuries and hazards has also increased (2). Hence, proper training and education of the radiation professional, which encompasses the radiation protection and safety aspects, instills confidence in the radiation professionals and reduces the anxiety and fear that surrounds radiation use. This training program can be conducted by the medical physicists in their respective hospitals on a regular basis.

Studies assessing the knowledge about radiation risks and radiation protection among healthcare professionals have been conducted worldwide (3-6). Studies conducted in the country are few in the literature.

The aim of our study was to assess the radiation protection and radiation safety awareness among radiation professionals in our institute. In addition the objective was to impart optimum awareness of exposure hazards of various radiological procedures and protective measures among the radiation professionals of various departments in our institute.

2. MATERIAL AND METHODS

The study was carried out at a tertiary care multispecialty medical college and hospitals with total inpatient bed strength of 9374. The hospitals are situated in the capital city of the State catering to the healthcare needs of patients from the State and neighboring States.

The study included faculty, staff and post graduate residents of the departments of Anesthesiology, Cardiology, Gastroenterology, Orthopedics, Radiology and Radiotherapy. A questionnaire related to radiation protection, safety, regulatory norms and safe practices was formulated and the radiation professionals were asked to fill it. They then underwent a training program on radiation safety and were asked to submit the same questionnaire. A comparison was done to analyze the improvement through the training program.

2.1 Questionnaire analysis

A questionnaire related to radiation protection, safety, regulatory norms and safe practices was formulated. It was comprised of 30 questions intended to evaluate the basic awareness of radiation safety and protection among the participants. The radiation professionals of various departments were asked to answer the questionnaire. They then underwent a training program on radiation safety and were asked to answer the same questionnaire. A comparison was done to analyze the improvement through the training program.

2.2 Educational lecture series

A series of educational lectures were conducted for the faculty staff and post graduate residents of various departments of the institute who uses ionizing radiation for diagnostic and therapeutic procedures. Basic radiation safety and protection, biological effects of ionizing radiation, radiation hazards, department specific safety protocols for radiological procedures and regulatory requirements in general and specific to each department were discussed in the lectures.

2.3 Statistical analysis

The data analysis was performed using tabulations and percentages. Descriptive statistics included mean, median, mode, percentage and standard deviation.

3. RESULTS

The questionnaire was distributed to 515 radiation professionals (including post graduate residents) of various departments of the institute pre and post lecture

series. A 100% response rate was observed in both pre and post evaluation. On comparing the results of pre and post questionnaires, an increase in the score was seen for almost every participant. The average score of the group increased from 67% to 78%. The median score increased from 22 to 25 while the mode value of score increased from 24 (scored by 7 participants) to 26 (scored by 8 participants).

Table 1 *Specialty wise distribution of Participants.*

Specialty	No. of participants
Anesthesiology	100
Cardiology	30
Gastroenterology	25
Orthopedics	20
Radiology	300
Radiotherapy	40

3.1 Educational lecture series

Notable interest was observed among all professionals especially the post graduate residents of all participating departments. 100% response to the questionnaire analysis shows the interest of the participants to understand the safety aspects of the use of ionizing radiation in routine clinical practice.

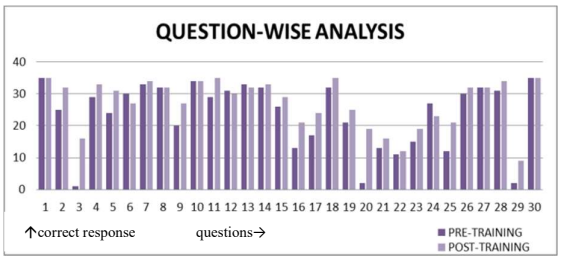

Figure 1 *Question-wise analysis of pre and post evaluation of radiation safety and protection awareness lecture series.*

4. DISCUSSION

Similar studies conducted in developed and developing countries as well as in the country (1-6) emphasize the importance of the need for radiation safety and protection awareness among radiation professionals.

The 100% response to pre and post questionnaire evaluation and the enthusiastic participation in the lecture series was an important characteristic of our study. In this evaluation equal marks were assigned to all questions and the same questionnaire was given to all participants irrespective their field of specialization. These may be the limitations of the analysis as the weightage of some questions to a particular specialty professional is subjective. Also this was a single institutional study.

The awareness and knowledge of radiation safety and protection among radiation professionals may vary depending on the field of specialization, the professional roles, the level of training and institutional adherence and implementation of regulatory norms for various departments.

4.1 Radiation safety awareness

Although the radiation workers and professionals are trained to work in radiation field, constant reassessment and updating is also required to keep them abreast with the technological and safety advances. With an increase in the use of radiation, the probability of occurrence of radiation injuries and hazards (in case of inadvertent accidents or malpractices) also increases. This training, however, should not be restricted to learning the functioning of a department but must encompass the radiation protection and safety aspects. Inclusion of radiation safety with special emphasis on safe work practices and safety protocols instills confidence in the radiation professionals and reduces the anxiety and fear that surrounds radiation usage. We have conducted specialized awareness programme for all radiation workers of the institute, radiological diagnosticians, interventionists, anesthesiologists, post-graduate trainees, paramedical and nursing staff and trainees. Although the radiation professionals have undergone training for radiation safety, they were found to be less confident in applying it in routine practice. A lacuna was also observed in the awareness about regulatory aspects and dose limits. The training programme showed some improvement but it threw light on the importance of regular and periodic training sessions.

5. CONCLUSION

The radiation professionals were found to be less confident in applying radiation safety knowledge in routine practice. The training program threw light on the importance of regular training sessions and the role of medical physicist in radiation protection and safety. The medical/ radiation physicists are the key persons in establishing a safe and fearless atmosphere in a hospital when it comes to radiation usage. It is hence a responsibility of the medical physicist to hold regular training sessions for all the radiation professionals.

ACKNOWLEDGEMENTS

The authors would like to acknowledge the cooperation and participation of the faculty, staff and students of the Department of Anesthesiology, Department of Cardiology, Department of Gastroenterology, Department of Orthopedics, Department of Radiology and the Department of Radiotherapy of the institute.

REFERENCES

1. Gothoskar S, Anand S, Walvekar P. Comparison of physicians' knowledge regarding radiation exposure and risks in common radiological investigations – A cross-sectional study. Int J Med Sci Public Health 2018; 7(4):305-310.

2. Azman R R, Md Shah M N, Kwan-Hoong Ng. Radiation safety in emergency medicine: balancing the benefits and risks. Korean J Radiol 2019; 20(3): 399-404.
3. Hayda R A, Hsu R Y, DePasse J M, Gil J A. Radiation exposure and health risks for orthopedic surgeons. J Am Acad Orthop Surg 2018; 26: 268-77.
4. Faggioni L, Paolicchi F, Bastiani L, Guido D, Caramella D. Awareness of radiation protection and dose levels of imaging procedures among medical students, radiography students, and radiology residents at an academic hospital: Results of a comprehensive survey. European Journal of Radiology 2017; 86: 135–142.
5. Zhonghua S, Kwan-Hoong Ng. Use of radiation in medicine in the Asia-Pacific region. Singapore Med J 2012; 53(12): 784–788.
6. Osullivan J, Oconnor O, Oregan K, et al. An assessment of medical students' awareness of radiation exposures associated with diagnostic imaging investigations. Insights Imaging 2010; 1(1): 86-92.

Localization accuracy of off-isocenter multi-target brain stereotactic radiosurgery using SyncTraX FX4

Jun Tomihara[1, 2], Jun Takatsu[3], Naoya Hara[2], Naoto Shikama[3], Keisuke Sasai[3]

1 Department of Radiation Oncology, Graduate School of Medicine, Juntendo University,
2 Department of Radiology, Juntendo University Hospital,
3 Department of Radiation Oncology, Faculty of Medicine, Juntendo University.

Abstract

Purpose: SyncTraX FX4 (Shimadzu, Kyoto, Japan) is a new image-guided radiotherapy (IGRT) device that is useful for patient positioning of linac-based brain stereotactic radiosurgery (SRS). In patient alignments using SyncTraX, the off-isocenter irradiation accuracy when irradiating multiple targets with a single isocenter has not been clarified. The purpose of this study was to evaluate the localization accuracy of SyncTraX FX4 for off-isocenter targets. In addition, the correlation between the intracranial isocenter position and positioning accuracy was investigated.

Methods: First, the localization accuracy of off-isocenter targets was investigated using MAX-EI phantom (Integrated Medical Technologies, Troy, NY). The MAX-EI phantom comprises anthropomorphic bone structures and two targets, one each at a center and an offset position. A plan with 15 fields was created, and each field had different couch and gantry angles. After phantom positioning with SyncTraX, an approximately 2×2 cm^2 irradiation field was delivered to the electronic portal imaging device (EPID) toward the off-isocenter target. Afterward, EPID images were analyzed. Second, RAND phantom (The Phantom Laboratory, NY) was used for evaluating positioning accuracy against the intracranial isocenter position. The isocenter was shifted from the phantom center in three different directions from –6 to +6 cm. Following image registration using SyncTraX, cone-beam computed tomography (CBCT) images were taken. The setup differences between SyncTraX and CBCT images were then analyzed.

Results: The maximum localization error of an off-isocenter target was 0.57 mm. The results of setup accuracy relative to isocenter shift between SyncTraX and CBCT were 0.0 ± 0.2 mm (mean ± 1 standard deviation), 0.2 ± 0.2 mm, and 0.3 ± 0.1 mm for anterior–posterior, superior–inferior, and left–right directions, respectively. Additionally, rotational errors were −0.1 ± 0.1 degree, 0.0 ± 0.1 degree, and −0.1 ± 0.1 degree for yaw, pitch, and roll, respectively.

Conclusion: We clarified that SyncTraX provides satisfactory setup accuracy for brain SRS.

Keywords: *SyncTraX FX4, Single isocenter, Multiple targets, Stereotactic radiosurgery.*

1. INTRODUCTION

The feasibility of linac-based brain stereotactic radiosurgery (SRS) using volumetric modulated arc therapy (VMAT) technique was reported.[1] Brain SRS creates very steep dose distributions and requires positioning accuracy within 1 mm.[2] The localization accuracy of several image-guided radiotherapy (IGRT) devices for linac-based brain SRS was investigated.[2–5] Recently, SyncTraX FX4 (Shimadzu, Kyoto, Japan) was introduced as a new IGRT device for brain SRS.

The advantage of linac-based SRS is shortened treatment time by irradiating multiple targets with a single isocenter. However, previous research reported the correlation between rotational setup errors and dosimetric impacts when irradiating off-isocenter targets with a single isocenter, particularly for a small target.[6] Therefore, in linac-based brain SRS, it is necessary to verify the off-isocenter irradiation accuracy as well as high position-matching accuracy. Although Tanabe et al. reported localization accuracy at the isocenter position using SyncTraX, the localization accuracy of off-isocenter targets using SyncTraX has not been revealed.

The purpose of this study was to evaluate the localization accuracy of off-isocenter targets using SyncTraX. In addition, the correlation between intracranial isocenter position and positioning accuracy using SyncTraX was investigated.

2. MATERIAL AND METHODS

2.1 Phantom design and imaging

Two types of anthropomorphic head phantoms were used in this study. First, the localization accuracy of an off-isocenter target was evaluated using the MAX-EI phantom (Integrated Medical Technologies, Troy, NY). The MAX-EI phantom was designed for the end-to-end Winston–Lutz test. The MAX-EI phantom comprises anthropomorphic bone structures and two targets. Figure 1 shows an image and three-dimensional (3D) view of the MAX-EI phantom. The two targets are spheres with a diameter of 9 mm, and the off-isocenter targets are located 3.7 cm away from the center of the phantom. Second, the RAND head phantom (The Phantom Laboratory, Salem, NY) was used for evaluating the correlation between the intracranial isocenter position and localization accuracy.

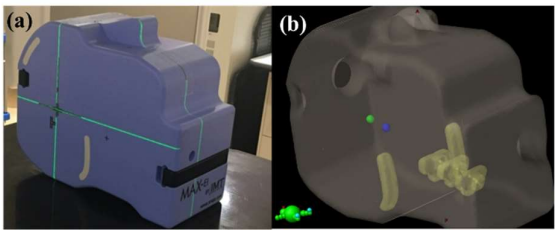

Figure 1 *(a) An image of the MAX-EI phantom; (b) a 3D view of the MAX-EI phantom. The green, blue, and yellow structures represent a target at the isocenter, an off-isocenter target, and a dummy bone, respectively.*

Computed tomography (CT) images of two head phantoms were acquired using Aquilion LB (Canon Medical Systems, Ōtawara, Japan). The resolution of the CT images was 1.07 × 1.07 mm^2, and the slice thickness was 1.0 mm. To reduce rotational setup errors, the RAND head phantom was fixed with an ESFORM thermoplastic mask (Engineering System, Matsumoto, Japan) and a Vac-fix bag (Engineering System). Treatment plans for evaluating localization accuracy were created with Eclipse ver. 13.6 (Varian Medical Systems, Palo Alto, CA).

2.2 SyncTraX FX4 system

SyncTraX FX4 comprises four X-ray tubes and flat-panel detectors (FPDs). Two SyncTraX imagers were selected for patient positioning using bony structure matching. SyncTraX can correct the patient position at any gantry and couch angle by combining imager sets. The resolution of the FPD image was 1516 × 1516 pixels (0.201 mm/pixel). SyncTraX was installed with TrueBeam (Varian Medical Systems), which is equipped with a Millennium 120 MLC in our hospital. The kV imaging conditions used in this study was 100 kV, 200 mA, and 100 ms.

2.3 Evaluation of the localization accuracy of the off-isocenter target

A 15-field Winston–Lutz test was created for the MAX-EI phantom. Table 1 lists the combinations of gantry and couch angles. All fields were created with a 5-mm leaf margin for the off-isocenter target (approximately 2 × 2 cm^2). Irradiation was performed with a 6-MV photon beam. Figure 2 shows a beam's eye view of the Winston–Lutz test. After phantom positioning with SyncTraX, 15 fields were delivered to the electronic portal imaging device (EPID). The localization accuracy of the off-isocenter target was analyzed with DoseLab ver. 6.7 (Varian Medical Systems). The radiation field threshold was adjusted between 50% and 64% because targets overlapped and bone structure affected the analysis results.

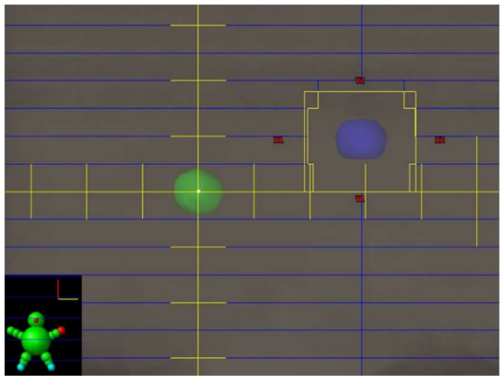

Figure 2 *Beam's eye view of the Winston–Lutz test. In this figure, gantry and couch angles are 0 degrees. The green sphere is a target at the isocenter. The blue sphere is an off-isocenter target.*

2.4 Evaluation of localization accuracy against various intracranial isocenter positions

To evaluate localization accuracy against intracranial isocenter positions, 12 plans with difference isocenter positions were created for the RAND head phantom. All plans were created with a couch angle at 0 degrees. The isocenter positions were shifted from the phantom center in a longitudinal, vertical, and lateral direction from –6 to +6 cm, respectively. After bony structure based positioning was performed using SyncTraX, cone-beam CT (CBCT) images were acquired. The localization accuracy of SyncTraX was then calculated from image registration errors between planning CT and CBCT. The localization accuracy of SyncTraX against variations of isocenter positions was evaluated for each translation and rotation direction.

3. RESULTS

3.1 Evaluation of localization accuracy of the off-isocenter target

Table 1 summarizes the discrepancy of the off-isocenter target from the radiation field. The mean differences and root mean square (RMS) of the localization errors of the off-isocenter target were 0.4 ± 0.1 mm (mean ± 1 standard deviation) and 0.39 mm, respectively. The maximum error was 0.57 mm. SyncTraX achieved localization accuracy <1 mm, which is recommended by the American Association of Physicists in Medicine (AAPM) Task Group 142 (TG-142),[7] even with an off-isocenter target.

Table 1 *Discrepancies in the off-isocenter target from the radiation field.*

Couch (degree)	Gantry (degree)	Discrepancy (mm)
0	0	0.37
	135	0.42
	180	0.56
	315	0.38
30	0	0.20
	135	0.27
	180	0.52
	315	0.19
60	0	0.38
	135	0.12
	180	0.24
	315	0.48
90	0	0.57
	135	0.41
	180	0.44

3.2 Evaluation of localization accuracy against various intracranial isocenter positions

Table 2 shows the localization errors against variations of isocenter intracranial positions. The mean values of translational localization errors for anterior–posterior (AP), superior–inferior (SI), and left–right (LR) directions were 0.0 ± 0.2 mm, 0.2 ± 0.2 mm, and 0.3 ± 0.1 mm, respectively. Similarly, the mean values of rotational localization errors for yaw, pitch, and roll were −0.1 ± 0.1 degree, 0.0 ± 0.1 degree, and −0.1 ± 0.1 degree for yaw, pitch, and roll, respectively.

Table 2 *The translational and rotational localization errors against variations of isocenter position.*

	Localization errors (mm/degree)			
AP shift	−6 cm	−3 cm	+3 cm	+6 cm
AP	−0.3	−0.3	0.4	0.0
SI	−0.3	0.3	0.0	0.3
LR	0.4	0.3	0.3	0.3
Yaw	−0.1	−0.2	−0.1	−0.1
Pitch	0.0	0.0	0.0	0.0
Roll	0.0	0.0	-0.1	-0.1
SI shift	−6 cm	−3 cm	+3 cm	+6 cm
AP	0.0	-0.1	0.0	−0.1
SI	0.2	0.3	0.1	0.0
LR	0.4	0.2	0.4	0.5
Yaw	−0.2	−0.1	−0.1	−0.1
Pitch	−0.1	0.0	0.0	0.0
Roll	0.0	0.0	−0.1	−0.4
LR shift	−6 cm	−3 cm	+3 cm	+6 cm
AP	0.0	0.0	0.1	0.1
SI	0.1	0.1	0.3	0.5
LR	0.2	0.3	0.4	0.3
Yaw	−0.2	−0.2	−0.2	−0.1
Pitch	0.0	0.0	0.0	0.1
Roll	−0.1	−0.1	−0.2	0.0

Table 3 summarizes the results of localization errors against variations of isocenter positions. The maximum RMS value was 0.34 mm for the translational errors and 0.15 degree for the rotational errors. The localization accuracy of SyncTraX was comparable to CBCT without depending on the intracranial isocenter position.

Table 3 *A summary of localization errors against variations of isocenter position.*

	AP	*SI*	*LR*	*Yaw*	*Pitch*	*Roll*
	(mm)			*(degree)*		
Average	*−0.02*	*0.16*	*0.33*	*−0.14*	*0.00*	*−0.09*
SD	*0.19*	*0.21*	*0.09*	*0.05*	*0.04*	*0.12*
RMS	*0.16*	*0.24*	*0.33*	*0.15*	*0.04*	*0.14*

Abbreviations: SD = standard deviation, RMS = root mean square

4. DISCUSSION

Tanabe et al. evaluated the isocenter localization accuracy with SyncTraX.[8] They reported that differences between the center position of a gold marker at the isocenter position and the radiation field for phantom positioning with SyncTraX were within 0.4 mm. Similarly, the localization accuracy of the off-isocenter target was within 0.6 mm using SyncTraX (shown in Table 1). Thus, SyncTraX meets the tolerance derived by the AAPM TG-142 (<1 mm) and can be used for patient setup with multiple targets using a single isocenter.

Decreasing localization accuracy after couch rotation was reported using the ExacTrac system (BrainLAB A.G., Heimstetten, Germany)[5]. In this study, the localization accuracy within 1 mm was investigated, even after couch rotation in patient positioning, using SyncTraX. In comparison to ExacTrac, SyncTraX has four imager sets and can select an imager set with high registration accuracy.

The off-isocenter target was in a fixed position, away from the isocenter in this study. Meanwhile, previous research investigated that localization errors increased in proportion to the distance between isocenter and tumors.[9] Thus, further investigations are

required to establish the correlation between the distance of the off-isocenter target and localization accuracy.

Ma et al. evaluated the RMS value of the differences between ExacTrac and CBCT as being 0.5 mm and 0.2 degree for an anthropomorphic head phantom.[4] In addition, Tanabe et al. reported that the maximum RMS was 0.13 mm and 0.10 degree when the isocenter was placed at the center of an anthropomorphic head phantom. When an isocenter position moved away from the center of the phantom, the bony structure acquired in the sensitive area of the FPD became smaller, decreasing the registration accuracy decreased. However, this study showed adequate registration when the isocenter was located away from the center of the skull.

5. CONCLUSION

We clarified that SyncTraX FX4 provides satisfactory localization accuracy for intracranial SRS.

ACKNOWLEDGMENTS

We would like to thank to Fuji Denolo for providing MAX–EI phantom.

REFERENCES

1 A. Andrevska, K.A. Knight, and C.A. Sale, The feasibility and benefits of using volumetric arc therapy in patients with brain metastases: a systematic review, J. Med. Radiat. Sci. **61**(4), 267–276 (2014).
2 J.P. Kirkpatrick, Z. Wang, J.H. Sampson, *et al.*, Defining the Optimal Planning Target Volume in Image-Guided Stereotactic Radiosurgery of Brain Metastases: Results of a Randomized Trial, Int. J. Radiat. Oncol. **91**(1), 100–108 (2015).
3 D. Hartgerink, A. Swinnen, D. Roberge, *et al.*, LINAC based stereotactic radiosurgery for multiple brain metastases: guidance for clinical implementation, Acta Oncol. (Madr). **58**(9), 1275–1282 (2019).
4 J. Ma, Z. Chang, Z. Wang, Q. Jackie Wu, J.P. Kirkpatrick, and F.F. Yin, ExacTrac X-ray 6 degree-of-freedom image-guidance for intracranial non-invasive stereotactic radiotherapy: Comparison with kilo-voltage cone-beam CT, Radiother. Oncol. **93**(3), 602–608 (2009).
5 Y. Tanaka, M. Oita, S. Inomata, T. Fuse, Y. Akino, and K. Shimomura, Impact of patient positioning uncertainty in noncoplanar intracranial stereotactic radiotherapy, J. Appl. Clin. Med. Phys. **21**(2), 89–97 (2020).
6 G. Prentou, E.P. Pappas, A. Logothetis, *et al.*, Dosimetric impact of rotational errors on the quality of VMAT-SRS for multiple brain metastases: Comparison between single-and two-isocenter treatment planning techniques, J. Appl. Clin. Med. Phys. **21**(3), 32–44 (2020).
7 E.E. Klein, J. Hanley, J. Bayouth, *et al.*, Task group 142 report: Quality assurance of medical acceleratorsa, Med. Phys. **36**(9), 4197–4212 (2009).
8 S. Tanabe, O. Umetsu, T. Sasage, *et al.*, Clinical commissioning of a new patient positioning system, SyncTraX FX4, for intracranial stereotactic radiotherapy, J. Appl. Clin. Med. Phys. **19**(6), 149–158 (2018).
9 J. Roper, V. Chanyavanich, G. Betzel, J. Switchenko, and A. Dhabaan, Single-Isocenter Multiple-Target Stereotactic Radiosurgery: Risk of Compromised Coverage, Int. J. Radiat. Oncol. Biol. Phys. **93**(3), 540–546 (2015).

The current status of Medical Physics in Sri Lanka

Vijitha Ramanathan

Department of Radiography & Radiotherapy, Faculty of Allied Health Sciences, General Sir John Kotelawala Defence University, Sri Lanka
Email: vijitha.r@kdu.ac.lk

Abstract

Medical physics plays a major role in medicine. It uses concepts, theories, and applications of physics in medicine to prevent, diagnosis, and treat the diseases. And the most important areas of medical physics are radiation oncology, radiology, nuclear medicine, and radiation protection. The purpose of this study was to investigate the current practice, education, staffing, and continuous professional development program in medical physics. Radiotherapy treatment centers were identified all over the country. All information about medical physics such as staffing, education, medical physicist job requirement, and continuous development programs in the field of medical physics were collected by on site visit, conversation over the phone, and from other available cancer resources in Sri Lanka. There are 7 government and 2 private radiotherapy centers currently providing radiotherapy treatment facilities for 21 million Sri Lankan population. Total number of medical physicists are about 38. Only 3 medical physicists are working in radiology departments as a diagnostic medical physicist. None of the medical physicists are involved directly in nuclear medicine in Sri Lanka. The minimum education requirement for medical physicist is a special degree in physics which is a four-year program. The medical physicists are recruited by Sri Lanka Scientific Service (SLSS) in government radiotherapy treatment centers. The medical physicists are rarely involving in research and continuous development program. The current status of medical physics is well below the required level. In addition, it is necessary to expand the medical physicists service to diagnostic radiology and nuclear medicine as these areas also require dosimetry and radiation protection. The research activities related to medical physics need to be improved. Nationwide professional accreditation system for certification of medical physicist should be implemented.

Keywords: Medical physics, Radiation oncology, Sri Lanka

1. INTRODUCTION

Medical physics is a fascinating branch of applied physics, practiced by medical physicists. It uses the principles, methods and techniques of physics in practice for diagnosis, prevention, and treatment. In present, the medical physicists involve in the field of radiation oncology, radiology, nuclear medicine and radiation protection to ensure the accuracy of diagnosis and treatment, safety use of radiation in medical practices. Medical physics has been recognized as a health care profession by the International Labour Organization (ILO) [1]. Even though, it is not fully implemented in developing countries [2].

In Sri Lanka, the medical physics profession was started in 1958 with the establishment of first national cancer hospital - Maharagama currently called as Apesksha Hospital. The first postgraduate degree program in medical physics was initiated in 1996 at University of Peradeniya, following University of Colombo started the master degree program in Medical Physics in 2013. Currently, only these two universities offer master degree in Medical Physics.

New cancer cases are increasing enormously. Radiotherapy treatment modalities keep evolving. The modern radiotherapy techniques involve very complex treatment techniques. Highly qualified medical professionals are required to handle those new radiotherapy treatment modalities. Due to having the complex radiotherapy treatment facilities, it is necessary to ensure that all the radiotherapy centers have adequate and well qualified medical professionals. Therefore, it is necessary to investigate the current status of medical physics in Sri Lanka. This study analyzes the current practice, educational requirement, staffing, and continuous professional development in medical physics in Sri Lanka.

2. MATERIAL AND METHODS

Radiotherapy centers were identified island wide by contacting the relevant authority, Sri Lanka Atomic Energy Board. The data pertaining to medical physics staffing, education system, and continuous development program for medical physicists were collected by onsite visit to Radiotherapy centers, conversation over the phone, and from other available cancer resources in Sri Lanka.

3. RESULTS

7 government and 2 private radiotherapy centers were identified all over the country. About 38 medical physicists are working as clinical medical physicists among 3 of them are working at radiology departments. None of the medical physicists are not involved directly in Nuclear medicine. Identified radiotherapy centers and medical physics staffing at radiotherapy centers are shown in table 1. In addition, 6 linear accelerators, 9 cobalt teletherapy machines, and 3 high dose rate (HDR)

brachytherapy units are operated to provide radiotherapy treatment.

Table 1 *Radiotherapy treatment centers and medical physics staffing. * indicates private treatment center.*

Radiotherapy centers	Number of Medical Physicist
Apeksha Hospital-Maharagama	14
Teaching Hospital - Karapitiya	05
Teaching Hospital-Kandy	04
Base Hospital - Tellippalai	03
Teaching Hospital - Anuradhapura	02
Provincial Hospital-Badulla	02
Teaching Hospital-Batticaloa	01
*Ceylinco Health Care Center- Colombo	02
*Asiri surgical Hospital-Colombo	02

The minimum educational requirement for a medical physicist in Sri Lanka is a special degree in Physics (4 years program). Medical Physicists are recruited by Sri Lanka Scientific Service (SLSS). After the recruitment, they will get trained under senior medical physicist in any of the government cancer treatment centre. In addition, they need to complete the master degree program in medical physics. There is no residency program for medical physicist. And, there is no certification requirement to work as a medical physicist and there is no continuous professional development system for medical physicists in Sri Lanka.

4. DISCUSSION

Currently, there are 6- linear accelerators and 9– Cobalt teletherapy machines, and 3- high dose rate brachytherapy machines are operating to treat cancer patients. Looking at currently functioning mega-voltage machines, there are 15 machines available for about 21 million population. It provides 0.7 mega voltage machines per one million people. As per the International Atomic Energy Agency (IAEA) recommendations, the ideal ratio for radiation therapy treatment is 4 - 8.1 radiotherapy centers per 1 million population or 1 mega voltage machine per 250,000 population [3]. It shows that Sri Lanka faces a significant shortfall in radiotherapy facilities.

According to the IAEA recommendations for the staff of physicist requirements for clinical radiotherapy, up to 400 patients can be treated annually per centre. For the staff of radiotherapy treatment planning, either dosimetrist or physics assistant can manage 300 patients yearly [4]. In Sri Lanka, there is no dosimetrist. Medical physicist does the treatment planning.

In 2018, 23530 new cases of cancer were identified in Sri Lanka [5], approximately 15,687 new cancer patients might have been undergone for radiotherapy as generally two third of patients require radiotherapy during their course of treatment. It should be more than that since old patients also need to be treated for palliative treatment. Considering overall, to treat about 16 000 cancer patients using radiotherapy with about 34 medical physicists are obviously not adequate. Increasing number of staff to radiotherapy centers according to the international standard is important to efficiently treat the cancer patients. Further, it is important to expand the medical physicists service to diagnostic radiology and nuclear medicine as these areas also require dosimetry and radiation protection.

Continuous professional development (CPD) system for medical physicist is essential to upgrade their skill and knowledge according to the current clinical practices. About 26 countries implemented CPD systems for medical physicists [6]. The CPD system could include various activities such as attending hands-on workshop, seminars, and conferences, journal publications, teaching activities for higher degree, conference presentations, writing books, examining postgraduate and undergraduate research projects, supervising research projects, involving in own research activities. It was noted that the main duties and responsibilities of medical physicists in Sri Lanka are radiotherapy treatment planning, dosimetry, radiation protection, and quality assurance, and few of them involve in teaching. The research activities related to medical physics is relatively poor. It needs to be improved. CPD system for medical physicists is not practiced in Sri Lanka. Nationwide CPD system for certification of Medical Physicist should be implemented.

5. CONCLUSION

The purpose of this study was to investigate the current status of medical physics in Sri Lanka to ensure whether the medical physicists are in the required level of current clinical practices. The current status of medical physics in Sri Lanka is well below the required current clinical practices. It is important to recruit more medical physicists to reduce their work load. Then and only, they will be able to involve in research activities and continuous development programs. Finally, enough man power will lead to more precise radiotherapy treatment to the cancer patients. In addition, adequate medical physicists need to be appointed in radiology department and nuclear medicine department to ensure the safety procedures and accuracy. This study identified the scarcity of radiotherapy facilities, man power, and shortfall in medical physics in Sri Lanka. The results of this study could be used to improve the field of medical physics in Sri Lanka.

REFERENCES

1. 'Medical Physicist' now included in the international standard classification of occupation (ISCO-08), https://www.iomp.org/wp-content/uploads/2019/02/iomp_guidance_on_isco-08.pdf [accessed on 31 October 2020].
2. Diana Garcia Hernandez et.al; Present status of medical physics practice in Mexico: An occupational analysis; Physica Medica 76 (2020) 55-61.
3. Surbhi Grover et.al; A ssystematic review of radiotherapy capacity in low- and middle-income countries; Frontiers in Oncology, 2015; https://doi: 10.3389/fonc.2014.00380.
4. Planning National Radiotherapy Services: A practical tool IAEA Human health series, No. 14, International Atomic Energy Agency, Vienna, 2010.
5. World Health Organization, Global Health ObservatoryGeneva,https://gco.iarc.fr/today/data/factsheets/populations/144-sri-lanka-fact-sheets.pdf; 2018 [accessed on 31 October 2020]
6. W.H.Round; Medical Physics Continuing Professional Development Systems, IFMBE Proceedings 39, 2012 ; DOI: 10.1007/978-3-642-29305-4_442.

Dosimetric evaluation of uncorrectable rotational setup error in total body irradiation using helical tomotherapy

Akira Isobe[1,3], Keisuke Usui[2,4], Haruka Katou[3], Junpei Ohbuchi[3], Naoya Hara[3], Keisuke Sasai[4]

1 Department of Radiation Oncology, Graduated School of Medicine, Juntendo University, Tokyo, Japan
2 Department of Radiological Technology, Faculty of Health Science, Juntendo University, Tokyo, Japan
3 Department of Radiology, Juntendo University Hospital, Tokyo, Japan
4 Department of Radiation Oncology, Faculty of Medicine, Juntendo University, Tokyo, Japan

Abstract

Helical tomotherapy (HT) is a type of intensity-modulated radiation therapy that improves target dose uniformity and reduces the dose delivered to organs at risk. Thus, HT has been used as a safe method for total body irradiation (TBI). Because TBI targets the whole body, accurate setup positioning in the field edge is difficult because of the whole-body rotational posture. This study aimed to determine the tolerance for rotational setup error (SE) in the vertical (pitch) direction for TBI using HT and present the effects of rotational SE on whole body dose through a retrospective analysis of previous patients' irradiation data. In this study, we simulated rotational SE in the pitch direction and quantitatively determined the effects of this SE on the administered dose. The simulation results indicated that the dose uniformity within the target deteriorated as the rotational SE increased. Even with a rotational SE value of 1.0°, the high-dose region showed a significant difference in dose distribution compared with the planned dose distribution. When the rotational SE was <2.0°, dose heterogeneity within the clinical target volume was maintained within ±10% of the prescribed dose in at least 95% of the evaluated patients. Therefore, dose errors induced by rotational SE values of <2.0° were acceptable.

Keywords: TBI, helical tomotherapy, rotational setup error

1. INTRODUCTION

Total body irradiation (TBI) combined with chemotherapy is widely used as a pre-bone marrow transplant regimen in hematological malignancies and has superior treatment results compared with chemotherapy-only regimens [1]. Helical tomotherapy (HT) has been used as a safe TBI method and can simultaneously improve target dose uniformity and reduce the dose delivered to organs at risk using intensity-modulated radiation therapy [2]. Because TBI targets the whole body, accurate positioning in the field edge is difficult because of whole-body rotational posture. Additionally, when irradiating a large target, as in TBI, the couch sagging of patient peculiar to the HT apparatus increases so that a systematic pitch error is generated in the vertical (pitch) direction. However, HT systems are not equipped with a function to correct for the rotational setup error (SE) in the pitch direction. Furthermore, the effects of surface dose deviations owing to SE are significant in HT [3]. Takenaka et al. stated that the translational position error in the horizontal direction should be within 5 mm in TBI with HT [3]. Therefore, we usually create a virtual structure enlarged 5 mm from body contour and use it to adjust patient position in image-guided radiation therapy (IGRT) to perform TBI within the acceptable SE ranges. However, the effect of the dose distribution owing to rotational SE in the pitch direction in TBI using HT is unclear, and studies that assessed this disadvantage are still not available. It is difficult to manually modify the rotational SE. Additionally, retrying the IGRT process requires a considerably long treatment time, which increases patient distress.

This study aimed to determine the rotational SE tolerance in the pitch direction in TBI using HT.

2. MATERIAL AND METHODS

2.1 Patients and treatment planning

This study included 10 patients who underwent TBI and were enrolled between January and December 2018 as approved by the institutional review board of our hospital (reception number: 18-034).

A whole-body suction fixture and thermoplastic head mask were used to ensure fixation accuracy. A 5-mm-thick image was obtained using a 16-sensor data acquisition system-type whole-body computed tomography (CT) system (Aquilion LB, Canon Medical Systems, Tochigi, Japan). The field of view was 550 mm. The planning CT data of patients who underwent TBI were obtained with a length of 120 cm for the upper body and 100 cm for the lower body, which were shorter than the longest irradiation range of the HT system (i.e., 135 cm). Separate treatment plans were created for the upper and lower parts of the body. The plan for the upper body was defined as "head-first (HF) plan" and that for the lower body was defined as "feet-first (FF) plan" by reversing the head-to-tail direction. The clinical target volume (CTV) was the whole-body contour, excluding the lung, which is an organ at risk. Considering the setup margin, the planning target volume (PTV) was set at a volume obtained by measuring the CTV and adding 5 mm toward the lung contour. According to a previous study [3], no margin was added to the body contour to prevent an increase in excessively high-dose areas on the body surface. The prescription dose was optimized by a radiation treatment planning system (TomoHDA System Planning Station, version 5.1.1.6, Accuray, WI, USA) using a constraint to cover 95% of the PTV with

12 Gy. In the FF plan, both the CTV and PTV were set in the body contour. In the HT plan, the field width was 5.0 cm, the pitch was 0.287, and the modulation factor was determined by adjusting each patient's value by 2.5 as a reference value. Additionally, one region was defined as the prediction area of large dose deviations. The region within 5 mm from the body surface was defined as CTVbs.

2.2 Effect of rotational SE on dose distribution

To simulate the effects of rotational SE on dose distribution, planning CT images of each patient were rotated 1°–4° in the pitch direction. Simultaneously, each organ structure dataset attached to the planning CT image was rotated using commercially available software (MIM Maestro, version 6.5.9, MIM Software, Inc., Cleveland, USA). Subsequently, we recalculated the dose distribution on each rotational SE image under the plans presented in Section 2.1. The dose indices of $D_{98\%}$ (the minimum absorbed dose that covers 98% of the CTV), $D_{95\%}$, and $D_{2\%}$ were compared for the quantitative evaluation of CTV coverage for all dose distributions. Furthermore, $D_{98\%}$ and $D_{2\%}$ of CTVbs were evaluated. In accordance with the American College of Radiology and American Society for Radiation Oncology guidelines [4], V110% (the volume receiving at least 110% of the prescription dose) and V90% were used as indicators of high- and low-dose regions, respectively. We compared the high- and low-dose regions' change in CTVs between the original and simulation doses quantitatively. The lungs were evaluated for mean dose and the volume receiving at least 10 Gy (V_{10Gy}). The volume receiving >10 Gy was not allowed to exceed 40% of the whole lung volume, with reference to the predictors of radiation pneumonia in patients receiving radiation therapy [5]. Therefore, changes in the dose distribution in CTVs and lungs owing to increased rotational SE were compared with the original plan dose to establish SE tolerance. The difference between the means of original plan dose and the means of simulation dose with rotational SE was considered statistically significant at a p-value of <0.05. (two-tailed test). R version.1.41 (www.r-project.org) was used for paired *t*-test.

3. RESULTS

The mean CTV $D_{95\%}$ values of the original HF and FF plans were 12.0 Gy and 11.9 Gy, respectively, and the standard deviation (SD) was <0.1. Tables 1 and 2 show the dose index with various rotational SE values using the HF and FF plans, respectively.

In the HF plan, CTV $D_{95\%}$ and $D_{98\%}$ decreased with increasing SE. There was a significant difference in $D_{95\%}$ and $D_{98\%}$ between the original planned and simulation doses when the SE was >2.0°. CTV $D_{2\%}$ increased with an increase in SE, with a significant difference from the original planned dose shown for SE of >1.0°. CTV V110% increased with an increase in SE, with a significant difference from the original planned dose shown in SE of >1.0°. CTV V90% decreased with increase in SE, with a significant difference from the original planned dose shown in SE of >3.0°. The mean lung dose was significantly different from the original planned dose when the SE was >1.0°, with a gradual increase noted with an increase in SE. CTVbs $D_{98\%}$ decreased with increasing SE. CTVbs $D_{2\%}$ reached its maximum value with an increase in SE at 3.0°, but subsequently decreased at an SE of >4.0°. Both CTVbs $D_{98\%}$ and $D_{2\%}$ were significantly different from the original planned dose with SE values of >1.0°. The mean lung V_{10Gy} showed a significant difference from the planned dose when the SE was >4.0°. Lung V_{10Gy} slightly decreased at the SE value of 1.0° and increased at ≥2.0°. Furthermore, at SE of ≥3.0°, the mean value of lung V_{10Gy} exceeded 40% of the allowable value.

Dosimetric effects caused by SE in the pitch direction were almost the same between the FF and HF plans. Significant differences from the planned dose were observed with SE values of >1.0° for all indices, except CTV V90%.

4. DISCUSSION

TBI using HT is a promising treatment modality. However, it is necessary to improve the accuracy of the treatment position. In this study, the permissible range of uncorrectable rotational SE in the pitch direction was evaluated with a focus on the impact on irradiated patient dose distribution.

Increasing the rotational SE in the pitch direction results in a higher dose inhomogeneity in the target volume. When the SE in the pitch direction is 2.0°, the mean V110% and V90% of CTV in the HF plan for 10 patients are 5.4% (SD ± 1.3) and 99.4% (SD ± 0.1), respectively (Table 1). The mean V110% and V90% of CTV in the FF plan for 10 patients are 5.9% (SD ± 1.5) and 99.6% (SD ± 0.5), respectively (Table 2). Assuming a normal distribution, the mean ± 3SD for CTV V110% is <10% in the HF plan. This indicates that almost 99% of patients have a CTV V110% of <10%. In the FF plan, the mean ± 2SD of CTV V110% is <10%; hence, >95% of patients have a CTV V110% of <10%. Figure 1 shows the changes in the high-dose regions of CTV owing to rotational SE. Conversely, the mean value of the dose index exceeded the tolerance deviation of 10% with an SE value of 4°. Dose heterogeneity needs to be maintained within ±10% of the prescription dose [4]. Figure 2 shows the results of lung simulation. The mean value of V_{10Gy} was maintained below 40% for an SE value of up to 2.0°. The CTV results showed that a high-dose region was caused by the SE, with $D_{2\%}$ and V110% showing significant increases even with the rotational SE value of 1.0°. Specifically, the maximum dose increased at the body surface area (CTVbs) with an increase in rotational SE. Areas of high-dose distribution were observed with an increase in rotational SE.

These issues were more significant in terms of the CTVbs value. Figure 3 shows the effect of rotational SE on the near-maximum dose in CTVbs. The $D_{2\%}$ value increased by 13.7% of the mean value with an SE value of only 1.0°. There is a high beamlet fluence area around the body surface to maintain a sufficient dose in the buildup region. Therefore, the rotational SEs increase the radiation dose at the patient's body surface. The results of the FF plan showed more significant dose deviations than those of the HF plan. Because the contour of the foot was more complex owing to structures such as the toes or heel, these beamlet fluences were associated with steep distributions. Therefore, even small SEs induced a significant dosimetric error in the FF plan.

Prolonging the treatment time with IGRT and improving the reproducibility by SE correction are trade-offs; hence, rationalization of SE correction can be expected through quantification of the allowable SE value. Rotational SE causes enlargement of unexpected high-dose areas on the patient's body surface. Furthermore, SE is a result of combining large irradiation volume with long treatment time in TBI using HT. Therefore, studies to improve treatment planning methods to reduce the dosimetric effects of rotational SE should be conducted in the future.

5. CONCLUSION

The simulation results indicated that dose errors owing to an SE of <2.0° are acceptable. Even if rotational SE of ≤2° is present, re-setup and IGRT rerun is not required. Thus, there is no need to increase patient distress. However, rotational SE may increase radiation doses, particularly on the patient's body surface.

REFERENCES

1. Kröger N et al. Comparison of total body irradiation vs busulfan in combination with cyclophosphamide as conditioning for unrelated stem cell transplantation in CML patients. Bone Marrow Transplant 2001;27:349–54.
2. T Hui SK et al. Feasibility study of helical tomotherapy for total body or total marrow irradiation. Med Phys 2005;32:3214–24.
3. Takenaka R et al. Adequate target volume in total-body irradiation by intensity-modulated radiation therapy using helical tomotherapy: A simulation study. J Radiat Res 2017;58:210–6.
4. Wolden SL et al. American college of radiology (ACR) and american society for radiation oncology (ASTRO) practice guideline for the performance of total body irradiation (TBI). Am J Clin Oncol Cancer Clin Trials 2013;36:97–101.
5. Pinnix CC et al. Predictors of radiation pneumonitis in patients receiving intensity modulated radiation therapy for Hodgkin and non-Hodgkin lymphoma. Int J Radiat Oncol Biol Phys 2015;92:175–82.

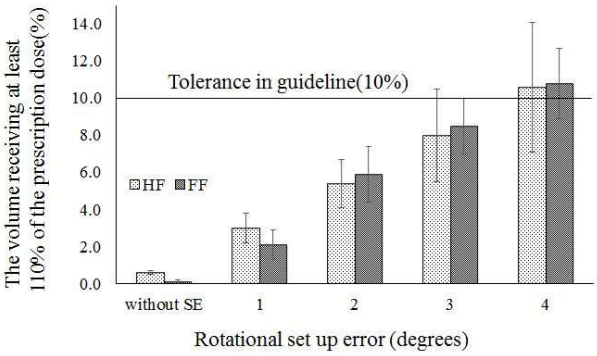

Figure 1. *Changes in high-dose regions within the clinical target volume owing to increased rotational SE in the pitch direction*

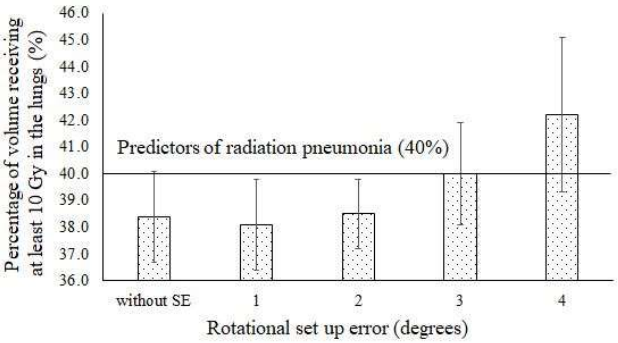

Figure 2. *Changes in the high-dose region in the lung owing to an increase in rotational SE in the pitch direction*

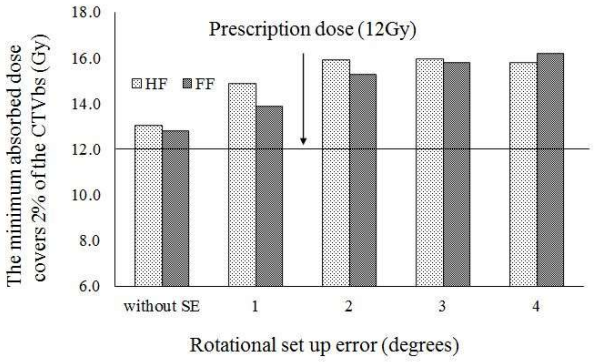

Figure 3. *Changes in maximum dose within the CTVbs owing to increased rotational SE in the pitch direction*

Table 1. *Effect on dose distribution owing to the rotational SE in the head-first plan*

Average±SD		Rotational SE in pitch direction. (degrees)				
		Plan	1.0	2.0	3.0	4.0
CTV	$D_{98\%}$ (Gy)	11.7±0.1	11.7±0.0	11.6±0.0*	11.3±0.0*	11.0±0.0*
	$D_{95\%}$ (Gy)	12.0±0.0	12.0±0.0	11.9±0.0*	11.8±0.0*	11.7±0.0*
	$D_{2\%}$ (Gy)	12.9±0.1	13.5±0.2*	14.5±0.5*	15.0±0.5*	15.2±0.5*
	$V_{110\%}$ (%)	0.6±0.1	3.0±0.8*	5.4±1.3*	8.0±2.5*	10.6±3.5*
	$V_{90\%}$ (%)	99.4±0.4	99.7±0.1	99.4±0.1	99.0±0.1*	98.3±0.2*
Lung	Mean (Gy)	9.5±0.1	9.5±0.1*	9.5±0.1*	9.6±0.1*	9.7±0.1*
	V_{10Gy} (%)	38.4±1.7	38.1±1.7	38.5±1.3	40.0±1.9*	42.2±2.9*
CTV_{bs}	$D_{98\%}$ (Gy)	11.0±0.4	10.7±0.3*	10.4±0.2*	10.1±0.2*	9.5±0.4*
	$D_{2\%}$ (Gy)	13.1±0.1	14.9±0.4*	15.9±0.4*	15.9±0.4*	15.8±0.3*

* (p <0.05)

Table 2. *Effect on dose distribution owing to the rotational SE in the feet-first plan*

Average±SD		Rotational SE in pitch direction (degrees)				
		Plan	1.0	2.0	3.0	4.0
CTV	$D_{98\%}$ (Gy)	11.8±0.1	11.6±0.2*	11.5±0.2*	11.3±0.2*	11.2±0.2*
	$D_{95\%}$ (Gy)	11.9±0.0	11.8±0.1*	11.8±0.1*	11.7±0.1*	11.6±0.1*
	$D_{2\%}$ (Gy)	12.6±0.1	13.2±0.2*	14.4±0.5*	15.1±0.7*	15.6±0.8*
	$V_{110\%}$ (%)	0.1±0.1	2.1±0.8*	5.9±1.5*	8.5±1.5*	10.8±1.9*
	$V_{90\%}$ (%)	100.0±0.1	99.8±0.2	99.6±0.5*	99.3±0.5*	98.9±0.4*
CTV_{bs}	$D_{98\%}$ (Gy)	11.6±0.3	11.1±0.3*	10.9±0.3*	10.7±0.3*	10.3±0.1*
	$D_{2\%}$ (Gy)	12.8±0.2	13.9±0.4*	15.3±0.8*	15.8±0.8*	16.2±1.0*

* (p <0.05)

Investigation of dose perturbations around brachytherapy seeds in high-energy photon beams

Shuta Ogawa[1], Keisuke Yasui[2], Yasunori Saito[3], Kazuki Ouchi[1], Junya Nagata[1], and Naoki Hayashi[2]

1 Graduate School of Health Sciences, Fujita Health University
2 School of Medical Sciences, Fujita Health University
3 Division of Radiology, Fujita Health University Hospital

Abstract

Purpose: The purpose of this study was to investigate the dose perturbations around seeds in high-energy photon beams (6 MV, 10 MV; with flattening filter (WFF), flattening filter-free (FFF)).

Methods: Two kinds of seed models, TheraAgX100 (TAX) and Bard BRACHYSOURCE STM125I (BBS), were used for the simulation. We calculated the dose distribution around seeds by Monte Carlo (MC) code (PHITS ver.3.11) under the following geometric conditions: (a) One seed at the depth of 50 mm on the beam axis in water (b) Three seeds at the depths of 48, 50 and 52 mm on the beam axis in water (c) One seed at the center of the elliptical columnar water phantom. It was irradiated perpendicular beam under the condition (a) and (b); static five beams under the condition (c). The measurement using GafchromicEBT3 films under the condition (a) with TAX carried out to verify the accuracy of the MC simulation. The dose perturbation is defined as the difference between the dose with and without the seed.

Results: The result of MC simulations indicated the coincident with film measurements within 4%. The dose perturbations were ranging from -14.9% (condition (b), on the downstream of TAX, 10 MV-WFF) to 13.0% (condition (b), on the upstream of BBS, 6 MV-WFF) on the beam axis under the condition (a) and (b). Only dose increases of up to 9.0% were observed under the condition (c).

Conclusion: The dose perturbations around seeds in high-energy photon beams were investigated by the MC simulation and film measurements. The seeds located close to organs at risk may cause excessive irradiation.

Keywords: Monte Carlo simulation, prostate cancer, brachytherapy, external-beam radiation therapy

1. INTRODUCTION

The treatment options for prostate cancer are radiation therapy, radical prostatectomy, and hormonal therapy. Radiation therapy for prostate cancer has been established. The main advantage of radiation therapy is that it may help to control the growth of the malignant cell without surgical invasion. Because of high precision technology such as image-guided radiation therapy, the prescription dose was escalated, and the control rate of prostate cancer was improved. Radiation therapy for prostate cancer is distinguished into two treatment methods: external beam radiation therapy (EBRT) and, brachytherapy. In addition, the combination of EBRT and brachytherapy (combo-RT) is proposed for specific case. Combo-RT means the integration of EBRT and brachytherapy. As the first step, the partial prescription dose was irradiated by brachytherapy, then EBRT is performed to complete the prescription dose. The details of these treatments are determined in consideration of the stage and aggressiveness of cancer and the impacts on the patient quality of life. The NCCN Guidelines recommend combo-RT for high or very high-risk groups[1]. Combo-RT performs EBRT on inhomogeneous prostate with the permanent seed implants inserted. Materials of the seed are classified as high atomic number (high-Z) materials[2]. The seeds of high-Z materials cause dose perturbations due to backscatter and attenuation of the photon beam during combo-RT. The composition and size of the seed are different among the manufacturer and model. Therefore, the dose perturbation may be different depending on the seed type. These problems are unable to be calculated and considered by the treatment planning system.

Given the above, it has not been clarified as to the difference in the magnitude of dose perturbation by seed type, position, number of seeds, and photon beam type. Similarly, it has not also been clarified how much the dose distribution changes with it. The purpose of this study was to investigate the dose perturbation around the seed in high-energy photon beams.

2. MATERIAL AND METHODS

2.1 Seed implants

Combo-RT uses permanent seed implants. The seed in use for prostate cancer is only iodine-125 (125-I) in japan. The type of seed used in our institution is TheraAgX100 (TAX: Theragenics Corporation, Fig. 1(a)) and Bard BRACHYSOURCE STM125I (BBS: C.R. Bard, Inc., Fig. 1(b)). The external dimensions of these seeds are nearly identical, but the materials of their internal composition differ greatly. Therefore, two kinds of the 125-I seed models, TAX and BBS were featured for the Monte Carlo (MC) simulation in this study.

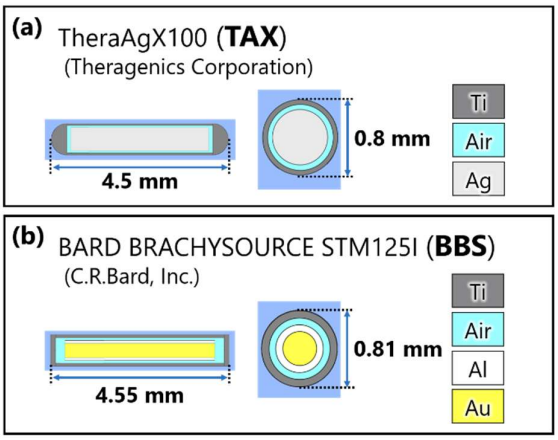

Figure 1 *Schematic diagram of I-125 seeds, TAX and BBS.*

2.2 Monte Carlo simulation

Dose calculations were performed by the Monte Carlo (MC) code (Particle and Heavy Ion Transport code System: PHITS, version 3.11). In this study, phase-space files (PSF) of the photon beam for the Varian TrueBeam linear accelerator (Varian Medical Systems, Palo Alto, USA) were used to simulate conventional (with-flattening filter: WFF) and the flattening-filter-free (FFF) beams. Beam energies of PSF are 6 MV and 10 MV. MC simulations with TAX and BBS were undergone in two geometric conditions (Fig. 2). The field size was set at 10 x 10 cm^2. The percentage depth dose (PDD) and off-axis ratio (OAR) were calculated under the above conditions: irradiation by perpendicular beam to a seed (a) and three seeds (b). The dose perturbation is defined as the difference between the dose with the seed and the dose without the seed.

In a clinical, the seed will be irradiated by multiple fields. The source position was moved to reproduce the situation, and an elliptical columnar water phantom was irradiated by five static beams (Fig. 3).

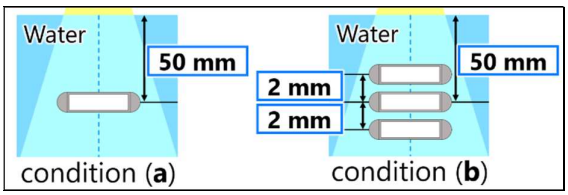

Figure 2 *Placements of seeds for MC calculation*

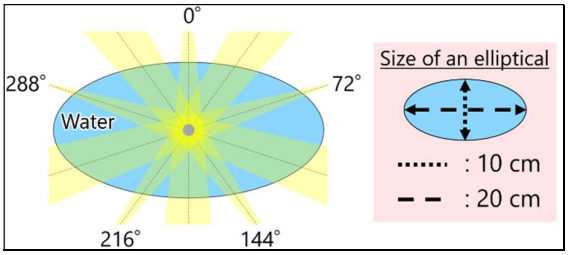

Figure 3 *The geometry of the MC simulation by using multiple fields. A seed was inserted the center of the phantom.*

2.3 Film measurement

The dose due to radioactive seeds itself causes dosimetric problems while used for film measurements. Therefore, film measurements were performed using a non-radioactive TAX. The measurement using GafchromicEBT3 (Ashland, NJ, USA) films was carried out to verify the accuracy of the MC simulation in the presence of seeds. Film measurements were performed using TAX. The EBT3 films were scanned and analyzed using a flatbed scanner (Epson Expression 11000 XL, Epson America Inc., Long Beach, CA, USA) and ImageJ 1.52v (National Institutes of Health). The measured results with EBT3 film evaluated the dose perturbation as in the MC simulation results.

3. RESULTS

Figure 4 shows the results of the MC simulation and the measurement with TAX on condition (a). The dose perturbations with TAX and BBS did not differ in the dose differences and the tendency. The results of MC simulations and measurements showed good agreement within 4%. WFF beam tended to have a slightly wider backscattering range. The magnitude of dose perturbations did not depend on the seed type and the beam energy.

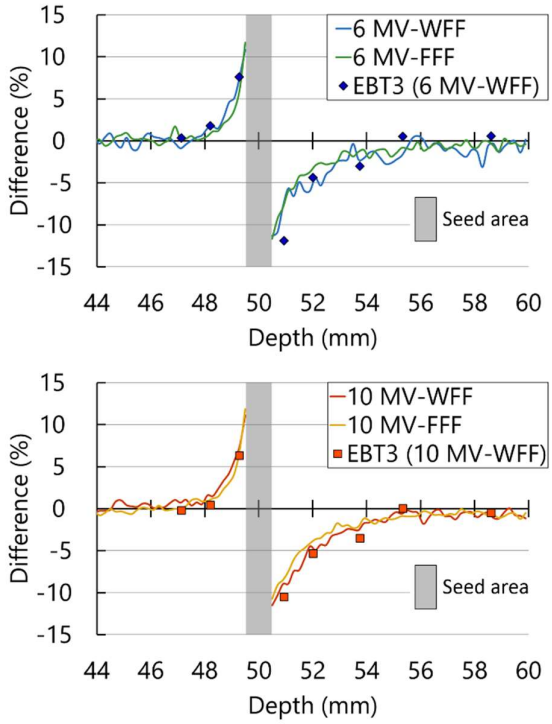

Figure 4 *Dose differences with TAX for the (i) 6 MV and (ii) 10 MV photon beam under condition (a)*

The Maximum dose increase of OAR was 9%. The range of dose perturbation to lateral direction was 2 mm around the seed. The dose perturbation of OAR did not depend on the seed type and beam energy. The dose decrease to lateral direction was not observed.

Figure 5 shows the results of MC simulation on condition (b). The tendency of dose perturbation was the same as under condition (a). Maximum dose decreases

under condition (b) tended to be much greater than that under condition (a). The dose after passing through three seeds was always reduced by 1%.

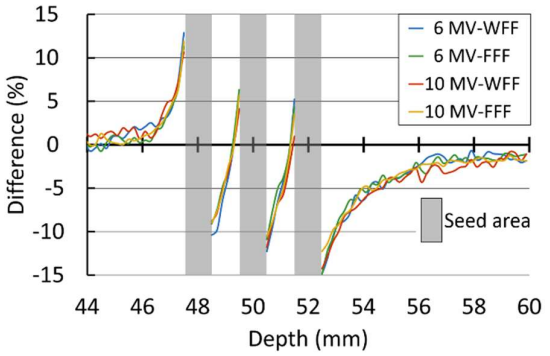

Figure 5 *Dose differences with TAX under condition (b)*

Fig. 6 shows the dose difference distribution around TAX in the MC simulation using multiple fields (10 MV-WFF). The higher the beam energy, the wider the range of dose perturbations. In the result of multiple fields, only dose increases were observed; dose decreases are not observed as in the case of using a single field.

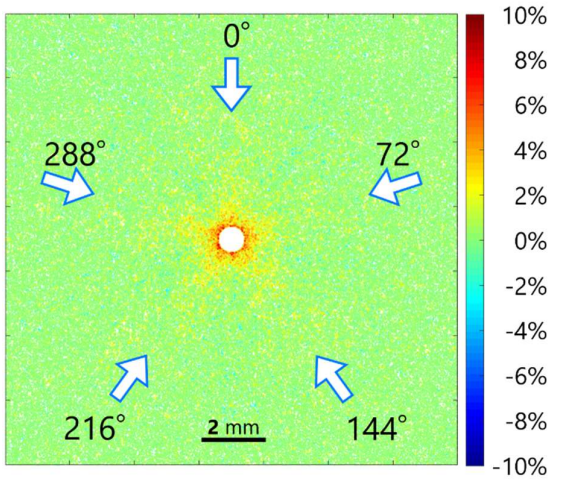

Figure 6 *Dose difference distribution around TAX differences with TAX under condition (b)*

4. DISCUSSION

The magnitude of dose perturbations did not depend on the seed type and the beam energy. That is because the seed size is small. The MC simulations with plates (8 x 8 cm^2) of the same composition as the seed showed the backscattering increased with a higher effective atomic number and higher beam energy. Those results coincide with a previous study[3].

WFF beam tends to have a slightly wider backscattering range. This is because the WFF beam contains high energy components than the FFF beam.

Maximum dose decreases under condition (b) tended to be much greater (1.5-4.0%) than that under condition (a). This is caused by the attenuation of the photon beam due to the arrangement of multiple seeds.

Only dose increases were observed in the results of multiple fields irradiation. Cancellation of dose perturbation due to multi fields irradiation does not occur because of lateral scattering. This phenomenon suggests that not only backscattering and attenuation but also lateral scattering contribute to dose perturbations. This dose increase becomes more pronounced as the number of radiation gates increases.

The results of MC simulation and measurement showed agreement within 4%. The dose difference is not suitable for evaluating the displacement in the depth direction. Evaluation by distance to agreement needs to be added as well.

5. CONCLUSION

Dose perturbations around seeds in high-energy photon beams were investigated by the MC simulation and measurements. The magnitude of dose perturbations varies with seeds position and type, and photon beam type. Only dose increases occur in the multiple fields irradiation. The seeds located close to organs at risk may cause excessive irradiation.

The limitation of this study is the actual clinical effect of combo-RT has not been considered yet. The MC simulation should be performed with the clinical computed tomography images inserted virtual seeds in the future.

REFERENCES

[1] National Comprehensive Cancer Network (NCCN). Prostate cancer. In: National Comprehensive Cancer Network Clinical Practice Guidelines in Oncology, version 2. 2019-April 24, 2019. Available at: https://www.nccn.org/professionals/physician_gls/default.aspx Accessed: October 24, 2020.

[2] AAPM. Tissue Inhomogeneity Corrections for Megavoltage Photon Beams. Report of the American Association of Physicists in Medicine (AAPM) Task Group No. 85 [online], available: https://www.aapm.org/pubs/reports/RPT_85.pdf; 2004 [accessed 24/10/2020].

[3] Das IJ, Kahn FM. Backscatter Dose Perturbation at High Atomic Number Interfaces in Megavoltage Photon Beams. Med Phys. 1989;16:367–375. https://doi.org/10.1118/1.596345.

Efficiency of EPID dosimetry based software compared with ion chamber

Wanwanat Sumanaphan[1], Jumneanphan Rueansri[2], Wannita Malila[2], Patsuree Cheebsumon[1]

1 Department of Radiological Technology, Faculty of Allied Health Science, Naresuan University, Thailand
2 Division of Medical Physics, Department of Radiation Therapy, Lampang Cancer Hospital, Thailand

Abstract

This study validated EPID dosimetry program by measuring point doses compared with ion chamber measurement. Square field sizes between 3×3 and 20×20 cm^2 at 5, 10, and 15 cm of depth were investigated. PerFRACTION™ is EPID dosimetry program that obtained data from TPS and ELEKTA Versa HD™. EPID measured dose delivered directly to EPID in the air without couch or phantom to calculate point dose. Dose difference from ion chamber and PerFRACTION™ was evaluated, compared with TPS. The average percentage difference from ion chamber was less than 1.40, except 15 cm depth. In contrast, the average percentage difference obtained from PerFRACTION™ remained relatively stable < 0.74. Small field size less than 5x5 cm^2 did not receive full scatter factor, and back scatter effect to depth especially at depth 15 cm of pinpoint ion chamber. Therefore, errors and maximum dose difference were found in the small field sizes. In conclusion, point doses obtained data from various measurements were good agreements (<3%) for 6 and 10 MV.

Keywords: EPID, Dosimetry, PerFRACTION™, Delta4+™, Validation

1. INTRODUCTION

Radiation therapy is one of the cancer treatments. In modern LINAC, Electronic portal imaging device (EPID) is an essential part for patient verification. Recently, it was highly developed to dosimeter because of convenience and reduces time to setup. PerFRACTION™ (Sun Nuclear Corp., Melbourne, FL, USA) is EPID dosimetry program. ***This program was used for pretreatment QA in Lampang Cancer Hospital.*** Before using EPID dosimetry program, point dose measurement is necessary to confirm software efficiency, machine output and position. The purpose of this study was to validate point dose measurement in EPID dosimetry program with ion chamber.

2. MATERIAL AND METHODS

Elekta iViewGT amorphous silicon (a-Si) AP detector panel (PerkinElmer Optoelectronics, Fremont, the United States – California) was irradiated for 6 and 10 MV photon beams. All squares fields (3×3 cm^2, 5×5 cm^2, 8×8 cm^2, 10×10 cm^2, 15×15 cm^2, and 20×20 cm^2) were determined by using Raysearch version 9A treatment planning system (TPS) with collapsed cone convolution superposition algorithm. The sensitive area of imager was 41×41 cm^2 (1024 × 1024 pixels set at pitch of 400 µm). The detector panel used 16-bit ADCs for high dynamic range. Contrast and readout rate of 15 frames per second were performed (1,2). All square fields sizes at 5, 10, and 15 cm depth were assessed in virtual water phantom size of 30×30×30 cm^3. 100 cGy irradiation for each point was conducted by 6 and 10 MV photons. Dose obtained from TPS using reference data was exported to Record and verify (RV) system and PerFRACTION™ to validate point dose. Ion chamber measurement and PerFRACTION™ were compared with reference.

2.1 Ion chamber (IC) measurement

The output of linear accelerator was measured by ion chamber farmer 0.6 cc (PTW, Freiburg) as TRS-398 condition (Equation 1) with SAD technique in one-dimension water phantom. Then PinPoint ion chamber 0.016 cc (PTW, Freiburg) was investigated in water phantom with the same condition using all square fields at depths 5, 10, and 15 cm for 6 and 10 MV photons. All delivered doses obtained from ion chamber measurement were compared with reference.

$$D_{w,D} = k_{TP} \times k_S \times k_P \times k_{elec} \times N_{D,W,Q0} \times k_{Q,Q0} \times M(cGy/MU) \quad (1)$$

where

k_{TP} is factor to correct IC between the standard reference temperature and pressure with the user facility.

k_s is factor to correct IC for the lack of complete charge collection.

k_p is factor to correct of an IC for the effect of a change in polarity of the polarizing voltage applied to the chamber.

k_{elec} is calibration factor of an electrometer.

$_{D,W,Q0}$ is calibration factor in terms of absorbed dose to water for a dosimeter at a reference beam quality Qo.

$k_{Q,Q0}$ is factor to correct for the difference between the response of an ionization chamber in the reference beam quality Qo used for calibrating the chamber and in the actual user beam quality.

M is average reading of dosimeter..

2.2 PerFRACTION™ implementation

EPID dosimetry program used an independent Graphic processing unit accelerated convolution/ superposition algorithm (3). The PerFRACTION™ beam model was created by Sun nuclear corporation. Vender required percentage depth dose, profile, and output factor data for IMRT and VMAT plans to ensure accurate MLC parameters. In pretreatment QA, the program produced an entire dose volume to confirm

data against data from TPS. Fraction 0 was able to perform a 2D dose determination at EPID level.

In this study, the program received data from TPS to evaluate. Measured dose delivered directly to EPID in the air without couch or phantom. In additional, EPID images and log file were reconstructed to confirm point dose. Percentage dose difference between PerFRACTION^{TM} and reference measurement were compared. However, percentage dose difference were calculated as equation 2, and would not exceed than 3% as AAPM TG 119 (4).

$$\text{Percentage dose difference} = \left(\frac{\text{Measured dose} - \text{Pla dose}}{\text{Plan dose}}\right) \times 100 \quad (2)$$

when

Measure dose is data from method that want to study.

Plan dose is data from TPS using reference.

3. RESULTS

For 6 MV, all doses obtained from ion chamber were higher than dose from TPS. **Average of p**ercentage difference between ion chamber and TPS in 6 MV was 1.16±0.59, 0.66±0.24 and 2.21±0.50 for depth 5, 10 and 15 cm, respectively. Percentage differences for depth 5 cm (range 0.65 to 1.21±0.16) and 10 cm (range 0.50 to 1.12) were reasonably close in all field sizes, except 3x3 cm^2. However, higher percentage difference for depth 15 cm (range 1.30 to 2.47) were found in all field sizes compared various depths as shown in Figure 1. Similar trend for 10 MV was presented in Figure 2. A**verage of p**ercentage difference of every field sizes from ion chamber was less than 1.40, except 2.54 at 15 cm depth. Percentage differences between doses obtained from ion chamber and that from TPS in various depths and field sizes were not more than 3%. Percentage differences between doses obtained from PerFRACTION^{TM} and that from TPS were showed in Figure 3-4. Average percentage different showed trend remained relatively stable < 0.74. Percentage differences were found no more than 2% for all depths and field sizes. In 6 MV, slight differences were found ranging from 0.86±0.16 to -1.03±0.12 for 3x3 cm^2 and ranging from -0.27±0.06 to -1.37±0.15 for 5x5 cm^2. The same trend was presented for 10 MV.

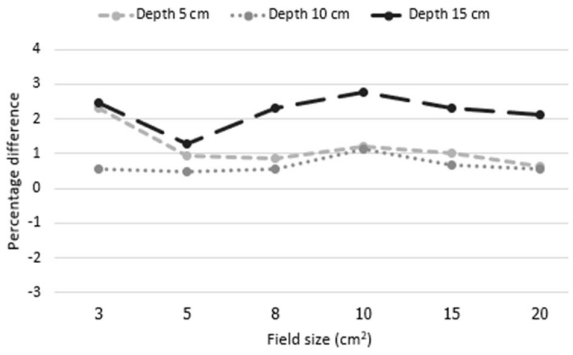

Figure 1 *Percentage difference between doses obtained from ion chamber and doses obtained from TPS in various depths for 6 MV*

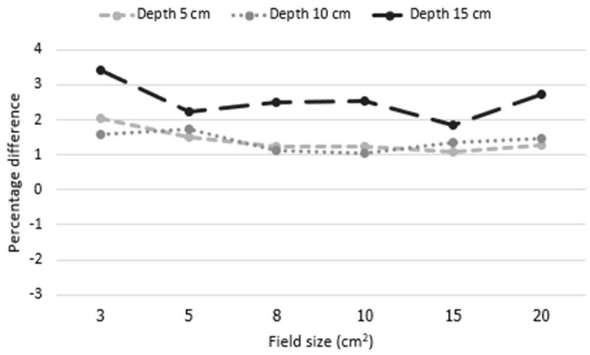

Figure 2 *Percentage difference between doses obtained from ion chamber and doses obtained from TPS in various depths for 10 MV*

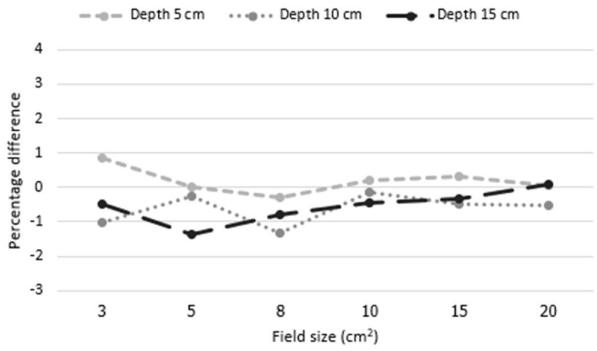

Figure 3 *Percentage difference between doses obtained from PerFRACTION^{TM} and doses obtained from TPS in various depths for 6 MV*

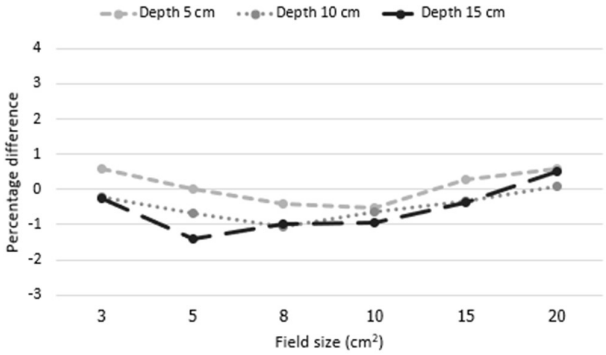

Figure 4 *Percentage difference between doses obtained from PerFRACTION^{TM} and doses obtained from TPS in various depths for 10 MV*

4. DISCUSSION

EPID measured dose was effected by many parameters. Different field sizes, depths and photon energies were investigated in this study. All measured doses obtained from ion chamber were higher compared with that from TPS. This might be received extra dose from central axis due to scatter from collimator and back scatter. The scatter form collimator in small field sizes, less than 5x5 cm^2 did not take into account. Therefore, high percentage difference was found. Size of ion chamber and precision of setup could be considered. In cases of depth 15 cm, it was to be noted that TPS modeling data did not require data deeper than 10 cm. Therefore, all values of percentage difference were high and depth got effect form back scatter than other. Validation of measured dose in depth over than 10 cm should learn more.

Percentage differences between doses obtained from PerFRACTION™ and that from TPS showed interestingly good agreement less than 2%. Small field sizes, 3x3 and5x5 cm^2. had small different values both in two energies, although back scatter effect was not enough. Good agreement of doses obtained from PerFRACTION™ and that from TPS because of using same modelling data and algorithm.

To concluded, point dose measurement from two devices compared dose obtained from TPS were not exceeded 3%. EPID dosimetry program could be use for pretreatment QA. In the future study, gamma index and clinical cases will recommended to examine for EPID dosimetry program.

ACKNOWLEDGEMENTS

Many thanks for all information from Lampang cancer hospital. Authors are very grateful for the cooperate of all staff in the department of radiation therapy.

REFERENCES

1. Limited E. Elekta Medical Linear Accelerator iViewGT™ Instruction for Use2018.
2. Sait AA, Figueredo J, Jones GW, Jones K, McGowan T, Kapatoes J, et al. Validation of three-dimensional electronic portal imaging device-based PerFRACTION™ software for patient-specific quality assurance. Journal of medical physics. 2019;44(1):16.
3. Bresciani S, Poli M, Miranti A, Maggio A, Di Dia A, Bracco C, et al. Comparison of two different EPID-based solutions performing pretreatment quality assurance: 2D portal dosimetry versus 3D forward projection method. Physica Medica. 2018;52:65-71.
4. AAPM. TG-119 IMRT Commissioning Tests Instructions for Planning, Measurement, and Analysis Version 10/21/2009. American Association of Physicists in Medicine. 2009(119).
5. Han B, Ding A, Lu M, Xing L. Pixel response-based EPID dosimetry for patient specific QA. Journal of applied clinical medical physics. 2017;18(1):9-17.
6. Ezzell GA, Burmeister JW, Dogan N, LoSasso TJ, Mechalakos JG, Mihailidis D, Molineu A, Palta JR, Ramsey CR, Salter BJ, Shi J, Xia P, Yue NJ, Xiao Y. IMRT commissioning: multiple institution planning and dosimetry comparisons, a report from AAPM Task Group 119. Med Phys. 2009 Nov;36(11):5359-73

Improvement of the spatial resolution with a deconvolution method in a pinhole SPECT system

Michi Okoshi[1], Kazumi Murata[2], Koichi Ogawa[3]

1 Graduate School of Science and Engineering, Hosei University,
2 National Astronomical Observatory of Japan,
3 Faculty of Science and Engineering, Hosei University

Abstract

We propose a resolution improvement method for a single photon emission CT (SPECT) system. A recently developed SPECT system can be applied for measuring dynamical function of organs owing to the data acquisition method without a detector rotation. Despite the advantage, it has serious problem; the spatial resolution is significantly degraded in case of a large pinhole size. Although a conventional method called 7-rays method for resolution compensation is widely used, the degradation could not be sufficiently corrected. Hence, we propose a new method with a point spread function deconvolution. The feasibility of our method is investigated with an image-reconstruction simulation. We assume a multi-head SPECT system with a pinhole collimator for simplicity. The image corrected with our method shows more detail structures and higher PSNR than the conventional one. These results indicate the effectiveness of our method for improving the spatial resolution of the SPECT system.

Keywords: static SPECT system, deconvolution, point spread function, pinhole collimator

1. INTRODUCTION

To measure the dynamical function of organs, a multi-detector SPECT system with multiple pinholes has generated considerable recent research interest [1], [2]. It can acquire the projection data without rotating the detectors, providing time information in contrast with a conventional SPECT system. However, the image quality is sensitive to pinhole sizes; although a large pinhole improves the sensitivity, it degrades the spatial resolution. A conventional method to compensate the spatial resolution, the 7-rays method [3], has widely been applied. Nonetheless, it could not sufficiently correct the spatial resolution especially in case of a large-pinhole system. Clearly, a new improvement method of the spatial resolution is required.

In this study, we propose a deconvolution method with a point spread function (PSF). The degradation of SPECT images is due to the pinhole size, and a projection of a point source with an infinitesimal pinhole system should be a point image. Hence, we approximate the degradation function as a PSF. In this case, PSF deconvolution on projection domain leads to a significant improvement in spatial resolution. In this study, we investigate the feasibility of this method via an image-reconstruction simulation.

2. METHODS

The simulation was performed with a static multi-head SPECT system. We assumed 18 detectors uniformly set around the target. Each detector had a single pinhole. We did not use a multi-pinhole collimator for the sake of simplicity and only focused on the principal feasibility. The detector size was 512×256 pixels (pixel size was $0.8\,mm \times 0.8\,mm$), the distance between the object center and collimator was 25 cm, and that between the collimator and detector was 7.5 cm. The collimator had a thickness of 1 cm and the diameter of the pinhole was 5 mm. A pinhole has a knife-edge at the half depth of the collimator plate and the aperture angle was 48 degrees in diameter.

The projection data of a brain phantom were obtained with a Monte-Carlo photon transportation. We assumed a perfect detection efficiency and the spatial resolution of the detector to only reproduce the resolution degradation caused by the pinhole collimator. We also assumed a perfect removal of the scattered photons and no energy resolution was considered. We corrected the non-uniformity due to the incident angle of each photon by a Monte-Carlo method (4). Fig. 1 (a) and (b) show example projection images with infinitesimal and 5 mm pinholes, respectively. The latter is clearly blurred owing to the large pinhole size.

To compensate the spatial resolution, we performed a PSF deconvolution on Fourier domain. We analytically estimated the PSF on the detector center, where we assumed that the photons were incident from the target center and the PSF was shift-invariant. The high-frequency component was suppressed by a Butterworth filter with a cut-off frequency of 0.08 (cycles/pixel) and an order of 1.

The image reconstruction was conducted with a maximum likelihood – expectation maximization (ML-EM) method. In this process, we assumed an infinitesimal pinhole as in the deconvolution process. We also reconstructed the image with the 7-rays method using the projection data without a deconvolution process for comparison.

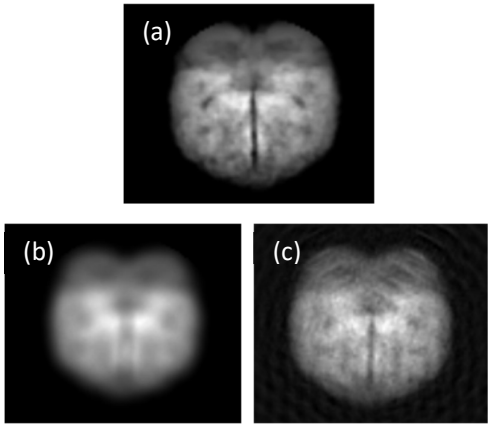

Figure 1 Examples of a projection image : (a) an ideal projection with infinitesimal pinhole, (b) measured with a 5mm pinhole system, and (c) after deconvolution process proposed in this study.

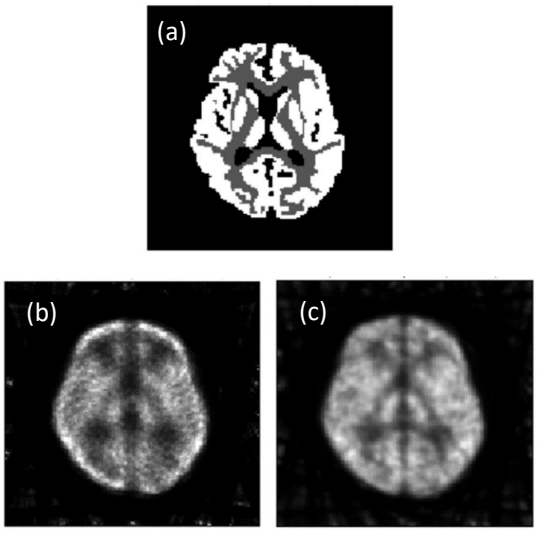

Figure 2 Reconstructed brain images : (a) original image(#70), (b) image corrected with the 7-rays method, and (c) image with proposed method. Our proposed method shows more detail structures than the conventional one and is more similar to the original image than the conventional one.

3. RESULTS AND DISCUSSION

Fig. 1 (c) shows a projection image after the deconvolution process proposed in this study. It is much more similar to the original ideal projection image (a) than that before the deconvolution process (b). Fig. 2 shows the original image (a), reconstructed images corrected with the 7-rays method (b), and with our proposed method (c). The image with our proposed method shows more detail structures than that with the 7-rays method and more similar to the original image than that with the 7-rays method. We evaluated the image quality with a PSNR, and ours had 13.1 dB, higher than the conventional one, 11.7 dB. Fig. 3 shows the horizontal profiles at the center of reconstructed images. Again, our image has a more similar profile to the original one compared with the image corrected with the conventional method. This is because the proposed method is more accurate in estimating the blur caused by the size of a pinhole than the conventional method. These results indicate that the proposed method is effective to compensate the spatial resolution degraded by a large pinhole.

Nonetheless, there is a lot of room for improvement. We assumed only a single pinhole and shift-invariant PSF. A multi-pinhole SPECT system has clearly different PSF at each pinhole, and they are different at different position. They are, therefore, investigated in a future study.

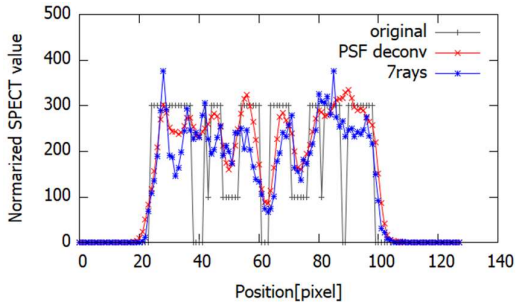

Figure 3 Horizontal profiles at the center of reconstructed images. Ours (red) is more similar to the original one (grey) than conventional one (blue).

4. CONCLUSION

In this study, we proposed a PSF deconvolution method for improving the spatial resolution of a multi-head static SPECT system. The feasibility of out method was investigated with a simulation. The reconstructed image with our method showed more detail structures and higher PSNR than that with a conventional method. These results suggest the effectiveness of the proposed method for improving the spatial resolution of the SPECT system.

ACKNOWLEDGEMENTS

This work was supported in part by JSPS KAKENHI Grant number JP19K12849.

REFERENCES

1. H. Kubota, et al., “Multi-pinhole SPECT system with a triple head gamma camera,” IEEE Nuclear Science Symposium, Medical Imaging Conference (NSS/MIC), DOI:10.1109/NSSMIC.2016.8069609, 2016.
2. Y. Fujishiro, et al., “Comparison of a Multi-pinhole Stationary SPECT System and a Parallel-hole High Speed Rotational SPECT system,” IEEE Nuclear Science Symposium and Medical Imaging

Conference (NSS/MIC), DOI:10.1109/NSSMIC.42101.2019.9059796, 2019.
3. A. Andreyev, et al., "Pinhole SPECT Reconstruction Using Blobs and Resolution Recovery," IEEE Transaction on Nuclear Science, vol. 53, No. 5, pp. 2719-2728, 2006.
4. F. P. Jansen, et al., "Uniformity correction using non-uniform floods," IEEE Nuclear Science Symposium and Medical Imaging Conference (NSS/MIC), pp.2314-2318, 2010.

The effective methods for liver cyst labelling in ultrasound images by using R-CNN

Sutthirak Tangruangkiat[1], Anchali Krisanachinda[2], Supatana Auetavekiat[3]

1 Ph.D. program in Medical Physics, Faculty of Medicine, Chulalongkorn University, Thailand.
2 Department of Radiology, Faculty of Medicine, Chulalongkorn University, Thailand.
3 Department of Electrical Engineering, Faculty of Engineering, Chulalongkorn University, Thailand.

Abstract

Introduction: Ultrasound imaging is one of the most popular medical imaging modality because of its non-ionizing radiation and real time imaging. Deep learning has been successfully applied in medical imaging as computer aided diagnosis (CAD). However, the limitation on ultrasound imaging of the same target can be variable according to the users' technique and the equipment setup, leading to the inaccurate classification.

Purpose: To design the training data for a region-based convolution neural network (R-CNN) for cyst detection in liver ultrasound images.

Methods: R-CNN using ResNet50 as a classifier was used as an object detector. The ground truth of a cyst was provided in two sets. In the first set, only the area of the cyst was used as a ground truth. In the second set, in addition to the cyst, the acoustic enhancement artefact below the cyst, the distinct feature of the cyst, was included into the ground truth. The five-fold cross validation was performed on 615 liver cyst images to evaluate the classification accuracy.

Results: The classification accuracy were 84.39% and 90.73% for the R-CNN trained using only cysts and the combination of a cyst and its enhancement artefact, respectively. There were four main causes of error: (1) the detection of a vessel as a cyst, (2) the detection of acoustic enhancement of other tissues/organs as the border of a cyst, (3) the failure to detect a cyst in low contrast image and (4) the failure to detect the cyst with incomplete border. The errors were reduced when the artefact was included to the training image.

Conclusion: The distinct feature of a target should be included into the training data of R-CNN to improve classification accuracy.

Keywords: Deep learning, ultrasound, liver, artefact, R-CNN

1. INTRODUCTION

The capability of deep learning (DL) to detect and classify pattern leads to the wide adoption of DL in medical imaging. It has been applied in all imaging modals. However, compared to computed tomography (CT), magnetic resonance imaging (MRI) and X-rays, the adoption rate of ultrasound (US) is far less, because US offers lowest image quality and contains ~~much~~ highest noise. Furthermore, the appearance of tissues in US varies not only from the equipment settings (brightness, depth of penetration, pixel size, window width, 2D or 3D, single frame or multi-frames) but also on how an operator directs the US beam. In order to cope with high variation, a large number of training data as well as high performance computer system were required.

Despite the above difficulties, some researchers attempt to design DL using a small dataset (on average, <100 images for each group). Jamieson et al. (1) used adaptive deconvolutional networks (ADN) for tumor classification in breast ultrasound imaging. Zhang et al (2) used convolutional neural network (CNN) in fatty liver classification, while Hassan et al.(3) and Schmauch (4) applied convolutional neural network (CNN) for liver lesion detection. Though radiologists have no difficulty differentiating hepatic cyst and hepatic vessels, the DL often misclassifies these two tissues. Though both tissues are the black area, they appear differently during the scanning. However, the input of DL is the image of one particular instance and the change during the scanning is not available. Radiologists and sonographers can detect a cyst from the posterior acoustic enhancement (Figure 1), which is the brighter region (increased echoes) below the fluid filled structure.

In this paper, we hypothesize that the number of required training images will be reduced, if we include the prior information of posterior acoustic enhancement into the training. Region-based convolution neural network (R-CNN) (5) is used for cyst detection in liver ultrasound images. Five-fold cross validation is used to evaluate the classification accuracy.

2. MATERIALS AND METHODS

615 conventional B-mode liver US images were collected. All images contain at least one cyst. The data were taken by various US machine so the image quality varied. The study was divided into 3 main stages: preprocessing, training and classification experiments.

2.1 Preprocessing

Brightness and contrast were greatly varied among 615 liver US images. In this investigation, all images were normalized such that the mean intensity of abdominal tissues is approximately 70 in 0(black) to 255 (white) scales. First, the patient's information was removed. Then the image was cropped to 442 x 442 pixels. The abdominal tissues were located at the top part of the liver image, so their intensities were approximated form the non-black pixels at the top 20% area (Figure 2B). All pixels were normalized as follows.

$$x_{ij} \leftarrow x_{ij} \times \frac{70}{m},$$

where x_{ij} and m are the intensity at (i,j) and the intensity median of the non-black pixels in the top 20% area, respectively. The effect of the normalization is shown in Figure 2.

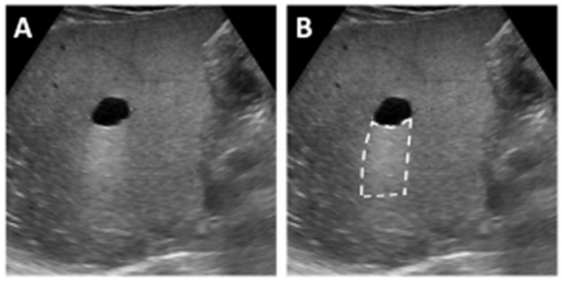

Figure 1 The example of a hepatic cyst. (A) shows an original image and (B) shows the cyst (black oval) and its distinct feature, posterior acoustic enhancement in the dashed line area.

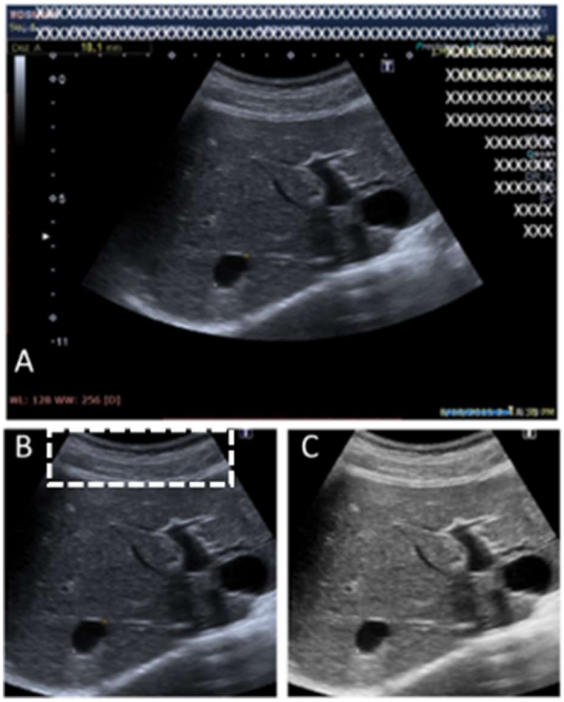

Figure 2. The normalization of input US images. (A) shows the original image. The dashed windows in (B) shows the area used to approximate the intensity of abdominal tissues. The normalized images is depicted in (C).

2.2 Training of R-CNN

Cysts in the training images were labelled by a sonographer with more than 10-year experience. Two training sets were constructed with different region of interest (ROI). In the first set, ROI consisted of only the area of a cyst (the solid window in Figure 3A). In the second set, ROI consisted of both a cyst and its distinct feature, the acoustic enhancement below the cyst (the dashed window in Feature 3B). The first and the second sets were named "Cyst Ground Truth" and "Cyst with Acoustic Enhancement Ground Truth," respectively.

ResNet50 was adopted as the feature extractor in our work. Transfer learning was used to train the last three layers (fully connected, Softmax and the classification layers). In R-CNN, the selective search was applied to find regions in an image to be used for the training. A binary support vector machine (SVM) and the regression model for constructing the bounding box of a detected object was also trained.

All networks were implemented in MATLAB 2019a program on the computer with Intel® Core™ i7-8700 CPU, 16 GB RAM, NVIDIA GeForce GTX 1060 6GB Display Card and MS Windows 10 OS. Stochastic gradient descent method was used for the training. The mini-batch size was set to 32. The training rate was fixed at 0.0001. All networks were trained for 10 epochs, where their training were converged. Since we would like to clearly see the effect of the inclusion of the distinct feature, the negative overlapped range was not fine-tuned. The range was fixed between 0 and 0.3.

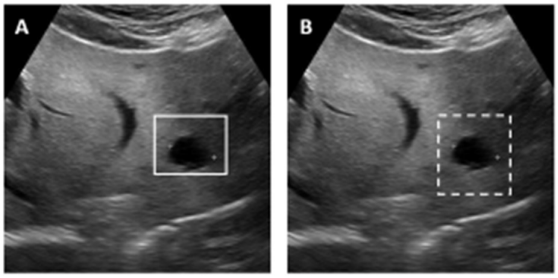

Figure 3 Sample of two training sets in this study. (A) shows the sample in Cyst Ground Truth set. The ROI contains only one cyst. (B) shows the sample in Cyst with Acoustic Enhancement Ground Truth set. The ROI contains both cyst and the bright artefact below the cyst.

2.3 Classification Experiment

Five-fold cross validation was used to evaluate the classification accuracy. 615 images were randomly separated into 5 sets. Each set has 123 images. Four sets were combined to form the training set and the remaining set was used for the testing. Each set was used as the testing set once, so the experiment was repeated 5 times. It should be noted that some images contain more than one cyst. All cysts were used for training, so the number of training data was different in each experiment. We did not attempt to make the number of training data equal in all experiments, because cysts from the same image have similar image characteristics. To equalize the number of training data, we risk getting the bias from having cysts in the same image for both training and testing data.

The parameters used to evaluate the accuracy was the percent of false negative, false positive and true

positive. The positive was the detection of a cyst. So the meaning of the three parameters were as follows.

– False negative is the failure to detect a cyst in an image.
– False positive is the detection of others tissues as a cyst.
– True positive is the correct detection of a cyst.

In this study, we considered the area of a cyst if it has the highest confidence in an image and the confidence was larger than 0.5.

The Pearson's chi-squared (X^2) statistical hypothesis was used X^2 to check whether the parameters were statistically difference.

3. RESULTS

The results of the classifier using Cyst and Cyst with Acoustic Enhancement Ground Truth sets are shown in Table 1. True positive can be considered as the classification accuracy. The addition of the distinct features help increase the accuracy from 84.39% to 90.73% as well as reduce the errors from both the false negative (11.2% to 7.64%) and the false positive (4.39% to 1.63%). The experiment indicated that the Cyst with Acoustic Enhancement was statistically better than the one without enhancement (p-value = 0.001).

Table 1 *Results of the different ground truth labelling for detections.*

Ground truth set	Number of images (percentage)		
	False Negative	False Positive	True Positive*
Cyst	69 (11.2%)	27 (4.39%)	519 (84.39%)
Cyst with Acoustic Enhancement	47 (7.64%)	10 (1.63%)	558 (90.73%)

*True positive was considered as the classification accuracy.

4. DISCUSSION

In this study, data were not augmented. However, when we compared our data to the published articles (2-4), our data (615 images) were much larger and more variations in the equipment settings (ignore demography). From our study, we found four major causes of errors as follows.

(1) Cysts and vessels were similar. In the ultrasound image, main vessels, hepatic veins and portal veins appear as black area, which was the same as a cyst. Though both classifiers mistakenly detected some vessels as cysts (Figures 4A and 5A), the classifier having the information of acoustic enhancement, incorrectly detected only the vessels that closely resembled the cyst (round with acoustic enhancement, Figure 5A). Note that this error was also reported by Schmauch (4).

(2) Acoustic enhancement is not the unique property of a cyst. Organs such as hepatic capsule, diaphragm and esophagus, etc. were also presented with enhanced edge (bright line). In some cases, the classifier mistakenly detected the bright line as the border of a cyst as shown in Figures 4B and 5B.

(3) Cysts were not detected in an image with low contrast. As shown in Figure 4C and 5C, a cyst and its posterior acoustic enhancement were not distinct in the low contrast images. Furthermore, the cyst and vessels are more similar in appearance, so the classifier may also incorrectly detect vessels as a cyst. This error can be reduced if better preprocessing has been used, instead of globally normalizing image intensity based on the non-black pixels at the top 20% area. The top 20% area was fixed and may not reflect the real intensity distribution in the image.

(4) The border of the cyst was missing or blended with the background (hepatic parenchyma) as shown in Figures 4D and 5D.

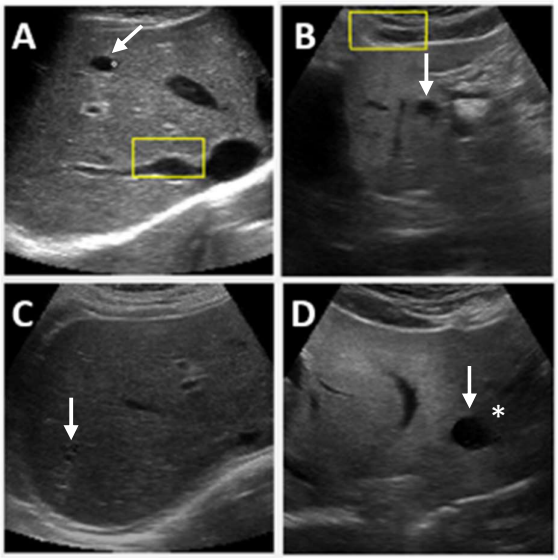

Figure 4 Examples of errors from the classifier trained with Cyst Ground Truth set. Actual cysts were indicated by arrows. The solid box was the cyst detected by the classifier. The classifier detected a branch of right hepatic vein as a cyst in (A) and a part of subcapsular as a cyst in (B). The classifier failed to detect a cyst in an image with low contrast in (C) and a cyst with incomplete border in (D).
* indicates a missing border.

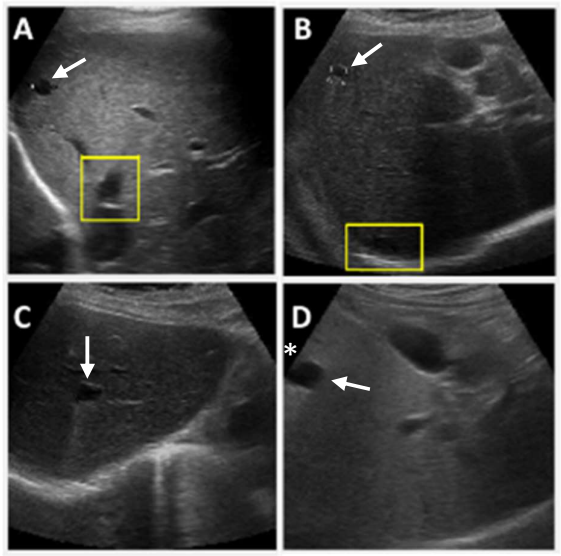

Figure 5 Examples of errors from the classifier trained with Cyst with Acoustic Enhancement Ground Truth set. Actual cysts are indicated by arrows. The windows are the cysts detected by the classifier. The classifier detected a branch of hepatic vein as a cyst in (A) and a part of diaphragm as a cyst in (B). The classifier failed to detect a cyst in an image with low contrast in (C) and a cyst with incomplete border in (D).
* indicates a missing border.

4. CONCLUSION

In this study, we investigated the effect of the inclusion of the distinct feature around the object of interest to the training data. The experiment indicated that the inclusion led to a classifier with higher accuracy. The distinct feature may not be unique to one particular tissue/organ. The classifier may still incorrectly classify other tissues/organs as the object of interest. Therefore, in addition to the area around the object, the image properties of the object should also be investigated and included into the training data.

In addition to the distinct features, the accuracy also depends on the classifier. Currently, the original R-CNN (5) was used. The feature was extracted by ResNet50 which was pre-trained by non-medical images and fine-tuned for the cyst detection. However, medical and non-medical images are greatly different. In this sense, the R-CNN in this study was not the best classifier. The accuracy can also be improved if networks dedicatedly trained or designed for medical images such as Nifty-Net (6) is used.

ACKNOWLEDGEMENTS

The authors would like to express their deepest gratitude to the support fund from Radiological Society of Thailand.

REFERENCES

1. Jamieson A, Drukker K, Giger M, editors. Breast image feature learning with adaptive deconvolutional networks. Medical Imaging 2012: Computer-Aided Diagnosis; 2012: International Society for Optics and Photonics.
2. Zhang L, Zhu H, Yang T, editors. Deep Neural Networks for fatty liver ultrasound images classification. 2019 Chinese Control And Decision Conference (CCDC); 2019: IEEE.
3. Hassan TM, Elmogy M, Sallam E. Diagnosis of focal liver diseases based on deep learning technique for ultrasound images. Arabian Journal for Science Engineering 2017;42:3127-40.
4. Schmauch B, Herent P, Jehanno P, Dehaene O, Saillard C, Aubé C, et al. Diagnosis of focal liver lesions from ultrasound using deep learning. Diagnostic interventional imaging 2019;100:227-33.
5. Girshick R, Donahue J, Darrell T, Malik J, editors. Rich feature hierarchies for accurate object detection and semantic segmentation. Proceedings of the IEEE conference on computer vision and pattern recognition; 2014.
6. Gibson E, Li W, Sudre C, Fidon L, Shakir DI, Wang G, et al. NiftyNet: a deep-learning platform for medical imaging. 2018;158:113-22.

Image reconstruction method based on a deep learning in a multi-pinhole SPECT system

Hiroaki KONNO[1], Michi OKOSHI[1], Kazumi MURATA[2, 3], Koichi OGAWA[2]

1 Graduate School of Science and Engineering, Hosei University,
2 Faculty of Science and Engineering, Hosei University,
3 National Astronomical Observatory of Japan

Abstract

A multi-detector SPECT system equipped with multi-pinhole collimators has great advantages compared with a conventional one owing to a data acquisition without rotating a gamma camera. It reduces the data acquisition time and obtains dynamic information of tracers. However, it has a problem in the image reconstruction; reconstructed images are highly degraded when the size of a pinhole is large. This is caused by the exact detection probability could not be calculated and a correction method such as a 7-rays method could not compensate the influence of the large pinhole size. Hence, a new image reconstruction method is required for the case with a large pinhole collimator. In this study, we propose a deep-learning based image-reconstruction method for a multi-pinhole static SPECT system. Our network successfully reconstructed the images. Our results indicate that the machine-learning based method is effective for the image reconstruction of a multi-pinhole static SPECT system.

Keywords: *SPECT, image reconstruction, deep learning*

1. INTRODUCTION

Recent developments of a static multi-head SPECT system have enabled us to observe the dynamical function of organs. Owing to multi-pinhole collimators equipped with the gamma cameras providing directional information, the system can acquire the projection data without a detector rotation. The stationary data acquisition, furthermore, can reduce the data-acquisition time and motion artifacts.

However, the spatial resolution of the system is sensitive to the pinhole size; a large pinhole leads to significantly blurred images. In principle, this can be compensated with the complete detection probability, that is, the perfect system matrix in the reconstruction process with a maximum likelihood estimation / expected value maximization (ML-EM) method [1]. Nonetheless, it requires huge computational costs which could not be calculated in practical term. On the other hand, the 7 rays method [2] is widely applied, but could not perform a sufficient correction in case of a large-pinhole system.

Currently, deep learning plays an important role in the medical image processing fields, e.g. noise reduction, super-resolution, and image reconstruction [3], [4]. These studies successfully showed significant improvements in image quality owing to the machine learning. As a natural consequence, deep learning would also be effective for image-reconstruction of a multi-pinhole static SPECT system. As far as the authors know, however, no such research has been conducted.

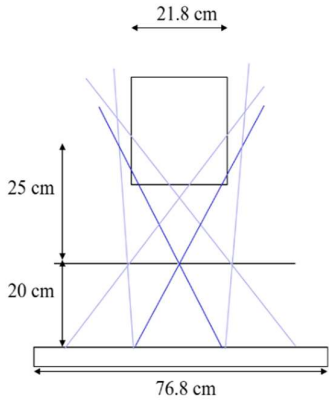

Fig.1 Multi-pinhole geometry. Projected images were acquired using a ray tracing method for a multi-pinhole collimator.

Therefore, in this study, we investigate the feasibility of deep learning for image reconstruction of the SPECT system. We constructed a CNN-based learning network producing reconstructed images from sinograms. The effectiveness of this network was evaluated with a simulation.

2. MATERIAL AND METHODS

We performed an image-reconstruction simulation with a neural network. Following a previous study [5], we applied a geometry shown in Fig. 1. The distance between the target center and collimator was 25 cm and that between the collimator and detector was 20 cm. The detector had 256 pixels and a collimator with three horizontally aligned infinitesimal pinholes. The distance between collimators was 12 cm.

We used a brain phantom (Fig. 2 left) with a size of 128 x 128 x 72 [pixels] (pixel size: 1.7 mm). For the sake of simplicity, each slice was projected to produce sinogram (Fig. 2 right). We added Gaussian noises with 1-10 % onto the sinograms, and produced augmented data set of 720 sinograms, in addition to the original noiseless 72 sinograms. Among them, we used 90 % for training data and 10 % for test data, respectively.

We constructed a network as shown in Fig. 3 in order to reconstruct an image. The network consisted of a convolutional layer, activation function, and batch normalization. The number of convolutional layers was

20, and the basic kernel size was 3 x 3 x 64. We finely adjusted the image size by changing the kernel size to 5 x 5 x 64 in some layers, or by using the max pooling layer or zero padding. The batch size was 32, and the number of learning epoch 2000, Adam was used for parameter update.

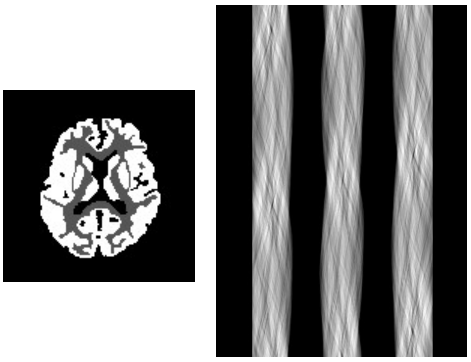

Fig.2 An example of the original image (left) and the sinogram (right).

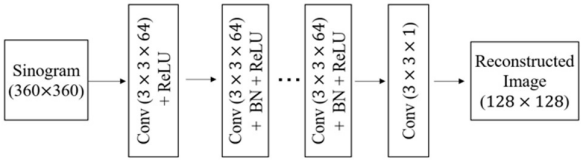

Fig.3 Network architecture. A sinogram is transformed into a reconstructed image through the convolutional layers. Each layer consists of a convolution (Conv), batch normalization (BN), and activation function (ReLU).

3. RESULTS & DISCUSSION

Figure 4 shows example reconstructed images from noiseless (center) and 5.0 % noise (right) sinograms. They are very similar to the original image (left). The relative mean square error between the original and reconstructed image was 1.03 % (noiseless), 1.42 % (5.0 % noise), respectively. Figure 5 shows horizontal profiles at the center of two reconstructed images (blue, red). These profiles are also similar to the original one (black). These results suggest that our network works well for both a noise reduction and improvement of spatial resolution.

Despite the successful reconstruction with deep learning for a multi-pinhole SPECT system shown above, our study has some caveats. Our results were based on small data set and could be affected by overfitting. Furthermore, we assumed a pinhole size of infinitesimal and 2D geometry. These issues will be explored in a future work.

5. CONCLUSION

In this study, we proposed an image reconstruction method with deep learning for a multi-pinhole SPECT system. The network constructed in this study successfully reproduced the reconstructed images. This result indicates that deep learning is effective in the image reconstruction of the system.

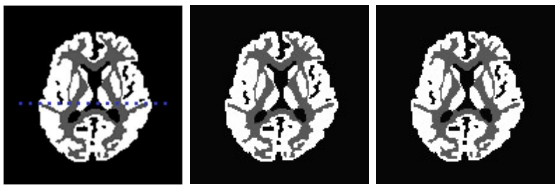

Fig.4 Original image (left), and reconstructed images from noiseless sinogram (center), and from sinogram with 5.0 % noise (right).

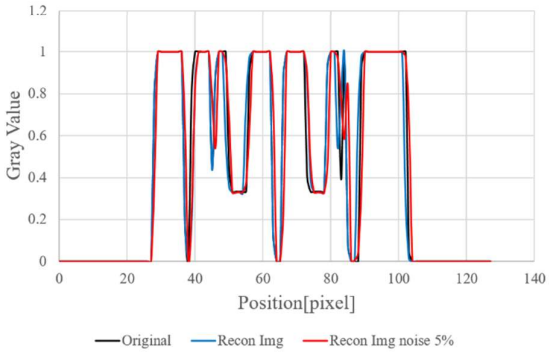

Fig.5 Horizontal profiles of the original image and two different reconstructed images. The similarity of these profiles indicates that the image reconstruction works well even for a noisy sinogram.

ACKNOWLEDGEMENTS

This work was supported in part by JSPS KAKENHI Grant number JP19K12849.

REFERENCES

1. L. A Shepp, Y. Vardi, “Maximum likelihood reconstruction for emission tomography,” IEEE Trans. Med. Imag., vol.1, pp. 113-122, 1982.
2. A. Andreyev, et al., “Pinhole SPECT reconstruction using blobs and resolution recovery,” IEEE Trans. Nucl. Sci., vol. 53, no. 5, pp.2719-2728, 2006.
3. H. Gupta, K. H. Jin, H. Q. Nguyen, M. T. McCann, et al., "CNN-Based Projected Gradient Descent for Consistent CT Image Reconstruction," in IEEE Trans. Med. Imag., vol. 37, no. 6, pp. 1440-1453, 2018.
4. C. Chrysostomou, L. Koutsantonis, C. Lemesios and C. N. Papanicolas, “SPECT Imaging Reconstruction Method Based on Deep Convolutional Neural Network,” IEEE Nuclear Science Symposium and Medical Imaging Conference (NSS/MIC), pp. 1-4, 2019.
5. Y. Fujishiro, et al., “List Mode Image Reconstruction With a Multi-pinhole Triple Head SPECT System,” IEEE Nuclear Science Symposium and Medical Imaging Conference Proceedings(NSS/MIC), 2018.

Preliminary investigation on performance of photodiode sensor as a dosimeter

Nur Farah Huda Zulkafli[1], Yasmin Md. Radzi[1], Ahmad Fairuz Omar[1]

1 School of Physics, Universiti Sains Malaysia, Minden, Penang, Malaysia

Abstract

Radiation dosimetry in the health and medicine field is crucial to ensure there is no unnecessary ionizing radiation exposure to patients and personnel. While various type of semiconductor dosimeters are available, photodiode sensors are seen as a reliable and cost-effective immediate dosimeter. This study investigates the capabilities of a monolithic photodiode with an on-chip trans-impedance amplifier as a dosimeter in diagnostic radiology. A photodiode sensor covered with black insulation tape is irradiated with the diagnostic x-ray of energy range between 40 to 90 kV with constant tube current-time product, 50 mAs at 60 cm source-to-detector distance (SDD). Exposures of different tube current at the range of 10 to 250 mA with a constant tube voltage of 70 kVp at the same setup are made. The photodiode sensor connected to the electrometer gives out reading in the millivolt (mV) and the output of the photodiode and semiconductor detector is recorded. The photodiode's energy dependency, reproducibility, dose response, and distance dependency were evaluated as the capabilities of the photodiode to use as a dosimeter. For energy dependency, it shows the linearity of 0.9458. While for the response to increasing tube current with a constant tube voltage shows the R2 of 0.912. The photodiode shows good dependency on the tube voltage and tube current. Other than that, it also showed a linear coefficient of 0.5138 for distance dependence which is considered as a good linearity fit value for a photodiode as initial performance. However, its reproducibility is poor due to its large capacitance. This monolithic photodiode with an on-chip trans-impedance amplifier has demonstrated good results for energy dependency but poor results for reproducibility. However, the photodiode can be improvised in the future to ensure it is suitable as a dosimeter.

Keywords: radiation dosimetry, dosimeter, photodiode sensor

1. INTRODUCTION

Radiation dosimetry is an important method to measure the exposure of ionizing radiation to the patients, personnel, and the public. To measure and evaluates the ionizing radiation, a radiation detector or dosimeter is used. The dosimeter is the essential equipment required for radiation detection especially in radiation monitoring and radiation protection. Radiation detectors or dosimeters operate in three types of operation modes which are pulse mode, current mode, and voltage mode. The most common mode of dosimeters is the pulse mode. For pulse mode, the signal from each interaction is processed individually thus it is impractical for high event rates because it will increase the dead time and a lot of signals could not be detected [1]. There are properties that a dosimeter must possess at least one for it to function as a radiation dosimeter, which are linearity, precision and accuracy, dose rate dependence, energy dependence, and directional dependence.

In the market, nowadays, various dosimeters had developed over the years, which can be used in specific energy range, type of radiation, and type of detection. There are radiation detectors that provide instant read-outs like survey meter and display accumulated exposure doses such as optically stimulated luminescence (OSL) dosimeter and thermal luminescence dosimeter (TLD). The one that provides instant reading usually uses in radiation protection to inspect leakage or spillage of the radioactive source. TLD and OSLD are the essential dosimeter that is compulsory for workers in the radiation-related department as an example in the oncology department and diagnostic radiology department.

There are various types of dosimeters such as gas-filled detectors and semiconductor detectors. Geiger-Muller survey meter is one kind of gas-filled dosimeter that operates in the Geiger-Muller region. Farmer's type of ionization chamber (IC) is another type of gas-filled detector. It is used in quality assurance in radiotherapy. For semiconductor detectors, there are metal-oxide semiconductor field effect transistor (MOSFET) and silicon diode dosimetry. Both semiconductor detectors usually use for in-vivo dosimetry in radiotherapy due to its small sizes and good energy resolution.

The Silicon diode dosimetry system is used in clinical dosimetry for measurements of depth-dose, dose profiles, and output factors. It is increasingly used for small field dosimetry in modern therapy techniques as they have a very small size of the sensitive volume [2]. Silicon diodes have found utility in radiation dosimetry principally because a diode produces a current approximately 18,000 times that of an ionization chamber of equal sensitive volume [3]. It is mentioned by Yarahmadi, M. et, al., that diode has high spatial resolution and high sensitivity, but it gives response dependence to energy [2]. Unlike MOSFET, the silicon diode dosimetry system is harder to set up since they required a long wire connected from them to the reader for read-out since it provides immediate read-out that is not recorded by any system.

The photodiode is the alternative to the silicon diode dosimeter because it has small size, real-time operation, low cost, high accuracy, and precision attainable in a wide range of doses [4]. The only lack of photodiode is its sensitivity that varied with temperature, dose rate, and its efficiency degrade over

time. In this study, photodiode sensitivity is evaluated by comparing the OPT101 photodiode to the commercialized semiconductor detector, PTW detector. The photodiode is selected as an alternative device for silicon diode dosimetry due to its fundamental properties which are energy dependency and dose linearity.

In term of energy dependency, a study conducted by Oliveira, where they used four photodiodes with different specifications found that there is a higher dependency in the 33 keV up to 100 keV energy range, but it could be the result of attenuation due to the coatings [5]. And there are another two studies found that the photodiode output increases with the tube voltage, at the maximum energy of X-rays [4,6]. While, for dose linearity, a study by Paschoal, Souza, and Santos found that the tested BPW 34S photodiode presents a linear response with air kerma [7]. Also, another study used photodiode found that the output of photodiode linearly proportional to the dose delivered [4]. Therefore, the objectives of this study are to analyze the reproducibility and consistency of OPT101 photodiode performances and to evaluate the OPT101 photodiode efficiency and sensitivity.

2. MATERIAL AND METHODS

The OPT101 monolithic photodiode with built-in transimpedance amplifier as shown in Fig. 1 is used as the sensor for detecting the ionizing radiation from the x-ray machine. This photodiode has a sensitive area of 2.29 mm x 2.29 mm and a large capacitance of 1200 pF. It has high responsitivity to the ambient light with a wavelength of 650 nm. The OPT101 photodiode is connected to the digital multimeter to obtain the output response of the photodiode after being irradiated with the x-rays from Toshiba KX0-50s x-ray machine with energy range from 40 kV to 90 kV. Att 60 cm source-to-detector distance (SDD), a semiconductor detector is also placed to measure the dose received by the photodiode. The OPT101 photodiode and PTW semiconductor detector are placed side-by-side with the same separation from the center of the light field. They are not placed along with the direction of the x-ray tube (anode-cathode) due to the anode heel effect. The PTW detector is connected to an electrometer and gives read-out in mGy unit. The results obtained from the PTW detector and photodiode are compared to investigates the capabilities of the photodiode as a dosimeter.

To ensure the result obtained is not influenced by the ambient light, the photodiode is covered with black tape since the photodiode is sensitive to the ambient light and high responsitivity to the light with a wavelength of 650 nm. Other than that, a lead shield is placed below the photodiode and PTW semiconductor detector to reduce the backscattered radiation from the table. Without the lead shield, the result obtained may be influenced by the backscattered radiation and leads to increases in readings. ***Figure 1*** *demonstrates the experimental setup for this project.*

To evaluate the photodiode performance as a dosimeter, the characterization of the photodiode is assessed. Energy dependence, dose response, distance dependence, and reproducibility of the photodiode are tested. Also, the sensitivity of the photodiode is analyzed by comparing it to a commercialized semiconductor detector, R/F/D PTW semiconductor detector.

The setup for energy dependence, dose response, reproducibility, and sensitivity are the same. However, for energy dependence and sensitivity tests, the tube potential is increasing from 40 kVp to 90 kVp of 10 kVp increment with a fixed tube current of 50 mA. The graph of output-dose response is obtained to evaluate the rate of output response increment with dose, while for the dose response test, the tube current increases from 10 mA to 250 mA fixed tube potential of 70 kVp. For the reproducibility test, where the exposure factors are fixed at 70 kVp and 50 mAs, three exposures are made every day for five consecutive days. Also, the distance dependency test is performed with fixed exposure factors of 70 kVp and 50 mAs, with increasing SDD from 60 cm to 100 cm of 10 cm increment. For sensitivity test, where the dose of the photodiode is comparing to the dose by the PTW R/F/D semiconductor detector, the rate of output increases with dose of the dose-output response is extracted. The characterization of the photodiode is analyzed based on the result obtained.

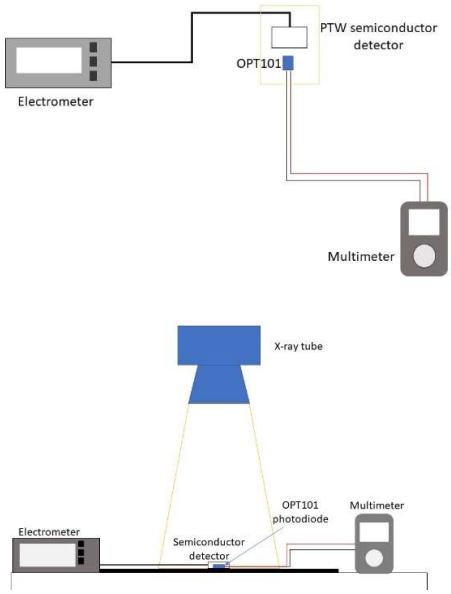

Figure 1 Experimental setup of photodiode and semiconductor detector under the light field of x-ray.

3. RESULTS

3.1 Energy dependency

In the energy dependence study where the tube potential increases by a factor of 10 with a fixed tube current of 50 mA, the result in Fig. 2 showed a linear coefficient of 0.9458, which is a good linear fit value. Fig. 2 also shows the output response of OPT101 photodiode as the tube voltage increases from 40 kVp to 90 kVp. Based on the graph, the output response of photodiode for 40 kVp is greater than 50 kVp, and at 60 kVp and above, the output responses increase with tube potential.

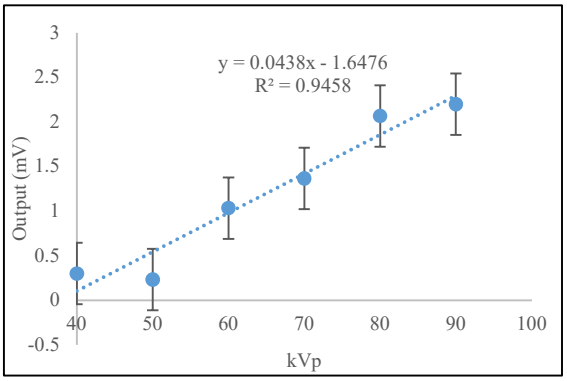

Figure 2 Output response of photodiode as tube potential increases.

3.2 Dose response

Figure 3 presents the result of the output response of OPT101 photodiode with increasing tube current and fixed tube potential of 70 kVp. The graph shows the increasing pattern of the output signals as the tube current increases. As the tube current increases from 10 mA to 20 mA, the increment of the output signals is quite small however, the output signal started increasing above 50 mA to 250 mA. The linear coefficient for dose response of OPT101 photodiode is 0.912, which is a good linearity fit value.

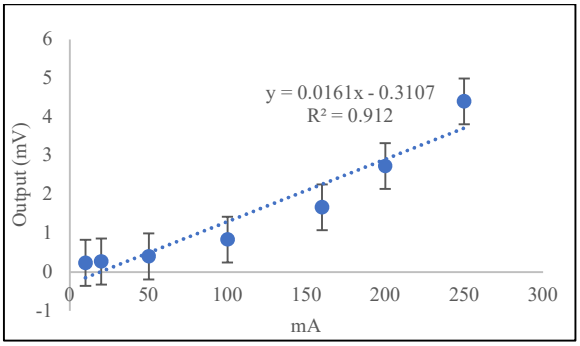

Figure 3 Output response of photodiode with varied tube current

3.3 Distance dependency

Figure 4 shows the output signals of the OPT101 photodiode as the distance between the photodiode and the x-ray source increasing from 60 cm to 100 cm with a 10 cm increment. At 100 cm SDD, the output signal is the lowest while at 70 cm SDD, the output signal is the highest. The linear coefficient for the distance dependence test is 0.5012 which is considerable as low linearity fit value however, it is good enough for a performance of a photodiode. The highest deviation is 1.721 of 70 cm SDD, while the lowest deviation is 0.404 of 80 cm SDD.

3.4 Reproducibility

Figure 5 presents the reproducibility of the output response of OPT101 photodiode with the same technical factors of 70 kVp, 50 mAs, and 60 cm SDD. The readings are taken for five days. The graph shows the linear coefficient for reproducibility is 0.5138, and a standard deviation of 2.0220. The value of linearity fit is low since the deviation is large.

3.5 Sensitivity

Figure 6 presents the graph of output response to dose with a linear coefficient of 0.9711 which shows that the output response of photodiode proportional to dose. The higher the dose, the greater the output signal detected by the photodiode. While Figure 7 presents the graph for measured doses of OPT101 photodiode and PTW detector. The dose measured by the PTW detector increases as the energy increases. However, for the photodiode, the increase of output signals as the energy increases are not noticeable. In terms of sensitivity, the PTW detector is more sensitive than the OPT101 photodiode since the slope of the increment of the dose is steeper than the slope of the photodiode.

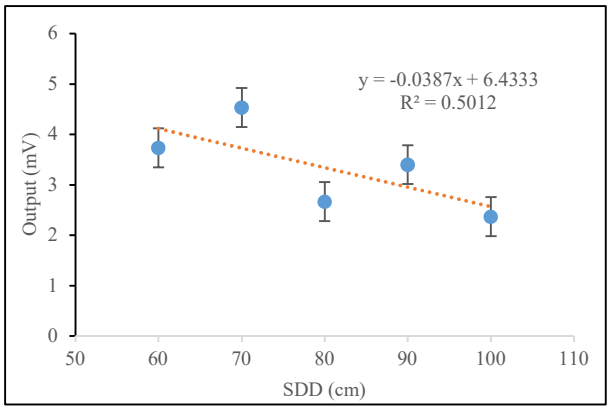

Figure 4 Output response of photodiode to variation in distance.

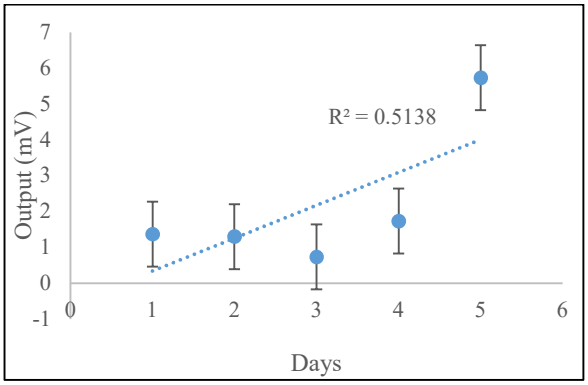

Figure 5 The result for reproducibility of the photodiode for five days

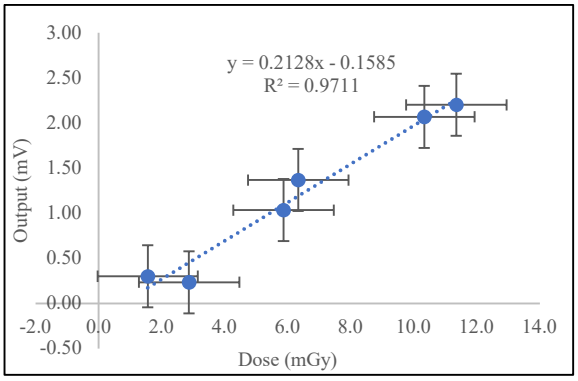

Figure 6 Dose-output response to increasing energy.

4. DISCUSSION

For the energy dependence test where the tube potential increases from 40 kVp to 90 kVp, the output response of the photodiode increases with the tube potential. Tube potential indicates the energy of the photons. The greater the tube potential, the higher the energy of the photons. Thus, the photodiode's output response increases as the energy increases. A study by Nazififard, Suh and Mahmoudieh also has the same finding where they stated that the PIN photodiode output increases with tube potential that is the maximum energy of x-rays [6].

In dose response test, radiation exposure is made at a fixed 70 kVp and increasing tube current, from 10 mA to 250 mA. The tube current indicates the number of photons. Therefore, the higher the tube current, the greater the number of radiation-generated carriers collected by the electrometer since the number of photons increases with tube current. The good linear coefficient for increasing tube current for OPT101 photodiode coincide with the findings from Damulira's study where the number of charges drift in PN junctions was linear to the number of photons in the x-ray beam [8].

Distance plays role in measuring radiation exposure. Based on inverse square law, where the greater the distance between the x-ray source and the detector, the lower the intensity of radiation. In this work, the tested photodiode showed a linear coefficient of 0.5138 on the increasing distance, SDD due to the high capacitance of photodiode. The linear fit value is considered a good response for varied distances for a photodiode. The distance dependence of the photodiode is related to the Compton effect and photoelectric effect that occurs during the irradiation of the photodiode.

OPT101 photodiode showed poor reproducibility when it was tested for five consecutive days. The large capacitance of the photodiode leads to poor reproducibility due to the storage of charges. The discharge of stored charges leads to fluctuation of the output signal of the photodiode that resulted in a large deviation.

Lastly, the OPT101 photodiode has poor sensitivity since the increasing dose measured by the photodiode is small and not noticeable due to the low output signals. To increase the output response of the photodiode, adding numbers of photodiodes will improve the sensitivity.

5. CONCLUSION

In this paper, the experimental evaluation of the OPT101 photodiode is performed to assess its performance as an immediate dosimeter. The OPT101 photodiode displays a good linear coefficient for energy dependence and dose response. For distance dependence, even though the linear coefficient is poor, it is considered good enough for a photodiode. The response of the photodiode to distance still could be improved. However, the OPT101 photodiode showed poor reproducibility and sensitivity. Since OPT101 photodiode possesses the properties of the dosimeter, further study could be performed to improvise the photodiode to be used as an immediate dosimeter.

ACKNOWLEDGEMENTS

The authors appreciate the School of Physics, Universiti Sains Malaysia for full support of this project.

CONFLICT OF INTEREST

The authors have no conflict of interest to disclose.

REFERENCES

1. Seco, J., Clasie, B., & Partridge, M. (2014). Review on the characteristics of radiation detectors for dosimetry and imaging. Physics in Medicine and Biology, 59(20), R303–R347. https://doi.org/10.1088/0031-9155/59/20/R303
2. Yarahmadi, M., Wegener, S., & Sauer, O. A. (2016). Energy and field size dependence of a silicon diode designed for small-field dosimetry. 1. https://doi.org/10.1002/mp.12195
3. Dixon, R. L., & Ekstrand, K. E. (1982). Silicon diode dosimetry. The International Journal of Applied Radiation And Isotopes, 33(11), 1171–

1176. https://doi.org/10.1016/0020-708X(82)90242-3
4. Romei, C., Di Fulvio, A., Traino, C. A., Ciolini, R., & d'Errico, F. (2015). Characterization of a low-cost PIN photodiode for dosimetry in diagnostic radiology. Physica Medica, 31(1), 112–116. https://doi.org/10.1016/j.ejmp.2014.11.001
5. Oliveira, C. N. P., Khoury, H. J., & Santos, E. J. P. (2016). PiN photodiode performance comparison for dosimetry in radiology applications. Physica Medica, 32(12), 1495–1501. https://doi.org/10.1016/j.ejmp.2016.10.018
6. Nazififard, M., Suh, K. Y., & Mahmoudieh, A. (2016). Experimental analysis of a novel and low-cost pin photodiode dosimetry system for diagnostic radiology. Review of Scientific Instruments, 87(7). https://doi.org/10.1063/1.4955170
7. Paschoal, C. M. M., Souza, D. N., & Santos, L. A. P. (2011). Characterization of three photodetector types for computed tomography dosimetry. World Academy of Science, Engineering and Technology, 80(8), 92–95.
8. Damulira, E., Yusoff, M. N. S., Omar, A. F., & Taib, N. H. M. (2019). A review: Photonic devices used for dosimetry in medical radiation. Sensors (Switzerland), 19(10), 1–28. https://doi.org/10.3390/s19102226
9. AAPM Report No. 87. (2005). Diode in vivo dosimetry for patients receiving external beam radiation therapy: Report of Task Group 62 of the Radiation Therapy Committee. In Medicine (Vol. 87, Issue 87).
10. Ahmed, S. N. (2007). Physics and Engineering of Radiation Detection. Academic Press Inc.
11. Asensio, L. J., Carvajal, M. A., López-Villanueva, J. A., Vilches, M., Lallena, A. M., & Palma, A. J. (2006). Evaluation of a low-cost commercial mosfet as radiation dosimeter. Sensors and Actuators, A: Physical, 125(2), 288–295. https://doi.org/10.1016/j.sna.2005.08.020
12. Attix, F. H. (2004). Introduction To Radiological Physics and. John Wiley & Sons, Inc, 1–607.
13. Bower, M. W. (n.d.). THE CHARACTERIZATION OF A COMMERCIAL MOSFET.
14. Damulira, E., Yusoff, M. N. S., Omar, A. F., & Taib, N. H. M. (2019). A review: Photonic devices used for dosimetry in medical radiation. Sensors (Switzerland), 19(10), 1–28. https://doi.org/10.3390/s19102226
15. Emirhan, E., Bayrak, A., Yücel, E. B., Yücel, M., & Ozben, C. S. (2016). A low cost X-ray imaging device based on BPW-34 Si-PIN photodiode. Nuclear Instruments and Methods in Physics Research, Section A: Accelerators, Spectrometers, Detectors and Associated Equipment, 819, 1–5. https://doi.org/10.1016/j.nima.2016.02.022
16. Izweska, J., & Rajan, G. (2003). Radiation Dosimetry. https://doi.org/10.1016/B978-012436603-9/50020-X
17. Kumar, A. S., Sharma, S. D., & Ravindran, B. P. (2014). Characteristics of mobile MOSFET dosimetry system for megavoltage photon beams. Journal of Medical Physics, 39(3), 142–149. https://doi.org/10.4103/0971-6203.139002
18. OMNES, F. (2009). Introduction to Semiconductor Photodetectors. In D. Decoster & J. Harari (Eds.), Optoelectronic Sensors (Issue January, pp. 175–437). https://doi.org/https://doi.org/10.1002/9780470611630.ch1
19. Rosenfeld, A. B., Lerch, M. L. F., Kron, T., Brauer-Krisch, E., Bravin, A., Holmes-Siedle, A., & Allen, B. J. (2001). Feasibility study of online high-spatial-resolution MOSFET dosimetry in static and pulsed X-ray radiation fields. IEEE Transactions on Nuclear Science, 48(6 I), 2061–2068. https://doi.org/10.1109/23.983173
20. Shi, J., Simon, W. E., & Zhu, T. C. (2003). Modeling the instantaneous dose rate dependence of radiation diode detectors. Medical Physics, 30(9), 2509–2519. https://doi.org/10.1118/1.1602171
21. Suyama, M. (2015). Optoelectronic sensors. In Handbook of Optical Metrology: Principles and Applications, Second Edition. https://doi.org/10.1201/b18328-3
22. Thomson, I., Thomas, R. E., & Berndt, L. P. (1983). Radiation Dosimetry with MOS Sensors. In Radiation Protection Dosimetry (Vol. 6, Issues 1–4, pp.121–124). https://doi.org/10.1093/oxfordjournals.rpd.a082883
23. Vicoroski, N., Espinoza, A., Duncan, M., Oborn, B. M., Carolan, M., Metcalfe, P., Menichelli, D., Perevertaylo, Vladimir L., M. L. F. L., Rosenfeld, A. B., & Petasecca, M. (2016). Development of a Silicon Diode Detector for Skin Dosimetry in Radiotherapy. https://doi.org/10.1002/mp.12469

Flexible, Lightweight and Lead-free Radiation Shielding for Nuclear Medicine from Natural Rubber with Barium Sulfate Composite

Nattha Plangpleng[1], Kartpan Sakulkaew[2], Nichapa Buasuwan[2], Putthiporn Charoenphan[3], Krisanat Chuamsaamarkkee[3*]

1 Master of Science Program in Medical Physics, Department of Diagnostic and Therapeutic Radiology, Faculty of Medicine Ramathibodi Hospital, Mahidol University, Thailand,
2 Department of Science Services, Ministry of Higher Education, Science, Research and Innovation, Thailand,
3 Division of Nuclear Medicine, Department of Diagnostic and Therapeutic Radiology, Faculty of Medicine Ramathibodi Hospital, Mahidol University, Thailand
**Corresponding Author – Krisanat Chuamsaamarkkee (E-mail krisanat.chu@mahidol.ac.th)*

Abstract

Radiation shielding is an important tool for the protection of patient and medical staffs from ionizing radiation. Flexible, lightweight and lead-free radiation shielding was developed for replacement of lead shielding. Natural rubber with barium sulfate ($BaSO_4$) of 0, 10, 20, 30 and 50 parts per hundred of natural rubber (phr) were studied the physical and mechanical properties. The shielding properties of these shielding were measured using NaI(Tl) scintillation detector with ^{57}Co (122.06 keV) and ^{133}Ba (356.01 keV) in nuclear medicine. The results showed that increasing of $BaSO_4$ into natural rubber raised the hardness and density whereas the flexible properties were reduced. For radiation shielding properties, the mass attenuation coefficient (μ_m) were found to increase with the $BaSO_4$ concentration for ^{57}Co and ^{133}Ba radionuclides. The highest mass attenuation coefficient was observed in natural rubber with $BaSO_4$ 50 phr, the μ_m were calculated to be 0.29 cm^2/g and 0.21 cm^2/g for ^{57}Co and ^{133}Ba respectively. Natural rubber with $BaSO_4$ showed a promising result for developing potential shielding in nuclear medicine due to their flexibility, lightweight and lead-free composite. However, it is important to note that this study used the ^{57}Co and ^{133}Ba to represent the energy peak of ^{99m}Tc and ^{131}I respectively. Hence, it might not be the same in the term of radioactivity.

Keywords: Natural rubber, Barium sulfate, Flexible shielding, Radiation shielding

1. INTRODUCTION

The radiation usages in diagnostic and therapeutic nuclear medicine have been increasing in the past decades. Indeed, not only the number of procedures is increasing but also the staff radiation exposure (e.g. nuclear medicine physician, radiopharmacist, technologist and nurse) is elevating. According to the United Nations Scientific Committee on the Effects of Atomic Radiation (UNSCEAR), the average annual dose for radiation workers was 0.86 to 1.14 mSv per year in the 1990s [1]. After 21st Century, there were increasing used of hybrid imaging equipment, positron emission tomography and therapeutic radiopharmaceuticals. Then, the data of nuclear medicine department around the world as well as the International Agency of Atomic Energy (IAEA) report showed that the average annual radiation exposure from nuclear medicine worker was ranged from 3 – 5 mSv [2-3]. Consequently, the demand for radiation protection equipment has also been raising in order to protect the radiation worker as well as the patient from unnecessary radiation exposures [4].

Generally, lead shielding is the preferred material because it can provide the efficient high atomic number, high density with greatest attenuated radiation [5-6]. On the other hand, lead is heavy and cause health problems due to its toxicity which may present an insidious hazard in the production process and environmental problem after waste disposal. For these reasons, many research groups have been growing interest in the development and study on materials that could replace lead for radiation shielding [7]. Practically, most of lead shielding used in nuclear medicine is heavy, sharp edges and inflexible making shield inconvenient. Consequently, nonlead-rubber material is attractive material as the rubber could add with the filler composition such as iron oxide (Fe_3O_4), tungsten oxide (W_2O_3), bismuth oxide (Bi_2O_3) and barium sulfate ($BaSO_4$) for possible use as lead-free flexible shielding [8-11]. In hospital, barium sulfate is used clinically as contrast agent for the upper gastrointestinal tract study [12]. Additionally, barium sulfate is non-toxic material and low cost which is suitable for using as filler particles.

Therefore, this work aims to develop novel flexible, lightweight and lead-free shielding from natural rubber with barium sulfate composite for radiation shielding mainly for the standard radiation sources of ^{57}Co (122.06 keV gamma rays) and ^{133}Ba (356.02 keV gamma rays) which represent the commonly used radionuclides in nuclear medicine ^{99m}Tc (140.50 keV gamma rays) and ^{131}I (364.49 keV gamma rays) respectively. This work also aims to study the physical and mechanical properties of natural rubber with barium sulfate composite for different filler concentration in order to optimize the filler concentration for flexible application in nuclear medicine.

2. MATERIAL AND METHODS

2.1 Production of lead-free flexible shielding material

Natural rubber (Standard Thai Rubber Grade 5L or STR 5L) used in this work was provided by Department of Science Services, Ministry of Higher Education, Science, Research and Innovation. The chemical grade $BaSO_4$ as a filler was purchased from Gammaco (Bangkok, Thailand). $BaSO_4$ has a high purity (>97.0 wt%) with average particle size of 0.4 micrometer.

Natural rubber was masticated using the Two roll mill (Gumix, Barcelona, Spain) at temperature of 60 °C. The masticated natural rubber was mixed with the other chemicals including processing aid, accelerator, activator, vulcanizing agent and filler particles until all chemicals uniformly dispersed. In this work, natural rubber composites of 0, 10, 20, 30 and 50 phr (parts per hundred of rubber) were prepared. To produce the 2 mm thickness with 10×10 cm^2 of natural rubber composite sheet, the hot compression molding (Model C, Carver, USA) at the temperature of 160 °C (according to ASTM D5289) with a hydraulic pressure was used.

2.2 Physical and mechanical properties

All rubber composites were tested the tensile properties including tensile modulus and elongation at break using universal testing machine (Zwick/Roell, model Z005, Singapore) according to ASTM (American Society for Testing and Materials) D412. The density was measured using the procedures of ASTM D792.

2.3 Radiation attenuation properties

As stated earlier, the standard sources ^{57}Co (122.06 keV gamma rays) and ^{133}Ba (356.01 keV gamma rays) were used in this work to represent the gamma rays of ^{99m}Tc (140.50 keV) and ^{131}I (364.49 keV). The 3 inch x 3 inch NaI(Tl) scintillation detector (ORTEC, USA) was used in this work. Linear attenuation coefficient for each sample was test using a narrow beam geometry. The thin sheet of natural rubber was placed between a radiation beam and scintillation detector, the transmitted gamma ray intensity (I_1) was recorded, then, the thin sheet of natural rubber was added. The transmitted gamma ray intensity (I_2) was recorded. In this work, the five thin sheets were added, then, the graph between ln (I_2/I_1) and thickness have been drawn using Microsoft Excel (Microsoft Office 365, version 13231.20418). According to the well-known Lambert's law (equation 1). The linear attenuation coefficient was obtained from slope of graph and the mass attenuation coefficient (μ_m) was also calculated using equation (2). The half-value layer (HVL) was also calculated using equation (3). The density (ρ) of the shielding was obtained from previous part.

$$\ln\left({}^{I_2}/_{I_1}\right) = -\mu x \quad (1)$$

$$\mu_m = {}^{\mu}/_{\rho} \quad (2)$$

$$HVL = \ln 2/\mu \quad (3)$$

3. RESULTS

In this work, the natural rubber was filled with $BaSO_4$ concentration of 0, 10, 20, 30 and 50 phr. The 2 mm thickness with 10×10 cm^2 sheet of shielding was produce. The density and weight for each sheet is illustrated in Table 1. In addition, the tensile modulus and elongation at break were tested to evaluate the flexible property of novel shielding.

The tensile modulus and elongation at break of a natural rubber flexible shielding with different filler concentration (unit of phr) are plotted in Figure 1 and 2 respectively.

Table 1 *Density and weight (2 mm thickness with 10×10 cm^2 sheet) of natural rubber with $BaSO_4$ of 0, 10, 20, 30 and 50 phr.*

Filler concentration (phr)	Density (g/cm^3)	Weight (g)
0	0.961 ± 0.002	1.32 ± 0.05
10	1.023 ± 0.001	1.46 ± 0.06
20	1.073 ± 0.002	1.52 ± 0.01
30	1.139 ± 0.002	1.68 ± 0.03
50	1.250 ± 0.001	1.84 ± 0.02

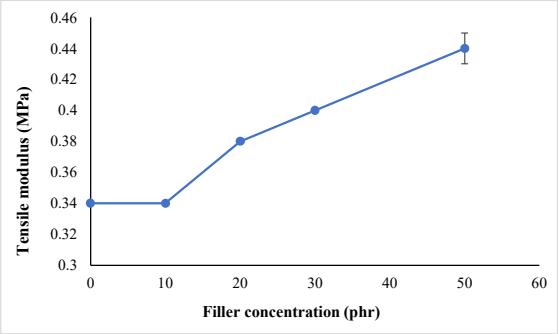

Figure 1 *Tensile modulus of natural rubber shielding with $BaSO_4$ of 0, 10, 20, 30 and 50 phr.*

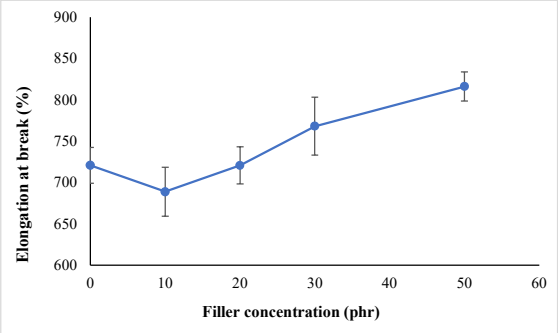

Figure 2 *Percentage elongation at break of natural rubber shielding with $BaSO_4$ of 0, 10, 20, 30 and 50 phr.*

For shielding properties of 122-keV and 356-keV gamma radiation, the mass attenuation coefficient as a function of $BaSO_4$ filler concentration are illustrated in

Figure 3. The results showed that the increasing of filler concentration improved the radiation attenuation properties as seen by mass attenuation coefficient. The highest mass attenuation coefficient was observed in natural rubber with $BaSO_4$ 50 phr for ^{57}Co and ^{133}Ba radionuclides. Moreover, ^{57}Co which emitted 122.06 keV gamma-ray obtained higher the ability to shield radiation than ^{133}Ba which emitted 356.01 keV gamma-ray. The half-value layer (HVL) was calculated from linear attenuation coefficient are shown in Table 2 and 3 for ^{57}Co and ^{133}Ba respectively.

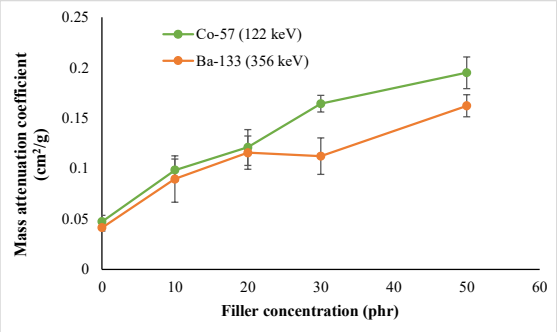

Figure 3 *Mass attenuation coefficient of natural rubber with $BaSO_4$ of 0, 10, 20, 30 and 50 phr.*

Table 2 *Linear attenuation coefficient (μ), mass attenuation coefficient (μ_m) and HVL of natural rubber with $BaSO_4$ of 0, 10, 20, 30 and 50 phr for ^{57}Co.*

Filler (phr)	μ (cm^{-1})	μ_m (cm^2/g)	HVL (cm)
0	0.05 ± 0.01	0.05 ± 0.01	15.26 ± 2.09
10	0.10 ± 0.01	0.10 ± 0.01	6.88 ± 0.77
20	0.13 ± 0.02	0.12 ± 0.02	5.34 ± 0.78
30	0.19 ± 0.01	0.16 ± 0.01	3.70 ± 0.19
50	0.24 ± 0.02	0.20 ± 0.02	2.84 ± 0.23

Table 3 *Linear attenuation coefficient (μ), mass attenuation coefficient (μ_m) and HVL of natural rubber with $BaSO_4$ of 0, 10, 20, 30 and 50 phr for ^{133}Ba.*

Filler (phr)	μ (cm^{-1})	μ_m (cm^2/g)	HVL (cm)
0	0.04 ± 0.00	0.04 ± 0.00	17.48 ± 1.36
10	0.09 ± 0.02	0.09 ± 0.02	7.56 ± 1.94
20	0.12 ± 0.02	0.12 ± 0.02	5.58 ± 0.79
30	0.13 ± 0.02	0.11 ± 0.02	5.42 ± 0.87
50	0.20 ± 0.01	0.16 ± 0.01	3.42 ± 0.23

4. DISCUSSION

As shown in Table 1, the density and weight of the 2 mm thick (10 × 10 cm^2) natural rubber composites increased, as the $BaSO_4$ filler concentration raised. According to manufacturer specification, the density of $BaSO_4$ is ranged from 4.25 – 4.50 g/cm3, whereas the density of natural rubber (no filler) was reported to be 0.961 ± 0.002 g/cm3.

The tensile modulus and elongation at break were investigated to indicate the flexible properties of shielding material. Our results showed that the value of tensile modulus increased with respect to filler concentration. Previous works used different fillers found similar results [9-11]. This might be due to interaction between the intercross-linking chains of natural rubber and filler particles [13]. In general, the high tensile modulus indicates that the material is resisted elastic deformation. In addition, the percentage elongation at break (also known as “fracture strain”) is related to resist changes of shape without cracking. Our findings showed similar trends with other published works. Principally, the dense nature of $BaSO_4$ filler caused in reducing the flexibility properties of natural rubber, thus the elongation at break should be decreased. However, the large variation (high standard deviation) in Figure 2 might be related to the heterogenous distribution of $BaSO_4$ fillers [10-11].

For radiation shielding properties, the μ was obtained from the slope of the values of ln (I_2/I_1) plotted against thickness of the natural rubber shielding. Then, the values μ_m and HVL were later calculated. Regarding to our results, the radiation shielding properties were escalated as the increasing of $BaSO_4$ filler concentration. These were indicated by increase in the values μ of and μ_m and decrease in the values of HVL. Our results showed that the values of μ_m were surged 4.1 and 3.9 times when compared 0 and 50 phr for 122.06 keV gamma rays from ^{57}Co and 356.01 keV from ^{133}Ba respectively. Additionally, the shielding ability to shield lower energy gamma rays from ^{57}Co was better than higher energy gamma rays from ^{133}Ba due to the stronger probability of gamma interactions for the lower-energy gamma ray. It is worth reminding here that the effective atomic number of natural rubbers with barium composite (atomic number of $BaSO_4$ 56) is increased from the pure natural rubber. Therefore, the adding high atomic number filler particles into natural rubber improved radiation shielding properties. In addition, amount of filler particles can increase the probability of gamma-ray interaction [14].

It also can be seen in Figure 3 that the ability of radiation shielding also depended on the gamma-ray energy. In nuclear medicine practice, the two most used radionuclides are the ^{99m}Tc and ^{131}I which emitted gamma ray energy 140.50 keV and 364.49 keV respectively. In this work, the ^{57}Co and ^{133}Ba were used to simulate the most common gamma ray energies. The experimental values of μ_m of natural rubber with $BaSO_4$

filler of 50 phr were calculated to be 0.29 cm^2/g and 0.21 cm^2/g for ^{57}Co (122.06 keV) and ^{133}Ba (356.01 keV) respectively. This indicated that the μ_m decreased with the increasing of gamma ray energy. As the primary interaction in shielding is the photoelectric effect, thus, the probability of the photoelectric effect is decreased with increasing of gamma-ray energy [5-6,9].

It is worth reminding hear that the flexible properties (tensile modulus and elongation at break) still maintain at 50 phr, hence adding more filler is still possible. This could improve the radiation properties of the novel shielding. Future research is needed to confirm this. The application in nuclear medicine practice should also further develop for example the flexible shielding sheet or lead glove from natural rubber with $BaSO_4$ composite.

5. CONCLUSION

Natural rubber with $BaSO_4$ composites showed a promising result for developing potential radiation shielding material for radiation protection in nuclear medicine. It is less toxic material compare with conventional lead shielding and also offers many attractive properties for example flexibility and lightweight. However, it is important to note that this study used the ^{57}Co and ^{133}Ba to represent the energy peak of ^{99m}Tc and ^{131}I respectively. Hence, it might not be the same in the term of radioactivity. Further study could be focused on enhancing the shielding properties by increasing the concentration of $BaSO_4$ filler or adding novel composites such as nanofiller in natural rubber and testing the shielding with the clinical used radionuclide.

ACKNOWLEDGEMENTS

Some material and equipment in this work were supported by Department of Science Services, Ministry of Higher Education, Science, Research and Innovation, Thailand.

REFERENCES

1. Charles, M., UNSCEAR Report 2000: sources and effects of ionizing radiation. Journal of Radiological Protection, 2001; 21(1): p. 83.
2. McEwan, A., Assessment of occupational exposure in New Zealand from personal monitoring records. Radiation Protection in Australasia, 2000; 17(2): p. 60-66.
3. Etherington, G., et al., Technical recommendations for monitoring individuals for occupational intakes of radionuclides. Radiation protection dosimetry, 2016; 170(1-4): p. 8-12.
4. Holmberg, O., R. Czarwinski, and F. Mettler, The importance and unique aspects of radiation protection in medicine. European journal of radiology, 2010; 76(1): p. 6-10.
5. McAlister DR. Gamma ray attenuation properties of common shielding materials, University Lane Lisle, USA; 2018
6. Nelson G, Reilly D, Gamma-Ray Interactions with Matter, in Passive Nondestructive Analysis of Nuclear Materials, Los Alamos National Laboratory, NUREG/CR-5550, LAUR-90-732 ,1991:p.27-42.
7. Wani AL, Ara A, Usmani JA. Lead toxicity: a review Interdisciplinary Toxicology. 2015; 8(2): p. 55-64.
8. Jaiyen S, Phumsuwan A, Thongpool V, Phunpueok A. Determination of Radiation Attenuation Coefficients of Rubber Containing Barite. Applied Mechanics and Materials. 2017; 866: p. 204-207.
9. Intom S, Kalkornsurapranee E, Johns J, Kaewjaeng, S, Kothan S, Hongtong W, Chaiphaksa W, Kaewkhao J. Mechanical and radiation shielding properties of flexible material based on natural rubber/Bi_2O_3 composites. Radiation Physics and Chemistry. 2020; doi:org/10.1016/j.radphyschem.2020.108772
10. Toyen D, Rittirong A, Poltabtim W, Saenboonruang K. Flexible, lead-free, gamma-shielding materials based on natural rubber/metal oxide composites. Iranian Polymer Journal. 2018; 27: p. 33-41.
11. Lim P, Wimolmala E, Sombatsompop N, Saenboonruang K. Manufacturing process and properties of lead-free natural rubber sponge for use in X-ray and gamma ray shielding applications. IOP Conference Series: Materials Science and Engineering. 2019; 526: p. 012-015. doi:10.1088/1757-899x/526/1/012015
12. Diós P, Szigeti K, Budán F, Pócsik M, Veres D, Máthé D, Nagy S. Influence of barium sulfate X-ray imaging contrast material on properties of floating drug delivery tablets. European Journal of Pharmaceutical Sciences. 2016; 95: p. 46-53.
13. Zhao F, Bi W, Zhao S. Infuence of crosslink density on mechanical properties of natural rubber vulcanizates. J Macromol Sci. 2011; 50: p. 1460-1469.
14. Saion E, Sulaiman ZA, Sulaiman MY. Gamma-ray attenuations in natural rubber. Journal of Natural Rubber Research. 1994; 9(1): p. 13-22.

Predicting Treatment Response in Nasopharyngeal Cancer Using Radiomics: a Preliminary Study

Sasawan Wongpisarn[1,5], Chawalit Lertbutsayanukul[2], Nutchawan Jittapiromsak[3], Yothin Rakvongthai[4,5]

1 Medical Physics Program, Department of Radiology, Faculty of Medicine, Chulalongkorn University, Bangkok, Thailand
2 Division of Radiation Oncology, Department of Radiology, Faculty of Medicine, Chulalongkorn University, Bangkok, Thailand
3 Division of Diagnostic Radiology, Department of Radiology, Faculty of Medicine, Chulalongkorn University, Bangkok, Thailand
4 Division of Nuclear Medicine, Department of Radiology, Faculty of Medicine, Chulalongkorn University, Bangkok, Thailand
5 Chulalongkorn University Biomedical Imaging Group, Department of Radiology, Faculty of Medicine, Chulalongkorn University, Bangkok, Thailand

Abstract

Radiomics is a new technique that extracts large amount of data from medical images in terms of features which reflect tumor characteristics. In patient management, it is necessary to monitor a treatment for nasopharyngeal cancer (NPC) to assess its response. Our hypothesis was that radiomics features from diffusion-weighted imaging (DWI) could be used as imaging biomarkers for concurrent chemoradiation therapy (CCRT) treatment response. Here we investigated the use of such radiomics features for treatment response prediction in NPC patients. In this study, we collected seventeen patient datasets including thirteen complete response (CR) patients and four partial response (PR) patients where one patient dataset consisted of DWI and apparent diffusion coefficient (ADC) data acquired before (i.e. pre-treatment) and at five weeks after (i.e. mid-treatment) initiation of CCRT. For each dataset, we calculated the radiomic feature values using PyRadiomics software from pre-treatment and mid-treatment, and computed the percentage change of each feature, called Delta Radiomic (ΔRadiomic) feature. To validate the performance in differentiating CR and PR patients, we calculated the mean, standard deviation (SD) across CR and PR patients, and area under the receiver operating characteristic (ROC) curve (AUC) of each feature and its ΔRadiomic, where tumor response was from 6-month follow-up data using RECIST1.1 guideline. The result showed that there were 2 radiomic feature values at pre-treatment and 25 ΔRadiomic feature values that yielded a significant difference ($p<0.05$) between CR and PR groups. The AUC values from these 25 ΔRadiomic feature values ranged from 0.85 to 0.94, which were all higher than those from percentage change values of conventional imaging biomarkers such as volume, mean, uniformity and entropy. Therefore, radiomics-based biomarkers could potentially be used for early treatment response prediction in NPC patients.

Keywords: Radiomics, Nasopharyngeal cancer, DWI

1. INTRODUCTION

The highest incidence and mortality rate of nasopharyngeal cancer (NPC) were found in Southeast Asia. In terms of treatment, concurrent chemoradiation therapy (CCRT) is used to cure the disease. Although it seems to be satisfactory with high overall survival, there are side effects of CCRT toxicity for NPC patients. Therefore, it is important to monitor the treatment response for individual patients. In terms of treatment response assessment, medical imaging is important for monitoring the status of the patients. Current imaging tools for monitoring in NPC are computed tomography (CT) or magnetic resonance imaging (MRI) because of its high tissue contrast that can characterize the normal tissue and the tumor very well. Although CT is a good modality to monitor the treatment response, some patients may be injected with contrast media for contrast enhancement. Due to its higher sensitivity as compared to structural imaging, functional imaging from MRI plays a key role in assessing tumor characteristics for early treatment response prediction. There are several MRI techniques for functional imaging. Diffusion-weighted image (DWI) is one of functional imaging techniques that analyzes differences in intracellular and extracellular space via random Brownian motion of water protons to image tissues of varying cellularity without injection the contrast media. According to RECIST1.1 guideline, a cancer patient is classified as a complete responder or partial responder by comparing change of tumor's size and volume. However, these two parameters do not comprehensively represent the heterogeneity within tumor. To overcome this problem, there is a need to use a new method that can represent the intratumoral heterogeneity. Radiomics is a technique that extracts large amount of data from medical images in terms of features which reflect tumor characteristics. Radiomics uses standard-of-care imaging that can capture tumor characteristics over space and time noninvasively at lower cost as compared with repeated samplings of tumors.

A number of studies have been conducted to investigate performance of the radiomics approach in predicting treatment response of tumors. According to Qin *et al*. (2018) (6), pre-treatment texture features based on DWI may have the potential to predict the early response to chemoradiotherapy for NPC. In another study (Rao et al., 2016), it has been reported that relative differences in CT texture occurring after treatment hold

Figure 1 *Study flow diagram in this study.*

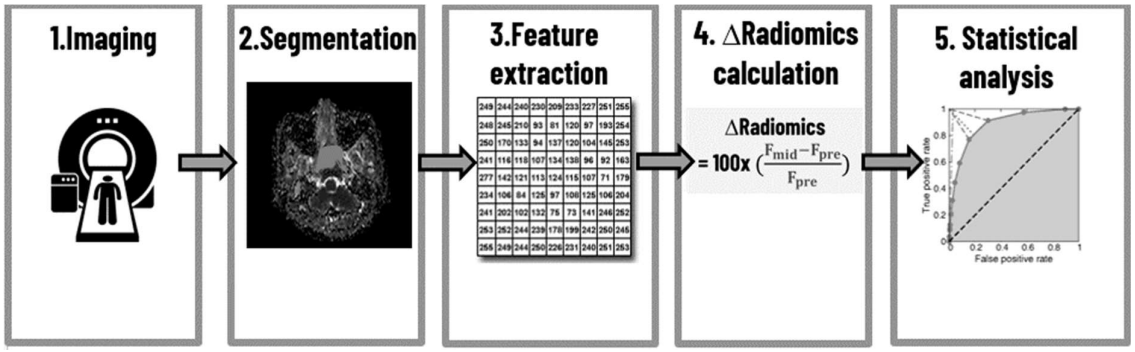

promise to assess the pathologic response to chemotherapy in patients with colorectal liver metastases (CRLMs) and may be better predictors of response than changes in lesion size or volume. In our study, based on DWI data, we investigated the use of relative difference in radiomic features called Delta Radiomics features for early treatment response prediction in NPC patients, and compared them with relative difference of conventional texture features and with radiomics features from only pretreatment data.

2. MATERIAL AND METHODS

2.1 Patient Selection

This study is a retrospective study. The study sample consisted of 17 patients. The inclusion criteria: (a) treated by CCRT; (b) first diagnosed of nasopharyngeal cancer with proved pathology; (c) age of more than 18 years old; (d) no prior radiation and chemotherapy; (e) evaluated with MRI simulation for radiation treatment planning before treatment verification; (f) complete clinical and MRI data; (g) informed consent; (h) no loss of follow up within 6 months and (i) no contraindications to MRI. Tumor response was from 6-month follow-up data using RECIST1.1 guideline. One patient dataset consisted of DWI and apparent diffusion coefficient (ADC) data acquired before (i.e. pre-treatment) and at five weeks after (i.e. mid-treatment) initiation of CCRT.

2.2 Tumor Segmentation and Feature Extraction

The ROI will be drawn over each tumor slice at pre-treatment and at mid-treatment by a board-certified neuroradiologist. For each dataset, we extracted the radiomics feature values using PyRadiomics (version 3.5) software from pre-treatment and mid-treatment. We computed the percentage change of each feature, called Delta Radiomics (ΔRadiomic) feature according to the following formula:

$$\Delta Radiomic = 100 \times \frac{F_{mid} - F_{pre}}{F_{pre}} ,$$

Where F_{mid} is radiomics feature at mid-treatment, F_{pre} is radiomics feature at pre-treatment.

2.3 Statistical Analysis

To validate the performance in differentiating CR and PR patients, A Mann-Witney U test was used in all statistical analyses with the level of statistical significance determined as p<0.05. We calculated the mean, standard deviation (SD) across CR and PR patients, and area under the receiver operating characteristic (ROC) curve (AUC) of each feature and its ΔRadiomic using Logistic regression. All statistical analysis were done through STATA software (version15)

3. RESULTS

Thirteen patients were in the CR group, while the 4 were in the PR group. After extraction, we obtained 842 radiomics feature which consisted of 4 types of radiomics features: shape, texture, first order and wavelet. Therefore, there were 842 radiomics features at pre- treatment and 842 ΔRadiomics for each patient. Among those 842 radiomics feature at pre-treatment, there were 2 radiomics feature values at pre-treatment which were original_firstorder_Minimum and wavelet-LLL_firstorder_Median that yielded a significant difference (p<0.05) between CR and PR there were 25 ΔRadiomics feature values that yielded significant difference between CR and PR groups as presented in Table2. Using the logistic regression, we obtained the AUC value of each of these 25 ΔRadiomics features. The AUC values ranged from 0.53 to 0.94. Most of them were higher than those from percentage change values of conventional imaging biomarkers such as volume, mean, uniformity and entropy (0.53, 0.46 and 0.46, respectively) except mean (0.88) as shown in Table3. ΔRadiomics feature values that yielded the highest AUC value were from sphericity and wavelet-LLH_glcm_DifferenceVariance (AUC=0.94 for both features).

Table 1 *Differences in the values of radiomics at pre-treatment between the complete responders and partial responders.*

Feature	CR (n=13)	PR (n=4)
original_firstorder_Minimum	1709.31±1679.14	3574.75±338.82
wavelet-LLL_firstorder_Median	21945.68±(3301.78)	25019.76±2236.94

Table 2 *Differences in the values of △radiomics between the complete responders and partial responders.*

Feature	CR (n=13)	PR (n=4)
original_firstorder_90Percentile	45.29±25.33	14.57±16.77
original_firstorder_10Percentile	103.72±52.59	41.71±37.01
wavelet-LLH_firstorder_90Percentile	-13.96±51.05	93.88±114.95
wavelet-LLH_ngtdm_Coarseness	902.16±1377.02	190.65±73.42
original_firstorder_Median	76.41±31.74	41.61±17.78
wavelet-LHL_firstorder_Mean	-78.38±104.32	31.17±111.99
wavelet-LLH_glcm_DifferenceAverage	-16.77±27.75	42.12±48.22
wavelet-LLL_firstorder_Median	72.59±32.17	36.13±16.86
wavelet-LLL_firstorder_Maximum	7.37±25.85	-12.78±10.79
wavelet-LLL_firstorder_RootMeanSquared	62.02±32.09	24.39±12.78
wavelet-LLL_firstorder_90Percentile	42.61±27.24	10.11±12.31
wavelet-LLL_firstorder_Minimum	227.85±141.35	55.25±73.58
wavelet-LLL_firstorder_10Percentile	101.95±60.93	43.03±27.20
original_firstorder_RootMeanSquared	63.89±28.97	28.68±14.06
original_firstorder_Mean	69.03±30.61	31.25±14.02
wavelet-LHH_glcm_DifferenceEntropy	-9.06±14.69	-4.70±14.95
wavelet-LHH_glcm_Idm	-3.09±41.45	-51.52±29.68
wavelet-LHH_glcm_Id	-4.43±31.12	-39.28±20.90
wavelet-LHH_glrlm_RunVariance	-16.61±50.44	-69.03±29.92
wavelet-LLH_glcm_Contrast	-31.11±42.56	91.51±102.08
wavelet-LLL_firstorder_Mean	66.29±33.64	26.76±13.30
original_firstorder_Skewness	-80.84±81.31	-184.92±110.38
wavelet-LHL_glcm_ClusterShade	4676.01±17052.82	-2850.19±3339.04
wavelet-LLH_glcm_DifferenceVariance	21.56±13.61	56.94±73.43
original_shape_Sphericity	-50.37±18.76	3.18±4.91

Table 3 *Area under the ROC curve (AUC) of conventional ΔRadiomics feature and the highest AUC value of ΔRadiomics*

Delta Radiomics Feature based on	AUC
Volume	0.54
Uniformity	0.46
Entropy	0.46
Mean	0.88
Wavelet-LLH_glcm_DifferenceVariance	0.94
Original_shape_Sphericity	0.94

4. DISCUSSIONS

This study focused on the performance of ΔRadiomic features based on DWI on predicting the early treatment response to chemoradiotherapy for NPC patients. Our results showed that there were ΔRadiomic features that yielded a significant difference between CR and PR groups more than radiomics features at pre-treatment. In addition, we compared the performance of ΔRadiomic of conventional features (volume, uniformity, entropy and mean) and found that there were ΔRadiomic features that have higher AUC value that the ΔRadiomic of conventional features.

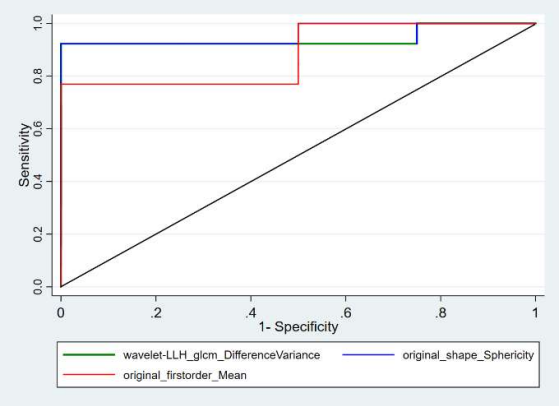

Figure2*: Receiver operating characteristic (ROC) curve of each ΔRadiomic features which have highest AUC (Wavelet-LLH_glcm_DifferenceVariance and Original_shape_Sphericity) compared with mean from percentage change values of conventional feature.*

In conclusion, ΔRadiomics feature from the full set of features outperformed ΔRadiomics based on 4 conventional features. This indicated that ΔRadiomics, difference of radiomics-based biomarkers from two time points, could potentially be used for early treatment response prediction in NPC patients.

REFERENCES

1. Mimi C. Epidemiology of nasopharyngeal carcinoma. Seminars in Cancer Biology [Internet].2002 [cited2020 Mar 3];2002:421. Available from:https://www.sciencedirect.com/science/article/pii/S1044579X02000858
2. Francesco Sciacca, Assoc Prof Frank Gaillard et al. MR spectroscopy. Radiopaedia [Internet].2020 [Cited2020 Mar 3];2020:1. Available from: https://radiopaedia.org/articles/mr-spectroscopy-1
3. Yaron Gordon, Sasan Partovi, Matthias Müller-Eschner, Erick Amarteifio, et al. Dynamic contrast-enhanced magnetic resonance imaging: fundamentals and application to the evaluation of the peripheral perfusion. Cardiovascular Diagnosis and Therapy 2014;4(2):147-164.
4. Koh DM, Padhani AR. Diffusion-weighted MRI: a new functional clinical technique for tumour imaging. Br J Radiol2006;79:633-5.
5. Henry Knipe, Muhammad Idris, et al.Radiomics. Radiopaedia [Internet].2020 [Cited2020 Mar 3];2020:1. Available from: https://radiopaedia.org/articles/radiomics
6. Yuhui Qin, Xiaoping Yu, Jing Hou, Ying Hu, el al. Predicting chemoradiotherapy response of nasopharyngeal carcinoma using texture features based on intravoxel incoherent motion diffusion-weighted imaging: Medicine 2018;97:30.
7. Sheng-Xiang Rao, Doenja MJ Lambregts, Roald S Schnerr, Rianne CJ Beckers, et al. CT texture analysis in colorectal liver metastases: A better way than size and volume measurements to assess response to chemotherapy: eugjournal 2016;257-263.

The Labeling of ^{99m}Tc-PSMA-HBED-CC for Prostate Cancer Imaging

Benchamat Phromphao[1,3], Shuichi Shiratori[2,3]

1 Department of Radiology, Faculty of Medicine, Chulalongkorn University, Bangkok 10330, Thailand
2 Department of Radiology, Faculty of Medicine Siriraj Hospital, Mahidol University, Bangkok 10700, Thailand
3 Chulalongkorn University Biomedical Imaging Group, Department of Radiology, Faculty of Medicine, Chulalongkorn University, Bangkok 10330, Thailand

Abstract

Introduction: Prostate cancer (PCa) is the second most common cancer and the fifth leading cause of death worldwide in 2018 [1]. Mostly, PCa diagnosis based on Prostate-Specific Antigen (PSA) blood test, sonography guided needle biopsy which is an invasive manner. Moreover, these two methods provided low sensitivity and low specificity. Therefore, molecular imaging recently enrolls as an important technique in PCa diagnosis using some small molecules which are well developed to bind to overexpressed Prostate Specific Membrane Antigen (PSMA). The small molecules, for example PSMA-HBED-CC, PSMA I&T, PSMA-617 can chelate with Ga-68, a PET radionuclide for diagnostic purpose. However, these PET tracers are limited in clinical PET center. Herein, we report a new SPECT tracer using Tc-99m labeled with PSMA-HBED-CC aim to alternative option for PCa diagnosis.
Purpose: To develop in-house preparation of ^{99m}Tc-PSMA-HBED-CC for prostate cancer imaging.
Methods: ^{99m}Tc-pertechnetate 370 MBq was added to mixture solution of PSMA-HBED-CC 10 µg and 4% $SnCl_2$•$2H_2O$, then heated to 100 ºC 15 minutes and incubated while cool down to room temperature. Labeling parameters were optimized to obtain the maximum radiochemical yield of ^{99m}Tc-PSMA-HBED-CC. The completeness of chelation was determined by instant thin layer chromatography (iTLC) and pH of ^{99m}Tc-PSMA-HBED-CC was measured.
Results: ^{99m}Tc-PSMA HBED-CC was successfully chelated using ^{99m}Tc-pertechnetate solution in high radiochemical yield and radiochemical purity which is sufficient to administer to patient for SPECT imaging of PCa diagnosis.
Conclusion: The preliminary labeling method of ^{99m}Tc-PSMA-HBED-CC can effectively prepare a new promising SPECT tracer for PCa diagnosis. Animal experiment using PCa xenograft nude mouses is under investigation in our laboratory before applying to clinical use of ^{99m}Tc-PSMA-HBED-CC in human.

Keywords: Prostate cancer imaging, Technetium-99m, PSMA, ^{99m}Tc-PSMA, SPECT tracer

1. INTRODUCTION

Prostate cancer (PCa) is the second most common cancer and the fifth leading cause of death worldwide in 2018 [1]. Early and accurate detection is necessary, which has a beneficial effect for staging, treatment management and prognosis. Elevated plasmatic levels of prostate-specific antigen (PSA) and sonography-guide needle biopsy are the most frequently used for diagnostic method in PCa [2]. PSA level as a biomarker for PCa has low sensitivity and low specificity because of possible false positive. Meanwhile, sonography-guide needle biopsy is the only technique to find out certain cancer stage but biopsy is an invasive method and cancer might be possibly missed. In case of PSA test and biopsy results can not confirmed pathologic PCa, CT and/or MRI scan will be acquired. However, CT localization provides poor soft tissue contrast and high radiation. On the other hands, MRI requires long acquisition time and not always reliably identifies local recurrence lymph node involvement or visceral metastasis. Therefore, molecular imaging allowing specific detection is highly considerable which is potentially employed to accurately diagnose PCa.

The molecular imaging of PCa became mighty tool under the concept of specific binding of radiopharmaceuticals to the surface receptor on prostate cancer cell, called Prostate Specific Membrane Antigen (PSMA). PSMA is a glycoprotein type II transmembrane, which has 750 amino acids, 19 amino acids intracellular portion, 24 amino acids transmembrane portion and 707 amino acids extracellular portion [3]. PSMA is expressed primarily in prostate epithelial and found in normal cell slightly such as proximal intestine, kidney and salivary gland.

PSMA has a short intracellular domain containing a binding site for 7E11 antibody [4], [5], [6]. Two decades ago, this binding site was a target for PCa imaging but the antibody has long pharmacokinetics, therefore long half-life radionuclide is necessary to chelate to 7E11. Moreover, it was difficult to penetrate into PCa cell. Recent research publications revealed large extracellular domain contains another binding site for J591 antibody. However, 7E11 antibody also requires long pharmacokinetics that is not appropriate as a tracer for PCa imaging. This extracellular binding site guided an idea to develop the small molecule for imaging, as PSMA inhibitor.

PSMA inhibitor divided into three families; phosphorous-based, thiol-based and urea based [FIG.1]. Urea-based inhibitors showed highest affinity for PSMA among them. These urea-based inhibitors are a small molecule developed from the binding part of J591 antibody. Currently, several commercially available PSMA inhibitors are used in PCa imaging. For example, Glu-NH-CO-NH-Lsy (Ahx)-HBED-CC (PSMA-11® or PSMA-HBED-CC), suitable for only Ga-68 labeling. PSMA inhibitor Vipivotide tetraxetan (PSMA-617®) [7]

and PSMA I&T® (imaging and therapeutic) contains DOTA chelator that suitable for Ga-68 and Lu-177. Recently, ^{18}F-PSMA is also available in clinical use. Both ^{68}Ga-PSMA and ^{18}F-PSMA are diagnostic radiopharmaceuticals which required the positron emission tomography (PET) facility.

In spite of superior imaging quality, PET tracer is less widely available and more costly to implement in many aspects. While, SPECT tracer is more routinely used with much more affordable.

Recently, ^{99m}Tc-PSMA had been report [8], [9], [10], [11], [12]. There are some drawbacks that could be improved in methodology to provide more practical labeling. Our rationale of ^{99m}Tc-PSMA labeling was derived from similarity of molecular structure between PSMA-HBED-CC and diethylene triamine pentaacetate (DTPA) [FIG.2].

Therefore, we aim to develop ^{99m}Tc-PSMA as a new promising in-house preparing tracer to potentially apply to PCa diagnosis in cost-effective manner.

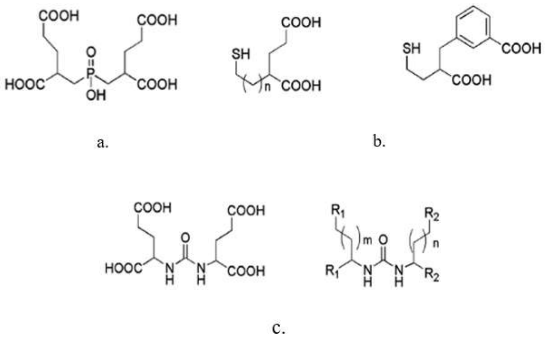

Figure 1 Three PSMA inhibitor families; (a.) Phosphate-based, (b.) Thiol-based, (c.) Urea-based family.

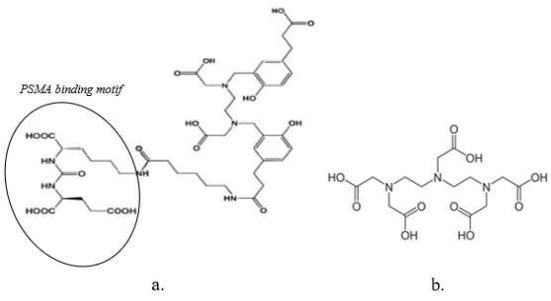

Figure 2 Chemical structures of (a) PSMA-HBED-CC and (b) DTPA

2. MATERIAL AND METHODS

This study is approved research ethic by committee of faculty of medicine, Chulalongkorn university. No personal data is involved and no beneficence and no justice apply to our research.

Reagents and equipment

Stannous chloride dihydrate ($SnCl_2 \cdot 2H_2O$) in hydrochloric acid (HCl) was prepared as reducing agent. ^{99m}Tc-pertechnetate ($^{99m}TcO_4^-$) was freshly eluted with saline from ^{99}Mo/^{99m}Tc generator by purchasing from Global Medical Solution (Thailand) CO., LTD. The ligand PSMA-HBED-CC were imported by Biomedia (Thailand) CO., LTD. All radioactive counting associated with the radiochemical studies was carried out using CRC-25R dose calibrator. The analytical of radiochemical yield (RCY) and radiochemical purity (RCP) were performed, using thin layer chromatograph (TLC) system. The crude product was purified by solid phase extraction (SPE) C-18 Cartridge.

Labeling of ^{99m}Tc-PSMA-HBEC-CC

The labelling methodology of ^{99m}Tc-PSMA-HBEC-CC is adopted according to the standard Tc-99m labeling. However, factors in labeling process are investigated and formulated to reach the requirement criteria for radiopharmaceutical injection as following; $SnCl_2 \cdot 2H_2O$ 0.144 mg was added to concentrate HCl 0.75 mL, heated 100 ºC 5 minutes. After cool down to room temperature, 6 N HCl 2.25 mL was added to be 4% $SnCl_2 \cdot 2H_2O$ solution.

4% $SnCl_2 \cdot 2H_2O$ solution were added to PSMA-HBED-CC 10 µg in sterile vial. After mixing, ^{99m}Tc-pertechnetate 370 MBq was added to the reaction vial, heated 100 ºC 15 minutes. Incubate 10-15 minutes while cool down to room temperature. Crude product is loaded into SPE C-18 cartridge and 0.9% NSS was used to flood the product retention. Finally, washing with ethanol and water 1:1 ratio (2 mL) obtained 100% radiochemical purity and confirmed by TLC system.

Quality control

^{99m}Tc-PSMA-HBED-CC was determined pH by colorimetric evaluation with universal indicators. Radiochemical yield and radiochemical purity are analyzed by TLC using silica paper strips in acetone system to determine the amount of free $^{99m}TcO^-_4$ and 0.9% saline to determine the amount of hydrolyzed form. The radioactivity is determined by using a dose calibrator.

Radiochemical yield and radiochemical purity are calculated by percentage of activity with counts in product divide by total counts in each system (free $^{99m}TcO^-_4$ and hydrolyzed form) [FIG.3]. The specification should be greater than 95% [13] or recommend value in related monograph.

$$\%\ \text{Free}\ ^{99m}TcO_4^- = \frac{\text{Count in product (free } TcO_4^-\text{)}}{\text{Total count}} \times 100$$

$$\%\ \text{Hydrolyzed form} = \frac{\text{Count in product (Hydrolyze form)}}{\text{Total count}} \times 100$$

$$\%\ \text{Yield} = 100 - (\%\text{Free}\ ^{99m}TcO_4^- + \%\text{Hydrolyzed form})$$

Figure 3 Radiochemical yield and radiochemical purity calculation

Stability

The stability test of ^{99m}Tc-PSMA-HBED-CC was performed by incubation of ^{99m}Tc-PSMA-HBED-CC at room temperature and monitored by TLC every hour up to 6 h.

Statistical analysis

The best condition of ^{99m}Tc-PSMA-HBED-CC labeling was replicated (n=6) and quantitative data were expressed as Mean±SD, descriptive statistic parameters in this study.

3. RESULTS

Radiochemical yields and radiochemical purity

The labeling of PSMA with ^{99m}Tc-pertechnetate was investigated by vary parameters in labeling process [Table 1]. PSMA-HBED-CC is fixed at 10 µg which is same quantity in clinical practice. Amount of $SnCl_2 \cdot 2H_2O$ is increased to reach the highest radiochemical yield in experiment 6th. However, amount of $SnCl_2 \cdot 2H_2O$ is key factor to cause free form of Tc-99m and hydrolyzed form, which the optimal amount of $SnCl_2 \cdot 2H_2O$ is 3 µg under 100 ºC 15 mins [FIG.4].

Table 1 Labeling condition of ^{99m}Tc-PSMA-HBED-CC

Exp.	PSMA (µg)	$SnCl_2 \cdot 2H_2O$ (µg)	$^{99m}TcO_4^-$ (mCi)	Labeling Condition (ºC)	pH	Free (%)	Hydrolyze (%)	% Yield
1	10	0.5	10.02	room temperature	5	99.58	0.17	0.25
2	10	0.5	10.32	100 ºC , 15 mins.	5	88.89	0.00	11.11
3	10	1.0	9.97	100 ºC , 15 mins.	5	81.82	0.00	18.18
4	10	2.0	10.16	100 ºC , 15 mins.	5	64.29	10.00	25.71
5	10	2.5	10.61	100 ºC , 15 mins.	5	20.00	20.00	60.00
6	10	3.0	11.02	100 ºC , 15 mins.	5	9.09	25.00	65.91
7	10	3.5	11.64	100 ºC , 15 mins.	5	0.00	41.67	58.33
8	10	4.0	11.15	100 ºC , 15 mins.	4	0.00	50.00	50.00

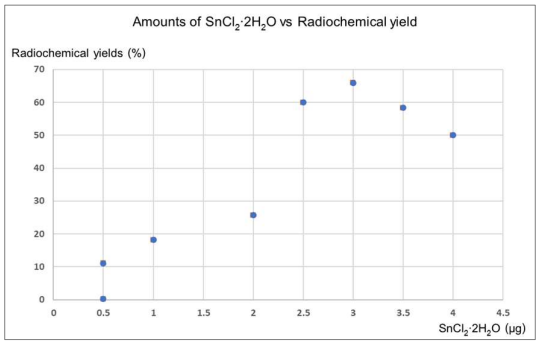

Figure 4 Amount of $SnCl_2 \cdot 2H_2O$ (µg) and radiochemical yield (%)

Replications of the best condition of ^{99m}Tc-PSMA-HBED-CC were performed to confirm reproducibility for 6 times. The radiochemical yields are about 67-75% (71.49±2.42) and radiochemical purity is 95-100% (98.29±2.65) [Table 2] after purification confirmed by TLC.

Table 2 Replication of the best condition of ^{99m}Tc-PSMA-HBED-CC labeling

Exp.	PSMA (µg)	$SnCl_2 \cdot 2H_2O$ (µg)	$^{99m}TcO_4^-$ (mCi)	pH	Free (%)	Hydrolyze (%)	% Yield	% Purity
9	10	3.0	11.35	5	14.29	12.50	73.21	100.00
10	10	3.0	10.61	5	20.00	12.50	67.50	100.00
11	10	3.0	10.13	5	9.09	20.00	70.91	100.00
12	10	3.0	10.94	5	14.29	11.11	74.60	94.74
13	10	3.0	10.81	5	13.33	15.79	70.88	95.00
14	10	3.0	10.48	5	18.18	10.00	71.82	100.00

^{99m}Tc-PSMA-HBED-CC Stability

^{99m}Tc-PSMA-HBED-CC Stability is higher 95% purity at 4 hrs. and higher 90% at 6 hrs (incubate at room temperature).

4. DISCUSSION

PSMA motif with HBED-CC, an open-chain chelator was successfully chelated with Tc-99m at high temperature because the entropy of reaction at room temperature was not enough to force the chelation forward. This study revealed that general procedure of ^{99m}Tc-PSMA-HBED-CC labeling should be performed at 100 ºC 15 mins with appropriate amount of 3 µg $SnCl_2 \cdot 2H_2O$ to reduce oxidation state of Tc-99m 370 MBq.

In table 2, purification process is strongly recommended to obtain radiochemical purity 95-100%. By the way, the consistent of washing speed should be well controlled in order to confirm that a final product was transferred from SPE C-18 cartridge.

However, TLC silica paper strips in QC process should be kept away from moisture because it can lead to high hydrolyzed form result. Therefore, silica paper strips are recommended storage at temperatures 18-20ºC with regulated humidity in desiccator [14].

In addition, ^{99m}Tc-PSMA-HBED-CC should be used in clinical practice immediately or keep in refrigerator no longer than 4 hrs after preparation.

5. CONCLUSION

We can improve the labeling of PSMA-HBED-CC with ^{99m}Tc-pertectnetate for prostate cancer imaging in high radiochemical yield and more than 95% radiochemical purity.

We plan to investigate efficacy of this new SPECT tracer in xenograft nude mice before utilizing in clinical application.

ACKNOWLEDGMENTS

The authors would like to thank Division of Nuclear Medicine, *Department of Radiology, King Chulalongkorn Memorial Hospital Bangkok, Thailand, and.* Nanomedicine Research Unit, Faculty of Medicine, Chulalongkorn University, *Bangkok, Thailand, and. Division of Nuclear Medicine, Department of*

Radiology, Faculty of Medicine Siriraj Hospital, Bangkok, Thailand

REFERENCES

1. Bray F, Ferlay J, Soerjomataram I, Siegel RL, Torre LA, Jemal A, et al. Global cancer statistics 2018: GLOBOCAN estimates of incidence and mortality worldwide for 36 cancers in 185 countries. CA Cancer J Clin 2018; 68:394-424.
2. Mottet N, Bellmunt J; European Association of Urology. Guidelines on prostate cancer 2015-2017 [cited 2019 Aug 05]; Available from: http://uroweb.org/guideline/prostate-cancer/
3. Gourni E and Henrifsen G. Metal-Base PSMA Radioligands. MDPI journal; molecules 2017, 22, 523.
4. Maurer T, Eiber M, Schweiger M, Gschwend JE. Current use of PSMA-PET in prostate cancer management. Nature 2016; 13: 226-35.
5. Chang SS. Overview of Prostate-Specific

Membrane Antigen. Rev Urol. 2004; VOL.6 SUPPL 10: S13-S18.

6. Denmeade S, Schwab M [editor]. Encyclopedia of cancer; prostate specific membrane antigen. Springer 3068-3072.
7. Puttemans J, Lahoutte T, Huyvette MD and Devoogdt N. Beyond the barrier: Targeted radionuclide therapy in brain tumors and metastasis. Pharmaceutics journal 2019, 11, 376.
8. Reinfelder J, Kuwert T, Beck M, Sanders JC, Ritt P, Schmidkonz C, et al. First experience with SPECT/CT using a ^{99m}Tc-labeled inhibitor for prostate-specific membrane antigen in patients with biochemical recurrence of prostate cancer. Clinical Nuclear Medicine 2017; 42: 26-33.
9. Goffin K, Joniau S, Tenke P, Slawin K, Ellis W, Babich J, et al. A phase 2 study of ^{99m}Tc-trofolastat (MIP-1404) to identify prostate cancer (PCa) in high-risk patients (pts) undergoing radical prostectomy (RP) and extended pelvic lymph node (ePLN) dissection: An interim analysis. Journal of Nuclear Medicine 2014; 55.
10. Hillier SM, Maresca KP, Lu G, Merkin RD, Marquis JC, Zimmerman CN, et al. ^{99m}Tc-labeled small molecule inhibitors of Prostate Specific Membrane Antigen for molecular imaging of prostate cancer. J Nucl Med 2013; 54:1369-76.
11. Xu X, Zhang J, Hu S, He S, Bao X, Ma G, et al. ^{99m}Tc-labeling and evaluation of a HYNIC modified small-molecular inhibitor of prostate-specific membrane antigen. ELSEVIER 2017, nuclear medicine and biology; 48:69-75.
12. Flores GF, Gutierrez ML, Garcia BO, Cuevas CS, Vega EA, et al. Clinical translation of a PSMA inhibitor for ^{99m}Tc-base SPECT. ELSEVIER 2017, nuclear medicine and biology; 48:36-44.
13. International Atomic Energy Agency. Quality control in the production of radiopharmaceuticals, TECDOC-1856. IAEA library cataloguing in publication data document 2018.
14. International Atomic Energy Agency. Operational guidance on hospital radiopharmacy, a safe and effective approach. IAEA library cataloguing in publication data document 2008.

Development of method to cancel the calculation direction dependence for image processing applying diffusion equation

Kentaro Doi [1], Yusuke Anetai [2], Hideki Takegawa [2], Yuhei Koike[2], Satoaki Nakamura [2], and Masahiko Koizumi1

1 Department of medical physics and engineering, Osaka University Graduate School of Medicine, Osaka, Japan,
2 Department of radiation oncology, Kansai Medical University Hospital, Osaka, Japan

Abstract

Manually extracting bone metastases lesions (BML) from computed tomography (CT) images generally depends on individual criteria and leads to overlooking lesions. Therefore, a system for efficiently extracting BML is needed, and we are developing a BML extraction system for screening[1)]. We reported calculation model applying diffusion equation (DEQ) for BML extraction in the previous study[1)]. To improve the accuracy of calculation model, a method for cancelling calculation direction dependence (CDD) was developed in this study, which is well-known in numerical fluid physics fields. DICOM CT images of patients with multiple BMs were used for this study. The cases of dependency for calculation starting point (CSP) and end point (CEP) were verified. Calculated images for evaluation were obtained from two calculation methods using our previous DEQ model, assuming calculation direction dependence. Noise reduction were compared with the DEQ calculated image regarding upper-left CSP to CEP as a control. As a result, we succeeded 26% decrease in high-CT value regions due to physiological reactions and couch. This result indicated that considering CDD can be efficient for extracting BMLs using the DEQ.

Keywords: Image processing, Diffusion equation, Bone metastasis

1. INTRODUCTION

Bone metastases lesions (BML) are diagnosed with medical images such as computed tomography (CT) images. Manually extracting BML from CT images typically depends on individual criteria of diagnosis and lead to overlooking the lesions. Therefore, a system for efficiently extracting BML is required, and we are developing a BML extraction system for screening and reported method applying diffusion equation (DEQ) in 119th JSMP conference[1)]. However, the calculation method extracted noises containing obvious BM false-negative regions and couch, which induce preventing extraction of BML. In this study, to improve the accuracy of calculation model, we developed a method for reducing noises to cancel the calculation direction dependence (CDD), which is well-known in numerical fluid physics fields.

2. MATERIAL AND METHODS

2.1 Numerically Calculation of DEQ

In this study, DEQ (Eq. (1)) has been numerically applied to image processing using the Crank-Nicolson method. DEQ is typical method for the image to smooth the areas which have different gradations[2)]. Using DEQ, we differentiated the osteoblastic BML which have higher CT value than that of other normal tissues. The DEQ is generally represented as Eq. (1). We used the form of Eq. (2) accompany with Eq. (3) to numerically calculate, and the diffusion coefficient D was defined as a time function in this model, excluded the spatial differentiation term.

$$\frac{\partial \phi}{\partial t} = (\nabla D(t) \cdot \nabla \phi) + D(t)\nabla^2 \phi, \tag{1}$$

$$\frac{\partial \phi}{\partial t} = D(t)\left(\frac{\partial^2}{\partial x^2} + \frac{\partial^2}{\partial y^2}\right)\phi(x, y, t), \tag{2}$$

$$D(t) = \frac{1}{2}|cos(\phi) + sin(\phi)|, \tag{3}$$

$$\begin{aligned}\phi_{i,j}^{k+1} - \phi_{i,j}^{k} = \frac{D_{i,j}^{k}}{2}\Big(&\big(\phi_{i+1,j}^{k+1} \\ &- 2\phi_{i,j}^{k+1} + \phi_{i-1,j}^{k+1} \\ &+ \phi_{i+1,j}^{k} \\ &- 2\phi_{i,j}^{k} + \phi_{i-1,j}^{k}\big) \\ &+ \big(\phi_{i,j+1}^{k+1} \\ &- 2\phi_{i,j}^{k+1} + \phi_{i,j-1}^{k+1} \\ &+ \phi_{i,j+1}^{k} \\ &- 2\phi_{i,j}^{k} + \phi_{i,j-1}^{k}\big)\Big),\end{aligned} \tag{4}$$

$$D_{i,j}^{k} = \frac{1}{2}\left|cos\left(\phi_{i,j}^{k}\right) + sin\left(\phi_{i,j}^{k}\right)\right|, \tag{5}$$

where ϕ represents the CT value in the DICOM CT images. For numerical calculation, Eqs. (2) and (3) were expanded as tensor form of Eqs. (4) and (5). CT images were calculated iteratively using the DEQ. Isotropic diffusion was used in this study, because anisotropic diffusion, which is typically used in image processing such as Perona and Malik model[3)], is not efficient for calculation without assuming the effective direction. The following calculation conditions were defined in

this study: dx = 1, dy = 1, and dt = 1, and an increase of calculating iteration represents all pixels of the image are calculated completely.

2.1 Calculation Direction Dependence (CDD) of Diffusion equation

Dependency for a calculation starting point (CSP) and an end point (CEP) were verified. CSP was selected a corner out of the four and CEP was defined as the diagonal point of CSP. A total calculated image for evaluation was obtained by following Method (i) and (ii): (i) the calculated four image sets received DEQ calculation after 20 iterations of each CSP to CEP were combined by Hadamard products with normalization in the range of 0 to 1, (ii) one image set was calculated taken over every four CSP to CEP with the condition that the previous CSP to CEP calculation received 20-iterated DEQ calculation was rescaled to original CT, then the four calculated images were combined with normalization in the range of 0 to 1 (Fig. 1(a) and (b)). Noise reductions were evaluated using following Eq. (6), and this compares the differentiation from the calculated case of upper-left CSP to lower-right CEP (the control case),

$$\sum_{i=1}^{512}\sum_{j=1}^{512}\frac{A_{i,j}-B_{i,j}}{A_{i,j}}\times 100, \qquad (6)$$

where A represents the calculated image of the control case, and B represents the calculated image processed by Method (i) or (ii), respectively.

3. RESULTS

3.1 Verification of the Calculation Direction

DEQ calculated images using the four different CSP to CEP, which indicates that the calculation direction has effects on image processing.

3.2 The Effect of Canceling CDD

The effect of CDD was verified by using method (i) and (ii). The control calculation image was shown in Fig. 3(a), *the lower part of the image showed a lot of noise due to influence by the couch.* By using Method (i) and (ii) successfully achieved noise reduction by 26% and 17% against the control, respectively (Fig. 4). Calculated using the method (i) suppressed to extract BM false-positive region more efficiently than that of using the method (ii).

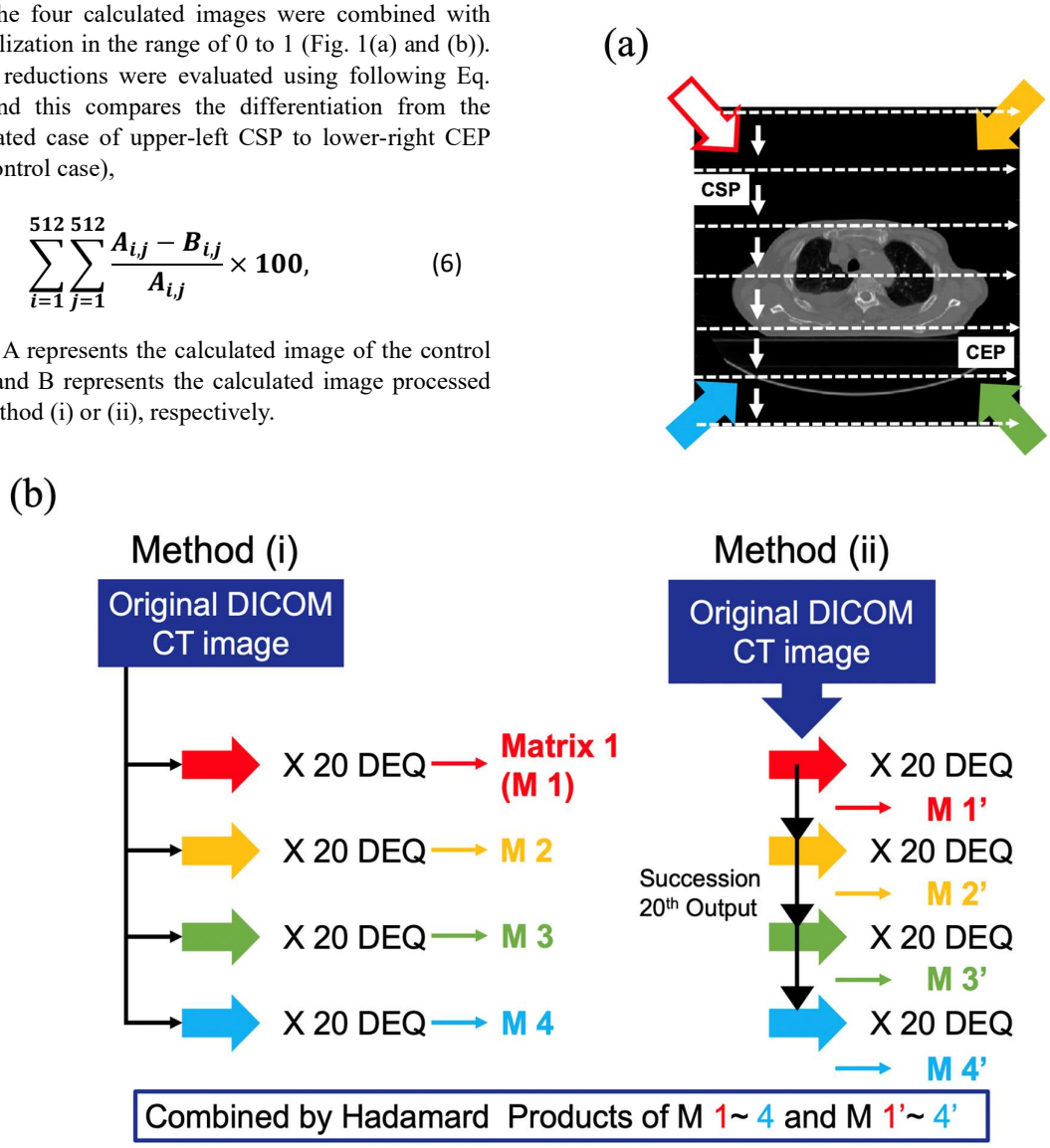

Fig. 1. *(a) shows calculation direction of Red allow. Dotted lines indicate detailed calculation direction. (b) represents the schemes of Method (i) and (ii).*

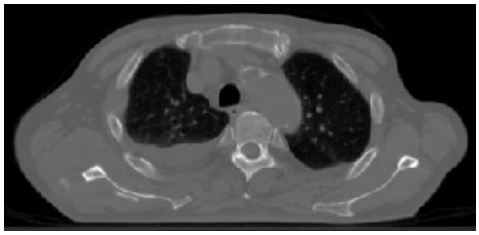

Fig. 2. *Original DICOM CT image of the patient with multiple BMs used for DEQ calculations in this study.*

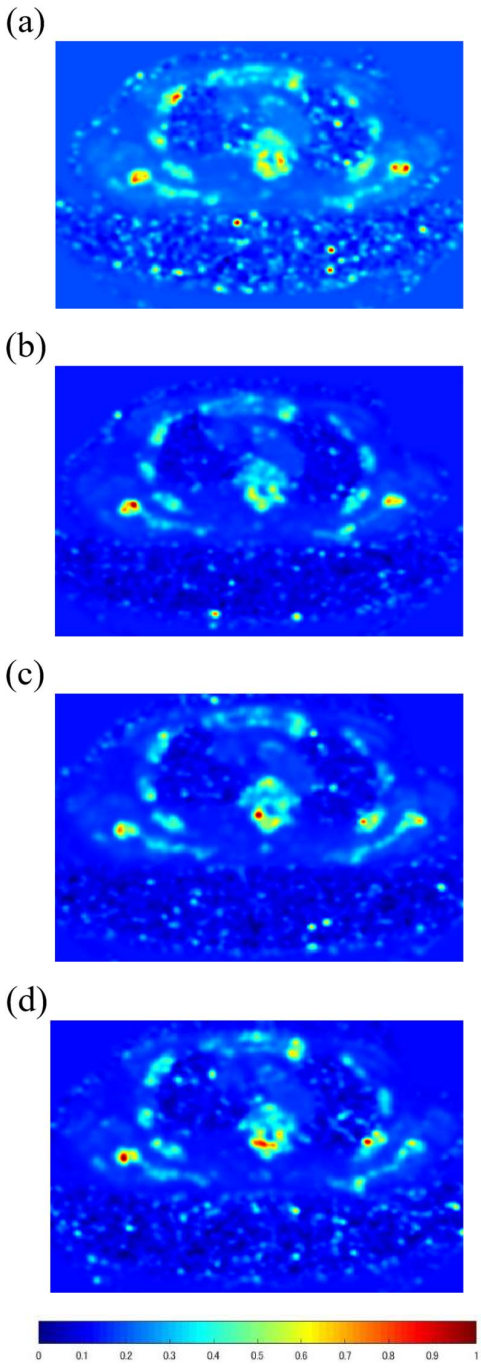

Fig. 3. *Results of the DEQ calculation with the four different directions of CSP to CEP: (a) upper-left to lower-right (b) upper-right to lower-left (c) lower-right to upper-left, and (d) lower-left to upper-right.*

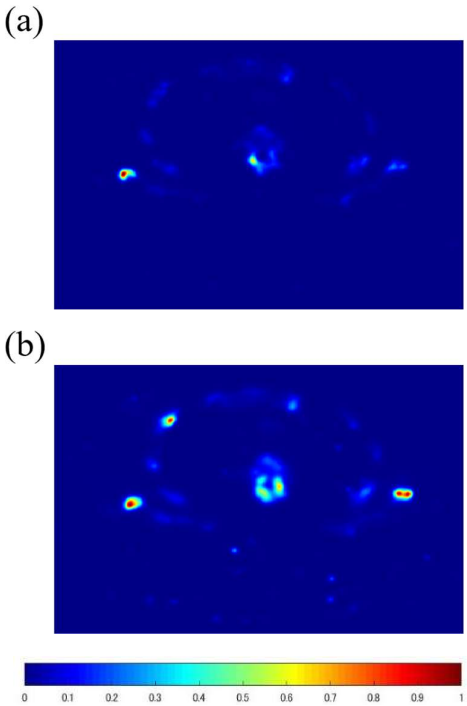

Fig. 4. *The effect of canceling CDD. (a) and (b) show results produced by Method (i) and (ii), respectively.*

4. DISCUSSION

We proposed two methods to cancel the effect of CDD for DEQ calculation, and successfully achieved to suppress BML false-positive regions and the couch. CDD effect is derived from the numerical calculation of the derivative term of DEQ, and its iterative dependency for the Gauss–Seidel solution. To cancel it out, the averaging method is expected to be effective, because the numerical accuracy is not required for the image processing. Although CDD was canceled by using our methods, our purpose is extraction of the BMLs, which was not sufficiently satisfied in this study. The methods for distinguishing between osteoblastic bone metastasis regions and non-BM regions such as enostoses were reported[4), 5), 6)]. These methods are still empirical, which induce BML to be overlooked. On the other hand, numerical methods uniquely extract BMLs superior to empirical methods. Thus, to improve numerical methods is more effective than that of them. In the current study, our methods achieved to partly suppress extracting BM false-positive region. To improve the accuracy of the extraction, we should focus the term of the diffusion coefficient represented by Eq. 3. Using trigonometric function in this study, the diffusion coefficient term has influence on the periodic effect for the calculation. This has advantages for suppressing the numerical divergence of the calculation, whereas it allows the intensifying the particular phase of iteration. Balancing term for relaxing the periodic effect is might be required.

Although canceling of CDD was effective on noise suppression, but not directly committing to extract BMLs in the current study. Therefore, we need to focus on improving the accuracy of extracting BMLs with sustaining the suppression of noises and considering of calculation conditions, in the future.

5. CONCLUSION

We developed the method for canceling CDD to improve the accuracy of the DEQ model. Noises in the calculated image decreased, however, the accuracy for extraction of BML requires more improvement.

ACKNOWLEDGEMENTS

I appreciate Hirokazu Mizuno for introducing to study in Kansai Medical University and for giving clinical educations.

REFERENCES

1. K. Doi, et al., “Extraction of osteoblastic metastases images from diagnostic CT image using diffusion equation.”, Japanese Journal of Medical Physics, Japan Society of Medical Physics, Vol. 40(1), pp151, 2020.
2. Guichard F., L. Moisan, and J-M. Morel, “A review of PDE models in image processing and image analysis.”, *Journal de Physique IV (Proceedings)*, Vol. 12(1), EDP sciences, 2002.
3. Perona P., and Jitendra M., “Scale-space and edge detection using anisotropic diffusion.”, *IEEE Transactions on pattern analysis and machine intelligence,* Vol. 12(7), pp629-39, 1990.
4. Elangovan S. M., and Ronnie Sebro., “Accuracy of CT attenuation measurement for differentiating treated osteoblastic metastases from enostoses.”, *American Journal of Roentgenology*, Vol. 210(3), pp615-20, 2018.
5. Sala F., et al., “Bone islands incidentally detected on computed tomography: frequency of enostosis and differentiation from untreated osteoblastic metastases based on CT attenuation value.”, *The British journal of radiology*, Vol. 92(1103), 2019.
6. Ulano A., et al., “Distinguishing untreated osteoblastic metastases from enostoses using CT attenuation measurements.”, *American Journal of Roentgenology*, Vol. 207(2), 362-8, 2016.

Impact of automatic image registration with contrast enhancement filter in head and neck cancer

Kouta Hirotaki[1,2], Tsunemichi Akita[1], Satoe Kitou[1], Vijay Raturi[4,5], Syunsuke Moriya[3]

1 National Cancer Center Hospital East Department of Radiology
2 University of Tsukuba Master's Program in Medical Sciences
3 Graduate School of Comprehensive Human Sciences, University of Tsukuba
4 National Cancer Center Hospital East, Department of Radiation Oncology and Particle Therapy
5 Course of Advance Clinical Cancer Research, Juntendo University

Abstract

Introduction: Automatic image registration benefits from objectivity in the registrations as the registration quality is observer independent. Current image-guided proton beam therapy (IGPBT) utilize orthogonal two-dimensional (2D) kV X-ray images. Automatic image registration performance is dependent on the quality of the image and there is some pre-processing filter in commercial IGPBT systems.
Purpose: To evaluate the effectiveness of using the contrast enhancement filter for improvement of the matching accuracy of automatic image registration.
Methods: A retrospective analysis of 13 head and neck cancer patients who received proton beam therapy was performed. The 2D-kV images were acquired per fraction. Bone registration was performed on each pretreatment daily 2D-kV image using the VeriSuite software (MedCom, Germany). The algorithms used in the software were based on a mutual information algorithm. The weights of contrast enhancement filter were set 0%, 60%, 75%, and 95%. The accuracy of automatic image registration using different contrast enhancement filters were compared with the manual registration. A typically acceptable clinical specifications was set at <1.0 mm and <0.5 degree.
Results: The automatic image registration without filter and with filter (i.e. 60%-, 75%-, and 95%-contrast enhancement filter) provided acceptable matches in >35.0% and >92.5% of registrations, respectively. The computed mean translational difference was 0.65±0.98 (mean±1SD), 0.32±0.37, 0.34±0.37, and 0.27±0.34 mm and the computed mean rotational difference was 0.71±1.32, 0.18±0.25, 0.16±0.20, and 0.08±0.11 degree in the 0%-, 60%-, 75%-, and 95%-contrast enhancement filter, respectively.
Conclusion: Automatic image registration with the contrast enhancement filter would achieve a higher accuracy. The increase of weight may contribute to the improvement of the rotation-error.

Keywords: IGRT, Automatic image registration, 2D-Xray image, Head and Neck cancer

1. INTRODUCTION

Image registration in proton therapy using 2D X-ray images leads to setup error in translational axis [Anterior-Posterior (AP)/Superior-Inferior (SI)/Right-Left (RL)]and rotational axis (Yaw/Roll/Pitch) these errors are corrected using 6D couch. However, the magnitude and direction of position-error are difficult to recognize with 6-D image registration using 2D images in comparison to the 3D images. Hence, the difference is observed during image registration accuracy and speed between the experienced therapists. On the other hand, automatic image registration (AIR) obtains stable registration accuracy and is not user-dependent [1]. In comparison to manual image registration (MIR), the AIR accuracy is found to be inferior [2]. As per the previously published data, the registration accuracy of AIR using mutual information (MI) [3] depends on the image contrast and the image background environment [4]. Therefore, to improve the registration accuracy of AIR, we focused on the filter processing method that enhances the contrast of registration images. In our study, we performed the AIR using 2D X-ray images with and without contrast enhancement filter and compared the registration accuracy. We further evaluated the influence of filter strength on image registration accuracy.

2. Material and Methods

This study is a retrospective study using 13 patients with head and neck cancer treated using proton beam therapy. Image registration was performed between Digitally Reconstructed Radiograph (DRR) created from the CT simulation images and 2D X-ray images obtained before each fraction of radiation. The VeriSuite software (MedCom, Germany) with MI-based algorism (Eq.1) was used to perform the AIR.

$$\mathrm{MI}(X,Y) = \sum_{Y}\sum_{X} P(X,Y)\log_2 \frac{P(X,Y)}{P(X)P(Y)} \quad \text{(Eq.1)}$$

The contrast enhancement filter in VeriSuite software was used for filter processing of 2D X-ray images before image registration. The contrast enhancement filter had two functions, first is the process of extracting the edge component followed by enhancement to the gradient of their image values. The second was to process the finest smooth original image followed by its subtraction from the original image. The filter strength represents the rate at which a subtracted smoothed image is processed, and has a range from 0% to 100%. In our study, a filter strength of 60% (normal), 75%(strong), and 95% (very strong) were used for image processing.

2.1 Accuracy of image registration

To evaluate image registration accuracy, we used set-up error in 6D to compared AIR (with and without contrast enhancement filter) and MIR. Clinical tolerance error was set as the translational error < 1 mm and rotational error < 0.5 degree. The result of MIR was assessed by two experienced radiation therapists.

2.2 Normalized mutual information

To evaluate the similarity between DRR and registration images, the normalized mutual information (NMI) [5] was used. The NMI was calculated using in-house software written in python, the following calculation was used as shown in equation (Eq.2).

$$NMI(X, Y) = \frac{MI(X, Y)}{\sqrt{H(X)H(Y)}} \qquad \text{(Eq.2)}$$

In the above equation, H denotes the entropy of the image (X and Y). The NMI range from 0 to 1, and if the image X and Y are the same, NMI is considered to have a value of 1 (NMI (X, X) = 1).

3. RESULTS

The achieved ratio of clinical tolerance was 35% and 92.5% for AIR without and with filter respectively. Under the condition of non-filter and with the filter strength of 60%, 75%, and 95%, the average translational error was RL: 0.86±1.20 (mean±1SD) / SI: 0.51±0.81, / AP: 0.35±0.74 mm, RL: 0.39±0.41 / SI: 0.31±0.21, / AP: 0.31±0.38 mm, RL: 0.40±0.36 / SI: 0.35±0.26, / AP: 0.32±0.40 mm, RL: 0.25±0.27 / SI: 0.30±0.27, / AP: 0.26±0.33 mm respectively(Table1), the average rotation error was Yaw: 0.63±1.41 / Pitch: 0.22±1.25, / Roll: 0.54±1.10 degrees, Yaw: 0.15±0.25 / Pitch: 0.10±0.13, / Roll: 0.16±0.31 degrees, Yaw: 0.12±0.19 / Pitch: 0.13±0.15, / Roll: 0.16±0.22 degrees, Yaw: 0.08±0.11 / Pitch: 0.10±0.13, / Roll: 0.06±0.08 degrees, respectively(Table2). Using non-filter and filter strength 60%, 75% and 95%, the result of NMI in 13 patients was 0.50 ± 0.05 (mean ± 1SD), 0.64 ± 0.04, 0.64 ± 0.04, 0.63 ± 0.04 respectively as shown in Table3.

4. DISCUSSION

The MI-based AIR with the contrast-enhancement filter achieved high registration accuracy that does not require manual modification in 92.5% of the measurements, and it improved the registration accuracy by 60% in comparison to the non-filter. The average translational and rotational error was greatly improved by using the contrast-enhancement filter, and modifying the filter strength contributed to a small improvement in registration accuracy. The NMI was significantly improved by using the contrast-enhancement filter as shown in Figure 1, but increasing the filter strength didn't contribute to improving the NMI. Using the MI-based AIR system in image registration between DRR and 2D X-ray images, may improve the registration accuracy and achieve the high accuracy image registration that needs no manual modification.

5. CONCLUSION

Image processing that enhances the edge and subtracts the smoothing image from the original, enhanced the 2D X-ray images characteristics almost similar to the DRR, and hence lead to an improvement in NMI. Image processing by the contrast-enhancement filter can improve the registration accuracy that needs no manual modification. The MI-based AIR with the contrast-enhancement filter may be able to eliminate manual workflow in image registration and can provide better accuracy and speed.

REFERENCES

1 A. Sawada, K. Yoda, M. Numano, et al., Patient positioning method based on binary image correlation between two images for proton-beam radiation therapy, Med. Phys. 32(10), 3106–3111 (2005).

2 M. Yoon, M. Cheong, J. Kim, D.H. Shin, S.Y. Park, and S.B. Lee, Accuracy of an automatic patient-positioning system based on the correlation of two edge images in radiotherapy, J. Digit. Imaging 24(2), 322–330 (2011).

3 Viola P, Wells WM. Alignment by maximization of mutual information. Proceedings of IEEE International Conference on Computer Vision. 2002.

4 T. Itou, H. Shinohara, K. Sakaguchi, T. Hashimoto, T. Yokoi, and T. Souma, Multimodal image registration using IECC as the similarity measure, Med. Phys. 38(2), 1103–1115 (2011).

5 Studholme C, Hill DLG, Hawkes DJ. An overlap invariant entropy measure of 3D medical image alignment. Pattern Recogn. 1999; 32:71–86.

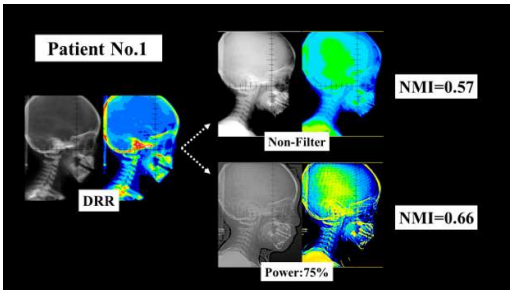

***Figure* 1** *Improvement of the difference in characteristics between 2D-image and DRR by the contrast-enhancement filter*

Table 1 *Translation error(mm)*

	Non-filter	60%	75%	95%
Average				
RL	0.86	0.38	0.40	0.25
SI	0.51	0.31	0.34	0.30
AP	0.35	0.31	0.32	0.26
Standard Deviation				
RL	1.20	0.41	0.36	0.27
SI	0.81	0.21	0.26	0.27
AP	0.74	0.38	0.40	0.33
Max				
RL	3.95	1.22	1.21	0.78
SI	2.10	0.59	0.81	0.76
AP	0.85	0.85	0.86	0.77

Table 2 *Rotation error(degree)*

	Non-filter	60%	75%	95%
Average				
RL	0.63	0.15	0.12	0.08
SI	0.22	0.10	0.13	0.10
AP	0.54	0.16	0.16	0.06
Standard Deviation				
RL	1.41	0.25	0.19	0.11
SI	1.25	0.13	0.15	0.13
AP	1.10	0.31	0.22	0.08
Max				
RL	5.58	0.73	0.62	0.27
SI	0.57	0.21	0.25	0.2
AP	1.90	0.47	0.42	0.2

Table 3 *NMI between DRR and 2D-Xray image*

Patient	Non-filter	60%	75%	95%
1	0.57	0.66	0.66	0.65
2	0.47	0.61	0.61	0.60
3	0.50	0.65	0.65	0.65
4	0.53	0.69	0.69	0.69
5	0.47	0.66	0.66	0.66
6	0.52	0.65	0.65	0.65
7	0.46	0.57	0.57	0.56
8	0.41	0.59	0.59	0.59
9	0.53	0.66	0.66	0.66
10	0.53	0.66	0.66	0.66
11	0.54	0.66	0.66	0.66
12	0.52	0.64	0.64	0.64
13	0.57	0.64	0.64	0.63
Average	0.50	0.64	0.64	0.63
SD	0.05	0.04	0.04	0.04

Monte Carlo calculation of beam quality correction factors in proton beams using PTSIM/GEANT4

Masaya Ichihara[1], Keisuke Yasui[2], Chihiro Omachi[3], Toshiyuki Toshito[3], Junya Nagata[1], Riki Oshika[1], Shun Kurata[1], and Naoki Hayashi[2]

1 Graduate School of Health Sciences, Fujita Health University,
2 School of Medical Sciences, Fujita Health University,
3 Nagoya Proton Therapy Center

Abstract

The beam quality correction factor (k_Q) which correct for the difference in the ionization chamber response between the reference and clinical beam quality, is an integral part of radiation therapy dosimetry. However, there are few data on the k_Q required for calculating the absolute dose for the proton beam. Furthermore, the perturbation correction factor (P_Q) of ionization chambers is assumed to be unity for proton beams in the IAEA TRS-398 CoP. The aim of this study was to calculate k_Q and P_Q for monoenergetic proton beams using PTSIM/GEANT4 Monte Carlo calculation system. The k_Q factors calculated between this study and Baumann et al (2020) agree within 0.3% at all energies. Between this study and Goma and Sterpin (2019) agree within 0.6% for low energies. However, there was a difference of up to 1.2% at 250 MeV. These results seem to suggest that the higher the proton energy, a significant effect of the physics processes on k_Q. The P_Q was different than unity in contrast to the assumption from the IAEA TRS-398 CoP.

Keywords: proton dosimetry, beam quality correction factors, perturbation correction factors, Monte Carlo

1. INTRODUCTION

In radiotherapy, determination and management of delivery dose by measuring the absolute dose are important. The reference dose for clinical proton beams is based on ionization chamber dosimetry. The beam quality correction factors (k_Q) which correct for the difference in the ionization chamber response between the reference and clinical beam quality, is an integral part of radiation therapy dosimetry using an ionization chamber. However, there are few data on the k_Q required for calculating the absolute dose for the proton beam. Hence, the aim of this study is to calculate k_Q for ionization chambers in clinical proton beams using the Monte Carlo (MC) simulation. To calculated k_Q, we calculated f-see eq. (1) below-for the user beam quality (Q) and the reference beam quality (Q_0). Note that f_Q/f_{Q0} ratios, which are the basis for the MC calculated k_Q, are the only part of the k_Q that can be calculated using MC methods. When using the term 'Monte Carlo calculated k_Q ' it means the MC calculation of f_Q/f_{Q0} ratios and subsequent derivation of k_Q by using the $W_{air,Q}$ values. Furthermore, the perturbation correction factors (P_Q) of ionization chambers is assumed to be unity for proton beams in the IAEA TRS-398 CoP. We also calculated P_Q to clarify whether the assumption from the IAEA TRS-398 CoP is sufficiently accurate or not.

2. MATERIAL AND METHODS

2.1 Monte Carlo code PTSIM/GEANT4

We used PTSIM a particle therapy simulation flamework based on Monte Carlo code GEANT4 version 10.05.p01. Since, PTSIM is based on GEANT4, physics models and nuclear interaction models are the same as in Geant4. O'Brien et al (2016) and Wulff et al (2018) showed that the Fano cavity test passes within 0.1% for photons and 0.1%-0.2% for protons by setting the appropriate physical parameters in Geant4. Based on the findings of O'Brien et al (2016) and Wulff et al (2018), Baumann et al (2020) calculated the k_Q using TOPAS/GEANT4. In this study, we used the same physics models as Baumann et al (2020). We used physics list G4E for photon simulations and physics list g4em-standard_opt4 for proton simulations. We used physics list g4h-phy_QGSP_BIC_HP to simulate the nuclear interactions. O'Brien et al (2016) showed Fano cavity test results can be improved by limited the step size. To control the length of a step, the parameters dRoverR and finalRange are used in Geant4. dRoverR is describes the maximum length of a step in relation to the residual range of the particle. The dRoverR and finalRange are set to 0.003 and 1 nm for the photon simulations and 0.05 and 100 nm for the proton simulation.

2.2 Geometries and source parameters

To validate the simulation, we compared the results of previous studies with reference beam quality. A uniform and parallel beam of 10 × 10 cm^2 was used for the Q_0 of ^{60}Co. That reference depth is 5 gcm^{-2} . We simulated a photon source is located 95 cm away from the water phantom surface, i.e. 100 cm away from the ionization chamber. As proton beams, we investigated four different monoenergetic beams (150, 160, 200 and 250 MeV) at a depth of 2 gcm^{-2}. We reproduced a spot scanning nozzle at the Nagoya Proton Therapy Center and calculated the k_Q for the cylindrical ionization chamber (30013: PTW). The scanning nozzle contained a titanium vacuum window, a beam profile monitor that consisted of a multiwire ionization chamber, x and y magnets, a helium chamber, two plane-parallel ionization chambers (main and sub dose monitors), and a spot-position monitor that consisted of a multiwire ionization chamber (see Figure 1). Spot scanning

irradiation is an advanced method in which narrow proton beams delivered from an accelerator is irradiated to the cancerous area using scanning magnets. In PTSIM, the scanning beam was defined by the parameters of proton energy in each spot layer, spot position at the isocenter, and intensity of proton beam at each spot.

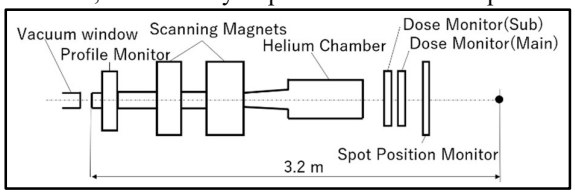

Figure 1 *Components of proton scanning beam nozzle.*

2.3 Calculation of k_Q

The Monte Carlo k_Q was calculated as follows.

$$k_Q = \frac{f_Q}{f_{Q_0}} \frac{W_{air,Q}}{W_{air,Q_0}} = \frac{(D_w/\bar{D}_{air})_Q}{(D_w/\bar{D}_{air})_{Q_0}} \frac{W_{air,Q}}{W_{air,Q_0}} \quad (1)$$

f is determined by the ratio of the absorbed dose of water D_w to the dose of cavity $\bar{D}_{air}$ in the chamber. f is a chamber specific parameter and dependent on beam quality. The absorbed dose to water D_w was calculated in the region of 1 cm radius and 250 µm thickness. The absorbed dose to air $\bar{D}_{air}$ was calculated in the cavity of the ionization chamber. D_w and $\bar{D}_{air}$ were calculated by Monte Carlo simulation, while W_{air} value was adopted from ICRU 90.

2.4 Calculation of P_Q

The P_Q is to correct the inequivalence caused by the difference in material between water and cavity of the ionization chamber due to the insertion of the ionization chamber in the water phantom. The Monte Carlo P_Q was calculated as follows.

$$P_Q = f_Q/(S_{w,air})_Q \quad (2)$$

Spencer-Attix water/air stopping power ratios ($S_{w,air}$) calculated in the previous report were used for each beam.

3. RESULTS AND DISCUSSION

3.1 Monte Carlo calculated f_{Q0} for ^{60}Co spectrum

In table 1, the Monte Carlo calculated f_{Q0} for the ^{60}Co photon beam are shown. Goma and Sterpin (2019) used MC code PENH. The I-values for all materials are the same for the two references.

The f_{Q0} in this study were in good agreement with the literature values. The f_{Q0} calculated for farmer chamber 30013 in this study agreed within 0.5% to the value presented by Goma and Sterpin (2019). Furthermore, the results are agreement with the values calculated by Baumann et al. (2020) using TOPAS/GEANT4 to within 0.1%.

Table 1 *Monte Carlo calculated f_{Q0} for ^{60}Co radiation in a cylindrical ionization chamber and comparison with values from the literature.*

Chamber	This study	Goma et al (2019)	Baumann et al (2020)
PTW 30013	1.111	1.106	1.112

3.2 Monte Carlo calculated f_Q for monoenergetic proton beams

Table 2 shows the Monte Carlo calculated f_Q for different monoenergetic proton beams in this study are shown. Figure 2 shows the f_Q from this study along with the f_Q published in the literature.

For the maximum difference, the f_Q between this work and Baumann et al (2020) was 0.4%. Interestingly, the values calculated in this work approached to Baumann et al (2020) at higher energy and agreed within 0.1% at 250 MeV. The value calculated by Goma and Sterpin (2019) agree with this study only low energies within 0.2 %. For higher energies, there was a difference of up to 0.8% at 250 MeV. The reason for the difference in f_Q is assumed to be difference in physics models. In this study we used the same physical models as Baumann et al (2020). The results of this study and the differences between the two references suggest that physical models, such as nuclear interaction models and parameters controlling step size, have a significant impact on f_Q at higher energies.

Table 2 *Monte Carlo calculated f_Q for different monoenergetic proton beams in this study.*

Energy (MeV)	*150*	*160*	*200*	*250*
f_Q	*1.1260*	*1.1265*	*1.1233*	*1.1169*

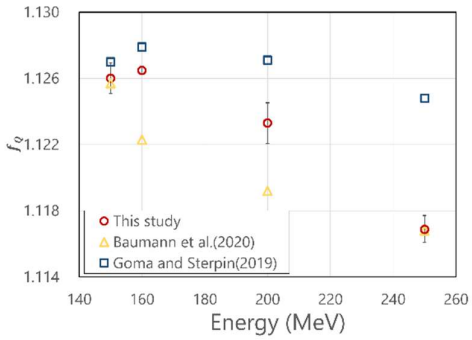

Figure 2 *Monte Carlo calculated f_Q for monoenergetic proton beams in a cylindrical ionization chamber and comparison with values from previous studies. The error bars correspond to one standard uncertainly of the three times measurements.*

3.3 Monte Carlo calculated k_Q and P_Q for monoenergetic proton beams

In tables 3 and 4, the Monte Carlo calculated k_Q and P_Q for different monoenergetic proton beams in this study are shown. The k_Q is calculated from equation (1) and the P_Q is calculated from equation (2). Note that this study used the same W_{air} values as both Goma and Sterpin (2019) and Baumann et al (2020). Figure 3 shows the k_Q from this study along with the f_Q published in the literature.

The k_Q calculated between this study and Baumann et al (2020) agreed within 0.3% at all energies. This agreement indicates that the literature based on the reference condition is also valid for clinical conditions. Between this study and Goma and Sterpin (2019) agreed within 0.6% for low energies. However, there was a difference of up to 1.2% at 250 MeV. These results seem to suggest again that the higher the proton energy, the larger the influence of physical models in the k_Q. The P_Q was about 1.0% different than unity at 250 MeV. This difference cannot be neglect and P_Q should be account for the calculation of k_Q.

Table 3 *Monte Carlo calculated k_Q for different monoenergetic proton beams in this study.*

Energy (MeV)	*150*	*160*	*200*	*250*
k_Q	*1.0275*	*1.0279*	*1.0249*	*1.0189*

Table 4 *Monte Carlo calculated P_Q for different monoenergetic proton beams in this study.*

Energy (MeV)	*150*	*160*	*200*	*250*
P_Q	*0.9973*	*0.9949*	*0.9950*	*0.9893*

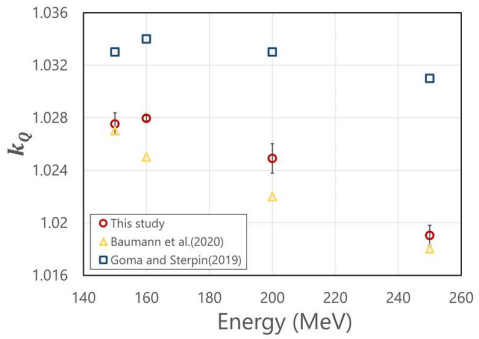

Figure 3 *Monte Carlo calculated k_Q for monoenergetic proton beams in a cylindrical ionization chamber and comparison with values from previous studies. The error bars correspond to one standard uncertainly of the three times measurements.*

5. CONCLUSION

We calculated the k_Q under the clinical condition in proton beams using PTSIM/GEANT4. The k_Q at high energies were affected by physical models significantly such as nuclear interaction models. However, these results cannot to identify the role of the physical models in the calculation of the k_Q at high energies. This need to be examine in further investigations. Additionally, P_Q was different than unity in contrast to the assumption from the IAEA TRS-398 CoP.

REFERENCES

Andreo P, Burns D T, Hohlfeld K, Huq M S, Kanai T, Laitano F, Smyth V and Vynicker S 2000 Absorbed dose determination in external beam radiotherapy: an international code of practice for dosimetry based on standards of absorbed dose to water *Technical Report* Technical Report Series TRS-398 (Vienna: International Atomic Energy Agency) (http://www-naweb.iaea.org/nahu/DMRP/documents/)

Baumann K-S, Kaupa S, Bach C, Engenhart-Cabillic R, Zink K. 2020 Monte Carlo calculation of beam quality correction factors in proton beams using TOPAS/GEANT4 *Phys. Med. Biol.* 65 055015

Gomà C and Sterpin E 2019 Monte Carlo calculation of beam quality correction factors in proton beams using PENH *Phys. Med. Biol.* 64 185009

O'Brien D J, Roberts D A, Ibbot G S and Sawakuchi G O 2016 Reference dosimetry in magnetic fileds: formalism and ionization chamber correction factors *Med. Phys.* 43 4915-27

Wulff J, Baumann K S, Verbeek N, Bäumer C, Timmermann B and Zink K 2018 TOPAS/GEANT4 configuration for ionization chamber calculations in proton beams *Phys. Med. Biol.* 63 115013

The comparison between planar gated blood pool imaging and gated blood pool SPECT to evaluate ventricular function in breast cancer patients receiving cardiotoxic cancer treatments

Kanokpich Khwaiphan[1], Benjapa Khiewvan [2], Pinyaporn On-Ekkasit [2], Thonnapong Thongpraparn[2], Sunanta Chiewvit[2]

Division of Radiological Science, Department of Radiology, Faculty of Medicine Siriraj Hospital, Mahidol University 1, Division of Nuclear Medicine, Department of Radiology, Faculty of Medicine Siriraj Hospital, Mahidol University 2,

Abstract

Introduction: Multiple Gated Acquisition (MUGA) is the study for evaluation of ventricular functions. Planar gated blood pool (GBP) imaging is commonly used to evaluate left ventricle performance in cancer patients who received treatment related cardiotoxicity. There are two techniques of GBP which are planar and SPECT techniques. This study was performed to compare left ventricular ejection fraction (LVEF), right ventricular ejection fraction (RVEF), left end diastolic volume (LEDV), left end systolic volume (LESV) and wall motion between planar and Single Photon Emission Tomography (SPECT) GBP techniques in breast cancer patients.

Method: Fifty-seven MUGA studies in 20 breast cancer patients were performed. Planar and SPECT MUGA were performed in patients who received treatment related cardiotoxicity (Anthracyclines and/or Transtuzumab) before and during chemotherapy every 3 months in Siriraj hospital between April 1, 2019 and July 21,2020.The correlation and agreement of LVEF, RVEF, ESV, and EDV were compared between two techniques. Wall motions of both ventricles were also observed.

Results: The mean LVEF, RVEF, left EDV and left ESV of planar GBP were 66.12±5.21%, 45.07±6.19%, 117.67±28.38 mL and 40.04±12.62 mL. The mean LVEF, RVEF, left EDV and left ESV of SPECT GBP were 67.21±8.11%, 45.35±6.44%, 87.75±13.22mL, 29.14±9.95mL. There was no significant different LVEF (p=0.082) and RVEF (p=0.760) between both techniques using Paired samples t-test. However, there was significantly different in EDV and ESV (p<0.001) between both techniques. LVEF showed good agreement (ICC=0.865, 95% confidence interval (CI) 0.771-0.921) and strong correlation (r=0.846, p-value<0.001). RVEF showed moderate agreement (ICC=0.577, 95% CI 0.278-0.751) with low correlation (r=0.402, p-value=0.002). EDV showed very poor agreement (ICC=0.167, 95% CI-0.165-0.440) and very poor correlation (r=0.225, p-value=0.092).ESV showed moderate agreement (ICC=0.559, 95% CI -0.095-0.799) with moderate correlation (r=0.579, p-value<0.001). SPECT GBP showed abnormal wall motion in 11 patients (55%) which is normal on planar images.

Conclusion: Gated blood pool SPECT technique can be used to evaluate left ventricular function in cancer patients receiving treatment related cardiotoxicity because there were no differences between planar and SPECT techniques. In addition, SPECT seems to detect abnormality of wall motion which cannot be determined by planar technique.

Keywords: Gated blood pool, Left ventricular ejection fraction, Planar gated blood pool, Gated blood pool SPECT

1. INTRODUCTION

Gated blood pool imaging (GBP) or Multiple Gated Acquisition (MUGA) is the nuclear medicine study for evaluation of ventricular functions. MUGA will collect a trigger signal from R wave from ECG signal. Planar gated blood pool technique is the common technique using to evaluate the performance of left ventricle in cancer patients who received treatment related cardiotoxicity. For example, Anthracyclines, a group of chemotherapy, that causes cumulative dose-dependent cardiac toxicity or Transtuzumab that affected to monoclonal antibodies. Those effects can also lead to left ventricular dysfunction. Such side effect can be prevented when left ventricular dysfunction can be early detected and provide timely treatment. A useful indicator of left ventricular ejection is the left ventricular ejection fraction (LVEF). Planar gated blood pool imaging is the first choice for assessment cardiac function because of ability of reproducibility. However, the disadvantage is the overlap of the cardiac structures (1), which affects the separation of between left and right ventricular function.

The single Photon Emission Computed Tomography (SPECT) technique is also used to examinate for LVEF calculation. SPECT can produce images in multiple planes to create a three-dimensional image. Therefore, this technique can clearly separate the parts of the heart chambers and also helps to assess the wall motion (2). In previous studies, Massardo et al (1). has found that planar and SPECT have good agreement and correlation to assess heart function as well as heart volume with linear correlations were 0.845, 0.688, 0.927 and 0.94 for LVEF, RVEF, end diastolic volume (EDV) and end systolic volume (ESV) of the left ventricle, respectively. Many breast cancer patients are offered cardiac function assessments before and

after initiating cardiac cancer drug therapy in Nuclear medicine at Siriraj Hospital. In present, planar technique is selected as a standard examination. This study aimed to compare between planar gated blood pool and Single Photon Emission Tomography (SPECT) gated blood pool technique in breast cancer patients. To study the agreement and additional benefits, the SPECT technique in the terms of left ventricular ejection fraction (LVEF), right ventrocular ejection fraction (RVEF), left end diastolic volume (LEDV), left end systolic volume (LESV) and wall motion were analyzed.

2. MATERIAL AND METHODS

Inclusion criteria were ≥ 18 years old participants assessed the cardiac function for baseline and during chemotherapy cardiotoxic in Department of Nuclear Medicine at Siriraj hospital. This research approved by IRB-Approved research at Siriraj hospital (no. Si 160/2019). All participants must be voluntarily. Hemodynamic instability, cardiac arrhythmia and pregnant were excluded.

2.1 Population

Fifty-seven studies from 20 breast cancer patients receiving treatment related cardiotoxicity (Anthracyclines and/or Transtuzumab) were collected. All patients were required to MUGA scan by both techniques (Planar and SPECT). Each patient will be examined before chemotherapy until terminate the program with 90 days intervals.

2.2 Acquisition and processing

Radiopharmaceutical injection red blood cells (RBC) were labeled approximately 20 mCi of technetium-99m pertechnetate (Tc-99m) in-vivo 20 minutes after intravenous administration of stannous pyrophosphate (Sn2 +) by intravenous.

Both techniques were performed using the SPECT/CT Discovery NM 670 Pro model (General electric health care), Dual head detector, collimator low energy high resolution, Matrix size 64x64, Zoom 2.0, setting window width at 140 ± 10% energy. All data processing was performed by 1 physicist (same operators).

2.2.1 Planar gated blood pool imaging

Planar gated blood pool imaging was collected the cardiac cycle (R-R interval) divided into 24 frames per cycle. Forward/Backward gate frame were taken 33 msec / frame, PVC threshold was 25%. The data were collected until total kcounts of anterior, LAO 45° (best septal) and LAO 70° were 5000. The EF analysis within Xeleris software was used for Planar technique. The ROI (region of interest) were defined over the LAO 45° image covering the position of left and right ventricle to calculate the ejection fraction, end-diastolic, end-systolic, stroke volume and paradox image.

2.2.2 Gated blood pool SPECT imaging

SPECT technique imaging was collected the cardiac cycle (R-R interval) divided into 16 frames per cycle, PVC threshold was 25%, and collected data. To acquire SPECT images, the detector projections in L-mode were clock wise rotated from right anterior oblique (RAO) 45° to left posterior oblique (LPO) 45° with 3° intervals by step and shoot technique (total duration was about 20 min per study).

In reconstruction method, SPECT data were reconstructed into an 3D image using a back-projection filter, ramp filter with low pass filter and butterworth. After that, such 3D matrix was separated into 3 planes followed vertical long axis, short axis and horizontal long axis. Quantitative blood pool SPECT (QBS) was performed using Cedars blood pool gated (BPGS). To obtain all research outcome, the septal line, both end-diastolic and end-systolic situation, was adjusted by manual and LV's and RV's ROI were automatically defined.

2.3 Ejection function calculation

The formula for calculating EF is:

$$EF = \frac{(EDV - ESV)}{EDV}$$

Where EF was ejection fraction, EDV and ESV were end diastolic and end systolic volume, which obtained from ROI area, respectively.

Data images obtained from processing were transferred to 3 observers: 1 residence and 2 nuclear medicine physicians. The results were displayed as a blind technique to compare and evaluate LVEF, RVEF, EDV, ESV, and wall motion, quantitatively. If the results were difference, 3 observers would consensus to reach a conclusion one.

2.4 Statistical analysis

Data were analyzed by SPSS statistics program version 25.0. Values were expressed as mean ± standard deviation (SD). Pearson's correlation coefficient and Interclass correlation coefficient (ICC) were used to compare the results of planar and SPECT techniques. The correlation and agreement of four-paired outcomes (LVEF, RVEF, EDV and ESV) were individually analyzed using above coefficient, respectively. The different values were presented in Bland and Almans plot.

3. RESULTS

The mean LVEF, RVEF, left EDV and left ESV of planar technique were 66.12 ± 5.21%, 45.07 ± 6.19%, 117.67 ± 28.38 mL and 40.04 ± 12.62 mL, respectively. The mean of SPECT technique was 67.21 ± 8.11%, 45.35 ± 6.44%, 87.75 ± 13.22mL, 29.14 ± 9.95mL. From the results of paired samples t-test, LVEF and RVEF had no significant differences with p-values were

0.082 and 0.760, respectively. There was significant difference in EDV and ESV (p<0.001). The correlation results demonstrated in Table 1. From Pearson's and ICC analysis, LVEF showed good agreement (ICC=0.865, 95% confidence interval (CI) 0.771-0.921) and strong correlation (r=0.846, p-value<0.001). RVEF showed moderate agreement (ICC=0.577, 95% CI 0.278-0.751) with low correlation (r=0.402, p-value=0.002). EDV showed very poor agreement (ICC=0.167, 95% CI-0.165-0.440) and very poor correlation (r=0.225, p-value=0.092).ESV showed moderate agreement (ICC=0.559, 95% CI -0.095-0.799) with moderate correlation (r=0.579, p-value<0.001). Bland - Altman plots of LVEF, RVEF, EDV and ESV with mean differences were -1.1% (range of agreement from -10.2% to 8.0%), 0.3% (range of agreement from -13.3% to 13.8%), 10.9%(range of agreement from -9.9% to 31.7%), and 29.9% (range of agreement from -25.9% to 85.7%), were shown in *Figure 1-4,* respectively. In addition, abnormality of heart's wall motions was found in 11 cases.

Table 1 *Correlation results*

Planar-SPECT	r	p-value	ICC
LVEF	0.846 (p<0.001)	0.082	0.865
RVEF	0.402 (p=0.002)	0.760	0.577
EDV	0.225 (p=0.092)	<0.001	0.167
ESV	0.579 (p<0.001)	<0.001	0.559

*p-value < 0.05

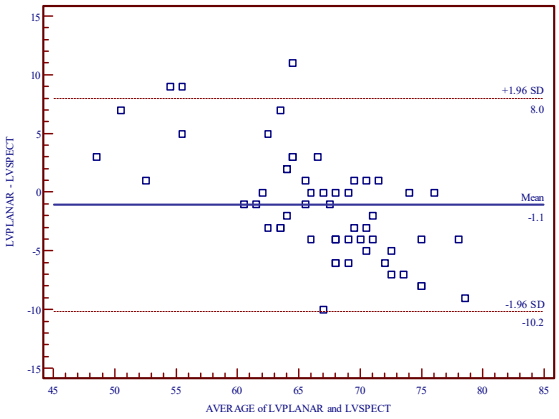

Figure 1 *LVEF defined by Planar versus SPECT GBP technique.*

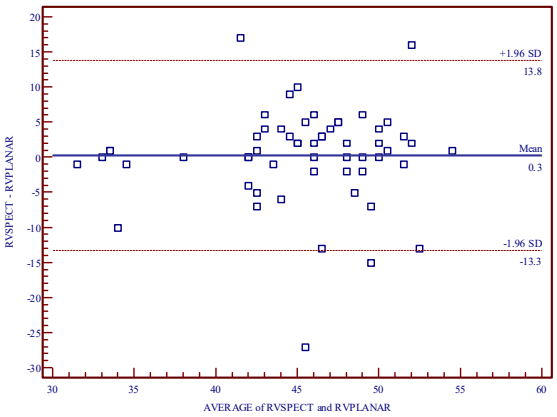

Figure 2 *RVEF defined by Planar versus SPECT GBP technique.*

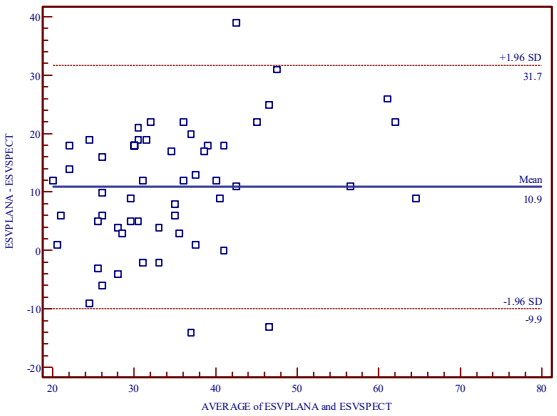

Figure 3 *LESV defined by Planar versus SPECT GBP technique.*

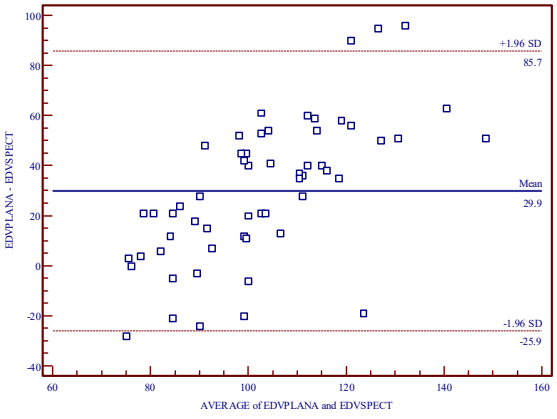

Figure 4 *LEDV defined by Planar versus SPECT GBP technique.*

4. DISCUSSION

Gated blood pool imaging or Multiple Gated Acquisition (MUGA) is the common technique using to evaluate the performance of left ventricle in cancer patients who received treatment related cardiotoxicity. LVEF is highly acceptable for evaluation. Additionally,

also find RVEF, ventricular volumes and wall motion from GBP (3).

A total 57 cases in 20 patients were studied in this research. The value of LVEF, RVEF, left EDV, left ESV and wall motion were compared between planar versus SPECT technique.

4.1 Left ventricular ejection fraction (LVEF)

The mean of LVEF from planar and SPECT technique were not difference (p-value = 0.082), strong correlation (r=0.846) and good agreement (ICC=0.865). This result was compatible with previous studies (1-2). However, Hacker et.al (5) has the dissimilarity results. Their LVEF agreement shown in moderated level (r=0.65) and planar values were over than SPECT with no significant difference (p-value=0.001). The research author argues that QBS program for processed SPECT GBP cannot flexible enough to separate left ventricle from left atrium. Due to the patient in their study has congestive heart failure, which may have associated of mitral regurgitation.

4.2 Right ventricular ejection fraction (RVEF)

Planar GBP technique showed the mean of RVEF from planar and SPECT technique were no difference (p-value = 0.760), low correlation (r=0.402) and moderate agreement (ICC=0.577). This result was incompatible with previous studies (1,5). has founded that RVEF values of planar less than SPECT techniques, with no significant difference (p-value=0.0017). RVEF from planar and SPECT showed moderate correlation (r=0.688) and agreement (ICC=0.5775). The reasons of such differences as well as found in LVEF section.

4.3 Left ventricular end diastolic volume (LVEDV) and Left ventricular end systolic volume (LVESV)

Because automated ROI of QBS could not be adjusted and incompletely covered left ventricular area, furthermore, both LVEDV and LVESV in this study differed to previous one (1). Our results of LVEDV and LVESV presented in very poor (r=0.225, ICC=0.167) and moderate (r=0.579, ICC=0.559) correlation, respectively. While literature study shown strong correlation (r=0.927, ICC=0.9138 and r=0.94, ICC=0.9385 for LVEDV and LVESV, respectively). Those differences caused by constant of automated ROI. QBS in this study used threshold method with constant threshold value that might be not suitable for every condition to defined ROI.

4.5 Wall motion

By 3D volume evaluation of SPECT GBP, the abnormal wall motions, including subtle one, could be detected. From 20 patients or 57 cases, there were 11 cases (55%) that abnormal wall motion were found by SPECT. By planar technique, all of cases were reported as normal motion because 2D operation presented the unclear heart's movements. The 3D volume operations of SPECT, therefore, were more accurate.

The limitation of study is that the results were not compared with gold standard of cardiac function analysis (4) and fully automatic software (QBS) with pre-defined parameters, such as segmented threshold value, was performed for SPECT technique. To improve the research quality in future study, the results of cardiac MRI will be represented as the reference values and QBS parameters will be considered to improve processing performances.

5. CONCLUSION

Gated blood pool SPECT technique could be used to evaluate left ventricular function in cancer patients receiving treatment related cardiotoxicity. SPECT technique seems to detect abnormal wall motion, which could not be determined by planar technique.

ACKNOWLEDGEMENTS

This research was performed with the support of nuclear medicine staff in Department of Nuclear Medicine. A scholarship grant was supported by the Siriraj Research Development Fund (managed by Routine to Research: R2R).

REFERENCES

1. Massardo T, Jaimovich R, Lavados H, Gutiérrez D, Rodríguez JC, Saavedra JM, et al. Comparison of radionuclide ventriculography using SPECT and planar techniques in different cardiac conditions. European journal of nuclear medicine and molecular imaging. 2007;34(11):1735-46.
2. Wright GA, Thackray S, Howey S, Cleland JG. Left ventricular ejection fraction and volumes from gated blood-pool SPECT: comparison with planar gated blood-pool imaging and assessment of repeatability in patients with heart failure. Journal of Nuclear Medicine. 2003;44(4):494-8.
3. Mettler Fred A., Guiberteau Milton J. Essentials of Nuclear Medicine and Molecular Imaging. 7th ed. Philadelphia, PA: Elsevier; 2019.
4. Harel F, Finnerty V, Grégoire J, Thibault B, Marcotte F, Ugolini P, et al. Gated blood-pool SPECT versus cardiac magnetic resonance imaging for the assessment of left ventricular volumes and ejection fraction. Journal of Nuclear Cardiology. 2010;17(3):427-34.
5. Hacker M, Hoyer X, Kupzyk S, La Fougere C, Kois J, Stempfle H-U, et al. Clinical validation of the gated blood pool SPECT QBS® processing software in congestive heart failure patients: correlation with MUGA, first-pass RNV and 2D-echocardiography. The international journal of cardiovascular imaging. 2006;22(3-4):407-16.

Patient-specific organ dose calculated using dose tracking software based on Monte Carlo simulation in pediatric abdominal CT

Yuparak Innan1,2,4, Kitiwat Khamwan1,3,4*

1 Medical Physics Program, Faculty of Medicine, Chulalongkorn University, Bangkok 10330, Thailand
2 Division of Diagnostic Imaging, Department of Radiology, Praram9 Hospital, Bangkok 10310, Thailand
3 Division of Nuclear Medicine, Department of Radiology, Faculty of Medicine, Chulalongkorn University and King Chulalongkorn Memorial Hospital, The Thai Red Cross Society, Bangkok 10300, Thailand
4 Chulalongkorn University Biomedical Imaging Group, Department of Radiology, Faculty of Medicine, Chulalongkorn University, Bangkok 10330, Thailand

Abstract

Objective: To determine the patient-specific organ doses using dose tracking software in pediatric abdominal CT.

Materials and Methods: The retrospective data were collected from 78 pediatric patients (164 studies, age range 0-15 years-old), who underwent single phase abdominal CT at Praram9 Hospital. The tube voltages ranged between 80 and 135 kVp were adjusted according to the size and age of patients, and rotation time 0.35-0.5 sec. All patients were acquired using the automatic exposure control (AEC) protocol. The organ dose calculations were based on the Monte Carlo simulation using the Radimetrics dose tracking software in accordance with patient age that derived from stylized computational phantom model. The size-specific dose estimates (SSDE) were calculated based on the effective diameter method. The organ doses obtained from pediatric abdominal CT were then compared between age group.

Results: Average patient body weights of 38.6±18.5 kg (range 3.89 - 94.00 kg) were obtained in this study. Five highest organ doses were found in kidneys, stomach, urinary bladder, upper large intestine and spleen for 15-yr patients, with the values of 18.44, 17.07, 16.74, 16.47 and 16.14 mGy, respectively. The average effective dose (ED) for pediatrics abdominal CT in newborn, 1, 5, 10 and 15 years-old were 2.24, 3.23, 3.82, 4.89 and 9.19 mSv, respectively. Average SSDE were 2.72, 4.52, 5.82, 8.02 and 13.05 mGy, respectively.

Conclusion: Patient-specific organ and effective doses from 0 through 15-years-old can be determined effectively using dose tracking software. As the various sizes of pediatrics, the patient ED and SSDE were correlated with patient's body weight rather than the patient age.

Keywords*:* CT organ dose, effective dose, size-specific dose estimates, dose tracking software, pediatric CT

1. INTRODUCTION

Computed tomography (CT) is mainly used in the diagnosis as the CT scan can be performed rapidly while proving good image contrast in various cross-sectional planes. CT scans in pediatrics have increased considerably in clinical, resulting increased the probability of cancer induction in the future for pediatric patients as well. As the children are more sensitive from ionizing radiation compared to the adults, assessing the individual organ doses accurately in CT scan is a challenging task. The assessment approach of radiation risk in CT leads to the development of strategies to prevent excessive radiation exposure for children. The patient dose in CT examination is dependent on the amount of radiation output by the scanner and patient size. Presently, all CT scanners are mandated to report radiation dose at least by two values: volumetric CT dose index ($CTDI_{vol}$), and dose-length product (DLP). $CTDI_{vol}$ is a standardized measurement in PMMA (polymethyl methacrylate) phantoms with a diameter of either 16 or 32 cm. However, $CTDI_{vol}$ does not represent real patients' dose and can be underestimated especially in small patients (1). In case of pediatric patients, they have a radiosensitivity higher than the adult's due to smaller body size, more rapidly growing tissue, and longer potential lifespan to express any radiation-related detriment (2). Since the increasing concern of radiation dose from CT scans, it is crucial to have a dosimetry tool that offers accurate evaluation of patient-specific organ doses in an automatic manner to efficiently perform the calculation and to accurately analyze the associated effects. Recent efforts have focused on developing patient dose tracking software to calculate the radiation dose for monitoring and reporting of cumulative radiation dose from various medical imaging modalities, and to analyze big data for patient safety inspections. By these software packages, the patient dose can be calculated based on the Monte Carlo simulation that uses the library of computational phantoms and matches patients to a particular phantom based on age, weight, or diameter. The patient dose tracking software namely Radimetrics, is one of the commercial dosimetric software packages that widely used as a gold standard software for monitoring and reporting radiation dose by devices or by patients (3). Therefore, it is of great interest to calculate the patient-specific organ doses from abdominal CT examination in different ages of pediatric patients based on the Monte Carlo method using this dose tracking software as preliminary data to support the CT clinical dosimetry in pediatric patients.

2. MATERIALS AND METHODS

2.1 Patients data collection

We collected the retrospective data of pediatric patients who underwent abdomen CT examination from CT Toshiba Aquilion ONE 320-detector-row and Siemens SOMATOM Sensation 64-detector-row at Praram9 Hospital, Bangkok, Thailand. Monte Carlo-based patient dose tracking program, Radimetrics, was used to collect and calculate patient specific organ dose (Figure 1). The patient information such as gender, patient height, body weight, displayed $CTDI_{vol}$ and DLP from CT monitor or PACS system were collected from the Radimetrics software. The CT scanning parameters were collected as followings: CT scanner, kVp, mAs, scan length, beam collimation, pitch, rotation time. All of patients were acquired using the automatic exposure control (AEC) protocol. The patient age based on Radimetrics dose monitoring program were sub-divided into 0, 1,5,10 and 15 years-old.

In order to perform the CT quality control and CTDI verification according to IAEA Human health series no. 19, the PMMA phantom and pencil ionization chamber with 10 cm active length were used. Prior collcting the data, the anthropomorphic Rando phantom and radiophotoluminescent glass dosimeters (RPLGDs) were used to measure the organ dose based on the scanning clinical protocol in order to verify the organ doses calculated by Radimetrics program.

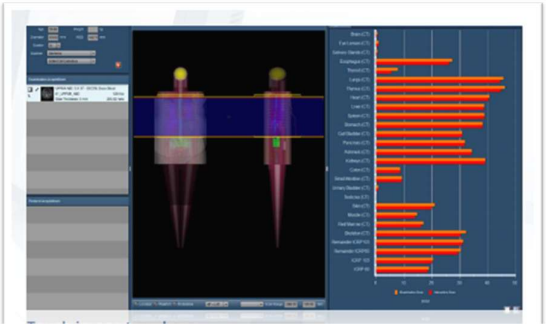

Figure 1 The Radimetrics™ Enterprise Platform (REP).

2.2 Size Specific Dose Estimates (SSDE) Calculation

The SSDE was obtained using the corresponding conversion factor published in the AAPM Task Group reports 204 and 220 (1). The water-equivalent diameter (WED or D_w), the diameter the body would have if it had the same attenuation property as water, does account for the differences in body composition and therefore is a more popular metric for patient size estimate. There are two ways to estimate the WED: one is from the axial images, and the other is from the localizers. Using the axial images, for each slice, the area of the body is isolated from the background, and the pixel values (Hounsfield Units) within the body area are summed and converted to a water-equivalent area to derive the WED. In Radimetrics™ software 2.1 and later, the WED, effective diameter and the SSDE are estimated for each slice of each acquisition, and the $CTDI_{vol}$ at each slice is used to account for the z-axis current modulation. The overall acquisition level SSDE is then the average of the SSDE from all slices within the torso region from that acquisition. The SSDE can be selected either the mid-slice SSDE or the average SSDE. This work, the reported SSDE based on the average of the average acquisition level SSDE was used.

2.3 Pediatric organ dose calculation

The organ dose and effective dose based on patient age computational phantom model using the Radimetrics Monte Carlo-based program were calculated. The major components of the Radimetrics™ Enterprise Platform (REP) Monte Carlo simulator include the modeling of the x-ray source, the patient phantoms, and the interaction between x-ray photons with the patient. The x-ray source spectrum is based on the model described by the National Radiological Protection Board (NRPB) R204 (4). The REP phantom library contains a set of 9 reference computational phantoms that represent the average of the population, as well as a set of bariatric phantoms. The reference phantom set used in this study includes the original 6 Cristy-Eckerman (CE) phantoms, i.e. newborn, 1, 5, 10, 15 years, and adult as illustrated in Figure 2. The patient to phantom mapping is based on age, gender, weight and/or diameter. The criteria for age and gender mapping are listed in Table 1. The selection of patient dose calculation was based on weight and diameter. The simulations are pre-run for various scan protocols with different parameters (such as kVp) for each phantom in library. In each run, the phantom is "scanned" from head to toe along the z-axis in a series of slices. At each slice position, the energy deposited in each organ is recorded and stored in a lookup table.

Table 1. Patient-phantom age and gender mapping.

Patient age range	Matched phantom
0 month < age <= 5 months	Newborn (F, M)
5 months < age <= 3 yrs	Age 1 (F, M)
3 yrs < age < = 7.5 yrs	Age 5 (F, M)
7.5 yrs < age <= 12.5 yrs	Age 10 (F, M)
age > 12.5 yrs	Age 15 (F); Adult (M)

When a CT exam is sent to the REP, the scan parameters and patient information are used to determine which simulation is run under the setup that is the closest to the actual exam, and the lookup table from that simulation is used. For a given procedure, the total energy deposited in each organ is the sum of the deposited energy from all slices that fall in the scan region as shown in Figure 1. The absorbed organ dose is then the total energy deposited in each organ divided by the total mass of the organ regardless whether that organ is fully or partially irradiated (5). Total organ dose is

calculated first for each slice using the $CTDI_{vol}$ at that slice and then summed over the slices that all into the scan region: The organ dose can be calculated using the equation as follows:

$$D_{organ} = \sum_i (coeff * CTDIvol_i) \quad (1)$$

where *coeff* is the ratio of the simulated organ to the simulated $CTDI_{vol}$, and i indicates slice specific values.

The effective dose (E) is defined as the sum of equivalent doses from all organs, weighted by tissue weighting factors to reflect their different radiation sensitivities: The effective dose can be calculated using the equation as follows:

$$E = \sum_T w_T H_T \quad (2)$$

where H_T is the equivalent organ dose, W_T is the tissue weighting factor. The organ doses and effective doses obtained from pediatric CT abdominal exam were then compared among the age group.

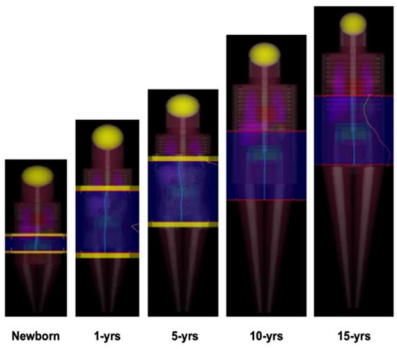

Figure 2 A set of CE computational pediatric phantoms used for patient organ dose mapping calculation for Radimetrics™ Enterprise Platform (REP).

3. RESULTS

For this work, the retrospective data were collected from 78 pediatric patients who underwent single phase abdominal CT, age range between 0-15 years old. Totally, 164 studies were used to calculate the organ doses. The patients were 112 males and 52 females. Average patient body weights of 38.6±18.5 kg (range 3.89 - 94.00 kg) were obtained in this study. The data were carried out by Toshiba CT machines in 133 examinations and from Siemens machines 31 examination. The tube voltages ranged between 80 and 135 kVp were adjusted according to the size and age of patients. Table 2 depicts the average effective dose (ED) for pediatrics abdominal CT in this study. There were found that the ED of 2.24, 3.23, 4.05, 4.46 and 8.46 mSv and the average SSDE of 2.72, 4.52, 6.15, 7.28 and 14.21 mGy, were seen in newborn, 1, 5, 10 and 15 years-old, respectively.

Table 2 Summary of CT scanning technique and patient effective dose.

Age	kVp	mAs	$CTDI_{vol}$ (mGy)	SSDE* (mGy)	ED* (mSv)
0 (M=3, F=0)	**80**	**22**	**1-1.1**	**2.72 (2.71-2.72)**	**2.24 (2.16-2.29)**
1 (M=1, F=0)	**80**	**43**	**2.1**	**4.52**	**3.23**
5 (M=25, F=11)	**80-120**	**28-94**	**1.7-5.1**	**6.15 (3.27-10.70)**	**4.05 (1.92-7.64)**
10 (M=44, F=15)	**80-120**	**26-176**	**1.6-15.3**	**7.28 (3.22-26.33)**	**4.46 (1.86-17.32)**
15 (M=39, F=26)	**120-135**	**30-247**	**3.1-25.9**	**14.21 (5.68-30.87)**	**8.46 (1.60-20.64)**

* Data presents in mean (min-max)

Five highest organ doses for 0-yr patients were found in skeleton, testicles, gall bladder, stomach and liver, with the values of 5.06, 3.53, 3.20, 3.19 and 3.16 mGy, respectively. For 1-yr, the highest organ doses were found in testicles, skeleton, kidneys, stomach and liver with the values of 6.25, 5.84, 4.94, 4.93 and 4.87 mGy, respectively, 5-yr patients were found in kidneys, urinary bladder, stomach, upper large intestine, and liver with the values of 7.75, 7.53, 7.52, 7.41 and 7.32 mGy, respectively, 10-yr patients were found in testicles, kidneys, urinary bladder, upper large intestine, and stomach with the values of 9.68, 8.58, 8.44, 8.12 and 7.98 mGy, respectively, for 15-yr patients were found in kidneys, stomach, urinary bladder, upper large intestine and spleen, with the values of 18.44, 17.07, 16.74, 16.47 and 16.14 mGy, respectively (Figure 3).

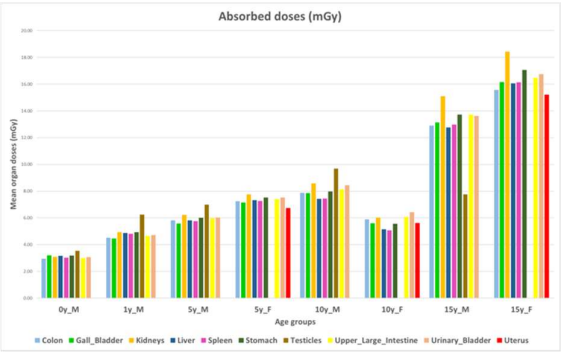

Figure 3 Organ doses for pediatric abdominal CT.

4. DISCUSSION

In this study, the $CTDI_{vol}$ and DLP were no greater than from all previous literatures (6,7). The scanning parameters will change as the patient size changes. The patient whose body size increases, the scanning parameter will also increase due to the use of AEC. The calculated mean ED and SSDE for CT scans of the abdomen CT showed that the highest dose was in age group 15 yrs, which was estimated to be 8.46 mSv. The ED for this age group ranged from 1.60 to 20.64 mSv, and the SSDE ranged 5.56 to 30.87 mGy.

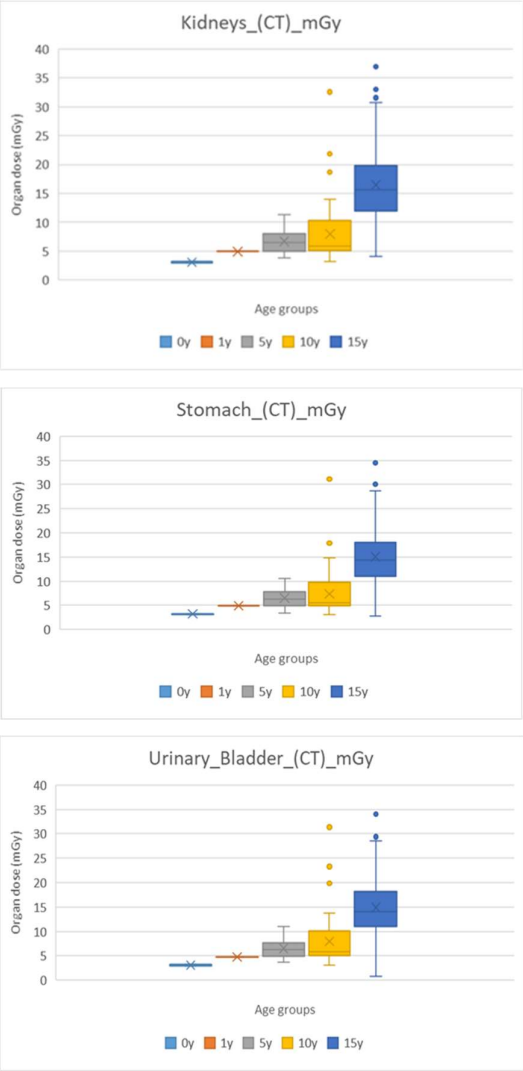

Figure 4 Comparison of organ doses for 0 through 15 years pediatric abdominal CT in kidneys, stomach and urinary bladder.

Organ doses in each organ where was found has a higher radiation dose in patients with older age groups, because the increased average size due to increased organ doses. When separated by gender and machines, it was demonstrated that the highest average organ doses also found in female 15 years. They underwent CT lower abdomen from Siemens SOMATOM Sensation 64 detector-row, which were as high as 23.82, 22.19, 22.08, 21.32 and 21.02 mGy in kidneys, stomach, urinary bladder, upper large intestine and spleen, respectively.

Organ doses of female 15 years in this study were greater than Gao et al (8) when compared to 11–15 years and 16–20 years groups. Since most of the patients in this group have the tendency of high body weight, resulting in higher scanning parameters and higher patient doses. As a result, tube current modulation was increased to 203-247 mAs in each patient. As only four pediatric patients were collected in age group less than 1-yr, the results of organ doses may not reflect the findings toward these patients due to limited number of patient data. This was the limitation in this study.

5. CONCLUSION

Patient-specific organ and effective doses from 0 through 15-years-old can be determined effectively using dose tracking software. As the various sizes of pediatrics, the patient ED and SSDE were correlated with patient's body weight according to earlier results reported by the ICRP classification rather than the patient age.

ACKNOWLEDGEMENTS

This work was supported by Praram9 Hospital Bangkok Thailand.

REFERENCES

1. American Association of Physicists in Medicine Task Group 204. Size-specific dose estimates (SSDE) in pediatric and adult body CT examinations. Report of AAPM Task Group 204. College Park, MD: American Association of Physicists in Medicine; 2011.
2. Communicating radiation risks in paediatric imaging. World Health Organization 2016.
3. Parakh A, Kortesniemi M, Schindera ST. CT Radiation Dose Management: A Comprehensive Optimization Process for Improving Patient Safety1. Radiology: Volume 280: Number 3 September 2016.
4. NRPB. NRPB-R204: The Computation of Bremsstrahlung X-ray Spectra over an Energy Range 15 KeV to 300 keV. 1987.
5. Radimetrics™ Enterprise Platform by Bayer, radiology.bayer.com
6. Galanski M, Nagel H.D., Stamm G. Paediatric CT Exposure Practice in the Federal Republic of Germany. Results of a Nation-wide Survey in 2005/2006.
7. Shrimpton P, Hillier M, Lewis M, Dunn M. Doses from computed tomography (CT) examinations in the UK-2003 review. Chilton, UK: National Radiological Protection Board (NRPB); 2005. NRPB-W67 ed.
8. Gao Y, Mahmood U, Liu T, Quinn B, Gollub MJ, Xu XG, Dauer LT, et al. Patient-Specific Organ and Effective Dose Estimates in Adult Oncologic CT. AJR 2020; 214:1–9 0361–803X/20/2144–1.

*Corresponding author: Kitiwat Khamwan, PhD
Email: kitiwat.k@chula.ac.th

Material decomposition of photon-counting CT spectra with machine learning

Kazumi Murata[1,2], Koichi Ogawa[2]

1 National Astronomical Observatory of Japan,
2 Faculty of Science and Engineering, Hosei University

Abstract

Photon-counting CT is an emergence technology which measures X-ray intensity with multiple energy bins. These data enable us to perform material decomposition and multi-contrast-agent imaging. However, simple material decomposition such as a singular value decomposition method is highly affected by statistical and systematic noises. Hence, material decomposition with less dependence on these noises should be provided. **The aim of this study is to provide a machine-learning based method which simultaneously performs both denoising and material decomposition.** We performed a material-decomposition simulation using a photon-counting CT system with attenuation spectra with solutions having various concentrations of water, iodine, and gold. Statistical Gaussian noises with a standard deviation of 1 % were also added to the spectra. Material decomposition was conducted on these spectra with a network similar to a denoising auto encoder. The network compressed input spectra and estimated concentration of each material, from which predicted spectra were produced. The optimization was conducted to minimize square of difference between predicted and input spectra. Our network successfully reduced the spectral noise; from 1.0 to 0.5 %. Furthermore, the concentrations produced from the network were consistent with the original values. The RMSEs were 0.7-0.8 wt% for all material (i.e. water, iodine, and gold). These results were valid for any concentrations adopted in this work. Our results suggest that the material decomposition based on a machine-learning method is effective even for a spectrum with strong noises.

Keywords: photon-counting CT, material decomposition, machine learning

1. INTRODUCTION

Photon-counting CT is an emergence technology that measures X-ray transmitted spectra in stark contrast with a conventional CT system [1]. Spectral measurements enable us to measure densities of material in the objects [2]. Making use of this advantage, we can perform dual-contrast imaging and measurements of dynamical functions of organs [3]. Furthermore, photon-counting CT can also produce high contrast images [4].

However, material decomposition derived from X-ray transmitted spectra is sensitive to noise. Since the material decomposition is a non-linear process, it amplifies the noise and causes the ring-artefacts [5]. Hence, a new material-decomposition method being less sensitive to noise is required.

In this work, we focus on machine learning. It has been considerable recent research interest owing to its versatility [6]. The most famous argument of applying machine learning is the fact that it is a black box. This leads to a difficulty of quality assurance confirmation. Hence, we include an analytical term in the network using linear attenuation coefficients. The feasibility of this method is investigated with a simulation.

2. MATERIAL AND METHODS

We constructed a neural network estimating material density from input spectrum. The architecture is shown in Fig.1. The input spectrum is compressed with convolution and fully connected layers into material densities. They are converted into a synthesised attenuation spectrum with an attenuation coefficient of each material. The network learns the weight parameters to reduce the MSEs between original noiseless spectra and output spectra. Hence, this process is similar to a spectral fitting method.

We randomly produced transmitted spectra as a data set. We assumed that the targets consist of water, gold, and iodine, and weight fractions of these materials were randomly determined. X-ray spectra with a tube voltage of 100 kV and 2-mm Al filter were incident on the mixtures, and transmitted spectra were obtained. The energy range was 31-90 keV with a bin size of 1 keV, and energy resolution of 5 keV in FWHM was assumed. We added 1.0 % Gaussian noise into the transmitted spectra. They were converted into the attenuation

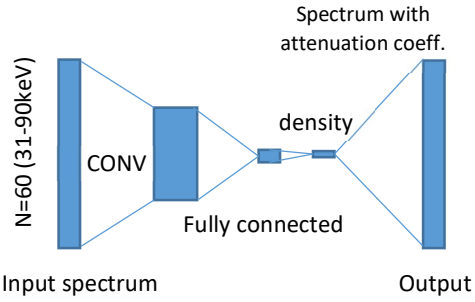

Figure 1 *Network architecture. Input spectrum is compressed with convolution and fully connected layers to estimate material density. It is converted into synthesized spectrum with linear attenuation coefficient.*

spectra. We used 600 spectra for training data and 300 spectra for test data.

3. RESULTS AND DISCUSSION

Figure 2 shows an example spectrum. As can be seen, the model is well fitted. The typical uncertainty of the output spectra was estimated with the original noiseless spectra. We found the uncertainty was reduced from 1.0 % to 0.5 %. This is because the loss function in the network was calculated with noiseless spectra. Hence, our network simultaneously performed both fitting and denoising.

Figure 3 shows a comparison of predicted and original material fractions for water, gold, and iodine. The predicted fractions clearly agreed with the original values and the typical errors were 0.7-0.8 wt% for all materials. These results suggest that the network constructed in this work is effective for precise material decomposition.

4. CONCLUSION

In this work, we provide a machine-learning based material decomposition method. Including an analytical term in the network, our network simultaneously performed both denoising and spectral fitting. The weight fractions of each material predicted by the network precisely agreed with the original values. These results indicate the effectiveness of our method for material decomposition.

ACKNOWLEDGEMENTS

This work was supported by JSPS KAKENHI Grant Number JP20K20232.

REFERENCES

1. K. Ogawa, T. Kobayashi, F. Kaibuki et al., "Development of an energy-binned photon-counting detector for X-ray and gamma-ray imaging", Nuclear Instruments and Methods in Physics Research A, Vol. 664, pp. 29-37, 2012
2. K. Taguchi, C. E. Frey, and X. Wang et al., "An analytical model of the effects of pulse pileup on the energy spectrum recorded by energy resolved photon counting x-ray detectors", Med. Phys., Vol. 37, No. 8, pp. 3957-3969, 2010
3. D. P. Cormode, S. Si-Mohamed, D. Bar-Ness et al., " Multicolor spectral photon-counting computed tomography: *in vivo* dual contrast imaging with a high count rate scanner", Scientific reports, 7: 4784, 2017
4. Jürgen Giersch, Daniel Niederlöhner, and Gisela Anton, "Influence of energy weighting on X-ray imaging quality", Nuclear Instruments and Methods in Physics Research A, Vol. 531, pp. 68-74, 2004
5. K. Murata & K. Ogawa, "Ring-artifact correction with total-variation regularization for material images in photon-counting CT", IEEE Transactions on Radiation and Plasma Medical Sciences, Early Access, 2020
6. Z. Chen and L. Li, "Robust multimaterial decomposition of spectral CT using convolutional neural networks", *SPIE Opt. Eng.*, 58 (1), 013104, 2019

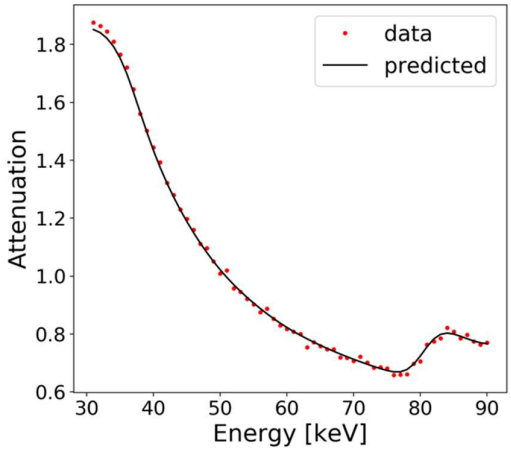

Figure 2 *Example spectra. Red point indicates an input spectrum while the black line indicates the predicted spectrum.*

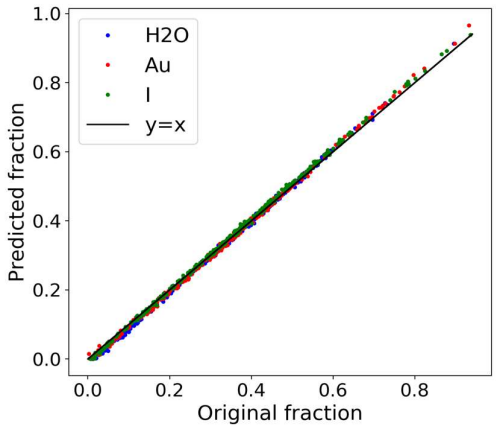

Figure 3 *Comparison of material fractions. Blue, red, and green points indicate the water, gold, and iodine fractions, respectively.*

How to create a conversion IMRT plan for lung / esophageal cancer using the fluence reversible computing function on Halcyon™

Toshiya Rachi[1], Yuki tanaka[1], Haruki Togo[1], Vijay Raturi[2,3]

1 Department of Radiological Technology, National Cancer Center Hospital East
2 Department of Radiation Oncology and Particle Therapy, National Cancer Center Hospital East
3 Course of Advance Clinical Research of Cancer, Graduate School of Medicine, Juntendo University

Abstract

If a C-arm type linac fails, a linac that has the same mechanical structure may be able to perform the treatment without changing the plan. However, Halcyon has a mechanical structure of Flattening Filter Free, so the structure is different from the existing linac. Therefore, to change the IMRT plan created on Halcyon to another linac plan, it is necessary to reconsider the optimization in TPS. In this study, we propose a simple method to convert the lung/esophageal IMRT plan created on Halcyon into other linac plans. Fall back Planning with RayStation which converts the created dose distribution into that of other linac was used. The subjects were 6 patients with esophagus cancer and 10 patients with lung cancer who were treated with IMRT. These converted plans were evaluated using DVH. The evaluated DVH are as follows, *CI* and *HI*, PTV, LUNG, Spinal cord, Heart. Also, the shapes of these iso-dose curves for each 10% were compared using the dice coefficient. All ROIs evaluated satisfied the specified values, indicating that the patient's treatment was curable using the conversion plan. The results of the dice coefficient showed that the shapes of the iso-dose curves were about the same. The plan converted to C-arm linac showed excellent dose distribution equal to or better than Halcyon's original plan and a simple re-planning method was proposed.

Keywords: Halcyon, C-arm type linac, convert plan

1. INTRODUCTION

VARIAN Medical Systems has been operating an O-ring type Linear Accelerator (linac) called Halcyon™. Halcyon has a dual-layer multi-leaf collimator (MLC) with flattening filter-free (FFF) and is a 6X-FFF single beam only specification. In Halcyon, it is possible to perform 3D conformal irradiation (3DCRT) treatment and Intensity Modulated Radiation Therapy (IMRT), which is a high-precision radiotherapy[1].

Generally, when linac fails, the converted irradiation between C-arm typed linac (C-linac) has the same mechanical structure, so it is possible to perform converted irradiation without re-calculating the dose distribution by the radiation therapy planning system (TPS). However, since the mechanical structure of Halcyon has FFF, the process for forming the dose distribution is different from that of the C-linac[2]. Therefore, if Halcyon becomes unusable due to a breakdown or inspection, it will be necessary to formulate a treatment plan from scratch, which will take a great deal of time. The situation is such that radiation therapy cannot be provided to the patient immediately. It is of great benefit to patients to clarify the consistency of treatment plans between these linacs and to establish a simpler converted plan creation method.

There are many reports on the comparison between Halcyon and C-linac. Li Y et al. reported the difference in quality control from C-linac[3], O'Grady F et al. compared the characteristics and safety of the dose distribution of each linac[4]. In a report similar to this study, Li C et al. compared the dose distribution of IMRT created by C-linac on TPS with that produced by Halcyon[2]. No specific method for performing the converted irradiation has been shown worldwide. Proposals for ways to reshape treatment plans are considered to be globally useful. In this study, we investigate a method for more easily performing converted irradiation from Halcyon to C-linac. Extension of radiation therapy may affect the therapeutic effect of patients, so it is considered to be a very meaningful study.

2. MATERIAL AND METHODS

2.1 Treatment plans and target patients

RaySearch's RayStation™ and VARIAN's Eclipse™ were used for the TPS. The target patients are 6 cases of esophageal cancer and 10 cases of lung cancer created using the Halcyon 6X-FFF beam on Eclipse, all of which are being treated by IMRT. The targeted cases of lung cancer are small-cell lung cancer and non-small cell lung cancer, and stage III lung cancer according to the Unio Internationalis Contra Cancrum 8th[5]. Prescription doses range from 45 Gy to 60 Gy. The cases of esophageal cancer were those with postoperative irradiation of 50.4 Gy and chemotherapy combined with 60 Gy in stages I to IV.

All plans on Halcyon were created with 2 or 3 arcs using 6X-FFF and treated with Volumetric-modulated Arc Therapy (VMAT). The dose constraints of the Dose Volume Histogram (DVH) for lung cancer patients treated are as follows, PTV is $D95 \geq 100\%$, LUNG is $V20 \leq 40\%$, $V10 \leq 40\%$, $V5 \leq 60\%$, Spinal Cord is $Dmax \leq 45$ Gy, and Heart is $V50 \leq 25\%$. In esophageal cancer cases, PTV is created with $D98 \geq 98\%$, and OAR constraints are similar to those in lung cancer cases. The dose constraint index refers to the treatment planning

guidelines by the Japanese Society for Radiation Oncology[6].

2.2 How to create a converted plan

By using Fall Back Planning (FBP) in RayStation, Halcyon's dose distribution was converted to a dose distribution using a 6X beam with TrueBeam. The function of FBP is to convert the dose data of the original plan into energy fluence. The alternative linac MLC is then optimized to achieve energy fluence. If there are unachieved constraints of the region of interest (ROI) on the in the plan converted by FBP, the plan is completed by adding the optimization parameters of the corresponding elements and performing optimization. The time required to convert one plan by FBP is about 20-30 minutes.

2.3 Evaluation of the converted plan

The evaluation method used was the DVH. The *Homogeneity Index (HI)*, *Conformity Index (CI)*, and PTV (*D98%*, *D2%*) of the modified plan using TrueBeam's 6X were evaluated. For Organ at Risk (OAR), the DVH of LUNG (*V5 Gy, V10 Gy, V20 Gy*), Spinal Cord (*Dmax* ≤ 45 Gy), and Heart (*V40 Gy, V50 Gy, V60 Gy*) were evaluated. The evaluation confirmed whether there was a difference between the DVH of the original plan and the converted plan. The *HI* and *CI* are defined as follows.

$$HI = \frac{D_{max} - D_{min}}{D_{pres}},\ CI = \frac{(V_{PTV} \cap V_{Pres})^2}{V_{PTV} + V_{pres}}$$

Also, the shapes of the iso-dose curves for each 10% in each plan were compared. For this, the evaluation index of similarity by the *Dice coefficient (DC)* was used. *DC* is defined as follows.

$$Dice\ coefficient = \frac{2\left|V_{iso\_Hal} \cap V_{iso\_True}\right|}{\left|V_{iso\_Hal}\right| + \left|V_{iso\_True}\right|}$$

V_{iso_Hal} and V_{iso_true} are the same iso-dose curves for Halcyon and TrueBeam, respectively. An index of the *DC*, which is the threshold for similarity ($DC \geqq 0.8$), is shown in Task Group 132 published by the American Association of Physicist in Medicine[7]. Objective evaluation is possible by using these quantitative indexes.

3. RESULTS

Table 1 *p-value of dose constraint when using the same evaluation DVH-index in ROI shown in Figure 1 (p> 0.05)*

		P
	HI	**0.8**
	CI	**0.34**
PTV	***D98***	**0.62**
	D2	**0.61**
Lung	***V5***	**0.92**
	V10	**0.82**
	V20	**0.85**
Heart	***V40***	**0.99**
	V50	**0.94**
	V60	**0.77**
Cord(Gy)	***Dmax***	**0.77**

Figure 1 shows the comparison results of the dose constraints of PTV and OAR between the original plan on Halcyon and the converted plan on TrueBeam for 10 cases of lung cancer. Table 1 shows the comparison results of the *t-test* ($p < 0.05$) in the ROI of patients with lung cancer that have been evaluated. These differences were not statistically significant ($p > 0.05$).

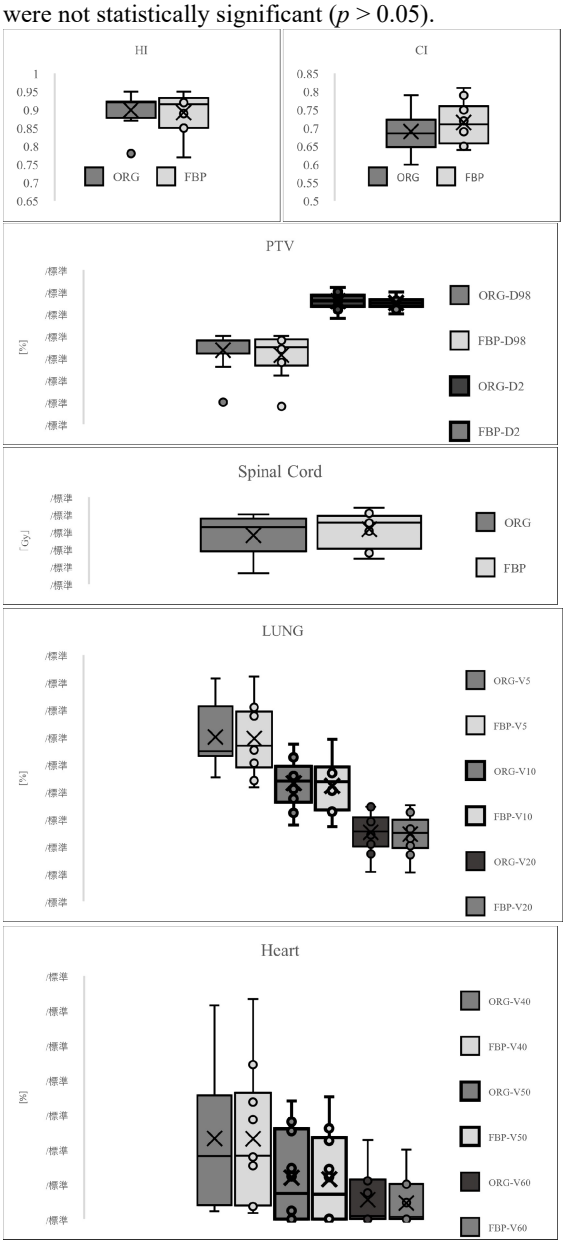

Figure 1 *Comparison of dose constraints in treatment plans created by Halcyon 6X-FFF and TrueBeam 6X for 10 cases of stage III lung cancer*

Similarly, Figure 2 shows the comparison of dose constraints in the treatment plan created by Halcyon and TrueBeam for 6 cases of esophageal cancer. The evaluated ROI is the same as in lung cancer cases. Table 2 shows the comparison results using the *t-test* ($p < 0.05$) in esophageal cancer cases.

Table 2 *p-value of dose constraint when using the same evaluation index in ROI shown in Figure 2 (p> 0.05)*

		P
PTV	*HI*	0.94
	CI	0.94
	D98	0.99
	D2	0.63
Lung	*V5*	0.98
	V10	0.67
	V20	0.63
Heart	*V40*	0.82
	V50	0.81
	V60	0.72
Cord(Gy)	*Dmax*	0.72

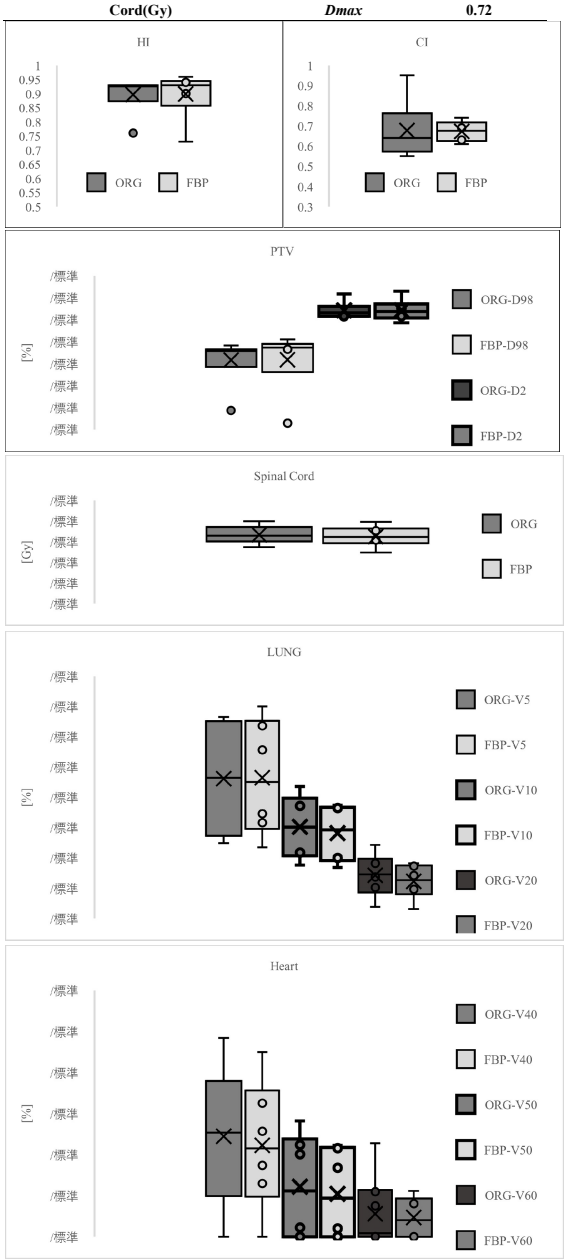

Figure 2 *Comparison of dose constraints in treatment plans created by Halcyon 6X-FFF and TrueBeam 6X for 6 cases of esophageal cancer*

3.1 Evaluation of PTV and OARs

The *p-value* results in 10 lung cancer patients were 0.80, 0.34, 0.62, and 0.61 for *HI*, *CI*, *D98 %,* and *D2* for PTV, respectively. Similarly, the *p-values* results in 6 cases of esophageal cancer patients were 0.94, 0.94, 1.00, and 0.63 for *HI*, *CI*, *D98* %, and *D2* for PTV, respectively. There was no significant difference between the plans created using Halcyon and TrueBeam (p > 0.05).On the other hand, in the case of OAR, no significant difference was observed by *p-value* in all cases of lung cancer and esophageal cancer in *V20%*, *V10%,* and *V5%* of LUNG, *Dmax* of Spinal Cord, *V40%*, *V50%,* and *V60%* of Heart. Also, the converted plan suggests a treatable plan, with all PTV and OAR DVHs meeting the tolerances set out in the guidelines.

3.2 Dice coefficient of the iso-dose curve

Figures 3 and 4 show the *DCs* calculated from each iso-dose curve for lung and esophageal cancer in all target patients, respectively. In all patients with lung and esophageal cancer, the 30% to 100% iso-dose curve of the prescribed dose is almost above 0.8. This is an indicator of the DC shown on the TG132. These show a great match. On the other hand, there was also a result that the iso-dose curve of less than 20% was less than 0.8. And, in the high dose range above 105%, the dice coefficients were well below 0.8.

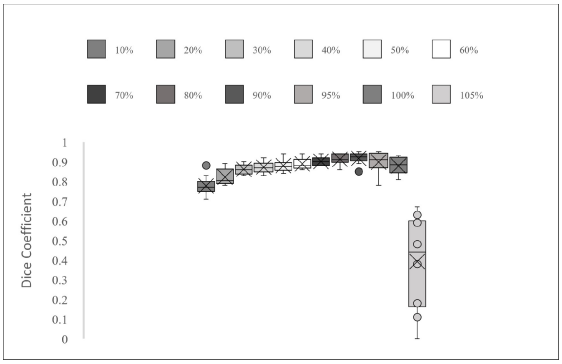

Figure 3 *Dice coefficient of the iso dose curve of the treatment plan created by Halcyon 6X-FFF and TrueBeam 6X in 10 cases of stage III lung cancer*

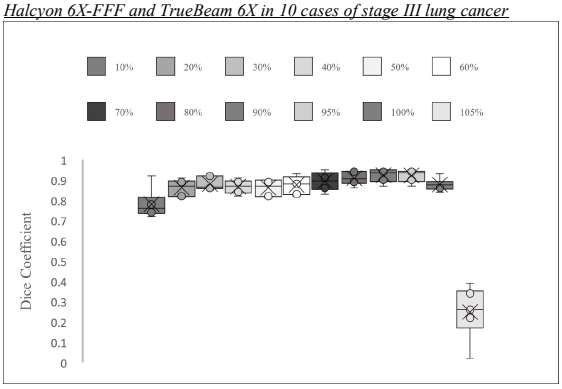

Figure 4 *Dice coefficient of the iso dose curve of the treatment plan created by Halcyon 6X-FFF and TrueBeam 6X in 6 cases of esophageal cancer*

4. DISCUSSION

It hasn't been a long time since Halcyon was widely used worldwide. Currently, several studies have been published on the safety and quality control of treatment plans made with Halcyon. Li C et al. conducted IMRT dose planning for cervical cancer in each of Halcyon and C-arm linac. The dose distribution in Halcyon showed the same coverage as the C-linac in the target, and the dose distribution in Halcyon was more reduced in OAR. Also, Halcyon has a faster gantry speed than the C-linac,

so treatment can be completed in a short time[8]. Riley et al. created an IMRT dose distribution for prostate and head and neck cancers on Halcyon. They compared the dose distribution with C-linac as reported by Li C et al. and showed the effectiveness of Halcyon[9]. Based on these reports, it is considered that Halcyon can be performed the radiotherapy equal to or better than C-linac. However, there are no reports of converting the treatment plan created by Halcyon into a treatment plan using a C-linac. We consider that the easy way to convert the treatment plan created using Halcyon to other C-linac will be of great benefit in clinical practice.

This study found no significant differences in *CI, HI*, PTV, and OARs (Lung, Heart, and Spinal Cord) between the original plan and the conversion plan created using FBP for lung and esophageal cancer. From this result, it is considered that the original plan and the FBP plan are equivalent plans.

We then used *DC* to calculate the similarity of the shapes of the iso-dose curves. According to TG-132, the tolerance of *DC* is 0.8 or more. From the results of the *DC*, it was found that there is no significant difference in the shape of the iso-dose curve between the original plan and the converted plan in the iso-dose range of 20% to 100%. However, the similarity was low in the regions of the iso-dose curve of 10% or less and 105% or more. It is considered that these differences are largely due to the structural difference between Halcyon and C-linac. Halcyon has dual-layer MLC with FFF, and the C-linac has single-layer MLC with a flattening filter. The transmission of MLC is an important factor in IMRT. Li C et al. and Yao W et al. reported that the transmittance of VARIAN millennium 120 MLC is about 1.5%[10,11]. On the other hand, the transmittance of dual-layer MLC in Halcyon has also been reported. Roover et al. reported 0.42%[12], Lim et al. reported 0.41% for distal MLC and 0.4% for proximal MLC[13]. Also, the FFF beam reduces transmission from MLC[14]. Due to the characteristics of these FFF beams and the structural differences of MLC, it is considered that the *DC* was greatly reduced due to the difference in the generation position and dose-volume in the high dose region of 105% or more.

Vassiliev et al. also reported that the FFF beam had a small change in the deep lateral dose curve and was suitable for the protection of normal tissues[15]. Similarly, Halcyon does not have jaws, so less scattered radiation is generated from it. Rovert et al. point out that Halcyon can reduce the dose of normal tissue by reducing the influence of scattered radiation in the lateral direction compared to the C-linac[16]. Since the dose profile of Halcyon is convex, it is difficult to compare and evaluate the quantitative penumbra with the flat profile of the C-linac. However, it is highly probable that the slight difference in the low dose range was caused by the small transmission from the MLC mentioned above and the structure without Jaw. In this study, Halcyon's treatment plan was converted to a treatment plan using 2 arcs full rotation using the TrueBeam 6X beam. The problem with this study is that these are not the most optimal parameters in the treatment plan using TrueBeam, such as the energy, beam angle, and a number of beams of the plan to be converted.

5. CONCLUSION

It was possible to convert the dose distribution planned on Halcyon to the dose distribution of the conventional C-arm type linac. A simple replanning method called FBP, which is a method of performing MLC fitting after converting from dose to energy fluence, has been proposed. This is a very effective means as one method for dealing with a failure or the like that may occur in an actual treatment site.

ACKNOWLEDGEMENTS

We thank all colleagues who helped us write this study.

REFERENCES

1. Pawlicki T, Atwood T, McConnell K, Kim GY, Clinical safety assessment of the Halcyon system. Med Phys. 2019 Oct;46(10):4340-4345.
2. Li C, Chen J, Zhu J, Gong G, Tao C, Li Z, Lu J, Yin Y, Plan quality comparison for cervical carcinoma treated with Halcyon and Trilogy intensity-modulated radiotherapy. J Cancer. 2019 Oct 15;10(24):6135-6141.
3. Li Y, Netherton T, Nitsch PL, Gao S, et al, Independent validation of machine performance check for the Halcyon and TrueBeam linacs for daily quality assurance. J Appl Clin Med Phys. 2018 Sep;19(5):375-382.
4. O'Grady F, Barsky AR, Anamalayil S, Freedman GM, et al. Increase in Superficial Dose in Whole-Breast Irradiation With Halcyon Straight-Through Linac Compared With Traditional C-arm Linac With Flattening Filter: In vivo Dosimetry and Planning Study. Adv Radiat Oncol. 2019 Aug 21;5(1):120-126.
5. J.D.Brierley, M.K.Gospodarowicz & C.Wittekind, TNM Classification of Malignant Tumours, 8th ed.
6. Edited by the Japanese Society for Radiation Oncology, Radiation Therapy Planning Guidelines 2016
7. Kristy K. Brock, Sasa Mutic, Todd R. McNutt, et al, Use of image registration and fusion algorithms and techniques in radiotherapy: Report of the AAPM Radiation Therapy Committee Task Group No. 132, Med. Phys., 44: e43–e76.
8. Michiels S, Poels K, Crijns W. et al. Volumetric modulated arc therapy of head-neck cancer on a fast -rotating O-ring linac: Plan quality and delivery time comparison with a C-arm linac. Radiother Oncol.2018; 35:206-215.
9. Riley C, Cox C, Graham S, et al, Varian Halcyon Dosimetric comparison for multiarc VMAT prostate and head-and-neck cancers: Med Dosim. 2018 Sep 6:S0958-3947(18)30084-0.
10. Li Y, Chen L, Zhu J. et al. A quantitative method to the analysis of MLC leaf position and speed based on EPID and EBT3 film for dynamic IMRT treatment with different types of MLC. J Appl Clin Med Phys. 2017;18:106-115.
11. Yao W, Farr JB. Determining the optimal dosimetric leaf gap setting for rounded leaf-end multileaf collimator systems by simple test fields. J Appl Clin Med Phys. 2015;16(4):65-77.
12. Roover RD, Crijns W, Poels K. et al. Validation and IMRT/VMAT delivery quality of a pre-configured fast-rotating O-ring linac system. Med Phys. 2018;46:328-339
13. Lim TY, Dragojevic I, Hoffman D. et al. Characterization of the HalcyonTM multileaf collimator system. J Appl Clin Med Phys. 2019;20:1-9
14. Dzierma Y, Licht N, Nuesken F. et al. Beam properties and stability of a flattening filter free 7 MV beam-An overview. Med Phys. 2012;39:2595-2602
15. Vassiliev ON, Titt U, Pönisch F. et al. Dosimetric properties of photon beams from a flattening filter free clinical accelerator. Phys Med Biol. 2006;51:1907-1917
16. Robert M, Eric L, Jessica H, et al. Field-in-field breast planning for a jawless, double-stack MLC linac using flattening-filter-free beams, ournal of Applied Clinical Medical Physics 20(11).

Evaluation of patient doses from ^{177}Lu-PSMA in metastases prostate cancer treatment at King Chulalongkorn Memorial Hospital

Kotchakorn Chatachot[1,2,4], Kitiwat Khamwan[1,3,4*]

1 Medical Physics Program, Faculty of Medicine, Chulalongkorn University, Bangkok, Thailand
2 Division of Nuclear Medicine, Department of Radiology, Buddhachinaraj Hospital, Phitsanulok, Thailand
3 Division of Nuclear Medicine, Department of Radiology, Faculty of Medicine, Chulalongkorn University and King Chulalongkorn Memorial Hospital, The Thai Red Cross Society, Bangkok, Thailand
4 Chulalongkorn University Biomedical Imaging Group, Department of Radiology, Faculty of Medicine, Chulalongkorn University, Bangkok, Thailand

Abstract

Introduction: ^{177}Lu-PSMA has increasingly used for targeted radionuclide therapy of prostate cancer and its metastases. Dosimetric calculation, therefore, is critical to achieve the optimal therapeutic activity with limited side effects. **Purpose**: To perform the image-based absorbed doses calculation to the normal organs for patients who treated by ^{177}Lu-PSMA for prostate cancer. **Methods**: Whole-body planar images and SPECT/CT images were acquired in six patients (8 cycles) at immediately, 4 and 24 h after injection of ^{177}Lu-PSMA (range 4.37 to 8.58 GBq) at King Chulalongkorn Memorial Hospital. To generate the time-integrated activity (TIA) in source organs, region of interests (ROIs) were manually contoured in whole-body, liver, spleen, urinary bladder, lacrimal gland, and bone marrow using the Osirix MD program. The geometric mean of anterior and posterior counts was determined through the ROI analysis. The TIA in each source organ was calculated by integrating area under time-activity curve using MATLAB. The s-values were extracted from OLINDA/EXM version 2.0 based on the NURBS computational phantoms in order to calculate the absorbed dose coefficient in target organs according to the Medical Internal Radiation Dose (MIRD) scheme. The absorbed doses to bone marrow were estimated using the two-compartment method by dividing high-uptake and low-uptake compartment. The spherical model was used to calculate the lacrimal gland absorbed doses. **Results**: The average absorbed dose coefficients per cycle were 0.56±0.16 Gy/GBq for the bone marrow, 0.62±0.13 Gy/GBq for the kidneys, 0.11±0.08 Gy/GBq for the liver, 0.18±0.14 Gy/GBq for the urinary bladder wall, 0.14±0.05 Gy/GBq for the spleen, and 2.86±0.78 Gy/GBq for the lacrimal glands. The critical absorbed doses reported for the kidneys of 23 Gy, and for bone marrow of 2 Gy were not reached in any patients. **Conclusion**: Our dosimetry results suggest that ^{177}Lu-PSMA treatment with higher activities and more cycles is possible without the risk of damaging the critical organ in metastasis prostate cancer patients.

Keywords: ^{177}Lu-PSMA; theranostics; MIRD; radionuclide therapy; prostate cancer

1. INTRODUCTION

According to the report on global cancer incidence from American Institute for Cancer Research, prostate cancer (PCa) is the second most common cancer found in men worldwide, and most of them presented with localized or indolent disease. There were reported that 9.5 million cases of estimate 18 million cancer cases worldwide were found in men in 2018. Approximately 30% of men have experience in biochemical recurrence and often followed by progression to metastatic castration-resistant prostate cancer (mCRPC). Treatment choices in prostate cancer are surgery, hormonal therapy, chemotherapy, external beam radiation therapy, and radionuclides therapy which uses the internal radiation dosimetry concept (1).

Since the precision medicine has been introduced, Lutetium-177 has been recognized as an option for radioisotope in targeted radionuclide therapy. Prostate-specific membrane antigen (PSMA) is a favorable target for both of diagnostic imaging and targeted radionuclide therapy of prostate cancer, called theranostics. The idea of theranostic signifies the combination of the two medical terms therapy and diagnostic. The goal of theranostics in reference to nuclear oncology is to identify the relevant molecular targets in cancer. ^{177}Lu-PSMA, therefore has increasingly used in metastatic prostate cancer for theranostics in nuclear medicine. The biological effects of radioactive sources in the human body can be evaluated through the physical quantity of the absorbed dose by estimated based on the Medical Internal Radiation Dose (MIRD) scheme (2).

However, the radiation doses to the normal tissues for the patients who treated by the Lu-177 should be evaluated as the high amount of radioactivity is administered. So, the treatment is restricted because of limitations imposed by irradiation of the critical organs such as kidneys and red bone marrow. Current evidence indicates that the kidneys can tolerate mean absorbed doses above the general dose limit of 23 Gy, and 2 Gy to the red bone marrow is based on treatments with ^{131}I and blood-based dosimetry. Therefore, this study aimed to determine the organ doses and biokinetic of ^{177}Lu-PSMA in prostate cancer patients to obtain the preliminary data in Thai patients.

2. MATERIAL AND METHODS

2.1 Patients

Retrospective data of six patients (mean age; 68±7.69 yrs) with metastasis prostate cancer treated by ^{177}Lu-PSMA at Division of Nuclear Medicine, King Chulalongkorn Memorial Hospital (KCMH) were collected in between January 2018 - May 2019. Totally, eight treatment cycles were performed (n = 4 for first cycle, and n = 2 for first and second cycle). The mean administered activity of ^{177}Lu-PSMA for all cycles was 6.21±1.33 GBq, range 6.70-8.54 GBq.

2.2 Image acquisition

The planar whole-body scan using a dual-headed gamma camera was used to acquire the patient data. The 113- and 208-keV photopeaks with 10% energy window was set for imaging studies. The medium-energy collimators, and the table speed of 10 cm per min was used. ^{177}Lu-PSMA planar images was acquired at 3 time-point (immediately, 4, 24 hrs.) after the injection by using SPECT/CT system at Division of Nuclear Medicine, KCMH. The planar images were manually drawn with ROI covering the whole body and source organs (kidneys, urinary bladder, liver, spleen, lacrimal gland, bone marrow) using the Osirix MD program to determine time-integrated activity (TIA). The patients were not allowed for voiding for the immediately scan in order to calibrate the correlation between the counts and injected activity. Next processing, the time integrated activity coefficient (TIAC) was computed by fitting time–activity curve (TAC) using MATLAB program. Then fitting the curve and interpolated for 48 and 120 hr. Consequently, the absorbed doses in target organs can be calculated according to MIRD method.

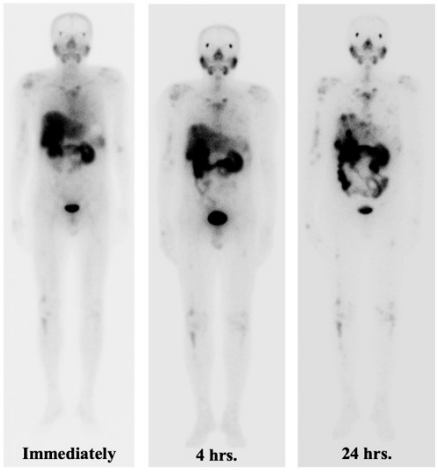

Figure 1 *^{177}Lu-PSMA whole-body scintigraphy images at immediately, 4 and 24 hrs. post injection.*

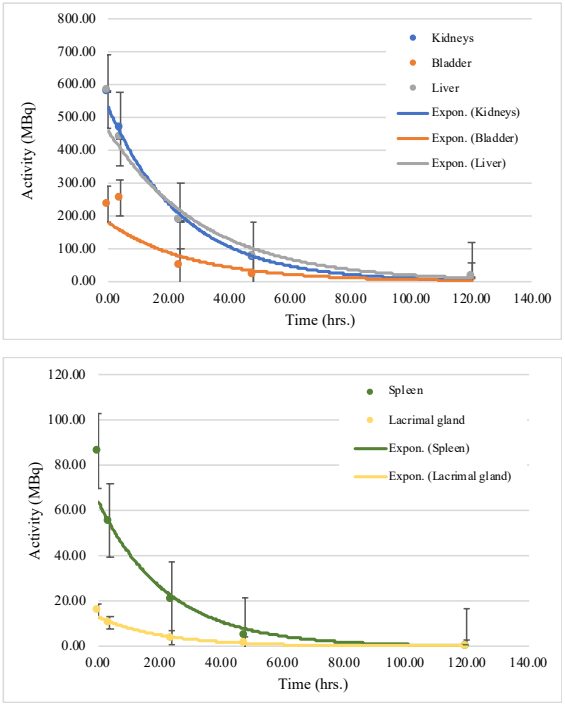

Figure 2 *Time–activity curve (TAC) in various source organs investigated in this work.*

2.3 Dosimetry

The absorbed dose, $D(r_T)$, to target region, r_T, was calculated in accordance with the methodology described by the Medical Internal Radiation Dose (MIRD) Committee Pamphlet No. 21. The MIRD formulation in Equation 1 is created to calculate radiation dose delivered to the target organ from the radionuclides that are deposited in source organ as follows.

$$D(r_T) = \sum_{r_S} \tilde{A}(r_S) \cdot S(r_T \leftarrow r_S), \qquad \text{(eq.1)}$$

where $D(r_T)$ is the mean absorbed dose to the target organ (mGy), $\tilde{A}(r_s)$ is the time-integrated activity; TIA (MBq.hr) in the source organ r_s over dose-integration period, $S(r_T \leftarrow r_S)$ is the radionuclide-specific quantity representing the mean absorbed dose rate to target organ r_T at time t after administration per unit activity present in source organ r_s, (mGy/MBq.hr). The absorbed doses calculated in this study was performed following the recommendation in the European Association of Nuclear Medicine (EANM) dosimetry guidelines.

The TIA is total number of disintegration nuclear transformation in the source tissue. It's depends on the amount of activity administered to patients and life-time of the radiotracer within the body. The TIA can be obtained by integrating the area under time-activity curve in source tissues. The TIA was then divided by the injected activity in order to obtain the time-integrated activity coefficient (TIAC), former name residence time, in source tissue. The S value is the mean absorbed

dose to the target organ per unit of time-integrated activity in a specified source organ based on the Monte Carlo Simulation with 70 kg reference man phantom. The S value is given by:

$$S(r_T \leftarrow r_S) = \frac{1}{M(r_T)} \sum_i E_i Y_i \phi(r_T \leftarrow r_S, E_i), \quad \text{(eq.2)}$$

where E_i is the mean energy of the i^{th} radiation, $\phi(r_T \leftarrow r_S, E_i)$ is the fraction of radiation energy E_i emitted by the source region (r_S) that is absorbed by a target region (r_T), Y_i is the yield for the i^{th} radiation per nuclear transformation, and $M(r_T)$ is the mass of the target region. The S values in this work were extracted from the OLINDA/EXM software version 2.0 that utilizes the non-uniform rational B-spline (NURBS) technology which combines the flexibility of mathematical organ geometry representation with the anatomical reality (3).

The absorbed doses coefficient (mGy/MBq) from ^{177}Lu-PSMA was then obtained by normalizing the mean absorbed dose in target organ with the injected activity. In case of the lacrimal gland, the absorbed dose was calculated using the spheres model method derived from OLINDA/EXM ver. 2.0. The organ mass of lacrimal gland at 1.4 g was used for this calculation (4). The absorbed dose in red bone marrow was calculated using the two-compartment method following Hagmarker et al. Starting from manually drawn of ROI using the Osirix MD program to segment the whole-body area, then used the 3D ROI isocontour to separate the high uptake area from the low uptake area. The high uptake compartment includes organs with physiologically high somatostatin receptor expression such as the liver, spleen, kidneys and tumors, while the low uptake compartment corresponds to the remainder of the body was used to represent the bone marrow.

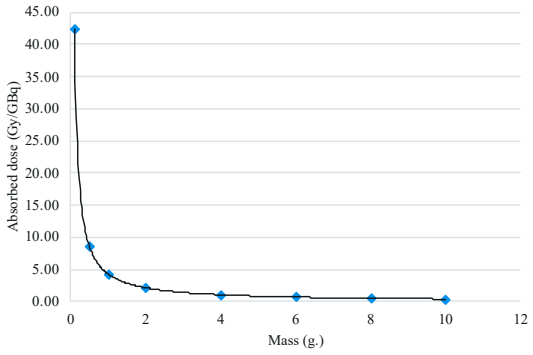

Figure 3 *The relationship between absorbed dose and mass of organ in lacrimal gland.*

2.4 Data analysis

According to the recommendations of EANM guideline, the critical organs in radionuclide therapy with ^{177}Lu-PSMA are bone marrow with accumulative dose limit of 2 Gy (6), kidneys accumulative dose limit of 23 Gy, and lacrimal glands with accumulative dose limit of 40 Gy. The absorbed doses in theses target organs in each cycle treatment were analyzed in order to avoid the toxicity.

3. RESULTS

The average absorbed dose coefficients per treatment cycle were 0.56±0.16 Gy/GBq for the bone marrow, 0.62±0.13 Gy/GBq for the kidneys, 0.11±0.08 Gy/GBq for the liver, 0.18±0.14 Gy/GBq for the urinary bladder wall, 0.14±0.05 Gy/GBq for the spleen, and 2.69±0.73 Gy/GBq for the lacrimal glands. The absorbed doses in all target organs were not reached those report for the kidneys of 23 Gy, bone marrow 2 Gy, and liver 32 Gy. Table 1 depicts the results of TIAC in source organs obtained in this study. The correlation between the absorbed dose and the sphere mass (g) for interpolating the radiation dose is shown in Figure 3. Figure 4 and Figure 5 depict the results of absorbed doses in target organs in each treatment cycle.

Table 1 *The time-integrated activity coefficient: TIAC (h).*

Patient	WB	Kidneys	Bladder	Liver	Spleen	Lacrimal gland	Bone marrow
1 (cycle 1)	16.09	2.30	0.61	1.75	0.15	0.055	12.71
1 (cycle 2)	17.91	2.02	0.46	1.67	0.24	0.039	9.93
2 (cycle 1)	22.05	2.57	0.72	3.55	0.21	0.059	17.53
2 (cycle 2)	21.50	2.00	1.09	5.99	0.18	0.038	11.30
3	25.55	1.65	0.78	1.28	0.18	0.068	19.71
4	24.38	2.54	2.44	1.39	0.25	0.039	8.26
5	20.84	3.08	0.50	1.33	0.41	0.054	13.76
6	30.14	1.81	0.31	1.05	0.28	0.030	15.32
Mean	22.31	2.25	0.87	2.25	0.24	0.05	13.57
SD	4.42	0.47	0.68	1.70	0.08	0.013	3.85

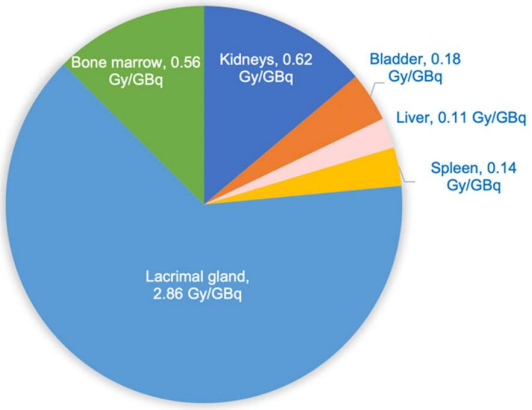

Figure 4 *The contribution of the average absorbed doses in target organs from ^{177}Lu-PSMA.*

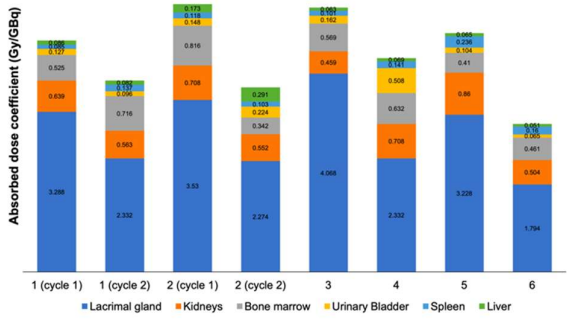

Figure 5 *The distribution of absorbed doses coefficient (Gy/GBq) in target organs obtained from eight treatment cycle in six prostate cancer patients.*

4. DISCUSSION

We present the data for radiation dosimetry for normal organs using ^{177}Lu-PSMA radionuclides therapy at KCMH and found that the highest amount of radiation dose was seen in the lacrimal glands of 2.69±0.74 Gy/GBq. Our results agreed with the earlier study of Shozo Okamoto, et al. (4) and Melanie Hohberg, et al. (5). They found that lacrimal glands gave the highest level of absorbed doses 3.8±1.4 Gy/GBq and 2.82 Gy/GBq respectively. Other previous studies mentioned that lacrimal glands were not likely a critical organ for ^{177}Lu-PSMA and has the limits dose over 40 Gy, which corresponds to our study with the absorbed doses of 17.24±4.28 Gy. However, all of the patients who have the absorbed dose greater that 40 Gy should be follow-up the treatment in order to observe the toxicity in lacrimal gland. In addition, kidneys were also take into accounted for critical organ for ^{177}Lu-PSMA. Regarding the results in this study, the average absorbed dose coefficients for the kidneys of 0.62±0.13 Gy/GBq was obtained. Our result was lower than those the values reported by the study of Shozo Okamoto et al (4) and Melanie Hohberg et al, with the average absorbed dose coefficients of 0.72±4.28 Gy/GBq and 0.53 Gy/GBq respectively. Therefore, this study indicated that the average absorbed dose for kidney was within the dose limits at 23 Gy, which is in safe and no toxicity found for patients. Figure 6 illustrates the comparison of the absorbed dose in kidneys and lacrimal gland between this work and literatures.

5. CONCLUSION

This study utilized the planar image-based method in calculating absorbed doses in target organs of metastasis prostate cancer patients treated by ^{177}Lu-PSMA. We found that in critical organs, the level of absorbed doses was lower than recommended dose limits. Therefore, the treatment with ^{177}Lu-PSMA is safe for patient. From this study, it is possible to increase the number of treatment cycles or the amount of injected activity while sparing the toxicity to the patients in order to achieve the treatment concept for theranostics in nuclear medicine.

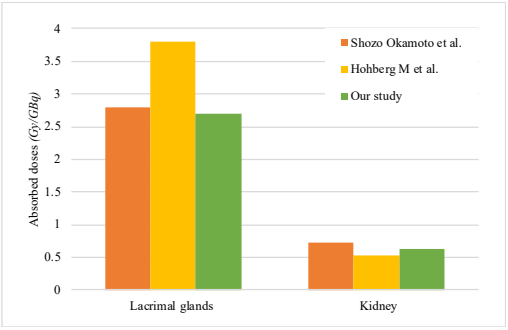

Figure 6 *Comparison of absorbed doses per administrated activity (Gy/GBq) in kidney and lacrimal glands with other studies.*

ACKNOWLEDGEMENTS

This study become a reality with the kind support and help of many individuals. I wish to express thankfulness and deepest appreciation to Medical Physics Program, Faculty of Medicine, Chulalongkorn University, Bangkok, Thailand.

REFERENCES

1. Worldwide cancer data Global cancer statistics for the most common cancers. Available from: https://www.wcrf.org/dietandcancer/cancer-trends/worldwide-cancer-data
2. *E. Hoseinian-Azghadi, L. Rafat-Motavalli, et al. Internal dosimetry estimates using voxelized reference phantoms for thyroid agents. J Radiat Res. 2014 May; 55(3): 407–422.*
3. Stabin MG, Sparks RB, Crowe E. OLINDA/EXM: the second-generation personal computer software for internal dose assessment in nuclear medicine. J Nucl Med. 2005;46:1023–1027
4. Melanie Hohberg, et al. Lacrimal Glands May Represent Organs at Risk for Radionuclide Therapy of Prostate Cancer with [177Lu]DKFZ-PSMA-617. Mol Imaging Biol (2016) 18:437Y445.
5. Shozo Okamoto, et al. Radiation Dosimetry for 177Lu-PSMA I&T in Metastatic Castration-Resistant Prostate Cancer: Absorbed Dose in Normal Organs and Tumor Lesions. J Nucl Med 2017; 58:445–450.
6. Linn Hagmarker, et al. Bone Marrow Absorbed Doses and Correlations with Hematologic Response During 177Lu-DOTATATE Treatments Are Influenced by Image-Based Dosimetry Method and Presence of Skeletal Metastases. J Nucl Med 2019; 60:1406–1413.

*Corresponding author: Kitiwat Khamwan, PhD
Email: kitiwat.k@chula.ac.th

Development of facial recognition system for patient safety : Analysis of benchmark data

Takatomo Ezura[1,2], Atsushi Myojoyama[1], Terufumi Kusunoki[2] and Daisaku Yoshida[3]

1 Graduate School of Human Health Sciences, Tokyo Metropolitan University, Tokyo, Japan,
2 Division of Radiation Medical Physics, Kanagawa Cancer Center, Kanagawa, Japan,
3 Department of Radiation Oncology, Kanagawa Cancer Center, Kanagawa, Japan

Abstract

Authentication of patients is indispensable for safety in medical practice. For patient safety, we developed a 3D camera-based facial recognition system that can identify individuals with more than 95% probability. This study aimed to quantitatively analyze the variability of daily scans as part of developing the present system. For facial identification, arbitrary 31 points were selectively used from 1347 points of feature points, and the matching algorithm is based on the comparison of coordinates between facial characteristic points in a reference data and collected real-time data. To verify the accuracy of the system, the identical person was scanned once or twice a day for 2 months and 80 facial mapping data were collected. In the current system environment, only one case deviated from the threshold range set for personal identification. The characteristic points with a small variability were located around the inner canthus and from the upper lip to below the nose, while the points of high movement were located on the whole nose and outer corners of the mouth. This study clarified that a facial recognition system using 3D camera is correct for day-to-day identification. The present system was shown to have satisfactory performance for use in clinical practice.

Keywords: Radiation therapy, Patient safety, Facial recognition, Kinect

1. INTRODUCTION

Authentication of individuals using two or more identifiers from their name, date of birth, and registration number is indispensable in providing secure healthcare to patients (1). The majority of medical errors due to misidentification can be prevented by systematic constraints of implementing integrated IT (2, 3). Radiofrequency identification is the next-generation technology for tracking and data collection, and this technology has been successfully applied in several clinics (4, 5). However, several challenges and barriers exist, including high adoption costs, lack of industry standards, lack of privacy and security protocols, and low awareness of its importance in the healthcare industry (6).

As an emerging technique, fingerprint recognition used in clinics can determine high performance (7). However, physical contact through biometric systems increases the likelihood of inoculating the respiratory tract with harmful microbial pathogens, thereby potentially triggering infections (8). Therefore, contactless biometric face recognition has been attracting a lot of attention. For patient safety, we developed a three-dimensional (3D) camera-based facial recognition system that can identify individuals with more than 95% probability. As part of the current system development, this study aimed to analyze the variation in daily scans and check the stability of the system.

2. MATERIAL AND METHODS

Kinect for Xbox One sensor was used to retrieve facial data. It is a multidevice equipped with an RGB camera, an infrared (IR) camera, and a microphone. The specifications are shown in Table 1. Qt 5.7.0 on Visual C++ 2015 was used as the development environment for the system. Kinect for Windows software development kit (SDK) 2.0, OpenCV 3.1, was applied as the development library, and MySQL 5.7.18 was used as the database management system. Kinect for Windows SDK 2.0 includes a high-definition face tracking application programming interface (HD Face API) that creates a 3D face model from the depth information acquired from the IR sensor and extracts facial feature points.

2.1 Process for acquiring facial feature point data

Figure 1 shows the process of creating a 3D face model using the Kinect sensor and the HD Face API. As the first step in the process of acquiring facial information, the whole-body joint information of the person closest to the IR sensor was acquired, as it is necessary to keep track of a specific individual. Tracking ID was then issued to track the head after the distance from the reference point of the head to the IR sensor had been measured. Detailed facial information frames were obtained in four poses to create a 3D facial model of the subject for which a tracking ID was issued. The created face mapping model consisted of 1347 feature points with 3D coordinates. All these feature point data were registered into a database built to perform specific personal authentication.

Table 1 *Kinect for Xbox One sensor specification.*

		RGB camera	IR camera
Resolution (pixels)		1920 × 1080	512 × 424
Frame rate (fps)		30	30
Depth range (m)		–	0.5–4.5
Viewing angle (°)	Horizontal	84.1	70.6
	Vertical	53.8	60

2.2 Matching process to authentication

Figure 2 shows the locations of the 1347 facial feature points retrieved by the HD Face API. The orange dots represent the 31 representative points that have been given anatomical names in SDK (9), which were also used in the present procedure to identify individuals. Four feature points near the corners of the mouth were excluded because of the possibility of movement (10).

A flowchart of the matching process to identify a specific individual is shown in Figure 3. In this study, the matching score is calculated from the standard deviation (SD) of the difference value of each 3D coordinate between the reference data and the new data. Matching scores were calculated for all data contained in the database. A correct authentication was determined as correct if the score between the reference and target data was the minimum value. In addition, the matching score was also used as a trigger to perform the final approval in personal authentication. The matching score is explained in the following.

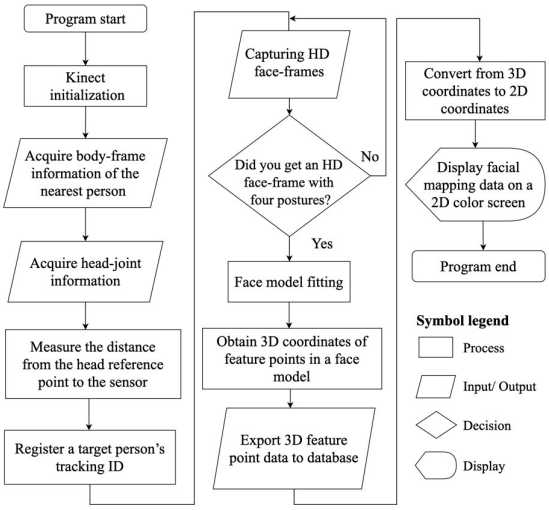

Figure 1 *Flowchart of the process of acquiring facial feature point data using the HD Face API. Personal authentication needs to be created as a separate process.*

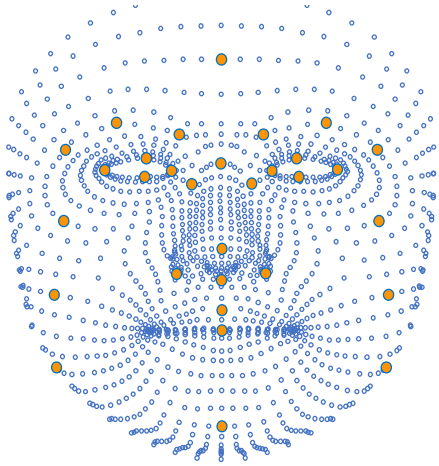

Figure 2 *Plot of the facial feature point data used throughout the face-matching process. Thirty-one feature points (orange plot) with data near the corners of the mouth were removed from the 35 reference points presented by Kinect SDK.*

The SD of the X-axis (s_x) is formulated as

$$s_x = \sqrt{\frac{1}{n-1}\sum_{i=1}^{n}(x_i - \bar{x})^2}\,, (1)$$

where $(x_1, x_2, \cdots, x_n)$ are the difference values of the X-axis, $\bar{x}$ is the mean of these difference values, and n is the number of the feature points. Similarly, the SD of the Y-axis (s_y) is written as

$$s_y = \sqrt{\frac{1}{n-1}\sum_{i=1}^{n}(y_i - \bar{y})^2}\,, (2)$$

and the Z-axis (s_z) is written as

$$s_z = \sqrt{\frac{1}{n-1}\sum_{i=1}^{n}(z_i - \bar{z})^2}\,. (3)$$

Combining Equations (1) to (3), the matching score S is expressed as

$$S = \sqrt{{s_x}^2 + {s_y}^2 + {s_z}^2}. (4)$$

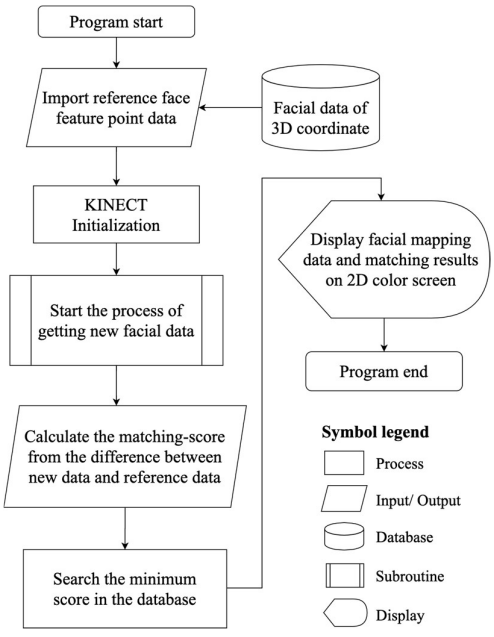

Figure 3 *Flowchart of the personal authentication process. The personal authentication process searches for the person with the lowest matching score value in the database.*

2.3 Benchmark for personal authentication

Facial recognition for benchmark testing was performed under identical conditions, considering that the measured data may vary due to the effects of different ambient light (10). The authentication process was carried out with a geometry of 100 cm distance from the target person to the Kinect sensor. A total of 80 facial mapping data were collected through one or two scans per day attempted on the same person over 2 months.

In the present study, two analyses were performed using the benchmark test results. The stability of the facial recognition process in the current system and the movement of facial feature points were studied.

3. RESULTS

3.1 Distribution of matching scores

The results of a benchmark test in which daily scans were performed on the same person are shown in Figure 4. In the present study, 80 face mapping images were acquired. The last data scanned was used as the reference data for calculating the matching score. Most of the data were distributed around the 1.0 mm matching score value, with 98.7% of all data being less than 1.5 mm.

3.2 Variation of facial feature points

A graph plotting the feature points of high/low variability in facial mapping for the 80 data is shown in Figure 5. These points included all feature points regardless of whether they were used or not to calculate the matching score. The feature points that returned stable values with little variability are shown in Figure 5 (a) and (b), plotted in blue. In contrast, the feature points that returned drifted values with greater variability are shown in Figure 5 (c) and (d), plotted in orange. The amount of feature point variability includes a combination of aspects caused by anatomical movements and aspects caused by the processing of the HD Face API.

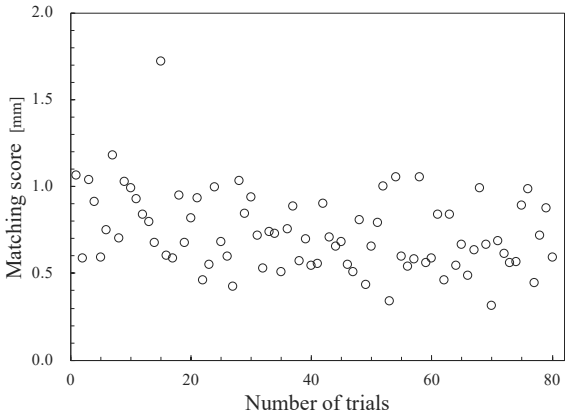

Figure 4 *Graph of the daily matching scores in the benchmark scan. Smaller matching score values are judged to be similar in facial contours and features between the two persons.*

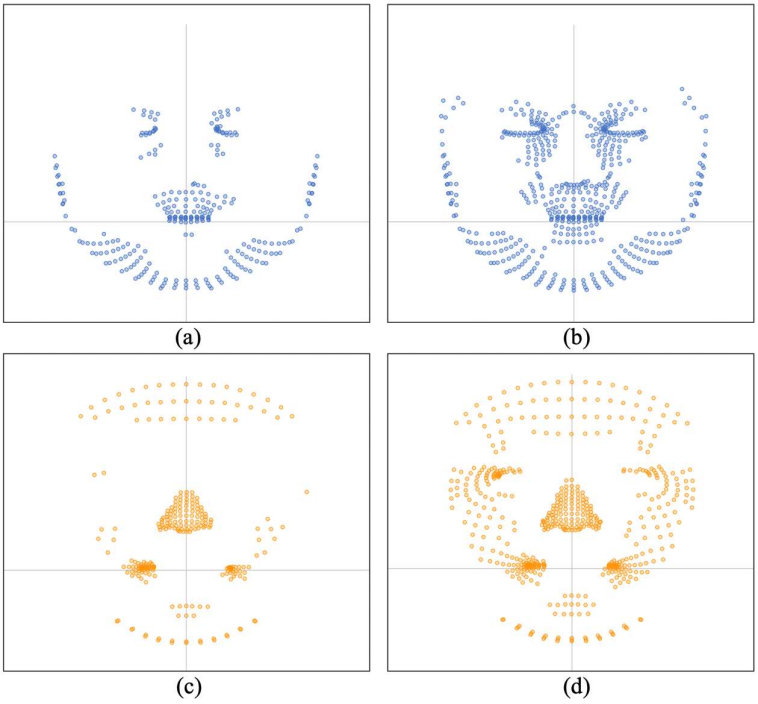

Figure 5 *Facial mapping of stable and drifted points extracted from the results of the benchmark test (daily personal authentication) for the identical person. The blue plot is a stable point cloud, and the orange plot is a drifting point cloud. (a) Top 20% stable points, (b) top 40% stable points, (c) worst 20% drifted points, and (d) worst 40% drifted points.*

4. DISCUSSION

4.1 Stability of the facial recognition system

The present facial recognition system has a matching score value of 1.5 mm as the threshold value for determining the "correct" judgment in the last step of the authentication process. The results of this benchmarking test indicate that the system was sufficiently robust for daily patient authentication in radiotherapy, as most data were within the threshold for correct determination. Given the potential influence of ambient light on the outcome, the best thing to do is obtain the initial facial data in the room where the radiation treatment is actually received.

The system showed sufficient potential, although one case was found to deviate from the decision threshold range. The reason for the outliers in the score in this case may lie in the process of obtaining the four postures for which the 3D face model was created, as shown in Figure 1. These four poses are directed in the order determined by the SDK. If a suitable face frame is not satisfied, the missing pose must be obtained again. This disappointing result can be attributed to the fact that the face model was created with a different angle of frame data in this re-acquisition procedure than in the past.

4.2 Trend of variation in feature points

The groups of feature points in Figure 5 (a) and (b) were considered stable points with little anatomical movement. Feature points around the eyes are considered an important area used as a reference point for research- and commercial-based face recognition (11, 12). Particularly low points of variation were shown in the vicinity of the inner canthus.

Figure 5 (c) and (d) suggest that the anatomical structure of the outer canthus and corner of the mouth is strongly influenced by differences in facial expressions. As daily changes in facial expressions are sensitively reflected in the face models even for the same subject, data handling of these points must be done with caution. Those points should not be uniquely excluded because of their high variability, and the anatomical differences between feature points with other persons should be fully considered. The large variation in the vicinity of the nose may be due to the accuracy of the constructed facial modeling and depth data (13), which is one of the issues to be considered in the future.

5. CONCLUSION

This study clarified that a facial recognition system using a 3D camera is correct for day-to-day identification. The present system has been shown to have satisfactory performance for use in clinical practice.

ACKNOWLEDGEMENTS

The authors have no conflicts of interest directly relevant to the content of this article.

REFERENCES

1. The Joint Commission. Hospital national patient safety goals. Hosp Natl Patient Saf Goals 2020. Published 2020. Accessed October 20, 2020. https://www.jointcommission.org/-/media/tjc/documents/standards/national-patient-safety-goals/2020/npsg_chapter_hap_jul2020.pdf
2. Hendee WR, Herman MG. Improving patient safety in radiation oncology. *Med Phys*. 2011;38(1):78-82. doi:10.1118/1.3522875
3. Yao W, Chu CH, Li Z. The adoption and implementation of RFID technologies in healthcare: A literature review. *J Med Syst*. 2012;36(6):3507-3525. doi:10.1007/s10916-011-9789-8
4. Arunachalam SP, Sir M, Marisamy G, et al. Optimizing emergency department workflow using radio frequency identification device (RFID) data analytics. *Front Biomed Devices, BIOMED - 2017 Des Med Devices Conf DMD 2017*. Published online 2017:10-11. doi:10.1115/DMD2017-3402
5. Ajami S, Rajabzadeh A. Radio frequency identification (RFID) technology and patient safety. *J Res Med Sci*. 2013;18(9):809-813.
6. Haddara M, Staaby A. RFID applications and adoptions in healthcare: A review on patient safety. *Procedia Comput Sci*. 2018;138:80-88. doi:10.1016/j.procs.2018.10.012
7. Palmgren JE, Lahtinen T. Fingerprint recognition to assist daily identification of radiotherapy patients. *J Radiother Pract*. 2009;8(1):17-22. doi:10.1017/S1460396908006493
8. Okereafor K, Ekong I, Okon Markson I, Enwere K. Fingerprint biometric system hygiene and the risk of COVID-19 transmission. JMIR Biomed Eng. 2020;5(1):e19623. doi:10.2196/19623
9. HighDetailFacePoints Enumeration | Microsoft Docs. Accessed October 22, 2020. https://docs.microsoft.com/en-us/previous-versions/windows/kinect/dn791778(v=ieb.10)
10. Silverstein E, Snyder M. Implementation of facial recognition with Microsoft Kinect v2 sensor for patient verification. *Med Phys*. 2017;44(6):2391-2399. doi:10.1002/mp.12241
11. Jeon B, Jeong B, Jee S, et al. A facial recognition mobile app for patient safety and biometric identification: Design, development, and validation. *J Med Internet Res*. 2019;21(4). doi:10.2196/11472
12. Sato A, Imaoka H, Suzuki T, Hosoi T. Advances in face detection and recognition technologies. *NEC J Adv Technol*. 2005;2(1):28-34.
13. Smolyanskiy N, Huitema C, Liang L, Anderson SE. Real-time 3D face tracking based on active appearance model constrained by depth data. *Image Vis Comput*. 2014;32(11):860-869. doi:10.1016/j.imavis.2014.08.005

Dosimetric effect of the baseline shift in the phase and amplitude gating lung SBRT

Kenji Yasue[1,2], Hiraku Fuse[3], Kazuya Shinoda[2], Hideaki Ikoma[2], Tatsuya Fujisaki[3], Yoshio Tamaki[4]

1 Graduate School of Health Sciences, Department of Radiological Sciences, Ibaraki Prefectural University of Health Sciences,
2 Ibaraki Prefectural Central Hospital, Department of Radiation Technology
3 Ibaraki Prefectural University of Health Sciences, Department of Radiological Sciences
4 Ibaraki Prefectural Central Hospital, Department of Radiation Oncology

Abstract

To clarify the dosimetric effect of the baseline shift on the phase and amplitude lung Stereotactic body radiation therapy (SBRT), the dose distribution in the phase and amplitude gating were measured by the respiratory motion phantom inserted Gafchromic EBT-XD. The respiratory motion phantom was employed in reproducing the patient's respiratory motion using the clinical data during the lung SBRT. The results obtained show that the gamma passing rate was 75.0±7.9%, 75.9 ±7.0% in phase, amplitude gating methods. For the phase gating, the linear increment of width depends on the baseline shift in contrast to that of the amplitude gating. Our results suggest that the dose distribution of the phase gating had more impact on the baseline shift. Thus, the amplitude gating is a more robust method for the patients with the baseline shift, compared with phase gating.

Keywords: Respiratory gating method, Baseline shift, Phase gating, Amplitude gating

1. INTRODUCTION

Lung stereotactic body radiation therapy (SBRT) considers the respiratory motion during treatment for prescribing a high radiation dose per fraction using a small complicated field. Various respiratory management strategies have been developed for minimizing the effect of target coverage and also reduces damages to organs (1, 2). The baseline shift defined as the change in the position of exhalation is a challenge in SBRT because of the decreased target coverage (3, 4).

The respiratory gating method in which the radiation is administrated within the phase by setting the gate window in the respiratory signal is one of the respiratory management strategies (1, 2). The two gating methods used during the clinical administration of radiation involve either phase gating or amplitude gating. However, the former is applied more frequently (5–8). Previous studies have shown the effectiveness of the amplitude gating method in increasing the target coverage by decreasing the residual motion (5, 6). Lee *et al.* showed a 5.2% difference in the gamma passing rate between the phase and amplitude gating method (5). Berbeco *et al.* reported a 30% reduction in the residual motion for patients with respiratory irregularity using the amplitude gating when compared with the phase gating method (6). However, the dosimetric effect of the baseline shift was not clarified in the phase and amplitude gating SBRT.

2. MATERIAL AND METHODS

2.1 Design of the respiratory motion phantom

The respiratory motion phantom was designed by QUASAR™ Respiratory Motion Platform (Modus Medical Devices, London, Canada) and a water equivalent solid phantom (Tough-water™ phantom, WD type; Kyoto Kagaku, Kyoto, Japan). The phantom was made to move in a superior-inferior direction depending on the respiratory waves acquired from the internal gold marker position of patients that had been treated using a Real-Time Tracking Radiotherapy (RTRT) system (Shimadzu, Kyoto, Japan) to reproduce the respiratory motion during treatment. This study was approved by the Ethics Committee in Ibaraki Prefectural Central Hospital to use the data collected from the respiratory motion of patients.

Detailed information about the five respiratory waves was shown in Table 1. The baseline positions were detected in each respiratory cycle using Python 3.6.6. The mean and standard deviation (SD) of the baseline positions were computed. To evaluate the dosimetric effect of the baseline shift, CV_{BS} was defined as

$$CV_{\mathrm{BS}} = |SD/Ave| \quad (1)$$

where, CV_{BS} represents the coefficient of variation, *SD* is the standard deviation of the baseline positions and *Ave* is the mean of the baseline positions.

2.2 Design of the dose distribution

The dose distribution of the lung SBRT was calculated using the RayStation TPS (RaySearch Laboratories, Stockholm, Sweden). The shape of the target was assumed to be a sphere. The conditions of the calculated dose distribution have been tabulated in Table 2. The dose distribution was calculated using a 6-MV high-energy photon beam (600 MU/min) from the True beam STx (Varian Medical Systems, Palo Alto, CA). The planning target volume (PTV) was covered with 80% isodose.

2.3 Irradiation and Measurement of the dose distribution

The Real-time Position Management (RPM; Varian medical systems, Palo Alto, CA, USA) system was used for respiratory gating. The RPM block was placed on the

respiratory motion phantom. The breathing cycle was evenly divided into ten phases and the gating window was set in 35–65% and 0–30%, to irradiate in the exhalation position for the phase and amplitude gating lung SBRT. The respiratory motion phantom was continually repeated to obtain the beam delivery. Fig. 1 shows the pictorial representation of the respiratory motion phantom. The measurements were performed using the EBT-XD films batch #12191801. The films were inserted at a depth of 10 cm in a water equivalent solid phantom. The region representing the PTV was positioned at the centre of the respiratory motion phantom and the two-dimensional (2D) dose distribution was measured in a coronal plane. The control data was measured the dose distribution without the respiratory motion due to analyze the gamma index by comparing it with the respiratory motion.

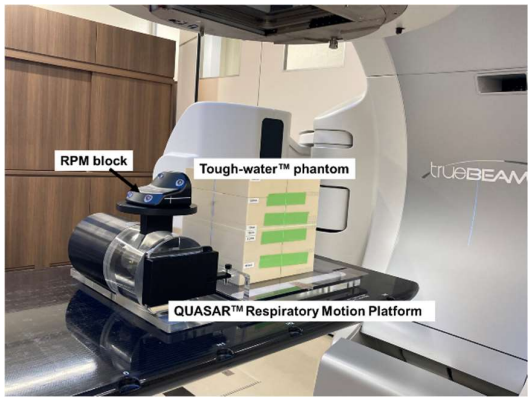

Figure 1. *The respiratory motion phantom.*

The respiratory motion phantom was designed by the water equivalent solid phantom and QUASAR™ Respiratory Motion Platform. This phantom was moved by the patient's respiratory data during the lung SBRT to reproduce the patient's respiratory motion.

2.3 Analysis of the gamma index

EBT-XD films were scanned in RGB (Red Green Blue) format using a 48-bit scanner (Epson Expression DS-G20000) at 72 dpi (pixel size: 0.35 mm) and were measured and analyzed using the DD-System (R-Tech Inc., Tokyo, Japan). The film response was calibrated with ten EBT-XD films exposed in the range of 0–24 Gy. All calibrated and measured films were scanned at a consistent 24 h post-exposure. To evaluate the dose distribution of the phase and amplitude gating lung SBRT with the baseline shift, the gamma index under 10% dose threshold, 2% dose difference (DD) and 1 mm distance-to-agreement criteria were analyzed by comparing with the control data.

2.5 Analysis of the penumbra

The dose profiles in the superior-inferior direction were computed from the EBT-XD films using the DD-system to evaluate the penumbra. The penumbra was defined as

$$PW_{\text{superior or inferior}}[\text{cm}] = |W_{80\%} - W_{20\%}| \qquad (2)$$

where, $PW_{\text{superior or inferior}}$ stands for the penumbra in a superior or inferior direction, $W_{80\%}$ represents the width of the 80% dose level and $W_{20\%}$ stands for the width of the 20% dose level.

Table 1. *The profile of the respiratory waves;*

Sample No.	Amplitude [cm]	baseline position[cm]	CV_{BS}
1	1.56 cm±0.27	−0.87 cm±0.06	6.8
2	1.41 cm±0.26	−0.78 cm±0.10	13.5
3	1.47 cm±0.16	−0.85 cm±0.08	9.0
4	1.34 cm±0.35	−0.72 cm±0.13	18.6
5	1.36 cm±0.20	−0.66 cm±0.17	25.0

Table 2. *The conditions of the calculated dose distribution.*

TPS	RayStation ver 6.2.0.7
Energy	6 MV-X
Number of beams	5 non-coplanar
CTV	3.4 cm sphere
PTV	CTV+0.5 cm
Gy/fr	48 Gy/4 fr

3. RESULTS

3.1 Analysis of the gamma index

The results of gamma analysis under the 2%/1 mm criterion according to the phase and amplitude gating methods are shown in Fig. 2. There were differences in the gamma passing rate according to the gating method. On average, the gamma passing rate was 75.0±7.9%, 75.9 ± 7.0% in phase and amplitude gating methods, respectively. When CV_{BS} exceeded 15 in the phase gating, the gamma passing rate was worse in comparison with the amplitude gating.

3.2 Analysis of the penumbra

The penumbra in the superior and inferior directions are shown in Figs. 3(a) and (b), respectively. When the CV_{BS} was 6.8, the PW_{superior} were 0.5 and 0.6 cm, and 0.5 and 0.7 cm for the phase and amplitude gating, respectively. When the CV_{BS} was 25.0, the PW_{superior} were 0.8 and 0.6 cm, and 0.8 and 0.6 cm for both the phase and the amplitude gating. In the phase gating, the increase in the penumbra depends on the CV_{BS}. Conversely, that of the amplitude gating does not

depend on the CV_{BS} in comparison with the phase gating. The results were similar in both directions.

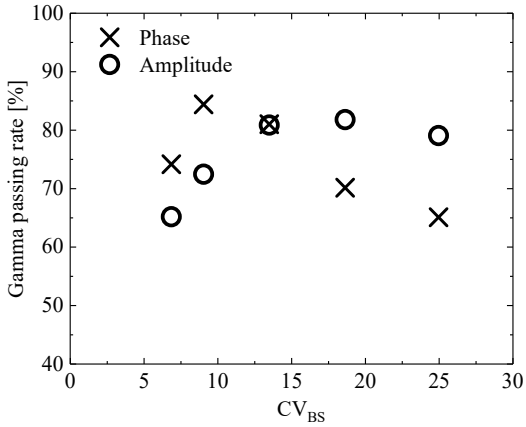

Figure 2. *Gamma passing rate in the phase and amplitude gating SBRT.*

The gamma passing rate under 2%/1 mm was computed by comparing the control data without the respiratory motion. CV_{BS} was determined using eq. 1 for evaluating the baseline shift of the patient's respiratory wave.

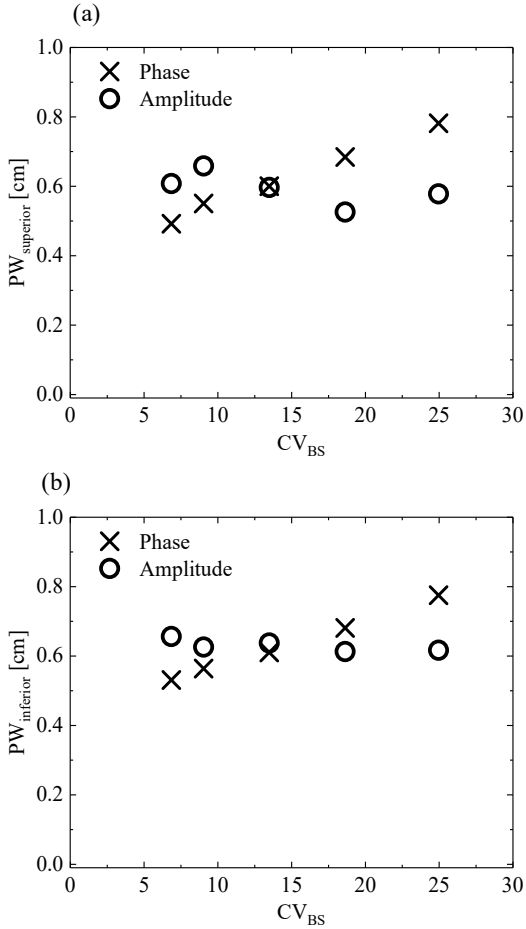

Figure 3 *(a) and (b). The relationship between the penumbra in the superior and inferior directions and the baseline shift.*

The $PW_{\text{superior or inferior}}$ was determined using eq.2.The relationship between the penumbra region and the baseline shift was evaluated in the phase and amplitude gating lung SBRT.

4. DISCUSSION

The dosimetric effect of the baseline shift in the different respiratory gating methods was investigated using the respiratory motion phantom reproduced from the patient's respiratory motion during treatment. The dose distribution in the phase and amplitude gating lung SBRT were measured by the EBT-XD films. On average, the gamma passing rate was 75.0±7.9%, 75.9 ±7.0% in phase, amplitude gating methods. Lee *et al.* analyzed the dose distribution in the phase and amplitude gating volumetric modulated arc therapy (VMAT) (5). The result revealed that the gamma passing rate under 2%/1 mm of the amplitude gating was 5.2% higher than the phase gating. The results obtained in this study are in agreement with that obtained in the previous study.

This study shows that if the CV_{BS} is greater than 15 in the phase gating, the gamma passing rate was worse in comparison with the amplitude gating. The linear increment of the penumbra depends on the magnitude of the baseline shift in the phase gating, while that of the amplitude gating remained consistent.

Takao *et al.* reported that the baseline shift was observed to be more than normal individuals in 70% of lung cancer patients (3). Zhao *et al.* showed that the increment of the residual motion during treatment depends on the baseline shift (4). Therefore, the baseline shift should be taken into account to perform a high precision treatment in the lung SBRT.

Our results suggest that the dose distribution of the phase gating was more impactful on the baseline shift in comparison with the amplitude gating. Thus, the amplitude gating lung SBRT is a more robust method in the lung SBRT with the baseline shift in comparison with the phase gating.

5. CONCLUSIONS AND FUTURE SCOPE

The dose distribution was measured by the respiratory motion phantom which reproduced the respiratory motion of the patient during treatment to clarify the dosimetric effect of baseline shift on the phase and amplitude lung SBRT. The amplitude gating was found to be a more robust method for the patients with the baseline shift since the dose distribution had less impact on the baseline shift in this method, compared with the phase gating. In the future, this experimental will be performed with more respiratory samples. In addition, the residual motion and gating irradiation timing will be investigated in the phase and amplitude gating lung SBRT using the log file from the True Beam STx.

ACKNOWLEDGEMENTS

I am grateful to the laboratory members at Ibaraki Prefectural University and colleagues at Ibaraki Prefectural Central Hospital for collaboration in this work.

REFERENCES

1. Keall, P. J. *et al.* The management of respiratory motion in radiation oncology report of AAPM Task Group 76 a. Med. Phys. 33, 3874-3900 (2006).
2. Tsang, M. W. K. Stereotactic body radiotherapy: current strategies and future development. J Thorac Dis. Suppl 6, S517-527 (2016).
3. Takao, S. *et al.* Intrafractional baseline shift or drift of lung tumor motion during gated radiation therapy with a real-time tumor-tracking system. Int. J. Radiat. Oncol. Biol. Phys. 94,172-180 (2016).
4. Zhao, B. *et al.* Statistical analysis of target motion in gated lung stereotactic body radiation therapy. Phys. Med. Biol. 56,1385-1389 (2011).
5. Lee, M. *et al.* Comparing phase- and amplitude-gated volumetric modulated arc therapy for stereotactic body radiation therapy using 3D printed lung phantom. J. Appl. Clin. Med. Phys. 20, 107-113 (2019).
6. Berbeco, R. I. *et al.* Residual motion of lung tumours in gated radiotherapy with external respiratory surrogates. Phys. Med. Biol. 50,3655-3667 (2005).
7. Vedam, S. *et al.* Determining parameters for respiration-gated radiotherapy. Med. Phys. 28, 2139-2146 (2001).
8. Oh, S. A., Yea, J. W., Kim, S. K. Statistical determination of the gating windows for respiratory-gated radiotherapy using a visible guiding system. PloS One 11, e0156357 (2016).

Paper ID 117

Development and dosimetric verification of 3D customized bolus in radiotherapy

Nichakan Chatchumnan[1], Sakda Kingkeaw [2], Chuanchom Aumnate[3], Taweap Sanghangthum[4,*]

1 Master of Science in Medical Physics Program, Faculty of Medicine, Chulalongkorn University, Bangkok, Thailand
2 Division of Radiation Oncology, Department of Radiology, King Chulalongkorn Memorial Hospital, Bangkok, Thailand
3 Metallurgy and Materials Science Research Institute Chulalongkorn University, Bangkok, Thailand
4 Division of Radiation Oncology, Department of Radiology, Faculty of Medicine, Chulalongkorn University, Bangkok, Thailand
**Corresponding Author*

Abstract

Introduction: Bolus is a tissue equivalent material that commonly used to reduce skin-sparing effect in radiotherapy. The commercial flat bolus cannot form perfect contact with irregular surface of the patient's skin, resulting in air gap, especially in irregular surface shape.

Purpose: The purpose of this study was to evaluate the feasibility of two kinds of silicone rubber bolus, RA-00AB and RA-05AB that were made as the fabricated flat and 3D customized bolus using 3D printing technology.

Methods: The 1 cm boluses were made from two kinds of silicone rubber solutions. The point dose and planar dose differences were evaluated by comparing with virtual bolus using gamma index from SNC-patient software. The physical properties were also evaluated by comparing with commercial one. For 3D customized bolus, the bolus shell was designed at nose, cheek and neck region from Fusion 360 program. Then print out the shell by 3D printer and filled the shell with silicone rubber solution. The dosimetric effect of 3D customized bolus was compared to without bolus situation.

Results: The point dose differences between RA-00AB and RA-05AB silicone rubber model compared with commercial bolus was lesser than 0.4%, while the planar dose differences of both model at 2%/2mmm gamma criteria was the same result at 100% pass. The hardness, thickness, density, Hounsfield unit (HU), and dose attenuation of customized bolus were quite the same as commercial bolus. When 3D customized bolus was placed on the RANDO phantom, it showed very good fit against the irregular surface shape compared with commercial bolus, build up doses increased and the target volume obviously presented more uniform doses compared to the without bolus situation.

Conclusion: A silicone rubber bolus produced the feasible dosimetric properties to a commercial bolus and could save cost when compared to commercial bolus. The 3D printed customized bolus is a good buildup material and could potentially to replace and improve treatment efficiency.

Keywords: silicone rubber, flat bolus, 3D Customize bolus

1. INTRODUCTION

Radiotherapy is one of the most common methods used for the treatment of cancer patients. In order to deliver a sufficient radiation dose to the tumor, adequate types of radiation are selected depending on the tumor location. Conventionally, electron is applied for the treatment of superficial lesions such as skin cancer, while high-energy photon is used to treat deeply located lesions. With high-energy photon treatment, a sufficient dose cannot be delivered to the surface due to the skin sparing effect. To avoid this limitation, several types of commercially available boluses are often used [1]. These bolus materials should be nearly tissue equivalent and allow a sufficient surface dose enhancement. In practice, most commonly used commercial flat boluses cannot form perfect contact with the irregular surface of the patient's skin, particularly the nose, ear, and scalp, and the resulting air gap affects the second skin sparing effect and reduces both the maximum and surface dose [2-6]. Thus, commercial flat boluses need to be used with great care, especially when the skin has a particularly irregular shape. Recently, there have been significant advances in 3-dimensional (3D) printer technology [7-8]. In this study, the customized boluses using a 3D printer were fabricated and assessed whether it could overcome the disadvantages of currently used commercial flat boluses.

2. MATERIAL AND METHODS

2.1 Bolus materials

The 1 cm commercial bolus is Bolx-I (CIVCO Medical Solution, Orange City, FL) [9] with a density of 1.03 g/cm^3 and a main component is polymer gel. There were two kinds of silicone rubber customized bolus, RA-00AB and RA-05AB. The former is based on vinyl silicone oil and white carbon black, while the latter one is based on Hydroxy-terminated Polydimenthylailoxane, Aqua and Titanium Dioxide.

2.2 Bolus fabrication

The silicone rubber solution (RA-05AB) component A and B as shown in Fig.1 (a), weight in a ratio of 1:1 by digital weighting machine, then pour into the container with size of 10×10 cm^2 [Fig. 2(a)] and keep in the room temperature for 24 hr. Then repeat the same process in silicone rubber solution (RA-00AB) [Fig. 1(b)] and the finished bolus is presented in Fig. 2(b).

2.3 Physical properties verification

The 1 cm boluses produced from two kinds of silicone rubber solutions with size of 10×10 cm^2 were evaluated in dosimetric from point dose differences at 0.5, 1.0 and 1.5 cm depths and planar dose differences at 1.5 cm depth by comparing with virtual bolus created in Eclipse treatment planning system (TPS) (Varian Medical Systems, Palo Alto, CA) using gamma index from SNC-patient software (Sun Nuclear Corporation, Melbourne, FL).

Then, the bolus presented better dosimetric results and basic physics properties (RA-00AB) was selected to fabricate flat bolus with size of 30×30 cm^2. The bolus characteristics of this silicone rubber bolus such as hardness, thickness, density, Hounsfield unit (HU), and dose attenuation, were also confirmed and compared to commercial flat bolus. To evaluate the physical characteristics of the boluses, hardness was measured by Shore A Durometer as displayed in Fig.3, thicknesses was measured with Vernier Caliper (inox), and density was calculated using the density formula. The HU of the bolus was measured for 9 positions on TPS. The dose attenuation verification part was measured by FG65-P detector in solid phantom as presented in Fig. 4.

Fig. 1. The silicone rubber solution of (a) RA-05AB, (b) RA-00AB

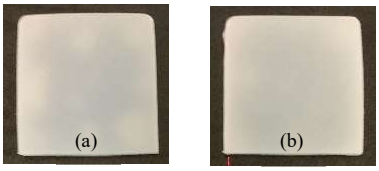

Fig. 2. The silicone rubber bolus of (a) RA-05AB size, (b) RA-00AB.

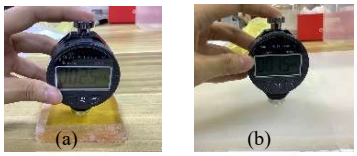

Fig. 3. The hardness measurement of boluses for (a) commercial bolus, (b) customized bolus.

Fig. 4. The dose attenuation measurement setting up for (a) commercial bolus, (b) customized bolus

2.4 Clinical application

The 3 pieces of bolus shells were design to create boluses at nose, cheek and neck region by 3D slicer program. The STL files (3D bolus shell) were print out by 3D printer. The 1 cm silicone rubber solution was filled to the shells and placed on Rando phantom in specified areas compared with commercial bolus.

3. RESULTS

3.1 Physical evaluation

The bolus of RA-00AB model was softer than RA-05AB model. For the point dose differences, both types of bolus showed less than 0.4% deviation from commercial for all depths as presented in Table 1.

Table 1. *The point dose at 0.5, 1.0 and 1.5 cm depth between commercial and in-house boluses.*

Depth (cm)	Commercial (cGy)	RA-05AB (cGy)	RA-00AB (cGy)
0.5	209.3	209.8	209.8
1.0	206.7	206.5	206.1
1.5	202.3	201.9	201.6

Moreover, the planar dose differences were also evaluated at 1.5 cm depth using gamma index from SNC-patient software as shown in Fig. 5.

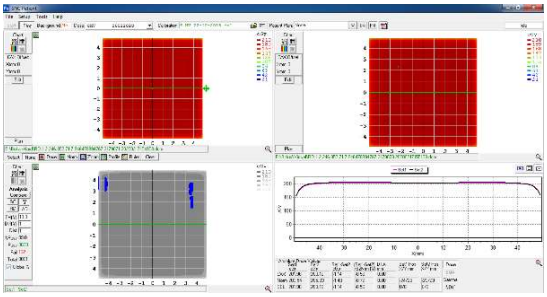

Fig. 5. The planar dose differences were evaluated at 1.5 cm depth using gamma index from SNC-patient software.

The planar dose differences were also presented the excellent agreement with 100% pass rate at 2%/2 mm gamma criteria in both types of bolus. However, RA-00AB model was softer than RA-05AB model. The RA-00AB model bolus was selected for the next step.

The physical properties of two types of boluses, commercial bolus and customized bolus with size 30×30 cm^2, were compared. From the hardness range of 0-100 HA, the hardness measured by Shore A Durometer for commercial bolus was 2.5 HA and customized bolus was 1.5 HA. The average thickness of commercial bolus was 1.05±0.00 cm and customized bolus were 1.07±0.01 cm, while density was 1.03 and 0.99 g/cm^3, respectively. The HU of commercial bolus and customized bolus were -124±63.33 and -73±42.57, respectively. There were good agreements between the

dose attenuation at 5 cm within solid water phantom, that commercial bolus and customized bolus were 167.2 and 167.6, respectively. The point dose differences were only 0.2%.

3.2 Clinical application

The 3D slicer and Fusion360 program were used to design the bolus shells, and the 3D printing technology was used to print the shells. The shells were filled with silicone rubber RA-00AB as shown in Fig. 6.

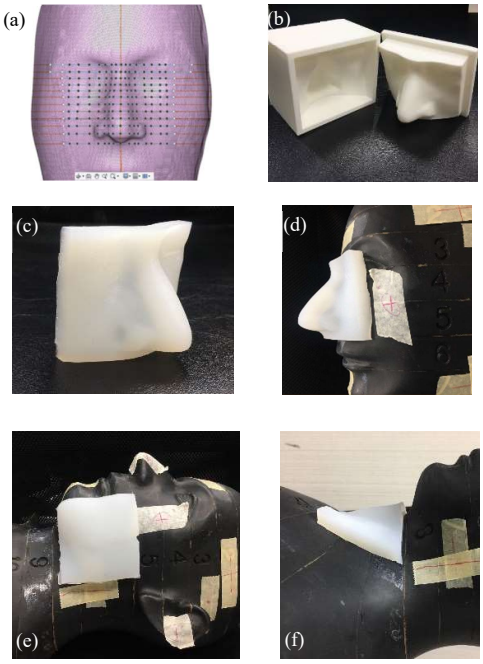

Fig. 6. The procedure of making silicone rubber bolus based on 3D printing technology at nose area from (a) the Fusion 360 program for bolus shell designed, (b) the bolus shell fabricated by 3D printer, (c) the silicone rubber bolus, (d), (e), and (f) the silicone rubber bolus on rando phantom for nose, cheek and neck, respectively.

4. DISCUSSION

Between two models of silicone rubber, the RA-00AB model was softer than RA-05AB model, while the gamma passing rate at 2%/2mm gamma criteria were also presented the excellent agreement with 100% pass rate in both types of bolus and the point dose differences were not differences. However, the bolus from RA-00AB model was softer and that represented to contact to surface than another model. When the size of 30×30 cm^2 was fabricated, the physical characteristics were quite the same as commercial bolus for all hardness, thickness, density, Hounsfield unit (HU), and dose attenuation properties that means the RA-00AB silicone rubber can be replaced the commercial super flab bolus. However, commercial super flab bolus has limitation in case of irregular shape surface. The 3D printing technology can be solved this problem.

The 3D printing skills was applied to create individually customized boluses, which were designed to compensate for the irregular surface in radiotherapy. In general, two ways have been reported of making a bolus in past studies. One method was to print a bolus directly with 3D printing materials after the design stage. Polylactic acid (PLA), was a commonly used printing material, which had been demonstrated to be a bolus material in a previous study [10]. Studies reported that the doses of 3D printed PLA bolus in phantom simulating radiotherapy of breast cancer after radical resection were more uniform than with the commercial bolus [11, 12]. Acrylonitrile butadiene styrene (ABS) copolymer is another printing material commonly used except PLA, but both the two materials are too hard and with poor comfort. Another method is to print the shell of the bolus and then fill it with other soft materials, that our studied use this method. Richard R et.al.[13] printed the shell in PLA using the 3D printer and filled it with silicone rubber for non-melanoma skin cancer electron beam radiotherapy. Silicone rubber has the advantage when making a bolus due to its excellent biocompatibility, chemical stability, and good mechanical properties, but its density is 1.1–1.2 g/cm^3 which differs from that of human tissue. In this study, our silicone rubber as filling materials was better than their studied with of the 0.99 g/cm^3.

The 3D printed bolus was very good fit against the irregular surface of the RANDO phantom that can significantly reduce the air gap between bolus and phantom compared with commercial bolus. With the bolus, the skin dose was increase that showed the same result of Shin W K et al [14] who fabricated a customized 3D bolus using a 3D printer and evaluated its feasibility in clinical practice by comparing its performance without a bolus in treatment planning system. It means that the 3D printed customized bolus is a good buildup material. Furthermore, the treatment plan with the 3D printed customized bolus could be clinically effective, help to overcome the problem of variable air gaps, and improve reproducibility of daily setup conditions on irregular surfaces compared to commercial flat boluses.

5. CONCLUSION

A silicone rubber bolus produced the feasible physical and dosimetric properties to a commercial bolus and could save cost when compared to commercial bolus. The 3D printed customized bolus is a good buildup material and could potentially replace and improve commercially flat bolus and therefore also increase the efficacy of the radiotherapy.

ACKNOWLEDGEMENTS

Ratchadapiseksompotch Fund, Faculty of Medicine, Chulalongkorn University

REFERENCES

1. Khan FM (2010) The physics of radiation therapy. 4th ed. Philadelphia: Lippincott Williams & Wilkins.
2. Butson MJ, Cheung T, Yu P, Metcalfe P (2000) Effects on skin dose from unwanted air gaps under bolus in photon beam radiotherapy. Radiat Meas 32: 201–204.
3. Khan Y, Villarreal-Barajas JE, Udowicz M, Sinha R, Muhammad W, et al. (2013) Clinical and dosimetric implications of air gaps between bolus and skin surface during radiation therapy. J Cancer Ther 4: 1251–1255.
4. Benoit J, Pruitt AF, Thrall DE (2009) Effect of wetness level on the suitability ofwet gauze as a substitute for Superflab as a bolus material for use with 6 mv photons. Vet Radiol Ultrasound 50: 555–559.
5. Sharma SC, Johnson MW (1993) Surface dose perturbation due to air gap between patient and bolus for electron beams. Med Phys 20: 377–378.
6. Kong M, Holloway L (2007) an investigation of central axis depth dose distribution perturbation due to an air gap between patient and bolus for electron beams. Australas Phys Eng Sci Med 30: 111–119.
7. Schubert C, van Langeveld MC, Donoso LA (2014) Innovations in 3D printing: a 3D overview from optics to organs. Br J Ophthalmol 98: 159–161.
8. Ju SG, Kim MK, Hong CS, Kim JS, Han Y, et al. (2014) New Technique for developing a proton range compensator with use of a 3-dimensional printer. Int J Radiat Oncol Biol Phys 88: 453–458.
9. Kong Y, et al. A dosimetric study on the use of 3D-printed customized boluses in photon therapy: A hydrogel and silica gel study, J Appl Clin Med Phys, Radiotherapy and Oncology 2018; DOI: 10.1002/acm2.12489.
10. Burleson S, Baker J, Hsia AT, et al. Use of 3D printers to create a patient-specific 3D bolus for external beam therapy. J Appl Clin Med Phys. 2015; 16:166–178.
11. Ha JS, Jung JH, Kim MJ, et al. Customized 3D printed bolus for breast reconstruction for modified radical mastectomy (MRM). Prog Med Phys. 2016; 27:196–202.
12. Park SY, Choi CH, Park JM, et al. A patient-specific polylactic acid bolus made by a 3d printer for breast cancer radiationtherapy. PLoSONE. 2016; 11:0168063.
13. Ricotti R, Ciardo D, Pansini F, et al. Dosimetric characterization of 3D printed bolus at different infill percentage for external photon beam radiotherapy. Phys Med. 2017; 39:25–32.
14. Kim SW, Shin HJ, Kay CS, Son SH. A customized bolus produced using a 3-dimensional printer for radiotherapy. PLoS ONE 9(10): e110746. doi: 10.1371 /journal .pone . PubMed 2014 PMID: 0110746.

Remote clinical dosimetry auditing for IMRT using virtual EPID standard phantom audit (VESPA) in Thailand: Preliminary results

Pavarit Pojanapreecha[1], Puangpen Tangboonduangjit[4], Sangutid Thongsawad[1], Peter Greer[2,3], Todsaporn Fuangrod[1]

1 Faculty of Medicine and Public Health, HRH Princess Chulabhorn College of Medical Science, Chulabhorn Royal Academy, Bangkok,10210, Thailand
2 Department of Radiation Oncology, Calvary Mater Hospital Newcastle, NSW, 2298, Australia
3 School of Mathematical and Physical Sciences, University of Newcastle, Newcastle, NSW, 2308, Australia
4 Department of Radiology, Faculty of Medicine, Ramathibodi Hospital, Mahidol University, Bangkok 10400, Thailand

Abstract

Since multiple centers apply the modern radiotherapy technique in radiation therapy, it requires an elaborate treatment plan, resulting in highly efficient quality assurance (QA) to ensure the beam is delivered precisely. The standard of QA (such as TG-142) is recommended for execution in all centers, the variation across center-to-center remains exist. The external audit with simulated beam delivery in end-to-end process test becomes essential. However, a traditional (on-site) audit process requires high resource intensive and time-consuming. To deal with these limitations, the remote auditing concept has been recently introduced as an alternative auditing. In this research, the remote auditing for intensity-modulated radiation therapy (IMRT) using virtual electronic portal imaging device (EPID) standard phantom was designed and implemented under Thailand context. A single institution (local center) was implemented as the pilot study. The remote auditing workflow was designed and used to communicate between the auditors and participants. All data is transferred online using commercial cloud platform and is analyzed using in-house software developed using MATLAB/Simulink. The evaluation results will be in the form of beam delivery accuracy using 3D gamma evaluation method. Based on our preliminary study, the results presented that the local center machines were passed the tolerance, which used 3%/2mm and 2%/2mm .The mean percentage gamma pass rates for the Varian TrueBeam was 100.0 % (for the 3%/2 mm criterion) and 99.93 % (for the 2%/2 mm criterion) , while the Varian Trilogy was 99.3% (for the 3%/2 mm criterion) and 99.0 % (for the 2%/2 mm criterion). In conclusion, the remote clinical dosimetry auditing protocol can monitor the radiotherapy treatment process from the participant center.

Keywords: Intensity modulated radiotherapy; Quality Assurance; External Dosimetry Auditing, Patient-Specific Quality Assurance

1. INTRODUCTION

Cancer is a genetic disease that progresses by accumulated molecular alterations in the genome of somatic cells (1). According to Public Health of Thailand, cancer diseases mainly cause deaths in 2018 (2).Cancer or tumor site is determined the treatment options, as a case in point surgery treatment is the recommended treatment for Tis, T1 and some T2 carcinoma of the esophagus or chemo-radiation is a standard treatment option for unresectable pancreatic cancer (3), (4). Radiotherapy is a locoregional cancer treatment modality that relies on accurate delivery of very high doses of radiation to a target whilst minimizing dose to surrounding healthy structures(5). Depending on staging, radiation treatment is the primary decision for cancers inoperable or invade to other regions (6). The dominance of radiotherapy over other treatment options is the survival rate, local control and toxicity profiles(7). Therefore the demand of radiotherapy as a treatment option has become world trend. The novel techniques will improve radiotherapy quality assurance. Prior the treatment delivery, IMRT technique requires to verify the beam delivery with the dosimetry method. It's called patient-specific QA (PSQA). There are functional tools that is implemented in routine clinical work (8). One of the dosimetry tools is electronic portal imaging device (EPID), which offers the availability to reduce time compared to film dosimetry because it offers a finer spatial resolution than array devices. In the IMRT application, EPID have been used for pretreatment and transit dosimetry applications. Some study shows the feasibility of EPID dosimetry for both applications (9) (10). At present, the local hospitals of Thailand apply the treatment process and a modern technique by using LINAC connected EPID. Thereby portal dosimetry audit can easily provide IMRT QA. External dosimetry audit is a valuable tool to ensure the quality and safety of radiotherapy, secure best-practice, enable improvements, and reduce the risk of treatment error. In 2000s, there was a research introduced the model for external dosimetry audit with a physical phantom or an anthropomorphic phantom which is embedded ion chamber (11). Some study performed an onsite audit program by using the ArcCheck helical diode (12). The limitation of on-site audit process are resource intensive and time consuming (13). The appearance of EPID influence to external dosimetry audit. As the pretreatment quality assurance, the study compare the performance of using EPID dosimetry algorithms as the dosimetry tools and analyzes dosimetry measurements made alongside the results

obtained with a standard diode array (14). For this reason, it support the applicable method for using EPID as the external dosimetry audit. The research objective is design the protocol and implement at the Local center as a pilot study.

2. MATERIAL AND METHODS

2.1 Remote dosimetry audit procedure

In this work, the remote dosimetry audit protocol was designed and implemented at the local center as the pilot study. We set the selection criteria for the audit participant. Firstly, we selected the center that has Varian LINAC. Second, each center is required to use the EPID dosimetry for the patient-specific QA as their protocol. Lastly, each center usually is planned for the IMRT technique as the clinical protocol.

Following the criteria, the local center equipped with linear accelerators (linacs) with two types of Varian (Varian Medical Systems, Palo Alto, CA) participated in this pilot study. Type 1 was Varian TrueBeam 2.5 with aS1000 type EPID, and Type 2 was Varian Trilogy 9.01 with aS1000 type EPID. A medical physicist from the institute received the documents and information via online cloud storage. They requested to create a treatment plan according to the specifics of the clinical trial followed the constraint. These clinical trial plans were transferred to virtual water-equivalent phantoms as the verification plan.

After planning, the verification plan was delivered to the treatment machine for patient-specific QA test. Additionally, calibration fields are delivered to determine the central axis and sag characteristics for software configuration.

The calibration plan can be delivered in about 10 minutes. The collected EPID images and the treatment planning data are sent back to the auditor for analysis.

3D combined dose distribution map of actual dose, that was generated by conversion model on software tool and treatment planning dose distribution map were compared using in-house software developed in MATLAB (The Mathworks, Natick, USA. Previously, the result was to show the mean gamma passing rate and percentage of gamma passing on various criteria. The research framework is shown in figure 1.

2.2 Calculation and Evaluation process

To calculate the delivered dose distributions the EPID images are converted to dose-in-water using a previously developed and published algorithm and clinically established patient-specific QA procedures at The Local center. TPS dose distributions compared the calculated delivered dose distributions.

The acceptance criteria was based on TG218's (15) for 2D and 3D Gamma analysis.. Tolerance levels applied for IMRT auditing will be greater than 95% pass-rate for 3%, 2 mm. And more than 90% pass rate for 2%, 2 mm. In this study, we extended the gamma index criteria from 3%/3mm to 1%/1mm with a threshold 10% for testing the auditing tool's capability.

2.3 Instruction for participates in the audit

The remote dosimetry auditing was used the EPID to dose conversion model for dosimetry audit. The virtual phantom concept introduces a web-based method to exchange data between participant and auditor. The original instructions were developed and provided to the author by P.Greer, including a configuration instruction, IMRT assessment instruction. The Trans-Tasman Radiation Oncology Group (TROG) supplied IMRT head and neck (HN) trial benchmarking plan instructions and CT data sets. Prescriptions, PTV and OAR constraints for both cases are shown in Table 1. The CT datasets of two standard virtual water-equivalent QA phantoms were provided; a VCP. The VCP is 40 cm in length and 20 cm diameter in cross section.

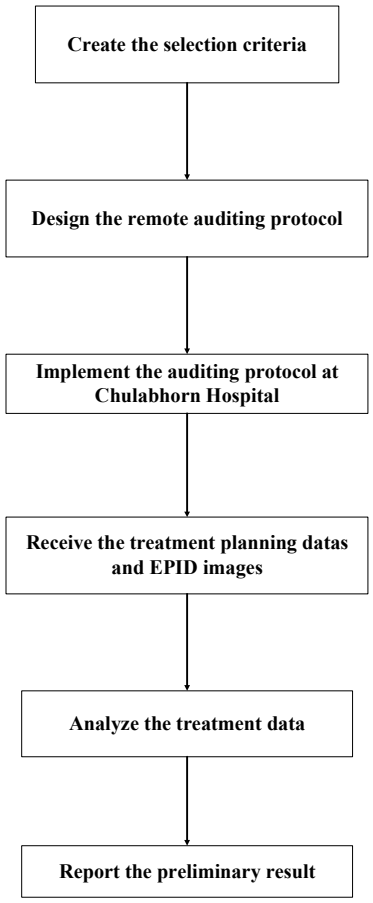

Figure 1 Research framework

3. RESULTS

Following the acceptance criteria, results from the preliminary study were 98.6-100.0% with the tolerance. While extending criteria were founded the low percentage of point passing rate and high mean gamma rate from Trilogy LINAC. The percentage difference of point dose from Varian TrueBeam auditing was 0.6%, while the percentage difference of point dose from Varian Trilogy auditing was 1.3%, respectively. Table 1 to Table 3 shows the result of dosimetry auditing on the local center, which evaluated % of point passing rate, means gamma pass and point dose at the central axis of dose distribution.

Table 1 *Result of percentage of points passing with γ ≤ 1 from preliminary result at Local center.*

	Parameters	% of points passing rate			
		3%/ 3mm	3%/ 2mm	2%/ 2mm	1%/ 1mm
A	Whole 3D volume	100.0	100.0	100.0	98.6
	2D coronal Plane	100.0	100.0	99.8	100.0
	2D sagittal Plane	100.0	100.0	100.0	98.5
B	Whole 3D volume	100.0	100.0	99.6	82.8
	2D coronal Plane	100.0	99.8	98.8	76.2
	2D sagittal Plane	100.0	100.0	98.6	81.3

(A = Varian TrueBeam, B = Varian Trilogy)

Table 2 *Result of mean gamma passing rate from preliminary result at Local center*

	Parameters	Mean gamma pass			
		3%/ 3mm	3%/ 2mm	2%/ 2mm	1%/ 1mm
A	Whole 3D volume	0.10	0.10	0.15	0.29
	2D coronal Plane	0.08	0.11	0.12	0.24
	2D sagittal Plane	0.10	0.11	0.15	0.30
B	Whole 3D volume	0.22	0.25	0.33	0.65
	2D coronal Plane	0.22	0.25	0.33	0.66
	2D sagittal Plane	0.24	0.27	0.36	0.72

(A = Varian TrueBeam, B = Varian Trilogy)

Table 3 *Result of point dose at central axis from preliminary result at Local center*

Machine	Point dose (cGy)		
	TPS dose	EPID dose	% Difference
A	95.5	96.1	0.6
B	212.0	209.3	1.3

4. DISCUSSION

From the pilot study results, there is some issue that was found by auditing the local center. With protocol design, there was a misunderstanding from the participant about the process resulting in delayed audit time.

4.1 Preliminary result from local center

For 3D Gamma analysis, this study was used only VCP to audit the patient-specific QA protocol. The pass of the percentage of point passing rate and mean gamma pass were supported the idea to implement this tool for the other medical center auditing. Otherwise, the small scale of data is less to persuade for standard audit tools. Comparing with Miri et al, They had 21 treatment centers on their study with the same tool indicating their result was more perspective than this study. Further study needs to improve the data to the large scale and discuss various factors that affected patient-specific QA protocol audits.

Comparing the result from two machines, Varian Trilogy audit result showed the low percentage of points passing rate, high mean gamma pass and percentage difference of point dose at central axis at the criteria 1%/1mm with threshold 10%. About the dosimetry parameter, Li et al concluded the dosimeter parameter of two type have a same variation range when comparing with Varian Golden Beam Data (16). The only cause of this difference in values is the age of treatment unit which the Varian Trilogy was established in 2009 as the Varian Truebeam was established in 2015.

4.2 The remote dosimetry audit protocol

The remote dosimetry auditing is a designed for patient specific QA auditing. The protocol was developed and tried out on local center specified on IMRT plan with photon energy 6 MV and performed on the Varian LINAC. We uploaded the guideline and the requirement data on cloud storage. The feedback was moderate because there was a lack of clarifying protocol and some process was increasing the participant's workload.

5. CONCLUSION

A new EPID-based remote dosimetry audit has been designed and implemented to the local center for end-

to-end test using IMRT scenario. 3D dose analysis from both machines (Varian TrueBeam and Varian Trilogy) were passed the TG218 criteria. From the feedback, the remote dosimetry auditing protocol was needed to improve efficiency for implementation in the other centers, such as communication, clarity of workflow, and assistance. This work is only a preliminary study and requires further validation to determine these tools' feasibility.

ACKNOWLEDGEMENTS

The authors are grateful for the assistance of the many physicists and therapists at Chulabhorn Hospital who planned the trial plan and measured EPID data.

REFERENCES

1. DeVita VT, Lawrence TS, Rosenberg SA. Cancer: Principles & Practice of Oncology: Primer of the Molecular Biology of Cancer: Wolters Kluwer Health; 2012.
2. Health MoP. Public Health Statistics A.D.2018 2019 [Available from: http://dmsic.moph.go.th/index/detail/7892.
3. Napier KJ, Scheerer M, Misra S. Esophageal cancer: A Review of epidemiology, pathogenesis, staging workup and treatment modalities. World J Gastrointest Oncol. 2014;6(5):112-20.
4. Warsame R, Grothey A. Treatment options for advanced pancreatic cancer: a review. Expert Review of Anticancer Therapy. 2012;12(10):1327-36.
5. Kron T, Haworth A, Williams I. Dosimetry for audit and clinical trials: challenges and requirements. Journal of Physics: Conference Series. 2013;444:012014.
6. Creutzberg CL, van Putten WLJ, Koper PCM, Lybeert MLM, Jobsen JJ, Wárlám-Rodenhuis CC, et al. Surgery and postoperative radiotherapy versus surgery alone for patients with stage-1 endometrial carcinoma: multicentre randomised trial. The Lancet. 2000;355(9213):1404-11.
7. Delaney G, Jacob S, Featherstone C, Barton M. The role of radiotherapy in cancer treatment. Cancer. 2005;104(6):1129-37.
8. Low DA, Moran JM, Dempsey JF, Dong L, Oldham M. Dosimetry tools and techniques for IMRT. Medical Physics. 2011;38(3):1313-38.
9. McDermott LN, Wendling M, Sonke J-J, van Herk M, Mijnheer BJ. Replacing Pretreatment Verification With In Vivo EPID Dosimetry for Prostate IMRT. International Journal of Radiation Oncology*Biology*Physics. 2007;67(5):1568-77.
10. Sabet M, Rowshanfarzad P, Vial P, Menk FW, Greer PB. Transit dosimetry in IMRT with an a-Si EPID in direct detection configuration. Phys Med Biol. 2012;57(15):N295-N306.
11. Ibbott GS, Molineu A, Followill DS. Independent Evaluations of IMRT through the Use of an Anthropomorphic Phantom. Technology in Cancer Research & Treatment. 2006;5(5):481-7.
12. Eaton DJ, Tyler J, Backshall A, Bernstein D, Carver A, Gasnier A, et al. An external dosimetry audit programme to credential static and rotational IMRT delivery for clinical trials quality assurance. Physica Medica. 2017;35:25-30.
13. Miri N, Legge K, Colyvas K, Lehmann J, Vial P, Moore A, et al. A remote EPID-based dosimetric TPS-planned audit of centers for clinical trials: outcomes and analysis of contributing factors. Radiation Oncology. 2018;13(1).
14. Bailey DW, Kumaraswamy L, Bakhtiari M, Malhotra HK, Podgorsak MB. EPID dosimetry for pretreatment quality assurance with two commercial systems. Journal of Applied Clinical Medical Physics. 2012;13(4):82-99.
15. Miften M, Olch A, Mihailidis D, Moran J, Pawlicki T, Molineu A, et al. Tolerance limits and methodologies for IMRT measurement-based verification QA: Recommendations of AAPM Task Group No. 218. Medical Physics. 2018;45(4):e53-e83.
16. Li R, Xue T, Song C. SU-E-T-243: Dosimeter Parameters Comparison of TrueBeam, Trilogy, and IX Machines. Medical Physics. 2012;39(6Part13):3759-.

Evaluation of Scattering Spectra from Examinee during CT Scans

Kota Tsurusawa[1], Daisuke Shimao[1,2]

1 Hokkaido University of Science Graduate School of Health Science,
2 Hokkaido University of Science

Abstract

Medical staff must be present in a CT room for various purposes, such as biopsy and patient care, during CT scans. In these cases, they are exposed to scattered X-rays from the patients. When considering the effects of occupational exposure on various tissues in terms of operational quantities, the X-ray quality is important, and effective energy has often been used hitherto. However, it is important to reveal the scattered X-ray spectra to evaluate the effect of the scattered X-rays more accurately because several energy spectra possess the same effective energy. In this study, we measured the scattered X-ray energy spectra during X-ray CT scans using an X-ray spectrometer. The result shows that several energy peaks appeared in the scattered X-ray energy spectra, which are assumed to be fluorescent X-rays from the constituent materials in the gantry and the human body phantom used in the measurement. The shape of the energy spectra did not change significantly based on the measurement position. This result suggests that the energy spectra at one measurement position can be used as a representative scattered X-ray energy spectrum in that space for future measurements. In the future, it will be possible to compare the operational quantities calculated from the effective energy with that calculated from each photon energy based on scattered X-ray energy spectra to investigate the difference.

Keywords: X-ray CT, scatter, spectrum

1. INTRODUCTION

Medical staff must often be present in a CT room during CT scans to perform fluoroscopic biopsies and assist patients. In recent years, the effects of occupational exposure on the eye lens and other parts of the body have received considerable attention[1)]. The tissue effects of occupational exposure are often assessed using operational quantities (e.g., 3 mm dose equivalent)[2)]. At this time, the scattered X-rays quality is important when performing evaluations. X-ray spectra of different shapes that possess the same effective energy have been reported. But the effective energy has been used hitherto as it enables simple measurements[3)]. Therefore, it is important to know the scattered X-ray energy spectra in order to properly evaluate the effects of occupational exposure.

The purpose of this study is to reveal the scattered X-ray spectra from objects during X-ray CT scans by measuring at various positions using an X-ray spectrometer.

2. MATERIAL AND METHODS

A diagnostic X-ray CT scanner (4row MDCT) (Alexion, Canon) was used to scan the chest level of the human body phantom [PBU-50 Xray-Man, Kyoto Kagaku] via non-helical scanning.

The scan conditions were as follows: tube voltage, 120 kV; tube current, 10 mA; scan speed, 0.75 s/rot; and beam width, 8 mm. A CdTe semiconductor detector (EMF Japan) was placed during these X-ray CT scans, and the energy spectra were measured.

The measurements were performed under an incidence count per scan of less than 10,000 to prevent the pile-up-effect of the detector, and the scans were repeated until the total count exceeded 100,000. In addition, the Cd and Te absorption edges and the escape peaks at the low energy side were corrected for the measured energy spectra by the stripping correction[4)] software. Furthermore, the effective energy was calculated from the measured energy spectra.

2.1 Reproducibility

We defined measurement points at 45° from the long axis of the scanner's bed and 270 cm away from the isocenter in the horizontal direction as position [C]. In addition, the point that moved in the gantry direction and the scanner's bed direction from position [C] was defined as position [L] and position [R]. It is noteworthy that the distance from the isocenter to the detector did not change by 270 cm.

The detector was measured from three heights: 190, 140, and 95 cm from the floor at each position [C, L, and R, respectively]. The reproducibility of the energy spectra measurements was confirmed by performing five measurements on five different days at each measurement position.

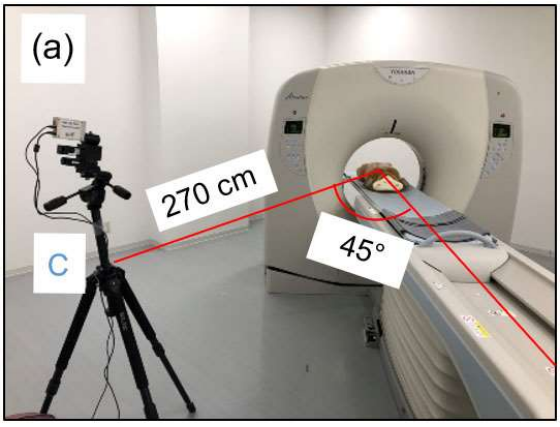

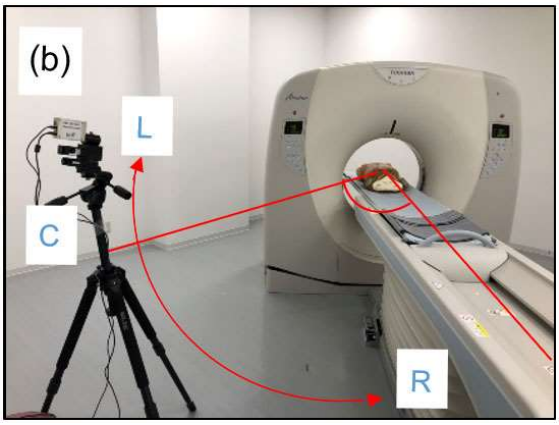

Figure 1 *(a) Define the position [C]*
(b) Define the position [L] and [R]

2.2 Spectral variation with measurement position

We compared the energy spectra at detector heights of 190, 140, and 95 cm at position [C]. A similar comparison was confirmed at positions [L][R]. Furthermore, we compared the energy spectra at positions [C][L][R] at the same detector height.

3. RESULTS

3.1 Reproducibility

The energy spectra at the measurement positions [C][L][R] are shown in Figs. 2–4. The horizontal axis of the graph represents the energy of the photon [keV], and the vertical axis represents the relative number of photons normalized by the number of incident photons. In addition, the effective energy calculated from the energy spectra at the measurement positions [C][L][R] are summarized in Tables 1 to 3.

The shape of the energy spectra at each detector height at position [C] did not change significantly. The average effective energies (standard deviation) at 190, 140, and 95 cm were 36.9 keV (0.41), 36.6 keV (0.39), and 36.8 keV (0.24), respectively.

The results for position [C] were reflected at positions [L] and [R] as well.

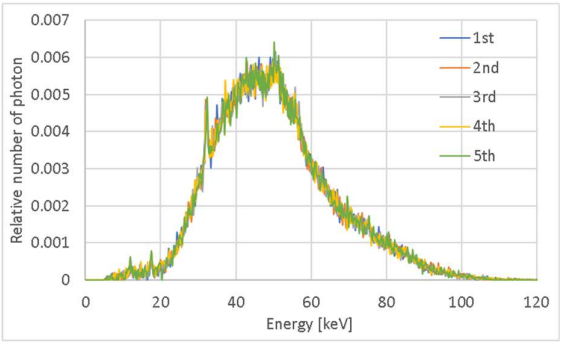

Figure 2 *Changes in energy spectra with the number of measurements: position [C]*

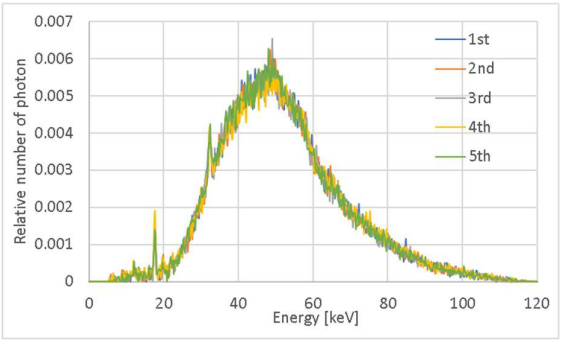

Figure 3 *Changes in energy spectra with the number of measurements: position [L]*

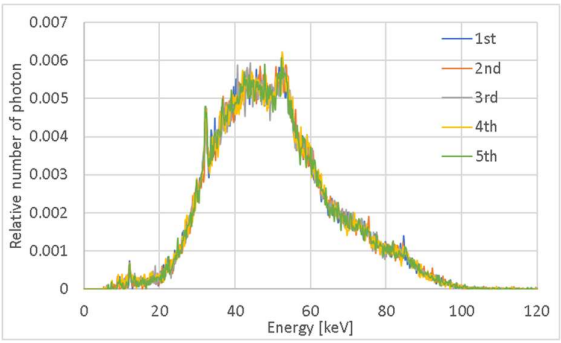

Figure 4 *Changes in energy spectra with the number of measurements: position [R]*

3.2 Spectra variation in measurement position

Fig. 5 shows the changes in the energy spectra at measurement position [C] at different heights of the detector. The shape of the energy spectra based on the detector height did not change significantly. The average effective energy at each height ranged from 36.6. to 36.9 keV, whereas the standard deviation ranged from 0.24 to 0.41.

In addition, the same results as those for position [C] were reflected at positions [L] and [R]. In addition, Fig. 6 shows a comparison of the changes in the energy spectra at a detector height of 140 cm.

Table 1 *Changes in effective energy [keV] with the number of measurements: position [C]*

	190 cm	140 cm	95 cm
1st	37.3	36.7	36.9
2nd	36.8	36.3	36.7
3rd	37	37.3	36.4
4th	36.1	36.2	37.1
5th	37.1	36.5	36.9
Average	36.9	36.6	36.8
SD	0.41	0.39	0.24

Table 2 *Changes in effective energy [keV] with the number of measurements: position [L]*

	190 cm	140 cm	95 cm
1st	37.8	37	37.4
2nd	37.4	36.7	37.1
3rd	37.5	37.4	37.5
4th	37.4	36.2	37.3
5th	38.0	37.7	37.6
Average	37.6	37.0	37.4
SD	0.24	0.53	0.17

Table 3 *Changes in effective energy [keV] with the number of measurements: position [R]*

	190 cm	140 cm	95 cm
1st	37.2	37.3	36
2nd	37.2	37.3	36.5
3rd	37.2	36.4	36.3
4th	36.5	36.2	36.2
5th	36.5	37.2	36.8
Average	36.9	36.9	36.4
SD	0.34	0.48	0.27

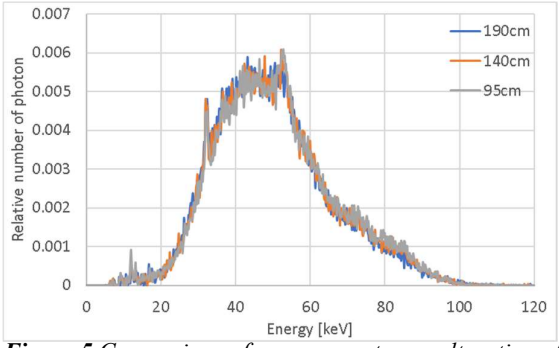

Figure 5 *Comparison of energy spectra as alteration of the detector height: position [C]*

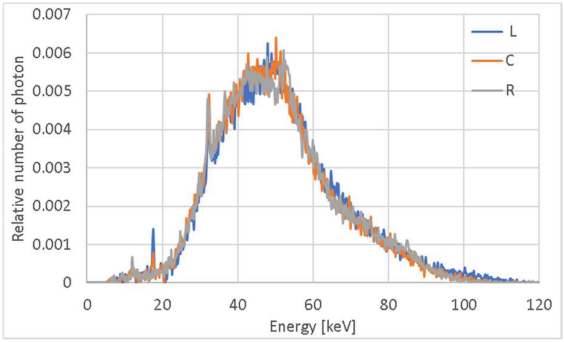

Figure 6 *Comparison of energy spectra as alteration of the measurement position: 140 cm of detector height*

Figure 7 *Energy peaks of fluorescent X-ray*

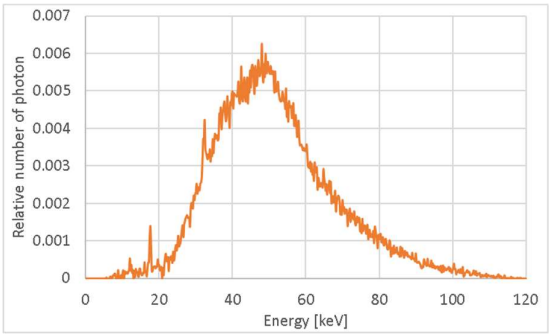

Similarly, the shape of the energy spectra based on the measurement position did not change significantly, and the maximum change in the effective energy was 0.4 keV.

4. DISCUSSION

4.1 Energy peaks

The measured energy spectra show two noticeable energy peaks of 17.5 and 32.2 keV. In an exploratory experiment study, an energy peak of 17.5 keV was observed even when the measurement was performed with nothing in the gantry. Hence, it was assumed that the energy peak at 17.5 keV was derived from the constituent materials in the gantry. Hereinafter, we assume that components with Mo exist in the gantry. Therefore, the energy peak of 17.5 keV was assumed to be a fluorescent X-ray from Mo in the gantry. Furthermore, we confirmed that the human phantom uses BaSO4 as a coating for the bone equivalent material. Hence, the energy peak at 32.2 keV was attributed to fluorescent X-rays from Ba. Therefore, fluorescent X-rays from the gantry components and other materials may also be measured from the scattered X-ray energy spectra.

To recognize the existence of fluorescent X-rays are useful for the further analysis of scattered X-ray energy spectra using another X-ray CT scanner.

4.2 Measurements of energy spectra

The measured scattered X-ray energy spectra did not exhibit any significant change in shape when the measurement position and detector height were changed. This suggests that the measurement at one position can be used as a representative scattered X-ray energy spectrum if the measurement is performed within the range of the present measurement.

In future studies, it will be possible to compare the operational quantities (e.g., 3 mm dose equivalent) calculated from the effective energy and those calculated from the photon energy based on the scattered X-ray energy spectra for the evaluation of occupational exposure to scattered X-rays in consideration of the X-ray quality.

5. CONCLUSION

Scattered X-ray energy spectra were measured during X-ray CT scans, and several noticeable energy peaks were observed in the measured spectra, which were inferred to be fluorescent X-rays from the components of the gantry and the human phantom.

The shape of the energy spectra did not change significantly when the measurement position was varied.

Therefore, it is suggested that the measurement at one position can be used as a representative scattered X-ray energy spectrum in the future if it is within the range of the present measurement.

ACKNOWLEDGEMENTS

We would like to thank Editage (www.editage.com) for English language editing.

REFERENCES

1. ICRP. Tissue Reactions and Early and Late Effects of Radiation in Normal Tissues and Organs. Publication 118 (2011).
2. ICRP. Conversion Coefficients for Radiological Protection Quantities for External Radiation Exposures. Publication 116 (2010).
3. Hideki Kato, Naoki Hayashi, Shoichi Suzuki, et al. Problems of the Effective Energy Used as a Quality Expression of Diagnostic X-ray. Journal of the Japanese Society of Radiological Technology 2011; 67(10): 1320-1326.
4. Seelentag W. W, Panzer W. Stripping of X-ray Bremsstrahlung Spectra up to 300 kVp on a Desk Type Computer. Phys, Med, Biol, 1979; 24(6): 767-780.
5. Hideki Kato. X-ray Spectrum. Journal of the Japanese Society of Radiological Technology 2010; 66(3): 238-245.

Diagnostic performance of I-131 MIBG scintigraphy in 101 patients suspected for pheochromocytoma/paraganglioma: a comparison between visual and semi-quantitative planar analyses and a hybrid SPECT/CT imaging

Pikom Sirisopausa, MD.[1], Chulaluk Komontri, PhD.[2], Jiraporn Sriprapaporn, MD.[3]

1 Diagnostic Radiology and Nuclear Medicine Unit, National Cancer Institute of Thailand,
2 Division of Research and Development, Faculty of Medicine Siriraj Hospital, Mahidol University,
3 Division of Nuclear Medicine, Department of Radiology, Faculty of Medicine Siriraj Hospital, Mahidol University

Abstract

Introduction: Pheochromocytoma and paraganglioma (PPGL) are rare. The diagnosis is based on clinical context, biochemical testing for catecholamine excess, and imaging localization. I-131 MIBG imaging provides high specificity for these diseases, however, only a few studies had compared different techniques for image interpretation.

Purpose: To compare the diagnostic performance of planar I-131 MIBG imaging using visual and semi-quantitative techniques and visual interpretation of SPECT/CT imaging in the diagnosis of PPGL.

Methods: This was a cross-sectional retrospective review of I-131 MIBG scintigraphy performed in 101 consecutive patients, being suspected for PPGL. I-131 MIBG imaging was performed 24 hours and 48 hours after intravenous administration of 37 MBq I-131 MIBG. All I-131 MIBG images were blindly interpreted by two nuclear medicine physicians. The planar images were read by visual analysis and semi-quantitative scoring (score 0-3, relative to the uptake in the liver). I-131 MIBG SPECT/CT images were read as positive or negative. Pathological diagnosis was used as the gold standard, otherwise clinical follow-up and a contrast CT scan were incorporated in the cases showing negative imaging results.

Results: The study included thirty-eight patients with pheochromocytoma/metastatic pheochromocytoma and eight patients with paraganglioma. The prevalence of PPGL was 45.5%. Out of 214 lesions, 69 were pathologically proved. The sensitivity, specificity, and accuracy of planar imaging using visual analysis were 92.59%, 97.5%, and 96.26%, respectively. Those interpreted using semi-quantitative method were 92.59%, 96.88%, and 95.79%, respectively. Those for I-131 MIBG SPECT/CT imaging were 90.48%, 98.26%, and 96.18%, respectively. Each technique showed similar diagnostic performance.

Conclusion: This study revealed excellent diagnostic performance of I-131 MIBG scan for the diagnosis of PPGL, both interpreted by visual analysis and semi-quantitative technique. SPECT/CT imaging provided additional benefit in a few cases with visualized physiologic adrenal gland uptake.

Keywords: I-131 MIBG; Pheochromocytoma; Paraganglioma; Semiquantitative; SPECT/CT

Address correspondence to: J. Sriprapaporn,
E-mail: jiraporn.spp@mahidol.ac.th

1. INTRODUCTION

Pheochromocytoma and paraganglioma (PPGL) are rare. The incidence of pheochomocytoma (PHEO) in coronial autopsies was around 0.05% in the general population (1). The classic symptoms of PHEO include headache, palpitations, and diaphoresis. The diagnosis is based on documentation of catecholamine excess and imaging localization of the tumor. Several imaging modalities have been used, such as ultrasound, CT scan, MRI, radioiodinated metaiodobenzylguanidine (I-123 or I-131 MIBG) imaging, somatostatin receptor imaging, and PET/CT scan. Contrast CT scan of the adrenal glands is primarily performed when the biochemical tests are positive. Radiolabeled MIBG scan has high specificity for the diagnosis of PPGL and to localize metastatic lesions (2). Although, PET/CT scans become more and more popular in this field due to better contrast and spatial resolution, radiolabeled MIBG imaging has been routinely used because of lower cost and wider availability.

The MIBG can be labeled with either I-131 or I-123. While I-123 MIBG is preferred for imaging due to favorable dosimetry and better image resolution, it's not available in Thailand. There had been a few MIBG imaging studies dealing with comparison between interpretation techniques and the reader's experience (3, 4). This study is to compare the diagnostic performance between visual and semi-quantitative planar methods and SPECT/CT imaging to diagnose PPGL.

2. MATERIAL AND METHODS

2.1 Patient selection

This study was a retrospective cross-sectional analysis of 120 consecutive patients, who underwent the first I-131 MIBG scan at Siriraj hospital between January 2013 and July 2018. The inclusion criteria involved the patients with suspected PPGL by clinical features, or biochemical investigation, or radiographic imaging. Patients who were less than 18-year-old, or had incomplete I-131 MIBG imaging data, or lost

follow-up that the final diagnosis could not be made were excluded from the study.

Pathological diagnosis from the biopsy or surgical specimens was used as the gold standard. In the case that I-131 MIBG scan was negative and the patients were not operated, clinical follow-up and an abdominal CT scan were used to confirm the negative results. A total of 101 patients or 214 adrenal/extraadrenal lesions were finally included for the analysis (Figure 1).

This study was ethically approved by institutional review board, faculty of medicine Siriraj hospital.

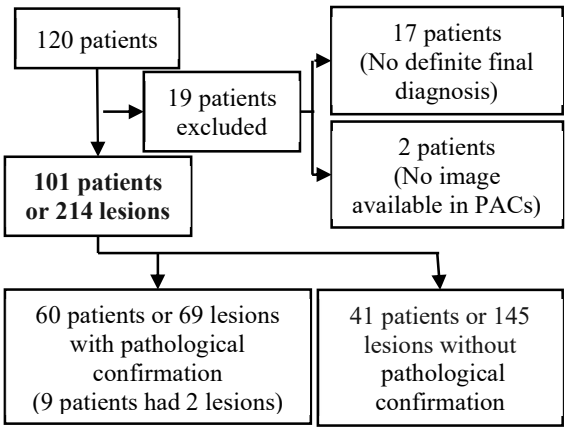

Figure 1 *Flow chart of patient selection*

2.2 Imaging procedures

Medications that could interfere with I-131 MIBG uptake were discontinued (5). Thyroid blockade of free iodide was introduced 24 hours before the radiotracer injection and had been extended for seven days by prescribing oral administration of 5% Lugol's solution for two drops three times a day.

Whole-body imaging from vertex to mid-thigh and static imaging in suspected areas were performed 24 and 48 hours after intravenous administration of 37 MBq (1 mCi) I-131 MIBG. The SPECT/CT scan was obtained as necessary. The imaging procedure was acquired using the Discovery NM/CT 670 Pro or Discovery NM/CT 670 dual-head gamma camera with SPECT/CT capability (GE Healthcare, IL, USA) equipped with a high-energy, parallel hole collimator, an energy peak at 364 keV ± 10%. The whole-body imaging was performed in a continuous acquisition mode with detector speed of 8 cm per minute and 256 × 1024 matrix, while static imaging was acquired with 256 × 256 matrix for 10 minutes. SPECT/CT imaging was performed by step and shoot mode with 30 steps for each detector, at 6 degrees and 60 seconds/step with 64 × 64 matrix. The CT portion was acquired using tube voltage of 100 kV with automatic exposure control and slice thickness of 3.75 millimetre.

2.3 Imaging interpretation

I-131 MIBG planar and SPECT/CT images in the picture archiving and communication system were separately interpreted blindly by two nuclear medicine physicians. The planar images were read by visual analysis as positive or negative and semi-quantitative analysis as scoring (0-3; score 0 = no uptake, score 1= mild uptake, less than the liver, score 2 = uptake equal to the liver, score 3 = uptake more than the liver). Each technique was separately interpreted at least 4-week apart. I-131 MIBG SPECT/CT images were also interpreted as positive or negative. A consensus diagnosis was achieved when the interpretations from the two readers are distinct. The pathological report, if available, was used as the gold standard.

2.4 Statistical analysis

Diagnostic performances such as sensitivity, specificity, accuracy, predictive values, and likelihood ratios were analyzed by using SPSS statistics 21.0 (IBM Corp.).

In addition, agreement of the two readers was obtained with the quadratic weighted kappa coefficient by using MedCalc statistical software.

3. RESULTS

This study included 48 (47.5%) males and 53 (52.5%) females with mean age of 50 years (range, 18-82 years). The most common sign and symptom at presentation were hypertension (63 patients, 62.38%), and palpitation (26 patients, 25.74%). The prevalence of PPGL in this study was 45.5%, including 34 PHEOs, 4 metastatic PHEOs, and 8 paragangliomas. The patient's characteristics and baseline parameters were summarized in Table 1.

Table 1 *Characteristics of the 101 patients suspected for PPGL*

Variables	Numbers
Total patients	101
Total lesions (right/ left adrenal/ extra-adrenal)	214 (98/98/18)
Age	
- Range (years)	18-82 years
- Mean ± SD	49.89 ±17
Sex	
- Men	48 (47.52%)
- Women	53 (52.48%)
Symptomatic* (N = 79)	79 (78.22%)
- Hypertension	63 (62.38%)
- Palpitation	26 (25.74%)
- Abdominal discomfort	16 (15.84%)
- Headache	14 (13.86%)
- Diaphoresis	8 (7.92%)
- Fatigue	4 (3.96%)
- Weight loss	5 (4.95%)
Asymptomatic (N = 22)	22 (21.78%)
- Adrenal incidentaloma	13 (12.87%)
- Genetic-related	9 (8.91%)

** Some patients had more than one sign and symptoms*

All patients (214 lesions) underwent planar imaging and 73 patients (157 lesions) had SPECT/CT imaging performed. Sixty patients had 69 pathologically proven lesions including 53 adrenal and 16 extra-adrenal lesions. The remaining 41 patients had no surgery because of a normal CT scan and had been clinically followed up, with a duration ranging from 0 to 2,233 days, average 780 days.

Concordance between 2 readers for each technique was very good. The quadratic weighted kappa for planar visual interpretation was 1.000 for both 24-hour and 48-hour images and those for planar semi-quantitative interpretations are 0.9620 and 0.9723 respectively.

Concordance between interpretations of 24-hour and 48-hour planar images was also very good. The quadratic weighted kappa for visual interpretation was 1.000 and that for semi-quantitative interpretation was 0.9808. So, we used 24-hour planar images for analyses of the diagnostic performance.

3.1 Planar images: visual analysis

The diagnostic accuracies of visual interpretation of planar images were listed in table 2. We found 4 false-positive results (2 physiologic uptake and 2 neuroendocrine tumors) and 4 false-negative results (2 lesions less than 1 cm, 1 small intra-abdominal lymph node metastasis, and a 5.3x4.4x4.3 cm adrenal tumor).

3.2 Planar images: semi-quantitative analysis

The diagnostic performance by using a semi-quantitative method for each score cut-point was presented in table 2. The highest accuracy was on score cut-point 2, that the sensitivity, specificity, and accuracy were 92.59% (95% CI: 82.11-97.94), 96.88% (95% CI: 92.86-98.98), 95.79% (95% CI: 92.17-98.06), respectively.

3.3 SPECT/CT images analysis

The SPECT/CT imaging was obtained in 73 patients and 157 lesions were detected, resulting in the diagnostic performance as shown in table 2.

4. DISCUSSION

Only I-131 labeled MIBG is available in Thailand. I-131 MIBG is primarily used in the localization of PPGL due to excellent sensitivity and specificity. We performed a retrospective cross-sectional study of 101 patients suspected for PPGL on clinical, or biochemical, or radiological basis.

The prevalence of PPGL in this study was 45.5%, nearly close to the previous studies, which reported 39% to 44% (4, 6) and The concordant interpretations between two different experienced nuclear medicine physicians in both visual and semi-quantitative techniques were very good, similar to those observed with I-131 and I-123 MIBG imaging studies (3, 6). It's concluded that the interpretation of radiolabeled MIBG imaging has very high precision.

The interpretation of 24-hour and 48-hour I-131 MIBG planar images shows no significant differences in both visual and semi-quantitative analyses. Only 9 lesions had different scoring between 24- and 48-hour images, which only single lesion changed the meaning (from score 1 to score 2). This could be explained by higher image contrast at 48 hours than 24 hours. Thus, I-131 MIBG scintigraphy could be generally obtained at 24 or 48 hours after the radiotracer administration, except in cases of equivocal findings that the images should be obtained at both 24 hours and 48 hours or even delayed further.

The sensitivity and specificity of I-131 MIBG planar imaging for the diagnosis of PPGL in this study are as high as 92.59% and 97.5%, respectively, which are slightly higher than those observed by Berglund, et al. (sensitivity 88% and specificity 89%) (6). Our data have somewhat lower sensitivity as compared to the sensitivity of 94% in the meta-analysis of I-123 MIBG scintigraphy, which is likely due to lower image quality but slightly higher specificity (97.5% vs. 92%) (7).

As proposed by Cecchin, et al. (3) that the scoring interpretation could enhance the diagnostic accuracy of I-123 MIBG scintigraphy, using uptake higher than the liver, score 3, as positive findings. In our study with

Table 2 *Comparative diagnostic performance of each technique interpretation and divided scoring cut-point for semi-quantitative technique*

		Sensitivity % (95% CI)	Specificity % (95% CI)	Accuracy % (95% CI)	PPV % (95% CI)	NPV % (95% CI)	Positive likelihood ratio (95% CI)	Negative likelihood ratio (95% CI)
Planar (visual analysis)		92.59 (82.11-97.94)	97.50 (93.72-99.31)	96.26 (92.77-98.37)	92.59 (85.57-97.06)	97.50 (93.82-99.01)	37.04 (14.03-97.76)	0.08 (0.03-0.20)
Planar (semi-quantitative) : Score cut-point	**1**	94.44 (84.61-98.84)	93.75 (88.81-96.96)	93.93 (89.84-96.73)	83.61 (73.61-90.32)	98.04 (94.33-99.34)	15.11 (8.26-27.63)	0.06 (0.02-0.18)
	2	92.59 (82.11-97.94)	96.88 (92.86-98.98)	95.79 (92.17-98.06)	90.91 (80-79-95.96)	97.48 (93.78-99.01)	29.63 (12.46-70.44)	0.08 (0.03-0.20)
	3	79.63 (66.47-89.37)	98.75 (95.56-99.85)	93.93 (89.84-96.73)	95.56 (84.35-98.85)	93.49 (89.45-96.05)	63.70 (15.97-254.19)	0.21 (0.12-0.35)
SPECT-CT		90.48 (77.38-97.34)	98.26 (93.86-99.79)	96.18 (91.87-98.58)	95.00 (82.74-98.69)	96.58 (91.75-98.63)	52.02 (13.12-206.24)	0.10 (0.04-0.25)

I-131 MIBG scoring, we found that score 2 or uptake equal to the liver provided the highest accuracy about 96% (95% CI: 92-98). Our cut-point has slight difference and may be related to delayed I-131 MIBG scanning resulting higher target-to-background ratio. Unlike, I-123 MIBG imaging, physiologic adrenal visualization with I-131 MIBG has less problematic due to lower incidence and usually very faint uptake.

In this study, physiologic adrenal uptake was only 4% at 24 hours and 5.4% at 48 hours, which are similar to the figures of 2% and 5.4% respectively reported by Nakajo and coworkers (8). Furthermore, Lynn, et al. reported that physiologic adrenal uptake was as high as 75% for I-123 MIBG and only 12.5% for I-131 MIBG, which is still higher than we found in this study (9).

The diagnostic performance of planar visual and semi-quantitative analysis, using cut-point score 2 is quite similar. Thus, to make a diagnosis of PPGL, visual interpretation of I-131 MIBG imaging is appropriate and more simply applicable.

Regarding I-131 MIBG SPECT/CT scan, we have reported here the sensitivity of 90.48% and the specificity of 98.26%, which are very close to those reported by Sharma and colleagues (sensitivity 90% and specificity 100%) (4).

As compared with the planar imaging, SPECT/CT images reveal slightly lower sensitivity (SPECT/CT 90.48% vs. planar 92.59%) due to presence of one false-negative result of image misregistration, but similar high specificity (SPECT/CT 98.26% vs. planar 97.50 %).

The main advantage of SPECT/CT is to clarify pathologic from physiologic uptake in the adrenal glands.

The limitations of this research include a retrospective study that limits some imaging or follow-up data, conducted in a single institution and a small number of patients having scores 1 and 2.

5. CONCLUSION

This research study shows excellent concordance between 2 readers and high diagnostic performance of the I-131 MIBG scan for the diagnosis of PPGL. Interpretation of planar images by a simple visual analysis is comparable to a semi-quantitative method, using score 2 or above as a cut-point.

SPECT/CT provides more benefit in the case of presence of physiologic adrenal gland uptake.

ACKNOWLEDGEMENTS

We would like to thank Assistant Professor Thonnapong Thongpraparn for his academic advice.

REFERENCES

1. McNeil AR, Blok BH, Koelmeyer TD, Burke MP, Hilton JM. Phaeochromocytomas discovered during coronial autopsies in Sydney, Melbourne and Auckland. Aust N Z J Med. 2000;30(6):648-52.
2. Shapiro B, Copp JE, Sisson JC, Eyre PL, Wallis J, Beierwaltes WH. Iodine-131 metaiodobenzylguanidine for the locating of suspected pheochromocytoma: experience in 400 cases. J Nucl Med. 1985;26(6):576-85.
3. Cecchin D, Lumachi F, Marzola MC, Opocher G, Scaroni C, Zucchetta P, et al. A meta-iodobenzylguanidine scintigraphic scoring system increases accuracy in the diagnostic management of pheochromocytoma. Endocr Relat Cancer. 2006;13(2):525-33.
4. Sharma P, Dhull VS, Jeph S, Reddy RM, Singh H, Naswa N, et al. Can hybrid SPECT-CT overcome the limitations associated with poor imaging properties of 131I-MIBG?: Comparison with planar scintigraphy and SPECT in pheochromocytoma. Clin Nucl Med. 2013;38(9):e346-53.
5. Bombardieri E, Giammarile F, Aktolun C, Baum RP, Bischof Delaloye A, Maffioli L, et al. 131I/123I-metaiodobenzylguanidine (mIBG) scintigraphy: procedure guidelines for tumour imaging. Eur J Nucl Med Mol Imaging. 2010;37(12):2436-46.
6. Berglund AS, Hulthen UL, Manhem P, Thorsson O, Wollmer P, Tornquist C. Metaiodobenzylguanidine (MIBG) scintigraphy and computed tomography (CT) in clinical practice. Primary and secondary evaluation for localization of phaeochromocytomas. J Intern Med. 2001;249(3):247-51.
7. Jacobson AF, Deng H, Lombard J, Lessig HJ, Black RR. 123I-meta-iodobenzylguanidine scintigraphy for the detection of neuroblastoma and pheochromocytoma: results of a meta-analysis. J Clin Endocrinol Metab. 2010;95(6):2596-606.
8. Nakajo M, Shapiro B, Copp J, Kalff V, Gross MD, Sisson JC, et al. The normal and abnormal distribution of the adrenomedullary imaging agent m-[I-131]iodobenzylguanidine (I-131 MIBG) in man: evaluation by scintigraphy. J Nucl Med. 1983;24(8):672-82.
9. Lynn MD, Shapiro B, Sisson JC, Swanson DP, Mangner TJ, Wieland DM, et al. Portrayal of pheochromocytoma and normal human adrenal medulla by m-[123I]iodobenzylguanidine: concise communication. J Nucl Med. 1984;25(4):436-40.

Paper ID 122

Detection of multi-leaf collimator errors in a small-field volumetric modulated arc therapy plan using portal dosimetry

Yuichi Saito[1], Suguru Kimura[1], Hiroaki Kobayashi[1], Kohei Shibayama[1], Takahisa Suzuki[1], Koudai Hoshino[1], Yuki Murayama[1], Kento Miyata[1], Katsumi Shima[1]

1 National Hospital Organization Hokkaido Cancer Center, Sapporo, Hokkaido, 003-0804, Japan,

Abstract

In volumetric modulated arc therapy (VMAT), multi-leaf collimator (MLC) errors cause significant dose discrepancy, especially in small fields. Therefore, patient-specific quality assurance (QA) using any metrics should be performed to detect MLC errors in advance. This study was conducted to investigate the effect of MLC errors on dose distribution in small-field VMAT plans and to determine the suitable criteria for detecting MLC errors using the gamma index in portal dosimetry (PD) for patient-specific QA. A small-field VMAT plan for a sphere considered as a PTV of 1-cm diameter in the phantom was created as an original plan. The original plan was modified according to the following three error types: (1) both MLC banks are open, (2) both MLC banks are closed, and (3) both MLC banks are shifted. The sizes of MLC errors for the original plan were 0.2 and 0.5 mm, respectively. The predicted fluence of the original plan was calculated in a treatment planning system, and the fluence of the original plan and error plans were measured by Digital Megavolt Imager (DMI) detector. The consistency of the predicted and measured fluence distribution was evaluated using the gamma index of 2%/0.5 and 1%/1 mm. The minimum MLC errors that failed the >97% criteria with the gamma index of 2%/0.5 mm were (1) 0.2 mm, (2) 0.2 mm, and (3) 0.5 mm, corresponding to the error types. In contrast, no MLC errors were detected with the gamma index of 1%/1 mm because all error plans passed the >97% criteria. Small-field VMAT plans for a sphere of 1-cm diameter are required to pass the >97% criteria in the gamma index of 2%/0.5 mm, which was also determined as the criteria for detecting MLC errors in patient-specific QA with PD.

Keywords: Quality assurance, Portal dosimetry, Gamma-index

1. INTRODUCTION

In volumetric modulated arc therapy (VMAT), multi-leaf collimator (MLC) errors cause significant dose discrepancy, especially in small fields (such as metastatic brain tumor). Therefore, to detect MLC errors in advance, patient-specific quality assurance (QA) using any metric should be performed. This study investigates the effect of MLC errors on dose distribution in small-field VMAT plans, and it also determines the suitable criteria for detecting MLC errors using the gamma index in portal dosimetry (PD) for patient-specific QA.

2. MATERIAL AND METHODS

For a sphere considered as a planning target volume (PTV), a small-field VMAT plan of 10-mm diameter in the phantom was developed as an original plan using a single arc. The original plan was modified based on the following three error types: (1) both MLC banks are open, (2) both MLC banks are closed, and (3) both MLC banks are shifted (Figure 1). The sizes of MLC errors for the original plan were 0.2 mm and 0.5 mm. Additionally, the error plan was recalculated using Eclipse treatment planning system (TPS) and compared with dose-volume histogram (DVH), D98, D95, and D2 of PTV of the original plan. The predicted fluence of the original plan was calculated using a TPS, and the fluence of the original and error plans was measured using a Digital Megavolt Imager (DMI) detector. The Varian DMI detector was pixel size (0.336 mm). The consistency of the predicted and measured fluence distribution was evaluated using the gamma index of 2%/0.5 and 1%/1 mm, respectively.

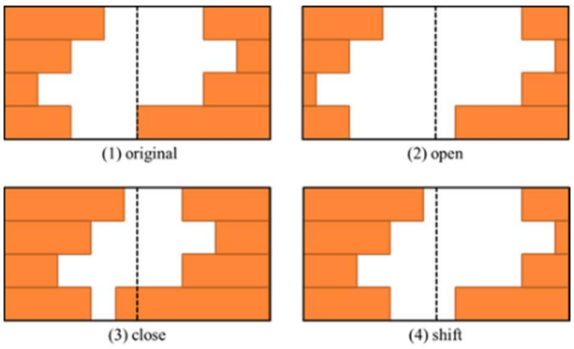

Figure 1 *The MLC error patterns: (1) original, (2) open, (3) close, and (4) shift.*

3. RESULTS

For D98 and D95 of PTV, the errors of 0.2 mm and 0.5 mm were all greater than ±3% compared to the original plan (Figure2 and Table 1). The impact of 0.2 mm shift was within 3% but 0.5 mm greater than 3% for D95 and D98 of PTV. In addition, the impact of D2 of PTV was not as much as that of D98 and D95.

The minimum MLC errors that failed the more than 97% criteria using the gamma index of 2%/0.5 mm were (1) 0.2 mm, (2) 0.2 mm, and (3) 0.5 mm, corresponding to the error types (Table 2). Moreover, the 1 mm/1% criteria showed a pass rate of more than 97% for most error plans. Using the gamma index criteria of 2%/0.5

mm, PD can detect almost all MLC errors (Figure 3 and Table 3).

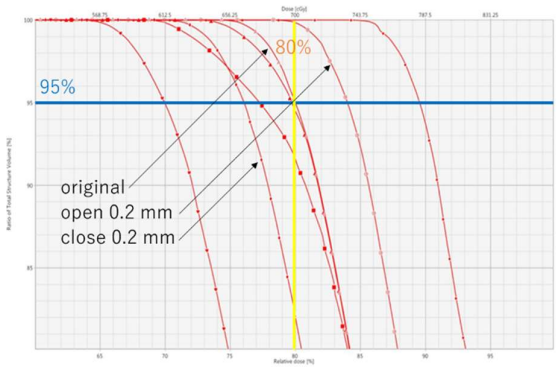

Figure 2 *DVH of the original (A) and 0.2 mm and 0.5 mm open (☼ and ○), 0.2 mm and 0.5 mm close (◊ and ♡), and 0.2 mm and 0.5 mm shift plans (△ and □). The blue and yellow lines represent 95% and 80% of the PTV volume and prescription dose, respectively.*

Table 1 *Comparison of the original and error plans for PTV.*

	D98	D95	D2
original	0.00%	0.00%	0.00%
close 0.2mm	-5.33%	-4.92%	-2.36%
close 0.5mm	-13.32%	-12.56%	-5.98%
open 0.2mm	5.12%	5.00%	2.12%
open 0.5mm	12.36%	11.93%	4.94%
shift 0.2mm	-1.23%	-0.35%	-0.10%
shift 0.5mm	-5.98%	-3.43%	-0.18%

Figure 3 *Passing rates using the gamma index 2%/0.5 mm criteria for MLC error types.*

Table 2 *Comparison of the MLC error type QA results using the gamma index 2%/0.5 mm, and 1%/1 mm criteria.*

Passing rates	portal dosimetry	
(in %) for	2%/0.5mm	1%/1mm
original	98.4%	100.0%
close 0.2mm	94.7%	99.8%
close 0.5mm	57.0%	97.6%
open 0.2mm	93.6%	99.6%
open 0.5mm	41.0%	89.0%
shift 0.2mm	98.5%	100.0%
shift 0.5mm	90.5%	100.0%

4. DISCUSSION

In head and neck VMAT, Heilemann et al. (1) reported that open and closed 1 mm MLC errors gave a 2% difference in the mean PTV dose. Besides, for the prostate, the same MLC error showed a dose difference of more than 4%. The impact of MLC errors on the PTV has a significant impact on its size. For 10 mm spheres, MLC error of 0.2 mm in VMAT can cause a dose difference of more than 3% with respect to PTV. To detect this error, a DTA of 0.5 mm was applied in the gamma analysis. The high resolution of the PD may have made it possible to detect the MLC error in small-field VMAT.

5. CONCLUSION

For a sphere of 10-mm diameter, small-field VMAT plans were required to pass the more than 97% criteria in the gamma index of 2%/0.5 mm, which was also determined as the criteria for detecting MLC errors in patient-specific QA with PD. Furthermore, it was necessary to determine the appropriate gamma analysis criteria for PTV size.

REFERENCES

1. Heilemann G: On the sensitivity of common gamma-index evaluation methods to MLC misalignments in Rapidarc quality assurance, Med Phys, 2013; 40: 031702.

Tuning effective spot size parameter in Acuros XB algorithm for Edge™ radiosurgery machine

Warinthorn Rattanaareeyakorn[1], Suphalak Khachonkham[1,2], Pimolpun Changkaew[2], Panun Sritubtim[1], Surendra Dhungana[1], Nauljun Stansook[1,2], Pornpan Yongvithisatid[3], Puangpen Tangboonduangjit[1,2]

1 Master of Science Program in Medical Physics, Department of Diagnostic and Therapeutic Radiology, Faculty of Medicine Ramathibodi Hospital, Mahidol University, Thailand
2 Division of Radiation Oncology, Department of Diagnostic and Therapeutic Radiology, Faculty of Medicine Ramathibodi Hospital, Mahidol University, Thailand
3 Radiosurgery center, Faculty of Medicine Ramathibodi Hospital, Mahidol University, Thailand

Abstract

The effective spot size parameter (ESS) can affect a beam profile shaping and output factor in a small beam. The main purpose of the study was tuning an ESS for Acuros XB by matching the beam profile of an MLC field. The selecting ESS was evaluated by field output factor compared with the measured field output factor by following the TRS-483 CoP. The result showed the excellent agreement of beam profile matching in selecting ESS of 0.75-1 mm and 0-0.25 mm in X and Y directions, respectively. The field output factor for selecting ESS showed good agreement in the 0.5 cm MLC delimited field (within 3%), while the default demonstrates poor agreement (6.71%). But the larger field is independent of ESS. The selecting ESS can improve the accuracy of field output factor calculation in the Acuros XB algorithm for a radiosurgical beam.

Keywords: effective spot size parameter (ESS), Acuros XB algorithm (AXB), field output factor, small MLC field

1. INTRODUCTION

The stereotactic radiosurgery (SRS) has become a major treatment for a small lesion disease where most of the SRS field used a small MLC field delimited. Nevertheless, the accuracy of dose calculation to the target depends on the dose calculation algorithm which can be challenged in the case of inhomogeneity tissue and especially in small target volumes. The Acuros XB (AXB) algorithm has been introduced in the Varian eclipse treatment planning system (TPS) for photon beam calculation. AXB is based on Linear Boltzmann Transport Equation (LBTE) solver. Several studies showed that the AXB can accurately predict doses on heterogeneity situations comparable to the Monte Carlo method [1,2] as well as improve in dose accuracy under the lack of CPE in small field conditions [2].

However, the dose calculation algorithm is not a complete program, the beam data configuration is needed to be performed. Varian published the white paper in 2013 [3]. This paper stated that the effective spot size parameter (ESS) could cause the inaccuracy of the small field dosimetry calculation. The fine-tuning ESS by beam profile matching using a high-resolution detector such as film is recommended. In 2016, Fogliata et al. discovered that the ESS could affect output factors, especially in small field sizes that are less than 1 cm. [4]. Moreover, in 2017 Gardner studied the effect of ESS in a small intracranial target VMAT plan and found that improper selection of the ESS can affect the isodose distribution in the planned dose compared to the measured dose using film [5]. Therefore, the selection of proper ESS should be investigated in the process of model configuration of AXB algorithm for small field dosimetry. Since recently high-resolution detectors e.g. scintillation, microDiamond have been also used to perform dose measurement in small field dosimetry although, previous studies recommended to use film for tuning ESS. However, the film processing is quite arduous, the microDiamond was used in this study.

The purpose of this study was to tune an effective spot size parameter in the Acuros XB using the microDiamond detector for radiosurgical beam defined by MLCs for Edge™ machine.

2. MATERIAL AND METHODS

The method was divided into three phases i.e., modelling phase, experiment phase, and selecting and testing phase

2.1 Modelling phase

The ESS can be varied in the beam configuration module in the Eclipse treatment planning system. For the Acuros XB algorithm, the default ESS is 1 mm in both directions (X or crossline, Y or inline). In this study, the ESS was varied separately in X and Y direction from 0 to 1.5 mm with a 0.25 mm increment.

Next, each ESS was used to plan the single beam of MLC square field sizes of 0.5, 1, 2 cm^2 with 3×3 cm^2 Jaw size in the virtual water phantom at the depth of 10 cm, SAD technique. Beam profile (0.1 mm dose grid size) in both direction (crossline and inline) and field output factor normalized at 10×10 cm^2 Jaw field were calculated

2.2 Experiment phase

The blue phantom (IBA dosimetry) tank scan with the PTW 60019 microDiamond detector (PTW Freiburg GmbH) was used to collect the beam profile in the same fields as collected in the treatment planning system that described in the previous phase. This measurement was

performed in 0.1 mm increment in the step by step mode, 10 mm/s in scan speed. The detector was set at depth of 10 cm and SSD 90 cm from the Edge™ linac (Varian medical system).

The 6 MV with the flattening filter (WFF) was used. The field output factor for the MLC field was measured with the microDiamond detector and the PTW 60018 SRS diode (PTW Freiburg GmbH) after the beam profile was scanned for centering correction according to TRS-483 CoP [6]. The field output correction factor was also applied. The reading for each detector was repeated 3 times and performed twice settings to reduce the uncertainty (note: the field width for finding a correction factor was only derived from the microDiamond detector for both detectors measurement). After that, the corrected field output factor was averaged from both detectors, and the standard error of the mean (SE) was also calculated for each field size. ($SE = \frac{SD}{\sqrt{n}}$) where SD is the standard deviation.

1.3 Selecting and testing phase

The ESS was selected by the beam profile matching and penumbra difference evaluation. The beam profile agreement was evaluated by qualitative beam profile analysis in both directions between the planned profile and measured profile of MLC field. Then, the penumbra difference in both directions were evaluated.

Finally, the beam model performance from the selecting ESS beam model was tested by comparing the calculated MLC field output factor with the measured field output factor.

3. RESULTS

Table 1. *The penumbra difference between calculated from each ESS and measured data for crossline and inline of 0.5 MLC square field.*

ESS (X, Y) mm	Penumbra difference (mm)	
	Crossline (X)	Inline (Y)
0,0	0.72	0.07
0.75,0	0.25	0.08
1.5,0	0.53	0.07
1,1	0.10	0.51
1,0	0.07	0.08
1,0.25	0.10	0.03
0.75,0.75	0.29	0.39
1.25,1.25	0.32	0.77

3.1 Beam profile matching

The crossline 0.5 cm MLC square field beam profile between measured and planned shows in Figure 1A, and the inline profile shows in Figure 1B. The red dot arrow shows the shoulder of the high dose region and the black arrow shows the penumbra region. And also, Table 1 show the penumbra difference for each ESS in 0.5 cm MLC square field. By visual inspection from Figure 1 and the penumbra difference from Table 1, it was found that in the crossline, the 0.75-1 mm ESS shows good agreement to the measured profile while in the inline, the excellent agreement shows in 0-0.25 mm ESS calculated profile. The same agreement was obtained for 1 cm and 2 cm MLC square field as well although the results were not displayed

3.2 Comparison of field output factor

Table 2. *The measured MLC field output factor. The 2 standard error of the mean was also calculated.*

MLC field (mm)	Average field output factor
0.5	0.559±0.0002
1	0.709±0.01
2	0.802±0.008

Table 2 shows the average field output factor from both detectors and ±2SE.

Table 3. *The calculated 0.5 cm MLC field output factor (FOF) for each ESS and the %difference between Calculated and Measured FOF.*

ESS (X, Y) mm	0.5 cm MLC field	
	Calculated FOF	%difference from the measured
0,0	0.566	1.10
0.75,0	0.559	0.05
1.5,0	0.514	8.09
1,1	0.522	6.71
1,0	0.551	1.43
1,0.25	0.548	2.12
0.75,0.75	0.539	3.73
1.25,1.25	0.472	15.68

The 0.75,0 mm (X and Y direction) ESS shows an excellent agreement between calculated and measured field output factors, while default ESS (1,1) demonstrates poor deal. This result shows the effect of ESS on the field output factor in a very small field. However, for the larger field as shown in Table 4, the field output factors are independent of ESS.

Table 4. *The calculated (Cal) 1 cm and 2 cm MLC field output factor (FOF) for each ESS and the %difference between Calculated and Measured FOF (%diff).*

ESS (X, Y) mm	1 cm MLC field		2 cm MLC field	
	Cal. FOF.	%diff	Cal. FOF.	%diff
0,0	0.719	1.31	0.807	0.70
0.75,0	0.720	1.5	0.807	0.70
1,1	0.716	0.95	0.806	0.54
1.5,0	0.715	0.78	0.806	0.54

4. DISCUSSION

The Varian white paper [3] suggested that fine-tuning the ESS is necessary for individual machines and recommended using a high-resolution detector such as film for measurement. But the film is complicated for processing. Moreover, the reviewed studies illustrated that the tuning of ESS could affect small MLC field dosimetry. So, the purpose of this study was tuning an effective spot size parameter (ESS) in the Acuros XB

algorithm using the microDiamond detector by comparing the beam profile and field output factor.

The small field stereotactic radiosurgery has become popular techniques, but most of the planning has been planned in VMAT or IMRT technique that uses the MLC field. So, that is why we selected to tuning the ESS as an MLC spot size.

Many studies show that the dosimetric characteristic of the microDiamond is suitable for measuring the beam profile, especially the penumbra region in very small field because of the less dose rate dependence, good water equivalent, and high spatial resolution [7,8]. And previous studies (1,9) used the natural diamond and microDiamond to measure the small field dosimetry as well.

The ESS was varied separately in X and Y direction from 0 to 1.5 mm with a 0.25 mm increment. We think it is appropriate, according to recommendation ESS, from many previous studies such as 1.5 and 0 in X and Y direction [3], 1 mm in both directions [9], 0.75 mm in both directions [5]. However, in the process of tuning ESS, the user can vary with any increments.

The beam profile matching between measured and calculated was evaluated by qualitative visual analysis. All of the profile was normalized to the central axis. We discovered that the beam profile for each crossline or inline only depends on the ESS in the same direction of the profile. For example, changing the X direction in ESS can affect only beam profile in crossline direction but no change in inline shape. Evaluation of beam profile matching was focus on 2-part of the profile, shoulder of the high dose region and the penumbra region. However, we focus more on the shoulder of the high dose region because this region can affect isodose distribution in treatment planning [5].

In the left side of Figure 1A, the profile shows that the X of 0.75 and 1 mm are more agreeable than 1.5 and 0 mm in the penumbra region (black arrow) as well as, in the shoulder of the high dose region (red dot arrow). However, on the right side of the curve shows, the line is not the same. But the curve of the line for 0.75 and 1 mm are parallel to the measured line with spacing around 0.3 mm. This result may come from the leaf positioning uncertainty. Although the digital readout of the MLC position of the HDMLC in the Edge machine is positioned down to 0.01 cm (or 0.1 mm). The study by Sharma DS showed that the unity of HDMLC digital readout and radiation field agree to within ±0.03 cm or 0.3 mm [10]. This effect could be seen in a larger field but less than a very small field. Where in Figure 1B, the profile shows an excellent agreement for ESS 0-0.25 mm. ESS in X is higher than Y because of the scatter from the round leaf end of the MLC in crossline [3].

For the penumbra difference in Table 1, we note that low difference of penumbra should be more reliable although the beam profile matching is essential as well. But in this table, the lower penumbra difference appears in 0.75-1 mm in the X direction and 0-0.25 mm in Y-direction.

The field output factor was analyzed with SE to evaluate the uncertainty of the mean. However, it is only type A uncertainty. We expect that the good agreement between calculated and measured field output factor should fall within ±2SE (95% confidence interval). So, the selecting ESS (0.75-1 mm in the X direction and 0-0.25 mm in Y-direction) shows the excellent agreement of field output factor in very small MLC field (within 3%), while default demonstrates low deal (6.71%) (Table 3). However, the field output factors were independent with an ESS for larger fields (Table 4).

5. CONCLUSION

The ESS can improve the accuracy of field output factor calculation in the Acuros XB algorithm for a radiosurgical beam size, but this parameter is not affected in a large field. However, other parameters should be considered, such as DLG. More evaluation in the clinical treatment fields should be performed to make more confidence in selecting ESS.

ACKNOWLEDGEMENTS

This research was supported by the staff of the Radiosurgery department and Division of radiation therapy, Faculty of Ramathibodi Hospital, Mahidol University.

REFERENCES

1. Fogliata A, Nicolini G, Clivio A, Vanetti E, Cozzi L. Dosimetric evaluation of Acuros XB Advanced Dose Calculation algorithm in heterogeneous media. Radiation Oncology. 2011;6(1):82.
2. Han T, Mikell JK, Salehpour M, Mourtada F. Dosimetric comparison of Acuros XB deterministic radiation transport method with Monte Carlo and model-based convolution methods in heterogeneous media. Med Phys. 2011; 38:2651–2664.
3. Torsti T, Korhonen L, Petäjä V. Using Varian Photon Beam Source Model for Dose Calculation of Small Fields. Palo Alto (CA): Varian Medical Systems; 2013
4. Fogliata A, Lobefalo F, Reggiori G, Stravato A, Tomatis S, Scorsetti M, et al. Evaluation of the dose calculation accuracy for small fields defined by jaw or MLC for AAA and Acuros XB algorithms. Med Phys. 2016;43(10):5685-94.
5. Gardner SJ, Lu S, Liu C, Wen N, Chetty IJ. Tuning of AcurosXB source size setting for small intracranial targets. J Appl Clin Med Phys. 2017;18(3):170-81.
6. International Atomic Energy Agency. Dosimetry of Small Static Fields Used in External Beam Radiotherapy, Technical Reports Series No. 483. Vienna: International Atomic Energy Agency; 2017.
7. J. M. Lárraga-Gutiérrez, P. Ballesteros-Zebadúa, M. Rodríguez-Ponce, O. A. García-Garduño, and O. O. de la Cruz, “Properties of a commercialPTW-60019 synthetic diamond detector for the dosimetry of

small radiotherapy beams," Phys. Med. Biol. 2015; 60:905–924.
8. I. Cincaglioni, M. Marinelli, E. Milani, G. Prestopino, C. Verona, and G. Verona-Rinati, "Dosimetric characterization of a synthetic single crystal diamond detector in clinical radiation therapy small photon beams," Med. Phys. 2012;39:4493–4501.
9. Fogliata A, Nicolini G, Clivio A, Vanetti E, Cozzi L. Accuracy of Acuros XB and AAA dose calculation for small fields with reference to RapidArc® stereotactic treatments. Med Phys. 2011;38(11):6228-37
10. Sharma DS, Dongre PM, Mhatre V, Heigrujam M. Physical and dosimetric characteristic of high-definition multileaf collimator (HDMLC) for SRS and IMRT. J Appl Clin Med Phys. 2011;12(3):3475.

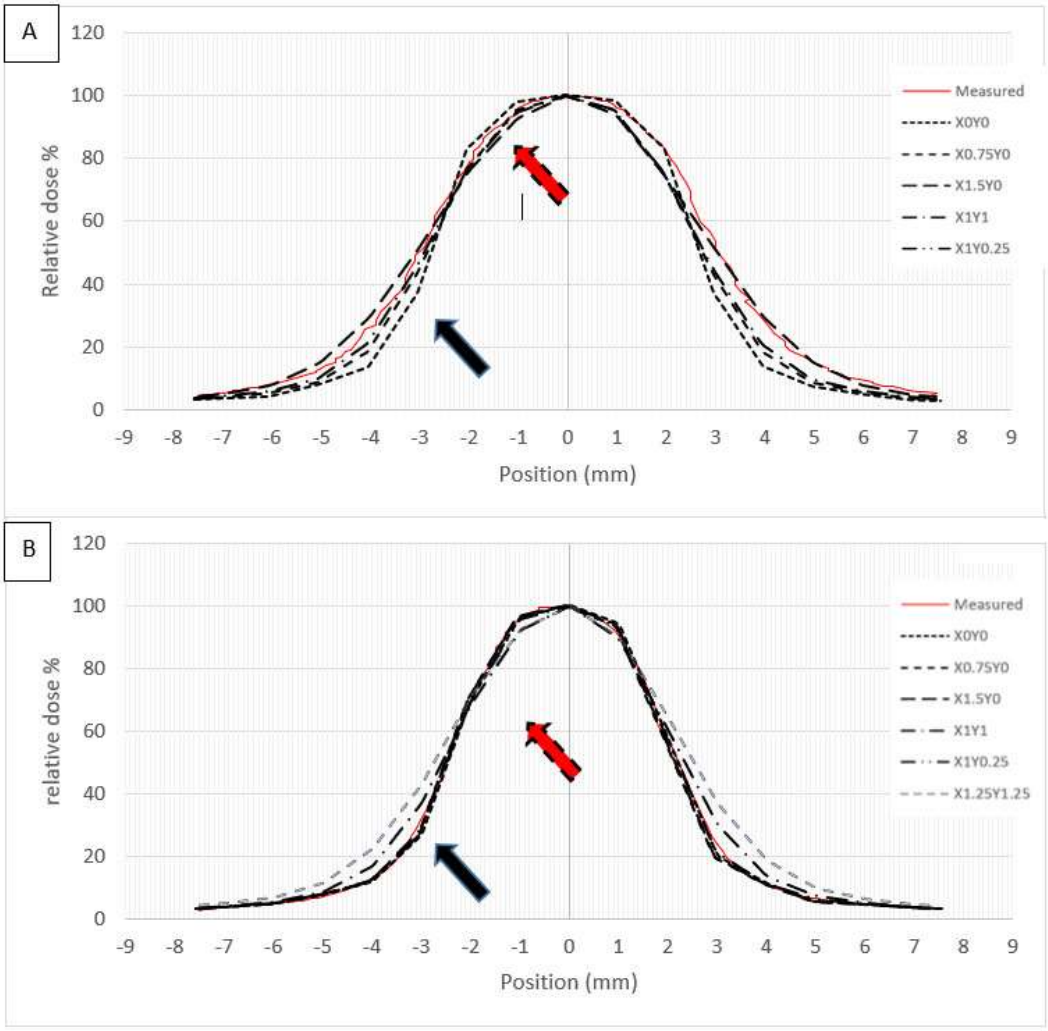

Figure 1 *Comparison of measured and calculated profile for each ESS. A is the crossline of 0.5 cm MLC field while B is the inline. The red dot arrow is the shoulder of the high dose region, and black arrow is the penumbra region.*

Denoising of OCT images with a bandelet transform for feature extractions

Keito Sato[1], Kazumi Murata[2,3], Koichi Ogawa[2]

1 Graduate School of Science and Engineering, Hosei University,
2 Faculty of Science and Engineering, Hosei University,
3 National Astronomical Observatory of Japan

Abstract

Optical coherence tomography (OCT) is a diagnostic imaging system for ophthalmologic applications. Making use of interferometry, the OCT system provides high resolution images, from which retinal layers are extracted for ophthalmologic diagnostics. However, the images tend to be degraded by speckle noise produced by coherent light. Although many studies have addressed this issue, the state-of-the-art noise reduction method is still far from optimal. In this work, we focus on the layer shape as *a priori* knowledge and produce a denoising method based on a bandelet transform. The aim of this study is to provide a new bandelet-based denoising method optimized for feature extractions from OCT images. **We investigated the** feasibility of our method with OCT images. **The proposed method** identified the directions of retinal layers in the OCT images with the bandelet transform and smoothed the images along with the directions. This analysis produced a flat profile of each layer. Our method successfully reduced the noise in the OCT images along the direction of each layer without degradation of detail features. This enables us to easily extract each retinal layer. **The results suggest that our method is appropriate for noise reduction in OCT images for feature extractions.**

Keywords: optical coherence tomography, denoising, bandelet transform, wavelet transform

1. INTRODUCTION

Optical Coherence Tomography (OCT) is a technique for imaging the internal structure of a sample with high resolution and speed by making use of interferometry. In contrast with X-ray CT and PET, OCT uses near infrared light and has no risk of radiation exposure. The typical penetration is about 1 mm and the resolution is about 10 μm. It is suitable for cross-sectional imaging of microtissues with shallow depths, such as the retina of eye and skin.

However, OCT images have a serious problem; a speckle noise. This is caused by the interference of light with different wavelengths, derived from scattered light in the target sample. The degradation leads to failures of image processing (e.g., edge or feature extraction). A lot of research has been carried out to remove the noise in OCT images [1], a mainstream of which is the noise removal with wavelet transform and related techniques.

Among them, we focus on a bandelet transform [2-5]. The bandelet transform is a transformation method using geometric regularities in images. Conventional wavelet transforms cannot make use of this regularity. It leads to blurring the edges during the noise reduction process. In contrast, the bandelet transform makes use of directional information, i.e. transformation is performed along the direction of geometric regularity. Hence, the effective noise reduction with less feature degradation can be conducted. The geometric regularity is also evident in the retinal layer images acquired by an OCT system. As a natural consequence, the bandelet transform would be appropriate for retinal layer images. Nonetheless, few researchers make use of the bandelet transform for noise reduction in such images.

In this paper, we propose a noise reduction method with a bandelet transform for retinal layer images. This would lead to an accurate feature extraction for a diagnosis with OCT images.

2. MATERIAL AND METHODS

In this section, we explain our noise reduction method with a bandelet transform. First, it identifies the direction of features in the image using a quadrant search. Second, a 1D wavelet transform is applied along the feature direction. Finally, the coefficients of the wavelet transform are thresholded for a noise reduction. In this process, features can be smoothed out in the direction and have a clear contrast. We performed this process on Harr-wavelet transformed images which wavelet decomposition level is one. This is because a bandelet transform directly applying on images leads to strong block artifacts whereas that on wavelet transformed images tends to avoid these artifacts. This method is a second-generation bandelet transform. Normally, the vertical, horizontal, and diagonal components are thresholded, but in our method, we also processed the approximate components. This allows the characteristics of the layers to be more clearly defined while suppressing block artifacts than when the original image is processed directly. We used Normal Shrink [6-8] in the threshold process.

We evaluated this method using OCT images obtained with 3D-OCT 2000 (Topcon, Japan). We performed a noise reduction with our method. For comparison, we also performed that with a Haar wavelet transform with the Normal Shrink thresholding.

3. RESULTS AND DISCUSSION

Figure 1 shows the noise reduction results. It shows two original images (top), denoised images with a Haar wavelet transform (middle), and with our method (bottom). As can be seen, images with our method have less noise and clearer features than the others.

For quantitative evaluation we defined the ROI 1-4 shown in the figure and calculated the standard deviation normalized with mean value in each region. In all cases, our method shows the minimum values.

Finally, we show profiles of a 1-pixel line parallel to the layers in the ROIs in Figure 2. The profiles with our method show profiles with small variations in all the cases.

These results suggest that our method is effective for reducing noise and emphasizing the features, which facilitates to easily extract features for an ophthalmologic diagnosis with OCT images.

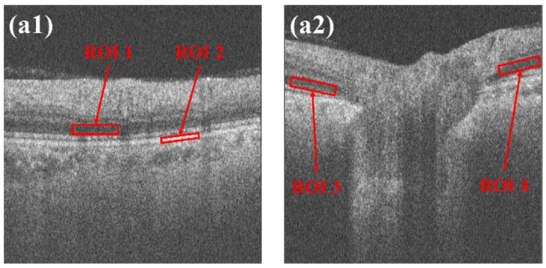

(a) Original images

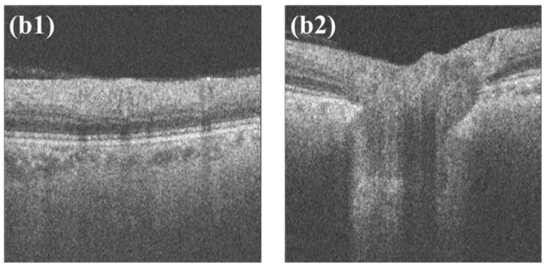

(b) Denoised images with a Haar wavelet transform

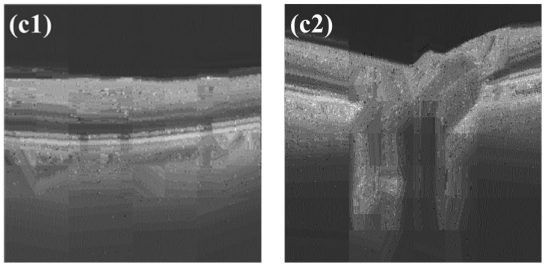

(c) Denoised images with proposed method

Fig. 1 Comparison of noise reduction methods with two images: (a) original, (b) denoised with a Haar wavelet transform, and (c) denoised with the proposed method.

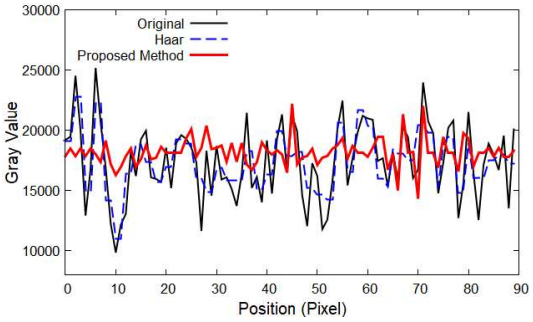

(a) Profile of ROI 1

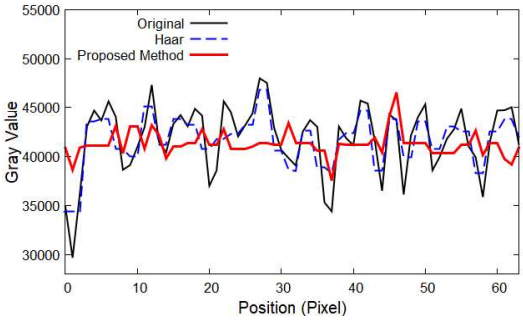

(b) Profile of ROI 2

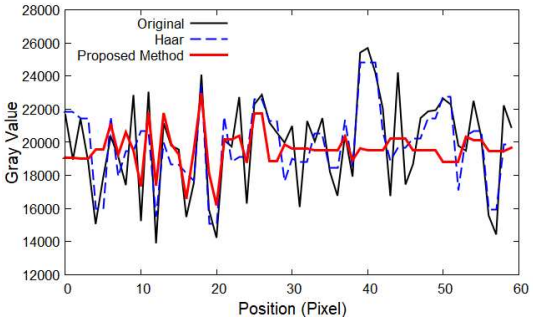

(c) Profile of ROI 3

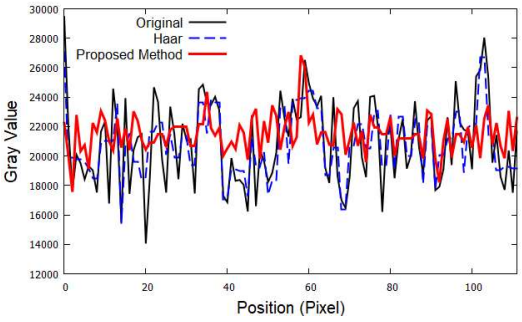

(d) Profile of ROI 4

Fig. 2 Profiles along each ROI. Black, blue, and red lines indicate an original profile, denoised one with a wavelet transform, and that with the proposed method, respectively.

Table 1 *Standard deviations normalized with the mean value in each ROI.*

	Original[%]	Wavelet[%]	Proposed[%]
ROI 1	15.7	13.2	9.1
ROI 2	16.8	14.6	9.5
ROI 3	18.9	16.2	10.3
ROI 4	10.1	8.9	6.0

4. CONCLUSION

The proposed method successfully reduced the noise in OCT images while preserving the features. Quantitative evaluation also supports that our method is more appropriate than a conventional method. This could be useful for feature extractions for an ophthalmologic diagnosis.

REFERENCES

1. R. Ramachandiran, et al. "A Survey on Speckle Removal for Optical Coherence Tomography Images," IEEE ICSCAN, pp. 1-5, 2019.
2. E. L. Pennec, S. Mallat, "Sparse geometric image representations with bandelets," IEEE Trans. Imag. Proc., vol. 14, no. 4, pp. 423-438, 2005
3. G. Peyré, E. Le Pennec, C. Dossal, S. Mallat, "Geometrical image estimation with orthogonal bandlet bases," Proc. SPIE, vol. 6701, pp. 67010M. 1-67010M. 10, 2007.
4. G. Peyré, S. Mallat, "A matlab tour of second generation bandelets," CMAP, Ecole Polytechnique, vol. 395, pp. 1-7, 2005.
5. G. Peyré, S. Mallat, "Surface compression with geometric bandelets," ACM Trans. Graph, vol. 24, no. 3, pp. 601-608, 2005.
6. R. Kafieh, H. Rabbani, G. Unal, “Bandlets on Oriented Graph: Application to Medical Image Enhancement,” IEEE Access, vol. 9, pp. 32589-32601, 2019.
7. R. Sihag, R. Sharma, V. Setia, "Wavelet thresholding for image denoising," IJNSA, vol. 3, no. 4, pp. 21-24, 2011.
8. S. Sutha, E. J. Leavline, D. A. A. G. Singh, "A comprehensive study on wavelet based shrinkage methods for denoising natural images," WSEAS Trans. Signal Proc., vol. 9, no. 4, pp. 203-215, 2013.

Evaluation of dose calculation algorithm accuracy in Eclipse treatment planning system for jaw-defined and MLC-defined small fields

Panun Sritubtim[1], Suphalak Khachonkham[1], Pimolpun Changkaew[1], Warinthorn Rattanaareeyakorn[1], Surendra Dhungana[1], Nauljun Stansook[1], Pornpan Yongvithisatid[2], Puangpen Tangboonduangjit [1]

1 Master of Science Program in Medical Physics, Division of Radiotherapy and Oncology, Department of Diagnostic and Therapeutic Radiology, Faculty of Medicine Ramathibodi Hospital, Mahidol University, Thailand
2 Radiosurgery center, Faculty of Medicine Ramathibodi Hospital, Mahidol University, Thailand

Abstract

The basic concepts of the Analytical Anisotropic Algorithm (AAA) and the Acuros XB (AXB) implemented in the Eclipse TPS are designed adequately for large conventional photon beams [1] in contrast with a specific condition as small fields that are still challenging to calculate dose accurately [2] and might lead to dosimetric errors in the stereotactic field technique planning if the commissioning process is not properly verified [3]. Therefore, preclinical validation tests in this condition are needed to determine their accuracy before clinical usage [3]. The purpose of this study is to evaluate the dosimetric calculation accuracy of the AAA and AXB algorithms implemented in the Eclipse treatment planning system version 13.6.23 in a homogeneous phantom for the range of small static fields delimited by the multileaf collimators (MLCs) and collimation jaws. The comparison of the AXB and AAA dose calculation against the measurement of small field dosimetry based on the TRS-483 recommendation. The experiment was performed for the 6MV photon beams from the Varian Edge linear accelerator with field sizes from 0.6×0.6 cm^2 to 3×3 cm^2 defined either by MLCs or collimation jaws. Results found that the AXB provides better agreement than AAA for all sizes of the MLC-defined field, while both produce the worse results on jaws-defined fields smaller than 2×2 cm^2. The maximum differences found in the smallest field size are about 19.14% and 12.18% for a jaws-defined field calculated by AXB and an MLC-defined field calculated by AAA, respectively. In brief, the agreement of both algorithms is within 3% for the 2×2 cm^2 field size and larger. The impact of radiation scattering caused by varying jaw positions for the MLC-defined field is negligible and uncertain trend.

Keywords: small fields, MLC defined field, Eclipse dose algorithms, AAA, Acuros XB, dose calculation accuracy

1. INTRODUCTION

The Analytical Anisotropic Algorithm (AAA) and Acuros XB (AXB) algorithms, complemented in the Eclipse™ treatment planning system, are essential software to calculate the required radiation dose distribution in the target organ on the patient. These two algorithms are based on different theories i.e., the 3D pencil beam convolution-superposition for the AAA algorithm and the Linear Boltzmann transport equation for the AXB algorithm, which can affect the different computation accuracy [4]. However, both algorithms are designed adequately for planning in the large conventional photon fields [1] in contrast with the specific condition as small fields that are still challenging for accurate calculation and measurement. As shown in dosimetric errors of SBRT calculation at centers in France and Missouri, more than 200 patients were receiving a 200% overdosage [2]. The cause of these radiation incidents were the improper procedures and detectors used in the field output factor measurement during the commissioning process.

Additionally, Liu et al. have indicated the inaccurate calculation in small fields delimited by collimator jaws [5]. Thus, Varian's clinical perspective recommends avoiding configured a field output factor smaller than 3×3 cm^2 into the TPS and using a multileaf collimator (MLC) to define the small fields [6]. However, this aspect was suggested before the TRS-483 Technical Report was released in 2017 as the first standard for small field dosimetry used in external photon beams [7].

Therefore, it is interesting whether this topic remains valid. *Therefore, the aim of this work was to evaluate dosimetric accuracy of the AAA and Acuros XB algorithms implemented in the Eclipse TPS version 13.6.23 in a homogeneous phantom for small static fields defined by the MLCs and jaws.*

2. MATERIAL AND METHODS

Calculated field output factors from the Eclipse dose algorithms version 13.6.23 were compared against the measurement based on the TRS-483 for the 6MV photon beam. The calculation and measurement were performed for the area ranged from 0.5×0.5 cm^2 to 3×3 cm^2 defined either by MLCs or collimation jaws at the 10 cm depth of the homogeneous phantom*, which is the simple condition for calculations in a small area. To verify the accuracy of basic calculations,* two sets of data were compared in terms of percentage difference with the reference measurements.

2.1 Dose measurement in a homogeneous phantom

The measured field output factors were acquired in a water phantom with a PTW microDiamond and the SRS diode (PTW GmbH, Freiburg, Germany). These two detectors were considered as a suitable detector for small field dosimetry following the TRS-483 CoP due to their properties, including the high spatial resolution,

minimal dose rate and dose per pulse detector as well as a small sensitive volume [8,9]. Also, the voltage bias is not required for both detectors.

The measurements were performed on the central beam axis at 10 cm depth (SSD = 90 cm). The detector orientation was set to its sensitive volume parallel to the beam axis. The centering of the detector was positioned according to the inline and crossline beam profile of 2×2 cm^2 at the measuring depth and confirmed with the beam profile of 1×1 cm^2 at the same depth.

The reading for each field size was collected with three repeats in short time intervals, and all measurement sets were repeated on two different days (two different time of settings). The average of each data set was normalized with the reading of a 10×10 cm^2 jaw-defined field to acquire the measured field output factor. The Varian Edge® linear accelerator (Varian Medical Systems, Palo Alto, USA) equipped with the high-definition MLC having 2.5 mm leaves width was used for the experiments.

The following field sizes were carried out:

– Jaws-defined field sizes including: 0.6×0.6, 1×1, 2×2, 3×3, 5×5, and 10×10 cm^2 with retracted MLC. The field sizes were selected as an even in millimeter to achieve a symmetrical jaw setting with a precision of 1 mm.
– MLC-defined fields sizes including: 0.5×0.5, 1×1, 2×2, 3×3, and 5×5 cm^2 with the jaw setting between 1×1 to 7×7 cm^2 as shown in Table 1.

Table 1. *Jaw settings for MLC-defined fields.*

MLC-defined field (cm^2)	Jaw setting (cm^2)
0.5×0.5	1×1
	2×2
	3×3
1×1	2×2
	3×3
	4×4
2×2	2×2
	3×3
	4×4
3×3	3×3
	4×4
	5×5
5×5	5×5
	7×7

According to the TRS-483 recommendation [7], a field output correction factor ($k_{Q_{clin},Q_{msr}}^{f_{clin},f_{msr}}$) was multiplied to the measured ratio of detector readings to correct for the size and material of the detectors [10,11]. Factors were acquired from Table 26 of this CoP using the field width obtained from the measurement in solid phantom with the EBT3 Gafchromic film with the same experimental setting condition.

2.2 Treatment planning and dose calculation

The 3D plans with the same experimental settings of the measurement were created on the virtual water phantom (size of $50 \times 50 \times 60$ cm^3) in the Eclipse treatment planning system (*Varian Medical Systems, Palo Alto, USA*), as shown in Figure 1. All plans were calculated using both AAA and AXB dose algorithms with the calculation grid size of 1 mm to provide the better resolution of the structure voxels sampling to the calculation grid [10], and the calculation volume was expanded to cover the whole virtual phantom. Calculated doses at the isocenter of each field size were normalized with the absorbed dose of 10×10 cm^2 field defined by jaws to achieve the calculated field output factors. Both algorithms are based on the implementation of the same photon source model to determine the physical parameters in dose calculation [12]. In this study, the TPS was operated without altering the beam configurated setting used currently in the clinic (the smallest field output factor configured to the TPS is 2×2 cm^2). Also the modeling parameters were set as the manufacturer's default in order to evaluate the limitations of each algorithm and provide recommendations for future actions. *The default values* include the effective spot sizes of 0 and 1 mm for AAA and AXB, the dosimetric leaf gap of 0.0255 cm, and the leaf transmission factor of 0.011.

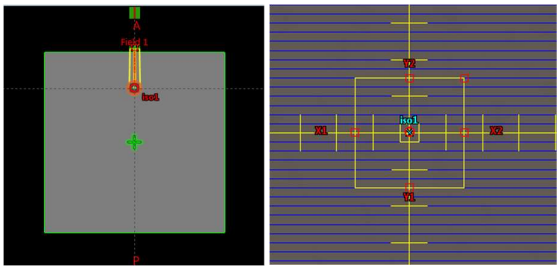

Figure 1. *Example of MLC-defined field (0.5×0.5 cm^2 with jaw setting of 3×3 cm^2) on the virtual water phantom in the Eclipse TPS.*

3. RESULTS

3.1 Field output factor of jaw-defined fields

Calculated and measured field output factors (corrected following TRS-483) are reported in the first part of Table 2. Percentage differences are summarized in Figure 2. For fields equal or larger than 2×2 cm^2, the calculated OF agree with measurements within 2% (range +0.26% to +1.16% for AAA, –0.37% to +1.52% for AXB) while the maximum differences found in the smallest field size are 15.74% and 19.14% for the AAA and AXB, respectively. Both algorithms tend to be overestimated in smaller fields. Generally, AAA is in better agreement with measurements than AXB for calculating in the jaw-defined field.

Table 2. *Calculated and Measured field output factors of jaw-defined fields and MLC-defined fields.*

Jaw setting (cm^2)	MLC setting (cm^2)	OF_{AAA}	OF_{AXB}	OF_{Mea}
0.6×0.6	Retract	0.577	0.594	0.499
1×1	Retract	0.694	0.698	0.672
2×2	Retract	0.799	0.802	0.790
3×3	Retract	0.839	0.835	0.832
5×5	Retract	0.897	0.892	0.895
1×1		0.508	0.497	0.554
2×2	**0.5×0.5**	0.509	0.540	0.557
3×3		0.510	0.513	0.560
2×2		0.689	0.714	0.707
3×3	**1×1**	0.690	0.714	0.709
4×4		0.695	0.721	0.710
2×2		0.797	0.801	0.790
3×3	**2×2**	0.799	0.805	0.802
4×4		0.806	0.810	0.808
3×3		0.838	0.834	0.832
4×4	**3×3**	0.844	0.842	0.843
5×5		0.852	0.848	0.851
5×5	**5×5**	0.896	0.890	0.893
7×7		0.909	0.903	0.911

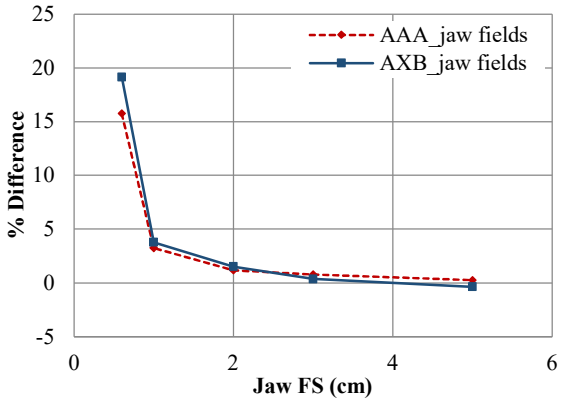

Figure 2. *Difference between measured and calculated field output factors for jaw-defined fields.*

3.2 Field output factor of MLC-defined fields

Calculated and measured corrected field output factors shown in the second part of Table 2. Percentage differences between calculations and measurements are summarized in Figure 3. For fields equal or larger than 2×2 cm^2 (considering all jaw settings), the calculated OF agreed with measurements in the average of 0.14% for AAA (range –0.34%, +0.82%) and in the average of 0.06% for AXB (range –0.85%, +1.33%). The calculation in MLC-defined fields tend to be underestimated for both algorithms. For the smallest field size, the difference was in the range of –8.95% to +3.98% for AAA (average –6.02%), and in the range of –8.49% to +7.39% for AXB (average –3.83%).

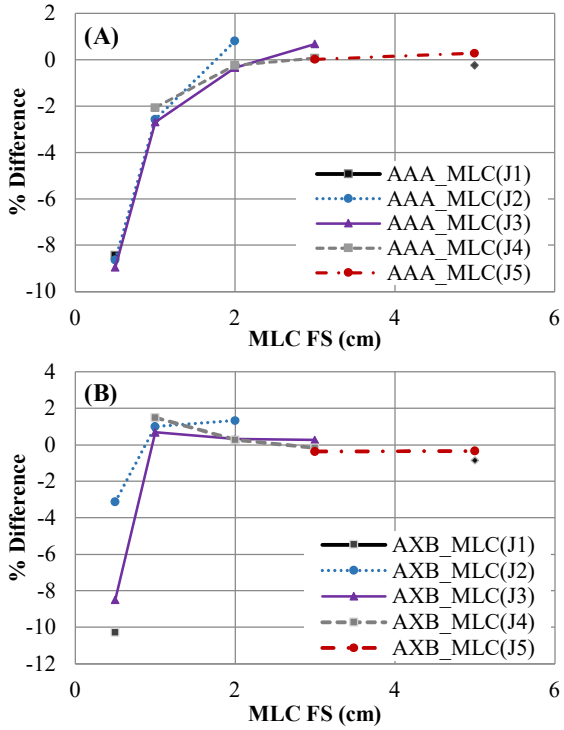

Figure 3. *Difference between measured and calculated field output factors for MLC-defined fields. Results of AAA and AXB are showed with (A) and (B).*

For AXB, size of the jaw setting slightly affects the agreement for field size equal to or larger than 2×2 cm^2 *while the maximum difference is found in the extreme case of* 0.5×0.5 cm^2. *For AAA, the minimum difference of agreement is found in the smallest field size. In general, both algorithms tend to underestimate the MLC-defined field as opposed to the behavior for jaw-defined fields.*

4. DISCUSSION

This study presents a comparison between measured output factors based on the TRS-483 for small static fields defined by jaws or MLC, and the data calculated by AAA and AXB dose algorithms implemented in the Eclipse treatment planning system version 13.6.23.

The overall results for field sizes equal to or greater than 2×2 cm^2 showed good agreement within ±3% corresponding with the results published by Fogliata et al. [13]. The results have shown that using small MLC-fields instead of jaws provides a better agreement in most field sizes.

The larger size of jaw setting in MLC-defined fields negligibly impact absorbed dose at the central axis due to the increasing of photon scattering into the field. The AXB is more sensitive to the size of the jaw setting, especially in a smaller field. However, the suitable size of the jaw setting for each MLC-defined field size is not distinct because the chosen jaw settings are only in the narrow range. The investigation in a broader range of

jaw settings used in clinical is advised to represent more clearly trends.

The worse agreement found in the field sizes smaller than 2×2 cm^2, especially in the extreme cases as 0.6×0.6 cm^2 jaw-defined fields that the difference is up to 19% because the collimator backscatter factor (CBSF) used for dose calculation in those cases were inaccurately estimated [13]. As well as the smallest field size 0.5×0.5 cm^2 field defined by MLC, the agreement still exceeds 3% difference even if the CBSF is no use for calculating in this case. It must be noted that the cause of the difference between the measurements and the calculations cannot be attributed to any single parameters. There are other parameters also impact the dose calculation, including the focal spot size and DLG which need to be in consideration [14,15]. While the uncertainty for small field dosimetry should be necessary. Accurately measured field output factors can be obtained from the appropriate procedure and detector, as well as applying the factor $k_{Q_{clin},Q_{msr}}^{f_{clin},f_{msr}}$ to correct the individual detector response.

The limitation of this study is that only one photon energy was studied (6 MV WFF) in a homogeneous media. The accuracy of AAA and AXB algorithms in heterogeneous media, as well as for other beam qualities, was beyond the scope of this present work.

5. CONCLUSION

The AAA and AXB dose algorithms implemented in the Eclipse treatment planning system version 13.6.23 have been investigated for the calculation accuracy in small fields defined by jaws and MLCs. The agreement of both algorithms against the measurement was within ±3% for all field sizes equal to or larger than 2×2 cm^2. For smaller fields, both algorithms tend to overestimate for jaw-defined fields and underestimate for MLC-defined fields. The AXB achieve better agreement than the AAA in all MLC-defined fields. The worse agreement was found in the smallest field size which might be caused by the uncertainty of the detector positioning (±0.1 mm).

ACKNOWLEDGEMENTS

The author especially grateful to the medical physics and staff of Radiation Therapy, Department of Diagnostic and Therapeutic Radiology, Faculty of Medicine Ramathibodi Hospital who supported and helped with the experimental measurements and calculations. We also thank the Radiosurgery Center of Ramathibodi Hospital that facilitated and allowed the use of the facility and machine for this study.

REFERENCES

1. Swinnen AC et al., Influence of the jaw tracking technique on the dose calculation accuracy of small field VMAT plans. J Appl Clin Med Phys. 2017;18(1):186-95.
2. Torsti T, Korhonen L, Petäjä V. Using Varian Photon Beam Source Model for Dose Calculation of Small Fields. Clinical Perspectives. 2013.
3. S. Derreumaux et al., Concerns in France Over the Dose Delivered to the Patients in Stereotactic Radiation Therapy. Standards, Applications and Quality Assurance in Medical Radiation Dosimetry (IDOS). 2011.
4. Lechner W, Wesolowska P, Azangwe G, Arib M, Alves VGL, Suming L, et al. A multinational audit of small field output factors calculated by treatment planning systems used in radiotherapy. Physics and Imaging in Radiation Oncology. 2018;5:58-63.
5. Lechner W, Wesolowska P, Azangwe G, Arib M, Alves VGL, Suming L, et al. A multinational audit of small field output factors calculated by treatment planning systems used in radiotherapy. Physics and Imaging in Radiation Oncology. 2018;5:58-63.
6. Torsti T, Korhonen L, Petäjä V. Using Varian Photon Beam Source Model for Dose Calculation of Small Fields. Clinical Perspectives. 2013.
7. INTERNATIONAL ATOMIC ENERGY ANGENCY. Dosimetry of Small Static Fields Used in External Beam Radiotherapy: An International Code of Practice for Reference and Relative Dose Determination. Technical Reports Series No. 483. Vienna: IAEA; 2017.
8. P. Francescon, S. Cora, and N. Satariano, "Calculation of $k_{Q_{clin},Q_{msr}}^{f_{clin},f_{msr}}$ for several small detectors and for two linear accelerators using Monte Carlo simulations," Med. Phys. 38. 2011.
9. I. Cincaglioni, M. Marinelli, E. Milani, G. Prestopino, C. Verona, and G. Verona-Rinati, "Dosimetric characterization of a synthetic single crystal diamond detector in clinical radiation therapy small photon beams," Med. Phys. 39, 4493–4501, 2012.
10. Kan MW, Leung LH, Yu PK. Verification and dosimetric impact of Acuros XB algorithm on intensity modulated stereotactic radiotherapy for locally persistent nasopharyngeal carcinoma. Med Phys. 2012;39:4705–14.
11. A. Ralston, M. Tyler, P. Liu, D. McKenzie, and N. Suchowerska, "Overresponse of synthetic microDiamond detectors in small radiation fields," Phys. Med. Biol. 59, 5873–5881. 2014.
12. M. Pimpinella, M. Anton, M. Rouijaa, and A. Stravato, "Comparison of D_w measurements by alanine and synthetic diamond dosimeters in photon beams with 1 cm ⇥ 1 cm field size," Metrologia 49,. 2012.
13. Fogliata A, Lobefalo F, Reggiori G, Stravato A, Tomatis S, Scorsetti M, et al. Evaluation of the dose calculation accuracy for small fields defined by jaw or MLC for AAA and Acuros XB algorithms. Med Phys. 2016.
14. Fogliata A, Nicolini G, Clivio A, Vanetti E, Cozzi L. Accuracy of Acuros XB and AAA dose calculation for small fields with reference to RapidArc((R)) stereotactic treatments. Med Phys. 2011.
15. Kron T, Clivio A, Vanetti E, Nicolini G, Cramb J, Lonski P, et al. Small field segments surrounded by large areas only shielded by a multileaf collimator: comparison of experiments and dose calculation. Med Phys. 2012;39(12):7480-9.

Spectral distortion correction caused by pulse-pileup effects with a machine learning technique for a photon counting x-ray detector

Kohei Koyama[1], Kazumi Murata[2,3], Koichi Ogawa[2]

1 Graduate School of Science and Engineering, Hosei University,
2 Faculty of Science and Engineering, Hosei University,
3 National Astronomical Observatory Japan

Abstract

Introduction: Owing to the spectral capabilities, a photon counting CT system has generated considerable recent research interest. It can distinguish materials of target objects and enables us to perform a K-edge imaging. However, the photon-counting CT has a serious issue; spectral distortion mainly due to a pulse-pileup effect, which is caused by multiple photons simultaneously incident on the detector. In this work, we focus on the capability of nonlinear regression of machine learning and propose a neural network-based method to correct the spectral distortion. The aim of this study is to develop a neural-network based correction method of spectral distortion due to pulse-pileup effects for a photon-counting detector. We investigated the feasibility of our method with a simulation. We produced a training network which transformed a distorted spectrum to an original spectrum. The distorted spectra were produced with an analytical pulse-pileup model for a non-paralyzable detector. The original spectra were obtained by using the IPEM program. We trained the network using distorted/original spectral pairs with various levels of pulse-pileup effects. The correction accuracy was investigated via a mean absolute error of output spectra from the trained network. Our trained network significantly reduced the spectral distortion and the output spectra were in good agreement with the original spectra for any pileup levels adopted in our study. The results demonstrate the feasibility of our neural network-based correction method for spectral distortion caused by pulse-pileup effects.

Keywords: photon-counting CT, pulse-pileup, distortion correction, machine learning

1. INTRODUCTION

Photon-counting CT systems (PCCTs) have attracted increasing attention in medical imaging [1], [2]. Compared to conventional energy-integrating CT systems (EICTs), PCCTs introduce a spectral information by counting x-ray photons into multiple energy bins. This spectral capability enables us to decompose target objects into basis materials, which is especially helpful to K-edge imaging [3], [4].

However, the current capability of PCCTs is limited by technical problems; a pulse-pileup effect caused by simultaneously incident photons at high count rate. The pulse-pileup effect leads to not only a counting loss but also a spectral distortion which significantly degrades an accuracy of physical parameters derived from the spectra [5].

Recently, machine learning techniques have been widely used in medical imaging and successfully applied for many tasks, such as denoising, super-resolution, segmentation, and image reconstruction. In nonlinear regression problem, machine learning has the great advantage of autonomously finding hidden laws. Spectral distortion correction is also a nonlinear regression problem, so machine learning can be suitable for addressing it. A recent study demonstrated the spectral distortion correction by using a fully connected neural network and improved an accuracy of material decomposition [6]. However, they focused only on detector response functions and did not address the spectral distortion caused by pulse-pileup effects.

In this work, we focus on the capability of nonlinear regression of machine learning and propose an artificial neural network (ANN) based method for spectral distortion correction caused by pulse-pileup effects. We have developed a learning model of ANN that directly corrects the spectral distortion. To investigate the correction accuracy for any pileup levels, we calculated a mean absolute error of output spectra from the trained network.

2. MATERIAL AND METHODS

2.1 Machine learning model

Figure 1 shows the learning model of ANN in which input data and output data are a spectrum. The model consists of a fully connected cascade ANN with one input layer, two hidden layers, and one output layer. The number of units of the input and output layers corresponded to the number of energy bins. As an activation function, rectified linear units (ReLU) were used in two hidden layers. The model predicts the original spectrum from the distorted spectrum via learning distorted/original spectral pairs.

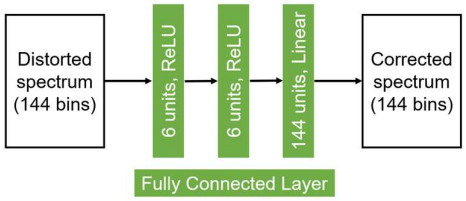

Figure 1 *Overall learning model. This model consists of a fully connected cascade ANN with 2 hidden layers.*

2.2 Distorted spectra caused by pulse pileup effects

As training data, distorted spectra and original spectra are required. We simulated both spectra with an energy range from 7 to 150 keV and an energy bin width of 1 keV. The original spectrum was produced in three steps. First, the incident spectrum was obtained using the IPEM program [7] with a 90 kV tube voltage, a 1-mm Aluminum filter, and tungsten target. The spectrum has an energy range from 7 to 90 keV. Second, the transmitted spectrum was calculated with a linear attenuation coefficient of water from the NIST database [8] with an attenuation path for the incident spectrum. Third, the original spectrum was obtained calculating the mean number of incident photons with the incident count rate a and detection time duration Δt for the transmitted spectrum. The distorted spectrum caused by the pulse-pileup was generated in the simulation by using the analytical pulse-pileup model for the original spectrum [9]. Following the previous research [9], parameters of the pulse-pileup model were set as follows: deadtime τ =100 ns, t_1=0.284 $\times$ τ , and t_2=0.850$\times$ τ . In the current study, we considered only the distortion due to peak pulse-pileup effects in a non-paralyzable detector for basic verification.

2.3 Evaluation of distortion correction accuracy

To evaluate the correction accuracy of output spectra from the trained network, mean absolute error (MAE) were calculated between normalized original and output spectra. In this study, we investigated the performance of ANN for various spectral distortions with various levels of pileup effects. Each level of pileup effects corresponded to the attenuating path. It was set 11 values between 0 and 10 cm. This is because the levels of pileup effects are determined on the incident count rate a, which depends on the attenuation length.

3. RESULTS AND DISCUSSION

Figure 2 shows the results of distortion correction for three pileup levels. As can be seen, output spectra with our method reduce distortions and clearly restore original spectra.

Figure 3 shows the mean absolute error between output spectra and distorted spectra where spectra were normalized with the maximum values. The errors were significantly reduced by the correction for any attenuation paths corresponding to pileup levels.

These results demonstrated the effectiveness of our correction method for spectral distortion caused by pulse-pileup effects. It can improve the accuracy of material decomposition applications.

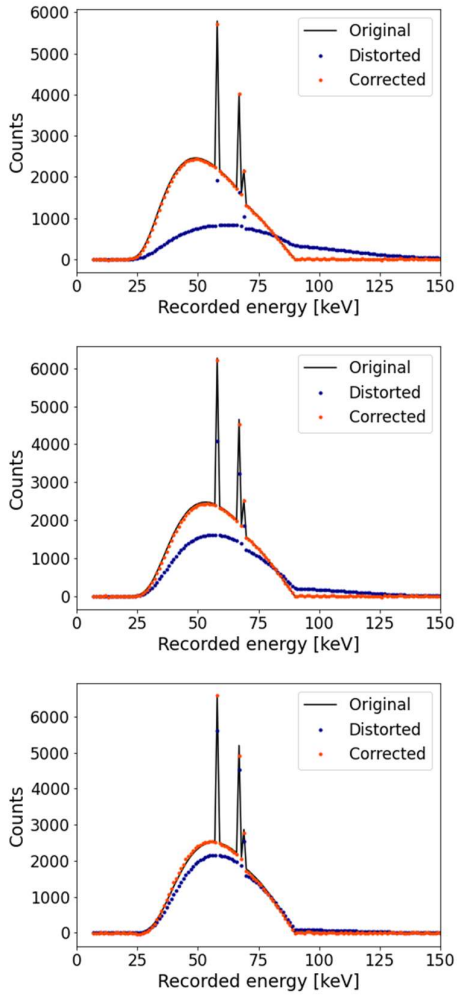

Figure 2 *Corrected spectra with various pileup levels. (top) 0 cm attenuation, (middle) 5 cm attenuation, and (bottom) 10 cm attenuation.*

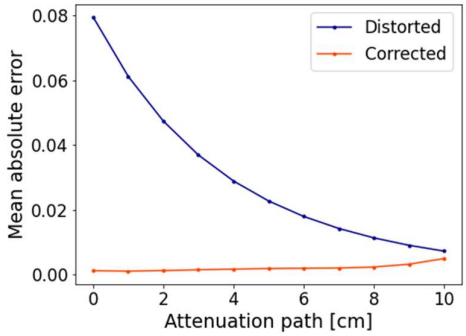

Figure 3 *Mean absolute error normalized with the maximum value in each spectrum with a different attenuation path.*

4. CONCLUSION

The proposed method significantly reduced the spectral distortion and the output spectra were in good agreement. This could be useful for material decomposition applications.

ACKNOWLEDGEMENTS

This work was supported by JSPS KAKENHI Grant Number JP20K20232.

REFERENCES

1. R. Symons, et al., "Feasibility of Dose-reduced Chest CT with Photon-counting Detectors: Initial Results in Humans," *Radiology*, vol. 285, no. 3, pp. 980-989, 2017.
2. W. A. Kalender, et al., "Technical feasibility proof for high-resolution low-dose photon-counting CT of the breast," *European Radiology*, vol. 27, no. 3, pp. 1081-1086, 2017.
3. A. M. Alessio, et al., "Quantitative material characterization from multi-energy photon counting CT," *Med Phys.*, vol. 40, no. 3, 031108, 2013.
4. S. Si-Mohamed, et al., "Evaluation of spectral photon counting computed tomography K-edge imaging for determination of gold nanoparticle biodistribution in vivo," *Nanoscale*, vol. 9, no. 46, pp. 18246-18257, 2018.
5. A. S. Wang, et al., "Pulse pileup statistics for energy discriminating photon counting x-ray detectors," *Med Phys.*, vol. 38, no. 7, pp. 4265-4275, 2011.
6. M. Touch, et al., "A Neural Network-based Method for Spectral Distortion Correction in Photon Counting X-ray CT," *Phys. Med. Biol.*, vol. 61, no. 16, pp. 6132-6153, 2016.
7. K. Cranley, et al., "Catalogue of diagnostic x-ray spectra and other data," IPEM Report No.78, 2006.
8. M. J. Berger, et al., "XCOM: Photon Cross Section Database (version 1.5)," [Online] Available: http://physics.nist.gov/xcom, National Institute of Standards and Technology, Gaithersburg, MD, 2010.
9. K. Taguchi, et al., "An analytical model of the effects of pulse pileup on the energy spectrum recorded by energy resolved photon counting x-ray detectors," *Med. Phys.*, vol. 37, no. 8, pp. 3957-3969, 2010.

Determination for current status of environmental radioactivity in Fukushima, using NaI(Tl) scintillation survey meter

Natsuki Miura[1], Daisuke Shimao[1], Tetsuya Sanada[1]

1 Department of Radiological Technology, Faculty of Health, Hokkaido University of Science,

Abstract

Fukushima Daiichi nuclear power plant accident following the Great East Japan Earthquake and tsunami on March 11, 2011 caused radiation contamination in Fukushima prefecture. The evaluation of the environmental radiation dose measured artificial radionuclides in Fukushima has been carried out by governments and many researchers. According to published investigation, in the environment the level of radiation reduced to a level of background radiation in major cities in Fukushima prefecture due to decontamination and reaching half-life. Nevertheless, there is concerned about the external radiation exposure over Fukushima prefecture. The purpose of this research is to evaluate the environmental radiation dose at major sightseeing areas and at roadside stations in Fukushima, and to provide the current status to the public. Ambient dose rates were measured in the air 1 m above the ground at all sampling points using a NaI (Tl) scintillation survey meter (TCS-172B, Hitachi-Aloka Medical, Ltd., Tokyo, Japan), which can measure gamma rays with a time constant of 30 sec. Environmental radioactivity measurements were carried out at 16 places where over 800 thousand people visit annually in Aizu, Iwaki and the northern area of Fukushima prefecture, at main stations and a limestone cave. The environmental radiation dose was derived from 5 measurement points at each of the 16 places. The environmental radiation doses obtained this study suggested that the level of radiation has become a level of background radiation and is almost the same as other areas. These results could be useful an available date to obtain understanding about safety in Fukushima prefecture. We measured the current environmental radiation doses at major sightseeing areas and roadside stations in Fukushima. The results indicate that there is no health hazard because the external radiation exposure is the same level as other cities in Japan and thus there is no reason for concern about additional exposure even when visiting Fukushima.

Keywords: Fukushima, environmental radioactivity measurement, NaI (Tl) scintillation survey meter

1. INTRODUCTION

On March 11, 2011, Fukushima Daiichi Nuclear Power Plant lost all of its power supply facilities and colling systems due to tsunami which is caused Great East Japan Earthquake, following which a hydrogen explosion occurred. ^{131}I (half-life: 8 days), ^{137}Cs (half-life: 30 years), ^{134}Cs (half-life: 2 years), ^{90}Sr (half-life: 19 years) and other radionuclides were released in large quantities into the environment. Decontamination of ^{134}Cs and ^{137}Cs, which have long half-lives, is still a concern, especially in the vicinity of Fukushima Daiichi. (1). However, in areas further from Fukushima Daiichi, environmental radiation levels have been reduced to pre-accident levels of background radiation due to decontamination work and the decay of dispersed radionuclides. There is no statistically significant difference in the deposition of radioactive Cs in the soil compared to the pre-accident level, except for some cities near Fukushima Daiichi (2). In 2011, when the accident occurred, the number of tourists in Fukushima fell from 57 million to 35 million in one year compared to 2010. The number of tourists to Fukushima generally tends to increase every year and was 56 million as of 2018, but currently the number has yet to exceed pre-accident levels (3). This is probably because people in Japan and around the world are concerned about high air dose rates over a wide area, including major cities in Fukushima prefecture. In this study, environmental radiation levels at tourist sites and stations in Fukushima prefecture were measured using a NaI (Tl) scintillation survey meter to determine the level and distribution of environmental radiation. In addition, the environmental radiation levels were compared with those of other areas in Japan to confirm that the environmental radiation levels in those areas have been reduced to the levels of background radiation.

2. MATERIAL AND METHODS.

2.1 Methods

Measurements at 14 spots (over 4 different sites) were taken in three regions (the northern part of the prefecture, Aizu and Iwaki regions), including tourist sites and roadside stations, as well as major stations and a limestone cave, the former of which welcome more than 800 thousand visitors with the highest number of visitors being in 2018: The 1cm dose equivalent rate [μSv/h] was measured using a NaI (Tl) scintillation survey meter (TCS-172B, Hitachi-Aolka Medical, Ltd., Tokyo, Japan). The detectors were kept at a height of 1m above the ground surface and the levels were measured for 90 seconds, which is three times the time constant, and then measured five times every 30 seconds, which is the time constant. These measurements were taken at five points surrounding each of the tourist sites, and over as wide an area as possible on large plateaus; the average of these measurements was taken as the 1cm dose equivalent rate [μSv/h] at each location.

2.2 Conversion factor

The measured 1 cm dose equivalent rate [μSv/h] needs to be converted to air absorbed dose rate [μGy/h]

for comparison with the Japanese each place. The conversion factor was obtained to be 0.82 using a gamma ray spectrometer (EMF211, EMF JAPAN). 0.82 has been used in previous studies (4). This value can be multiplied by the measured 1 cm dose equivalent rate [μSv/h] to calculate the air absorbed rate [μGy/h].

3. RESULTS

3.1 Air absorbed dose rate

Table 1 shows the air absorbed dose rates at each measurement point in Fukushima prefecture. The measurement points in the northern area, Aizu and Iwaki regions were labelled A-E, F-J, K-M, respectively, and a limestone cave in Fukushima was labelled N. The ground where the measurements were taken are as follows: D-1 is asphalt, D-2: grass, and D-3 is in a tunnel. The unit for air absorbed dose rate is [μGy/h], and the value is calculated by multiplying the measured value by 0.82. Where there was rainfall, it was marked Y, and where there was no rainfall, it was marked N.

Table 1 *Air absorbed dose rates in Fukushima prefecture.*

Site	No.	Air absorbed dose rate $\times 10^{-2}$[μGy/h]	Rainfall
Northern Area	A	5.18	Y
	B	5.58	Y
	C	3.48	N
	D-1	5.90	Y
	D-2	4.46	Y
	D-3	8.52	Y
	E	6.20	Y
Aizu	F	4.59	N
	G	5.12	N
	H	4.79	N
	I	5.31	N
	J	5.90	N
Iwaki	K	5.44	N
	L	4.79	N
	M	5.15	N
Limestone Cave	N	1.96	N

3.2 Distribution of air dose rate

Figure 1 shows the distribution of Table 1 and the location of the Fukushima Daiichi Nuclear Power Plant. At Point D in the northern part of the prefecture where three measurements were obtained, the inside of the tunnel is excluded and the value of D-1 on the asphalt where higher dose rate was obtained compared to the grass is shown. The limestone cave is not shown because the surrounding area is covered with limestone and the conditions are different from others because it is surrounded by limestone.

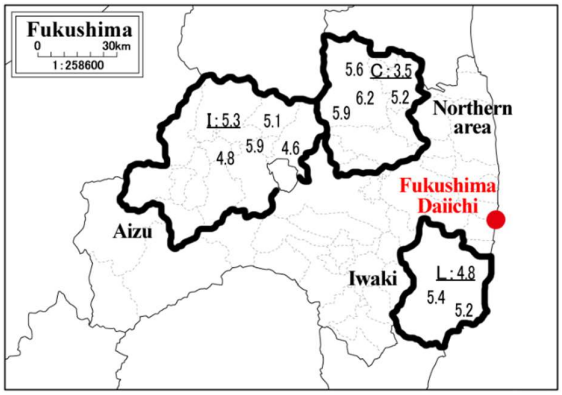

Figure 1 *Distribution of air dose rates [μGy/h]*

4. DISCUSSION

4.1 The differences in air absorbed dose rate by condition

As shown in Figure 1, there is no tendency for the radiation dose to increase closer to Fukushima prefecture. Point L (Figure 1), where 4.8μGy/h was measured in the Iwaki area, is about 40km from the nuclear power plant, and is the closest in distance; the level of radiation was also lower than the two points in the same Iwaki area that are further away from Fukushima Daiichi. At the farthest Point I, approximately 60 km from the plant, the radiation dose rate was 5.3μGy/h; thus there was no tendency for the dose rate to decrease with distance, At Point C in the northern part, particularly low doses were obtained compared to other northern sites. Rainfall was observed at the time of measurement at the measurement points, except at C in the northern area. Descendant nuclides of ^{222}Rn, naturally occurring radionuclides in the atmosphere, were washed out by the rain and deposited on the earth's surface, resulting in an increase in air dose rates near the surface (5). Therefore, only C is considered about being lower than the others, even though it is in the same northern region of the prefecture. In Furukawa (6), the dose rate was found to be higher in tunnels surrounded by concrete and rocks, and lower in limestone caves as they are generally covered with low radionuclide content. The dose rate in the tunnel was 8.52μGy/h for the same tourist site, while the dose rate in the limestone cave was 1.96μGy/h, which was relatively low. Dose rates varied depending whether the ground surface was asphalt or grass at the measurement points. These results indicate that the dose measured can vary greatly depending on the weather and various ambient conditions.

4.2 Comparison with other parts of Japan

Table 2 shows the air absorbed dose rates measured in Fukushima and the five major Japanese largest cities, Sapporo, Tokyo, Nagoya, Osaka, and Fukuoka. The values for Fukushima prefecture are averaged over the 9 points without rainfall, except for a limestone cave. The values for the five largest cities are based on the

radiation monitoring information in each city (7). These are all air absorbed dose rates [μGy/h] measured at the same time when there was no rainfall.

Table 2 *Air absorbed dose rates in Japan.*

City	Air absorbed dose rate $\times 10^{-2}$[μGy/h]	Rainfall
Fukushima	5.0	N
Sapporo	3.7	N
Tokyo	3.6	N
Nagoya	7.5	N
Osaka	6.5	N
Fukuoka	6.0	N

Figure 2 shows the respective distributions. There was no increase in radiation dose in Fukushima prefecture compared to the other areas in this study. In addition, no increase in dose rates was observed due to proximity to Fukushima prefecture.

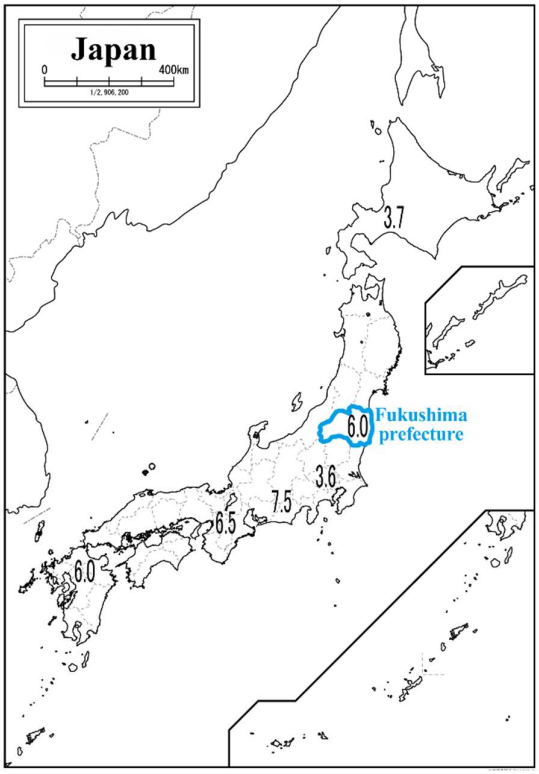

Figure 2 *Distribution of air absorbed rates in Japan.*

5. CONCLUSION

We measured rates of current environmental air absorbed dose rate in the air at tourist sites in Fukushima, and clarified the levels and distribution. The results show that a level of background radiation in the tourist areas have declined to pre-accident levels of background radiation which are comparable to levels in other major cities. The dose in the limestone cave was relatively lower than the surface level due to the limestone. In addition, no trend of higher dose rates were observed getting near Fukushima Daiichi Nuclear Power Plant at the points where the measurements were taken, suggesting that the decontamination process has already reduced the doses in major cities in the prefecture to a level off background radiation. In this study, environmental radiation levels were measured with an NaI (Tl) scintillation survey meter mainly in the major tourist areas in Fukushima prefecture where a large number of people gather. The results confirmed that in the tourist areas, the levels of background radiation were comparable to those in other parts of Japan. We hope that this information will be publicized in Japan and around the world, and that the number of tourists to Fukushima prefecture will increase in the future.

REFERENCES

1. Sato T. Background and Problematics of Radioactive Contamination by the Accidnt at Fukushima Dai-ichi Nuclear Power Plant. Clay Science, 5, 2, 26-32. 2011.
2. Local Nuclear Emergency Response Headquarters. Fukushima Prefecture Disaster Response Headquarters. Results of soil radiation monitoring in Fukushima prefecture. 2012.
3. Fukushima Prefecture Department of Commerce, Industry and Labor. Visitors to Fukushima Prefecture. 2018.
4. Iino N, Kanagaki C. Measurement of Environmental Radiation with a Simple Device. Bulletin of Faculty of Education Kumamoto University, 63, 357-362. 2014.
5. Radiation Monitoring Center, Disaster Prevention Bureau. Niigata Prefectural Government. Why do air radiation rates vary depending on the weather and location. 2020. Accessed 2020-10-15.
6. Furukawa K, Measurement of radiation dose in a limestone cave. Journal of General Education, 57, 1-3, 2019.
7. Nuclear regulatory Commission. Radiation Monitoring Information. Accessed 2020-10-15

Effect of plan complexity to gantry angle uncertainty for VMAT delivery

Thananya Chanpanya[1], Sangutid Thongsawad[1], Todsaporn Fuangrod[1]

1 Medical Physics Program, Faculty of Medicine and Public Health, HRH Princess Chulabhorn College of Medical Science, Chulabhorn Royal Academy, Bangkok, Thailand

Abstract

The aim of this study was to investigate the correlation between gantry angle uncertainty and plan complexity in VMAT plan by using in-house Quality Assurance (QA) tool. Twenty VMAT plans included head and neck (10 plans) and prostate (10 plans) were selected for measurement gantry angle uncertainty and assessment beam complexity. Gantry speed and acceleration were used to determined plan complexity by retrieving from DICOM plan. The gantry angle measurement was performed using in-house QA tool namely double dot QA. Briefly explain here, double dot QA is gantry angle measurement tool using VDO processing method. To evaluate gantry angle uncertainty, the gantry difference between measurement and plan were determined. Finally, the correlation between gantry angle uncertainty and plan complexity was evaluated with Spearman's correlation method. The result of 20 VMAT plans showed a strong correlation between plan complexity and gantry angle uncertainty. This study indicated that the beam complexity in term of gantry speed and acceleration has a strong correlation with gantry uncertainty, and the optimal gantry speed and acceleration was suggested to reduce gantry uncertainty for VMAT plan.

Keywords: Volumetric modulated arc therapy (VMAT), gantry speed and acceleration, gantry angle QA

1. INTRODUCTION

Volumetric modulated arc therapy (VMAT) is the radiation therapy technique with a radiation delivered to the patient by rotating the linear accelerator (linac) gantry around the patient whereas a radiation beam is continuously on. During this process, several delivery parameters are varied such as the dose rate, the MLC aperture shape, and the gantry rotation speed [1]. Unlike 3 dimensional-conformal radiation therapy (3D-CRT), VMAT deliveries the radiation beam with complicated method. This technique has a benefit to treat at a complexed cancer region such as head and neck (H&N) [2-6] and prostate cancer [7-9] because it can decrease a dose in overlapping region between normal organ and target. Although this technique can reduce the dose at normal organ, it requires an understanding of each parameter's error on the final dosimetric effect. Several studies have reported the dosimetric accuracy related to the plan complexity. In particular, the accuracy of gantry speed rotation greatly affects to the treatment dose delivery. The deliverability metrics of plan complexity focus on machine capability of delivering the treatment as planned due to the variation of mechanical (gantry, MLC) and dosimetric (dose rate, MU) machine parameters. Park et al.[10] suggested a new metric of beam complexity score by utilizing multileaf collimator (MLC) speeds and accelerations to predict plan delivery accuracy of VMAT, and the result was found that the increasing of MLC speeds and accelerations may reduce the accuracy of beam delivery. Due to the complexity of modulated plans, machine quality assurance and patient-specific Quality Assurance (QA) is strongly recommended to verify the beam delivery accuracy. There is a variety of instrument and experimental methods in a clinical use for patient-specific QA. Code of Practice for the QA and Control for VMAT Report task group 24 [11] has also recommended the QA tool for patient-specific QA such as ionization chambers, thermoluminescent dosimetry (TLD), film dosimetry, detector arrays and Electronic Portal Imaging Device (EPID). However, some suggested QA tool is difficult for a practical use in routine such as detector arrays which attached on gantry may be causes mechanical sag in the linear accelerator (linac) gantry and some QA tool is not recognized as an independent measurement such as EPID based-dosimetry and log file method. Hence, our previous research [12] have developed the in-house QA tool to verify the gantry angle accuracy with the benefit in high resolution gantry angle measurement and easy to set up.

The objective of this study was to investigate the correlation between gantry angle uncertainty and plan complexity in VMAT plan by using in-house QA tool.

2. MATERIAL AND METHODS

2.1 Patient selection and treatment planning

Ten H&N and ten prostate VMAT plans were retrospectively selected from plans previously used for treating patients. Total twenty VMAT plans were selected for assessment plan complexity and measurement gantry angle uncertainty. The plans were generated by using Eclipse treatment planning system version 13.6 (Varian Medical System, Palo Alto,CF, USA.).

2.2 Quantification of plan complexity

MLC speed and acceleration were used to determined plan complexity by retrieving from DICOM-RT plan. To compute the plan complexity metrics, MATLAB version R2020a program (Mathworks, Massachusetts, USA) was used. This software reads the DICOM-RT plan as exported from the TPS and computes complexity metrics using the data contained in the DICOM-RT plan and calculate independently for each bank of MLC (Bank A and B)

position then calculate Leaf speed (LS) and leaf acceleration (LA) in each bank from Equation (1) and Equation (2) respectively.

$$Leaf\ speed_i = \frac{Leaf_i + Leaf_{i+1}}{Time_i} \quad \text{Eq. (1)}$$

$$Leaf\ accelleration_i = \frac{Leaf\ speed_i + Leaf speed_{i+1}}{Time_i} \quad \text{Eq. (2)}$$

2.3 Gantry angle measurement

TrueBeam (Varian Medical Systems, Palo Alto, CA, USA) was used for delivery of the VMAT plans in QA mode to determine the gantry angle uncertainty. The Double Dot (DD) hardware consists of HD VDO camera for recording the gantry movement, DD marker for displaying two dots during gantry rotation, two laser pointers for detecting double dot marker on front of gantry stand, Geiger muller counter for starting a measurement when beam on, and port USB flash drive for collecting the VDO data. Figure 1 shows the DD QA setup for measurement the gantry angle. To align the DD marker as the centre of VDO images, the DD QA was placed on the couch and the laser from DD was projected on DD marker. The DD QA was recorded VDO in gray scale. The software can compare gantry angle between measurement and DICOM file by importing the DICOM-RP format to the software.

Figure 1. The DD setup for measurement gantry angle.

2.4 Data analysis

The correlation between gantry angle uncertainty and plan complexity was evaluated with Spearman's correlation coefficient. To describe the strength level of the correlation, the following guide line were used [13]; the r_s between 0.00 - 0.19 is very weak correlation, r_s between 0.20 - 0.39 is weak correlation, the r_s between 0.40 - 0.59 is moderate correlation, r_s between 0.60 - 0.79 is strong correlation, and r_s between 0.80 - 1.0 is very strong correlation.

3. RESULTS

3.1 Quantification of plan complexity

Table 1 summarizes the complexity of leaf speed and leaf acceleration.

MLC Bank	Parameter/Site	H&N	Prostate
A	Max LS	19.72933	19.40079
	Mean LS	10.89134	9.465445
	SD LS	7.183374	7.113532
	LS 0-4 per sec	0.62481	0.822101
	LS 4-8 per sec	0.09314	0.045464
	LS 8-12 per sec	0.055242	0.025596
	LS 12-16 per sec	0.03349	0.016335
	LS 16-20 per sec	0.193317	0.090504
	Max LA	19.72933	19.40079
	Mean LA	11.37548	9.892395
	SD LA	7.268241	7.259687
	LA 0-4 per sec^2	0.599418	0.81669
	LA 4-8 per sec^2	0.090247	0.043924
	LA 8-12 per sec^2	0.055373	0.024836
	LA 12-16 per sec^2	0.03593	0.016871
	LA16-20 per sec^2	0.219032	0.097679
B	Max LS	47.30996	46.50589
	Mean LS	15.51459	14.14819
	SD LS	13.25502	12.57423
	LS 0-4 per sec	0.553093	0.752063
	LS 4-8 per sec	0.100431	0.077913
	LS 8-12 per sec	0.041457	0.02116
	LS 12-16 per sec	0.088404	0.044539
	LS 16-20 per sec	0.210966	0.098676
	Max LA	47.31694	46.51741
	Mean LA	15.75142	14.55788
	SD LA	13.70782	13.04979
	LA 0-4 per sec^2	0.555593	0.759235
	LA 4-8 per sec^2	0.096693	0.070165
	LA 8-12 per sec^2	0.043982	0.021657
	LA 12-16 per sec^2	0.076942	0.042558
	LA16-20 per sec^2	0.221141	0.100734

Figure 2 shows the example of leaf speed pattern after extracting from dicom file.

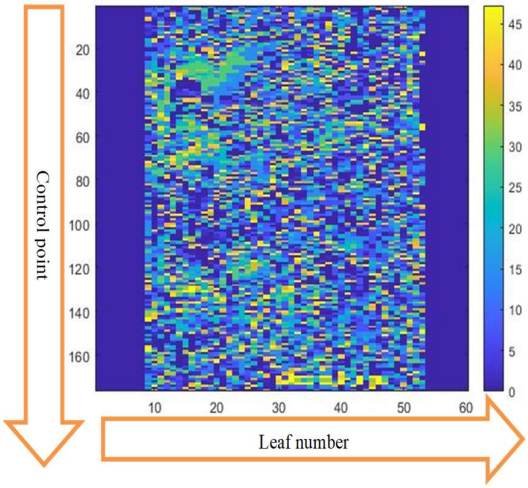

Figure 2. Example of leaf speed pattern map.

3.2 Gantry angle determination

Gantry angle difference between DD measurement and dicom file was ***0.35±0.25*** degree.

3.3 Data analysis

Figure 3 shows heat map correlation of leaf speed/acceleration and gantry angle uncertainty. The highest correlation was found at leaf acceleration bank A fraction of 160-200 mm/s^2 with Spear man correlation (r_s) 0.65, the second correlation was found at leaf speed bank A fraction of 140-160 mm/s with r_s = 0.63, and the lowest correlation was found at maximum leaf speed bank A with r_s 0.07.

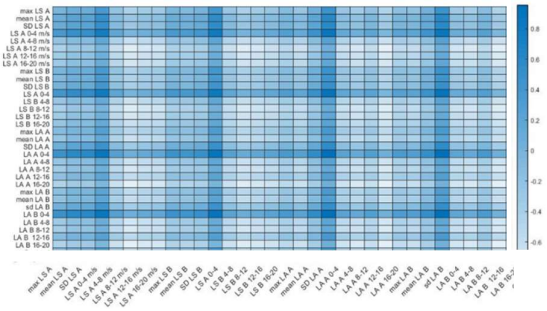

Figure 3 Heat map correlation between leaf speed/acceleration characteristics and gantry angle uncertainty

4. DISCUSSION

In this study, the characterization of leaf speed and acceleration was selected to find the correlation with gantry uncertainty because the other complexity matrices such as the small fraction aperture, leaf cross center, mean field area may not influenced to gantry uncertainty. The mean (±sd.) leaf speed fraction of 140-160 was found 0.19 (±0.035) mm/s, and mean (±sd.) leaf acceleration fraction of 160-200 was found 0.22 (±0.034) mm/s^2. The result indicated that increasing of the both leaf speed and acceleration fraction can increase the gantry angle uncertainty. Hence, the mean leaf speed fraction of 140-160 mm/s, and mean leaf acceleration fraction of 160-200 mm/s can be used to suggest as the optimal parameter for VMAT plan.

5. CONCLUSION

The correlation between leaf speed/acceleration and gantry angle uncertainty was found at leaf acceleration fraction of 160-200 mm/s^2 with strong correlation of r_s = 0.65, and leaf speed fraction of 140-160 mm/s with strong correlation of r_s = 0.63. The optimal leaf speed was suggested the leaf speed fraction of 140-160 should be ≤ 0.19 mm/s, whereas the optimal leaf acceleration was suggested the leaf acceleration fraction of 160-200 should be ≤ 0.22 mm/s^2.

ACKNOWLEDGEMENTS

I would like to thank the various Medical physicists and radiation therapists of Department of Radiation Oncology, Chulabhorn Hospital who were accessible and helped to answer any questions I had during this learning experience. Finally, thank you to Mr. Kritsada for suggestion about the tool.

REFERENCES

1. Otto, K., Volumetric modulated arc therapy: IMRT in a single gantry arc. Medical physics, 2008. 35(1): p. 310-317.
2. Wiehle, R., et al., VMAT and step-and-shoot IMRT in head and neck cancer. Strahlentherapie und Onkologie, 2011. 187(12): p. 820-825.
3. Osborn, J., Is VMAT beneficial for patients undergoing radiotherapy to the head and neck? Radiography, 2017. 23(1): p. 73-76.
4. Stieler, F., et al., A comparison of several modulated radiotherapy techniques for head and neck cancer and dosimetric validation of VMAT. Radiotherapy and Oncology, 2011. 101(3): p. 388-393.
5. Alvarez-Moret, J., et al., Evaluation of volumetric modulated arc therapy (VMAT) with Oncentra MasterPlan® for the treatment of head and neck cancer. Radiation Oncology, 2010. 5(1): p. 110.
6. Studenski, M.T., et al., Clinical experience transitioning from IMRT to VMAT for head and neck cancer. Medical Dosimetry, 2013. 38(2): p. 171-175.
7. Onal, C., et al., Comparison of IMRT and VMAT plans with different energy levels using Monte-Carlo algorithm for prostate cancer. Japanese journal of radiology, 2014. 32(4): p. 224-232.

8. Kopp, R.W., et al., VMAT vs. 7-field-IMRT: assessing the dosimetric parameters of prostate cancer treatment with a 292-patient sample. Medical Dosimetry, 2011. 36(4): p. 365-372.
9. Tsai, C.-L., et al., Treatment and dosimetric advantages between VMAT, IMRT, and helical tomotherapy in prostate cancer. Medical Dosimetry, 2011. 36(3): p. 264-271.
10. Park, J.M., et al., The effect of MLC speed and acceleration on the plan delivery accuracy of VMAT. The British journal of radiology, 2015. 88(1049): p. 20140698.
11. Stralingsdosimetrie, N.C.V., Code of Practice for the Quality Assurance and Control for Volumetric Modulated Arc Therapy. Report, 2015. 24: p. 9-59.
12. Fuangrod, T., et al., A novel and independent method for time-resolved gantry angle quality assurance for VMAT. Journal of applied clinical medical physics, 2017. 18(5): p. 134-142.
13. Spearman's correlation. www.statstutor.ac.uk/resources/uploaded/spearmans.pdf

Calculation of an automatic irradiation path for dynamic-wave-arc irradiation

Kouichi Murashima[1], Akira Sawada[2], Masaki Sueoka[3], Yoshitomo Ishihara[4], Masaki Kokubo[3], Masamitsu Moriyama[1]

1 Kindai University, Osaka, Japan,
2 Kyoto College of Medical Science, Kyoto, Japan,
3 Kobe City Medical Center General Hospital, Hyogo, Japan,
4 Japanese Red Cross Wakayama Medical Center, Wakayama, Japan

Abstract

Dynamic-wave-arc irradiation enables 3D rotational irradiation along a unicursal path with dynamic tumor tracking functionality of Vero4DRT system. It is a burden to determine an irradiation path. The purpose of this study was to calculate a dynamic-wave-arc irradiation path which has passed over normal tissues reduced as much as possible. First, distance from each point inside irradiation area to normal tissue was measured using the structure data of DICOM. From a starting point to the end, points having the smallest value among 8-neighborhood points on the above distance map showing risk score were selected successively. The treatment plan along the calculated irradiation path for a phantom was created and dose distribution was calculated using a treatment planning system (Eclipse TPS Ver. 15.1 (Varian Medical Systems, Palo Alto, USA)). For the lung phantom, an irradiation path and the DVH were calculated. It has been observed that radiation dose to normal tissue was minimized while the prescribed dose was delivered to the target. From this preliminary phantom study, it will be feasible to calculate a dynamic-wave-arc irradiation path which has passed over normal tissues reduced as much as possible, further investigation is required though.

Keywords: dynamic-wave-arc, dynamic tumor tracking, Vero4DRT

1. INTRODUCTION

The Vero4DRT is the world's first radiation therapy device developed by Mitsubishi Heavy Industries, Ltd. that can track and deliver radiation to a dynamic tumor. Conventional radiotherapists use either the entire area where the tumor moves or ambush the dynamic tumor to be irradiated. However, Dynamic-wave-arc irradiation with dynamic tumor tracking functionality of Vero4DRT system enables 3D rotational irradiation along a unicursal path. Therefore, we can reduce the side-effects of irradiation to normal tissues compared with conventional radiotherapy systems. For the development of Vero4DRT, Takashi Mizowaki et al. showed the usefulness of this irradiation technique, which is the predecessor of dynamic-wave-arc irradiation (1). They called the irradiation technique in which the rotation of the Vero4DRT ring and the gantry rotate continuously and simultaneously as three-dimensional (3D) unicursal irradiation. They performed a dose comparison between 3D unicursal irradiation and a treatment plan that envisioned the treatment of pancreatic tumor patients with 2D-DCART and IMRT. Figure 1 shows the path of 3D unicursal irradiation. It showed that 3D unicursal irradiation avoided as much of the normal tissue as possible. The dose distribution of 3D unicursal irradiation treatment plan was similar to that of 2D-DCART and IMRT treatment plans in tumors and risk tissues. They also measured the number of monitor units. The number of monitored units in 3D unicursal irradiation was only 7% higher than in 2D-DCART and 22.1% lower than in IMRT. As a result, their study showed that 3D unicursal irradiation was useful in both treatment time and dose distribution. Vero4DRT is currently implemented with dynamic-wave-arc irradiation, which is a modification of 3D unicursal irradiation.

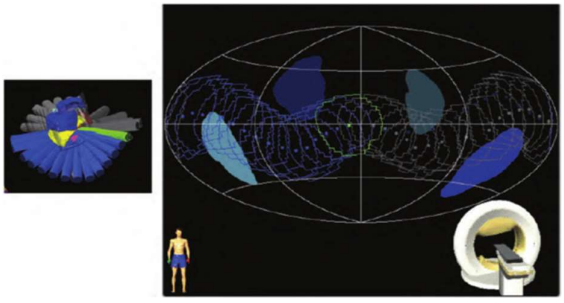

Figure 1 *path of 3D unicursal irradiation (1)*

In preparing the treatment plan of radiation therapy, physicians should determine the angle of irradiation to the tumor using a model of an actual tissue and the location of the tumor and the number of times the tumor has been irradiated using a treatment planning device. Physicians repeats the calculation of the dose distribution for each site of normal tissue and the area where tumor cells may remain around it. This takes a long time and places a burden on the physician. In addition, the introduction of Vero4DRT, which is capable of dynamic-wave-arc irradiation, has made the planning of radiotherapy more difficult, which has increased the burden on physicians. Therefore, in order to reduce the burden of physicians, we developed a system to calculate an irradiation path of treatment plan of radiation therapy for dynamic-wave-arc instead of physicians. The purpose of this study was to calculate a dynamic-wave-arc irradiation path which has passed over normal tissues reduced as much as possible and evaluating the treatment plan along the calculated irradiation path.

2. MATERIAL AND METHODS

First, we calculated the distance from each point in the irradiation area to each tissue using the structural data of DICOM. Next, we created a distance map showing the risk score based on the above results and calculated the irradiation path from the starting point to the end of the path using the distance map. Finally, we calculated the dose distribution of the above irradiation path using the treatment planning system.

2.1 Distance map creating

We obtained point cloud coordinates of tissue from the structure data of DICOM, tissue labels, and the coordinates of the center position of the radiotherapy device's irradiation range from the plan data of DICOM. Based on the above data, we created a model of each tissue point cloud and radiation. We rotated the radiation model along the operating range of Vero4DRT with the tumor as the center, and we calculated the distance to each tissue, and the result is the risk score. In this section, we explain the procedure to obtain the risk score of each tissue. Since the operation range of Vero4DRT is spherical, the irradiation position can be indicated by irradiation latitude φ and irradiation longitude θ (Figure 2). The latitude φ range is set -90 to 90 degrees, and the longitude θ range is set 0 to 360 degrees. In order to prioritize each tissue risk score, we gave each tissue risk score a weight W which range set 0 to 1, and the importance of the tissue risk score in the user's mind is W_i. Therefore, the equation for finding the risk score $D_{\theta\varphi}$ is given as

$$D_{\theta\varphi} = \sum_{i=0}^{n} W_i \times D_{i\theta\varphi}.$$

Here, n is the number of tissues, W_i is the importance of each tissue, and $D_{i\theta\varphi}$ is the risk score of each tissue.

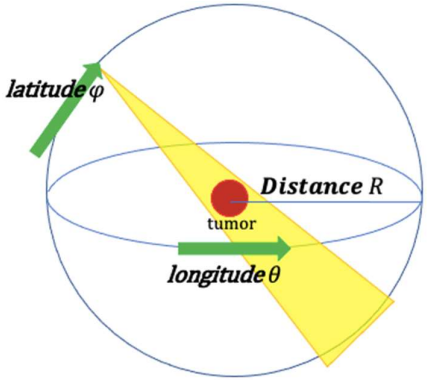

Figure 2 *operation range of Vero4DRT*

We created a distance map using the risk scores of each tissue within the range set in the above procedure. In order to judge the combined risk score and the combined risk score, we judged whether the risk score is high or low by the intensity of red color. Colors are represented by the three primary colors of light, with red, green, and blue represented by 256 colors each.

Therefore, the value $A_{\theta\varphi}$ in red is given as

$$A_{\theta\varphi} = 255 - \left(255 \times \left(\frac{D_{\theta\varphi}}{D_{max}}\right)\right).$$

Here, $D_{\theta\Phi}$ is the risk score of irradiation position (θ, φ) and D_{max} is the largest risk score. Figure 3 shows the screen design of the distance map showing the risk score.

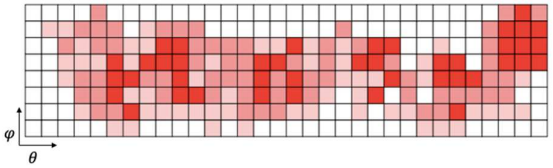

Figure 3 *distance map showing the risk score*

2.2 Irradiation path calculating

We calculated the irradiation path using the distance map created in section 2.1. We calculated the irradiation path by selecting the point with the smallest value of 8-neighborhood points from a starting point to the end and searching the best path by A* algorithm. The A* algorithm is basically one of the algorithms used for two-dimensional graph search (2). The A* algorithm uses the distance from the start position to the current position and a heuristic function to search the path. A heuristic function is an expectation or estimate of the value from the current position to the destination position. In this study, we have mapped objects in three dimensions to two dimensions based on the latitude and longitude information. Therefore, the distance $dist(\theta, \varphi)$ in 3 dimensions when the current position is longitude θ and latitude φ is given as

$$dist(\theta, \varphi) = Rcos^{-1}(sin\theta sin\Theta + cos\theta cos\Theta \cos(\Phi - \varphi)).$$

Here, R is the distance between the gantry and the tumor, and Θ and Φ are the longitude and latitude of the arrival point. In this study, we use a risk score for $dist(\theta, \varphi)$ as a heuristic function. The heuristic function $H(\theta, \varphi)$ when the current position is longitude θ and latitude φ is given as

$$H(\theta, \varphi) = dist(\theta, \varphi) + I \times \frac{D_{\theta\varphi}}{D_{max}}.$$

Here, $dist(\theta, \varphi)$ is when the current position is longitude θ and latitude φ, I is influence on searching the path, $D_{\theta\Phi}$ is the risk score of irradiation position (θ, φ) and D_{max} is the largest risk score. Figure 4 shows the screen design of irradiation path on the distance map showing the risk score. Here, blue line indicates irradiation path.

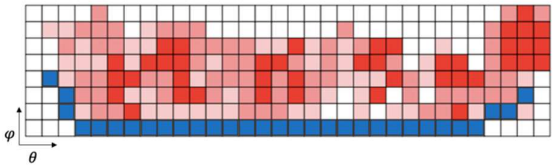

Figure 4 irradiation path on the distance map

2.3 Evaluation using a treatment planning system

We evaluated the treatment plan along the calculated irradiation path using the treatment planning system. We calculated the dose distribution and DVH of the treatment plan created by adding the irradiation model and dose, along the irradiation path calculated in section 2.2.

3. RESULTS

We conducted an evaluation experiment of calculated irradiation path. In this experiment, we used a lung phantom with the spinal cord set as normal tissue for a lung tumor patient. We calculated the dose distribution of treatment plan using a treatment planning system (Eclipse TPS Ver. 15.1 (Varian Medical Systems, Palo Alto, USA)).

3.1 Distance map and irradiation path

We created a distance map of irradiation longitude from 0 to 360 and irradiation latitude from -90 to 90 by setting the weight of the spinal cord as 1. Figure 5 shows the distance map of lung phantom. Here, Red shading indicates the variation of the risk score and yellow line indicates the position of longitude 0 and latitude 0.

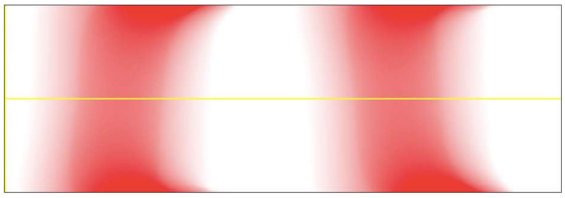

Figure 5 *distance map of lung phantom*

We calculated the irradiation path using the above distance map. Figure 6 shows the irradiation path on the distance map. Here, blue line indicates the irradiation path, red shading indicates the variation of the risk and yellow line indicates the position of longitude 0 and latitude 0.

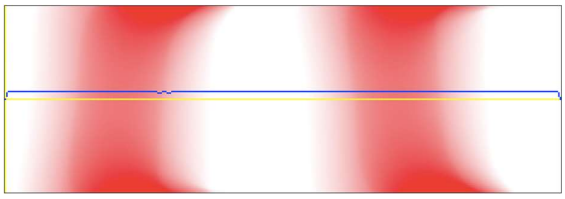

Figure 6 *irradiation path on distance map*

From Figure 6, we observed that the irradiation path passes through a low risk score position. Therefore, we thought that searching the best path by A* algorithm did exactly what we expected it to do.

3.2 Dose distribution of treatment plan

We calculated the dose distribution in treatment plan of lung phantom using the treatment planning system along the irradiation path calculated in section 3.1. Figure 7 shows the dose distribution of treatment plan of lung phantom. Here, pink issue indicated spinal cord, yellow issue indicated GTV.

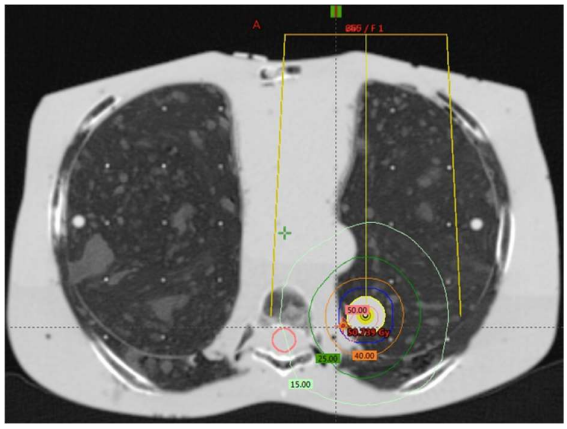

Figure 7 *dose distribution of treatment plan*

4. DISCUSSION

We calculated DVH of treatment plan of lung phantom. using a treatment planning system. Figure 8 shows that DVH of treatment plan of lung phantom. Here, spinal cord indicates the pink line, GTV indicates the yellow line.

Figure 8 *DVH of treatment plan*

From Figure 7 and Figure 8, we observed that the dose distribution focuses GTV and radiation dose to spinal cord was minimized as much as possible. We thought that this calculated irradiation path is radiation dose to normal tissues was minimized while the prescribed dose was delivered to the target. There is a limitation to this study. In the lung phantom used in this experiment, Normal tissue position was close to target position. Therefore, the distribution of risk score in the distance map was not as simple as shown in the Figure 5 and irradiation path was almost straight path as shown in the Figure 6. Therefore, Future outlook for this study include conducting experiments on complex tissue phantoms such as the brain. The experiments allow us to evaluate a better the performance of this system.

5. CONCLUSION

In order to reduce the burden of physicians, we developed a system to calculate an irradiation path of treatment plan of radiation therapy for dynamic-wave-arc irradiation instead of physicians. The purpose of this study was to calculate a dynamic-wave-arc irradiation path which has passed over normal tissues reduced as much as possible. In this experiment, we used a lung phantom with the spinal cord set as normal tissue for a

lung tumor patient. The dose distribution and DVH were calculated using a treatment planning system. As a result, calculated irradiation path is radiation dose to normal tissues was minimized while the prescribed dose was delivered to the target. From this preliminary phantom study, it will be feasible to calculate a dynamic-wave-arc irradiation path which has passed over normal tissues reduced as much as possible, further investigation is required though.

ACKNOWLEDGEMENTS

This study was partly supported by JSPS KAKENHI Grant Number JP 18K07650.

REFERENCES

1. Takashi Mizowaki et al (2013) Feasibility evaluation of a new irradiation technique: three dimensional unicursal irradiation with the Vero4DRT (MHI-TM2000). Journal of Radiation Research. 54:330-336
2. Peter E. Hart, Nils J. Nilsson, Bertram Raphael (1968) A Formal Basis for the Heuristic Determination of Minimal Cost Paths. IEEE Transactions on Systems Science and Cybernetics. 4(2)

Comparison of field output factors of different detectors in small field for 6 MV flattening filter and flattening filter free photon beams

Surendra Dhungana [1], Suphalak Khachonkham [1], Pimolpun Changkaew [1], Warinthorn Rattanaareeyakorn [1], Panun Sritubtim [1], Nauljun Stansook [1], Supakiet Piasanthia [1] Pornpan Yongvithisatid [2], Puangpen Tangboonduangjit [1]

1. Masters of Science Program in Medical Physics, Department of Diagnostic and Therapeutic Radiology, Faculty of Medicine Ramathibodi Hospital, Mahidol University, Thailand,
2. Radiosurgery Centre, Faculty of Medicine Ramathibodi Hospital, Mahidol University, Thailand,

Abstract

This work aims to compare the small field output factors (FOF) of detectors in WFF and FFF modes. FOF was measured with 5 detectors (Electron Field Diode-3G, Microdiamond, Ionization chamber - CC01, Dosimetric diode SRS and Edge) for 6 MV WFF and FFF modes in Varian's Edge accelerator. Field sizes (FS) range of 0.6×0.6 - 3×3 cm^2 with a reference field of 10×10 cm^2 were scanned in Blue Phantom^2 system controlled by OMNIPRO-ACCEPT software. Individual detector equivalent square field sizes (S_{clin}) were used for calculation of FOF except for CC01 for which Microdiamond's S_{clin} was considered. The mean (reference) corrected FOF of all detectors for nominal square fields of 0.6, 1, 1.5, 2, 2.5, and 3 cm^2 are 0.498, 0.671, 0.751, 0.790, 0.813, 0.831 in WFF mode and 0.529, 0.688, 0.762, 0.797, 0.821, 0.839 in FFF mode respectively. The Standard error of the mean (SEM) are 0.0032, 0.0016, 0.0013, 0.0014, 0.0011, 0.0013 for WFF and 0.0014, 0.0033, 0.0032, 0.0030, 0.0029, 0.0025 for FFF modes for the respective field sizes mentioned above. The SEM of corrected output factors is higher for FFF than WFF mode in all FS except 0.6×0.6 cm^2. There is the decreasing trend of SEM with an increase in F.S in both modes for FS >0.6 ×0.6 cm^2.

Keywords: Small field output factors, Detectors, Flattening filter, Flattening filter free

1. INTRODUCTION

The use of radiation in small fields have increased dramatically due to the availability of advanced techniques and radiotherapy has become the precision medicine in modern days. The radiation behaviour in larger fields have come to the limelight due to extensive experimentation in the last few decades and dosimetry process are within acceptable limits. However, for small fields, no extensive researches have been made and scientific literatures are sparsely distributed [1]. International Atomic Energy Association (IAEA) and American Association of Physicists in Medicine (AAPM) jointly produced the standardized codes of practices (COPs), Technical Report Series no. 483 (TRS- 483) for small fields recently. Considering the limitations of conventional COPs; TRS-483 has developed standardized guidance for absorbed dose determination in small fields and for those systems where reference conditions cannot be achieved by introducing the concept of machine-specific reference (msr) field. Furthermore, for standardization purpose, TRS-483 also have provided the detector specific correction factors (CF) for different field sizes and the commonly used detectors.

Modern linear accelerators are equipped with dual options; with flattening filter (WFF) and flattening filter-free (FFF). The possibility of prescribing a higher dose per fraction in a short time are favoring the use of FFF [2,3]. The higher dose rate and density effects of the detectors for the softer spectrum in FFF mode compared to WFF beams can alter detector responses in small fields. Till date; a huge amount of publications is available for WFF beams whereas limited publication can be seen for FFF beams and if the recent modalities are to be used with FFF mode, it needs better understanding [1,4,5].

The conventional output factors (OF) differ significantly from small field output factors. At small fields; application of CF (values derived experimentally or calculated by Monte Carlo) is essential [1,4]. The difference in detectors response in clinical and reference field size are considered by these CF. The OF in broad beam commonly uses the approach of the ratio of detector readings at clinical field size to reference field size at specified depth due to approximate constancy of stopping power and perturbations ratios with field size. In the small field, these quantities vary due to detector related effects, mostly perturbation factors including volume averaging and hence may result in inaccuracy if conventional method of calculation is used and unsuitable detectors are used [6].

2. MATERIAL AND METHODS

The study was performed at the Department of Diagnostic and Therapeutic Radiology in Ramathibodi Hospital using Varian's Edge linear accelerator with flattening filter and flattening filter-free 6 MV photon beams. Five small field detectors; namely EFD-3G and CC01 (IBA), Edge detector (Sun Nuclear), PTW60018 and microdiamond detector (PTW) were used for the experiment for determining the output factors. The Blue Phantom^2, a 3D water phantom system from IBA with its scanning software OmniPro-Accept 7 (version 7.4 c) was used for the experimentation.

2.1 Experimental setup

Mechanical QA of the accelerator for gantry angle indicators was performed with the spirit level and was set at 0^0 each time before the start of experimentation. For the scanning system using OMNIPRO ACCEPT 7; scan speed, step size, sensitivity, penumbra margins etc. were predetermined through optimization for a range of field sizes under study and consecutively used during the experimentation.

A 3-D full scatter water phantom (Blue Phantom 2, IBA Dosimetry) was set up with the help of machine crosshair and the marks at the base of the phantom system. Connections to the water reservoir, levelling of the apparatus with the 4-point levelling mechanism, connections between the detector and common control unit (CCU) and to computer unit with OMNIPRO ACCEPT 7 software and detector holder placement were done. Isocentric setup with SSD of 90 cm, measurement depth of 10 cm was set. The initial alignment of the detector with the beam central axis was performed with the help of machine cross-hair, room lasers and the marks on the detectors; further refinement was done using the scanning system by measuring the beam profiles in two dimensions [6]. Each detector under study was set at its effective point of measurement at 10 cm depth except for CC01 for which the chamber's center was kept at the depth 10 cm (as stated in TRS 483 for the CC01). The software's capability to offset the detector depth was utilized to precisely position the depth of each of the detectors relative to detector-specific landmarks [4,6,7]. Jaw defined nominal field sizes were set at 0.6 × 0.6, 1 × 1, 1.5 × 1.5, 2 × 2, 2.5 × 2.5, 3 × 3, and 10 × 10 cm^2 with multi-leaf collimators fully retracted.

The detector orientation either perpendicular or parallel was performed considering the smallest dimension of its sensitive volume is perpendicular to the scanning direction whenever possible [6,9]. CC01 and Edge were positioned with their axis perpendicular to the beam axis. The microdiamond, SRS diode, and EFD-3G were set with their axis parallel to the beam axis as given in Table 1. For CC01 ionization chamber, the readings were corrected for influence quantities ($K_{T,P}$, K_{Pol} and K_s). Biasing voltage (+300V) was used for CC01 and no biasing voltage for other detectors.

Table 1. Detectors setup

S.N	Detectors	Offset Point	Orientation
1	EFD-3G	(+) 1.2mm	Parallel
2	Microdiamond	(+) 1mm	Parallel
3	Edge	0 mm	Perpendicular
4	CC01	0 mm	Perpendicular
5	SRS Diode	(+) 0.7	Parallel

The conventional field size of 10 × 10 cm^2 was used as reference field size. For the experiment; 100 - 500 MU with a dose rate of 400 - 800 MU /Min was delivered to each nominal field sizes under study in WFF and FFF modes. The details of the scan and measurement parameters are given in Table 2. FWHM in inline and crossline direction was determined to find actual clinical field size (s_{clin}) [6]. The S_{clin} is calculated as per the equation below initially suggested by Cranmer-Sargison et al [8] and accepted in COP of TRS-483.

$$S_{clin} = \sqrt{A\,B} \qquad (1)$$

Table 2. Scan and measurement parameters

S.N	Detectors	Sensitivity	Voltage applied	MU and Dose rate (WFF)	MU and Dose rate (FFF)	Scan speed, step size and penumbra margin
1	EFD-3G	Medium	0	100 ,400 MU/Min	100 ,800 MU/Min	Scan speed 10mm/s 0.1 mm step size and 5mm penumbera in step by step mode for small FS. 1 mm step size and relative 20 % penumbra margin in continuous mode for reference FS.
2	MID	High	0	200 ,400 MU/Min	200 ,800 MU/Min	
3	Edge	Medium	0	100 ,400 MU/Min	100 ,800 MU/Min	
4	CC01	High	(±) 300, (+100)	500 ,600 MU/Min	500 ,800 MU/Min	
5	SRS diode	Medium	0	100 ,400 MU/Min	100 ,800 MU/Min	

Where; A= FWHM in y-axis (in-plane)

B= FWHM in x-axis (cross plane)

For output factor measurement of smaller fields (≤ 2 × 2 cm^2); the central axis alignment of the detector with radiation isocenter of the beam was performed by generating the inline and crossline profiles in WFF mode. At first, it was performed in 2 × 2 cm^2 position and the necessary shifting of the detector with the help of software was done to align detector with the isocenter. Rescanning was performed at 2 × 2 cm^2 to reconfirm it. If within the tolerance level of ± 0.1mm

then further scanning was done at 1 × 1 cm^2 for verification. If the result was seen to be within the tolerance for 1 × 1 cm^2 then only the output factors were measured for other fields. This was the iterative process until radiation iso-centre and the central axis matches.

Small field output factor is calculated using the equation as follows by interpolating and applying the CF from Table 26 of TRS 483.

$$\Omega_{Q_{clin},Q_{msr}}^{f_{clin},f_{msr}} = \frac{M_{Q_{clin}}^{f_{clin}}}{M_{Q_{msr}}^{f_{msr}}} k_{Q_{clin},Q_{msr}}^{f_{clin},f_{msr}} \qquad (2)$$

2.2 Statistical calculations

The mean value of 3 readings of each detectors reading per field sizes was obtained and then the mean of the means was obtained following for one field size of all detectors for calculation of the standard error of the mean.

3. RESULTS

The conventional (uncorrected / TRS 398 method) output factors of each detector are seen to deviate more from the mean in both WFF and FFF mode. The small field (corrected / TRS 483 method) output factors of each detector are seen to deviate less from the mean in comparison to the conventional method and all detectors output appears to be in close agreement to the mean. Microdiamond has slightly higher small field output factor than the mean in both modes (exception seen in 0.6×0.6 cm^2 in WFF mode). Edge values are lower than the mean throughout the fields for FFF mode and in WFF mode fluctuations are noted. EFD-3G values are slightly lower but in a consistent manner lesser than the mean for both modes. CC01 corrected outputs are the same as the mean in FS ≥ 1.5 × 1.5 cm^2 in WFF mode whereas in FFF modes the values are greater than mean for FS 1 × 1 cm^2 to 2 × 2 cm^2. SRS diode has consistently lower output factors than the mean in both modes (exception FS 0.6 × 0.6 cm^2 in WFF mode). The discrete values and the SEM are given in Table 3.

The uncorrected, as well as corrected small field output factors, are larger for FFF mode in comparison to WFF mode as shown in Table 3 for all the detectors measured in Varian's Edge system. SEM is higher for uncorrected output factors in both WFF and FFF modes. The SEM seems to decrease significantly in corrected small field output factors for both modes. Similarly, in the comparison between the modes; SEM seems greater for FFF mode except for small sizes ≤ 1 × 1 cm^2 for uncorrected output factors and field size 0.6 × 0.6 cm^2 for corrected output factors.

The mean (reference) FOF of all detectors for nominal square fields of 0.6, 1, 1.5 ,2, 2.5 and 3 cm^2 after the application of the correction factors are 0.498, 0.671 ,0.751 ,0.790, 0.813, 0.831 in WFF mode and 0.529 ,0.688,0.762, 0.797, 0.821, 0.839 in FFF mode respectively. The Standard error of the mean (SEM) are 0.0032, 0.0016, 0.0013, 0.0014, 0.0011, 0.0013 for WFF and 0.0014, 0.0033, 0.0032, 0.0030, 0.0029, 0.0025 for FFF modes for the respective field sizes mentioned above.

Table 3. Discrete values of corrected output factors, mean, SD and SEM in FFF and WFF mode.

Corrected – Small field output factors								
WFF Mode								
F.S (cm^2)	Edge	MID	EFD-3G	CC01	SRS diode	Mean FOF	S.D	SE of the mean
0.6		0.497	0.494		0.504	0.498	0.0055	0.0032
1	0.671	0.677	0.670	0.668	0.669	0.671	0.0036	0.0016
1.5	0.752	0.756	0.749	0.751	0.747	0.751	0.0032	0.0015
2	0.790	0.795	0.787	0.790	0.787	0.790	0.0034	0.0015
2.5	0.811	0.818	0.811	0.813	0.811	0.813	0.0028	0.0013
3	0.828	0.836	0.829	0.831	0.830	0.831	0.0032	0.0014
FFF mode								
0.6		0.531	0.526		0.528	0.529	0.0024	0.0014
1	0.682	0.700	0.687	0.689	0.682	0.688	0.0073	0.0033
1.5	0.760	0.773	0.758	0.765	0.754	0.762	0.0072	0.0032
2	0.795	0.808	0.793	0.799	0.791	0.797	0.0068	0.0030
2.5	0.819	0.832	0.816	0.820	0.816	0.821	0.0064	0.0029
3	0.836	0.849	0.835	0.839	0.836	0.839	0.0056	0.0025

4. DISCUSSION

For centering the detector with the radiation field, the process was performed in WFF mode only and subsequently used for FFF mode as we had verified pre-experimentally that the center of the detector with the

radiation beam are almost equal for both WFF and FFF modes.

The density effects of the detector in flattening filter free (FFF) with soft spectrum compared to with flattening filter (WFF) beams can alter detector responses in small fields and hence the output factors in FFF are higher than the WFF modes; similar are the results in a study by Casar et al [2,4]. The small field corrected output factors of each detector are seen to deviate less from the mean in comparison to the conventional method and all detectors output appears to be in close agreement to the mean. Hence the SEM of the corrected output factors are in general less than the uncorrected ones for both modes.

Similarly, in the comparison between the modes; SEM seems greater for FFF mode except for small sizes $\leq 1 \times 1$ cm^2 for uncorrected output factors and field size 0.6×0.6 cm^2 for corrected output factors. The reason for SEM generally high for FFF mode can be explained as the higher uncertainties associated with FFF mode and the beam itself being less stable in comparison to WFF [1,10].

There is an overall decreasing trend of SEM with the increase in FS (exception 0.6×0.6 cm^2 in FFF mode). The reason for this trend is that perturbation related with FS and detector decreases as the FS increases or the small field condition vanishes [4,6,8].

An exception; dose rate of 600 MU/Min was given for CC01 in WFF mode. The ionization chamber is dose rate-independent and after performing the corrections for the recombination of the ions the detector response with changing dose per pulse remains stable (< 0.1 %) [6]. Hence this may not have caused any difference for the obtained results.

5. CONCLUSION

Microdiamond's small field output factors are slightly higher than the mean in both modes (exception for FS 0.6×0.6 cm^2 in WFF mode). Edge values are lower than mean throughout the fields for FFF mode (fluctuating values for WFF mode). EFD-3G and SRS diode values are consistently lesser than the mean for both modes (exception 0.6×0.6 cm^2 for SRS diode in WFF mode). CC01 values are the same as the mean in FS $\geq 1.5 \times 1.5$ cm^2 in WFF mode whereas in FFF modes the values are greater than mean for FS 1×1 cm^2 - 2×2 cm^2.

The SEM of corrected output factors is higher for FFF than WFF mode in all FS except 0.6×0.6 cm^2. There is the decreasing trend of SEM with an increase in FS in both modes for FS $>0.6 \times 0.6$ cm^2.

ACKNOWLEDGEMENTS

The authors would like to acknowledge Radiosurgery Centre, Faculty of Medicine Ramathibodi Hospital for authorizing to perform the experimentation in Varian's Edge Linear accelerator. This study is partially supported by the Faculty of Graduate Studies and Graduate Studies of Mahidol Alumni Association.

REFERENCES

1. Palmans H, Andreo P, Huq MS, Seuntjens J, Christaki KE, Meghzifene A. Dosimetry of small static fields used in external photon beam radiotherapy: Summary of TRS-483, the IAEA–AAPM International Code of Practice for reference and relative dose determination. Med Phys; 2018; 45: e1123– e1145
2. Reggiori G, Mancosu P, Suchowerska N, Lobefalo F, Stravato A, Tomatis S, et al. Characterization of a new unshielded diode for small field dosimetry under flattening filter-free beams. Phys Med; 2016;32(2):408-13.
3. Cashmore J. The characterization of unflattened photon beams from a 6 MV linear accelerator. Physics in medicine and biology. 2008;53(7):1933-46.
4. Casar B, Gershkevitsh E, Mendez I, Jurković S, Huq MSJMp. A novel method for the determination of field output factors and output correction factors for small static fields for six diodes and a microdiamond detector in megavoltage photon beams. 2019;46(2):944-63
5. Tyler M, Liu P, Lee C, McKenzie D, Suchowerska N. Small field detector correction factors: Effects of the flattening filter for Elekta and Varian linear accelerators. Journal of applied clinical medical physics / American College of Medical Physics. 2016; 17:6059
6. International Atomic Energy Agency. Technical Reports Series No. 483. Dosimetry of Small Static Fields Used in External Beam Radiotherapy. An International Code of Practice for Reference and Relative Dose Determination. IAEA. Vienna, 2017
7. Kragl G, Wetterstedtaf S, Knausl B, Lind M, McCavana P, Knoos T, et al. Dosimetric characteristics of 6 and 10 MV unflattened photon beams: Radiother Oncol; 2009;93(1):141-6
8. Cranmer-Sargison G, Charles PH, Trapp JV, Thwaites DIJR, Oncology. A methodological approach to reporting corrected small field relative outputs. Radiother Oncol; 2013;109(3):350-5
9. Alfonso R, Andreo P, Capote R, Huq MS, Kilby W, Kjall P, et al. A new formalism for reference dosimetry of small and nonstandard fields. Transl Biophotonics; 2008;35(11):5179-86.
10. Tyler M, Liu P, Lee C, McKenzie D, Suchowerska N. Small field detector correction factors: Effects of the flattening filter for Elekta and Varian linear accelerators. J Appl Clin Med Phys; 2016; 17:6059

Paper ID 142

Grey Matter Segmentation of T1-Weighted MR Image in Ischemic Stroke Patients using *k*-Means Clustering

Dian Yuliani Alam[1]

1 Department of Physics, University of Brawijaya, Malang, Indonesia

Abstract

The grey matter in the brain plays an important role to process the information. In ischemic stroke patients, it could experience some neurological dysfunctions. This could be diagnosed through the T1-weighted MR (Magnetic Resonance) image, since it shows the grey matter brighter. The T1-weighted MR image is based on the longitudinal relaxation, which the energy of radio-frequency is released to the surrounding tissue. In this research, the T1-weighted images of ischemic stroke patients was used for the grey matter segmentation with *k*-means clustering to analyze the correlation of T1-weighted image and ischemic stroke towards the grey matter. The Time Echo (TE) parameter in the T1-weighted image also was analyzed. The data were taken from 7 ischemic stroke patients and 6 normal patients. The obtained result showed that the T1-weighted images of all patients had short TE values. This made the T1-weighted image disallows the contrast swap between grey matter and cerebrospinal fluid (CSF). This also proved by the *k*-means clustering segmentation method, which showed the mean pixel intensity of grey matter in between white matter and CSF, while the mean pixel intensity of white matter is highest in both patient image type. Furthermore, the mean pixel number or grey matter area of ischemic stroke patient images was less than the normal patient images. This is more likely due to the infarction in the brain of ischemic stroke patients.

Keywords: Grey matter, T1-weighted image, ischemic stroke, *k*-means clustering

1. INTRODUCTION

The human central nervous system consists of two tissues: grey matter and white matter. The grey matter is mainly composed by nerve cell bodies (perikarya) and unmyelinated axons, while the white matter is composed mostly of myelinated axons and very small numbers of perikarya.

The grey matter plays an important role to process information in the brain. It processes the signals from the sensory organs or other grey matter areas. Then, the signals are transmitted to neurons in central nervous system and responded by synapses (1).

In ischemic stroke patients, the grey matter experiences some neurological dysfunctions. Diao *et al.* found that the grey matter volume (GMV) decrease in the motor cortex of right-handed chronic subcortical ischemic stroke patients causes the motor deficit. Furthermore, the partial recovery patients had significant GMV decrease than the complete recovery patients and healthy controls in the right somatomotor cortex. This is due to the lesion-side effect (2). Stebbins *et al*. also found that the GMV reductions in ischemic stroke patients cause the impairment in one or more cognitive domains, including orientation, attention, working memory, language, visuospatial skills, psychomotor speed, and memory (3). Wang *et al*. confirmed more about the GMV reduction in their study of pontine ischemic stroke (4).

The studies above used the Magnetic Resonance Imaging (MRI) because it is able to localize the brain infarction area. Moreover, one of its basic pulse sequences, T1-weighted image, could show the grey matter quite bright (5), so the GMV decrease could be diagnosed. The T1-weighted image uses the longitudinal relaxation, which the energy of radio-frequency is released to the surrounding tissue (6).

In this research, the T1-weighted images of ischemic stroke patients was used for the grey matter segmentation with *k*-means clustering to analyze the correlation of T1-weighted image with grey matter, as well as the correlation of grey matter with ischemic stroke. The Time Echo (TE) image parameter also was analyzed.

2. MATERIAL AND METHODS

2.1 Patient Images

The T1-weighted axial images of 7 ischemic stroke patients (age range 8 – 61 years) and 6 normal patients (age range 10 – 47 years) were taken in the Radiology Installation of Saiful Anwar Regional Public Hospital, Malang, Indonesia. The images were acquired using MRI 1.5 T SIGNA Explorer GE and MRI 3 T Ingenia Philips.

2.2 Grey Matter Segmentation

The DICOM image files were opened in RadiAnt DICOM Viewer version 2020.1.1 (64-bit). The selected image parameter for analysis was the Time Echo (TE). Then, the files were converted into .jpg extension with size 512 × 512 pixels.

MATLAB software version 2014b was used for image segmentation. The input .jpg image in RGB color space was converted into the grayscale to obtain a one channel (green channel) image, which can more easily distinguish the contrasts in grayscale intensity and also has less noise.

Next, the cranium part was stripped by thresholding to obtain more accurate results when clustering brain tissues. The used functions were *bwlabel* (to label all blobs), *ismember* (to strip the outermost blob or cranium), and *imdilate* (to thicken edges).

The *k*-means was used to cluster brain tissues by 4 clusters. The stripped image was converted into the double-precision array to obtain the grey level, which indicates the pixel intensity. The initial cluster centroid (representation of each cluster) positions were chosen by applying the *k*-means++ algorithm. It uses a heuristic to find the seeds of centroid.

Furthermore, the cluster centroids were computed with the squared Euclidean distance to obtain the mean of the cluster points. The replication (number of times to repeat clustering) was 10 with maximum iteration of 30. Then, the cluster indexes were reshaped into the clustered image.

To distinguish the clusters better, each cluster was assigned with different colors by converting the clustered image into the RGB image using the *label2rgb* function. It determined the color for each cluster based on the number of objects in the label matrix and color range in the colormap. The used colormap was *hsv*.

To segment the grey matter tissue, the RGB image was converted into the HSV image. Its main advantage was to separate hue (color component) from saturation (color intensity) and value (color brightness). These were threshold set for grey matter segmentation, with hue had a minimum value of 0.396 and a maximum value of 0.709, while the saturation and value had a minimum value of 0 and a maximum value of 1. Then, the HSV image was masked to count the pixel numbers.

3. RESULTS

3.1 The Time Echo (TE) Parameter Data

The TE data of patients are shown in Table 1 and Table 2. The values are quite varied because two different magnetic fields were used. The images of patient D, L, N, O, and P were acquired in 1.5 T, while the others were in 3 T.

Table 1 *TE parameter of ischemic stroke patient images.*

Patient (age)	TE (ms)
A (8)	3.15
B (32)	3.17
C (35)	3.16
D (36)	13.0
E (48)	3.27
F (60)	6.58
G (61)	3.16

Table 2 *TE parameter of normal patient images.*

Patient (age)	TE (ms)
H (10)	3.28
I (19)	13.0
J (27)	3.18
K (33)	13.0
L (40)	13.0
M (47)	10.0

3.2 Image Processing

The T1-weighted axial images of ischemic stroke and normal patients are processed through RGB image conversion into grayscale, skull stripping, k-means clustering, label coloring, and grey matter segmentation. The processes can be seen in Figure 1.

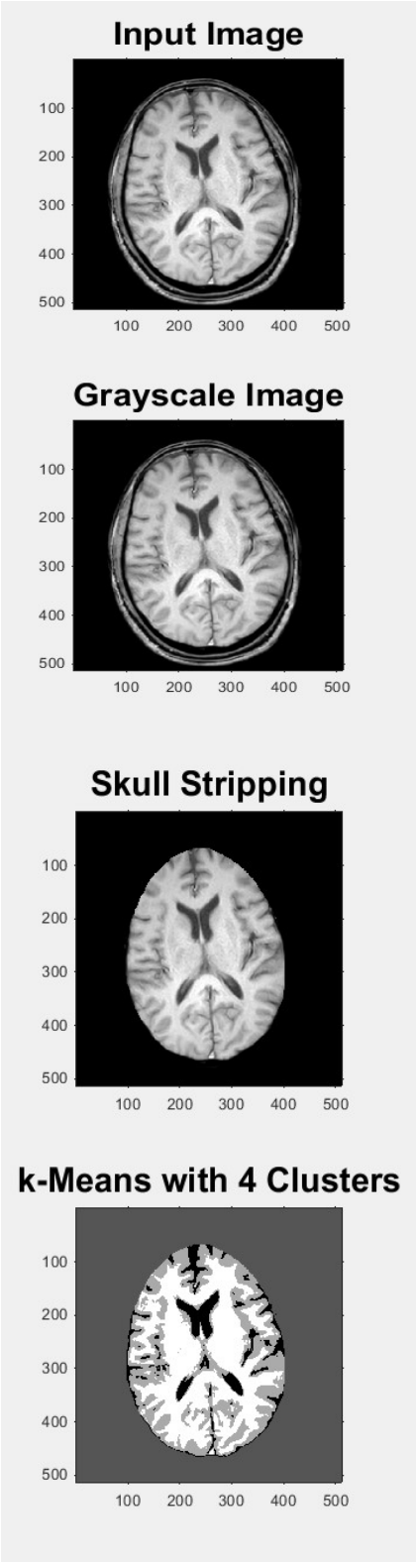

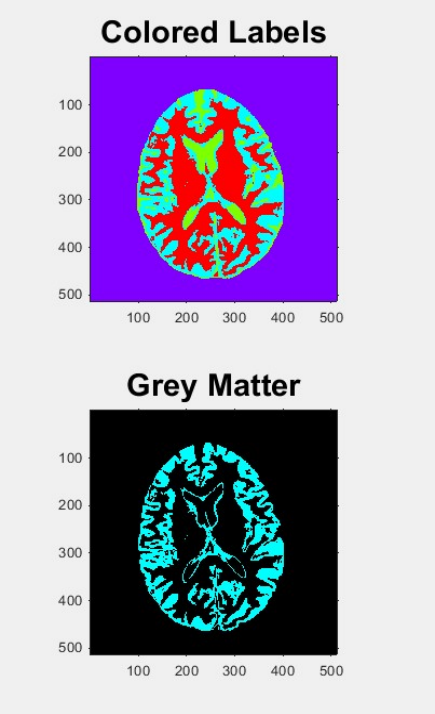

Figure 1 *The T1-weighted axial image processing of patient F*

3.3 Mean Pixel Intensity

The mean pixel intensity is obtained from the calculation of cluster centroids. There are four clusters, which consist of the background (first cluster), CSF (second cluster), grey matter (third cluster), and white matter (fourth cluster). The data are shown in Table 3 and Table 4.

Table 3 *Mean pixel intensities of ischemic stroke patient images.*

Patient	*Cluster Number*			
(Age)	*1*	*2*	*3*	*4*
A (8)	*0.094*	*203.149*	*88.682*	*115.963*
B (32)	*0.115*	*81.604*	*119.494*	*151.518*
C (35)	*0.246*	*85.792*	*130.359*	*173.536*
D (36)	*0.076*	*35.442*	*59.189*	*75.524*
E (48)	*0.105*	*82.725*	*130.270*	*175.027*
F (60)	*0.150*	*93.684*	*161.964*	*209.436*
G (61)	*0.390*	*48.184*	*90.657*	*122.824*

Table 4 *Mean pixel intensities of normal patient images.*

Patient	*Cluster Number*			
(Age)	*1*	*2*	*3*	*4*
H (10)	*0.052*	*97.530*	*127.553*	*159.462*
I (19)	*0.032*	*37.526*	*61.075*	*77.784*
J (27)	*0.643*	*91.229*	*137.703*	*185.164*
K (33)	*0.067*	*39.005*	*60.298*	*76.275*
L (40)	*0.063*	*33.904*	*57.299*	*73.239*
M (47)	*0.050*	*33.661*	*56.354*	*70.672*

3.4 Grey Matter Pixel Number

The pixel number is obtained from the area calculation of masked HSV image. It represents the grey matter area in pixel unit. The data can be seen in Table 5 and the data significance test can be seen in Table 6.

Table 5 *The pixel number of all patient images.*

Ischemic Stroke Patient (age)	*Pixel Number*	Normal Patient (age)	*Pixel Number*
A (8)	*42,576*	H (10)	*32,072*
B (32)	*28,736*	I (19)	*33,947*
C (35)	*30,535*	J (27)	*34,393*
D (36)	*38,582*	K (33)	*36,778*
E (48)	*30,674*	L (40)	*37,172*
F (60)	*36,342*	M (47)	*34,624*
G (61)	*31,157*		

Table 6 *Mean pixel number significance test.*

Patient Image Type	*Mean Pixel Number*	*Mean Difference*	*p-value*
Ischemic Stroke	*34,086*	*- 0.745*	*0.745*
Normal	*34,831*		

4. DISCUSSION

4.1 The T1-Weighted Image and Grey Matter

Basically, a MR image is a water distribution map. It has limited clinical values, since the water density varies relative slightly between tissues. Its contrast can be manipulated through weighting according to the tissue relaxation time.

One of the MR image weightings, the T1-weighting, is based on the longitudinal relaxation. It is caused by the hydrogen nucleus releasing its energy to the surrounding environment or tissue (spin-lattice relaxation). The released energy then makes a magnetization recovery in the longitudinal plane. This recovery is exponential and has a time constant, which called T1 or longitudinal relaxation time (6).

The T1-weighted image depends on many parameters. One of them is time echo (TE). It is the time between the 90^0 excitation pulse and the peak of the induced signal in the coil (echo). It is also an important parameter because it can influence the image contrast extremely in all sequences (5).

In Table 1 and Table 2, TE values in all patient images are short (less than 30 ms) (7). The shorter TEs are found in the higher field strength (3 T), which less than 10 ms, because the shorter TE and high field strength allow more longitudinal relaxation, less spin dephasing or transversal relaxation, and more signal.

The shorter TE also disallows the contrast swap between grey matter and cerebrospinal fluid (CSF). The early echo shows grey matter brighter than CSF, while the late one shows the vice versa (5). This can be seen in Table 3 and Table 4 where the mean pixel intensity of grey matter cluster is higher than CSF one in all patient images, except patient A. It might be related to the shorter TE than other patients, but it needs further study.

Table 3 and Table 4 also show that the mean pixel intensity of white matter cluster is highest in all patient images, except patient A. The results correspond well with a study of the T1 MEMP (Multi Echo Multi Planar) image that used the short TE (8). Other references (5, 7) also confirm that the white matter has the highest signal intensity in the T1-weighted image. Therefore, the T1-weighted image shows grey matter intensity somewhere in between white matter and CSF intensities.

4.2 The Grey Matter and Ischemic Stroke

The *k*-means clustering is one of the most useful methods for brain image segmentation. It is the simplest unsupervised clustering algorithm that classifies the pixel intensities through a predefined number of clusters without any preceding information (9). It also can be combined with other techniques, for instance the object counting (10). In this study, the *k*-means clustering is used for grey matter segmentation followed by the mean pixel intensity calculation and object (pixel number) counting for grey matter area calculation.

Table 5 shows the grey matter area or pixel number of all patient images. The data can be grouped into four age groups (11); pediatric patients (A and H), adolescent patient (I), adult patients (B, C, D, J, K, and L), and elderly patients (E, F, G, and M). The pixel number of ischemic stroke patient A's image is greater than the normal patient H's image due to the shorter TE. The mean pixel number of ischemic stroke adult patient images (32,618) is less than the normal adult patient images (36,114). The mean pixel number of ischemic stroke elderly patient images (32,724) also is less than the normal elderly patient image (34,624).

Furthermore, without seeing the age group, the mean pixel number of ischemic stroke patient images is less than the normal patient images. It is more likely due to the infarction in the brain of ischemic stroke patients. This result corresponds well with other researches (2,3,4), which they used the GMV data. The GMV itself is more related to surface area (12) and it is represented as the grey matter area or pixel number in this study.

However, the mean pixel number difference in both patient image type is not significant, because its *p*-value is greater than 0.05, despite the mean pixel number of ischemic stroke patient images is smaller (Table 6). It is related to the differences in patient age range, TE parameter, and small number of images. The further studies should consider these aspects for accurate result.

5. CONCLUSION

The T1-weighted images of ischemic stroke and normal patients had short TE values. This made the T1-weighted image disallows the contrast swap between grey matter and CSF. It also shows the grey matter intensity in between white matter and CSF intensities, since the mean pixel intensity of white matter is highest in both patient image type. Furthermore, the mean pixel number or grey matter area of ischemic stroke patient images was less than the normal patient images. This is more likely due to the infarction in the brain of ischemic stroke patients. For accurate result, it is important to consider the patient age range, TE parameter, and number of images.

ACKNOWLEDGEMENTS

None. No funding to declare.

REFERENCES

1. Robertson S 2018 *What is Grey Matter?* Available on: http://www.newsmedical.net/health/What-is-Grey-Matter.aspx. Accessed on 27 September 2020
2. Diao Q, Liu J, Wang C, Cao C, Guo J, Han T, Cheng J, Zhang X and Yu C 2017 Gray matter volume changes in chronic subcortical stroke: A cross-sectional study *NeuroImage: Clinical* **14** 679–84
3. Stebbins G T *et al.* 2008 Gray Matter Atrophy in Patients with Ischemic Stroke with Cognitive Impairment *Stroke* **39** 785–93
4. Wang P *et al.* 2018 Correlation of Longitudinal Gray Matter Volume Changes and Motor Recovery in Patients After Pontine Infarction *Frontiers in Neurology* **9** 1–8
5. Blink E J 2004 *MRI: Physics.* Available on: http://mri-physics.net/bin/mriphysics-en rev1.3.pdf. Accessed on 3 October 2020
6. Brown M A and Semelka R C 2003 *MRI: Basic Principles and Applications Third Edition* (New Jersey: John Wiley & Sons Inc.)
7. Schild H H 1990 *MRI Made Easy* (Berlin: Schering AG)
8. Alam D Y, Milani, Rauf N and Samad B A 2020 Study of Longitudinal Relaxation Time Multi Echo Multi Planar (T1 MEMP) and Diffusion Weighted Imaging (DWI) on Magnetic Resonance Imaging (MRI) Image *J.Phys.: Conf. Ser.* **1505** 012033
9. Selvaraj D and Dhanasekaran R 2013 MRI Brain Image Segmentation Techniques – A Review *Indian Journal of Computer Science and Engineering (IJCSE)* **4** 364–81
10. Nasor M and Obaid W 2020 Detection and Localization of Early-Stage Multiple Brain Tumors Using a Hybrid Technique of Patch-Based Processing, k-means Clustering and Object Counting *International Journal of Biomedical Imaging* 1–9
11. Departemen Kesehatan RI 2009 *Sistem Kesehatan Nasional* Jakarta
12. Winkler A M, Kochunov P, Blangero J, Almasy L, Zilles K, Fox P T, Duggirala R and Glahn D C 2011 Cortical Thickness or Grey Matter Volume? The Importance of Selecting the Phenotype for Imaging Genetics Studies *NeuroImage* 53 1135–46

Paper ID 144

Evaluation of the effectiveness of gonad shielding in digital radiography

E.W Kombo[1] J. H. D. Wong[1,2] M.S Nizam[1] K.H Ng[1,2]

1 Department of Biomedical Imaging, Faculty of Medicine, University of Malaya, Kuala Lumpur 50603, Malaysia
2University of Malaya Research Imaging Centre, Faculty of Medicine, University of Malaya, Kuala Lumpur, 50603, Malaysia

Abstract

Objective

This study evaluates the effectiveness of gonads shield in terms of dose reduction factor. It establishes how much reduction is achieved when gonad shields are in place and how it is affected by varying the radiographic parameters, which include tube potential, current-time product (mAs), and automatic exposure control (AEC).

Materials and Methods

An adult anthropomorphic phantom was exposed in anteroposterior pelvic (AP) projection examination. Exposure was done for shielded and unshielded gonads in various adjustments. Using tube voltages (70-100kVp) and mAs (16-25mAs) adjustments when AEC turned off and measured organ absorbed dose at five internal sites and three on the surface points for male study using nanoDot™ optically stimulated luminescent dosimeter (OSLD).

Results

In the male examination, when the AEC was switched on, gonad shield reduced the absorbed dose to the testes by > 87%, dose reduction ranged from 60-70% in the female examination. With manual control of mAs and standard voltage (70kVp), a similar dose reduction in males was observed. However, the dose reduction in female reduction was lesser (45-70%). Various tube potential values with constant mAs dose reductions with values > 84% (85- 89%) and female 57-70% range were obtained.

Conclusion

The effectiveness of gonad shielding is affected by the location of gonads. Male gonads located externally were easily identified and shielded, thus benefited from a larger dose of reduction[2]. In contrast, the actual positions of the female ovaries are not visible and often estimated. This resulted in poorer gonad shielding.

Keywords: contact shields, dose reduction factor, mAs, tube voltage, AEC

1. INTRODUCTION

Gonad shielding in radiography was introduced to limit doses to the gonads both for women and men. When gonad shielding was introduced more than 50 years ago, it was expected to reduce radiation dose to gonads by 95% and for female adults by 50% [1].

Shielding of the gonads requires that gonads to be within 5cm of the X-ray field during exposure; the only exception to this is if the shielding degrades diagnostic information or radiation is more than 5cm away from the pelvis area [2]. This practice is useful for both diagnostic and therapeutic procedures. Usually, a protective shield of either lead or aluminum is placed outside the body to cover the pelvis region. For males, this region is defined below the pelvis girdle being the sensitive region around the testicular region. For females, the part of interest is the pelvis region with sensitive organs such as the uterus and the ovaries. Pelvic shielding was aimed at preventing infertility due to sterility.[1]

The effectiveness of gonad shielding was questioned, especially in the female examination. Subsequently, recommendations have been put forward to halt the practice. This recommendation was based on image quality issues; that the gonad shield obstructs radiological information obstruction. These studies did not include dosimetry assessment. With there being a likelihood of dose increase to organs due to scattering, absorbed dose analysis would be particularly important[3]. A study based on air kerma measurements had shown an increase in absorbed to the gonads when shields are placed[4]. However, air kerma does not represent the actual radiation dose to the gonads.

In the male examination, similar studies have been conducted and shown that gonad shielding resulted in up to 42% of dose reduction for the lumbar spine[5].

The International Commission on Radiological Protection (ICRP), report 103 had reduced the values of radiation risk to the gonads to 0.08[6]. This means that the irradiation of gonads contributes to only 8% risk of stochastic effect due to radiation. Whilst it may seem that radiation risk from diagnostic imaging is too low due to a combination of low dose and risk, there is still justification nonetheless that protection is always a better policy.

With X-ray imaging being widely available and a standard modality of examination, there is an increase in population exposure. Dracham et al. reported that with each Gray (Gy) of radiation exposure, there is an increased rate of solid cancer by about 35% in males and 58% in females[7]. Pelvic and lower abdomen radiography being near reproductive organs, thus is important to consider the efficacy of shielding.

In this study, we attempted to do a wholesome quantitative efficacy analysis of gonad shielding. We examined several physical adjustable parameters disposable to the radiographers to ensure quality pelvic examinations. These parameters are tube voltage, tube current-time, and AEC control.

2. MATERIAL AND METHODS

An anthropomorphic phantom (model no: ART-702G, CIRS Radiology Support Devices, Inc., Norfolk, Virginia, USA) composed of tissue and bone equivalent epoxy resin was irradiated using a Carestream DRX-Evolution system (CARESTREAM HEALTH, USA, New York Inc) digital X-ray system.

For organ dose measurements, the Al_2O_3: C based nanoDot^{TM} dosimeter (Landeur Inc., Glenwood, US) were used (Figure 1). The InLight® microStar reader (Landauer Inc., Glenwood, IL, USA) was used to read the dosimeters.

Figure 1: *The nanoDot^{TM}, microStar reader, barcode reader with a processing unit*

2.1 OSLD preparation.

The OSL dosimeters were optically bleached using a high luminescence LED light for 12-24 hours to erase residual doses. Initial readings were then recorded for individual dosimeters before being used for dose measurement.

2.2 Positioning and parameters selection.

For the female phantom, the OSL dosimeters were inserted in the phantom at the position of the uterus (3x) and on the left and right side of each ovary, shown in Figure 2 (a,b). For the male examination, three units of nanoDots places were selected on the surface of the pelvis to represent the testis position, as shown in Figure 2 (c). Figure 3 shows the positioning of the gonad shields.

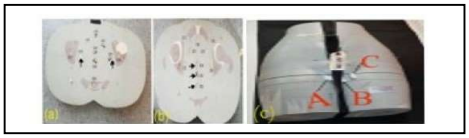

Figure 2: *(a) A section of female phantom ovary position. (b) placement of the chip in uterus position (c) NanoDot™ chips placed on the surface of the phantom.*

Figure 3: *(a) Position of the gonad shield for male phantom analysis. (b) Positioning for gonad shield female phantom analysis*

The pelvic part of the phantom was placed in a supine position with the median sagittal plane of the body at right angles to and in the mid-line of the table and AP pelvic examinations were performed. The tube was adjusted to a source surface distance (SSD) of 100 cm. The collimator was open wide to 35 x 43 cm^2 to include both the pelvic region and the lower abdomen.

We evaluate the percentage of dose reduction with the use of gonad shield in various clinical settings (i) using the AEC technique, (ii) without the use of AEC technique, i.e. with a fixed tube potential and with fixed mAs. The dosimeters were read three times; the mean and 1 standard deviation (SD) of the mean was computed.

3. RESULTS

A pair of 22 AP pelvic and lower abdomen images were obtained. A sample of the image is shown in Figure 4. The image (4d) represents a clinically unacceptable image for female pelvic examination but useful for lower abdomen examination.

Figure 4: *Sample images of gonad shield placement; a) male examination without shield (b) shielded gonad for male 80 kVp with AEC switched on (c) female phantom image 70 kVp sample of gonad shield placement (d) shielded gonads.*

3.1 Absorbed dose measurements

The gonad doses from a supine pelvic radiographic examination, over a range of clinically used tube voltages and tube current-time, produces were obtained. Table 1 to 3 shows the mean dose, comparing the doses with and without gonad shielding. Mean absorbed dose for both female and male examinations was between 0.3 – 5.0 mGy for unshielded gonads, while for shielded gonads the dose was in the range of 0.09 - 0.8 mGy.

The absorbed doses measured with AEC in place were for the unshielded gonads were notably low (Table 3) a range of 0.8 to 2.5 mGy in males, compared

to manual adjustment of tube voltages resulted in absorbed doses ranging from 2.3 to 4.9 mGy (Table 1).

This trend was also similar in female examination with the absorbed doses ranged from 0.3 to 1.7 mGy. With the use of the AEC, a larger dose reduction (0.1-0.3mGy) was observed.

Notably, a variation of tube current-time resulted in absorbed doses of 2.2 to 1.4 mGy and 0.2 to 0.3mGy in the male and female examinations, respectively. When the shields were in place, the measured doses were reduced to 0.1-0.3 mGy and 0.11-0.13mGy in the male and female examination, respectively (Table 2).

With tube voltage of range of 70- 100kV absorbed dose, a primary indicator of the dose received to the gonad was significantly reduced in males by more than 84%(85-89%), deviation of ±2.9% and female (57-70%) deviation±11.7% range of values in the presence of the gonad shield when AEC is off for a standard tube current (25mAs) as shown in Figure 5.

By adjusting the mAs, both female and male examinations demonstrated a significantly high dose reduction of >88.5% (88.5 - 88.7%) deviation of ±0.2% from the optimized value in males, however, in the female, the reduction was slightly lower with 50-70% with deviations of ±9.9%.

Table 1 *Mean dose comparison for various energies at a constant tube current second.*

Tube-potential (kVp)	**Mean Absorbed Dose(mGy) at (25mAs)**			
	Male (n=3)		**Female (n=5)**	
	Unshielded	**Shielded**	*Unshielded*	**Shielded**
70	2.29 ±0.11	0.26±0.06	0.39±0.09	0.12±0.05
80	3.23±0.09	0.29±0.04	0.54±0.12	0.19±0.04
90	4.02±0.12	0.57±0.05	0.86±0.05	0.37±0.08
100	4.88±0.23	0.74±0.14	1.26±0.17	0.47±0.05

n is the detector position. mGy is the absorbed dose

Table 2 *Mean dose and percentage dose reduction for various tube current seconds at a constant tube voltage of 70 kVp.*

Tube current -time (mAs)	**Absorbed Dose(mGy)**			
	70kV			
	Male (n=3)		**Female (n=5)**	
	Unshielded	**Shielded**	**Unshielded**	**Shielded**
16	1.48±0.10	0.17±0.05	0.27±0.05	0.13±0.06
20	1.93±0.10	0.22±0.07	0.33±0.07	0.15±0.06
25	2.29±0.05	0.26±0.08	0.38±0.09	0.11±0.05

Table 3 *Mean dose comparison for various kVp with AEC control switched on.*

kVp	**Mean Absorbed Dose(mGy)**			
	AEC			
	Male (n=3)		**Female (n=5)**	
	Unshielded	**Shielded**	*Unshielded*	**Shielded**
70	2.34±0.10	0.22±0.08	0.38±0.16	0.10±0.05
80	1.26±0.10	0.14±0.03	0.24±0.03	0.10±0.03
90	0.10±0.04	0.1±0.04	0.19±0.14	0.11±0.05
100	0.81±0.07	0.1±0.03	0.24±0.15	0.10±0.05

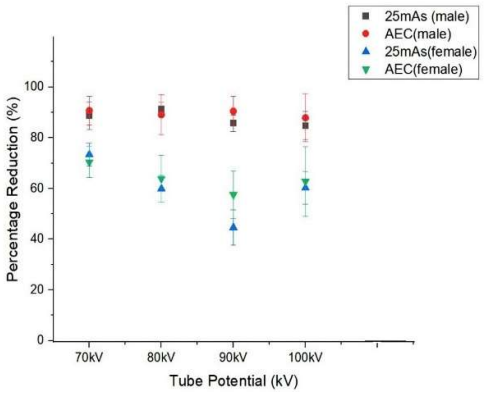

Figure 5: *Comparison of percentage dose reduction for various kVp for male and female examination when AEC is on and off.*

When the AEC is turned on for shielded gonads, there is a significant dose reduction (mean> 50), 87- 91% deviation ±1.3%, and in females 60-70% deviation of ±5.28% as shown in Figure 6.

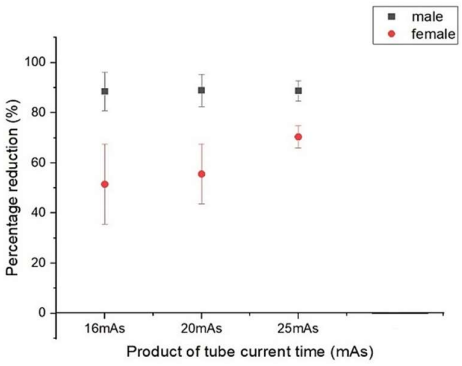

Figure 6: *A comparison of percentage dose reduction for various mAs for both male and female examination.*

4. DISCUSSION

The images obtained for all shielded examinations of male's bony landmarks showed that the whole pelvis, sacrum, and pubic symphysis were visible (Figure 4). For the female examination, the obscured pubic symphysis would be of great concern for patients with pubic symphysis diastasis, prevalent in pregnant women. Generally, an acceptable female radiograph for

patients who have incurred trauma injuries must have all threshold landmarks to assess fractured bones; it is therefore not a useful image for this type of scan.

To effectively shield the female gonads, a customized design for each patient may be needed because of the anatomic variation of the pelvic cavity. Furthermore, it is difficult to establish the exact geometry of the pubic cavity because of its internal location, unlike male patients where the gonads are visible externally.

4.1 Tube voltage potential

The use of gonad shields results in > 50% dose reduction when used under tube potentials ranging from 70 to 100 kVp. The protection value to the gonads outweighs the risk of positioning errors, statistically would give room for a second radiograph, if needed.

The tube voltage of 70kVp and 25mAs were the current standard practice of the department. This setting was primarily based on experience and standard settings by the manufacturer. The main emphasis was to ensure that the gonad shield does not obstruct anatomy of interest and there is a relatively lower dose. The so-called optimized settings were not based on an extensive evaluation of image contrast and resolution. One of the reasons is, as long as there is sufficient exposure to the digital receptor, suboptimal image quality can be post-process digitally to adjust the image on the digital display.

4.2 Tube current seconds

A Similarity in the trend of male and female (> 80%, >50%), respectively is not surprising given that male gonads are located on the surface and receive a minimal contribution from scattered radiation.

This difference in dose reduction was clinically significant for males and indicates a greater benefit with no impact on image quality when correctly placed.

4.3 Automated exposure control (AEC)

As opposed to previous KAP dependent studies [4], the gonad shield placed does not increase the dose to the gonads when a shield is used. Absorbed dose is a true representation of the dose being received to the gonads as compared to KERMA, which is the dose reaching the detector.

For comparison on the sufficiency of AEC without the need for shielding, the following is established; Absorbed dose (mGy) at higher tube voltage is significantly reduced indicating AEC is even more effective than optimized mAs values at higher voltages. It is likely that the effect of AEC in radiation protection at higher tube voltage is more conspicuous and can replace optimized parameters with shields in place.

5. CONCLUSION

With a range of parameters, kVp and mAs measurements were made for shielded and unshielded gonads. Male shielding is recommended due to its effectiveness in easy to identify gonads and has a higher shielding factor. However, for female shielding is likely non-effective (errors in positioning and finding the right shield) and slightly lower shielding factor.

ACKNOWLEDGEMENTS

We thank the radiographers from the Department of Bio-Medical Imaging of the University of Malaya Medical Centre for the successful completion of this study.

REFERENCES

1. Frantzen MJ, Robben S, Postma AA, Zoetelief J, Wildberger JE, Kemerink GJ. Gonad shielding in paediatric pelvic radiography: Disadvantages prevail over benefit. *Insights Imaging*. 2012;3(1):23-32. doi:10.1007/s13244-011-0130-3
2. Sowby, F. D., Valentin J. International Commission on Radiological Protection (2007) ICRP publication 103: the 2007 recommendations of the International Commission on Radiological Protection. Ann ICRP 37:1–332. *Ann ICRP,*. 2007;103(4):332. doi:10.1016/0146-6453(81)90127-5
3. Karami V, Zabihzadeh M. Ovarian Shielding during Pelvis Radiography : Risk Versus Benefit. 2016;4(May):5-6.
4. Kaplan SL, Magill D, Felice MA, Xiao R, Ali S, Zhu X. Female gonadal shielding with automatic exposure control increases radiation risks. *Pediatr Radiol*. 2018;48(2):227-234. doi:10.1007/s00247-017-3996-5
5. Clancy CL, Reilly GO, Brennan PC, Mcentee MF. The effect of patient shield position on gonad dose during lumbar spine radiography. *Radiography*. 2010;16(2):131-135. doi:10.1016/j.radi.2009.10.004
6. Sowby FD, D.Valentine.J. International Commission on Radiological Protection (1981) ICRP publication 34: the 1981 recommendations of the International Commission on Radiological Protection. Ann ICRP 37:1–332. *Ann ICRP*. 1981;6(1):237. doi:10.1016/0146-6453(81)90127-5
7. Dracham CB, Shankar A, Madan R. Radiation induced secondary malignancies: A review article. *Radiat Oncol J*. 2018;36(2):85-94. doi:10.3857/roj.2018.00290

Focus control of electron beam for arbitrary field formation

Atsushi Myojoyama[1], Minami Nakao[1] and Hidetoshi Saitoh[1]

1 Graduate Schools of Human Health Sciences, Tokyo Metropolitan University

Abstract

Currently, scanning irradiation is used to form irradiation fields in proton beam and heavy particle beam therapy. In contrast, electron beam therapy uses a mold and a bolus to form an appropriate dose distribution. If an equivalent dose distribution can be produced without using them, high-accuracy and short-time electron beam therapy can be realized. Moreover, if the irradiation field dependence of the electron beam is used, there is a possibility that the maximum treatment depth can be changed and the treatment depth can be adjusted by changing the size of the electron beam. In scanning irradiation with an electron beam, it is necessary to realize convergence and deflection of the electron beam with high accuracy. The purpose of this study was to confirm the convergence of the electron beam using a solenoid and its effect on the dose distribution by simulation. Monte Carlo simulation was performed using Geant4, and the solenoid conditions suitable for convergence control were obtained. The simulation geometry assumed that a solenoid coil was attached to the accelerator gantry. When the energy of the electron beam was changed, the magnetic flux density was changed, and the solenoid shape was devised. From the result of Monte Carlo simulation, it was confirmed that the electron beam could be converged by using a solenoid. It was suggested that the conditions suitable for convergence differ depending on the energy of the electron beam, and the conditions of the appropriate solenoid differ, and that the solenoids of the same size and shape can be used for all energies by adjusting the applied voltage. It was confirmed that the electron beam was converged by Lorentz force based on the theoretical formula when irradiated in a magnetic field. Detailed experiments are ongoing.

Keywords: *Monte Carlo, electron beam therapy*

1. INTRODUCTION

Currently, scanning irradiation is used to form irradiation fields in proton beam and heavy particle beam therapy. In contrast, electron beam therapy uses a mold and a bolus to form an appropriate dose distribution. In this case, there are problems such as the time required to create the mold and the difficulty in ensuring the reproducibility of the bolus during treatment planning and actual treatment. If an equivalent dose distribution can be produced without using them, high-accuracy and short-time electron beam therapy can be realized. In addition, electron beams have a field size dependence that the maximum treatment depth changes depending on the size of the irradiation field. By taking advantage of this property, it is possible to adjust the treatment depth by changing the size of the electron beam. In scanning irradiation with an electron beam, it is necessary to realize convergence and deflection of the electron beam with high accuracy. We confirmed electron beam deflection by previous research. Therefore, the purpose of this study was to confirm the convergence of the electron beam using magnetic fields and its effect on the dose distribution by simulation.

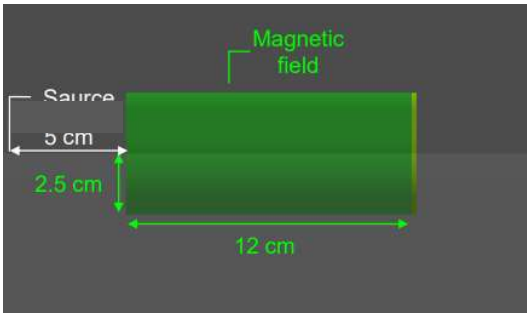

Fig.1 the magnetic field of solenoid in MC simulation.

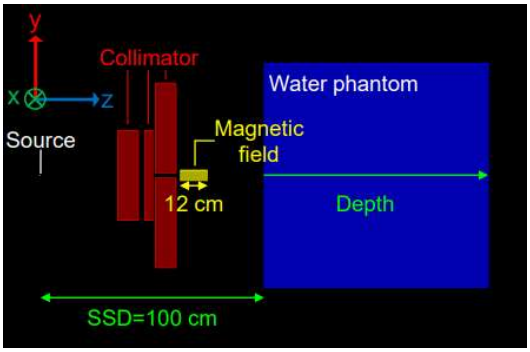

Fig.2 simulation geometry in MC simulation

2. MATERIAL AND METHODS

Geant4[1] was adopted as the Monte Carlo simulation because the magnetic field simulation can be constructed relatively easily. The convergence of the electron beam using magnetic fields and its effect on the dose distribution were obtained. The conditions of the solenoid coil include the material of the conductor, the diameter of the conductor, the number of turns of the coil, and the applied voltage. These conditions determine the condition of the uniform magnetic field generated by the solenoid coil. In the case that μ is the magnetic permeability, H is the strength of the magnetic

field, n is the number of turns per meter [m-1], and I is the current [A], the magnetic flux density B is determined by equation

$$B = \mu H = \mu n I. \quad (1)$$

Since the permeability depends on the material of the conductor and the current depends on the diameter of the conductor and the applied voltage, the optimal parameters of solenoid for convergence could be obtain if the magnetic flux density is known. The simulation geometry assumed that electromagnets were attached to the accelerator gantry. The effect of the incident electron beam on the magnetic field from the accelerator was detected using a water phantom. The simulation conditions were as follows: the distance between the collimators in the x and y directions was 2 cm, the SSD was 100 cm, and the number of incident electron beams was 500,000. Then, in the case that the magnetic flux density was changed, we measured the depth dose and OAR at the maximum dose depth.

3. RESULTS

The behavior of the electron beam in the solenoid when there was no magnetic flux density and when it was 1.0 Tesla were shown in Fig.3. It was confirmed that the electron beam spreads radially at 0.0 tesla, and it draws a spiral orbit due to the magnetic field and converges toward the center at 1.0 tesla.

The difference in dose due to the strength of the magnetic flux density is shown in Fig.4 and Fig.5. And irradiation field in cross-line direction due to difference of the strength of the magnetic flux density is shown in Table 1. From the result of Monte Carlo simulation, it was confirmed that the electron beam can be converged by using magnetic fields. However it was found that the stronger the magnetic field, the larger the effect was not necessarily. It was also found that the maximum dose depth does not change much, but the central dose increases in the case the electron beam converges. Furthermore, since it was possible to converge with the same type of solenoid coil, it was suggested that the same solenoid could be used for all energies by adjusting the applied voltage. Fig.6 shows the percentage depth dose of the result of Fig.5. It had almost the same shape at all magnetic flux densities, but showed a different shape only at 1.0 Tesla.

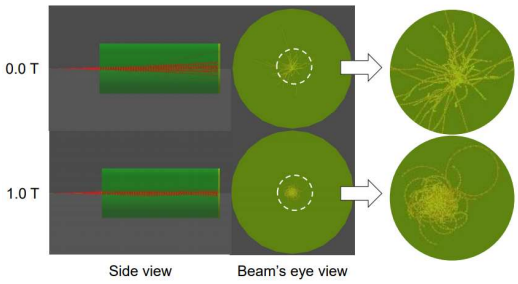

Fig. 3 behavior of electron beam in solenoid coil, at 0.0 tesla, the electron beam spreads radially, and at 1.0 tesla, it draws a spiral orbit due to the magnetic field.

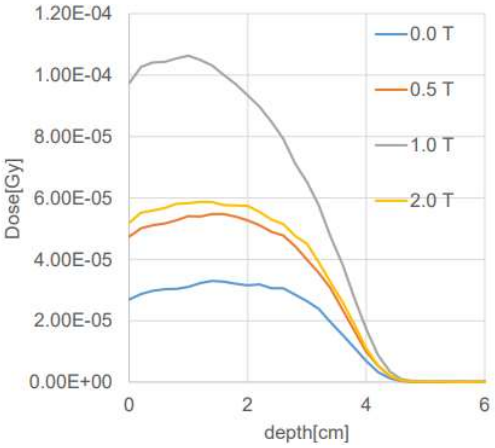

Fig.4 depth dose of the electron beams with / without magnetic flux density

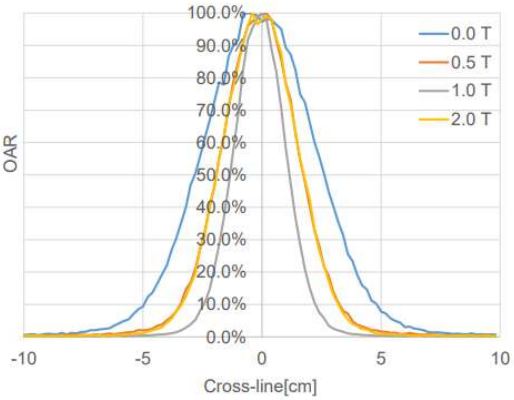

Fig.5 cross line profiles of the electron beams with / without magnetic flux density

Table 1 *FWHM of the cross line profile of the electron beams with\without magnetic flux density*

Mag. flux dens. [T]	0.0	0.5	**1.0**	2.0
FWHM [cm]	5.44	3.66	**2.50**	3.66

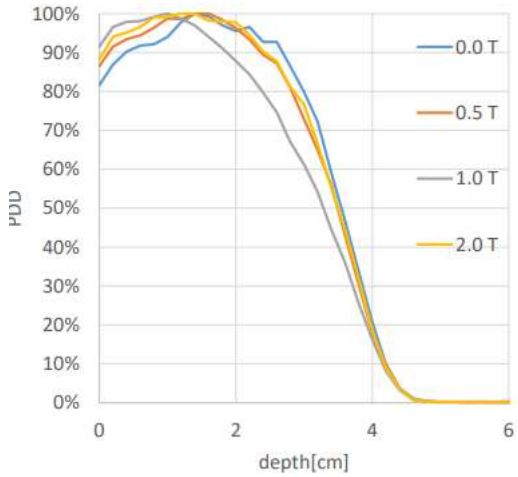

Fig.6 percentage depth dose of the electron beams with / without magnetic flux density

4. DISCUSSION

It became clear that in order to converge the electron beam using a solenoid, it is necessary to investigate strictly the magnetic flux density suitable for the energy of the electron beam. In addition, the dose on the beam axis of the most converged electron beam increased significantly, and the PDD changed in a shallower direction compared to the non-converged electron beam. In this study, the electron beam converged most at a magnetic flux density of 1.0 Tesla, because this experiment incidents a single energy. Since the electron beam generated from the accelerator has a distribution from the maximum energy to the low energy, it is considered necessary to create the shape and number of stages of the solenoid.

5. CONCLUSION

It was confirmed that the electron beam was converged by Lorentz force by magnetic field, and that the convergence of the electron beam affected the dose distribution. It is essential to develop a solenoid that is compact in size and produces a magnetic flux density of 1.0 Tesla.

REFERENCES

1. 10.5 Geant4 Collaboration Book For Application Developers Release, 2019.

Quantitative Assessment of Breast Density Using Pixel Intensity Threshold

Jaroonroj Wongnil[1], Rajalida Lipikorn[2], Anchali Krisanachinda[1]

1 Medical Physics program, Department of Radiology Faculty of Medicine, Chulalongkorn University, Bangkok, Thailand,
2 Department of Mathematics and Computer Science, Faculty of Science, Chulalongkorn University, Bangkok, Thailand,

Abstract

The purpose of this study is to evaluate quantitative breast density using pixel intensity threshold correlate to visual assessment method. Materials and Methods: The study consists of 880 full-field digital screening mammogram with 440 craniocaudal (CC) and 440 mediolateral oblique (MLO) views in Thai patients. Breast density of almost entirely fatty (AF), scatter areas of fibro-glandular density (SD), heterogeneous dense (HD) and extremely dense (ED) at 80, 200, 400 and 200 images had been collected on both views (CC and MLO). All mammograms were classified using BI-RADS, along with the radiologist classification and retrieved from PACS (Picture Archiving and Communication System). The pre-process covers the identification of the breast region, the background removal, and labelling pectoral muscle areas using MATLAB Image segmentation. The ratio of breast density was calculated by specific breast pixel density such as fibro-glandular tissue divided by total breast density. The breast density ratio of each breast classification was obtained and validated by using the new set of mammographic images. Results: The average (min-max) breast density ratio of AF, SD, HD and ED were 0.377 (0.326-0.448), 0.403 (0.316-0.499), 0.449 (0.339-0.571) and 0.485 (0.383-0.600), respectively. The results were concordant with visual assessment by radiologist which is difficult to distinguish between HD and ED. Discussion and Conclusion: The quantitative assessment of breast density using pixel intensity threshold conformed to visual assessment methods. The classification of breast density between HD and ED are still challenging, using both quantitative and qualitative methods to assess which may improve the accuracy and consistency of breast density classification.

Keywords: Breast density, BI-RADS, pixel intensity threshold.

1. INTRODUCTION

Breast cancer is the most common cancer with the highest mortality in women worldwide. In 2018, the World Health Organization (WHO) reported that the new cancer cases in Thai women is breast cancer with 19,510 patients (22.8%) from total cancer patient of 85,579 and ranked the third highest cause of death in the same year.

Breast density is one of the main risk factors of breast cancer. These is an amount of fibrous and glandular tissue in a woman breast compared with the amount of fatty tissue in the breasts. The high breast density usually indicates more difficult to detect abnormality, especially calcification malignancy, because dense tissue layers produce a masking effect.

Digital mammography or full-field digital mammography (FFDM) is one of several medical imaging techniques widely used to examine the breast. The test involves taking images of each breast from two standard views at different angles (CC and MLO).

The American College of Radiology (ACR) established Breast Imaging-Reporting And Data System (BI-RADS) of 5th edition has become a standard in the medical community. The BI-RADS can be classified breast density into four categories: the first is almost entirely fat (AF), second is scattered fibroglandular densities (SD), third is heterogeneously dense (HD) and fourth is extremely dense (ED). The higher breast density causes the sensitivity of mammography to be lower. In clinical practice, BI-RADS is routinely used for reporting mammographic breast density.

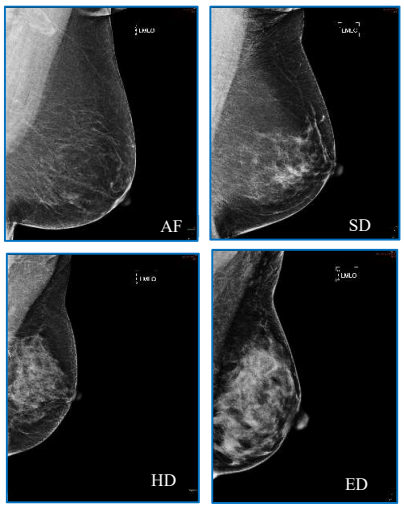

Figure 1: The four BI-RADS breast density. AF (Almost entirely fat), SD (Scattered fibroglandular densities), HD (Heterogeneously dense) and ED (Extremely dense). (By the courtesy of King Chulalongkorn Memorial Hospital).

Breast density has several approaches to classification. Attribution of breast density category has usually been based on a visual assessment. Generally, radiologists use the BI-RADS density classification to assign women to one of four categories. BI-RADS breast density classification is subjective. Therefore, different observer can assign a different BI-RADS density level.

The aim of this study is to evaluate quantitative breast density using pixel intensity threshold correlate to

visual assessment method in reporting mammographic breast density according to BI-RADS categories. This will assist in determining the visual method to be valid and clinically reliable.

2. MATERIAL AND METHODS

The study is a retrospective study. The data used in this study is a clinically realistic data set which consists of complete full-field digital mammographic studies in 500 Thai patients which properly anonymized. The full-field digital mammography includes the standard four views of both MLO and CC views from both breasts of a patient in screening mammography. The Hologic Selenia system (Hologic Inc, MA, USA) has been used to obtain screening mammograms and stored in Picture Archiving and Communication System (PACS).

All computations were performed on a consumer-grade desktop computer equipped with an Intel Core i7 CPU with 24 GB random access memory and an NVIDIA processing unit with 64-bit operating system. All images were resized from their originals.

2.1 Database

The data consists of 880 full-field digital screening mammogram images with 440 CC and 440 MLO views from Thai patients. All mammogram images were classified along with the radiologist classification using BI-RADS. The mammogram images were divided into four groups according to the density patterns of almost entirely fatty (AF), scatter areas of fibro-glandular density (SD), heterogeneous dense (HD) and extremely dense (ED) at 80, 200, 400 and 200 images, respectively. Mammogram images of implant, operation, breast calcification, breast cancer, and breast mass/lump had been excluded.

2.2 Quantitative classification

The mammogram images with a size of 4096x3328 pixels or 3328×2560 pixels, depend on the breast size were included. The preprocessing step was used to all mammogram images to reduce the effects of the normal anatomy of the breast. There are manually segmented breast areas as the ground truth. Any non-breast areas, such as, the pectoral muscle, belly tissue, paddle shadow, and electronic marker had been removed from the resulting ground truth mask for the breast area by using Image segmenter App, MATLAB version R2020a. All images were resized from their initial dimensions to 600 × 600 pixels. Using a MATLAB version R2020a.

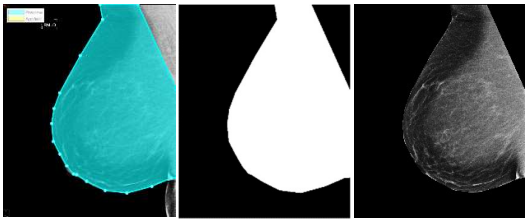

Figure 2: The segmentation mammogram images using image segmenter app.

The manual segmented breast area, to establish the ground truth for the dense fibro-glandular area per images had been performed. The images were converted from a gray scale image into a binary image using adaptive thresholding. Then, two breast imaging experts with broad experience in mammography confirmed a threshold of four breast density categories on binary images.

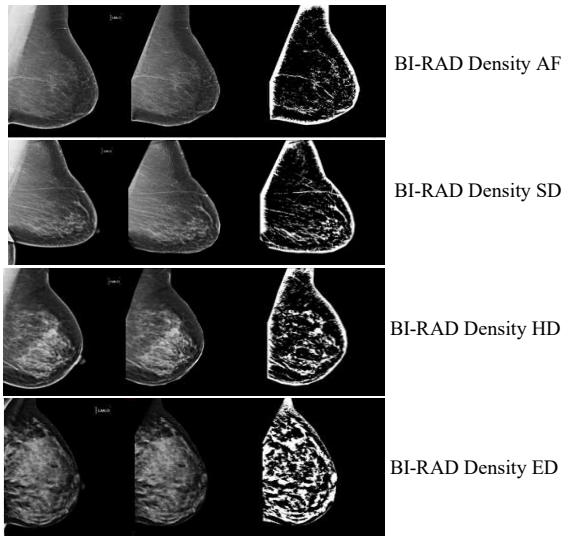

Figure 3: The established ground truth mask for dense fibroglandular area. Images on the left side show the original mammograms, the middle shows the results after applying manually image segmented breast area mask and the third shows an application of a thresholding method to get ground truth mask for dense fibroglandular area.

All binary images were computing the ratio between dense area masks and breast area mask. For each binary image using the following equation:

Density ratio = Dense pixel density masks / Breast pixel density mask

This study utilized manually segmented breast areas as the ground truth. The pixel intensity shows inside the breast area.

3. RESULTS

The 220 female patients underwent full-field digital screening mammogram. The results are shown in Table 1 of average ages with range and the number of images per view in each breast composition.

Table 1: Patient age and number of images.

Breast composition	AF		SD		HD		ED	
	CC	MLO	CC	MLO	CC	MLO	CC	MLO
Age (year)	62(39-77)		58(39-77)		50(35-74)		45(35-60)	
Number of images	40	40	100	100	200	200	100	100

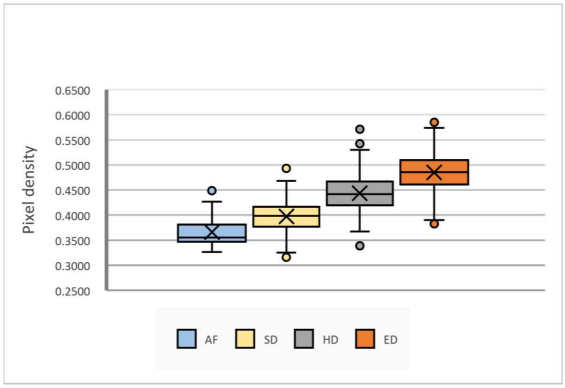

Figure 4: The box plots of BI-RADS and pixel density of the segmentation result in CC view.

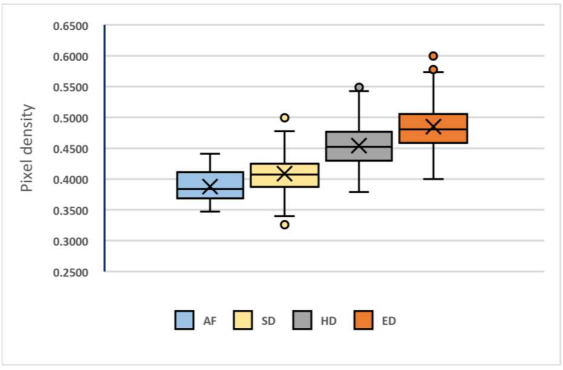

Figure 5: The box plots of BI-RADS and pixel density of the segmentation result in MLO view.

Figure 4 and 5 present a box-and-whisker plot representation of the mammographic density according to the BIRADS classification given by breast imaging experts. A box is drawn enclosing the first and third quartiles of the data, and the median value divides the box into two parts. Moreover, the whiskers show the variability outside the upper and lower quartiles. In addition, each box represents the variability of the automatic estimation of the pixel density clustered according to the expert qualitative assessment.

The pixel density in CC view were calculated as the follwings: Q2, (Q1-Q3) BI-RADS AF: 0.355(0.346-0.381), BI-RADS SD: 0.398(0.376-0.416), BI-RADS HD: 0.441(0.419-0.467), BI-RADS ED: 0.485(0.461-0.509).

In MLO view, BI-RADS AF: were 0.383(0.368-0.411), BI-RADS SD: were 0.407(0.387-0.424), BI-RADS HD: were 0.452(0.429-0.476), BI-RADS ED: were 0.480(0.458-0.505) respectively.

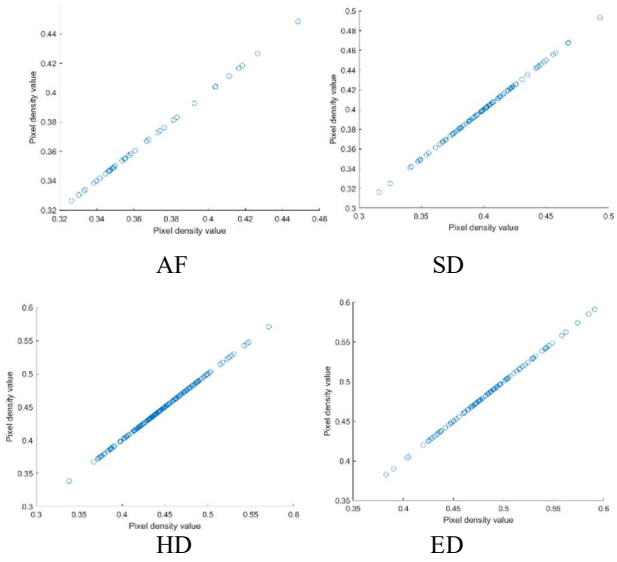

Figure 6: The scatter plot of pixel density of BI-RADS for both breasts in CC views.

The distribution of the pixel density of all left and right breasts in CC view are shown in figure 6. For MLO view, the similar trend is similar to the CC views.

The average (min-max) breast density of AF, SD, HD and ED were 0.377(0.326-0.448), 0.403(0.316-0.499), 0.449(0.339-0.571) and 0.485(0.383-0.600), respectively. We obtained the pixel density threshold of 95% of mean $\pm$ 2SD which could be used for the interpretation at the breast center having no pixel density information on the four BI-RADS or at the center with junior mammogram radiologists.

The results were concordant with visual assessment by radiologists which are difficult to distinguish between AF versus HD, and HD versus ED.

4. DISCUSSION

When the breast density is increasing, the BI-RADS class is also increases, showing high correlation between qualitative and quantitative assessment.

If we compare the breast density of the same side, we will obtain a very strong correlation. The BI-RADS SD and HD are significantly different.

The limitations of this study are the lack of number of BI-RADS AF. The segmentation of the breast density is not an easy task because it is not feasible to obtain a ground truth detailing all the dense regions in a large set of mammograms. Moreover, the computational task is difficult, the variability is high if multi-expert is looking at the breast densities.

5. CONCLUSION

The quantitative breast density using pixel intensity threshold correlated the visual assessment method and has been validated in this work. The quantitative assessment of breast density using pixel intensity threshold conformed to visual assessment methods. The classification of breast density between HD and ED are still challenging, using both quantitative and qualitative methods to assess which may improve the accuracy and consistency of breast density classification.

ACKNOWLEDGEMENTS

I would like to thank Department of Radiology, King Chulalongkorn Memorial Hospital for their equipment support, breast imaging experts, and all teachers in Medical Imaging, Faculty of Medicine Chulalongkorn University for their suggestions in this work.

REFERENCES

1. Ciritsis A, Rossi C, Vittoria I, et al. Determination of mammographic breast density using a deep convolutional neural network. Br J Radiol 2019; 92: 20180691.
2. Lee J, Nishikawa M. J, Automated mammographic breast density estimation using a fully convolutional network. Med. Phys 2018; 45(3).
3. Destounis S, Arieno A, Morgan R, et al. Qualitative Versus Quantitative Mammographic Breast Density Assessment: Applications for the US and Abroad. MDPI 2017; 7, 30; doi:10.3390/diagnostics7020030
4. Wu N, Geras J. K, Shen Y, et al. Breast Density Classification with deep convolutional neural networks. ArXiv, Cornell University 2017; 1711. 03674.
5. Oliver A, Tortajada M, Llado X, et al. Breast Density Analysis Using an Automatic Density Segmentation Algorithm. Society for Imaging Informatics in Medicine 2015; 28:604–612.
6. He W, Juette A, Denton R.E.E, et al. A Review on Automatic Mammographic Density and Parenchymal Segmentation. International Journal of Breast Cancer 2015, 31 http://dx.doi.org /10.1155/ /2015/276217.
7. Arora P, Singh M, New Intensity Based Features for Classification of Mammograms. Canadian Conference on Electrical and Computer Engineering 2014, 978-1-4799-3010-9/14.
8. Mustra M, Grgic M, Delac K, Breast Density Classification Using Multiple Feature Selection. DOI 10.7305/automatika.53-4.281, 2012; 53(4), 362–372.
9. Raundahl J, Kokkedal, Loog M, et al. Breast Tissue Density Measure. United States Patent 2008; 12/317,530.
10. Malich A, Fischer R.D, Facius M, et al. Effect of Breast Density on Computer Aided Detection. Journal of Digital Imaging 2005; 18 (3), 227-223.
11. Ciatto S, Houssami N, Apruzzese A, et al. Categorizing breast mammographic density: intra- and interobserver reproducibility of BI-RADS density categories. The Breast (2005) 14, 269–275.

Diagnostic performance of dual-tracer subtraction, single-tracer dual-phase 99mTc-MIBI parathyroid scintigraphy, and 99mTc-MIBI SPECT/CT for preoperative localization in patients with hyperparathyroidism.

Warissara Wittayapasitti[1], Kijja Rhoongsittichai[2], Jiraporn Sriprapaporn[2]

1 Master of Science Program in Medical Physics, Faculty of medicine, Siriraj hospital, Mahidol University,
2 Division of Nuclear Medicine, Department of Radiology, Faculty of medicine Siriraj hospital, Mahidol University

Abstract

Introduction: Preoperative imaging is usually performed to localize the hyper-functioning parathyroid glands to facilitate a minimally invasive surgical approach. Parathyroid scintigraphy has been the investigation of choice for decades. However, it is still in doubt that which technique is the best.

Purpose: To evaluate the diagnostic performance of dual-tracer subtraction (DT), dual-phase 99mTc-MIBI (DP), and 99mTc-MIBI SPECT/CT parathyroid scintigraphy for preoperative localization in patients with hyperparathyroidism.

Methods: This is a retrospective study of 481 consecutive patients with biochemically confirmed hyperparathyroidism who were referred for parathyroid scintigraphy. All patients had routinely underwent three techniques of parathyroid scintigraphy; i.e. DT, DP, and 99mTc-MIBI SPECT/CT. One hundred patients, who had complete imaging data and had pathologically confirmed diagnosis within eight months, were included for the analysis.

All the parathyroid scintigraphy images retrieved from the PACS system were blindly reinterpreted by two nuclear medicine physicians at least three weeks apart for each imaging set. A consensus interpretation was made if the readings were distinct.

Results: A total of 243 parathyroid lesions were analyzed, consisting of 205 hyperplastic glands, 28 adenomas, and two carcinomas. The remaining eight foci reveal a normal parathyroid gland. According to the lesion-based analysis, the overall pooled sensitivities for DT, DP, and SPECT/CT were 48.09%, 39.57%, and 53.19%, respectively. However, subgroup analysis showed better sensitivities for parathyroid adenoma of 82.14%, 78.57%, 92.86% than those for hyperplastic glands of 42.93%, 33.66%, 47.32%, respectively.

A comparison between techniques of parathyroid scintigraphy revealed statistically significant differences between DT and DP ($p = 0.01$) and between DP and SPECT/CT ($p < 0.001$) but there was no statistically significant difference between DT and SPECT/CT ($p = 0.182$).

Conclusion: Parathyroid scintigraphy has higher sensitivity for parathyroid adenoma rather than hyperplastic glands in all three techniques. DT and SPECT/CT techniques provide similar sensitivities and are superior to DP technique.

Keywords: Hyperparathyroidism, Parathyroid scan, Dual-tracer, MIBI, SPECT/CT

Address correspondence to: J. Sriprapaporn,
E-mail: jiraporn.spp@mahidol.ac.th

1. INTRODUCTION

Hyperparathyroidism (HPT) is a common endocrine disorder, which is caused by an excess secretion of parathyroid hormone from one or more hyper-functioning parathyroid glands, leading to high serum calcium or hypercalcemia.

Since surgery is a definitive treatment for this condition, preoperative imaging is usually performed to localize the hyperfunctioning parathyroid glands to facilitate a minimally invasive surgical approach to short the operative time and to reduce postoperative complications and chance for reoperation. The parathyroid glands can be imaged with different modalities (1), however, parathyroid scintigraphy has been the investigation of choice for decades. Several techniques have been used including double-phase (DP), dual-tracer subtraction (DT), and SPECT/CT methods. Furthermore, it is still debated, which techniques should be preferred for localizing hyperfunctioning parathyroid glands (2-6).

This study was to compare the diagnostic performance of dual-tracer subtraction, dual-phase 99mTc-MIBI, and 99mTc-MIBI SPECT/CT parathyroid scintigraphy for preoperative localization in patients with different types of hyperparathyroidism.

2. MATERIAL AND METHODS

All related medical information including demographic data, laboratory results, details of surgeries, and pathological findings were recorded.

The parathyroid imaging procedures routinely include all three techniques, i.e. DT, DP, and SPECT/CT imaging. All the images were blindly reinterpreted by two nuclear medicine physicians, who read 3 sets of image data of DT, DP, and SPECT/CT at least three weeks apart. A consensus of interpretation was used if the two readers had different opinions.

The data were analyzed on the patient basis, lateralization, and also on the lesion basis using pathological results as the gold standard. Subgroup analysis for parathyroid adenomas and hyperplastic glands was also performed.

This study was ethically approved by Human Research Protection Unit from Institutional Review Board, Faculty of Medicine Siriraj Hospital (SIRB).

2.1 Patient selection

Out of 481 consecutive patients with clinical hyperparathyroidism, who underwent parathyroid scintigraphy at the division of nuclear medicine, department of radiology, Siriraj hospital from 30 July 2013 to 10 September 2019, only 100 patients who were older than 18 years old and had parathyroid surgery within eight months of the imaging study were included for analysis (Figure 1).

2.2 Imaging techniques

All examinations were performed on a Discovery NM/CT 670 (GE Healthcare) or Siemens Symbia T2 (Siemens Healthcare) equipped with low-energy, high-resolution parallel collimator.

Anterior planar static image of the neck was acquired 10 minutes and performed with 256×256 matrix a with an energy peak set at 140 keV$\pm$ 20%.

All patients initially had 2 mCi of 99mTc-pertechnetate intravenously injected and the scan had been 20 minutes afterward. Subsequently, 20 mCi of 99mTc-MIBI was intravenously administered and the planar imaging over the neck and mediastinum was obtained 10 minutes later (early 99mTc-MIBI images).

SPECT/CT imaging of the neck and chest was acquired following the early 99mTc-MIBI images. SPECT acquisition settings were as follows: 360 degrees, 30 sec/view, 128×128 matrix size, and zoom 1.28. CT scan settings were as follows: 120 kVp, smart mA (100 - 200 mA).

After a 3-hour delay from 99mTc-MIBI injection, the patient is repositioned to duplicate the initial images and the scan was repeated using the same parameters (delayed 99mTc-MIBI images).

2.3 Image interpretation

Planar and SPECT/CT images were independently and blindly reinterpreted by two nuclear medicine physicians at least three weeks apart for each imaging technique. In case of discrepant readings, they were solved by a consensus.

Abnormal parathyroid lesions were categorized per head, per side, and also per lesion based on anatomical four quadrant position; right upper, right lower, left upper and left lower quadrants.

Positive scan findings include the presence of remaining abnormal radioactivity after subtraction for DT technique, focal abnormal 99mTc-MIBI uptake in early or delayed images for DP technique, and presence of abnormal 99mTc-MIBI uptake and/or presence of soft tissue lesion that is not classified as thyroid lesions. Pathological findings were used as the gold standard.

2.4 Statistical analysis

Means, median, and standard deviations were used for continuous variables. Percentages were used for categorical data.

Data were analyzed by SPSS statistical software version 10.0 for Mac. The sensitivity, specificity, positive predictive value (PPV), negative predictive value (NPV), likelihood ratios (LR) with 95% confidence intervals (CI) were calculated for each technique.

A McNemar test was applied to compare the diagnostic performance of 3 techniques of parathyroid scan results and p-value less than 0.05 was considered statistically significant.

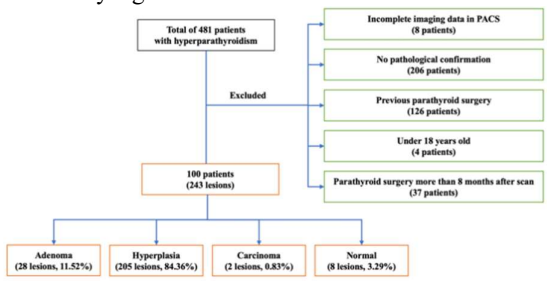

Figure 1 *Flowchart of patient selection*

3. RESULTS

The patients' characteristics in our study were shown in Table 1. The majority of the patients in this group have parathyroid hyperplasia (70 cases, 70%). Twenty-eight patients (28%) had parathyroid adenoma and 2 patients (2%) had parathyroid carcinoma. In the hyperplasia group, 13 cases had chronic kidney disease (CKD) stage 1-2 and 8 cases had CKD stage 3-4, and 49 patients had CKD stage 5, which was end-stage renal disease (ESRD). The prevalence of CKD in adenoma group were 12, 15, and only one ESRD.

Preoperative intact parathyroid hormone (PTH), and serum creatinine, serum total calcium, and serum phosphorus levels had also been measured in Table 2.

Table 1 *Patients' characteristics.*

Variable	Numbers
Total patients	100 patients
Total lesions	243 lesions
Age Range (years), Mean±SD	 21-87 years 56.7±15.2
Sex • Female • Male	 63 37
Type of parathyroid lesions • Adenoma • Hyperplasia • Carcinoma • Normal gland	 28 (11.12%) 205 (84.77%) 2 (0.82%) 8 (3.29%)
Underlying ESRD*	50 (50.00%)
Time of parathyroid surgery Range (days) Mean±SD	 1-240 97.3±66.53

**ESRD: end-stage renal disease*

3.1 Lesion-based analysis

Among 243 excised parathyroid lesions, 205 were parathyroid hyperplasia, 28 were parathyroid adenoma and two carcinomas. The rest eight lesions represented normal parathyroid tissue.

The results of sensitivities and specificities among these three techniques analyzed on the lesion basis were shown in Table 3 Subgroup analysis for adenomas and hyperplastic glands was also applied.

Table 2 *Laboratory Results*

Test	Range	Mean±SD
PTH (pg/mL)	59.7 – 4564.0	1162.1±1013.2
Total calcium (mg/mL)	7.0 – 13.7	10.8±1.4
Phosphorus (mg/mL)	1.4 – 9.8	4.0±2.0
Creatinine (mg/mL)	0.4 – 18.6	5.0±4.5

A summary of diagnostic performance of all techniques was provided in Table 3.

3.2 Lateralization

Once concerning lateralization, DT, DP, SPECT/CT techniques can correctly predict the correct side of all the lesions in 105 of 152 (69.08%), 94 of 152 (61.84%), and 111 of 152 (73.03%), respectively.

For hyperplastic glands, these techniques provided correct lateralization in 79 of 120 (65.83%), 68 of 120 (56.67%), and 82 of 120 (68.33%), respectively.

The percentages for correct lateralization in the groups of parathyroid adenomas were 85.71% (24 of 28), 89.29% (25 of 28), and 96.43% (27 of 28), respectively.

3.3 Patient-based analysis

The DT, DP, and SPECT/CT techniques could pick up the diseased patients in 82 of 100 (82.00%), 80 of 100 (80.00%), and 85 of 100 (85.00%) respectively. The efficacies of these techniques for hyperplastic glands were (81.43%), (57 of 70), 77.14% (54 of 70) and 81.43% (57 of 70), and those for detecting parathyroid adenoma were 85.71% (24 of 28), 89.29% (25 of 28), and 96.43% (27 of 28), respectively.

4. DISCUSSION

Actually, the diagnostic performance of parathyroid scintigraphy for localization of hyperfunctioning parathyroid glands in the patients with HPT depends on several factors, such as types of HPT, types of hyper-functioning glands (adenoma or hyperplasia), imaging protocols including types of radiotracer used for imaging, the experience of the readers, and partly related to the type of instrument used for image acquisition. Thus, different situations can lead to different results.

The common radionuclide imaging techniques for parathyroid scintigraphy mainly involve dual-tracer subtraction (using technetium pertechnetate or I-123 in conjunction with 99mTc-MIBI or 99mTc-tetrofosmin, or 201Thallium) and single-tracer, dual-phase technique, which 99mTc-MIBI is most popular (2,3,5).

The overall sensitivities of parathyroid scintigraphy (all three techniques) in this study are lower than the mean sensitivity of 71.5% reported by Gotthardt et al. (7), but it is still in the wide range of the studied papers, which varies from 39% to 92.5%.

The reason why the overall sensitivity is low is related to the high proportion of the patients with multiglandular hyperplastic glands in this study (84.77%). Since it's well documented that the sensitivity in this group of patients is much lower than that observed in the adenoma group (5).

Table 3 *A summary of diagnostic performance of all techniques*

	Dual tracer		Dual phase		SPECT/CT	
	Value	**95% C.I.**	**Value**	**95% C.I.**	**Value**	**95% C.I.**
Overall (243 lesions)						
Sensitivity	48.09%	41.54% - 54.68%	39.57%	33.28% - 46.14%	53.19%	46.59% - 59.71%
Specificity	75.00%	34.91% - 96.82%	87.50%	47.35% - 99.68%	75.00%	34.91% - 96.82%
Accuracy	48.97%	42.53% - 55.44%	41.15%	34.90% - 47.62%	53.91%	47.42% - 60.30%
PPV	98.26%	94.41% - 99.47%	98.94%	93.66% - 99.83%	98.43%	94.93% - 99.52%
NPV	4.69%	3.14% - 6.96%	4.70%	3.59% - 6.13%	5.17%	3.45% - 7.68%
LR+	1.92	0.57 - 6.43	3.16	0.50 - 19.40	2.13	0.64 - 7.11
LR-	0.69	0.46 - 1.05	0.69	0.52 - 0.92	0.62	0.41 - 0.95
Adenoma (28 lesions)						
Sensitivity	82.14%	63.11% - 93.94%	78.57%	59.05% - 91.70%	92.86%	76.50% - 99.12%
Specificity	60.00%	14.66% - 94.73%	80.0%	28.36% - 99.50%	80.00%	28.36% - 99.50%
Accuracy	78.79%	61.09% - 91.02%	78.79%	61.09% - 91.02%	90.91%	75.67% - 98.09%
PPV	92.00%	79.50% - 97.15%	95.65%	79.04% - 99.23%	96.30%	81.79% - 99.34%
NPV	37.50%	17.08% - 63.61%	40.00%	22.46% - 60.55%	66.67%	32.91% - 89.08%
LR+	2.05	0.69 – 6.09	3.93	0.67 - 22.92	4.64	0.80 - 26.88
LR-	0.29	0.10 – 0.87	0.27	0.12 - 0.62	0.09	0.02 - 0.36
Hyperplasia (205 lesions)						
Sensitivity	42.93%	36.05% - 50.00%	33.66%	27.23% - 40.57%	47.32%	40.32% - 54.39%
Specificity	100%	29.24% - 100.0%	100%	29.24% - 100.0%	66.67%	9.43% - 99.16%
Accuracy	43.75%	36.90% - 50.78%	34.62%	28.17% - 41.51%	47.60%	40.65% - 54.62%
PPV	100%		100%		98.98%	95.11% - 99.79%
NPV	2.50%	2.23% - 2.81%	2.16%	1.96% - 2.37%	1.82%	0.82% - 4.0%
LR+*					1.42	0.29 - 7.08
LR-	0.571	0.51 – 0.64	0.66	0.60 – 0.73	0.79	0.35 - 1.78

PPV: positive predictive value, NPV: negative predictive value, LR+: positive likelihood ratio, LR-: negative likelihood ratio
**LR+ cannot be calculated due to lack of false-positive*

Thus, it's better to evaluate the diagnostic accuracy in each group separately. For localization of parathyroid adenoma, the sensitivities of parathyroid scintigraphy range from about 76% to 82%, and those for hyperplastic glands vary from 33% to 47%, which are closed to reported in one meta-analysis (88.44% and 44.46% respectively) (8).

According to the meta-analysis by Ruda et al. (9), which included 54 studies between 1995 and 2003 showed an overall sensitivity of 88% for the detection of a single adenoma, and sensitivity had been decreased to 44.5% in patients found to have 4-gland hyperplasia.

As compared to primary hyperparathyroidism, there are fewer studies have been conducted in the group of secondary hyperparathyroidism. According to a meta-analysis done by Caldarella et al. (10), they found that pooled sensitivity of 99mTc-MIBI parathyroid scintigraphy was only 58%, which seems to be not impressive.

When comparing the techniques of parathyroid scintigraphy, our results suggest that DT and SPECT/CT are superior to DP technique since DT technique displays the outline of the thyroid gland and several hyperfunctioning parathyroid lesions do not obviously show higher radiotracer uptake than the thyroid tissue making 99mTc-MIBI alone difficult for localization. For SPECT/CT imaging, it's clear that 3-dimensional image localization is helpful.

Our results are similar to Leslie WD et al. (11), who found that DT technique (99mTc-pertechnetate and 99mTc-MIBI) was superior to DP 99mTc-MIBI protocol with detection rate 85% vs. 72% respectively while combine DT and DP imaging would result in highest yield of 90%.

Similar results that DT was more sensitive than DP were also confirmed using additional pinhole collimator and the localization was even higher if SPECT/CT acquisition was combined (4).

A recent meta-analysis has been showed that SPECT/CT had higher sensitivity in localizing parathyroid lesions when compared with planar imaging (84 vs. 63%) (6).

On contrary, in the recent studies demonstrated that 99mTc-MIBI DP protocol was found to be more sensitive than DT technique (2,12).

Our study had some limitations Firstly, it is a retrospective study that some patients had lost follow-up and were not operated or operate long after the scintigraphy. Secondly, the parathyroid lesions are usually small size, which are difficult to be localized on a low-dose, non-contrast SPECT/CT images. Finally, several factors being related to diagnostic accuracy in localization of hyper-functioning parathyroid glands were not mentioned in this study such as concomitant thyroid disorders, level of parathyroid hormone, and size of the parathyroid lesions.

5. CONCLUSION

Parathyroid scintigraphy has higher sensitivity for parathyroid adenoma rather than hyperplastic glands in all three techniques. DT and SPECT/CT techniques provide similar sensitivities and are superior to DP technique.

ACKNOWLEDGEMENTS

The author would like to thank Dr. Chulaluk Komontri for statistical advice.

REFERENCES

1. Cox MD, Stack BC. Minimally Invasive Radioguided Parathyroidectomy. Medical and Surgical Treatment of Parathyroid Diseases: Springer; 2017. p. 181-201.
2. Raruenrom Y, Theerakulpisut D, Wongsurawat N, Somboonporn C. Diagnostic accuracy of planar, SPECT, and SPECT/CT parathyroid scintigraphy protocols in patients with hyperparathyroidism. Nuclear medicine review Central & Eastern Europe. 2018;21(1):20-5
3. Saengsuda Y. The accuracy of 99m Tc-MIBI scintigraphy for preoperative parathyroid localization in primary and secondary-tertiary hyperparathyroidism. J Med Assoc Thai. 2012;95 Suppl 3:S81-91.
4. Heiba SI, Jiang M, Rivera J, Genden E, Inabnet W, 3rd, Machac J, et al. Direct comparison of neck pinhole dual-tracer and dual-phase MIBI accuracies with and without SPECT/CT for parathyroid adenoma detection and localization. Clin Nucl Med. 2015;40(6):476-82.
5. Chen CC, Holder LE, Scovill WA, Tehan AM, Gann DS. Comparison of parathyroid imaging with technetium-99m-pertechnetate/sestamibi subtraction, double-phase technetium-99m-sestamibi and technetium-99m-sestamibi SPECT. J Nucl Med. 1997;38(6):834-9.
6. Wei WJ, Shen CT, Song HJ, Qiu ZL, Luo QY. Comparison of SPET/CT, SPET and planar imaging using 99mTc-MIBI as independent techniques to support minimally invasive parathyroidectomy in primary hyperparathyroidism: A meta-analysis. Hell J Nucl Med. 2015;18(2):127-35.
7. Gotthardt M, Lohmann B, Behr TM, Bauhofer A, Franzius C, Schipper ML, et al. Clinical value of parathyroid scintigraphy with technetium-99m methoxyisobutylisonitrile: discrepancies in clinical data and a systematic metaanalysis of the literature. World J Surg. 2004;28(1):100-7.
8. Cheung K, Wang TS, Farrokhyar F, Roman SA, Sosa JA. A meta-analysis of preoperative localization techniques for patients with primary hyperparathyroidism. Ann Surg Oncol. 2012;19(2):577-83.
9. Ruda JM, Hollenbeak CS, Stack BC, Jr. A systematic review of the diagnosis and treatment of primary hyperparathyroidism from 1995 to 2003. Otolaryngol Head Neck Surg. 2005;132(3):359-72.
10. Caldarella C, Treglia G, Pontecorvi A, Giordano A. Diagnostic performance of planar scintigraphy using mTc-MIBI in patients with secondary hyperparathyroidism: a meta- analysis. Ann Nucl Med. 2012;26(10):794–803
11. Leslie WD, Dupont JO, Bybel B, Riese KT. Parathyroid 99mTc-sestamibi scintigraphy: dual-tracer subtraction is superior to double-phase washout. Eur J Nucl Med Mol Imaging. 2002;29(12):1566-70.
12. Maccora D, Rizzo V, Fortini D, Mariani M, Giraldi L, Giordano A, et al. Parathyroid scintigraphy in primary hyperparathyroidism: comparison between double-phase and subtraction techniques and possible affecting factors. J Endocrinol Invest. 2019;42(8):889-95.

Linear accelerator performance monitoring through clinical treatment delivery using Statistical Process Control and MobiusFX

Piyakan Wongsaroj[1], Kittipol Dachaworakul[1], Taweap Sanghangthum[2], Todsaporn Fuangrod[1]

1 Medical Physics Program, Faculty of Medicine and Pubic Health, HRH Princess Chulabhorn College of Medical Science, Chulabhorn Royal Academy, Bangkok, Thailand,
2 Division of Radiation Oncology, Department of Radiology, Faculty of Medicine, Chulalongkorn University, Bangkok, Thailand

Abstract

Linear accelerator (Linac) quality assurance (QA) aims to check if the machine does not significantly deviate from the controlled values in various mechanics and dosimetric parts. The QA can be routinely taken in daily, monthly, and annual periods. However, there is no current quality management system, which monitors the individual linac machine performance through the evaluation of clinical treatment delivery. This study aims to develop linac performance monitoring using MobiusFX (machine log-file) with the statistical process control (SPC) method. Linac log-file of patient delivery data in daily bias from Varian Clinac iX LINAC were captured for 62 days. Total data of 398 log-files were analyzed using MobiusFX (Version 2.1.2). SPC in form of average and standard deviation ($\bar{X}/S$) control charts were constructed from the first 30 days, then used to monitor linac machine performance including 3D gamma analysis values, root-mean-square (RMS) error analysis values for gantry, collimator, jaw and MLC motor. The $\bar{X}/S$ control charts showed the lower control limits (LCL) of 3D gamma at 95% (as baseline). The upper control limits (UCL) of RMS error for the gantry, collimator, jaws in X1, X2, Y1, Y2, and MLC leaf positions were 0.422 mm, 0.052 mm, 0.184 mm, 0.204 mm, 0.308 mm, 0.269 mm, and 1.005 mm, respectively. During the linac machine monitoring (day 31 to 62), the system flagged issues on Y1-jaw, Y2-jaw, and collimator angle. In conclusion, the linac machine performance monitoring through the clinical treatment delivery using MobiusFX with SPC demonstrates the potential system to flag the high risks of machine parts (focusing on finding systematic errors). The system can help medical physicists manage their preventive maintenance efficiently and minimize unexpected machine downtime in the future.

Keywords: Daily machine-specific performance monitoring, Statistical process control, MobiusFX

1. INTRODUCTION

Linac is a sophisticated machine, which can produce beams of photons and electrons with various energies to deliver precise radiation doses to exterminate cancer. The linac comprises several subsystems, which facilitate cancer treatment in clinical approaches. The subsystems such as the gantry, beam defining system, and the patient support system requires high-quality mechanical engineering (1). Furthermore, modern radiotherapy techniques such as intensity-modulated radiotherapy (IMRT) and volumetric modulated radiotherapy (VMAT) have been used in the linac. These techniques are considered complex treatment methods in external beam radiation therapy. Therefore, the linac is necessary to implement a comprehensive quality assurance (QA) program. The goal of QA program for the linac is to evaluate the functional performance of linac by determining the machine parameters does not significantly deviate from the controlled values in various both mechanics and dosimetric parts. The QA program be routinely taken in daily, monthly and annual periods (2). However, the QA program tests uncover all types of errors, which occur at the time of treatment, and there is no current quality management system, which monitors the individual linac machine performance through the evaluation of clinical treatment delivery outcomes.

MobiusFX (Varian Medical Systems, Palo Alto, CA, USA) is one of the Mobius system software modules, which can be applied for treatment delivery QA. Analysis of the delivered dose uses automatic measurements in machine log-files recorded the linac machine performance during each fraction of treatment delivery to the patients (3, 4). Usually, the machine log-files contain the clinical treatment delivery data, such as fractional dose, planned MLC leaf positions, delivered MLC leaf positions, jaw positions, collimator angle, and gantry angle.

SPC is a quality control method that uses statistical techniques to monitor and control the process performance to ensure that this process's operation is stable. A control chart is an essential tool of the SPC used for time-series process data and constructed the centerline, the lower control limits (LCL), and the upper control limits (UCL) to indicate this process. The SPC has been widely applied for healthcare improvement in the QA of radiotherapy (5-8).

This study aims to develop linac performance monitoring using MobiusFX based on machine log-file with SPC. The Control chart will be applied to monitor linac machine performance through the machine log-files outcomes ofmobiusFX to flag the possible malfunction (in the sense of high risk) of machine components, which will focus on finding the systematic errors to enhance the quality of this system. Therefore, an additional machine-specific performance monitoring through this process may improve the treatment quality, reduce the systematic errors, and benefit proactive linac maintenance management.

2. MATERIAL AND METHODS

In this study, the linac performance monitoring was performed to capture treatment delivery data of the patient (machine log-file) in everyday bias from Varian Clinac iX linac (Varian Medical Systems, Palo Alto, CA, USA) for 62 days between November 2019 and February 2020 at Division of Radiation Oncology, Bhumibol Adulyadej Hospital, Bangkok, Thailand. The machine log-file of the Varian Clinac iX linac is named "DynaLog file". Total DynaLog file data of 398 log-files were analyzed using MobiusFX (Version 2.1.2). Patient treatment with IMRT and VMAT techniques with photon energies at 6 MV and 10 MV treatment will be recorded. The analysis of machine log-files in MobiusFX contained the clinical treatment delivery (patient delivery) data in mechanics parts, such as root-mean-square (RMS) error analysis of gantry angle, collimator angle, jaw position, and MLC leaf positions, and dosimetric components such as 3D gamma analysis. MobiusFX determined RMS errors by comparing delivered values to prescribed values, of which RMS error is calculated from equation 1. The setting of 3D gamma in MobiusFX decided a gamma comparison within 3%/3 mm criteria, and a gamma passing rate was above 95%.

$$RMS\ error = \sqrt{\frac{(error)^2}{n}} \quad (1)$$

When the error is a set of n errors (differences between prescribed and delivered positions) and n is the number of errors.

SPC was applied as the $\bar{X}/S$ control charts in this study. The $\bar{X}/S$ control chart consists of an upper control limit (UCL), centerline (CL), lower control limit (LCL), and data points. The control chart is used to monitor and control the variation in daily linac machine performance. If the data are within the control limits, the data will be an in-control process. When some of the data are outside the control limits, which indicates a systematic error might have occurred. These data point to the outside of the control limit should be removed to return the process to control. The CL and control limits of the $\bar{X}/S$ control chart is calculated from equation 2-4.

$$CL_{\bar{X}} = \bar{\bar{X}} \quad (2)$$

$$UCL_{\bar{X}} = \bar{\bar{X}} + A_3\bar{S} \quad (3)$$

$$LCL_{\bar{x}} = \bar{\bar{X}} - A_3\bar{S} \quad (4)$$

When $\bar{\bar{X}}$ is the average values of the several subgroups of each patient delivery data in MobiusFX. The constant A_3 depends on various subgroup size. The standard deviation value is calculated from equation 5.

$$\bar{S} = \sqrt{\frac{\sum_{i=1}^{m}(n_i-1){S_i}^2}{\sum_{i=1}^{m} n_i - m}} \quad (5)$$

The $\bar{X}/S$ control charts were constructed; the prior data points form the first 30 days were used to calculate the control limits. However, the 3D gamma analysis value cannot exceed 100%, so the UCL is not calculated. The LCL of the RMS error analysis values for gantry angle, collimator angle, jaw position, and MLC leaf positions are determined to be equal to 0 mm, so the LCL is not calculated. If there were any data points of out-of-control, these data points were removed. The CL and control limits were recalculated to the corrected control limits and then the control charts were used to continuously monitor the linac machine performance for 3D gamma analysis values, RMS error analysis values for gantry, collimator, jaw and MLC motor since day 31 to 62.

3. RESULTS

The result of the linac machine performance monitoring using the SPC. The CL, UCL, and LCL of the $\bar{X}/S$ control chart of each patient data in MobiusFX was calculated from the first 30 days. When the control limit thresholds were calculated, there were two data points of Y1-jaw, and three data points of Y2-jaw were removed (Exceeded the control limit thresholds). The new threshold of the control limits of the RMS errors on Y1-jaw and Y2-jaw was recalculated, shown in table 1.

Table 1 *The previous and new control limits of the patient delivery data were removed from out-of-control data points and recalculated control limits.*

Parameters	Previous control limits (mm)		New control limits (mm)	
	UCL	*CL*	*UCL*	*CL*
RMS error of MLC	1.007	0.910	1.005	0.907
RMS error of collimator angle	0.054	0.021	0.052	0.020

The $\bar{X}/S$ control charts of SPC showed the LCL of 3D gamma was 95% (as baseline). The UCL of RMS error for the gantry, collimator, jaw in X1, X2, Y1, Y2, and MLC leaf positions were 0.422 mm, 0.052 mm, 0.184 mm, 0.204 mm, 0.308 mm, 0.269 mm, and 1.005 mm, respectively. Then the $\bar{X}/S$ control charts were used to continuously monitor the linac machine performance since day 31 to 62. In figure 1-5 show the $\bar{X}/S$ control charts of the 3D gamma analysis, the RMS error analysis of MLC leaf positions, gantry angle and X-jaw position, respectively, which can demonstrate the ability to control the variation in the process of the daily linac machine performance to stabilize. We found the system flagged on Y1-jaw, Y2-jaw, and collimator angle during the linac machine monitoring, which are

shown in figure 6-8. Therefore, this required to the setup of preventive maintenance for the Y-jaw and collimator angle.

Figure 1 *The $\bar{X}/S$ control chart of 3D Gamma*

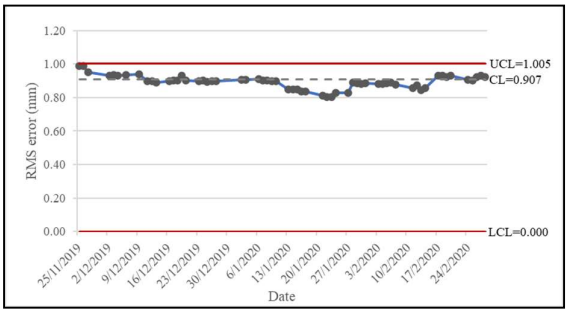

Figure 2 *The $\bar{X}/S$ control chart of RMS error of MLC leaf positions*

Figure 3 *The $\bar{X}/S$ control chart of RMS error of X1-jaw position*

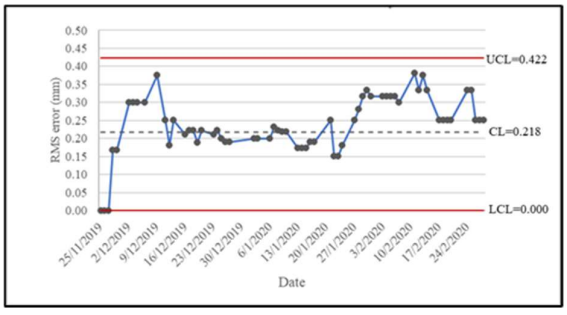

Figure 4 *The $\bar{X}/S$ control chart of RMS error of Gantry angle*

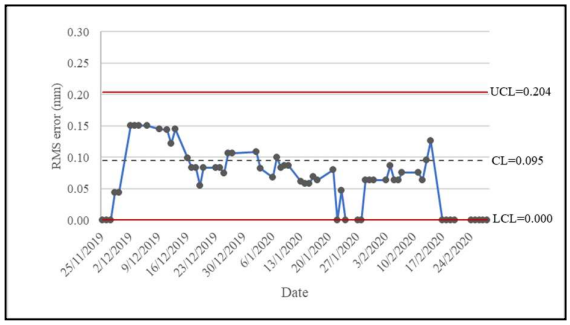

Figure 5 *The $\bar{X}/S$ control chart of RMS error of X2-jaw position*

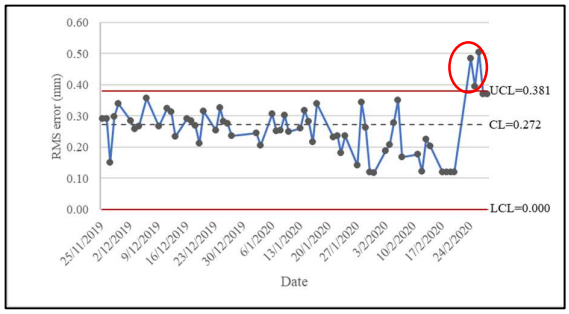

Figure 6 *The $\bar{X}/S$ control chart of RMS error of Y1-jaw position*

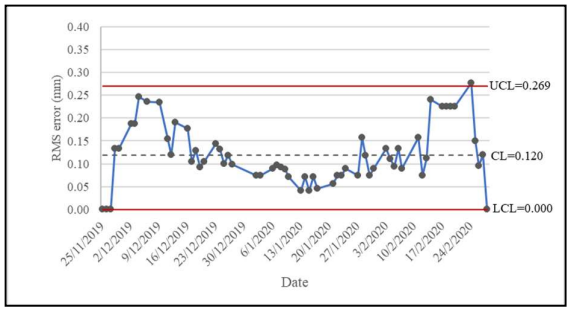

Figure 7 *The $\bar{X}/S$ control chart of RMS error of Y2-jaw position*

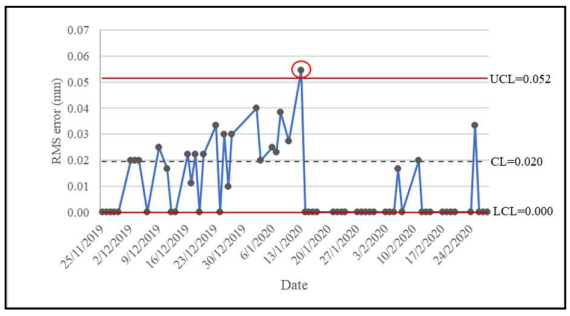

Figure 8 *The $\bar{X}/S$ control chart of RMS error of Collimator angle*

4. DISCUSSION

This study was a retrospective study, which applied the SPC in form the $\bar{X}/S$ control chart for monitoring the daily linac machine performance thought the clinical treatment delivery outcome using MobiusFX.

The implementation of SPC, the $\bar{X}/S$ control charts were constructed the prior data points from the first 30 days were used to calculate the control limits, which at least 20 data points are recommended to construct the control limits (9). When the data points are within the control limits, we can assume that the error occurs randomly. On the other hand, when the data points are out-of-control of the control limits. If we can find the root cause of errors from the out-of-control point, these points can be called systematic errors, which we should eliminate and bring the systematic error points back to within the control limits.

The SPC has been performed to be a suitable tool for quickly detecting the systematic errors, which occur at the time of treatment. The medical physicists will flag any possible cause when data points exceed control limits. Preventative actions should be taken to minimize treatment variability and to produce treatment quality (7).

However, there are several concerns regarding the application of SPC to the procedures of the QA programs. First, the user should know which SPC analysis is most appropriate for the QA's intended purposes. The selection of the SPC method will depend on the data type or goal of the procedures of the QA programs. Therefore, the medical physicists should understand the implementation of SPC and interpret to detect abnormalities of the data (8).

5. CONCLUSION

The linac machine performance monitoring through the clinical treatment delivery evaluation using MobiusFX with SPC can demonstrate the potential system to flag the possible malfunction of machine parts. This system can help medical physicists manage their preventive maintenance efficiently and minimize unexpected machine downtime in the future.

ACKNOWLEDGEMENTS

I am grateful to Dr. Todsaporn Fuangrod, Dr. Taweap Sanghangthum, and Mr. Kittipol Dachaworakul for useful advice and knowledge, and all medical physicists, radiation technologist and staff at Division of Radiation Oncology, Bhumibol Adulyadej hospital for their kind support of this study.

REFERENCES

1. Podgorsak E, Kainz K. Radiation oncology physics: A handbook for teachers and students. International Atomic Energy Agency. 2006;98.
2. Klein EE, Hanley J, Bayouth J, Yin FF, Simon W, Dresser S, et al. Task Group 142 report: Quality assurance of medical acceleratorsa. Med Phys. 2009;36(9Part1):4197-212.
3. Vazquez-Quino LA, Huerta-Hernandez CI, Rangaraj D, editors. Clinical experience with machine log file software for volumetric-modulated arc therapy techniques. Baylor University Medical Center Proceedings; 2017: Taylor & Francis.
4. Varian Medical Systems I. Mobius3D User Guide Version 2.1.2 rev 1.1. 2018.
5. Pawlicki T, Whitaker M, Boyer AL. Statistical process control for radiotherapy quality assurance. Med Phys. 2005;32(9):2777-86.
6. Gérard K, Grandhaye JP, Marchesi V, Kafrouni H, Husson F, Aletti P. A comprehensive analysis of the IMRT dose delivery process using statistical process control (SPC). Med Phys. 2009;36(4):1275-85.
7. Fuangrod T, Greer PB, Simpson J, Zwan BJ, Middleton RH. A method for evaluating treatment quality using in vivo EPID dosimetry and statistical process control in radiation therapy. Int J Health Care Qual Assur. 2017.
8. Cheong K-H, Lee M-Y, Kang S-K, Yoon J-W, Park S, Hwang T, et al. Statistical quality control for volumetric modulated arc therapy (VMAT) delivery by using the machine's log data. Journal of the Korean Physical Society. 2015;67(1):63-70.
9. Sanghangthum T, Suriyapee S, Srisatit S, Pawlicki T. Retrospective analysis of linear accelerator output constancy checks using process control techniques. J Appl Clin Med Phys. 2013;14(1):147-60.

Surface and Buildup Doses Comparison between Analytical Anisotropic Algorithm and Acuros XB for Various Treatment Parameters

Sonam Choki[1], Chulee Vannavijit[2], Taweap Sanghangthum[3,*]

1 Medical Physics Program, Department of Radiology, Faculty of Medicine, Chulalongkorn University, Bangkok, Thailand
2 Division of Radiation Oncology, Department of Radiology, King Chulalongkorn Memorial Hospital, Thai Red Cross Society, Bangkok, Thailand
3 Division of Radiation Oncology, Department of Radiology, Faculty of Medicine, Chulalongkorn University, Bangkok, Thailand
** Corresponding Author*

Abstract

The aim of this study was to compare the surface and build-up region doses under various treatment parameters between AAA and AXB algorithms and compare the surface dose with the measured values using EBT3 film. Surface and build up region doses were calculated in a solid water phantom using AAA and Acuros XB algorithms and the measurements were made in a water equivalent solid phantom. The measurements were performed for the surface and depth of maximum dose in phantom under the same parameters as used in treatment planning. Doses at the surface and build up region were calculated based on four treatment parameters of energy (6, 10 and 15 MV), field size (1×1-40×40 cm^2), dynamic wedge angle (10-60 degree), and bolus thickness (0-1.5 cm). Moreover, the out-of-field doses from 0-20 cm from field edge were evaluated. Surface dose increases linearly with field size and photon energy, with AAA showing higher dose than AXB. The measured surface doses using 6MV photon beams for field size 10x10 cm^2 and less were found to be closer to AXB values. The dose differences between two algorithms ranged approximately from 22.7 % to 36% at depth 0.07 cm and 0 cm. Dynamic wedges have negligible impact on the surface dose for both algorithms, with difference of about 23% and AAA also showed higher doses. But doses in AXB were closer to the measured doses. The out-of-field surface dose decreases with distance from the beam edge for both algorithms and in measured doses as well. The calculated surface dose increases linearly with respect to bolus thickness for both algorithms for all the depths and this result agrees with the measured surface doses.

Keywords: Surface dose, buildup region, AAA, Acuros XB, treatment parameters, EBT3 film

1. INTRODUCTION

Dose deposited at the boundary between the air and the patient's skin is defined as the surface dose [1]. In radiotherapy, megavoltage photons generated by medical linear accelerators are used for the treatment of cancer and these megavoltage X-rays have a skin-sparing effect, whereby the maximum dose is deposited in the deep tissues than in the skin. Therefore, the dose at the surface should be negligible but it is not. The surface dose is also affected by various treatment parameters such as field size, source to skin distance (SSD), beam angle, beam energy, and beam modifiers such as wedges, blocks and multi-leaf collimator (MLC) systems. Charged particle equilibrium does not exist at this depth and the dose gradient is high in the buildup region [2]. Therefore, accurate knowledge of surface dose is important, but the measurement at such depths is a challenging issue.

Knowledge of surface dose is important particularly when skin becomes a limiting factor in dose delivery to the deep-seated tumors and when they become part of the target volume in the treatment area. This can result in excessive radiation dose to the skin, thereby causing early radiation effects such as erythema or late effects such as hypoxia, fibrosis, etc.

In external radiotherapy, treatment planning systems (TPS) are used to calculate dose distributions in the target volume and organs at risk in order to provide maximum tumor control while minimizing critical organ doses [3]. The accuracy of the dose delivered depends on the accuracy of treatment planning calculation algorithm. The Eclipse treatment planning system has dose calculation algorithms standards like Analytical Anisotropic Algorithm (AAA) and new algorithm of Acuros XB (AXB). Due to the electronic disequilibrium, many treatment planning systems aim to develop the algorithm for tissue heterogeneity correction. The Analytical Anisotropic Algorithm, AAA, is a 3D pencil beam convolution-superposition algorithm and implemented in Varian's treatment planning system Eclipse. There's a good agreement between Monte Carlo and experimental measurements. AAA is generally in compliance with MC, but does not account for all scattering effects in the interface between different mediums [4]. On the other hand, another new calculation algorithm called Acuros XB (AXB) of Eclipse treatment planning system has been introduced to correct dose in tissue heterogeneity. It uses the Linear Boltzmann transport equation for heterogeneity correction in patient dose calculation AXB is recommended for tissue heterogeneity correction according to the report by Oonsiri et al. [5]. The aim of this study was to compare the dosimetric impact of the Acuros XB algorithm (AXB) with Anisotropic Analytical Algorithm (AAA) calculations and validate with the measured doses using EBT3 film for surface dose.

2. MATERIALS AND METHODS

Surface and build up region doses were calculated in a water equivalent homogeneous solid phantom using Acuros XB and AAA algorithm and compared with the measured surface dose using EBT3

film. The results presented in this paper were based on beam data for 6, 10 and 15 MV photon beams from Varian Clinac iX and 23EX linear accelerator (Varian Medical Systems, Palo Alto, CA). The machines are equipped with 120 MLC.

2.1 TPS Calculations

Several treatment parameters were applied to the AAA and AXB single field plan for the calculation of surface and buildup doses. The various plans were created in a water equivalent homogeneous phantom (30×30×30 cm^3) with SAD technique. Doses at the surface and buildup region were calculated based on different treatment parameters including beam energy, field size, wedge factor, out-of-field locations and bolus effect. The four different surface dose calculations were made

1) at the depth ranging from 0 cm to 1 cm depth for 6 MV, 10 MV and 15 MV beam for 1×1 till 40×40 cm^2 field sizes

2) with dynamic wedges ranging from 10 to 60 degrees with 6 MV beam for 10×10 cm^2 field size

3) varying bolus thickness with different depth at 10×10 cm^2 field size for 6 MV beam

4) out-of-field dose with distance ranging from 0 cm to 20 cm from the beam edge at surface of the phantom for 10×10 cm^2 field size and 6 MV photon energy.

2.2 Film Measurements

In this study, GafChromic EBT3 film (Ashland ISP Advanced Materials, NJ) was used for measurement to verify the treatment planning. It is a radiochromic dosimetry film that has been developed specifically to quantify dose measurement applications in external beam radiotherapy. The EBT3 film is a self-developing (develops in real time without post exposure treatment), energy independent, near tissue equivalent, water resistant, high spatial resolution and can handle in room light. The wide dose range of Gafchromic EBT3 film is 0.2 to 10 Gy. This film features symmetrical construction and anti-Newton ring coatings for enhanced ease-of-use and accuracy. The EBT3 film has a single active layer (30 μ m), which is sandwiched between two 125 μ m matte polyester sheets. The effective point of measurement for the EBT3 film was defined at 0.153 mm depth [1,6]. For the investigation of surface dose, a calibration curve was created before irradiation to make correct evaluation. The EBT3 film was cut into small pieces of 2×2 cm^2 size and placed perpendicularly between solid water slab phantoms. The phantom used in this study was the solid water phantoms (Gammex rmi, Middleton, WI), which has the density of 1.02 g/cm^3, and atomic number of 5.95 is made in square slabs of 30×30×30 cm^3. The film was calibrated at d_{max} in range from 0 to 310 cGy with 10×10 cm^2 field sizes. For field size effect, the films were placed on the surface and at the depth of maximum dose for 1, 5, 10, 20, 30 and 40 cm^2 field sizes at 100 cm fixed SAD and 6MV beam as shown in Fig 1. To evaluate the surface dose on of photon energy effect, films were irradiated with 6, 10 and 15 MV for 10×10 cm^2 field size at surface and their d_{max}. Moreover, films were irradiated with varying wedge angles from 10 to 45 degrees at 10×10 cm^2 field size for 6MV. Effects of bolus were also evaluated with bolus thickness ranging from 0.5, 1.0 and 1.5 cm for 10×10 cm^2 field size of 6 MV photon beams. The out-of-field surface doses were also studied for 6 MV photon beam at 10×10 cm^2 field size with distance ranging from 0 cm to 20 cm from the beam edge at surface of the phantom. The EBT3 films showed instant change in color on radiation dose. After a period of 24 hours after irradiation, the exposed films were scanned using the Epson perfection V700 flat-bed color CCD (model V700, Epson Seiko Corp., Nagano, Japan). After the scanning process, the optical densities (OD) of the film pieces were acquired in the red channel using imageJ software. The calibrations curve was then used to covert the net ODs to the dose.

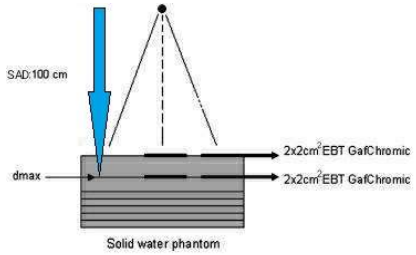

Fig 1. The phantom setting up for film measurement.

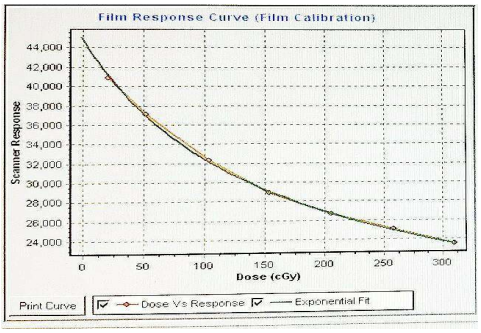

Fig 2. Calibration Curve of EBT3 film

3. RESULTS

The film calibration curve is presented in Fig 2. The calculated and measured surface and buildup region doses were expressed as percentage of maximum dose at depth for that photon energy. Fig.3 (a), (b), and (c) shows surface dose for 6, 10 and 15 MV beam at various field sizes. Surface dose increases with field size linearly for photon energy ranging from 6 to 15 MV. AAA showed higher surface dose than Acuros XB. The variation of calculated dose difference between AXB and AAA algorithm ranges from 22.7 % to 36% at depth 0.07 cm and depth 0 cm, respectively. Dynamic wedge angles have negligible impact on the surface dose for both calculation algorithms and also EBT3 film measurement as presented in Table 2. The out-of-field surface dose decreases with distance from the beam edge for both algorithms. The calculated surface dose increases linearly with respect to bolus thickness for

both algorithms for all the depths. The measured surface doses using EBT3 film agreed well with the relationship of the calculated surface dose (as a percentage of D_{max}) for various treatment parameters for both AAA and AXB. For some parameters, the measured surface dose agrees well with AAA while for some parameters it agrees more with AXB as presented in Table 1 and Table 2.

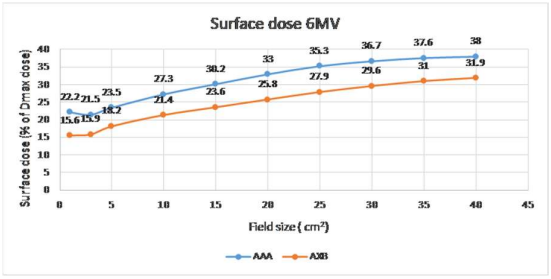

(a)

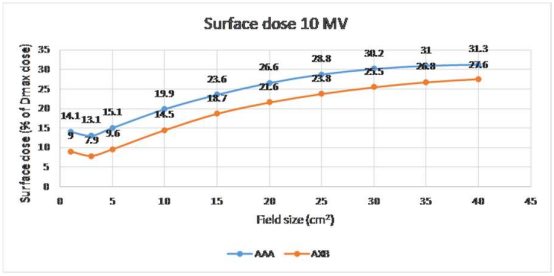

(b)

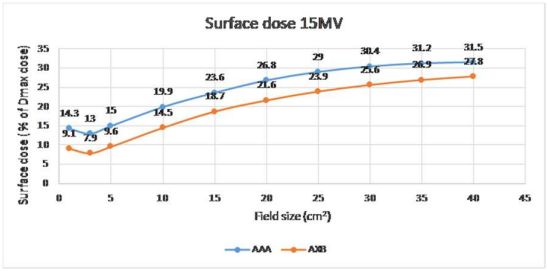

(c)

Fig.3 The calculated percentage surface doses of (a) 6 MV, (b) 10 MV and, (c) 15 MV beams at various field sizes.

Table 1. Surface dose comparison between AAA, AXB and EBT3 for various energies and some treatment parameters.

Surface Dose (%)					
Technique	6 MV	10 MV	15 MV	Bolus (0.5cm)	Out-of-field (10cm)
AAA	27.3	19.9	23.8	88.4	0.7
AXB	21.4	14.5	17.5	90.2	0.6
EBT3	23.6	16.8	17.2	85.7	3.3

Table 2. Surface dose comparison between AAA, AXB and EBT3 for various wedge angles.

Surface Dose (%)					
Technique	10º	15º	30º	45º	60º
AAA	27.0	27.1	27.2	27.2	27.2
AXB	21.3	21.4	21.4	21.4	21.5
EBT3	23.7	24.7	24.5	24.1	24.0

4. DISCUSSION

Measuring dose at surface and buildup region is very challenging and significant for clinical dosimetry in radiotherapy. The surface and buildup region doses can be affected by different treatment parameters such as field sizes, photon energy, SAD and beam modifying devices such as collimators, blocks and wedges. Therefore, the use of a suitable tool for surface dosimetry is necessary. In this study, it was seen that for both measurement and calculation, increasing field sizes also increases the surface dose. This is due to extra electron contamination and scattered photon. For all field sizes, surface dose was lower for AXB than AAA, while the EBT3 measured doses were in between these 2 algorithms. The measured surface doses were closer to AXB than AAA because more consideration of scattered radiation in AXB algorithm. This would suggest that AAA could be overestimating the dose at the surface. Our results showed close agreement with publications by Oonsiri et al. [5] and another studied by Bush et al. [7]. By comparing the values with the measured surface doses, it has been observed that for field size 10×10 cm^2 and less, the values agreed more with AXB and for field sizes larger than 10×10 cm^2, the values agreed more with AAA. At 10×10 cm^2 field size, for 6 MV, the percentage difference seen for surface dose between AXB and EBT3 was found to be 9.7% and between AAA and EBT3 was found to be 14.5%. As for the energy effect, the surface dose increases slightly with energy for 15MV in this study. This is due to electron contamination from high energy photon as represented in the paper by Kry.et al. [8]. Regardless, overall, there is only a small difference in surface dose with beam energy. It has been observed that dynamic wedges have less impact on the surface dose when wedge angle changes from 10 to 60 degrees for both AAA and AXB. The measured values also showed negligible impact from wedges at the surface. The calculated out-of-field surface dose decreases as the distance from the beam edge increases at the surface of the phantom. The relative dose difference between the calculated surface dose for AAA and AXB ranges from approximately 41% at 0 cm to 0% at 20 cm distance from the beam edge. This result also agrees with our measured values from EBT3 film. Bolus minimizes the skin sparing effect of MV photon beams by increasing the surface dose. It is a tissue equivalent material, which increases dose in the buildup region for relevant photon

energies. Surface dose increases with bolus thickness as evident in the calculated doses using AAA and AXB and also in the measured dose values using different bolus thickness. In this study EBT3 film was used only for the surface dose measurement comparison. Therefore, further comparisons can be made by measuring in the buildup region for further studies.

5. CONCLUSION

Differences in surface dose calculations have been observed between AXB and AAA treatment algorithms and also with the measured values using EBT3 film. At deeper depths calculated doses between AAA and AXB became closer. For some parameters, AAA agreed well with the EBT3 measurements and for some parameters, AXB agreed more with the measured surface doses using EBT3 film.

REFERENCES

1. Devic S, Seuntjens J, Abdel-Rahman W, Evans M, Olivares M, Podgorsak EB, et al. Accurate skin dose measurements using radiochromic film in clinical applications. Medical Physics. 2006;33(4):1116–24
2. Akbas U, Donmez Kesen N, Koksal C, Bilge H. Surface and Buildup Region Dose Measurements with Markus Parallel-Plate Ionization Chamber, GafChromic EBT3 Film, and MOSFET Detector for High-Energy Photon Beams. Advances in High Energy Physics. 2016;2016:8361028.
3. Kesen ND, Akbas U, Koksal C, Bilge H. Investigation of AAA dose calculation algorithm accuracy in surface and buildup region for 6MV photon beam using markus parallel-plate ion chamber. J Xray Sci Technol. 2019;27(2):361-369. doi: 10.3233/XST-180489. PMID: 30856153.
4. Nilsson E, Back A, Chakarova R. Evaluation of the Analytical Anisotropic Algorithm (AAA) in lung tumors for 6MV photon energy. Göteborg University.2009
5. Oonsiri P, Saksornchai K, Suriyapee S. Dosimetric evaluation of Acuros XB and AAA on lung volumetric modulated radiation therapy plan for stereotactic body radiation therapy technique. J Thai Assn of Radiat Oncol[Internet].2016Dec.29[cited2020Nov.7];22(2):306.Availablefrom:https://he01.tcithaijo.org/index.php/jtaro/article/view/203075.
6. Van Battum LJ, Hoffmans D, Piersma H, Heukelom S. Accurate dosimetry with GafChromic EBT film of a 6 MV photon beam in water: what level is achievable?. *Med Phys*. 2008;35(2):704-716. doi:10.1118/1.2828196
7. Bush K, Gange IM, Zavgorodni S, Ansbacher W and Beckham W: Dosimetric validation of Acuros XB with Monte Carlo methods for photon dose calculations. Med Phy 2011, 38(suppl 4): 2208-2221
8. Kry SF, Smith SA, Weathers R, Stovall M. Skin dose during radiotherapy: a summary and general estimation technique. *J* Appl *Clin Med Phys*. 2012;13(3):3734. Published 2012 May 10. doi:10.1120/jacmp.v13i3.3734

Determination of small field output factors and specific correction factors for various diodes and microDiamond detector for CyberKnife M6 system equipped with fixed collimator

Penpisuth Suksawang[1], Sawwanee Asavaphatiboon[1] Lakkana Apipunyasopon[2], Wisawa Phongprapun[3], Chumpot Kakanaporn[3*]

1 Master of Science Program in Medical Physics, Faculty of Medicine Ramathibodi Hospital, Mahidol University, Bangkok 10400, Thailand,
2 Department of Radiological Technology and Medical Physics, Faculty of Allied Health Sciences, Chulalongkorn University, Bangkok 10330, Thailand,
3 Division of Radiation Oncology, Faculty of Medicine Siriraj Hospital, Mahidol University, Bangkok 10700, Thailand
**Corresponding author E-mail: kakanaporn@yahoo.com*

Abstract

The purpose of this study was designed to determine small field output factors and specific output correction factors of CyberKnife M6 equipped with fixed collimators using various type of solid-state detectors and a synthetic diamond detector. The relative output factors measurements were performed by PTW60017 diode E, PTW60018 diode SRS, IBA RAZOR diode and PTW60019 microDiamond. Then calculate the output factors for each detector and using microDiamond as the reference detector to calculate the specific output correction factors for various detectors. The results have shown a good agreement of output factors between PTW60017, PTW60018 and IBA RAZOR diode compare to PTW60019 at smallest circular field sizes of 7.5mm and 5mm, which the percentage difference compared to PTW60019 is 1.4%, 1.8%, and 0.6%, respectively. Specific output correction factors do not exceed than 1%, when compared to TRS 483(1) percentage difference within. 1%. In conclusion, the result has shown the comparable output factor of CyberKnife M6 with fixed collimator between various diodes.

Keywords*:* CyberKnife M6, Small field, Output factors, Specific output correction factors

1. INTRODUCTION

Over the last decades, development of radiosurgery technique has improved to deliver high radiation dose to very small targets while mostly sparing normal organs. To accomplish the goal, the small photon beams usually used in radiosurgery. According to the TRS483(1), small photon beam defined follow three conditions; the range of secondary electron larger than the field width, collimators obstructs the part of the beam, and hardening in photon energy spectrum. The following condition of dosimetric measurement on small photon beam shown the significant considerable uncertainty(2, 3) in terms of output factors. To correct the uncertainty of the measurement, TRS483(1) provide the measurement procedure guideline and also the $k_{Q_{clin},Q_{msr}}^{f_{clin},f_{msr}}$ (output correction factor) calculated from Monte Carlo method. Another method is a measurement, normally the ionization chamber often used as the standard detector. For small field sizes, unshielded diodes with small active areas appear to be a reasonable choice(4). These devices have been the detector of choice in most centers to perform CyberKnife® system dosimetric characterization and output factor measurements(5) but the detector material made from high atomic number component that can cause of detector overresponse. Francescon et al. (6) designated that preference should be given to a microDiamond or diode detector for small field output factor measurement because these have smaller corrections than other detectors and it also has the characteristic equivalent to the tissue. Recently, IBA has introduced an unshielded p-type silicon diode, the Razor for small field dosimetry. The present study, the PTW60019 microDiamond has been evaluated for relative measurement in term of reference for output factor and $k_{Q_{clin},Q_{msr}}^{f_{clin},f_{msr}}$ (output correction factor) and compare to others detectors, which are PTW60017, PTW60018, and IBA RAZOR diode.

2. MATERIAL AND METHODS

2.1 CyberKnife stereotactic system

The measurements were performed on the CyberKnife M6 system with 6 MV flattening filter free beams at dose rate of 1000 MU/min with fixed collimators. The study were performed at the Division of Radiation Oncology, Department of Radiology, Faculty of medicine Siriraj Hospital, Mahidol University.

2.2 Dosimeters

To determine the accurate dosimetric measurement in small field condition required the detector characteristic; high accuracy and precision, high spatial resolution, high sensitivity, beam quality independent, constant response, and material composition equivalent to soft tissue. According to Veselsky T. et al.(7) , the PTW60019 (microDiamond) can use as the reference detector due to characteristic of near tissue-equivalence

and high specific sensitivity (8-10). Nevertheless, the studies by Dieterich S. et al. (5) and Francescon P. et al. (6) suggested using small volume unshield p-type diode measured small field in CyberKnife . Thus, our study conducted three p-type silicon detectors: the PTW60017 E diode, PTW60018 SRS diode, and IBA RAZOR diode as a comparable detectors.

2.3. Measurement condition

According to the TRS483(1) defined machine specific reference (msr) field size of CyberKnife at circular diameter 60 mm at 80 cm SAD. Output factor obtains in circular field diameter 5, 7.5, 10, 15, 20, 30, 40, and 60 mm. Before the output measurement, scan beam profile to centering the detectors. The output factor measured with 80 cm source to detector distance and depth 1.5cm in water with 6 MV FFF. Then alignment of the detectors at the level of sensitive volume and perpendicular to the central axis. Calculated the PTW60019 output factor and apply $k_{Q_{clin},Q_{msr}}^{f_{clin},f_{msr}}$ on TRS483(1). Then calculated the output factor of the other detectors and calculated the output correction factor using the corrected PTW60019 output factor as a reference.

2.4 Data analysis

2.4.1 Field output factor

The CyberKnife output factor measurements were analyzed in terms of a ratio of detector readings OF_{det} defined according to Alfonso et al. formalism (11) for relative dosimetry of small fields. In detail:

$$OF_{det}^{fclin,fmsr} = \left(\frac{M_{Qclin}^{fclin}}{M_{Qmsr}^{fmsr}}\right)$$

Where M_{Qclin}^{fclin} and M_{Qmsr}^{fmsr} are the readings per MU of each detector in the clinical field (f_{clin}) and in the machine-specific reference field (f_{msr}), respectively.

2.4.2 Specific output correction factors

For the CyberKnife system, f_{msr} is defined by the fixed 60mm collimator.

The field output factor $\Omega_{Qclin.Qmsr}^{fclin,fmsr}$, that converts the absorbed dose to water for f_{msr} to the absorbed dose to water for f_{clin} can be written as

$$\Omega_{Qclin.Qmsr}^{fclin,fmsr} = OF_{det}^{fclin,fmsr} \cdot k_{Q_{clin},Q_{msr}}^{f_{clin},f_{msr}}$$

Where $k_{Q_{clin},Q_{msr}}^{f_{clin},f_{msr}}$ is the correction factor accounting for the difference between detector response in the fields f_{clin} and f_{msr}. Monte Carlo simulations could be used to estimated. In this study, we used microDiamond be the reference detector for output correction factors. $k_{Q_{clin},Q_{msr}}^{f_{clin},f_{msr}}$

3. RESULTS

3.1 Field output factors

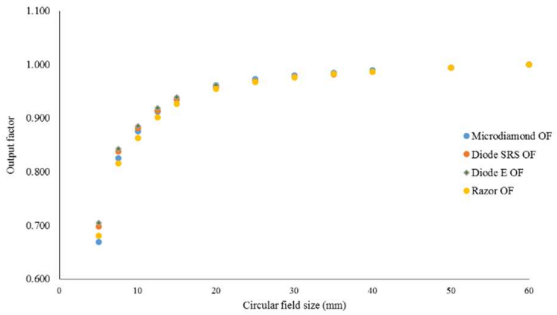

Figure 1 *Relationship between circular field size and output factors measured by various solid-state detectors without corrected.*

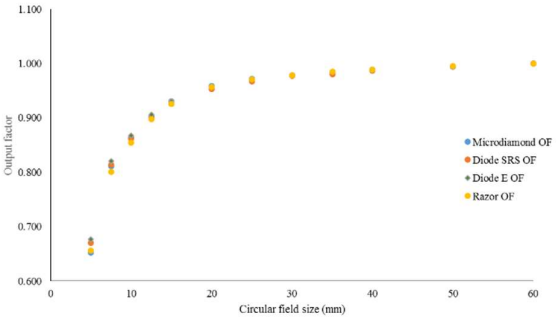

Figure 2 *Relationship between circular field size and output factors measured by various solid-state detectors after corrected according to TRS 483.*

Table 1 *Measured output factor with various type of detector on CyberKnife M6 system defined with fixed collimators.*

Field size (mm)	PTW 60019	PTW 60017	PTW 60018	IBA RAZOR diode
60	1.0000	1.0000	1.0000	1.0000
50	0.9945	0.9939	0.9941	0.9951
40	0.9891	0.9883	0.9873	0.9888
35	0.9845	0.9844	0.9808	0.9854
30	0.9788	0.9784	0.9771	0.9786
25	0.9716	0.9702	0.9677	0.9708
20	0.9591	0.9577	0.9534	0.9571
15	0.9304	0.9311	0.9257	0.9259
12.5	0.9034	0.9061	0.8993	0.8978
10	0.8643	0.8680	0.8620	0.8549
7.5	0.8109	0.8207	0.8144	0.8009
5	0.6523	0.6766	0.6707	0.6564
Average percentage different		0.26	0.13	0.26
Maximum percentage different		1.84	1.39	0.63

The table 1 and Figure 1, 2 show the results of output factor measurements by various solid-state detectors.

The maximum different before corrected follow to TRS483(1) is 2.61%, decrease to 1.84% at the smallest field size. All of the measurements has a good agreement with the mean output factors. Then compared to Wilcox E. et al.(12), the measurement slightly higher in field size less than 15 mm.

Overall output factors of PTW60017 and PTW60018 diodes are very close, the percentage different are within 0.7% and show the excellent agreement on Pearson correlation test (r = 0.999) when compared to PTW60019. For output factor of IBA Razor diode compare to PTW60019 also shown the good agreement (r=0.982). Nevertheless, the measurement with the smallest field size 5 mm shows the maximum difference in PTW60017, PTW60018, and IBA RAZOR diode about 1.84%, 1.39%, and 0.63%, respectively.

3.2 Specific output correction factors

The result in table 2 shows the output correction factor calculated by used the microDiamond output factors corrected by TRS483(1) as a reference. When compare to output correction factors of PTW60017, PTW60018 on TRS483(1) has a good correlation about 0.983 and 0.955 on Pearson correlation test, respectively. Then compared to mean output factors of Francescon et al. (13, 14), which measured by PTW60017, PTW60008, and Sun nuclear EDGE detector on 800MU/min CyberKnife with fixed collimator, in order to determine the correlation within 0.965 in five smallest field sizes, respectively. IBA RAZOR diode output correction factors only publish on Francescon et al. study(15) also provides a good correlation (0.912). Bassinet C. et al.(16), that measurement performed by EDGE diode, PTW60016, PTW60017, PTW31014 pin point chamber, PTW 60003 diamond, and SFD diode in five smallest field sizes, correlation within 0.915.

Table 2 *Calculated output correction factor with various type of detector on CyberKnife M6 system.*

Field size (mm)	PTW60017	PTW60018	IBA RAZOR diode
60	1.0000	1.0000	1.0000
50	1.0006	1.0004	1.0004
40	1.0018	1.0028	1.0024
35	1.0010	1.0028	1.0021
30	1.0003	1.0016	1.0033
25	1.0003	1.0019	1.0047
20	0.9983	1.0008	1.0049
15	0.9909	0.9947	1.0046
12.5	0.9838	0.9883	1.0020
10	0.9764	0.9812	1.0013
7.5	0.9629	0.9684	0.9947
5	0.9254	0.9346	0.9588
Maximum percentage different	1.84	1.39	0.32

4. DISCUSSION

4.1 Output factors

Comparison of the output factors in each detector without applied the output correction factor shown the massive difference due to the physical properties perturbation of detectors and volume averaging effect (17). The results from Wilcox E. et al. (12), which measured by PTW60008, compare to this study is lower because the detector volume of PTW60008 is larger that cause of volume averaging effect to under response.

In smallest field size has a large difference between detectors such as in PTW60019 microDiamond and IBA RAZOR diode, the measurements are the lowest in the condition of with or without applying correction factor, because the volume of detector exceeds than the field width. Another reason is the PTW60017 and PTW60018 made from silicon diode which composed of high atomic number component, which can reduce secondary electrons range effect to measurements slightly over response.

4.2 Comparison Specific output correction factors with data given in TRS 483

The ideal method to calculated output correction factor is Monte Carlo simulation. Nevertheless, this study used measurements base calculation. Then compare to TRS 483 that calculated from Monte Carlo simulation output correction factor has a very good agreement for PTW 60017 E and PTW 60018 SRS diodes. Nevertheless, output correction factor of IBA RAZOR diode has not provided by TRS 483 yet. Therefore, the study of Francescon et al. (6, 13-15) which provide the measurements by simulated the detectors on Monte Carlo simulation with the uncertainty less than 1% used as the comparable measurement for IBA RAZOR diode and PTW 60018 SRS diodes others detectors. According to the results have been shown the slight difference of the measurement.

5. CONCLUSION

It is able to conclusion the result in term of output factors and specific output correction factors have a good agreement when compared to other studies. In the case of microDiamond used as a reference also shown a good agreement. However, to use the result in clinical practice should be investigated with other detectors or Monte Carlo simulation.

In future work we plan to investigate the measurements of reference detector with Extradin W1 scintillator, radiochromic film or Monte Carlo simulation in IRIS and Incise MLC on CyberKnife M6 series.

REFERENCES

1. Dosimetry of Small Static Fields Used in External Beam Radiotherapy. Vienna: INTERNATIONAL ATOMIC ENERGY AGENCY; 2017.
2. Tsai JS, Rivard MJ, Engler MJ, Mignano JE, Wazer DE, Shucart WA. Determination of the 4 mm Gamma Knife helmet relative output factor using a variety of detectors. Medical Physics. 2003;30(5):986-92.
3. Haryanto F, Fippel M, Laub W, Dohm O, Nüsslin F. Investigation of photon beam output factors for conformal radiation therapy—Monte Carlo simulations and measurements. Physics in Medicine & Biology. 2002;47(11):N133.
4. Cranmer-Sargison G, Weston S, Sidhu NP, Thwaites DI. Experimental small field 6 MV output ratio analysis for various diode detector and accelerator combinations. Radiotherapy and Oncology. 2011;100(3):429-35.
5. Dieterich S, Cavedon C, Chuang CF, Cohen AB, Garrett JA, Lee CL, et al. Erratum:" Report of AAPM TG 135: Quality assurance for robotic radiosurgery". Medical physics. 2011;38(9):5264.
6. Francescon P, Cora S, Cavedon C, Scalchi P, Stancanello J. CyberKnife dosimetric beam characteristics: Comparison between experimental results and Monte Carlo simulation Robotic Radiosurgery. Radiosurgery. 2005;1(1):71-80.
7. Veselsky T, Novotny Jr J, Pastykova V, Koniarova I. Determination of small field synthetic single-crystal diamond detector correction factors for CyberKnife, Leksell Gamma Knife Perfexion and linear accelerator. Physica Medica. 2017;44:66-71.
8. Zani M, Bucciolini M, Casati M, Talamonti C, Marinelli M, Prestopino G, et al. A synthetic diamond diode in volumetric modulated arc therapy dosimetry. Medical physics. 2013;40(9):092103.
9. Pimpinella M, Ciancaglioni I, Consorti R, Di Venanzio C, Guerra A, Petrucci A, et al. A synthetic diamond detector as transfer dosimeter for Dw measurements in photon beams with small field sizes. Metrologia. 2012;49(5):S207.
10. Almaviva S, Ciancaglioni I, Consorti R, De Notaristefani F, Manfredotti C, Marinelli M, et al. Synthetic single crystal diamond dosimeters for Intensity Modulated Radiation Therapy applications. Nuclear Instruments and Methods in Physics Research Section A: Accelerators, Spectrometers, Detectors and Associated Equipment. 2009;608(1):191-4.
11. Alfonso R, Andreo P, Capote R, Huq MS, Kilby W, Kjäll P, et al. A new formalism for reference dosimetry of small and nonstandard fields. Medical physics. 2008;35(11):5179-86.
12. Wilcox EE, Daskalov GM. Evaluation of GAFCHROMIC® EBT film for CyberKnife® dosimetry. Medical physics. 2007;34(6Part1):1967-74.
13. Francescon P, Kilby W, Satariano N, Cora S. Monte Carlo simulated correction factors for machine specific reference field dose calibration and output factor measurement using fixed and iris collimators on the CyberKnife system. Physics in Medicine & Biology. 2012;57(12):3741.
14. Francescon P, Kilby W, Satariano N. Monte Carlo simulated correction factors for output factor measurement with the CyberKnife system—results for new detectors and correction factor dependence on measurement distance and detector orientation. Physics in Medicine & Biology. 2014;59(6):N11.
15. Francescon P, Kilby W, Noll J, Masi L, Satariano N, Russo S. Monte Carlo simulated corrections for beam commissioning measurements with circular and MLC shaped fields on the CyberKnife M6 System: a study including diode, microchamber, point scintillator, and synthetic microdiamond detectors. Physics in Medicine & Biology. 2017;62(3):1076.
16. Bassinet C, Huet C, Derreumaux S, Brunet G, Chéa M, Baumann M, et al. Small fields output factors measurements and correction factors determination for several detectors for a CyberKnife® and linear accelerators equipped with microMLC and circular cones. Medical physics. 2013;40(7):071725.
17. Palmans H, editor Small and composite field dosimetry: the problems and recent progress. Proceedings of IAEA International Symposium on Standards, Applications and Quality Assurance in Medical Radiation Dosimetry; 2011.

Tolerance level determination for automated EPID-based deep inspiration breath-hold (DIBH) instability evaluation in breast cancer patients

Aphisara Deeharing[1], Puangpen Tangboonduangjit[1, 2], Todsaporn Fuangdrod[3]

1 Master of Science Program in Medical Physics, Department of Diagnostic and Therapeutic Radiology, Faculty of Medicine Ramathibodi Hospital, Mahidol University, Bangkok, Thailand
2 Division of Radiation Oncology, Department of Diagnostic and Therapeutic Radiology, Faculty of Medicine Ramathibodi Hospital, Mahidol University, Bangkok, Thailand
3 Faculty of Medicine and Public Health, HRH Princess Chulabhorn College of Medical Science, Chulabhorn Royal Academy, Bangkok, Thailand

Abstract

Introduction: Deep Inspiration Breath Hold (DIBH) is used during radiotherapy for left-sided breast cancer to reduce the cardiac dose. This technique requires monitoring for the stability of DIBH during treatment. The cinematographic image (cine) is selected for DIBH monitoring because it does not add the dose to the patient. Then, it can measure geometrical setup errors in Beam's-Eye-View (BEV) according to the actual field

Purpose: To develop a daily patient DIBH instability assessment as an intra-fractional motion verification tool using a cine-electronic portal imaging device (cine-EPID).

Methods: The cine images were acquired and analyzed to find the stability of the breath-hold during treatment by using in house MATLAB program with Canny's edge algorithm. Then the lung depth distance was calculated automatically to evaluate the stability of DIBH. Moreover, the performance of assessment tools was studied from the phantom by testing accuracy and capability. Then applying in clinical from three patients.

Results: The maximum difference of the accuracy test of the in house assessment tool from the phantom is -0.996 ±0.246 mm. For capability test with adding blur in the image, this program can be analyzed quite accurately with a maximum difference of 1.400 ±0.460 mm but reduce noise very poorly with a maximum difference of 73.2±13.89 mm. However, in clinical found that the results correspond amplitude setting from the treatment room.

Conclusion: The in-house automated program with EPID based is suitable for clinical treatment with a millimeter error**.**

Keywords: Deep Inspiration Breath Hold (DIBH), cine EPID, Whole Breast Radiation Therapy (WBRT)

1. INTRODUCTION

Breast cancer is the most common cancer, and also the primary cause of cancer death, approximately 15.0% in women [1]. For early-stage breast cancer, surgery with radiation therapy is the most recommended treatment to reduce the local recurrence and improves the survival rate [2]. Nevertheless, respiratory motion is a significant challenging problem in breast radiotherapy, essentially on the left side owing to near heart and left anterior descending coronary artery (LAD). Moreover, the risk of subsequent has been reported to induce relevant cardiac death that is assessed from mean heart dose (MHD) [3-5]. Currently, deep inspiration breath-hold (DIBH) is used in radiotherapy with left-sided breast cancer to reduce the cardiac and LAD dose. In this technique, patients hold their breath while radiation is delivered, the diaphragm descends, and the heart moves away from the chest wall [6-8]. Though there is a significant reduction of heart dose, this technique is also required monitoring the stability of DIBH during treatment. Besides, several methods have been developed to monitoring the stability of DIBH, such as using a respiratory gating system, EPID, and surface guided radiotherapy. In this study, the cine-EPID is selected for DIBH monitoring because it does not add the dose to the patient. Then, it can measure geometrical setup errors in Beam's-Eye-View (BEV) according to the actual field [9-11]. As a result, an in-house automated DIBH stability evaluation tool from cine was developed by using MATLAB software.

2. MATERIAL AND METHODS

The automated EPID-based DIBH evaluation tool was developed using MATLAB/SIMULINK version 2018b. Cine images were obtained during treatment delivery. After patients were treated, the cine images were saved in the ARIA database. Then, the images were analyzed the results by the in house MATLAB. In the first step, the cine images were used for an input image. Also, the Canny edge detection of MATLAB code was written and used a Gaussian smoothing filter, which removed the majority of image artifacts yet preserved the chest wall boundary. Besides, the image was rotated to zero degrees, and the median filter and Wiener filter were applied. Next, the program displays the edges image. Finally, the line profile was built at the center of the image along the horizontal direction. The distance of lung depth was measured from the peak as shown in Figure 1.

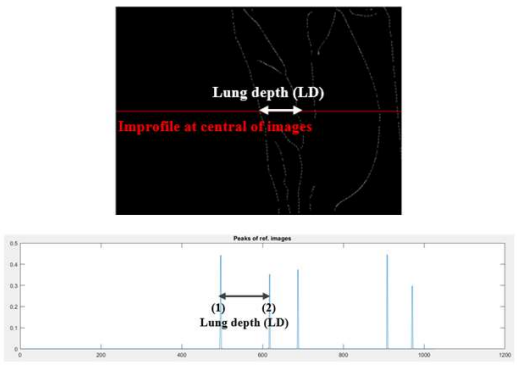

Figure 1 *The profile along a horizontal.*

2.1 Testing the performance of the assessment tool

The Rando phantom combine with MotionSim-4D/XY has moved the different motion by vary amplitude and speed then the cine images were acquired during radiation delivery by using EPID. The pattern of motion can be separated into eight groups, as presented in Table 1. Besides, the cine imaging was used for assessing the performance of MATLAB in house programs, including accuracy and capability.

Table 1 *The pattern of phantom motion*

Group	Gantry angle (°)	Amplitude (mm)	Time (second)
1	239	0	0
2	239	2.5	1
3	239	2.5	0.5
4	239	5.0	1
5	39	0	0
6	39	2.5	1
7	39	2.5	0.5
8	39	5.0	1

A. Accuracy test

All cine images of phantom motion were used to verify the accuracy of the DIBH assessment tool. the data were compared with the prediction value that was calculated from the sine wave.

B. Capability test

The cine images have been introduced an error to test the ability to analyze the results of the program in abnormal conditions that were divided into three scenarios consist of simulated the blurring images, added Gaussian noise, and salt and pepper noise. Moreover, each scenario also had three levels. For scenario 1, the blurring image which is a different point spread function (PSF) consists of blurring 7,10, 10,10, and 15,15. For scenario 2, the Gaussian noise was introduced into an image in different values consist of 0.000001, 0.00001, 0.000025. For the scenario 3, the salt and pepper noise was also added into the image. consists of 0.0005, 0.001, and 0.002.

2.2 Applying in clinical

The cine image of three patients with left side breast cancer without SPC who were treated with the DIBH technique was selected in this study for evaluating the stability of DIBH. The number of the fraction was ten, and the number of cine images was used for analysis is 115. In each patient have a different character. The first, the patient, has large breast conservative surgery. Second, breast mastectomy is both with and without a bolus plan: the last, the small breast conservative surgery. The images were analyzed by a measured distance of lung depth in each field.

3. RESULTS

3.1 Testing the performance of the assessment tool

A. Accuracy test

All eight series of cine imaging were used for assessing accuracy. The results were compared between prediction value and measurement value in each pattern of motion. The results are shown in Table 2.

Table 2 *The results of testing the accuracy of the assessment tool.*

Group	**Maximum difference (mm)**	**RMSE (mm)**
1	-0.300	0.195
2	0.934	0.444
3	0.686	0.366
4	-0.807	0.385
5	0.500	0.264
6	-0.996	0.353
7	-0.989	0.425
8	-0.714	0.395
Absolute mean difference	0.741	0.353
SD	0.246	0.084

B. Capability test

All eight series of cine imaging were used for assessing the capability by introduced an error to images that were divided into three scenarios consist of simulated the blurring images, added Gaussian noise (GN), and salt and pepper noise (SP). The result is shown in Table 3

Table 3 *The testing capability of the assessment tool.*

Group	Maximum difference (mm)			RMSE (mm)		
	PSF	GB	SP	PSF	GN	SP
1	0.30	14.10	55.20	0.25	3.50	32.87
2	0.50	14.10	34.50	0.26	4.57	28.60
3	0.30	35.60	35.80	0.21	28.27	32.46
4	0.30	36.90	36.30	0.25	30.04	30.47
5	-1.40	-35.80	-41.80	0.59	23.42	30.66
6	0.80	-44.70	-73.20	0.40	22.48	27.79
7	-1.30	37.20	-35.80	0.57	20.18	18.90
8	-1.00	-44.10	-54.60	0.31	23.61	20.62
Mean	0.74	32.81	45.90	0.36	19.51	27.80
SD	0.46	12.08	13.89	0.15	10.06	5.27

3.2 Applying in clinical

The cine images of the patient were analyzed in this study consist of 3 patients that have a different character. The first, the patient, has large breast conservative surgery. Second, breast mastectomy is both with and without bolus treatment planning. The last, the small breast conservative surgery. The results of detecting the stability of the DIBH technique as shown in Figure 2.

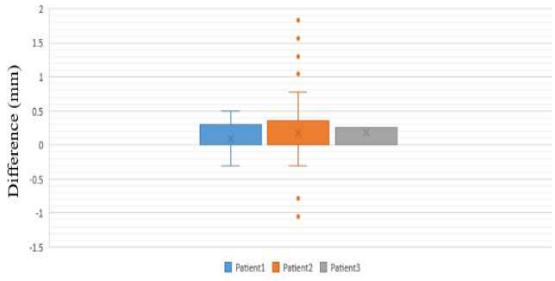

Figure 2 The difference in measuring the stability of breath-hold in patients who treat with the DIBH technique.

4. DISCUSSION

Canny's edge detection algorithm was used in this study because it can reduce the number of false edges and create a better starting point for a farther process like Hough Transformation due to 2 steps consist of non-maximum suppression process and hysteresis process

4.1 Testing the performance of the assessment tool

For testing accuracy, the maximum difference from prediction is -0.996±0.246 mm in gantry angle 39º with amplitude 2.5 mm and time 1 second. This error is according to the study by Jensen [9] using MATLAB algorithms to apply with the Canny filter with a reported error of 1.2–1.5 mm. The uncertainty of this in-house program may be caused by a low frame rate of cine image that is 2 frames per second. Using a low frame rate, it may lead to a lack of image motion as the study by Yip [12]. Also, this in-house program was applied with 3 filters consisting of Gaussian filter, median filter, and Wiener filter that was resulted in degrading the information of images. Moreover, the EPID maybe occur a ghosting effect as the study by Alshanqity [13]. The effect of ghosting is present at the beginning of irradiation delivery established as a decreased total integrated signal per MU at low dose range (1–10 MU) and because of hardware limitations. The last, the distance of lung depth was measured from only one line profile, which will result in a systematic error from a subpixel error. Furthermore, the capability testing consists of blurring and noise images; this in-house program can detect the blurring image with a quite high accuracy due to the Wiener filter with the maximum RMSE is 0.59 mm and the maximum difference is 1.4 mm. The Wiener filter is the MSE optimal stationary linear filter for images degraded by additive noise and blurring. Normally, the blurring image can occur from movement during the image capture process. However, in the noise image found that this program cannot detect accuracy with a maximum difference of 73.2 mm for 'salt and pepper noise' and 44.1 mm for 'Gaussian noise'. Thirumavalavan [14] studied the performance under noisy environment and found that the Canny edge is distorted and deviate widely from the true edges with Gaussian and impulse noises. For the salt and pepper noise is a random pixel being set to black or white such as dead pixels from EPID that can occur from the electronic part. It can be found rarely owing to calibrated regularly. For Gaussian noise, it is statistical noise that is scattered from EPID, patient, and treatment head. In this study, setting too many noises that effect to program are unable to get rid of it.

4.2 Applying in clinical

After the test program from the phantom, it was applied in clinical usage. That analyzed the images of data from 3 patients who were treated with the DIBH technique. The standard gating window of 2 mm was

used for all patients [11]. Each day in the same patient will have different amplitudes, which will depend on the position of the patient. As a result, an offline review of cine images was analyzed and seem to be quite a stable result of BH. However, it has just an image over a limitation of 2 mm. Manual hold RT may cause readability over 2 mm if the patient breathes more than the setting of amplitude, which may be pressed delay time. Alternatively, it may be caused by the error of the program at almost 1 mm. Nevertheless, this experiment cannot use DRR for reference images but use the first cine image as a reference image due to the setting amplitude by the radiation therapist. The study by Jensen [9], also uses the first image of each beam to be the reference image. Thomsen [10] and Lutz [11] use DRR as the reference image by manually registering with portal images. The limitation of this program only use in the tangential breast without the SPC field because the image acquires full-field so the whole lune can be imaged but if the SPC field is also included, only the upper lung can be imaged.

5. CONCLUSION

The cine EPID images were used to measure the stability of DIBH by using in house MATLAB program with Canny's edge detection algorithm. The evaluation of the accuracy of the in-house MATLAB assessment tool from the phantom found that the maximum difference from prediction is less than 1 mm. Also, the in-house MATLAB program has good repeatability. Testing capability with added blurring in the image, this program can be analyzed quite accurately with a maximum difference of 1.4 mm but reduce noise very poorly with a maximum difference of 73.2 mm. However, the in-house MATLAB program was used to detect the stability of breath-hold in patients which found that the results correspond amplitude setting from the treatment room. The in-house automated MATLAB program with EPID based is suitable for clinical treatment with a millimeter error.

ACKNOWLEDGEMENTS

The authors would like to thank my advisor, co-advisor, and all staff at Radiation oncology, Chulabhorn hospital for their help, assistance, and kind cooperation entire my study.

REFERENCES

1. World Health Organization. Latest global cancer data: Cancer burden rises to 18.1 million new cases and 9.6 million cancer deaths in 2018 [Internet].Available from:https://www.iarc.fr/wpcontent/uploads/2018/09/pr263_E.pdf
2. Miller, K. D., et al. "Cancer treatment and survivorship statistics, 2019." CA: a cancer journal for clinicians 69.5 (2019): 363
3. Taylor CW, Nisbet A, McGale P, Darby SC. Cardiac exposures in breast cancer radiotherapy: 1950s–1990s. International Journal of Radiation Oncology* Biology* Physics. 2007;69(5):1484-95.
4. Darby SC, Ewertz M, McGale P, Bennet AM, Blom-Goldman U, Bronnum D, et al. Risk of ischemic heart disease in women after radiotherapy for breast cancer. N Engl J Med. 2013;368(11):987-98.
5. Beaton L, Bergman A, Nichol A, Aparicio M, Wong G, Gondara L, et al. Cardiac death after breast radiotherapy and the QUANTEC cardiac guidelines. Clinical and Translational Radiation Oncology. 2019;19:39-45.
6. Nissen HD, Appelt AL. Improved heart, lung and target dose with deep inspiration breath hold in a large clinical series of breast cancer patients. Radiotherapy and Oncology. 2013;106(1):28-32.
7. Sung K, Lee KC, Lee SH, Ahn SH, Lee SH, Choi J. Cardiac dose reduction with breathing adapted radiotherapy using self respiration monitoring system for left-sided breast cancer. Radiation oncology journal. 2014;32(2):84.
8. Bruzzaniti V, Abate A, Pinnarò P, D'Andrea M, Infusino E, Landoni V, et al. Dosimetric and clinical advantages of deep inspiration breath-hold (DIBH) during radiotherapy of breast cancer. Journal of Experimental & Clinical Cancer Research
9. Jensen C, Urribarri J, Cail D, Rottmann J, Mishra P, Lingos T, et al. Cine EPID evaluation of two non-commercial techniques for DIBH. Medical physics. 2014;41(2).
10. Thomsen MS, Harrov U, Fledelius W, Poulsen PR. Inter-and intra-fraction geometric errors in daily image-guided radiotherapy of free-breathing breast cancer patients measured with continuous portal imaging. Acta Oncologica. 2014;53(6):802-8.
11. Lutz CM, Poulsen PR, Fledelius W, Offersen BV, Thomsen MS. Setup error and motion during deep inspiration breath-hold breast radiotherapy measured with continuous portal imaging. Acta Oncologica. 2016;55(2):193-200.
12. Yip S, Rottmann J, Berbeco R. The impact of cine EPID image acquisition frame rate on markerless soft-tissue tracking. Medical physics. 2014;41(6Part1):061702.
13. Alshanqity M, Duane S, Nisbet A. A simple approach for EPID dosimetric calibration to overcome the effect of image-lag and ghosting. Applied Radiation and Isotopes. 2012;70(7):1154-7.
14. Thirumavalavan S, Jayaraman S. An improved teaching–learning based robust edge detection algorithm for noisy images. Journal of Advanced Research. 2016;7(6):979-89.5.

Fabrication and validation of cubic phantom embed with an accelerometer sensor for verifying six-degrees-of-freedom couch

T. Popreeda[1], S. Thongsawad[2], N. Udee[1]

1 Department of Radiological Technology, Faculty of Allied Health Sciences, Naresuan University, Mueang, Phitsanulok 65000, Thailand.
2 Radiation Oncology Unit, Chulabhorn Hospital, HRH Princess Chulabhorn College of Medical Science, Chulabhorn Royal Academy, Laksi, Bangkok 10210, Thailand.

Abstract

The research purpose was to fabricate a cubic printed phantom embed with an accelerometer sensor for verifying the six-degrees-of-freedom couch. In addition, the measurement accuracy was validated in the study. The study was classified in three main tests: printing accuracy test, accuracy of calibration procedure, and 6DOF perfectPitch test. The printing accuracy of cubic phantom was assessed by comparing between the dimensional in printing software and a vernier caliper/ CT images. The accuracy of calibration procedure was determined by repeating measurement with and without re-set position. After completed calibration, accelerometer was inserted to the phantom for verifying the angle of 6DOF.

Keywords: six-degrees-of-freedom (6DOF) couch QA, 3D printing, Accelerometer sensor, cubic phantom

1. INTRODUCTION

Nowadays, the six degrees-of-freedom (DOF) couch is a new technology that improves the efficiency of external beam radiotherapy. The 6DOF couch is a relatively new technology that two additional directions of rotational movement. The additional directions have delivered a more accurate treatment and to decrease target margins in clinical. Hence, The quality assurance (QA) of localization and patient positioning system is critical for accurately treating the patient in their exact treatment location. As the suggestion by the American Association in Physicists in Medicine (AAPM) task group report 142 (TG-142) and Medical Physics Practice Guidelines 8.a. (MPPG 8.a.) is to measure position accuracy of couch (1). The report recommends the tolerance of a treatment couch position test is 2 mm for translation movement and 1° for rotation movement (2,3).

Due to the lack of a commercial QA phantom cannot verified in all directions of treatment couch positioning. The QA phantom tools for a 6DOF couch is usually expensive. Since a 3D printer was introduced to a medical health care field, many medical devices can be fabricated by 3D printer. There are several reports on the accuracy of 3D printer, and the report indicated that the Fused Deposition Modelling (FDM) 3D printers has submillimeter accuracy for fabrication (1-5). *Msallem et al.* developed a phantom for verifying the 6DOF couch, and they found the phantom reconstructed by 3D printing has efficiently for implementation in QA (6).

In this study, we have developed a QA phantom using CAD software to design model and fabricate it with 3D printer (FULLSCALE MAX450). In addition, accelerometer sensor was embedded inside a phantom to measure the couch tilt.

2. MATERIAL AND METHODS

Tests were performed on a 6DOF perfectPitch couch of TrueBeam linacs (Varian Medical Systems, Palo Alto, CA, USA).

2.1 Cube phantom design and fabrication

The cube phantom was designed and modeled using a computer-aided design (autoCAD) software. The FullScale Max 450 (Neotech Co., Ltd., Thailand) 3D printer was used to fabricated the phantom, and it utilizes a fused deposition modelling (FDM) method for printing. The 3 mm off-white polylactic acid (PLA) plastic filament were used as a material.

The cube dimension was 7 x 7 x 7 cm which has an isocenter and offset marks. The offset location was designed to be exactly 2.00 cm away from the isocenter in each translational direction. Figure 1 shows the model of cube phantom and the 3D printed phantoms.

The 3D model final version of the design was saved as a stereolithography (STL) file, and then the STL was converted to a GCODE file for printing process. A GCODE file is the printer-specific language for the 3D printing control, as follows: speed, temperature, and fill density.

2.2 Dimensional accuracy

To determine the accuracy of the cubic phantom, the nominal model dimension was compared to dimension of computed tomography (CT) images and dimension of digital Vernier caliper (IP67) measurement. The dimension of cubic phantom was measured in three different directions via sagittal, transverse, and frontal planes.

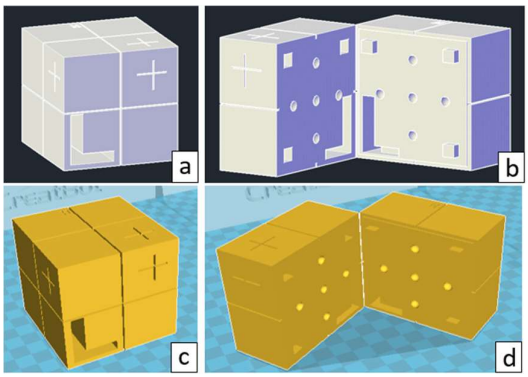

Figure 1: *Cube phantom in different views: (a) surface view, (b) inside phantom view using AutoCAD, (c) surface view, (d) inside phantom view using the CreatWare™ program.*

2.3 Accelerometer sensor

The signal of accelerometer was calibrated with referent spirit level to measure couch tilt. However, the residual errors still occurred in angle measurement. Hence, offset and gain parameter were taken account to remove these errors. Offset and gain can be calculated as equation 1 and 2, respectively.

$$A_{offset} = 0.5 \times \left(A_{+1g} + A_{-1g}\right) \quad \text{equation 1}$$

$$Gain = 0.5 \times \frac{A_{+1g} - A_{-1g}}{2} \quad \text{equation 2}$$

Where the +1g and -1g is measurements at angle A_{+1g} *and* A_{-1g} .

The corrected angle measurement ($A_{correct}$) can be calculated using equation 3.

$$A_{correct} = \frac{A_{out} - A_{offset}}{Gain} \quad \text{equation 3}$$

Where A_{out} are measurement without correction.

The accuracy and reproducibility of were performed before insertion the accelerometer to cubic phantom. Accuracy and reproducibility tests were determined by repeating ten-time measurements with different scenarios. For accuracy test, repeating ten-time measurements with placing the same position were performed, and spirit level was used to compare as a referent angle. For reproducibility test, repeating ten-time measurement with re-set position were performed, and standard deviation (SD.) was used to assess the reproducibility score. The angle measurements were performed with varying angle between -3° and +3°, and interval step of 1° for pitch and roll directions.

2.4 Couch positioning test of 6DOF perfectPitch

In couch position test, accelerometer was inserted to cubic phantom, and the absolute couch angle was measured against the digital readout monitor. The couch angle measurement was performed in pitch, roll, and yaw directions with angle between -3°and +3°. Figure 3 shows the cubic phantom setup for verifying 6DOF.

3. RESULTS

Figure 2 shows different image views of cubic phantom which were used to measure the dimensional error. The dimensional error of printed cubic phantom was found less than 0.05 cm for the both measurements (vernier caliper and the CT image) as summarized in Table 1.

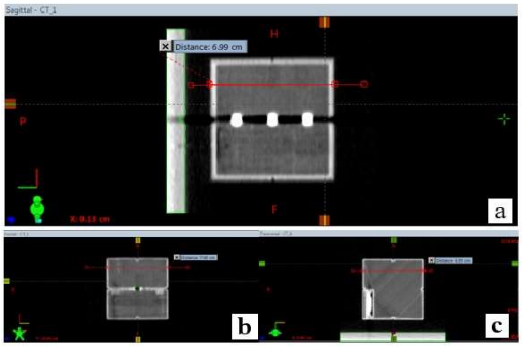

Figure 2: *The 3D printed cube phantom (a) sagittal, (b) frontal, and (c) transverse computed tomography views of the cube phantom with the accelerometer sensor.*

Table 1 *The results of the dimension measurement with the IP67 digital Vernier caliper and the CT image tools.*

Directions	Nominal model (cm)	IP67 caliper		CT images	
		Mean (cm)	Accuracy (%)	Mean (cm)	Accuracy (%)
Transversal	7.00	6.98	99.77	6.98	99.71
Frontal	7.00	6.98	99.77	6.99	99.83
Sagittal	7.00	7.00	99.94	6.99	99.80

3.1 Accelerometer calibration

For accuracy test, the maximum errors across the entire calibration procedure was 0.05° for the both angles (pitch and roll). Table 2 summarizes the result of accuracy test. For reproducibility test, the difference between accelerometer and spirit level was found with in ±0.05°, and maximum SD. was found 0.04°, and 0.03° for pitch and roll, respectively. Table 3 summarizes the result of reproducibility test.

Table 2 *Accuracy measurement of the accelerometer sensor.*

Spirit level	Pitch	Roll
	Mean (deg) ±SD.	Mean (deg) ±SD.
-3.0°	-3.02 ± 0.04	-3.00 ± 0.19
-2.0°	-2.05 ± 0.04	-2.01 ± 0.21
-1.0°	-1.01 ± 0.05	-0.99 ± 0.21
0.0°	-0.05 ± 0.04	0.00 ± 0.17
1.0°	0.99 ± 0.03	1.04 ± 0.19
2.0°	1.98 ± 0.06	2.01 ± 0.17
3.0°	3.00 ± 0.06	3.05 ± 0.18

Table 3 *Reproducibility results of the accelerometer sensor.*

Spirit level	Pitch	Roll
	Mean (deg), SD	Mean (deg), SD
-3.0°	-3.01 ± 0.02	-3.00 ± 0.01
-2.0°	-1.99 ± 0.04	-2.03 ± 0.03
-1.0°	-0.99 ± 0.02	-0.99 ± 0.01
0.0°	-0.00 ± 0.04	-0.01 ± 0.00
1.0°	1.02 ± 0.02	1.02 ± 0.01
2.0°	2.03 ± 0.03	2.02 ± 0.02
3.0°	3.03 ± 0.02	3.02 ± 0.02

3.2 Couch positioning test

The maximum couch angle error was found 0.07º at 0º of pitch direction, and 0.12º at +1º of roll direction. Table 4 summarizes the results of couch position test.

Table 4 *The results of couch rotation test with 6DOF perfectPitch couch.*

Couch shift	Pitch (deg)	Roll (deg)
-3°	-2.97	-3.03
-2°	-1.98	-2.00
-1°	-0.94	-0.91
0°	-0.07	0.04
+1°	+1.06	+1.12
+2°	+2.05	+2.09
+3°	+3.01	+3.09

4. DISCUSSION

In thus study, we demonstrated how to calibrate the accelerator signal to angle measurement by taking account gain and offset correction to reduce the residual error from the sensor. The both corrections (gain and offset) are the important factor to improve angle accuracy.

The accuracy and reproducibility tests were designed to asset the performance of accelerator sensor before inserting in phantom. The accuracy was determined by comparing accelerator measurement with spirit level (referent angle measurement), and the difference was found less than 0.05º. The reproducibility was determined by using SD. with ten-time re-set position, and SD. was found less than 0.04º. This result indicated that our cubic phantom has a good performance for measurement angle. However, the measurement was validated only for the angle between ±3º because the perfectPitch couch has limitation of couch angle accuracy with in ±3º according to vendor recommendation (7).

The couch angle QA using our cubic phantom embed an accelerometer sensor is helpful medical physicist to verify couch rotation accuracy with a good efficiency compared to the traditional method which was used image registration. The accelerator self-report the angle measurement without additional process. Unlike couch angle QA with images registration, it required multiple steps to measure the couch angle and evaluation process may introduced the intra observer error (8).

According to TG-142 recommendation (9), couch positioning/repositioning error could be within 2 mm and 1° for Stereotactic Radio Surgery (SRS) and Stereotactic Radiation Therapy (SRT). The result of couch rotation test using our in-house QA indicated that 6DOF perfectPitch has enough accuracy for SRS/SRT with error less than 0.2º for pitch and roll direction.

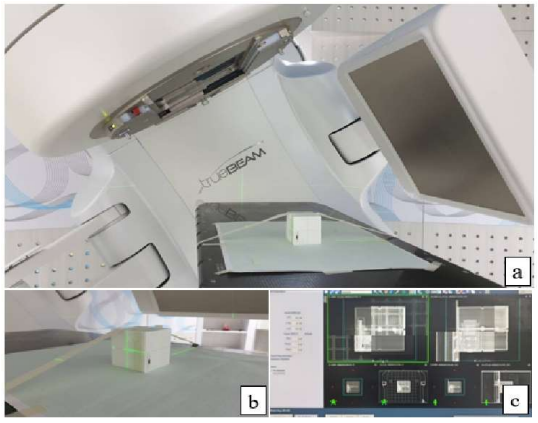

Figure 3 *Experimental setup for the evaluation of the 6DOF couch positioning: (a) a cubic phantom placed on the top of 6DOF couch , (b) align with external lasers, and (c) X-ray view of phantom.*

5. CONCLUSION

In this study, we have successfully developed the new QA tool for verifying 6DOF couch with self-measurement method using accelerometer sensor, and the accuracy was enough for verifying six-degrees-of-freedom couch. In addition, in-house QA tool was implemented in the 6DOF QA, and the result indicated that 6DOF perfectPitch has enough accuracy for SRS/SRT.

ACKNOWLEDGEMENTS

The authors would like to thank the Radiation Oncology Unit, Chulabhorn Hospital, HRH Princess Chulabhorn College of Medical Science, Chulabhorn Royal Academy of Thailand for the equipment and materials support under Fundamental Research.

REFERENCES

1. Chan MF, Lim SB, Li X, Tang X, Zhang P, Shi C. Commissioning and Evaluation of a Third-Party 6 Degrees-of-Freedom Couch Used in Radiotherapy. Technol Cancer Res Treat. 2019;18:1533033819870778.
2. Belcher AH, Liu X, Grelewicz Z, Pearson E, Wiersma RD. Development of a 6DOF robotic motion phantom for radiation therapy. Med Phys. 2014;41(12):121704.

3. Ehler ED, Barney BM, Higgins PD, Dusenbery KE. Patient specific 3D printed phantom for IMRT quality assurance. Phys Med Biol. 2014;59(19):5763-73.
4. Schmidhalter D, Fix MK, Wyss M, Schaer N, Munro P, Scheib S, et al. Evaluation of a new six degrees of freedom couch for radiation therapy. Med Phys. 2013;40(11):111710.
5. Woods K, Ayan AS, Woollard J, Gupta N. Quality assurance for a six degrees-of-freedom table using a 3D printed phantom. J Appl Clin Med Phys. 2018;19(1):115-24.
6. Msallem B, Sharma N, Cao S, Halbeisen FS, Zeilhofer HF, Thieringer FM. Evaluation of the Dimensional Accuracy of 3D-Printed Anatomical Mandibular Models Using FFF, SLA, SLS, MJ, and BJ Printing Technology. Journal of clinical medicine. 2020;9(3).
7. Chan MF, Lim S-B, Li X, Tang X, Zhang P, Shi C. Commissioning and Evaluation of a Third-Party 6 Degrees-of-Freedom Couch Used in Radiotherapy. Technology in cancer research & treatment. 2019;18:1533033819870778.
8. systems Vm. PerfectPitch 6 degrees of freedom couch. 2013.
9. Klein EE, Hanley J, Bayouth J, Yin F-F, Simon W, Dresser S, et al. Task Group 142 report: Quality assurance of medical accelerators. Medical Physics. 2009;36(9).

Automatic QC Analysis Program in Digital Radiography System

Jongwat Cheewakul[1], Natee Ina [2]

1,2 Department of Radiology Faculty of Medicine Prince of Songkla University, Songkla, Thailand

Abstract

Quality Control of the diagnostic radiology system is the test of the quality and function of the X-ray machine and to observe the defects, deterioration or damage of the equipment by Medical Physicist. The developed program analyses the automatic image quality control in digital x-ray systems can help Medical Physicist to reduce the time spent in the analysis the test results with more convenience. The purpose of this study was to design automatic quality control analysis program and to compare the test results from this program with the results from three observers. This developed analysis program using MATLAB could assess the image quality in terms of the spatial resolution, low contrast detail detectability and high contrast detail detectability. The Routine Test Object for conventional and non-subtractive digital radiography, TOR CDR test tool was exposed by three digital X-ray machines, one image for each X-ray machine was obtained. Then three images were assessed by developed software and three observers. The results show that the evaluation from the developed software and three observers are comparable. The spatial resolution evaluated by the developed software were 3.55, 3.15, 2.80 lp/mm and by three observers was 3.55, 2.80, 2.80 lp/mm respectively. The low-contrast detectability evaluated by the developed software was 16, 15, 17 and by three observers were 16, 16, 15 respectively. The high-contrast detectability evaluated by the developed software was 17, 17, 17, and by three observers were 16, 17, 17 respectively. The average assessment time evaluated by the developed software was 1.30 min and by manual procedure was 3.15 min. This automatic QC analysis program can be used with the reduction in the assessment time and be able to record the results to compare with the previous results.

Keywords: Quality Control, Spatial Resolution, Low and High Contrast Detectability, Digital Radiography System

1. INTRODUCTION

Quality Control is a test of the quality and function of the X-ray machine to know the defects, Deterioration or damage to equipment. This is to maintain the quality of the radiograph well and sufficient for diagnosis with an appropriate dose. The problem of quality control is that it takes a long time to analyze the results and not easy to do on a routine[1] if hospital has many x-ray machines are installed, if there is a defect or damage to the unresolved X-ray machine, may affect the quality of the image[1]. Causing the doctor to not be able to clearly distinguish the details of the disease or see small abnormalities. Therefore, the program analyzes the automatic image quality control results in digital x-ray systems[2,3,4]. Which is developed Program. It helps to reduce the time spent in the analysis control test results of the quality control[5] In order to be able to test the image quality control faster and more conveniently

2. MATERIAL AND METHODS

used in this research are list as follows :

A. TOR CDR Phantom[6] (Figure 1)

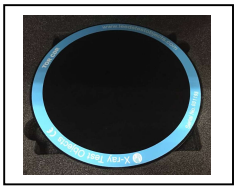

Figure 1 *TOR CDR Phantom serial no.001195.*

B. X-ray SAMSUNG XGEO-GC85A serial no. 50FGM3EH200001E (Figure 2A)

C. X-ray SAMSUNG GU60A-65 serial no. 502UM3AF700001J (Figure 2B)

D. X-ray SAMSUNG XGEO GC80 serial no. S06QM3AD9000024 (Figure 2C)

Figure 2 *X-ray SAMSUNG : (A)XGEO-GC85A, (B) GU60A-65, (C) XGEO GC80*

E. MATLAB software R2019b

2.1 Study design : Comparative analytical study

2.2 Study procedures

Study the quality control data on Spatial Resolution, Low Contrast Detectability, High Contrast Detectability in digital x-ray and program design using MATLAB With TOR CDR phantom serial no.001195 as recommended by AAPM (American Association of Physicist in Medicine).

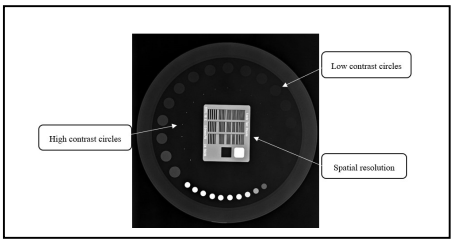

Figure 3 *TOR CDR Phantom Detail.*

2.2.1 Design an automatic image quality control result analysis program in digital x-ray system using MATLAB program. (Figure 4) Testing the automatic analysis program for image quality control results in digital x-ray systems.

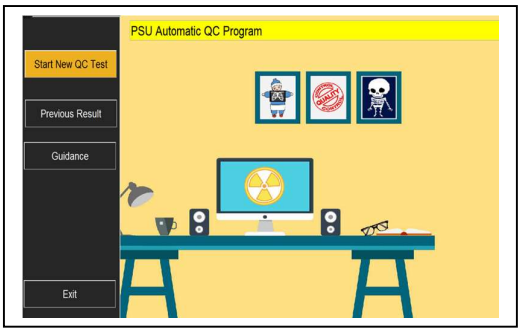

Figure 4 *GUI of* program developed software

2.2.2 Take X-ray by TOR CDR phantom in digital radiography SID 100 cm (Figure 5)

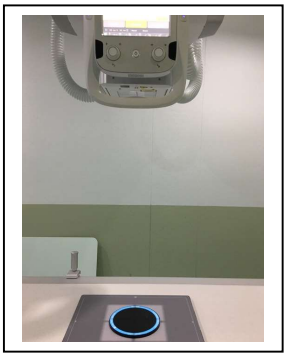

Figure 4 *Setting of TOR CDR*

2.2.3 Assessment of low and high contrast detail detectability : Features of detecting the center of the object (center) .(Figure 5A) and diameter of the object. Trimming the edges.(Figure 5B,5C) of the phantom sheet to only the low contrast circles.(Figure 6) , then detecting the circle boundary from a diameter equal to 11 mm to approximately 79 pixels.Contrast can be calculated using the equation

$$C_{object} = \frac{GS_{object} - GS_{background}}{GS_{background}}$$

Where C_{object} is the contrast of the object. GS_{object} is the blackness of the object. $GS_{background}$ is the blackness of the background.

and in the detection section High contrast is the same. Cut to only the High contrast circles. (Figure 7A) and detect circles with a diameter of 0.5 mm, approximately 4 pixels. (Figure 7B)

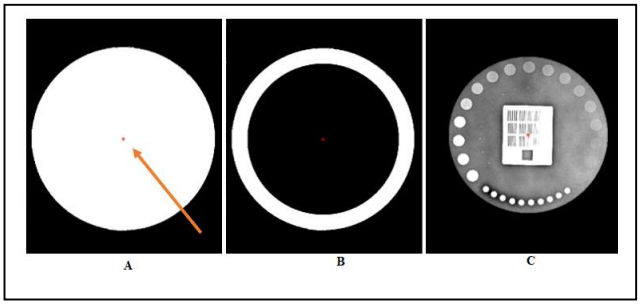

Figure 5 *(A) Detecting object center, (B) Edge of test strip, (C) trimmed image*

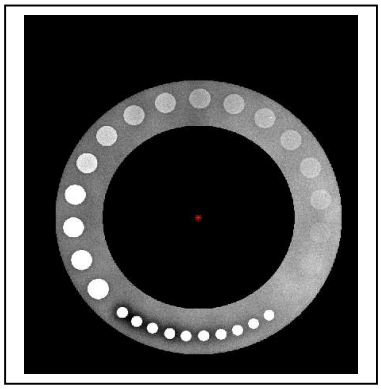

Figure 6 test strip cut to only Low contrast circles.

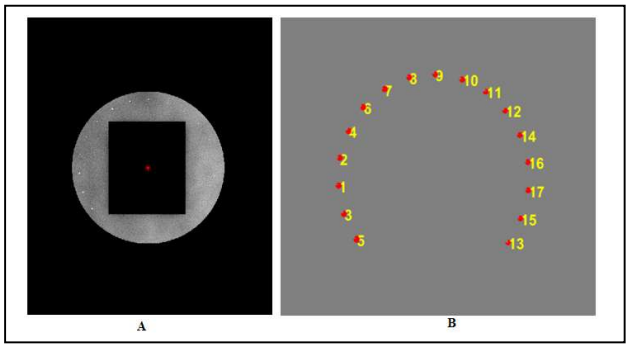

Figure 7 *Image showing test sheet (A) Image with only cut High contrast circles (B) High contrast detected image*

2.2.4 *Assessment of* spatial resolution : Only the bar pattern part has to be cut, then three lines are drawn in the middle of the bar pattern in each row to create a line profile, then the program will graph each row. .(Figure 8) Will be a graph showing the signal of each group Then count the number of groups of bar pattern, where all 4 peak signals (peak) are counted as 1 group. .(Figure 9)

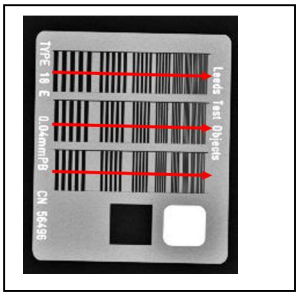

Figure 8 *shows how to draw a line through the bar pattern in each group.*

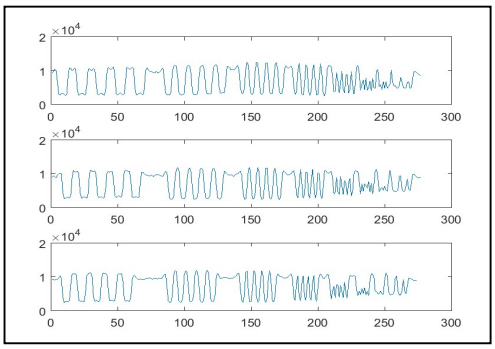

Figure 9 *shows the signal curve of the spatial resolution obtained by drawing the line profile.*

2.2.5 The three observers , who have experience in digital image quality control, analyze the all results and record the time spent in analyzing each method for comparison.

3. RESULTS

The results show that the evaluation from the developed software and three observers are comparable. The spatial resolution evaluated by the developed software were 3.55, 3.15, 2.80 lp/mm and by three observers was 3.55, 2.80, 2.80 lp/mm respectively. The low-contrast detectability evaluated by the developed software was 16, 15, 17 and by three observers were 16, 16, 15 respectively. The high-contrast detectability evaluated by the developed software was 17, 17, 17, and by three observers were 16, 17, 17 respectively. The average assessment time evaluated by the developed software was 1.30 min and by manual procedure was 3.15 min.

Table 1 *Results of assessment, Spatial resolution, low and high contrast detail detectability by* software

	Spatial resolution (lp/mm)	Low contrast Detectability (discs)	High contrast Detectability (discs)	The average assessment time evaluated by the developed software (mins)
Image 1	18 (3.55)	16	17	1.30
Image 2	17 (3.15)	15	17	1.30
Image 3	16 (2.80)	17	17	1.30

Table 2 *Results of assessment Spatial resolution, low and high contrast detail detectability by 3 observers.*

	Spatial resolution (lp/mm)	Low contrast Detectability (discs)	High contrast Detectability (discs)	The average assessment time evaluated by the developed software (mins)
observers A	18 (3.55)	16	16	2.40
observers B	16 (2.80)	16	17	3.01
observers C	16 (2.80)	15	17	4.04

4. DISCUSSION

The programmed analysis values are saved in Microsoft Excel, allowing the data to be stored for future reference.

4.1 Using a program to analyze results can help reduce the uncertainty of visual evaluation that can be caused by human errors.

4.2 For the analysis of results using a program, the TOR CDR test must be extracted image from the PACS system.

4.3 *The program is semi-automatic program. due to time constraints and different placement of TOR CDR test for each shot. Make the rotation of the image not the same Therefore cannot create fully automatic programs In order to analyze the results of the* spatial resolution*, the analyst has to crop the bar pattern for drawing Line profiles to analyze the results manually.*

4.4 *May be affected by the Anode heel effect, cause the signal distribution. In the image not uniformity This can be solved by placing a TOR CDR test disc so that the high signal intensity side on the Anode tube.*

4.5 *Using Different Post-processing in each image It will make the image that has been scaled in the image, which affect the results analysis of the program.*

5. CONCLUSION

This automatic QC analysis program can be used with the reduction in the assessment time and be able to record the results to compare with the previous results.

ACKNOWLEDGEMENTS

This project was supported by ***Prince of Songkla University***. We thank the ***Department of Radiology Faculty of Medicine***, for the use of Phantom TOR CDR in this research.

REFERENCES

1. Périard MA, Chaloner P. Diagnostic X-ray imaging quality assurance: an overview. Can JMed Radiat Technol 1996;27:171–177.
2. Efstathopoulos EP, Benekos O, Molfetas M, et al. Quality assurance (QA) procedures for software:

evaluation of an ADC quality system. Radiat Prot Dosimetry 2005;117:291–297.
3. Oliveira M, Lopez G, Geambastiani P, et al. Application of newly developed Fluoro-QCsoftware for image quality evaluation in cardiac X-ray systems. Radiography 2018;24:e44–e47.
4. Desai N, Valentino DJ. A software tool for Quality Assurance of Computed/DigitalRadiography (CR/DR) systems. In: Medical Imaging 2011: Physics of Medical Imaging International Society for Optics and Photonics; 2011. p. 79614E.
5. Williams MB, Krupinski EA, Strauss KJ, et al. Digital radiography image quality: image acquisition. JAm Coll Radiol JACR 2007 Jun;4:371–88.
6. TOR CDR [Internet]. Leeds Test Objects. [cited 2019 Feb11]. Availablefrom: http://www.leedstestobjects.com/index.php/phantom/tor-cdr/
7. Schreiner-Karoussou A. Review of image quality standards to control digital X-ray systems.Radiat Prot Dosimetry 2005;117:23–5.

Investigation of position and angle effects of nanoDot OSL dosimeter for the eye lens dose measurement

Pattaravarin Rattanamongkonkul[1], Putthiporn Charoenphun[1], Krisanat Chuamsaamarkkee[2], Tanapol Dachviriyakij[3], Korawee Saejia[3]

1 Master of Science Program in Medical Physics, Department of Diagnostic and Therapeutic Radiology, Faculty of Medicine Ramathibodi Hospital, Mahidol University, Thailand,
2 Division of Nuclear Medicine, Department of Diagnostic and Therapeutic Radiology, Faculty of Medicine Ramathibodi Hospital, Mahidol University, Thailand,
3 Regulatory Technical Support Division, Office of Atoms for Peace, Thailand.

Abstract

Radiation dose to the eye lens of the medical personnel should be more considered since ICRP had decreased the equivalent dose limit of the eye lens in 2011. The nanoDot dosimeter has been used to measure the eye lens dose due to its characteristic which should be appropriate for point dose measurement in term of Hp(3). However, several studies showed angular dependence of the nanoDot OSL. Moreover, the position of nanoDot could be varied, depending on the individual face. The aim of the study was to investigate the effects of position and angle of the nanoDot OSL upon the radiation source position for the eye lens dose measurement. The responses of nanoDot OSL dosimeters were carried out on the PMMA water-filled cylindrical phantom behind the build-up region using ^{137}Cs as a calibration and reference source. The position and angular dependence were tested by setting up the ^{137}Cs source at 0^{o} to the phantom. The nanoDots were placed at the centre (0^{o}) and the other angles of 15^{o}, 30^{o}, 45^{o}, 60^{o}, 75^{o} and 90^{o} to the left and right side of the ^{137}Cs source. Then Hp(3) was evaluated corresponding to each dosimeter. The mean, standard deviation and the range of evaluated Hp(3) at the left and right sides were 1137.13 ± 74.13 µSv ranging of 988.87 - 1285.39 µSv and 1152.36 ± 51.64 µSv ranging of 1049.08 - 1255.65 µSv, respectively. The Hp(3) results from various positions and angles indicated no difference at 95% confidence interval. The nanoDot OSL dosimeter exhibited no effects of position and angle for the eye lens dose measurement in term of Hp(3). Therefore, nanoDot OSL dosimeter could be feasible for measurement of the eye lens dose whether the workers wear nanoDots in different positions and angles on their faces.

Keywords: nanoDot OSL dosimeter, Hp(3), effect of position and angle

1. INTRODUCTION

A cataract is the lens opacity resulting in visual impairment. One cause of cataract is the radiation exposure to the eye lens over the threshold (1). The eye lens dose limit has been recognized that it is necessary to avoid the effects of the eye lens. The International Commission on Radiological Protection (ICRP) Publication 103 had published the limit on the eye lens dose of 150 mSv in a year (2). In 2011, the ICRP statement on tissue reactions was considered to decrease the threshold dose of the absorbed dose of the eye lens to be 0.5 Gy and recommended to reduce the limit on the equivalent dose of the eye lens to 20 mSv per year (1). Based on the ICRP recommendation to decrease the eye lens dose limit, the eye lens dose measurement has to be a crucial consideration.

In routine practice, the eye lens doses are estimated in terms of operational quantities as a personal dose equivalent at 3 mm depth below surface body - Hp(3) which corresponds to the center of the eye lens then Hp(3) represents a personal equivalent dose of the eye lens (3). Meanwhile, a small-type OSL dosimeter, namely nanoDot OSL dosimeter, was developed to measure the single point of radiation. It has an aluminum oxide chip doped with carbon, Al_2O_3: C as a detector inside a plastic pouch. The size and thickness of the nanoDot OSL dosimeter are 10×10 mm^2 and 2 mm, respectively (4). Then it would be appropriated to assess at the point area of the eye to represent the eye lens dose equivalent. However, many studies of the characteristic of nanoDot dosimeter showed angular dependence (5-8). From several publications, they suggested to wear the eye lens dosimeter as close as the eye (9, 10). However, the workers' faces are different. So the position and angle of the dosimeters on the individual faces should be concerned. Under this condition, the effect to the dose measurement of nanoDot dosimeter might be different from only angular dependence. Therefore, the study aimed to investigate the effects of position and angle of the nanoDot OSL for the eye lens dose measurement simultaneously.

2. MATERIAL AND METHODS

The effect of position and angle of the nanoDot OSL (Landauer Inc., USA) for the eye lens dose measurement was performed on a PMMA water-filled cylindrical phantom and ^{137}Cs source was used as the reference radiation source. The PMMA water-filled cylindrical phantom was set at an angle of 0^{o} (center) to the ^{137}Cs reference radiation source and the distance between phantom and radiation source was 2.5 m. The irradiation time was 12 min 4 sec to deliver the dose of 1000 **µ**Sv, which was calculated from the conversion coefficient at 0^{o} of ^{137}Cs source incidence according to certificate of ^{137}Cs reference source. The effects of

position and angle were investigated at the different angles of 15º, 30º, 45º, 60º, 75º, and 90º to the left and right side of the radiation source (different distances) demonstrated in figure 1.

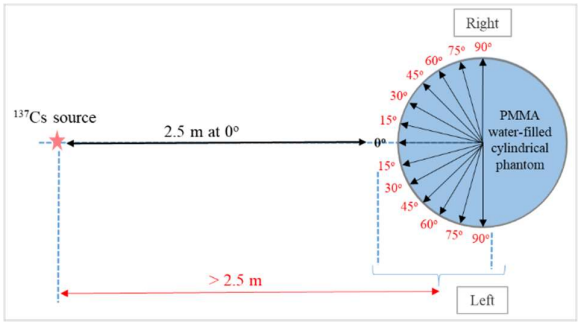

Figure 1 The positions of nanoDot dosimeters on the PMMA cylindrical phantom at the various distances and angles to the ^{137}Cs source.

In each irradiation, nanoDot dosimeters placed at the same angle on the left and right side of the ^{137}Cs source, were simultaneously exposed to the ^{137}Cs source. Two nanoDot dosimeters were used to irradiate in each position. In addition, following ISO 4037-3 recommendation, a solid PMMA slabs 3 mm thick were attached in front of nanoDot dosimeters as a build-up layer to establish secondary electron equilibrium in the case of photon fields with ^{137}Cs energy, as shown in figure 2.

Figure 2 Setting up nanoDot dosimeters on the PMMA water-filled cylindrical phantom with solid PMMA slabs.

After irradiation, MicroStar reader (Landuer Inc., USA) was used to read the nanoDot dosimeter's radiation response in terms of Hp(3). Each irradiated nanoDot dosimeter was repeatedly read three times to decrease the uncertainty of measurement. Then at the same angle, average of the Hp(3) was calculated and normalized by averaged Hp(3) at incidence angle (0º). The mean and standard deviation of Hp(3) on the left and right side were utilized to evaluate the correspondence of position and angle using statistical evaluation with a 95% confidence interval.

3. RESULTS

The normalized responses of nanoDot dosimeters (Hp(3)) at varied positions and angles to ^{137}Cs radiation source are exhibited in figure 3. The mean and standard deviation of evaluated Hp(3) on the left and right sides were 1137.13 ± 74.13 µSv, with the range of 988.87 µSv to 1285.39 µSv and 1152.36 ± 51.64 µSv, with the range of 1049.08 µSv to 1255.65 µSv, respectively. Slightly different among Hp(3) was revealed. However, there was no effect of various positions and angles to nanoDot dosimeter response in term of Hp(3) on ^{137}Cs at a 95% confidence interval.

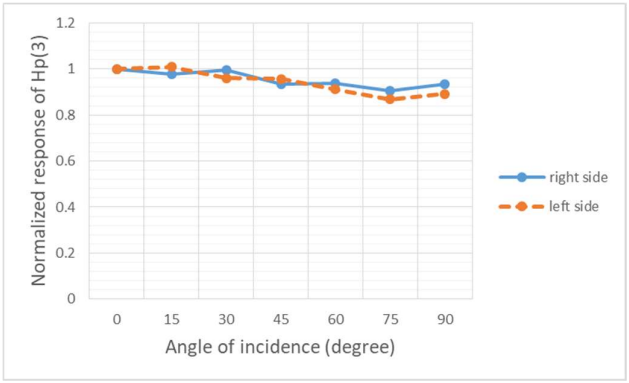

Figure 3 The normalized response of Hp(3) dose assessment to ^{137}Cs source at various positions and angles on PMMA cylindrical phantom.

4. DISCUSSION

Several studies showed that angular dependent was one of nanoDot OSL dosimeter characteristics (5-8). Al-Senan and Hatab found that the response of nanoDot OSL at 90º and 270º to the radiation source were lower than that of the other angles (7). A similar result was demonstrated by Cruz et al. (6). They reported that response of the nanoDot OSL dosimeter was also decrease at 90º and 270º when exposed with 1500 keV photon and 40 kV X-rays (6). However, the previous studies only accounted for the angle effect of the nanoDot dosimeters toward the radiation source. Whereas the distance between the source and dosimeter, which should represent the position of the dosimeter, was certainly constant as demonstrated in figure 4.

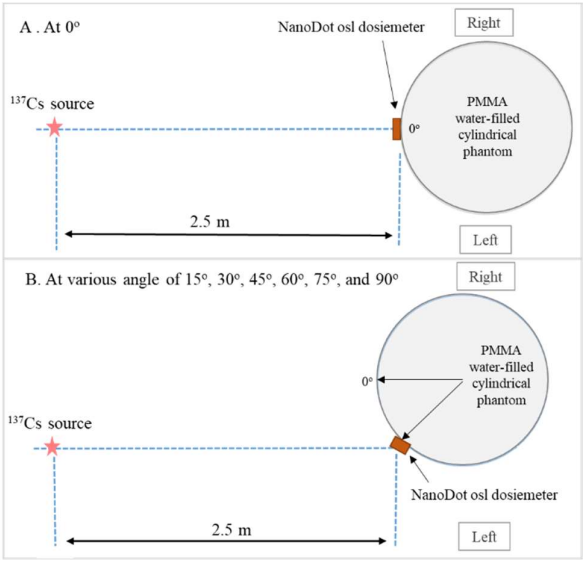

Figure 4 Setting up dosimeters to assess the angular effect.

On the other hand, setting up experimental exposures in this study were varied both positions and angles of nanoDot OSL dosimeters simultaneously by placing dosimeters on the different distances and angles on the PMMA water-filled cylindrical phantom illustrated in figure 1. This setting should surrogate general situation that face shape of radiation workers are different. As a result, the position and angle of the nanoDot OSLs toward radiation source might be varied among the workers when they wear the dosimeters near their eyes. Consequently, nanoDot OSL response in term of Hp(3) might be affected. However, result from this study suggested that Hp(3) doses were no different responses at a 95% confidence interval when the nanoDot dosimeter were placed in various positions and angles and the radiation source was located in front of dosimeters.

5. CONCLUSION

This study suggested that no effect of position and angle of nanoDot OSL dosimeter for the eye lens dose measurement in terms of Hp(3) when ^{137}Cs was used as radiation source. Therefore, the nanoDot OSL dosimeter could be feasible for measuring the eye lens dose whether the workers wear nanoDots in different positions and angles near the eyes.

ACKNOWLEDGEMENTS

The authors would gratefully acknowledges the Division of Regulatory Technical Support, Office of Atoms for Peace (OAP) for supporting equipment as well as giving technical support throughout the experiment.

REFERENCES

1. Stewart, F. A., Akleyev, A. V., Hauer-Jensen, M., Hendry, J. H., Kleiman, N. J., Macvittie, T. J., ... & Shore, R. E. (2012). ICRP publication 118: ICRP statement on tissue reactions and early and late effects of radiation in normal tissues and organs–threshold doses for tissue reactions in a radiation protection context. Annals of the ICRP, 41(1-2), 1-322.
2. International Commission on Radiological Protection. (2007). ICRP publication 103: the 2007 recommendations of the International Commission on Radiological Protection. Ann ICRP, 37(2–4), 1-34.
3. Mattsson, S., & Söderberg, M. (2013). Dose quantities and units for radiation protection. In Radiation Protection in Nuclear Medicine (pp. 7-18). Springer, Berlin, Heidelberg.
4. nanoDot® single point dose measurement. (2018). URL:https://www.landauer.eu/voy_content/uploads/sites/3/2019/01/FT-NAN-002-RevC_nanoDot_dec18_EN.pdf
5. Jursinic P.A., Characterization of optically stimulated luminescence dosimeters, OSLDs, for clinical dosimetric measurements, Medical Physics 34 (2007), pp. 4594-4604.
6. Cruza, V. L. E., Okazakia, T., Hayashib, H., Miharab, Y., Asaharab, T., Kimotob, N., & Kobayashia, I. (2019). Energy and angular dependence of the small-type OSL dosimeter in nuclear medicine regions using Monte Carlo simulation.
7. Al-Senan RM and Hatab MR. (2011). Characteristics of an OSLD in the diagnostic energy range, Medical Physics 38(7), 4396-4405
8. Kerns JR, Kry SF, Sahoo N, et al. Angular dependence of the nano-Dot OSL dosimeter. Med Phys. 2011;38:3955–3962
9. International Atomic Energy Agency (2013). Implications for occupational radiation protection of the new dose limit for the lens of the eye. —IAEA Vienna.
10. International Organization of Standardization (ISO), ISO 15382: Radiological protection – Procedures for monitoring the dose to the lens of the eye, the skin and the extremities. 2015.
11. International Organization of Standardization (ISO), ISO 4037. X and gamma reference radiations for calibrating dosemeters and dose rate meters and for determining their response as a function of photon energy.
ISO 4037-3 (2019) - Part 3: Calibration of area and personal dosemeters and the measurement of their response as a function of energy and angle of incidence.

Development of an In-house MATLAB code for dynamic multileaf collimator quality assurance based on EPID

Aiyara Pishyapan[1], Nauljun Stansook[1], Pimolpun Changkaew[1], Suphalak Khachonkham[1], Puangpen Tangboonduangjit[1], Sithiphong Suphaphong[1]

1. Master of Science Program in Medical Physics, Department of Diagnostic and Therapeutic Radiology, Faculty of Medicine Ramathibodi Hospital, Mahidol University, Thailand

Abstract

In advanced radiotherapy treatments, verification of the performance of the multileaf collimator (MLC) is an essential part of the linac QA program. Electronic portal imaging device (EPID) is very useful for MLC QA due to the EPID is high special resolution including the data are digitized and available for repeated visual and analysis. However, time-consuming is one of the issues of the MLC QA analysis procedure. There are some commercial software product that can be used in combination with EPID information in saving time for MLC QA analysis. Unfortunately, the software is an expensive product. To ameliorate this issue, In-house MATLAB code was developed and introduced, which aim for evaluating the MLC positional accuracy with picket fence test based on EPID images. In this study, the error of MLC positions at the gantry zero angle were intended to validated the accuracy of the In-house MATLAB code. The error-detection corresponding to leaf position and agrees to within ±0.15 mm of the intentional preset value by showing 1.05 mm and 1.85 mm for 1 mm and 2 mm intent errors, respectively. The results showed, that the developing In-house MATLAB code provide an accuracy inspection of the leaf disposition and precise numerical values. Thus, this developing MATLAB code is an effective tool and useful for routine MLC QA.

Keywords: Multileaf collimator, EPID, quality assurance, MATLAB

1. INTRODUCTION

The goal of radiotherapy is to determine the high-dose conformal to the target while keeping the controlled dose in a normal organ. Nowadays, the advanced radiotherapy technique irradiated including 3D-conformal, a fix-gantry modulated intensity radiotherapy (IMRT) and Volumetric Modulated Arc Therapy (VMAT) are used worldwide (1,2). The multileaf collimator (MLC) is an essential component that utilize to achieve the conformal and complex dose distribution in the treatment. Thus, the MLC required high accuracy of quality assurance (QA) (1). The mechanical part and the dosimetric part are the main concern for MLC QA. Essentially, the MLC transmission dose and dosimetric leaf gap are the parameters that highly affect the dose deviation for the planning (3,4). However, the accuracy of the dosimetric part depends on the speed of motion and position for the individual each leaf. As the study of LoSasso *et al*. showed, the shift of the MLC position 0.5 mm from the offset position increase the dose error up to 5% (4). In addition, the influence of gap error on delivery dose error is greater in a small size of a nominal leaf gap than a wide leaf gap (4). Therefore, the mechanical part should be realized. The American Association of Physicists in Medicine (AAPM) task group (TG)142 is a recommendation document for MLC QA procedure and general devices (5). The stability of the paired leaf is an important factor in the IMRT technique, and it is necessary for the QA MLC process, such as picket fence test, travel speed, and leaf position accuracy. Commonly, the film is used to verify the leaf position error due to its high resolution. By visual evaluated, films are enabled to detect the leaf positions errors by 0.5 mm (6). However, it hard to clarify which leaf number error including the process of measuring the film is quite complicated and time-consuming. The log file based analysis is the one of method that increasingly uses. The method of log file based is analyzed by using a machine delivery information that usually automatically storing in text files format within the computer of the machine (8). This method can detect all the characteristics of each MLC, but the results refer to the leaf motor (7).

Several studies have been emphasized the use of EPID and state it is very useful for MLC QA due to the EPID is already mounted on the linac machine and provide a high spatial resolution, including the digital data information that available for repeated visual and analysis. Li Y *et al*. (9) have been studied the leaf position and leaf speed of MLC comparing between EPID and EBT3 films and found that EPID can validate the error as same as EBT3 measurement. Similarly, the results of the high efficiency of EPID are also showed in the study of Rajesh Kumar *et al*. (8) and Agnew CE *et al*. (10), who studied the EPID compared with Log file for MLC QA. However, the information is analyzed by visual method remain the time-consuming and depend on the inspector determine and judgment the error detection. There are some commercial software that can be used in combination with EPID information in saving time of MLC QA analysis. Unfortunately, the product cost is an expensive.

The purpose of this study is to develop the In-house MATLAB code for routine MLC QA verification based on the EPID image data analysis.

2. MATERIAL AND METHODS

All experiments performed with 6 MV photon beams by using Clinac iX™ linear accelerator (Varian Medical Systems, Palo Alto, USA) equipped with Millennium-120 MLC that utilizes 40 inner leaf pairs with 0.5 cm width, and 20 outer leaf pairs with 1 cm width. The leaves attached on a carriage allowing the maximum extended each individual leaf movement is 14.5 cm. Images integrated over the delivery were acquired in DICOM format with on-board Varian aS1000 EPID (Varian Medical Systems, Palo Alto, USA). The detector has (1024 × 768 pixels, each pixel size is 0.39 mm with cover an active area of 40× 30 cm^2 in isocenter). The EPID is attached to the linacs by an exact-type arm positioned at 100 cm source to detector distance.

2.1 Pre-experimental

The EPID image quality can effect by its configuration and clinical conditions used. The EPID require a calibration to remove back ground noise (Dark field) and provide a uniform image, high quality image and responses consistently (Flood field) in routine use. In this study, the calibration was performed following the Varian procedure. The setup measurement, perform using a source to image distance (SID) 100 cm at field size 30×40 cm^2 which cover the entire sensitive area of the detector and dose not be irradiated the electronic part of the EPID. This calibration performed all dose rate of 100 to 600 MU/min. An image of a dark field was acquired 30 images while the beam was off. This can eliminate variation in sensitivity between different detector elements and areas of the panel. Flood field image is acquired 200 images while irradiating the EPID with an open field. In addition, pixel correction is the method to verify the dead pixel in EPID and gain it.

2.2 Experimental

In this study, we focus on picket fence at a static gantry MLC verification. However, it is necessary to initialize the various forms of irradiated areas to validate the generated MATLAB code. MLC static fields are essential for initial quality assurance before being examined with other tests. For each trial, the MLC was characterized using the commercial MLC shaper software (Varian Medical Systems Inc., Palo Alto, CA) before being sent to the treatment room, and the portal image was recorded in CD-ROM. The portal image was used to create the standard MATLAB code.

I. **MLC static field**

The various shape of radiation field determined using the commercial MLC shaper software (Varian Medical Systems Inc., Palo Alto, CA). The simple radiation field size of circle, square, and diamond was created with a diameter of 50 and 100 mm. In additional, the small static gap of 3 and 5 mm were created within the 10×10 cm^2 field size. This part implemented source to image distance (SID) 100 cm at 0º gantry angle. These geometry in term of DICOM image (Figure 1), were generated to validate MATLAB code.

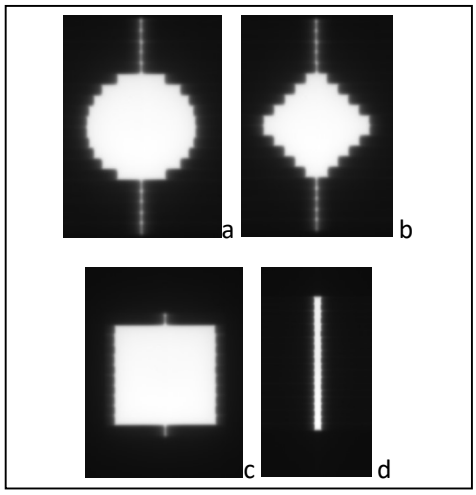

Figure 1. *The results of the EPID image in various shape, (a) Circle, (b) diamond, (c) square, (d) static gap.*

II. **Picket fence (PF) test and Validation of MATLAB code**

The Picket Fence plan with and without intentional error position were created. The first one was standard PF plan which consisted of the 11 narrow lines with a 1 mm gap widths and 20 mm interval. The other was intended the position of 0.5 mm, 1 mm and 2 mm at the leaf position of A30. All plans were performed at the source to image distance (SID) of EPID as 100cm at gantry angle with 0º. The collimator was 90º, and the field size was 16×40 cm^2 in order to cover all leaf pairs because we want to validate overall leaf MLC. The dose rate of 600 MU/min and 100 MU are used.

In assessing the accuracy of In-house software based on MATLAB, first, we must ensure that the software design has the potential to be accurately measured. The preset leaf position DICOM file from EPID was recorded and transferred to create the MATLAB code to evaluate MLC's characteristics. The data used for the baseline to compare with the MLC intent error.

III. **MATLAB code description**

This MATLAB code is designed as a MATLAB (version R2019a) graphical user interface (GUI). The portal image from EPID in any experiment was collected in terms of the DICOM file. The image processing for all experiments, was compounded the region of exposed radiation and blocked radiation. The two set images separated from background by Otsu's method (11), so the automatic optimum threshold is gotten to the group black and white image. Then finding the distance of various shapes and the size of the intent error that differs from the baseline. The size of the image in longitudinal and horizontal provided the bounding box. It found the top-left, top-right, width, and height of the object binary.

3. RESULTS

The size of MLC defined by using MLC shaper software has to correlate with the output image. The MATLAB code was able to detect the error with 0.26 mm per pixel resolution. It was the default value in this code to define the binary object or intent error size. Otherwise, SID has to vary until getting the correct size to allow the plan.

Table 1 *The differences result between the MLC static field shape plan and MATLAB code measurement.*

Shapes	Diameter (mm)	Measured (mm)	Difference between plan and measurement (mm)
Circle	50	49.1	0.9
	100	98.0	2.0
Diamond	50	49.1	0.9
	100	98.1	1.9
Square	50	49.5	0.5
	100	98.3	1.7
Static gap	3	3.3	0.3
	5	5.5	0.5

3.1 MLC static field

Table 1 shows the resulting MATLAB code analysis where the various irradiated static shapes are observed. The difference value between plans and MATLAB code analysis were within 2 mm for all various shape and diameter of static MLC. However, the MATLAB code performed a closer agreement for the diameter of 50 mm by show the difference were within 1 mm. A good agreement is also show for the static gap test, the differences were 0.3 and 0.5 mm for static gap of 3 and 5 mm, respectively.

3.2 Picket fence (PF) test

Figure 2 demonstrates the leaf position for the intent error of 1 mm and 2 mm at the preset leaf number of A30. The MATLAB code analysis shows that the error detection corresponds both leaf number and position with the agreement of position were within ±0.15 mm. Unfortunately, the intend error of 0.5 mm cannot detect by this MATLAB code.

4. DISCUSSION

Before using an image dosimetric tool for quality assurance purposes, the image QA and the calibration of EPID was necessary. Due to the pixel values of EPID, the response should be converted to the dose for evaluation. If the pixel values in some locations are counted incorrectly without checking or noise coming into the EPID will result in incorrect intensity measurements, causing dose error measurement and object size error.

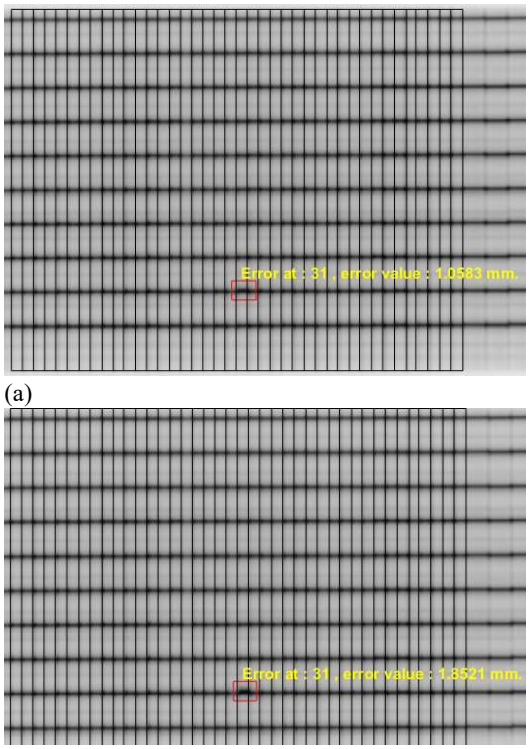

Figure 2 *Results of the Picket fence test which added intent error by (a)1 mm and (b)2 mm at the leaf number 30.*

In this study, the imager calibration is essential for verifying the size of the MLC static field and detect the leaf error in order to validate the MATLAB code too.

4.1 MLC static field

This MATLAB code in this part can adjust the size to detect the binary object to get optimal size. It's more affect in the small binary object to detect them.

Although, the difference between shape plans and MATLAB code analysis were within 2 mm for all shape type. The difference value of a 100 mm diameter was showed greater than a difference of a 50 mm diameter. This may cause by the backscatter radiation from its metallic support arm. Rowshanfarzad *et al*. (12) reported that in the small field, there is no arm backscatter, while for the large field, a substantial amount of backscatter is there, which increases the low dose in the image measured by EPID. The correction of a large field should be involved.

For the small static gap test, the calculation of the size of the object is considered the average of the pixel threshold, then the code is rounded up or down according to the set threshold, so the object's size in the image may be in the pixel subsection, which is the reason for displaying greater error values. The difference value can decrease by the subpixel arrangement method. It can increase the apparent resolution of an image by separate the subpixel from one pixel (13,14). The use of this is rather than direct pixel-by-pixel analysis.

4.2 Picket fence (PF) test

The intent error for all plan in 0º gantry angle agrees within ±0.15 mm. The intent error 1 mm was correlated with the measurement, while the intent error 1.85 mm was detected for 2 mm. Due to the pixel resolution was 0.26 mm, so the number of pixels for 1.05 and 1.85 mm were 4 and 7, respectively. The number of pixels was from the code using pixel-by-pixel. For the intent error, 2 mm should be getting 8 pixels that mean 2.11 mm. It may cause the intensity of pixel number 8 less than the threshold set. A further image analysis code is possible through the using of subpixel covers all object binary, the decreasing of error deviation value can be estimated. Although the intent error of 0.5 mm was made in this experiment and can be detected by visual inspection, the MATLAB code could not detect the value. The image intensity of intent error 0.5 mm was similar to baseline. In the study of Shahla Ebrahimi Moghadam *et al*. (15) showed the MATLAB code provide the maximum difference detection for the intentional of a 0.5 mm error up to 0.1 mm. However, this deviation considered to be within the AAPM TG 142 tolerance limit, which provide the tolerance for the IMRT technique is 1 mm. Thus, the initial verifying leaf error ≥ 1 mm well capable of detecting. The additional test of intent error of 0.5 mm may be randomly performed.

5. CONCLUSION

This developing MATLAB code was found to be an effective, accurate and convenient tool for routine MLC QA, static field shape and picket fence test. The small size of object binary should be provided with complex code, such as the subpixel arrangement method.

ACKNOWLEDGEMENTS

The authors wish to thank all members of the diagnostic and therapeutic radiology department, faculty of Medicine Ramathibodi Hospital, for their sincere cooperation and help.

REFERENCES

1. Bortfeld T. The number of beams in IMRT--theoretical investigations and implications for single-arc IMRT. Phys Med Biol. 2010;55(1):83-97.
2. Chen DZ, Craft D, Yang L. A circular matrix-merging algorithm with application in Volumetric Intensity-Modulated Arc Therapy. Theoretical Computer Science. 2015;607:126-34.
3. Kim J, Han JS, Hsia AT, Li S, Xu Z, Ryu S. Relationship between dosimetric leaf gap and dose calculation errors for high definition multi-leaf collimators in radiotherapy. Physics and Imaging in Radiation Oncology. 2018;5:31-6.
4. LoSasso T, Chui CS, Ling CC. Physical and dosimetric aspects of a multileaf collimation system used in the dynamic mode for implementing intensity modulated radiotherapy. Med Phys. 1998;25(10):1919-1927.
5. Klein EE, Hanley J, Bayouth J, Yin FF, Simon W, Dresser S, et al. Task Group 142 report: quality assurance of medical accelerators. Med Phys. 2009;36(9):4197-212.
6. Ezzell GA, Galvin JM, Low D, Palta JR, Rosen I, Sharpe MB, et al. Guidance document on delivery, treatment planning, and clinical implementation of IMRT: report of the IMRT Subcommittee of the AAPM Radiation Therapy Committee. Med Phys. 2003;30(8):2089-115.
7. Drashanfarzad P, Sabet M, Barnes MP, O'Connor DJ, Greer PB. EPID-based verification of the MLC performance for dynamic IMRT and VMAT. Med Phys. 2012;39(10):6192-207.
8. Kumar R, Amols HI, Lovelock M, Sharma SD, Datta D. Quick, efficient and effective patient-specific intensity-modulated radiation therapy quality assurance using log file and electronic portal imaging device. J Cancer Res Ther. 2017;13(2):297-303.
9. Li Y, Chen L, Zhu J, Wang B, Liu X. A quantitative method to the analysis of MLC leaf position and speed based on EPID and EBT3 film for dynamic IMRT treatment with different types of MLC. J Appl Clin Med Phys. 2017;18(4):106-15.
10. Agnew A, Agnew CE, Grattan MW, Hounsell AR, McGarry CK. Monitoring daily MLC positional errors using trajectory log files and EPID measurements for IMRT and VMAT deliveries. Phys Med Biol. 2014;59(9):N49-63.
11. Liu D, Yu J. Otsu Method and K-means. 2009 Ninth International Conference on Hybrid Intelligent Systems2009. p. 344-9.
12. Rowshanfarzad P, McCurdy BM, Sabet M, Lee C, O'Connor DJ, Greer PB. Measurement and modeling of the effect of support arm backscatter on dosimetry with a varian EPID. Med Phys. 2010;37(5):2269-78.
13. Choh H-K. Subpixel arrangements and color image rendering methods for multiprimary displays. Journal of Electronic Imaging. 2006;15(2).
14. Mamalui-Hunter M, Li H, Low DA. MLC quality assurance using EPID: a fitting technique with subpixel precision. Med Phys. 2008;35(6):2347-55.
15. Moghadam SE, Nasseri S, Seyedi SS, Gholamhosseinian H, Momennezhad M. Evaluation of application of EPID for rapid QC testing of linear accelerator. Rep Pract Oncol Radiother. 2018;23(5):369-77.

Predicting 3D dose distribution from patient CT images alone for prostate VMAT using deep learning

Patiparn Kummanee[1], Sangutid Thongsawad[1,2], Wares Chancharoen[1], Todsaporn Fuangrod[1]

1 Faculty of Medicine and Public Health, HRH Princess Chulabhorn College of Medical Science, Chulabhorn Royal Academy, Bangkok, Thailand
2 Department of Radiation Oncology, Chulabhorn Hospital, Chulabhorn Royal Academy, Bangkok, Thailand

Abstract

Volumetric modulated arc therapy (VMAT) planning is a time-consuming process of radiation therapy system. because of the iteration of manual trail-and-errors inverse planning process, long dose calculation time and replan iterations. With the deep learning approach, the 3D dose distribution can be predicted without traditional dose calculation from treatment planning system (TPS). This will accelerate the process by guiding and confirming the achievable dose distribution by reducing the number of replan iterations while maintain the plan quality. In this work, the prostate VMAT dose distribution prediction model from CT images alone was developed using generative adversarial network (GAN) model. The GAN model was constructed by a pair of deep learning model including U-NET generator and patchGAN discriminator. Total of eleven prostate VMAT plan were randomly selected. Ten plan data were used to develop the prediction model as the training data set, including patient CT images and 3D dose distribution from TPS. A single plan was tested to determine the preliminary model accuracy. The predicted 3D dose distribution was compared to the calculated 3D dose distribution from TPS using 2D gamma evaluation method for each slide. The result showed the prediction model can generate 3D dose distribution from CT image alone with the accuracy 70.35% ± 20.48% of mean passing rates from 2D gamma analysis with 3%/3 mm criteria. Our proposed CT-alone prostate VMAT dose distribution prediction model could generate accurate dose distribution from input CT images which could help medical physicists to get the acceptable quality of treatment plan with less time in the process.

Keywords: VMAT, deep learning, prostate cancer, dose distribution prediction

1. INTRODUCTION

Volumetric modulated arc therapy (VMAT) and intensity modulated arc therapy (IMRT) are the widely used External Beam Radiation Therapy (EBRT) technique more than 3D conformal radiation therapy (3DCRT) and become the standard treatment for many cancers in many institutes (1, 2). From the complex dose distribution in VMAT and IMRT, it can increase conformity of dose to the target and can significantly decrease dose to OARs, which reduce the risk of normal tissue complication after treatment (3). However, to achieve more complex dose distribution, the complexity of treatment planning process also increases (3, 4). VMAT treatment planning may be very time-consuming process due to iteration of manual trail-and-errors and iteration of planning process. In order to achieve the desired dose distribution, planners have to manually try input optimization parameters to the treatment planning system (TPS) and repeat the processes to adjust the parameters, which take a long time for each cycle. Moreover, the process may be iterated again form an unapproved plan and more requirements from oncologists.

In recent years, researchers have started to use deep learning and neural network in various medical applications (5). To solve these problems, the deep learning also is acquired for accelerating and to assist the treatment planning process in various dimensions, one of that is predicting dose distribution. Deep learning can be used for predicting dose distributions from inputting anatomical information (such as CT or contour) either in a 2D or 3D data (6). The predicted dose distribution can be used as an objective to automatically generate a treatment plan later (6). However, the VMAT dose distribution prediction system is not published by now.

The goal of this study is to develop the VMAT prostate cancer dose distribution prediction framework using GAN deep learning mode from patients CT data without organ contour data.

2. MATERIAL AND METHODS

The research framework of this study is shown in Figure 1. The framework used a generative adversarial network to predict the dose distribution of VMAT for prostate cancer which did not require the contour information as input data. This framework used only CT images as inputs and its corresponding dose distribution as labels to train the predictive model. To evaluate the accuracy of the CT alone prediction model, various dosimetric parameters were compared between the predicted dose distribution and actual dose distribution.

2.1 Patients data

Prostate cancer patient's data were used for training and testing the model. All patients were treated between 2015 to 2020 at Chulabhorn Oncology Medical Centre, Chulabhorn Hospital, Thailand, by using VMAT technique with 78 Gy/39 fractions prescription dose to a planning target volume (PTV). Patient's CT images,

contour structures and corresponding RT-dose files were export from eclipse treatment planning system.

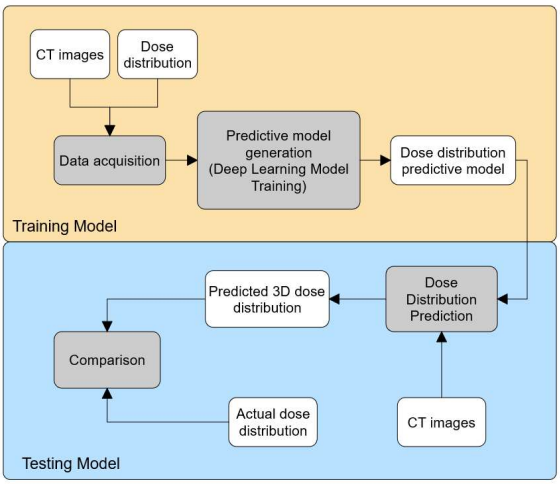

Figure 1 *Overall framework of this study, CT based dose distribution prediction model was trained using GAN. The predicted dose distributions were compared to corresponding actual dose distribution.*

2.2 Data preprocessing

Each slice of CT image was resized from 512 × 512 pixels to 256 × 256 pixels. The RT-dose images which different in each patient due to the variation in body size were processed to be the size 256 × 256 pixels as of CT images. The same size of CT images and corresponding dose distributions were paired and created the dataset of input (CT image) and target (dose distribution) for image-to-image translation deep learning model. All CT and RT-dose images were normalized from 0 to 1 before input to GAN model as shown in Figure 2.

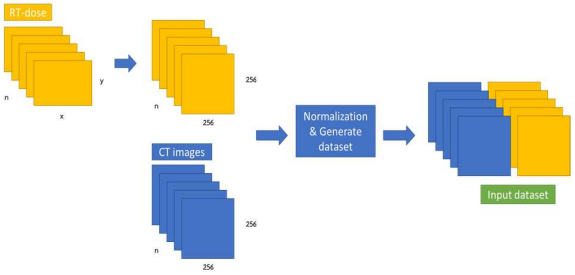

Figure 2 *Data preprocessing process, to create the datasets for training and testing the model with the paired CT images and the resized dose distribution.*

2.3 Generative adversarial network model

In this study, the pix2pix model was chosen to generate VMAT dose distribution from CT images. The pix2pix is the supervised learning techniques adopted in GANs. As showing in Figure 3, the GANs model is constructed by using two deep learning models, the generator and discriminator. The U-net model was used as the generator, while a convolutional patchGAN classifier was used for the discriminator. These two models were trained and competed to each other at the same time, the generator was trained to generate the dose distribution which cannot be distinguish by the discriminator, while the discriminator was trained to distinguish dose distribution that generated by generator and the actual corresponding dose distribution from the input CT image. In each round of training, the discriminator would give more accurate of dose distribution distinguishing and the generator would generate more accurate dose distribution.

2.4 Model training

The patient's data were divided into two groups, first was training dataset which 80% of all patient's data and for the rest of patient data (20%) are testing dataset. The prediction models were trained with a tensorflow module in Python. The Adam optimization were applied to the model. The training iterations of the prediction model were selected as 200 epochs which based on the preliminary experiment. The dose distributions of the testing dataset were predicted by using the corresponding trained model with only CT of the testing set.

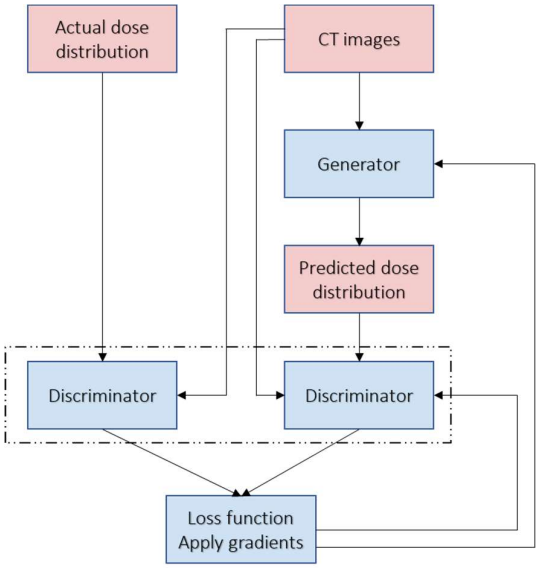

Figure 3 *GAN pix2pix framework, two deep learning model were used as generator and discriminator.*

2.5 Evaluation

To compare the prediction performance between the CT-based prediction model and the actual dose plan, 3D gamma analysis was used to evaluate the accuracy of the predicted dose distributions with the corresponding actual dose distributions. The agreement was assessed at tolerance levels of 3%/3 (7).

3. RESULTS

3.1 Dose distribution

The results of the dose-distribution comparison of one sample testing data are showing in Figure 4. The dos difference and gamma distribution are showing in Figure 5, mean passing rates of 2D gamma analysis were 70.35% with 3%/3 mm criteria.

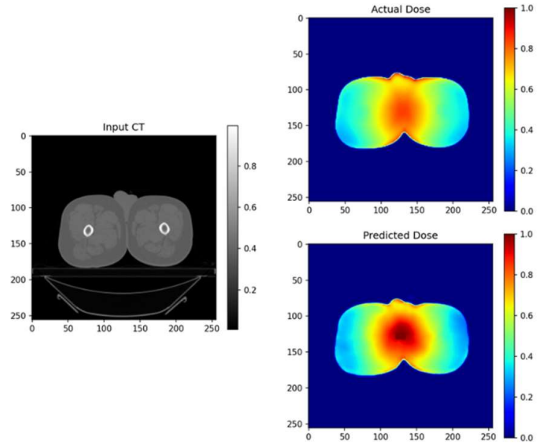

Figure 4 *Input CT, corresponding actual dose distribution and predicted dose distribution.*

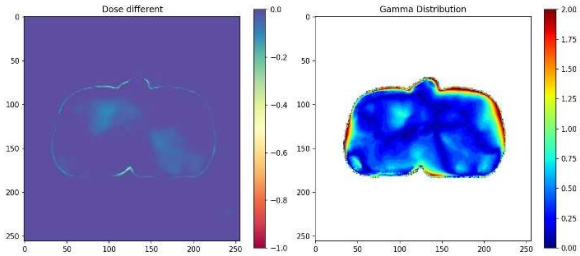

Figure 5 *Dose difference and gamma analysis distribution.*

4. DISCUSSION

In this study, prostate VMAT dose distribution predictive model based on GAN deep learning was developed by learning the GAN model from prostate cancer patient CT images and its corresponding dose distributions. The prediction accuracy of the model which evaluated by 2D gamma analysis was lower than the acceptable criteria, which should be more than 95% pass rate. Murakami et al. was studied the dose prediction of IMRT of prostate cancer patients from 90 patient CT-alone images using generative adversarial network (GAN), and reported that dose differences of all dosimetric parameters except for D98% and D95% for PTV were within approximately 2% and approximately 3% for OARs. The obviously superior result of Murakami et al. comparered to our study, may cause of the numbers of patient sample which is the based of accuracy of neural network and deep learning process.

The PatchGAN was used for the the discriminator that only look at small patches in an image and try to determine whether each is real or fake. In this study, the 30×30 receptive fields was used to discriminate predicted dose and actual dose. But according to a previous report, the use of 70×70 PatchGAN gives better results for the image-to-image translation (8). The more receptive fields should used in this study for achieved the better accuracy result.

The first limitation of this study is the number of patient's data, small dataset compared to others previous study, which could affect to predictive model in term of over fitting model. The small dataset could let the training model train over the same data and create strong pattern of the model which cannot effectively work on the others dataset even in testing dataset. Future work will be developing the model by increasing a greater number of patients in the training dataset and adjust the predictive model architecture to achieve the acceptable dose distribution.

5. CONCLUSION

The accurate prediction model of prostate VMAT dose distribution from CT-alone based on GAN deep learning model was developed. The predictive model could instantly predict dose distribution from the CT images which could reduce the usage time for the iterative optimization process. Therefore, the total usage time of treatment planning process would be smaller.

REFERENCES

1. Smitsmans MHP. Towards image-guided radiotherapy of prostate cancer: Citeseer; 2010.
2. Shiraishi S, Moore KL. Knowledge-based prediction of three-dimensional dose distributions for external beam radiotherapy. Medical physics. 2016;43(1):378-87.
3. Murakami Y, Magome T, Matsumoto K, Sato T, Yoshioka Y, Oguchi M. Fully automated dose prediction using generative adversarial networks in prostate cancer patients. PloS one. 2020;15(5):e0232697.
4. Nguyen D, Long T, Jia X, Lu W, Gu X, Iqbal Z, et al. A feasibility study for predicting optimal radiation therapy dose distributions of prostate cancer patients from patient anatomy using deep learning. Scientific reports. 2019;9(1):1-10.
5. Shen D, Wu G, Suk H-I. Deep learning in medical image analysis. Annual review of biomedical engineering. 2017;19:221-48.
6. Barragán-Montero AM, Nguyen D, Lu W, Lin M-H, Norouzi-Kandalan R, Geets X, et al. Three-dimensional dose prediction for lung IMRT patients with deep neural networks: robust learning from heterogeneous beam configurations. Medical physics. 2019;46(8):3679-91.
7. Chen X, Men K, Li Y, Yi J, Dai J. A feasibility study on an automated method to generate patient-specific dose distributions for radiotherapy using deep learning. Medical physics. 2019;46(1):56-64.
8. Isola P, Zhu J-Y, Zhou T, Efros AA, editors. Image-to-image translation with conditional adversarial networks. Proceedings of the IEEE conference on computer vision and pattern recognition; 2017.

Size-Specific Dose Estimates (SSDE) for Head CT in Pediatric Patients

Saowapark Poosiri[1,2], Kanokkwan Chuboonlap[1], Nuttita Kaewlaied[1],
Supika Kritsaneepaiboon[1], Anchali Krisanachinda[2]

1 Department of Radiology, Faculty of Medicine, Prince of Songkla University, Hat Yai, Thailand.
2 Medical Physics, Department of Radiology, Faculty of Medicine, Chulalongkorn University, Bangkok, Thailand

Abstract

Introduction: The dose from CT examination is normally displayed as volume CT dose index ($CTDI_{VOL}$). Actually, $CTDI_{VOL}$ is estimated by using two cylindrical phantoms of different diameters. $CTDI_{VOL}$ is only an indicator as it does not address the patient size. AAPM Report no.293 on the size-specific dose estimates (SSDEs) for CT head examination provides the conversion factors for the estimation of the patient radiation dose at higher accuracy.

Purpose: The purpose of this study is to estimate the size-specific dose estimation (SSDE) for head examination in the Computed Tomography of pediatric patients.

Methods: This study is the retrospective analysis of 191 cases with the inclusion criteria for the age range from 0 to 15 years old. The patients had been scanned by CT Toshiba Aquilion Prime with 80 detectors without contrast media enhancement, from September 2015 to October 2019. The conversion factors from AAPM Report no.293 was selected to calculate $SSDE_{Dw}$ by using the equation, $SSDE_{Dw}$ = conversion factor x $CTDI_{VOL}$.

Results: The mean $SSDE_{Dw}$ with four age ranges of less than 1, 1 to less than 5, 5 to less than 10 and 10 to 15 years old were 19.38, 22.82, 28.74 and 38.20 mGy, respectively while the mean $CTDI_{VOL}$ were 18.82, 24.36, 31.87, and 43.71 mGy respectively.

Conclusion: The $SSDE_{Dw}$ were less than $CTDI_{VOL}$ except at the age of less than 1, the $SSDE_{Dw}$ were greater than $CTDI_{VOL}$ due to the conversion factor that included the patient body composition. The $SSDE_{Dw}$ is more appropriate indicator for CT patient dose because the patient size and body composition had been considered to provide higher accuracy.

Keywords: Size-specific dose estimates (SSDE), Volume CT dose index ($CTDI_{VOL}$), Radiation dose

1. INTRODUCTION

Computed Tomography (CT) is one of the best modalities for low contrast imaging in human. As the CT has been invented since the 1970s, the clinical applications increase rapidly and become the major source of human exposure in diagnostic X-rays (1-2). CT head examination in pediatric patients can demonstrate brain disorders such as brain infection and brain tumor. The radiation dose delivered to the pediatric patient should be concerned because of the increasing use of MDCT in patient studies and the head region has several sensitive organs to radiation especially, the lens of the eye (3).

The patient dose from CT scan is displayed in terms of Dose Length Product (DLP) with the unit of mGy.cm and the volumetric CT dose index ($CTDI_{VOL}$), in mGy. $CTDI_{VOL}$ represented the scanner output, depends on several parameters such as tube current time product (mAs), tube potential (kVp), pitch, gantry rotation time and filters (4). Actually, $CTDI_{VOL}$ has not been considered to patient size and only be used to estimate patient radiation dose but the value is inaccurate and determined from the polymethyl methacrylate (PMMA) cylindrical phantom of particular size. One phantom size is 16 cm diameter to approximate the size of head and the other is 32 cm diameter to approximate the size of adult body. Both phantoms are 16 cm length (5-6).

In fact, patient radiation dose should be considered for both output radiation dose from CT and the patient characteristics. Therefore, patient size and tissue as well as organ composition should be considered to estimate patient radiation dose by using the concept of the size-specific dose estimates (SSDEs). AAPM Report no.293 (5) recommended the estimation of patient dose based on $CTDI_{vol}$ and patient size. The patient radiation dose was calculated by the equation- SSDE=fsize (the conversion factor that takes into account the patient size (water equivalent diameter (Dw)) x $CTDI_{VOL}$.

$CTDI_{VOL}$ and DLP have been used for the patient radiation dose estimation at most institutions in Thailand. It is not realistic and inaccurate. When the radiation delivered to small or large patients displayed the same amount of $CTDI_{VOL}$, estimated from same size of cylindrical phantom.

At Songklanagarind Hospital, the pediatric patients had been examined for the diagnosis and follow up brain disease using non-contrast enhancement protocol in CT study. Regarding to the scanner, the radiation output ($CTDI_{VOL}$) had been determined by using 16 cm in diameter of homogeneous cylindrical phantoms. On the contrary, the human thoracic region is neither cylindrical shape, nor uniform in size and density, therefore, the SSDE should be implemented for patient dose from CT scan in thoracic region. The purpose of this study is to estimate the size-specific dose estimation ($SSDE_{DW}$) for head examination by the Computed Tomography of pediatric patients.

2. MATERIAL AND METHODS

2.1 Patient population

The patient data in terms of body weight, body mass index (BMI), height, gender and age were collected from the image DICOM header from September 2015 to October 2019. The study was approved by Institutional Review Board (IRB) of Faculty of Medicine, Prince of Songkla University.This study was retrospective analysis in 191 pediatric patients of the age range from 0 to 15 years old. The patients had been scanned by CT Toshiba Aquilion Prime with 80 detectors without contrast media enhancement. Patients with a tumor size of more than 5 cm in diameter, hydrocephalus disease, the contour skin of head region not visible on the FOV reconstruction were excluded from this study.

2.2 Patient radiation dose determination

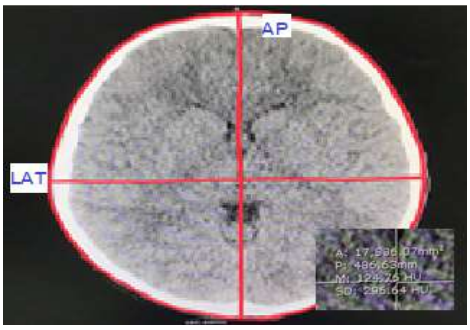

Figure1. Region of interest (ROI) contouring and AP-LAT dimensions from the CT brain

The patient's size (water equivalent diameter (Dw)) and the region of interest (ROI) were manually drawn at the mid brain level from the CT axial image including the brain cross section using digital calipers and free hand ROI on image tools. The patient dimension, anterior-posterior (AP) and lateral (LAT) dimension, mean CT number (HU), image noise (SD) and the area of the ROI were recorded as shown in Figure1. The patient radiation dose was calculated in terms of SSDE, product of conversion factor (f_{Dw}) and $CTDI_{VOL}$ (5). The calculation of SSDE is as the following equation:

$$SSDE = f_{Dw} \times CTDI_{vol}$$

Where, f_{Dw} is the conversion factor that takes into account the patient size (water equivalent diameter (Dw)).

Water equivalent diameter (Dw) was calculated by this equation;

$$Dw \equiv 2 \times \sqrt{\left(\frac{\overline{CT(x,y)_{ROI}}}{1000} + 1 \right) \times A_{ROI} / \pi}$$

Where, average $CT(x,y)_{ROI}$ is the mean CT number in the ROI and A_{ROI} is the total area of ROI.

3. RESULTS

3.1 Patient radiation dose

The mean $SSDE_{Dw}$ with four age ranges of less than 1 (26 cases), 1 to less than 5 (54 cases), 5 to less than 10 (55 cases), and 10 to 15 years old (56 cases), were 19.38, 22.82, 28.74 and 38.20 mGy, respectively while the mean $CTDI_{VOL}$ were 18.82, 24.36, 31.87, and 43.71 mGy respectively as shown in table1.

Table 1 *Patient radiation dose, $CTDI_{VOL}$ and $SSDE_{Dw}$ of head CT examination.*

Age group (year)	$CTDI_{vol}$ (mGy) Mean±SD	Conversion Factor Mean±SD	$SSDE_{Dw}$ (mGy) Mean±SD
0-1	18.82±4.56	1.03±0.06	19.38±4.88
>1-5	24.36±5.23	0.94±0.03	22.82±4.78
>5-10	31.87±7.77	0.90±0.02	28.74±6.99
>10-15	43.71±9.38	0.88±0.03	38.20±7.94

3.2 The correlation between water equivalent diameter (Dw) and $SSDE_{Dw}$

The correlation between water equivalent diameter (Dw) and $SSDE_{Dw}$ of pediatric patients for head CT examination, the weak linear relationship between the water equivalent diameter (Dw) and $SSDE_{Dw}$, R^2 was 0.2956. as shown in Figure2.

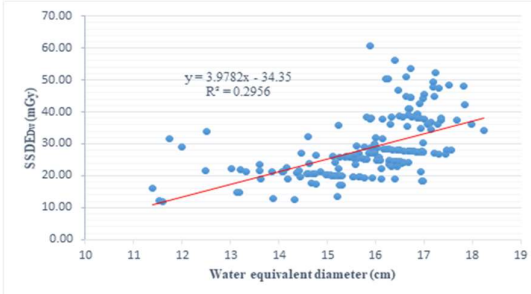

Figure 2. The correlation between water equivalent diameter (Dw) and $SSDE_{Dw}$

The correlation between age (year) and water equivalent diameter (Dw) (cm) of pediatric patients for head CT examination, the moderate linear relationship with R^2 was 0.538 as shown in Figure3.

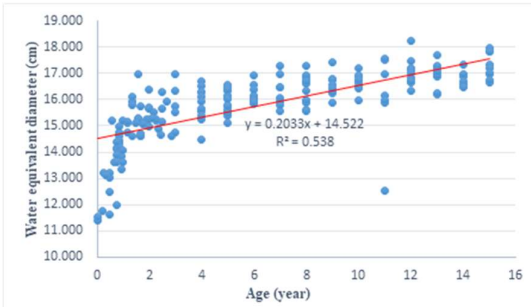

Figure 3. The correlation between age (year) and water equivalent diameter (Dw)

4. DISCUSSION

In this study, 191 pediatric patients of the age range from 0 to 15 years old were included to determine the SSDE. The conversion factors (f_{size}) from the AAPM Reports no.293 (5) was applied to determine SSDE for head imaging in 80 row detectors computed tomography.

$CTDI_{vol}$ has been used as the patient radiation dose estimation but it is not realistic and inaccurate as it was determined from 16 cm diameter PMMA cylindrical and homogeneous phantom, on the contrary head region is not in the cylindrical shape, non-uniform in size and density. Our study, the mean $CTDI_{VOL}$ was less than $SSDE_{Dw}$ at the age range 0-1 year old but the other three groups, the mean $CTDI_{vol}$ were higher than $SSDE_{Dw}$ as shown in Table1.

In previous study, Anam C et al (7) reported on 'A fully automated calculation of size-specific dose estimate (SSDE) in thoracic and head CT examinations'. The results showed SSDE was less than $CTDI_{VOL}$ while our study, $SSDE_{Dw}$ were less than $CTDI_{VOL}$ except at the age of less than 1, the $SSDE_{Dw}$ were greater than $CTDI_{VOL}$ due to the head diameter was smaller than 16-cm cylindrical phantom and conversion factor, when Dw decreased, the mean CT number decreased. On the other hand, the conversion factor (f_{Dw}) to calculate SSDEDW will increase, so $SSDE_{Dw}$ was also increased, therefore $SSDE_{Dw}$ of age of less than 1 is higher than other groups.

The correlation of age and Dw was moderately correlated, R^2 was 0.538. Dw can be determined from age for pediatric patients with the age range from 0 to 15 years old and underwent head CT examination by this equation:

$$y = 0.2033x + 14.522,$$

where x is the age, and y is the water equivalent diameter.

The patient size in terms of water equivalent diameter was measured by manual contour at the middle slice of head. The benefit of manual measuring is suitable for clinical users (physicians and radiological technologists) and save the cost instead of purchasing commercial software.

$SSDE_{Dw}$ has been considered in details on patient size and body composition. So, the concepts of the size-specific dose estimates (SSDEs) is appropriate to be used as in clinical studies for patient dose estimation of different attenuations especially in pediatric patients.

5. CONCLUSION

In conclusion, the $SSDE_{Dw}$ of the brain CT in pediatric patients were less than $CTDI_{VOL}$ except at the age of less than 1, the $SSDE_{Dw}$ were greater than $CTDI_{VOL}$ due to the conversion factor that included the patient body composition. The $SSDE_{Dw}$ is an appropriate indicator for CT patient dose because the patient size and composition had been considered to provide higher accuracy.

ACKNOWLEDGEMENTS

The authors are thankful to Mr. Natee Ina, Head of Radiological Technology Division, Department of Radiology, Faculty of Medicine, Prince of Songkla University, Hat Yai, Thailand. for his guidance and contribution.

REFERENCES

1. Kak, A.C. and M. Slaney, Principles of Computerized Tomographic Imaging. 1988, New York: IEEE Press.
2. Hsieh, J., Computed Tomography: Principles, Design, Artifacts, and Recent Advances. 2009, Bellingham, WA, USA: SPIE Press.
3. ICRP., 1990 Recommendations of the International Commission on Radiological Protection. Ann ICRP, 1991. 21(1-3): p. 1-201.
4. Bushberg, J.T., et al., The Essential Physics of Medical Imaging. second edition. 2001, Philadelphia, PA, USA: Lippincott Williams & Wilkins.
5. John M, Keith J, Anthony H, Kimberly E, Nathan S, Nima K, et al. AAPM report no.293 size-specific dose estimate (SSDE) for head ct. American Association of Physicists in Medicine 2019:1-19.
6. Cynthia M, FAAPM C, Donovan M, Maryam B, Samuel B, Kristen B, et al. AAPM report no.220 use of water equivalent diameter for calculating patient size and ssde in ct. Association of Physicists in Medicine 2014:1-18.
7. Anam C, Haryanto F, Widita R, Arif I and Dougherty G. A fully automated calculation of size-specific dose estimate (SSDE) in thoracic and head CT examinations. Article in Journal of Physics Conference 2016;694:1-9.
8. John M, Keith J, Dianna D, Cynthia H, Michael F, Thomas L. AAPM report no.204 size-specific dose estimate (SSDE) in pediatric and adult body ct examinations. American Association of Physicists in Medicine 2011:1-21.
9. Rehani M. Managing Patient Dose in Multi-Detector Computed Tomography (MDCT) [Internet]. International Commission on Radiological Protection (ICRP) [cited 2019 Nov 20].Availablefrom: http://www.icrp.org/docs/ICRP-MDCT-for_web_cons_32_219_06.pdf

Conflicts of interest: None
Corresponding author: Anchali Krisanachinda, Ph.D.
Institute: Department of Radiology, Faculty of Medicine Chulalongkorn University
Street: Rama IV Road, Pathumwan
City: Bangkok10330
Country: Thailand
Email: anchali.kris@gmail.com

Design of universal 3D-printed oral stent for head and neck radiotherapy

Thunphisit Mundee[1], Teerawit Eakpatcha[2], Chavin Jongwannasiri[1], Todsaporn Fuangrod[1]

1 Faculty of Medicine and Public Health, HRH Princess Chulabhorn College of Medical Science, Chulabhorn Royal Academy, Bangkok, Thailand
2 Department of Radiation Oncology, Chulabhorn Hospital, Chulabhorn Royal Academy, Bangkok, Thailand

Abstract

Introduction: The primary treatment of head and neck cancer is external beam radiation therapy. The complications from radiation include speech, taste, saliva production, and swallowing. An oral stent, immobilized equipment, is applied to minimize dose in the tongue (or hard palate). It can improve the accuracy of patient's setup between fractions. However, the oral stent is not widely used due to the unaffordable price.
Purpose: This study aims to design the universal oral stent (UOS), which has low cost but high efficiency.
Methods: The structural components and physical properties were evaluated using the Finite element analysis (FEA). It was simulated by mimicking the realistic environment parameters, including maximum bite force (350 N) and average human breath airflow (1.3 m/s). The 3D model was designed by CAD modeling and fabricated by 3D printing. It consists of two parts, namely, mouthpiece and tongue displacer. The tongue displacer has three sizes of 37, 40, and 43 mm in length, according to the average value of Asian's tongue length.
Results: The results showed that total deformation from the maximum bite force on the mouthpiece was 0.15 mm, indicating an unbreakable mouthpiece. The total airflow velocity was in the range of 1.3-4.5 m/s through the airway, but the mainline speed was 1.3-2.3 m/s. It indicated that the patient could breathe during treatment.
Conclusion: The UOS can be considered beneficial for use in the treatment due to the less deformation and easy to breathe.

Keywords: Head and neck cancer, Oral stent, 3D printing

1. INTRODUCTION

One of the main treatments in head and neck cancer is external beam radiation therapy, which applies the maximum radiation dose deposition to cancer cells while minimizes the radiation dose to normal tissues. However, the head and neck region have complex and overlap structures so that the normal tissues and cancerous region are located adjacently. It is difficult to evade the normal tissues from the radiation beam. The patient's tongue position in the oral cavity is difficult to setup. The effects of overdose on the patient's tongue lead to an error in speech, taste, saliva production, and swallowing(1-3). The modern techniques of radiation therapy, such as intensity modulated radiation therapy (IMRT) and volumetric modulated arc therapy (VMAT), improve dose distribution precision and evade the radiation beam. However, the radiation beam must travel through the tongue to deposit the radiation dose to a cancer cell in some situations. The total dose is divided into 20-30 fractions based on techniques, prescribed dose, and patient's anatomy in radiotherapy. Minimizing the patient position variation for fraction-to-fraction is a key role; the patient needs to be set up with the same position in every fraction to ensure the radiation beam hits the target precisely. However, the tongue region can be moved during the treatment because of the saliva swallowing. Moreover, the thermoplastic mask cannot be used to immobilize the patient's tongue.

Oral stent, also known as tongue displacer, mouthpiece, and bite block, is used in head and neck cancer patients for minimizing radiation dose to the tongue or hard palate. It will separate between the maxillary and mandible and press the tongue down away from the hard palate(4, 5). Generally, an oral stent is applied with a thermoplastic mask to immobilize the tongue during treatment. Therefore, it can minimize radiation dose and improve patient setup accuracy between fractions. In developing countries, the major limitation of using oral stents is the unaffordable price for budgeted patients. Many centers have invented alternative equipment instead of the oral stent, such as a cut syringe. It can separate the tongue from the hard palate to evade the radiation beam. However, its cylindrical shape can affect less contact area, generating the radiation dose on both sides of the tongue. Besides, the tongue's position can change over the treatment course, and the patient can get the wound from the sharpness of the cut syringe. Therefore, this study aims to fabricate an oral stent with a comfortable design at a low price.

2. MATERIAL AND METHODS

2.1 Design of universal oral stent (UOS)

The UOS was designed to meet users' needs (radiologists and patients). The key design factors are personalized patient, comfort, user friendly, and ability to reduce radiation dose. There are several design iterations to ensure the design met these design factors where were validated by the target users initially. The 3D model of UOS was designed and illustrated using Autodesk Fusion 360 software. The final design consists of two main parts, namely, mouthpiece and tongue displacer.

2.2 Finite element analysis (FEA)

In FEA process, the bite and tongue resistance forces and airflow velocity were evaluated using ANSYS 2020 R1 software. The defined criteria for UOS FEA is shown in Table 1. The bite resistance force is simulated on the top and bottom of the biting area on the mouthpiece (1 x 25 mm). The tongue resistance force is simulated in a connector part of the tongue displacer. Airflow velocity is also simulated in the airway through the mouthpiece.

Table 1 The criteria for evaluation by FEA

Topic of testing	Criteria
bite resistance force	50 - 450 Newton (N) (50 N increment)
tongue resistance force	20 - 100 Newton (N) (20 N increment)
Airflow velocity	1.3 meter per second

2.3 Fabrication of UOS prototype

Once the 3D model design is analyzed and evaluated through the FEA. The Standard Triangle Language (STL) file is exported for UOS prototype fabrication. The STL file is transformed into a G-code file by a 3D Printing slicer (Create Bot). The G-code was then sent to Create Bot DE+ 3D printer to produce the prototype. The polylactic acid (PLA) material with 100% fill-in will be used for 3D printing. The parameters for printing are shown in table 2.

Table 2 The parameters of printing.

Parameters	Value
Layer height	0.3 mm
Fill density	100 %
Material	Plastic PLA
Bad temperature	45 ℃
Printing temperature	210 ℃

3. RESULTS

3.1 Design of universal oral stent

The dimensional shape of UOS is shown in Figure 1. The mouthpiece illustrates an airway, which is designed to use with alginate. The tongue displacer has three sizes; 37, 40, and 43 mm in length, to cover various patient conditions. Figure 1(A) shows the mouthpiece's front view designed to connect with a thermoplastic mask for immobilizing the patient during treatment. Figure 1(B) shows the mouthpiece's side view, which has both connector and airway. The connector was designed to fasten with a tongue displacer, as shown in Figure 1(C) and 1(D).

3.2 Finite element analysis (FEA)

The bite and tongue force resistances were evaluated to consider the total deformation on the boundary of bite and tongue forces followed the criteria, as shown in Figure 2(A) and 2(C). The total deformations generated by maximum bite and tongue forces are 0.15 and 0.25 mm, respectively, as shown in Figure 2(B) and 2(D). Moreover, the airflow velocity was simulated in the airway of the mouthpiece. The result showed that an air velocity increases from 1.3 m/s to 4.57 m/s when passing through the airway. Figure 3 presents the streamline of air particles through the airway.

3.3 Fabrication of UOS prototype

The workpieces fabricated by 3D printing are shown in Figure 4. The 3D model consists of two parts, mouthpiece and tongue displacer.

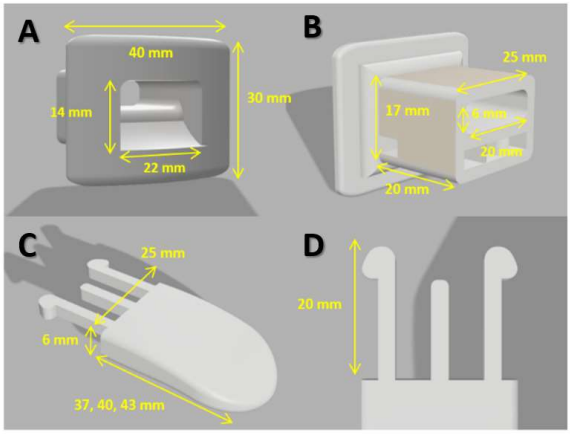

Figure 2 A dimensional shape of the universal oral stent. (A) front view of mouthpiece, (B) side view of mouthpiece, (C) overview of tongue displacer, and (D) Connector of tongue displacer.

4. DISCUSSION

The UOS was designed to use alginate for creating a marking on it. This design is personalization. The airway on a mouthpiece can help a patient to breathe via the oral cavity. A front of the mouthpiece was used to grip with a thermoplastic mask.

The UOS was evaluated by using FEA method to optimize the oral stent morphology and size. There are three factors influence during the design phase; Asian tongue size and mouth space, bio-compatible material, and usability. The single mouthpiece and three different length of tongue displacers were created. The prototype was fabricated using 3D printing with PLA material. However, we found that the shape of 3D printing universal oral stent had the uncertainty of size because of the limitation of the printing process's resolution and the support part's non-smooth surface. These problems made the tongue displacer can't connect to the mouthpiece. The troubleshooting is polishing on the surface of the connecter of the tongue displacer.

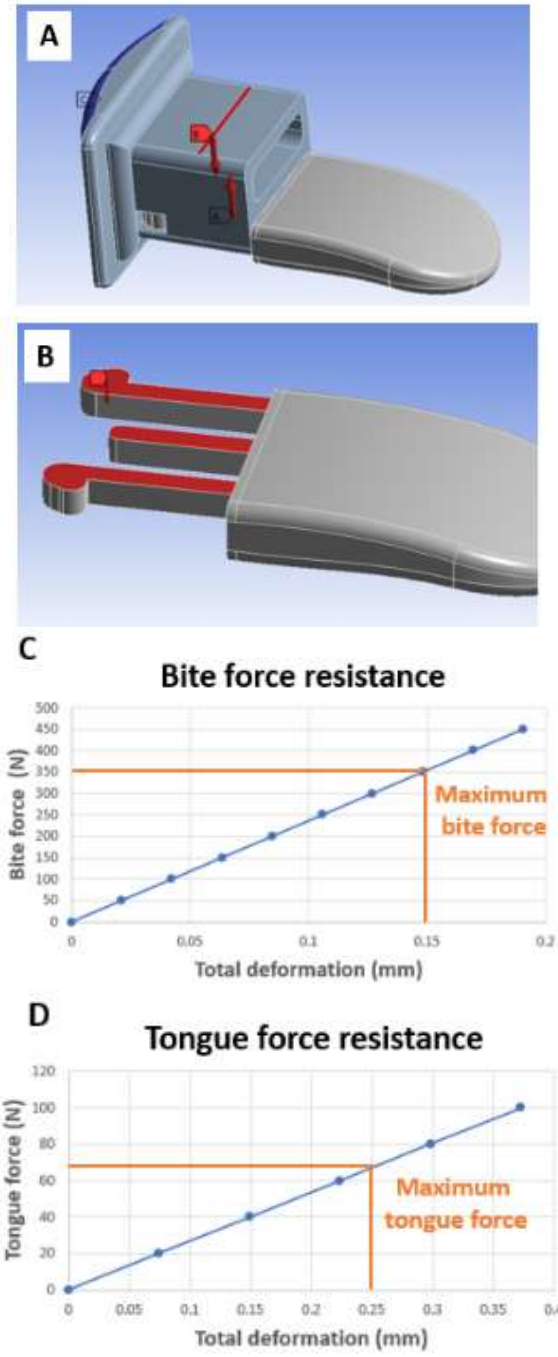

Figure 2 The results from Finite element analysis. (A) boundary of bite force and direction, (B) boundary of reaction force of tongue force and direction, (C) bite force resistance, and (D) tongue force resistance.

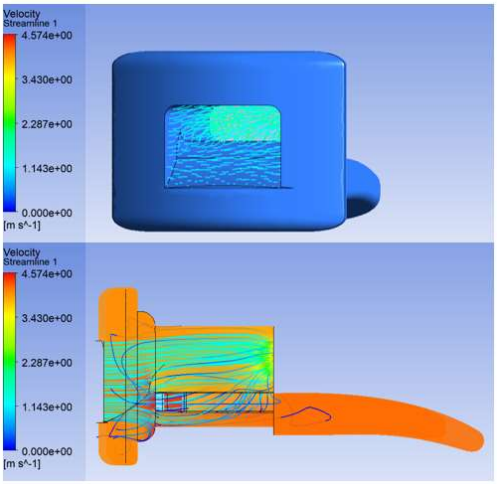

Figure 3 The results of the fluent test from Finite element analysis.

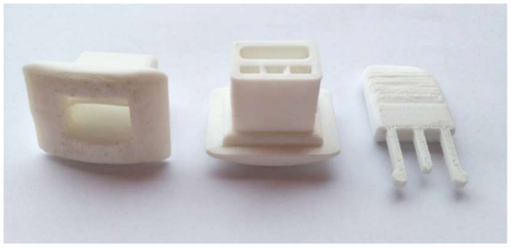

Figure 4 The 3D printed UOS.

The maximum of human bite and tongue forces are 350 N and 65 N, respectively. The results indicated that total deformation on the mouthpiece and tongue displacer from the maximum human bite and tongue forces are lower than 0.3 mm. In practical use, the biting force is in the range of 50-70 N, and the maximum deformation on the mouthpiece is lower than 0.05 mm. This value is minimal. It was thought that there is no deformation on the mouthpiece in practical use. The airflow analysis results show that the air particle can pass through the airway with an average velocity 2.3 m/s. It indicated an easy to breathe when using the UOS.

The 3D-printed UOS prototype will perform practical use of durability tests and comfortable patient tests in future works. For practical use durability test, we plan to simulate the full treatment course (30 fractions 30 min per fraction) that use the UOS during treatment. The length and degree of swelling of UOS will measure every 5 fractions. For a comfortable test, the UOS will be trialed and rated by three radiotherapists. The parameter to rated is the preparation process, suitable size of the mouthpiece and tongue displacer, sharpness, and breathable.

5. CONCLUSION

The universal oral stent was designed and evaluated using Finite element analysis. 3D printing method was used to fabricate the prototype version. The results showed that UOS possessed physical strength due to

less deformation on the model. Moreover, the level of airflow was suitable for the patient's normal breathing. Therefore, it can be concluded that 3D printed UOS can be considered beneficial for use in the treatment.

ACKNOWLEDGEMENTS

We appreciate Asst. Prof. Nuntawat Udee from the Department of Radiological Technology, Faculty of Allied Health Sciences, Naresuan University, provided valuable suggestions.

REFERENCES

1. Eisbruch A, Kim HM, Terrell JE, Marsh LH, Dawson LA, Ship JA. Xerostomia and its predictors following parotid-sparing irradiation of head-and-neck cancer. Int J Radiat Oncol Biol Phys. 2001;50(3):695-704.
2. Jacobi I, Navran A, van der Molen L, Heemsbergen W, Hilgers F, van den Brekel M. Radiation dose to the tongue and velopharynx predicts acoustic-articulatory changes after chemo-IMRT treatment for advanced head and neck cancer. European Archives of Oto-Rhino-Laryngology. 2015;273.
3. Sapir E, Tao Y, Feng F, Samuels S, El Naqa I, Murdoch-Kinch CA, et al. Predictors of Dysgeusia in Patients With Oropharyngeal Cancer Treated With Chemotherapy and Intensity Modulated Radiation Therapy. Int J Radiat Oncol Biol Phys. 2016;96(2):354-61.
4. Allan E, Lu L, Hamedani H, Diavolitsis V, Bhatt A, Grecula J, et al. Dosimetric verification of dental stent efficacy in head and neck radiation therapy using modern radiation therapy techniques: quality of life and treatment compliance implications. Journal of Radiation Oncology. 2016;5(4):351-8.
5. Hong C-S, Oh D, Ju SG, Ahn YC, Na CH, Kwon DY, et al. Development of a semi-customized tongue displacement device using a 3D printer for head and neck IMRT. Radiation Oncology. 2019;14(1):79.

The Breast Microcalcification Detection in Mammogram Image by Using the Deep Convolutional Neural Network

Chatsuda Songsaeng[1], Sitthichok Chaichulee[2]

1 Department of Radiology, Faculty of Medicine, Prince of Songkla University, Hat Yai, Songkhla 90110, Thailand.
2 Institute of Biomedical Engineering, Department of Biomedical Sciences and Biomedical Engineering, Faculty of Medicine, Prince of Songkla University, Hat Yai, Songkhla 90110, Thailand.

Abstract

Introduction: The deep convolutional neural network (DCNN) is one of the methods in artificial intelligence to automatically recognize and classify the images. The method has a potential to help radiologists to detect microcalcifications in mammography assessment.

Purpose: To develop and evaluate the efficiency of the computer model in the detection of microcalcification in mammogram images and compare with the radiologist's assessment.

Methods: This retrospective study included 814 mammogram images of the patients who undertaken screening mammogram between 1 January 2017 to 30 September 2019 at Tanyawej Breast Cancer, Songklanagarind Hospital. The data was collected 214 mammogram images with breast calcification and 600 mammogram images without breast calcification. The following data were collected: age (year), breast side, type of microcalcification, position of calcification and BI-RADS assessment. In this study, the data were divided into 2 sets, the first set was used for training a model and the second set was used for testing the model. We tried out three different model architectures using the same dataset. The training and testing of the models were performed on MATLAB R2019a.

Results: Our best performing DCNN model has a sensitivity of 82.1%, a specificity of 87.5%, a precision of 88.5%, a negative value prediction of 80.8%, an accuracy of 84.6%. The model has the area under the receiver operating characteristic curve (AUC-ROC) of 0.92.

Conclusion: The deep learning model was efficient to predict the groups of microcalcification in mammogram images which resembles to the radiologists' assessments.

Keywords: Microcalcification, Deep Convolutional Neural Network (DCNN), Mammogram images, MATLAB

1. INTRODUCTION

Nowadays artificial intelligence (AI) techniques have been frequently applied in healthcare industry and computer added diagnostics systems have been witnessed with significant impact to mold the traditional procedures into computerized DSS (decision support systems) for diagnosis and prognosis of various diseases such as rectal cancer, lung cancer, breast cancer and so on. Breast cancer accounts for 1.7 million deaths per year worldwide (1) and many people are badly suffering from such type of cancer. Mammography is a non-invasive technique to diagnose the breast cancer. However, it is difficulties to differentiate between malignant and non-malignant microcalcification from the mammography images frequently led to an unnecessary biopsy, which eventually revealed no malignancy (2,3).

Microcalcifications appear as the regions with high intensity compared to the background, and they can vary in size and shapes ranging from circular geometries to strongly irregular ones with sharp or soft contours. They are classified by morphology to be benign and suspicious for malignancy. It is really challenging to differentiate between the malignant and non-malignant from the mammography image because of variations in breast composition such as fat tissue, connective tissue, and glandular tissue. And that could cause radiologist to make error assessment. The suspicious calcifications are further categorized to be amorphous (BI-RADS 4B), coarse heterogeneous (BI-RADS 4B), fine pleomorphic (BI-RADS 4C) and fine linear or fine linear branching (BI-RADS 4C). Sometimes, the radiologist cannot classify the morphology of the calcification, therefore they need the biopsy method to confirm the morphology of calcification. It increases the risk for the patients in biopsy method.

The Convolutional neural network (CNN) is one of the methods in artificial intelligence to automatically recognize and classify the images. Due to the intrinsic limitations of classical methods, with this work, we propose a system based on deep learning (4,5), demonstrating the potentialities of convolutional neural networks (CNN) to electively detect the microcalcifications in mammogram images to support radiologists in mammography assessment.

2. MATERIAL AND METHODS

2.1 Mammography image

This retrospective study included 814 mammogram images of the patients who undertaken screening mammogram between 1 January 2017 to 30 September 2019 at Tanyawej Breast Cancer, Songklanagarind Hospital. The data was collected 214 mammogram images with breast calcification and 600 mammogram images without breast calcification. The following data were collected: age (year), breast side, type of microcalcification, position of calcification and BI-RADS assessment.

2.2 The Deep convolution neural network

In this study we use the deep convolution neural network to build the model for detection and separate the calcification (benign and malignant). The data were divided into 2 sets, using the mammography image (data1) with BIRAD category 1-5 for training the model and using the mammography image (data2) with BIRAD category 1-5 for testing the model. We tried out three different model architectures using the same dataset. The training and testing of the models were performed on MATLAB R2019a. The MATLAB program was used to assess the model for reading the mammography image and classify the calcification.

3. RESULTS

3.1 Confusion Matrix Model

Table1 The confusion matrix model in test1,2 and 3.

Model	True Negative (TN)	True Positive (TP)	False Positive (FP)	False Negative (FN)
1	32.7%	50.0%	0.0%	17.3%
2	40.4%	44.2%	5.8%	9.6%
3	34.6%	50.0%	0.0%	15.4%
total	35.9%	48.1%	1.9%	14.1%

3.2 The ROC curves from the three models

The ROC curves show the efficiency in the detection of calcification in mammogram image of three models. (Figure 1,2,3)

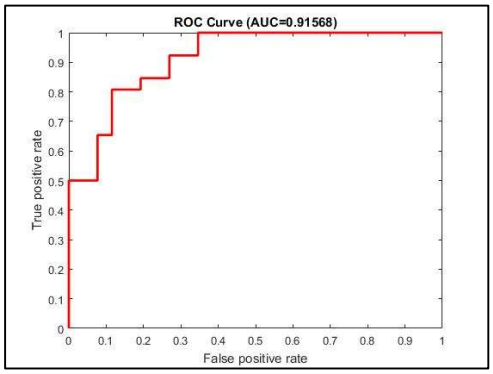

Figure 1 *The graph shows the relationship between true positive rate (Sensitivity) and false positive rate (1–Specificity) of the model1.*

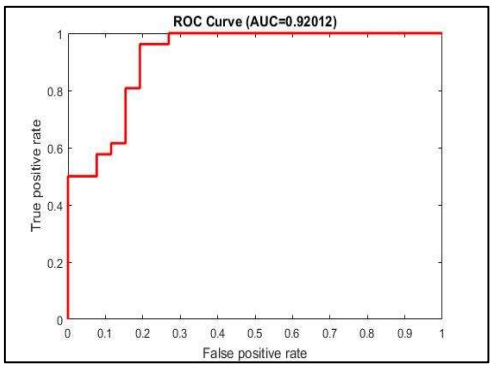

Figure 2 *The graph shows the relationship between true positive rate (Sensitivity) and false positive rate (1–Specificity) of the model2.*

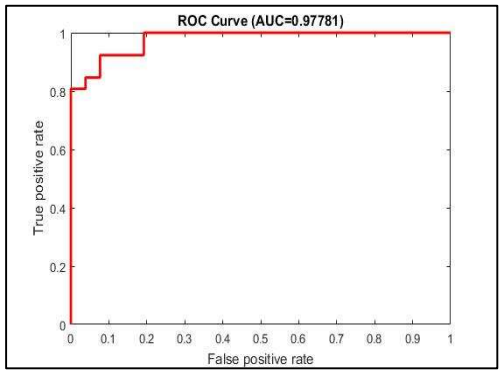

Figure 3 *The graph shows the relationship between true positive rate (Sensitivity) and false positive rate (1–Specificity) of the model3.*

4. DISCUSSION

Table2 *The table shows the efficiency in the detection of calcification in mammogram image of three models.*

Model	Sensitivity	Specificity	Precision	Negative Predictive Value	Accuracy
1	74.3%	100%	100%	65.4%	82.7%
2	82.1%	87.5%	88.5%	80.8%	84.6%
3	76.5%	100%	100%	69.2%	84.6%
total	77.6%	95.8%	96.2%	71.8%	84.0%

From Table2, the total sensitivity of the three models is 77.6%. These results show the sensitivity of diagnostic in false negative. The total specificity, precision, and the accuracy in Table2 are 95.8%, 96.2% and 84% respectively. These results show the high efficiency in the calcification detection in the mammogram image.

The Receiver Operating Characteristic curve (ROC curve) in Figure1,2,3 show the ROC cure in the upper left of the curve because of high sensitivity and the specificity. The AUC of the three models are 0.92, 0.92 and 0.97, respectively. The average AUC of the three model is 0.94, that in the range between 0.9-1.0. This

result shows the high performant in predict diagnostic of calcification detection in mammography image.

Our results are similar to Gabriele Valvano et al who study about Convolutional Neural Networks for the Segmentation of Microcalcification in Mammography Imaging. The accuracy and the false positive rate are 99.99% and 0.005%, respectively. Our results are 84% and 1.9%, respectively.

5. CONCLUSION

The deep learning model was efficient to predict the groups of microcalcification in mammogram images which resembles to the radiologists' assessments.

ACKNOWLEDGEMENTS

The authors wish to thank the staff and colleague at Thanyavej Breast Center and the staff at Department of Diagnostic Radiology, Songklanagarind Hospital, Songkhla, Thailand for help in data collection and analysis.

REFERENCES

1. Dengler J, Behrens S, Desaga JF. Segmentation of microcalcifications in mammograms. IEEE Trans Med Imaging. 1993 Dec;12(4):634–42.
2. Richardson WB. Applying wavelets to mammograms. IEEE Eng Med Biol Mag. 1995 Oct;14(5):551–60.
3. McKinney SM, Sieniek M, Godbole V, Godwin J, Antropova N, Ashrafian H, et al. International evaluation of an AI system for breast cancer screening. Nature. 2020 Jan;577(7788):89–94.
4. Yala A, Lehman C, Schuster T, Portnoi T, Barzilay R. A Deep Learning Mammography-based Model for Improved Breast Cancer Risk Prediction. Radiology. 2019 Jul;292(1):60–6.
5. Kontos D, Conant EF. Can AI Help Make Screening Mammography "Lean"? Radiology. 2019 Oct;293(1):47–8.
6. Abdul M, Ahmed J, Waqas A, Sawand A. Intelligent System for Detection of Micro-Calcification in Breast Cancer. Int J Adv Comput Sci Appl [Internet]. 2017 [cited 2020 Jun 10];8(7).
7. Valvano G, Santini G, Martini N, Ripoli A, Iacconi C, Chiappino D, et al. Convolutional Neural Networks for the Segmentation of Microcalcification in Mammography Imaging. J Healthc Eng. 2019 Apr 9;2019:1–9.
8. Yala A, Schuster T, Miles R, Barzilay R, Lehman C. A Deep Learning Model to Triage Screening Mammograms: A Simulation Study. Radiology. 2019 Oct;293(1):38–46.

Participants

Invited Speaker

Amornwichet Napapat	Thailand
Anupama Azhari hasin	Bangladesh
Arimura Hidetaka	Japan
Bezak Eva	Australia
Carlone Marco	Canada
Chantadisai Maythinee	Thailand
Cheung Kin Yin	Hong Kong
Chougule Arun	India
Chuamsaamarkkee Krisanat	Thailand
Das J Indra	United States of America
Fuangrod Todsaporn	Thailand
Gia Huy Truong	Vietnam
Golam Abu Zakaria	Bangladesh
Hanaoka Kohei	Japan
Haryanto Freddy	Indonesia
Hara Takahiro	Japan
Hensley F.	Germany
Hong Chai Yeong	Malaysia
Jin Xiance	China
Khorprasert Chonlakiet	Thailand
Kirisits Christian	Austrian
Kron Tomas	Australia
Kwan Ng Hoong	Malaysia
Lamey Michael	Canada
Lee James Lei Cheow	Singapore
Loreti Giorgia	Austria
Mahesh Mahadevappa	United States of America
Matsubara Kosuke	Japan
Pongnapang Napapong	Thailand
Prayongrat Anussara	Thailand
Rajapakshe Rasika	Thailand
Rakvongthai Yothin	Thailand
Rehani Madan	United States of America
Sakata Dousatsu	Japan
Sarasanandarajah Sivananthan (Siva)	Australia
Seuntjens Jan	Canada
Shiraishi Junji	Japan
Shiratori Shuichi	Thailand
Somanesan S.	Singapore
Srimahachota Suphot	Thailand
Steil V.	Germany
Sudchai Waraporn	Thailand
Tabakov Slavik	United Kingdom
Tabakova Vassilka	United Kingdom
Takatsu Yasuo	Japan
Tawara Noriyoki	Japan
Theerakul Kanlayanee	Thailand
Trinavarat Panruethai	Thailand
Uber Pichet	Thailand
Wong Hsiu Jeanie Ding	Malaysia
Wu Keng-Yi	China (Taiwan)
Zain Azleen Mohd	Malaysia

Committee

Apipunyasopon Lukkana	Thailand
Chaiwatanarat Tawatchai	Thailand
Chakrapong Apawadee	Thailand
Chatachot Kotchakorn	Thailand
Chatchumnan Nichakan	Thailand

Chirdchid Thamonwan	Thailand
Choki Sonam	Thailand
Fukuda Shigekazu	Japan
Funsian Amporn	Thailand
Hayashi Naoki	Japan
Hematulin Arunee	Thailand
Innan Yuparak	Thailand
Intaprom Rudjaya	Thailand
Intarak Sararas	Thailand
Jantawong Hataipat	Thailand
Kakanaporn Chumpot	Thailand
Kanematsu Nobuyuki	Japan
Khamwan Kitiwat	Thailand
Krisanachinda Anchali	Thailand
Lee Shen-Hao	China (Taiwan)
Mahasub Sutasinee	Thailand
Netprasert Sa-angtip	Thailand
Nobnop Wannapha	Thailand
Noipinit Nut	Thailand
Oonsiri Sornjarod	Thailand
Panyura Pongpitch	Thailand
Pasawang Panya	Thailand
Phimolasawakun Laksamon	Thailand
Phromphao Benchamat	Thailand
Poolnapol Vanida	Thailand
Ruenjit Sakultala	Thailand
Sanghangthum Taweap	Thailand
Sanoesan Viyada	Thailand
Shunhavanich Picha	Thailand
Sontrapornpol Tanawat	Thailand
Stansook Nauljun	Thailand
Sukwijit Kanjana	Thailand
Suriyapee Sivalee	Thailand
Tangboonduangjit Puangpen	Thailand
Tannanonta Chirapha	Thailand
Thasasi Phatthraporn	Thailand
Tiajaroen Tanapat	Thailand
Tippayamontri Thititip	Thailand
Wongnil Jaroonroj	Thailand
Wongpisarn Sasawan	Thailand
Yoykaew Saowapark	Thailand

Participant

A. Latiff Rukiah	Malaysia
Abdul Hadi Muhammad Fahmi Rizal	Malaysia
Adhikari Tirthraj	Nepal
Afif Nur Faadhilah	Indonesia
Ahmad Sabri Anis Suhana Binti	Malaysia
Alam Dian Yuliani	Indonesia
Alonzo Robert Dave	Philippines
Aphiwatthanasumet Kingkarn	Thailand
Arphasetthasakul Nussara	Thailand
Arphasetthasakul Wisan	Thailand
Binti Talik Sisin Noor Nabilah	Malaysia
Boonserm Petarpa	Thailand
Boontad Rattiya	Thailand
Bozhikov Stanislav	Bulgaria
Buakaew Nataporn	Thailand
Burgonio Mark Anthony	Philippines
Chaisuttee Rusdchai	Thailand
Chanayota Julaluck	Thailand
Changtoongyai Chaiya	Thailand
Chanpanya Thananya	Thailand

Chatchaipaiboon Nongnuch	Thailand
Chawana Nuengruthai	Thailand
Chawengsaksopak Kornkanok	Thailand
Cheewakul Jongwat	Thailand
Chitnok Manatchanok	Thailand
Cho Byungchul	South Korea
Chongsan Thanaphat	Thailand
Chotmit Yupawadee	Thailand
Chumsuwan Nipha	Thailand
Chung Hyun-Tai	South Korea
Chunpenmongkol Sranut	Thailand
Dachaworakul Kittipol	Thailand
Damrongkijudom Nuanpen	Thailand
Dardaranonda Paya	Thailand
Deeharing Aphisara	Thailand
Dhungana Surendra	Thailand
Duangsuphan Phothong	Thailand
Ezura Takatomo	Japan
Furuo Koki	Japan
Fuse Hiraku	Japan
Gani Ernawatil	Indonesia
Gemanam Sylvester	Malaysia
Gonzales John Maru Gabriel	Philippines
Haekal Mohammad	Indonesia
Hairunpijit Surapa	Thailand
Hayakawa Yuki	Japan
Hirai Nanako	Japan
Hirai Ryuta	Japan
Hirano Shunta	Japan
Hiranrat Pantajaree	Thailand
Hirotaki Kouta	Japan
Ho Chung	China (Taiwan)
Hongkham Nattapong	Thailand
Hori Kensuke	Japan
Ichihara Masaya	Japan
Inphavong Viphaphone	Laos
Ishida Tomoya	Japan
Isobe Akira	Japan
Jaikuna Tanwiwat	Thailand
Jaiphian Jeeraporn	Thailand
Jamal Noriah	Malaysia
Jamalludin Zulaikha	Malaysia
Junhong Jittima	Thailand
Junios Junios	Indonesia
Junrach Pimpida	Thailand
Kadman Boriphat	Thailand
Kaewbunperm Urairat	Thailand
Kamezawa Hidemi	Japan
Kamiguchi Nagaaki	Japan
Kanai Takayuki	Japan
Kanchanawaleekun Chanidapa	Thailand
Kanyakham Kannikar	Thailand
Karinchai Piraya	Thailand
Kawamura Shinji	Japan
Kawvised Supannika	Thailand
Keawsamur Mintra	Thailand
Khadsiri Patchareewan	Thailand
Khaijaitrong Sirintha	Thailand
Khamchompoo Darat	Thailand
Khayaiwong Paowarin	Thailand
Khuenchana Somsak	Thailand
Khwaiphan Kanokpich	Thailand
Kingkaew Sakda	Thailand
Kittipayak Samrit	Thailand

Kladsomboon Sumana	Thailand
Konno Hiroaki	Japan
Koyama Kohei	Japan
Kraitong Natchaya	Thailand
Kuekkong Kanokkarn	Thailand
Kumkhwao Jumnong	Thailand
Kummanee Patiparn	Thailand
Lalrinmawia Jonathan	India
Lee Chia-jung	China (Taiwan)
Lekkong Issara	Thailand
Lestari Fauzia Puspa	Indonesia
Li Ting Chuan	China (Taiwan)
Lian Cheryl	Singapore
Lipikorn Rajalida	Thailand
Lowong Thanatchaya	Thailand
Maknitikul Sitanan	Thailand
Manpuen Supamas	Thailand
Masanga Wilai	Thailand
Mayomthong Prajaree	Thailand
McLean Donald	Australia
Md Ariffin Nurmazaina	Malaysia
Md Radzi Yasmin	Malaysia
Michi Okoshi	Japan
Mitsui Yuki	Japan
Miura Natsuki	Japan
Miyazaki Kengo	Japan
Mizuno Hideyuki	Japan
Mohamed Aminah	Malaysia
Mouri Shiina	Japan
Muangkhamporn Kanokporn	Thailand
Mundee Thunphisit	Thailand
Murashima Kouichi	Japan
Murata Kazumi	Japan
Myojoyama Atsushi	Japan
Nagami Noriyuki	Japan
Nair Sarath	India
Nakaji Taku	Japan
Nakanishi Kouhei	Japan
Narawong Taratip	Thailand
Ng Aik Hao	Malaysia
Ngoenthuan Woraya	Thailand
Nguyen Lam	Vietnam
Nimjaroen Kampheang	Thailand
Noda Shigetoshi	Japan
Nualsutha Panicha	Thailand
Numpinit Piya	Thailand
Nuntue Chatnapa	Thailand
Ogata Ryosei	Japan
Ogawa Koichi	Japan
Ogawa Shuta	Japan
Oguchi Hiroshi	Japan
Ohta Tomohiro	Japan
Ohtani Hiroki	Japan
Pairodsantikul Phornpailin	Thailand
Pamarapa Chayanon	Thailand
Panyala Papitchaya	Thailand
Passawee Peach	Thailand
Phatarachaiworapat Aunchalee	Thailand
Phongphiriyadecha Khanit	Thailand
Phongprapun Wisawa	Thailand
Piahyan Aiyara	Thailand
Pihusut Chonlathorn	Thailand
Pischom Narueporn	Thailand
Plangpleng Nattha	Thailand

Pojanapreecha Pavarit	Thailand
Popreeda Tippawan	Thailand
Prajamchuea Kornkamol	Thailand
Prasartvit Kanogpan	Thailand
Prasert Prathana	Thailand
Pratama Sra H.	Indonesia
Prommetta Promporn	Thailand
Promwan Siriporn	Thailand
Pyone Yin Yin	Myanmar
Rachi Toshiya	Japan
Ramanathan Vijitha	Sri Lanka
Rattanaareeyakorn Warinthorn	Thailand
Rattanamongkonkul Pattaravarin	Thailand
Rattanarungruangchai Natch	Thailand
Ravindran Paul	India
Remigio Adrian	Philippines
Ritlumlert Napat	Thailand
Ruangchan Sirinya	Thailand
Rueansri Jumneanphan	Thailand
Rugpong Panupat	Thailand
Rungpin Nittima	Thailand
Saenbandit Prapapan	Thailand
Saenchon Phattanapong	Thailand
Saenkla Warocha	Thailand
Sah Suraj	Nepal
Saito Hidetoshi	Japan
Saito Yuichi	Japan
Saiyo Nipon	Thailand
Sakulsingharoj Siwaporn	Thailand
Salvador Eleanor	Philippines
Sangounsub Ravipim	Thailand
Sanklaa Khemipa	Thailand
Satharasinghe Duminda	Sri Lanka
Sato Keito	Japan
Sayed Inayatullah Shah	Malaysia
Septiawan Reza Rendian	Indonesia
Singlaem Sittaporn	Thailand
Singusaha Orathai	Thailand
Sintuprom Rosarin	Thailand
Siripongsakun Surachate	Thailand
Sirisopausa Pikom	Thailand
Sisai Siriwan	Thailand
Songprakhon Rangsee	Thailand
Songseang Chatsuda	Thailand
Sriklay Sawinee	Thailand
Srisittimongkon Songpon	Thailand
Sritubtim Panun	Thailand
Sudloy Nuntawuth	Thailand
Sueangamiam Kamonrat	Thailand
Sugai Yuto	Japan
Sukantamala Singhadeth	Thailand
Suksawang Penpisuth	Thailand
Sumanaphan Wanwanat	Thailand
Suntiwong Sawanee	Thailand
Suphaphong Sithiphong	Thailand
Suwandi Galih Restu Fardian	Indonesia
Suwannarat Achawee	Thailand
Suwanraksa Chitchaya	Thailand
Suzuki Kentaro	Japan
Syajaah Khoerun Nisa	Indonesia
Takeda Masakatsu	Japan
Takemura Akihiro	Japan
Tamura Mikoto	Japan
Tanabe Shumpei	Japan

Tanaka Yuki	Japan
Tangruangkiat Sutthirak	Thailand
Tasomkan Sasithorn	Thailand
Tawara Noriyuki	Japan
Tawonwong Tanawat	Thailand
Thana Rasalin	Thailand
Thanakijsombat Natcha	Thailand
Thirapong sukanya	Thailand
Thongsawad Sangutid	Thailand
Thongthanom Siwika	Thailand
Tinlapat Jongchai	Thailand
Tippanya Damrongsak	Thailand
Tomihara Jun	China (Peoples Rep.)
Tongngarm Wimonmart	Thailand
Trinate Rachawadee	Thailand
Tsujioka Katsumi	Japan
Tsurusawa Kota	Japan
Uadrang Surin	Thailand
Urago Yuka	Japan
Urakami Akimasa	Japan
Usui Keisuke	Japan
Utapom Kitsana	Thailand
Utitsarn Kananan	Thailand
Vannavijit Chulee	Thailand
Vimolnoch Mananchaya	Thailand
Wahabi Janatul Madinah	Malaysia
Wakisaka Yushi	Japan
Wanotayan Rujira	Thailand
Wisetrintong Metinee	Thailand
Wittayapasitti Warissara	Thailand
Wong Jeannie	Malaysia
Wong Siriporn	Thailand
Wong Yin How	Malaysia
Wongsa Paramest	Thailand
Wongsaroj Piyakan	Thailand
Yani Sitti	Indonesia
Yasue Kenji	Japan
Yawichai Kannika	Thailand
Yeenang Nuttawut	Thailand
Yoshida Masato	Japan
Yoshimoto Manabu	Japan

Commercial Exhibitor

Diebold Johannes	Germany
Jirawatwanith Titiya	Thailand
Jomkaew Tanut	Thailand
khaosomboon kritsada	Thailand
Lertkittiamornkul Seksan	Thailand
Onnomdee Chanakarn	Thailand
Pleanngamwong Thanyaporn	Thailand
Punjapratheep Warangkana	Thailand
Sakthumjaroen Puncharat	Thailand
Sangchang Wasana	Thailand
Sangsrijan Anchasa	Thailand
Singh manmohan	Singapore
Thakasem Nongpanga	Thailand
Thuechart Thiranan	Thailand

Author Index

Afif N.F. 254
Akhtaruzzaman M. 117
Alam D.Y. 173, 475
Arimura H. 58, 72
Ashaari A.E. 260
Aye K.T.N. 106
Aye Thidar Moe Moe 262
Azhari H.A. 50
Azlan C.A. 197
Bezak E. 43, 44
Burgonio M.A.C. 249
Carlone M. 64
Chanpanya T. 132, 463
Chantadisai M. 56
Chatachot K. 214, 416
Chatchumnan N. 87, 428
Cheewakul J. 168, 514
Cheung K.Y. 40, 45, 66
Choki S. 92, 498
Chougule A. 61, 67
Chuamsaamarkkee K. 57
Chumsuwan N. 107
Dardaranonda P. 269
Das I.J. 60
Deeharing A. 140, 506
Dell'Oro M. 43
Dhungana S. 90, 471
Doi K. 236, 392
Ezura T. 238, 420
Fahmi M.R. 212
Furuo K. 226
Fuse H. 232
Gani A.M. 257
Gemanam S.J. 108
Gia Huy T. 180
Haekal M. 182
Hanaoka K. 48
Hayakawa Y. 263, 332
Hirai R. 227, 299
Hiranrat P. 163, 274
Hirotaki K. 237, 396
Hirunpijit S. 196, 320
Ho C.H. 231
Hori K. 245, 311
Huang Y. 123
Hull A. 171
Ichihara M. 103, 399
Innan Y. 185, 406
Inphavong V. 113
Intarak S. 177
Ishida T. 118
Isobe A. 152, 356
Jaikuna T. 115
Jamalludin Z. 220
Jamil A. 109, 110
Jantawong H. 167
Joan M. 147, 156, 344, 346
Junios J. 153
Kamiguchi N. 138
Kawamura S. 222
Keawsamur M. 137
Khwaiphan K. 201, 402
Kingkaew S. 150
Kittiva N. 136
Kombo E.W. 194, 479
Konno H. 267, 373
Koyama K. 244, 457
Krisanachinda A. 76, 77
Kron T. 71
Kummanee P. 121, 525
Lamey M. 65
Latiff R.A. 213
Leong S.S. 169
Li C. 141
Liu H. 122
Loreti G. 49
Madin F. 266
Mahamud S. 151
Matsubara K. 46, 53
Mayomthong P. 206, 328
Miura N. 209, 460
Miyazaki K. 223
Mizuno H. 218
Mohammad Shazmi bin Sapeei 336
Mouri S. 124
Mundee T. 157, 532
Murashima K. 228, 467
Murata K. 242, 410
Myojoyama A. 234, 483
Nagami N. 259
Nakaji T. 235
Nakanishi K. 204, 251
Ng A.H. 160
Nuntue C. 253
Nur Aina Najwa Mohamad Feriza 248
Nur Diyana Afrina Hizam 129
Nur Emirah Zain 116
Nur Farah Huda Zulkafli 187, 375
Nur Farrah Ezlyn Mohammad Rusdi 172
Ogata R. 148
Ogawa S. 99, 360
Ohtani H. 261
Okoshi M. 268, 366
Oonsiri S. 84
Pamarapa C. 178
Phongprapun W. 91
Phromphao B. 211, 388
Pihusut C. 145
Pishyapan A. 154, 521
Plangpleng N. 207, 380
Pojanapreecha P. 130, 432
Pongnapang N. 55
Poolnapol V. 86
Poosiri S. 186, 528
Popreeda T. 158, 510
Poudel S. 100
Prajamchuea K. 190, 285
Prasartvit K. 155
Pratama S.H. 241, 257
Pyone Y.Y. 119
Rachi T. 412
Radzi Y.M. 128
Rahman M. 198
Rakvongthai Y. 63, 83

Ramanathan V. 255, 353
Rattanaareeyakorn T. 446
Rattanaareeyakorn W. 88
Rattanamongkonkul P. 208, 518
Rehani M.M. 68, 69, 73
Reid P. 44
Remigio A. 293
Remigio A.S. 258
Roskhahar N.N. 128
Ruangchan S. 135
Rungpin N. 272
Saito Y. 233, 444
Sakata D. 41
Sarasanandarajah S. 62
Satharasinghe D.M. 193
Satharasinghe DM. 307
Sato K. 250, 450
Septiawan R.R. 183
Shazmi M.R. 102
Shiratori S. 81, 82
Shunhavanich P. 70
Sirisopausa P. 265, 440
Siti Hajar Abdul Rahman 217
Somanesan S. 78, 79
Songsaeng C. 179, 536
Srimahachota S. 52, 74
Srisittimongkon S. 165, 340
Sritubtim P. 114, 453
Sudchai W. 74
Sugai Y. 126
Sukprakun C. 203
Suksawang P. 93, 502
Sumanaphan W. 94, 363
Suwanbut P. 97
Suwandi G.R.F. 199
Suzuki K. 133, 143
Syaja'ah K.N. 243, 324
Tabakov S. 39
Tabakova V. 59
Takatsu Y. 47
Takeda M. 221
Talik Sisin N.N. 111
Tanabe S. 125
Tanaka Y. 230
Tangruangkiat S. 175, 369
Tawara N. 75
Tawonwong T. 146
Tecson M.R.Z. 271, 279
Thana R. 191
Thanakijsombat N. 164, 289
Theerakul K. 76
Thiangsook W. 270
Tomihara J. 142, 349
Trinavarat P. 54
Tsujioka K. 246, 252
Tsurusawa K. 188, 436
Urago Y. 225
Urakami A. 170
Usui K. 181, 315
Vannavijit C. 131
Vimlnoch M. 89
Wahabi J.M. 95, 239
Wakisaka Y. 224
Wittayapasitti W. 202, 490
Wong J.H.D. 197
Wong Y.H. 215, 260
Wongnil J. 176, 486
Wongpisarn S. 166, 384
Wongsaroj P. 159, 494
Wu K.Y. 192
Yabsantia S. 98
Yani S. 104
Yasue K. 229, 424
Yeong C.H. 80
Yi Y.S. 219
Yoshida M. 247, 303
Yoshimoto M. 256, 297
Zakaria G.A. 51
Zuber S.H. 101, 161

Commercial Exhibition Floor Plan

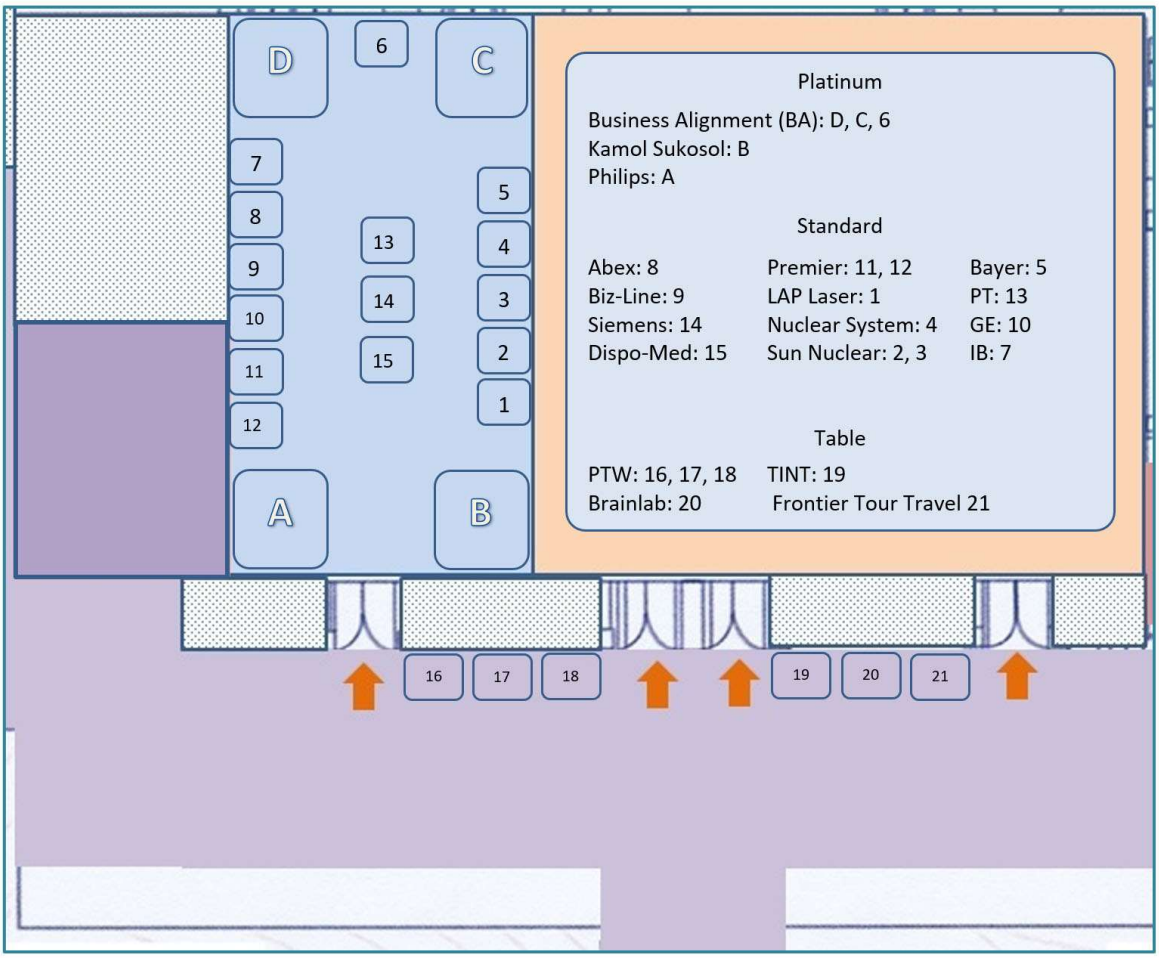

Sponsors

Platinum

Standard

Table

Frontier Tour Travel